GARY S. WAS

Fundamentals of Radiation Materials Science

Metals and Alloys

Second Edition

Springer

Fundamentals of Radiation Materials Science

Gary S. Was

Fundamentals of Radiation Materials Science

Metals and Alloys

Second Edition

Springer

Gary S. Was
Department of Nuclear Engineering
and Radiological Sciences
University of Michigan
Ann Arbor, MI
USA

ISBN 978-1-4939-3436-2 ISBN 978-1-4939-3438-6 (eBook)
DOI 10.1007/978-1-4939-3438-6

Library of Congress Control Number: 2015955871

Printed on acid-free paper

This Springer imprint is published by SpringerNature
The registered company is Springer-Verlag GmbH Berlin Heidelberg

This book is dedicated to my wife, LeeAnn, and to my sons Adam and Alex for their support and encouragement.

Preface

The purpose of this text is to provide a foundation for understanding the theory and mechanisms behind the effects of irradiation on metals and alloys. The subject is divided into three parts, each of which is subdivided into individual chapters that together provide a unified picture of how radiation interacts with and alters the structure and properties of metallic materials. Part I consists of five chapters that together, focus on the *radiation damage process* and provide the formalism for the prediction of the amount and spatial configuration of the damage produced by bombarding particles. Chapter 1 treats the interactions between particles that result in the transfer of energy from the incident particle to the target atoms. Chapter 2 focuses on determination of the number of displacements produced by the bombarding particles, and Chap. 3 describes the spatial configurations of the resulting defects. Chapter 4 provides background on the equilibrium concentration of point defects and their diffusion. Chapter 5 treats diffusion and reactions between point defects under irradiation that are fundamental to all of the observable effects.

While radiation damage describes the state of the irradiated material, radiation effects are concerned with defect behaviour in the solid after formation. Part II (Chaps. 6–11) covers the *physical effects* of irradiation on metals. Chapter 6 describes radiation-induced segregation, which is a direct consequence of radiation-enhanced diffusion. Chapters 7 and 8 address the nucleation and growth of dislocation loops and voids, the defect aggregates that determine much of the behavior of irradiated alloys. Chapter 9 covers the stability of phases under irradiation and irradiation-induced precipitation and precipitate dissolution. Chapter 10 extends the effects of irradiation to the unique processes resulting from ion irradiation such as composition changes, sputtering, and exfoliation. Finally, Chap. 11 describes the use of ion irradiation to emulate the effects of neutron irradiation in reactor components.

Mechanical and environmental effects of radiation damage (Part III) are distinguished from physical effects by the application of stress and a corrosive environment. Hardening and deformation of alloys under irradiation are discussed in

Chap. 12. Creep deformation and growth are treated in Chap. 13, and the effect of irradiation on crack nucleation and propagation resulting either from static or fatigue loading is discussed in Chap. 14. Irradiation also has a profound effect on corrosion and stress corrosion cracking as these degradation modes often constitute the limiting processes for many reactor designs. Chapter 15 includes the basics of corrosion and stress corrosion cracking that are required for understanding the combined effects of irradiation, corrosion, and stress discussed in Chap. 16.

The chapters contain examples and illustrations of radiation effects and sample calculations to quantify and describe the observations. Problems at the end of each chapter are designed to reinforce the main concepts of each chapter and to challenge the reader on his or her comprehension of the topics covered within. Taken together, the chapter text, examples, illustrations, and end-of-chapter problems provide a comprehensive treatment of the effects of irradiation on metals and alloys.

The subject matter in this text will likely require two academic terms to complete. Many of the topics rely on a basic knowledge of disciplines that constitute the underlying basis for irradiation effects: thermodynamics and kinetics of solids, crystal structure, defects and dislocations, physical metallurgy, elasticity and plasticity, deformation and fracture and corrosion and stress corrosion cracking. The text either presents the requisite background for each of these topics, or provides references of other sources where good treatments can be found.

This book should also be useful to researchers who would like to learn more about the subject, or who would like a more complete and integrated treatment of the topics than can be found in individual papers on the subject. While the chapters are integrated with one another and each chapter builds upon the sum of the previous chapters, it is possible to read selected chapters for just that topic.

As a final comment, the author would like to note that this book was written by sorting, organizing, and condensing information from several texts and numerous journal and conference papers to arrive at a comprehensive description of the processes constituting radiation materials science. A conscientious effort was made to acknowledge and give credit to the original sources of the ideas, theories, mathematical developments, and drawings contained herein. For occasional oversights that may have occurred during the condensation process, the author offers his apologies. He is indebted to the many authors and publishers who provided material and illustrations for this text.

Finally, the author wishes to acknowledge the many colleagues, students, and friends who aided and advised him in this work. In particular, special thanks go to Jeremy Busby, Todd Allen, Michael Atzmon, Roger Stoller, Yuri Osetsky, Ian Robertson, and Brian Wirth, for their substantive contributions to the content, to Elaine West, Brian Wagner, Sean Lemecha, Gerrit Vancoevering, and Bryan Eyers for their work on the illustrations, to Gerrit Vancoevering for completing and compiling the end of chapter problem solutions, to Cherilyn Davis and Ovidiu

Toader for their help in manuscript and movie preparation, to Lynn Rehn, Don Olander, Arthur Motta, Michael Nastasi, Steve Zinkle, K. Linga Murty, Lou Mansur, and Peter Andresen for their chapter reviews, and to John King and Arden Bement for providing the inspiration to the author to pursue this field of study many years ago.

Ann Arbor Gary S. Was
August 2015

Contents

Movies accompanying the text are located at: http://rmsbook2ed.engin.umich.edu/movies/

Part III Mechanical and Environmental Effects of Radiation Damage

Values of Physical Constants

Name	Symbol	Value
Atomic mass unit	u	1.6605×10^{-27} kg
Avagadro's number	N_0	6.0221×10^{23}/g mole
Barn	–	10^{-24} cm^2
Bohr radius	a_0	5.2918×10^{-11} m
Bohr magnetron	μ_B	9.2730×10^{-24} J m^2/weber
Boltzmann's constant	k	1.3807×10^{-23} J/K
		8.6173×10^{-5} eV/K
Classical electron radius	r_0	2.8179×10^{-15} m
Rydberg energy	E_R	13.606 eV
Electric constant	ε_0	8.8542×10^{-12} F/m
Elementary charge	ε	1.6022×10^{-19} C
		4.8029×10^{-10} esu
	ε^2	1.44 eV nm (CGS system)
Electron Compton wavelength	λ_e	2.4263×10^{-12} m
Electron density/mass ratio	ε/m_e	1.7588×10^{11} C/kg
Faraday constant	F	96485.3415 C/mole
Gravitational constant	G	6.6743×10^{-11} Nm/kg^2
Ionization energy of hydrogen atom	I_0	13.6057 eV
Magnetic constant	μ_0	1.2566×10^{-6} NA^{-2}
Planck's constant	h	6.6261×10^{-34} J s
		4.1357×10^{-15} eV s
Quantum/charge ratio	h/ε	4.1357×10^{-15} J s/C
Rest mass		
Electron	m_e	9.1094×10^{-31} kg
		5.4860×10^{-4} amu
Neutron	m_n	1.6749×10^{-27} kg
		1.0089 amu

(continued)

(continued)

Name	Symbol	Value
Proton	m_p	1.6726×10^{-27} kg
		1.0073 amu
Rydberg constant	R_∞	1.0974×10^{7} m^{-1}
Speed of light	c	2.9979×10^{8} m/s
Standard volume of ideal gas	–	22.4140 l/g mole
Stefan–Boltzmann constant	σ	5.6704×10^{-8} w/m^2 K^4
Universal gas constant	R	8.3145 J/g mole K
		1.9855 cal/g mole K

Introduction

Radiation materials science describes the interaction of radiation with matter—a broad subject covering many forms of irradiation and of matter. Some of the most profound effects of irradiation on materials occur in the core of nuclear power reactors where atoms comprising the structural components are displaced numerous times over the course of their engineering lifetimes. The consequences of radiation to core components include changes in shape and volume by tens of percent, increases in hardness by factors of five or more, severe reduction in ductility and increased embrittlement, and susceptibility to environmentally induced cracking. For these structures to fulfill their purpose, a firm understanding of the effect of radiation on materials is required in order to account for its effect in design, to mitigate its effect by changing operating conditions, or to serve as a guide for creating new, more radiation-tolerant materials that can better achieve their purpose.

The attractiveness of nuclear power as a present-day and future energy source is due to the vast improvements that have been made in the way reactors are operated and in our understanding of how these engineering systems degrade and fail. But the attractiveness of nuclear power is also driven by new concepts for advanced reactors that offer improvements in safety and reliability, radioactive waste production, energy efficiency, and cost-effectiveness. Nuclear power holds the promise for producing hydrogen in a clean and low-cost process that would power a future hydrogen economy. Yet all of these improvements come at a cost. That cost is a greater demand on the materials used to build and operate these reactors. New concepts that promise better performance from this energy source also include more aggressive environments, higher temperatures, and greater levels of irradiation. In his article in *Nature*, Butler [1] summarizes the challenges facing several promising advanced reactor concepts. In all of these concepts, material behavior is the *leading* challenge in bridging the gap from concept to reality. The pivotal role of material behavior in the unique radiation environment created in a reactor core makes radiation materials science a subject of paramount importance in the future of nuclear energy in the world. It is with this perspective that the objective of this text was formulated, that is, to provide a sound, fundamental understanding of radiation effects in structural materials.

Structural materials in reactor systems are predominantly crystalline, metallic alloys. Virtually, all of the structural materials in reactors are metallic, and many of the materials proposed for the more aggressive conditions in advanced reactor concepts are metals as well. The types of radiation that can alter structural materials consist of neutrons, ions, electrons, and gamma rays. All of these forms of radiation have the capability to displace atoms from their lattice sites, which is the fundamental process that drives the changes in structural metals described earlier. The inclusion of ions among the irradiating particles provides a coupling to other fields and disciplines such as the use of accelerators for the transmutation of nuclear waste, or in the creation of new materials by ion implantation, ion beam mixing, plasma-assisted ion implantation, and ion beam–assisted deposition. All of the concepts developed in this text for the interactions of ions with solids are applicable to these fields as well.

The effect of irradiation on materials is rooted in the initial event in which an energetic projectile strikes a target. While the *event* is made up of several steps or processes, the primary result is the displacement of an atom from its lattice site. This book will address primarily crystalline solids in which the atom locations are defined by the crystalline structure. Irradiation displaces an atom from its site, leaving a vacant site behind (a *vacancy*), and the displaced atom eventually comes to rest in the interstices between lattice sites, becoming an *interstitial* atom. The vacancy–interstitial pair is central to radiation effects in crystalline solids and is known as a *Frenkel pair* (FP). The presence of the FP and other consequences of irradiation damage determine the physical effects and, with the application of stress and the environment, the mechanical and environmental effects of irradiation.

The radiation damage event, detailed in Chap. 1, is concluded when the displaced atom (also known as the *primary knock-on atom*, PKA) comes to rest in the lattice as an interstitial. This event consumes about 10^{-11} s. Subsequent events are classified as physical effects of irradiation. These effects include such phenomena as swelling, growth, phase change, and segregation. For example, it is possible to take a block of pure nickel, 1 cm on a side, irradiate it in a reactor (to a fluence of say, 10^{22} n/cm^2), and measure it to be 1.06 cm on a side, representing a volume change of 20 %! The volume change, or swelling, is isotropic and is due to the formation of voids in the solid (see, e.g., Fig. 8.1).

Another example is irradiation growth. Irradiation of a cylindrical rod of uranium, 10 cm in length and 1 cm in diameter (7.85 cm^3) to a fluence of $\sim 10^{20}$ n/cm^2, will cause it to grow to 30 cm in length and shrink to 0.58 cm in diameter. The volume is unchanged (7.85 cm^3), but the shape is highly distorted. Distortion at constant volume under irradiation is referred to as growth.

Phase changes under irradiation are also common. A Ni–12.8at%Al, solid solution alloy irradiated with 5 MeV Ni^+ ions to 10^{16} cm^{-2} will result in the formation of a Ni_3Al phase, which is separate and distinct from the parent phase (see, e.g., Fig. 9.3). The formation of a new phase is known as irradiation-induced phase formation and is of great significance in both ion and neutron irradiation.

A last example of physical changes of irradiation is segregation. If a Ni–1at%Si alloy is bombarded with Ni^+ ions at 525 °C, and to a dose of one displacement per

atom, the result is an enrichment of Si on the surface and at grain boundaries to values that are 20–60 times the amount in the bulk (see, e.g., Fig. 6.5). This redistribution of alloying elements to specific sites in the microstructure is known as radiation-induced segregation and occurs in many alloys to a significant extent when irradiated at high temperatures.

Irradiation-induced physical changes can indeed be dramatic. But how do they alter the structural integrity of components? This is the realm of mechanical effects of irradiation. Mechanical effects manifest themselves only under the application of a stress. The result is that alloys behave much differently than their unirradiated counterparts. For example, the impact energy of an irradiated steel can be drastically reduced. For unirradiated steels, the energy absorbed is a strong function of temperature, where at low temperatures, little energy is absorbed and the steel becomes very brittle, but with increasing temperature, the energy absorbing capacity of the steel increases dramatically. Irradiation of a steel with neutrons can cause a marked reduction in the strain and a several-fold increase in the strength of the steel. The result is an increase in strength by a factor of five and a decrease in ductility by over a factor of ten. Irradiation can also influence the way in which materials deform at high temperature. Under a constant load, there is almost a complete loss of creep strength due to severe embrittlement arising from irradiation.

Finally, irradiation to a neutron fluence of $>5 \times 10^{20}$ n/cm^2 ($E > 1$ MeV) results in accelerated corrosion and intergranular cracking of iron- and nickel-based austenitic alloys in light water reactors. This stress corrosion cracking phenomenon is very pervasive in that it affects most all austenitic alloys in all types of water reactors. Clearly, any of these effects will have profound consequences on reactor component integrity. Understanding how they work is the key to designing around their detrimental effects or to developing new alloys that are more radiation tolerant. As it turns out, almost all of these effects have a common link: defects such as isolated vacancies and interstitials, clusters of vacancies and interstitials, dislocation loops and lines, and voids and bubbles. The reader should keep these defect types in mind as they progress from the radiation damage event through the physical effects to the mechanical and environmental effects.

We will address the radiation damage event first as this is the basis for understanding all effects of irradiation. We will start by quantifying the extent of radiation damage and develop a physical description of the interaction process. In quantifying the displacement process, what we are seeking is a quantitative description of the number of vacancies and interstitials produced by an incoming projectile. Unless we can do this, we have no hope of understanding the extent of the damage. The importance of determining the effect of irradiation in terms of the production of defects is discussed in Chaps. 2 and 3 and is shown here with a simple illustration.

The number of displacements created by a neutron flux is a complicated function of the energy dependence of that flux. Note in the top graph in Fig. 1 that the dependence of the yield strength of a 316 stainless steel alloy on the neutron fluence is highly dependent on the particular neutron flux spectrum [2]. OWR is a test reactor with a typical LWR neutron spectrum, RTNS-II produced a pure 14 MeV source of neutrons, and LASREF had a broad spectrum of high neutron energies.

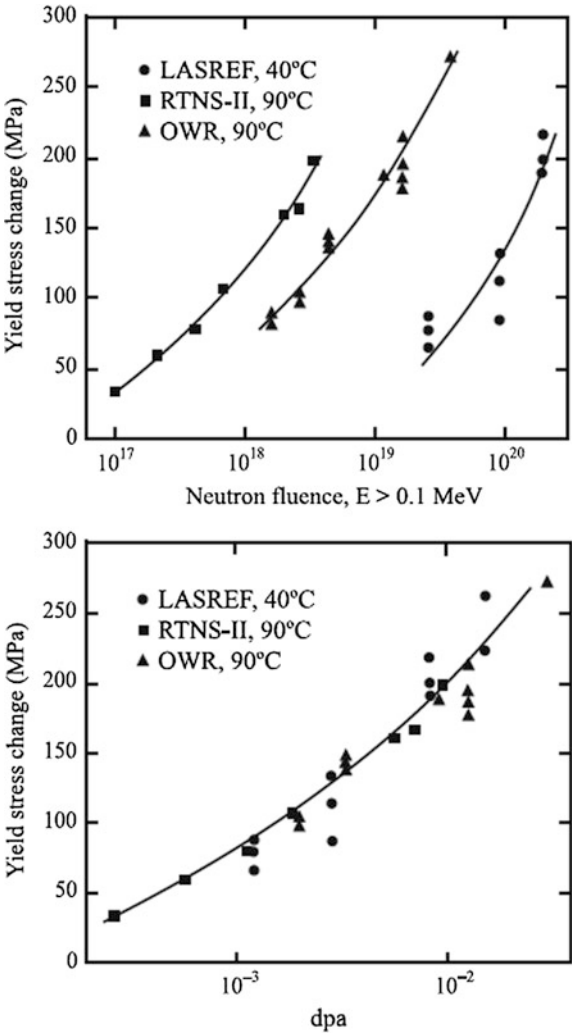

Fig. 1 Comparison of yield stress change in 316 stainless steel irradiated in three facilities with very different neutron energy flux spectra. While there is little correlation in terms of neutron fluence, the yield stress changes correlate well against displacements per atom, dpa (after [2])

However, if the yield strength is plotted as a function of the displacement damage in the alloy (dpa = displacements per atom in the solid), then data from all three neutron sources collapse beautifully onto a single trend line (bottom graph in Fig. 1) that is independent of the flux spectrum. The independence of the yield strength–dpa correlation on the neutron spectrum indicates that dpa is a better representation of the effect of irradiation on materials properties than is the fluence. This addresses our first objective; the determination of the quantity R, the number of displacements per unit volume per unit time:

$$R \equiv \frac{\#\text{displacements}}{\text{cm}^3\,\text{s}} = N \int_{\check{E}}^{\hat{E}} \phi(E_\text{i})\sigma_D(E_\text{i})\text{d}E_\text{i}, \tag{1}$$

where N is the atom number density, $\hat{E}$ is the maximum energy of the incoming particle, $\check{E}$ is the minimum energy of the incoming particle, $\phi(E_\text{i})$ is the energy-dependent particle flux, and $\sigma_\text{D}(E_\text{i})$ is the energy-dependent displacement cross section:

$$\sigma_\text{D}(E_i) = \int_{\check{T}}^{\hat{T}} \sigma(E_\text{i})\nu(T)\text{d}T, \tag{2}$$

where $\hat{T}$ is the maximum energy transferred in a collision of a particle of energy E_i and a lattice atom, $\check{T}$ is the minimum energy transferred in a collision of a particle of energy E_i and a lattice atom, $\sigma(E_\text{i}, T)$ is the cross section for the collision of a particle of energy E_i that results in a transfer of energy T to the struck atom, and $\nu(T)$ is the number of displacements per primary knock-on atom. So, ultimately, we want to determine:

$$R = N \int_{\check{E}}^{\hat{E}} \int_{\check{T}}^{\hat{T}} \phi(E_\text{i})\sigma(E_\text{i}, T)\nu(T)\text{d}T\text{d}E_\text{i}. \tag{3}$$

The two key variables in this equation are $\sigma(E_\text{i}, T)$ and $\nu(T)$. The term $\sigma(E_\text{i}, T)$ describes the transfer of energy from the incoming particle to the first atom it encounters in the target, the PKA. Determination of this quantity is the goal of Chap. 1. The second quantity is $\nu(T)$, the total number of displacements that the PKA goes on to make in the solid, and its determination is described in detail in Chap. 2. Taken together, they describe the total number of displacements caused by an incoming particle of energy E_i, and the flux term of Eq. (3) accounts for the energy distribution of the incoming particles. The result is the total number of displacements in the target from a flux of particles with a known energy distribution. We will return to this equation often, as it is the essence of the quantification of radiation damage in solids.

References

1. Butler D (2004) Nuclear power's new dawn. Nature 429:238–240
2. Greenwood LR (1994) J Nucl Mater 216:29–44

Part I
Radiation Damage

Chapter 1
The Radiation Damage Event

The radiation damage event is defined as the transfer of energy from an incident projectile to the solid and the resulting distribution of target atoms after completion of the event. The radiation damage event is actually composed of several distinct processes. These processes and their order of occurrence are as follows:

1. The interaction of an energetic incident particle with a lattice atom.
2. The transfer of kinetic energy to the lattice atom giving birth to a primary knock-on atom (PKA).
3. The displacement of the atom from its lattice site.
4. The passage of the displaced atom through the lattice and the accompanying creation of additional knock-on atoms.
5. The production of a displacement cascade (collection of point defects created by the PKA).
6. The termination of the PKA as an interstitial.

The radiation damage event is concluded when the PKA comes to rest in the lattice as an interstitial. The result of a radiation damage event is the creation of a collection of point defects (vacancies and interstitials) and clusters of these defects in the crystal lattice. It is worth noting that this entire chain of events consumes only about 10^{-11} s (see Table 1.1). Subsequent events involving the migration of the point defects and defect clusters and additional clustering or dissolution of the clusters are classified as *radiation damage effects*.

What we first need to know in order to understand and quantify radiation damage is how to describe the interaction between a particle and a solid that produces displacements, and later on how to quantify this process. The most simple model is one that approximates the event as colliding hard spheres with displacement occurring when the transferred energy is high enough to knock the struck atom off its lattice site. In addition to energy transfer by hard sphere collisions, the moving atom loses energy by interactions with electrons, the Coulomb field of nearby atoms, the periodicity of the crystalline lattice, etc. The problem is reduced to the following. If we can describe the energy-dependent flux of the incident particle and the energy transfer cross sections (probabilities) for collisions between atoms, then we can quantify the PKA production in a differential energy range and utilize this to determine the number of displaced atoms.

G.S. Was, *Fundamentals of Radiation Materials Science*,
DOI 10.1007/978-1-4939-3438-6_1

Table 1.1 Approximate timescale for the production of defects in irradiated metals (from [1])

Time (s)	Event	Result
10^{-18}	Energy transfer from the incident particle	Creation of a primary knock-on atom (PKA)
10^{-13}	Displacement of lattice atoms by the PKA	Displacement cascade
10^{-11}	Energy dissipation, spontaneous recombination, and clustering	Stable Frenkel pairs (single interstitial atoms (SIA) and vacancies) and defect clusters
$>10^{-8}$	Defect reactions by thermal migration	SIA and vacancy recombination, clustering, trapping, defect emission

In this chapter, we will concentrate on quantifying the energy transferred between interacting bodies as well as describing the energy transfer cross section. We will begin with neutron–nucleus reactions since the neutrality of the neutron makes the interaction particularly straightforward. Following creation of the PKA, subsequent interactions occur between atoms, and the positive charge of the nucleus and the negative charge of the electron cloud become important in understanding how atoms interact. In fact, atom–atom interaction is the low-energy limit of ion–atom interactions that occur in reactor cores and via ion irradiation using accelerators over a wide energy range and can lead to the last type of interaction: ionization collisions.

1.1 Neutron–Nucleus Interactions

1.1.1 Elastic Scattering

By virtue of their electrical neutrality, elastic collisions between neutrons and nuclei can be represented as colliding hard spheres. When neutrons pass through a solid, there is a finite probability that they will collide with a lattice atom, imparting a recoil energy to the struck atom. This probability is defined by the double differential scattering cross section (in energy and angle), σ_s (E_i, E_f, Ω), where E_i and E_f are the incident and final energies and Ω is the solid angle into which the neutron is scattered. We are often only interested in the scattering probability as a function of E_i and the scattering angle. The single differential scattering cross section is as follows:

$$\sigma_s(E_i, \Omega) = \int \sigma_s(E_i, E_f, \Omega) \mathrm{d}E_f. \tag{1.1}$$

The total scattering probability for neutrons of energy E_i is as follows:

$$\sigma_s(E_i) = \int \sigma_s(E_i, \Omega) \mathrm{d}\Omega. \tag{1.2}$$

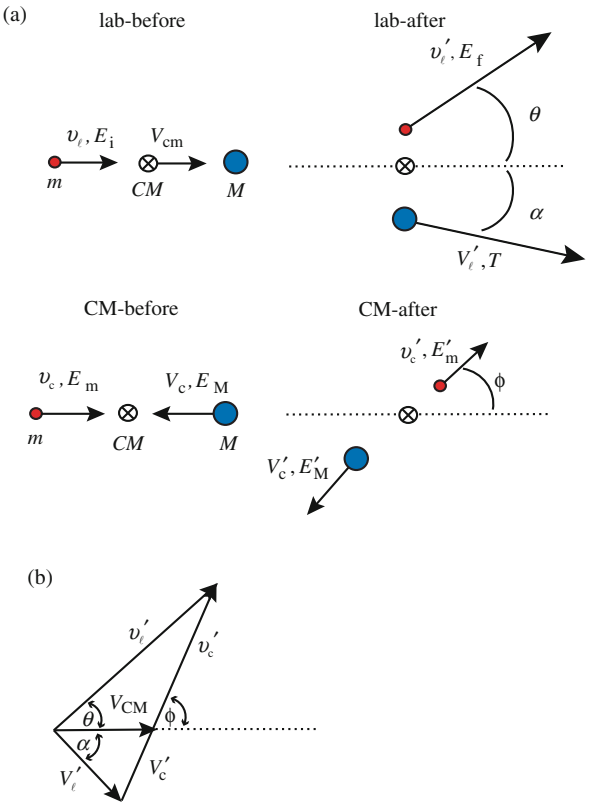

Fig. 1.1 Vector velocities (**a**) in the laboratory and center-of-mass (CM) systems and (**b**) composite diagram relating velocities in the two systems

In the study of irradiation effects, we are interested in the behavior of the struck atom. So we are seeking σ_s (E_i, T); the energy transfer cross section, or the probability that a neutron of energy E_i elastically scattering against an atom of mass M, will impart a recoil energy T to the struck atom. But first it is necessary to find T in terms of the neutron energy and the scattering angle. To do this, let us consider the dynamics of binary elastic collisions in the center-of-mass and laboratory frames.

Figure 1.1(a) shows the trajectories of a neutron and the target nucleus before and after scattering, as seen from both the laboratory reference system and the center-of-mass system. The easiest way to obtain a relationship between the incident neutron energy, scattering angle, and transferred energy is to analyze the dynamics of the collision in the center-of-mass (CM) system. When the collision is viewed in the center-of-mass system, the recoiling particles appear to move away from each other in opposite directions. Momentum conservation along the axes of approach and departure yields the following:

$$\begin{aligned} \upsilon_c m - V_c M &= 0 \\ \upsilon'_c m - V'_c M &= 0, \end{aligned} \tag{1.3}$$

and conservation of kinetic energy requires that:

$$\frac{1}{2}mv_c^2 + \frac{1}{2}MV_c^2 = \frac{1}{2}mv_c'^2 + \frac{1}{2}MV_c'^2. \tag{1.4}$$

Using Eq. (1.3) to eliminate v_c and v_c', we get:

$$\left[\frac{1}{2}m\left(\frac{M}{m}\right)^2 + \frac{1}{2}M\right]V_c^2 = \left[\frac{1}{2}m\left(\frac{M}{m}\right)^2 + \frac{1}{2}M\right]V_c'^2. \tag{1.5}$$

Therefore,

$$\begin{aligned} V_c &= V_c', \text{ and hence,} \\ v_c &= v_c'. \end{aligned} \tag{1.6}$$

Since the target nucleus is at rest in the laboratory system and moving to the left with speed V_c in the CM system, the CM system itself must be moving to the right relative to the laboratory system with the same speed, V_c. Thus, if we use V_{CM} to denote the speed of the CM system relative to the laboratory system, the magnitudes of V_{CM} and V_c are the same (but opposite in direction). This can be restated as follows:

$$v_c = v_\ell - V_{CM} = v_\ell - V_c, \tag{1.7}$$

and using Eq. (1.3), we find that:

$$V_{CM} = \left(\frac{m}{M+m}\right)v_\ell. \tag{1.8}$$

Recall that we want to relate T, the energy transferred to the struck atom, to ϕ, the scattering angle in the CM system. Using vector addition, we can relate the recoil target nucleus velocity in the laboratory system, V_ℓ', to ϕ as shown in Fig. 1.1(b), which is a composite of the interaction in the laboratory and CM systems as shown in Fig. 1.1(a). Using the law of cosines:

$$V_\ell'^2 = V_{CM}^2 + V_c'^2 - 2V_{CM}V_c'\cos\phi, \tag{1.9}$$

and rewriting the velocities in Eq. (1.9) in terms of energy gives:

$$V_\ell'^2 = \frac{2T}{M}, \quad V_{CM}^2 = \frac{2E_i}{m}\left(\frac{m}{m+M}\right)^2, \quad \text{and} \quad V_c'^2 = \frac{2m}{M^2}E_m',$$

and substituting these expressions into Eq. (1.9) gives:

$$T = \frac{mM}{(m+M)^2} E_\mathrm{i} + \frac{m}{M} E'_\mathrm{m} - 2\left(\frac{m}{m+M}\right)(E_\mathrm{i} E'_\mathrm{m})^{1/2} \cos\phi, \tag{1.10a}$$

or

$$T = \eta_1 \eta_2 E_\mathrm{i} + \frac{\eta_1}{\eta_2} E'_\mathrm{m} - 2\eta_1 (E_\mathrm{i} E'_\mathrm{m})^{1/2} \cos\phi, \tag{1.10b}$$

where $\eta_1 = m/(m + M)$ and $\eta_2 = M/(m + M)$.

Since we want to find the energy transferred, T, as a function of initial energy and scattering angle only, we use the relationship between E_i and E'_m to eliminate E'_m. From Eqs. (1.7) and (1.8), we know that:

$$\upsilon'_\mathrm{c} = \upsilon_\ell - \left(\frac{m}{m+M}\right)\upsilon_\ell = \upsilon_\ell \left(\frac{M}{m+M}\right). \tag{1.11}$$

Writing Eq. (1.11) in terms of energy gives:

$$E'_\mathrm{m} = E_\mathrm{i}\left(\frac{M}{m+M}\right)^2 = \eta_2^2 E_\mathrm{i}. \tag{1.12}$$

Substituting into Eq. (1.10b) and simplifying gives:

$$T = \frac{\gamma}{2} E_\mathrm{i}(1 - \cos\phi), \tag{1.13}$$

where we define

$$\gamma = \frac{4mM}{(M+m)^2} = \frac{4A}{(1+A)^2}, \tag{1.14}$$

where $1 = m$ and $A = M$. Hence, T depends upon only one unknown, ϕ. Note the angular dependence of T on ϕ as shown in Fig. 1.2. The energy transferred rises from 0 at $\phi = 0$ to a maximum of γE_i at $\phi = \pi$, or $T_\mathrm{max} = \hat{T} = \gamma E_\mathrm{i}$. That is, the energy transferred is a maximum when the particle backscatters and is a minimum when it misses the target, resulting in no change in course ($\phi = 0$).

Example 1.1. Neutron–nuclear interaction

For a neutron incident on a hydrogen atom, $\hat{T}_{n-H}/E_\mathrm{i} = 1.0$. For a neutron incident on a uranium atom, $\hat{T}_{n-U}/E_\mathrm{i} = 0.017$. Conversely, comparing the interaction of an iron atom with 100 keV Xe^+ ions or electrons, the value of γ for

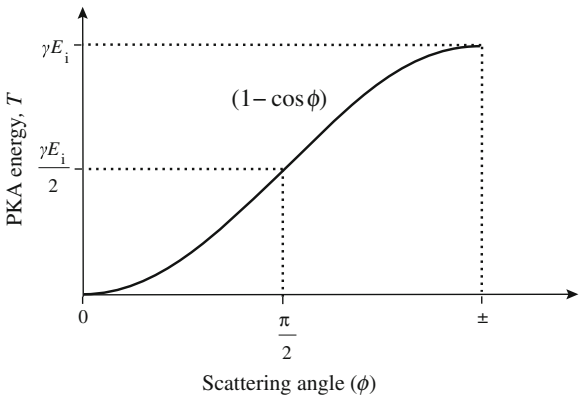

Fig. 1.2 Energy transfer as a function of center-of-mass scattering angle

the Xe–Fe interaction is 0.83, yielding a $\hat{T}$ of 83,000 eV. However, the value of γ for e^-–Fe interaction is 0.00004, giving a $\hat{T}$ of only 4 eV, which, as we will see in Chap. 2, is not enough to displace an iron atom from its lattice site.

The scattering angles in the laboratory system for the incident particle (θ) and the struck atom (α) can be written in terms of the scattering angle in the center-of-mass system (ϕ) using the vector diagram shown in Fig. 1.1(b). Applying the law of sines to Fig. 1.1(b) for the *scattered particle*:

$$\frac{v'_\ell}{\sin(\pi-\theta)} = \frac{v'_c}{\sin\theta},$$

where v'_c is given by Eqs. (1.6) and (1.7):

$$v'_c = V_{CM}\left(\frac{v_\ell}{V_{CM}} - 1\right),$$

and using Eq. (1.8), we have:

$$v'_c = V_{CM}\frac{M}{m}.$$

Applying the law of cosines to the same triangle gives:

$$v'^2_\ell = v'^2_c + V^2_{CM} - 2V_{CM}v'_c\cos(\pi-\phi),$$

and combining the last three equations to express θ as a function of ϕ yields:

$$\tan\theta = \frac{(M/m)\sin\phi}{1+(M/m)\cos\phi}.$$

Applying the law of sines to the vector diagram in Fig. 1.1(b) for the *struck atom* gives:

$$\frac{V_c'}{\sin\alpha} = \frac{V_\ell'}{\sin\phi},$$

and combining this result with Eqs. (1.6) and (1.9) where the energies are written in terms of velocities gives:

$$\tan\alpha = \frac{\sin\phi}{1-\cos\phi}.$$

We are still interested in obtaining the probability that a given T will be imparted to the recoil atom. This depends on the differential cross section. We define $\sigma_s(E_i, \phi)\,d\Omega$ as the probability of a collision that scatters the incident particle into a center-of-mass angle in the range $(\phi, d\Omega)$ where $d\Omega$ is an element of solid angle about the scattering direction ϕ. Since differential probabilities written in transformed variables are equivalent, $\sigma_s(E_i, \phi)$ can be written in terms of CM variables:

$$\sigma_s(E_i, \phi)d\Omega = \sigma_s(E_i, T)dT. \tag{1.15}$$

Using Fig. 1.3 to relate $d\Omega$ to $d\phi$, we have by definition:

$$d\Omega = dA/r^2, \tag{1.16}$$

and from Fig. 1.4, we have:

$$d\Omega = \frac{rd\phi(2\pi r\sin\phi)}{r^2} = 2\pi\sin\phi\,d\phi. \tag{1.17}$$

Substituting Eq. (1.17) into Eq. (1.15) yields:

$$\sigma_s(E_i, T)\,dT = \sigma_s(E_i, \phi)\,d\Omega = 2\pi\sigma_s(E_i, \phi)\sin\phi\,d\phi. \tag{1.18}$$

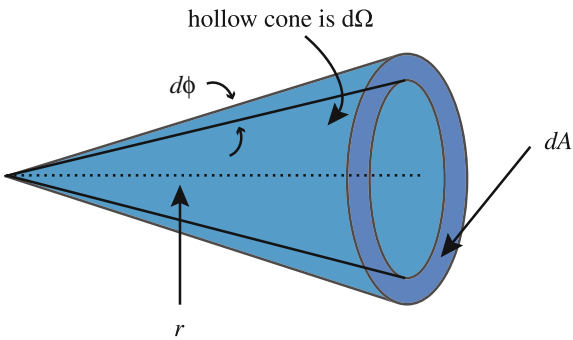

Fig. 1.3 Scattering into the solid angular element $d\Omega$ defined by dA/r^2

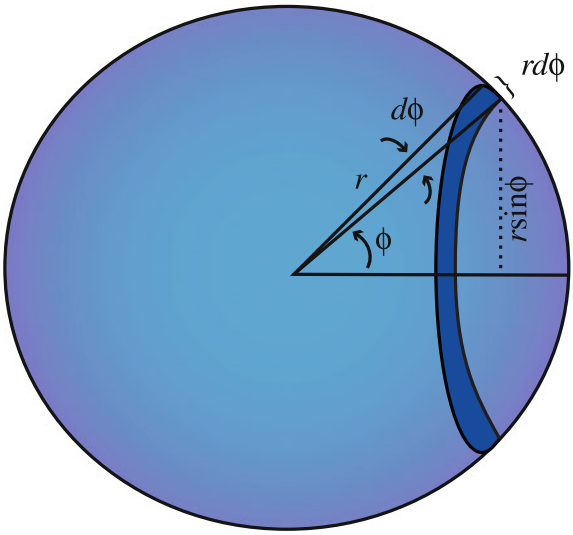

Fig. 1.4 The solid angle dΩ subtended at the scattering angle ϕ by the incremental angle dϕ

Since $T = \frac{\gamma}{2} E_\mathrm{i}(1 - \cos\phi)$ then $\mathrm{d}T = \frac{\gamma}{2} E_\mathrm{i} \sin\phi \, \mathrm{d}\phi$, and we have:

$$\sigma_\mathrm{s}(E_\mathrm{i}, T) = \frac{4\pi}{\gamma E_\mathrm{i}} \sigma_\mathrm{s}(E_\mathrm{i}, \phi). \tag{1.19}$$

Figure 1.5 shows the difference in the differential scattering cross section in units of area per unit solid angle versus area per unit angle as in Eq. (1.18). Although the number of atoms scattered through an angle increment dϕ about $\phi = \pi/2$ is greater than that through an angular increment dϕ about $\phi = 0$ or π (Fig. 1.5(a)), the number intercepting the spherical surface per unit of solid angle is constant over all angles, ϕ (Fig. 1.5(b)). Hence, dT/dϕ varies in a sinusoidal manner with ϕ, but dT/dΩ is independent of ϕ.

Using Eqs. (1.2) and (1.18), the total elastic scattering cross section is as follows:

$$\sigma_\mathrm{s}(E_\mathrm{i}) = \int \sigma_\mathrm{s}(E_\mathrm{i}, \phi) \, \mathrm{d}\Omega = 2\pi \int \sigma_\mathrm{s}(E_\mathrm{i}, \phi) \, \sin\phi \, \mathrm{d}\phi.$$

If we assume that elastic scattering in the CM system is independent of scattering angle (i.e., scattering is isotropic), Fig. 1.6, then:

$$\sigma_\mathrm{s}(E_\mathrm{i}) = \int \sigma_\mathrm{s}(E_\mathrm{i}, \phi) \, \mathrm{d}\Omega = 2\pi \, \sigma_\mathrm{s}(E_\mathrm{i}, \phi) \int \sin\phi \, \mathrm{d}\phi = 4\pi \, \sigma_\mathrm{s}(E_\mathrm{i}, \phi), \tag{1.20}$$

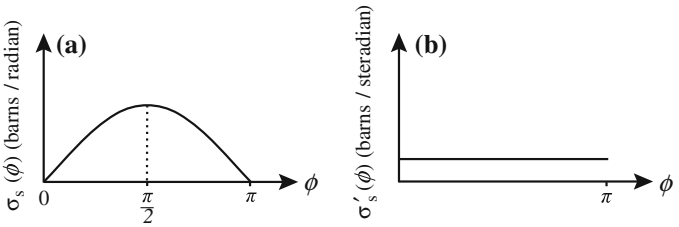

Fig. 1.5 Isotropic differential scattering cross sections in units of (**a**) area per unit scattering angle and (**b**) area per unit solid angle

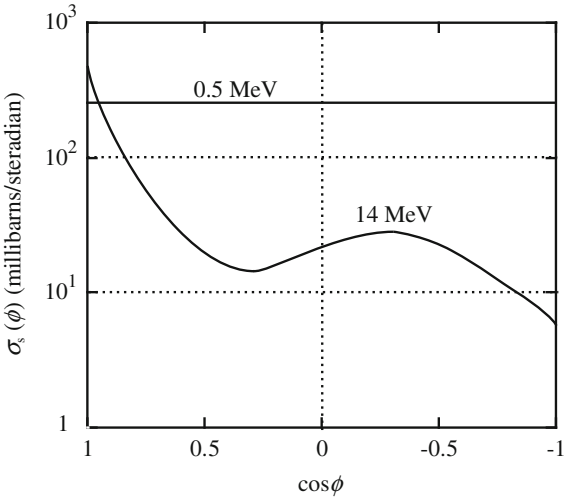

Fig. 1.6 Differential elastic scattering cross sections for C^{12} at 0.5 and 14 MeV neutrons as a function of the cosine of the center-of-mass scattering angle (from [2])

and

$$\sigma_s(E_i, T) = \frac{\sigma_s(E_i)}{\gamma E_i}, \tag{1.21}$$

which is independent of T! That is, σ_s (E_i, T), the probability that a neutron of energy E_i, elastically scattering against an atom of mass M, will impart a recoil energy T to the struck atom does not depend on the recoil energy. Now, the average recoil energy can be calculated as follows:

$$\overline{T} = \frac{\int_{\check{T}}^{\hat{T}} T\sigma_s(E_i, T)\,dT}{\int_{\check{T}}^{\hat{T}} \sigma_s(E_i, T)\,dT} = \frac{\check{T} + \hat{T}}{2} \approx \frac{\hat{T}}{2} = \frac{\gamma E_i}{2}. \tag{1.22}$$

Applying Eq. (1.22) to the case of a 1 MeV neutron incident on elements of varying mass, we have the following:

$$\begin{array}{lll} 1\,\text{MeV n on C:} & \gamma = 0.28 & \overline{T} = 0.14\,\text{MeV} \\ 1\,\text{MeV n on Fe:} & \gamma = 0.069 & \overline{T} = 0.035\,\text{MeV} \\ 1\,\text{MeV n on U:} & \gamma = 0.017 & \overline{T} = 0.009\,\text{MeV} \end{array}$$

In addition to the elastic scattering just discussed, we can have energy transfer by inelastic scattering, (n, 2n) reactions and (n, γ) reactions. The first two reactions become important above neutron energies of about 1.0 and 8.0 MeV, respectively, while the latter occurs at thermal neutron energies in ^{235}U.

1.1.2 Inelastic Scattering

Inelastic scattering is characterized by a reaction in which the emitted particle is experimentally the same as the captured particle, but there is a loss of kinetic energy in the system. The energy is found in the excitation energy of the product nucleus, e.g., N^{14} (p, p′)N^{14*} or C^{14}(n, n′)C^{14*}. The differences in the energies of groups of scattered particles correspond to the energy separations of excited levels in the product nucleus:

$$-Q = \sum_{\text{f}} KE_{\text{f}} - \sum_{\text{i}} KE_{\text{i}} = \sum_{\text{f}} M_{\text{f}}c^2 - \sum_{\text{i}} M_{\text{i}}c^2.$$

In an inelastic collision, a neutron is absorbed by the nucleus, forming a compound nucleus, which emits a neutron and a γ-ray. There may be more than one γ emitted and the nucleus may remain in an excited state during the course of an interaction. The inelastic scattering cross section can be divided into resolved and unresolved resonance components [3]. For a given resonance (jth resonance) of the target nucleus, the scattering cross section will be a function of Q_j, the γ decay energy of the residual nucleus that is always negative. Analogous to Eq. (1.15), we can write differential equalities σ_{sj} (E_{i}, Q_j, T) dT = σ_{sj} (E_{i}, Q_j, ϕ) dΩ, so that:

$$\sigma_{sj}(E_{\text{i}}, Q_j, T) = \sigma_{sj}(E_{\text{i}}, Q_j, \phi)\, 2\pi \sin\phi \frac{\text{d}\phi}{\text{d}T}. \tag{1.23}$$

However, the expression for T in Eq. (1.13) is not valid for inelastic collisions since kinetic energy is not conserved. Instead, we focus on the conservation of total energy. If the target nucleus M is at rest in the laboratory system and the particle m has energy E_{i}, then the energy balance in CM coordinates is as follows:

$$\frac{M}{M+m} E_{\text{i}} + Q_j = E'_{\text{m}} + E'_{\text{M}}, \tag{1.24}$$

where Q_j is the reaction energy and E'_{m} and E'_{M} are the kinetic energies in CM coordinates of the exit particle and nucleus, respectively. In order that momentum is conserved:

$$mE'_{\mathrm{m}} = ME'_{\mathrm{M}}, \tag{1.25}$$

and combining Eq. (1.24) with Eq. (1.25) (assuming that the masses of the projectile and target are unchanged after the reaction) yields:

$$E'_{\mathrm{m}} = \frac{M}{M+m}\left(Q_j + \frac{M}{M+m}E_{\mathrm{i}}\right)$$

or

$$E'_{\mathrm{m}} = \eta_2\left(Q_j + \eta_2 E_{\mathrm{i}}\right). \tag{1.26}$$

Recalling the general expression for T, Eq. (1.10b):

$$T = \eta_1\eta_2 E_{\mathrm{i}} + \frac{\eta_1}{\eta_2}E'_{\mathrm{m}} - 2\eta_1(E_{\mathrm{i}}E'_{\mathrm{m}})^{1/2}\cos\phi,$$

and substituting in for E'_{m} from Eq. (1.26) yields:

$$T(E_{\mathrm{i}}, Q_j, \phi) = \frac{\gamma}{2}E_{\mathrm{i}} - \frac{\gamma}{2}\left[E_{\mathrm{i}}\left(E_{\mathrm{i}} + Q_j\frac{A+1}{A}\right)\right]^{1/2}\cos\phi + \frac{Q_j}{A+1}. \tag{1.27}$$

Now, the expression for $\mathrm{d}T/\mathrm{d}\phi$ becomes:

$$\frac{\mathrm{d}T(E_{\mathrm{i}}, Q_j, \phi)}{\mathrm{d}\phi} = \frac{\gamma}{2}E_{\mathrm{i}}\left[1 + \frac{Q_j}{E_{\mathrm{i}}}\frac{A+1}{A}\right]^{1/2}\sin\phi. \tag{1.28}$$

Note that in the case of elastic collisions, Q_j = 0 and Eq. (1.27) reduces to Eq. (1.13).

If we now assume that inelastic scattering is isotropic in the CM system, then we have:

$$\sigma_{\mathrm{s}j}(E_{\mathrm{i}}, Q_j) = \int \sigma_{\mathrm{s}j}(E_{\mathrm{i}}, Q_j, \phi)\,\mathrm{d}\Omega = 4\pi\sigma_{\mathrm{s}j}(E_{\mathrm{i}}, Q_j, \phi). \tag{1.29}$$

Substituting Eqs. (1.28) and (1.29) into (1.23) yields:

$$\sigma_{\mathrm{s}j}(E_{\mathrm{i}}, Q_j, T) = \frac{\sigma_{\mathrm{s}j}(E_{\mathrm{i}}, Q_j)}{\gamma E_{\mathrm{i}}\left(1 + \dfrac{Q_j}{E_{\mathrm{i}}}\dfrac{A+1}{A}\right)^{1/2}}. \tag{1.30}$$

for inelastic collisions in the resolved resonance region.

When the compound nucleus is excited to high enough energies, the resonance levels overlap and are no longer individually distinguishable. The inelastic scattering cross section is treated as a continuum and is described by an evaporation model [3] with:

$$\sigma_{\mathrm{is}}(E_{\mathrm{i}}, E'_{\mathrm{m}}, T) = \sigma_{\mathrm{is}}(E_{\mathrm{i}}) \frac{f(E_{\mathrm{i}}, E'_{\mathrm{m}})}{4\dfrac{1}{A+1}(E_{\mathrm{i}}, E'_{\mathrm{m}})^{1/2}}, \text{ and}$$
$$\sigma_{\mathrm{is}}(E_{\mathrm{i}}, T) = \sigma_{\mathrm{is}}(E_{\mathrm{i}}) \int_0^{E'^{\max}_{\mathrm{m}}} \frac{f(E_{\mathrm{i}}, E'_{\mathrm{m}})}{4\dfrac{1}{A+1}(E_{\mathrm{i}}, E'_{\mathrm{m}})^{1/2}} \mathrm{d}E'_{\mathrm{m}}, \tag{1.31}$$

where $f(E_{\mathrm{i}}, E'_{\mathrm{m}})$ is a distribution function for the energy E'_{m} of the scattered neutron in the CM system that represents the probability that a neutron is evaporated from the moving compound nucleus, whose value in the CM system is a Maxwellian of nuclear temperature $E_{\mathrm{D}} = kT$:

$$f(E_{\mathrm{i}}, E'_{\mathrm{m}}) = \frac{E'_{\mathrm{m}}}{I(E_{\mathrm{i}})} \mathrm{e}^{(-E'_{\mathrm{m}}/E_{\mathrm{D}})}, \tag{1.32}$$

and

$$I(E_{\mathrm{i}}) = E_{\mathrm{D}}^2 \left[1 - \left(1 + \frac{E'^{\max}_{\mathrm{m}}}{E_{\mathrm{D}}}\right) \mathrm{e}^{(-E'^{\max}_{\mathrm{m}}/E_{\mathrm{D}})}\right], \tag{1.33}$$

is a normalization factor such that

$$\int_0^{E'^{\max}_{\mathrm{m}}} f(E_{\mathrm{i}}, E'_{\mathrm{m}}) \, \mathrm{d}E'_{\mathrm{m}} = 1. \tag{1.34}$$

The maximum value of E'_{m} is given by Eq. (1.26) with $Q = Q_1$, the lowest energy level, and the minimum value of E'_{m} is zero.

1.1.3 (n, 2n) Reactions

Reactions such as the (n, 2n) reaction are important in radiation effects since they produce additional neutrons that can either cause damage or transmutation reactions in components of interest. Following the 2n model, which is based on work by Odette [4] and Segev [5], a second neutron can only be emitted if the residual excitation of the nucleus after emission of the first neutron exceeds the binding energy of a neutron in the mass M nuclide. The recoil energy after emission of the

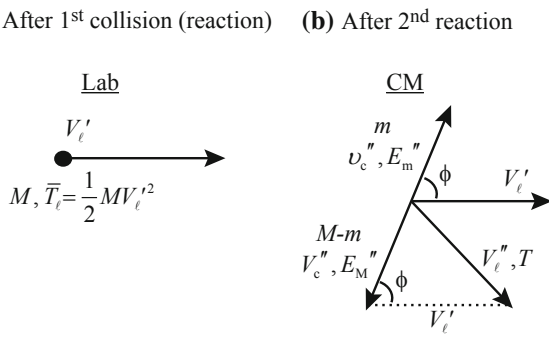

Fig. 1.7 Vector velocities for the (n, 2n) reaction in (**a**) the laboratory system and (**b**) the center-of-mass system

first neutron is taken to be the average value ($\cos\phi = 0$ in Eq. (1.10b)) and is shown in Fig. 1.7(a) in the laboratory system. We next analyze the second reaction (emission) in the CM system described in Fig. 1.7(b). We begin by using the law of cosines to relate V_c'' to ϕ:

$$V_\ell''^2 = V_\ell'^2 + V_c''^2 - 2V_\ell' V_c'' \cos\phi. \tag{1.35}$$

From Fig. 1.7(a), we have:

$$\frac{1}{2}MV_\ell'^2 = \overline{T}_\ell \quad \text{or} \quad V_\ell'^2 = \frac{2\overline{T}_\ell}{M},$$

and from Fig. 1.7(b), we have:

$$\frac{1}{2}(M-m)V_c''^2 = E_M'' \quad \text{or} \quad V_c''^2 = \frac{2E_M''}{M-m}.$$

Conservation of momentum requires:

$$(M-m)V_c'' = m\upsilon_c'', \tag{1.36}$$

and squaring gives:

$$V_c''^2 = \left(\frac{m}{M-m}\right)^2 \upsilon_c''^2 = \frac{2m}{(M-m)}E_m''. \tag{1.37}$$

Substituting into the law of cosines, Eq. (1.35), gives:

$$V_\ell''^2 = \frac{2\overline{T}_\ell}{M} + \frac{2m}{(M-m)}E_m'' - 2\left(\frac{2m}{(M-m)^2}\frac{2}{M}E_m''\overline{T}_\ell\right)^{1/2}\cos\phi, \tag{1.38}$$

where $\overline{T}_\ell = \eta_1\eta_2 E_\mathrm{i} + (\eta_1/\eta_2)E'_\mathrm{m}$ is the mean recoil energy after the emission of the first neutron. Writing V''^2_ℓ in terms of energy gives the recoil energy following the second emission:

$$\begin{aligned} T &= \frac{1}{2}(M-m)V''^2_\ell \\ &= \frac{M-m}{M}\overline{T}_\ell + \frac{m}{M-m}E''_\mathrm{m} - 2\left(\frac{m}{M}\right)^{1/2}(E''_\mathrm{m}\overline{T}_\ell)^{1/2}\cos\phi \\ &= \frac{A-1}{A}\overline{T}_\ell + \frac{1}{A-1}E''_\mathrm{m} - 2\left(\frac{1}{A}\right)^{1/2}(\overline{T}_\ell E''_\mathrm{m})^{1/2}\cos\phi \\ &= \frac{A}{A-1}\frac{\eta_1}{\eta_2}E''_\mathrm{m} + \frac{A-1}{A}\overline{T}_\ell - 2\left(\frac{\eta_1}{\eta_2}\right)^{1/2}(\overline{T}_\ell E''_\mathrm{m})^{1/2}\cos\phi. \end{aligned} \tag{1.39}$$

The (n, 2n) reaction cross section is a special case of the inelastic scattering cross section given in Eq. (1.31):

$$\begin{aligned} &\sigma_{\mathrm{n,2n}}(E_\mathrm{i}, E'_\mathrm{m}, E''_\mathrm{m}, T) \\ &\quad = \sigma_{\mathrm{n,2n}}(E_\mathrm{i})\frac{E'_\mathrm{m}}{I(E_\mathrm{i})}\mathrm{e}^{-E'_\mathrm{m}/E_\mathrm{D}}\frac{E''_\mathrm{m}}{I(E_\mathrm{i}, E'_\mathrm{m})}\mathrm{e}^{-E''_\mathrm{m}/E_\mathrm{D}}, \quad \text{and} \\ &\sigma_{\mathrm{n,2n}}(E_\mathrm{i}, T) \\ &\quad = \int_0^{E_\mathrm{i}-U}\frac{E'_\mathrm{m}}{I(E_\mathrm{i})}\mathrm{e}^{-E'_\mathrm{m}/E_\mathrm{D}}\int_0^{E_\mathrm{i}-U-E'_\mathrm{m}}\frac{E''_\mathrm{m}}{I(E_\mathrm{i}, E'_\mathrm{m})}\mathrm{e}^{-E''_\mathrm{m}/E_\mathrm{D}}\mathrm{d}E'_\mathrm{m}\mathrm{d}E''_\mathrm{m}, \end{aligned} \tag{1.40}$$

where $I(E_\mathrm{i})$ is given in Eq. (1.33) with $E'^{\max}_\mathrm{m} = E_\mathrm{i} - U$ and $I(E_\mathrm{i}, E'_\mathrm{m})$ is given in Eq. (1.33) with $E'^{\max}_\mathrm{m}$ replaced by $E''^{\max}_\mathrm{m} = E_\mathrm{i} - U - E'_\mathrm{m}$ and for (n, 2n) reactions, $U = 0$ [3].

1.1.4 (n, γ) Reactions

Another class of reactions that can affect the extent of radiation damage involves photon emission. This reaction is important since the energy of the recoiling nucleus is sufficient to displace an atom. As we will see later, this type of displacement is particularly important in radiation damage in reactor pressure vessels in which the gamma flux is more comparable to the fast neutron flux than in the reactor core. Recalling the momentum and energy conservation laws of Eqs. (1.3) and (1.4) and Fig. 1.1, which for (n, γ) reactions, $E_\mathrm{i} \sim 0$ (since these reactions occur with thermal neutrons of energy 0.025 eV), $E_\mathrm{f} \equiv 0$ (since there is no scattered neutron) and Q is the equivalent of the mass difference between the initial particles and the compound nucleus. When the compound nucleus (CN) de-excites, it emits a

γ-ray with this energy. Conservation of momentum says that the nucleus must recoil with momentum:

$$(m+M)V_c' = \frac{E_\gamma}{c}. \tag{1.41}$$

Note that this is an approximation since we have not subtracted the mass defect from the compound nucleus. Squaring both sides of Eq. (1.41) and dividing by 2 (m + M) gives:

$$\frac{1}{2}(m+M)V_c'^2 = \frac{E_\gamma^2}{2(m+M)c^2}.$$

As in the case of elastic scattering, T is given by:

$$T = (V_{CM}^2 + V_c'^2 - 2V_{CM}V_c'\cos\phi)\left(\frac{M+m}{2}\right),$$

but $V_{CM} \ll V_c'$ so to a good estimate:

$$T \cong \left(\frac{m+M}{2}\right)V_c'^2 = \frac{E_\gamma^2}{2(M+m)c^2}.$$

We will assume further that this value of T represents the maximum recoil energy. But since not all of Q will be emitted in a single γ-ray, we approximate the average recoil energy as half the value of the maximum recoil energy, giving:

$$\overline{T} \cong \frac{E_\gamma^2}{4(M+m)c^2}. \tag{1.42}$$

The radiative capture cross section is derived from the Breit–Wigner single-level formula when the target nucleus has zero intrinsic angular momentum and the compound nucleus has a neutron width Γ_n, a radiation width Γ_g, and a total width Γ, and E_0 is the resonance energy and λ is the wavelength [6]:

$$\sigma_{n,\gamma}(E_i) = \pi\lambda^2 \frac{\Gamma_n\Gamma_\gamma}{(E_i - E_0)^2 + (\Gamma/2)^2}. \tag{1.43}$$

Expressing Eq. (1.43) in terms of σ_0, the maximum value of the radiative capture cross section (at $E = E_0$) and taking Γ_n proportional to $1/\lambda$ and to $\sqrt{E}$ gives:

$$\sigma_{n,\gamma}(E_i) = \sigma_0\sqrt{\frac{E_0}{E_i}}\left\{\frac{1}{[(E_i - E_0)/(\Gamma/2)]^2 + 1}\right\}. \tag{1.44}$$

Table 1.2 Energy transfer and energy transfer cross sections for various types of neutron–nuclear collisions

Types of collision	Energy transfer and energy transfer cross section	Equation in text
Elastic scattering	$T = \frac{\gamma}{2} E_\mathrm{i}(1 - \cos\phi)$	(1.13)
	$\sigma_\mathrm{s}(E_\mathrm{i}, T) = \frac{\sigma_\mathrm{s}(E_\mathrm{i})}{\gamma E_\mathrm{i}}$	(1.21)
Inelastic scattering	$T(E_\mathrm{i}, Q_j, \phi) = \frac{\gamma}{2} E_\mathrm{i} - \frac{\gamma}{2}\left[E_\mathrm{i}\left(E_\mathrm{i} + Q_\mathrm{i}\frac{A+1}{A}\right)\right]^{1/2} \cos\phi + \frac{Q_j}{A+1}$	(1.27)
	resonance region	
	$\sigma_{\mathrm{s},j}(E_\mathrm{i}, Q_j, T) = \frac{\sigma_{\mathrm{s},j}(E_\mathrm{i}, Q_j)}{\gamma E_\mathrm{i}\left(1 + \frac{Q_j}{E_\mathrm{i}}\frac{1+A}{A}\right)^{1/2}}$	(1.30)
	unresolved resonance region	
	$\sigma_\mathrm{is}(E_\mathrm{i}, T) = \sigma_\mathrm{is}(E_\mathrm{i}) \int_0^{E_\mathrm{m}^\mathrm{max}} \frac{f(E_\mathrm{i}, E'_\mathrm{m})}{4\frac{1}{A+1}(E_\mathrm{i}, E'_\mathrm{m})^{1/2}}\, \mathrm{d}E'_\mathrm{m}$	(1.31)
(n, 2n)	$T = \frac{A}{A-1}\frac{\eta_1}{\eta_2} E''_\mathrm{m} + \frac{A-1}{A}\overline{T}_\ell - 2\left(\frac{\eta_1}{\eta_2}\right)^{1/2} (\overline{T}_\ell E''_\mathrm{m})^{1/2} \cos\phi$	(1.39)
	$\sigma_{\mathrm{n,2n}}(E_\mathrm{i}, T) = \int_0^{E_\mathrm{i}-U} \frac{E'_\mathrm{m}}{I(E_\mathrm{i})} \mathrm{e}^{-E'_\mathrm{m}/E_\mathrm{D}} \times \int_0^{E_\mathrm{i}-U-E'_\mathrm{m}} \frac{E''_\mathrm{m}}{I(E_\mathrm{i}, E'_\mathrm{m})} \mathrm{e}^{-E''_\mathrm{m}/E_\mathrm{D}} \mathrm{d}E'_\mathrm{m}\, \mathrm{d}E''_\mathrm{m}$	(1.40)
(n, γ)	$\overline{T} \cong \frac{E_\gamma^2}{4(M+m)c^2}$	(1.42)
	$\sigma_{\mathrm{n},\gamma}(E_\mathrm{i}) = \sigma_0 \sqrt{\frac{E_0}{E_\mathrm{i}}} \left\{ \frac{1}{[(E_\mathrm{i} - E_0)/(\Gamma/2)]^2 + 1} \right\}$	(1.44)

Table 1.2 provides a summary of the energy transfer and the energy transfer cross sections for the various types of reactions covered in Sect. 1.1.

1.2 Interactions Between Ions and Atoms

Ion–atom or atom–atom collisions are governed by interactions between the electron clouds, the electron cloud and the nucleus, and between the nuclei. These interactions are described by what are known as interatomic potentials. In order to develop descriptions of energy transfer cross sections for interactions between atoms, we need descriptions of the potential function that governs that interaction. Unfortunately, there exists no single function that describes all interactions, but rather, the nature of the interaction is a strong function of the atom energies, and hence the distance of closest approach of the nuclei. The following section provides a summary of interatomic potentials adapted from Chadderton [7].

1.2.1 Interatomic Potentials

The end product of the neutron–nuclear interaction is the creation of the primary knock-on atom with some amount of kinetic energy. This atom will, of course, make subsequent collisions with other atoms in the solid. Knowledge of the forces acting between two colliding atoms represents the most fundamental aspect of radiation damage, without which a proper description of the primary event and the ensuing defect structure is impossible. Our interest lies in the forces between like atoms, unlike atoms, or ions and atoms. The interaction between atoms is described by potential functions. Recall that the atoms are (usually) electrically neutral but are composed of positive and negative components that do not cancel at all points in space. It is well known that the potential energy between two point charges of the same sign separated by a distance r is described by the well-known Coulomb equation:

$$V(r) = k_e \frac{\varepsilon^2}{r}, \tag{1.45}$$

where $k_e = \dfrac{1}{4\pi\varepsilon_0}$ is the Coulomb constant (8.98755×10^9 Nm^2 C^{-2}), ε_0 is the electric constant, ε is the single unit electronic charge, and ε^2 = 1.44 eV-nm. When written in electrostatic units or Gaussian units, the unit charge (esu or statcoulomb) is defined in such a way that the Coulomb constant, k_e, disappears because it has the value of one and becomes dimensionless, and Eq. (1.45) is often written in abbreviated form without the Coulomb constant. In the case of atoms, we have a charged nucleus surrounded by an electron cloud of opposite charge. It is evident that the potential function describing the interaction between atoms is far more complicated than that describing neutron–nuclear interaction. Even in the simplest cases, $V(r)$ has never been determined exactly, but some simple considerations show that it must be dominated by two distinct contributions over the range of separation in which we are interested. Perhaps, the simplest of all potential functions is the "hard sphere" approximation. This potential is described as follows:

$$V(r) = \begin{cases} 0 & \text{for } r > r_0 \\ \infty & \text{for } r \leq r_0. \end{cases} \tag{1.46}$$

This potential function describes an interaction with an infinitely sharp cutoff at the atomic radius r_0. At distances greater than this radius, the interaction vanishes, while at distances equal to and less than r_0, the magnitude is infinity. This description is analogous to the behavior of billiard balls, and hence, the atoms in this model are described as acting as such. Clearly, this is not a very realistic description of atom–atom interaction since we know that the electron shells can overlap.

Figure 1.8 shows how the interatomic potential actually varies with separation. At large separation, the principal interaction is supplied by the Coulomb forces,

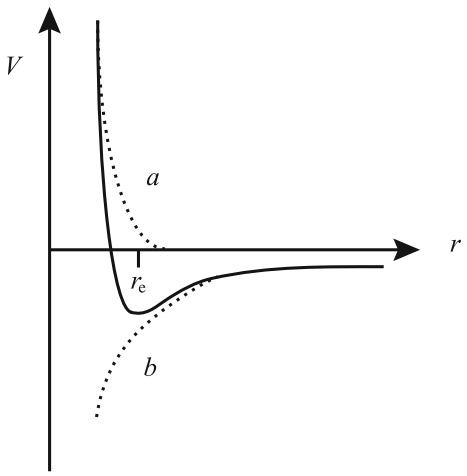

Fig. 1.8 Variation of interatomic potential with separation, *R*. Attractive forces dominate at large separations (*b*) and the central repulsive force dominates at small separations, (*a*) and at intermediate distances, there is a smooth transition between the two extremes with a minimum corresponding to the equilibrium separation distance, r_e or *D*

while for smaller separations, the central field repulsive force is dominant. A similar relationship applies to all crystals regardless of the nature of binding. In all cases, there is a smooth curve with a minimum at the separation distance corresponding to the nearest neighbor distance in the lattice, r_e (also referred to as *D*).

In describing the interaction between atoms, we will use two yardsticks for points of reference. One is the Bohr radius of the hydrogen atom, $a_0 = 0.053$ nm, which provides a measure of the position of the atomic shells. The other is r_e, the spacing between nearest neighbors in the crystal (typically ~ 0.25 nm). When $r \ll r_e$, electrons populate the lowest energy levels (closed shells) of the individual atoms and only the outer valence shells will have empty levels. As two atoms are brought together, the valence shells begin to overlap and weak attractive forces such as van der Waals forces may develop. When $a_0 < r \leq r_e$, the closed inner shells begin to overlap. Since the Pauli exclusion principle demands that some electrons change their levels, and hence move to higher energy levels, the extra energy supplied in forcing the atoms together constitutes a positive potential energy of interaction. This is known as closed shell repulsion and the potential that most accurately describes this region is the Born–Mayer potential:

$$V(r) = A \exp(-r/B), \tag{1.47}$$

where *A* and *B* are constants determined from the elastic moduli [8]. Although this function was first used by Born and Mayer to represent core ion repulsion in their theory of ionic crystals, it is perfectly valid for separations on the order of the

equilibrium separation, r_e, and is useful in treatments of threshold or near-threshold collisions where the impact parameter is of the order r_e.

When $r \ll a_0$, Coulomb interaction between the nuclei dominates all other terms in $V(r)$:

$$V(r) = \frac{Z_1 Z_2 \varepsilon^2}{r}. \tag{1.48}$$

At slightly larger distances, the nuclear charges are electrostatically "screened" by the space charge of the innermost electron shells that have entered the internuclear space. The potential describing this behavior is known as the screened Coulomb potential [8–12]:

$$V(r) = \left(\frac{Z_1 Z_2 \varepsilon^2}{r}\right) \exp(-r/a), \tag{1.49}$$

where $a = \left(\frac{9\pi^2}{128}\right)^{1/3} \frac{a_0}{(Z_1^{2/3} + Z_2^{2/3})^{1/2}} \approx \frac{Ca_0}{(Z_1 Z_2)^{1/6}}$ is the screening radius and $C = 0.8853$. More generally, screening by the electron cloud is described by a screening function, $\chi(r)$, that is defined as the ratio of the actual atomic potential at a radius r to the Coulomb potential. The function of $\chi(r)$ is to moderate the Coulomb potential to describe the interaction between atoms at all separation distances. For large distances, $\chi(r)$ will tend toward zero, and at very small distances, $\chi(r)$ will tend toward unity. This is one way in which a single interatomic potential function can be used to describe all collisions.

We have now described two regimes of interaction. At small separations ($r < a$), the screened Coulomb term dominates all others, with the screening effect decaying exponentially with the separation distance. In the region $r \lesssim r_e$, electronic interaction dominates and is best described by the Born–Mayer potential. At intermediate separations, there is no satisfactory description of the nature of atomic interaction. Unfortunately, it is exactly in this region where information is needed to provide a proper analytical description of radiation damage.

Nevertheless, we may make a first approximation to the total potential by summing the controlling potentials at large and small separations:

$$V(r) = \left(\frac{Z_1 Z_2 \varepsilon^2}{r}\right) \exp(-r/a) + A \exp(-r/B), \tag{1.50}$$

where $A = 2.58 \times 10^{-5} (Z_1 Z_2)^{11/4}$ eV and $B = 1.5 a_0/(Z_1 Z_2)^{1/6}$ are empirical formulae suggested by Brinkman [11], consistent with observed compressibilities and elastic moduli in the noble metals Cu, Ag, and Au. Unfortunately, there is little experimental information about the forces between metal atoms, which is our primary interest. Figure 1.9 shows that the first term dominates for small separation and the second for large.

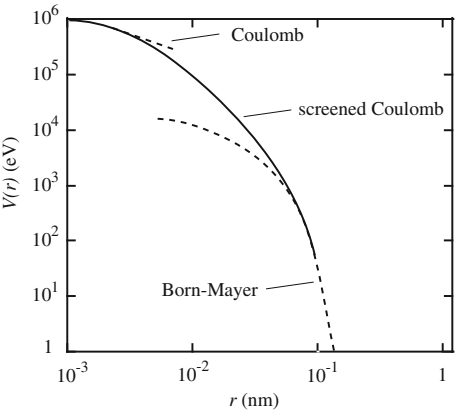

Fig. 1.9 Behavior of various potential functions over a range of separation distances between copper atoms

Brinkman suggested a model for the interaction between two identical atoms in which the nucleus is surrounded by a rigid charge distribution ρ_ε, and it is assumed that both atoms supply a screened Coulomb field of the same type:

$$V(r) = \frac{Z^2\varepsilon^2}{r} e^{-r/a}\left(1 - \frac{r}{2a}\right). \tag{1.51}$$

This relation approaches the Coulomb repulsion as r approaches zero and changes sign at $r = 2a$, becoming a weak attractive potential with a minimum at $r = a(1 + \sqrt{3})$. However, this potential predicts a strong interaction energy at large distances and may not represent the true physical picture for metals. Brinkman formulated a new potential function:

$$V(r) = \frac{AZ_1Z_2\varepsilon^2 \exp(-Br)}{1 - \exp(-Ar)}. \tag{1.52}$$

Note that for small values of r, the potential closely approximates the Coulomb repulsive interaction, i.e.,

$$\lim_{r\to 0} V(r) \to \frac{Z_1Z_2\varepsilon^2}{r},$$

and at large separation, the potential equation approximates the exponential repulsion of the Born–Mayer type:

$$\lim_{r\to\infty} V(r) \to AZ_1Z_2\varepsilon^2 \exp(-Br).$$

The constant B is defined as $B = Z_{\text{eff}}^{1/3}/Ca_0$, where $Z_{\text{eff}} = (Z_1Z_2)^{1/2}$, and C is of the order 1.0 or 1.5. The constant A depends on the compressibility and bulk modulus, which depend on the overlap of closed electron shells. An empirical

expression for A is $A = \dfrac{0.95 \times 10^{-6}}{a_0} Z_{\text{eff}}^{7/6}$ Substituting for A, B, and C (= 1.5) into Eq. (1.52) gives:

$$V(r) = 1.9 \times 10^{-6} Z_{\text{eff}}^{1/2} E_{\text{R}} \frac{\exp\left(-Z_{\text{eff}}^{1/3} r / 1.5 a_0\right)}{1 - \exp\left(-0.95 \times 10^{-6} Z_{\text{eff}}^{7/6} r / a_0\right)}, \tag{1.53}$$

where $E_{\text{R}} = \varepsilon^2/2a_0$ is the Rydberg energy (13.6 eV).

It should be noted that although the potential is a reasonably reliable function for all metals whose atomic number exceeds 25 over the range $r < 0.7 r_{\text{e}}$, it should not be used near $r = r_{\text{e}}$ since in the derivation it has been implicitly assumed that all interatomic distances are close to those of Cu, Ag, and Au. It is therefore not a valid potential to use in calculating formation and migration energies of point defects.

Two other potentials should be discussed. The first is the Firsov or Thomas–Fermi two-center potential. This potential function is an improvement over the screened Coulomb potential by virtue of the fact it takes into account the change in electron energy connected with the mutual approach of the nuclei. The potential can be written as follows:

$$V(r) = \frac{\chi(r)}{r},$$

where $\chi(r)$ is the screening function. In the case of the screened Coulomb potential:

$$\begin{aligned} \chi(r) &= \chi_{\text{B}}(r) \quad \text{and} \\ \chi_{\text{B}}(r) &= Z_1 Z_2 \varepsilon^2 \exp(-r/a), \end{aligned} \tag{1.54}$$

while in the Firsov potential:

$$\chi(r) = \chi_{\text{TF}}(r) = \chi\left[\left(Z_1^{1/2} + Z_2^{1/2}\right)^{2/3} \frac{r}{a}\right], \tag{1.55}$$

so that we have:

$$V(r) = \frac{Z_1 Z_2 \varepsilon^2}{r} \chi\left[\left(Z_1^{1/2} + Z_2^{1/2}\right)^{2/3} \frac{r}{a}\right], \tag{1.56}$$

where

$$\chi\left[\left(Z_1^{1/2} + Z_2^{1/2}\right)^{2/3} \frac{r}{a}\right]$$

is a screening function.

The second potential of interest is the Thomas–Fermi–Dirac two-center potential (TFD). The Thomas–Fermi–Dirac statistical model of the atom was employed to calculate a potential from first principles. As a consequence, this potential takes into account the exchange effects and places a finite boundary, defined by r_b, on the spatial distribution of the electron cloud density ρ_ε. The potential obtained for like atoms is as follows:

$$\overline{V}(r) = \frac{Z^2\varepsilon^2}{r}\chi\left(Z^{1/3}\frac{r}{a}\right) - \alpha Z + \overline{\Lambda}\,, \tag{1.57}$$

where $\alpha \cong 3.16 \times 10^{-3}\dfrac{\varepsilon^2}{a_0}$ and $\overline{\Lambda}$ is a set of integrals over exact single-center electron densities. Calculations using this potential have shown that for very small separations of less than $\sim 0.3a_0$, $\overline{V}(r)$ agrees well with other theoretical curves and with experiment, while in the range $\sim 0.3a_0$ to $3a_0$, $V(r)$ agrees with other theoretical and experiment results better than the screened Coulomb potential or the Firsov potential [7].

In selecting the appropriate potential for a specific collision problem, the range of separation can be determined by equating the available kinetic energy to the potential and hence obtaining the smallest separation. The important interaction terms for the calculated separation can then be determined. For interactions between metal atoms at low kinetic energies, 10^{-1} to 10^3 eV, the Born–Mayer term alone is sufficient with constants given in Eq. (1.50). In cases of atom–atom collisions in the collision cascade, where energies from 10^3 to 10^5 eV are involved, an inverse power potential is extremely convenient. Such a potential can be formulated by fitting a function C/r^s to one of the above potential functions over a limited range of r. For example, one can fit an inverse square ($s = 2$) function to the screened Coulomb potential at $r = a$, obtaining the same slope, ordinate, and curvature. This function is as follows[13]:

$$V(r) = \frac{Z_1 Z_2 \varepsilon^2 a}{r^2} e^{-1}. \tag{1.58}$$

For a limited range of r, this can be used as an approximate potential. Rewriting using the expression in Eq. (1.49) for a gives:

$$V(r) = \frac{2E_R}{e}(Z_1Z_2)^{5/6}\left(\frac{a_0}{r}\right)^2. \tag{1.59}$$

A convenient alternative for numerical calculations uses the fact that $\dfrac{2E_R}{e} \cong 10\,\text{eV}$, hence:

$$V(r) = 10(Z_1Z_2)^{5/6}\left(\frac{a_0}{r}\right)^2 \text{eV}. \tag{1.60}$$

Table 1.3 Summary of potential functions

Potential	Equation for $V(r)$ =	Range of applicability	Definitions	Eq. in text
Hard sphere	0 for $r > r_0$ ∞ for $r \leq r_0$	$10^{-1} < T < 10^3$ eV	r_0 = Atomic radius	(1.46)
Born–Mayer	$V(r) = A\exp(-r/B)$	$10^{-1} < T < 10^3$ eV $r \lesssim r_e$	A, B determined from elastic moduli	(1.47)
Simple Coulomb	$\frac{Z_1 Z_2 \varepsilon^2}{r}$	Light ions of high energy $r \ll a_0$		(1.48)
Screened Coulomb	$\left(\frac{Z_1 Z_2 \varepsilon^2}{r}\right) \exp(-r/a)$	Light ions $r < a$	a_0 = Bohr radius a = Screening radius	(1.49)
Brinkman I	$\frac{Z^2 \varepsilon^2}{r} e^{(-r/a)} \left(1 - \frac{r}{2a}\right)$	$r < a$	$a \cong a_0 / Z^{1/3}$	(1.51)
Brinkman II	$\frac{A Z_1 Z_2 \varepsilon^2 \exp(-Br)}{1 - \exp(-Ar)}$	Z > 25 $r < 0.7 r_e$	$A = \frac{0.95 \times 10^{-6}}{a_0} Z_{\text{eff}}^{7/6}$ $B = Z_{\text{eff}}^{1/3} / C a_0$ $C \cong 1.5$	(1.52)
Firsov	$\frac{Z_1 Z_2 \varepsilon^2}{r} \chi\left[\left(Z_1^{1/2} + Z_2^{1/2}\right)^{2/3} \frac{r}{a}\right]$	$r \leq a_0$	χ is screening function	(1.56)
TFD two-center	$\frac{Z^2 \varepsilon^2}{r} \chi\left(Z^{1/3} \frac{r}{a}\right) - \alpha Z + \overline{A}$	$r < r_b(3a_0)$	r_b = Radius at which the electron cloud density vanishes	(1.57)
Inverse square	$\frac{2E_R}{e} (Z_1 Z_2)^{5/6} \left(\frac{a_0}{r}\right)^2$	$a/2 < r < 5a$	E_R = Rydberg energy = 13.6 eV	(1.59)

This potential also applies to heavy ion bombardment in the energy range 10^3 to 10^5 eV. In the case of light ions at high energy, such as 5 MeV protons, the simple Coulomb potential is adequate.

Table 1.3 summarizes the various potential functions and their regions of applicability. But how do we go about verifying a potential function? For example, how do we determine the constants A and B in the Born–Mayer potential for a specific element? Since the Born–Mayer potential is based on small displacements from equilibrium (i.e., r_e), we can obtain these constants from bulk property measurement of the solid, e.g., compressibility and elastic moduli. If we expand the potential $V(r)$ as $V_0 + \left(\frac{dV}{dr}\right)_0 r + 1/2 \left(\frac{d^2V}{dr^2}\right)_0 r^2 + \cdots$, then the coefficient of $\left(\frac{d^2V}{dr^2}\right)_0$ is the curvature of the energy–distance curve at $r = r_e$ as shown in Fig. 1.8.

How then do we know that a given potential does or does not properly describe the interaction in a region of r? We can make this determination by scattering measurements or by measuring the range of ions in solids. Since $V(r)$ describes the nature of the interaction, it will also tell us about $\sigma_s(E_i)$ that can be determined by scattering experiments. Also, range measurements give a good indication of how many interactions must have occurred in order to place the ion in its deposited

location. Both of these sets of experiments will provide information on the adequacy of the chosen potential function to accurately describe the interaction between the atoms in the solid.

With some appreciation for the way in which neutral atoms or atoms and ions interact, we are now prepared to describe a collision between these species, which is in some ways very similar to and in other ways very different from neutron–nuclear collisions. The resulting formalism will provide us with the tools to determine the energy transferred from the incident atom to the struck atom along with the energy transfer cross section. The following treatment is adapted from Thompson [13].

1.2.2 Collision Kinematics

The orbits of two colliding atoms are shown in Fig. 1.10 relative to the center of mass of the masses M_1 and M_2. Particle locations are most conveniently denoted in polar coordinates (r_1, ψ) and (r_2, ψ) for masses M_1 and M_2, respectively. The impact parameter is b, ψ is the scattering angle of the struck atom in the laboratory system, and ϕ is the asymptotic scattering angle when the interparticle spacing approaches infinity. The impact parameter is defined as the distance between the asymptotic trajectories of the colliding particles as shown in Fig. 1.10. We are interested in determining the detailed orbits by expressing ϕ as a function of b. This result will then be used to determine the scattering cross section.

The radial and transverse velocities of mass M_1 are $\dot{r}_1$ and $r_1\dot{\psi}$ in polar coordinates, and the resultant velocity is $\left(\dot{r}_1^2 + r_1^2\dot{\psi}^2\right)^{1/2}$. The velocity components are the same for mass M_2 with the subscript 2 substituted for 1. Conservation of energy requires that the total energy of any system remains constant. The energy in the laboratory reference

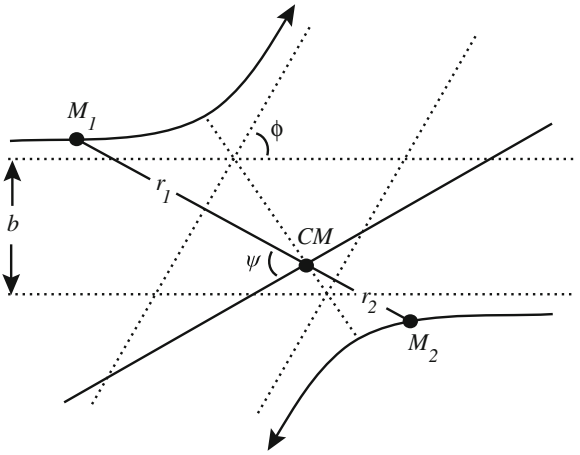

Fig. 1.10 Collision orbits in the center-of-mass system

system is just $E_i = \frac{1}{2}M_1 v_\ell^2 = E_T$ Recall that $V_{CM} = \frac{M_1}{M_1 + M_2} v_\ell$ and that the kinetic energy of the center of mass itself (in the laboratory system) is as follows:

$$E_{CM} = \frac{1}{2}(M_1 + M_2)V_{CM}^2 = \left(\frac{M_1}{M_1 + M_2}\right)E_i.$$

Hence, the energy in the CM system that is available for transformation is the total kinetic energy less the motion energy of the CM system:

$$E = E_T - E_{CM} = E_i - E_{CM} = E_i\left(\frac{M_2}{M_1 + M_2}\right). \tag{1.61}$$

In an elastic collision, the sum of the potential and kinetic energies at any point in the orbit must equal the asymptotic sum of kinetic energies, so:

$$\begin{array}{lll} E_i\left(\dfrac{M_2}{M_1 + M_2}\right) & = \dfrac{1}{2}M_1(\dot{r}_1^2 + r_1^2\dot{\psi}^2) + \dfrac{1}{2}M_2(\dot{r}_2^2 + r_2^2\dot{\psi}^2) + V(r_1 + r_2). & \\ \text{asymptotic} & \text{sum of kinetic energy at any point} & \text{potential} \\ \text{energy} & \text{in orbit} & \text{energy} \end{array} \tag{1.62}$$

Letting $r = r_1 + r_2$ be the total separation distance, $r_1 = \frac{M_2}{M_1 + M_2}r,\ r_2 = \frac{M_1}{M_1 + M_2}r$, and the energy balance of Eq. (1.62) simplifies to:

$$\eta E_i = \frac{1}{2}\mu(\dot{r}^2 + r^2\dot{\psi}^2) + V(r), \tag{1.63}$$

where $\eta = \frac{M_2}{M_1 + M_2}$ and $\mu = \frac{M_1 M_2}{M_1 + M_2}$ is the reduced mass.

The law of conservation of angular momentum demands that the value at any point in the orbit must equal the asymptotic value. Recall that:

$$v_\ell = v_\ell - V_{CM} = v_\ell\left(\frac{M_2}{M_1 + M_2}\right) \text{ and } V_2 = V_{CM} = v_\ell\left(\frac{M_1}{M_1 + M_2}\right),$$

so that the asymptotic value of the angular momentum is given by:

$$M_1 v_1 b_1 + M_2 v_2 b_2 = \left(\frac{M_1 M_2}{M_1 + M_2}\right) v_\ell(b_1 + b_2) = \mu b v_\ell. \tag{1.64}$$

The angular momentum at any point is given by:

$$\begin{aligned} M_1 r_1^2\dot{\psi} + M_2 r_2^2\dot{\psi} &= \left[M_1\left(\frac{M_2}{M_1 + M_2}r\right)^2 + M_2\left(\frac{M_1}{M_1 + M_2}r\right)^2\right]\dot{\psi} \\ &= \mu r^2\dot{\psi}, \end{aligned} \tag{1.65}$$

hence:

$$\mu r^2 \dot{\psi} = \mu b v_\ell. \tag{1.66}$$

Substituting from Eq. (1.66) into Eq. (1.63) to eliminate $\dot{\psi}$ and solving for $\dot{r}$, we obtain:

$$\dot{r} = \left(\frac{2}{\mu}\right)^{1/2} \left[\eta E_\mathrm{i}\left(1 - \frac{b^2}{r^2}\right) - V(r)\right]^{1/2}. \tag{1.67}$$

The algebra for this step is as follows. Multiplying out the terms of Eq. (1.63) gives:

$$\eta E_\mathrm{i} - \frac{1}{2}\mu \dot{r}^2 = \frac{1}{2}\mu \frac{v_\ell^2 b^2}{r^2} + V(r),$$

and rearranging gives:

$$\eta E_\mathrm{i} - \frac{1}{2}\mu \frac{v_\ell^2 b^2}{r^2} = \frac{1}{2}\mu \dot{r}^2 + V(r). \tag{1.68}$$

Recall that $E_\mathrm{i} = 1/2 M_1 v_\ell^2$ and therefore $v_\ell^2 = 2E_\mathrm{i}/M_1$, and we can eliminate v_ℓ so that the second term on the left-hand side of Eq. (1.68) becomes $-\dfrac{\mu b^2 E_\mathrm{i}}{M_1 r^2}$. Since $\mu = \dfrac{M_1 M_2}{M_1 + M_2}$ and $\mu/M_1 = \eta$, then:

$$\eta E_\mathrm{i} - \eta E_\mathrm{i} \frac{b^2}{r^2} = \frac{\mu \dot{r}^2}{2} + V(r), \quad \text{and} \quad \eta E_\mathrm{i}\left(1 - \frac{b^2}{r^2}\right) = \frac{\mu \dot{r}^2}{2} + V(r),$$

or

$$\dot{r} = \left(\frac{2}{\mu}\right)^{1/2} \left[\eta E_\mathrm{i}\left(1 - \frac{b^2}{r^2}\right) - V(r)\right]^{1/2},$$

which is the same as in Eq. (1.67). Note that r reaches the distance of closest approach, ρ, when $\dot{r} = 0$. At this point:

$$V(\rho) = \eta E_\mathrm{i}\left(1 - \frac{b^2}{\rho^2}\right), \tag{1.69}$$

and $V_\mathrm{max} = \eta E_\mathrm{i}$ (at $b = 0$) which represents a "head-on" collision. So if a particle strikes a target atom of equal mass, then $V_\mathrm{max} = 1/2 E_\mathrm{i}$. When $r \to \infty$, $V(r) \to 0$ and $\dot{r}^2 = \left(\dfrac{2}{\mu}\right)\eta E_\mathrm{i}$, or $\dot{r}^2 = 2E_\mathrm{i}/M_1$, $E_\mathrm{i} = 1/2 M_1 \dot{r}^2$ (and $\dot{r} = v_\ell$ at $r \to \infty$), so $E_\mathrm{i} = 1/2 M_1 v_\ell^2$.

Recall that we are looking for ϕ as a function of b. Going back to Eq. (1.67) and dividing $\dot{r}$ in Eq. (1.67) by $\dot{\psi}$ from Eq. (1.66), we have:

$$\frac{\dot{r}}{\dot{\psi}} = \frac{\mathrm{d}r}{\mathrm{d}\psi} = -\left(\frac{2}{\mu}\right)^{1/2}\left[\mu E_\mathrm{i}\left(1-\frac{b^2}{r^2}\right) - V(r)\right]^{1/2}\frac{r^2}{\upsilon_\ell b}. \tag{1.70}$$

The minus sign in front of the quantity to the right of the equality is because for the first half of the orbit, $\dot{r}$ decreases as ψ increases. Bringing the term r^2 under the square root gives:

$$\frac{\mathrm{d}r}{\mathrm{d}\psi} = -\frac{1}{\upsilon_\ell b}\left(\frac{2}{\mu}\right)^{1/2}\left[\mu E_\mathrm{i}(r^4 - r^2b^2) - r^4V(r)\right]^{1/2}. \tag{1.71}$$

Dividing the terms under the square root by $\eta E_\mathrm{i} b^2$ to bring this term out of the square root gives:

$$\frac{\mathrm{d}r}{\mathrm{d}\psi} = -\frac{1}{\upsilon_\ell b}\left(\frac{2}{\mu}\right)^{1/2}(\eta E_\mathrm{i})^{1/2} b\left[\frac{r^4}{b^2}\left(1-\frac{V(r)}{\eta E_\mathrm{i}}\right) - r^2\right]^{1/2}. \tag{1.72}$$

Since $1/2M_1\upsilon_\ell^2 = E_\mathrm{i}$, then $\upsilon_\ell = (2E_\mathrm{i}/M_1)^{1/2}$, and substituting for υ_ℓ gives:

$$\begin{aligned}\frac{\mathrm{d}r}{\mathrm{d}\psi} &= -\left(\frac{2}{\mu}\frac{M_1}{2E_\mathrm{i}}\eta E_\mathrm{i}\right)^{1/2}\left[\frac{r^4}{b^2}\left(1-\frac{V(r)}{\eta E_\mathrm{i}}\right) - r^2\right]^{1/2} \\ &= -\left(\frac{M_1}{\mu}\eta\right)^{1/2}\left[\frac{r^4}{b^2}\left(1-\frac{V(r)}{\eta E_\mathrm{i}}\right) - r^2\right]^{1/2} \\ &= -\left[\frac{r^4}{b^2}\left(1-\frac{V(r)}{\eta E_\mathrm{i}}\right) - r^2\right]^{1/2}.\end{aligned} \tag{1.73}$$

Substituting for $x = 1/r$ gives:

$$\frac{\mathrm{d}x}{\mathrm{d}\psi} = \left[\frac{1}{b^2}\left(1-\frac{V(x)}{\eta E_\mathrm{i}}\right) - x^2\right]^{1/2}. \tag{1.74}$$

This is the equation of orbit [$\psi = f(x)$].

The scattering angle ϕ is found by expressing $\mathrm{d}\psi$ as a function of x and $\mathrm{d}x$ and integrating from the limits on ψ corresponding to $x = 0$ and $1/\rho$. These limits are $\phi/2$

and $\pi/2$, respectively, as shown in Fig. 1.10. Performing this integration for the first half of the orbit yields:

$$\int_{\phi/2}^{\pi/2} \mathrm{d}\psi = \int_{0}^{1/\rho} \left[\frac{1}{b^2}\left(1 - \frac{V(x)}{\eta E_\mathrm{i}}\right) - x^2\right]^{-1/2} \mathrm{d}x, \tag{1.75}$$

and

$$\phi = \pi - 2\int_{0}^{1/\rho} \left[\frac{1}{b^2}\left(1 - \frac{V(x)}{\eta E_\mathrm{i}}\right) - x^2\right]^{-1/2} \mathrm{d}x. \tag{1.76}$$

The quantity ρ in the upper limit of x is the value of r when $\psi = \pi/2$ and hence is the distance of closest approach. Since $\mathrm{d}x/\mathrm{d}\psi = 0$ when $\psi = \pi/2$, ρ is given from Eq. (1.74) by:

$$\eta E_\mathrm{i} = \frac{V(\rho)}{1 - \dfrac{b^2}{\rho^2}}. \tag{1.77}$$

Equations (1.76) and (1.77) provide the relation between ϕ and b.

We have yet to determine the cross section for our scattering event. This may be done as follows. If particles M_1 are bombarding target atoms M_2, then in Fig. 1.11, those ions which cross an area $2\pi b\mathrm{d}b$ enclosed by circles of radii b and $b + \mathrm{d}b$ will be scattered into $\mathrm{d}\phi$ about ϕ. Since the relation between $\mathrm{d}b$ and $\mathrm{d}\phi$ can be obtained from Eq. (1.76) by differentiation, the differential cross section is given by:

$$\sigma_\mathrm{s}(E_\mathrm{i}, T)\mathrm{d}T = 2\pi b\mathrm{d}b \quad \text{and} \quad \sigma_\mathrm{s}(E_\mathrm{i}, T) = 2\pi b\frac{\mathrm{d}b}{\mathrm{d}\phi}\frac{\mathrm{d}\phi}{\mathrm{d}T}. \tag{1.78}$$

Knowing $V(r)$ enables ϕ to be written in terms of b^2 using Eq. (1.76) and then in terms of T using Eq. (1.13). Differentiating gives $2\pi b\mathrm{d}b$ as a function of T and $\mathrm{d}T$.

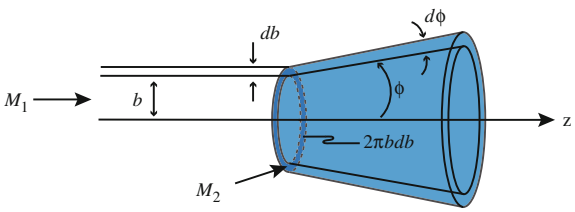

Fig. 1.11 Scattering of ions crossing an area $2\pi b\mathrm{d}b$ into an angular element $\mathrm{d}\phi$ about ϕ

Then from Eq. (1.78), the differential cross section for collisions having recoils in dT about T follows. The total cross section for collisions with T anywhere in the range $\check{T}$ to γE_i is as follows:

$$\sigma(E_i) = \int_{\check{T}}^{\gamma E_i} \sigma_s(E_i, T)\mathrm{d}T. \tag{1.79}$$

The process for finding the energy transfer cross section can be summarized as follows:

1. Select a potential function $V(r)$.
2. Use Eq. (1.76) to obtain b as a function of ϕ, $b = f(\phi)$.
3. Use Eq. (1.13) to obtain ϕ as a function of T, $\phi = g(T)$.
4. Use the relations between b and ϕ and between ϕ and T in Eq. (1.78) to obtain the energy transfer cross section.

The preceding description of the energy transfer cross section emphasizes the importance of knowing the potential function describing the particular ion–atom or atom–atom interaction of interest. Without accurate knowledge of the potential function, further description of the collision process and the ensuing defect structure become impossible. Unfortunately, explicit evaluation of the integral in Eq. (1.76) is possible only for simple potential functions. But before looking further at the various potential functions and their application in determining the energy transfer cross section, we must first consider the different possible classes of ions and their corresponding energies.

Classification of Ions

There are three important classes of ions in ion–atom collisions. The first is light energetic ions with $E_i > 1$ MeV. The second is highly energetic ($E_i \sim 10^2$ MeV) heavy ions such as fission fragments ($M \sim 10^2$). The third is lower energy heavy ions that may be produced by an accelerator or appear as a recoil that results from an earlier high-energy collision. The energy of these recoils is generally less than 1 MeV.

For each of these interactions, we must decide on the most appropriate potential function. A convenient guide is ρ/a, the ratio of the distance of closest approach to the screening radius as a function of the recoil energy, T. A rough graph of ρ/a versus T is provided in Fig. 1.12 to aid in the selection of the most appropriate potential. The three curves represent ions of each of the three classes just discussed: (1) 20 MeV protons, (2) 70 MeV fission fragments, and (3) 50 keV Cu ions. Curve (1) collisions apply to the regime where $\rho \ll a$ and the simple Coulomb potential is adequate. Curve (2) collisions that are head-on will have $\rho \ll a$ also. But for glancing collisions, $\rho \sim a$ and the screened Coulomb potential is most appropriate. Curve (3) represents the

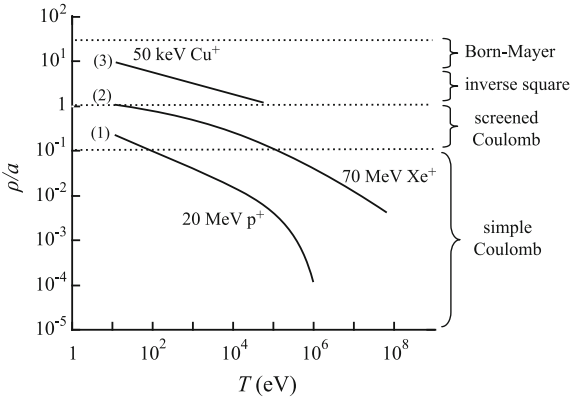

Fig. 1.12 Distance of closest approach ρ/a, as a function of T for (*1*) 20 MeV protons in Cu, (*2*) 70 MeV Xe^+ ions in Cu, and (*3*) 50 keV Cu^+ recoils in Cu (from [12])

region where $a < \rho \ll 5a$ and the inverse square potential or Brinkman potential would apply since both the Born–Mayer and screened Coulomb terms must be accounted for.

Hard Sphere-Type Collisions

The hard sphere potential is appropriate for ion energies below about 50 keV and for near head-on elastic collisions. Here, $\rho \sim r_e$ and atoms will act like hard spheres. In a head-on collision, $b = 0$ and from Eq. (1.77), we have:

$$\eta E_i = V(\rho). \tag{1.80}$$

When b is not quite zero, the collision may be pictured as shown in Fig. 1.13 where we define $R_1 = \rho \dfrac{M_2}{M_1 + M_2}$ and $R_2 = \rho \dfrac{M_1}{M_1 + M_2}$. If ρ is known, then from the figure:

$$b = \rho \cos \frac{\phi}{2}. \tag{1.81}$$

Now, recalling that:

$$\begin{aligned} \sigma_s(E_i, T)\, dT &= 2\pi b\, db \\ \sigma_s(E_i, T) &= 2\pi b \frac{db}{d\phi}\frac{d\phi}{dT}, \end{aligned} \tag{1.82}$$

where $\dfrac{db}{d\phi} = 1/2\rho \sin \phi/2$ from $b = \rho \cos \phi/2$ (using the absolute value of the derivative to maintain $\dfrac{db}{d\phi}$ as a positive value) and $\dfrac{d\phi}{dT} = \dfrac{2}{\gamma E_i \sin \phi}$ from $T = \dfrac{\gamma E_i}{2}(1 - \cos \phi)$. Then $\sigma_s(E_i, T) = 2\pi\rho \cos \phi/2 \dfrac{\rho}{2} \sin \phi/2 \dfrac{2}{\gamma E_i \sin \phi}$, and

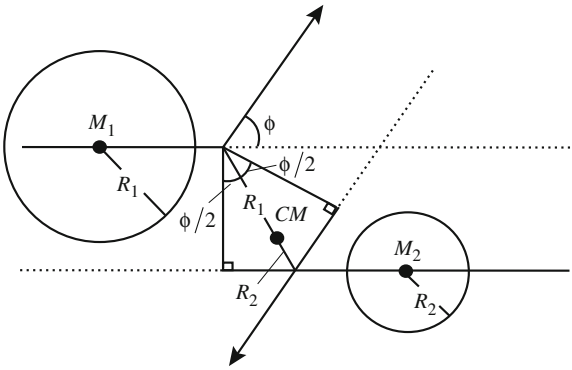

Fig. 1.13 Schematic of colliding atoms obeying the hard sphere approximation for collisions

$$\sigma_s(E_i, T) = \frac{\pi\rho^2}{\gamma E_i}. \tag{1.83}$$

Recall that for neutron–nuclear interactions, $\sigma_s(E_i, T) = \sigma_s(E_i)/\gamma E_i$. Using this relation, we can obtain an idea of the size of the energy transfer cross section for neutron–nuclear interactions versus atom–atom interactions: $\frac{\sigma_s(E_i, T)^{a-a}}{\sigma_s(E_i, T)^{\text{n-nuclear}}} = \frac{\pi\rho^2}{\sigma_s(E_i)} \sim \frac{\pi(10^{-8})^2}{10^{-24}} \sim 10^8$, and so the energy transfer cross section for atom–atom interactions is about eight orders of magnitude greater than that for neutron–nuclear interactions.

The total scattering cross section is as follows:

$$\sigma_s(E_i) = \int_{\check{T}}^{\gamma E_i} \sigma_s(E_i, T)\mathrm{d}T = \int_{\check{T}}^{\gamma E_i} \frac{\pi\rho^2}{\gamma E_i}\mathrm{d}T = \frac{\pi\rho^2}{\gamma E_i}[\gamma E_i - \check{T}] = \pi\rho^2. \tag{1.84}$$

Note that $\sigma_s(E_i)$ is independent of E_i (because $\rho \neq f(E_i)$) and that $\sigma_s(E_i, T) \propto 1/E_i$ and is independent of T. We can find $\sigma_s(E_i, T)$ explicitly by applying the appropriate potential function to find a value of ρ (determined by $V(r)$). Recall from our discussions in Sect. 1.2.1 that for collisions in which the impact parameter is on the order of the equilibrium separation of the atoms, the Born–Mayer potential is most appropriate. This corresponds to energies below about 10 keV. (Note that this means that we are also backing off from a pure hard sphere model.) Hence, we will use $V(r) = A\exp(-r/B)$, where A and B are defined in Eq. (1.47). Using Eq. (1.80) gives:

$$V(\rho) = A\exp(-\rho/B) = \eta E_i, \tag{1.85}$$

or

$$\rho = B \ln\left(\frac{A}{\eta E_{\mathrm{i}}}\right), \tag{1.86}$$

and since $b = \rho \cos \phi/2 = B\ln(A/\eta E_{\mathrm{i}})\cos \phi/2$, the energy transfer cross section is as follows:

$$\sigma_{\mathrm{s}}(E_{\mathrm{i}}, T) = \frac{\pi B^2}{\gamma E_{\mathrm{i}}}\left[\ln\frac{A}{\eta E_{\mathrm{i}}}\right]^2. \tag{1.87}$$

The total scattering cross section is then the integral of the energy transfer cross section between the limits $\check{T}$ and γE_{i}:

$$\sigma_{\mathrm{s}}(E_{\mathrm{i}}) = \int_{\check{T}}^{\gamma E_{\mathrm{i}}} \pi B^2 \left[\ln\frac{A}{\eta E_{\mathrm{i}}}\right]^2 \frac{1}{\gamma E_{\mathrm{i}}} \mathrm{d}T. \tag{1.88}$$

From this expression, we will be able to calculate the total cross section for displacement scattering events for all allowed T. Note that the total scattering cross section depends on E_{i}. Also, for typical values of A, B, and $\check{T}$ (40 eV), the value of $\sigma_{\mathrm{s}}(E_{\mathrm{i}})$ for atom–atom interactions is about 10^8 times that for neutron–nuclear events.

Rutherford Scattering

Let us turn now to a second example in which we will use the pure Coulomb scattering potential to demonstrate Rutherford scattering. From our classification of ions according to ion energy and mass, type 1 collisions involve light ($m \sim$ 1–4) energetic ($E >$ MeV) ions where $\rho \ll a$. Collisions of this sort are adequately represented by the simple Coulomb potential, which from Eq. (1.48) is as follows:

$$V(r) = \frac{Z_1 Z_2 \varepsilon^2}{r}.$$

We will assume that Z_1 and Z_2 represent the nuclear charges and that this collision occurs at high energies so that electrons are stripped from the nuclei and the only interaction is between the nuclei.

In our description of the trajectories of the particles in the CM system, we found that at the point of closest approach, $\mathrm{d}x/\mathrm{d}\psi = 0$ and from Eq. (1.77):

$$\eta E_{\mathrm{i}} = \frac{V(\rho)}{1 - \dfrac{b^2}{\rho^2}}.$$

Substituting in for $V(r)$ gives:

$$\frac{Z_1 Z_2 \varepsilon^2}{\rho} = \eta E_\mathrm{i}\left(1 - \frac{b^2}{\rho^2}\right). \tag{1.89}$$

Defining:

$$b_0 = \left(\frac{Z_1 Z_2 \varepsilon^2}{\eta E_\mathrm{i}}\right), \tag{1.90}$$

it follows that:

$$\frac{b_0}{\rho} = 1 - \frac{b^2}{\rho^2}, \tag{1.91}$$

and

$$\rho = \frac{b_0}{2}\left[1 + \left(1 + \frac{4b^2}{b_0^2}\right)^{1/2}\right]. \tag{1.92}$$

Hence, the distance of closest approach is a function of the impact parameter b, as expected. For head-on collisions, $b = 0$ and the minimum value of ρ depends on E_i:

$$\rho(b = 0) = \rho_0 = b_0 = \frac{Z_1 Z_2 \varepsilon^2}{\eta E_\mathrm{i}}. \tag{1.93}$$

Note that for this type of collision, ρ depends on E_i, in contrast to independence of E_i in the hard sphere model. Going back to the orbital Eq. (1.75), we will now evaluate it as a definite integral:

$$\int_{\pi/2}^{\phi/2} \mathrm{d}\psi = \int_{1/\rho}^{0} \left[\frac{1}{b^2} - \frac{b_0}{b^2}x - x^2\right]^{-1/2} \mathrm{d}x. \tag{1.94}$$

Since $\psi = \pi/2$ when $r = \rho(x = 1/\rho)$ and $\psi = \phi/2$ when $r = \infty$ $(x = 0)$, letting $y = x + \dfrac{b_0}{2b^2}$ gives:

$$\phi/2 - \pi/2 = \int_{\frac{1}{\rho} + \frac{b_0}{2b^2}}^{\frac{b_0}{2b^2}} [c^2 - y^2]^{-1/2} \mathrm{d}y, \tag{1.95}$$

where $c^2 = \left(\frac{1}{b^2} + \frac{b_0^2}{4b^4}\right)$. The orbits are then as follows:

$$\begin{aligned}\phi/2 - \pi/2 &= \left[\sin^{-1}\frac{y}{c}\right]_{\frac{1}{\rho}+\frac{b_0}{2b^2}}^{\frac{b_0}{2b^2}} \\ &= \sin^{-1}\frac{b_0}{2b^2 c} - \sin^{-1}\frac{1}{c}\left(\frac{1}{\rho} + \frac{b_0}{2b^2}\right).\end{aligned} \tag{1.96}$$

Since $\sin^{-1}\frac{1}{c}\left(\frac{1}{\rho} + \frac{b_0}{2b^2}\right) = \sin^{-1}(1) = \pi/2$, then:

$$\sin\phi/2 = \frac{b_0}{2b^2 c}. \tag{1.97}$$

Substituting for c (from above) into Eq. (1.97) yields:

$$\sin^2\phi/2 = \frac{1}{1 + \frac{4b^2}{b_0^2}}. \tag{1.98}$$

Using trigonometric relations for $\sin^2\phi/2$, we have:

$$b = \frac{b_0}{2}\cot\phi/2. \tag{1.99}$$

We now have a relationship between the impact parameter, b, and the asymptotic scattering angle, ϕ. Note that b is a function of E_i through b_0 (Eq. (1.93)).

We now want an expression for the scattering cross section. Using Eq. (1.82) for $\sigma_\mathrm{s}(E_\mathrm{i}, T)$, we have:

$$\sigma_\mathrm{s}(E_\mathrm{i}, T)\,\mathrm{d}T = \sigma_\mathrm{s}(E_\mathrm{i}, \phi)\,\mathrm{d}\Omega = 2\pi b\mathrm{d}b = \pi b_0 \cot\frac{\phi}{2}\,\mathrm{d}b, \tag{1.100}$$

and substituting for db from Eq. (1.99) gives:

$$\sigma_\mathrm{s}(E_\mathrm{i}, \phi) = \left(\frac{b_0}{4}\right)^2 \frac{1}{\sin^4(\phi/2)}, \tag{1.101}$$

which is the Rutherford inverse fourth power scattering law. The cross section for recoil is exactly the same as for elastic collisions, Eq. (1.13), and since:

$$\sigma_\mathrm{s}(E_\mathrm{i}, T) = \sigma_\mathrm{s}(E_\mathrm{i}, \phi)\frac{\mathrm{d}\Omega}{\mathrm{d}T},$$

we have:

$$\sigma_s(E_i, T) = \frac{\pi b_0^2}{4}\frac{\gamma E_i}{T^2}. \tag{1.102}$$

Note that unlike neutron–nuclear collisions and hard sphere scattering in general, the Rutherford scattering cross section is a strong function of T. This expression also shows that the scattering cross section $\sigma_s(E_i, T) \rightarrow \infty$ as $T \rightarrow 0$. But this is just a reflection of the fact that as $\phi \rightarrow 0$ and $b \rightarrow \infty$ and is representative of long-range Coulomb interactions. In reality, there is a cutoff in b and hence in ϕ due to electron screening. As we will see later, this cutoff is E_d, the displacement energy. The average energy transferred is then as follows:

$$\overline{T} = \frac{\int_{\check{T}}^{\hat{T}} T\sigma_s(E_i, T)\,dT}{\int_{\check{T}}^{\hat{T}} \sigma_s(E_i, T)\,dT} = \frac{\check{T}\ln(\hat{T}/\check{T})}{1 - \frac{\check{T}}{\hat{T}}}. \tag{1.103}$$

For $\hat{T} = \gamma E_i$ and $\check{T} = E_d$ and since $\gamma E_i \gg E_d$, then:

$$\overline{T} \approx E_d \ln\left(\frac{\gamma E_i}{E_d}\right), \tag{1.104}$$

which is quite small for all energies E_i, reflecting the strong T^{-2} dependence in Eq. (1.102).

The integral of Eq. (1.102) over T gives the total cross section for displacement events by an ion of energy E_i:

$$\sigma_s(E_i) = \frac{\pi}{4} b_0^2 \hat{T} \int_{E_d}^{\hat{T}} \frac{dT}{T^2} = \frac{\pi b_0^2}{4}\left(\frac{\hat{T}}{E_d} - 1\right), \tag{1.105}$$

and since at high energies $\hat{T}/E_d \gg 1$ then we have for $\hat{T} = \gamma E_i$:

$$\sigma_s(E_i) \approx \frac{\pi b_0^2}{4}\frac{\gamma E_i}{E_d}, \tag{1.106}$$

which is quite large.

A critical question in applying the above results is under what conditions can Rutherford scattering be applied? The answer is that we must require that during an

encounter, the major part of scattering occurs in the region where $r \ll a$ But this is a qualitative measure. What is needed is a means for determining quantitatively, when Rutherford scattering applies. To address this question, we consider two cases.

Case 1: Near "head-on" collisions (*high T*). For near head-on collision, $\rho_0 \ll a$ or $E_\mathrm{i} \gg E_a$, where E_a is the value of E_i that would give $\rho_0 = a$ assuming a screened Coulomb potential:

$$E_a = \frac{2E_\mathrm{R}}{C}(Z_1 Z_2)^{7/6}\frac{M_1 + M_2}{M_2 e}, \tag{1.107}$$

which is obtained by rewriting the screened Coulomb potential (Eq. (1.49)) in an inverse square law form (Eq. (1.59)), with $\varepsilon^2 = 2a_0 E_\mathrm{R}$ and equating at $r = a$ and setting $V(r) = \eta E_\mathrm{i} = \dfrac{M_2}{M_1 + M_2}E_\mathrm{i}$ for a head-on collision.

Case 2: Glancing collisions (*low T*). Here, we only consider those collisions in which $b \le a$, or that result in an energy transfer $\check{T} \sim E_\mathrm{d}$ for $b = a$. For a simple Coulomb collision with $b = a$, we have from Eqs. (1.98) and (1.13):

$$T = \frac{e^2\gamma E_a^2}{4E_\mathrm{i}}, \text{ or } E_\mathrm{i} = \frac{e^2\gamma E_a^2}{4T}, \tag{1.108}$$

and giving this value of E_i the name E_b at $T = \check{T}$, we have

$$E_b = \frac{e^2\gamma E_a^2}{4\check{T}}, \quad \text{where} \quad \check{T} = E_\mathrm{d}, \tag{1.109}$$

and this equation is valid for all $E_\mathrm{i} \gg E_b$. Essentially, E_b is the value of E_i that results in a transfer of energy $T \ge E_\mathrm{d}$ at $b = a$. Or looking at it another way, values of $E_b < E_\mathrm{i}$ give $T \ll \check{T}$ and can be neglected since $\rho \ge a$, and these encounters can be neglected. Table 1.4 provides examples of the values of E_a and E_b for different particle–target atom combinations and energies. From Table 1.4, since $E_a < E_b$, we can use the criterion that E_i must be $\gg E_b$ as an extreme test of the validity of the simple Coulomb scattering description.

In summary, if $E_\mathrm{i} \gg E_a$, the simple Coulomb potential may be used for near head-on collisions. If $E_\mathrm{i} \gg E_b$, it can be used for all collisions of interest in radiation damage. Light charged particles such as protons and alphas with $E_\mathrm{i} > 1$ MeV fall into this category, while fission fragments are in the regime $E_a < E_\mathrm{i} < E_b$ and recoils have $E_\mathrm{i} \le \mathrm{E}_a$. These will be discussed next. But first, we present an example of Rutherford scattering.

Table 1.4 Values of E_a and E_b for various particle–target atom combinations and energies (from [13])

Incident particle	Target atom	E_a (eV)	E_b (eV)
C	C	2×10^3	8×10^5
Al	Al	1×10^4	2×10^7
Cu	Cu	7×10^4	1×10^9
Au	Au	7×10^5	1×10^{11}
Xe	U	5×10^5	3×10^{10}
D	C	1.5×10^2	2×10^3
D	Cu	1×10^3	2×10^4
D	C	4×10^3	1×10^5

Example 1.2. 2 MeV protons on aluminum
For this case,

$$\hat{T} = \gamma E_\mathrm{i} = \frac{4(27)}{(27+1)^2} 2\,\mathrm{MeV} = 0.28\,\mathrm{MeV}$$

$$\check{T} = 40\,\mathrm{eV}$$

$$\overline{T} = E_\mathrm{d} \ln\left(\frac{\gamma E_\mathrm{i}}{E_\mathrm{d}}\right) = 354\,\mathrm{eV}$$

We can also calculate $E_a \sim 200$ eV and $E_b \sim 2500$ eV. (For comparison, 2 MeV He^+ on Al, $E_a \sim 1$ keV, and $E_b \sim 16$ keV. Also, for 2 MeV H^+ on Au, $E_a \sim 1.6$ keV, and $E_b \sim 24$ keV; and for 2 MeV He^+ on Au, $E_a \sim 8$ keV, and $E_b \sim 42$ keV.) Since $E_\mathrm{i} \gg E_b$, the simple Coulomb law is valid for this type of collision. Incidentally, $\sigma(E_\mathrm{i}) \sim 4 \times 10^{-22}$ cm^2, and since the mean free path between collisions is $\lambda = 1/\sigma N$ and $N \sim 6 \times 10^{22}$ a/cm^3, then $\lambda \sim 0.04$ cm or about 400 μm, or about 10 times the length of a 2 MeV proton track in Al. This means that there is, on average, only one Rutherford scattering collision for every 10 protons incident on Al.

Now, let us investigate the other classes of ion–atom collisions such as heavy energetic ions, heavy slow ions, and high-energy electrons.

Heavy Energetic Ions
For heavy energetic ions such as fission fragments, Fig. 1.12 shows that an appropriate potential must account for both screened Coulomb and closed shell repulsion. Let us look first at the simple Coulomb potential as a rough approximation, knowing that its use is only justified for recoil energies approaching γE_i where $\rho \ll a$. Recall that $\sigma_\mathrm{s}(E_\mathrm{i}) = \frac{\pi b_0^2}{4}\frac{\gamma E_\mathrm{i}}{E_\mathrm{d}}$, and $b_0 \propto \frac{Z_1}{\gamma E_\mathrm{i}}, \gamma = \frac{4M_1M_2}{(M_1+M_2)^2}, \eta = \frac{M_2}{M_1+M_2}$, which gives an increase in the cross section compared to the light ion by a factor of

$$\frac{\sigma_{\mathrm{s,heavy}}}{\sigma_{\mathrm{s,light}}} = \frac{\left.\dfrac{z_1^2 M_1}{E_\mathrm{i}}\right|_{\mathrm{heavy}}}{\left.\dfrac{z_1^2 M_1}{E_\mathrm{i}}\right|_{\mathrm{light}}} \approx 10^6$$

for the same value of E_i and for fission fragments at the peaks of the fission yield of uranium, $M_1^{\mathrm{light}} \simeq 96$ amu, $E_1^{\mathrm{light}} \simeq 95$ MeV and $M_1^{\mathrm{heavy}} \simeq 137$ amu, $E_1^{\mathrm{heavy}} \simeq 55$ MeV. Comparing to the example of the 2 MeV proton on Al, fission fragments have a cross section that is larger by a factor of 10^4! Therefore, the mean free path is 10^{-4} that of a proton in Al.

Recall that $\sigma_\mathrm{s}(E_\mathrm{i}, T)$ varies as $1/T^2$. But this is only true near $\gamma E_\mathrm{i}(\rho \ll a)$. At lower energies, screening will reduce the sensitivity to energy. So we must use a better description of the interaction between energetic, heavy ions, and target atoms. Brinkman's expression, Eq. (1.50), includes both terms, and if this is used in the impulse approximation (see [13]), the result is as follows:

$$T = \frac{M_1}{M_2}\frac{A^2}{E_\mathrm{i}}\left[F\left(\alpha, \frac{b}{B}\right) - (1-\alpha)F\left(1+\alpha, \frac{b}{B}\right)\right]^2, \tag{1.110}$$

where A and B are given in Eq. (1.50) and

$$\begin{aligned} F\left(\alpha, \frac{b}{B}\right) &= \frac{b}{B}\int_{b/a}^{\infty} \frac{-e^{-x}\mathrm{d}x}{\left(x^2 - b^2/a^2\right)^{1/2}\left(1-e^{-\alpha x}\right)^2} \\ &= \frac{b}{B}\sum_{n=0}^{\infty}(n+1)K_0\left\{\frac{b}{B}(1+n\alpha)\right\}, \end{aligned} \tag{1.111}$$

where $K_0(y)$ is a Bessel function of the third kind. The term α is the ratio of Born–Mayer and screened Coulomb terms at $r = a$, so in general, $\alpha < 1$. T can be found from b and Eq. (1.110), and by inversion, b is obtained as a function of T. Differentiation gives $\sigma = 2\pi b\mathrm{d}b$. However, because of the complexity of Eq. (1.110), numerical solutions are required. Nevertheless, we may calculate $\mathrm{d}N$, the number of recoils in $\mathrm{d}T$ at T produced by the fission fragment in slowing down to rest. This is found by:

$$\mathrm{d}N = n\sigma\mathrm{d}x = n\frac{\mathrm{d}\sigma}{\mathrm{d}T}\left(-\frac{\mathrm{d}E}{\mathrm{d}x}\right)^{-1}\mathrm{d}E\mathrm{d}T, \tag{1.112}$$

where n is the density of atoms, and

$$N(T)\mathrm{d}T = n\int_0^{E_\mathrm{i}} \frac{\sigma}{\mathrm{d}T}\left(\frac{\mathrm{d}E}{\mathrm{d}X}\right)^{-1}\mathrm{d}E\,\mathrm{d}T. \tag{1.113}$$

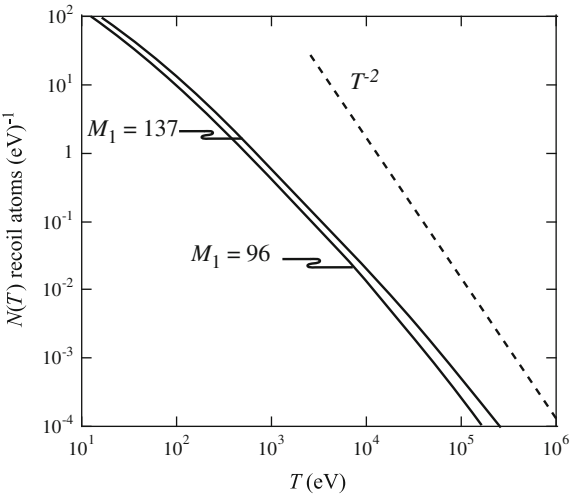

Fig. 1.14 The energy spectrum of recoils $N(T)$ dT produced by fission fragments slowing down to rest in uranium. Two cases are shown: $M_1 = 96$, $E_1 = 95$ MeV; and $M_1 = 137$, $E_1 = 55$ MeV (from [13])

Brinkman carried out these calculations for light and heavy fragments from ^{235}U fission slowing down in uranium. The results are shown in Fig. 1.14. Note that $N(T)$ decreases more rapidly than T^{-1}, and hence, the majority of displaced atoms are produced by low-energy recoils. Therefore, high-energy recoils can be neglected altogether. Another way of looking at this is that the simple Coulomb potential is only valid in an energy range that does not contribute significantly to displacements.

Heavy Slow Ions

These ions are classified by the curve labeled "3" as shown in Fig. 1.12. This is a very important class of collisions as it covers most of the applications of kV ion implanters and low MV accelerators in the fields of materials science and radiation damage that includes such topics as ion implantation and heavy ion radiation effects simulation. The figure shows that collisions must be dealt with over the range $a < \rho < 10a$. The formalism used for fission fragments in the previous section applies to glancing collisions, but for head-on collisions, another approach is needed. The appropriate potential for $a/5 \leq \rho \leq 5a$ is the inverse square approximation. We use a potential of the form:

$$V(r) = \frac{2E_R}{e}(Z_1 Z_2)^{5/6}\left(\frac{a_0}{r}\right)^2,$$

which is obtained by fitting a screened Coulomb potential to the inverse square potential and equating at $r = a$, Eq. (1.59). Substituting this potential function into the orbital equation (1.76) gives:

$$\frac{\phi}{\pi} = 1 - \left(1 + \frac{a^2 E_a}{b^2 E_\mathrm{i}}\right)^{-1/2}. \tag{1.114}$$

Using Eq. (1.13) to express ϕ in terms of T gives:

$$T = \gamma E_\mathrm{i} \cos^2 \left[\frac{\pi}{2}\left(1 + \frac{a^2 E_a}{b^2 E_\mathrm{i}}\right)^{-1/2}\right]. \tag{1.115}$$

Expressing b in terms of T and differentiating gives:

$$\sigma_\mathrm{s}(E_\mathrm{i}, T) = \frac{4E_a a^2 \alpha}{\gamma E_\mathrm{i}^2 (1 - 4\alpha^2)^2 [x(1-x)]^{1/2}}, \tag{1.116}$$

where $x = \dfrac{T}{\gamma E_\mathrm{i}}$ and $\pi\alpha = \cos^{-1} x^{1/2}$.

For small x (low-energy transfer), we have:

$$\sigma_\mathrm{s}(E_\mathrm{i}, T) = \frac{\pi^2 a^2 E_a \gamma^{1/2}}{8 E_\mathrm{i}^{1/2} T^{3/2}}. \tag{1.117}$$

Note that the energy transfer cross section is dependent on T. The mean recoil energy is as follows:

$$\overline{T} = \frac{\int_{\check{T}}^{\gamma E_\mathrm{i}} T \sigma_\mathrm{s}(E_\mathrm{i}, T)\, \mathrm{d}T}{\int_{\check{T}}^{\gamma E_\mathrm{i}} \sigma_\mathrm{s}(E_\mathrm{i}, T)\, \mathrm{d}T} = (\gamma E_\mathrm{i} \check{T})^{1/2}. \tag{1.118}$$

The total cross section for displacement is as follows:

$$\sigma_\mathrm{s}(E_\mathrm{i}) = \int_{\check{T}}^{\gamma E_\mathrm{i}} \sigma_\mathrm{s}(E_\mathrm{i}, T)\, \mathrm{d}T = \frac{\pi^2 a^2 E_a \gamma^{1/2}}{4 (E_\mathrm{i} \check{T})^{1/2}}. \tag{1.119}$$

Relativistic Electrons

Radiation damage from electrons is not so important in reactor core materials, but more so in the laboratory as they are commonly used in electron microscopes for radiation damage studies. Due to the low mass of the electron, very high energies must be attained in order to cause displacements of a lattice atom. These energies are high enough such that relativistic quantum mechanics must be used to describe the collision. Even so, the energy transferred is large enough to displace only the struck atom with no secondary displacements.

In relativistic form, the momentum of an electron with rest mass m_0 and kinetic energy E_i is as follows:

$$p_\mathrm{e}^2 = \frac{E_\mathrm{i}}{c^2}(E_\mathrm{i} + 2m_0c^2). \tag{1.120}$$

Since the struck atom (Z, M) recoils non-relativistically, the recoil expression is that given in Eq. (1.9):

$$V_\ell'^2 = V_\mathrm{CM}^2 + V_\mathrm{c}'^2 - 2V_\mathrm{CM}V_\mathrm{c}'\cos\phi = 2V_\mathrm{CM}^2(1-\cos\phi) = 4V_\mathrm{CM}^2\sin^2\frac{\phi}{2},$$

and conservation of momentum gives:

$$p_\mathrm{e} = (m_0 + M)V_\mathrm{CM} \cong MV_\mathrm{CM}.$$

Replacing the velocity terms with energies in the expression for $V_\ell'^2$ yields:

$$T = \frac{2E_\mathrm{i}}{Mc^2}(E_\mathrm{i} + 2m_0c^2)\sin^2\frac{\phi}{2}, \tag{1.121}$$

or

$$\hat{T} = \frac{2E_\mathrm{i}}{Mc^2}(E_\mathrm{i} + 2m_0c^2). \tag{1.122}$$

An approximate expression for the Dirac equation for light ions [13] yields the differential scattering cross section:

$$\begin{aligned}\sigma_\mathrm{s}(E_1,\phi) = {} & \frac{4\pi a_0^2 Z^2 E_\mathrm{R}^2}{m_0^2c^4}\frac{1-\beta^2}{\beta^4} \\ & \times [1 - \beta^2\sin^2(\phi/2) + \pi\alpha\beta\sin(\phi/2)(1-\sin(\phi/2))] \\ & \times \cos(\phi/2)\csc^3(\phi/2),\end{aligned} \tag{1.123}$$

where $\beta = \upsilon/c$ and $\alpha = Z_2/137$. This expression approaches the Rutherford scattering law for small β. Using Eqs. (1.121) and (1.122), the differential scattering cross section is written in terms of T and $\hat{T}$:

$$\sigma_\mathrm{s}(E_\mathrm{i},T) = \frac{4\pi a_0^2 Z^2 E_\mathrm{R}^2}{m_0^2c^4}\frac{1-\beta^2}{\beta^4}\left[1 - \beta^2\frac{T}{\hat{T}} + \pi\frac{\alpha}{\beta}\left\{\left(\frac{T}{\hat{T}}\right)^{1/2} - \frac{T}{\hat{T}}\right\}\right]\frac{\hat{T}}{T^2}. \tag{1.124}$$

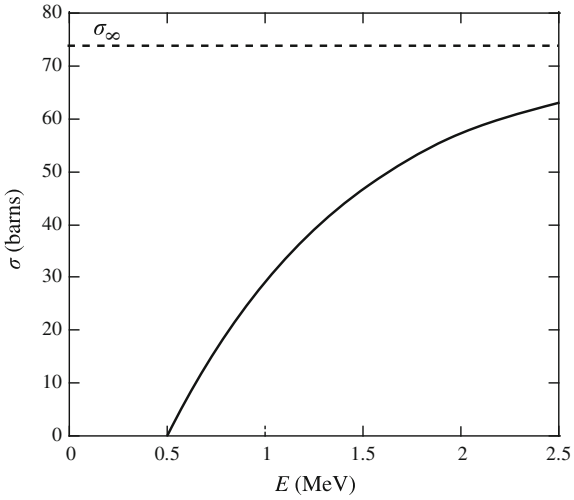

Fig. 1.15 Damage cross section for electrons bombarding copper where E_d = 25 eV (from [13])

The total cross section is found by integrating Eq. (1.124) from $\check{T}$ to $\hat{T}$:

$$\sigma_s(E_i) = \frac{4\pi a_0^2 Z^2 E_R^2}{m_0^2 c^4} \frac{1-\beta^2}{\beta^4} \left(\frac{\hat{T}}{\check{T}} - 1 \right) - \beta^2 \log \frac{\hat{T}}{\check{T}} + \alpha\beta 2 \left(\frac{\hat{T}}{\check{T}} \right)^{1/2} - 1 - \log \frac{\hat{T}}{\check{T}}. \tag{1.125}$$

For electrons with energies above the damage threshold and $\hat{T}/\check{T}$ slightly greater than unity:

$$\sigma_s(E_i) \cong \frac{4\pi a_0^2 Z^2 E_R^2}{m_0^2 c^4} \left(\frac{1-\beta^2}{\beta^4} \right)^2 \left(\frac{\hat{T}}{\check{T}} - 1 \right). \tag{1.126}$$

Figure 1.15 shows that at high enough energies, $E_i \gg m_0 c^2$, and $\sigma_s(E_i)$ approaches an asymptotic value:

$$\sigma_s(E_i) \to \frac{8\pi a_0^2 Z^2 E_R^2}{\check{T} M c^2} = \sigma_\infty. \tag{1.127}$$

It should be emphasized, however, that these cross sections are most accurate for light elements but seriously underestimate $\sigma_s(E_i)$ for heavy elements ($Z > 50$). Table 1.5 provides a summary of the energy transfer and the energy transfer cross sections for the various types of atom–atom interactions discussed in Sect. 1.2.

Table 1.5 Energy transfer and energy transfer cross sections for various types of atom–atom collisions

Type of collision	Energy transfer and energy transfer cross section	Equation in text
Hard sphere type (Born–Mayer potential) $\rho \sim r_e$	$\sigma_s(E_i, T) = \frac{\pi B^2}{\gamma E_i}\left[\ln\frac{A}{\eta E_i}\right]^2$	(1.87)
	$\overline{T} = \gamma E_i/2$	(1.13)
Rutherford scattering (simple Coulomb potential) $\rho \ll a$	$\sigma_s(E_i, T) = \frac{\pi b_0^2}{4}\frac{E_i\gamma}{T^2}$	(1.102)
	$\overline{T} \approx E_d \ln\left(\frac{\gamma E_i}{E_d}\right)$	(1.104)
Heavy ion (inverse square) $a/5 \le \rho \le 5a$	$\sigma_s(E_i, T) = \frac{\pi^2 a^2 E_a \gamma^{1/2}}{8E_i^{1/2}T^{3/2}}$	(1.117)
	$\overline{T} = \left(\gamma E_i \check{T}\right)^{1/2}$	(1.118)
Relativistic electrons	$\sigma_s(E_i, T) = \frac{4\pi a_0^2 Z^2 E_R^2}{m_0^2 c^4}\frac{1-\beta^2}{\beta^4} \times \left[1 - \beta^2\frac{T}{\hat{T}} + \pi\frac{\alpha}{\beta}\left\{\left(\frac{T}{\hat{T}}\right)^{1/2} - \frac{T}{\hat{T}}\right\}\right]\frac{\hat{T}}{T^2}$	(1.124)

1.3 Energy Loss

Up to this point, we have been treating collisions as discrete events. However, besides collision with or between nuclei, an ion or atom traveling through the lattice may lose energy by electronic excitation, by ionization, or by Bremsstrahlung (loss of energy of an electron passing through the Coulomb field of a nucleus by emission of X-rays). These events may be viewed as more or less continuous events. What follows is a treatment of energy loss in solids.

1.3.1 Energy Loss Theory

We are interested in finding the differential energy loss of an ion or atom traveling through a lattice. We begin by defining the energy loss per unit length as $-\mathrm{d}E/\mathrm{d}x$ (or $NS(E)$ where N is the target atom number density and S is the stopping power in units of energy × distance squared) so that the total energy loss can then be approximated by a sum of these components:

$$\left(-\frac{\mathrm{d}E}{\mathrm{d}x}\right)_{\text{total}} = \left(-\frac{\mathrm{d}E}{\mathrm{d}x}\right)_n + \left(-\frac{\mathrm{d}E}{\mathrm{d}x}\right)_e + \left(-\frac{\mathrm{d}E}{\mathrm{d}x}\right)_r = NS_n + NS_e + NS_r, \quad (1.128)$$

where the subscripts are defined as follows:
n = elastic,
e = electronic, and
r = radiation.

For most of the applications in which we will be interested, energy loss by radiation will be small and will be neglected.

From our discussion in Sect. 1.2.1, it is evident that in order to accurately describe the slowing down of an ion or atom over the entire energy range from $\hat{T}$ to $\check{T}$, where $\hat{T}$ may be in MeV and $\check{T} \sim 10$ eV, several potential functions would need to be "pieced" together (see Fig. 1.9). This would cause problems because of discontinuities at the cuts. Moreover, the cutoff points of these functions often differ depending on M and Z.

However, we can separate or subdivide stopping power according to the type of interaction and hence the energy regime. In the high-energy regime, $\rho \ll a$ and $S_e \gg S_n$, and these interactions are treated as pure Coulomb collisions. In the low-energy regime, $\rho \approx a$ and $S_n > S_e$. This is the region of importance in the deposition of displacement energy. In either case, we can establish a formalism for calculating stopping power, $-\mathrm{d}E/\mathrm{d}x = NS(E)$.

If we know the energy transfer cross section $\sigma(E_i, T)$ for either S_n or S_e, then we can calculate the average energy transfer:

$$\overline{T} = \frac{\int T\sigma \mathrm{d}T}{\int \sigma \mathrm{d}T} = \text{energy lost or transferred,}$$

and the mean free path (mfp) between collisions is $\lambda = \dfrac{1}{N\sigma}$. Then, the ratio of these two quantities is the energy loss per unit length:

$$\begin{aligned} \frac{\mathrm{d}E}{\mathrm{d}x} = NS_n = \frac{\overline{T}}{\lambda} &= \frac{\int_{\check{T}}^{\hat{T}} T\sigma(E_i, T)\,\mathrm{d}T}{\int_{\check{T}}^{\hat{T}} \sigma(E_i, T)\,\mathrm{d}T} \cdot N \int_{\check{T}}^{\hat{T}} \sigma(E_i, T)\,\mathrm{d}T \\ &= N \int_{\check{T}}^{\hat{T}} T\sigma(E_i, T)\,\mathrm{d}T. \end{aligned} \tag{1.129}$$

Another way to look at this is as follows: Consider a projectile incident on an amorphous target containing an average of N atoms/unit volume (Fig. 1.16). In traversing the slab of material between x and $x + \Delta x$, the projectile will come within a distance b_1 of $N\Delta x 2\pi b_1 \mathrm{d}b$ target particles and transfer an energy $T(E_i, b)$ to each.

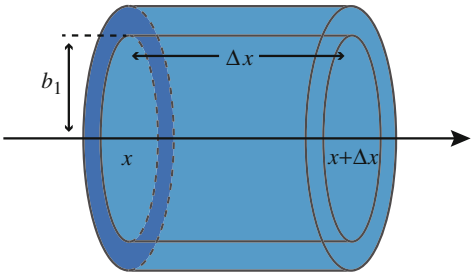

Fig. 1.16 Schematic of an incident projectile of energy E passing within a distance b_1 of an annular ring containing $N\Delta x 2\pi b_1 \mathrm{d}b$ atoms

The total energy transferred to all target particles in the slab is obtained by integrating over all possible impact parameters:

$$\Delta E = N\Delta x \int_0^\infty T 2\pi b \, \mathrm{d}b.$$

Assuming $\Delta E \ll E$ and dividing by Δx and taking the limit as $\Delta x \to 0$, we obtain:

$$\left.\frac{\Delta E}{\Delta x}\right|_{\lim \Delta x \to 0} = \frac{\mathrm{d}E}{\mathrm{d}x} = N \int_0^\infty T 2\pi b \, \mathrm{d}b.$$

We know that $\sigma\,(E_\mathrm{i},\, T)\,\mathrm{d}T = 2\pi b \mathrm{d}b$ so:

$$\frac{\mathrm{d}E}{\mathrm{d}x} = N \int_{\check{T}}^{\hat{T}} T\sigma(E_\mathrm{i}, T)\,\mathrm{d}T,$$

which is the same result as from Eq. (1.129). Let us first consider nuclear stopping, or energy loss from elastic collisions.

Nuclear Stopping Power

We define $\left(-\frac{\mathrm{d}E}{\mathrm{d}x}\right)_\mathrm{n}$ or $NS_\mathrm{n}(E_\mathrm{i})$ as the energy lost to target nuclei when a projectile of energy E_i traverses a differential thickness dx of a target of unit density. A simple formulation of $\left(-\frac{\mathrm{d}E}{\mathrm{d}x}\right)_\mathrm{n}$ can be made if we assume that each target nucleus acts independently of every other target nucleus in slowing down a projectile. In essence, we are neglecting any possible interactions between nuclei. This is a fair

approximation for amorphous targets and a good first approximation for crystalline targets also.

Case 1: High-energy elastic collisions, $\rho \ll a$.

Rutherford scattering describes this type of interaction accurately. Recall that for simple Coulomb scattering, the energy transfer cross section [Eq. (1.102)] is as follows:

$$\sigma_s(E_i, T) = \frac{\pi b_0^2}{4}\frac{\gamma E_i}{T^2}.$$

Therefore, the stopping power becomes:

$$\begin{aligned}\left.\frac{dE}{dx}\right|_n &= NS_n(E_i) = N\int_{\check{T}}^{\gamma E_i} T\frac{\pi b_0^2}{4}\frac{\gamma E_i}{T^2}dT \\ &= \frac{N\pi b_0^2}{4}\gamma E_i \ln\left(\frac{\gamma E_i}{\check{T}}\right),\end{aligned} \tag{1.130}$$

where $\hat{T} = \gamma E_i$ and $\check{T}$ is the value of T which yields $b = a$ or $\check{T}_b = \dfrac{e^2\gamma E_a^2}{4E_i}$.

Substituting for b_0 from Eq. (1.93) gives:

$$\left.\frac{dE}{dx}\right|_n = NS_n(E_i) = \frac{N\pi Z_1^2 Z_2^2 \varepsilon^4}{E_i}\frac{M_1}{M_2}\ln\left(\frac{\gamma E_i}{\check{T}_b}\right). \tag{1.131}$$

Note that for like atoms, $\gamma = 1$ and $M_1 = M_2$, so:

$$NS_n(E_i) = \frac{N\pi Z_1^2 Z_2^2 \varepsilon^4}{E_i}\ln\left(\frac{E_i}{\check{T}_b}\right). \tag{1.132}$$

Substituting for E_a from Eq. (1.107) into the expression for $\check{T}_b$ gives:

$$\check{T}_b = \frac{4E_R^2 (Z_1Z_2)^2 (Z_1Z_2)^{2/6}}{c^2 E_i}. \tag{1.133}$$

Using $a = a_0/(Z_1Z_2)^{1/6}$ and substituting for $(Z_1Z_2)^{1/6}$ gives:

$$\check{T}_b = \frac{4E_R^2 a_0^2 Z^4}{c^2 a^2 E_i},$$

for $Z_1 = Z_2$, and since $\varepsilon^2 = 2a_0E_R$, then Eq. (1.132) becomes:

$$\begin{aligned} NS_n(E_i) &= \frac{4N\pi Z^4 a_0^2 E_R^2}{E_i} \ln\left(\frac{E_i}{\check{T}_b}\right) \\ &= \frac{4N\pi Z^4 a_0^2 E_R^2}{E_i} \ln\left(\frac{c^2 a^2 E_i^2}{4a_0^2 E_R^2 Z^4}\right). \end{aligned} \tag{1.134}$$

Case 2: Low-energy elastic collisions, $\rho \sim a$.

At intermediate and lower energies, pure Coulomb scattering will not correctly capture the interaction. Here, we must use a screened Coulomb function to account for the effects of the electrons in the internuclear space. Bohr showed that the screened Coulomb potential could be accurately described using an inverse power potential of the form [14]:

$$\sigma(E,T) = \frac{C_m}{E^m T^{1+m}}, \tag{1.135}$$

where

$$C_m = \frac{\pi}{2}\lambda_m a^2 \left(\frac{2Z_1 Z_2 \varepsilon^2}{a}\right)^{2m} \left(\frac{M_1}{M_2}\right)^m, \tag{1.136}$$

and λ_m is a fitting variable. Inserting the potential function in Eq. (1.135) into Eq. (1.129) for the stopping power gives:

$$S_n(E) = \frac{1}{N}\left(\frac{dE}{dx}\right)_n = \frac{C_m}{E^m}\int_0^{\hat{T}} T^{-m} dT = \frac{C_m E^{-m} T^{1-m}}{1-m}\Bigg|_0^{\hat{T}}, \tag{1.137}$$

$$S_n(E) = \frac{C_m E^{1-2m}}{1-m}\gamma^{1-m}, \tag{1.138}$$

where γ has the usual definition, Eq. (1.14). Lindhard et al. [14] introduced a set of dimensionless or reduced variables for energy, $\in$, and distance, ρ_x:

$$\in = \frac{M_2}{(M_1+M_2)}\frac{a}{Z_1 Z_2 \varepsilon^2}E, \tag{1.139}$$

$$\rho_x = N4\pi a^2 \frac{M_1 M_2}{(M_1+M_2)^2}x. \tag{1.140}$$

They proposed a universal, one-parameter, differential scattering cross section in reduced notation that approximates the interaction potential $V(r) = \dfrac{Z_1 Z_2 \varepsilon^2}{r}\phi_0(r/a)$, where ϕ_0 is the Fermi function belonging to a single Thomas–Fermi atom:

$$\sigma = \frac{\pi a^2}{2}\frac{f(t^{1/2})}{t^{3/2}}, \tag{1.141}$$

where t is a dimensionless collision parameter defined by:

$$t = \in^2 \frac{T}{\hat{T}} = \frac{1}{2}\in^2 (1 - \cos\phi) = \in^2 \sin^2 \phi/2, \tag{1.142}$$

and t is proportional to the energy transfer, T, and to the energy, E_i, through $\in^2 /\hat{T}$, and ϕ is the CM scattering angle. Lindhard et al. [14] treated $f(t^{1/2})$ to be a simple scaling function where t was a measure of the depth of penetration into an atom during a collision and large t represents close approach. The function $f(t^{1/2})$ is plotted in Fig. 1.17, and Winterbon et al. [15] developed an analytical expression for the function:

$$f(t^{1/2}) = \lambda' t^{1/6}\left[1 + (2\lambda' t^{2/3})^{2/3}\right]^{-3/2}, \tag{1.143}$$

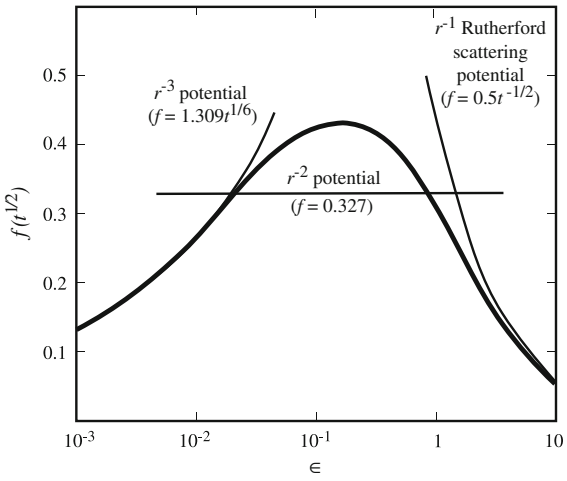

Fig. 1.17 Reduced differential cross section calculated from the Thomas–Fermi potential. Abscissa is $\in = t^{1/2}/\sin\phi/2$. The *thick solid line* ranging over $10^{-3} < \in < 10$ is from Eq. (1.141). The *thin solid lines* at *left* and *right* and the *horizontal line* in the *middle* are calculated using the power law cross section, Eq. (1.144) (after [15])

where $\lambda' = 1.309$. A generalization of Eq. (1.143) for power law scattering is as follows:

$$f(t^{1/2}) = \lambda_m t^{\frac{1}{2}-m}, \tag{1.144}$$

where $\lambda_{1/3} = 1.309$, $\lambda_{1/2} = 0.327$, and $\lambda_1 = 0.5$. Equation (1.144) approximately describes scattering from a potential of the form $V(r) \propto r^{-s} = r^{-1/m}$, where s is the power law exponent. At low energies (low $\in$), there is little penetration in the collision (t is small) and collisions are described by a power law with $V(r) \propto r^{-3}$ and $m = 1/3$, yielding a $t^{1/6}$ dependence. At higher energies, screening effects are minimal and are described by a $V(r) \propto r^{-1}$ potential and $m = 1$, giving $t^{-1/2}$ behavior. At intermediate energies, the function (cross section) is slowly varying and is best described by a power law potential for the form, $V(r) \propto r^{-2}$, with $m = 1/2$ giving no dependence on t, which means that the cross section is independent of $\in$. For the case of the inverse square law, $m = 1/2$ and the stopping power is given by Eq. (1.138):

$$S_n(E) = 4\pi\lambda_{1/2} a Z_1 Z_2 \varepsilon^2 \frac{M_1}{M_1 + M_2}. \tag{1.145}$$

The reduced stopping cross section, $S_n(\in)$, is given as follows:

$$S(\in) = \frac{\mathrm{d} \in}{\mathrm{d}\rho_x}, \tag{1.146}$$

and a relation between $S_n(E)$ and $S_n(\in)$ is as follows:

$$\frac{\mathrm{d} \in}{\mathrm{d}\rho_x} = \left(\frac{\mathrm{d} \in}{\mathrm{d}E}\frac{\mathrm{d}\rho_x}{\mathrm{d}x}\right)\frac{\mathrm{d}E}{\mathrm{d}x}. \tag{1.147}$$

Taking differentials of $\in$ with respect to E (Eq. (1.139)), and ρ_x with respect to x (Eq. (1.140)) gives:

$$S_n(\in) = \frac{M_1 + M_2}{M_1}\frac{1}{4\pi a Z_1 Z_2 \varepsilon^2} S_n(E) \tag{1.148}$$

$$= \frac{\in}{\pi a^2 \gamma E_i} S_n(E). \tag{1.149}$$

Substituting the expression for $S_n(E)$ from Eq. (1.145) into Eq. (1.148) gives:

$$S_n(\in) = \lambda_{1/2} = 0.327. \tag{1.150}$$

The stopping power can also be written using the energy transfer cross section in reduced notation from Eq. (1.141) giving:

$$S_{\mathrm{n}}(E) = \frac{1}{N}\left(\frac{\mathrm{d}E}{\mathrm{d}x}\right)_{\mathrm{n}} = \pi a^2 \int_0^{\hat{T}} T \frac{f(t^{1/2})}{2t^{3/2}}\,\mathrm{d}t = \frac{-\pi a^2 \hat{T}}{\in^2} \int_0^{\hat{T}} f(t^{1/2})\mathrm{d}t^{1/2}. \tag{1.151}$$

Substituting the stopping power $S_{\mathrm{n}}(E)$ in Eq. (1.151) into Eq. (1.149) for $\hat{T} = \gamma E_{\mathrm{i}}$ gives:

$$S_{\mathrm{n}}(\in) = \frac{1}{\in} \int_0^{\in} f(t^{1/2})\mathrm{d}t^{1/2}. \tag{1.152}$$

Setting $y = t^{1/2}$ in Eq. (1.144), Eq. (1.152) becomes:

$$S_{\mathrm{n}}(\in) = \frac{\lambda_m}{\in} \int_0^{\in} y^{1-2m} dy = \frac{\lambda_m}{\in} \frac{y^{2-2m}}{2(1-m)}\bigg|_0^{\in} = \frac{\lambda_m}{2(1-m)} \in^{1-2m}, \tag{1.153}$$

which is the power law approximation to the reduced nuclear stopping cross section. For the case of the inverse square law, $m = 1/2$ and $S_{\mathrm{n}}(\in) = \lambda_{1/2} = 0.327$.

Two approximations for $S_{\mathrm{n}}(E_{\mathrm{i}})$ for collisions in the intermediate energy regime are considered. The first is obtained by solving the orbital Eq. (1.76) using the inverse square potential in Eq. (1.59) [16]:

$$\frac{\phi}{\pi} = 1 - \frac{1}{\left(1 + \dfrac{a^2 E_a}{b^2 E_{\mathrm{i}}}\right)^{1/2}}.$$

Using Eq. (1.14) to determine T gives:

$$T = \gamma E_{\mathrm{i}} \cos^2 \left[\frac{\pi}{2}\left(1 + \frac{a^2 E_a}{b^2 E_{\mathrm{i}}}\right)^{1/2}\right]. \tag{1.154}$$

Expressing b^2 in terms of T and differentiating, and using the relation between $\sigma_{\mathrm{s}}(E_{\mathrm{i}}, T)$ and b from Eq. (1.78) gives:

$$\sigma_{\mathrm{s}}\left(E_{\mathrm{i}}, T\right) = \frac{4 E_a a^2 \alpha}{\gamma E_{\mathrm{i}}^2 \left(1 - 4\alpha^2\right)^2 \left(x(1-x)\right)^{1/2}}, \tag{1.155}$$

where $x = T/E_i$, $\pi\alpha = \cos^{-1}\sqrt{x}$, and for small x, Eq. (1.155) has the form:

$$\sigma_s\left(E_i, T\right) = \frac{\pi^2 a^2 E_a \gamma^{1/2}}{8 E_i^{1/2} T^{3/2}}. \tag{1.156}$$

The total cross section and mean recoil energy are calculated from Eq. (1.156) taking a cutoff to zero at $\overline{T} = \gamma E_i$:

$$\overline{T} = \left(\gamma E_i \check{T}\right)^{1/2}, \tag{1.157}$$

$$\sigma_s\left(E_i\right) = \frac{\pi^2 a^2 E_a \gamma^{1/2}}{4\left(E_i \check{T}\right)^{1/2}}. \tag{1.158}$$

The stopping power is determined using:

$$S_n(E_i) = \int_{\check{T}}^{\hat{T}} T\sigma(E_i, T)dT,$$

and substituting the energy transfer cross section from Eq. (1.158) yields:

$$S_n\left(E_i\right) = \frac{1}{N}\left(\frac{dE}{dx}\right)_n = \frac{\pi^2}{4} a^2 E_a \gamma. \tag{1.159}$$

Substitution for E_a from Eq. (1.107) gives a value of 0.327 for S_n. This same result can be obtained using the expression for average energy loss:

$$\frac{dE}{dx} = \frac{\overline{T}}{\lambda} = N\sigma_s \overline{T}, \tag{1.160}$$

where $\lambda = \dfrac{1}{N\sigma_s}$ is the mean free path between collisions, and substituting for $\sigma_s(E_i)$ and $\overline{T}$ from Eqs. (1.157) and (1.158).

The second approximation of $S_n(E_i)$ can be obtained using the Thomas–Fermi screening function. We will assume that a series of small-angle scattering events are responsible for most of the energy loss of a projectile in a target. When this is true, the energy transferred, T, can be expressed as a function of E_i and b by solving Eq. (1.76) for ϕ using the Thomas–Fermi screening function, Eq. (1.49), and expanding the solution on the assumption that f is small. Proceeding, we find:

$$\phi = \pi - 2\int_{\circ}^{\hat{x}} \left[\frac{1}{b^2}\left(1 - \frac{V(x)}{\eta E_i} - b^2 x^2\right)\right]^{-1/2} dx, \tag{1.161}$$

and for $V(r) = \dfrac{Z_1 Z_2 \varepsilon^2}{r} f(r/a)$, where $f(r/a) = a/r$, the solution is as follows:

$$\phi = \pi - b\left[b^2 + \frac{Z_1 Z_2 \varepsilon^2 a}{E_R}\right]^{-1/2}. \tag{1.162}$$

Solving for b and substituting in the expression:

$$\sigma_s\left(E_i, \phi\right)\, \mathrm{d}\Omega = 2\pi b\, \mathrm{d}b,$$

and using Eq. (1.15) to obtain $\sigma_s(E_i, T)\, dT$, we can then find $S_n(E_i)$ from Eq. (1.129). The result is as follows:

$$S_n^0 = \frac{\pi^2}{e}\varepsilon^2 a_0 Z_1 Z_2 \frac{M_1}{M_1 + M_2} Z^{-1/3}, \tag{1.163}$$

which is the standard stopping power and is shown in Fig. 1.18. Note that S_n^0 is independent of the projectile energy to a first approximation, and substitution of Eqs. (1.163) and (1.139) into Eq. (1.149) yields a value of 0.327 for S_n^0. Ranges estimated from S_n^0 will be reasonably close when small-angle scattering predominates.

Recall that the key assumption in deriving Eq. (1.163) was that energy loss of a projectile can be represented as a series of small-angle scattering events, allowing us to then assume that f remains small. Table 1.6 gives the scattering angles and energy loss for a 50 keV silicon projectile incident on a silicon target atom. Note that for $\rho/a \geq 1$, this assumption is clearly valid.

The nuclear stopping cross section in reduced notation is determined by using Eq. (1.149) for $S_n(\in)$ and substituting Eq. (1.129) for $S_n(E)$ giving:

$$S_n(\in) = \frac{\in}{\pi a_U^2 \gamma E_i} \int_0^{\hat{T}} T\sigma_s(E_i, T)\mathrm{d}T, \tag{1.164}$$

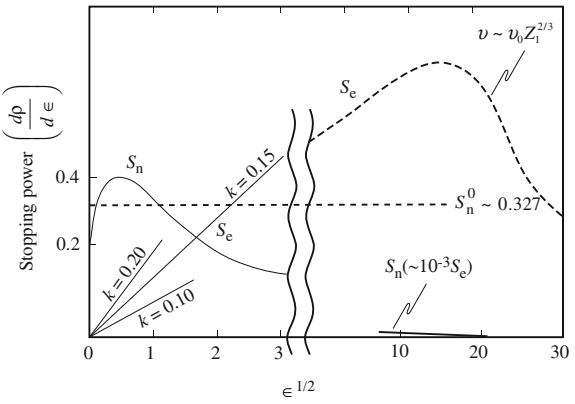

Fig. 1.18 The reduced nuclear and electronic stopping cross sections as a function of $\in^{1/2}$

Table 1.6 Scattering angles and energy loss for a 50 keV silicon projectile and a silicon target atom [17]

ρ/a =	10	1	0.1
ϕ (radians)	0.004π	0.26π	0.89π
θ (degrees)	0.36	23.4	80.5
T/E	4×10^{-5}	0.16	0.973
T (keV)	0.002	8	49

where the universal screening length a_U is substituted for the Thomas–Fermi screening length a, and using the identity:

$$\int_0^{\hat{T}} \sigma_s(E_i, T)\mathrm{d}T = \int_0^{b_{\max}} 2\pi b \mathrm{d}b, \tag{1.165}$$

yields an expression for the nuclear stopping cross section in reduced notation:

$$S_n(\in) = \frac{\in}{a_U^2} \int_0^{\infty} \sin^2 \frac{\phi}{2} \mathrm{d}b^2. \tag{1.166}$$

Ziegler [18] used the universal screening function, Fig. 1.19:

$$\chi_U = 0.1818e^{-3.2x} + 0.5099e^{-0.9423x} + 0.2802e^{-0.4028x} + 0.02817e^{-0.2016}, \tag{1.167}$$

and the numerical integration of Eq. (1.76) and Eq. (1.166) to calculate a universal reduced nuclear stopping cross section, the ZBL cross section shown in Fig. 1.20. An expression for the fit is as follows:

$$S_n(\in) = \frac{0.5 \ln(1 + 1.1383 \in)}{(\in + 0.01321 \in^{0.21226} + 0.19593 \in^{0.5})}, \tag{1.168}$$

and for practical calculations, the ZBL universal nuclear stopping for an ion with energy E_i in the laboratory system is as follows:

$$S_n(E_i) = \frac{8.462 \times 10^{-15} Z_1 Z_2 M_1 S_n(\in)}{(M_1 + M_2)(Z_1^{0.23} + Z_2^{0.23})} \frac{\mathrm{eV} \cdot \mathrm{cm}^2}{\mathrm{atom}}, \tag{1.169}$$

where the ZBL reduced energy is as follows:

$$\in = \frac{32.53 M_2 E_i}{Z_1 Z_2 (M_1 + M_2)(Z_1^{0.23} + Z_2^{0.23})}. \tag{1.170}$$

Let us now look at electronic energy loss.

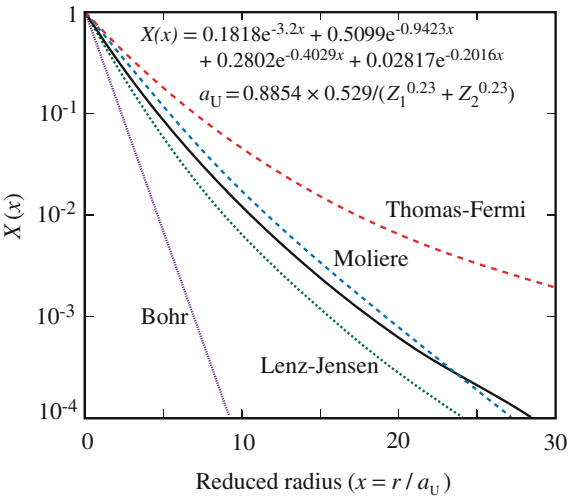

Fig. 1.19 The universal screening function χ_U (*solid thick line*) from Eq. (1.167) as a function of $x = r/a_{U,}$ where a_U is the universal screening length defined by $a_U = 0.8854a_0/(Z_1^{0.23} + Z_2^{0.23})$, along with several other screening functions (after [19])

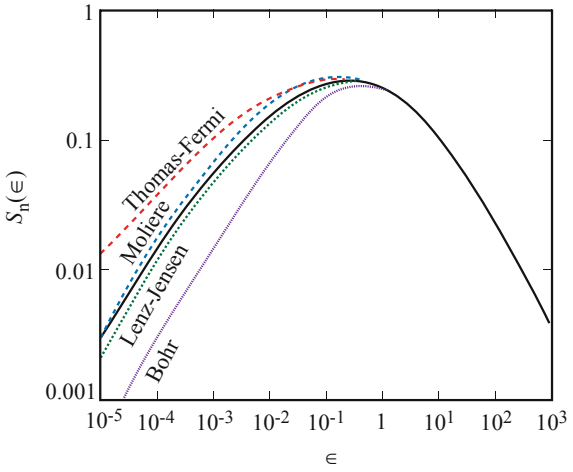

Fig. 1.20 Nuclear stopping power in reduced units from Eq. (1.168)

Electronic Stopping Power

The theoretical computation of electronic stopping power is a much more complicated problem than the calculation of S_n. For the description of collisions between ions and electrons, we may use the classical equation (Eq. (1.106)). But here we must consider that the binary collision is between a heavy moving ion and an electron in a solid. This approach is valid as long as all electrons participate and the ion velocity exceeds the velocity of the tightest bound electron. We may define T by:

$$\hat{T} \cong \gamma_e E_i, \tag{1.171}$$

where $\gamma_e = \dfrac{4m_e M}{(m_e + M)^2}$, and hence, $\hat{T}$ is very small. We will also define a lower limit for ion–electron interactions as the effective mean excitation–ionization level $\bar{I}$.[1] We also note that we must use the electron density, which is just Z_2 times the atom density:

$$n = NZ_2. \tag{1.172}$$

Writing an expression for stopping power due to excitation–ionization interactions that is equivalent to Eq. (1.130) yields:

$$\begin{aligned}\left(-\frac{dE}{dx}\right)_e &= \frac{n}{Z_2}\int_{\bar{I}}^{\gamma_e E_i} T\sigma_s(E_i, T)\,dT \\ &= \frac{n}{Z_2}\frac{\pi b_0^2}{4}\gamma_e E_i \ln\left(\frac{\gamma_e E_i}{\bar{I}}\right) \\ &= N\pi\frac{Z_1^2 Z_2 \varepsilon^4}{E_i}\frac{M}{m_e}\ln\left(\frac{\gamma_e E_i}{\bar{I}}\right).\end{aligned} \tag{1.173}$$

This formula is only approximate. A more exact expression is obtained from a quantum mechanical treatment based on the Born approximation, which is interpreted physically to mean that the perturbation due to the incident particle does not seriously disturb the electronic motion for large impact parameters. The result of this analysis is the addition of a factor of 2, which comes from the small-energy transfer processes where free Coulomb scattering is invalid. The Bethe–Bloch formula is a good approximation:

$$\left(-\frac{dE}{dx}\right)_e = \frac{2N\pi Z_1^2 Z_2 \varepsilon^4}{E_i}\frac{M}{m_e}\ln\left(\frac{\gamma_e E_i}{\bar{I}}\right) = \frac{2\pi N Z_1^2 M \varepsilon^4}{m_e E_i}B, \tag{1.174}$$

where $B = Z_2 \ln\left(\dfrac{\gamma_e E_i}{\bar{I}}\right)$ is the stopping number. For relativistic velocities:

$$B = Z_2\left\{\ln\left(\frac{\gamma_e E_i}{\bar{I}}\right) - \ln(1-\beta^2) - \beta^2\right\}, \tag{1.175}$$

where $\beta = \upsilon/c$ and c is the speed of light. Note that at high energies, S_n and S_e vary as $1/E_i$ very nearly, and:

$$\frac{S_e}{S_n} = \frac{2M_2}{m_e Z_2}\frac{\ln\left(\dfrac{\gamma_e E_i}{\bar{I}}\right)}{\ln\left(\dfrac{\gamma E_i}{E_d}\right)}. \tag{1.176}$$

[1] To a first approximation, $\bar{I} = kZ_2$ where $k = 11.5$ eV.

Applying Eq. (1.176) to the case of MeV protons, the value is ~2000 for $\bar{I} \sim 11.5Z_2$ eV, or the electronic stopping power is 2000 times that of the nuclear stopping power.

At low velocities, electrons in the inner shells contribute less to the stopping power. Also, the neutralization probability becomes so large that the collision between the projectiles and the surrounding electrons is almost elastic. The energy loss becomes proportional to the projectile velocity. Lindhard, Scharff, Schiott (LSS), and Firsov gave theoretical descriptions for this energy region. The LSS expression is based on elastic scattering of free target electrons in the static field of a screened point charge. Firsov's is based on a simple geometric model of momentum exchange between the projectile and target atom during interpenetration of electron clouds. Lindhard and Winther [17] have shown that as long as the ion velocity is less than the velocity of an electron having an energy equal to the Fermi energy, E_f of the free electron gas, S_e will be proportional to the velocity of the ion or the one-half power of its energy. Using a potential of the form:

$$V(r) = \frac{2(Z_1Z_2)^{1/2}\varepsilon^2}{r}\chi_{TF}\left[1.13\left(Z_1^{2/3}+Z_2^{2/3}\right)^{1/2}\frac{r}{a_0}\right], \tag{1.177}$$

the Lindhard–Scharff stopping power becomes:

$$S_e(E) = \left(-\frac{dE}{dx}\right)_e\frac{1}{N} = k'E^{1/2}, \tag{1.178}$$

$$k' = 3.83\frac{Z_1^{7/6}Z_2}{M_1^{1/2}\left(Z_1^{2/3}+Z_2^{2/3}\right)^{3/2}}, \tag{1.179}$$

where $S_e(E)$ is given in units of 10^{-15} eV cm^2/atom and E is in keV. Expressing the stopping cross section in reduced notation gives:

$$S_e(\in) = \left(\frac{d\in}{d\rho}\right)_e = k\in^{1/2}, \text{ where}$$
$$k = \frac{0.07937Z_1^{2/3}Z_2^{1/2}\left(1+\frac{M_2}{M_1}\right)^{3/2}}{\left(Z_1^{2/3}Z_2^{2/3}\right)^{3/4}M_2^{1/2}}. \tag{1.180}$$

The universal nuclear stopping cross section is shown in Fig. 1.18 where a single curve represents all possible projectile–atom collisions, and the electronic stopping cross section of Eq. (1.180) results in a family of lines or one for each combination of projectile and target atom.

An approximate treatment that results in an analytical expression is obtained in the following analysis. Consider an atom of mass M_1, moving with velocity v_1,

which makes a head-on collision with an electron moving in the opposite direction with velocity υ_e. The relative initial speed of the two particles is as follows:

$$\upsilon_{r0} = \upsilon_1 + \upsilon_e. \tag{1.181}$$

After collision, the velocity vector changes but not the magnitude:

$$\upsilon_{rf} = -(\upsilon_1 + \upsilon_e). \tag{1.182}$$

The speed of the atom following the collision with the electron is given by:

$$\begin{aligned} \upsilon_{1f} &= V_{CM} + \left(\frac{m_e}{M_1 + m_e}\right)\upsilon_{rf} \\ &= \frac{M_1\upsilon_1 - m_e\upsilon_e}{M_1 + m_e} - \left(\frac{m_e}{M_1 + m_e}\right)(\upsilon_1 + \upsilon_e) \\ &\cong \upsilon_1 - \frac{2m_e\upsilon_e}{M_1}, \end{aligned} \tag{1.183}$$

where m_e is neglected compared to M_1. The change in the energy of the atom due to the collision is as follows:

$$\Delta E = \Delta\left(\frac{1}{2}M_1\upsilon_1^2\right) \cong M_1\upsilon_1(\upsilon_1 - \upsilon_{1f}) = 2M_e\upsilon_e\upsilon_1. \tag{1.184}$$

The electron velocity after the collision is given as follows:

$$\begin{aligned} \upsilon_{ef} &= V_{CM} - \left(\frac{m_1}{M_1 + m_e}\right)\upsilon_{rf} \\ &= \frac{M_1\upsilon_1 - m_e\upsilon_e}{M_1 + m_e} + \left(\frac{M_1}{M_1 + m_e}\right)(\upsilon_1 + \upsilon_e) = 2\upsilon_1 + \upsilon_e, \end{aligned} \tag{1.185}$$

or the increase in the electron velocity is as follows:

$$\Delta\upsilon_e = \upsilon_{ef} - \upsilon_e = 2\upsilon_1. \tag{1.186}$$

The number of conduction electrons in a metal is approximately equal to the atom number density N. But only those electrons with velocities lying in the range $\Delta\upsilon_e$ of the Fermi velocity υ_f are able to participate in the slowing down process. Therefore, the effective density of electrons in the metal is as follows:

$$n_e \cong N\left(\frac{\Delta\upsilon_e/2}{\upsilon_f}\right) = \left(\frac{\upsilon_1}{\upsilon_f}\right)N. \tag{1.187}$$

The current of effective electrons impinging on the atom is as follows:

$$I_e = n_e \upsilon_{r0} = n_e(\upsilon_1 + \upsilon_e) \cong n_e \upsilon_e, \tag{1.188}$$

and the collision rate of effective electrons with a single atom is $\sigma_e I_e$, where σ_e is the cross section for interaction of the moving atom with conduction electrons. The stopping power is then the energy loss rate of a moving atom to effective electrons divided by the velocity of the atom:

$$\left(-\frac{dE}{dx}\right)_e = \frac{\sigma_e I_e \Delta E}{\upsilon_1}. \tag{1.189}$$

Substituting Eqs. (1.184), (1.187), and (1.188) into the above expression and writing υ_e and υ_1 as $(2E_f/m_e)^{1/2}$ and $(2E/M_1)^{1/2}$, respectively, yield:

$$\left(-\frac{dE}{dx}\right)_e = 8\sigma_e N\left(\frac{m_e}{M_1}\right)^{1/2} E^{1/2} = kE^{1/2}, \tag{1.190}$$

where

$$k = 8\sigma_e N\left(\frac{m_e}{M_1}\right)^{1/2}, \tag{1.191}$$

and $k = 3.0NZ^{2/3}\text{eV}^{1/2}/\text{nm}$ for like atoms, or $S_e = k'E^{1/2}$ where $k' = 3 \times 10^{-15}Z^{2/3}\ \text{eV}^{1/2}\ \text{cm}^2$ for like atoms. Both equations are valid for $0 < E\ (\text{keV}) < 37Z^{7/3}$. For example, for $M_2 = \text{Si}$, $k'_{\text{Si}} \sim 0.2 \times 10^{-15}\text{eV}^{1/2}\,\text{cm}^2$. Table 1.7 summarizes the nuclear and electronic energy loss rates for the various types of interactions used in Sect. 1.3.1.

1.3.2 Range Calculations

We have developed expressions for the two major forms of energy loss: (1) collisions of the ion with the target nuclei and (2) interactions of the ion with the electrons in the solid. We will assume that these two forms of energy loss are independent of each other. Because of this approximation, we may write the total energy loss of a single projectile as the sum of the individual contributions:

$$\left(-\frac{dE}{dx}\right)_T = NS_T = N[S_n(E) + S_e(E)]. \tag{1.192}$$

This expression can be integrated to give the total distance R that a projectile of initial energy E_i will travel before coming to rest:

Table 1.7 Summary of energy loss rates for various types of interactions

Type of interaction	Nuclear energy loss rate $\left(-\frac{dE}{dx}\right)_n$		Electronic energy loss rate $\left(-\frac{dE}{dx}\right)_e$	
High E Coulomb	$\frac{4N\pi Z^4 a_0^2 E_R^2}{E_i}\ln\left(\frac{a^2c^2E_i^2}{4a_0^2E_R^2Z^4}\right)$	(1.134)	$N\pi\frac{Z_1^2Z_2e^4}{E_i}\frac{M}{m_e}\ln\left(\frac{\gamma_e E_i}{\bar{I}}\right)$	(1.173)
Low E	General expression: $\frac{8.462\times10^{-15}NZ_1Z_2M_1S_n(\in)}{(M_1+M_2)(Z_1^{0.23}+Z_2^{0.23})}$	(1.169)	$k'E_i^{1/2}$ $k' = 3.83\frac{Z_1^{7/6}Z_2}{M_1^{1/2}\left(Z_1^{2/3}+Z_2^{2/3}\right)^{3/2}}$	(1.178) (1.179)
	Inverse square: $\frac{\pi^2}{4}a^2NE_a\gamma$	(1.159)	$kE_i^{1/2}$	(1.190)
	Thomas–Fermi screening: $K\frac{NZ_1Z_2}{Z^{1/3}}\frac{M_1}{M_1+M_2}$ where $Z^{1/3} = \left(Z_1^{2/3}+Z_2^{2/3}\right)^{1/2}$ and $K = \left(\frac{\pi}{e}\right)\varepsilon^2 a_0 = 2.8\times10^{-15}\,\text{eV}\cdot\text{cm}^2$	(1.163)	$k = 8\sigma_e N\left(\frac{m_e}{M_1}\right)^{1/2}$ valid for $0 < E\,(\text{keV}) < 37Z^{7/3}$	

$$R = \int_0^R dx = \frac{1}{N}\int_0^{E_i}\frac{dE}{[S_n(E)+S_e(E)]}. \tag{1.193}$$

This distance is called the average total range and is a useful quantity for making estimates of the average penetration depths of ions in amorphous targets. In general, the total path length due only to nuclear stopping can be obtained by substituting the nuclear stopping power from Eq. (1.138) into:

$$R = \int_0^{E_i}\frac{dE}{NS_n(E)}\frac{\pi}{2}, \tag{1.194}$$

to give:

$$R(E_i) = \left(\frac{1-m}{2m}\right)\frac{\gamma^{m-1}}{NC_m}E_i^{2m}, \tag{1.195}$$

and in reduced notation, substituting the stopping power given in Eq. (1.153) into:

$$\rho_x = \int_0^{\in}\frac{d\in}{S_n(\in)}, \tag{1.196}$$

to give:

$$\rho_x = \frac{1-m}{m\lambda_m} \in^{2m} . \tag{1.197}$$

An estimate of the total path length for the case of nuclear stopping only with application of the inverse square potential [see Eq. (1.156)] is as follows:

$$\begin{aligned} \frac{\mathrm{d}E}{\mathrm{d}x} &= N \int_{\check{T}}^{\gamma E_\mathrm{i}} T\sigma_\mathrm{s}(E_\mathrm{i}, T)\mathrm{d}T \quad \text{where} \quad \sigma_\mathrm{s}(E_\mathrm{i}, T) = \frac{\pi^2 a^2 E_a \gamma^{1/2}}{8E_\mathrm{i}^{1/2} T^{3/2}} \\ &= \frac{\pi^2}{4} a^2 N E_a \gamma, \end{aligned} \tag{1.198}$$

so,

$$\begin{aligned} \overline{x} = \overline{R}_\mathrm{total} &= \int_0^{E_\mathrm{i}} \frac{\mathrm{d}E'}{(\mathrm{d}E/\mathrm{d}x)_n} = \int_0^{E_\mathrm{i}} \frac{\mathrm{d}E'}{\frac{\pi^2}{4} a^2 N E_a \gamma} \\ &\frac{4E_\mathrm{i}}{\pi^2 a^2 N E_a \gamma} \quad \text{where} \quad E_\mathrm{i} \leq E_a. \end{aligned} \tag{1.199}$$

The quantity of interest is, however, the projection of the total range on the initial direction of the particle path (Fig. 1.21). In addition, we want to know the deviation in the projected range, which arises from the fact that all particles do not suffer the same sequence of collisions. We then define:

$\overline{R_\mathrm{p}} \equiv$ mean projected range and

$\overline{\Delta R_\mathrm{p}} \equiv$ standard deviation of the projected range.

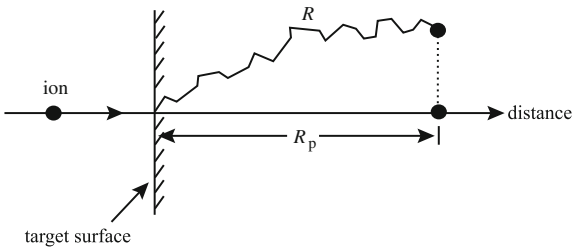

Fig. 1.21 Total path length R and projected range R_p for an ion incident on a target

Methods for computing $\overline{R_\mathrm{p}}$ have been developed by Lindhard et al. [16]. In cases where the energy transfer T is small compared to the total energy of the particle, the differential equation for $\overline{R_\mathrm{p}}$ has the solution:

$$\overline{R_\mathrm{p}} = \int_0^{E_\mathrm{i}} \frac{\mathrm{d}E'}{\beta_1(E')} \exp\left[\int_{E_\mathrm{i}}^{E'} \frac{\alpha_1(x)\,\mathrm{d}x}{\beta_1(x)}\right], \tag{1.200}$$

where $\alpha_1(E) = \dfrac{\mu}{2} N \dfrac{S_\mathrm{n}(E)}{E}$,

$$\beta_1(E) = N\left[S_\mathrm{n}(E) + S_\mathrm{e}(E) - \frac{\mu}{2}\frac{\Omega_\mathrm{n}^2(E)}{E}\right], \tag{1.201}$$

and $\Omega_\mathrm{n}^2(E) = \int_0^\infty T_\mathrm{n}^2 2\pi b\,\mathrm{d}b$.

The standard deviation is computed by defining the quantities R_c (chord range) and $R_\perp$ (range perpendicular to the initial direction) so that, from Fig. 1.22, we have the following relation:

$$\overline{R_\mathrm{c}^2} = \overline{R_\mathrm{p}^2} + \overline{R_\perp^2}, \tag{1.202}$$

and a related quantity:

$$\overline{R_\mathrm{r}^2} = \overline{R_\mathrm{p}^2} - \frac{1}{2}\overline{R_\perp^2}, \tag{1.203}$$

and for cases where $T \ll E$:

$$\overline{R_\mathrm{r}^2(E)} = \int_0^{E} \frac{2\overline{R_\mathrm{p}(E')}\,\mathrm{d}E'}{\beta_2(E')} \exp\left[\int_{E}^{E'} \frac{3\alpha_2(x)}{\beta_2(x)}\mathrm{d}x\right], \tag{1.204}$$

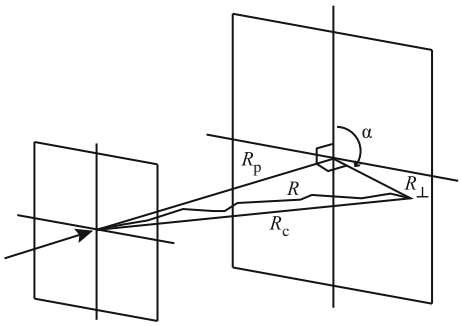

Fig. 1.22 Schematic of the definition of range parameters R, R_p, R_c, $R_\perp$

and

$$\overline{R_c^2(E)} = \int_0^E \frac{2\overline{R_p(E')}\,dE'}{N[S_n(E') + S_e(E')]}, \tag{1.205}$$

and then $\overline{\Delta R_p}$ is found from:

$$(\overline{\Delta R_p})^2 = \frac{2\overline{R_r^2}(E) + \overline{R_c^2}(E)}{3} - (\overline{R_p})^2, \tag{1.206}$$

where $\alpha_2(E) = \alpha_1(E)/2, \beta_2(E) = \beta_1(E) - \dfrac{N\mu\Omega_n^2(E)}{E}$.

The integrals can be evaluated numerically for the Thomas–Fermi potential or analytically if the approximate values of S_n and S_e are used together with the value:

$$\Omega_n^2(E) = \frac{4M_1M_2}{3(M_1 + M_2)} S_n^0 E. \tag{1.207}$$

In LSS formalism, the average total path length can be calculated from:

$$\rho_R = \int_0^{\in} \frac{d \in}{[S_n(\in) + S_e(\in)]} = \int_0^{\in} \frac{d \in}{[S_n(\in) + k \in^{1/2}]}. \tag{1.208}$$

This expression must be integrated numerically using different values of k. For a particular Z_1, Z_2, and E_i, we calculate $\in$ and k and then read off the value of ρ_R from Fig. 1.23 and convert to R using Eqs. (1.139), (1.140), and $\rho_R = 3.06\varepsilon$:

$$R(\text{nm}) = \frac{6EM_2(M_1 + M_2)\left(Z_1^{2/3} + Z_2^{2/3}\right)^{1/2}}{\rho Z_1 Z_2 M_1}, \tag{1.209}$$

where E is in keV and ρ is in g/cm^3. The most interesting range quantity of interest is the average projected range, R_p, and this is what is usually measured. At high energies, $S_e \gg S_n$ and $R \sim R_p$. At low energies where $S_n \sim S_e$, then $R_p < R$. This difference gets larger with M_2/M_1. LSS theory also analyzed this problem.

At low $\in$ or ρ_R (and small values of k):

$$\begin{aligned} \text{For} \quad & M_2/M_1 = \frac{1}{2}; \quad R/R_p \sim 1.2 \\ & M_2/M_1 = 1; \quad R/R_p \sim 1.6 \\ \text{and} \quad & M_2/M_1 = 2; \quad R/R_p \sim 2.2. \end{aligned}$$

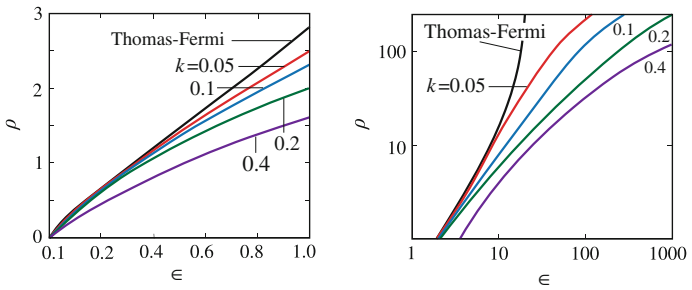

Fig. 1.23 Reduced range–energy plots for various values of the electronic stopping parameter, k

At high energies ($\in$ large), $R/R_p \rightarrow 1$ for all k. Finally as a general approximation [16]:

$$\frac{R}{R_p} \cong 1 + B\frac{M_2}{M_1}, \tag{1.210}$$

where B is a slowly varying function of E and R. In the energy region where nuclear stopping dominates and $M_1 > M_2$, $B = 1/3$. Increased electronic stopping at higher energies leads to smaller values of B. When $M_1 < M_2$, large-angle scattering increases the difference between R and R_p. However, for these collisions, electronic stopping is appreciable and partially offsets the increase in the difference. Therefore, $B = 1/3$ is a reasonable approximation for a wide range of conditions, giving:

$$R_p \cong \frac{R}{1 + (M_2/3M_1)}. \tag{1.211}$$

Range straggling can be calculated using the theory of Lindhard et al. [16]. For the case where nuclear stopping dominates and $M_1 > M_2$, i.e., small-angle scattering:

$$2.5\Delta R_p \cong 1.1R_p\left[\frac{2(M_1M_2)^{1/2}}{M_1 + M_2}\right], \tag{1.212}$$

or

$$\Delta R_p \cong R_p/2.5. \tag{1.213}$$

For a high-energy ion, the slowing down path is essentially a straight line in the original direction of motion, since the stopping is electronic with a small amount of straggle at the end due to nuclear collisions (Fig. 1.24(a)). At lower energies where S_n and S_e are more comparable, the ion path follows a zigzag course with many large deflections with the distance between collisions decreasing as the energy

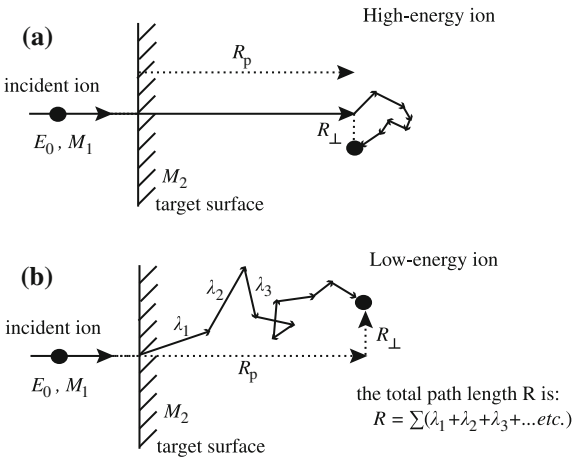

Fig. 1.24 Total path length, projected range, and perpendicular range for (**a**) high-energy ions and (**b**) low-energy ions incident on a target

decreases and the cross section increases (Fig. 1.24(b)). The incident particles are distributed according to a Gaussian as:

$$N(x) = N_p e^{-1/2X^2}, \tag{1.214}$$

where $X = \dfrac{x - R_p}{\Delta R_p}$ and ΔR_p is the standard deviation (Fig. 1.25). If the peak concentration is N_p at R_p, then this will fall to $\dfrac{1}{e^{1/2}} N_p$ at distances $x = R_p \pm \Delta R_p$. If we view the target perpendicularly through its surface, then the number of implanted ions per unit area will be N_s, given by:

$$N_s = \int_{-\infty}^{+\infty} N(x)\,dx, \tag{1.215}$$

or since $dx = \Delta R_p dX$ and the Gaussian curve is symmetrical, then:

$$N_s = 2\Delta R_p N_p \int_0^{\infty} e^{-1/2X^2}\,dX, \tag{1.216}$$

which can be written as follows:

$$N_s = \Delta R_p N_p \sqrt{2\pi} \left\{ \sqrt{\frac{2}{\pi}} \int_0^{\infty} e^{-1/2X^2}\,dX \right\}. \tag{1.217}$$

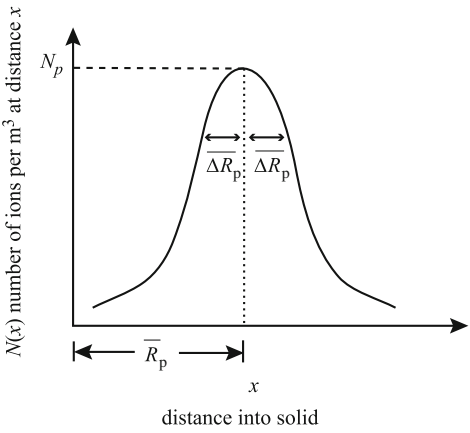

Fig. 1.25 Parameters of the Gaussian distribution applied to an ion implantation profile showing the projected range, $\overline{R}_p$, the straggling or standard deviation, $\overline{\Delta R}_p$, and the maximum concentration, N_p of the implanted ion

The integral inside the bracket is the error function and tends to unity as $X \rightarrow \infty$, so that if N_s is the number of ions/cm^2 implanted into the target, we have:

$$N_p = \frac{N_s}{\sqrt{2\pi}\Delta R_p} \cong \frac{0.4N_s}{\Delta R_p}, \tag{1.218}$$

so the density of implanted ions is as follows:

$$N(x) = \frac{0.4N_s}{\Delta R_p} \exp\left(-1/2\left\{\frac{x - R_p}{\Delta R_p}\right\}^2\right). \tag{1.219}$$

As an example, if we implant 5×10^{15} ions/cm^2 of 40 keV B into Si, then $R_p \sim 160$ nm, $\Delta R_p \sim 54$ nm, and $N_p \sim 4 \times 10^{20}$ atoms/cm^2. Note that from the properties of the Gaussian, the concentration will fall by one decade at $x \simeq R_p \pm 2\Delta R_p$ and by 2 decades at $x \simeq R_p \pm 3\Delta R_p$.

Using the LSS treatment to describe electronic and nuclear stopping, Littmark and Ziegler have solved for the ranges of atoms with atomic number between 1 and 92 in all elements [18]. For each atom serving as the target, the mean ion depth, longitudinal straggling, and transverse straggling are compiled in graphs for projectiles with $1 \leq Z \leq 92$ and over a wide energy range. The following example is taken from this handbook.

Example 1.3. MeV He implantation into Si
Zeigler [18] plots and tabulates the range parameters for a wide range of ions and target atoms. For 2 MeV He incident on a Si target, the range and straggling are 7.32 μm and 0.215 μm, respectively. If we assume a dose of 10^{15} He ions/cm^2, then applying Eq. (1.218) gives a peak concentration of $\sim 1.86 \times 10^{19}$ He atoms/cm^3 at a depth of 7.32 μm, which is approximately

620 appm. Equation (1.219) gives the distribution of deposited He atoms as follows:

$$N(x) = 1.86 \times 10^{19} \exp\left(-1/2\left\{\frac{x - 7.32}{0.215}\right\}^2\right) \text{He/cm}^3,$$

where x is in units of μm.

In addition to a tabulation of range data, Ziegler has developed a Monte Carlo-based computer program for calculating the transport of ions in matter [20]. The program is available on the Web at http://www.srim.org, and the reader is encouraged to try some examples using the SRIM simulation software. This program is downloadable at no cost to the user (subject to the terms of use posted on the site) and may be executed on your personal computer. The following example uses data taken from the SRIM program.

Example 1.4. Implantation of Al into Ni
A similar example can be worked for lower energy implantation of a heavier element such as Al, into a nickel target. In this case, we use the output of the SRIM program. Selecting 200 keV Al in Ni results in a projected range of ~135 nm with a longitudinal straggling of 44 nm. Substitution into Eq. (1.216) yields a peak concentration of 9.1×10^{19} Al/cm^3 for a dose of 10^{15} Al$^+$/cm^2. The SRIM software also yields a quantity that allows the user to determine concentration. The unit of concentration in the ion range plot is [atoms/cm^3/atoms cm^2], and the range of the implanted ion distribution on this plot has a maximum of $\sim 8 \times 10^4$ atoms/cm^3/atoms cm^2. Multiplying this value by the dose of 10^{15} Al$^+$/cm^2 gives $\sim 8 \times 10^{19}$ Al/cm^3 which is close to the analytical solution.

Chapter Review
The chapter began with a description of neutron–nuclear collisions, utilizing the absence of charge on the neutron to describe the interaction using a hard sphere approximation. Expressions for the energy transfer in elastic and inelastic scattering collisions were developed, and (n, 2n) and (n, γ) reactions were analyzed as well to determine the energy transferred. Table 1.2 summarizes the energy transfer and energy transfer cross sections for these types of reactions. The description of projectile–target interaction was broadened to include ion–atom and atom–atom collisions which are relevant for two important cases: ion irradiation or implantation and the interaction between atoms in a lattice after the initial collision with a neutron in reactor materials. Interatomic potentials form the basis for describing the

interaction between atoms and also for determining the energy transfer cross section. Table 1.3 summarizes the important potentials used to describe these interactions.

Collision kinematics was then used to develop a description of the orbit of colliding atoms and hence the transferred energy and the energy transfer cross section. Because there is not one single interatomic potential that describes the interaction over the entire distance (energy) range, the energy transfer and energy transfer cross sections are analyzed in various energy ranges and for various classes of interactions. Rutherford scattering is used to describe light energetic ions, and slow heavy ions, energetic heavy ions, and relativistic electrons are all treated separately. Table 1.5 summarizes the energy transfer and energy transfer cross section for various atom–atom collisions.

Energy loss theory is developed in order to determine the energy loss of energetic atoms/ions to the solid by elastic/nuclear collisions and by collisions with the electrons of the target. Collisions are analyzed in terms of their energy range for both nuclear stopping and electronic stopping. Table 1.7 summarizes the stopping powers for various types of interactions. Finally, the stopping powers are used to develop expressions for the range and projected range of ions in solids so that their penetration depth and concentration distribution can be determined.

Nomenclature

a	Screening radius
a_0	Bohr radius of the hydrogen atom
a_U	Universal screening length
A	Atomic mass, or Pre-exponential constant in Born–Mayer relation, Eq. (1.47)
b	Impact parameter
B	Constant in exponent in Born–Mayer relation, Eq. (1.47)
C	Constant in screened Coulomb potential, Eq. (1.49) = 0.8853
c	Speed of light
D	Nearest neighbor spacing between atoms
E_a	Value of E_i that yields $\rho_0 = a$
E_b	Value of E_i that gives $T \geq E_\mathrm{d}$ at $b = a$
E_d	Displacement energy
E_D	Maxwellian nuclear temperature = kT
E_f	Final energy
E_γ	Gamma ray energy
E_i	Incoming particle energy
$E^f_{\mathrm{v,i}}$	Vacancy and interstitial formation energy
$E^m_{\mathrm{v,i}}$	Vacancy and interstitial migration energy
E'_m	Kinetic energy of incoming particle in CM system
E''_m	Energy of neutron after (n, 2n) reaction
E'_M	Kinetic energy of target particle in CM system
E''_M	Energy of CM after (n, 2n) reaction

E_{R}	Rydberg energy
E_{T}	Total energy
$\bar{I}$	Excitation–ionization level
k_e	Coulomb constant
m	Mass of incoming particle
M	Mass of target
N	Atom number density
N_{p}	Peak implanted ion concentration
N_{s}	Implanted ion density in ions/unit area
p_{e}	Momentum of electron
Q	Excitation energy of nucleus
r_{e}	Nearest neighbor spacing between atoms
$\dot{r}$	Radial velocity in polar coordinates
R	Range of ion
R_{eff}	Recombination radius
R_{p}	Projected range
ΔR_{p}	Standard deviation of projected range
s	Power law exponent
S_{e}	Electronic stopping power
S_{n}	Nuclear stopping power
t	Time, or Dimensionless collision parameter, Eq. (1.142)
T	Energy transferred in collision
$\check{T}$	Minimum energy transferred
$\hat{T}$	Maximum energy transferred
$\overline{T}$	Average energy transferred
T_ℓ	Energy transferred to target atom after (n, 2n) reaction
$V(r)$	Potential energy
υ_{c}	Velocity of incoming particle in CM system
V_{c}	Velocity of target particle in CM system
υ'_{c}	Velocity of incoming particle in CM system after collision
V'_{c}	Velocity of target atom in CM system after collision
υ''_{c}	Velocity of neutron in CM system after (n, 2n) reaction
V''_{c}	Velocity of target atom in CM system after (n, 2n) reaction
V_{CM}	Velocity of CM in laboratory system
υ_ℓ	Velocity of incoming particle in laboratory system
υ'_ℓ	Velocity of incoming particle in laboratory system after collision
V'_ℓ	Velocity of target atom in laboratory system after collision
V''_ℓ	Velocity of target atom in laboratory system after (n, 2n) reaction
Z	Atomic number
β	υ/c
$\chi(r)$	Screening function
χ_U	Universal screening function
ε	Unit electronic charge
ε_0	Electric constant

$\in$	Dimensionless, reduced energy parameter, Eq. (1.139)
ϕ	Asymptotic scattering angle at infinity separation
ϕ	Scattering angle in CM system
$\dot{\psi}$	Angular velocity in polar coordinates
ψ	Scattering angle of struck atom in laboratory system
λ	Mean free path between collisions
λ_m	see Eq. (1.144)
λ'	1.309, Eq. (1.143)
μ	Reduced mass, Eq. (1.63)
$\nu(T)$	Displacement function
θ	Scattering angle in laboratory system
ρ	Distance between atom centers in a collision
ρ_e	Electron cloud density
ρ_0	Distance of closest approach, value of r when $\psi = \pi/2$
ρ_r	Dimensionless, reduced distance parameter, Eq. (1.140)
$\sigma\ (E_i)$	Total atomic collision cross section
$\sigma\ (E_i, T)$	Differential energy transfer cross section
$\sigma\ (E_i, \phi)$	Differential angular collision cross section
$\sigma\ (E_i, E_\phi, \Omega)$	Double differential collision cross section
$\sigma\ (E_i, Q_j, \phi)$	Differential angular cross section for inelastic collisions
$\sigma\ (E_i, Q_j, T)$	Differential energy transfer cross section for inelastic collisions
Ω	Solid angle into which incoming particle is scattered
$d\Omega$	Differential solid angular element
ξ_e	$Z_1^{1/6}$

Problems

1.1 A 0.5 MeV neutron strikes a target atom with mass A, which is initially at rest. Calculate the velocity and energy of both particles in the laboratory reference frame after a head-on collision for $A = 27$ (Al) and $A = 207.2$ (Pb).

1.2 A detector of 100 % efficiency (i.e., every particle entering the detector is registered) and area of 1 cm^2 is placed at a distance r from a target (taken to be of zero dimension, i.e., a point). The target is bombarded with neutrons. Assuming that only elastic scattering occurs, scattering is azimuthally symmetric, and the scattering cross section is isotropic:

(a) What is the ratio of the number of particles detected by the detector at positions 1 and 2 shown in the figure?

(b) What is the ratio of the number of particles scattered through an angular increment of 10° about $\theta_1 = 5°$ and $\theta_2 = 85°$?

(c) Repeat parts (a) and (b) assuming that instead of being isotropic, the differential scattering cross section varies as $\sigma_s(E_i, \theta) = \cos\theta$.

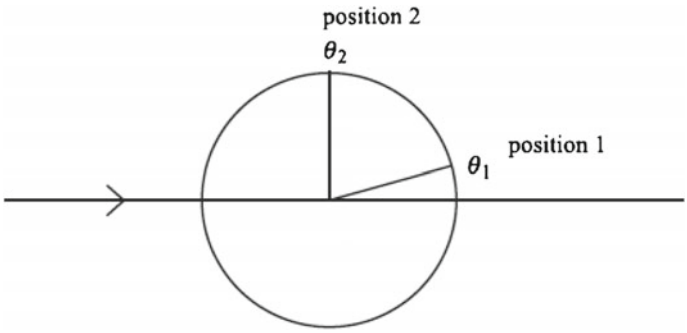

$d\theta$ = Increment of scattering angle
$d\Omega$ = Increment of solid angle about θ
θ = Scattering angle in the lab system

1.3 A Ti plate is bombarded with 10^{14} neutrons per cm^2 per second at perpendicular incidence. The entire plate is hit by the beam.

(a) Calculate the number of particles scattered per second at

(i) $85° \leq \theta = 86°$ and
(ii) $5° \leq \theta = 6°$.

The plate size is 1 cm^2 by 0.6 mm thick. Scattering is isotropic with a total scattering cross section of 2.87 barns (1 barn = 10^{-24} cm^2).

(b) The same target is bombarded with particles such that the differential angular scattering cross section is proportional to θ^2. Calculate the ratio of the atomic flux in interval (i) above to that in interval (ii). In both cases, perform full integration of the differential cross section.

(c) Approximate the integrals in (b) by assuming the differential angular scattering cross section to be constant in each integration interval and equal to the value at the interval's center.

1.4 Derive the kinematic factor K, defined as $K = E_f/E_i$, where E_i is the projectile energy before the collision and E_f is the projectile energy after the collision.

1.5 The following formula relates the scattering angles θ and ϕ in the laboratory and center-of-mass frames, respectively:

$$\tan\theta = (M/m)\sin\phi/[1 + (M/m)\cos\phi]$$

where m and M are the masses of the projectile and target, respectively. Discuss this expression for the following three cases: $m = M$, $m \gg M$, and $m \ll M$.

1.6 Derive Eq. (1.24) in the text.

1.7 Derive Eq. (1.39) in the text.

1.8 For two colliding particles write expressions for:

(a) E_T, the total energy of a system of n particles;
(b) E_{CM}, the energy of the center of mass (determined by V_{CM} and the total mass of the system); and
(c) E, the total energy in the CM system.
Show that $E = E_T - E_{CM}$ [Eq. (1.61)]

1.9 Derive a relation between b and ϕ from Eq. (1.76) for the hard sphere potential:

$$V_{HS}(r) = 0 \quad r > r_0$$
$$= \infty \quad r \leq r_0$$

Make sure your answer is correct for $b > r_0$.

1.10 As a means of describing atom–atom interaction at intermediate separation, i.e., between Coulombic repulsion and closed shell repulsion, an inverse power potential is often employed of the form

$$V(r) = \text{constant}/r^n.$$

For example, one can fit an inverse square ($n = 2$) function to the screened Coulomb potential at $r = a$ obtaining the same slope, ordinate, and curvature. This function is as follows:

$$V(r) = z_1 z_2 \varepsilon^2 a/(r^2 \exp[1]).$$

Formulate the cross sections $\sigma_s(E_i, T)$ and $\sigma_s(E_i, \phi)$ for atom–atom interactions obeying the inverse square potential function.

1.11 Compare your result in Problem 1.10 to that obtained using a Born–Mayer potential and a simple Coulomb potential. Comment on the similarities and differences.

1.12 Calculate the average energy transfer from a 100 keV Ni atom colliding with another Ni atom, using:

(a) The hard sphere potential and
(b) The inverse square potential.

1.13 Explain, in physical terms, why the scattering cross section resulting from Coulombic repulsion depends on the transferred energy, T, while that for neutron–nuclear interaction does not.

1.14 Assuming a pure Coulomb potential, determine the distance of closest approach for a 100 keV boron atom on silicon for an impact parameter, $b = 1$ nm. What is the significance of your answer?

1.15 1 MeV Al^+ ions are accelerated toward a pure Ni target. The ions are directed normal to the sample surface.

(a) Calculate the total path length and provide an estimate for the mean projected range of the ions.
(b) For a dose of 10^{16} ions/cm^2, estimate the maximum Al concentration and the FWHM of the Al distribution. Use $S_e(E) = k'E^{1/2}$, where $k' = 2 \times 10^{-16}$ eV$^{1/2}$ cm^2.

1.16 A 10 MeV Si ion penetrates a Si crystal.

(a) Calculate its energy as a function of distance traveled and its penetration depth. Assume that electronic stopping dominates.
(b) Write an expression for the depth distribution of implanted Si ions and give the straggling.

1.17 Calculate the energy threshold above which the Rutherford scattering cross section can be used for: (i) near head-on collisions and (ii) all collisions of He^{++} and H^+ in Si and Pd.

1.18 2 MeV He^{++} ions are backscattered ($\theta = 180°$) off of a 25-nm-thick gold foil. Determine the highest and lowest energy values of the backscattered ions as measured in a detector placed at 180° with respect to the incoming beam. Use $k = 0.14 \times 10^{-15}$ eV$^{1/2}$ cm^2.
Determine the stopping power by interpolation or extrapolation based on the following values of $1/N(dE/dx)$ (in eV/(10^{15} atoms/cm^2)):

Energy (MeV):	1.6	2.0
Au	122.3	115.5
Al	47.5	44.25

1.19 Assume the stopping power can be described by the following function:

$$S = C + KE^{1/2} \text{ where } C \text{ and } K \text{ are constants.}$$

(a) Derive an equation for the particle range as a function of energy.
(b) Does the range increase or decrease as:

(i) Energy increases;
(ii) K increases; and
(iii) C increases.

1.20 Which increases the high-energy electronic stopping power the most, increased charge, energy, or mass of the projectile ion?

1.21 A 2 MeV proton travels through lead.

(a) Assuming elastic collisions, calculate the maximum energy that can be transferred from the proton to the lead.

(b) What energy would a Pb ion need to have the same maximum energy transfer in a Pb–Pb collision as the proton–Pb collision in part (a)?

1.22 An Fe particle is fired at a block of natural uranium. To get the Fe as close to the uranium particle as possible, would you be better off using a higher charge state of Fe or a lighter isotope? Assume Coulomb potentials can be used.

1.23 A thin film containing F^{19} is bombarded with 1.85 MeV protons. The following reaction takes place:

$$F^{19} + p \rightarrow O^{16} + \alpha.$$

The reaction has a Q value of 8.13 MeV. After interaction, an alpha particle is seen to emerge at a right angle to the incident proton beam. What are the energies of the alpha particle and the oxygen atom? What is the maximum energy each of these particles could transfer to a stationary Fe atom?

1.24 A helium atom at 1 MeV is sent into iron. Assuming the electronic stopping cross section is a constant (88×10^{-5} eV cm^2), what is the energy of the helium atom after it travels 500 nm? If the He atom collides with an Fe atom after traveling 500 nm, what is the maximum energy transferred? Assume an atomic density of 8.5×10^{22} atoms/cm^3 for Fe. Was an assumption of constant stopping power valid?

References

1. Ullmaier H, Schilling W (1980) Radiation damage in metallic reactor materials. In: Physics of modern materials, vol I. IAEA, Vienna
2. Lamarsh JR (1971) Introduction to nuclear reactor theory. Addison-Wesley, Reading, MA
3. Doran DG (1972) Neutron Dispalcement Cross Sections for Stainless Steel and tantalum based on a Lindhard model. Nucl Sci Eng 49:130
4. Odette GR (1972) Energy Distribution of neutrons from (n,2n) reactions. Trans Am Nucl Soc 15:464
5. Segev M (1971) Inelastic matrices in multigroup calculation, ANL-7710. Argonne National Lab, Argonne, IL, p 374
6. Evans RD (1955) The atomic nucleus. McGraw-Hill, New York
7. Chadderton LT (1965) Radiation damage in crystals. Methuen, London
8. Born M, Mayer JE (1932) Zur gittertheorie der ionenkristalle. Z Physik 75:1
9. Firsov OB (1957) Calculation of the interaction potential of atoms for small nuclear separations. Zh Eksper Teor Fiz 32:1464
10. Firsov OB (1957) Calculation of atomic interaction potentials. Zh Eksper Teor Fiz 33:696
11. Brinkman JA (ed) (1962) Radiation damage in solids. Academic, New York
12. Abrahamson AA (1963) Repulsive interaction potentials between rare-gas atoms. Homonuclear two-center systems. Phys Rev 130:693
13. Thompson MW (1969) Defects and radiation damage in metals. Cambridge University Press, Cambridge

14. Lindhard J, Nielsen V, Scharff M (1968) Approximation method in classical scattering by screened Coulomb fields. Mat Fys Medd Dan Vid Selsk 36(10):1–32
15. Winterbon KB, Sigmund P, Sanders JB (1970) Spatial distribution of energy deposited by atomic particles in elastic collisions. Mat Fys Medd Dan Vid Selsk 37(14):1–73
16. Lindhard J, Scharff M, Schiott HE (1963) Range concepts and heavy ion ranges. Mat Fys Medd Dan Vid Selsk 33(14):3
17. Lindhard J, Winther A (1964) Stopping power of electron gas and equipartition. Mat Fys Medd Dan Vid Selsk 34:1
18. Littmark U, Ziegler JF (1980) Handbook of range distributions of energetic ions in all elements. Pergamon, New York
19. Nastasi M, Mayer JW, Hirvonen JK (1996) Ion-Solid Interactions: fundamentals and applications. Cambridge University Press, Cambridge
20. Ziegler JF (2015) SRIM The stopping and range of ions in solids. IIT Co. (www.srim.org)

Chapter 2
The Displacement of Atoms

2.1 Elementary Displacement Theory

The struck lattice atom of energy T is referred to as a primary knock-on atom, or PKA. This atom moves through the lattice encountering other lattice atoms. Such encounters may result in sufficient energy transfer to displace this lattice atom from its site resulting in two displaced atoms. If this collision sequence continues, a series of tertiary knock-ons is produced resulting in a collision cascade. A cascade is a spatial cluster of lattice vacancies and atoms residing as interstitials in a localized region of the lattice. Such a phenomenon can have a profound effect on the physical and mechanical properties of the alloy, as will become evident later. Here, we are concerned with being able to quantify the displacement cascade. That is, for a neutron of energy E_i, striking a lattice atom, how many lattice atom displacements will result? We have already discussed in detail the nature of neutron–nucleus and atom–atom collisions. Now, we will develop a model for determining the number of atoms displaced by a PKA of energy T.

Recall that to quantify radiation damage, we require a solution to the damage rate equation:

$$R_\mathrm{d} = N \int_{\underset{E}{\vee}}^{\hat{E}} \phi(E_\mathrm{i}) \sigma_\mathrm{D}(E_\mathrm{i})\, \mathrm{d}E_\mathrm{i}, \tag{2.1}$$

where N is the lattice atom number density, $\phi\,(E_\mathrm{i})$ is the energy-dependent particle flux, and $\sigma_\mathrm{D}\,(E_\mathrm{i})$ is the energy-dependent displacement cross section. The displacement cross section is a probability for the displacement of lattice atoms by incident particles:

$$\sigma_\mathrm{D}(E_\mathrm{i}) = \int_{\underset{T}{\vee}}^{\hat{T}} \sigma(E_\mathrm{i}, T)\, \nu\,(T)\, \mathrm{d}T, \tag{2.2}$$

G.S. Was, *Fundamentals of Radiation Materials Science*,
DOI 10.1007/978-1-4939-3438-6_2

where $\sigma(E_i, T)$ is the probability that a particle of energy E_i will impart a recoil energy T to a struck lattice atom, and $\nu(T)$ is the number of displaced atoms resulting from such a collision. Chapter 1 provided the energy transfer cross section appearing in Eq. (2.2) for various types of particles in various energy ranges. This chapter will be devoted to supplying the second term in the integrand, $\nu(T)$, the number of atom displacements resulting from a primary recoil atom of energy T, and the limits of T between which displacements occur. Finally, we will develop the displacement cross section and an expression for the displacement rate.

2.1.1 Displacement Probability

As a first step, we define $P_d(T)$ as the probability that a struck atom is displaced upon receipt of energy T. Clearly, there is some minimum energy that must be transferred in order to produce a displacement. We will call this energy, E_d. The magnitude of E_d is dependent upon the crystallographic structure of the lattice, the direction of the incident PKA, the thermal energy of the lattice atom, etc. These considerations will be discussed in detail later. By definition of E_d, the probability of displacement for $T < E_d$ is zero. If E_d is a fixed value under all conditions, then the probability of displacement for $T \geq E_d$ is one. Hence, our simplest model for the displacement probability is a step function:

$$\begin{aligned} P_d(T) &= 0 \quad \text{for} \quad T < E_d \\ &= 1 \quad \text{for} \quad T \geq E_d, \end{aligned} \tag{2.3}$$

and is shown in Fig. 2.1. However, E_d is not constant for all collisions due to the factors mentioned earlier. The effect of atomic vibrations of the lattice atoms would be expected to lower the value of E_d or introduce a natural "width" of the order kT to the displacement probability. Further, as will be discussed later, the effect of crystallinity will also contribute strongly to the blurring effect on E_d. In fact, the picture in Fig. 2.1 and Eq. (2.3) is only strictly true for an amorphous solid at 0 K. A more realistic representation is shown in Fig. 2.2 and is represented as:

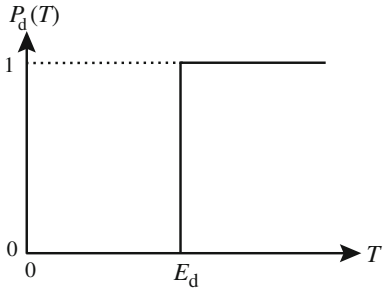

Fig. 2.1 The displacement probability $P_d(T)$ as a function of the kinetic energy transferred to a lattice atom, assuming a sharp displacement threshold

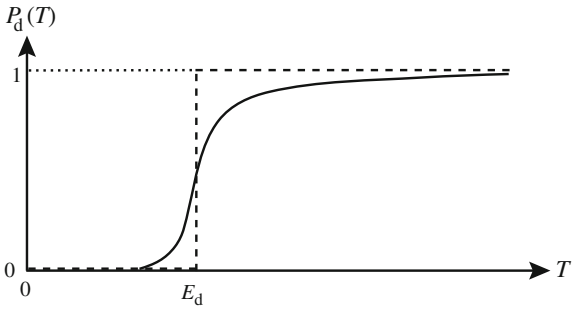

Fig. 2.2 The displacement probability as a function of the kinetic energy transferred to the lattice atom allowing for a blurring of the threshold due to atomic vibrations, impurity atoms, etc.

$$\begin{aligned} P_d(T) &= 0 \quad \text{for} \quad T < E_{d_{min}} \\ &= f(T) \quad \text{for} \quad E_{d_{min}} \leq T < E_{d_{max}} \\ &= 1 \quad \text{for} \quad T \geq E_{d_{max}}, \end{aligned} \tag{2.4}$$

where $f(T)$ is a smoothly varying function between 0 and 1. Given the displacement probability, the next task is to find the number of displacements as a function of the energy transferred. Kinchin and Pease [1] developed a simple theory to find the average number of displaced atoms initially created by a PKA of energy T in a given solid lattice. Their analysis is based on the following assumptions:

1. The cascade is created by a sequence of two-body elastic collisions between atoms.
2. The displacement probability is 1 for $T \geq E_d$ as given by Eq. (2.3).
3. When an atom with initial energy T emerges from a collision with energy T' and generates a new recoil with energy ε, it is assumed that no energy passes to the lattice and $T = T' + \varepsilon$.
4. Energy loss by electron stopping is given by a cutoff energy E_c. If the PKA energy is greater than E_c, no additional displacements occur until electron energy losses reduce the PKA energy to E_c. For all energies less than E_c, electronic stopping is ignored, and only atomic collisions occur.
5. The energy transfer cross section is given by the hard sphere model.
6. The arrangement of the atoms in the solid is random; effects due to crystal structure are neglected.

Assumption 1 is fundamental to all theories of a cascade consisting of isolated point defects. Elimination of this restriction allows the cascade to be represented by a displacement spike discussed in Chap. 3. Assumption 2 neglects crystallinity and atomic vibrations, which will add a natural width or "blurring" effect to the distribution. Later on, we will relax Assumptions 3, 4, 5 and 6.

2.1.2 The Kinchin and Pease Model for Atom Displacements

Consider the two moving atoms created when a PKA first strikes a stationary atom. After the collision, the PKA has residual energy $T - \varepsilon$ and the struck atom receives an energy $\varepsilon - E_d$, giving:

$$\nu(T) = \nu(T - \varepsilon) + \nu(\varepsilon - E_d), \tag{2.5}$$

where E_d is the energy consumed in the reaction. By neglecting E_d relative to ε, i.e., $\varepsilon \gg E_d$ according to Assumption 3, then Eq. (2.5) becomes:

$$\nu(T) = \nu(T - \varepsilon) + \nu(\varepsilon). \tag{2.6}$$

Equation (2.6) is not sufficient to determine $\nu(T)$ because the energy transfer ε is unknown. Since the PKA and lattice atoms are identical, ε may lie anywhere between 0 and T. However, if we know the probability of transferring energy in the range (ε, dε) in a collision, we can multiply Eq. (2.6) by this probability and integrate over all allowable values of ε. This will yield the average number of displacements.

Using the hard sphere Assumption 5, the energy transfer cross section is as follows:

$$\sigma(T, \varepsilon) = \frac{\sigma(T)}{\gamma T} = \frac{\sigma(T)}{T} \quad \text{for like atoms,} \tag{2.7}$$

and the probability that a PKA of energy T transfers energy in the range (ε, dε) to the struck atom is as follows:

$$\frac{\sigma(T, \varepsilon)\mathrm{d}\varepsilon}{\sigma(T)} = \frac{\mathrm{d}\varepsilon}{T}, \tag{2.8}$$

for $\gamma = 1$ (like atoms). Multiplying the right-hand side of Eq. (2.6) by dε/T and integrating from 0 to T yields:

$$\begin{aligned} \nu(T) &= \frac{1}{T}\int_0^T [\nu(T - \varepsilon) + \nu(\varepsilon)]\mathrm{d}\varepsilon \\ &= \frac{1}{T}\left[\int_0^T \nu(T - \varepsilon)\mathrm{d}\varepsilon + \int_0^T \nu(\varepsilon)\mathrm{d}\varepsilon\right]. \end{aligned} \tag{2.9}$$

A change in variables from ε to $\varepsilon' = T - \varepsilon$ in the first integral in Eq. (2.9) gives:

$$\nu(T) = \frac{1}{T}\int_0^T \nu(\varepsilon')\,\mathrm{d}\varepsilon' + \frac{1}{T}\int_0^T \nu(\varepsilon)\,\mathrm{d}\varepsilon, \tag{2.10}$$

which is really a sum of two identical integrals. Therefore,

$$\nu(T) = \frac{2}{T}\int_0^T \nu(\varepsilon)\,\mathrm{d}\varepsilon. \tag{2.11}$$

Before solving Eq. (2.11), let us examine the behavior of $\nu(\varepsilon)$ near the displacement threshold, E_d. Clearly when $T < E_\mathrm{d,}$ there are no displacements and:

$$\nu(T) = 0 \quad \text{for} \quad 0 < T < E_\mathrm{d}. \tag{2.12}$$

If T is greater than or equal to E_d but less than $2E_\mathrm{d}$, two results are possible. The first is that the struck atom is displaced from its lattice site, and the PKA, now left with energy less than E_d, falls into its place. However, if the original PKA does not transfer E_d, the struck atom remains in place and no displacement occurs. In either case, only one displacement in total is possible from a PKA with energy between E_d and $2E_\mathrm{d}$, and:

$$\nu(T) = 1 \quad \text{for } E_\mathrm{d} \le T < 2E_\mathrm{d}. \tag{2.13}$$

Using Eqs. (2.12) and (2.13), we may split the integral in Eq. (2.11) into ranges from 0 to E_d, E_d to $2E_\mathrm{d}$, and $2E_\mathrm{d}$ to T and evaluate:

$$\nu(T) = \frac{2}{T}\left[\int_0^{E_\mathrm{d}} 0\mathrm{d}\varepsilon + \int_{E_\mathrm{d}}^{2E_\mathrm{d}} 1\mathrm{d}\varepsilon + \int_{2E_\mathrm{d}}^{T} \nu(\varepsilon)\mathrm{d}\varepsilon\right],$$

yielding:

$$\nu(T) = \frac{2E_\mathrm{d}}{T} + \frac{2}{T}\int_{2E_\mathrm{d}}^{T} \nu(\varepsilon)\mathrm{d}\varepsilon. \tag{2.14}$$

We can solve Eq. (2.14) by multiplying by T and differentiating with respect to T giving:

$$T\frac{\mathrm{d}\nu}{\mathrm{d}T} = \nu, \tag{2.15}$$

with the solution:

$$\nu = CT. \tag{2.16}$$

Substituting Eq. (2.16) into Eq. (2.14) gives:

$$C = \frac{1}{E_\mathrm{d}}, \tag{2.17}$$

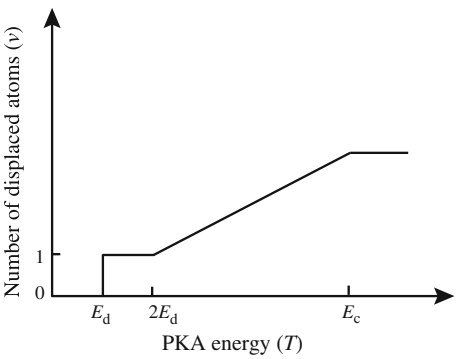

Fig. 2.3 The number of displaced atoms in the cascade as a function of the PKA energy according to the model of Kinchin and Pease

and therefore:

$$\nu(T) = \frac{T}{2E_d} \quad \text{for } 2E_d \leq T < E_c. \tag{2.18}$$

The upper limit is set by E_c (Assumption 4). When a PKA is born with $T \geq E_c$, the number of displacements is $\nu(T) = E_c/2E_d$. So the full Kinchin–Pease (K–P) result is as follows:

$$\nu(T) = \begin{cases} 0 & \text{for } T < E_d \\ 1 & \text{for } E_d \leq T < 2E_d \\ \dfrac{T}{2E_d} & \text{for } 2E_d \leq T < E_c. \\ \dfrac{E_c}{2E_d} & \text{for } T \geq E_c \end{cases} \tag{2.19}$$

Note that if E_c is ignored, $T/2E_d$ is a true average since the number of displacements can range from 0 (no energy transfers above E_d) to $T/E_d - 1$ (every collision transfers just enough), and for large T, $T/E_d \gg 1$. So the maximum value of $\nu(T)$ is T/E_d. The full displacement function described by Eq. (2.19) is shown in Fig. 2.3.

2.1.3 The Displacement Energy

A lattice atom must receive a minimum amount of energy in the collision in order to be displaced from its lattice site. This is the displacement energy or displacement threshold, E_d. If the energy transferred, T, is less than E_d, the struck atom will vibrate about its equilibrium position but will not be displaced. These vibrations will be transmitted to neighboring atoms through the interaction of their potential fields, and the energy will appear as heat. Hence, the potential fields of the atoms in the lattice form a barrier over which the stuck atom must pass in order to be displaced. This is the source of the displacement threshold energy.

Since metals are crystalline, the potential barrier surrounding an equilibrium lattice site is not uniform in all directions. In fact, there are directions in which the surrounding atoms will remove large amounts of energy from the struck atom yielding a high potential barrier. Along directions of high symmetry, there exist open directions along which the threshold displacement energy is low. Since the direction of the recoil is determined from the collision event which is itself a random process, the recoil direction is entirely random. The single value often quoted for displacement energy in radiation damage calculations then represents a spherical average of the potential barrier surrounding the equilibrium lattice site.

The value of E_d may be roughly estimated using an argument by Seitz [2]. The energy of sublimation, E_s, for most metals is about 5–6 eV. Since half as many bonds are broken by removing an atom from the surface of a crystal as opposed to the interior, the energy to remove an atom from the interior is then 10–12 eV. If an atom is moved from its lattice site to an interstitial position in the direction of least resistance and time is allowed for neighboring atoms to relax (an adiabatic movement), an energy of $2E_s$ is needed. Since in reality, the struck atom is not always projected in the direction of least resistance and time is not allowed for the relaxation of neighboring atoms, a greater amount of energy (perhaps 4–5 E_s) is needed. Thus, we would expect E_d to be 20–25 eV.

Accurate determination of the displacement energy can be made if the interaction potential between lattice atoms is known. This is accomplished by moving the atom in a given direction and summing the interaction energies between the moving atom and all other nearest neighbors along the trajectory of the struck atom. When the total potential energy reaches a maximum, the position corresponds to a saddle point and the difference between the energy of the atom at the saddle point, E^*, and its energy in the equilibrium position, E_{eq}, represents the displacement threshold for the particular direction. Since the interaction energy in these collisions is only tens of eV, the Born–Mayer potential would be the most appropriate potential to use in describing the interaction. These calculations can be carried out over all directions and averaged to obtain a mean E_d for a particular solid.

To appreciate the significance of the variation in interaction energies or potential barriers with crystal direction, we will consider the case of copper. In the cubic lattice, there are three crystallographic directions that may be considered easy directions for displacement: $\langle 100 \rangle$, $\langle 110 \rangle$ and $\langle 111 \rangle$. In particular, $\langle 110 \rangle$ is the close-packed direction in the fcc lattice and $\langle 111 \rangle$ is the close-packed direction in the bcc lattice. Figure 2.4 shows how an atom is displaced along each of these directions in the fcc lattice. In each case, the displaced atom K passes through the midpoint of a set of "barrier atoms," B, in the direction of the L atom, with the atom configuration dependent on the direction. For a K atom displaced in the $\langle 110 \rangle$ direction, the atoms are located at the corners of a rectangle to which the path of K is perpendicular. When the K atom passes through the barrier, it loses kinetic energy in glancing collisions, which initially becomes potential energy of the barrier atoms. The energy need not be shared equally between the four B atoms. This is illustrated by drawing a set of contours of constant E_d in the place of the B atoms (Fig. 2.5). Then, if K only receives a quantity of energy E_d $\langle 110 \rangle$ in the

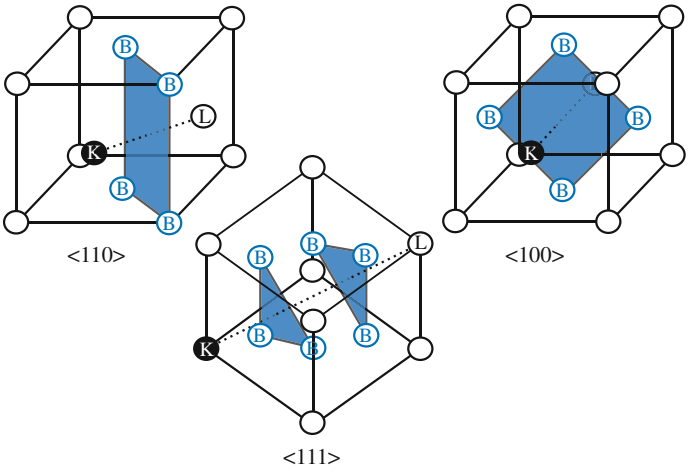

Fig. 2.4 Struck atom, K, and barrier atoms, B, for various directions of the struck atom in the fcc lattice

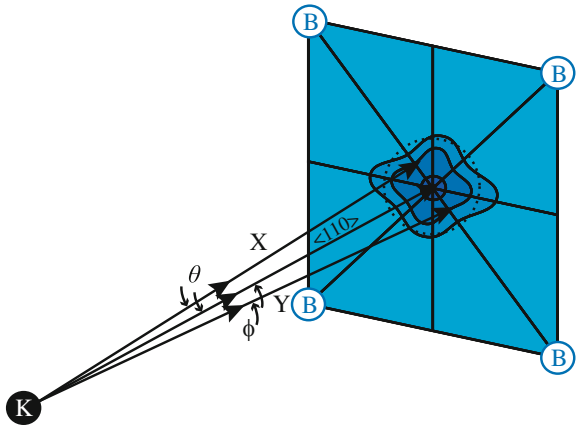

Fig. 2.5 Equi-potential contours in the barrier plane for a struck atom, K, traveling close to the <110> direction and heading toward the barrier plane defined by the barrier atoms, B (after [3])

collision event, it will be displaced if its initial direction is contained within a small cone of solid angle centered about the $\langle 110 \rangle$ direction. For small energies, the cone intersects the B atom plane in a circle, but as the energy transferred increases, the intersection deviates significantly from a right circular cone (Fig. 2.5). The contours are in fact generated by the intersection of a complex but symmetrical three-dimensional surface with a sphere which is described about the atom K as center. This contour pattern can be constructed by accounting for the interaction between the K atom and each of the B atoms at every point in time while simultaneously accounting for interactions between each of these five atoms and other atoms in the surrounding region of the crystal. This is a very difficult problem, the solution of which depends heavily on the interaction potential. In principle, at least,

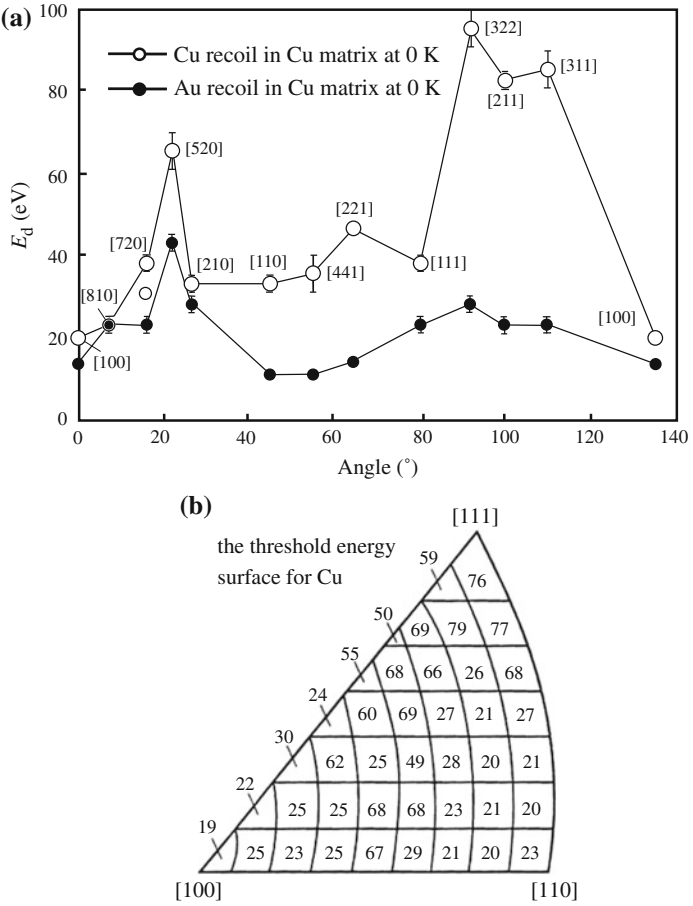

Fig. 2.6 Displacement energy as a function of direction in (**a**) fcc Cu and Au crystal (after [3]) and (**b**) in copper (after [4])

we can obtain all the information we need about the directional dependence of the thresholds. Figure 2.6 shows the displacement threshold as a function of direction in fcc copper and gold. Note that displacement threshold energies along ⟨100⟩ and ⟨110⟩ are low, but the value along ⟨111⟩ is high due to the large distance between barrier atoms in this direction and the two sets of barriers between the atoms on the body diagonal of the unit cell.

This dependence will be further illustrated in an example using the fcc lattice and a parabolic repulsion function. Figure 2.7 shows a lattice atom on the face of a unit cell in an fcc crystal receiving energy from a collision. Its flight trajectory is in the ⟨110⟩ direction, which is equidistant from four atoms located on the faces of the unit cell. In an fcc lattice, each atom is surrounded by 12 nearest neighbors. Displacement will be dependent on several important factors. They are the number

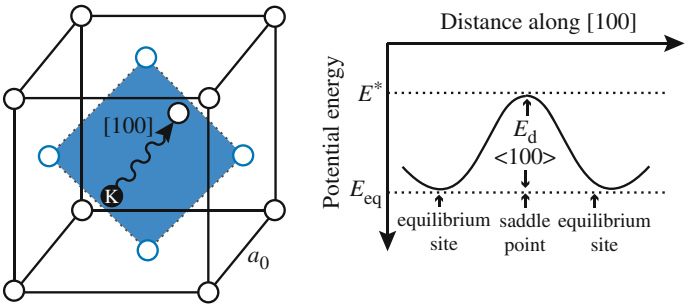

Fig. 2.7 Displacement of a lattice atom along the <100> direction in the fcc lattice and the variation of energy of the atom with position along its path (after [5])

Table 2.1 Parameters used for the determination of E_d in the fcc lattice

Direction	# B atoms	Impact parameter, z	Distance to barrier, y
$\langle 100 \rangle$	4	$\frac{a}{2}$	$\frac{a}{2}$
$\langle 110 \rangle$	4	$\frac{\sqrt{6}}{4}a$	$\frac{\sqrt{2}}{4}a$
$\langle 111 \rangle$	3	$\frac{a}{\sqrt{6}}$	$\frac{a}{3}$

of barrier atoms, B, the impact parameter, z (the distance of closest approach to the B atoms), and the distance from the K atom in its lattice site to the barrier, y. These quantities are given in Table 2.1 for the fcc lattice. The energy required to displace an atom will increase with B and y and decrease with z. Since z is smallest for the $\langle 110 \rangle$ direction, this will be the most difficult to penetrate. Also $z_{100} < z_{110}$ and $y_{100} > y_{110}$, so both factors will make displacement along $\langle 110 \rangle$ easier than along $\langle 100 \rangle$. Let us take the specific example of displacement in the $\langle 100 \rangle$ direction of the fcc example and calculate a value for E_d.

The energy of a single atom in a normal lattice site is as follows:

$$E_{eq} = -12U, \tag{2.20}$$

where U is the energy per atom of the crystal. Since only half as many bonds are broken in the sublimation process, this energy is just:

$$E_s \cong 6U, \tag{2.21}$$

and since $E_s \sim$ 4–5 eV, U is about 1 eV.

To describe the interaction of the lattice atoms as they are pushed together in the solid, we will use a simple parabolic repulsion as opposed to the Born–Mayer potential:

$$V(r) = -U + \frac{1}{2}k\left(r_{\text{eq}} - r\right)^2 \quad r < r_{\text{eq}}$$
$$V(r) = 0 \quad r \geq r_{\text{eq}}, \tag{2.22}$$

where k is the force constant characterizing the repulsive position of the potential. The force constant can be expressed as [5]:

$$ka^2 = \frac{3\upsilon}{\beta}, \tag{2.23}$$

where
k force constant
a lattice constant
υ $a^3/4$ = specific volume of an atom
β compressibility

In our example, the equilibrium spacing of the struck atom and the four atoms forming the square barrier is $r_{\text{eq}} = a/\sqrt{2}$. When the atom is at the center of the square, it interacts with the four atoms at the corners a distance $a/2$ away. Hence, the energy at the saddle point is as follows:

$$E^* = 4V\left(\frac{a}{2}\right) = 4\left[-U + \frac{1}{2}\left(ka^2\right)\left(\frac{1}{\sqrt{2}} - \frac{1}{2}\right)^2\right]. \tag{2.24}$$

The displacement energy in the $\langle 100 \rangle$ direction is then:

$$E_{\text{d}}\langle 100\rangle = \varepsilon^* - \varepsilon_{\text{eq}} = 8U + 2\left(ka^2\right)\left(\frac{1}{\sqrt{2}} - \frac{1}{2}\right)^2. \tag{2.25}$$

Typical values for ka^2 and U for metals are 60 and 1 eV, respectively, yielding $E_{\text{d}}\langle 100\rangle \cong 13.1$ eV. This value is in reasonable agreement with that given in Fig. 2.6. Table 2.2 gives values of E_{d} for various metals [6]. Note that for the transition metals, the accepted value of E_{d} is 40 eV.

2.1.4 The Electron Energy Loss Limit

Now that we have established a lower limit on the energy transfer necessary to cause a displacement, E_{d}, let us turn our attention to the high-energy regime of collisions. Recall that at low energies ($T < 10^3$eV), $S_{\text{n}} \gg S_{\text{e}}$, and we may assume that nearly all of the energy loss of the PKA goes toward elastic collisions (Fig. 1.18). However, as the PKA energy increases, the fraction of the total energy loss that is due to electron excitation and ionization increases until above the crossover energy, E_{x}, $S_{\text{e}} > S_{\text{n}}$.

Table 2.2 Recommended values of the effective displacement energy for use in displacement calculations (from [6])

Metal	Lattice (c/a)	E_d, min (eV)	E_d (eV)
Al	fcc	16	25
Ti	hcp (1.59)	19	30
V	bcc	–	40
Cr	bcc	28	40
Mn	bcc	–	40
Fe	bcc	20	40
Co	fcc	22	40
Ni	fcc	23	40
Cu	fcc	19	30
Zr	hcp	21	40
Nb	bcc	36	60
Mo	bcc	33	60
Ta	bcc	34	90
W	bcc	40	90
Pb	fcc	14	25
Stainless steel	fcc	–	40

Our expression for $\nu(T)$ in Eq. (2.19) must therefore be modified to account for this variation in the amount of kinetic energy available for displacement collisions.

Figure 2.8 shows $(\mathrm{d}E/\mathrm{d}x)_n$ for carbon recoils in graphite using Eq. (1.163) and Lindhard's Thomas–Fermi result, the latter showing that Eq. (1.163), which predicts a constant value of 250 eV/nm, is a good approximation for energies up to at least E_a. Note that at high energies ($T \gg E_x$), electronic energy losses predominate by several orders of magnitude. However, at low energies ($T \ll E_x$), the situation is reversed.

Fortunately, because of departures from the hard sphere model, the primary recoil creates secondaries with average energies far below $\hat{T}/2$. These will almost

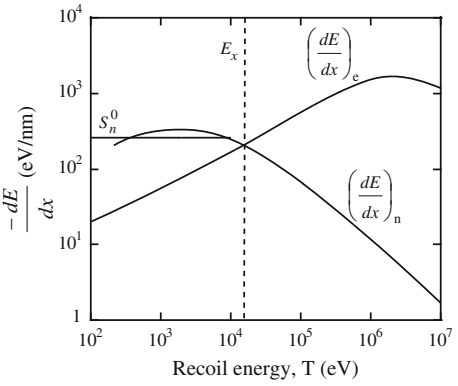

Fig. 2.8 Energy loss from electronic and nuclear stopping as a function of energy (after [7])

always be in the range where electronic excitation can be neglected. To obtain $\nu(T)$ to a fair approximation, we calculate the energy E_c, dissipated in elastic collisions by the PKA:

$$E_c = \int_0^{\check{T}} \frac{(dE/dx)_n dE}{(dE/dx)_n + (dE/dx)_e}. \tag{2.26}$$

We can then use Eq. (1.190) for $(dE/dx)_e$ and Eq. (1.130) for $(dE/dx)_n$ with $\check{T} = E_a$. The modified damage function is the original Eq. (2.19) with T replaced by E_c:

$$\nu(T) = \frac{E_c}{2E_d}. \tag{2.27}$$

As an estimate of E_c, we can use the maximum energy a moving atom (of energy E) can transfer to an electron as

$$\frac{4m_e}{M}E, \tag{2.28}$$

and equating this with the ionization energy of the struck electron belonging to the target atom, we have:

$$E_c = \frac{M}{4m_e}I. \tag{2.29}$$

Kinchin and Pease [1] equated E_c and E_x, implying that all energy above E_x is lost in electron excitation, and displacements account for all the energy loss below E_c. Figure 2.9 shows $\nu(T)$ for graphite using Lindhard's $(dE/dx)_n$. Note that for recoils with energy below E_c, the simple theory gives a fair description, but for $T > E_c$, the losses in electron excitation are important.

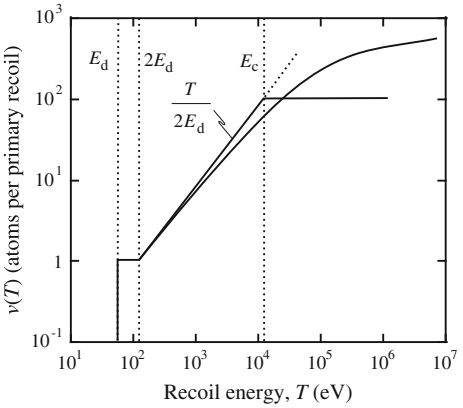

Fig. 2.9 Number of displaced atoms per primary recoil compared to the simple K–P result of $T/2E_d$ (after [7])

2.2 Modifications to the K–P Displacement Model

2.2.1 *Consideration of* E_d *in the Energy Balance*

Snyder and Neufeld [8] make the assumption that an energy E_d is consumed in each collision such that the relation in Assumption 3 of the K–P displacement model will read:

$$T = T' + \varepsilon + E_d, \tag{2.30}$$

and both atoms move off after collision, no matter how small their energy. When compared with the Kinchin–Pease model, it may be expected that $\nu(T)$ would decrease since an energy loss term is added. However, because atoms are allowed to leave the collision with energy less than E_d, an increase in $\nu(T)$ will occur. Since these two changes to $\nu(T)$ nearly cancel, the result is very similar to the K–P model:

$$\nu(T) = 0.56\left(1 + \frac{T}{E_d}\right) \quad \text{for } T > 4E_d. \tag{2.31}$$

2.2.2 *Realistic Energy Transfer Cross Sections*

The weakest point of the K–P displacement model is the assumption of hard sphere collisions (Assumption 5). In fact, more realistic energy transfer cross sections can be used while still maintaining the proportionality of Eq. (2.19). Sanders [9] solved Eq. (2.5) using an inverse power potential (r^{-s}) to obtain:

$$\nu(T) = s\left(2^{\frac{1}{s+1}} - 1\right)\frac{T}{2E_d}, \tag{2.32}$$

which for the inverse square potential becomes:

$$\nu(T) = 0.52\,\frac{T}{2E_d}, \tag{2.33}$$

reducing the Kinchin–Pease result by a factor of 2.

However, the use of this potential has its shortcomings because it is applied to all collisions in the cascade, while its region of validity is limited to those values of T such that $\rho < 5a$. Physically, the effect of realistic scattering is to make a larger number collisions generate T in the subthreshold regions below E_d where they are removed from multiplication chain.

For many years, investigators have been intrigued that Eq. (2.19) appears to overestimate $\nu(T)$ in metals by a factor of 2–10 [10] and yet attempts to measure the energy dependence of $\nu(T)$ over a large energy range (50–200 keV recoil atoms in gold) gave a quadratic rather than linear relationship. In 1969, Sigmund [11] took a

different approach to this problem by considering the *recoil density* $F(T, \varepsilon)\,\mathrm{d}\varepsilon$ defined as the average number of atoms recoiling with an energy in $(\varepsilon, \varepsilon + \mathrm{d}\varepsilon)$ as a consequence of a primary ion slowing down from T to zero energy. The recoil density can be expressed in a form that uses the power law approximation of the Thomas–Fermi differential cross section [12]:

$$\sigma(T, \varepsilon) \propto T^{-m}\varepsilon^{-1-m}, \tag{2.34}$$

where $0 \leq m \leq 1$, giving:

$$F(T, \varepsilon) = \frac{m}{\psi(1) - \psi(1-m)} \frac{T}{(\varepsilon + U_b)^{1-m}\varepsilon^{1+m}}, \tag{2.35}$$

for $T \gg \varepsilon \gg U_b$, where

$$\psi(x) = \mathrm{d}[\ln\Gamma(x)]/\mathrm{d}x, \tag{2.36}$$

U_b is the binding energy lost by an atom when leaving a lattice site, and $\Gamma(x)$ is the gamma function or the generalized factorial function. Since a recoiling atom is displaced when $\varepsilon > E_{\mathrm{d}}$, we obtain

$$\nu(T) = \int_{E_{\mathrm{d}}}^{T} \mathrm{d}\varepsilon F(T, \varepsilon) = \frac{(1 + U_b/E_{\mathrm{d}})^m - 1}{\psi(1) - \psi(1-m)} \left(\frac{T}{U_b}\right), \tag{2.37}$$

for $T \gg E_{\mathrm{d}} \gg U_b$. The value of m is chosen in such a way [13] that $\sigma(T, \varepsilon)$ describes collisions at *low* energies, i.e., $2E_{\mathrm{d}} \leq T \leq 100E_{\mathrm{d}}$. This constrains $m \leq 1/4$. For $m = 0$, Eq. (2.37) reads:

$$\nu(T) = \frac{6}{\pi^2}\frac{T}{U_b}\ln(1 + U_b/E_{\mathrm{d}}). \tag{2.38}$$

This is an upper limit for displacement processes since loss of defects by replacement collisions has been neglected.

A characteristic feature of displacements in metals is the large recombination volume of an isolated point defect, of the order of 100 atomic volumes or more. Hence, E_{d} is the energy lost to the environment by an atom trying to escape the recombination volume. This has the consequence that in cascades, many defects are lost by replacement collisions [14]. The binding energy U_b is only a few eV and thus negligible as compared to E_{d}, reducing Eq. (2.38) to:

$$\nu(T) = \frac{6}{\pi^2}\frac{T}{E_{\mathrm{d}}} = 1.22\left(\frac{T}{2E_{\mathrm{d}}}\right), \tag{2.39}$$

which is about 22 % greater than the result of Eq. (2.19) which accounted for replacement collisions.

2.2.3 Energy Loss by Electronic Excitation

Even for $E > E_c$, collisions of the PKA with electrons compete for energy loss against collisions with lattice atoms. These two processes can be treated independently, and each can be represented by separate energy transfer cross sections. The formulation originally presented by Lindhard et al. [15] is summarized here as presented by Olander in [5] as a more realistic treatment of energy loss by electronic excitation (Assumption 4).

As a PKA traverses a distance dx of a solid, three things may happen: (1) It collides with an electron, (2) it collides with an atom, or (3) nothing. Let $p_e\,d\varepsilon_e$ be the probability that a collision between the PKA and an electron in the interval dx transfers energy in the range (ε_e, dε_e) to the electron:

$$p_e d\varepsilon_e = N\sigma_e(T, \varepsilon_e)d\varepsilon_e dx, \tag{2.40}$$

where $\sigma_e(T, \varepsilon_e)$ is the energy transfer cross section from the PKA to the electron. Similarly, for a PKA and lattice atom:

$$p_a d\varepsilon_a = N\sigma_a(T, \varepsilon_a)d\varepsilon_a dx, \tag{2.41}$$

and the probability that nothing happens in dx is as follows:

$$\begin{aligned} p_0 &= 1 - \int_0^{\varepsilon_{e,max}} p_e d\varepsilon_e - \int_0^{\varepsilon_{a,max}} p_a d\varepsilon_a \\ &= 1 - N\,dx[\sigma_e(T) - \sigma_a(T)], \end{aligned} \tag{2.42}$$

and $\varepsilon_{e,max}$ and $\varepsilon_{a,max}$ are the maximum energies transferable to an electron and atom, respectively, by a PKA of energy T. We rewrite the conservation equation for $\nu(T)$ by weighting with the appropriate probability for the process by which it is created and integrating over the permissible ranges of energy transfers:

$$\begin{aligned} \nu(T) = &\int_0^{\varepsilon_{a,max}} [\nu(T - \varepsilon_a) + \nu(\varepsilon_a)]\,p_a\,d\varepsilon_a \\ &+ \int_0^{\varepsilon_{e,max}} \nu(T - \varepsilon_e)p_e\,d\varepsilon_e + p_0\nu(T). \end{aligned} \tag{2.43}$$

Substituting for p_e, p_a, and p_0 yields:

$$\begin{aligned} [\sigma_a(T) + \sigma_e(T)]\nu(T) = &\int_0^{\varepsilon_{a,max}} [\nu(T - \varepsilon_a) + \nu(\varepsilon_a)]\sigma_a(T, \varepsilon_a)\,d\varepsilon_a \\ &+ \int_0^{\varepsilon_e,max} \nu(T - \varepsilon_e)\sigma_e(T, \varepsilon_e)\,d\varepsilon_e. \end{aligned} \tag{2.44}$$

Since the maximum energy transferred to an electron is very small compared to T, $v(T - \varepsilon_e)$ can be expanded in a Taylor series and truncated after the second term:

$$v(T - \varepsilon_e) = v(T) - \frac{dv}{dT}\varepsilon_e, \tag{2.45}$$

and the last term in Eq. (2.44) can be written as:

$$\int_0^{\varepsilon_e,\max} v(T - \varepsilon_e)\,\sigma_e(T, \varepsilon_e)d\varepsilon_e = v(T)\int_0^{\varepsilon_e,\max} \sigma_e(T, \varepsilon_e)\,d\varepsilon_e - \frac{dv}{dT}\int_0^{\varepsilon_e,\max} \varepsilon_e\sigma_e(T, \varepsilon_e)\,d\varepsilon_e. \tag{2.46}$$

The first integral on the right of Eq. (2.46) is the total cross section for collisions of the PKA with the electron and cancels the corresponding term on the left in Eq. (2.44). The second integral on the right of Eq. (2.46) is the electronic stopping power of the solid divided by the atom density. Combining Eqs. (2.46) and (2.45), we have:

$$v(T) + \left[\frac{(dT/dx)_e}{N\sigma(T)}\right]\frac{dv}{dT} = \int_0^{T_{\max}} [v(T - \varepsilon) + v(\varepsilon)]\left[\frac{\sigma(T, \varepsilon)}{\sigma(T)}\right]d\varepsilon, \tag{2.47}$$

where the subscript "a" on T and σ has been dropped with the understanding that these quantities refer to atomic collisions. Equation (2.47) can be solved using the hard sphere assumption, but where $\left(\frac{dE}{dx}\right)_e$ is given by Eq. (1.190), i.e., $\left(\frac{dE}{dx}\right)_e = kE^{1/2}$, giving:

$$v(T) = \frac{2E_d}{T} + \frac{2}{T}\int_{2E_d}^{T} v(\varepsilon)d\varepsilon - \frac{kT^{1/2}}{\sigma N}\frac{dv}{dT}. \tag{2.48}$$

After simplification, the final result is as follows:

$$v(T) = \left[1 - \frac{4k}{\sigma N(2E_d)^{1/2}}\right]\left(\frac{T}{2E_d}\right), \quad \text{for } T \gg E_d, \tag{2.49}$$

where k is a constant depending on the atom number density, N, and the atomic number. The term σ is the energy-independent hard sphere collision cross section. Note that when electronic stopping is properly accounted for in the basic integral equation, the entire concept of a definite energy, E_c, separating regimes of electronic energy loss from atomic collisions can be dismissed.

However, Eq. (2.49) is still plagued by the use of the hard sphere assumption. Lindhard realized that in order to ensure that reliable predictions are obtained, a realistic energy transfer cross section must be used. Lindhard also realized that the

parameter $v(T)$ need not be interpreted solely as the number of displacements produced per PKA, but could be taken to be that part of the original PKA energy, which is transferred to the atoms of the lattice (rather than the electrons) in slowing down. In reality, collisions of the PKA with atoms compete with collisions with electrons. But the processes can be treated as independent events. Nevertheless, the expression for $v(T)$ needs to be reformulated.

In 1975, Norgett, Robinson, and Torrens [17] proposed a model to calculate the number of displacements per PKA according to:

$$v(T) = \frac{\kappa E_D}{2E_d} = \frac{\kappa(T-\eta)}{2E_d}, \tag{2.50}$$

where T is the total energy of the PKA, η is the energy lost in the cascade by electron excitation, and E_D is the energy available to generate atomic displacements by elastic collisions and is known as the *damage energy*. The displacement efficiency, κ, is 0.8 and is independent of M_2, T, and temperature. The quantity E_D is defined by:

$$E_D = \frac{T}{[1 + k_N g(\in)]}, \tag{2.51}$$

and inelastic energy loss is calculated according to the method of Lindhard using a numerical approximation to the universal function, $g(\in)$:

$$\begin{aligned} g(\in) &= 3.4008\ \in^{1/6} + 0.40244\ \in^{3/4} + \in \\ k_N &= 0.1337 Z_1^{1/6} \left(\frac{Z_1}{A_1}\right)^{1/2}, \end{aligned} \tag{2.52}$$

where $\in$ is the reduced energy given by:

$$\begin{aligned} \in &= \left(\frac{A_2 T}{A_1 + A_2}\right)\left(\frac{a}{Z_1 Z_2 \varepsilon^2}\right) \\ a &= \left(\frac{9\pi^2}{128}\right)^{1/3} a_0 (Z_1^{2/3} + Z_2^{2/3})^{-1/2}, \end{aligned} \tag{2.53}$$

a_0 is the Bohr radius, and ε is the unit electronic charge. If E_d ~40 eV, then $v = 10E_\mathrm{D}$, where E_D is in keV.

The displacement function can also be written as the Kinchin–Pease result modified by a damage energy function, ξ(T), given by:

$$v(T) = \xi(T)\left(\frac{T}{2E_d}\right), \tag{2.54}$$

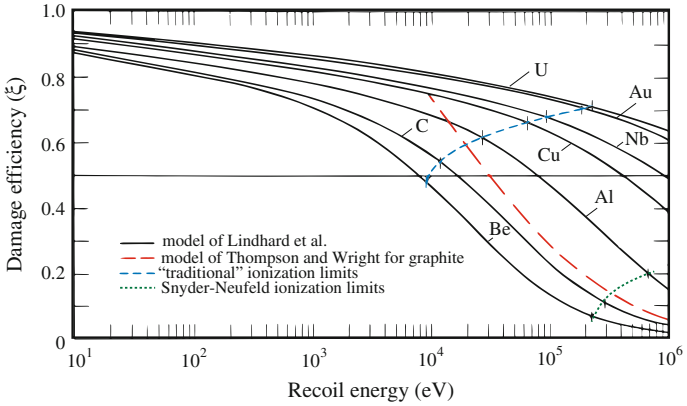

Fig. 2.10 The effect of electronic energy losses on the energy available for atomic displacements (after [16])

where

$$\xi(\in) = \frac{1}{1 + 0.1337 Z_1^{1/6} \left(\frac{Z_1}{A_1}\right)^{1/2} \left(3.4008 \in^{1/6} + 0.40244 \in^{3/4} + \in\right)}, \quad (2.55)$$

and giving the same result as in Eq. (2.50) except for the exclusion of the displacement efficiency, κ. Figure 2.10 shows the effect of accounting for damage efficiency in the Kinchin–Pease result. Note that the function approaches 1.0 as the recoil energy is reduced. As energy increases, the damage efficiency drops faster for light materials.

2.2.4 *Effects of Crystallinity*

The analysis thus far has assumed that the cascade occurs in a solid composed of a random array of atoms. However, when the order of a crystal structure is imposed (Assumption 6), two important effects occur that can alter the number of displacements produced by a PKA; focusing and channeling. *Focusing* is the transfer of energy and/or atoms by near head-on collisions along a row of atoms. *Channeling* is the long-range displacement of atoms along open directions (channels) in a crystal structure in which an atom travels by making glancing collisions with the walls of the channel which are just rows of atoms. Both processes can result in long-range transport of interstitials away from the initial PKA or the cascade. Both processes also reduce the number of displacements per PKA, $\nu(T)$, as calculated from the simple Kinchin–Pease model.

Focusing

The effects of focusing were first seen in the directional dependence of the threshold energy, E_d. In an fcc lattice, for example, displacements occur in the ⟨100⟩ and ⟨110⟩ directions with the lowest energy transfer of any crystalline direction. Since the direction of the primary knock-on is random, focusing must be possible for a sizable range of polar angles off the close-packed direction. If exact head-on collision were required to produce a linear collision chain, the phenomenon would be of little practical significance since this probability is extremely low.

Focusing along an atomic row can be analyzed using the hard sphere approximation. The distance between atoms along a particular crystallographic direction is denoted by D. Figure 2.11 shows two atoms of such a row in which a collision sequence is initiated by the atom which was initially centered at A. This atom receives energy T and moves off at an angle θ_0 to the atomic row. The dashed circle shows the atom position at the instant it strikes the next atom in the row. The radius of the colliding sphere, R, is obtained from the Born–Mayer potential. The impact transfers some of T to the second atom, which then moves off in the direction of the line joining P and B at an angle θ_1 to the row. From Fig. 2.11, we can also show that:

$$\overline{AP}\sin\theta_0 = \overline{PB}\sin\theta_1. \tag{2.56}$$

If θ_0 and θ_1 are small, Eq. (2.56) can be approximated by:

$$\overline{AP}\theta_0 \approx \overline{PB}\theta_1, \tag{2.57}$$

and if θ_0 and θ_1 are very small, then:

$$\begin{aligned} \overline{AP} &\approx \overline{AB} - \overline{PB} = D - 2R, \quad \text{and since } \overline{PB} = 2R \\ (D-2R)\theta_0 &= 2R\theta_1, \end{aligned} \tag{2.58}$$

and

$$\theta_0(D-2R) = \theta_1(2R). \tag{2.59}$$

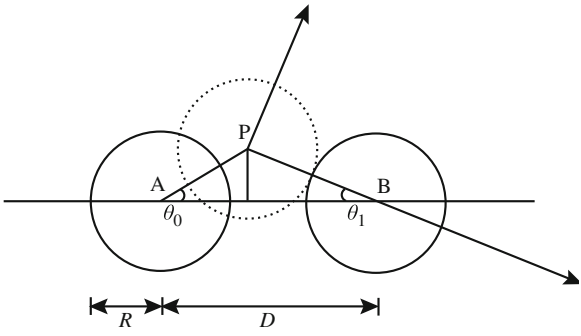

Fig. 2.11 The simple focusing effect assuming hard sphere collisions

If we further define a focusing parameter:

$$f \equiv \theta_1/\theta_0, \tag{2.60}$$

then by Eq. (2.59):

$$f = \frac{D}{2R} - 1. \tag{2.61}$$

This permits us to write the following inequalities:

$$\begin{aligned} &\text{for } f > 1, D > 4R \text{ and } |\theta_0| < |\theta_1| \\ &\text{for } f < 1, D < 4R \text{ and } |\theta_0| > |\theta_1|. \end{aligned} \tag{2.62}$$

Considering further collisions, by the time the momentum pulse reaches atom n, the relation between angles is given by:

$$\begin{aligned} \theta_n &= f\theta_{n-1} \\ &= f^2\theta_{n-2} \\ &= f^3\theta_{n-3} \\ &\vdots \\ &= f^n\theta_0 = \left(\frac{D}{2R} - 1\right)^n \theta_0, \end{aligned} \tag{2.63}$$

or finally:

$$\theta_n = (f)^n\theta_0 = \left(\frac{D}{2R} - 1\right)^n \theta_0. \tag{2.64}$$

This last relation shows that if $D > 4R$, the focusing parameter f is greater than unity so that the angles θ_n will increase in successive collisions. Conversely, if $D < 4R$, f is less than unity and the angles θ_n converges to zero.

A set of conditions also exist under which the scattering angle θ_n will neither diverge nor converge after successive collisions. These are the conditions for critical focusing ($\theta_n = \theta_{n+1} = \ldots$) which can be determined as follows. The recoil angle of atom B can be related to the initial direction of atom A by applying the law of sines to triangle $\overline{APB}$:

$$\frac{\sin(\pi - \theta_0 - \theta_1)}{\sin\theta_0} = \frac{D}{2R}, \tag{2.65}$$

which simplifies to:

$$\frac{\sin(\theta_0+\theta_1)}{\sin\theta_0}=\frac{D}{2R}. \tag{2.66}$$

The condition for critical focusing is $\theta_1 = \theta_0$. Applying this equality in Eq. (2.66) gives:

$$\frac{\sin 2\theta_0}{\sin\theta_0}=2\cos\theta_0=\frac{D}{2R}, \tag{2.67}$$

and

$$\cos\theta_0=\cos\theta_c=\frac{D}{4R}, \tag{2.68}$$

or focusing will occur when $\cos\theta_0 \leq \frac{D}{4R}$ and:

$$\cos\theta_c=\frac{D}{4R}. \tag{2.69}$$

Equation (2.60) also shows that focusing of momentum is favored along rows of atoms in the $\langle hkl\rangle$ directions for which the separation distance D^{hkl} is a minimum, or the close-packed directions.

If we treat the atoms as having an energy-dependent radius, we can determine the maximum possible energy for focusing at any given collision angle. The key is to allow the potential between atoms to vary with separation. The critical focusing energy, E_{fc}^{hkl}, is defined as that energy below which $f < 1$ and $D < 4R$, and focusing is possible. In the hard sphere model, the relation between kinetic energy, E, and potential energy $V(r)$ for a head-on collision is given by Eq. (1.80) as $V(2R)=\frac{1}{2}E$. If $V(r)$ is described by the Born–Mayer potential, Eq. (1.47), then $V(r) = A\exp(-Br)$, and:

$$E=2A\exp(-2R/B). \tag{2.70}$$

For a head-on collision, $\theta_c = 0$, so $\cos\theta_c=\frac{D}{4R}=1$, and we have:

$$E_{fc}=2A\exp\left(\frac{-D}{2B}\right). \tag{2.71}$$

This means that any angle greater than zero will result in defocusing for $E \geq E_{fc}$ or that focusing at an energy E_{fc} can only occur for $\theta = 0°$. Clearly then, the critical focusing angle depends on the energy of the projectile. The relation between angle and energy is developed by writing the expression for E_{fc} in terms of D:

$$D = 2B \ln\left(\frac{2A}{E_{\mathrm{fc}}}\right). \tag{2.72}$$

Now, for any atom of energy T reaching a separation of $4R$:

$$4R = 2B \ln\left(\frac{2A}{T}\right). \tag{2.73}$$

Combining these equations gives:

$$\frac{D}{4R} = \cos\theta_{\mathrm{c}} = \frac{\ln(2A/E_{\mathrm{fc}})}{\ln(2A/T)}, \quad T < E_{\mathrm{fc}}. \tag{2.74}$$

Note that the condition of critical focusing can be expressed in two ways:

1. $E_{\mathrm{fc}} = 2A \exp\left(\frac{-D}{2B}\right)$: This condition gives the energy E_{fc} for which focusing occurs for a head-on collision ($\theta_{\mathrm{c}} = 0$).
2. $\cos\theta_{\mathrm{c}} = \frac{\ln(2A/E_{\mathrm{fc}})}{\ln(2A/T)}$: This condition gives the maximum angular deviation from a head-on collision θ_{c}, at which a PKA of energy T can initiate a focused sequence.

From the first expression, it should be apparent that focusing is a function of crystallographic direction since D is a function of crystal structure. That is,

$$E_{\mathrm{f}}^{hkl} = 2A \exp\left(\frac{-D^{hkl}}{2B}\right). \tag{2.75}$$

For example, in the fcc lattice, we have:

$$D^{\langle 100\rangle} = a$$
$$D^{\langle 110\rangle} = \frac{\sqrt{2}}{2}a$$
$$D^{\langle 111\rangle} = \sqrt{3}a$$

therefore, since $D^{\langle 110\rangle} < D^{\langle 100\rangle} < D^{\langle 111\rangle}$, we have $E_{\mathrm{f}}^{\langle 110\rangle} > E_{\mathrm{f}}^{\langle 100\rangle} > E_{\mathrm{f}}^{\langle 111\rangle}$.

Typical values for $E_{\mathrm{f}}^{\langle 110\rangle}$ are 80 eV in copper and 600 eV for gold. In any case, E_{f} is much less than initial PKA energies.

From the preceding discussion, it should be apparent that focusing is only applicable if a scattered atom is within an angle θ_{c} of an atomic row. Then, a focused sequence can result. It is therefore important to determine the probability that the initial direction of a struck atom is within a cone of apex θ_{c} about an atomic row.

For a random starting direction, the probability of generating a focused collision sequence at energy T is as follows

$$P_f(T) = \frac{\theta_c^2}{4}. \tag{2.76}$$

Expanding cos θ_c in Eq. (2.69) gives:

$1 - \frac{1}{2}\theta_c^2 \approx \frac{D}{4R}$, for small θ_c. Substituting from Eq. (2.76) gives:

$$P_f(T) = \frac{1}{2}\left(1 - \frac{D}{4R}\right), \tag{2.77}$$

or

$$\begin{aligned} P_f(T) &= \frac{1}{2}\left[1 - \frac{\ln(2A/E_{fc})}{\ln(2A/T)}\right] \\ &= \frac{1}{2}\left[\frac{\ln(2T/E_{fc})}{\ln(E_{fc}/2A) + \ln(T/E_{fc})}\right]. \end{aligned} \tag{2.78}$$

Since $E_{fc}/2A \ll 1$ and $T/E_{fc} \sim 1$, then:

$$\begin{aligned} P_f(T) &= \frac{1}{2}\frac{\ln(T/E_{fc})}{\ln(E_{fc}/A)} \quad T < E_{fc} \\ &= 0 \quad T > E_{fc} \end{aligned} \tag{2.79}$$

For n equivalent directions in the crystal:

$$P_f(T) = n\frac{\ln(T/E_{fc})}{\ln(E_{fc}/A)}. \tag{2.80}$$

For example, in copper, $E_{fc} \sim 80$ eV, and for $A \sim 20{,}000$ eV, $P_f(60\text{ eV}) \sim 0.026n$. For $n = 12$, then $P_f \sim 0.3$ or 30 %. Focusing refers to the transfer of energy by elastic collisions along a line, but without involving the transfer of mass. We will next discuss replacement collisions in which both energy and mass are transferred.

Replacement Collisions

In addition to energy transfer, mass can be transferred by replacement of the struck atom with the striking atom if the center of the first atom moves beyond the midpoint of the two atoms as they reside in the lattice. In our analysis of focusing, we assumed hard sphere collisions. However, if we assume that there is a softness to the atom, three things occur:

1. The hard sphere model overestimates the angle of scattering for a particular impact parameter, and hence, the amount of focusing must be overestimated.

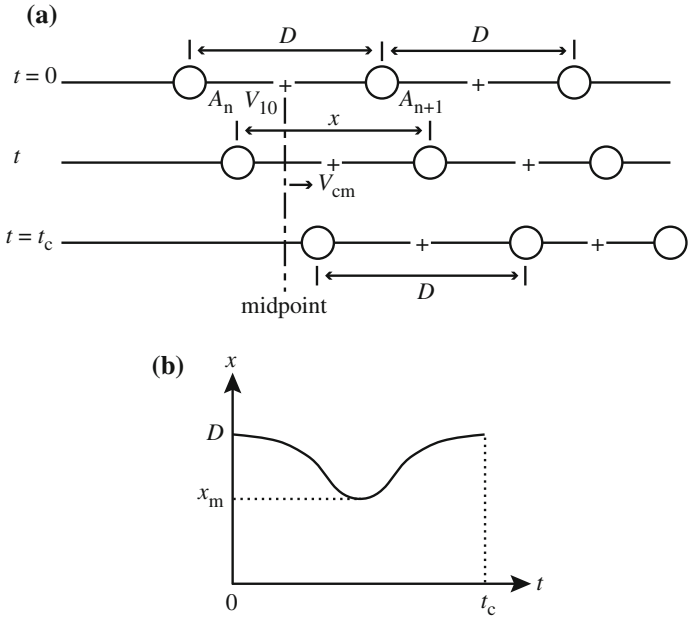

Fig. 2.12 Head-on collisions in a focused chain when the interaction potential acts continuously during the collision. (**a**) Atom positions during the collision initiated by the atom on the *left*. (**b**) Separation of atoms A_n and A_{n+1} during the collision (after [5])

2. Atoms in the row feel the influence of the oncoming disturbance long before it gets there so the atom is already moving. Since D is decreased, focusing is enhanced.
3. Replacement becomes possible.

Referring to Fig. 2.12, as the collision proceeds, the distance x between atoms A_n and A_{n+1} decreases continuously. The velocity of the center of mass (CM) is as follows:

$$V_{CM} = \left(\frac{M_1}{M_1 + M_2}\right)\upsilon_1 + \left(\frac{M_2}{M_1 + M_2}\right)\upsilon_2,$$

where υ_1 and υ_2 are in the laboratory system. The relative speed, defined by $g = \upsilon_1 - \upsilon_2$, gives:

$$\upsilon_1 = V_{CM} + \left(\frac{M_2}{M_1 + M_2}\right)g$$
$$\upsilon_2 = V_{CM} + \left(\frac{M_1}{M_1 + M_2}\right)g,$$

and the total kinetic energy of the two particles is as follows:

$$KE = 1/2M_1\upsilon_1^2 + 1/2M_2\upsilon_2^2,$$

and in terms of g and V_{CM} is as follows

$$KE = 1/2(M_1 + M_2)V_{CM}^2 + 1/2\mu g^2,$$

where μ is the reduced mass = $\left(\frac{M_1M_2}{M_1 + M_2}\right)$. The total kinetic energy is divided into two parts: one due to the motion of the system and another due to the relative motion of the two particles. Conservation of total energy is given as $E_{\mathrm{r}} + V(x) = E_{\mathrm{r0}}$, where $V(x)$ is the potential energy at a head-on separation distance of x, E_{r0} is the relative kinetic energy at infinite (initial) separation, and E_{r} is the relative kinetic energy at any point. Rewriting the kinetic energy in terms of g gives:

$$\frac{1}{2}\mu g^2 + V(x) = \frac{1}{2}\mu g_0^2$$

and

$$g_0 = \upsilon_{10},$$

where g_0 is the initial speed. This equation should be recognizable from our earlier analysis in Chap. 1, Sect. 1.2.2. Recall that at $x = x_{\min}$, $V(x_{\min}) = 1/2\mu g_0^2$, and for $M_1 = M_2$, then $g_0 = \upsilon_{10}$ and $V = E/2$.

We also assume that the interaction energy at the initial separation is $V(D) \ll \frac{1}{2}\mu g_0^2$. The time rate of change of the separation distance is equal to the relative speed:

$$\frac{\mathrm{d}x}{\mathrm{d}t} = -g. \tag{2.81}$$

Taking the collision time as twice the time needed to reach the distance of closest approach:

$$t_{\mathrm{c}} = -2\int_D^{x_{\mathrm{m}}} \frac{\mathrm{d}x}{g} = -2\int_{V(D)}^{V(x_{\mathrm{m}})} \frac{\mathrm{d}V}{g\mathrm{d}V/dx}, \tag{2.82}$$

where x_{m} is the distance of closest approach.

Since $V(x) = A\ \exp(-x/B)$, then:

$$\frac{\mathrm{d}V}{\mathrm{d}x} = -\frac{A}{B}\exp(-x/B) = -\frac{V}{B}\,, \tag{2.83}$$

and:

$$\begin{aligned} g &= \left\{ \left[\frac{1}{2}\mu g_0^2 - V(x) \right] \frac{4}{M} \right\}^{1/2} \\ &= \left\{ \left[\frac{E}{2} - V \right] \frac{4}{M} \right\}^{1/2} \\ &= 2\left\{ \frac{E}{2M} - \frac{V}{M} \right\}^{1/2}, \end{aligned} \tag{2.84}$$

where $\mu = M/2$ for like atoms and $1/2\mu g_0^2 = 1/4Mv_{10}^2 = E/2$. Substitution of Eqs. (2.83) and (2.84) into Eq. (2.82) yields:

$$t_c = B\left(\frac{2M}{E}\right)^{1/2} \int_{V(D)}^{E/2} \frac{dV}{V(1 - 2V/E)^{1/2}} \tag{2.85}$$

$$= 2B\left(\frac{2M}{E}\right)^{1/2} \tanh^{-1}\left[1 - \frac{2V(D)}{E}\right]^{1/2}. \tag{2.86}$$

Note that the definition of a hard sphere radius has been used for the upper limit, i.e., x_m is taken to be $2R(E)$. For $V(D)/E \ll 1$,

$$t_c = B\left(\frac{2M}{E}\right)^{1/2} \ln\left[\frac{2E}{V(D)}\right]. \tag{2.87}$$

Since the speed of the center of mass is $\frac{v_{10}}{2} = \left(\frac{E}{2M}\right)^{1/2}$, the distance moved by the CM during the collision time, t_c, is as follows:

$$x = t_c\left(\frac{E}{2M}\right)^{1/2}. \tag{2.88}$$

If $x > D/2$, atom A_n will end up to the right of the initial halfway point and replacement will occur, and A_n will occupy the lattice site occupied by atom A_{n+1}. Relating the distance x to energy by substituting for t_c from Eq. (2.87) into Eq. (2.88) gives:

$$\frac{x}{B} = \ln\left(\frac{2E_r}{V(D)}\right). \tag{2.89}$$

For $x = D/2$:

$$\exp\left(\frac{D}{2B}\right) = \frac{2E_r}{A\exp(-D/B)},$$

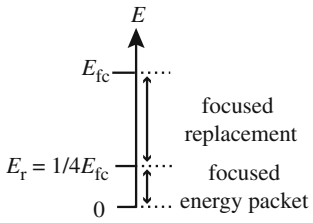

Fig. 2.13 Energy scale for focused energy transfer and focused replacement sequence

and the replacement energy becomes:

$$E_r = \frac{A}{2}\exp\left(\frac{-D}{2B}\right). \tag{2.90}$$

According to the above arguments, and comparing to Eq. (2.71), focused replacement is possible when the energy transported in the collision chain satisfies:

$$E > E_r = \frac{1}{2}A\exp\left(\frac{-D}{2B}\right) = \frac{1}{4}E_{fc}. \tag{2.91}$$

Therefore, we get focused replacement, or:
$E_{fc}/4 < T < E_{fc}$ focused replacement
$T < E_{fc}/4$ focused momentum/energy packet

Hence, mass transfer can occur when E is between $E_r = E_{fc}/4$ and E_{fc}, which from our previous example is about the same or slightly less than the displacement energy, E_d. Figure 2.13 shows where focusing and replacement collisions fall on the energy spectrum of the PKA.

Assisted Focusing

In our analysis of focusing, we have not accounted for the effects of surrounding atoms or nearest neighbors. Due to their repulsion of the moving atom, they tend to act as a lens and aid in the focusing process. The net result of this assisted focusing is to increase the critical energy for focusing, E_{fc}, rendering focusing more probable. Second, the ring of atoms surrounding a focusing event also tends to dissipate energy by glancing collisions. This effect is augmented by the vibrational motion of the atom rings, which can be increased with temperature. The length of the replacement chain and the number of collisions in the chain decrease as the temperature increases. The increased motion of the surrounding atoms increases the energy loss from the collision sequence. Other effects that destroy the sequence are alloying elements and defects such as interstitials, vacancies, and dislocations. Figure 2.14 shows the number of collisions in a focused chain of initial energy E in room temperature copper along with the focusing probability. Table 2.3 from Chadderton [18] gives the focusing and replacement energies in various directions in fcc and bcc lattices as

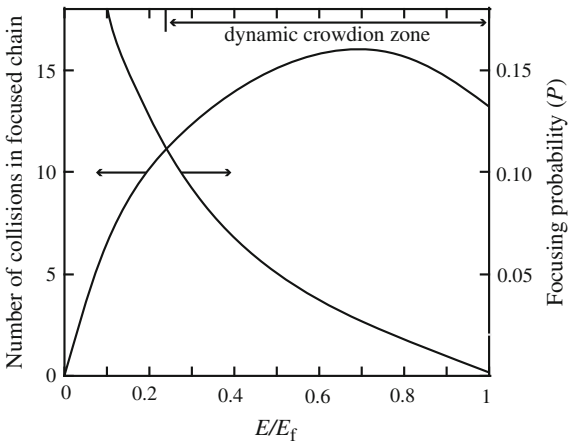

Fig. 2.14 Length and probability of the collision chain in a <110> collision sequence in copper at room temperature (after [5])

Table 2.3 (**a**) Equations for E_{fc}^{hkl} in the fcc and bcc lattices considering assisted focusing (after [18]). (**b**) Equations for replacement energies (E_r^{hkl}) in the fcc and bcc lattices (after [18])

(a)

$\langle hkl \rangle$	Face-centered cubic	Body-centered cubic
$\langle 100 \rangle$	$\frac{A(D^{110})^2}{2B^2}\exp\left(-\frac{D^{110}}{4B}\right)^{\uparrow}$	$2A\exp\left(-\frac{D^{111}}{B\sqrt{3}}\right)$
$\langle 110 \rangle$	$2A\exp\left(-\frac{D^{110}}{2B}\right)$	$\frac{4\sqrt{2}(D^{111})^2 A}{15B^2}\exp\left(-\frac{D^{111}\sqrt{5}}{2\sqrt{3}B}\right)^{\uparrow\uparrow}$
$\langle 111 \rangle$	$\left(\frac{6}{19}\right)^{1/2}\frac{A(D^{110})^2}{B^2}\exp\left(-\frac{D^{110}}{2B}\left(\frac{19}{12}\right)^{1/2}\right)^{\uparrow}$	$2A\exp\left(-\frac{D^{111}}{2B}\right)$

(b)

$\langle hkl \rangle$	Face-centered cubic	Body-centered cubic
$\langle 100 \rangle$	$5A\exp\left(-\frac{D^{110}}{D\sqrt{2}}\right)$	$\frac{A}{2}\exp\left(-\frac{D^{100}}{2B}\right)$
$\langle 110 \rangle$	$\frac{A}{2}\exp\left(-\frac{D^{110}}{2B}\right)$	$3A\exp\left(-\frac{D^{110}}{2B}\right)$
$\langle 111 \rangle$	$4A\exp\left(-\frac{D^{110}}{B\sqrt{3}}\right)$	$2A\exp\left(-\frac{D^{111}}{2B}\right)$

$^{\uparrow}$ In the (110) plane only
$^{\uparrow\uparrow}$ Assisted focusing

modified by surrounding atoms (assisted focusing). Note that in all cases, the focusing energies are larger when the surrounding atoms aid in the focusing process.

Channeling

Channeling is the long distance displacement of energetic knock-on atoms down an open direction in the crystal lattice. Figure 2.15a shows a schematic of an atom spiraling down an open channel in a crystal lattice, and Fig. 2.15b shows axial and

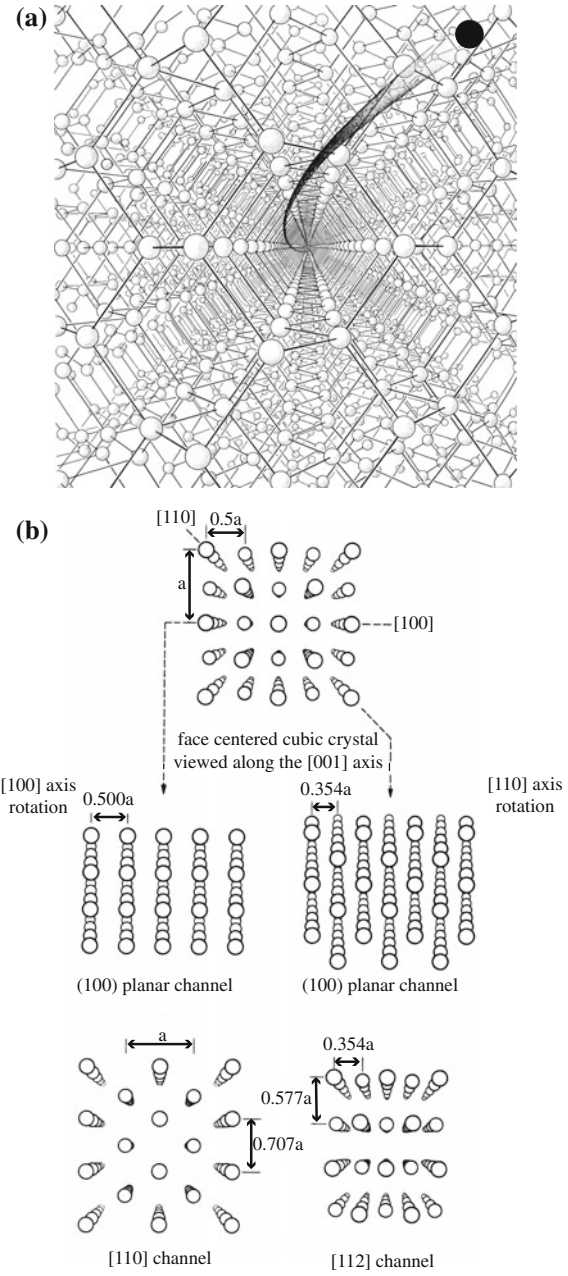

Fig. 2.15 (**a**) Schematic of an atom moving in a channel in a crystal lattice (after [19]), and (**b**) axial and planar channels in the fcc lattice (after [20])

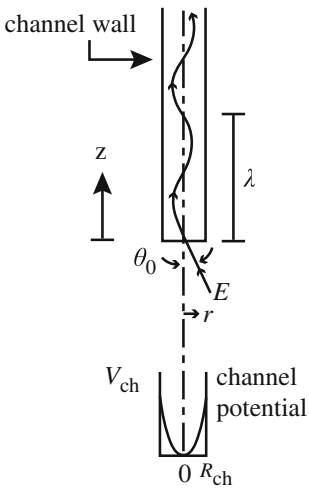

Fig. 2.16 Trajectory of a channeled atom (after [5])

planar channels along specific crystallographic directions in the fcc lattice. The walls of the passageway consist of atomic rows. If the rows surrounding the channel are close-packed, discrete repulsive forces between atoms are "smeared out" and the atom appears to be traveling in a long cylindrical tube with radius R_{ch}. The value of R_{ch} can be determined by equating πR_{ch}^2 with the cross-sectional area of the channel. If the amplitude of the lateral oscillations of the moving atom is small compared to R_{ch}, the potential well provided by the channel wall is roughly parabolic in the direction transverse to the channel axis.

The interaction of the moving atom with a channel wall (Fig. 2.16) can be described by a harmonic channel potential:

$$V_{ch}(r) = kr^2, \tag{2.92}$$

where r is the lateral distance from the axis, and k is the force constant that depends on the potential function describing atom–atom repulsion and channel dimension R_{ch}. Using the Born–Mayer potential to describe atom–atom interactions in this energy regime, k becomes:

$$k = \frac{A}{DB}\left(\frac{2\pi R_{ch}}{B}\right)\exp\left(\frac{-R_{ch}}{B}\right), \tag{2.93}$$

where D is the atom spacing in the rows forming the channels. Moving atoms enter the channel with a velocity component along the channel axis (Fig. 2.16) given by:

$$V_{z0} = \left(\frac{2E}{M}\right)^{1/2}\cos\theta_0, \tag{2.94}$$

where $(2E/M)^{1/2} = V_0$. The axial velocity is gradually reduced by inelastic energy loss to the electron cloud. The moving atom undergoes simple harmonic motion in the r direction with period τ given by:

$$\tau = 2\pi\left(\frac{M}{2k}\right)^{1/2}, \tag{2.95}$$

and the initial wavelength of the oscillation is equal to $V_{z0}\tau$ for $\theta_0 = 0$ or:

$$\lambda = 2\pi\left(\frac{E}{k}\right)^{1/2}. \tag{2.96}$$

The amplitude of lateral oscillation is determined by the injection angle, θ_0, and the kinetic energy of the injected atom, E. The r component of the atom velocity as it enters the channel is as follows:

$$V_{r0} = \left(\frac{2E}{M}\right)^{1/2}\sin\theta_0 \cong \left(\frac{2E}{M}\right)^{1/2}\theta_0. \tag{2.97}$$

So the radial component of the kinetic energy is $E\theta_0^2$, which is equal to the potential energy at the transverse amplitude, kr_{max}^2. Equating kinetic and potential energies and solving for r_{max} gives:

$$r_{max} = \left(\frac{E}{k}\right)^{1/2}\theta_0, \tag{2.98}$$

and the trajectory of the channeled atom is as follows:

$$r = \theta_0\left(\frac{E}{k}\right)^{1/2}\sin\left[\left(\frac{k}{E}\right)^{1/2}Z\right]. \tag{2.99}$$

The critical angle below which channeling can occur, θ_{ch}, is obtained by equating the transverse amplitude, r_{max}, and the channel radius, R_{ch}:

$$\theta_{ch} = R_{ch}\left(\frac{k}{E}\right)^{1/2}. \tag{2.100}$$

Note that θ_{ch} decreases as E increases, as expected. When the mean free path between collisions is of the order of a few atom spacings, large-angle collisions become probable and channeling dissipates. The channeling probability is difficult to determine since an atom must be knocked into the channel, but there are no atoms near the channel axis. The event probably starts with an impact on an atom forming the channel wall. If the entrance angle is small enough, it may begin to channel.

There is no upper limit on energy for channeling. Instead, θ_{ch} just becomes smaller as E increases. The minimum channeling energy occurs when the wavelength is $\sim nD$ or a few atom spacings ($n \sim 2$). Essentially, there develops a resonance between impulses from channel walls and transverse oscillations. The trajectory terminates in a violent collision. Recall that our treatment is only valid if $\lambda \gg D$. Solving for E in Eq. (2.96) and letting $\lambda = 2D$ yield $E_{ch} \sim 0.1\, kD^2$. For copper, E_{ch} is about 300 eV. E_{ch} is larger for large mass because k increases with mass. Channeling is a high-energy phenomenon and is most significant for light atoms, while focusing is a low-energy phenomenon that is most significant for heavy atoms.

Effect of Focusing and Channeling on Displacements

The probability of a crystal effect is a function of recoil energy. $P(T)$ is used for either P_f or P_{ch}, but since $E_f \sim 100$ eV, P_f is quite small. The equation governing cascade effects can be modified to account for crystal effects by modifying Eq. (2.14):

$$\nu(T) = P(T) + [1 - P(T)]\left[\frac{2E_d}{T} + \frac{2}{T}\int_{2E_d}^{T} \nu(\varepsilon)\mathrm{d}\varepsilon\right]. \tag{2.101}$$

The first term on the right of Eq. (2.101) represents the lone displaced atom, which results if the PKA is channeled or focused on the first collision. The second term gives the number of displacements created by a PKA that makes an ordinary displacement on the first collision. Assuming $P \neq P(T)$, Eq. (2.101) is differentiated with respect T to yield:

$$T\frac{\mathrm{d}\nu}{\mathrm{d}T} = (1 - 2P)\nu + P. \tag{2.102}$$

Integration gives

$$\nu(T) = \frac{CT^{(1-2P)} - P}{1 - 2P}, \tag{2.103}$$

and the constant, C can be found by substitution into Eq. (2.102):

$$C = \frac{1 - P}{(2E_d)^{(1-2P)}},$$

resulting in the final solution:

$$\nu(T) = \frac{1 - P}{1 - 2P}\left(\frac{T}{2E_d}\right)^{(1-2P)} - \frac{P}{1 - 2P}. \tag{2.104}$$

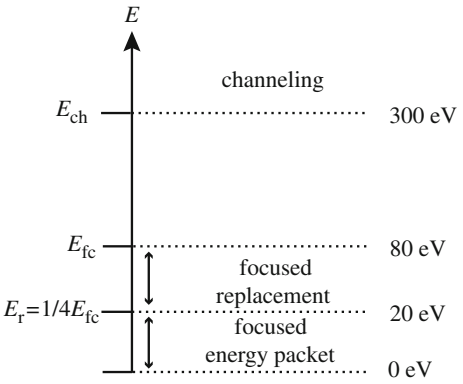

Fig. 2.17 Energy scale showing focused energy transfer and focused replacement sequence and channeling

For small P, $\nu(T)$ can be approximated by:

$$\nu(T) = \left(\frac{T}{2E_d}\right)^{(1-2P)}. \tag{2.105}$$

It should be noted that the most important crystal effect is channeling, which is most important at high energies. For example, for P = 7 %, a 10 keV PKA in iron produces 100 displacements or about half the amount with $P = 0$. Figure 2.17 shows where channeling occurs on the PKA energy scale. Note that channeling is a high-energy phenomenon and that there is a gap between the replacement energy, below which replacements or focused energy transfer occurs, and the channeling energy, above which channeling occurs. Given the K–P model for displacement and the various modifications to the basic model, we now turn to the determination of the number of displaced atoms.

2.3 The Displacement Cross Section

The results of previous sections may now be used to define the displacement cross section as:

$$\sigma_D(E_i) = \int_{\check{T}}^{\hat{T}} \nu(T)\sigma\left(E_i, Q_j, T\right) \mathrm{d}T, \tag{2.106}$$

where $\nu(T)$ is the number of displacements caused by a PKA of energy T, $\sigma(E_i, Q_j, T)$ is the general form of the energy transfer cross section, and $\check{T}$ and $\hat{T}$ are the minimum and maximum transfer energies. This quantity was first presented in Eq. (2.2) and gives the average number of displacements produced by an incoming neutron of energy E_i. We can apply this expression to the various regimes of scattering in order to determine their individual contributions to the total number of displacements.

We will first determine $\sigma_D(E_i)$ for each type of interaction using the basic K–P result and then go back and add in the modifications.

2.3.1 Elastic Scattering

Consider $\sigma_s(E_i, T)$ for elastic scattering. From Eq. (1.19),

$$\sigma_s(E_i, T) = \frac{4\pi}{\gamma E_i}\sigma_s(E_i, \phi).$$

In the case of isotropic scattering:

$$\sigma_s(E_i, \phi) = \frac{\sigma_s(E_i)}{4\pi}; \quad \sigma_s(E_i, T) = \frac{\sigma_s(E_i)}{\gamma E_i},$$

therefore,

$$\sigma_{Ds}(E_i) = \frac{\sigma_s(E_i)}{\gamma E_i}\int_{E_d}^{\gamma E_i} \nu(T)\mathrm{d}T. \tag{2.107}$$

Should we wish to consider anisotropic elastic scattering in systems such as fast reactors, the angular dependence of the elastic scattering cross section can be written in a series of Legendre polynomials:

$$\sigma_s(E_i, \phi) = \frac{\sigma_s(E_i)}{4\pi}\sum_{\ell=0}^{\infty} a_\ell(E_i)P_\ell(\cos\phi), \tag{2.108}$$

where $\sigma_s(E_i)$ is the total elastic scattering cross section for incident neutrons of energy E_i, P_ℓ is the ℓth Legendre polynomial, and values of a_ℓ are the energy-dependent coefficients of the cross section expansion. At neutron energies encountered in thermal or fast reactors, it is sufficient to retain only the first two terms, $\ell = 0$ and $\ell = 1$. Since $P_0 = 1$ and $P_1 = \cos\phi$:

$$\sigma_s(E_i, \phi) = \frac{\sigma_s(E_i)}{4\pi}[1 + a_1(E_i)\cos\phi]. \tag{2.109}$$

Also, given that $\cos\phi = 1\text{–}2T/\gamma E_i$ and substituting Eq. (2.109) into Eq. (2.106) gives:

$$\sigma_{Ds}(E_i) = \frac{\sigma_s(E_i)}{\gamma E_i}\int_{E_d}^{\gamma E_i} \nu(T)\left[1 + a_1(E_i)\left(1 - \frac{2T}{\gamma E_i}\right)\right]\mathrm{d}T. \tag{2.110}$$

2.3.2 Inelastic Scattering

Since inelastic scattering is isotropic in the center-of-mass system:

$$\sigma_{sj}(E_\mathrm{i}, Q_j, \phi) = \frac{\sigma_{sj}(E_\mathrm{i}, Q_j)}{4\pi}. \tag{2.111}$$

Equation (1.30) gives the energy transfer cross section for inelastic scattering in the resonance region as:

$$\sigma_{sj}(E_\mathrm{i}, Q_j, T) = \frac{\sigma_{sj}(E_\mathrm{i}, Q_j)}{\gamma E_\mathrm{i}} \left[1 + \frac{Q_j}{E_\mathrm{i}}\left(\frac{1+A}{A}\right)\right]^{-1/2},$$

so that

$$\sigma_{\mathrm{D}sj}(E_\mathrm{i}) = \sum_j \frac{\sigma_{sj}(E_\mathrm{i}, Q_j)}{\gamma E_\mathrm{i}} \left[1 + \frac{Q_j}{E_\mathrm{i}}\left(\frac{1+A}{A}\right)\right]^{-1/2} \int_{\check{T}_j}^{\hat{T}_j} \nu(T)\mathrm{d}T, \tag{2.112}$$

where the minimum and maximum values of $T(E_\mathrm{i}, Q_j, \phi)$ are given by Eq. (1.27), and setting cos $\phi = -1$ and 1, respectively, gives:

$$\hat{T}_j = \frac{\gamma E_\mathrm{i}}{2}\left[1 + \frac{1+A}{2A}\frac{Q_j}{E_\mathrm{i}} + \left(1 + \frac{Q_j}{E_\mathrm{i}}\frac{1+A}{A}\right)^{1/2}\right]$$

$$\check{T}_j = \frac{\gamma E_\mathrm{i}}{2}\left[1 + \frac{1+A}{2A}\frac{Q_j}{E_\mathrm{i}} - \left(1 + \frac{Q_j}{E_\mathrm{i}}\frac{1+A}{A}\right)^{1/2}\right].$$

2.3.3 (n, 2n) and (n, γ) Displacements

The displacement cross section for (n, 2n) reactions can be written as:

$$\sigma_{\mathrm{D(n,2n)}}(E_\mathrm{i}) = \int_0^{E_\mathrm{i}-E'_\mathrm{m}} \sigma_{(\mathrm{n},\,2\mathrm{n})}(E_i, T)\frac{T}{2E_\mathrm{d}}\mathrm{d}T, \tag{2.113}$$

where $\sigma_{(\mathrm{n},\ 2\mathrm{n})}(E_\mathrm{i}, T)$ is given by Eq. (1.40).

The displacement cross section due to (n, γ) reactions can be written as:

$$\sigma_{\mathrm{D}\gamma}(E_\mathrm{i}) = \sigma_\gamma \int_0^{\hat{T}} \frac{T}{2E_\mathrm{d}}\mathrm{d}T. \tag{2.114}$$

However, since we have assumed that the lattice atom recoils with an average energy

$$\overline{T} = \frac{\hat{T}}{2} = \frac{E_\gamma^2}{4(A+1)c^2},$$

and that E_γ for a given isotope is either known or can be measured, Eq. (2.114) can be simplified to:

$$\sigma_{D\gamma} = \sigma_\gamma \frac{\overline{T}}{2E_d} = \sigma_\gamma \frac{E_\gamma^2}{8E_d(A+1)c^2}. \tag{2.115}$$

The total displacement cross section due to these forms of neutron interaction then becomes:

$$\begin{aligned}\sigma_{\mathrm{D}}(E_{\mathrm{i}}) &= \sigma_{\mathrm{Ds}}(E_{\mathrm{i}}) + \sigma_{\mathrm{Ds}j}(E_{\mathrm{i}}) + \sigma_{\mathrm{D(n,2n)}}(E_{\mathrm{i}}) + \sigma_{\mathrm{D}\gamma} \\ &= \frac{\sigma_{\mathrm{s}}(E_{\mathrm{i}})}{\gamma E_{\mathrm{i}}} \int_{E_{\mathrm{d}}}^{\gamma E_{\mathrm{i}}} \frac{T}{2E_{\mathrm{d}}} \left[1 + a_1(E_{\mathrm{i}})\left(1 - \frac{2T}{\gamma E_{\mathrm{i}}}\right)\right] \mathrm{d}T \\ &\quad + \sum_j \frac{\sigma_{sj}(E_{\mathrm{i}}, Q_j)}{\gamma E_{\mathrm{i}}} \left[1 + \frac{Q_j}{E_{\mathrm{i}}}\left(\frac{1+A}{A}\right)\right]^{-1/2} \int_{\hat{T}_j}^{\hat{T}_j} \frac{T}{2E_{\mathrm{d}}} \mathrm{d}T \\ &\quad + \int_0^{E_{\mathrm{i}} - E'_{\mathrm{m}}} \sigma_{\mathrm{(n,2n)}}(E_{\mathrm{i}}, T) \frac{T}{2E_{\mathrm{d}}} \mathrm{d}T \\ &\quad + \sigma_\gamma \frac{E_\gamma^2}{8E_{\mathrm{d}}(A+1)c^2},\end{aligned} \tag{2.116}$$

where the terms are for elastic scattering, inelastic scattering in the resonance region, (n, 2n) reactions and (n, γ) reactions, respectively.

2.3.4 *Modifications to the K–P Model and Total Displacement Cross Section*

The displacement cross section can be modified to account for the relaxation of the various assumptions made to the basic K–P model as in Sect. 2.2. These modifications are summarized in Table 2.4. Applying these correction terms to the basic K–P result by consolidating Assumptions 1 and 3 into a single constant C' and using Eq. (2.104) for the effect of crystallinity transform Eq. (2.116) to read:

Table 2.4 Modifications to the displacement cross section

Assumption	Correction to $\nu(T) = T/2E_d$	Equation in text
3: Loss of E_d	$0.56\left(1+\frac{T}{2E_d}\right)$	Equation (2.31)
4: Electronic energy loss cutoff	$\xi(T)\left(\frac{T}{2E_d}\right)$	Equation (2.54)
5: Realistic energy transfer cross section	$C\frac{T}{2E_d}, \quad 0.52 < C \leq 1.22$	Equation (2.33), (2.39)
6: Crystallinity	$\frac{1-P}{1-2P}\left(\frac{T}{2E_d}\right)^{(1-2P)} - \frac{P}{1-2P}$	Equation (2.104)
	$\sim \left(\frac{T}{2E_d}\right)^{(1-2P)}$	Equation (2.105)

$$
\begin{aligned}
\sigma_D = {} & \frac{\sigma_s(E_i)}{\gamma E_i}\int_{E_d}^{\gamma E_i}\left[\frac{1-P}{1-2P}\left(C'\xi(T)\frac{T}{2E_d}\right)^{(1-2P)} - \frac{P}{1-2P}\right] \\
& \times \left[1 + a_1(E_i)\left(1 - \frac{2T}{\gamma E_i}\right)\right]dT \\
& + \sum_j \frac{\sigma_{sj}(E_i, Q_j)}{\gamma E_i}\left[1 + \frac{Q_j}{E_i}\left(\frac{1+A}{A}\right)\right]^{-1/2} \\
& \times \int_{\hat{T}_j}^{\hat{T}_j}\left[\frac{1-P}{1-2P}\left(C'\xi(T)\frac{T}{2E_d}\right)^{(1-2P)} - \frac{P}{1-2P}\right]dT \\
& + \int_0^{E_i - E'_m}\sigma_{(n,2n)}(E_i, T)\left[\frac{1-P}{1-2P}\left(C'\xi(T)\frac{T}{2E_d}\right)^{(1-2P)} - \frac{P}{1-2P}\right]dT \\
& + \sigma_\gamma\left[\frac{1-P}{1-2P}\left(C'\xi(T)\frac{E_\gamma^2}{8E_d(A+1)c^2}\right)^{1-2P} - \frac{P}{1-2P}\right].
\end{aligned}
\tag{2.117}
$$

Using the more simplified expression for the effect of crystallinity, Eq. (2.104) reduces Eq. (2.117) to:

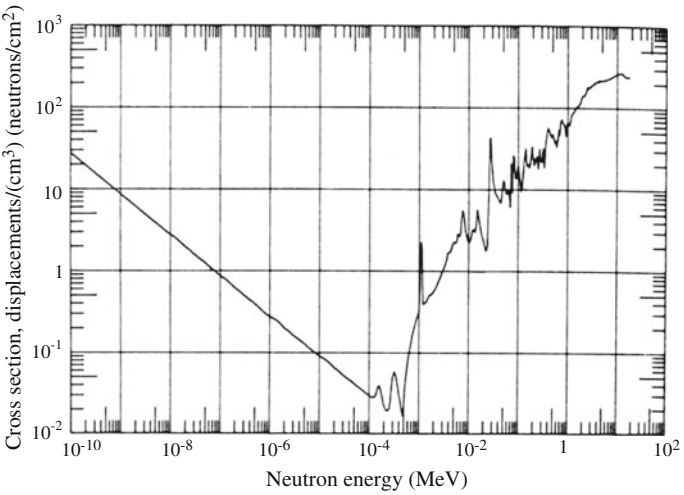

Fig. 2.18 The displacement cross section for stainless steel based on a Lindhard model and ENDF/B scattering cross sections (after [21])

$$\begin{aligned}\sigma_{\mathrm{D}} = {} & \frac{\sigma_{\mathrm{s}}(E_{\mathrm{i}})}{\gamma E_{\mathrm{i}}} \int_{E_{\mathrm{d}}}^{\gamma E_{\mathrm{i}}} \left[\left(C' \xi(T) \frac{T}{2E_{\mathrm{d}}} \right)^{(1-2P)} \right] \left[1 + a_1(E_{\mathrm{i}}) \left(1 - \frac{2T}{\gamma E_{\mathrm{i}}} \right) \right] \mathrm{d}T \\ & + \sum_j \frac{\sigma_{\mathrm{s}j}(E_{\mathrm{i}}, Q_j)}{\gamma E_{\mathrm{i}}} \left[1 + \frac{Q_j}{E_{\mathrm{i}}} \left(\frac{1+A}{A} \right) \right]^{-1/2} \int_{\check{T}_j}^{\hat{T}_j} \left(C' \xi(T) \frac{T}{2E_{\mathrm{d}}} \right)^{(1-2P)} \mathrm{d}T \\ & + \int_0^{E_{\mathrm{i}} - E'_{\mathrm{m}}} \sigma_{(\mathrm{n},2\mathrm{n})}(E_{\mathrm{i}}, T) \left(C' \xi(T) \frac{T}{2E_{\mathrm{d}}} \right)^{(1-2P)} \mathrm{d}T \\ & + \sigma_\gamma \left(C' \xi(T) \frac{E_\gamma^2}{8E_{\mathrm{d}}(A+1)c^2} \right)^{1-2P}, \end{aligned} \tag{2.118}$$

or,

$$\sigma_{\mathrm{D}} = \sigma_{\mathrm{Ds}} + \sigma_{\mathrm{Di}} + \sigma_{\mathrm{D(n,2n)}} + \sigma_{\mathrm{D}\gamma}. \tag{2.119}$$

The displacement cross section for stainless steel was calculated by Doran [21] using the energy partition theory of Lindhard and is shown in Fig. 2.18.

2.4 Displacement Rates

Recall that the displacement rate was given in Eq. (2.1) as:

$$R = \int_{\check{E}}^{\hat{E}} N\phi(E_\mathrm{i})\sigma_\mathrm{D}(E_\mathrm{i})\mathrm{d}E_\mathrm{i}.$$

This is the displacement rate density or total number of displacements per unit volume per unit time [#/cm^3 s]. To get a rough estimate of the order of magnitude of this number, let us simplify the displacement cross sections as follows. Neglecting (n, 2n) and (n, γ) contributions to displacements, all modifications to the simple K–P displacement model (i.e., using $\nu(T) = T/2E_\mathrm{d}$), and neglecting E_d relative to E_i, the displacement cross section due to elastically and inelastically scattered neutrons only becomes:

$$\begin{aligned}\sigma_\mathrm{D}(E_\mathrm{i}) = {} & \frac{\sigma_\mathrm{s}(E_\mathrm{i})}{\gamma E_\mathrm{i}}\int_{E_\mathrm{d}}^{\gamma E_\mathrm{i}}\frac{T}{2E_\mathrm{d}}\left[1 + a_1(E_\mathrm{i})\left(1 - \frac{2T}{\gamma E_\mathrm{i}}\right)\right]\mathrm{d}T \\ & + \sum_j \frac{\sigma_{\mathrm{s}j}\left(E_\mathrm{i}, Q_j\right)}{\gamma E_\mathrm{i}}\left[1 + \frac{Q_j}{E_\mathrm{i}}\left(\frac{1+A}{A}\right)\right]^{-1/2}\int_{\hat{T}_j}^{\hat{T}_j}\frac{T}{2E_\mathrm{d}}\mathrm{d}T.\end{aligned} \tag{2.120}$$

Assuming that elastic scattering is isotropic ($a_1 = 0$), neglecting inelastic scattering and integrating between the limits E_d and γE_i gives:

$$\sigma_\mathrm{D}(E_\mathrm{i}) = \frac{\sigma_\mathrm{s}(E_\mathrm{i})}{\gamma E_\mathrm{i}}\int_{E_\mathrm{d}}^{\gamma E_\mathrm{i}}\frac{T}{2E_\mathrm{d}}\mathrm{d}T, \tag{2.121}$$

and if $\gamma E_\mathrm{i} > E_\mathrm{c}$, then:

$$\begin{aligned}\sigma_D(E_i) &= \frac{\sigma_s(E_i)}{\gamma E_i}\left[\int_{E_d}^{2E_d} dT + \int_{2E_d}^{E_c}\frac{T}{2E_d}dT + \int_{E_c}^{\gamma E_i}\frac{E_c}{2E_d}dT\right] \\ &= \frac{\sigma_s(E_i)}{2\gamma E_i E_d}\left[\gamma E_i E_c - \frac{E_c^2}{2}\right].\end{aligned} \tag{2.122}$$

If we choose $\gamma E_i \sim E_\mathrm{c,}$ then we have:

$$\sigma_\mathrm{D}(E_\mathrm{i}) \approx \left(\frac{\gamma E_\mathrm{i}}{4E_\mathrm{d}}\right)\sigma_\mathrm{s}(E_\mathrm{i}), \tag{2.123}$$

and Eq. (2.1) becomes:

$$R_d = \frac{N\gamma}{4E_\mathrm{d}} \int_{E_{\mathrm{d}/\gamma}}^{\infty} \sigma_\mathrm{s}(E_\mathrm{i}) E_\mathrm{i} \phi(E_\mathrm{i})\, \mathrm{d}E_\mathrm{i} \tag{2.124}$$

$$= N\sigma_\mathrm{s} \left(\frac{\gamma \bar{E}_\mathrm{i}}{4E_\mathrm{d}} \right) \phi, \tag{2.125}$$

where $\bar{E}_\mathrm{i}$ is an average neutron energy and ϕ is the total neutron flux above energy E_d/γ, and the term in brackets is the number of displacements (Frenkel pairs) produced per neutron. The validity of assuming isotropic scattering and neglecting inelastic scattering is shown in Figs. 2.19 and 2.20. Essentially, both approximations are reasonable at energies below one to a few MeV.

Example 2.1. Neutron irradiation of iron
As an example, let us look at the damage caused by 0.5 MeV neutrons in Fe in a fast flux that may be representative of the core of a fast reactor:

$N = 0.85 \times 10^{23}$ atoms/cm^3
$\sigma_\mathrm{s} = 3 \times 10^{-24}$ cm^2
$\phi = 10^{15}$ neutrons cm^{-2}s^{-1}
$\frac{\gamma E_\mathrm{i}}{4E_\mathrm{d}} = 350$ displaced atoms/neutron

R_d is 9×10^{16} displaced atoms per cm^3 per second, or dividing R_d by N gives $\sim 10^{-6}$ dpa/s or about 32 dpa/year. This is equivalent to each atom being displaced from a normal lattice site once every 12 days.

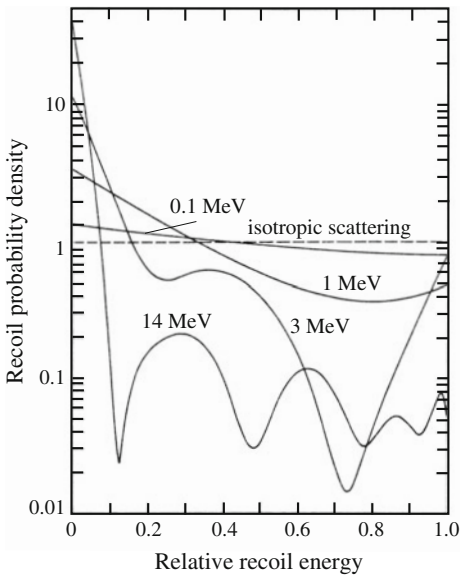

Fig. 2.19 Recoil energy spectra from the elastic scattering of fast neutrons using data from ENDF/B files (after [22])

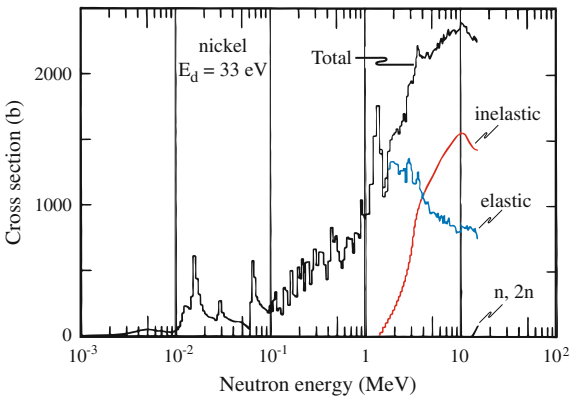

Fig. 2.20 Displacement cross section for nickel showing the elastic and inelastic components (after [21])

A second example can be worked for the displacement rate in the aluminum fuel plates in an MTR-type thermal neutron research reactor. In this case, we have:

$E_i \sim 0.5$ MeV
$N = 0.6 \times 10^{23}$ atoms/cm^3
$\sigma_s = 3 \times 10^{-24}$cm^2
$\phi = 3 \times 10^{13}$ neutrons cm^{-2}s^{-1}
$\frac{\gamma E_i}{4E_d} = 690$ displaced atoms/neutron

R_d is 4×10^{15} displaced atoms per cm^3 per second, or dividing R_d by N gives $\sim 7 \times 10^{-8}$ dpa/s or about 2 dpa/year. Note that even though the number of displacements per neutron is almost a factor of 2 higher in Al than in Fe, the damage rate is significantly lower because of the much lower fast flux in this type of reactor.

2.5 Correlation of Property Changes and Irradiation Dose

The ultimate objective of the calculation of R_d is to provide a prediction of the extent of change of a particular property of the material under irradiation. The mechanical property may be yield strength, swelling, degree of embrittlement, etc. Recall in the introduction that the determination of the number of displaced atoms was motivated by the inability of particle fluence to account for property changes (see Fig. 1 in the Introduction). While an improvement over units of exposure such as neutron fluence, displacement rate alone cannot account for the macroscopic changes observed, and a semiempirical method of correlating damage with

macroscopic property changes has evolved known as the damage function method. In this method, the atom displacement rate is replaced with the change in some macroscopic property after a time t of irradiation. The displacement cross section is replaced by the damage function for the particular mechanical property, $G_{\mathrm{i}}(E)$, hence:

$$\Delta P_{ij} = \int \int G_{\mathrm{i}}(E)\phi_j(E,t)\,\mathrm{d}E\,\mathrm{d}t, \tag{2.126}$$

where ΔP_{ij} is the change in the property labeled by the index i, during an irradiation time of t and in a neutron flux where $\phi_j(E,t)$ is the jth neutron differential spectrum. Assuming energy–time separability, $\phi_j(E,t) = \phi_j(E,)t$, then Eq. (2.126) can be rewritten as

$$\Delta P_{ij}^{(k)} = t \cdot \int G_{\mathrm{i}}^{(k)}(E)\phi_j(E)\,\mathrm{d}E, \tag{2.127}$$

where the superscript refers to the kth cycle of iteration.

The objective is to deduce a single function $G_{\mathrm{i}}(E)$ from a set of measured ΔP_{i} values. Given $\Delta P_{ij}^{(k)}$ and $\phi_j(E)$ as input along with an initial approximation of $G_{\mathrm{i}}(E)$ or $G_{\mathrm{i}}^{(0)}(E)$, a computer code is used to generate iterative solutions $G_{\mathrm{i}}^{(\mathrm{k})}(E)$. An appropriate solution is obtained when the standard deviation of the ratios of all measured-to-calculated values $\Delta P_{ij}/\Delta P_{ij}^{(k)}$ reaches a lower value that is consistent with experimental uncertainties. As it turns out, the resultant damage function is highly sensitive to the initial approximation as shown in Fig. 2.21. But note that since the shape of $G_{\mathrm{i}}(E)$ is the same as the displacement function, it is clear that they are related. However, this result tells us that we cannot fully understand radiation effects by only calculating the number of displaced atoms. We cannot treat radiation effects as a black box. Rather, in order to understand the effect of the damage on the properties of the material, we must understand the fate of these defects after they are formed. This realization is reinforced by the property dependence on dose shown in Fig. 2.22. Note that for the three property changes, resistivity, radiation-induced segregation, and hardening, the functional dependence on dose is strikingly different between them. While property change certainly relates to displacement damage, the nature of the change is not uniform but varies considerably depending on the property measured. The next chapter explores the spatial and temporal distribution of radiation damage. But before we examine the damage zone in detail, let us complete our picture of the production of displacements by addressing the damage created by charged particles such as ions and electrons.

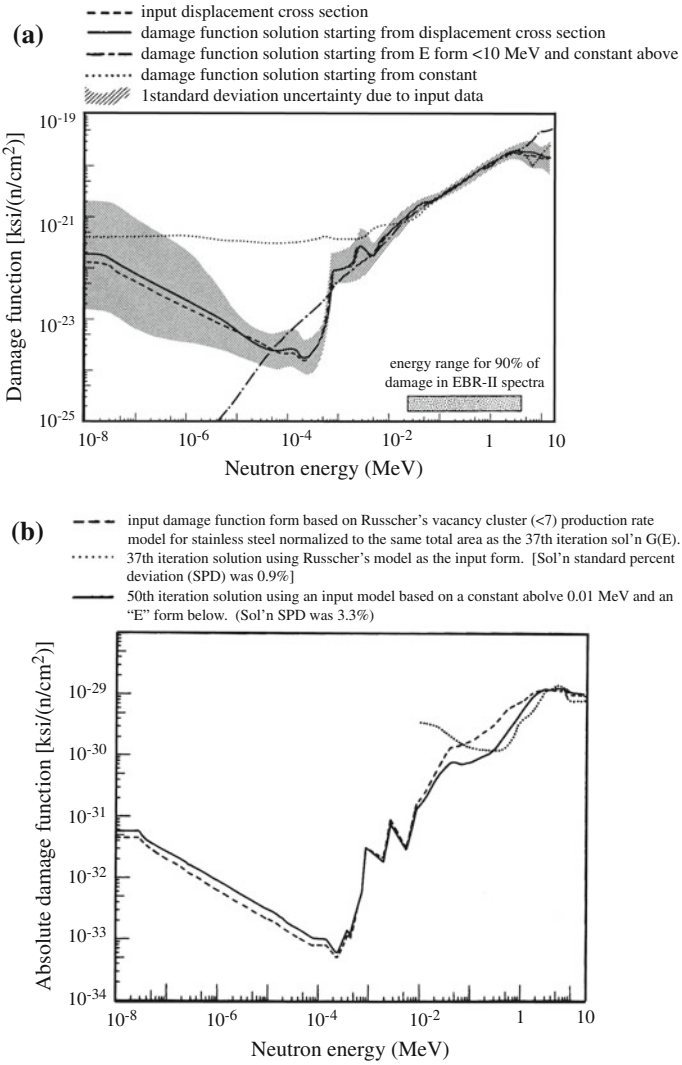

Fig. 2.21 (**a**) 60 ksi yield strength damage function for 304 stainless steel irradiated and tested at 480 °C (after [23]) (**b**) Damage function for a 2.0×10^{-8} psi^{-1} $\bar{\varepsilon}/\bar{\sigma}$ property change for stainless steel (after [24])

2.6 Displacements from Charged Particle Irradiation

Displacement from charged particles differs from that due to neutrons because as they travel through the lattice, they lose energy via electronic excitation in addition to via elastic collisions. Figure 2.23 shows the trade-off in energy loss mechanism dominance with energy in the energy range of relevance for ion–solid interaction,

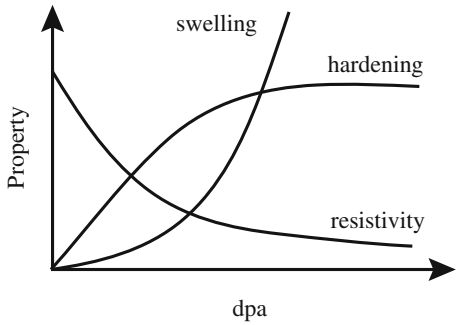

Fig. 2.22 Dose dependence of swelling, resistivity, and radiation-induced segregation

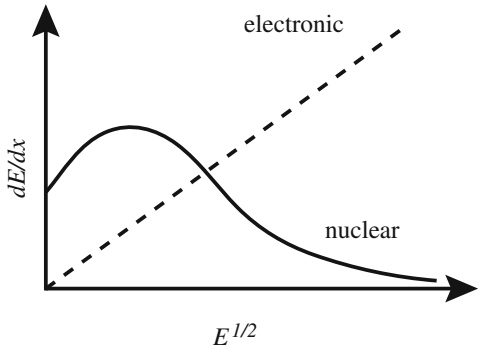

Fig. 2.23 Variation in nuclear and electronic stopping powers over the energy range of relevance to ion–solid interactions

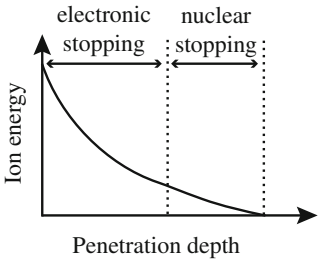

Fig. 2.24 Residual range of an ion incident on a target and the regimes of electronic and nuclear stopping dominance

and Fig. 2.24 shows the residual ion energy as a function of ion penetration depth. Note that electronic stopping will dominate at short depths, but elastic collisions will dominate near the end of range. An expression for the number of displacements from a charged particle can be derived from the analysis of energy lost from the

PKA by electronic excitation given in Sect. 2.2.3 and described by Eq. (2.40) through Eq. (2.49). Equation (2.44) describes the loss of energy to both atoms and electrons in the target by the PKA. We can revisit this analysis assuming that the particle we are tracking is the incident ion. As was done in Eq. (2.45), we can expand the terms for $\nu(T-\varepsilon_a)$ and $\nu(T-\varepsilon_e)$ in a Taylor series and truncate the series after the second term, giving:

$$\begin{aligned}\nu(T-\varepsilon_a) &= \nu(T) - \frac{d\nu}{dT}\varepsilon_a,\\ \nu(T-\varepsilon_e) &= \nu(T) - \frac{d\nu}{dT}\varepsilon_e,\end{aligned} \tag{2.128}$$

and the integrals involving the terms $\nu(T-\varepsilon_a)$ and $\nu(T-\varepsilon_e)$ can both be written in the general form:

$$\begin{aligned}\int_0^{\varepsilon_{max}} \nu(T-\varepsilon)\sigma(T,\varepsilon)d\varepsilon &= \nu(T)\int_0^{\varepsilon_{max}} \sigma(T,\varepsilon)d\varepsilon - \frac{d\nu}{dT}\int_0^{\varepsilon_{max}} \varepsilon\sigma(T,\varepsilon)\,d\varepsilon\\ &= \nu(T)\sigma(T) - \frac{d\nu(T)}{dT}S(T),\end{aligned} \tag{2.129}$$

where $S(T)$ is the stopping cross section. Since in this treatment, the ion is the incoming projectile, we will rewrite Eq. (2.129) using our established convention that the incoming particle is of energy E_i and it transfers energy T to the target atoms and electrons, and the maximum energy transfer is $\hat{T}$:

$$\begin{aligned}\int_0^{\hat{T}} \nu(E_i-T)\sigma(E_i,T)dT &= \nu(E_i)\int_0^{\hat{T}} \sigma(E_i,T)dT - \frac{d\nu}{dE}\int_0^{\hat{T}} T\sigma(E_i,T)\,dT\\ &= \nu(E_i)\sigma(E_i) - \frac{d\nu(E_i)}{dE}S(E_i),\end{aligned} \tag{2.130}$$

where Eq. (1.79) is used to transform the integral of the differential energy transfer cross section, $\sigma(E_i,T)$, to the total collision cross section, $\sigma(E_i)$, and Eq. (1.129) is used to transform the integral of $T\sigma(E_i,T)$ into the stopping cross section $S(E_i)$. Applying the results of Eqs. (2.129) and (2.130) into Eq. (2.44) gives:

$$d\nu(E_i) = \frac{dE}{S(E_i)}\int_0^{\hat{T}} \nu(T)\sigma(E_i,T)\,dT. \tag{2.131}$$

Since we are concerned with the total number of displacements over the entire range of the ion rather than the specific number of displacements over a distance dx of the sample, we can integrate Eq. (2.131) over the entire range of ion energy loss to obtain the number of displacements resulting from an incident ion with initial energy E_i:

$$\begin{aligned} \nu(E_\mathrm{i}) &= \int_0^{E_\mathrm{i}} \frac{\mathrm{d}E'}{S(E')} \int_{E_\mathrm{d}}^{\hat{T}} \nu(T)\sigma(E', T)\mathrm{d}T \\ &= \int_0^{E_\mathrm{i}} \sigma_\mathrm{d}(E') \frac{\mathrm{d}E'}{S(E')}, \end{aligned} \tag{2.132}$$

and

$$\int_{E_\mathrm{d}}^{\hat{T}} \nu(T)\sigma(E', T)\mathrm{d}T \equiv \sigma_\mathrm{d}(E'), \tag{2.133}$$

where $E' = E'(x)$ is the ion energy as a function of the traveled path length x as the ion travels down to zero energy. We can work a simple example using an approximation to the treatment given above. We are interested in the number of collisions made by an ion as it passes through a solid. We will take I as the ion flux in units of ions/cm^2 s, and we can write the number of collisions per second in a volume element of unit cross-sectional area and thickness dx which transfer energy in the range (T, dT) to atoms of this element as:

$$NI\sigma(E, T)\mathrm{d}x. \tag{2.134}$$

The number of collisions per unit volume per unit time which transfer energy in (T, dT) at depth x is $NI\sigma(E, T)$ [collisions/cm^3 s]. The number of displaced atoms for each collision that produces a PKA of energy T is $\nu(T)$. Therefore, the production rate of displaced atoms at depth x is as follows:

$$R_\mathrm{d}(x) = NI \int_{E_\mathrm{d}}^{\gamma E} \sigma(E, T)\nu(T)\,\mathrm{d}T \quad [\text{displacements/cm}^3\text{s}]. \tag{2.135}$$

(Note that we have not accounted for the fact that I is a function of x (or E) and that $I(x) \neq I_0$.) E is a function of x since the ion slows down by loss of energy to the electrons of the target. The functional form of $E(x)$ can be estimated using dE/dx = $kE^{1/2}$ as:

$$E(x) = \left[(E_\mathrm{i})^{1/2} - 1/2kx\right]^2, \tag{2.136}$$

where E_i is the initial energy of the ion when it strikes the target. The number of displaced atoms/atom/s is $R_\mathrm{d}(x)/N$, and the $\frac{\text{dpa}}{(\text{ions/cm}^2)}$ at a depth x is $R_\mathrm{d}(x)/NI$. We will assume that $\sigma(E, T)$ can be described by Rutherford scattering, and using the Lindhard treatment for $\nu(T)$ from the K–P model and assuming $\xi = 0.5$ gives:

$$\frac{R_\mathrm{d}}{NI} = \int_{E_\mathrm{d}}^{\gamma E_\mathrm{i}} \frac{1}{2} \frac{\pi Z_1^2 Z_2^2 \varepsilon^4}{4} \left(\frac{M + M_\mathrm{i}}{M}\right)^2 \frac{1}{E_\mathrm{i}} \frac{4 M_\mathrm{i} M}{(M + M_\mathrm{i})^2} \frac{1}{T^2} \frac{T}{2E_\mathrm{d}} \mathrm{d}T$$
$$= \frac{\pi Z_1^2 Z_2^2 \varepsilon^4}{4 E_\mathrm{i} E_\mathrm{d}} \left(\frac{M_\mathrm{i}}{M}\right) \ln \frac{\gamma E_\mathrm{i}}{E_\mathrm{d}} \frac{\mathrm{dpa}}{\mathrm{ion/cm^2}}. \tag{2.137}$$

Applying this result to 0.5 MeV protons in iron gives $\sim 10^{-18}$ dpa/(ions/cm^2) at the surface. 20 MeV C^+ ions incident on nickel produce $\sim 3 \times 10^{-18}$ dpa/(ions/cm^2) at the surface, but 50 times this amount at the damage peak. These values can be compared to the damage rate from 0.5 MeV neutrons in iron:

$$\frac{R_d}{N\phi} = \left(\frac{\gamma E_i}{4E_d}\right) \sigma_s$$
$$= 350 \times 3 \times 10^{-24} \tag{2.138}$$
$$= 1 \times 10^{-21} \frac{\mathrm{displacements}}{\mathrm{n/cm^2}}.$$

Comparing 0.5 MeV neutrons to 20 MeV C^+ ions shows that over their range C^+ ions produce 3000 times more displacements than do neutrons. Figure 2.25 compares the displacement rates as a function of penetration depth for ions of various mass and energy. As expected, for the same energy, ions of heavier mass deposit their energy over a shorter distance resulting in higher damage rates. Note that due

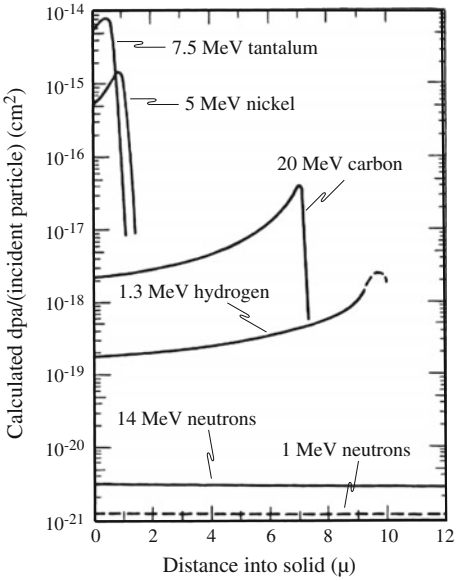

Fig. 2.25 Displacement-damage effectiveness for various energetic particles in nickel (after [25])

to the large collision mean free path of a neutron as compared to an ion, the neutron damage energy is low and constant over distances of millimeters.

Nomenclature

a	Lattice constant
a_0	Bohr radius of the hydrogen atom
A	Atomic mass
A	Pre-exponential constant in Born–Mayer relation, Eq. (1.47)
B	Spacing between barrier atoms in crystal lattice
B	Constant in exponent in Born–Mayer relation, Eq. (1.47)
c	Speed of light
D	Nearest neighbor spacing between atoms
E_c	Cutoff energy; critical energy for focusing
E_{ch}	Critical energy for channeling
E_{fc}	Critical focusing energy
E_d	Displacement energy
E_D	Damage energy
E_i	Projectile energy
E_r	Critical energy for replacement collisions; relative kinetic energy
E_s	Sublimation energy
E_γ	Gamma ray energy
E_i	Incoming particle energy
E'_m	Kinetic energy of incoming particle in CM system
E''_m	Energy of neutron after (n, 2n) reaction
E^*	Saddle point energy
E_{eq}	Energy of atom in equilibrium lattice site
f	Focusing parameter
g	Relative speed $v_1 - v_2$
G	Damage function
$\bar{I}$	Excitation–ionization level
k	Force constant; constant in the electronic energy loss term, $kE^{1/2}$
m	Mass of incoming particle; 1/s in power law expression
m_e	Mass of the electron
M_1	Mass of projectile
M_2	Mass of target
N	Atom number density
p, P_e, P_a	Probability, referring to electron and atom
P_{ch}	Channeling probability
P_d	Displacement probability
P_f	Focusing probability
Q	Excitation energy of nucleus
r_{eq}	Equilibrium spacing between atoms
r_{max}	Transverse amplitude of channeled atom
R	Atomic radius

R_{ch}	Radius of channel
R_d	Displacement rate [#/cm^3 s]
s	Exponent in the power law approximation
S, S_e, S_n	Stopping power electronic, nuclear
t_c	Collision time
T	Energy transferred in collision
$\check{T}$	Minimum energy transferred
$\hat{T}$	Maximum energy transferred
$\bar{T}$	Average energy transferred
T_ℓ	Energy transferred to target atom after (n, 2n) reaction
U	Energy per atom in a crystal
U_b	Binding energy lost by an atom when leaving a lattice site
$V(r)$	Potential energy
v_1	Velocity of projectile in laboratory system
v_2	Velocity of target in laboratory system
V_{CM}	Velocity of CM in laboratory system
Y	Distance to atom barrier
z	Impact parameter
Z	Atomic number
β	Compressibility
ε	Secondary atom knock-on energy unit charge in Eq. (2.52)
ε_{eq}	Energy of atom in a normal lattice site
ε^*	Energy of atom at saddle point
$\in$	Reduced PKA energy
ϕ, Φ	Neutron flux, fluence
γ	$4M_1M_2/(M_1 + M_2)^2$
η	Energy lost to electronic excitation in the NRT model
κ	Displacement efficiency
μ	Reduced mass
v	Specific volume of an atom
$\nu(T)$	Displacement function
θ	Scattering angle in laboratory system
θ_c	Critical focusing angle
θ_{ch}	Critical channeling angle
$\sigma(E_i)$	Total atomic collision cross section
$\sigma(E_i, T)$	Differential energy transfer cross section
σ_D	Displacement cross section
σ_s	Scattering cross section
σ_{sj}	Inelastic scattering cross section for the jth resonance
$\sigma_{(n, 2n)}$	Cross section for (n, 2n) reactions
σ_γ	Cross section for (n, γ) reactions
τ	Period for oscillation for a channeled atom
ξ	Damage energy efficiency, Eq. (2.50)

Problems

2.1 (a) Using the simple K–P model and assuming only elastic, isotropic scattering, calculate the number of displacements per atom (dpa) in nickel subjected to a fast neutron (2 MeV) fluence of 10^{22} n/cm^2

(b) Using the relativistic expression for the electron–atom energy transfer, calculate the minimum electron energy required to displace an atom in (i) Al and (ii) W.

2.2 In a (n, 2n) reaction, a second neutron can only be emitted if the residual excitation of the nucleus after emission of the first neutron exceeds the binding energy of a neutron in the mass M nuclide. The recoil energy after emission of the first neutron is taken to be the average value ($\cos \phi = 0$). Write an expression for the recoil energy following the second emission.

2.3 An ^{56}Fe nucleus undergoes an (n, γ) reaction resulting in the release of a single 7 MeV gamma ray, on average. If a steel component is located in a reactor where the peak thermal flux is 1×10^{14} n/cm^2 s and the thermal/fast flux ratio is one (where $E_{\text{ave}}^{\text{fast}} \geq 1\,\text{MeV}$), determine the relative displacement rates by fast neutrons, recoil nuclei, and gamma rays which undergo Compton scattering. Assume $\sigma_{(\text{n},\,\gamma)} \sim 4b$, $\sigma_{\text{s}} \sim 3b$.

2.4 A slab of iron is exposed to a 20 MeV gamma source.

(a) What is the most probable interaction between the gamma and the electrons in the Fe?

(b) Assume the reaction you chose in part (a) occurs. Can this lead to the displacement of an Fe atom if the displacement energy is 40 eV?

2.5 A thermal neutron causes the following reaction

$$^{27}\text{Al} + \text{n} \rightarrow ^{28}\text{Al} + \gamma.$$

The gamma energy is 1.1 keV. The gamma will interact with lattice electrons. What is the most probable event? For this event, what is the maximum energy transferred? Does the resultant electron have enough energy to displace an aluminum atom (assume the displacement energy is 25 eV). Can the recoil Al atom displace another aluminum atom?

2.6 The (n, γ) reaction in ^{56}Fe releases a prompt gamma ray of energy $E\gamma = 7$ MeV.

(a) What is the recoil energy of the ^{57}Fe product nucleus?

(b) Determine the number of displaced atoms per ^{57}Fe recoil assuming $E_{\text{d}} = 40$ eV.

(c) If the thermal component of the neutron flux in a fast reactor is 10^{13} n/cm^2 s, what is the damage production rate due to the (n, γ) reaction in ^{56}Fe?

(d) If the fast flux is given by $\phi_f(E_n) = 10^{15}\delta(E_n - 0.5)$, where E_n is in MeV, what is the damage production rate due to the fast flux in iron?

Use the K–P displacement formula in (c) and (d). The scattering cross section for 0.5 MeV neutrons is 3 barns. Also, $\sigma_a^{56} \sim 2.5$ barns for part (c).

2.7 Assuming that atom–atom interactions can be treated as near head-on collisions, the appropriate potential function is then the Born–Mayer potential. Write an expression for the threshold energy for unassisted critical focusing along the [110] direction in fcc nickel in terms of the lattice constant, a.

2.8 For iron (equilibrium phase for 400°C), assuming a focusing collision occurs, how much does the closest approach (the allowed equivalent hard sphere radius calculated using a Born–Mayer potential) change between a [100] collision chain and a [110] collision chain?

2.9 (a) Calculate the focusing energy of the $\langle 111 \rangle$ direction for gold under the condition of assisted focusing.

(b) Will focusing occur along the $\langle 111 \rangle$ direction in the absence of assisted focusing? Why?

(c) The experimental focusing energy of gold is 21,000 eV for the $\langle 111 \rangle$ direction. Compare your answer with this value.

2.10 (a) Determine the critical focusing energy for the $\langle 111 \rangle$, $\langle 110 \rangle$, and $\langle 100 \rangle$ directions in fcc copper and iron.

(b) Plot θ_c as a function of $T < E_c$ for the $\langle 111 \rangle$ directions in Ni and Fe. Comment on similarities and differences.

(c) Do the same for the $\langle 110 \rangle$ direction of each.

(d) Repeat parts (a) and (b) using the inverse square potential, $V(r) = A/r^2$, where $A = 1.25$ eV nm^2.

(e) Over what energy range does focused replacement occur? How about focused energy packets only?

2.11 For the focusing process as described in Problem 2.10, give a physical explanation of why the critical angle for focusing, θ_c, should depend on the projectile energy.

2.12 A 30 keV ion enters a channel in the solid lattice and loses energy only by electronic excitation. Using the Lindhard stopping power formula Eq. (1.191), determine the distance traveled by the ion before it is dechanneled. The minimum channeling energy is 300 eV. Use $k = 3.0NZ^{2/3}$ eV$^{1/2}$/nm, where N is the atomic density of the metal in nm^{-3}.

2.13 Show that when channeling is accounted for in the collision cascade, the average number of displaced atoms $\nu(T)$ is as follows:

$$\nu(T) = (T/2E_d)^{1-2p},$$

where p is the probability that an atom with energy, E being channeled is lost to the cascade. Assume that $p \neq f(E)$, $T \gg E_d$, and $p \ll 1$.

Assuming that all energy is lost by elastic collisions for 100 keV protons in nickel determine:

(a) The energy loss per unit length in the solid, dE/dx
(b) The range in the solid.

2.14 A crystal of copper is bombarded with monoenergetic (2 MeV) neutrons.

(a) Calculate the mean atomic displacement rate (displacements/cm^{3}s) using the simple Kinchin–Pease model and the following data:

Lattice parameter, Cu = 0 361 nm
Atomic weight of Cu = 63.54 amu
Displacement energy for Cu = 40 eV
$\phi = 10^{13}$ n/cm^{2}s (2 MeV)
$\sigma_s = 0.5 \times 10^{-24}$ cm^2 (2 MeV)

(b) Repeat part (a) but instead of 2 MeV neutrons, use a monoenergetic thermal neutron beam with the same value of flux, $\sigma_{th} = 3.78 \times 10^{-24}$ cm^2 and the recoil energy ~ 382 eV.
(c) What would be the effect on your answer to part (a) by including Lindhard's damage energy function $\xi(T)$?
(d) How would your answer in part (a) be affected by assuming that the channeling probability is 1, 5, 10 %?

2.15 For the 2 MeV neutron bombardment problem described in Problem 2.14, how would you go about calculating the threshold energy for unassisted critical focusing along the [110] direction?

2.16 Assume that the copper target in Problem 2.14 was bombarded by a beam of 2 MeV He ions instead of a beam of 2 MeV neutrons. Calculate the displacement rate at the surface of the sample and compare to your result for Problem 2.14.

2.17 The same copper sample as in Problem 2.14 is bombarded with 500 keV Cu^+ ions at a flux of 10^{15} cm^{-2} s^{-1}. Calculate:

(a) The displacement rate at the surface
(b) The location of the damage peak.

References

1. Kinchin GH, Pease RS (1955) Rep Prog Phys 18:1
2. Seitz F (1949) Disc Faraday Soc 5:271
3. Bacon DJ, Deng HF, Gao F (1993) J Nucl Mater 205:84
4. King WE, Merkle KL, Meshii M (1983) J Nucl Mater 117:12–25
5. Olander DR (1976) Fundamental aspects of nuclear reactor fuel elements. US DOE, Washington, DC
6. ASTM E521 (1996) Standard practice for neutron radiation damage simulation by charged-particle irradiation. Annual Book of ASTM Standards, vol 12.02. American Society for Testing and Materials, Philadelphia

7. Robinson MT (1969) Defects and radiation damage in metals. Cambridge University Press, Cambridge
8. Snyder WS, Neufeld J (1955) Phys Rev 97(6):1636
9. Sanders JB (1967) Dissertation, University of Leiden
10. Kohler W, Schilling W (1965) Nukleonik 7:389
11. Sigmund P (1969) Appl Phys Lett 14(3):114
12. Lindhard J, Nielsen V, Scharff M (1968) Kgl Dan Vidnsk Selsk Mat Fyf Medd 36(10)
13. Sigmund P (1969) Rad Eff 1:15–18
14. Erginsoy C, Vineyard GH, Englert A (1964) Phys Rev 133A:595
15. Lindhard J, Nielsen V, Scharff M, Thomsen PV (1963) Dan Vidnsk Selsk Mat Fyf Medd 33:1
16. Robinson MT (1972) The dependence of radiation effects on the primary recoil energy. In: Corbett JW, Ianiello LC (eds) Proceedings of radiation-induced in metals, CONF-710601, USAEC Technical Information Center, Oak Ridge, TN, 1972, p 397
17. Norgett MJ, Robinson MT, Torrens IM (1975) Nucl Eng Des 33:50–54
18. Chadderton LT (1965) Radiation damage in crystals. Wiley, New York
19. Brandt W (1968) Sci Am 218:90
20. Datz S, Noggle TS, Moak CT (1965) Nucl Instr Meth 38:221
21. Doran DG (1971) Displacement cross sections for stainless steel and tantalum based on a lindhard model, USAEC Report, HEDL-TME-71-42. WADCO Corporation, Hanford Engineering Development Laboratory, Hanford
22. Robinson MT (1996) J Nucl Mater 216:1–28
23. Simmons RL, McElroy WN, Blackburn LD (1972) Nucl Technol 16:14
24. McElroy WN, Dahl RE, Gilbert ER (1970) Nucl Eng Des 14:319
25. Kulcinski GL, Brimhall JL, Kissinger HE (1972) Production of voids in pure metals by high-energy heavy-ion bombardment. In: Corbett JW, Ianiello LC (eds) Proceedings of radiation-induced voids in metals, CONF-710601, USAEC Technical Information Center, Oak Ridge, p 453

Chapter 3
The Damage Cascade

3.1 Displacement Mean Free Path

In our discussion of cascade development, no consideration was given to the spatial arrangement of displaced atoms. We assumed that every Frenkel pair created was preserved and that no annihilation occurred. However, the spatial arrangement of these Frenkel pairs is crucial in determining the number that survive annihilation or immobilization by clustering. In order to understand what the damaged region looks like, we need to know whether the displacements are concentrated or distributed. A helpful tool in this regard is the mean free path for displacement collisions, i.e., collisions in which the energy transferred is greater than E_d. This will tell us how far apart the displacements occur and hence the separation distance between Frenkel pairs.

By definition, the mean free path $\lambda = \frac{1}{N\sigma}$ and the corresponding displacement cross section are:

$$\sigma_d'(E) = \int_{E_d}^{E} \sigma(E,T)\,dT. \tag{3.1}$$

This is the cross section for the transfer of energy in excess of E_d and is given in terms of the differential energy transfer cross section between lattice atoms. Note that σ_d' has nothing to do with the projectile, be it a neutron or an ion, or the source of the damage in general. Using the equivalent hard sphere model to evaluate σ_d' gives:

Additional material to this chapter can be downloaded from http://rmsbook2ed.engin.umich.edu/movies/

G.S. Was, *Fundamentals of Radiation Materials Science*,
DOI 10.1007/978-1-4939-3438-6_3

$$\sigma(E,T) = \frac{\sigma(E)}{\gamma E},$$

but $\gamma = 1$, so substituting into Eq. (3.1) and integrating yields:

$$\sigma'_{\mathrm{d}}(E) = \int_{E_{\mathrm{d}}}^{E} \frac{\sigma(E)}{E}\mathrm{d}T = \sigma(E)\left(1 - \frac{E_{\mathrm{d}}}{E}\right), \tag{3.2}$$

where $\sigma(E) = 4\pi r^2$ is the total collision cross section between lattice atoms, so:

$$\sigma'_{\mathrm{d}}(E) = 4\pi r^2\left(1 - \frac{E_{\mathrm{d}}}{E}\right), \tag{3.3}$$

and r is the energy-dependent, equivalent hard sphere radius, which, using the Born–Mayer potential, gives:

$$\sigma'_{\mathrm{d}}(E) = \pi B^2\left[\ln\left(\frac{2A}{E}\right)\right]^2\left(1 - \frac{E_{\mathrm{d}}}{E}\right), \tag{3.4}$$

and the mean free path, λ, becomes

$$\lambda = \frac{1}{N\pi B^2\left[\ln\left(\frac{2A}{E}\right)\right]^2\left(1 - \frac{E_{\mathrm{d}}}{E}\right)}. \tag{3.5}$$

The mean free path and the total collision cross section are plotted in Fig. 3.1 for copper atoms in copper and show that as the energy of the moving atom drops, the cross section increases slowly, but the mean free path becomes very small at energies just above E_{d}. Note that the critical region ($\lambda \sim 0.2$ nm), or the region in

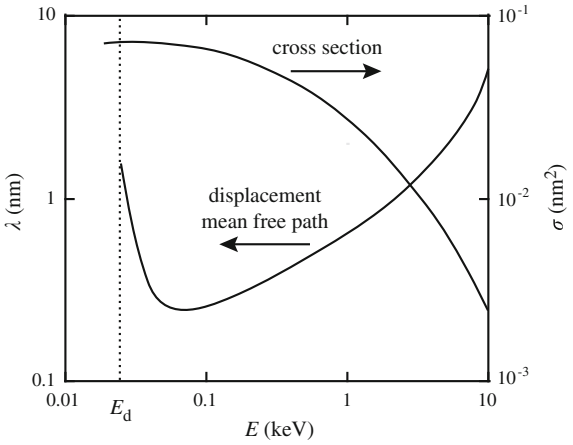

Fig. 3.1 Displacement mean free path and total collision cross section for copper atoms moving in copper (after [1])

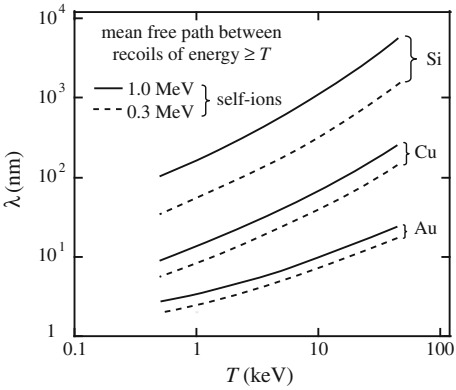

Fig. 3.2 Mean free paths of primary recoil atoms of 300 keV and 1 MeV, and self-ion irradiations of Si, Cu, and Au (after [2])

which every lattice atom in the path of the knock-on is displaced, lies in the energy range $\sim$50–100 eV.

The mean free paths for primary recoil atoms of 300 keV and 1 MeV resulting from self-ion irradiations of Si, Cu, and Au are shown in Fig. 3.2. Recall that $\bar{T} = \frac{\gamma E_\mathrm{i}}{2} \cong \frac{2E_\mathrm{i}}{A}$ (for n-Cu interactions), where E_i is the neutron energy and A is the atomic mass. Typically, $E_\mathrm{i} \sim 0.5$ MeV (for a thermal or fast reactor) and $A \sim 60$ (stainless steel), giving $\bar{T} \sim 15$ keV. So at large recoil energies, the displacements are well separated ($\sim$100 nm at 15 keV), but as the recoil energy decreases, the spacing approaches the atomic spacing, at which point each atom along the recoil path is displaced.

3.2 Primary Recoil Spectrum

The analysis of displacement mean free path gives us a first glimpse of what the spatial distribution of defects might look like. Brinkman [3] was the first to picture the cascade as a *displacement spike* with a high core density of vacancies surrounded by an interstitial shell (Fig. 3.3). Seeger [4] modified the picture to account for crystallinity such as focused energy packets (focusons), and long-range transport of mass by replacement collisions and channeling, and termed the vacancy core the *depleted zone* (Fig. 3.4).

Two additional quantities are helpful in developing a picture of the distribution of damage energy. The first is the deposited energy depth distribution, $F_\mathrm{D}(x)$, defined by:

$$F_\mathrm{D}(x)\,\mathrm{d}x = \mathrm{d}E = NS_n E(x)\,\mathrm{d}x. \tag{3.6}$$

Using the nuclear stopping power and range given by the power law potential [5] results in a simple form for $F_\mathrm{D}(x)$:

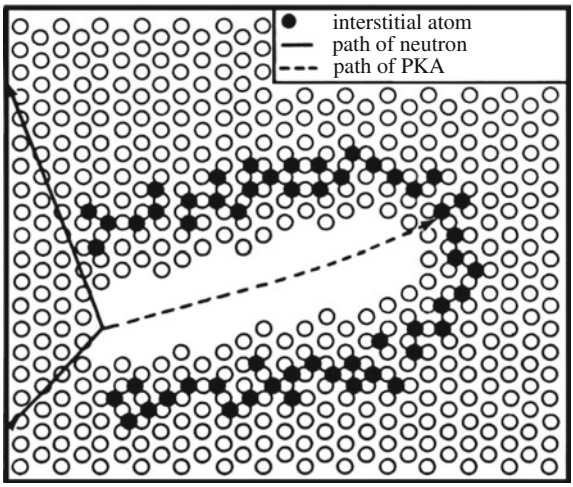

Fig. 3.3 Original version of the displacement spike as drawn by Brinkman (after [3])

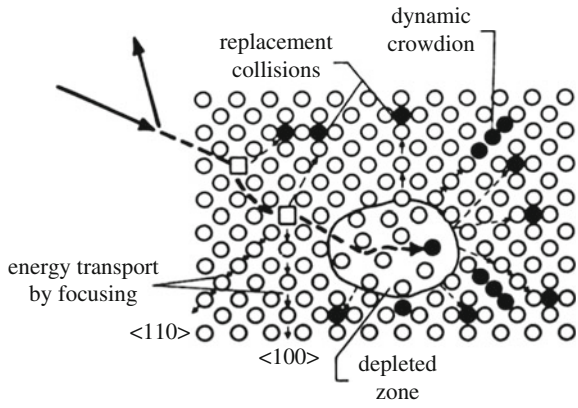

Fig. 3.4 Revised version of Brinkman's displacement spike as drawn by Seger (after [4]) accounting for crystallinity in the damage cascade

$$F_{\mathrm{D}}(x) = \frac{T}{2mR}(1 - x/R)^{\frac{1}{2m}-1}, \tag{3.7}$$

where T is the PKA energy, R is the PKA range, and $m = 1/s$ where s is the power law exponent. If $N_{\mathrm{d}}(x)$ is the number of displacements per unit depth at a depth x, then using the modified K–P model or the NRT model (e.g., Eq. 2.50) with $\kappa = 0.8$ and with $F_{\mathrm{D}}(x)$ replacing E_{D}, we can write that:

$$\frac{N_{\mathrm{d}}(x)}{\phi} = \frac{0.8F_{\mathrm{D}}(x)}{2E_{\mathrm{d}}}, \tag{3.8}$$

and the displacement rate as a function of depth in units of dpa becomes:

$$\text{dpa}(x) = \frac{N_\text{d}(x)}{N} = \frac{0.4F_\text{D}(x)}{NE_\text{d}}\phi. \tag{3.9}$$

The *total* dpa produced over the range of the recoil can be estimated by replacing $F_\text{D}(x)$ with the damage energy E_D from Eq. (2.51) over the range of the recoil, R:

$$\text{dpa} \cong \frac{\phi 0.4E_\text{D}}{NRE_\text{d}}. \tag{3.10}$$

The second important concept is the primary recoil spectrum. The density of recoil atoms with energies between T and $T + \text{d}T$ created during irradiation is an important quantity in radiation damage. The recoil density depends on the projectile energy and mass and gives a measure of the density of displacement damage in the target. The density of recoils as a function of recoil energy is known as the primary recoil spectrum and is given as:

$$P(E_\text{i}, T) = \frac{1}{N}\int_{E_\text{d}}^{T} \sigma(E_\text{i}, T')\,\text{d}T', \tag{3.11}$$

which is the fractional number of recoils between the minimum displacement energy E_d and energy T, N is the total number of primary recoils, and $\sigma(E_\text{i}, T)$ is the energy transfer cross section for a particle of energy E_i to create a recoil of energy T. The fraction of recoils is shown in Fig. 3.5 for 1-MeV projectiles of various mass incident on a copper target. Note that while higher-mass projectiles produce more recoils at higher energy, the difference does not appear to be large.

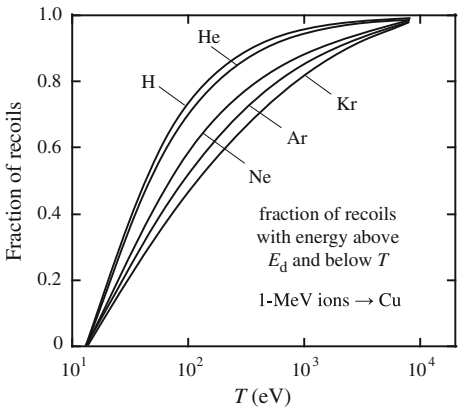

Fig. 3.5 Integral primary recoil spectra for 1 MeV particles in copper. Curves plotted are the integral fractions of primary recoils between the threshold energy and energy, T, from Eq. (3.11) (after [2])

For defect production, it is not the number of recoils of a particular energy that is of greatest importance; rather, it is the number of recoils weighted by the damage energy produced in each recoil that is most important. This quantity is determined by "weighting" the recoil spectra by the number of defects or the damage energy produced in each recoil:

$$W(E_\mathrm{i}, T) = \frac{1}{E_\mathrm{D}(E_\mathrm{i})} \int_{E_\mathrm{d}}^{T} \sigma(E_\mathrm{i}, T') E_\mathrm{D}(T')\, \mathrm{d}T', \tag{3.12}$$

where $E_\mathrm{D}(T)$ is the damage energy created by a recoil of energy T:

$$E_\mathrm{D}(E_\mathrm{i}) = \int_{E_\mathrm{d}}^{\hat{T}} \sigma(E_i, T') E_\mathrm{D}(T')\, \mathrm{d}T', \tag{3.13}$$

and $\hat{T} = \gamma E_\mathrm{i}$.

For the extremes of Coulomb and hard sphere interactions, the differential energy transfer cross sections are:

$$\sigma_\mathrm{Coul}(E_\mathrm{i}, T) = \frac{\pi M_1 (Z_1 Z_2 \varepsilon^2)^2}{E_\mathrm{i} T^2}, \tag{3.14}$$

and

$$\sigma_\mathrm{HS}(E_\mathrm{i}, T) = \frac{A}{E_\mathrm{i}}. \tag{3.15}$$

Ignoring electron excitations and allowing $E_\mathrm{D}(T) = T$ and substituting Eqs. (3.14) and (3.15) into Eq. (3.12) gives the weighted average recoil spectra for each type of interaction:

$$W_\mathrm{Coul}(T) = \frac{\ln T - \ln \check{T}}{\ln \hat{T} - \ln \check{T}}, \tag{3.16}$$

and

$$W_\mathrm{HS}(T) = \frac{T^2 - \check{T}^2}{\hat{T}^2}, \tag{3.17}$$

where $\check{T} = E_\mathrm{d}$. Equations (3.16) and (3.17) are graphed in Fig. 3.6 for 1 MeV particle irradiations of copper. The Coulomb potential is a good approximation for

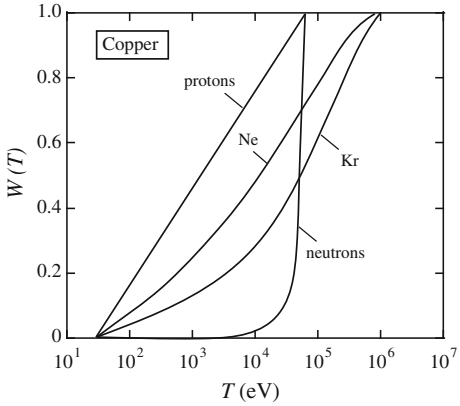

Fig. 3.6 Weighted recoil spectra for 1 MeV particles in copper (after [2]). Curves representing protons and neutrons are calculated using Eqs. (3.14) and (3.15), respectively. $W(T)$ for other particles were calculated using Lindhard cross sections and include electronic excitation

proton irradiation, while the hard sphere potential is a good approximation for neutron irradiation. The Coulomb forces extend to infinity and slowly increase as the particle approaches the target. In a hard sphere interaction, the particles and target do not "feel" each other until their separation reaches the hard sphere radius at which point the repulsive force goes to infinity. A screened Coulomb is most appropriate for heavy ion irradiation. The result is that Coulomb interactions tend to create many PKAs with low energy, while hard sphere collisions create fewer PKAs but with higher energy. Note the large difference in $W(T)$ between the various types of irradiations in Fig. 3.6. While heavy ions come closer to reproducing the energy distribution of recoils of neutrons than do light ions, neither is accurate in the "tails" of the distribution. This does not mean that ions are poor simulations of radiation damage, but it does mean that damage is produced differently and that this needs to be considered when assessing the microchemical and microstructural changes due to irradiation.

Figure 3.7 illustrates the difference in the types of damage that is produced by different types of particles. Light ions such as electrons and protons will produce damage as isolated Frenkel pairs or in small clusters, while heavy ions and neutrons produce damage in large clusters. For 1 MeV particle irradiation of nickel, half the recoils for protons are produced with energies less than ~1 keV but with an average energy of 60 eV, while the same number for Kr occurs at about 30 keV with an average energy of 5 keV. Recoils are weighted toward lower energies because of the screened Coulomb potential that controls the interactions of charged particles. For an unscreened Coulomb interaction, the probability of creating a recoil of energy T varies as $1/T^2$. Because neutrons interact as hard spheres, the probability of creating a recoil of energy T is independent of recoil energy.

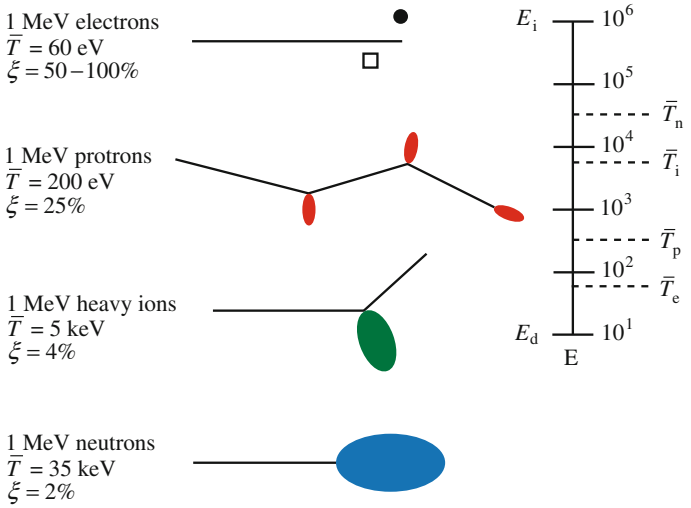

Fig. 3.7 Difference in damage morphology, displacement efficiency, and average recoil energy for 1 MeV particles of different types incident on nickel (after [6])

3.3 Cascade Damage Energy and Cascade Volume

The energy density in a cascade of volume V_{cas} formed by an energetic projectile of energy E_i is given by [7]:

$$\bar{\Theta}_D \cong \frac{E_D}{NV_{cas}}, \tag{3.18}$$

where E_D is the damage energy defined in Eq. (2.50) and N is the atom density of the target. To find the volume of the cascade requires knowledge of the depth distribution of the damage energy. Averback [2] showed that the volume of the cascade can be approximated by:

$$V_{cas} = \frac{4\pi}{3}\left((\delta\Delta X)^2 + 2(\delta Y)^2\right)^{3/2}, \tag{3.19}$$

where $(\Delta X)^2$ and Y^2 are the longitudinal and transverse moments of the deposited damage energy distribution for an individual cascade and δ is a contraction factor that accounts for the difference between an individual cascade and the average cascade determined by transport theory.

While Eqs. (3.18) and (3.19) provide a description of the spatial extent of a cascade, other characteristics of the cascade are the temperature and temporal lifetime. The effective temperature of the cascade can be estimated by the relation:

$$3k_B T_{max} = \bar{\Theta}_D, \tag{3.20}$$

where k_B is the Boltzmann's constant. The lifetime of the cascade or *thermal spike* can be estimated by solving the heat equation for the spread of energy from a point source in three dimensions. The variance in the temperature profile, R^2, is given by:

$$R^2 = 4D\tau, \tag{3.21}$$

where τ is the cascade lifetime and D is the thermal diffusivity = κ_T/C_p, where κ_T is the thermal conductivity and C_p is the specific heat capacity. The damage energy is then:

$$E_D = \frac{4}{3}\pi R^3 U_a N, \tag{3.22}$$

where U_a is the energy per atom. The cascade lifetime is determined by combining Eqs. (3.21) and (3.22) to solve for τ:

$$\tau = \frac{1}{4D}\left(\frac{3E_D}{4\pi N U_a}\right)^{2/3}. \tag{3.23}$$

If we estimate U_a from the melting temperature of the target, then $U_a \sim 0.3$ eV and $D \sim 10^{12}$ nm^2/s, and then the lifetime of a 1 keV cascade is of the order 10^{-12} s, or a few lattice vibration periods.

3.4 Computer Simulation of Radiation Damage

Analytical solutions to the space and time dependence of damage caused by an energetic particle incident on a target can take us only so far. And as we will see later, excellent instrumentation exists to observe defect clusters such as transmission electron microscopy, X-ray scattering, small-angle neutron scattering, and positron annihilation spectroscopy. But these instruments do not have the resolution to image individual defects and they cannot capture the temporal development of the cascade. To gain a better understanding of the spatial and temporal development of the cascade, we must turn to computer simulation. There are three principal techniques used to model the behavior of atoms in a displacement cascade; the binary collision approximation (BCA) method, the molecular dynamics (MD) method, and the kinetic Monte Carlo (KMC) method [8]. Each will be briefly discussed.

3.4.1 Binary Collision Approximation (BCA) Method

BCA simulations are useful for examining the collisional stages of high-energy cascades in statistically significant numbers. BCA simulations consider only the interactions between two colliding atoms at a time and in sequence [8]. The computation follows only the atoms having significant energies and is thus very efficient. The BCA approach provides a good approximation to the collision stage, since the neglected many-body interactions make little contribution to the atom trajectories at collision energies well above the atom displacement energy. At energies near or even less than the displacement energy, ballistic features of cascades such as replacement collision sequences and focused collision sequences (focusons) can be reasonably captured by BCA calculations. At primary recoil energies above approximately 20 keV, cascades may have more than one damage region. Because the mean free path between high-energy collisions of a recoil atom increases with energy, higher-energy cascades will consist of multiple damage regions or *subcascades* that are well separated in space due to high-energy collisions. Channeling of primary or high-energy secondary recoils also contributes to subcascade formation when the channeled recoils lose energy and dechannel.

There are two distinct types of BCA models. Those for crystalline targets are termed BC or binary crystal models and resemble MD models in that they assign all atoms to well-defined initial positions [9]. Models for materials without long-range order (amorphous solids) are termed MC or Monte Carlo models and use stochastic methods to locate target atoms and to determine collision parameters. The MC models are similar to transport theory models used in analytical theory to track neutron populations in a medium.

An example of a BC model is the MARLOWE code [10]. The program models crystalline targets with no restrictions on the crystal symmetry or on the chemical composition. All collision parameters are calculated from the particle positions. Several interatomic potentials are available for selection to describe atom collisions. Inelastic energy losses may be included in either local or non-local form, but the losses are limited to the velocity-proportional ($E^{1/2}$) range of kinetic energies. Figure 3.8 shows the spatial configuration of defects from an early computer simulation using the MARLOWE code for the case of a 200 keV cascade in copper. This is a very energetic cascade that would only be expected from extremely energetic neutrons such as are generated in a fusion reactor. The PKA is generated in the lower right-hand corner (arrow) and proceeds to the left with a kinetic energy of 200 keV. The dark spheres are displaced atoms, and the lighter spheres are vacant lattice sites. Note that the full cascade consists of several subcascades.

A second example, given in Fig. 3.9, shows how the cascade can become extended in space. The recoil trajectories and final configuration of interstitials and vacancies in bcc iron are shown after interaction with a 5 keV PKA at a temperature of 0 K [11]. All vacancies and interstitials within a sphere containing 30 lattice atom sites were assumed to recombine spontaneously. Note in Fig. 3.9(a) that the secondary knock-on in the center of the spike undergoes channeling, making possible the

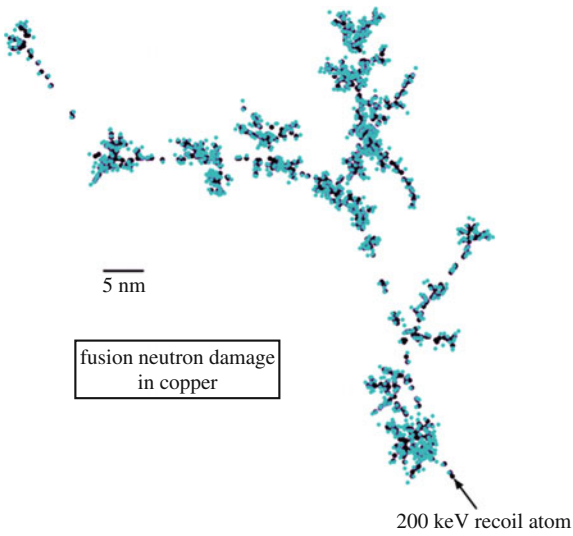

Fig. 3.8 Collisional stage of a 200 keV cascade in copper simulated using the binary collision approximation in MARLOWE (after [8])

extension of the cascade into the upper right half of the lattice shown in Fig. 3.9(b). Essentially, all of the damage to the upper right of the diagonal is due to channeling of the secondary knock-on.

SRIM [12] (previously called TRIM) is another BCA code that uses Monte Carlo techniques to describe the trajectory of the incident particle and the damage created by that particle in amorphous solids and was discussed briefly in Chap. 1. SRIM uses a maximum impact parameter set by the density of the medium and a constant mean free path between collisions which is related to this. Stochastic methods are used to select the impact parameter for each collision and to determine the scattering plane. The barycentric scattering angle is determined by a "magic" formula, tested against published integral tables, and represents the scattering from the ZBL "universal" potential. Inelastic energy losses are based on the effective charge formalism, using tables distributed with the code. Figure 3.10 shows a simulation of 3 MeV protons incident on a nickel target. Figure 3.10(a) shows the trajectories of the incident particles for 10,000 cases (MC runs), and Fig. 3.10(b) shows the ion concentration profile and the displacement rate profile as a function of depth.

3.4.2 Molecular Dynamics (MD) Method

Molecular dynamics (MD) is the second major type of methodology used to describe collision cascades. MD is an atomistic modeling and simulation method in which the particles are the atoms that constitute the material of interest [13]. The underlying assumption is that one can treat the ions and electrons as a single,

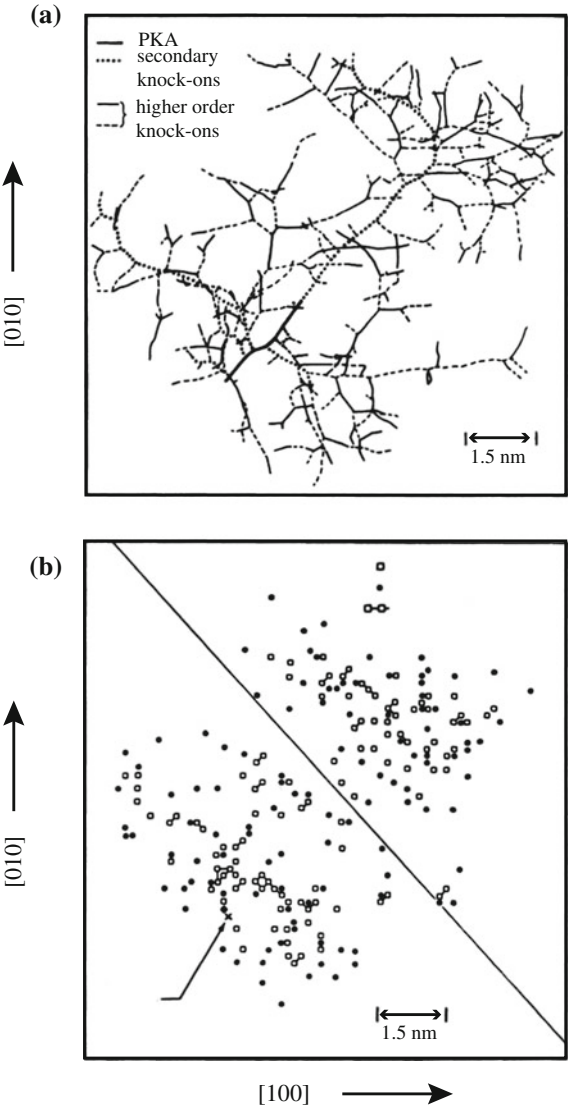

Fig. 3.9 Computer simulation of a displacement spike due to a 5 keV PKA in iron. All out-of-plane damage has been projected onto the (001) plane shown in the figure. (**a**) Recoil trajectories and (**b**) vacancies and interstitial atoms at the end of the collision cascade (0 K). The *diagonal line* in (**b**) shows the effect of channeling of a secondary knock-on atom (after [11])

classical entity. Thus, atoms behave according to the principles of classical mechanics as formulated by Newton and Hamilton. In the simplest physical terms, MD may be characterized as a method of "particle tracking." Operationally, it is a method for generating the trajectories of a system of N particles by direct numerical integration of Newton's equations of motion, with appropriate specification of an interatomic potential and suitable initial and boundary conditions.

Using realistic interatomic potentials and appropriate boundary conditions, the fate of all atoms in a volume containing the cascade can be described through the

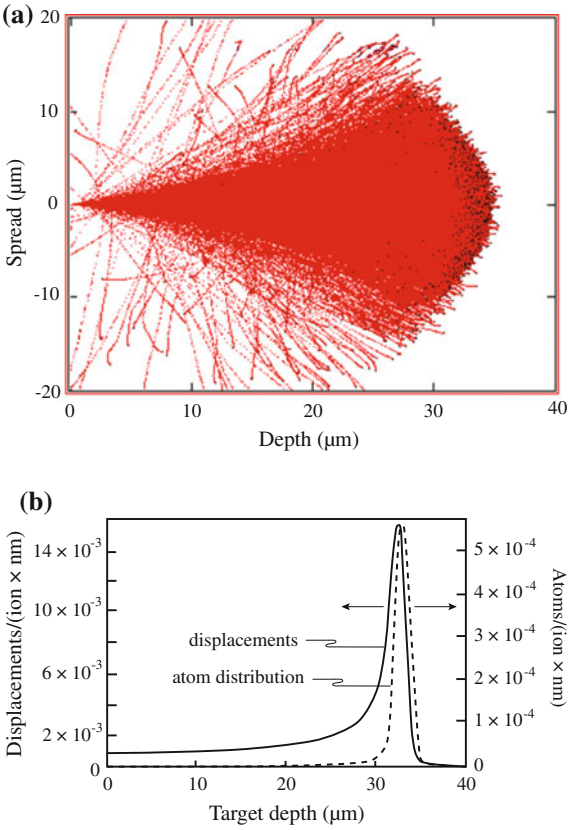

Fig. 3.10 A 3 MeV proton incident on nickel as modeled by the SRIM code: (**a**) trajectory and (**b**) concentration profile and displacement profile

various stages of cascade development. The analytical interatomic potential functions must describe the force on an atom as a function of the distance between it and the other atoms in the system. The results are physically as meaningful as the potential V that is used. It must account for both attractive and repulsive forces in order to obtain stable lattice configurations. When this interatomic potential has been derived, the total energy of the system of atoms being simulated can be calculated by summing over all the atoms. The forces on the atoms are obtained from the gradient of the interatomic potential and are used to calculate acceleration according to $F = ma$, yielding the equations of motions for the atoms, which can be solved by numerical integration using a suitably small time step. The computer code solves these equations numerically over very small time steps and then recalculates the forces at the end of the time step, to be applied in the calculations in the next time step. The process is repeated until the desired state is achieved. A typical flowchart for an MD code would look something like Fig. 3.11. Among these steps, the part that is the most computationally demanding is the force calculation. The efficiency of an MD simulation therefore depends on performing the force calculation as simply as possible without compromising the physical

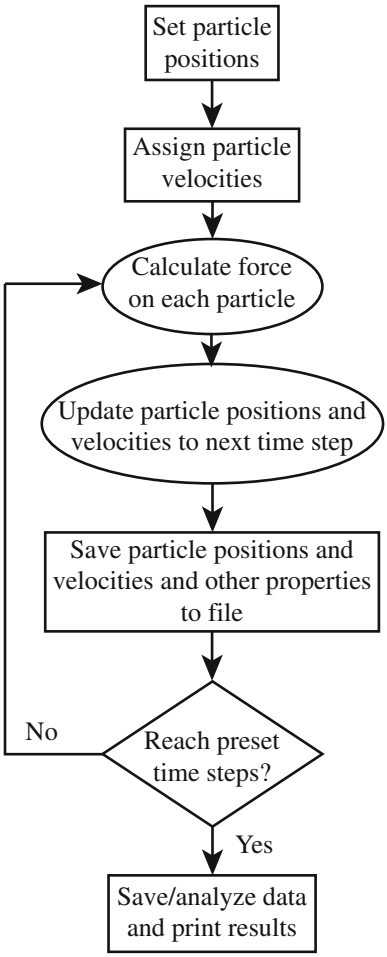

Fig. 3.11 Flowchart of MD simulation (from [13])

description (simulation fidelity). Since the force is calculated by taking the gradient of the potential V, the specification of V essentially determines the compromise between physical fidelity and computational efficiency [13].

Time steps in MD simulation must be very small ($5–10 \times 10^{-15}$s, or 5–10 fs), so MD simulations are generally run for no more than 100 ps. With periodic boundary conditions, the size of the simulation cell needs to be large enough to prevent the cascade from interacting with periodic images of itself. Higher-energy events therefore require a larger number of atoms in the cell. As the initial primary kinetic energy E increases, larger and larger numerical crystallites are required to contain the event. While the size of the crystallite is roughly proportional to E, the required computing time scales roughly as E^2. The demand on computing time limits the statistical capabilities of MD simulation. However, it provides a detailed view of the

spatial extent of the damage process on an atomic level that is not afforded by other techniques.

A cascade simulation begins by thermally equilibrating a block of atoms that constitutes the system to be studied. This process allows the determination of the lattice vibrations for the simulated temperature and typically requires a simulation time of approximately 10 ps. Next, the cascade simulation is initiated by giving one of the atoms a specified amount of kinetic energy and an initial direction. Several cascades must be run in order to generate enough results that can be used to represent the average behavior of the system at any energy and temperature. Statistical variability can be introduced by either further equilibration of the starting block, choosing a different PKA or PKA direction, or some combination of these. The number of simulations required at any one condition to obtain a good statistical description of defect production is not large. Typically, only about 8–10 simulations are required to obtain a small standard error about the mean number of defects produced.

One such code used for MD simulations is the MOLDY code written by Finnis that uses interatomic potentials developed by Finnis and Sinclair [14] and was later modified by Calder and Bacon for cascade simulations [15]. The code only describes elastic collisions between atoms and does not account for energy loss mechanisms such as electronic excitation and ionization. The energy given to the PKA in the MD simulation (cascade energy, E_{MD}) is that corresponding to the value of the damage energy E_D, given in Eq. (2.50). The corresponding values for T and ν_{NRT} for iron and the ratio of the damage energy to the PKA energy are listed in Table 3.1 along with the neutron energy that would yield T as the average recoil

Table 3.1 Typical atomic displacement cascade parameters in iron (from [16])

Neutron energy, E_i (MeV)	Average PKA energy, T (keV)[a]	Corresponding damage energy, E_d (keV)[b] $\sim E_{MD}$	NRT displacements	Ratio: E_d/E_{MD}	Simulation cell size (atoms)
0.00335	0.116	0.1	1	0.8634	3456
0.00682	0.236	0.2	2	0.8487	6750
0.0175	0.605	0.4	5	0.8269	
0.0358	1.24	1.0	10	0.8085	54,000
0.0734	2.54	2.0	20	0.7881	
0.191	6.60	5.0	50	0.7570	128,000
0.397	13.7	10.0	100	0.7292	250,000
0.832	28.8	20.0	200	0.6954	~0.5 M
2.28	78.7	50.0	500	0.6354	~2.5 M
5.09	175.8	100.0	1000	0.5690	~5–10 M
12.3	425.5	200.0	2000	0.4700	~10–20 M
14.1[c]	487.3	220.4	2204	0.4523	

[a]Average iron recoil energy from an elastic collision with a neutron of specified energy
[b]Damage energy defined in Eq. (2.50)
[c]Relevant to D–T fusion energy production

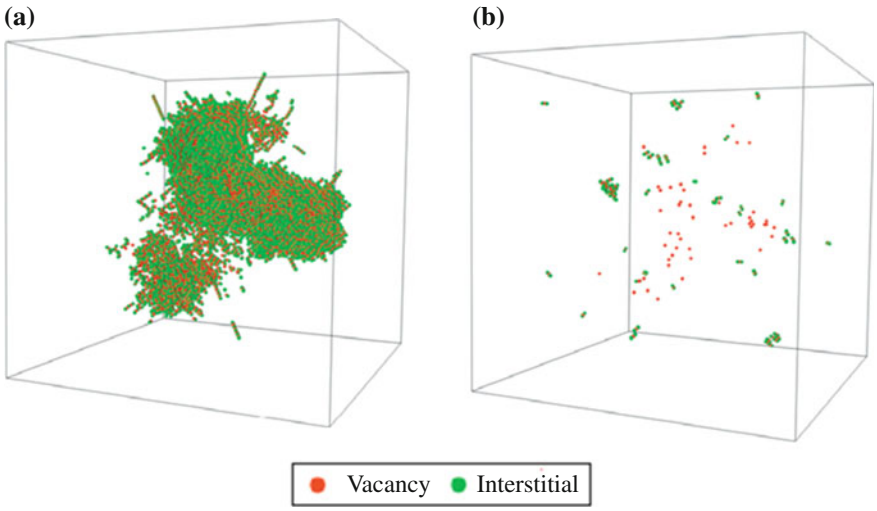

Fig. 3.12 Structure of a typical 20 keV cascade in iron at 100 K; (**a**) at peak damage state (0.48 ps) and (**b**) the final defect configuration (15 ps) (from Ref. [16])

energy in iron. Note that with increasing energy, the difference between the damage energy, E_D, and the PKA energy, T, increases. In reality, energetic atoms lose energy continuously by a combination of electronic and nuclear reactions, and the typical MD simulation effectively removes the electronic component at time zero.

Figure 3.12 shows typical point defect configurations from a 20 keV MD cascade simulation in iron at 100 K. Figure 3.12(a) shows the cascade at the point of peak disorder, and Fig. 3.12(b) shows the cascade following in-cascade recombination. Note the sizable reduction in the residual damage between 0.48 ps and 15 ps. This result shows that the actual damage resulting from the PKA is much less than the total aggregate number of displacements calculated from the K–P or NRT models. While "still" images of the stages of the cascade are useful in understanding how the cascade develops, a much better tool is to view the temporal evolution of the cascade directly. This can be done by viewing Movie 3.1 via the Web site at (http://rmsbook2ed.engin.umich.edu/movies/). This MD simulation shows the development of a cascade from a 20 keV recoil in iron at 100 K through to cascade quench at $\sim$5 ps. Note the striking difference in the defect density between the peak ballistic stage ($\sim$1 ps) and the end of the quench at $\sim$ 5 ps.

3.4.3 Kinetic Monte Carlo (KMC) Method

Our objective is to simulate the dynamical evolution of systems of atoms during and immediately following the displacement event. The most robust tool in this class of atomistic simulation methods is molecular dynamics. Integrating the classical

equations of motion forward in time, the behavior of the system emerges naturally, requiring no intuition or further input from the user. A serious limitation, however, is that accurate integration requires time steps short enough ($\sim 10^{-15}$ s) to resolve the atomic vibrations. Consequently, the total simulation time is typically limited to less than one nanosecond, while processes we wish to study (e.g., diffusion and annihilation of defects after a cascade event or evolution of the void dislocation microstructures) often take place on much longer timescales, up to many years. This is the "timescale problem."

Kinetic Monte Carlo attempts to overcome this limitation by exploiting the fact that the long-time dynamics of a system typically consist of diffusive jumps from state to state. Rather than following the trajectory through every vibrational period, these state-to-state transitions are treated directly. The KMC methods used in radiation damage studies represent a subset of Monte Carlo (MC) methods that provide a solution to the Master Equation which describes a physical system whose evolution is governed by a known set of transition rates between possible states [17]. The main ingredients of KMC models are a set of objects (point defects, point defect clusters, solutes, and impurities) and a set of reactions or (rules) that describe the manner in which these objects undergo diffusion, emission, and reaction, and their rates of occurrence. The solution proceeds by choosing randomly among the various possible transitions and accepting them on the basis of probabilities determined from the corresponding transition rates. The probabilities are calculated for physical transition mechanisms as Boltzmann factor frequencies, and the events take place according to their probabilities leading to an evolution of the microstructure.

Given a set of rate constants connecting states of a system, KMC offers a way to propagate dynamically correct trajectories through the state space. The basic steps in a KMC simulation can be summarized as follows:

1. Calculate the probability (rate) for a given event to occur.
2. Sum the probabilities of all events to obtain a cumulative distribution function.
3. Generate a random number to select an event from all possible events.
4. Increase the simulation time on the basis of the inverse sum of the rates of all possible events.
5. Perform the selected event and all spontaneous events as a result of the event performed.
6. Repeat Steps 1–4 until the desired simulation condition is reached.

Advantages of KMC models include the ability to capture spatial correlations in a full 3D simulation with atomic resolution, while ignoring the atomic vibration timescales captured by MD models. In KMC, individual point defects, point defect clusters, solutes, and impurities are treated as objects, either on or off an underlying crystallographic lattice, and the evolution of these objects is modeled over time. Two general approaches are object KMC (OKMC) and event KMC (EKMC) [18, 19], which differ in the treatment of timescales or steps between individual events. OKMC can be further subdivided into techniques that explicitly treat atoms and atomic interactions, denoted as atomic KMC (AKMC), or those that track the

defects on a lattice, but without complete resolution of the atomic arrangement, or lattice KMC (LKMC). The later technique is predominately referred to as object Monte Carlo and is used in such codes as BIGMA [20] or LAKIMOCA [21].

KMC modeling of radiation damage involves tracking the location and fate of all defects, impurities, and solutes as a function of time to predict microstructure evolution. The starting point in these simulations is the primary damage state that is obtained from MD simulations along with the displacement or damage rate, which sets the timescale for defect introduction. The rates of all reaction–diffusion events then control the subsequent evolution or progression in time and are determined from appropriate activation energies for diffusion and dissociation. The reactions and rates of these reactions that occur between species are key inputs, which are assumed to be known. The defects execute random diffusion jumps (in one, two, or three dimensions depending on the nature of the defect) with a probability (rate) proportional to their diffusivity. Similarly, cluster dissociation rates are governed by a dissociation probability that is proportional to the binding energy of a particle to the cluster. In these simulations, the events which are considered to take place are thus diffusion, emission, irradiation, and possibly transmutation.

If the rate catalog is constructed properly, KMC dynamics can give the exact state-to-state evolution of the system, in the sense that it will be statistically indistinguishable from a long molecular dynamics simulation. KMC is the most powerful approach available for making dynamical predictions at the meso-scale without resorting to more dubious model assumptions. It can also be used to provide input to and/or verification for higher-level treatments such as rate theory models or finite-element simulations. Moreover, even in situations where a more accurate simulation would be feasible (e.g., using accelerated molecular dynamics or on-the-fly kinetic Monte Carlo), the extreme efficiency of KMC makes it ideal for rapid scans over different conditions, for example, and for model studies. The result is that KMC can reach vastly longer timescales, typically seconds and often well beyond.

An example of the capability of KMC to capture processes on a larger timescale is given in Movie 3.2 (http://rmsbook2ed.engin.umich.edu/movies/), which shows a KMC simulation of a 20 keV cascade in Fe–0.2Cu–0.6Si–0.7Ni–12.4Mn (similar to a pressure vessel steel) at 327 °C. The simulation shows the enrichment of Ni (green), Mn (black), Si (blue), and Cu (red) at cascade debris (vacancies in yellow) covering a time period out to several years, or many orders of magnitude longer than the cascade quench time. Note the pairing of Ni and Si and the accumulation of solute atoms at the vacancy clusters.

Atomic KMC is a variant of KMC that can be used to simulate the evolution of materials with complex microstructure at the atomic scale by modeling the elementary atomic mechanisms. It has been used extensively to study phase transformations such as precipitation, phase separation, and/or ordering [17]. Despite the fact that the algorithm is fairly simple, the method is most of the time non-trivial to implement in the case of realistic materials (as opposed to binary alloys for instance). The total potential energy of the system, that is, the construction of the cohesive model, is difficult to obtain when the chemistry of the system under study is complex and involves many species or a complex crystallographic structure.

Furthermore, the knowledge of all the possible events and the rates at which they occur is non-trivial. On rigid lattices, the migration paths are easier to determine and cluster expansion-type methods may be extended to determine the saddle point energies as a function of the local chemical environment. This can, however, take a very large amount of calculation time when there is a drastic difference in the local environment. Furthermore, complicated correlated motions cannot be modeled within the simple scheme usually followed in AKMC of jumps to 1nn neighbor sites. Another drawback is that the use of rigid lattices (to gain efficiency) can lead to an approximate (or even unrealistic) treatment of microstructure elements such as incoherent carbide precipitates, SIA clusters, or interstitial dislocation loops.

In OKMC, the evolution of individual objects is simulated on the basis of timescales that encompass individual atomic diffusive jumps, dominated by the very fast events. This method is not efficient at high temperatures and/or high doses. The difficulty is the inability to model sufficiently high doses necessary for macroscopic material behavior due to the focus on fast dynamics. At the moment, OKMC methods have been mostly used to investigate the annealing of the primary damage or the effect of temperature change on the damage accumulation. But they can also be used to study 3D versus 1D motion, mobility of the SIA clusters [22–25], or corroboration of theoretical assumptions such as the analytical description of the sink strength [26]. The time step between events is much longer in EKMC models, which require that a reaction (e.g., clustering among like defects, annihilation among opposite defects, cluster dissolution, or new cascade introduction) occurs within each Monte Carlo sweep. EKMC can therefore simulate much longer times and therefore evolution of materials over higher doses.

Taken together, the MD and KMC methods cover the radiation timescale as shown in Fig. 3.13. MD simulations are practical up to the ns range, and KMC simulations extend the range to the order of seconds. Much occurs after this

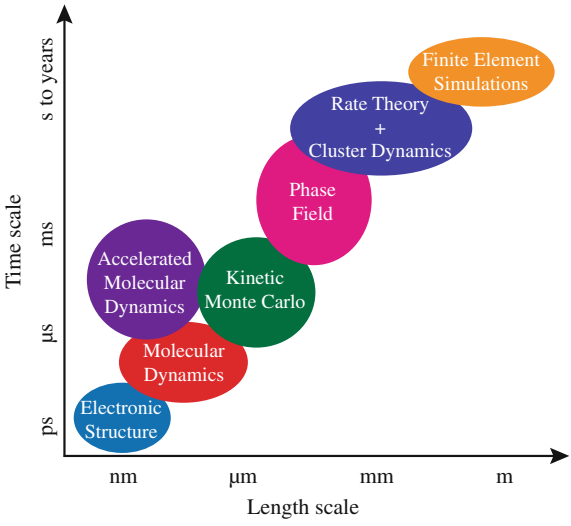

Fig. 3.13 Time and length scale for radiation damage evolution and the corresponding simulation methodologies (courtesy F. Gao)

timescale, and this is generally modeled using rate theory, which will be discussed in Chap. 5 and beyond.

3.5 Stages of Cascade Development

The final state of the cascade is extremely important because the end of the cascade is the starting point for defect diffusion, agglomeration, and destruction that forms the basis for the observable effects of irradiation to be covered in Part II of this text. Figure 3.14 shows another example in which a 2D cross section of a cascade is shown at times that correspond to the early stages of the cascade and near the final state. Here again, the damage state has relaxed to a very large degree between 2 ps

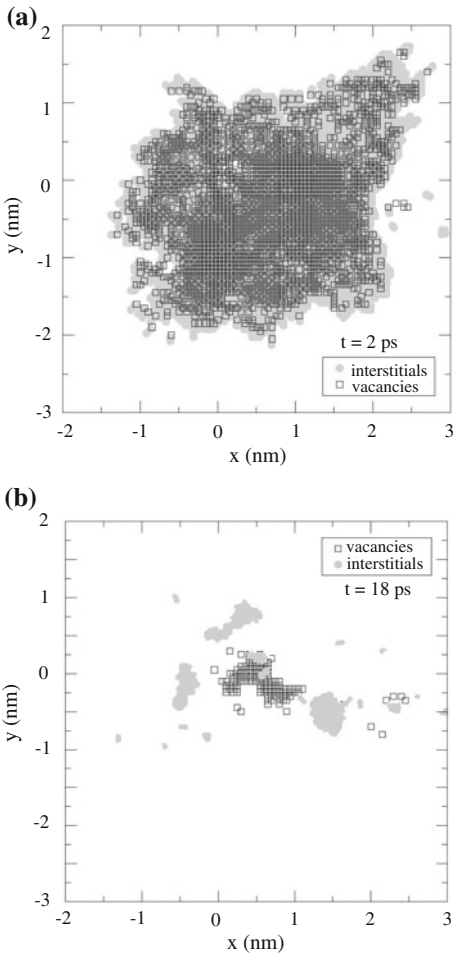

Fig. 3.14 MD simulation of a 30 keV displacement cascade in Cu at 300 K at (**a**) 2 ps and (**b**) 18 ps into the collision (calculations performed at the Barcelona Supercomputer Center, courtesy of M. Catula and Tomas Diaz de la Rubia)

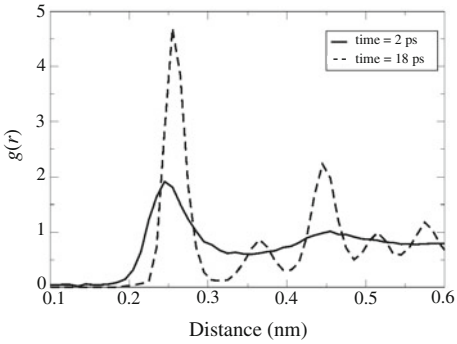

Fig. 3.15 Pair correlation function for the collision cascades in Fig. 3.14, showing the amorphous-like character of the displacement cascade zone at 2 ps and the considerable degree of recovery by 18 ps (calculations performed at the Barcelona Supercomputer Center, courtesy of M. Catula and Tomas Diaz de la Rubia)

(Fig. 3.14a) and 18 ps (Fig. 3.14b). Figure 3.15 shows the radial pair correlation function for the two times. The pair correlation function describes the separation of atoms and will appear as a series of spikes for crystalline solids (by virtue of their long-range order) and as a smoothly varying function for a liquid or amorphous solid (in which there is only nearest and second nearest neighbor correlation). As shown in the figure, the atom arrangement in the core of the displacement spike at short times is similar to that of a liquid, while the final arrangement is recovering its crystalline configuration. Figure 3.16 shows that the mean square atomic displacement of atoms in the cascade increases dramatically with time, indicating that the bulk of the aggregate movement of atoms in the displacement cascade occurs *after* the time to reach peak damage! Taken together, the results of Figs. 3.14–3.16

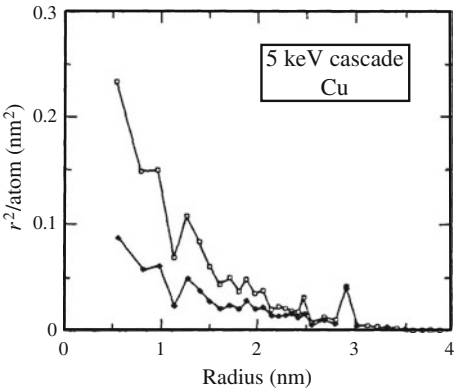

Fig. 3.16 Integrated diffusion coefficient as a function of distance from the center of the cascade at the end of the collisional phase, $t = 0.12$ ps (*bottom curve*), and at the end of the cooling phase, $t = 10$ ps (*top curve*), for a 5 keV cascade in copper (after [27])

tell us that damage is *annealing* out with time. This annealing is occurring as the energy of the cascade is dropping. In fact, annealing occurs at the tail end of the period during which the cascade energy drops, called the *quench* stage.

We now have a picture of how the cascade develops in time that we can describe. Cascades evolve in stages given as follows:

1. Collisional
2. Thermal spike
3. Quenching
4. Annealing.

In the collisional stage (1), the primary recoil atom initiates a cascade of displacive collisions that continues until no atom contains enough energy to create further displacements. At the end of this stage (lasting <1 ps), the damage consists of energetic displaced atoms and vacant lattice sites. However, stable lattice defects have not yet had time to form. During the thermal spike stage (2), the collisional energy of the displaced atoms is shared among their neighboring atoms in the region of high deposited energy density. The development of the spike requires about 0.1 ps, and the spike may occupy several zones in which the energy is high enough so that the atoms resemble molten material. As energy is transferred to the surrounding atoms, the molten zones return to the condensed, or quenched stage (3), and thermodynamic equilibrium is established (~10 ps). The quenching stage may take several ps, and during this time, stable lattice defects form either as point defects or as defect clusters. But the total number of defects at this stage is much less than the number of atoms displaced in the collisional stage. The annealing stage involves further rearrangement and interaction of defects and occurs by thermally activated diffusion of mobile lattice defects. By definition, the annealing stage (4) lasts until all mobile defects escape the cascade region or another cascade occurs within it. Thus, the timescale extends from nanoseconds to months, depending on the temperature and the irradiation conditions. The annealing stage is the subject of Part II on Physical Effects of Radiation Damage and is the link between the damage cascade and the observable effects of irradiation.

3.6 Behavior of Defects Within the Cascade

The actual number of defects that survive the displacement cascade and their spatial distribution in the solid will determine their effect on the irradiated microstructure. We define the *displacement efficiency* ξ, as the fraction of the "ballistically" produced Frenkel pairs (NRT dpa) that survive the cascade quench. MD simulation of the displacement cascade yields the recoil dependence of the displacement efficiency in iron irradiated at low temperature, as shown in Fig. 3.17. With decreasing cascade energy, the value of ξ increases rapidly from zero to > 1 at very low recoil energies. That ξ exceeds 1.0 is attributed to the inability of the modified K–P model

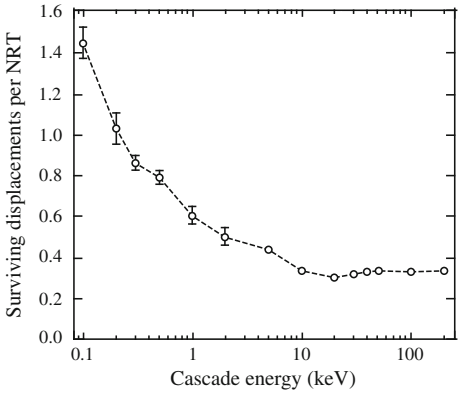

Fig. 3.17 Ratio of MD defects to NRT displacements as a function of cascade energy in 100 K iron (from [16])

to describe displacements in a polycrystalline material at recoil energies near the threshold displacement energy, E_d, due to the strong dependence of E_d on crystallographic orientation. The actual displacement threshold varies with crystallographic direction and is as low as $\sim$ 19 eV in the [100] direction (see Fig. 2.6). Thus, using the recommended average value of 40 eV for the displacement energy predicts fewer defects at low energies [28].

As recoil energy increases, ξ steadily decreases to a value of about 0.3 for 5 keV cascades in copper. The formation of multiple subcascades at high PKA energies (above $\sim$20 keV) causes ξ to remain nearly constant for PKA energies up to 500 keV. Comparing this plot to the recoil and weighted recoil spectra given in Figs. 3.5 and 3.6 shows that electrons and light ions with a low PKA energy will generate values of ξ close to 1, while heavy ions and neutrons that produce high PKA energies will result in ξ at the asymptotic value of 0.3.

The displacement cascade efficiency, ξ, is comprised of several components:

$\gamma_{i,v}$ The isolated point defect fraction

$\delta_{i,v}$ Clustered fraction including mobile defect clusters such as di-interstitials

ζ Fraction initially in isolated or clustered form after the cascade quench that undergoes recombination during subsequent short-term ($>10^{-11}$ s) intracascade thermal diffusion

They are related as follows:

$$\xi = \delta_i + \gamma_i + \zeta = \delta_v + \gamma_v + \zeta. \tag{3.24}$$

Figure 3.18 shows the history of defects born, according to the NRT model, as vacancies and interstitials. The fraction of defects that will be annihilated after the cascade quench by recombination events among defect clusters and point defects within the same cascade (intracascade recombination), ζ, is about 0.07, for a displacement efficiency of 0.3. The clustered fraction, δ, includes large, sessile clusters and small defect clusters that may be mobile at a given irradiation temperature and

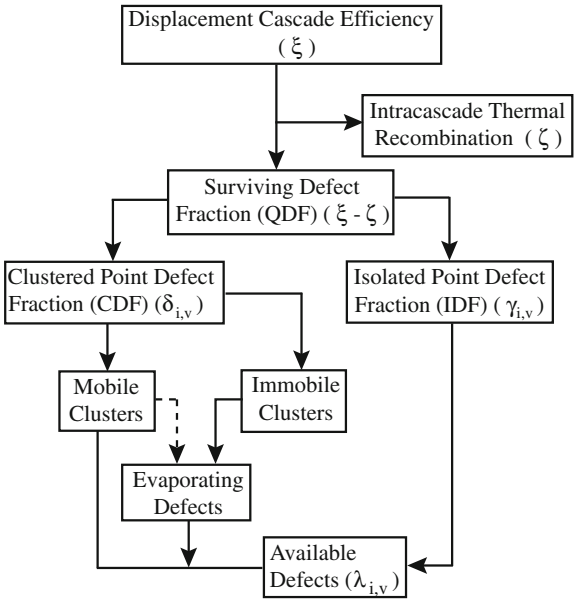

Fig. 3.18 Interdependence of isolated point defects, mobile defect clusters, and thermally evaporating defect clusters that contribute to the fraction of surviving defects that are "available" for radiation effects (after [28])

will be different for vacancies and interstitials. For a 5 keV cascade, δ_i is about 0.06 and δ_v is closer to 0.18. Some of these defects may be able to "evaporate" or escape the cluster and become "available" defects (Fig. 3.18).

This leaves γ, the isolated point defect fraction as yet to be determined. These defects are available to migrate to sinks, to form clusters, to interact with existing clusters, and to participate in the defect flow to grain boundaries that gives rise to radiation-induced segregation. Because of their potential to so strongly influence the irradiated microstructure, defects in this category, along with defects freed from clusters, make up the *freely migrating defects* (FMDs). Recall that electrons and light ions produce a large fraction of their defects as isolated Frenkel pairs, thus increasing the likelihood that they remain as isolated defects rather than in clusters. Despite the equivalence in energy among the four particle types described in Fig. 3.7, the average energy transferred and the defect production efficiencies vary by more than an order of magnitude! This is explained by the differences in the cascade morphology among the different particle types. Neutrons and heavy ions produce dense cascades that result in substantial recombination during the cooling or quenching phase. However, electrons are just capable of producing a few widely spaced Frenkel pairs (FPs) that have a low probability of recombination. Protons produce small widely spaced cascades and many isolated FPs due to the Coulomb interaction and therefore fall between the extremes in displacement efficiency defined by electrons and neutrons.

The value of γ has been estimated to range from 0.01 to 0.10 depending on PKA energy and irradiation temperature, with higher temperatures resulting in the lower values. Because of the importance of this parameter, we will estimate the freely

migrating defect fraction using an analytical treatment by Naundorf [29] that is based on two factors. The first is that energy transfer to atoms is only sufficient to create a single Frenkel pair. The second is that the Frenkel pair lies outside a recombination (interaction) radius so that the nearby FPs neither recombine nor cluster. The model follows each generation of the collision and calculates the fraction of all defects produced that remain free. According to Naundorf, the free single FPs are classified according to the generation i in which they were produced, i.e., the relative amount η_1 is that amount that is produced by primary collisions (first generation), while η_2 is the relative amount produced by secondary collisions (second generation). Thus, the total number of free single FPs produced is:

$$\eta = \sum_i \eta_i, \tag{3.25}$$

where that produced by primary collisions is:

$$\eta_1 = \left(\beta_\mathrm{p}/\sigma_\mathrm{d}\right) \int_{E_\mathrm{d}}^{\gamma E_\mathrm{i}} \sigma(E_\mathrm{i}, T)\, \mathrm{d}T, \tag{3.26}$$

and that produced by secondary collisions is:

$$\eta_2 = (1/\sigma_\mathrm{d}) \int_{E_\mathrm{d}}^{\gamma E_\mathrm{i}} \sigma(E_\mathrm{i}, T)[Z(T)\beta_\mathrm{A}(T)/\sigma_\mathrm{A}(T)]\, \mathrm{d}T \int_{E_\mathrm{d}}^{2.5E_\mathrm{d}} \sigma(T, T')\, \mathrm{d}T', \tag{3.27}$$

where $\sigma(E_\mathrm{i},T)$ is the energy transfer cross section for an incident particle to a lattice atom, $\sigma\ (T,T')$ is the energy transfer cross section between like atoms in the solid, and $Z(T)$ is the total number of secondary collisions produced above E_d by a PKA of energy T along its path. The primary displacement cross section for the incident ion, σ_p, is:

$$\sigma_\mathrm{p} = \int_{E_\mathrm{d}}^{\gamma E_\mathrm{i}} \sigma(E_\mathrm{i}, T)\, \mathrm{d}T, \tag{3.28}$$

and the total displacement cross section σ_d is given in the Kinchin–Pease model by:

$$\sigma_\mathrm{d} = \int_{E_\mathrm{d}}^{\gamma E_\mathrm{i}} \sigma(E_\mathrm{i}, T)\nu(T)\, \mathrm{d}T. \tag{3.29}$$

The distance λ between two primary collisions is distributed according to an exponential law:

$$W(\lambda) = 1/\lambda_p \exp\left(-\lambda/\lambda_p\right), \tag{3.30}$$

with the mean distance:

$$\lambda_p = \Omega/\sigma_p, \tag{3.31}$$

where Ω is the atomic volume. The condition that the distance between two consecutive collisions must be larger than an appropriate interaction radius r_{iv} (so that FPs produced near each other neither recombine nor cluster) reduces the amount of all possible free single FPs by:

$$\beta_p = \exp\left(-r_{iv}/\lambda_p\right), \tag{3.32}$$

and is illustrated in Fig. 3.19 [30]. The model provides the efficiency for the production of freely migrating defects. Results of this calculation are shown in Table 3.2 for several ions of varying mass and energy. Values of η range from 24 % for proton irradiation to 3 % for heavy ion (krypton) irradiation.

Applying this model to our illustration in Fig. 3.7 yields the following values for η:

MeV electrons	1.0
3.4 MeV protons	0.2
5.0 MeV Ni^{++} ions	0.04
Neutrons (fission spectrum)	0.02

These results can also be compared to those calculated by Rehn et al. [31] determined from the analysis of experiments and are shown in Fig. 3.20. The data in this figure are arbitrarily normalized to 1.0 for 1 MeV protons. These data along with

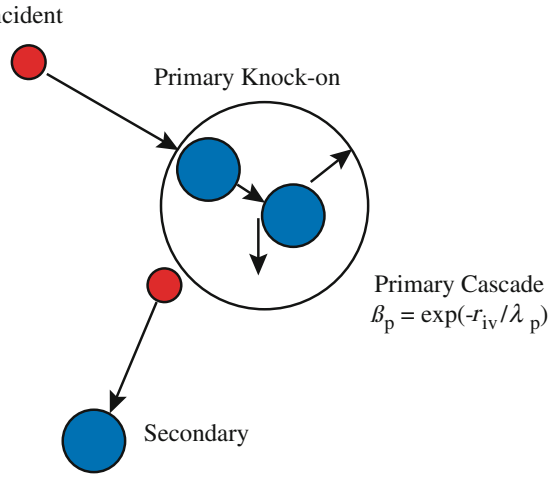

Fig. 3.19 Illustration of the effect of the interaction radius on single Frenkel pair production

Table 3.2 Calculated values for σ_p/σ_d and of the relative amounts η_{calc} of FP production in nickel by different kinds of irradiations (E_d = 40 eV, r_{iv} = 0.7 nm) using Lindhard's analytical differential collision cross section (from [29])

Irradiation	σ_p/σ_d (%)	η_{calc} (%)
1 MeV H^+	37.0	24.0
2 MeV H^+	30.0	19.2
2 MeV Li^+	27.0	16.9
1.8 MeV Ne^+	16.0	8.7
300 keV Ni^+	5.1	2.3
3 MeV Ni^+	7.5	3.8
3.5 MeV Kr^+	5.9	3.0
2 keV O^+	42.0	9.8

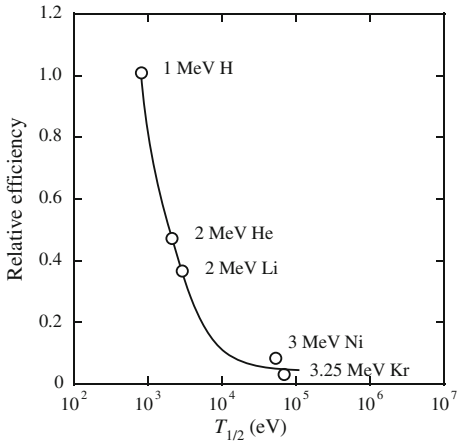

Fig. 3.20 Relative efficiency of freely migrating defect production for ions of various mass and energy (after [31])

the results just presented show that at low recoil energies, the fraction of defects that are freely migrating approaches 1.0, and as the recoil energy increases, that fraction drops to values in the range 0.02–0.05.

As discussed earlier and shown in Fig. 3.17, recent results [32] have established that such low values of FMD efficiency for heavy ion or neutron irradiation cannot be explained by defect annihilation within the parent cascade (*intra*cascade annihilation). In fact, cascade damage generates vacancy and interstitial clusters that act as annihilation sites for FMD, reducing the efficiency of FMD production. Thus, the cascade remnants result in an increase in the sink strength for point defects and along with recombination in the original cascade account for the low FMD efficiency measured by experiment.

While the NRT description of atom displacements provides an estimation of the number of Frenkel pairs produced by the PKA, it does not accurately describe atomic interactions in the thermal spike and hence is inadequate for describing the true configuration of defects. MD simulations can be used for this purpose and have confirmed that defect production by displacement cascades is not as efficient as predicted by the NRT formula. In fact, ν is about 20–40 % of ν_{NRT} for cascades with energy greater than 1–2 keV. From the analysis of MD results for several

metals [33], the number of Frenkel pairs is found to depend on the kinetic energy of the PKA, T, as:

$$\nu_{MD} = AT^n, \tag{3.33}$$

where A and n are constants that are only weakly dependent on the metal and temperature. Figure 3.21 shows the dependence of ν_{MD} on T for various metals. Note that the behavior of Frenkel pair production is well represented by this function over a large damage energy range. Also note that the results all fall below the NRT value as shown by the solid line in the figure. The lower efficiency is likely the result of SIA production at the periphery of the disordered core dominating that at the end of focused collision chains such that the close proximity to the vacancies and the high kinetic energy of the core during the thermal spike assist in SIA–vacancy recombination.

From the results shown in Fig. 3.21, there is no noticeable dependence on the crystal structure, as there are three fcc metals (Al, Ni, Cu), two hcp metals (Ti, Zr), one bcc metal (Fe), and one ordered $L1_2$ structure (Ni_3Al), and yet the magnitude of ν_{FP} is not separated along crystal structure lines. Second, there is a dependence on atomic mass of the metal as noted in the dependence of ν_{MD} and A on T. The dependence of n on atomic mass is weaker, though evident. The decrease in efficiency with atomic mass is likely due to the enhanced recombination due to thermal spike effects. As cascade energy increases, there is a tendency for cascades to break up into subcascades. Since one cascade produces fewer defects than two separate cascades of the same total energy, subcascade formation will increase the slope of the plots in Fig. 3.21. The transition to subcascades occurs at lower energy in lighter metals and may be the cause for the mass dependence on efficiency. Note that n is only weakly dependent on mass.

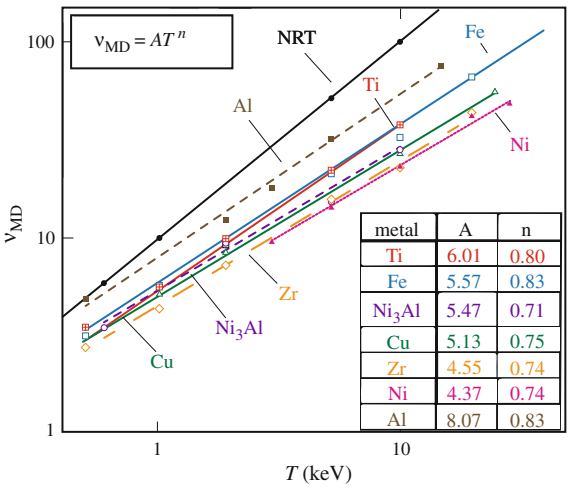

Fig. 3.21 Number of Frenkel pairs produced as a function of damage energy, T, for Cu, Fe, Ti, Zr, and Ni_3Al at 100 K and for Al and Ni at 10 K (after [33])

MD simulation has also been applied to the study of defect production in alloys [34, 35]. One might expect that the mass difference between solute atoms in an alloy will interrupt crystallographic processes such as focusing and channeling and result in the production of more Frenkel pairs as compared to the pure metal case. MD simulations in copper containing up to 15 at.% gold in solution show that the larger Au atoms decrease the length of focused displacement events in the ballistic phase and thereby enhance the intensity and lifetime of the disorder and temperature of the thermal spike. However, ν_{FP} was found to be independent on the alloy composition over a wide range of T. Similar studies conducted on Fe–Cr alloys substantiated these results. Movie 3.3 (http://rmsbook2ed.engin.umich.edu/movies/) shows cascade formation and cooling in an Fe–10 %Cr alloy in which the yellow balls are vacancies, the gray are iron interstitials, and the green are chromium interstitials. In this simulation, chromium is modeled as the larger solute, and after cooling, the remaining interstitial population is predominantly iron atoms as their distortion of the lattice is less than that from the oversized chromium atoms.

The results shown in Fig. 3.21 are for MD calculations at or below a temperature of 100 K. Irradiation temperature has a strong effect on the evolution of radiation damage in metals because of its effect on the motion of defects and their stability as clusters. Irradiation temperature also has an effect on the formation of Frenkel pairs. Figure 3.22 shows the Frenkel pair production as a function of temperature in α-iron up through 900 K (627 °C) and for several values of PKA energy. Note that there is a small but consistent effect of temperature in that higher irradiation temperatures produce fewer Frenkel pairs. The lower Frenkel pair production is believed to be due to the increase in the lifetime of the thermal spike as T_{irr} increases, which allows for more defect motion before cooling and hence more vacancy–interstitial recombination within the cascade region. A contributing factor may be the shorter length of the focused collision sequences (due to the higher kinetic energy of the atoms) that results in a reduction of the vacancy–interstitial separation distance.

In ordered alloys such as Ni_3Al (Fig. 3.21), the Frenkel pair production is similar to that in the pure metal (compare with Ni, for example). In addition to Frenkel

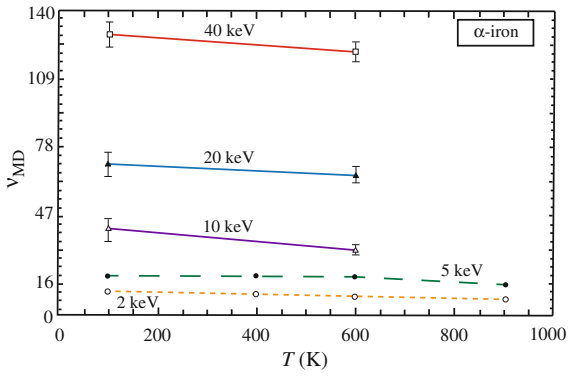

Fig. 3.22 Number of Frenkel pairs produced per cascade as a function of the PKA energy and irradiation temperature in α-iron (after [33])

pairs, anti-site defects or amorphization can occur in these systems. Anti-site defects consist of atoms of the wrong type occupying regular sites in the sublattice. These anti-site defects are observed to increase with T to the 1.25 power rather than to the 0.75 power as in the case of Frenkel pairs. If the amount of disorder is large enough, amorphization can occur. That the anti-site defects form in the molten core confirm that the thermal spike is important in the formation of these defects. The effect of increasing irradiation temperature on defect production in an ordered structure is to increase the number of anti-site defects, primarily due to the reduced length of focused collision sequences.

Because they were conducted in defect-free materials, results of MD simulations of cascades should be viewed as an approximation of what happens in engineering materials. Real materials contain interstitial and substitutional impurities, pre-existing defects such as dislocations, grain boundaries, free surfaces, etc. These microstructure features must be accounted for to obtain the true response of the material to a PKA.

The simplest microstructure imperfection is a collection of point defects. Consider the impact of three types of point defect clusters [36]: 1) As-quenched debris from a 10 keV cascade in a perfect crystal consisting of 30 vacancies and interstitials including one di- and one 7-interstitial cluster; 2) the same 30 vacancies reconfigured into a 6-vacancy void and a 9-vacancy loop and interstitial clusters consisting of four di-, one tri- and one 8-interstitial cluster; and 3) a third configuration consisting of a single 30-vacancy void. Surviving defects per NRT dpa following a 10 keV cascade in a region containing these defect configurations were on average, less that in a perfect crystal for the first two configurations, but greater for the case of the 30-vacancy void. Overall, MD simulations show a reduction in defect production when a cascade was initiated in materials containing defects.

Grain boundaries are indigenous to engineering alloys, and their effect on the radiation damage microstructure is potentially important. One of the key strategies for radiation damage control is to use microstructures with high defect sink densities, such as can be achieved with nanograins that have dimensions approaching the cascade size. MD simulation of defect production conducted in a nanocrystalline structure consisting of 10 nm grains in bcc iron and then subject to 10 or 20 keV cascades showed that while the number of surviving vacancies is similar to that for the single crystal, the number of interstitials is substantially lower, as shown in Fig. 3.23(a). Clustering of interstitials is also much lower in nanograin material as shown by the fractions of surviving interstitials and vacancies contained in clusters in both nanograined and single-crystal iron, as shown in Fig. 3.23(b). Also, the effect of temperature on clustering is reversed in nanograined material. Between 100 and 600 K, the fraction of interstitials in clusters increases for single-crystal iron but decreases for nanograined iron. However, the vacancy cluster fraction decreases for single-crystal iron and increases for nanograined iron.

The presence of a nearby free surface can influence primary damage formation. Contrary to cascade formation in bulk material, the number of surviving vacancies in cascades near the surface exceeds the number of interstitials because of loss of interstitials to the surface, resulting in the formation of larger vacancy clusters. Such

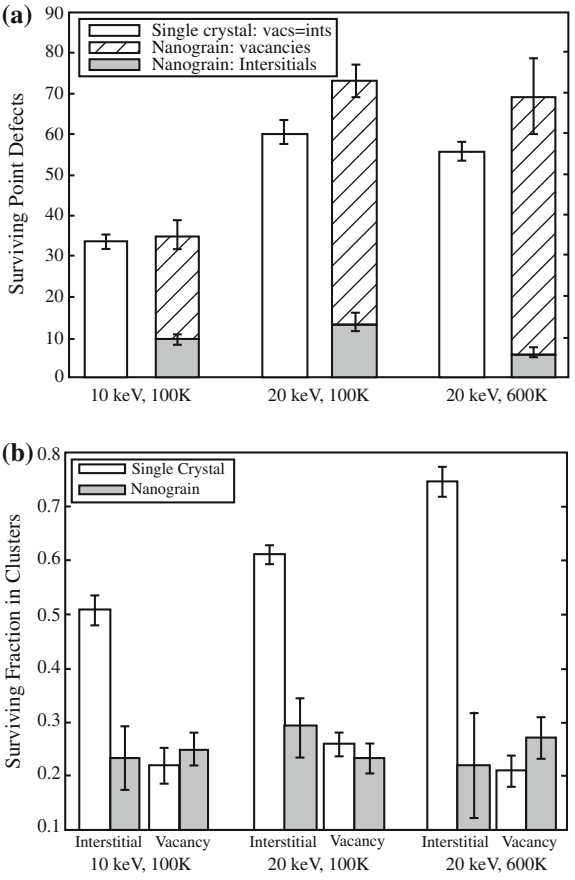

Fig. 3.23 Surviving point defect fraction (**a**) of interstitials and vacancies and (**b**) of surviving interstitials and vacancies, in single-crystal nanograined iron at 100 or 600 K, and for 10 and 20 keV clusters (from [16])

a process is of importance in both in situ ion irradiation experiments of thin (100 nm) foils and analysis of defects in bulk ion irradiations conducted at modest energies such that the analysis volume may be influenced by the proximity to the surface. MD simulations have shown that for 10–20 keV PKAs, the stable interstitial production in surface cascades is not significantly different than in bulk cascades. But the number of stable vacancies is significantly larger in the case of surface cascades as interstitials can be lost by sputtering or transport to the surface as single interstitials or small glissile clusters, thus reducing recombination. In-cascade clustering of interstitials is also relatively unchanged from the case of bulk irradiation, but the fraction of vacancies in clusters per NRT dpa increased by 20–40 % as compared to bulk irradiation. The vacancy cluster size distribution also changed significantly, with larger clusters produced in the surface cascades.

We now have the description of the damage state that we need in order to begin to describe the development of the physical and mechanical effects of irradiation. The K–P/NRT models along with the energy transfer cross sections provide a

means to calculate the number of displacements occurring in a solid from an incident particle of some mass and energy. The spatial, temporal, and thermal descriptions of the resulting cascade provide us with a means to estimate the number of defects surviving the cascade quench phase that are available to influence the microstructure at longer times. To this point, we have focused on developing both a physical and a quantitative description of the state of the material at the end of the quench phase of the cascade that is completed within $\sim$ 10 ps of the initial collision event. From that point forward in time, we will be concerned with the development of the microstructure. This development will continue to occur for weeks, months, and even years in a reactor core, spanning some 18 orders of magnitude in time, and constitutes the Physical Effects of Radiation Damage, which is the focus of Part II of this text.

Nomenclature

A	Atomic mass pre-exponential constant in Born–Mayer relation, Eq. (1.47)
B	Constant in exponent in Born–Mayer relation, Eq. (1.47)
C_p	Specific heat capacity
D	Thermal diffusivity
E_a	Energy per atom
E_d	Displacement energy
E_D	Damage energy
E_i	Projectile energy
F_D	Energy depth distribution
k_B	Boltzmann's constant
m	1/s
M_1	Mass of projectile
M_2	Mass of target
N	Atom number density
N_d	Number of displacements per unit depth
$P(E_i, T)$	Primary recoil spectrum
r_{iv}	Recombination radius
R	Ion/atom range in the lattice
R^2	Variance in temperature profile, Eq. (3.21)
s	Exponent in power law relationship
T	Energy transferred in collision
$\check{T}$	Minimum energy transferred
$\hat{T}$	Maximum energy transferred
$\bar{T}$	Average energy transferred
U_a	Energy per atom
V_{cas}	Cascade volume
$W(\lambda)$	Function describing distance between primary collisions
$W(E_i, T)$	Weighted primary recoil spectrum
ΔX	Longitudinal moment of the cascade
Y	Transverse moment of the cascade

Z	Atomic number
$Z(T)$	Fraction of secondary collisions produced above E_d by a PKA of energy T
β_p	Reduction factor in FPs due to recombination within r_{iv}
δ	Cascade contraction factor
$\delta_{i,v}$	Clustered fraction of vacancies and interstitials
ε	Unit charge
ϕ	Neutron flux
γ	$4M_1M_2/(M_1 + M_2)^2$
$\gamma_{i,v}$	Isolated point defect fraction
η	Energy lost to electronic excitation in the NRT model, also total # free FPs produced in cascade
η_1	Fraction of defects produced by primary collisions
η_2	Fraction of defects produced by secondary collisions
λ	Mean free path
$\nu(T)$	Displacement function
ν_{FP}	Number of Frenkel pairs
Θ	Cascade energy density
$\sigma(E, T)$	Differential energy transfer cross section
$\sigma'_D(E)$	Displacement cross section for collisions between atoms
σ_d	Total displacement cross section
σ_p	Primary displacement cross section for incident ion
τ	Cascade lifetime
ξ	Displacement efficiency
ζ	Fraction of vacancies and interstitials initially clustered that are subsequently annihilated in the cascade

Problems

3.1 Plot the mean free path for a Ni PKA in Ni for PKA energy in the range 1–10,000 eV, making calculations at each decade. At what energy is the mean free path the smallest? Use Eq. (1.50) to determine the Born–Mayer constants and a value of 40 eV for E_d.

3.2 What is the implication of the difference in shape in the weighted recoil spectra for neutrons and protons in the morphology of the damage cascade?

3.3 For 1 MeV neutrons incident on nickel, determine

(a) The damage energy
(b) The effective cascade temperature
(c) The cascade lifetime using $U_a \sim 0.3$ eV and $D \sim 10^{12}$ nm^2/s.

3.4 You would like to model displacement cascades. What is the appropriate modeling tool, kinetic Monte Carlo, or molecular dynamics? Why?

3.5 Based on your expertise using SRIM, you decide to irradiate a steel sample (Fe–18Cr–9Ni) with nickel ions. You have the choice of examining the

sample near the surface or near the damage peak. You are worried that the implanted nickel ions will change the local chemistry of the sample. To mitigate this concern, should you look in the region closer to the sample surface or the damage peak? Why?

References

1. Olander DR (1976) Fundamental aspects of nuclear reactor fuel elements, TID-26711-P1. Technical Information Service, Springfield
2. Averback RS (1994) J Nucl Mater 216:49
3. Brinkman JA (1956) Amer J Phys 24:251
4. Seeger A (1958) On the theory of radiation damage and radiation hardening. In: Proceedings of the Second United Nations international conference on the peaceful uses of atomic energy, Geneva, vol. 6. United Nations, New York, p 250
5. Nastasi M, Mayer JW, Hirvonen JK (1996) Ion-solid interactions: fundamentals and applications. Cambridge University Press, Cambridge
6. Was GS, Allen TR (1994) Mater Charact 32:239
7. Sigmund P (1981) Sputtering by ion bombardment: theoretical concepts. In: Behrisch R (ed) Sputtering by particle bombardment, Springer, Berlin, p 9
8. Heinisch HL (1996) J Metals, Dec:38
9. Robinson MT (1994) J Nucl Mater 216:1
10. Robinson MT, Torrens IM (1974) Phys Rev B 9:5008
11. Beeler JR (1966) Phys Rev 150:470
12. Ziegler JF, Biersack JP, Ziegler MD (2008) SRIM—The Stopping Range of Ions in Matter, Ion Implantation Press (http://www.srim.org)
13. Cai W, Li J, Yip S (2012) Molecular Dynamics in Konings RJM (ed.) Comprehensive nuclear materials, 1.09:249. Elsevier, Amsterdam
14. Finnis MW, Sinclair JE (1984) Phil Mag A50:45–55; (1986) Erratum Phil Mag A53:161
15. Calder AF, Bacon DJ (1993) J Nucl Mater 207:25–45
16. Stoller RE (2012) Primary radiation damage formation. In: Konings RJM (ed) Comprehensive nuclear materials, 1.11:293. Elsevier, Amsterdam
17. Becquart CS, Wirth BD (2012) Molecular dynamics. in Konings RJM (ed) Comprehensive nuclear materials, 1.14:393. Elsevier, Amsterdam
18. Dalla Torre, J, Bocquet, J-L, Doan NV, Adam E, Barbu A (2005) Phil Mag 85:549
19. Lanore JM (1974) Rad Eff 22:153
20. Caturla MJ, Soneda N, Alonso E, Wirth BD, Diaz de la Rubia T, Perlado JM (2000) J Nucl Mater 276:13
21. Domain C, Becquart CS, Malerba L (2004) J Nucl Mater 335:121
22. Heinisch HL, Singh BN, Golubov SI (2000) J Nucl Mater 276:59
23. Souidi A, Becquart CS, Domain C et al (2006) J Nucl Mater 355:89
24. Arevalo C, Caturla MJ, Perlado JM (2007) J Nucl Mater 362:293
25. Heinisch HL, Trinkaus H, Singh BN (2007) J Nucl Mater 367–370:332
26. Malerba L, Becquart CS, Domain C (2007) J Nucl Mater 360:159
27. Diaz de la Rubia T, Averback RS, Benedek R, King WE (1987) Phys Rev Lett 59(19):1930
28. Zinkle SJ, Singh BN (1993) J Nucl Mater 199:173
29. Naundorf V (1991) J Nucl Mater 182:254
30. Was GS, Allen TR (2007) Radiation effects in solids. In: Sickafus KE, Kotomin EA, Uberoage BP (eds) NATO science series, vol 235. Springer, Berlin, pp 65–98
31. Rehn LE, Okamoto PR, Averback RS (1984) Phys Rev B 30(6):3073
32. Iwase A, Rehn LE, Baldo PM, Funk L (1996) J Nucl Mater 238:224–236

33. Bacon DJ, Gao F, Osetsky YN (2000) J Nucl Mater 276:1–12
34. Deng HF, Bacon DJ (1996) Phys Rev B 54:11376
35. Calder AF, Bacon DJ (1997) In: Proceedings of symposium on microstructure evolution during irradiation, vol 439. Materials Research Society, Pittsburgh, PA, p 521
36. Stoller RE, Guiriec SC (2004) J Nucl Mater 329–333:1228

Chapter 4
Point Defect Formation and Diffusion

The first step in understanding the effects of irradiation on materials is to understand, on the atomic level, the nature of radiation damage. In the previous chapters, we developed a quantitative description of the process of displacing an atom from its lattice site by the transfer of kinetic energy from a high-energy particle. The recoiling lattice atom travels through the crystal, colliding with its neighbors and displacing these also from their sites. A cascade of atomic collisions is created by the original particle with the end result being a number of vacant lattice sites and an equal number of displaced atoms wedged into the interstices of the lattice. The basic *defects* (vacancies and interstitials) form the foundation for *all* observed effects of irradiation on the physical and mechanical properties of materials. Determination of the concentration and diffusion of these basic defects is the subject of this chapter.

4.1 Properties of Irradiation-Induced Defects

Various types of defects exist in any crystalline lattice. These include the following:

- Point defects (0D): vacancies and interstitials
- Line defects (1D): dislocation lines
- Planar defects (2D): dislocation loops and
- Volume defects (3D): voids, bubbles, stacking-fault tetrahedra.

The most basic of these are point defects. Following [1], we will start with interstitials.

4.1.1 Interstitials

An interstitial is an atom that is located in a position of a crystal that is not a regular lattice site. There are two broad classifications of interstitial sites in the various

Additional material to this chapter can be downloaded from http://rmsbook2ed.engin.umich.edu/movies/

G.S. Was, *Fundamentals of Radiation Materials Science*,
DOI 10.1007/978-1-4939-3438-6_4

cubic crystal lattices: octahedral sites and tetrahedral sites, and these will be briefly reviewed. The fcc lattice is cubic with unit cell of length a (lattice constant) and with atoms located at the corners and the faces of the cube (Fig. 4.1). Each corner atom is shared by eight unit cells and each face atom is shared by two unit cells, so the number of atoms per unit cell is 8 corner atoms × 1/8 atom/unit cell + 6 face atoms × 1/2 atoms/unit cell = 4. Octahedral sites are interstitial positions that are surrounded by an octahedron where the lattice atoms make up the six vertices of an octahedron. There are four octahedral sites per unit cell in the fcc lattice, the center of the unit cell and the edges. The center site is wholly within the unit cell, but the sites on the edges are each shared by four unit cells (Fig. 4.2(a)). So the total number of octahedral interstitial sites per unit cell is 1 + 12 edge sites × 1/4 site per unit cell = 4 sites. There are also tetrahedral interstitial sites in the fcc lattice in which the atom is located inside a tetrahedron formed by lattice atoms. These are located inside the corners of the unit cell (Fig. 4.2(b)). There are a total of 8 tetrahedral sites (one for each corner) in the fcc unit cell.

In the bcc lattice, the atoms reside at the corners of the unit cell with one in the center of the cell for a total of two atoms per unit cell; 1 + 8 corner sites × 1/8 site/unit cell = 2 sites (Fig. 4.3). Octahedral interstitial sites are located on the faces and the edges of the unit cell giving 6 faces × 1/2 site per face +12 edges × 1/4 sites per edge = 6 sites per unit cell (Fig. 4.4(a)). Tetrahedral interstitial sites are located on the faces and in the corners of the faces. There are 6 faces × 4 locations per face × 1/2 sites/face = 12 tetrahedral sites (Fig. 4.4(b)).

The hcp unit cell is not cubic but rather hexagonal and is defined by the c/a ratio where a is the length of a side of the regular hexagon and c is the height of the cell (Fig. 4.5). There are six atoms per unit cell in the hcp lattice; twelve on the corners shared by six cells (=2) plus two on the faces shared by two cells (=1) plus three inside the cell at a height of $1/2c$ (=3). There are six octahedral sites per unit cell, all wholly contained within the unit cell (Fig. 4.6(a)). There are also six tetrahedral

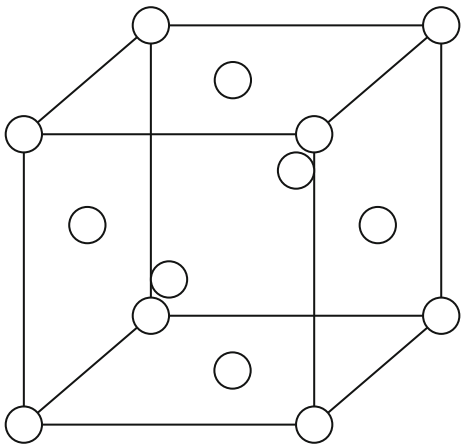

Fig. 4.1 Face-centered cubic (fcc) lattice unit cell

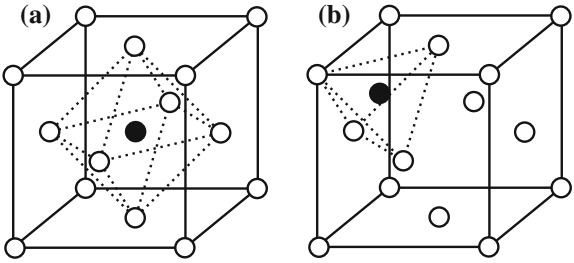

Fig. 4.2 Interstitial positions in the fcc unit cell, (**a**) octahedral site and (**b**) tetrahedral site

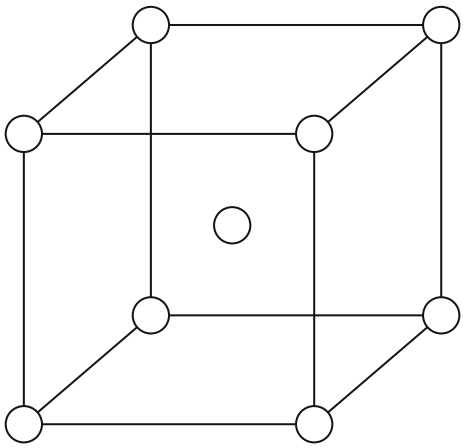

Fig. 4.3 Body-centered cubic (bcc) lattice unit cell

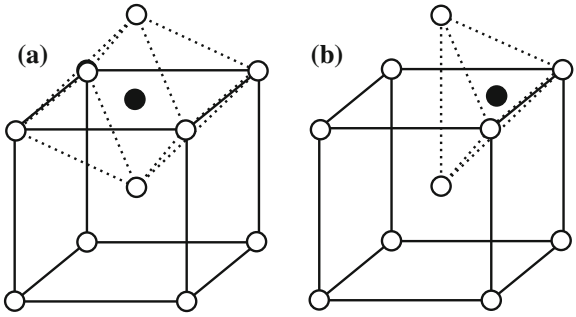

Fig. 4.4 Interstitial positions in the bcc unit cell, (**a**) octahedral site and (**b**) tetrahedral site

sites per unit cell, four wholly contained within the unit cell and six that are shared by each of three cells (Fig. 4.6(b)).

Our simple picture of interstitials is not a true physical picture because the stable configuration of self-interstitial atoms (SIA) in metals is the dumbbell or split-interstitial configuration where two atoms are associated with or "share" a single lattice site. Since the atom cores repel each other, the atoms arrange

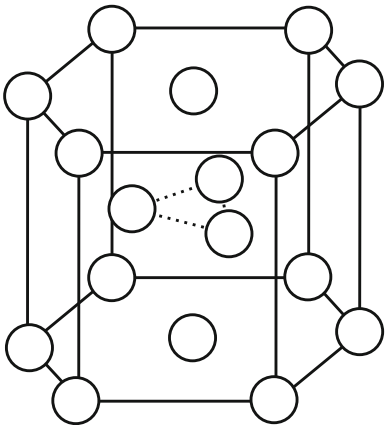

Fig. 4.5 Hexagonal close-packed (hcp) unit cell

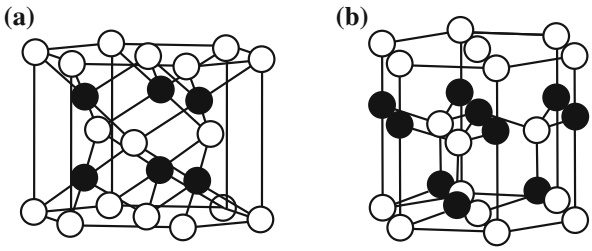

Fig. 4.6 Interstitial positions in the hcp unit cell (**a**) octahedral site and (**b**) tetrahedral site

themselves in the lowest energy orientation. This turns out to be with the dumbbell axis along the $\langle 100 \rangle$ direction for fcc metals, the $\langle 110 \rangle$ direction for bcc metals, and the $\langle 0001 \rangle$ direction for hcp crystals (Fig. 4.7).

To accommodate two atoms in one lattice site, atoms adjacent to the dumbbell are displaced slightly off their lattice positions which then perturbs neighboring atoms and so on. These displacements emanate from the defect, forming an elastic displacement field. The symmetry of the displacement field is reflected by the SIA configuration in the bcc lattice (Fig. 4.8).

Consider a $\langle 100 \rangle$ dumbbell interstitial configuration in fcc aluminum. The separation distance of the two dumbbells is about $0.6a$. The nearest neighbor spacing in the fcc lattice is along $\langle 110 \rangle$ and is $\left(a/\sqrt{2}\right)$, so the separation distance of a $\langle 100 \rangle$ dumbell is about 20 % smaller than the nearest neighbor distance in the undistorted lattice. The four nearest neighbors to each dumbbell are displaced outwards by about $0.1a$ and the total relaxation volume is about 2Ω, where Ω is the atomic volume. The relaxation volume is determined by treating the crystal as an

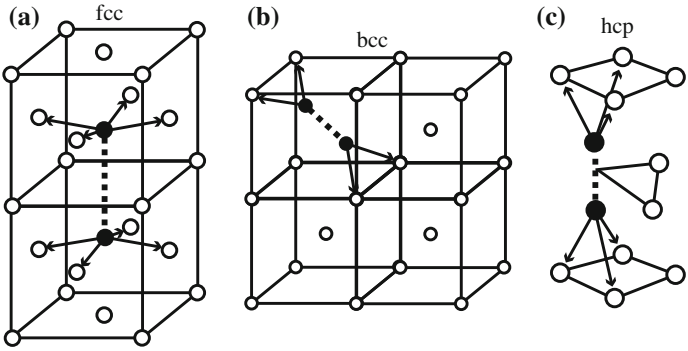

Fig. 4.7 Configurations of SIAs in (**a**) fcc, (**b**) bcc and (**c**) hcp lattices

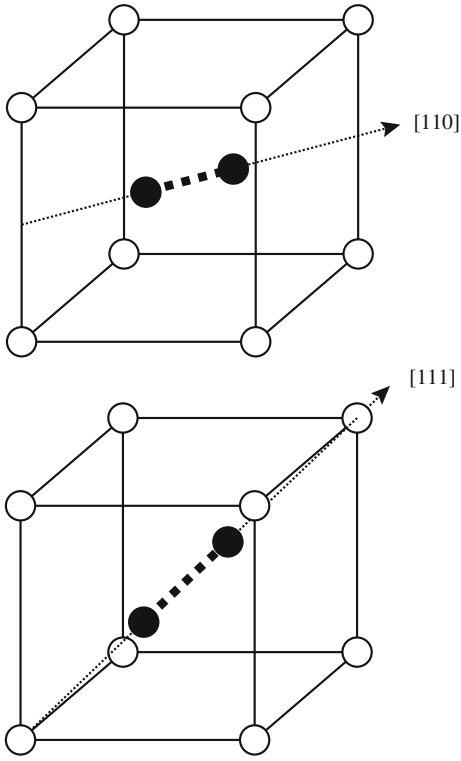

Fig. 4.8 Split interstitials in the bcc lattice

elastic continuum and inserting an atom as an interstitial (or removing one to create a vacancy) and determining the amount of distortion resulting in the lattice. The high relaxation volumes due to SIAs cause large lattice distortions, which lead to strong interaction with other SIAs and with other lattice defects (dislocation,

impurity atoms). The net effect of this elastic interaction is an attraction of mobile SIAs to these defects. Experimental values for the relaxation volume in several metals appear in Table 4.1.

4.1.2 Multiple Interstitials

Multiple interstitials form by the agglomeration of mobile SIAs at elevated temperatures. Multiple interstitials have a high binding energy on the order of 1 eV. Since the energy needed to dissociate a SIA from a large cluster approaches the SIA formation energy (2–4 eV), SIA clusters are very stable against dissociation at low temperatures.

Computer simulation predicts that the stable configuration of a di-interstitial in fcc metals is two parallel dumbbells on nearest neighbor sites (Fig. 4.9). The stable structure of tri-interstitials in fcc metals is predicted by computer simulation to be three orthogonal $\langle 100 \rangle$ dumbbells on nearest neighbor sites. The anticipated configuration of di-interstitials in the bcc lattice is two $\langle 110 \rangle$ dumbbells on nearest neighbor sites.

Table 4.1 Numerical values, compiled from different sources for some quantities characterizing properties of radiation-induced point defects in metals (from [1])

	Symbol	Unit	Al	Cu	Pt	Mo	W
Interstitials							
Relaxation volume	V^{i}_{relax}	Atomic vol.	1.9	1.4	2.0	1.1	
Formation energy	E^{i}_{f}	eV	3.2	2.2	3.5		
Equilibrium Concentration at T^{*}_{m}	$C_{i}(T_{m})$	–	10^{-18}	10^{-7}	10^{-6}		
Migration energy	E^{i}_{m}	eV	0.12	0.12	0.06		0.054
Vacancies							
Relaxation volume	V^{v}_{relax}	Atomic vol.	0.05	–0.2	–0.4		
Formation energy	E^{v}_{f}	eV	0.66	1.27	1.51	3.2	3.8
Formation entropy	S^{v}_{f}	k	0.7	2.4			2
Equilibrium Concentration at T_{m}	$C_{v}(T_{m})$	–	9×10^{-6}	2×10^{-6}			4×10^{-5}
Migration energy	E^{v}_{m}	eV	0.62	0.8	1.43	1.3	1.8
Activation energy for self-diffusion	Q_{vSD}	eV	1.28	2.07	2.9	4.5	5.7
Frenkel pairs							
Formation energy	E^{FP}_{f}	eV	3.9	3.5	5		

*Estimated by assuming $S^{f}_{i} = 8k$

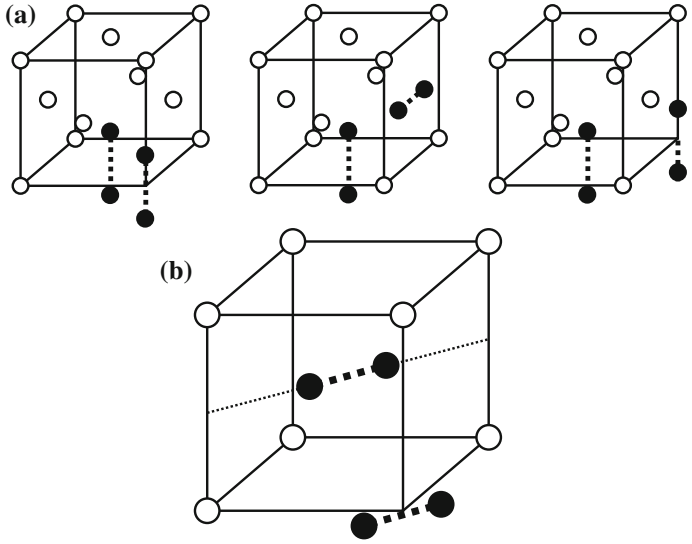

Fig. 4.9 Di-interstitials in the (**a**) fcc lattice in stable, metastable, and new stable positions and (**b**) in the bcc lattice

4.1.3 Interstitial–Impurity Complexes

Impurity atoms in metals are efficient traps for SIAs. Stable complexes consisting of undersized atoms and interstitials do not dissociate thermally below a temperature where vacancies become mobile. One possible configuration is the mixed dumbbell where one of the dumbbell atoms is replaced by the impurity atom (Fig. 4.10(a)). Binding energies are of the order of 0.5–1.0 eV. Weaker trapping is observed with oversized impurities (Fig. 4.10(b)).

Interstitial–impurity complexes require only a small activation energy to reorient themselves by so-called cage motion. Shown in Fig. 4.10(a), the impurity can jump between the indicated positions of the central octahedron, forming a new mixed dumbbell with the adjacent host atom. Since all of the mixed dumbbells have the impurity end toward the center of the cage, no long-range motion is associated with cage motion. The activation energy of the reorientation jump in the cage is about 0.01 eV.

Movies 4.1 and 4.2 (http://rmsbook2ed.engin.umich.edu/movies/) show the behavior of iron and chromium in an Fe–10 %Cr alloy following a displacement cascade as a function of the relative sizes of the solutes. In Movie 4.1, chromium is modeled as an oversized solute and in Movie 4.2 chromium is undersized. Note the difference in the interstitial clusters following the cascade cooling period. The undersize Cr in Movie 4.2 undergoes stronger trapping by the iron interstitials than

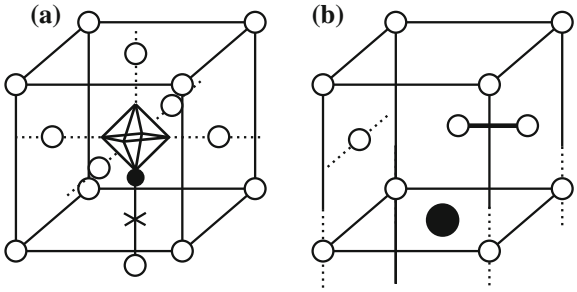

Fig. 4.10 (**a**) Mixed dumbbell configuration in the fcc lattice formed by an undersized impurity and an atom of the host lattice. The vertices of the octahedron are the other locations of the impurity as it makes a dumbbell with the other "face" atoms in the unit cell. (**b**) Trapping of an interstitial to make a dumbbell with an oversized impurity in the fcc lattice

in the case of oversize Cr in Movie 4.1, resulting is a greater number of small interstitial clusters containing Cr.

4.1.4 Vacancies

The vacancy, or missing lattice atom, is the simplest point defect in metal lattices. All calculations and computer simulations show that the single vacancy structure is a missing lattice atom with the nearest neighbors relaxing inward toward the vacancy.

SIAs have a high formation energy (>2.0 eV), a large relaxation volume ($\sim 2\Omega$) and a low migration energy (<0.15 eV) leading to a high mobility. Vacancies, on the other hand, have low formation energies (<2 eV), low relaxation volume (0.1–0.5Ω), and high migration energy (>0.5 eV) and are therefore much less mobile than SIAs (Table 4.1). Further, the strain field of vacancies is isotropic in cubic metals making them hard to investigate.

4.1.5 Multiple Vacancies

Multiple vacancies have small binding energies compared to interstitial clusters (0.1 eV) but are often observed in irradiated metals. The configuration of multiple vacancy clusters is shown for the fcc lattice in Fig. 4.11(a), and for the bcc lattice in Fig. 4.11(b). The migration energy of divacancies is less than for single vacancies (0.9 eV vs. 1.32 eV for Ni) but increases with increasing cluster size. It appears that since the tetra-vacancy can only migrate by dissociation, it is the first stable nucleus for further clustering.

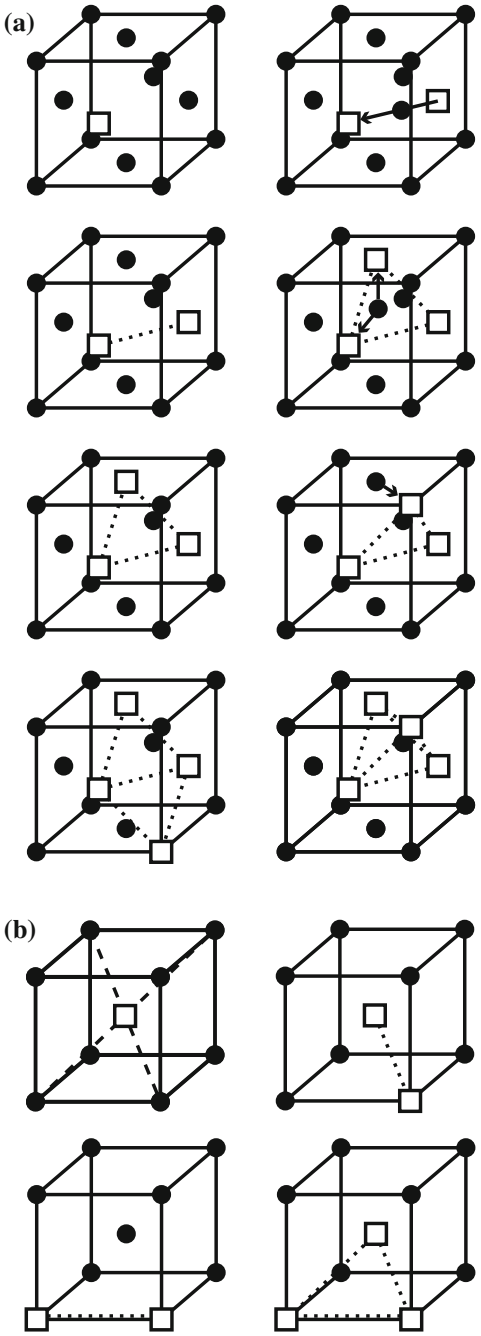

Fig. 4.11 Configurations of multiple vacancies in the (**a**) fcc lattice and (**b**) bcc lattice

4.1.6 Solute–Defect and Impurity–Defect Clusters

Vacancies can bind to oversize solute or oversize impurity atoms in order to lower the overall free energy of the solid. Estimates of the binding energy of a vacancy to an oversize solute in the fcc lattice range from 0.2 to 1.0 eV [2]. Hence, these solutes can act as efficient traps for vacancies in the lattice.

4.2 Thermodynamics of Point Defect Formation

Even in the absence of irradiation, a crystal cannot exist at a finite temperature in a state of absolute perfection. Statistically, there is a finite probability that sufficient energy will be concentrated, by local fluctuations, to form a defect in the crystal lattice. For most purposes, it is fair to assume that the volume of the crystal is constant, for which the Helmholtz free energy function applies. Following [3], if the system is at constant pressure, then:

$$F \cong G = U + pV - TS = H - TS, \tag{4.1}$$

where U is the internal energy, H is the total enthalpy of the N atoms comprising the system, S represents the disorder (entropy) in the system which can be characterized by:

$$S = k \ln w, \tag{4.2}$$

where w is the number of possible different configurations of atoms and k is Boltzmann's constant.

Suppose that a crystal has n defects with N available sites. The increase in free energy is:

$$\Delta G_{\mathrm{f}} = n\Delta H_{\mathrm{f}} - T\Delta S, \tag{4.3}$$

where ΔH_{f} is the increase in enthalpy brought about by the introduction (formation) of the defect and ΔS is the change in total entropy, determined as follows.

For one defect, there are N available sites and hence N possible configurations. For n defects, there are N for the first, $(N - 1)$ for the second, $(N - 2)$ for the third, etc., up to $(N - n + 1)$ for the nth. This leads to $N(N - 1)(N - 2)\ldots(N - n + 1)$ configurations in all. But because these are not all distinct and defects are indistinguishable, the number above allows for $n!$ ways of distributing N defects among n sites. Hence, the number of possible different configurations is:

$$w = \frac{N(N-1)(N-2)\ldots(N-n+1)}{n!}, \tag{4.4}$$

or

$$w = \frac{N!}{n!(N-n)!}. \tag{4.5}$$

The *mixing entropy* is then:

$$\Delta S_{\text{mix}} = k[\ln N! - \ln n! - \ln (N-n)!]. \tag{4.6}$$

Using Stirling's approximation of $\ln x! \simeq x \ln x$ for large x gives:

$$\Delta S_{\text{mix}} = k \ln w \cong k[N \ln N - n \ln n - (N-n) \ln (N-n)]. \tag{4.7}$$

In addition to ΔS_{mix}, there is a contribution to ΔS from the vibrational disorder of the presence of the defects. According to the Einstein model of lattice motion, the atoms are represented as $3N$ independent linear harmonic oscillators and the associated entropy is:

$$S_{\text{f}} = 3k \ln\left(\frac{kT}{\hbar \nu_{\text{E}}}\right), \tag{4.8}$$

where ν_{E} is the natural frequency of the oscillator and $\hbar$ is Planck's constant. If each defect changes the vibration frequency of z neighbors to ν_{r}, the entropy is:

$$S'_{\text{f}} = 3kz \ln\left(\frac{kT}{\hbar \nu_{\text{r}}}\right) = 3kz\left[\ln\left(\frac{kT}{\hbar \nu_{\text{E}}}\right) + \ln\left(\frac{\nu_{\text{E}}}{\nu_{\text{r}}}\right)\right], \tag{4.9}$$

and for n defects, the total change in entropy due to vibrational disorder is:

$$n\left(S'_{\text{f}} - zS_{\text{f}}\right) = \Delta S_{\text{f}} = 3nkz \ln\left(\frac{\nu_{\text{E}}}{\nu_{\text{r}}}\right). \tag{4.10}$$

Taking both contributions to the entropy change and inserting them into the free energy equation gives:

$$\Delta G_{\text{f}} = n\Delta H_{\text{f}} - kT\left[N \ln N - n \ln n - (N-n)\ln(N-n) + n \ln\left(\frac{\nu_{\text{E}}}{\nu_{\text{r}}}\right)^{3z}\right]. \tag{4.11}$$

In equilibrium, n will be such that it satisfies $\mathrm{d}\Delta G_{\text{f}}/\mathrm{d}n = 0$ giving:

$$\frac{\Delta H_{\text{f}}}{kT} = \ln\left[\frac{N-n}{n}\left(\frac{\nu_{\text{E}}}{\nu_{\text{r}}}\right)^{3z}\right]. \tag{4.12}$$

Assuming $n \ll N$ and letting $n/N = C$ (concentration fraction):

$$C = \left(\frac{\nu_E}{\nu_r}\right)^{3z} \exp\left(\frac{-\Delta H_f}{kT}\right). \tag{4.13}$$

Writing $\left(\frac{\nu_E}{\nu_r}\right)^{3z}$ in terms of entropy gives the familiar equation:

$$C = \frac{n}{N} = \exp\frac{\Delta S_f}{k} \exp\frac{-\Delta H_f}{kT} = \exp\left(\frac{-\Delta G_f}{kT}\right). \tag{4.14}$$

For vacancies, we have

$$C_v = \exp\left(\frac{S_f^v}{k}\right) \exp\left(\frac{-E_f^v}{kT}\right), \tag{4.15}$$

and for interstitials:

$$C_i = \exp\left(\frac{S_f^i}{k}\right) \exp\left(\frac{-E_f^i}{kT}\right), \tag{4.16}$$

where $E_f^v = \Delta H_f^v$ and $E_f^i = \Delta H_f^i$ are the formation energies for the respective defect type, and $\Delta S_f^v = S_f^v, \Delta S_f^i = S_f^i$. In metals, typical values for E_f^v are ~ 1 eV, and for $E_f^i \sim 4$ eV. Hence, the formation of vacancies requires considerably less energy than the formation of interstitials (see Table 4.1) and so at thermal equilibrium, $C_v \gg C_i$. Let us look at an example.

Example 4.1 Calculate the equilibrium concentration of vacancies and interstitials in aluminum at room temperature and 10 °C below the melting point.

(a) $RT \simeq 20$ °C or 293 K
From Table 4.1, we have

$$E_f^v \cong 0.66 \text{ eV} \quad S_f^v \sim 0.7k$$
$$E_f^i \cong 3.2 \text{ eV} \quad S_f^i \sim 8k,$$

and inserting into Eqs. (4.15) and (4.16) yields

$$C_v = \exp\left(S_f^v/k\right) \exp\left(-E_f^v/kT\right) \sim 1.6 \times 10^{-11}$$
$$C_i = \exp\left(S_f^i/k\right) \exp\left(-E_f^i/kT\right) \sim 5.0 \times 10^{-51}.$$

(b) At 10 °C below T_m or 650 °C (923 K)
Equations (4.15) and (4.16) yield

$$C_v = \exp\left(S_f^v/k\right)\exp\left(-E_f^v/kT\right) \sim 5.0 \times 10^{-4}$$
$$C_i = \exp\left(S_f^i/k\right)\exp\left(-E_f^i/kT\right) \sim 9.8 \times 10^{-15}.$$

Besides doing an experiment, how do we go about obtaining an estimate for E_f^v? Suppose we create a small cavity in a rigid crystal that has a volume $\Omega = 4/3\pi r_a^3$ equal to the volume occupied by one atom, where Ω is the atom volume and r_a is the atom radius. Since we must conserve volume, we spread the material from the cavity uniformly over the surface of a crystal. If the crystal is a sphere, we have:

$$R' = R + \Delta R. \tag{4.17}$$

Since the crystal is a rigid medium and volume is conserved:

$$4\pi R^2 \Delta R = 4/3\pi r_a^3, \tag{4.18}$$

and if the crystal is large compared to the size of the atom, then $R \gg r_a$ and $\Delta R \ll R$ and:

$$\Delta R = r_a^3/3R^2. \tag{4.19}$$

If E_f^v is the difference in surface energy of the crystal with and without a cavity and σ is the surface energy per unit area, then:

$$\begin{aligned} E_f^v &= 4\pi r_a^2\sigma + 4\pi\sigma(R+\Delta R)^2 - 4\pi R^2\sigma \\ &\sim 4\pi\sigma\left(r_a^2 + 2R\Delta R\right), \end{aligned} \tag{4.20}$$

where the first two terms on the right-hand side of the equation are the energies associated with the inner and outer surfaces after formation of the vacancy and the last term is the energy of the surface of the crystal before formation of the vacancy, and the ΔR^2 term has been neglected. Substituting for ΔR from Eq. (4.19) gives:

$$\begin{aligned} E_f^v &= 4\pi\sigma\left(r_a^2 + \frac{2}{3}\frac{r_a^3}{R}\right) \\ &= 4\pi\sigma r_a^2\left(1 + \frac{2}{3}\frac{r_a}{R}\right), \end{aligned} \tag{4.21}$$

and since $r_a \ll R$, we have:

$$E_f^v \sim 4\pi\sigma r_a^2. \tag{4.22}$$

In most metals, $\sigma \sim 10$ eV/nm^2 and $r_a \sim 0.15$ nm, so $E_f^v \sim 2$ eV.

If we treat the crystal as an elastic continuum, we get a different expression for E_f^v:

$$E_f^v = 4\pi r_a^2 \sigma - 12\pi r_a \frac{\sigma^2}{\mu} + 6\pi r_a \frac{\sigma^2}{\mu}, \tag{4.23}$$

where the first term is the surface energy of the cavity, the second term is the reduction in surface energy due to contraction of the surface by the surface tension, and the third term is the elastic energy stored in the solid, μ is the shear modulus of the crystal, and $E_f^v \sim 1\,\text{eV}$. Note that an interstitial will cause a displacement that is greater than r_a, resulting in a greater formation energy as we have seen already.

4.3 Diffusion of Point Defects

Atoms in a lattice are in a constant state of motion due to thermal vibration, and this means that point defects in the lattice are also in motion. The random nature of thermal vibration gives rise to random walk of the atoms via the defects that are in thermal equilibrium with their surroundings, known as *self-diffusion*. If foreign atoms are present in a pure metal, their diffusion is known as *heterodiffusion*. Self-diffusion arises when a local concentration gradient of defects appears in the crystal, driving atoms to move in the direction that eliminates the gradient. Diffusion is driven by forces other than the concentration gradient, such as stress or strain, electric fields, temperature, etc. In the most general sense, diffusion is driven by a difference in chemical potential. Diffusion in a polycrystal is a complex mechanism due to the presence of grain boundaries, internal surfaces, dislocations, etc. We will follow the analysis in [4] by starting with diffusion in a single crystal and then expanding our treatment to include the polycrystalline case later on.

4.3.1 Macroscopic Description of Diffusion

Diffusion is governed by two fundamental laws derived by Fick in 1880. They apply to any state of matter due to their general character regarding macroscopic diffusion processes. The first law is a relationship between the flux, J, and the concentration gradient of the diffusing specie:

$$J = -D\nabla C, \tag{4.24}$$

where D is the diffusion coefficient and ∇C is the composition gradient. For diffusion in one-dimension,

$$J = -D\frac{\partial C}{\partial x}. \tag{4.25}$$

The minus sign indicates that diffusion takes place in the direction of *decreasing* concentration of the diffusing specie. D is generally given in units of cm^2/s or m^2/s and for solids between 20 and 1500 °C, 10^{-20} $cm^2/s < D < 10^{-4}$ cm^2/s.

Fick's second law gives a relation between the concentration gradient and the rate of change of concentration caused by diffusion at a given point in the system:

$$\frac{\partial C}{\partial t} = -\nabla \cdot J = -\nabla \cdot D\nabla C,$$

which, in one-dimension simplifies to:

$$\frac{\partial C}{\partial t} = -\frac{\partial}{\partial x}\left(D\frac{\partial C}{\partial x}\right). \tag{4.26}$$

If D is not a function of the concentration, then we can write Eq. (4.26) as:

$$\begin{aligned}\frac{\partial C}{\partial t} &= -D\nabla^2 C \\ &= -D\frac{\partial^2 C}{\partial x^2}.\end{aligned} \tag{4.27}$$

Equations (4.26) or (4.27) can be solved for certain limiting conditions enabling D to be determined on the basis of various measurements.

While Fick's laws provide a description of diffusion on the macroscopic scale, we would like to understand diffusion on the microscopic level as well. Diffusion occurs by several possible mechanisms depending on the nature of the diffusing specie and the host lattice. We will examine these mechanisms and then derive a description of diffusion on the microscopic level.

4.3.2 Mechanisms of Diffusion

To obtain a theoretical description of diffusion, we first consider the elementary act of a jump of an atom from one stable position to another in the lattice. There are several mechanisms of lattice diffusion, some requiring the presence of defects, others not. The following types [5] can be distinguished.

Exchange and ring mechanisms: The exchange mechanism (Fig. 4.12) consists of the exchange of lattice positions involving two atoms located in adjacent crystal sites. It does not require the presence of defects, and it is highly improbable in close-packed crystals since it requires considerable deformation and hence an enormous activation energy. The ring mechanism (Fig. 4.13) is less energy

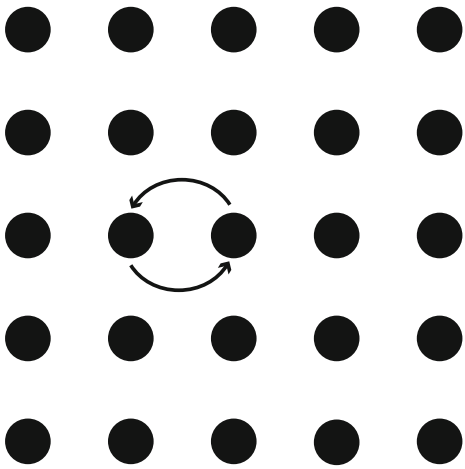

Fig. 4.12 Exchange mechanism of diffusion

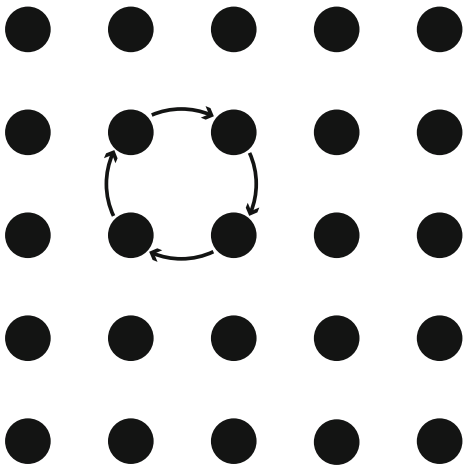

Fig. 4.13 Ring mechanism of diffusion

intensive but requires the coordinated movement of three to five atoms. Since the probability of this is low and the energy required is still high, both the exchange and ring mechanisms are unimportant in crystals containing defects.

Vacancy mechanism: This is the simplest mechanism of diffusion and occurs in metals and alloys (Fig. 4.14). Diffusion occurs by the jump of an atom from its lattice site to a vacant site. For an atom to move by this mechanism, the presence of a neighboring vacancy is required. Since movement of the vacancy is opposite that of the atom, vacancy-type diffusion is regarded as either a movement of the atom or the equivalent movement of the vacancy. However, as we will see, the diffusion coefficient for vacancy diffusion is *not* equal to that for atom diffusion.

Interstitial mechanism: This mechanism involves the movement of an atom from one interstitial position to another (Fig. 4.15). It requires considerable energy in

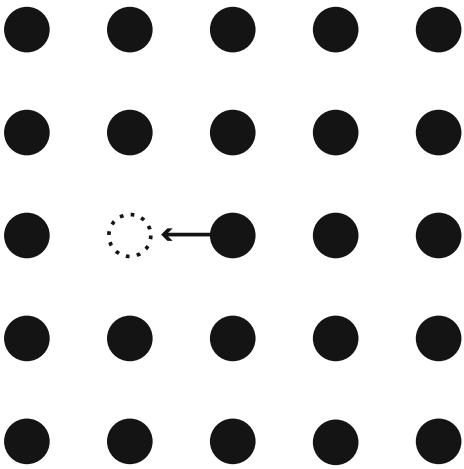

Fig. 4.14 Vacancy mechanism of diffusion

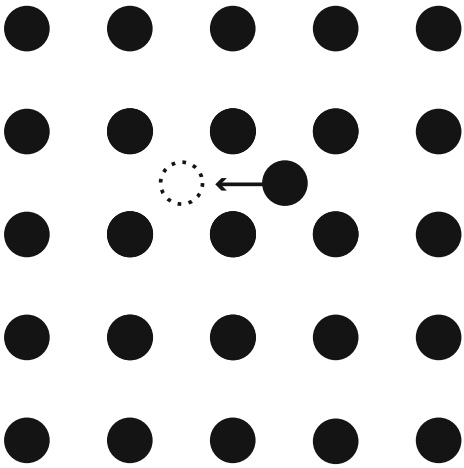

Fig. 4.15 Interstitial mechanism of diffusion

order to push its way through the barrier atoms separating the interstitial sites in the crystal (recall the role of barrier atoms in our calculation of displacement energy in Chap. 2). In reality, this mechanism only occurs when the diffusing species is of an atom type that is smaller than the host lattice atoms.

Interstitialcy mechanism: This mechanism involves the displacement of nearby lattice atoms to an interstitial site and generally occurs when atom diameters are comparable. There are two variants of this mechanism: the collinear variant in which displaced atoms move along a straight line (Fig. 4.16(a)) and the non-collinear variant in which the displaced atom moves to the interstitial position at an angle to the direction of movement of the displacing atom (Fig. 4.16(b)).

Dumbbell interstitial mechanism: This process involves the symmetrical placement of an interstitial and a lattice atom about a single lattice site such that they

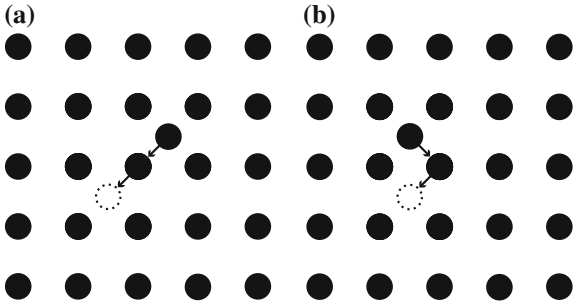

Fig. 4.16 Interstitialcy mechanism of diffusion (**a**) collinear variant and (**b**) non-collinear variant

share the lattice site. Figure 4.17 shows a 2D schematic of the sharing of a single lattice site by two atoms. Recall from our discussion in Sect. 4.1 that the dumbbell is a very stable configuration for the interstitial and that there are preferred directions for the dumbbell that depend on the lattice, and minimize the energy.

Crowding (*crowdion*) *mechanism*: This mechanism occurs when an atom is added to a lattice plane, but it does not reside in an interstitial position. To accommodate the atom, lattice atoms over, perhaps, 10 lattice constants are all shifted with respect to their lattice sites. The configuration can be thought of as a dumbbell spread over 10 atoms along a row, rather than two (Fig. 4.18). Actually, we have already seen a crowdion in our discussion of focusing collisions. Re-examine Fig. 3.4 and you will see a crowdion emanating from the displacement spike. This configuration is not a stable configuration and exists only temporarily as the energy for the knock-on atoms is expended.

Despite the numerous mechanisms for diffusion of atoms in a solid, diffusion usually occurs by either the vacancy or interstitialcy mechanisms. Ultimately, we want to obtain a mathematical relation between the macroscopic parameters for diffusion (i.e., the self-diffusion coefficient) and the elementary acts of defect jumps represented by the coefficients of diffusion for defects, or the microscopic process. We will assume that the self-diffusion process consists of a completely random walk of defects, i.e., there is no correlation between successive jumps of the defects.

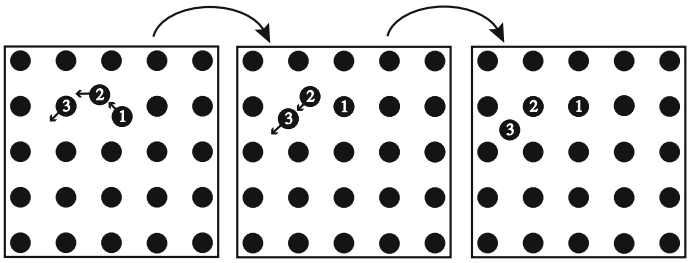

Fig. 4.17 Dumbbell interstitial mechanism of diffusion

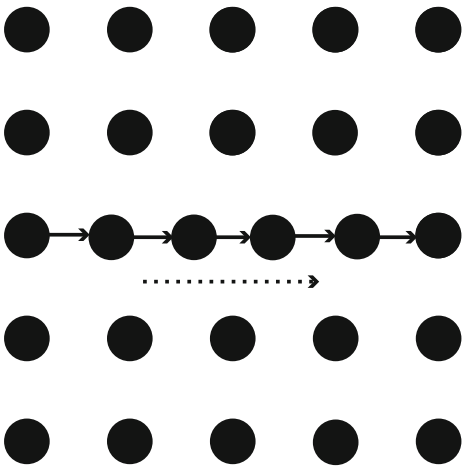

Fig. 4.18 Crowdion mechanism of diffusion

Although this is reasonable for defect diffusion, it is not strictly true for atom diffusion. As mentioned earlier, jumps of defects and hence, atoms, are due to thermal vibrations of very high frequency. The Debye frequency is $\sim 10^{13}\ \mathrm{s}^{-1}$. The frequency of atom jumps is orders of magnitude lower, $\sim 10^{8}\ \mathrm{s}^{-1}$ at say, 700 °C. This means that once every 10^5 vibrations, a thermal fluctuation is large enough for an atom to overcome the energy barrier separating it from the next stable position. Let us take a closer look at the jumping process.

4.3.3 Microscopic Description of Diffusion

Suppose that at time zero, a single impurity atom is placed in a position in a crystal which is designated as the origin. The atom proceeds to jump from one site to another in a completely random manner. Each jump is of distance λ, but since the medium is assumed to be isotropic, each jump is arbitrary and independent of previous jumps. After a time t, the displacement, r, of the particle from the origin is measured. If the experiment is repeated several times, r will not be the same because of the stochastic nature of the process. Rather, the displacements will be distributed according to a function $P_t(r)$ where $P_t d^3 r$ is the probability of finding the atom in a volume element $d^3 r$ a distance r from the origin after time t. The quantity that best describes the extent of migration is the mean square displacement, $\overline{r^2}$, which is given by the second moment of the distribution:

$$\overline{r^2} = \int_{\text{all space}} r^2 P_t(r) d^3 r = 4\pi \int_0^\infty r^4 P_t(r) dr. \tag{4.28}$$

We will first compute $\overline{r^2}$ without knowledge of $P_t(r)$.

If the atom makes Γ jumps per unit time, the time interval t corresponds to a number of n jumps given by:

$$n = \Gamma t. \tag{4.29}$$

Each jump is represented by a vector $\underline{\lambda_i}$, where the subscript, i, refers to the jump number. The vectors are all of the same length, λ_i, but of random direction. The position of the diffusing atom after n jumps (Fig. 4.19) is the vector sum of the $\underline{\lambda_i}$ or:

$$\underline{r} = \underline{\lambda}_1 + \underline{\lambda}_2 + \underline{\lambda}_3 \ldots + \underline{\lambda}_n. \tag{4.30}$$

The magnitude of the square of the displacement is obtained by taking the scalar product of $\underline{r}$ with itself:

$$r^2 = \underline{r} \cdot \underline{r} = (\underline{\lambda}_1 + \underline{\lambda}_2 + \underline{\lambda}_3 \ldots + \underline{\lambda}_n) \cdot (\underline{\lambda}_1 + \underline{\lambda}_2 + \underline{\lambda}_3 \ldots + \underline{\lambda}_n). \tag{4.31}$$

The scalar product of two sums is equivalent to squaring the sums, giving:

$$r^2 = \sum_{i=1}^{n} \underline{\lambda}_i \cdot \underline{\lambda}_i + 2 \sum_{i=1}^{n-1} \sum_{j \neq i}^{n} \underline{\lambda}_i \cdot \underline{\lambda}_j. \tag{4.32}$$

The first term is equal to $n\lambda^2$ and the second term can be rewritten as:

$$\underline{\lambda}_i \cdot \underline{\lambda}_j = \lambda^2 \cos \theta_{ij}, \tag{4.33}$$

and

$$r^2 = n\lambda^2 + 2\lambda^2 \sum_{i=1}^{n-1} \sum_{j \neq i}^{n} \cos \theta_{ij}, \tag{4.34}$$

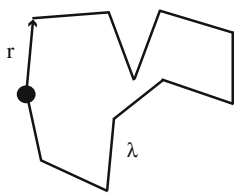

Fig. 4.19 Random jump of a defect in an isotropic solid

or

$$r^2 = n\lambda^2\left(1 + \frac{2}{n}\sum_{i=1}^{n-1}\sum_{j\neq i}^{n}\cos\theta_{ij}\right). \tag{4.35}$$

The mean square displacement is obtained by averaging r^2 over a large number of experiments. The term $\cos\theta_{ij}$ can range from -1 to 1, and by nature of the random hopping process, the average value of $\cos\theta_{ij}$ for any $i\,j$ combination is zero. Hence, the last term disappears and:

$$\overline{r^2} = n\lambda^2, \tag{4.36}$$

or

$$\overline{r^2} = \lambda^2\Gamma t. \tag{4.37}$$

Equation (4.37) relates the mean square displacement to the microscopic properties of jump distance and jump frequency. Now, we wish to compute $\overline{r^2}$ from a macroscopic viewpoint.

At $t = 0$, N impurity atoms are introduced into a restricted region of a host crystal. As a consequence of diffusion (random hopping), the N atoms spread out from the origin in a manner described by $C(r, t)$ which is obtained by solving Fick's second law (assuming D is not a function of concentration):

$$\frac{\partial C}{\partial t} = D\frac{1}{r^2}\frac{\partial}{\partial r}\left(r^2\frac{\partial C}{\partial r}\right), \tag{4.38}$$

with initial condition $C(r, 0) = 0$, for $r \neq 0$. Since the N atoms remain in the crystal, $C(r, t)$ is subject to the constraint:

$$\int_0^\infty 4\pi r^2 C(r,t)\mathrm{d}r = N, \tag{4.39}$$

with boundary condition that the concentration drops to 0 at infinity, $C(\infty, t) = 0$. The solution to Eq. (4.38) subject to the initial and boundary conditions becomes:

$$C(r,t) = N\frac{\exp(-r^2/4Dt)}{(4\pi Dt)^{3/2}}. \tag{4.40}$$

The probability of finding the single atom in a spherical shell between r and $r + \mathrm{d}r$ after time t is equivalent (in the macroscopic diffusion description of the

problem) to the fraction of the N atoms located in the same volume element after time t. $P_r(r)$ and $C(r, t)$ are related by:

$$P_t(r) = \frac{C(r,t)}{N} = \frac{\exp(-r^2/4Dt)}{(4\pi Dt)^{3/2}}. \tag{4.41}$$

The mean square displacement is:

$$\begin{aligned} \overline{r^2} &= 4\pi \int_0^\infty r^4 P_t(r) \mathrm{d}r \\ &= \frac{4\pi}{(4\pi Dt)^{3/2}} \int_0^\infty r^4 \exp\left(-r^2/4Dt\right) \mathrm{d}r, \end{aligned} \tag{4.42}$$

or

$$\overline{r^2} = 6Dt. \tag{4.43}$$

Comparing to $\overline{r^2} = \lambda^2 \Gamma t$ from our microscopic solution Eq. (4.37), we have:

$$D = \frac{1}{6}\lambda^2 \Gamma \tag{4.44}$$

which is the Einstein formula and is the link between the microscopic diffusion parameters λ and Γ, and the macroscopic diffusion parameter, D.

4.3.4 Jump Frequency, Γ

We define Γ as the total number of jumps per second for an atom. Therefore, in a time increment δt, we expect $\Gamma \delta t$ jumps. The quantity $\Gamma \delta t$ is proportional to z, the number of nearest neighbors (sites), p_v, the probability that a given neighboring site is vacant, and ω, the frequency with which an atom jumps to a particular site. Thus, the frequency with which an atom jumps to any neighboring equilibrium site, Γ, is the product of the jump frequency to a single site, ω, the number of nearest neighbor sites, z, and the probability that one site is vacant, p_v or:

$$\Gamma = z p_v \omega, \tag{4.45}$$

and

$$D_{\mathrm{a}}^{\mathrm{v}} = \frac{1}{6} z \lambda^2 p_{\mathrm{v}} \omega, \tag{4.46}$$

where we have properly included the subscript, a and superscript, v to indicate that this is the diffusion coefficient for *atom diffusion* via vacancies. Also note that the jump distance λ is related to the lattice constant by $\lambda = Aa$, where the coefficient, A, depends on the diffusion mechanism and the crystal structure. The terms $\frac{1}{6} z A^2$ are often lumped together into a single parameter, α, such that:

$$D_{\mathrm{a}}^{\mathrm{v}} = \alpha a^2 p_{\mathrm{v}} \omega, \tag{4.47}$$

and if vacancy motion is random, then $p_{\mathrm{v}} = N_{\mathrm{v}}$ and:

$$D_{\mathrm{a}}^{\mathrm{v}} = \alpha a^2 N_{\mathrm{v}} \omega. \tag{4.48}$$

Let us look at an example of how to determine α for a specific diffusion process and crystal structure.

Example 4.2. Vacancy diffusion in the bcc and fcc lattices
In the case of the vacancy mechanism of diffusion in a bcc structure, each atom has eight nearest neighbors ($z = 8$). The jump distance is related to a by $A = \frac{\sqrt{3}}{2}$, and hence, $\alpha = 1$. For the simple interstitial diffusion mechanism in a bcc lattice, $z = 4$ and $A = \frac{1}{2}$ giving $\alpha = \frac{1}{6}$.

For the fcc lattice, $z = 12$ and $A = \frac{1}{\sqrt{2}}$, giving $\alpha = 1$. For interstitials in the fcc lattice, $z = 12$ and $A = \frac{1}{2}$, and $\alpha = \frac{1}{2}$.

Before continuing, it is instructive to point out the difference between vacancy diffusion and atom diffusion via a vacancy mechanism (vacancy self-diffusion). In determining the components of Γ, we noted that Γ depends on the probability, p_{v}, that a neighboring lattice site is vacant. This is a necessary condition for an atom jump via a vacancy. However, if we are following the migration of the vacancy, then Γ depends on the probability that a neighboring lattice site to the vacancy is filled by an atom. Since in all but the most extreme cases this probability is ~1, and the equation for vacancy diffusion is given as follows:

$$D_{\mathrm{v}} = \alpha a^2 \omega, \tag{4.49}$$

and differs from that for vacancy self-diffusion by the factor N_{v}.

4.3.5 *Jump Frequency, ω*

In calculating ω, we will ignore detailed atomic movements and instead deal in terms of "activated complexes" or regions containing an atom midway between two equilibrium sites (Fig. 4.20). The number of atoms diffusing per second is then obtained by multiplying the number of activated complexes (n_m) by the average velocity of the atoms moving through this barrier ($\bar{\upsilon}$) divided by the width of the barrier (δ). The jump frequency is then:

$$\omega = \frac{N_m \bar{\upsilon}}{\delta}, \tag{4.50}$$

where N_m is the mole fraction of activated complexes. The work done in moving an atom across this barrier is equal to the change in Gibbs free energy for the region, ΔG_m:

$$\Delta G_m = \Delta H_m - T\Delta S_m. \tag{4.51}$$

Using ΔG_m, the equilibrium mole fraction of atoms in the region of the saddle point in Fig. 4.20, N_m can be calculated; in the same way, we calculated N_v. Instead of mixing vacancies to raise the free energy by ΔG_v per mole, we are mixing complexes to raise the free energy an amount ΔG_m per mole. The ideal entropy of mixing is the same for vacancies as for complexes so, at equilibrium, n_m out of N atoms will be in the neighborhood of the saddle point at any instant and:

$$\frac{n_m}{N} = N_m = \exp\left(\frac{-\Delta H_m + T\Delta S_m}{kT}\right) = \exp\left(\frac{-\Delta G_m}{kT}\right). \tag{4.52}$$

From Eq. (4.50), $\omega = \frac{N_m \bar{\upsilon}}{\delta}$ and $\bar{\upsilon}/\delta$ is the frequency (call it ν) at which atoms at the saddle point jump to the new site. Thus, $n_m\nu$ out of N atoms will jump from one site to a given site per second, and the average jump frequency is:

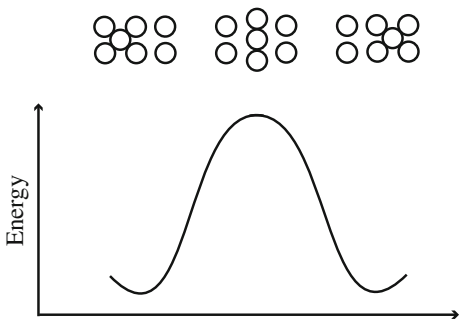

Fig. 4.20 Passage of the "activated complex" from one stable position, through a saddle point, to another stable position

$$\frac{n_m v}{N} = \omega = v \exp\left(\frac{-\Delta G_m}{kT}\right) = v \exp\left(\frac{-\Delta S_m}{k}\right) \exp\left(\frac{-\Delta H_m}{kT}\right)$$
$$= v \exp\left(\frac{S_m}{k}\right) \exp\left(\frac{-E_m}{kT}\right), \tag{4.53}$$

where v is the Debye frequency ($\sim 10^{13}$ s^{-1}) and $E_m = \Delta H_m$ and $S_m = \Delta S_m$.

A more precise treatment considers the fact that not all jump directions are equal and that inequality is reflected in the frequency. So-called multifrequency models are used to describe diffusion in dilute alloys [6]. For vacancy-atom jumps in fcc alloys, there are five frequencies of interest, as shown in Fig. 4.21. The solute atom, shown as shaded, will exchange with the vacancy with a jump frequency ω_2. Near to the solute atom, solvent atoms may have jump frequencies that are different from the value ω_0 characteristic of pure solvent. ω_1 is the frequency for solvent-vacancy jumps between a pair of sites that are both nearest neighbors of a solute. ω_3 is for vacancy jumps from first to more distant neighbor sites (second, third, or fourth) and are referred to as dissociative jumps. Finally, ω_4 is the frequency for the reverse, or associative jumps onto first neighbor sites. All other solvent-vacancy jumps are assumed to occur with the frequency ω_0. Thus, each jump frequency, ω_j, will have an Arrhenius-type temperature dependence with activation enthalpy, H_j, and pre-exponential factor, v_j, yielding equations of the form:

$$\omega_j = v_j \exp\left(\frac{-H_j}{kT}\right). \tag{4.54}$$

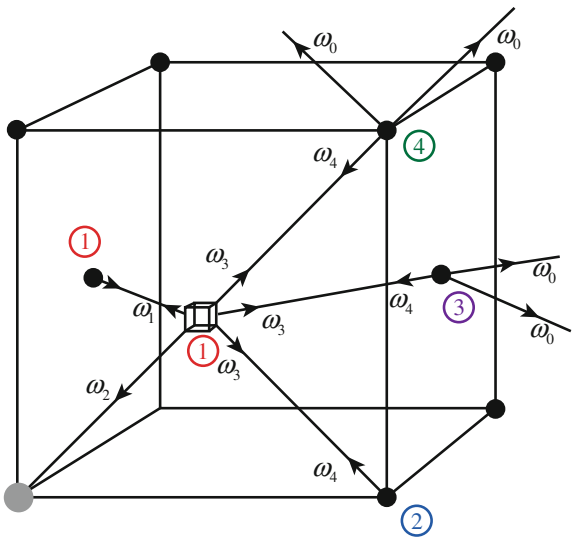

Fig. 4.21 Frequencies ω_j for vacancy-atom jumps in fcc crystals. The *arrows* indicate the direction the vacancy moves. The *circled numbers* indicate the order of neighbors to the solute atom at the origin (after [6])

4.3.6 *Equations for* D

We are now in a position to write the expressions for the diffusion coefficients for the motion of the defects and of the atoms by way of the defects.

1. The vacancy diffusion coefficient is given by:

$$D_{\mathrm{v}} = \alpha a^2 \omega,$$

where

$$\omega = v \exp\left(\frac{-\Delta G_{\mathrm{m}}^{\mathrm{v}}}{k\mathrm{T}}\right) = v \exp\left(\frac{S_{\mathrm{m}}^{\mathrm{v}}}{k}\right) \exp\left(\frac{-E_{\mathrm{m}}^{\mathrm{v}}}{kT}\right),$$

then

$$D_{\mathrm{v}} = \alpha a^2 \omega = \alpha a^2 v \exp\left(\frac{S_{\mathrm{m}}^{\mathrm{v}}}{k}\right) \exp\left(\frac{-E_{\mathrm{m}}^{\mathrm{v}}}{kT}\right). \tag{4.55}$$

2. The vacancy self-diffusion coefficient is the product of the vacancy diffusion coefficient and the probability that the nearest neighbor site is vacant, N_{v}:

$$D_{\mathrm{v}SD} = D_a^{\mathrm{v}} = \alpha a^2 N_{\mathrm{v}} \omega,$$

where

$$N_{\mathrm{v}} = \exp\left(\frac{-\Delta G_{\mathrm{f}}^{\mathrm{v}}}{kT}\right) = \exp\left(\frac{S_{\mathrm{f}}^{\mathrm{v}}}{k}\right) \exp\left(\frac{-E_{\mathrm{f}}^{\mathrm{v}}}{kT}\right),$$

giving

$$D_{\mathrm{vSD}} = D_{\mathrm{a}}^{\mathrm{v}} = \alpha a^2 v \exp\left(\frac{S_{\mathrm{f}}^{\mathrm{v}} + S_{\mathrm{m}}^{\mathrm{v}}}{k}\right) \exp\left(\frac{-E_{\mathrm{f}}^{\mathrm{v}} - E_{\mathrm{m}}^{\mathrm{v}}}{kT}\right). \tag{4.56}$$

3. The interstitial diffusion coefficient is:

$$D_{\mathrm{i}} = \alpha a^2 \omega,$$

or

$$D_{\mathrm{i}} = \alpha a^2 v \exp\left(\frac{S_{\mathrm{m}}^{\mathrm{i}}}{k}\right) \exp\left(\frac{-E_{\mathrm{m}}^{\mathrm{i}}}{kT}\right). \tag{4.57}$$

4. The interstitial self-diffusion coefficient is the interstitial diffusion coefficient times the probability that a neighboring site contains an interstitial, N_i:

$$D_a^i = \alpha a^2 N_i \omega,$$

where

$$N_i = \exp\left(\frac{-\Delta G_f^i}{kT}\right) = \exp\left(\frac{S_f^i}{k}\right)\exp\left(\frac{-E_f^i}{kT}\right),$$

giving

$$D_a^i = \alpha a^2 \nu \exp\left(\frac{S_f^i + S_m^i}{k}\right)\exp\left(\frac{-E_f^i - E_m^i}{kT}\right). \tag{4.58}$$

The diffusion coefficients are all different in detail, but similar in form as they consist of two factors: a constant that is independent of temperature and an exponential of temperature containing an energy term. All equations for D can be rewritten in the form:

$$D = D_0 \exp(-Q/kT), \tag{4.59}$$

where $D_0 = \alpha a^2 \nu$ is the temperature-independent term and Q is the activation energy. For vacancy diffusion, we have:

$$Q_v = E_m^v, \tag{4.60}$$

and for vacancy self-diffusion we have:

$$Q_a^v = E_f^v + E_m^v. \tag{4.61}$$

For interstitials, we have:

$$Q_i = E_m^i, \tag{4.62}$$

and for interstitial self-diffusion, we have:

$$Q_a^i = E_f^i + E_m^i. \tag{4.63}$$

It follows that the activation energy for diffusion of atoms in a crystal depends on both the energy of formation of defects and the energy required for their migration in the periodic field of the crystal lattice. Experiments can be conducted to confirm the temperature dependence of D and also the values of Q. The terms in the pre-exponential factor for the various diffusion mechanisms are provided in Table 4.2 for the fcc and bcc lattices.

Table 4.2 Parameters in the expression for the diffusion coefficient, $D = \alpha a^2 N \omega$, where $\alpha = \frac{1}{6} z A^2$ for the various diffusion mechanisms in the fcc and bcc lattices

Diffusion mechanism	z	A	α	N	D
fcc					
Vacancy	12	$1/\sqrt{2}$	1	1	$a^2\omega$
Vacancy self-diffusion	12	$1/\sqrt{2}$	1	N_V	$a^2 N_v \omega$
Interstitial	12	1/2	1/2	1	$\frac{1}{2}a^2\omega$
Interstitial self-diffusion	12	1/2	1/2	N_i	$\frac{1}{2}a^2 N_i \omega$
bcc					
Vacancy	8	$3/\sqrt{2}$	1	1	$a^2\omega$
Vacancy self-diffusion	8	$3/\sqrt{2}$	1	N_v	$a^2 N_v \omega$
Interstitial	4	1/2	1/6	1	$\frac{1}{6}a^2\omega$
Interstitial self-diffusion	4	1/2	1/6	N_i	$\frac{1}{6}a^2 N_i \omega$

Example 4.3. Determination of D_a^v and D_a^i for fcc copper at 500 °C
For copper:

$$\begin{aligned} E_f^v &= 1.27 \text{ eV}, \quad E_f^i = 2.2 \text{ eV} \\ E_m^v &= 0.8 \text{ eV}, \quad E_m^i = 0.12 \text{ eV} \\ S_f^v &= 2.4k, \quad\quad S_f^i = \sim 0 \end{aligned}$$

and we neglect S_m^v and S_m^i.
For the fcc lattice, $z = 12$, $A = 1/\sqrt{2}$, and $a \sim 0.3$ nm, giving:

$$\begin{aligned} D_v &= \alpha a^2 v \exp\left(\frac{-0.8}{kT}\right) \\ &\cong 5 \times 10^{-6} \text{ cm}^2/\text{s} \\ D_i &= \alpha a^2 v \exp\left(\frac{-0.12}{kT}\right) \\ &\cong 7 \times 10^{-2} \text{ cm}^2/\text{s} \\ D_a^v &= \alpha a^2 v \exp\left(\frac{2.4k}{k}\right) \exp\left(\frac{-1.27 - 0.8}{kT}\right) \\ &\cong 3 \times 10^{-13} \text{ cm}^2/\text{s} \\ D_a^i &= \alpha a^2 v \exp\left(\frac{-2.2 - 0.12}{kT}\right) \\ &\cong 3 \times 10^{-16} \text{ cm}^2/\text{s} \end{aligned}$$

Note that while $D_i/D_v \sim 10^4$ due to the smaller migration energy for interstitials than for vacancies, $D_a^i/D_a^v \sim 10^{-3}$ because of the very high interstitial formation energy compared to that for vacancies. Plots of the

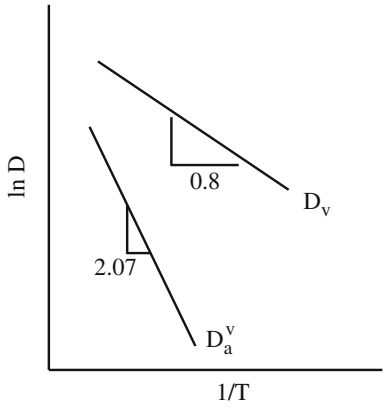

Fig. 4.22 Comparison of plots of ln D versus $1/T$ for vacancy diffusion and vacancy self-diffusion

diffusion coefficients are shown in Fig. 4.22. Note that the vacancy diffusion coefficient is larger than the vacancy self-diffusion coefficient and has a smaller slope.

The behavior of self-interstitial atoms in bcc iron at 323 °C is illustrated in Movie 4.3 (http://rmsbook2ed.engin.umich.edu/movies/). In this movie, the green balls are the interstitials and the red ball is the vacant lattice site, and together they form a SIA dumbbell in which the two green atoms share a single lattice site. The SIA originates as a ⟨110⟩ split-dumbbell interstitial and then rotates into a ⟨111⟩ interstitial and moves in one-dimension through the ⟨111⟩ crowdion saddle position. Movie 4.4 shows a di-SIA consisting of two parallel ⟨111⟩ split-dumbbells that migrates along the ⟨111⟩ direction and also rotates to different ⟨111⟩-type orientations.

4.4 Correlated Diffusion

Earlier we assumed that irrespective of the kinds of defects present in a crystal lattice, successive jumps of atoms are completely random or uncorrelated. This means that after n jumps, all possible directions for the $(n + 1)$th jump are equally probable. This is true for vacancies or interstitials since all structural elements surrounding them are at all times identical. Since the vibrational frequency of a lattice atom is several orders of magnitude greater than the jump frequency, equilibrium in the region surrounding the defect is rapidly established between successive jumps and the next jump occurs with no effect of the previous jump on its direction. But this does not always hold true for atom diffusion as described in [5] and in the following.

If we consider the case of a radioactive tracer to track atom diffusion, a tracer will make a jump if a vacancy is in its immediate vicinity. The second jump is uncorrelated with the first if the probability of the second jump is the same for all directions. However, the tracer arrives from a position that is vacant at the time of its arrival. Hence, when it is "preparing" for the next jump, the chance that the position from which it has arrived is unoccupied is greater than for any other position around the atom. The two jumps are correlated since the probability of the tracer returning to its former position is higher than for making a jump in any other direction. In other words, the tracer has a greater tendency to move in the direction from which it came than in the direction it is headed, or from Eq. (4.35), $\overline{\cos\theta_2} < 0$.

Since jumps in the direction from which it came are most probable, the tracer will have traveled a shorter (net) distance than that traveled by the vacancy. Therefore, the self-diffusion coefficient of the tracer (which is a measure of the rate of this process) is smaller than that of the atoms constituting the lattice, since the self-diffusion of the tracer is a correlated random walk, whereas the movement of the vacancies and consequently of the atoms constituting the lattice are not correlated.

The correlation effect is absent in the simple interstitial mechanism, but there is correlation of motion by the interstitialcy mechanism. In both, the vacancy and the interstitialcy mechanisms, $D_{\text{tracer}} < D_{\text{lattice}}$, and:

$$f = \frac{D_{\text{tracer}}}{D_{\text{lattice}}}, \tag{4.64}$$

and f is known as the *Haven coefficient* and is a measure of the degree to which diffusion is random. Recall our earlier discussion of the measurement of the square of the displacement by random walk given by Eq. (4.35):

$$r^2 = n\lambda^2\left(1 + \frac{2}{n}\sum_{i=1}^{n-1}\sum_{j\neq i}^{n}\cos\theta_{ij}\right),$$

where the mean square displacement is obtained by averaging over all values of $\cos\theta_{ij}$. In this expression, the term in brackets is f and the value of f for random walk is 1 since the average over all $\cos\theta_{ij}$ is 0. But when there is correlation between successive jumps, f is $\neq 1$. For the vacancy mechanism of diffusion of a tracer in a regular lattice [5]:

$$f_{\text{v}} = \frac{1 + \overline{\cos\theta}}{1 - \overline{\cos\theta}}, \tag{4.65}$$

and for interstitial diffusion,

$$f_i = 1 + \overline{\cos\theta}. \tag{4.66}$$

Since in both cases, $\overline{\cos\theta} < 0$, then $f < 1$.

A simpler treatment of f_v is that $f_v = \dfrac{1-P}{1+P}$, where P is the probability of a jump of a tracer to a neighboring vacancy, and $1 - P$ is the probability that a neighboring vacancy will move away as a result of jumps of lattice atoms. To a first approximation, P is equal to the reciprocal of the number of nearest lattice sites, z, around the tracer. Therefore:

$$f = \frac{1-1/z}{1+1/z} = \frac{z-1}{z+1}. \tag{4.67}$$

For the fcc lattice:

$$f = \frac{1-1/12}{1+1/12} = \frac{12-1}{12+1} = 0.85.$$

For the bcc lattice:

$$f = \frac{1-1/8}{1+1/8} = \frac{8-1}{8+1} = 0.78.$$

For the simple cubic (sc) lattice:

$$f = \frac{1-1/6}{1+1/6} = \frac{6-1}{6+1} = 0.71.$$

So, in our microscopic description of the diffusion coefficient, D, Eq. (4.44), we account for correlated diffusion by including the correlation coefficient:

$$D = 1/6 f \lambda^2 \Gamma = f \alpha a^2 \omega. \tag{4.68}$$

As an aside, the true correlation coefficient, f, actually consists of two terms, f' and f'' such that $f = f'\,f''$. The quantity f'' was described in the previous paragraph (as f) and f' is related to the difference between the distances traveled during the elementary act by the tracer atom and the defect:

$$f' = \frac{\lambda_{\text{tracer}}}{\lambda_{\text{defect}}}. \tag{4.69}$$

In the case of a vacancy, $f' = 1$ since $\lambda_{\text{tracer}} = \lambda_{\text{vacancy}}$, or the distance traveled by the tracer and the defect are equal in one jump. The same is true for the simple interstitial mechanism. But in the case of the interstitialcy mechanism, the tracer

Table 4.3 Correlation coefficients for the most common diffusion mechanisms in the various crystal lattices (from [5])

Crystal lattice	Diffusion mechanism	Correlation factor
Simple cubic	Vacancy	0.65311
	Interstitial	
	Collinear	0.80000
	Non-collinear	0.96970
Face-centered cubic	Vacancy	0.72722
	Interstitial	
	Collinear	0.66666
	Non-collinear	0.72740
Body-centered cubic	Vacancy	0.72722
Hexagonal close-packed	Vacancy	0.78121

moves from an interstitial position to a lattice site (or vice versa). In both cases, it travels a distance λ_{tracer}. However, the passage of a lattice atom from an interstitial position to a lattice site is equivalent to the appearance of an identical atom displaced from the lattice site in a neighboring interstitial position. Therefore, the jump of a lattice atom from the interstitial position to a lattice site requires (for the collinear case) a displacement of the lattice atom by a distance $2\lambda_{\text{tracer}}$, or $f' = \lambda_{\text{tracer}}/2\lambda_{\text{tracer}} = 0.5$. For the non-collinear case, $f' = \lambda_{\text{tracer}}/6\lambda_{\text{tracer}} = 2/3$. Table 4.3 summarizes the correlation coefficient for various diffusion mechanisms in the common crystal lattices.

4.5 Diffusion in Multicomponent Systems

Our discussion on diffusion so far has applied only to pure or single-component systems. We have not accounted for multiple components such as impurities in a pure metals and alloys. Diffusion in these systems was treated in experiments conducted by Smigelskas and Kirkendall in 1947 [7] and analyzed by Darken in 1948 [8]. The result is that the diffusion coefficients of the two components in a binary (A–B) system can be expressed as:

$$\tilde{D} = D_{\text{A}} N_{\text{B}} + D_{\text{B}} N_{\text{A}}, \tag{4.70}$$

where $D_{\text{A,B}}$ are the intrinsic diffusion coefficients and are functions of composition, and $\tilde{D}$ is the interdiffusion coefficient. Since the partial diffusion coefficients depend on the alloy composition, $\tilde{D}$ is a complex, nonlinear function of concentration. However, in the case of dilute solutions ($N_{\text{B}} \rightarrow 0$, $N_{\text{A}} \rightarrow 1$), the interdiffusion coefficient is approximately equal to the partial diffusion coefficient of the solute.

The significance of this result can be appreciated by a brief review of the elegance and implications of the experiment. In Kirkendall's experiment,

molybdenum wires were wound around a block of brass (70Cu–30Zn) which was then plated with a thick coating of copper. The molybdenum wires are insoluble in copper and act as inert markers to locate the original interface. When the assembly is heated in a furnace, the wire markers on opposite sides of the brass moved toward each other, indicating that more material has left the brass than entered it, implying that the diffusion coefficient of zinc is greater than that of copper.

The vacancy mechanism is the only diffusion mechanism that can account for marker motion. If zinc diffuses by a vacancy mechanism, then the flux of zinc atoms in one direction must equal the flux of vacancies in the opposite direction and the number of zinc atoms leaving the brass is balanced by an equal number of vacancies entering the brass. But the vacancies are absorbed by internal sinks, so the result is that the volume of the brass diminishes and the markers move closer together. The concept of a flux of atoms giving rise to a flux of defects will be explored in depth in Chap. 6 on Radiation-Induced Segregation, which occurs by the *inverse* Kirkendall effect.

4.6 Diffusion Along High-Diffusivity Paths

Metals and alloys used as structural engineering materials are polycrystals and are thus, inhomogeneous, as they contain grain boundaries, dislocations, internal interfaces due to precipitates or second phases, etc. To understand diffusion in these systems, we must discuss the effect of these linear, planar and area defects on the diffusion process. The primary difference between mono- and polycrystals is that the latter consists of aggregates of crystals oriented (generally) at random. This latter type of structure rarely shows anisotropy of diffusion. The important difference is that linear and planar defects represent high-diffusivity paths along which diffusion can occur much faster than via point defects (bulk diffusion).

Grain boundaries are important high-diffusivity paths since the atom packing density is lower. There exist several models of grain boundary diffusion, and all assume that the boundary has a width, $\delta \sim 0.3–0.5$ nm. One model that is based on the dislocation model of grain boundaries deserves special attention. In this model, the grain boundary is regarded as a number of edge dislocations. The dislocation density (#/unit length) increases with increasing misorientation angle, θ, between two grains in contact (Fig. 4.23). From the figure:

$$d \sin\frac{\theta}{2} = \frac{b}{2}. \tag{4.71}$$

Hence, the distance between neighboring dislocations decreases with increasing misorientation angle. A low-angle grain boundary consisting of many edge dislocations can be regarded as a row of parallel channels in which packing of atoms is loosest. In this region, the strain is high and the packing of atoms is loose, and the diffusion coefficient will be the highest along the dislocation lines (cores).

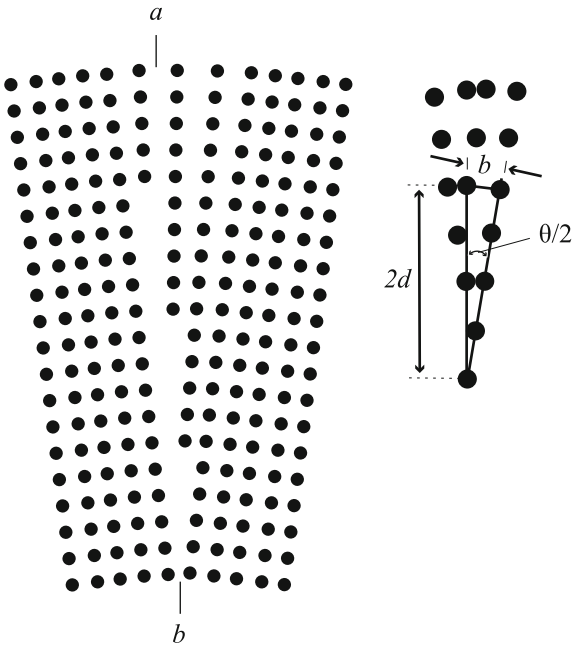

Fig. 4.23 Dislocation model of a small-angle grain boundary and the geometrical relationship between the angle of tilt, θ, the Burgers vector, b, and the spacing between the dislocations, d

According to this model, diffusion along grain boundaries should be anisotropic and depends on the angle θ. The grain boundary described as a slab of uniform thick δ, and diffusion coefficient D_{gb} can also be viewed as a planar array of pipes of radius p and spacing d. Grain boundary diffusion is related to diffusion along dislocation cores (also known as *pipe diffusion*), described by D_p, by the following relation:

$$D_{gb}\delta = D_p\left(\pi p^2/d\right), \tag{4.72}$$

and substituting for d from Eq. (4.71) gives:

$$\begin{aligned} &= D_p \pi p^2 \left(\frac{2\ \sin\theta/2}{b}\right) \\ &\cong \frac{D_p \pi p^2 \theta}{b}. \end{aligned} \tag{4.73}$$

The dislocation model of the grain boundary shown in Fig. 4.23 is expanded in Fig. 4.24 to show that the extra half-planes of atoms can be regarded as edge dislocations. In fact, the rate of diffusion along the grain boundary increases with increasing misorientation angle, θ, and reaches a maximum at $\theta = 45°$ (Fig. 4.25). At angles greater than 45°, the dislocation model of grain boundaries breaks down since the distance between dislocations, d, would have to be smaller than the lattice constant.

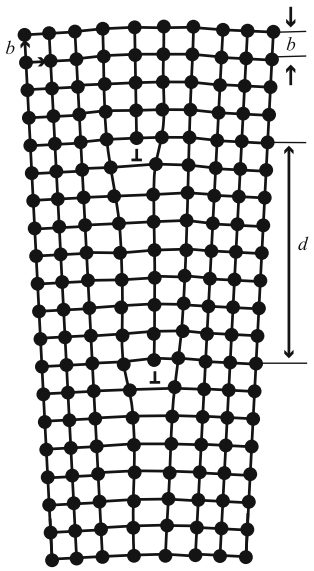

Fig. 4.24 Expanded view of the dislocation model of the grain boundary shown in Fig. 4.23

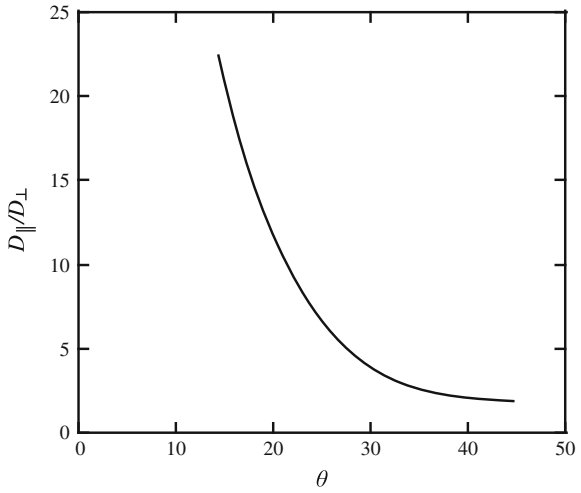

Fig. 4.25 Effect of grain boundary misorientation angle on the diffusion of atoms along grain boundaries (after [5])

This result also indicates that there should be a relationship between the mean value of the diffusion coefficient, $\bar{D}$, in a polycrystalline material and the grain size, d, since as the grain size decreases, the grain boundary area per unit volume increases. Therefore, $\bar{D}$ should increase with decreasing grain size as shown in Fig. 4.26. We can write the diffusion coefficient of a solid in which diffusion occurs by bulk diffusion (vacancy mechanism) and grain boundary diffusion as:

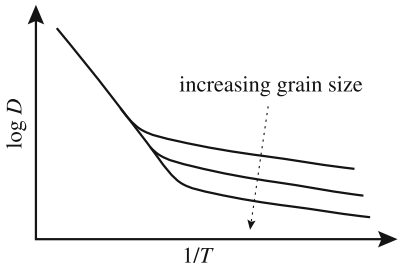

Fig. 4.26 The effect of grain size on the character of diffusion in polycrystalline solids

$$\bar{D} = D_{\mathrm{a}}^{\mathrm{v}} \exp\left(\frac{-Q_{\mathrm{a}}^{\mathrm{v}}}{kT}\right) + D_{\mathrm{gb}} \exp\left(\frac{-Q_{\mathrm{gb}}}{kT}\right), \tag{4.74}$$

where $D_{\mathrm{a}}^{\mathrm{v}}$ and $Q_{\mathrm{a}}^{\mathrm{v}}$ refer to vacancy self-diffusion, and D_{gb} and Q_{gb} refer to grain boundary diffusion. In most metals, $Q_{\mathrm{a}}^{\mathrm{v}} \sim 2Q_{\mathrm{gb}}$, so at low temperature, grain boundary diffusion dominates and at high temperature, diffusion is dominated by bulk, or volume diffusion (Fig. 4.26).

Pipe diffusion along dislocation cores can also influence low temperature lattice diffusion and the total diffusion coefficient can be estimated simply by:

$$\bar{D} = gD_{\mathrm{p}} + (1-g)D_{\mathrm{a}}^{\mathrm{v}}, \tag{4.75}$$

where $\bar{D}$ is the mean diffusion coefficient, D_{p} is the diffusion coefficient for dislocations and $D_{\mathrm{a}}^{\mathrm{v}}$ is the self-diffusion coefficient, and g is the fraction of time that the diffusing atom spends within the dislocation. As the dislocation density increases, g increases, and since $D_{\mathrm{p}} > D_{\mathrm{a}}^{\mathrm{v}}$, then $\bar{D}$ increases as well.

This general formulation can also be applied to interface or surface diffusion occurring on internal and external surfaces of solids. In general, for defects in the lattice, the more loosely bound the atoms, the lower is the activation energy and the higher is the diffusion coefficient. So surface diffusion requires a lower activation energy than for other forms of diffusion since each surface atom has only half the nearest neighbors as it does in the bulk, and generally:

$$Q_{\mathrm{surface}} < Q_{\mathrm{gb}} < Q_{\mathrm{p}} < Q_{\mathrm{a}}^{\mathrm{v}}, \quad \text{and so} \quad D_{\mathrm{surface}} > D_{\mathrm{gb}} > D_{\mathrm{p}} > D_{\mathrm{a}}^{\mathrm{v}}. \tag{4.76}$$

Nomenclature

a	Lattice constant
A	Factor depending on geometry and diffusion mechanism
C	Concentration
D_x^y	Diffusion coefficient of species x via y
D_{gb}	Diffusion coefficient for grain boundary diffusion

$\tilde{D}$ Interdiffusion coefficient
$\bar{D}$ Mean value of diffusion coefficient in a polycrystalline material
D_{lattice} Diffusion coefficient of lattice atom
D_{p} Diffusion coefficient for pipe diffusion
D_{tracer} Diffusion coefficient of tracer atom
E Energy
f Correlation (Haven) coefficient
F Helmholtz free energy
g Fraction of time a diffusing specie spends within a dislocation
G Gibbs free energy
H Enthalpy
J Flux [cm^{-2}]
k Boltzmann's constant
n Number of defects
n_{m} Number of activated complexes
N Number of sites
p_{v} Probability that a lattice site is vacant
P Pressure, also probability
Q Activation energy
R Radius
r_{a} Radius of an atom
S Entropy
T Temperature
U Internal energy
V Volume
z Number of nearest neighbors
α $\frac{1}{6}zA^2$
δ Width of the barrier in an activated complex, also grain boundary width
γ Stacking fault energy
Γ Jump frequency
κ_{r} Thermal conductivity
Λ Jump distance
μ Shear modulus
ν Frequency, also Poisson's ratio
ν_{E} Natural frequency of an oscillator
ν_{r} Perturbed frequency of an oscillator
σ Surface energy
$\bar{v}$ Average velocity of atoms moving through barrier in activated complex, Eq. (4.50)
ω Jump frequency to a single site
Ω Volume of an atom

Subscripts

a Atom
E Natural contribution to v
f Formation
gb Grain boundary
i,v Interstitials, vacancies
m Migration
p Pipe
r Vibrational contribution to v
th Thermal

Superscripts

FP Frenkel pair
i,v Interstitials, vacancies
mix Mixing

Acronyms

SIA Single interstitial atom

Problems

4.1 Many metals occur with both bcc and fcc structure, and it is observed that the transition from one structure to the other involves only insignificant volume change. Assuming *no* volume change, find the ratio D_{fcc}/D_{bcc} where D_{fcc} and D_{bcc} are the closest distances between metal atoms in the respective structures.

4.2 For a Ni lattice, calculate the following parameters for atomic chains along the (110) direction:

(a) the number of atoms per unit chain length,
(b) the number of chains per unit area, and
(c) the product of the two. What is this product?

4.3 In the past, investigators have sometimes considered an interstitial atom as having been produced by the transfer of an atom from a normal lattice site to an interstitial site, thus resulting in a one-to-one correspondence between the concentrations of vacancies and interstitials. However, the equilibrium number of vacancies is generally orders of magnitude greater than the equilibrium number of interstitials at a given temperature. Explain.

4.4 The magnitude of the relaxation volume, $|V|$, is greater than 1.0 for interstitials and is less than 1.0 for vacancies. Explain.

4.5 In terms of the jump frequency to a particular neighboring site, ω, and the lattice constant, a, what is the diffusion coefficient for impurity atoms whose equilibrium position is the octahedral interstitial site in:

(a) the fcc lattice?
(b) the bcc lattice?

4.6 Consider a rigid crystal in the shape of a sphere of radius R. We create a small cavity of radius r (one atomic volume) in the center of the sphere. The material that was in this volume is spread uniformly over the surface of the sphere (assuming this can be done), increasing the radius of the sphere to R'.

(a) Show that for an atomic radius of 0.15 nm and an intrinsic surface energy, $\sigma \sim 10$ eV/nm^2, the formation energy of a vacancy is of order $\simeq$2 eV
(b) If instead of a rigid solid, the crystal is treated as an elastic continuum, how would this affect the value of E_f^v you calculated for part (a)? Why?

4.7 Calculate the diffusion coefficients for interstitials and vacancies in copper at 484 °C. Neglect the contributions of mixing entropy. Use 0.361 nm for the lattice constant. Also, calculate the vacancy self-diffusion coefficient. Why is this so much lower than the diffusion coefficients for vacancies?

4.8 In a laboratory experiment conducted at 10 °C below the melting point of copper, 0.02 % of the atom sites are vacant. At 500 °C, the vacant atom fraction was 5.7×10^{-8}.

(a) What is the vacancy formation energy?
(b) How many vacancies are there per cm^3 at 800 °C?

4.9 For the case in Problem 4.7, determine the thermal equilibrium concentrations of vacancies and interstitials.

References

1. Ullmaier H, Schilling W (1980) Radiation damage in metallic reactor materials. In: Physics of modern materials, (vol. 1). IAEA, Vienna
2. Hackett MJ, Was GS, Simonen EP (2005). J ASTM Int 2(7)
3. Thompson MW (1969) Defects and radiation damage in metals. Cambridge University Press, Cambridge
4. Shewmon PG (1989) Diffusion in solids. The Minerals, Metals and Materials Society, PA
5. Mrowec S (1980) Defects and diffusion in solids, an introduction. Elsevier, New York
6. LeClaire AD (1978) J Nucl Mater 69–70:70
7. Smigelskas A, Kirkendall E (1947) Trans AIME 171:130
8. Darken L (1948). Trans AIME 175:184–201

Chapter 5
Radiation-Enhanced Diffusion and Defect Reaction Rate Theory

We have developed an understanding of the formation of point defects, their motion or diffusion in a solid, and the configurations of some of the common types of defect clusters encountered in irradiated and unirradiated metals. Clearly, the formation, growth, and dissolution of defect aggregates such as voids, dislocation loops, etc., depend upon the diffusion of point defects and their reaction with the defect aggregates. But they also depend upon the concentration of point defects in the solid. The concentration at any point and time is a balance between the production rate and the loss rate of point defects and is adequately described by the *point defect balance equations*. The increase in diffusion or enhancement of atom mobility in an irradiated metal is due to two factors: (1) the enhanced concentration of the defects and (2) the creation of new defect species.

Recall that the diffusion of lattice atoms by way of the vacancy mechanism is given by:

$$D_a^v = f_v D_v C_v,$$

where D_v is the vacancy diffusion coefficient, C_v is the vacancy concentration, and f_v is the correlation coefficient. Thus, increasing the concentration of vacancies will increase the diffusion coefficient for the atoms in the metal. However, if other mechanisms of diffusion are operative, such as interstitials or divacancies, then the total diffusion coefficient for atoms, D_a is written as follows:

$$D_a = f_v D_v C_v + f_i D_i C_i + f_{2v} D_{2v} C_{2v} + \cdots$$

and diffusion of atoms in the metal is increased by opening new channels via defect species which are usually not present in significant concentration at thermal equilibrium. Under irradiation, D_a is also written as D_{rad}.

In this chapter, we will develop the transient and steady-state solutions to the point defect balance equations in different temperature and microstructure regimes within the framework of radiation-enhanced diffusion [1, 2]. The solutions to the equations are used to determine the radiation-enhanced diffusion coefficient. Reaction rate theory is then presented to develop an understanding of how point

G.S. Was, *Fundamentals of Radiation Materials Science*,
DOI 10.1007/978-1-4939-3438-6_5

defects interact with the various defect aggregates. Radiation-enhanced diffusion and defect reaction rate theory are essential to understanding the evolution of the irradiated microstructure developed in Chaps. 6–10.

5.1 Point Defect Balance Equations

The development of radiation-induced vacancy and interstitial concentrations occurs due to competing processes. Frenkel defects are created from the collisions between high-energy particles and lattice atoms. These defects can be lost either through recombination of vacancies and interstitials or by reaction with a defect sink (void, dislocation, dislocation loop, grain boundary, or precipitate). The local change in defect concentration of the various defect species can be written as the net result of (1) the local production rate, (2) reaction with other species, and (3) diffusion into or out of the local volume or the divergence of the flow. The main reactions we will focus on in this treatment are vacancy–interstitial recombination ($v + i \rightarrow \square$, where $\square$ represents a lattice site) and point defect reactions with sinks ($v + s \rightarrow s$, and $i + s \rightarrow s$). These competing processes can be mathematically described by the *chemical rate equations*:

$$\begin{aligned} \frac{dC_v}{dt} &= K_0 - K_{iv}C_iC_v - K_{vs}C_vC_s \\ \frac{dC_i}{dt} &= K_0 - K_{iv}C_iC_v - K_{is}C_iC_s, \end{aligned} \tag{5.1}$$

where

C_v vacancy concentration
C_i interstitial concentration
K_0 defect production rate
K_{iv} vacancy–interstitial recombination rate coefficient
K_{vs} vacancy–sink reaction rate coefficient
K_{is} interstitial–sink reaction rate coefficient

The terms K_{iv}, K_{vs}, and K_{is} are the rate constants of the general form, $K_{jX,}$ that describe the loss rate of point defects, j per unit point defect concentration to sinks of type, X. Similar equations can be written for defect agglomerates such as di- and trivacancies and interstitials. Note that the equations are nonlinear differential equations and they are not mutually symmetric with respect to vacancy and interstitial concentrations because of the difference in K_{is} and K_{vs}, making an analytical solution difficult. The term "chemical" refers to homogeneous reactions, where the rate depends only on concentration ("law of mass action") and not on the local distribution $C(r)$ of the reactants. Thus, uniformity and thereby chemical kinetics require that $\nabla C \approx 0$. This gives rise to a problem when considering localized sinks, e.g., dislocations, grain boundaries, voids, and precipitate interfaces. Such local sinks violate the supposition of spatial uniformity in the host metal

in that there is now locally a directed net flow of mobile point defects toward the closest sinks. The divergence of the flow is equivalent to another "reaction" term, $\nabla \cdot D\nabla C$, in the kinetic balance equations. The locally valid rate equations are as follows:

$$\begin{aligned}\frac{\partial C_\mathrm{v}}{\partial t} &= K_0 - K_\mathrm{iv}C_\mathrm{i}C_\mathrm{v} - K_\mathrm{vs}C_\mathrm{v}C_\mathrm{s} + \nabla \cdot D_\mathrm{v}\nabla C_\mathrm{v} \\ \frac{\partial C_\mathrm{i}}{\partial t} &= K_0 - K_\mathrm{iv}C_\mathrm{i}C_\mathrm{v} - K_\mathrm{is}C_\mathrm{i}C_\mathrm{s} + \nabla \cdot D_\mathrm{i}\nabla C_\mathrm{i}.\end{aligned} \tag{5.2}$$

The solution to these equations requires the statement of boundary conditions in addition to the initial local concentrations of the mobile defects (vacancies and interstitials). However, we can assume that $\nabla C \approx 0$ if the mean defect separation is greater than the mean distance between sinks, that is, the sink density is higher than the defect density. This amounts to treating the sink as being uniformly distributed and Eq. (5.1) applies.

We consider the following model for the solution to Eq. (5.1). A pure metal is irradiated to produce only single vacancies and single interstitials in equal numbers with no spatial correlation of the interstitial with its vacancy. The interstitials and vacancies migrate by random walk diffusion, annihilating each other by mutual recombination or at unsaturable fixed sinks. Sinks and defects are distributed homogeneously in the metal. The diffusion coefficient of the metal is given by the sum of terms due to its diffusion by vacancies and interstitials. The model will have the following limitations:

1. The model applies to a pure metal. Binding of defects to atomic species and limitation of defect motion due to binding and correlation effects are neglected, $f = 1$.
2. The sink concentrations and strengths are time independent, or unsaturable.
3. Other than mutual recombination, defect–defect interactions (e.g., the formation of divacancies or di-interstitials) are ignored.
4. Bias factors for diffusion of defects to sinks are set to unity (no preferential absorption of specific point defects at specific sinks).
5. Diffusion terms in and out of a specific volume are not considered.
6. The thermal equilibrium vacancy concentration is neglected.

The rate constants are as follows:

$$K_\mathrm{iv} = 4\pi r_\mathrm{iv}(D_\mathrm{i} + D_\mathrm{v}) \approx 4\pi r_\mathrm{iv}D_\mathrm{i} \tag{5.3}$$

since $D_\mathrm{i} \gg D_\mathrm{v}$,

$$K_\mathrm{is} = 4\pi r_\mathrm{is}D_\mathrm{i} \tag{5.4}$$

$$K_\mathrm{vs} = 4\pi r_\mathrm{vs}D_\mathrm{v}, \tag{5.5}$$

where r_{iv}, $r_{vs,}$ and r_{is} are interaction radii for the reaction between the species given by the subscripts and represent the radii of surfaces such that if crossed by the defect, it is annihilated. The terms D_i and D_v are the interstitial and vacancy diffusion coefficients, respectively. The production term, K_0, is the *effective* point defect production rate in that it refers to the production of only freely migrating defects that can give rise to long-range diffusion (see Chap. 3). The derivations of the terms in Eqs. (5.3), (5.4), and (5.5) will be given in the Sect. 5.3.

Note that since the rate constants can differ by several orders of magnitude, the equations are stiff. That is, the time increment needed to follow interstitial motion is orders of magnitude too small to show any vacancy motion. Therefore, the equations must be solved using numerical techniques for stiff equations. But we can gain insight into the processes by looking at analytical solutions to limiting cases. For example, the defect concentrations initially increase linearly, with $C_v = C_i = K_0 t$. Further development depends on the values of the temperature and sink concentration, C_s. We will develop analytical solutions to Eq. (5.1) for four different regimes (combinations of T and C_s): (1) low T and low C_s, (2) low T and intermediate C_s, (3) low T and high C_s, and (4) high T.

5.1.1 Case 1: Low Temperature, Low Sink Density

The approximate solutions to Eq. (5.1) for low temperature and low sink density are given in Fig. 5.1. Initially, defect concentrations build up according to $dC/dt = K_0$ with $C_i \sim C_v$, so $C_i = C_v = C = K_0 t$. Initially, the concentrations are too low for either recombination or sinks to have an effect on the buildup. The buildup of point defects will start to level off when the production rate is compensated by the recombination rate. In the time regime where the production rate is balanced by the recombination rate, we drop the last two terms from Eq. (5.1) and solve for the "quasi-steady-state" concentrations:

$$\frac{dC}{dt} = K_0 - K_{iv} C^2 = 0 \quad (C = C_i = C_v), \tag{5.6}$$

with the solution:

$$C = \left(\frac{K_0}{K_{iv}}\right)^{1/2}. \tag{5.7}$$

Equating this concentration with that during the buildup phase:

$$K_0 t = \left(\frac{K_0}{K_{iv}}\right)^{1/2}, \tag{5.8}$$

yields the time at which losses to recombination compensate for the production rate from irradiation:

$$t = \tau_1 = (K_0 K_{iv})^{-1/2}, \tag{5.9}$$

where τ_1 is a time constant or characteristic time for the *onset of mutual recombination*.

Eventually, the interstitials (first) and then the vacancies (later) will begin to find the sinks, and sinks will start to contribute to annihilation. C_i and C_v remain approximately equal until a time τ_2, which is the time constant for the process of interstitials reacting with the sinks. Because $D_i > D_v$, more interstitials are lost to sinks than vacancies, which is described by:

$$\frac{dC_i}{dt} = -K_{is} C_i C_s, \tag{5.10}$$

so the interstitial concentration will decay and the vacancy concentration will rise (since their only sink is interstitials and interstitials are being lost to sinks), yielding:

$$\begin{aligned} C_v(t) &= \left[\frac{K_0 K_{is} C_s t}{K_{iv}}\right]^{1/2} \\ C_i(t) &= \left[\frac{K_0}{K_{iv} K_{is} C_s t}\right]^{1/2}. \end{aligned} \tag{5.11}$$

(The derivation of Eq. (5.11) is Problem 5.15 at the end of the chapter.) The time at which these equalities occur is obtained by equating the concentrations in the bounding time regimes of quasi-steady state and buildup of interstitials/decay of vacancies (Fig. 5.1):

$$\begin{aligned} C_v &= \left(\frac{K_0}{K_{iv}}\right)^{1/2} = \left[\frac{K_0 K_{is} C_s t}{K_{iv}}\right]^{1/2} \\ C_i &= \left(\frac{K_0}{K_{iv}}\right)^{1/2} = \left[\frac{K_0}{K_{iv} K_{is} C_s t}\right]^{1/2}, \end{aligned} \tag{5.12}$$

and solving for the time yields the time constant for the *onset of the buildup regime*:

$$t = \tau_2 = (K_{is} C_s)^{-1}. \tag{5.13}$$

After a while, at time τ_3, true steady state will be achieved. τ_3 is the time constant for the slowest process, which is the interaction of vacancies with sinks. Solving

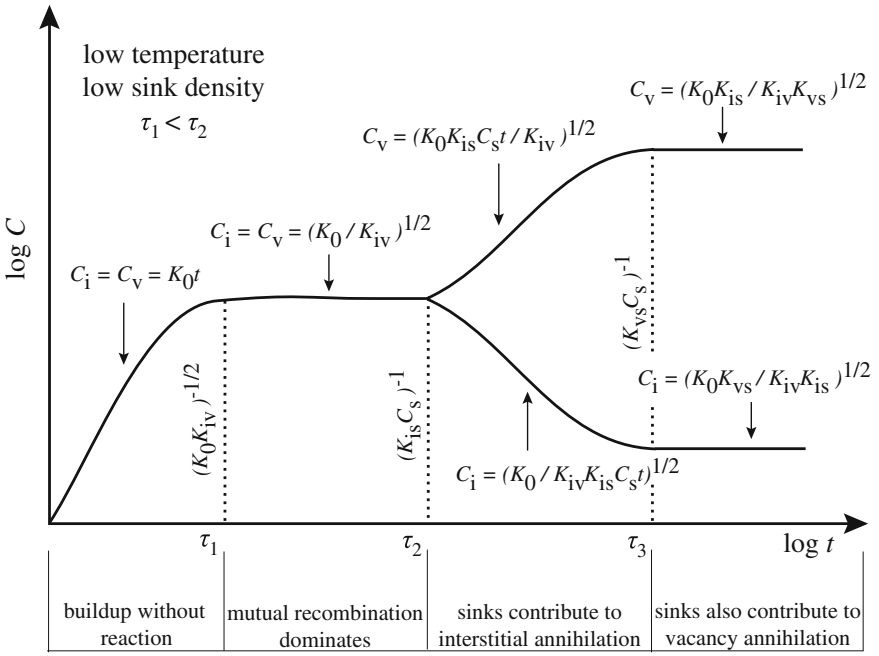

Fig. 5.1 Log–log plot of vacancy and interstitial concentration versus time for case (1) low temperature and low sink density (after [2])

Eq. (5.1) for the steady-state concentration of vacancies and interstitials by setting $dC_v/dt = dC_i/dt = 0$ gives:

$$C_v^{ss} = -\frac{K_{is} C_s}{2K_{iv}} + \left[\frac{K_0 K_{is}}{K_{iv} K_{vs}} + \frac{K_{is}^2 C_s^2}{4K_{iv}^2}\right]^{1/2}$$
$$C_i^{ss} = -\frac{K_{vs} C_s}{2K_{iv}} + \left[\frac{K_0 K_{vs}}{K_{iv} K_{is}} + \frac{K_{vs}^2 C_s^2}{4K_{iv}^2}\right]^{1/2}. \tag{5.14}$$

Since vacancies and interstitials are produced in equal numbers and equal numbers are lost to recombination, the loss of each to sinks must be equal at steady state, and:

$$K_{vs} C_v = K_{is} C_i. \tag{5.15}$$

For the case of low temperature and low sink density, C_s is small, and the vacancy and interstitial concentrations in Eq. (5.14) are approximated as:

$$C_v^{ss} \cong \sqrt{\frac{K_0 K_{is}}{K_{iv} K_{vs}}}; \quad C_i^{ss} \cong \sqrt{\frac{K_0 K_{vs}}{K_{iv} K_{is}}}. \tag{5.16}$$

Equating these expressions to those from the previous (buildup) region gives:

$$C_v = \left[\frac{K_0 K_{is} C_s t}{K_{iv}}\right]^{1/2} = \left[\frac{K_0 K_{is}}{K_{iv} K_{vs}}\right]^{1/2}. \tag{5.17}$$

and solving for the time gives the time constant for the *onset of steady state*:

$$t = \tau_3 = (K_{vs} C_s)^{-1}. \tag{5.18}$$

The buildup shown in Fig. 5.1 is really a schematic and not the actual buildup. The transitions between regimes are not so sudden. For example, if the sink density is assumed to be zero, the exact solution to Eq. (5.1) is as follows:

$$C_v(t) = \sqrt{\frac{K_0}{K_{iv}}} \tanh\left(\sqrt{K_{iv} K_0 t}\right). \tag{5.19}$$

5.1.2 Case 2: Low Temperature, Intermediate Sink Density

Increasing the sink density has the effect of bringing τ_2 closer to τ_1 (see Fig. 5.2). That is, the region of mutual recombination is shrunk at the expense of annihilation at sinks. In fact, when:

$$\tau_1 = \tau_2 \text{ or } (K_0 K_{iv})^{-1/2} = (K_{is} C_s)^{-1}, \tag{5.20}$$

the plateau disappears.

5.1.3 Case 3: Low Temperature, High Sink Density

The main effect of a high sink density is that interstitials find the sinks before they find vacancies because $C_s \gg C_v$ at short time (Fig. 5.3). That is, the time to reach linear buildup (loss of interstitials to sinks), τ_2, becomes shorter than the time to reach quasi-steady state due to vacancy–interstitial interaction, τ_1. In this case, the

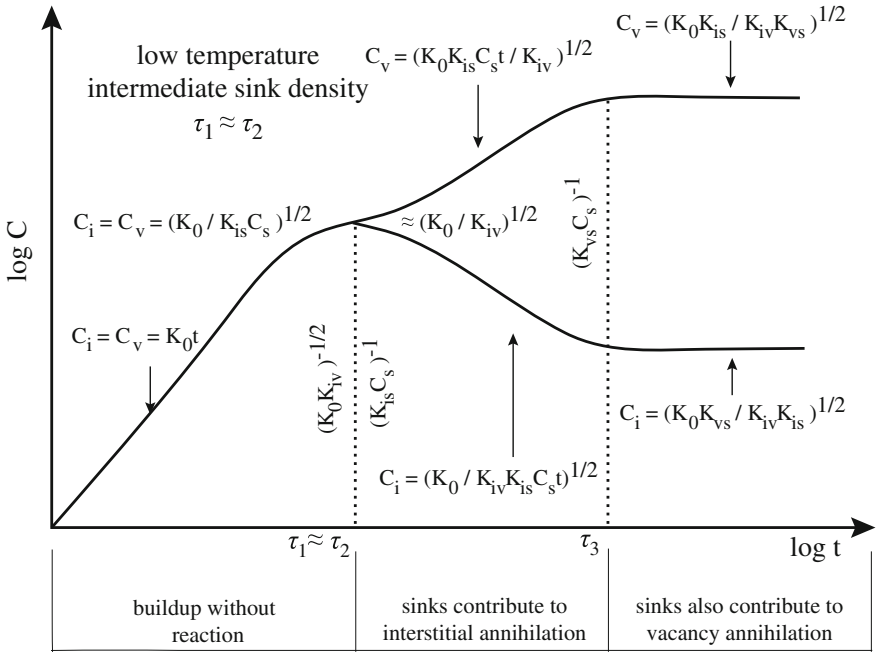

Fig. 5.2 Log–log plot of vacancy and interstitial concentration versus time for case (2) low temperature and intermediate sink density (after [2])

interstitial concentration comes into a quasi-steady state with production and annihilation at sinks:

$$\frac{dC_i}{dt} = 0 = K_0 - K_{is} C_i C_s; \tag{5.21}$$

resulting in the quasi-steady-state concentration:

$$C_i = \frac{K_0}{K_{is} C_s}. \tag{5.22}$$

Equating interstitial concentrations in the linear buildup regime with the quasi-steady-state regime gives the following:

$$K_0 t = \frac{K_0}{K_{is} C_s}, \tag{5.23}$$

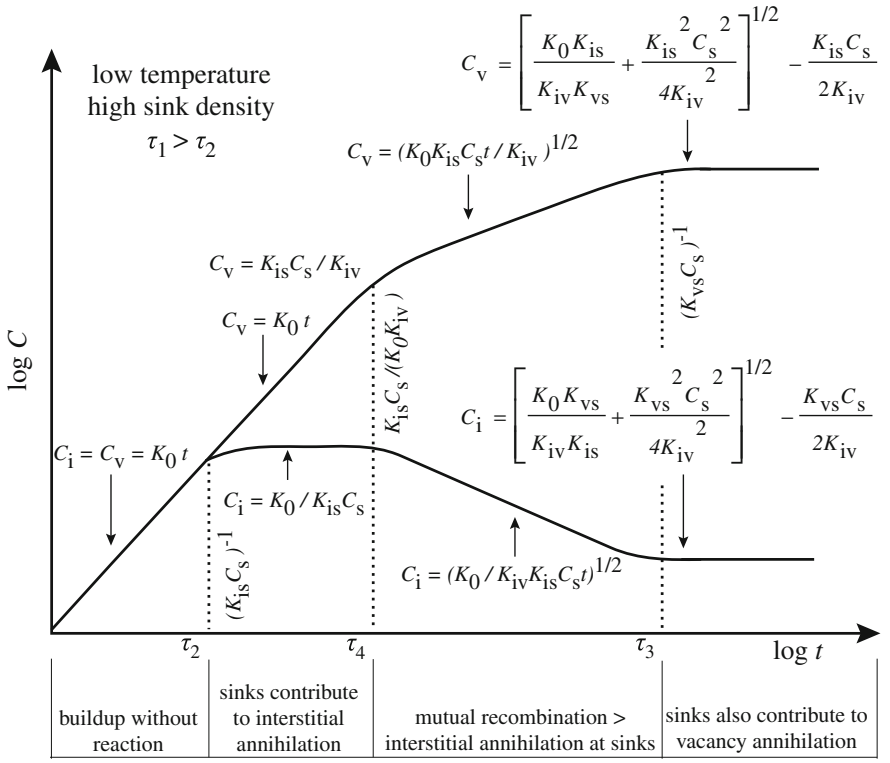

Fig. 5.3 Log–log plot of vacancy and interstitial concentration versus time for case (3) low temperature and high sink density (after [2])

and solving for t gives the value for the time constant τ_2:

$$t = \tau_2 = (K_{is} C_s)^{-1}. \tag{5.24}$$

Note that since interstitials have found the sinks before finding the slower vacancies, the vacancy concentration continues to rise according to $C_v = K_0 t$. A competition soon arises between annihilation of interstitials at sinks and recombination with vacancies:

$$K_{is} C_i C_s = K_{iv} C_i C_v \cong K_{iv} C_i K_0 t, \tag{5.25}$$

yielding the time constant for the transition between the regimes where interstitials go to sinks and mutual recombination dominates:

$$t = \tau_4 = \frac{K_{is} C_s}{K_{iv} K_0}. \tag{5.26}$$

In the regime following τ_4, C_v rises but more slowly, and C_i decreases slowly according to:

$$\begin{aligned} C_v &= (K_0 K_{is} C_s t / K_{iv})^{1/2} \\ C_i &= (K_0 / K_{is} K_{iv} C_s t)^{1/2}. \end{aligned} \tag{5.27}$$

Steady state arrives at:

$$\tau_3 = \frac{1}{K_{vs} C_s}, \tag{5.28}$$

with

$$\begin{aligned} C_v^{ss} &= -\frac{K_{is} C_s}{2K_{iv}} + \left[\frac{K_0 K_{is}}{K_{iv} K_{vs}} + \frac{K_{is}^2 C_s^2}{4K_{iv}^2}\right]^{1/2} \\ C_v^{ss} &= -\frac{K_{vs} C_s}{2K_{iv}} + \left[\frac{K_0 K_{vs}}{K_{iv} K_{is}} + \frac{K_{vs}^2 C_s^2}{4K_{iv}^2}\right]^{1/2}. \end{aligned} \tag{5.29}$$

Note that the steady-state concentrations are the same as Eq. (5.14) given earlier in case (1), but without the simplification of dropping the terms in C_s since in this case, the sink density is high and cannot be neglected.

5.1.4 Case 4: High Temperature

At high temperature, the defect annihilation rate at the sinks keeps the concentration of interstitials low (Fig. 5.4). Since recombination does not contribute much, the rate equations become the following:

$$\begin{aligned} \frac{dC_v}{dt} &= K_0 - K_{vs} C_s C_v \\ \frac{dC_i}{dt} &= K_0 - K_{is} C_s C_i, \end{aligned} \tag{5.30}$$

with steady-state solutions:

$$C_v = \frac{K_0}{K_{vs} C_s}, \quad C_i = \frac{K_0}{K_{is} C_s}, \tag{5.31}$$

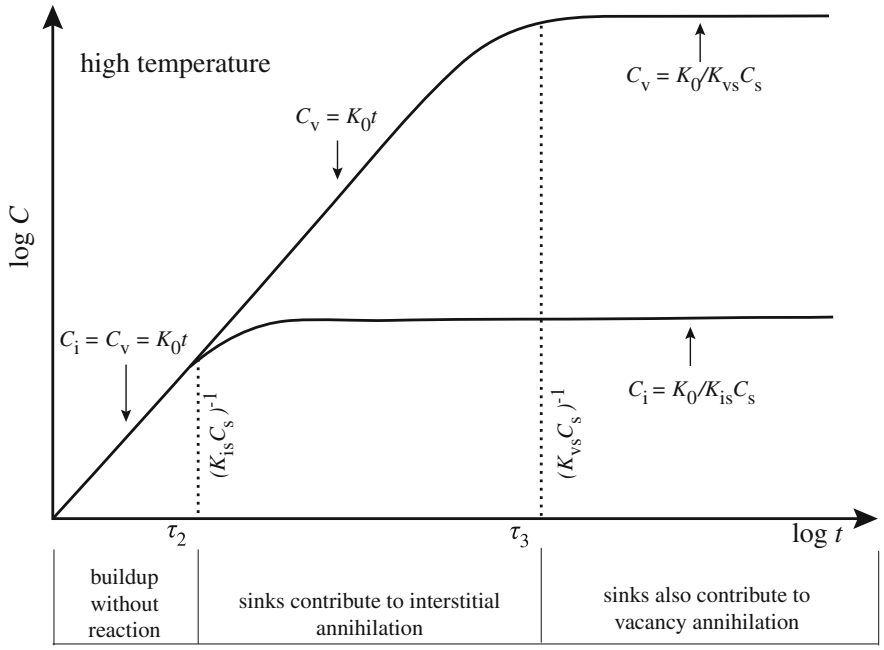

Fig. 5.4 Log–log plot of vacancy and interstitial concentration versus time for case (4) high temperature (after [2])

with characteristic times given by:

$$\text{interstitial annihilation at sinks: } K_0 t = \frac{K_0}{K_{is}C_s} \Rightarrow t = \tau_2 = (K_{is}C_s)^{-1} \tag{5.32}$$

$$\text{vacancy annihilation at sinks: } K_0 t = \frac{K_0}{K_{vs}C_s} \Rightarrow t = \tau_3 = (K_{vs}C_s)^{-1}. \tag{5.33}$$

The time evolution of vacancy and interstitial concentrations displayed in Fig. 5.4 ignores the presence of thermal vacancies, which may be significant at higher temperatures. The buildup of radiation-induced vacancies and interstitials at high temperature, including an initial presence of thermal equilibrium vacancies, is shown in Fig. 5.5. Note the effect of sink (dislocation) density and defect production rate.

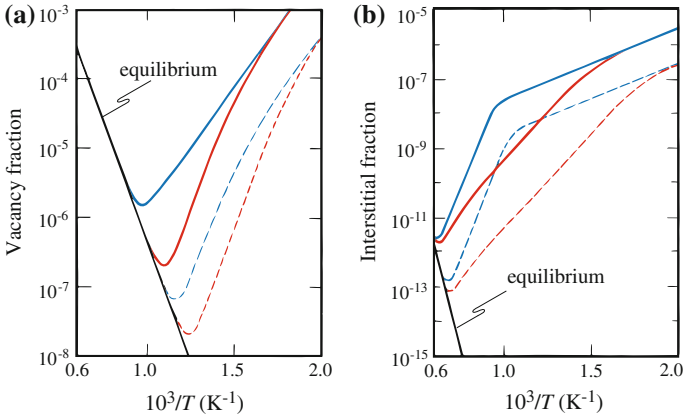

Fig. 5.5 Steady state (**a**) vacancy and (**b**) interstitial concentrations in an irradiated metal at a high production rate (*solid line*) and at a low defect production rate (*dashed line*). The upper (*blue*) and lower (*red*) curves for each defect production rate represent small and large dislocation densities, respectively (after [3])

Figure 5.5a shows that increasing the sink density lowers the vacancy concentration since sinks absorb the vacancies (loss term is proportional to K_{vs}). Also for a fixed sink density, a higher displacement rate results in a higher vacancy concentration because the production rate is higher than the loss rate to sinks. The same is true for interstitials shown in Fig. 5.5b. The kinks in the interstitial concentration curves correspond to the temperature at which vacancies become mobile and contribute to interstitial loss by mutual recombination as in Fig. 5.3. Comparing Fig. 5.5a and b shows that the equilibrium concentration of interstitials is negligible over the practical range of reactor component temperatures, while this is not the case for vacancies.

The main objective of solving the point defect balance equations is to obtain values for C_i and C_v to determine D_{rad}, which is just the sum of C_iD_i and C_vD_v. The preceding discussion shows that we can interpret radiation-enhanced diffusion experiments after an isothermal irradiation at a constant flux for a time t in terms of characteristic times. Table 5.1 summarizes the time constants for the various

Table 5.1 Time constants for rate-limiting processes in the point defect balance equations

Time constant	Value	Process
τ_1	$(K_0K_{iv})^{-1/2}$	Onset of mutual recombination
τ_2	$(K_{is}C_s)^{-1}$	Onset of interstitial loss to sinks
τ_3	$(K_{vs}C_s)^{-1}$	Onset of vacancy loss to sinks
τ_4	$\tau_1^2/\tau_2 = \dfrac{K_{is}C_s}{K_0K_{iv}}$	Mutual recombination dominates interstitial loss to sinks

rate-limiting mechanisms. For low sink density, recombination dominates at short times, followed by interstitial annihilation at sinks and then vacancy annihilation at sinks, which is the slowest process and controls the achievement of steady state. At high sink density, interstitial annihilation at sinks dominates early, followed by mutual recombination and then vacancy loss to sinks. As a rule, when $\tau_1 < \tau_2$, mutual recombination dominates and when $\tau_2 < \tau_1$, sinks dominate. In summary, the key factors affecting C_i and C_v are production rate, defect mobility, and sink concentration.

5.1.5 Properties of the Point Defect Balance Equations

The point defect balance equations and their solutions possess interesting properties, which provide further insight into the behavior of vacancies and interstitials in the diffusion of lattice atoms. They are the following:

1. The vacancy concentration referred to in the last section is really $C_v - C_v^0$ where C_v^0 is the thermal equilibrium concentration of vacancies. In high-temperature irradiations ($T/T_m \geq 0.5$), this concentration is non-negligible. However, over all irradiation temperatures of interest, $C_i^0/C_i \leq 1$.
2. In the absence of sinks and thermal vacancies, C_v can be exchanged with C_i; that is, $C_v = C_i$ at any instant:

$$\begin{aligned} \frac{dC_v}{dt} &= K_0 - K_{iv}C_iC_v \\ \frac{dC_i}{dt} &= K_0 - K_{iv}C_iC_v \end{aligned} \tag{5.34}$$

   Since $D_{rad} = D_iC_i + D_vC_v$, and $C_i = C_v$, but since $D_i \gg D_v$, then interstitials contribute much more to atom mobility than do vacancies.
3. If there is only one type of sink, then at steady state:

$$\begin{aligned} K_0 &= K_{iv}C_iC_v + K_{vs}C_vC_s \\ K_0 &= K_{iv}C_iC_v + K_{is}C_iC_s, \end{aligned} \tag{5.35}$$

   or

$$K_{vs}C_v = K_{is}C_i, \tag{5.36}$$

   and the absorption rate of interstitials and vacancies at sinks is equal, or the net absorption rate at the sink is zero. Even for the case of multiple sink types, if the sinks have the same "strength" for vacancies and interstitials, then the net flow to any sink is zero.

4. Inclusion of sink terms violates the symmetry with respect to C_i and C_v because of the different values of $K(K_{vs} \neq K_{is})$. Symmetry *is* present in the steady state with regard to D_iC_i and D_vC_v (since $K_{is} \propto D_i$ and $K_{vs} \propto D_v$). The consequence is that vacancies and interstitials contribute to atom mobility to the same extent and their actions cannot be discriminated. At steady state:

$$\begin{aligned} 0 &= K_0 - K_{iv}C_iC_v - K'_{vs}D_vC_vC_s \\ 0 &= K_0 - K_{iv}C_iC_v - K'_{is}D_iC_iC_s, \end{aligned} \tag{5.37}$$

where the K terms have been written as $K = K'D$, giving:

$$D_vC_vK'_{vs}C_s = D_iC_iK'_{is}C_s. \tag{5.38}$$

So if $K'_{vs} \sim K'_{is}$, then $D_iC_i = D_vC_v$ which means that vacancies and interstitials contribute *equally* to atom mobility. Even though the steady-state concentration of interstitials is much lower than the steady-state concentration of vacancies, they each contribute equally to atom mobility because of the faster rate of diffusion of interstitials. For any particular sink to grow, it must have a net bias for either vacancies or interstitials. In real metals, K_{vs} and K_{is} are not equal. Specific sinks have a bias for certain point defects, allowing that sink to grow. This behavior is described in more detail in Sect. 5.3.

5.1.6 *Deficiencies of the Simple Point Defect Balance Model*

The simple point defect model neglects numerous features of realistic systems that must be incorporated in order to obtain accurate results. For example, no account is taken for changing sink strengths, which occur as dose buildup continues due to the formation of depleted zones and defect clusters. Also, sink bias is neglected. Bias is an important factor affecting the development of the irradiated microstructure as will become evident in Chaps. 7 and 8. Defect–defect interaction and defect–impurity interaction have also been neglected. Defect–defect interaction will be important in the formation of void and interstitial loop nuclei and cannot be neglected if larger clusters are to be properly accounted for. These small clusters will serve as traps or sinks for mobile defects. In fact, vacancy clusters have been found to increase D_{rad} in the mutual recombination range, but are insignificant for high sink concentrations and temperatures where annealing to fixed sinks dominates [4]. Finally, the equations are unable to account for defect gradients (and in the simple form, for concentration gradients). These become very important in processes such as radiation-induced segregation (Chap. 6), in which defect fluxes give rise to concentration gradients in the alloying elements. Such processes may significantly alter the behavior of sinks and the bias of the sinks.

5.1.7 Point Defect Balance Equations in the Presence of Cascades

In a cascade, vacancies and interstitials are produced simultaneously but in a segregated fashion such that their distributions are separated from each other in space [5]. After the initial thermal annealing period, vacancies segregate in a vacancy-rich region (e.g., Figs. 3.3 and 3.4). Because of their high concentration and high mobility, the interstitials immediately start to form clusters [6] and diffuse at the same time. In molecular dynamics simulation of cascades, the interstitials are consistently observed to form clusters even in low energy (≈1–2 keV) cascades. More interstitial clustering is likely to occur in higher energy cascades since the concentration of interstitials in these cascades is likely to be higher. These clusters have been found to be stable even at high temperatures. In general, the interstitial population is likely to be partitioned into three portions: one that back diffuses into the vacancy-rich zone and is lost through recombination with the vacancies, one that is immobilized through interaction and clustering, and one that escapes the cascade zone and engages in long-range migration. The relative proportion of these three portions may be affected by the size and morphology of cascades and the disposition of sinks in the vicinity of the cascade.

The vacancy population in the cascade core agglomerates during the "cool down" period after the collision event and eventually collapses to form vacancy loops or stacking fault tetrahedra. In the temperature range of interest, the immobilization of vacancies in vacancy loops is only temporary. They will soon be re-emitted during thermal annealing and become available to various sinks, including voids, as freely migrating vacancies. At elevated temperatures (e.g., the peak swelling temperature), vacancy loops are thermally unstable because of the high line tension and would shrink by vacancy emission. The evaporation of vacancies from the loops and their escape from the vacancy-rich zone provides the mobile vacancies for microstructural evolution (e.g., void growth) and macroscopic deformation.

On the other hand, the immobilization of interstitials in the interstitial loops is permanent. Due to their high formation energy, they remain locked in interstitial loops from the moment they are created. They are unavailable to the voids, whether they grow to a network by receiving a net flow of interstitials, or shrink out of existence by absorbing a net flow of vacancies, or are destroyed by dislocation sweep or cascade overlap. The lifetime of vacancy loops is dominated by thermal annealing and that of the interstitial loops is dominated by destruction.

This description of vacancies and interstitials in the cascade process means that there is an *asymmetry* in the production of mobile point defects (that enters into the mean-field description of microstructure evolution followed by the rate theory approach). First, the proportion of vacancies that agglomerate into clusters is not likely to be the same as that of the interstitials. Second, even if they are, while the vacancy loops can still provide mobile vacancies by evaporation, the interstitial clusters cannot. Thus, it is the difference in the stability and lifetime between

vacancy and interstitial clusters generated during the cascade process that gives rise to a biased production of available vacancies and interstitials. This *production bias* could be a potent driving force for void growth and swelling during cascade damage conditions.

It should be noted that the concept of production bias is valid not only for low doses but also for high doses. One process that could maintain operation of the production bias even at high doses is the climb or/and glide of dislocation segments during irradiation. The mobile dislocation segments would keep sweeping the interstitial clusters and would prevent the buildup of a high concentration of interstitials in the form of clusters. However, bias is absent in the case of electron irradiation when only Frenkel pairs are produced.

In case of cascade production, Eq. (5.1) must be modified to incorporate the effect of production bias. If ε_r is the fraction of defects that recombine in the cascade and ε_v and ε_i are the fractions of clustered vacancies and interstitials, respectively, then the production of isolated vacancies and interstitials is given as:

$$\begin{aligned} K_v &= K_0(1-\varepsilon_r)(1-\varepsilon_v) \\ K_i &= K_0(1-\varepsilon_r)(1-\varepsilon_i), \end{aligned} \tag{5.39}$$

and the point defect balance equations become the following:

$$\begin{aligned} \frac{dC_v}{dt} &= K_0(1-\varepsilon_r)(1-\varepsilon_v) - K_{iv}D_vC_v - K_{vs}C_vC_s + L_v \\ \frac{dC_i}{dt} &= K_0(1-\varepsilon_r)(1-\varepsilon_i) - K_{iv}D_vC_v - K_{is}C_iC_s, \end{aligned} \tag{5.40}$$

where L_v is the production of thermal vacancies from the various sinks (discussed in more detail in Sect. 8.2.1). The continuous production of single interstitial atom (SIA) clusters in displacement cascades is a key process that makes microstructure evolution under cascade conditions qualitatively different from that during Frenkel pair (FP) producing electron irradiation. For electron irradiation, Eq. (5.1) describes the evolution of the defect concentration. In the case of production of clusters in irradiations that generate cascades, Eq. (5.40) should be used.

However, another factor that impacts isolated defect concentration is the mobility of SIA clusters. These clusters have been found to exhibit one-dimensional (1D) migration rather than 3D migration characteristic of isolated point defects. This high mobility results in the constant removal of SIA clusters from the bulk, further increasing the defect imbalance. Note that SIA cluster removal by 1D migration means that dislocation sweeping of clusters is not required to prevent the buildup of the interstitial cluster concentration at high dose.

Damage accumulation under cascade conditions requires the inclusion of the mobile (glissile) SIA cluster concentration, $C_{giL}(x)$, in the defect balance equations of Eq. (5.40):

$$\begin{aligned}\frac{dC_v}{dt} &= K_0(1-\varepsilon_r)(1-\varepsilon_v) - K_{iv}D_vC_v - K_{vs}C_vC_s + L_v \\ \frac{dC_i}{dt} &= K_0(1-\varepsilon_r)(1-\varepsilon_i) - K_{iv}D_vC_v - K_{is}C_iC_s \\ \frac{dC_{giL}(x)}{dt} &= K_{giL}(x) - K_g(x)C_iC_{giL}(x),\end{aligned} \tag{5.41}$$

where $C_{giL}(x)$ is the concentration, $K_{giL}(x)$ is the production rate, and $K_g(x)$ is the rate constant for interstitial interaction with glissile SIA loops (clusters) of size x. The solution of Eq. (5.41) will be discussed in Chap. 8, Sect. 8.3.8 on void swelling.

5.2 Radiation-Enhanced Diffusion

In a pure metal, the diffusion coefficient under radiation is given by:

$$D_{rad} = D_vC_v + D_iC_i. \tag{5.42}$$

Because the concentrations of vacancies and interstitials under irradiation are much greater than those produced thermally, the radiation-enhanced diffusion coefficients are much larger than thermal diffusion coefficients. Despite the shortcomings, it is interesting to see how well the simple point defect balance equations are able to estimate the effect of irradiation on diffusion. Figure 5.6 shows a plot of log D_{rad}

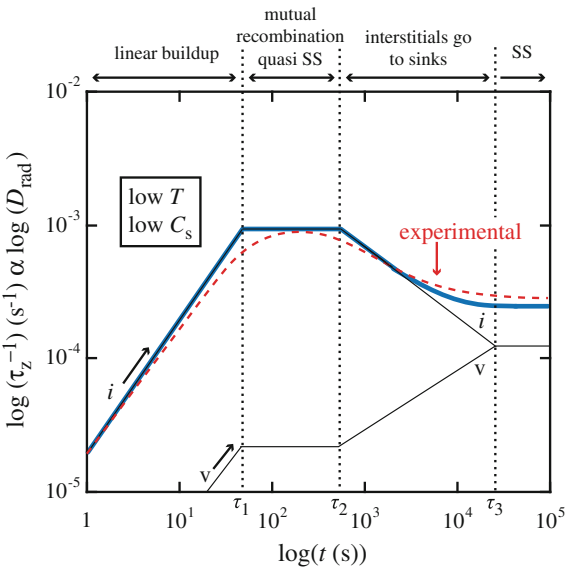

Fig. 5.6 Time dependence of log(D_{rad}) versus log(t) for both calculation (*solid line*) and measurement (*dashed red line*). *Thin solid black lines* are for the vacancy and interstitial components and the *heavy solid blue line* is the sum of the components (after [2])

versus log t for the case of annealed Ag-30 % Zn at 40 °C irradiated with 2.5 MeV electrons at a flux of 3.7×10^{15} m^{-2} s^{-1} [2]. The thin solid black lines are the interstitial and vacancy components and the thick solid blue line is their sum as calculated from Eq. (5.42) by Sizeman [2], and the dashed red line is the experimental data. The experiment actually measures the Zener relaxation time, τ_z (see [1]), which is proportional to D_{rad}. The experimental result confirms the existence of a maximum in D_{rad} as in case (1) for low temperature and low sink density. This result also shows that the interstitial component dominates at times less than that to achieve steady state, τ_3, since $D_i > D_v$ (by assumption) and $C_i > C_v$ for $\tau < \tau_3$.

Another excellent example of calculation of D_{rad} verses measurement is provided by Rothman [1] for self-diffusion in copper at 200 °C in a crystal containing a dislocation density of 10^{11} m^{-2} under irradiation with a net damage rate, $K_0 = 10^{-6}$ dpa/s (similar to that experienced by a fast reactor core structural material). In this case, $D_{rad} \sim 6.5 \times 10^{-21}$ m^2 s^{-1}. Given that the thermal diffusion coefficient is $\sim 1.4 \times 10^{-27}$ m^2 s^{-1}, this represents an extremely large (>10^6) increase due to irradiation. Figure 5.7 shows that at temperatures below 575 °C, D_{rad} exceeds the thermal equilibrium self-diffusion coefficient for this defect production rate (curve 1). The various curves in Fig. 5.7 represent different combinations of production rates and defect densities. Note that at low temperature, mutual recombination dominates and D_{rad} has an activation energy of $E_m^v/2$ (all curves). At low sink density (10^{11} dislocations m^{-2} (curve 1), where $\rho_d \sim 4\pi r_{vs} C_s = 4\pi r_{is} C_s$), the mutual recombination region ties indirectly to diffusion by

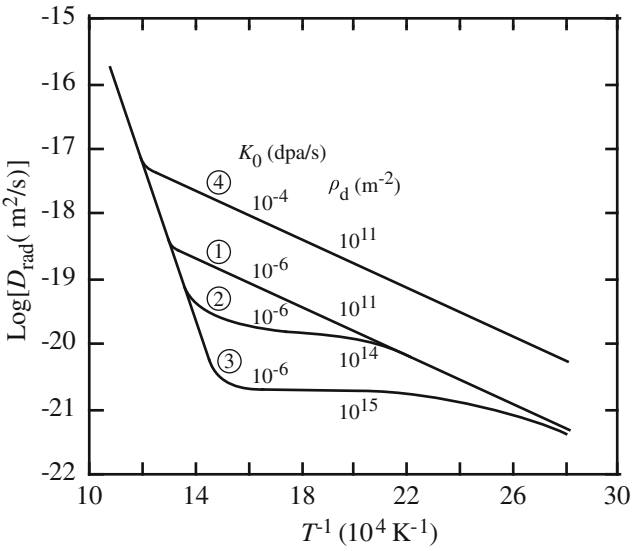

Fig. 5.7 Calculated D_{rad} for self-diffusion of copper as a function of temperature for different combinations of defect production rates and dislocation densities. (1) $K_0 = 10^{-6}$ dpa/s, $\rho_d = 10^{11}$ m^{-2}, (2) $K_0 = 10^{-6}$ dpa/s, $\rho_d = 10^{14}$ m^{-2}, (3) $K_0 = 10^{-6}$ dpa/s, $\rho_d = 10^{15}$ m^{-2}, (4) $K_0 = 10^{-4}$ dpa/s, $\rho_d = 10^{11}$ m^{-2} (after [1])

thermal equilibrium vacancies with increasing temperature. At high sink densities, [10^{14} m^{-2} (curve 2) and 10^{15} m^{-2} (curve 3)], mutual recombination gives way to annealing at fixed sinks at a critical temperature, determined as follows.

According to Eq. (5.36), for a single sink type:

$$C_i K_{is} = C_v K_{vs} \quad \text{or} \quad C_i = \frac{C_v K_{vs}}{K_{is}}. \tag{5.43}$$

At steady state, Eq. (5.29) is applied and they can be rewritten in the following form:

$$\begin{aligned} C_v &= \frac{K_{is} C_s}{2K_{iv}} \left[\left(1 + \frac{4K_0 K_{iv}}{K_{is} K_{vs} C_s^2} \right)^{1/2} - 1 \right] \\ C_i &= \frac{K_{vs} C_s}{2K_{iv}} \left[\left(1 + \frac{4K_0 K_{iv}}{K_{is} K_{vs} C_s^2} \right)^{1/2} - 1 \right]. \end{aligned} \tag{5.44}$$

We define a parameter, η, such that:

$$\eta = \frac{4K_0 K_{iv}}{K_{vs} K_{is} C_s^2}. \tag{5.45}$$

Then using Eq. (5.44), C_v can be written as:

$$C_v = \frac{F(\eta) K_0}{K_{vs} C_s}, \quad \text{or} \quad C_v K_{vs} C_s = F(\eta) K_0. \tag{5.46}$$

where

$$F(\eta) = \frac{2}{\eta} [1 + \eta)^{1/2} - 1]. \tag{5.47}$$

Equation (5.46) shows that $F(\eta)$ determines the number of defects absorbed by sinks in relation to the total rate of formation of the defects. If $\eta \rightarrow 0$, then $F(\eta) \rightarrow 1$, i.e., all of the defects are lost to sinks and none to recombination. In the limit of large η, $F(\eta) \sim 2/\eta^{1/2}$ and $F(\eta) \rightarrow 0$, indicating that mutual recombination dominates defect loss. When $F(\eta) = 1/2$, the loss of defects to sinks and recombination is equal. This occurs at a value of η of:

$$\eta = 8 = \frac{4K_0 K_{iv}}{K_{vs} K_{is} C_s^2}. \tag{5.48}$$

Equation (5.48) can be solved for the critical temperature below which mutual recombination will dominate, and above which loss to sinks will dominate. (The term η will be revisited in Chap. 8 in describing the effect of recombination on

void growth). Using Eqs. (5.3), (5.4), and (5.5) for K_{iv}, K_{is}, and K_{vs}, and defining $K'_{iv} = 4\pi r_{iv}$, $K'_{is} = 4\pi r_{is}$, and $K'_{vs} = 4\pi r_{vs}$, Eq. (5.48) can be written as:

$$8 = \frac{4K_0 K'_{iv} D^{i}_0 \exp\left(\dfrac{-E^{i}_m}{kT}\right)}{K'_{vs} D^{v}_0 \exp\left(\dfrac{-E^{v}_m}{kT}\right) K'_{is} D^{i}_0 \exp\left(\dfrac{-E^{i}_m}{kT}\right) C_s^2}, \tag{5.49}$$

where $E^{v}_{i,m}$ is the migration energy and $D^{i,v}_0$ is the pre-exponential factor in the diffusion coefficient for interstitials and vacancies, respectively. Equation (5.49) simplifies to:

$$T_c = \frac{E^{v}_m}{k \ln\left[\dfrac{2D^{v}_0 C_s^2 K'_{is} K'_{vs}}{K_0 K'_{iv}}\right]}. \tag{5.50}$$

At the highest temperatures, D_{rad} is overwhelmed by thermal vacancies (all curves in Fig. 5.7), and increasing K_0 to 10^{-4} dpa/s (curve 4) raises D_{rad} in the mutual recombination range by a factor of 10.

Figure 5.8 shows the radiation-enhanced diffusion coefficient calculated for a sample of nickel undergoing irradiation at a rate of 10^{-6} dpa/s for different sink annihilation probabilities, p, where p^{-1} is the average number of jumps of a defect between creation and annihilation at a sink [7]. The diffusion coefficient describing radiation-enhanced diffusion, D_{rad}, is shown by the solid line. The dashed line to the left is the thermal diffusion coefficient and the solid horizontal line at the right is the diffusion coefficient due to ballistic mixing, D_m [8], and will be discussed in Chap. 10.

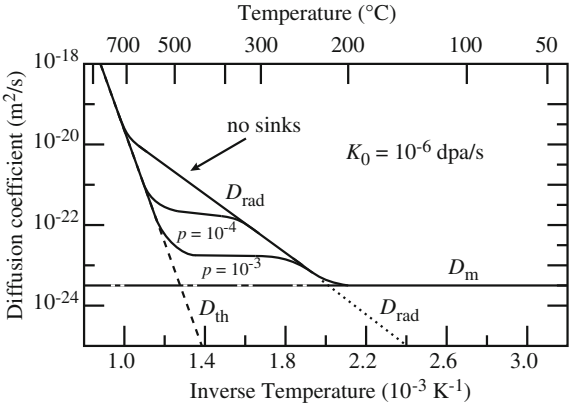

Fig. 5.8 Diffusion coefficient as a function of $1/T$ for a nickel-base alloy during irradiation at a displacement rate of 10^{-6} dpa/s. D_{rad} is calculated from rate theory for various sink annihilation probabilities, p. The diffusion coefficient from displacement mixing is D_m and the thermal diffusion coefficient is D_{th} (after [7])

The difference between the curves for D_{rad} and D_{th} is the effect of radiation-enhanced diffusion. As shown, irradiation can result in a several orders of magnitude increase in the diffusion coefficient.

5.3 Defect Reactions

Each of the terms in the point defect balance equations represents a reaction. The rate at which the reaction occurs will depend on the nature of the reacting species. Following [3], we will develop expressions for the rates of each of the reactions in the point defect balance equations, as they will be used in describing processes such as void growth and dislocation climb. We have seen that the motion of mobile point defects can be considered a random walk process. When one of these defects encounters a specie in the crystal to which it becomes tightly bound, one or both of the partners in the encounter are considered to disappear from the solid. Examples include a vacancy or interstitial intersecting a free surface, grain boundary, dislocation, void, etc., or a vacancy encountering a vacancy, an interstitial encountering an interstitial, or a vacancy encountering an interstitial. Clearly, the rate of such reactions is proportional to the concentrations of both species, or:

$$\text{reaction rate of A and B} = K_{AB} C_A C_B \text{ reaction/cm}^3\,\text{s}, \tag{5.51}$$

where C_A and C_B are the concentrations of species A and B in units of particles/cm^3, and K_{AB} is the rate constant of the reaction in cm^3/s. Reactions can be between two mobile particles (vacancy and interstitial at high temperature) or between one mobile and one stationary defect, e.g., low temperature where vacancies are immobile and interstitials are mobile, or between interstitials and dislocation, grain boundaries, and voids.

There are two types of processes that will be of interest in dealing with the reaction between point defects and sinks; reaction rate-controlled and diffusion-controlled. In reaction rate-governed processes, there must be no macroscopic concentration gradients of either partner. If one partner is large compared to the atomic-sized reactant, or if one is a strong sink, a concentration gradient may be established in the vicinity of the stationary defect. Reactions between point defects are examples of reaction rate-controlled processes. If a defect concentration gradient is established, the overall process is governed by the rate of diffusion of the mobile species to the stationary sink. This is the case with free surfaces, voids, and grain boundaries. These defects are usually not treated by reaction rate theory.

As a first example of a reaction rate-controlled process, let us look at the vacancy–vacancy reaction. Consider the reaction:

$$v + v \rightarrow v_2, \tag{5.52}$$

that proceeds in the forward direction only and is characterized by the rate constant K_{2v}. In this example, one vacancy is assumed to be stationary and the other is mobile. The rate of divacancy formation per cm^3 is given as:

$$R_{2v} = P_{2v} C_v, \tag{5.53}$$

where C_v is the concentration of monovacancies and P_{2v} is the probability per second that another vacancy jumps into a site that is a nearest neighbor to a particular vacancy (Fig. 5.9). A divacancy will form if a nearest neighbor site to a vacancy is occupied by another vacancy, thus P_{2v} depends on the crystal structure. Taking the fcc lattice, all 12 nearest neighbor sites are equivalent, yielding:

$$P_{2v} = 12 P_x, \tag{5.54}$$

where P_x is the probability per second that another vacancy jumps into one of the nearest neighbor positions surrounding the vacancy. P_x is proportional to:

1. The number of sites surrounding the nearest neighbor site from which another vacancy could jump (seven sites as shown by the open red circles in Fig. 5.9)
2. The probability that one of these lattice positions is occupied by a vacancy, N_v
3. The jump frequency of a vacancy, ω, or

$$P_x = 7 N_v \omega, \tag{5.55}$$

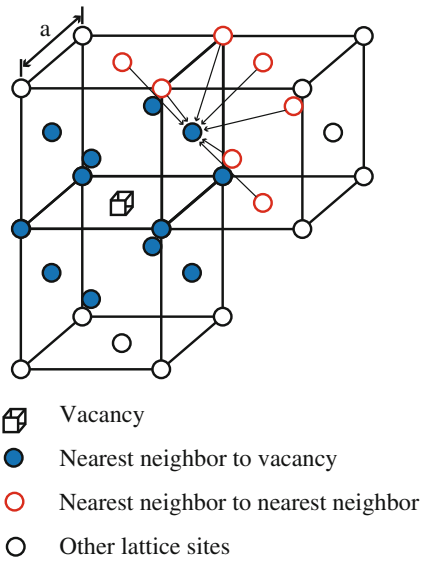

Fig. 5.9 Locations of nearest neighbors for the formation of a divacancy in the fcc lattice (after ref. [3])

and we can write the vacancy site fraction as $N_v = C_v\Omega$, where C_v is the volumetric vacancy concentration and Ω is the atomic volume. Back substitution of Eqs. (5.54) and (5.55) into Eq. (5.53) yields:

$$R_{2v} = 84\omega\Omega C_v^2 [\text{cm}^{-3}\,\text{s}^{-1}]. \tag{5.56}$$

Comparison with the definition of the reaction rate, Eq. (5.51) gives the reaction rate constant K_{2v}:

$$K_{2v} = 84\omega\Omega. \tag{5.57}$$

In the fcc lattice, $D = a^2\omega$, then:

$$K_{2v} = \frac{84\Omega D_v}{a^2}. \tag{5.58}$$

Although the expression for the rate constant was derived for a vacancy–vacancy reaction, the same formulation applies to any reaction between any specie (e.g., impurity) that occupies substitutional positions in the fcc lattice. It can also be used for other lattice types, but the factor, 84, called the combinatorial factor, or z, is dependent on the crystal structure. The combinatorial factor is the solid-state analog of the cross section in particle interactions.

In the previous example, we forced one of the reactants to be stationary. When the reaction is between two mobile species, the rate is $(K_{AB} + K_{BA})\, C_A C_B$, where K_{AB} is the rate constant calculated assuming that B is immobile and vice versa for K_{BA}. Therefore, if both vacancies are mobile, the result would be multiplied by a factor of 2; $K_{2v} + K_{2v} = 2K_{2v}$. Given this background, we now turn our attention to the various terms in the point defect balance equations in order to develop expressions for the reaction rate coefficients.

5.3.1 Defect Production

The first term in the defect balance equations of Eq. (5.1) is the production rate of vacancies and interstitials and this was determined in Chap. 2, Eq. (2.125), where the term in brackets is given the designation, ν_{FP}

$$K_0 = \xi\nu_{FP}\sigma_s N\phi [\text{cm}^{-3}\,\text{s}^{-1}]. \tag{5.59}$$

For stainless steel, $\nu_{FP} \sim 30$ Frenkel pairs per collision, $\sigma_s \sim 3 \times 10^{-24}$ cm^2 and $N \sim 7 \times 10^{22}$ cm^{-3}. The term, ξ, is the displacement efficiency (Chap. 3) that accounts for the reduction in freely migrating point defects due to in-cascade recombination and clustering.

5.3.2 Recombination

The second term in Eq. (5.1), $K_{iv}C_vC_i$, is the recombination rate. The rate constant K_{iv} is the same for both vacancies and interstitials since they must recombine with each other at the same rate. Reactions between vacancies and interstitials are of great importance since the result is mutual annihilation or return to the perfect lattice. Assuming a stationary vacancy and a mobile interstitial, and that recombination occurs only when the interstitial jumps into a site that is nearest neighbor to the vacancy, we can determine the recombination rate constant for an octahedral interstitial in the fcc lattice. There are six octahedral sites as nearest neighbors to the vacant lattice site and each interstitial site has eight octahedral nearest neighbors, giving a value of 48 for the combinatorial factor:

$$K_{iv} = \frac{48\Omega D_i}{a^2}. \tag{5.60}$$

However, this is a bit unrealistic since (1) the stable form of the interstitial is the split interstitial and (2) the vacancy and interstitial are attracted to each other by virtue of their strain fields, causing spontaneous recombination to occur over distances greater than the nearest neighbor spacing. Therefore, a more realistic estimate of the combinatorial factor, z_{iv}, is ~ 500:

$$K_{iv} = \frac{z_{iv}\Omega D_i}{a^2}, \quad \text{and} \quad z_{iv} \sim 500. \tag{5.61}$$

5.3.3 Loss to Sinks

The loss term represents all the possible sinks for vacancy and interstitial loss. These sinks can be divided into three categories:

1. *Neutral* (*unbiased*) *sinks* show no preference for capturing one type of defect over the other type. The rate of absorption is proportional to the product of the diffusion coefficient of the point defect and the difference in the concentrations of the point defect in the bulk metal and at the sink surface. The types of sinks in this category are voids, incoherent precipitates, and grain boundaries.
2. *Biased sinks* exhibit preferential attraction for one defect type over the other. Dislocations exhibit a stronger preference for interstitials than for vacancies. The bias is due to the drift of interstitials down the stress gradient near the dislocation core. Since absorption of interstitials enhances dislocation climb, the dislocation is an unsaturable sink. Two types of dislocations are considered:

networks in unirradiated metal and from unfaulted Frank loops, and interstitial dislocation loops.

3. *Variable bias sinks* such as coherent precipitates act as traps that capture a defect but preserve its identity until it is annihilated by the opposite type defect. Impurity atoms and coherent precipitates act as recombination centers with a limited capacity.

5.3.4 Sink Strengths

Reaction rate constants describe the reaction between a point defect and a sink (which may be another point defect), and are designated K_{jX} where j is the mobile point defect and X is the sink. As such, they include the diffusion coefficient of the point defect as well as a description of the tendency for the reaction to occur. It is often useful to describe the tendency of a sink to absorb defects that is independent of the defect properties. The sink strength, with units of [cm^{-2}], is such a description and it reflects the strength or affinity of a sink for defects. Sink strength is independent of defect properties for neutral sinks. The sink strength is denoted by k_{jX}^2, and is defined as:

$$\text{absorption rate} = K_{jX} C_j C_X = k_{jX}^2 C_j D_j, \tag{5.62}$$

so

$$k_{jX}^2 = \frac{K_{jX} C_X}{D_j}, \tag{5.63}$$

or

$$k_j^2 = \sum_X k_{jX}^2. \tag{5.64}$$

Both the rate constant and the sink strength are terms commonly used to describe the action of sinks on the defects in the solid. Physically, k_j^{-1} is the mean distance a free defect of type j travels in the solid before becoming trapped.

Before we treat the various sink types, we will first look at the rate constants for the two basic reaction processes: reaction rate-controlled processes and diffusion-limited processes. We begin with reaction rate-controlled processes.

5.4 Reaction Rate-Controlled Processes

5.4.1 Defect–Void Interaction

For reactions where capture is controlled by the rate at which the point defects enter the trap site, we can use Eq. (5.61). For defect–void reactions, the term to be determined is the combinatorial factor. For a void, the number of lattice points on the surface of the sphere is $4\pi R^2/a^2$, where the area occupied by a lattice point is approximated by a^2. The rate constant then becomes:

$$K_{vV} = \frac{4\pi R^2 \Omega D_v}{a^4} = \frac{4\pi R^2 D_v}{a}, \quad \text{where } \Omega \sim a^3, k_V^2 = \frac{4\pi R^2 \rho_V}{a}, \tag{5.65}$$

where ρ_V is the concentration of voids in the solid.

5.4.2 Defect–Dislocation Interaction

Consider a cylinder about a dislocation line whose axis is coincident with the dislocation line such that capture is certain for any vacancy entering the cylinder (Fig. 5.10). The cylinder consists of z_{vd} atomic sites on each of the crystal planes intersected by the dislocation line. The cylinder defines the capture radius of the dislocation, or the radius inside which entering defects are lost to the sink. If the spacing between atom planes in the lattice is $\sim a$, then there are z_{vd}/a capture sites per unit length of dislocation. Letting ρ_d be the density of dislocation lines in the crystal (in units of centimeters of dislocation line per cm^3 of solid or cm^{-2}), then there are z_{vd} ρ_d/a capture sites per unit volume. If the concentration of vacancies per unit volume

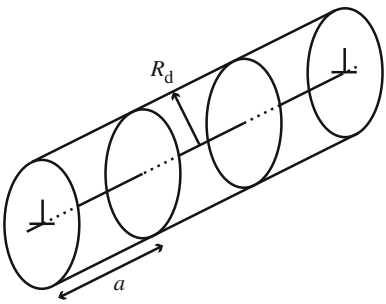

Fig. 5.10 Capture volume around a dislocation line, defined by the cylinder of radius R_d and with sink sites lying on crystal planes separated by a distance a

is C_v, then the vacancy site fraction is $C_v\Omega$. For a vacancy jump rate of ω, the rate of vacancy capture rate by the dislocation per cm^3 is given as:

$$R_{vd} = \frac{z_{vd}\rho_d}{a} C_v \Omega \omega \ [\mathrm{cm}^{-3}\,\mathrm{s}^{-1}]. \tag{5.66}$$

Since $\Omega \sim a^3$ and $D_v = a^2\omega$, we have:

$$\begin{aligned} R_{vd} &= D_v z_{vd}\rho_d C_v \text{ and reaction rate constant } K_{vd} = D_v z_{vd}, k_{vd}^2 = z_{vd}\rho_d \\ R_{id} &= D_i z_{id}\rho_d C_i \text{ and reaction rate constant } K_{id} = D_i z_{id}, k_{id}^2 = z_{id}\rho_d \end{aligned} \tag{5.67}$$

and $z_{vd} \neq z_{id}$.

5.5 Diffusion-Limited Reactions

Reactions between defects and sinks cannot always be characterized as reaction rate-limited. Reactions driven by defect concentration gradients are diffusion-limited and must be treated differently. Such reactions are defect–void, defect–grain boundary, and sometimes defect–dislocation interactions. Following [3], these reactions are addressed here starting with defect–void reactions.

5.5.1 Defect–Void Reactions

Consider the case of ρ_V voids per unit volume, each of radius, R, which absorb a particular type of point defect present in the solid and between the spherical sinks. Focusing on a single sphere, the unit cell or capture volume surrounding each sphere is defined as the portion of the solid that can be associated with each sphere. The radius of the capture volume (see Fig. 5.11) around each sphere is defined by:

$$\left(\frac{4}{3}\pi\mathscr{R}^3\right)\rho_V = 1. \tag{5.68}$$

The diffusion equation for the point defects will be solved in the spherical shell $R \le r \le \mathscr{R}$. The concentration of point defects at a radial position r in the capture volume at time t is denoted by $C(r, t)$. The definition of the capture volume implies that there is no net flux of point defects across the boundary at $r = \mathscr{R}$, which is written as:

$$\left(\frac{\partial C}{\partial r}\right)_{\mathscr{R}} = 0, \tag{5.69}$$

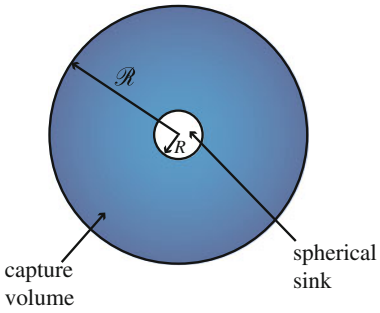

Fig. 5.11 The unit cell for determination of the diffusion-controlled rate constant for defect absorption by a spherical sink

and the point defect concentration at the surface of the sphere is given as:

$$C(R,t) = C_{\mathrm{R}}. \tag{5.70}$$

The value of C_{R} depends on the process. For insoluble gas atoms where the spheres represent gas bubbles, $C_{\mathrm{R}} = 0$. For bubbles or voids where the point defects are vacancies or interstitials, $C_{\mathrm{R}} = C^0_{\mathrm{v,i}}$, the thermal equilibrium defect concentration.

If the defects are created uniformly in the capture volume and no sinks other than the sphere are present, then the concentration $C(r, t)$ is determined by solution of the volumetric diffusion equation with a volumetric source term:

$$\frac{\partial C}{\partial t} = \frac{D}{r^2}\frac{\partial}{\partial r}\left(r^2\frac{\partial C}{\mathrm{d}r}\right) + K_0, \tag{5.71}$$

where D is the diffusion coefficient of the defects (assumed to be independent of concentration) and K_0 is the defect production rate per unit volume given by Eq. (5.59).

When a solid is irradiated at a temperature where point defects are mobile, the loss of particles to the sink is partially compensated by the production rate so the concentration changes slowly with time $\left(\frac{\partial C}{\partial t} \sim 0\right)$ and Eq. (5.71) can be approximated as:

$$\frac{D}{r^2}\frac{\mathrm{d}}{\mathrm{d}r}\left(r^2\frac{\mathrm{d}C}{\mathrm{d}r}\right) = -K_0. \tag{5.72}$$

The solution to Eq. (5.72) subject to the boundary conditions given by Eqs. (5.69) and (5.70) is given as:

$$C(r) = C_{\mathrm{R}} + \frac{K_0}{6D}\left[\frac{2\mathscr{R}^2(r-R)}{rR} - (r^2 - R^2)\right]. \tag{5.73}$$

Since in many cases, the capture volume radius is much larger than the sink radius and the defect concentration changes rapidly only very close to the sink, the capture volume is divided into two regions (Fig. 5.12). In region 1, the diffusion term is much greater than the source term and Eq. (5.72) can be approximated by:

$$\frac{1}{r^2}\frac{\mathrm{d}}{\mathrm{d}r}\left(r^2\frac{\mathrm{d}C}{\mathrm{d}r}\right) = 0, \tag{5.74}$$

with boundary conditions:

$$C(R) = C_{\mathrm{R}} \tag{5.75}$$

$$C(\infty) = C(\mathscr{R}). \tag{5.76}$$

The solution of Eq. (5.74) subject to the boundary conditions given by Eqs. (5.75) and (5.76) gives:

$$C(r) = C_{\mathrm{R}} + [C(\mathscr{R}) - C_{\mathrm{R}}]\left[1 - \left(\frac{R}{r}\right)\right]. \tag{5.77}$$

The flux of particles at the void surface is defined by:

$$J = -D\left(\frac{\mathrm{d}C}{\mathrm{d}r}\right)_R. \tag{5.78}$$

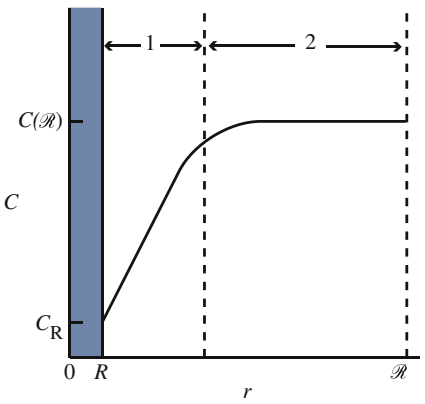

Fig. 5.12 Regions of interest in the solution of the diffusion equation in a spherical shell with a uniform volumetric production rate of defects

Using Eq. (5.77) gives:

$$J = \frac{-D[C(\mathscr{R}) - C_{\mathrm{R}}]}{R}. \tag{5.79}$$

The absorption rate of point defects by the void is given as:

$$-(4\pi R^2)J = 4\pi RD[C(\mathscr{R}) - C_{\mathrm{R}}]. \tag{5.80}$$

Requiring that point defects produced in the capture volume be absorbed by the void gives:

$$\frac{4}{3}\pi\left(\mathscr{R}^3 - R^3\right)K_0 = 4\pi RD[C(\mathscr{R}) - C_{\mathrm{R}}]. \tag{5.81}$$

If $\mathscr{R}^3 \gg R^3$, the balance becomes as follows:

$$C(\mathscr{R}) = C_{\mathrm{R}} + \frac{K_0\mathscr{R}^3}{3RD}. \tag{5.82}$$

Assuming that $C(\mathscr{R}) \gg C_{\mathrm{R}}$ in Eq. (5.80) and replacing $C(\mathscr{R})$ by C, we obtain the total rate of diffusion-controlled absorption of point defects by the void by multiplying Eq. (5.80) by the number of voids per unit volume ρ_{V}:

$$\text{Rate of absorption/cm}^3 = 4\pi RD\rho_{\mathrm{V}}C. \tag{5.83}$$

The rate constant for diffusion-controlled reaction of point defects and a perfect spherical sink of radius R is then:

$$\begin{aligned} K_{\mathrm{iV}} &= 4\pi RD_{\mathrm{i}}, \\ K_{\mathrm{vV}} &= 4\pi RD_{\mathrm{v}}, \\ k_{\mathrm{V}}^2 &= 4\pi R\rho_{\mathrm{V}}, \end{aligned} \tag{5.84}$$

where the subscripts on K refer to the reacting species, vacancies or interstitials (v, i), and voids V.

5.5.2 Defect–Dislocation Reactions

Diffusion-controlled reactions between defects and dislocations occur in much the same way as in the case of spherical sinks, but in cylindrical coordinates. Taking the

capture radius of the sink to be R_d and the dislocation density to be ρ_d, we define the unit cell such that:

$$(\pi \mathscr{R}^2)\rho_d = 1. \tag{5.85}$$

The diffusion equation is given as:

$$\frac{D}{r}\frac{d}{dr}\left(r\frac{dC}{dr}\right) + K_0 = 0, \tag{5.86}$$

with boundary conditions:

$$C(R_d) = C_{Rd} \tag{5.87}$$

$$\left(\frac{dC}{dr}\right)_{\mathscr{R}} = 0, \tag{5.88}$$

and solution:

$$C(r) = C_{R_d} + \frac{K_0 \mathscr{R}^2}{2D}\left[\ln\left(\frac{r}{R_d}\right) - 1/2\left(\frac{r^2 - R_d^2}{\mathscr{R}^2}\right)\right]. \tag{5.89}$$

Analogous to the case for spherical sinks in region 1, but in cylindrical geometry instead, the diffusion equation is given as:

$$\frac{1}{r}\frac{d}{dr}\left(r\frac{dC}{dr}\right) = 0, \tag{5.90}$$

with boundary conditions:

$$C(R_d) = C_{Rd} \tag{5.91}$$

$$C(\mathscr{R}) = C, \tag{5.92}$$

with solution:

$$C(r) = C_{R_d} + [C(\mathscr{R}) - C_{R_d}]\frac{\ln(r/R_d)}{\ln(\mathscr{R}/R_d)}. \tag{5.93}$$

The flux of defects to the dislocation line is given as:

$$J = -D\left(\frac{dC}{dr}\right)_{R_d} = \frac{-D[C(\mathscr{R}) - C_{R_d}]}{R_d \ln(\mathscr{R}/R_d)}. \tag{5.94}$$

The absorption rate per unit length of dislocation line $= -(2\pi R_d)J$

$$= \frac{2\pi D[C(\mathscr{R}) - C_{R_d}]}{\ln(\mathscr{R}/R_d)}. \tag{5.95}$$

The rate of defect production in the capture volume

$$= \pi(\mathscr{R}^2 - R_d^2)K_0, \tag{5.96}$$

and since all defects produced in the capture volume are captured by the dislocation:

$$\frac{2\pi D[C(\mathscr{R}) - C_{R_d}]}{\ln(\mathscr{R}/R_d)} = \pi(\mathscr{R}^2 - R_d^2)K_0, \tag{5.97}$$

and

$$C(\mathscr{R}) = C_{R_d} + \frac{K_0\mathscr{R}^2}{2D}\ln(\mathscr{R}/R_d) \qquad \text{for } R_d/\mathscr{R} \ll 1, \tag{5.98}$$

so from Eq. (5.94) the rate of defect capture by dislocations per unit volume $= \dfrac{2\pi D\rho_d C}{\ln(\mathscr{R}/R_d)}$, and the rate constants for vacancies and interstitials are as follows:

$$\begin{aligned} K_{vd} &= \frac{2\pi D_v}{\ln(\mathscr{R}/R_{vd})} \\ K_{id} &= \frac{2\pi D_i}{\ln(\mathscr{R}/R_{id})}, \end{aligned} \tag{5.99}$$

and

$$\begin{aligned} k_{vd}^2 &= \frac{2\pi\rho_d}{\ln(\mathscr{R}/R_{vd})} \\ k_{id}^2 &= \frac{2\pi\rho_d}{\ln(\mathscr{R}/R_{id})}. \end{aligned} \tag{5.100}$$

Note that the combinatorial factors for vacancies and interstitials differ by the capture radius. The capture radius for interstitials is slightly greater than that for vacancies and is the origin of the dislocation bias for interstitials.

5.6 Mixed Rate Control

Mixed rate control occurs when the reaction rate is determined by a combination of processes. We can determine the rate constant for the combined processes by adding the reciprocals of the rate constants to give the resistance due to series steps of diffusion and surface attachment. For the case of voids, we use the rate constants given by Eqs. (5.65) and (5.84) giving:

$$\frac{1}{K_{\text{eff}}} = \frac{1}{K_{\text{reaction}}} + \frac{1}{K_{\text{diffusion}}}, \tag{5.101}$$

to yield the effective rate constant:

$$K_{\text{eff}} = \frac{4\pi RD}{1 + \dfrac{a}{R}}, \quad k^2_{\text{eff}} = \frac{4\pi R\rho_{\text{V}}}{1 + \dfrac{a}{R}}. \tag{5.102}$$

For large spheres, $a/R \rightarrow 0$ and the rate constant is that for diffusion only. This result shows that reaction rate limitations to capture kinetics for spherical sinks are only significant if the sphere radius is small, approaching the lattice constant.

For dislocations, the capture rates calculated from a diffusion-controlled process verses a reaction rate-controlled process are as follows:

$$\begin{aligned} K_{\text{diffusion}} &= \frac{2\pi D}{\ln(\mathscr{R}/R_{\text{d}})} \\ K_{\text{reaction}} &= z_{\text{d}} D, \end{aligned} \tag{5.103}$$

giving the effective rate constant for mixed-control:

$$K_{\text{eff}} = \frac{D}{\dfrac{1}{z_{\text{d}}} + \dfrac{\ln(\mathscr{R}/R_{\text{d}})}{2\pi}}, \quad k^2_{\text{eff}} = \frac{\rho_{\text{d}}}{\dfrac{1}{z_{\text{d}}} + \dfrac{\ln(\mathscr{R}/R_{\text{d}})}{2\pi}} \tag{5.104}$$

Consider z_{d} to be the area of a circular region of radius R_{d} multiplied by the number of atoms per unit area. For the (100) plane of the fcc lattice, the number of atoms/unit area is $2/a^2$ and:

$$K_{\text{reaction}}/D = z_{\text{d}} = \frac{2\pi R_{\text{d}}^2}{a^2} = 24 \qquad \text{for } R_{\text{d}} \sim 0.6\,\text{nm and } a \sim 0.3\,\text{nm}. \tag{5.105}$$

For a dislocation line density of 10^{10} cm^{-2}, $K_{\text{diffusion}}/D = \dfrac{2\pi}{\ln(\mathscr{R}/R_{\text{d}})} = 1.4$. So capture of defects by dislocations is diffusion-controlled.

5.7 Defect–Grain Boundary Reactions

Interactions between point defects and grain boundaries are important in the case of radiation-induced segregation, discussed in Chap. 6. Following the analysis of Heald and Harbottle [9], the sink strength of the grain boundary is determined by considering a spherical grain of radius a, with grain boundary defect concentration equal to the thermal equilibrium value, which will be neglected compared to the irradiated-induced concentration. The loss to sinks within the grain is given as:

$$k^2 DC = (z_d \rho_d + 4\pi R_V \rho_V) DC, \tag{5.106}$$

where k^2 is the sink strength for the grain interior due to dislocations and voids, and the diffusion equation is given as:

$$\frac{d^2 C}{dr^2} + \frac{2}{r}\frac{dC}{dr} + \frac{K_0}{D} - k^2 C = 0, \tag{5.107}$$

subject to boundary conditions $C(r = a) = 0$ and $C(r = 0) =$ finite. The solution to Eq. (5.107) subject to the boundary conditions is given as:

$$C(r) = \frac{K_0}{Dk^2}\left[1 - \frac{a \sinh(kr)}{r \sinh(ka)}\right], \tag{5.108}$$

and the total flow of point defects to the grain boundary, A, is given as:

$$A = -4\pi r^2 D \left.\frac{\partial C}{\partial r}\right|_{r=a} = \frac{4\pi K_0 a}{k^2}[ka \cot(ka) - 1]. \tag{5.109}$$

Written in rate theory formalism, Eq. (5.109) becomes as follows:

$$A = z_{gb} D C_0, \tag{5.110}$$

where z_{gb} is the sink strength for an individual grain boundary and C_0 is the concentration at the grain center ($r = 0$), Fig. 5.13:

$$C_0 = C(r = 0) = \frac{K_0}{Dk^2}\left[1 - \frac{ka}{\sinh(ka)}\right]. \tag{5.111}$$

From Eqs. (5.109), (5.110), and (5.111), the grain boundary sink strength, z_{gb}, is given as:

$$z_{gb} = 4\pi a \left[\frac{ka \cosh(ka) - \sinh(ka)}{\sinh(ka) - ka}\right]. \tag{5.112}$$

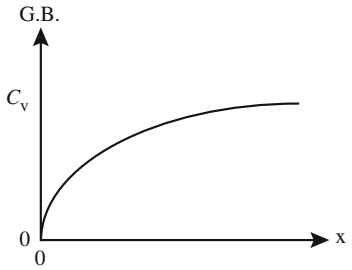

Fig. 5.13 Diffusion-controlled reaction between vacancies and a grain boundary

For small grains and low sink strengths, $ka \rightarrow 0$, and:

$$z_{gb}(ka \rightarrow 0) = 8\pi a = 4\pi d, \tag{5.113}$$

where $d(=2a)$ is the grain diameter. When the sink strength is large, $ka \rightarrow \infty$, and:

$$z_{gb}(ka \rightarrow \infty) = 4\pi k a^2 = \pi k d^2. \tag{5.114}$$

The grain boundary sink strength is the product of z_{gb} and the grain density in grains per unit volume, or $\rho_{gb} = 6/\pi d^3$, giving:

$$k_{gb}^2(ka \rightarrow 0) = 24/d^2, \quad K_{jgb} = 4\pi D_j d, \tag{5.115}$$

and

$$k_{gb}^2(ka \rightarrow \infty) = 6k/d, \quad K_{jgb} = \pi k D_j d^2, \tag{5.116}$$

where j = i or v.

Generally, $k^2 \sim 10^{11}$ cm^{-2} and $d > 10^{-3}$ cm so that Eq. (5.116) is the appropriate expression for the grain boundary sink strength. In fact, the grain boundary sink strength is given by Eq. (5.116) whenever $(z_d\rho_d + 4\pi R_V\rho_V) > 1/d$.

5.8 Coherent Precipitates and Solutes

These types of sinks are known as variable bias sinks in that they act as traps for vacancies and interstitials rather than as infinite sinks, in which the defect loses its identity after being absorbed. The source of the attraction of vacancies and interstitials to the trap is the relief of the strain field produced by the coherency between

the trap and the lattice. The coherent precipitate is of a structure in which the lattice planes of the precipitate are continuous with those of the matrix, but due to the difference in lattice parameters, there is a strain field at the interface where the lattice planes from each are forced to match. The over- or undersized solute is a limiting case of a coherent precipitate. The trap strength is limited by the capacity of the interface to hold or trap a defect until the anti-defect arrives and results in annihilation. Hence, no matter accumulates at this defect and thermal emission does not occur. The interface does exhibit a bias for defects and this bias is a function of the biased sinks in the solid. For example, if the biased sinks in the solid favor interstitials, then $k_i^2 > k_v^2$ and the trap interface will acquire slightly more vacancies than interstitials. This excess of vacancies then causes the trap surface to become a more effective sink for interstitials than for vacancies. The biases for the trap are denoted by Y_v and Y_i (Brailsford and Bullough [10] and Olander [3] provide detailed analyses of the bias factors), and the absorption rates of vacancies and interstitials at the trap are given by:

$$\begin{aligned} A_v^{CP} &= 4\pi R_{CP} D_v C_v \rho_{CP} Y_v = K_{vCP} C_v \rho_{CP} \\ A_i^{CP} &= 4\pi R_{CP} D_i C_i \rho_{CP} Y_i = K_{iCP} C_i \rho_{CP}. \end{aligned} \tag{5.117}$$

If there can be no steady-state accumulation of defects at the trap, then there is no net matter flow to or from the sinks and:

$$4\pi R_{CP} \rho_{CP} D_v C_v Y_v = 4\pi R_{CP} \rho_{CP} D_i C_i Y_i, \tag{5.118}$$

so

$$Y_i = \frac{D_v C_v}{D_i C_i} Y_v, \tag{5.119}$$

and the rate constants and sink strengths are as follows:

$$\begin{aligned} K_{vCP} &= 4\pi R_{CP} D_v Y_v; \quad & k_{vCP}^2 &= 4\pi R_{CP} \rho_{CP} Y_v \\ K_{iCP} &= 4\pi R_{CP} D_i Y_i; \quad & k_{iCP}^2 &= 4\pi R_{CP} \rho_{CP} Y_i. \end{aligned} \tag{5.120}$$

So variable bias sinks play an interesting role in that they adjust their preference for point defects in response to the relative sink strengths in the bulk.

The reaction rate constants for the various reactions are summarized in Table 5.2 for the various defect–defect and defect–sink reactions.

Table 5.2 Reaction rate constants for defect–sink reactions

Reaction	Rate constant	Sink strength	Eq. #
v + v	$K_{2v} = \dfrac{z_{2v}\Omega D_v}{a^2}$	–	Equation (5.58)
i + i	$K_{2i} = \dfrac{z_{2i}\Omega D_i}{a^2}$	–	Equation (5.58)
v + i	$K_{iv} = \dfrac{z_{iv}\Omega D_i}{a^2}$	–	Equation (5.61)
v, i + void			
Reaction rate control	$K_{vV} = \dfrac{4\pi R^2 D_v}{a} \quad K_{iV} = \dfrac{4\pi R^2 D_i}{a}$	$k^2_{vV} = k^2_{iV} = \dfrac{4\pi R^2 \rho_V}{a}$	Equation (5.65)
Diffusion control	$K_{vV} = 4\pi R D_v \quad K_{iV} = 4\pi R D_i$	$k^2_{vV} = k^2_{iV} = 4\pi R \rho_V$	Equation (5.84)
Mixed rate control	$K_{vV} = \dfrac{4\pi R D_v}{1 + \dfrac{a}{R}} \quad K_{iV} = \dfrac{4\pi R D_i}{1 + \dfrac{a}{R}}$	$k^2_{vV} = k^2_{iV} = \dfrac{4\pi R \rho_V}{1 + \dfrac{a}{R}}$	Equation (5.102)
v, i + dislocation			
Diffusion control	$K_{vd} = \dfrac{2\pi D_v}{\ln(\mathscr{R}/R_{vd})} \quad K_{id} = \dfrac{2\pi D_i}{\ln(\mathscr{R}/R_{id})}$	$k^2_{vd} = \dfrac{2\pi \rho_d}{\ln(\mathscr{R}/R_{vd})} \quad k^2_{id} = \dfrac{2\pi \rho_d}{\ln(\mathscr{R}/R_{id})}$	Equations (5.99, 5.100)
Reaction rate control	$K_{vd} = z_{vd} D_v \quad K_{id} = z_{id} D_i$	$k^2_{vd} = z_{vd}\rho_d \quad k^2_{id} = z_{id}\rho_d$	Equation (5.67)
Mixed rate control	$K_{vd} = \dfrac{D_v}{\dfrac{1}{z_{vd}} + \dfrac{\ln(\mathscr{R}/R_{vd})}{2\pi}} \quad K_{id} = \dfrac{D_i}{\dfrac{1}{z_{id}} + \dfrac{\ln(\mathscr{R}/R_{id})}{2\pi}}$	$k^2_{vd} = \dfrac{\rho_d}{\dfrac{1}{z_{vd}} + \dfrac{\ln(\mathscr{R}/R_{vd})}{2\pi}} \quad k^2_{id} = \dfrac{\rho_d}{\dfrac{1}{z_{id}} + \dfrac{\ln(\mathscr{R}/R_{id})}{2\pi}}$	Equation (5.104)
v, i + grain boundary			
Diffusion control	$K_{vgb} = 4\pi D_v d \quad K_{igb} = 4\pi D_i d$ $K_{vgb} = \pi k D_v d^2 \quad K_{igb} = \pi k D_i d^2$	$k^2_{gb} = 24/d^2, \quad d < 10^{-3}$ cm $k^2_{gb} = 6k/d, \quad d > 10^{-3}$ cm	Equation (5.115) Equation (5.116)
v, i + coherent ppt	$K_{vCP} = 4\pi R_{CP} D_v Y_v, \quad K_{iCP} = 4\pi R_{CP} D_i Y_i$	$k^2_{vCP} = 4\pi R_{CP}\rho_{CP} Y_v, \quad k^2_{iCP} = 4\pi R_{CP}\rho_{CP} Y_i$	Equation (5.120)

5.9 Point Defect Recovery

When irradiated materials are annealed, they exhibit stages, or temperature regimes, that correspond to the loss of defects by mutual annihilation or by diffusion to sinks. Experimental studies use isochronal annealing followed by electrical resistivity at low temperature to identify the major defect recovery processes. Irradiation and electrical resistivity measurements are conducted at low temperature (e.g., 4 K) where defects are immobile and thermal scattering contributions to resistivity are minimal. The appearance of any given stage depends on the time and temperature used in the annealing experiment, and often on the time and temperature of irradiation. Therefore, they are not precisely defined.

Since electrical resistivity is proportional to the total concentration of all irradiation-produced point defects, the resistivity increase per unit irradiation dose is therefore a measure of the concentration of stable defects produced at a given irradiation temperature. Measurements of the change in electrical resistivity, $\Delta\rho$, as a function of annealing temperature provide information on the kinetics of defect reactions. For example, if recombination of vacancies and interstitials occurs, a decrease of $\Delta\rho$ with temperature follows. Figure 5.14 shows a plot of the fractional change in defect concentration ($\Delta\rho/\Delta\rho_0$ is proportional to N/N_0) as a function of temperature in pure copper after electron irradiation at 4 K. Note that there are five major stages of annealing.

Based on the one-interstitial model, Stage I corresponds to the onset of SIA migration. In fact, Stage I consists of five substages, I_A–I_E, as shown in Fig. 5.15. Details of Stage I annealing of copper are shown in Table 5.3. The lower temperature substages, I_A, I_B, and I_C, are due to collapse of close Frenkel pairs. That is, recombination of vacancy–interstitial pairs that were not created far enough away from each other to escape the attractive forces and thus the interstitial recombines with its vacancy counterpart. The differences between stages I_A, I_B, and I_C may be due to alternative interstitial structures or to directions of separation in the lattice.

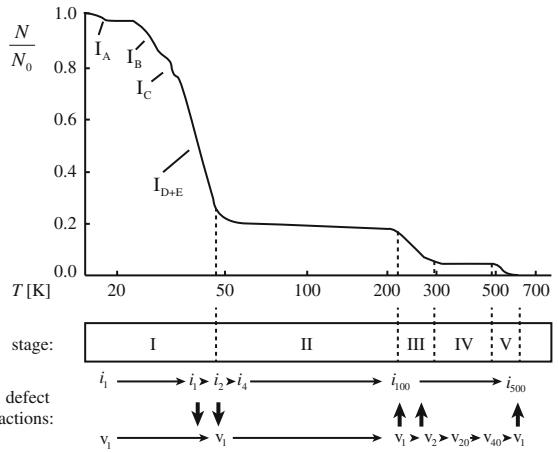

Fig. 5.14 Annealing stages and defect reactions in pure copper after electron irradiation; i_1 and v_1 denote single interstitials and vacancies, respectively, i_2 and v_2 di-interstitials and divacancies (after [11])

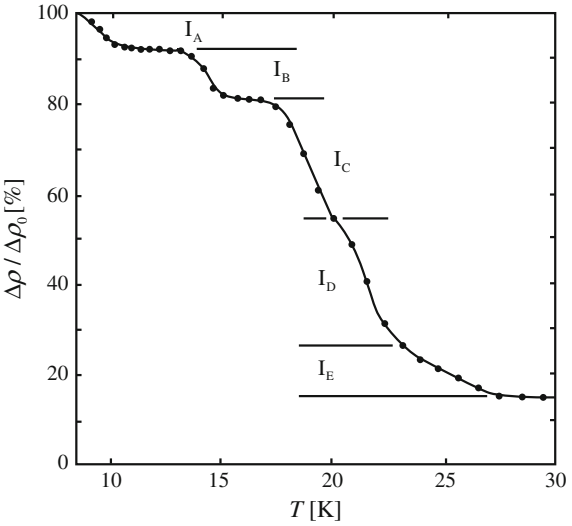

Fig. 5.15 Isochronal annealing curves of a Pt sample irradiated at 4.5 K with 3 MeV electrons to $\Delta\rho_0 = 4 \times 10^{-9}\ \Omega$ cm. Isochronal holding times were 20 min for temperature steps of $\Delta T/T = 3.5$ % (after [11])

Table 5.3 Stage 1 annealing of copper (after [12])

	I_A	I_B	I_C	I_D	I_E
Temperature (K)	16	28	32	39	53
Activation energy (eV)	0.05	0.085	0.095	0.12	0.12
Reaction order	1	1	1	1	1
Number of jumps	1	1	1	10	10^4
Impurity effect	–	Small reduction	–	Large reduction	Large reduction
Dose effect	–	–	–	–	Moves to lower T
Increasing e^- energy	Increase		Reduce		Increase

Stages I_D and I_E are due to recombination by long-range migration of interstitials. Stage I_D is due to correlated recombination in which the interstitial atom recombines with the vacancy created by the same displacement event. Stage I_E is due to uncorrelated recombination of an interstitial with a vacancy from a different displacement event. In these cases, recovery may consist of tens or hundreds of jumps. Stages I_D and I_E are observed when the Frenkel pair density is small enough so that the average distance of an interstitial atom to a vacancy from a different displacement event is much larger than that to a vacancy from the same displacement event. Note that interstitial clustering occurs simultaneously with recombination and is responsible for the survival of interstitials at the end of Stage I and for the incompleteness of recovery in this stage.

Stage II recovery describes migration and growth of small interstitial clusters and SIA-impurity clusters and occurs in the temperature range 50–200 K in copper. The

minimal change in resistivity of Stage II is indicative of the importance of impurities in this stage. Impurities can trap interstitials, delaying interstitial clustering reactions. Stage II is more prominent in impure materials or when pure materials are doped with impurities that could form SIA-impurity clusters.

In Stage III, vacancies migrate and annihilate at interstitial clusters. Vacancy migration also results in vacancy agglomeration and at the end of Stage III, surviving defects consist of small vacancy clusters and larger interstitial loops. Vacancy clusters grow in Stage IV to such a size that they are visible in the transmission electron microscope as small voids. Impurities may affect vacancy clustering and alter Stage IV recovery. Stage V corresponds to the thermal dissociation of vacancy clusters followed by vacancy annihilation at interstitial loops such that at the end of stage V all damage is removed.

The specific processes that occur after Stage III are less well defined for several reasons. For a number of metals (Al, Pt, Au), recovery is complete after Stage III since the loss of mobile vacancies to interstitial clusters is apparently so great that the residual vacancy clusters are not large enough to survive Stage III. Multiple-defect structures are not easily formed by electron irradiation and so stages IV and V are rather ill-defined. Defect clusters are more readily formed by neutron or ion irradiation that produce large defect cascades in which separation of the vacancy core from the interstitial shell enhances agglomeration reactions. In this case, a much larger fraction of vacancies and interstitials survive Stage I and Stage III, respectively. It also means that annealing behavior is dependent on the irradiating particle. Further, the wide range of cluster geometries that can nucleate and evolve make for a very complex microstructure with many recovery pathways.

Nomenclature

A	Flow rate of defects to sink
a	Lattice constant, also grain radius
C	Concentration
C_{giL}	Mobile SIA cluster concentration
C_{iv}	Interstitial, vacancy concentration
C_{R}	Vacancy concentration at void boundary
C_{s}	Sink concentration
d	Grain diameter
D_{rad}	Radiation-enhanced diffusion coefficient
D_{th}	Thermal diffusion coefficient
D_{m}	Ballistic mixing diffusion coefficient
D_0^y	Pre-exponential factor in the diffusion coefficient via defect y
D_x^y	Diffusion coefficient for species x via y
E_{m}^y	Migration energy of defect y
f	Correlation coefficient
i	Interstitial
v	Vacancy
s	Sink

J_x Flux of atom or defect x across a marker plane
k Boltzmann's constant
k^2_{jX} Strength of sink X for defect j
K_0 Defect production rate
K_{gb} Rate constant for defect–grain boundary interaction
K_g Rate constant for interstitial interaction with glissile SIA loops
K_{giL} Production rate of glissile interstitial loops
K_{id} Rate constant for interstitial–dislocation interaction
K_{iv} Vacancy–interstitial recombination rate constant
K_{is} Interstitial–sink reaction rate constant
K_{vd} Rate constant for vacancy–dislocation interaction
K_{vs} Vacancy–sink reaction rate constant
K_{2v} Divacancy formation rate constant
L_v Thermal vacancy production term
N Atom fraction
r_{iv} Vacancy–interstitial recombination radius
r_{is} Interstitial–sink recombination radius
r_{vs} Vacancy–sink recombination radius
p Sink annihilation probability
P_{2v} Probability/second of forming a divacancy
P_x Probability/second that a vacancy jumps to a nearest neighbor to a vacancy
R_d Dislocation core radius
R_{id} Reaction rate between interstitials and dislocations
R_{vd} Reaction rate between vacancies and dislocations
R_{2v} Rate of divacancy formation
$\mathscr{R}$ Radius of unit cell or capture volume surrounding a spherical sink
t Time
T Temperature
T_c Critical temperature defined by Eq. (5.50)
v_2 Divacancy designation
z_{gb} Sink strength for an individual grain boundary
z_{xy} Combinatorial number for a reaction between x and y
$\varepsilon_{i,v}$ Fraction of clustered interstitials, vacancies
ε_r Fraction of defects recombining in cascade
ϕ Particle flux
ρ_d Dislocation density
η Parameter defined by Eq. (5.45)
σ_s Microscopic scattering cross section
τ_x Time constant for process x
ω Jump frequency
Ω Atomic volume
ξ Production efficiency term

Subscripts

a	Atoms
CP	Coherent precipitate
d	Dislocation
g	Glissile
gb	Grain boundary
giL	Glissile interstitial loop
i,v	Interstitials, vacancies
m	Migration
Rad	Under irradiation
r	Recombination
R	Void radius
s	Sink
V	Void

Superscripts

i, v	Interstitials, vacancies

Problems

5.1 Point defect concentration buildup during irradiation can be described by:

$$\frac{dC_v}{dt} = K_0 - K_{iv}C_iC_v - K_{vs}C_vC_s + \nabla \cdot (D_v \nabla C_v)$$
$$\frac{dC_i}{dt} = K_0 - K_{iv}C_iC_v - K_{is}C_iC_s + \nabla \cdot (D_i \nabla C_i)$$

How do these equations simplify if you are irradiating a single crystal with no defects present? In that case, what is the relationship between vacancy and interstitial concentrations? Do the vacancy and interstitial concentrations differ if you start with a sample that contains defects?

5.2 For pure nickel irradiated at 500 °C:

(a) Calculate the steady-state concentration of vacancies and interstitials.

$$K_0 = 5 \times 10^{-4}\text{dpa/s} \quad \Delta H_m^v = 0.82\,\text{eV}$$
$$C_s = 10^9\,\text{cm}^{-3} \quad \Delta H_m^i = 0.12\,\text{eV}$$
$$r_{iv} = r_{is} = r_{vs} = 10a \quad \Delta S_m^v = \Delta S_m^i = 0$$
$$\nu = 10^{13}\text{s}^{-1} \quad a = 0.352\,\text{nm}$$

(b) For a dislocation density of 10^{12} cm^{-2}, determine the temperature at which mutual recombination gives way to annealing at fixed sinks.

5.3 A perfect, single crystal Cu wire (cylinder) of radius R = 10 nm and length $L \gg R$ is irradiated at 400 °C. The only sink present is the surface.

(a) Assuming negligible recombination, solve the diffusion equation:

$$\frac{\partial C_x}{\partial t} = K_0 + D_x \nabla^2 C_x$$

at steady state for x = interstitial or vacancy, to obtain the vacancy and interstitial concentration profiles. What boundary condition do you use at the surface? When you solve the equation pay attention to the symmetry of the problem to eliminate terms in the expression for $\nabla^2 C_x$.

(b) Calculate the rates of absorption (number of defects per unit area and time) at the surface.

(Hint: remember that $\nabla^2 C$ is continuous.)

5.4 Calculate the steady-state radiation-enhanced diffusion coefficient for copper at T/T_m = 0.5 in terms of K_0, the defect production rate, and ρ_d, the dislocation sink density.

5.5 Assume for a metal of interest that the interstitial–sink interaction radius and the vacancy–sink interaction radius are equal. Two irradiations are performed at low, but non-negligible sink density. The displacement rate is the same for both irradiations. In the second irradiation, a minor alloying addition doubles the diffusion coefficient of interstitials but does not change the diffusion coefficient for vacancies. By how much does the ratio of the steady-state vacancy to interstitial concentrations change? Explain physically what happens to the point defects.

5.6 A sample of aluminum is held at room temperature (20 °C) and irradiated with a monoenergetic beam of 1 MeV neutrons at a flux of 10^{14} n/cm^{2}s. Assume that the capture radii $r_{iv} = r_{is} = r_{vs}$ are all approximately 10a.

(a) At what sink density does defect annihilation at sinks overtake mutual recombination?

(b) What is the value of the radiation-enhanced steady-state diffusion coefficient of aluminum atoms? How does this compare to the diffusion coefficient in the absence of irradiation?

(c) Verify that your calculations in part (b) do indeed represent a steady-state condition, i.e., $dC_v/dt = dC_i/dt = 0$.

5.7 A defect-free Al crystal is irradiated at a displacement rate of 10^{-5} dpa/s.

(a) Calculate the steady-state concentration of point defects at T = 100 °C and 500 °C.

(b) Once steady state is reached, the irradiation is stopped. Calculate the time constant for recombination as a function of temperature.

(c) One wishes to measure the defect concentration in the irradiated Al, a process assumed to take 100 s. Determine the temperature range for which the defect concentration can be kept within 1 % of its value at the end of the irradiation for this length of time.
Assume the combinatorial factor, $z = 500$.

5.8 Following the analysis for the diffusion rate of point defects to spherical sinks, derive an expression for the vacancy concentration profile around a dislocation. What is the vacancy capture rate by dislocations?

5.9 For fcc nickel, determine whether vacancy capture by dislocations is a diffusion-controlled or reaction rate-controlled process. What about interstitial capture by dislocations?

z_d Area of the circular region about the dislocation (defined by the capture radius) multiplied by the number of atoms per unit area
r_{vd} Capture radius for vacancies = 0.6 nm
r_{id} Capture radius for interstitials = 0.7 nm
ρ_d 10^{10} cm^{-2}

5.10 It can be shown that the time constant (characteristic time) for the process $v + s \rightarrow s$ is $\tau_3 = (K_{vs}C_s)^{-1}$. At sufficiently high temperature, vacancies may be mobile so that the reaction $v + v \rightarrow v_2$ may terminate the increase in vacancy concentration with time. If the consumption rate of vacancies in divacancy formation is $K_{vv}C_v^2$, determine the time constant for the onset of steady state.

5.11 A sample of fcc copper with a low sink density ($\tau_1 < \tau_2$) is irradiated at low temperature ($T/T_m = 0.3$) until steady state is reached. Some time later, all sinks instantly disappear and a new steady state is reached. Determine the magnitude of the change in C_v and C_i between the two steady states.

5.12 Explain the reason (or likely reasons) for the following observations:

(a) The displacement rate at the surface of a copper sample is 1000 times higher when irradiated with 1 MeV Cu^+ ions than with 1 MeV protons at the same flux.
(b) A scattering experiment using 3 MeV B^+ ions on Cu produces yields that disagree sharply with calculations using the Rutherford scattering formula.
(c) A single crystal of copper is irradiated with 2 MeV He^+ ions and the backscatter yield is only 5 % of that of a polycrystal.
(d) Irradiation of a metal with a high neutron flux does not produce a measurable increase in the atom diffusion coefficient.
(e) Two metals are pressed together and heated to $0.5T_m$. It is observed that atoms from the metals intermix at the interface. Attempts to determine the defect(s) responsible for the intermixing reveal that vacancies account for 100 % of the atom mixing. True or false? Why?

5.13 Two engineers are arguing over how to test the effect of the high point defect concentration developed during irradiation on the deformation rate of nickel at 500 °C. Engineer #1 maintains that one can irradiate the sample to the appropriate fluence at the temperature of interest, remove it from the reactor, and heat it back up to temperature to perform the test. Engineer #2 insists that the concentration of point defects decays almost immediately after irradiation ceases and therefore, tests must be performed in situ. Who is right? Why? (Hint: consider the point defect equation for the slowest defect (vacancy) only, neglect recombination, and consider that the only sinks present are dislocations at a concentration of 10^9 cm^{-2}).

$$D_v^{Ni}(500\,^\circ\text{C}) \sim 10^{-8}\,\text{cm}^2/\text{s}$$
$$a \sim 0.3\,\text{nm}$$

5.14 Assume a solid containing defect sinks is irradiated at a temperature T_0, at which only vacancies are mobile.

(a) For the case of a high sink density, estimate the time, t_1, at which sinks will contribute to interstitial annihilation. Neglect recombination.
(b) For the case of a low sink density, estimate the time, t_2, at which recombination will contribute to vacancy annihilation. Neglect the effect of sinks.
(c) Describe what changes can be made in either the irradiation process or the material microstructure to force $t_1 = t_2$.

Assume a quasi-steady-state condition exists, beginning at t_1 in part (a) and at t_2 in part (b).

5.15 Show that, for a metal with a low sink density undergoing neutron irradiation at low temperature ($T/T_m < 0.2$), when sinks contribute to interstitial annihilation, the vacancy and interstitial concentrations as a function of time can be written as:

$$C_v = (K_0 K_{is} C_s t / K_{iv})^{1/2}$$
$$C_i = (K_0 / K_{iv} K_{is} C_s t)^{1/2}$$

(Hint: consider this case to be intermediary to the quasi-steady state and steady-state cases such that $dC_i/dt < 0$ and $dC_v/dt > 0$ and write the point defect balance equations as inequalities.)

5.16 Two bilayer samples with low sink strengths are being irradiated at low temperature as part of a radiation-enhanced diffusion experiment. If the displacement rate of the second sample is five times that of the first sample, what is the difference in the radiation-enhanced diffusion coefficient?

References

1. Rothman SJ (1983) Effects of irradiation and diffusion in metals and alloys. In: Nolfi FV (ed) Phase transformations during irradiation. Applied Science Publisher, New York, pp 189–211
2. Sizmann R (1978) The effect of radiation upon diffusion in metals. J Nucl Mater 69(70):386–412
3. Olander DR (1976) Fundamental aspects of nuclear reactor fuel elements, TID-26711-P1. Technical Information Service, Springfield, VA
4. Lam NQ (1975) J Nucl Mater 56:125–135
5. Woo CH, Singh BN (1990) Phys Stat Sol (b) 159:609
6. Woo CH, Singh BN, Heinisch HL (1991) J Nucl Mater 179–181:951
7. Wiedersich H (1986) In: Johnson RA, Orlov AN (eds) Physics of radiation effects in crystals. Elsevier Science, New York, p 237
8. Matteson S, Roth J, Nicolet M (1979) Rad Eff 42:217–226
9. Heald PT, Harbottle JE (1977) J Nucl Mater 67:229–233
10. Brailsford AD, Bullough R (1972) J Nucl Mater 44:121–135
11. Ehrhart P, Robrock KH, Schober HR (1986) Basic defects in metals. In: Johnson RA, Orlov AN (eds) Physics of radiation effects in crystals. Elsevier Science Publishers, Amsterdam, p 3
12. Agullo-Lopez F, Catlow CRA, Towsend PD (1988) Point defects in materials. Academic Press Inc, San Diego, pp 198–203

Part II
Physical Effects of Radiation Damage

Chapter 6
Radiation-Induced Segregation

A profound consequence of irradiation at elevated temperature is the spatial redistribution of solute and impurity elements in the metal. This phenomenon leads to the enrichment or depletion of alloying elements in regions near surfaces, dislocations, voids, grain boundaries, and phase boundaries. Figure 6.1 shows a plot of solute element profiles across a grain boundary in stainless steel irradiated in a reactor to a dose of several dpa at about 300 °C. There is significant depletion of chromium, molybdenum, and iron and enrichment of nickel and silicon. Such drastic changes at the grain boundary will cause changes in the local properties of the solid and may induce susceptibility to a host of processes that can degrade the integrity of the component. For this reason, understanding radiation-induced segregation (RIS) is of great importance for reactor performance.

First postulated by Anthony in 1972 [2], and observed by Okamoto and Weidersich in 1973 [3], RIS has its origin in the coupling between defect fluxes and fluxes of alloying elements. Irradiation produces point defects and defect clusters with an approximately random distribution throughout the material. Those defects that are mobile and escape recombination are reincorporated into the crystal structure at dislocations, grain boundaries, and other defect sinks. As shown in Chap. 5, point defects flow to spatially discrete sinks. Since the motion of atoms is by way of defects, atom fluxes are associated with defect fluxes. Any preferential association of defects with a particular alloying component and/or preferential participation of a component in defect diffusion will couple a net flux of the alloying element to the defect fluxes. The flux of an element causes its buildup or depletion in the vicinity of defect sinks and, therefore, concentration gradients in initially homogeneous alloy phases. The concentration gradients induce back diffusion of the segregating elements, and a quasi-steady state may be set up during irradiation whenever the defect-driven alloying element fluxes are balanced by diffusion-driven back diffusion.

Figure 6.2 presents a schematic of processes driving segregation in a binary, 50 % A–50 %B alloy, under irradiation at an elevated temperature. As described in Chap. 5, vacancies and interstitials flow to the grain boundary causing a concentration profile to develop. In case of vacancies (Fig. 6.2(a)), the flux of vacancies to the grain boundary is balanced by an equal flux of atoms in the opposite direction. However, if the participation of A atoms in the vacancy flux is larger than the atom

G.S. Was, *Fundamentals of Radiation Materials Science*,
DOI 10.1007/978-1-4939-3438-6_6

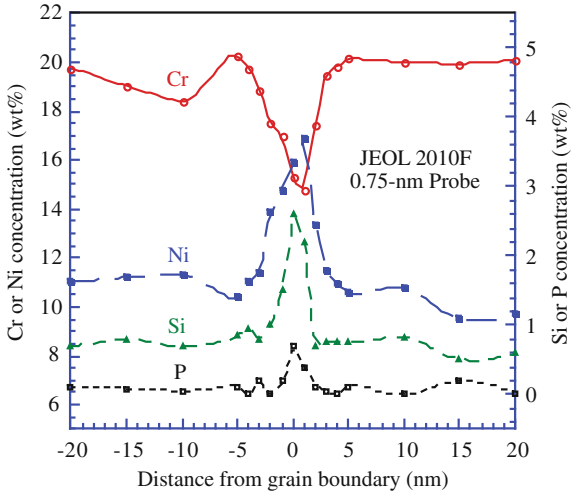

Fig. 6.1 Radiation-induced segregation of Cr, Ni, Si, and P at the grain boundary of a 300 series stainless steel irradiated in a light water reactor core to several dpa at ~300 °C (after [1])

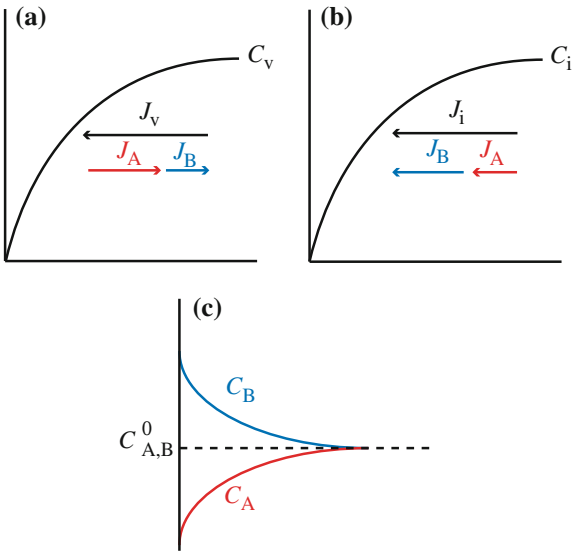

Fig. 6.2 Schematic of radiation-induced segregation in a binary, 50 % A–50 % B system showing (**a**) the development of the vacancy concentration profile by the flow of vacancies to the grain boundary balanced by an equal and opposite flow of A and B atoms, but not necessarily in equal numbers, (**b**) the development of the interstitial concentration profile by the flow of interstitials to the grain boundary balanced by an equal flow of A and B atoms migrating as interstitials, but not necessarily in equal numbers, (**c**) the resulting concentration profiles for A and B

fraction in the alloy (and consequently the participation of B atoms is less), then there will be a net loss of A atoms, and a net gain of B atoms at the boundary, giving rise to concentration gradients, such as shown in Fig. 6.2(c). Considering interstitials, their flux to the grain boundary is also made up of a flux of A and B atoms. If the participation of B atoms in the interstitial flux is greater than the atom fraction in the alloy (and necessarily, the participation of A atoms in the flux is less than the atom fraction in the alloy), then a net increase in B atoms and a corresponding net decrease in A atoms will result. These processes are shown in Fig. 6.2(b). This example shows that both vacancy and interstitial flow to the grain boundary can result in the net accumulation of one alloying element and a corresponding depletion of the other alloying element. Whether element A enriches or depletes when both processes are included depends on the relative strengths of atom association with the respective defect fluxes.

In this chapter, we will focus on radiation-induced segregation in concentrated binary and ternary alloy systems and we will explore the dependence of RIS on temperature, dose, and dose rate.

6.1 Radiation-Induced Segregation in Concentrated Binary Alloys

To distinguish a concentrated alloy from a dilute alloy, it will be assumed that a concentrated alloy is one in which the substitutional solute concentration is above a few percent. The following segregation model is also well-suited to describe alloy systems with significant atomic size differences, including the limit in which the undersized component is present in dilute solution.

The model for solute segregation as developed by Wiedersich [4] follows. We will consider a binary solid solution of elements A and B that are distributed randomly throughout the solid. Due to irradiation, the local vacancy and interstitial concentrations change with time according to the point defect balance equations:

$$\begin{aligned} \frac{\partial C_\mathrm{v}}{\partial t} &= -\nabla J_\mathrm{v} + K_0 - R \\ \frac{\partial C_\mathrm{i}}{\partial t} &= -\nabla J_\mathrm{i} + K_0 - R, \end{aligned} \tag{6.1}$$

where $-\nabla J_\mathrm{v}$ and $-\nabla J_\mathrm{i}$ are the divergences of the vacancy and interstitial fluxes, respectively, K_0 is the Frenkel pair production rate and $R = K_\mathrm{iv} C_\mathrm{i} C_\mathrm{v}$ is the rate of recombination of vacancies and interstitials. Note also that we have dropped the vector notation for sake of simplicity, and thus, we will need to keep track of direction. Equations (6.1) are identical to Eq. (5.1) in the absence of sinks and with the gradient term included. The conservation equations for the alloying elements A and B are given as:

$$\frac{\partial C_A}{\partial t} = -\nabla J_A$$
$$\frac{\partial C_B}{\partial t} = -\nabla J_B. \tag{6.2}$$

The defect and atom fluxes in Eqs. (6.1) and (6.2) arise from forces due to chemical potential gradients. In reality, the equations should be solved for chemical potential, but for simplicity, we will use relations between fluxes and concentration gradients. The coupling between atom and defect fluxes is based on simple physical models. Note that in the case of self-ion bombardment, we would also include a production term due to the implanted element concentration.

It is assumed that diffusive motions of A and B atoms occur only by vacancy and by interstitial jumps. An important coupling between atom and defect fluxes is that a flux of interstitials drives a flux of A and B atoms, equal in size and direction to that of the interstitials, across any fixed lattice or "marker" plane:

$$J_i = J_A^i + J_B^i, \tag{6.3}$$

and, similarly, a flux of vacancies drives a flux of A and B atoms equal in size, but opposite in direction, across the marker plane:

$$J_v = -\left(J_A^v + J_B^v\right). \tag{6.4}$$

In Eqs. (6.3) and (6.4) and in subsequent notation, the subscripts indicate the species of flux considered, and superscripts the complementary species by which the flux occurs. In general, the division of vacancy and interstitial fluxes via A and B atoms will not be in the same proportion as the atom fractions in the alloy, N_A, N_B. That is, vacancies may migrate preferentially via A atoms and interstitials via B atoms, as described earlier and shown in Fig. 6.2.

The fluxes of atoms and defects can be expressed in terms of the gradients of the different species by the *partial diffusion coefficient*:

$$D_A^v = \frac{1}{6}\lambda_v^2 z_v N_v \omega_A^v f_A^v, \tag{6.5}$$

where ω_A^v is the jump frequency with which an A atom exchanges with a vacancy on a given neighboring site, N_v is the atomic fraction of vacancies, z_v is the number of nearest neighbors to the A atom, and λ_v is the jump distance. The term f_A^v is the correlation factor for A atoms migrating by vacancies, which accounts for the greater than random probability that after an initial jump, subsequent jumps of the A atom will have a displacement component opposite to that of the initial jump. In alloys, f is highly composition-dependent and is neglected in the following for simplicity, giving:

$$D_{\mathrm{A}}^{\mathrm{v}} = \frac{1}{6}\lambda_{\mathrm{v}}^{2} z_{\mathrm{v}} N_{\mathrm{v}} \omega_{\mathrm{A}}^{\mathrm{v}}, \tag{6.6}$$

and the partial diffusion coefficient for vacancies via A atoms is given as:

$$D_{\mathrm{v}}^{A} = \frac{1}{6}\lambda_{\mathrm{v}}^{2} z_{\mathrm{v}} N_{A} \omega_{\mathrm{v}}^{A}. \tag{6.7}$$

Note that $\omega_{\mathrm{A}}^{\mathrm{v}} = \omega_{\mathrm{v}}^{\mathrm{A}} = (\omega_{\mathrm{Av}})$, since either jump frequency involves the exchange of a given A atom–vacancy pair. Combining those factors on the RHS of Eqs. (6.6) and (6.7) that are common to both, the *diffusivity coefficient* is defined as follows:

$$d_{\mathrm{Av}} = \frac{1}{6}\lambda_{\mathrm{v}}^{2} z_{\mathrm{v}} \omega_{\mathrm{Av}}, \tag{6.8}$$

so that we have:

$$\begin{aligned} D_{\mathrm{A}}^{\mathrm{v}} &= d_{\mathrm{Av}} N_{\mathrm{v}} \\ D_{\mathrm{v}}^{\mathrm{A}} &= d_{\mathrm{Av}} N_{\mathrm{A}}. \end{aligned} \tag{6.9}$$

For B atoms, the complementary equations are given as:

$$\begin{aligned} D_{\mathrm{B}}^{\mathrm{v}} &= d_{\mathrm{Bv}} N_{\mathrm{v}} \\ D_{\mathrm{v}}^{\mathrm{B}} &= d_{\mathrm{Bv}} N_{\mathrm{B}} \end{aligned} \tag{6.10}$$

with

$$d_{\mathrm{Bv}} = \frac{1}{6}\lambda_{\mathrm{v}}^{2} z_{\mathrm{v}} \omega_{\mathrm{Bv}}, \tag{6.11}$$

where ω_{Bv} is the effective exchange-jump frequency of a B atom–vacancy pair that includes a factor accounting for possible binding or repulsion between vacancies and B atoms.

The partial diffusion coefficients of A and B atoms via interstitials, and interstitials via the elements, provided migration occurs by an interstitial mechanism, are similarly:

$$D_{\mathrm{A}}^{\mathrm{i}} = \frac{1}{6}\lambda_{\mathrm{i}}^{2} z_{\mathrm{i}} \omega_{\mathrm{A}}^{\mathrm{i}}, \tag{6.12}$$

which is analogous to Eq. (6.6). We are, however, neglecting the fact that interstitial migration is more complex because more than one atom is significantly involved in any interstitial jump. The partial diffusion coefficients for interstitials are thus:

$$\begin{aligned} D_{\mathrm{A}}^{\mathrm{i}} &= d_{\mathrm{Ai}} N_{\mathrm{i}} \\ D_{\mathrm{i}}^{\mathrm{A}} &= d_{\mathrm{Ai}} N_{\mathrm{A}} \end{aligned} \tag{6.13}$$

and

$$\begin{aligned} D_{\mathrm{B}}^{\mathrm{i}} &= d_{\mathrm{Bi}} N_{\mathrm{i}} \\ D_{\mathrm{i}}^{\mathrm{B}} &= d_{\mathrm{Bi}} N_{\mathrm{B}}. \end{aligned} \tag{6.14}$$

The expression for d_{Ai} and d_{Bi} will depend on the interstitialcy mechanism and will be more complicated than Eqs. (6.8) and (6.11). In writing the partial diffusion coefficients in the form $D = dN$, we further assume that the spatial dependence resides in the factor N, whereas the ds are composition-independent.

The "average" or "total" diffusion coefficients for the various species are given as:

$$\begin{aligned} D_{\mathrm{v}} &= d_{\mathrm{Av}} N_{\mathrm{A}} + d_{\mathrm{Bv}} N_{\mathrm{B}} \\ D_{\mathrm{i}} &= d_{\mathrm{Ai}} N_{\mathrm{A}} + d_{\mathrm{Bi}} N_{\mathrm{B}} \end{aligned} \tag{6.15}$$

$$\begin{aligned} D_{\mathrm{A}} &= d_{\mathrm{Av}} N_{\mathrm{v}} + d_{\mathrm{Ai}} N_{\mathrm{i}} \\ D_{\mathrm{B}} &= d_{\mathrm{Bv}} N_{\mathrm{v}} + d_{\mathrm{Bi}} N_{\mathrm{i}}. \end{aligned} \tag{6.16}$$

Using the partial and total diffusion coefficients, we can write the fluxes of atoms and defects with respect to a coordinate system fixed on the crystal lattice:

$$\begin{aligned} J_{\mathrm{A}} &= -D_{\mathrm{A}} \chi \nabla \mathrm{C}_{\mathrm{A}} + d_{\mathrm{Av}} N_{\mathrm{A}} \nabla \mathrm{C}_{\mathrm{v}} - d_{\mathrm{Ai}} N_{\mathrm{A}} \nabla \mathrm{C}_{\mathrm{i}} \\ J_{\mathrm{B}} &= -D_{\mathrm{B}} \chi \nabla \mathrm{C}_{\mathrm{B}} + d_{\mathrm{Bv}} N_{\mathrm{B}} \nabla \mathrm{C}_{\mathrm{v}} - d_{\mathrm{Bi}} N_{\mathrm{B}} \nabla \mathrm{C}_{\mathrm{i}} \end{aligned} \tag{6.17}$$

$$\begin{aligned} J_{\mathrm{v}} &= d_{\mathrm{Av}} N_{\mathrm{v}} \chi \nabla \mathrm{C}_{\mathrm{A}} + d_{\mathrm{Bv}} N_{\mathrm{v}} \chi \nabla \mathrm{C}_{\mathrm{B}} - D_{\mathrm{v}} \nabla \mathrm{C}_{\mathrm{v}} \\ &= (d_{\mathrm{Av}} - d_{\mathrm{Bv}}) N_{\mathrm{v}} \chi \nabla \mathrm{C}_{\mathrm{A}} - D_{\mathrm{v}} \nabla \mathrm{C}_{\mathrm{v}} \\ J_{\mathrm{i}} &= -d_{\mathrm{Ai}} N_{\mathrm{i}} \chi \nabla \mathrm{C}_{\mathrm{A}} - d_{\mathrm{Bi}} N_{\mathrm{i}} \chi \nabla \mathrm{C}_{\mathrm{B}} - D_{\mathrm{i}} \nabla \mathrm{C}_{\mathrm{i}} \\ &= -(d_{\mathrm{Ai}} - d_{\mathrm{Bi}}) N_{\mathrm{i}} \chi \nabla \mathrm{C}_{\mathrm{A}} - D_{\mathrm{i}} \nabla \mathrm{C}_{\mathrm{i}}, \end{aligned} \tag{6.18}$$

where $\chi = \left(1 + \dfrac{\partial \ln \gamma_{\mathrm{A}}}{\partial \ln N_{\mathrm{A}}}\right) = \left(1 + \dfrac{\partial \ln \gamma_{\mathrm{B}}}{\partial \ln N_{\mathrm{B}}}\right)$, accounts for the difference between the chemical potential gradient (the true driving force for the diffusion of A and B atoms) and the concentration gradient, and γ_{A} and γ_{B} are activity coefficients. The second equality in the expressions for J_{v} and J_{i} is obtained by neglecting small perturbations arising from the presence of defects, so that $\nabla C_{\mathrm{B}} = -\nabla C_{\mathrm{A}}$. This equality describes the Kirkendall effect from the vacancy and interstitial mechanisms, respectively. That is, the difference in the A atom and B atom fluxes in opposite directions past a marker plane must be made up by an appropriate defect flux.

We briefly digress to address the thermodynamic factor, χ. In the description of fluxes of species, A, B, i, v, we assumed that the flux was driven by the concentration gradient:

$$J_k = -\sum_{j=1} D_{kj} \nabla C_k. \tag{6.19}$$

In fact, fluxes are driven by the gradient in the chemical potential, μ_k, and so we should write as:

$$J_k = -\sum_{j=1} L_{kj} X_k, \tag{6.20}$$

where the L_{kj} are the transport or Onsager coefficients for species k and j that contain the kinetics information similar to D_{kj} in Eq. (6.19), and X_k is the driving force for species k, which for diffusion is the gradient of the chemical potential for species k. The L_{kj} are fundamental kinetic quantities that can be used to predict RIS and transport behavior in general. Of particular interest are the off-diagonal terms $L_{kj(k \neq j)}$ that contain kinetic information about coupled fluxes between species k and j. These cross terms are essential for a quantitative understanding of RIS as they include information about solute-defect coupling, e.g., vacancy drag, which is not available from just the diagonal terms.

The driving force, X_k, for diffusion of species k is the gradient of the chemical potential for species k:

$$X_k = -\nabla \mu_k. \tag{6.21}$$

The chemical potential gradient is given as:

$$\nabla \mu_k = kT \frac{\nabla C_k}{C_k} \left(1 + \frac{\partial \ln \gamma}{\partial C_k}\right), \tag{6.22}$$

where

$$\chi = \left(1 + \frac{\partial \ln \gamma}{\partial C_k}\right). \tag{6.23}$$

Substituting the expression for χ into Eq. (6.22) gives:

$$\nabla \mu_k = \chi_k \frac{\nabla C_k}{C_k} kT, \tag{6.24}$$

and substituting Eq. (6.24) into Eq. (6.21) and writing in general form yields:

$$X_k = -\chi_k \frac{\nabla C_k}{C_k} kT. \tag{6.25}$$

The terms D_A and D_B in Eqs. (6.16) can be written in terms of the Onsager coefficients as:

$$\begin{aligned} D_A &= kT\left[\left(\frac{L_{AA}^v}{C_A}-\frac{L_{AB}^v}{C_B}\right)+\left(\frac{L_{AA}^i}{C_A}-\frac{L_{AB}^i}{C_B}\right)\right]\chi \\ D_B &= kT\left[\left(\frac{L_{BB}^v}{C_B}-\frac{L_{AB}^v}{C_A}\right)+\left(\frac{L_{BB}^i}{C_B}-\frac{L_{AB}^i}{C_A}\right)\right]\chi, \end{aligned} \tag{6.26}$$

and the terms d_{Av}, d_{Ai}, d_{Bv}, d_{Bi} from Eqs. (6.16) can be written as:

$$\begin{aligned} d_{Av} &= \frac{L_{AA}^v+L_{AB}^v}{C_A C_v}, \quad d_{Ai} = \frac{L_{AA}^i+L_{AB}^i}{C_A C_i} \\ d_{Bv} &= \frac{L_{BB}^v+L_{AB}^v}{C_B C_v}, \quad d_{Bi} = \frac{L_{BB}^i+L_{AB}^i}{C_B C_i}, \end{aligned} \tag{6.27}$$

where superscripts i, v indicate interstitial- and vacancy-mediated coefficients, respectively. Substitution of Eqs. (6.26) and (6.27) into Eqs. (6.17) and (6.18) yields the atom and defect fluxes in terms of the L-coefficients. The L_{kj} are generally not directly measurable, making them difficult to obtain from experiment. Rather, they can be obtained if the jump rates of the solute, solvent, vacancy, and interstitial are known. Recall from Sect. 4.3.5 that multifrequency models can provide jump frequencies for each of the species of interest, and L-coefficients can be calculated from these frequencies. Values of specific jump frequencies can be determined using ab initio methods. Reference [5] provides an example of the determination of jump frequencies using ab initio, and the calculation of L-coefficients using the method in [6].

Returning to the determination of concentration profiles, of the four flux equations, Eqs. (6.17) to (6.18), only three are independent because atom fluxes and defect fluxes through a marker plane must balance:

$$J_A + J_B = -J_v + J_i. \tag{6.28}$$

To obtain the atom and defect distributions in time and space, the set of coupled partial differential equations in Eqs. (6.1) and (6.2) must be solved for the appropriate initial and boundary conditions. Inserting the fluxes given in Eqs. (6.17), (6.18) and (6.28) into Eqs. (6.1) and (6.2) gives:

$$\begin{aligned} \frac{\partial C_v}{\partial t} &= \nabla[-(d_{Av}-d_{Bv})\chi\Omega C_v\nabla C_A + D_v\nabla C_v] + K_0 - R \\ \frac{\partial C_i}{\partial t} &= \nabla[(d_{Ai}-d_{Bi})\chi\Omega C_i\nabla C_A + D_i\nabla C_i] + K_0 - R \\ \frac{\partial C_A}{\partial t} &= \nabla[(D_A\chi\nabla C_A) + \Omega C_A(d_{Ai}\nabla C_i - d_{Av}\nabla C_v)]. \end{aligned} \tag{6.29}$$

Note that the terms in brackets are just the fluxes, J, of the respective species. The atomic fractions N have been corrected to volume concentration according to $N = \Omega C$, where Ω is the average atomic volume of the alloy. The equation for element B is $C_B = 1 - C_A$ when small defect concentrations are neglected.

Assuming that steady state has been reached, we can make some qualitative conclusions about the flux equations in Eqs. (6.17), (6.18), and (6.28). At steady state:

$$J_A = J_B = 0, \tag{6.30}$$

and neglecting defect bias effects in the solid:

$$J_i = J_v, \tag{6.31}$$

since vacancies and interstitials are produced and recombine in equal numbers. Eliminating ∇C_i in relation for J_A in Eq. (6.17) using Eqs. (6.28), (6.30), and (6.31) gives the following:

$$\nabla C_A = \frac{N_A N_B d_{Bi} d_{Ai}}{\chi(d_{Bi} N_B D_A + d_{Ai} N_A D_B)} \left(\frac{d_{Av}}{d_{Bv}} - \frac{d_{Ai}}{d_{Bi}}\right) \nabla C_v. \tag{6.32}$$

Equation (6.32) is a relation between the vacancy concentration gradient and the A atom concentration gradient. It is evident that the relation between the direction of the gradient of alloy component A and that of the vacancy gradient is determined by the relative magnitude of the ratios $\frac{d_{Av}}{d_{Bv}}$ and $\frac{d_{Ai}}{d_{Bi}}$. Recall from Eqs. (6.8) and (6.11) that:

$$d_{Av} = \frac{1}{6}\lambda_v^2 z_v \omega_{Av}$$
$$d_{Bv} = \frac{1}{6}\lambda_v^2 z_v \omega_{Bv},$$

and

$$\omega_{Av} = \nu \exp\left(\frac{\Delta S_m^{Av}}{k}\right) \exp\left(\frac{-E_m^{Av}}{kT}\right), \quad \omega_{Bv} = \nu \exp\left(\frac{\Delta S_m^{Bv}}{k}\right) \exp\left(\frac{-E_m^{Bv}}{kT}\right),$$

therefore:

$$\frac{d_{Av}}{d_{Bv}} \approx \exp\left(\frac{E_m^{Bv} - E_m^{Av}}{kT}\right), \tag{6.33}$$

since differences in ΔS_m between A and B atoms are small. Similarly:

$$\frac{d_{Ai}}{d_{Bi}} \approx \exp\left(\frac{E_m^{Bi} - E_m^{Ai}}{kT}\right). \tag{6.34}$$

During irradiation, the vacancy concentration always decreases toward a defect sink, and Eq. (6.32) predicts that the element A becomes enriched at sinks if $\frac{d_{Ai}}{d_{Bi}} > \frac{d_{Av}}{d_{Bv}}$, i.e., if preferential transport of A atoms via interstitials outweighs preferential transport via vacancies and vice versa.

Example 6.1. Segregation in a B–25 %A alloy.
Let us look at a B–25 %A alloy (where B = Ni and A = Cu), and assume that there is no preferential association of defects with either A or B atoms. Given the following values for migration energies of the two components via vacancies and interstitials:

$$E_m^{Av} \sim 0.77\,\text{eV} \quad E_m^{Ai} \sim 0.10\,\text{eV}$$
$$E_m^{Bv} \sim 1.28\,\text{eV} \quad E_m^{Bi} \sim 0.15\,\text{eV},$$

Then, from Eqs. (6.33) and (6.34), we have:

$$\begin{aligned}\left(\frac{d_{Av}}{d_{Bv}} - \frac{d_{Ai}}{d_{Bi}}\right) &= \exp\left(\frac{1.28 - 0.77}{kT}\right) - \exp\left(\frac{0.15 - 0.1}{kT}\right) \\ &= \exp\left(\frac{0.51}{kT}\right) - \exp\left(\frac{0.05}{kT}\right) \\ &\gg 0\end{aligned}$$

Since $\left(\frac{d_{Av}}{d_{Bv}} - \frac{d_{Ai}}{d_{Bi}}\right)$ is positive and the concentration gradient of A follows that of vacancies, we have depletion of A at the sink. If this sink is a free surface, then A is depleted at the surface. If it is a grain boundary, then A is depleted at the grain boundary. More A atoms move away from the sink via vacancies than to the sink via interstitials. Figure 6.3 shows the behavior of the A concentration at a temperature of 500 °C and a dose rate of 10^{-3} dpa/s. Note that the drop in the concentration of A at the sink surface is balanced by a buildup behind the depleted zone. With increasing dose, the depleted zone increases in depth and width until back diffusion due to the large concentration gradient causes a leveling off and the establishment of a "steady-state" condition at $t > 10^4$ s.

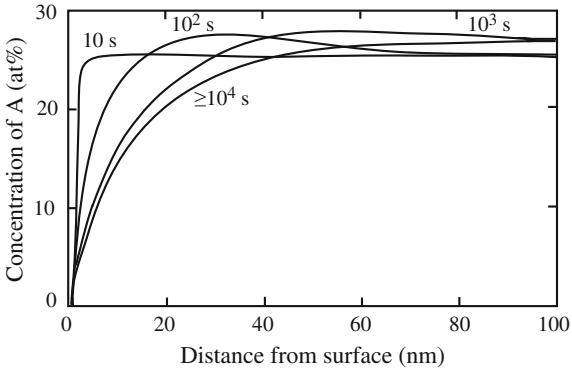

Fig. 6.3 Concentration profiles of element A in a B–25 %A alloy as a function of irradiation time at a temperature of 500 °C and for a displacement rate of 10^{-3} dpa/s; $E_m^{Av} = 0.77\,eV$, $E_m^{Bv} = 1.28\,eV$, $E_m^{Ai} = 0.10\,eV$, $E_m^{Bi} = 0.15\,eV$ (after [4])

6.1.1 Solution to the Coupled Partial Differential Equations

Solution to the system of partial differential equations given in Eq. (6.29) must be obtained numerically. Solutions can be obtained in either planar geometry (free surface) or spherical geometry (grain boundary). In the Perks code [7], segregation of the alloying elements is modeled adjacent to a plane, which is a perfect sink for point defects, such as a grain boundary or a free surface. Another plane is sufficiently far away to model the conditions in the middle of the grain where there are no concentration gradients. The model calculates the concentrations of the major elements by considering the fluxes of each species caused by the migration of point defects created thermally and by irradiation. Point defect losses occur due to mutual recombination and annihilation at fixed sinks, the boundary surfaces, and a uniform and time-independent distribution of dislocations. The detailed radiation-induced microstructure is not considered explicitly, but the sink strength can be adjusted with dose to simulate the buildup of sinks in the microstructure.

Once the fluxes are calculated, the divergences can be used to perform the time integration required by the continuity equations in Eq. (6.29). The program calculates the concentration of each species independently. An advantage of this method is that any errors in the calculations are evident when the partial concentrations are summed.

The deep boundary condition is representative of the bulk material where there are no concentration gradients for atomic and defect species so that the net flux of each species is always zero. The surface or grain boundary is created as a perfect sink for point defects, thus their concentration at the sink is maintained at their initial values ($dC_k/dt = 0$). In order to conserve atoms in the solid, the atomic fluxes at the boundary are all zero.

6.1.2 Interstitial Binding

Undersize solutes can tightly bind to interstitials forming interstitial–solute complexes that migrate as solute interstitials. The RIS model described in Sect. 6.1 can account for solute–interstitial binding by accounting for the non-random occupation of interstitials by A and B atoms in the diffusivity coefficients, d_{Ai} and d_{Bi}, respectively [4]. The concentrations of A and B interstitials are given as:

$$C_{Ai} = C_i \frac{C_A \exp\left(E_b^{Ai}/kT\right)}{C_A \exp\left(E_b^{Ai}/kT\right) + C_B}, \tag{6.35}$$

$$C_{Bi} = C_i \frac{C_B}{C_A \exp\left(E_b^{Ai}/kT\right) + C_B}, \tag{6.36}$$

where E_b^{Ai} is the average energy gained by converting a B interstitial into an A interstitial. The term E_b^{Ai} is referred to as the effective A interstitial binding energy. Clearly, solutes that bind to interstitials will undergo enrichment at sinks by virtue of the flow of interstitials to the sink.

Example 6.2. Segregation with interstitial binding in Ni–Si.
Segregation will occur in systems where strong binding of the interstitials to undersize atoms occurs. Consider the system of B–5 %A where B is Ni and A is Si and preferential interstitial association with A atoms occurs. Figure 6.4 shows the calculated concentration profile of alloy component A (Si) for an irradiation temperature of 500 °C. Note that element A strongly segregates to the surface. This can be understood by referring to the parameters of Eq. (6.36). We have chosen $E_m^{Av} = E_m^{Bv} = 1.28\,\text{eV}$ and E_m^{Ai} = 0.09 eV, E_m^{Bi} = 0.15 eV and a binding energy of E_b^{Ai} = 1.0 eV so that:

$$\frac{d_{Av}}{d_{Bv}} - \frac{d_{Ai}}{d_{Bi}} = 1 - \exp\left[\left(E_b^{Ai} - E_m^{Ai} + E_m^{Bi}\right)/kT\right] < 0$$

and from Eq. (6.32), the surface becomes strongly enriched in Si. The binding energy in part results from the size difference between Ni and Si. Here the solute atom, Si, is considerably smaller and is expected to segregate to the surface according to the argument given in Sect. 6.1.3. Results are supported by the preceding calculation and confirmed by experiment. Figure 6.5 shows that segregation of silicon to the surface does indeed occur in a Ni–1 %Si alloy irradiated at moderate temperature. It should also be noted that in the Ni–Si system, the solubility limit for Si is ~10 at.%, and that segregation of Si to values of above the solubility limit will result in precipitation of Ni_3Si. Hence, one important result of irradiation-induced segregation is that it can lead to local solute concentration that exceeds the solubility limit and results

in precipitation. Irradiation can also act to stabilize a second phase that would otherwise not be present in thermodynamic equilibrium and vice versa. These processes are discussed in Chap. 9.

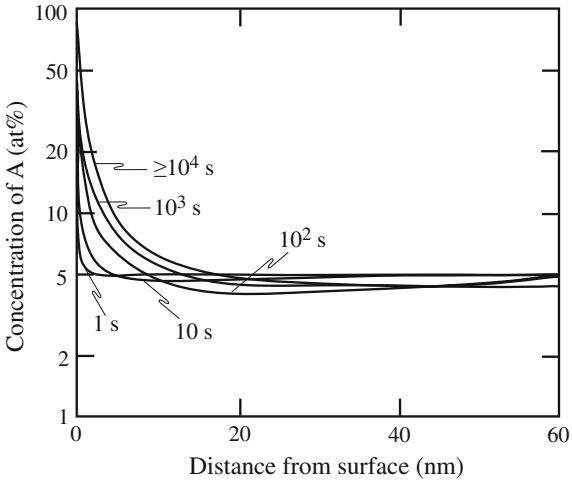

Fig. 6.4 Concentration profiles of element A in a B–5 %A alloy as a function of irradiation time at temperature of 500 °C and for a displacement rate of 10^{-3} dpa/s; $E_m^{Av} = E_m^{Bv} = 1.28\,eV, E_b^{Ai} = 1.0\,eV, E_m^{Ai} = 0.09\,eV, E_m^{Bi} = 0.15\,eV$ (after [4])

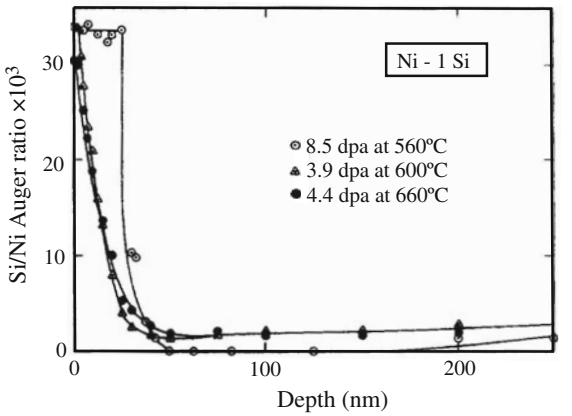

Fig. 6.5 Measured concentration versus depth profiles for a Ni–1 %Si alloy irradiated to doses between 3.9 and 8.5 dpa at temperatures between 560 and 660 °C with 3.5 MeV $^{58}Ni^+$ ions at a displacement rate of ~10^{-3} dpa/s at the sample surface (after [8])

6.1.3 Solute Size Effect

Size difference between solute atoms plays a major role in determining the magnitude and the direction of segregation [8]. To reduce the strain energy stored in the lattice, undersize solute substitutional atoms will preferentially exchange with solvent atoms in interstitial positions, whereas oversize solute atoms will tend to remain on, or return to, substitutional sites. Strain-energy considerations also predict that vacancies will preferentially exchange with oversize solute atoms. During irradiation at elevated temperatures, the fraction of undersize solute atoms migrating as interstitials, or of oversize solute atoms migrating against the vacancy flux, may therefore greatly exceed the fraction of solute in the alloy. In other words, any variation in size between solute and solvent atoms will cause the chemical composition of the irradiation-induced interstitial and vacancy fluxes toward sinks to differ from the chemical composition of the alloy. This disproportionate participation of misfitting solute atoms in the defect fluxes to sinks will cause a redistribution of solute, which will produce an enrichment of undersize solute and a depletion of oversize solute near defect sinks. Since the surface of an irradiated solid serves as an unsaturable sink for both vacancy and interstitial-type defects, concentration gradients will be created near the surface of alloys that contain misfitting solute atoms during irradiation at appropriate temperatures. Table 6.1 shows the volume misfit for several solute–solvent combinations and the predicted and observed direction of segregation under irradiation. Note that positive misfits should result in depletion (−) at sinks while negative misfits should result in enrichment (+) at sinks.

Example 6.3. Segregation driven by the size effect in Ni–1 %Al.
An example of the size effect is the Ni–Al system. According to Table 6.1, Al is an oversized solute in the Ni lattice, and E_m^{Al-v} will be less than E_m^{Ni-v} since the oversize Al atoms will preferentially exchange with vacancies. According to Eqs. (6.33) and (6.34), $\frac{d_{Av}}{d_{Bv}} > \frac{d_{Ai}}{d_{Bi}}$ and depletion at the surface is predicted. In fact, measurement of the segregation of Al in Ni–1 %Al irradiated to 10.3 dpa at 510 °C and to 10.7 dpa at 620 °C shows strong depletion of Al at the surface followed by redistribution behind the surface (Fig. 6.6). The buildup of Al just below the surface results in an Al concentration that exceeds the solubility limit and induces second phase formation as discussed in detail in Chap. 9.

Table 6.1 Effect of solute size on radiation-induced segregation (from [9–11])

Solvent–solute	Volume misfit (%)	Predicted direction of segregation	Observed direction of segregation
Pd–Cu	−20	+	+
Pd–Fe	−27	+	+
Pd–Mo	−3	+	+
Pd–Ni	−26	+	+
Pd–W	−2	+	+
Al–Ge	−37	+	+
Al–Si	−45	+	+
Al–Zn	−19	+	+
Fe–Cr	+4	−	−
Mg–Cd	−19	+	+
Ti–Al	−3	+	+
Ti–V	−26	+	+
Ni–Al	+52	−	−
Ni–Au	+55	−	−
Ni–Be	−29	+	+
Ni–Cr	+1	−	−
Ni–Ge	−5	+	+
Ni–Mn	+32	−	
Ni–Mo	+31	−	−
Ni–Sb	+21	−	−
Ni–Si	−16	+	+
Ni–Ti	+57	−	−
Cu–Ag	+44	−	−
Cu–Be	−34	+	+
Cu–Fe	−8	+	+
Cu–Ni	−7	+	+
[a]SS–Ni	−3	+	+
[a]SS–Cr	+5	−	−
[a]SS–Si	−3	+	+
[a]SS–C	+54	−	−
[a]SS–Mn	+3	−	−
[a]SS–Mo	+36	−	−
[a]SS–Cu	+9	−	−

[a]SS refers to 316 stainless steel from [10]

6.1.4 *Effect of Temperature*

The temperature dependence of RIS is shown in Fig. 6.7 for a B–25 % A alloy, as determined by solution of Eq. (6.29). Note that with increasing temperature, the profile flattens. This is because the difference between $\frac{d_{Av}}{d_{Bv}}$ and $\frac{d_{Ai}}{d_{Bi}}$ decreases with

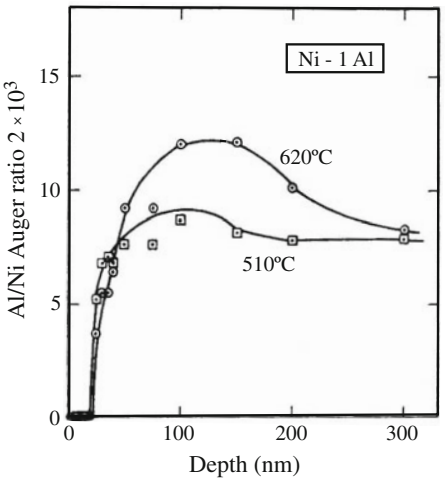

Fig. 6.6 Measured concentration versus depth profiles for a Ni–1 %Al alloy irradiated to 10.3 dpa at 510 °C and to 10.7 dpa at 620 °C with 3.5 MeV $^{58}Ni^{+}$ ions at a displacement rate of $\sim 10^{-3}$ dpa/s at the sample surface (after [8])

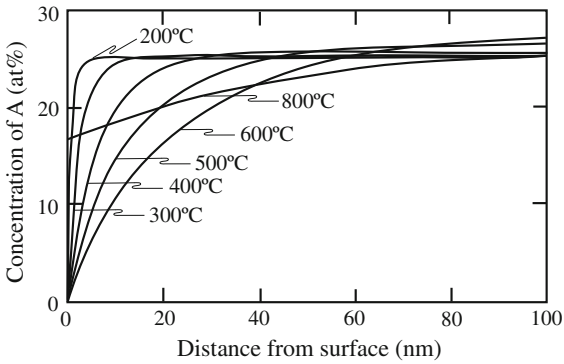

Fig. 6.7 Steady-state concentration profiles of element A as a function of temperature for the same alloy and irradiation conditions as shown in Fig. 6.3 (after [4])

temperature. Figure 6.8 shows that the steady-state concentration at the sink surface passes through a minima/maxima as a function of temperature and can be explained as follows. At high temperatures, a large thermal vacancy concentration leads to a high diffusion rate of alloying elements as well as to a high defect recombination rate; the latter reduces the defect fluxes to sinks, and hence, the amount of solute segregation, while the former increases the back diffusion of segregated alloying elements. At low temperatures, the vacancy mobility is low, the radiation-induced excess vacancy concentration is correspondingly high so that defect recombination becomes dominant, and hence, the defect fluxes to sinks decrease and segregation is reduced. At intermediate temperatures, the thermal vacancy concentration becomes insignificant and the radiation-induced excess vacancy concentration is relatively low. The defect recombination rate is low, and hence defects migrate predominantly to sinks and significant segregation occurs.

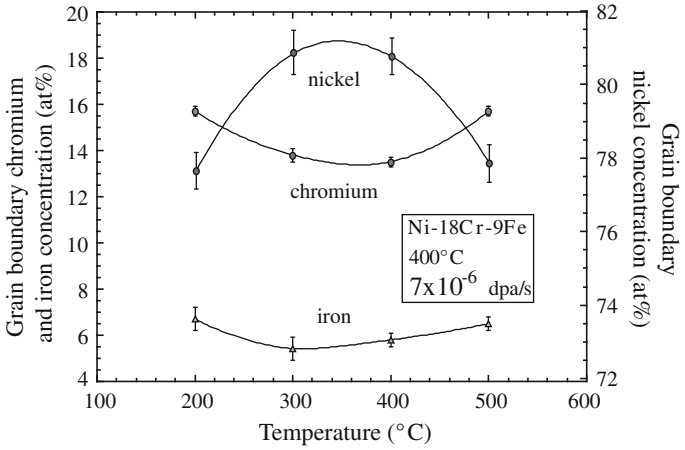

Fig. 6.8 Temperature dependence of grain boundary segregation of Ni, Cr, and Fe in a Ni–18Cr–9Fe alloy irradiated with 3.4 MeV protons at 400 °C to 1 dpa and at a displacement rate of 7×10^{-6} dpa/s (after [12])

6.1.5 *Effect of Dose Rate*

Decreasing the dose rate will shift the temperature dependence of RIS to lower temperatures as shown in Fig. 6.9. The shift of the curve toward lower temperatures for lower displacement rates can be explained as follows. At a given temperature, a lower point defect generation rate means that vacancies and interstitials are added to the lattice more slowly, or more widely spaced in time. However, their thermal mobility is unchanged and with the lower numbers of defects in the lattice, the probability of finding a sink versus recombination is increased. Thus, at a given temperature, lower displacement rates tend to increase the role of the sink over the

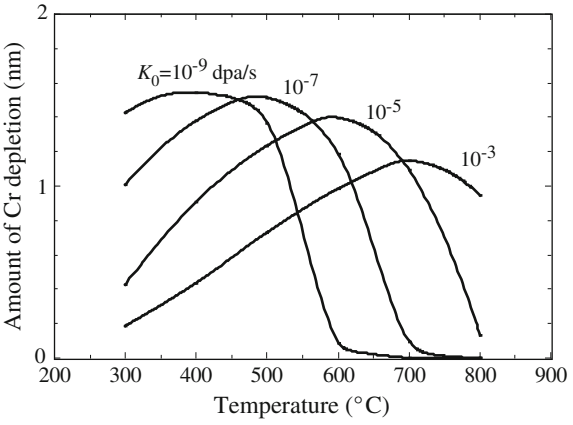

Fig. 6.9 Dose rate dependence of grain boundary chromium depletion calculated using the MIK model for RIS (after [13, 14])

role of recombination, resulting in greater segregation. At high temperatures, a lower displacement rate means that irradiation-produced vacancies will have less of an impact, so that their effect on segregation is less than that at higher dose rate and the amount of segregation drops with decreasing dose rate.

6.2 RIS in Ternary Alloys

Engineering alloys are rarely simple binary alloys. Most structural alloys contain many solutes, each with a specific role in the properties of the alloy. Because of the significance of structural stainless steels that are predominantly composed of iron, chromium, and nickel, we will reproduce the development of the time- and space-dependent concentration equations for a ternary alloy under irradiation. The following description is a condensation of that given by Lam et al. [15] for a ternary alloy whose components A, B, and C are present in concentrations C_A, C_B, and C_C (number of atoms per unit volume). We start by writing the defect fluxes partitioned into those occurring via A, B, and C atoms in the alloy according to:

$$\begin{aligned} J_i &= J_i^A + J_i^B + J_i^C \\ J_v &= J_v^A + J_v^B + J_v^C, \end{aligned} \tag{6.37}$$

where the subscripts indicate the species of flux (interstitial or vacancy) and the superscripts indicate the complementary species by which the flux occurs (atom A, B, or C). The partial interstitial fluxes are in the same direction as the corresponding atom fluxes while the partial vacancy fluxes are in the opposite direction to the atom fluxes:

$$\begin{aligned} J_i^A &= J_A^i; \quad & J_i^B &= J_B^i; \quad & J_i^C &= J_C^i \\ J_v^A &= -J_A^v; \quad & J_v^B &= -J_B^v; \quad & J_v^C &= -J_C^v, \end{aligned} \tag{6.38}$$

and Eq. (6.37) can be written as:

$$\begin{aligned} J_i &= J_A^i + J_B^i + J_C^i \\ J_v &= -\left(J_A^v + J_B^v + J_C^v\right). \end{aligned} \tag{6.39}$$

These equations express the coupling between defect and atom fluxes across any fixed lattice plane.

As with the defect compositions, the alloy composition in time and space can be described by the conservation equations:

$$\begin{aligned}\frac{\partial C_{\mathrm{A}}}{\partial t} &= -\nabla \cdot J_{\mathrm{A}} \\ \frac{\partial C_{\mathrm{B}}}{\partial t} &= -\nabla \cdot J_{\mathrm{B}} \\ \frac{\partial C_{\mathrm{C}}}{\partial t} &= -\nabla \cdot J_{\mathrm{C}},\end{aligned} \tag{6.40}$$

where J_{A}, J_{B}, and J_{C} are the total fluxes of the alloying elements, which can be partitioned into partial fluxes occurring by vacancies and interstitials:

$$\begin{aligned}J_{\mathrm{A}} &= J_{\mathrm{A}}^{\mathrm{v}} + J_{\mathrm{A}}^{\mathrm{i}} \\ J_{\mathrm{B}} &= J_{\mathrm{B}}^{\mathrm{v}} + J_{\mathrm{B}}^{\mathrm{i}} \\ J_{\mathrm{C}} &= J_{\mathrm{C}}^{\mathrm{v}} + J_{\mathrm{C}}^{\mathrm{i}}.\end{aligned} \tag{6.41}$$

The defect and atom fluxes are expressed in terms of the concentration gradients of the different species:

$$\begin{aligned}J_k^{\mathrm{i}}\left(\equiv J_{\mathrm{i}}^{\mathrm{k}}\right) &= -D_k^{\mathrm{i}}\chi\nabla C_k - D_{\mathrm{i}}^k\nabla C_{\mathrm{i}} \\ J_k^{\mathrm{v}}\left(\equiv -J_{\mathrm{v}}^k\right) &= -D_k^{\mathrm{v}}\chi\nabla C_k + D_{\mathrm{v}}^k\nabla C_{\mathrm{v}},\end{aligned} \tag{6.42}$$

where k = A, B, or C, χ is the thermodynamic factor which relates the concentration gradient to the chemical potential gradient of atoms (as in Eqs. (6.17) and (6.18)), and D_k^{i}, D_k^{v}, D_{i}^k and D_{v}^k are the partial diffusion coefficients of atoms k by interstitials, and vacancies, and of interstitials and vacancies by atoms, respectively. The partial diffusion coefficients have the form:

$$\begin{aligned}D_k^j &= d_{kj}N_j \\ D_j^k &= d_{kj}N_k,\end{aligned} \tag{6.43}$$

where j = i or v, $N_j = \Omega C_j$ and $N_k = \Omega C_k$ are the atomic fractions of defects and of k atoms, respectively, Ω is the average atomic volume in the alloy, and d_{kj} are the diffusivity coefficients for conjugate atom-defect pairs kj:

$$d_{kj} = \frac{1}{6}\lambda_k^2 z_k \omega_{kj}^{\mathrm{eff}}. \tag{6.44}$$

Here, λ_k is the jump distance, z_k the coordination number, and $\omega_{kj}^{\mathrm{eff}}$ the effective jump or exchange frequency of the pair. The total diffusion coefficients for interstitials and vacancies are defined as:

$$D_{\mathrm{i}} = \sum_k d_{k\mathrm{i}} N_k$$
$$D_{\mathrm{v}} = \sum_k d_{k\mathrm{v}} N_k, \tag{6.45}$$

and for atoms:

$$D_k = d_{k\mathrm{i}} N_{\mathrm{i}} + d_{k\mathrm{v}} N_{\mathrm{v}}. \tag{6.46}$$

For alloy systems in which atoms of one alloy component interact with interstitials to form bound atom–interstitial complexes, the non-random occupation of interstitials by A, B, and C atoms is accounted for in the same manner as for a binary alloy system. For preferential A atom–interstitial binding, we have by analogy with Eqs. (6.35) and (6.36):

$$C_{\mathrm{Ai}} = C_{\mathrm{i}} \frac{C_{\mathrm{A}} \exp\left(E_{\mathrm{b}}^{\mathrm{Ai}}/kT\right)}{C_{\mathrm{A}} \exp\left(E_{\mathrm{b}}^{Ai}/kT\right) + C_{\mathrm{B}} + C_{\mathrm{C}}},$$
$$C_{\mathrm{Bi}} = C_{\mathrm{i}} \frac{C_{\mathrm{B}}}{C_{\mathrm{A}} \exp\left(E_{\mathrm{b}}^{\mathrm{Ai}}/kT\right) + C_{\mathrm{B}} + C_{\mathrm{C}}}, \tag{6.47}$$
$$C_{\mathrm{Ci}} = C_{\mathrm{i}} \frac{C_{\mathrm{C}}}{C_{\mathrm{A}} \exp\left(E_{\mathrm{b}}^{\mathrm{Ai}}/kT\right) + C_{\mathrm{B}} + C_{\mathrm{C}}},$$

where $E_{\mathrm{b}}^{\mathrm{Ai}}$ is the average energy gained by converting a B interstitial or a C interstitial into an A interstitial. From Eqs. (6.40), (6.42), (6.43), (6.44), and (6.37), the defect and atom fluxes with respect to a coordinate system fixed on the crystal lattice are given as:

$$\begin{aligned}
J_{\mathrm{i}} &= -(d_{\mathrm{Ai}} - d_{\mathrm{Ci}})\Omega C_{\mathrm{i}} \chi \nabla C_{\mathrm{A}} - (d_{\mathrm{Bi}} - d_{\mathrm{Ci}})\Omega C_{\mathrm{i}} \chi \nabla C_{\mathrm{B}} - D_{\mathrm{i}} \nabla C_{\mathrm{i}} \\
J_{\mathrm{v}} &= (d_{\mathrm{Av}} - d_{\mathrm{Cv}})\Omega C_{\mathrm{v}} \chi \nabla C_{\mathrm{A}} + (d_{\mathrm{Bv}} - d_{\mathrm{Cv}})\Omega C_{\mathrm{v}} \chi \nabla C_{\mathrm{B}} - D_{\mathrm{v}} \nabla C_{\mathrm{v}} \\
J_{\mathrm{A}} &= -D_{\mathrm{A}} \chi \nabla C_{\mathrm{A}} + d_{\mathrm{Av}} \Omega C_{\mathrm{A}} \nabla C_{\mathrm{v}} - d_{\mathrm{Ai}} \Omega C_{\mathrm{A}} \nabla C_{\mathrm{i}} \\
J_{\mathrm{B}} &= -D_{\mathrm{B}} \chi \nabla C_{\mathrm{B}} + d_{\mathrm{Bv}} \Omega C_{\mathrm{B}} \nabla C_{\mathrm{v}} - d_{Bi} \Omega C_{\mathrm{B}} \nabla C_{\mathrm{i}} \\
J_{\mathrm{C}} &= -D_{\mathrm{C}} \chi \nabla C_{\mathrm{C}} + d_{\mathrm{Cv}} \Omega C_{\mathrm{C}} \nabla C_{\mathrm{v}} - d_{\mathrm{Ci}} \Omega C_{\mathrm{C}} \nabla C_{\mathrm{i}}.
\end{aligned} \tag{6.48}$$

Small perturbations arising from the presence of point defects are neglected so that $C_{\mathrm{A}} + C_{\mathrm{B}} + C_{\mathrm{C}} = 1$ and $\nabla C_{\mathrm{C}} = -(\nabla C_{\mathrm{A}} + \nabla C_{\mathrm{B}})$. Of the five fluxes in Eq. (6.48), only four are independent because the defect and atom fluxes across a marker plane must balance:

$$J_{\mathrm{A}} + J_{\mathrm{B}} + J_{\mathrm{C}} = J_{\mathrm{i}} - J_{\mathrm{v}}. \tag{6.49}$$

A system of four coupled partial differential equations describing the space and time dependence of the atoms and defects in the solid is determined by substituting the defect and atom fluxes given by Eq. (6.48) into Eqs. (6.40) and (6.1):

$$\begin{aligned}
\frac{\partial C_\mathrm{v}}{\partial t} &= \nabla \cdot [-(d_\mathrm{Av} - d_\mathrm{Cv})\Omega C_\mathrm{v}\chi\nabla C_\mathrm{A} - (d_\mathrm{Bv} - d_\mathrm{Cv})\Omega C_\mathrm{v}\chi\nabla C_\mathrm{B} + D_\mathrm{v}\nabla C_\mathrm{v}] + K - R \\
\frac{\partial C_\mathrm{i}}{\partial t} &= \nabla \cdot [(d_\mathrm{Ai} - d_\mathrm{Ci})\Omega C_\mathrm{i}\chi\nabla C_\mathrm{A} + (d_\mathrm{Bi} - d_\mathrm{Ci})\Omega C_\mathrm{i}\chi\nabla C_\mathrm{B} + D_\mathrm{i}\nabla C_\mathrm{i}] + K - R \\
\frac{\partial C_\mathrm{A}}{\partial t} &= \nabla \cdot [D_\mathrm{A}\chi\nabla C_\mathrm{A} + \Omega C_\mathrm{A}(d_\mathrm{Ai}\nabla C_\mathrm{i} - d_\mathrm{Av}\nabla C_\mathrm{v})] \\
\frac{\partial C_\mathrm{B}}{\partial t} &= \nabla \cdot [D_\mathrm{B}\chi\nabla C_\mathrm{B} + \Omega C_\mathrm{B}(d_\mathrm{Bi}\nabla C_\mathrm{i} - d_\mathrm{Bv}\nabla C_\mathrm{v})].
\end{aligned} \tag{6.50}$$

Numerical solutions of Eq. (6.50) are obtained for a planar sample under irradiation. The grain boundary is equated to a free surface and the calculations are performed for only a single grain, taking advantage of the symmetry of the problem. The initial conditions are those for thermodynamic equilibrium of the alloy. Conditions at the boundary are defined as follows. At the grain center, all concentration gradients are set equal to zero. At the grain boundary, the concentrations of interstitials and vacancies are fixed at their thermal equilibrium values. The grain boundary atom concentrations are determined by the conservation of the numbers of atoms in the specimen. Atom concentrations are assumed to be initially uniform. Parameters used in the calculation of segregation in Fe–Cr–Ni alloys are given in [15] for the Lam model and in [7] for the Perks model.

Equation (6.50) can be solved at steady state to provide a relationship between the vacancy gradient and the atom gradient. This relationship is known as a determinant, *M,* and is a function of the concentrations and diffusivities. The determinant for a three-component alloy is determined in the same way as was done for the binary alloy case Eq. (6.32) and is given by [16]:

$$M_j = \frac{\nabla C_j}{\nabla C_\mathrm{v}} = \frac{\dfrac{d_{j\mathrm{v}}C_j}{D_j}\displaystyle\sum_{k\neq j}\frac{d_{ki}C_k}{D_k} - \frac{d_{ji}C_j}{D_j}\sum_{k\neq j}\frac{d_{k\mathrm{v}}C_k}{D_k}}{\chi\displaystyle\sum_k \frac{d_{ki}C_k}{D_k}}. \tag{6.51}$$

The determinant can be used to help determine the primary mechanism of segregation in Fe–Cr–Ni alloys. Table 6.2 shows the determinant calculated for Cr, Fe, and Ni for a total of seven alloys *assuming that preferential coupling with the vacancy flux causes the segregation*, i.e., setting the interstitial diffusion coefficients for Cr, Fe, and Ni to be equal to each other. The segregation trends (enrichment or depletion at the grain boundary) for Cr, Fe, and Ni that were measured on the grain boundaries of these alloys by Auger electron spectroscopy (AES) and energy dispersive spectroscopy in scanning transmission electron microscopy (STEM/EDS) are also listed. For each alloy where the determinant for the element is positive, depletion occurs; where the determinant is negative enrichment occurs. Note that for each element in each of the seven alloys studied, the sign of the determinant agrees with the measurement (by either STEM/EDS or AES) and calculation. This

Table 6.2 Segregation behavior in Ni–Cr–Fe and Fe–Cr–Ni alloys compared to inverse Kirkendall predictions. Determinants (M) calculated using Eq. (6.51)

Alloy	M_{Cr}	M_{Fe}	M_{Ni}	Ref.	Cr	Fe	Ni	Analysis method
Ni–18Cr	3.9	–	−3.9	[16]	Depletes	–	Enriches	AES & STEM/EDS
Ni–18Cr–9Fe	5.0	0.4	−5.4	[17]	Depletes	Depletes	Enriches	AES & STEM/EDS
Fe–16Cr–24Ni	4.0	3.6	−7.6	[18]	Depletes	Depletes	Enriches	AES
Fe–20Cr–24Ni	5.0	2.4	−7.4	[18]	Depletes	Depletes	Enriches	AES & STEM/EDS
Fe–24Cr–24Ni	6.3	1.8	−8.5	[18]	Depletes	Depletes	Enriches	AES
Fe–24Cr–19Ni	6.5	−1.8	−4.7	[18]	Depletes	Enriches	Enriches	AES
Fe–20Cr–9Ni	5.0	−3.0	−2.0	[18]	Depletes	Enriches	Enriches	AES & STEM/EDS

example also shows that while chromium always depletes and nickel always enriches, iron can either enrich or deplete depending on the relative concentrations of nickel and chromium. In the Fe–Cr–Ni system, Cr is the fast diffuser and Ni is the slow diffuser and Fe is between the two. When the nickel level is high relative to the Cr level, the large amount of enrichment of Ni at the grain boundary cannot be fully compensated by depletion of Cr, so Fe also must deplete. But when the Cr level is high relative to Ni, the reverse occurs and Fe enriches. Note that Cr and Ni do not exactly cancel as can be seen in the case of the Fe–24Cr–24Ni alloy in which Ni enrichment is stronger than Cr depletion and Fe must also deplete.

This example exposes a key process in RIS, the role of composition in the segregation behavior. When the composition near a sink starts to change, the diffusivities of the elements in that region will also change as diffusion is composition-dependent. The effect of changing local composition needs to be accounted for to properly determine the extent of RIS, as will be covered in the next section.

6.3 Effect of Local Composition Changes on RIS

We have established that RIS occurs because of differences in the coupling of the various solutes with defects. Further, the difference in the strength of the coupling influences the degree of segregation. Therefore, when the concentration near the sink is significantly different from that in the bulk, the diffusivities of the solutes will change as well, and this change needs to be accounted for to accurately determine the composition profile [14].

In the Perks model, the rate of segregation of element k by defect j is described by a diffusivity of the general form given by Eq. (6.33):

$$d_{\mathrm{kj}} = \frac{1}{6}\lambda_{\mathrm{j}}^{2} z_{\mathrm{j}} \nu \exp\left(\frac{S_{\mathrm{m}}^{\mathrm{j}}}{k}\right) \exp\left(\frac{-E_{\mathrm{m}}^{\mathrm{kj}}}{kT}\right),$$

or in simplified notation:

$$d_{\mathrm{kj}} = d_{0}^{\mathrm{kj}} \exp\left(\frac{-E_{\mathrm{m}}^{\mathrm{kj}}}{kT}\right), \tag{6.52}$$

where the pre-exponential terms are lumped into a single term, d_0^{kj}. In most solutions to Eq. (6.50), the migration energies for each element are assumed to be equal, with differences in segregation rates arising from differences in the pre-exponential factors. To account for diffusion in a solution of varying composition, the migration energy term in the exponential must be described as a function of composition [13, 17, 18] as presented in the following paragraphs.

For an atom to migrate (Cr migrating in a Fe–Cr–Ni lattice will be used as an example), it must move from its equilibrium position in the lattice (with equilibrium energy E_{eq}^{Cr}) and travel through a position of maximum potential (known as the saddle point, with saddle point energy $ES_{Fe-Cr-Ni}^{Cr}$), before moving to a new lattice site. This relationship between the energies is shown schematically in Fig. 6.10. For atom–vacancy exchange, the migration energy is the difference between the saddle point energy and the equilibrium energy:

$$E_{\mathrm{m}}^{\mathrm{Cr-v}} = ES_{\mathrm{Fe-Cr-Ni}}^{\mathrm{Cr}} - E_{\mathrm{eq}}^{\mathrm{Cr}}. \tag{6.53}$$

In a simple model, the equilibrium energy can be described as the interaction energy between nearest neighbors:

$$E_{\mathrm{eq}}^{\mathrm{Cr-v}} = Z[C_{\mathrm{Cr}}E_{\mathrm{CrCr}} + C_{\mathrm{Ni}}E_{\mathrm{NiCr}} + C_{\mathrm{Fe}}E_{\mathrm{FeCr}} + C_{\mathrm{v}}E_{\mathrm{Cr-v}}], \tag{6.54}$$

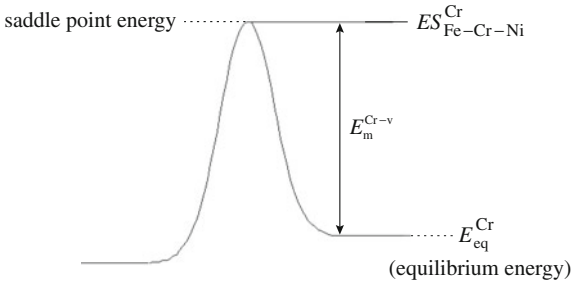

Fig. 6.10 Determination of the migration energy for an atom–vacancy exchange in an Fe–Cr–Ni alloy (after [14])

where Z is the number of nearest neighbors, C is the atomic concentration of atoms and/or defects, and E_{kj} is the pair interaction energy between an atom k and an atom or vacancy j. Pair interaction energies between unlike neighbors are defined to be a linear average of the like-atom pair energies minus any ordering energy:

$$E_{\mathrm{NiCr}} = \frac{E_{\mathrm{NiNi}} + E_{\mathrm{CrCr}}}{2} - E^{\mathrm{ord}}_{\mathrm{NiCr}}. \tag{6.55}$$

Combining Eq. (6.53) to Eq. (6.55) and requiring that $C_{\mathrm{Fe}} + C_{\mathrm{Cr}} + C_{\mathrm{Ni}} = 1$, the migration energy for Cr, Ni, and Fe via vacancies can be expressed as:

$$E_{\mathrm{m}}^{\mathrm{Cr-v}} = ES^{\mathrm{Cr}}_{\mathrm{Fe-Cr-Ni}} - Z\left[\frac{1}{2}(C_{\mathrm{Cr}}+1)E_{\mathrm{CrCr}} + \frac{C_{\mathrm{Ni}}}{2}E_{\mathrm{NiNi}} + \frac{C_{\mathrm{Fe}}}{2}E_{\mathrm{FeFe}} + C_{\mathrm{v}}E_{\mathrm{Cr-v}}\right] + ZC_{\mathrm{Ni}}E^{\mathrm{ord}}_{\mathrm{NiCr}} + ZC_{\mathrm{Fe}}E^{\mathrm{ord}}_{\mathrm{FeCr}} \tag{6.56a}$$

$$E_{\mathrm{m}}^{\mathrm{Ni-v}} = ES^{\mathrm{Ni}}_{\mathrm{Fe-Cr-Ni}} - Z\left[\frac{1}{2}(C_{\mathrm{Ni}}+1)E_{\mathrm{NiNi}} + \frac{C_{\mathrm{Cr}}}{2}E_{\mathrm{CrCr}} + \frac{C_{\mathrm{Fe}}}{2}E_{\mathrm{FeFe}} + C_{\mathrm{v}}E_{\mathrm{Ni-v}}\right] + ZC_{\mathrm{Cr}}E^{\mathrm{ord}}_{\mathrm{NiCr}} + ZC_{\mathrm{Fe}}E^{\mathrm{ord}}_{\mathrm{FeNi}} \tag{6.56b}$$

$$E_{\mathrm{m}}^{\mathrm{Fe-v}} = ES^{\mathrm{Fe}}_{\mathrm{Fe-Cr-Ni}} - Z\left[\frac{1}{2}(C_{\mathrm{Fe}}+1)E_{\mathrm{FeFe}} + \frac{C_{\mathrm{Cr}}}{2}E_{\mathrm{CrCr}} + \frac{C_{\mathrm{Ni}}}{2}E_{\mathrm{NiNi}} + C_{\mathrm{v}}E_{\mathrm{Fe-v}}\right] + ZC_{\mathrm{Cr}}E^{\mathrm{ord}}_{\mathrm{FeCr}} + ZC_{\mathrm{Ni}}E^{\mathrm{ord}}_{\mathrm{FeNi}} \tag{6.56c}$$

In order to determine the migration energies in Eq. (6.56), pair interaction energies and saddle point energies must be calculated. For like atoms, the pair interaction energy is the cohesive energy, E_{coh} divided by the number of nearest neighbor bond pairs:

$$E_{\mathrm{CrCr}} = E^{\mathrm{Cr}}_{\mathrm{coh}}/(Z/2), \tag{6.57a}$$

$$E_{\mathrm{FeFe}} = E^{\mathrm{Fe}}_{\mathrm{coh}}/(Z/2), \tag{6.57b}$$

$$E_{\mathrm{NiNi}} = E^{\mathrm{Ni}}_{\mathrm{coh}}/(Z/2). \tag{6.57c}$$

Since pure Fe and pure Cr occur in the bcc structure, the energy required to convert Fe and Cr to the fcc structure for application to stainless steels must be included in the determination of E_{CrCr} and E_{FeFe} to properly describe the equilibrium energy:

$$E_{\mathrm{CrCr}}^{fcc} = E_{\mathrm{CrCr}}^{bcc} + \Delta G_{\mathrm{Cr}}^{bcc \rightarrow fcc}, \tag{6.58a}$$

$$E_{\mathrm{FeFe}}^{fcc} = E_{\mathrm{FeFe}}^{bcc} + \Delta G_{\mathrm{Fe}}^{bcc \rightarrow fcc}. \tag{6.58b}$$

Pair interaction energies between unlike atoms are determined from the average value of the like-atom pair energies less any ordering energy:

$$E_{\mathrm{NiCr}} = \frac{(E_{\mathrm{NiNi}} + E_{\mathrm{CrCr}})}{2} - E_{\mathrm{NiCr}}^{\mathrm{ord}}, \tag{6.59a}$$

$$E_{\mathrm{FeCr}} = \frac{(E_{\mathrm{FeFe}} + E_{\mathrm{CrCr}})}{2} - E_{\mathrm{FeCr}}^{\mathrm{ord}}, \tag{6.59b}$$

$$E_{\mathrm{FeNi}} = \frac{(E_{\mathrm{FeFe}} + E_{\mathrm{NiNi}})}{2} - E_{\mathrm{FeNi}}^{\mathrm{ord}}. \tag{6.59c}$$

Finally, the pair interaction energy for atoms and vacancies is fitted to the formation energy of the pure metal and is given by:

$$E_{\mathrm{Cr-v}} = \left(\frac{E_{\mathrm{coh}}^{\mathrm{Cr}} + E_{\mathrm{f}}^{\mathrm{Cr-v}}}{Z}\right), \tag{6.60a}$$

$$E_{\mathrm{Ni-v}} = \left(\frac{E_{\mathrm{coh}}^{\mathrm{Ni}} + E_{\mathrm{f}}^{\mathrm{Ni-v}}}{Z}\right), \tag{6.60b}$$

$$E_{\mathrm{Fe-v}} = \left(\frac{E_{\mathrm{coh}}^{\mathrm{Fe}} + E_{\mathrm{f}}^{\mathrm{Fe-v}}}{Z}\right), \tag{6.60c}$$

where $E_{\mathrm{f}}^{\mathrm{k-v}}$ is the vacancy formation energy in pure k.

The last quantity remaining to be determined is the saddle point energy, which is calculated using the saddle point energy of pure Fe, Cr, and Ni. The saddle point energy in the pure metal is calculated to reproduce the vacancy migration energy in the pure metal. For example, assuming that in pure Cr both an atom and a vacancy are extracted and placed at a saddle point, then the energy to extract the Cr atom is given by:

$$E_{\mathrm{Cr}} = Z(C_{\mathrm{Cr}} E_{\mathrm{CrCr}} + C_{\mathrm{v}} E_{\mathrm{Cr-v}}). \tag{6.61}$$

The energy to extract the vacancy is:

$$E_{\mathrm{v}} = Z(C_{\mathrm{v}} E_{\mathrm{vv}} + C_{\mathrm{Cr}} E_{\mathrm{Cr-v}}) \tag{6.62}$$

Since $C_{Cr} + C_v = 1$ in a pure metal and since $C_v \ll C_{Cr}$, the sum of $E_{Cr} + E_v$ becomes the following:

$$E_{Cr} + E_v = Z(E_{CrCr} + E_{Cr-v}). \tag{6.63}$$

Equation (6.63) represents the equilibrium energy for pure Cr. We want to place the atom at a saddle point with an energy such that:

$$E_m^{Cr-v} = ES_{pure}^{Cr} - (E_{Cr} + E_v) = ES_{pure}^{Cr} - Z(E_{CrCr} + E_{Cr-v}). \tag{6.64}$$

The saddle point energy in the pure metal is then given as:

$$ES_{pure}^{Cr} = E_m^{Cr-v} + Z(E_{CrCr} + E_{Cr-v}). \tag{6.65}$$

This approach, described in the modified inverse Kirkendall (Perks) model called the MIK model [14], was used to model RIS and results were compared to measurements taken on a range of Fe-base and Ni-base austenitic alloys irradiated at temperatures from 200 to 600 °C and at doses up to 3 dpa. The RIS results shown in Fig. 6.11 clearly demonstrate the importance of accounting for composition changes near the sinks in the determination of the RIS composition profiles. The MIK model calculations agree with AES measurements of grain boundary nickel concentration in irradiated Fe–20Cr–24Ni much better than the original Perks model. Also, over a range of alloys, doses, and irradiation temperatures (Fig. 6.12), the inclusion of local composition changes on RIS results in much better agreement with the data. These data also serve to illustrate the importance of vacancies in RIS in Fe–Cr–Ni alloys at intermediate temperatures. The MIK model calculations did *not* include either

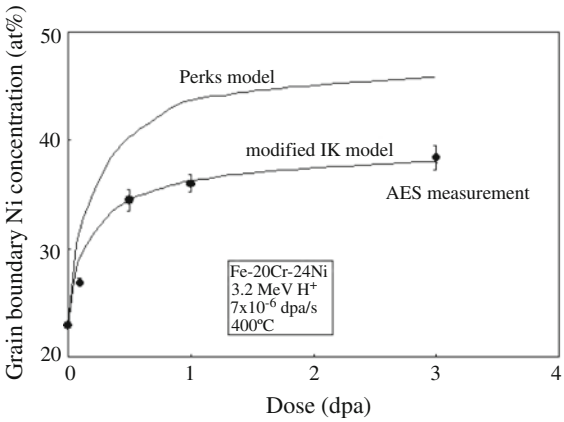

Fig. 6.11 The modified inverse Kirkendall (MIK) model result compared to the Perks model result and to measurement showing the importance in accounting for the changing local composition at sinks in RIS. Experiment was conducted on Fe–20Cr–24Ni using 3.2 MeV protons at 400 °C and at a displacement rate of 7×10^{-6} dpa/s (after [14])

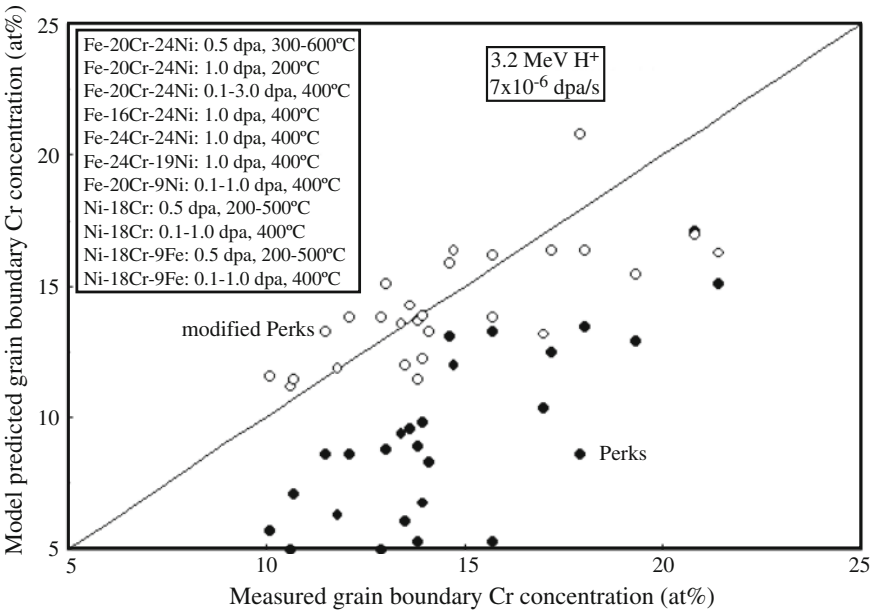

Fig. 6.12 MIK model applied to several alloys under a range of doses and temperatures and comparison to measurement (after [14])

interstitial binding (that is, $E_b^{ik} = 0$) or preferential participation of any of the alloying elements in the interstitial flux. Excellent agreement between model and measurement is achieved solely by preferential participation of alloying elements in the vacancy flux. Hence, in the Fe–Cr–Ni system, atom migration via vacancies appears to be the dominant mechanism of RIS.

6.4 Effect of Solutes on RIS

The presence of impurities in a solid can influence the propensity for RIS at the grain boundary. It has been hypothesized that solutes that are oversized or undersized with respect to the lattice atoms can act as traps for vacancies or interstitials. Trapping of point defects by solutes could increase the fraction of vacancies and interstitials undergoing mutual recombination, thus reducing the fraction flowing to sinks and hence the degree of segregation. Mansur and Yoo [19] generalized the point defect balance equations to include point defect trapping. Trapping is accommodated by subtracting and adding terms corresponding to trapping and recombination at traps, and the release of point defects from traps. In addition, equations describing the conservation of the trapped defects are also added. As a result, the point defect balances, from Eq. (6.1), are given as follows:

Free vacancies:

$$\frac{\partial C_{\mathrm{v}}}{\partial t} = \nabla \cdot D_{\mathrm{v}} \nabla C_{\mathrm{v}} + K_0 - K_{i\mathrm{v}} C_i C_{\mathrm{v}} + \sum_l \tau_{\mathrm{v}l}^{-1} C_{\mathrm{v}l} - C_{\mathrm{v}} \sum_l K_{il} C'_{il} - C_{\mathrm{v}} \sum_l \kappa_{\mathrm{v}l} \left(C_l^t - C'_{\mathrm{v}l} - C'_{il} \right) - K_{\mathrm{v}s} C_{\mathrm{v}}. \tag{6.66}$$

Free interstitials:

$$\frac{\partial C_i}{\partial t} = \nabla \cdot D_i \nabla C_i + K_0 - K_{i\mathrm{v}} C_i C_{\mathrm{v}} + \sum_l \tau_{il}^{-1} C_{il} - C_i \sum_l K_{\mathrm{v}l} C'_{\mathrm{v}l} - C_i \sum_l \kappa_{il} (C_l^t - C'_{\mathrm{v}l} - C'_{il}) - K_{is} C_i. \tag{6.67}$$

In Eqs. (6.66) and (6.67), the summations extend over the l = 1, 2,…, n types of traps. Similarly, the following equations apply to each of the l = 1, 2,…, n types of traps.

Traps (concentration in general is a function of position and time):

$$\frac{\partial C_l^t}{\partial t} = f_l(r, t). \tag{6.68}$$

Trapped vacancies:

$$\frac{\partial C_{\mathrm{v}l}^t}{\partial t} = C_{\mathrm{v}} \kappa_{\mathrm{v}l} \left(C_l^t - C'_{\mathrm{v}l} - C'_{\mathrm{i}l} \right) - \tau_{\mathrm{v}l}^{-1} C'_{\mathrm{v}l} - C_{\mathrm{i}} K_{\mathrm{v}l} C'_{\mathrm{v}l}. \tag{6.69}$$

Trapped interstitials:

$$\frac{\partial C_{\mathrm{i}l}^t}{\partial t} = C_{\mathrm{i}} \kappa_{\mathrm{i}l} \left(C_l^t - C'_{\mathrm{v}l} - C'_{\mathrm{i}l} \right) - \tau_{\mathrm{i}l}^{-1} C'_{\mathrm{i}l} - C_{\mathrm{v}} K_{\mathrm{i}l} C'_{\mathrm{i}l}. \tag{6.70}$$

In Eqs. (6.66) and (6.67), the first three terms are the same as in Eq. (6.1). The remaining terms have the following meaning. Referring to the equation for free vacancies, the fourth term is the release of trapped vacancies from the sink and the variable $\tau_{\mathrm{v}l}^{-1}$ is the mean time that the vacancy is trapped at the lth trapping site. The mean trapping time is denoted by $\tau_{jl} = \left(b^2 \Big/ D_j^0 \right) \exp\left[\left(E_{\mathrm{b}}^{jl} + E_{\mathrm{m}}^{j} \right) \Big/ kT \right]$, where j denotes i or v, D_j^0 is the pre-exponential of the diffusion coefficient $\left[D_j = D_j^0 \exp\left(-E_{\mathrm{m}}^{j} / kT \right) \right]$, b is the order of atomic distance, E_{b}^{jl} is the binding energy of the point defect at the lth type trap, and E_{m}^{j} is the point defect migration energy. The fifth term is the recombination rate of vacancies with trapped interstitials, where K_{jl} is the recombination rate constant for that reaction and is given by $K_{\mathrm{i}l} = 4\pi r_{\mathrm{i}l} D_{\mathrm{v}}$ or $K_{\mathrm{v}l} = 4\pi r_{\mathrm{v}l} D_{\mathrm{i}}$, where $r_{\mathrm{i}l}$ and $r_{\mathrm{v}l}$ denote the respective radii of the

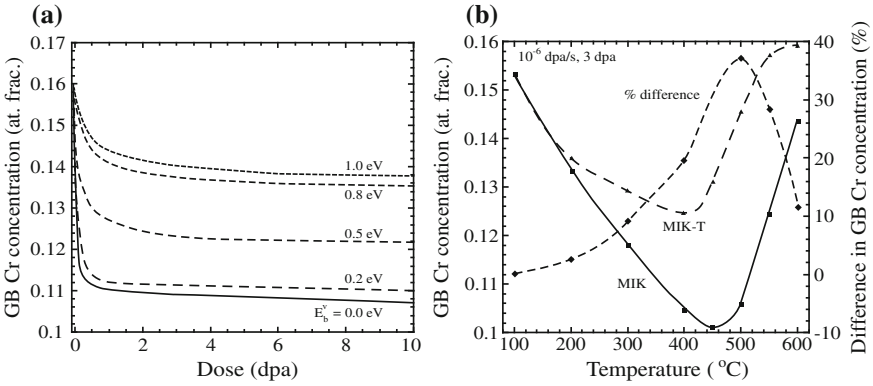

Fig. 6.13 Calculated grain boundary Cr composition (**a**) as a function of binding energy for the MIK-T model at 400 °C and 1×10^{-5} dpa/s for Fe–16Cr–13Ni, and (**b**) as a function of temperature at a constant dose rate of 10^{-5} dpa/s at 3 dpa. Percent difference calculated by (MIK-T − MIK)/MIK * 100 % (after [20])

recombination volumes. The sixth term describes the trapping of free vacancies at a trap of type l. The concentration difference $\left(C_l^t - C'_{\mathrm{v}l} - C'_{\mathrm{i}l}\right)$ accounts for the fact that the fraction $C'_{\mathrm{v}l}/C_l^t + C'_{\mathrm{i}l}/C_l^t$ of traps of type l are already occupied by vacancies and interstitials and hence are not available as traps for free defects. It also accounts for the fact that a given trap may have a binding energy for both vacancies and interstitials but would not trap both simultaneously, since when one is trapped, the site is then a recombination center. The terms $\kappa_{\mathrm{v}l} = 4\pi r'_{\mathrm{v}l} D_{\mathrm{v}}$ and $\kappa_{\mathrm{i}l} = 4\pi r'_{\mathrm{i}l} D_{\mathrm{i}}$ denote the capture coefficients similar to recombination coefficients, and the $r'_{\mathrm{v}l}$ and $r'_{\mathrm{i}l}$ are the capture radii of the trap type l for the respective point defects. Finally, the seventh term is the loss of defects to all internal sinks and K_{js} describes the rate constant for all sinks.

Equations (6.66) through Eq. (6.70) are substituted for the vacancy and interstitial concentrations in Eq. (6.50) and solved in the same manner as before in a version of the MIK code designated MIK-T. The results of trapping in Fe–16Cr–13Ni containing an oversized solute concentration of 1 % are shown in the plot of grain boundary chromium content versus dose for the case of irradiation at a dose rate of 10^{-5} dpa/s at a temperature of 400 °C and for interstitial and vacancy binding energies up 1.0 eV (Fig. 6.13(a)). Note that high binding energies on the order 1.0 eV are required for trapping to reduce the amount of RIS. The main effect is a reduction in the amount of grain boundary Cr depletion, but a secondary effect is a slowing of the rate of segregation with dose. Figure 6.13(b) shows that trapping moves the temperature at which RIS is a maximum to a slightly lower temperature. Figure 6.14 shows the effect of oversize solute addition on grain boundary chromium depletion and nickel enrichment in Fe–Cr–Ni alloys irradiated with protons, and that experimental results qualitatively follow those of the model.

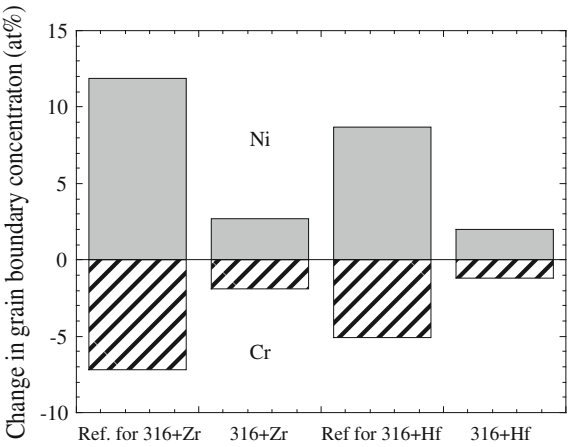

Fig. 6.14 Grain boundary Cr and Ni composition for reference and oversize impurity-doped Fe–Cr–Ni alloys irradiated at 400 °C to 3.0 dpa (Zr) and 2.5 dpa (Hf) (after [20, 21])

As successful as these models are in predicting the direction and magnitude of segregation, they are very incomplete. The models have been developed for binary and ternary systems only, whereas real engineering alloys may contain 10–20 alloying elements. Even though some may be present in very small quantities, they can exert a very large influence on the behavior of the alloy. The Perks and MIK models apply only to solute atoms and not to small interstitial atoms such as B, C, and N. Further, many of the thermodynamic parameters required for accurate simulation of RIS are unknown and must be estimated, introducing uncertainty into the results. Despite these shortcomings, they can serve to rationalize RIS in real systems.

6.5 Examples of RIS in Austenitic Alloys

As stated earlier, RIS is an extremely important problem in structural materials exposed to irradiation at elevated temperatures. The changes in grain boundary composition can give rise to microstructure changes (precipitation, dislocation loop structure, void structure) in addition to changes in susceptibility to processes such as intergranular corrosion and stress corrosion cracking. For example, we determined that Cr always depletes in irradiated stainless steels, and the loss of chromium at grain boundaries could cause an increased susceptibility to intergranular corrosion and intergranular stress corrosion cracking, since chromium provides *passivity* to the alloy by forming a very thin, protective, Cr_2O_3 film. As will be discussed in Chap. 15, with increases in dose above some *pseudo-threshold* level, the amount of intergranular stress corrosion cracking (IGSCC), measured as the percentage of the fracture surface that displays intergranular facets, increases steeply in slow strain rate tests in 288 °C normal water chemistry used in boiling water reactors (BWR). Figure 6.15 shows that the grain boundary Cr content also

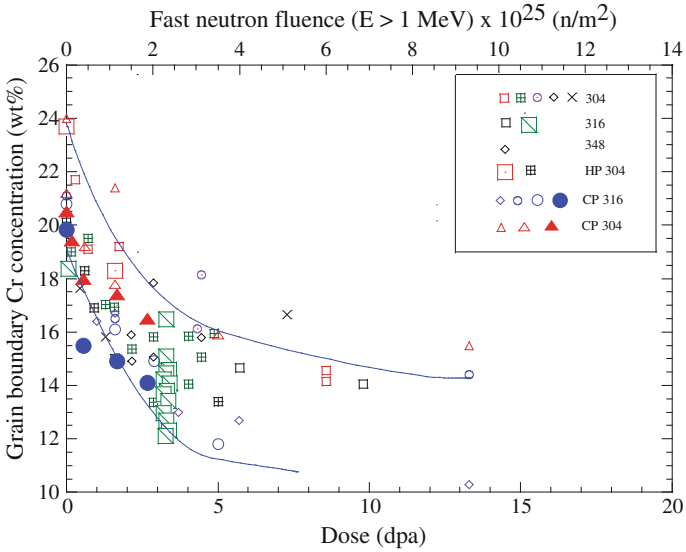

Fig. 6.15 Dependence of grain boundary chromium concentration on dose for a range of 300 series stainless steels irradiated under various conditions. Note that RIS increases with dose through about 5 dpa after which the change is minimal (after [22])

decreases rapidly with dose due to RIS. The loss of Cr may raise the susceptibility of the alloy to IASCC, although other changes are occurring in the microstructure at the same time.

Silicon is also observed to segregate very strongly with dose, as shown in Fig. 6.16 for austenitic stainless steels irradiated at ~288 °C. These measurements of high levels of Si were made by STEM/EDS. Due to the spatial resolution limit of this technique, the actual grain boundary level of Si may be underestimated by as much as a factor of 3–5, giving concentrations of over 20 % Si at the grain

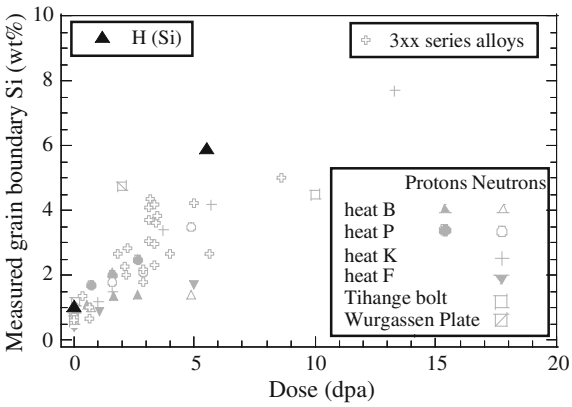

Fig. 6.16 Grain boundary segregation of silicon in 300 series austenitic alloys irradiated with neutrons or protons to 13 dpa

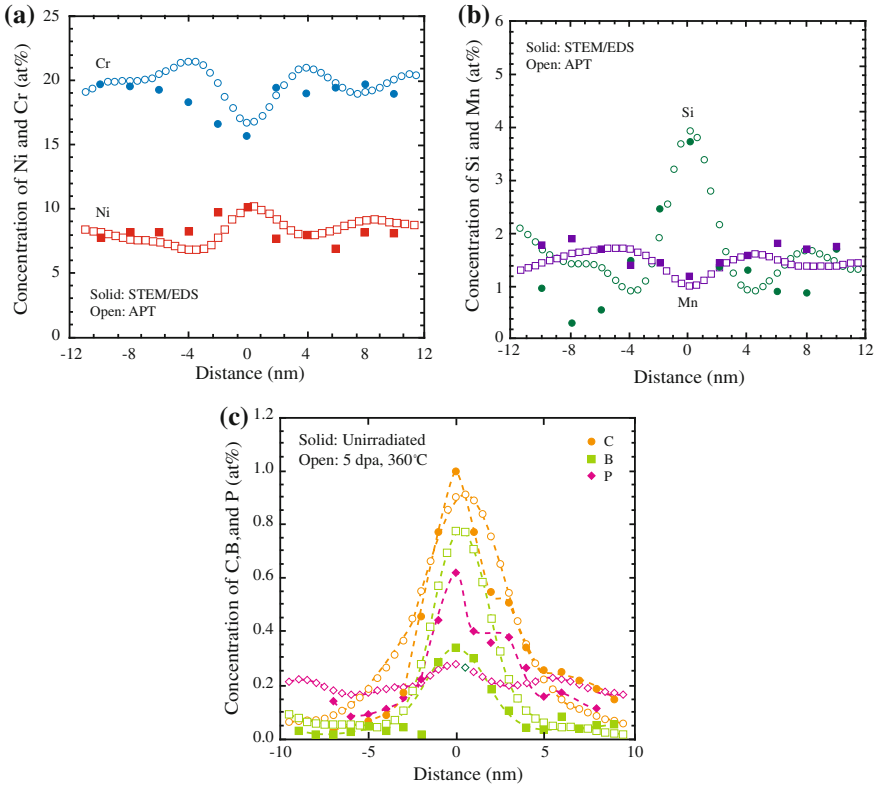

Fig. 6.17 Composition profiles across the grain boundary in commercial purity 304 stainless steel following irradiation to 5 dpa at 360 °C, (**a**) major alloying elements Cr and Ni, (**b**) minor alloying elements Mn and Si, and (**c**) elements B, C, and P (after [23])

boundary. Since Si is soluble in high-temperature water, it is possible that it could be enhancing dissolution at the grain boundary giving rise to increased rates of intergranular corrosion (IGC) and IGSCC.

In addition to the Fe, Cr, and Ni segregation, the minor alloying elements also exhibit RIS under irradiation. Figure 6.17(a) shows the behavior of Cr and Ni in a commercial purity 304 alloy irradiated with 2 MeV protons to 5 dpa at 360 °C. In addition to the depletion of Cr, Mn also depletes at the grain boundary, Fig. 6.17(b). The behavior of Mn is similar to that of Cr as both are oversize solute and deplete under irradiation. Conversely, similar to Ni, Si strongly enriches at the grain boundary. In fact, Si does not exhibit saturation up through a dose of 13 dpa, as shown in Fig. 6.16.

Trace elements also undergo RIS. These elements are difficult to measure using energy dispersive spectroscopy because of their low mass. However, atom probe tomography is able to track the behavior of these elements at the grain boundary. Figure 6.17(c) shows the composition profiles of B, C, and P at a grain boundary in

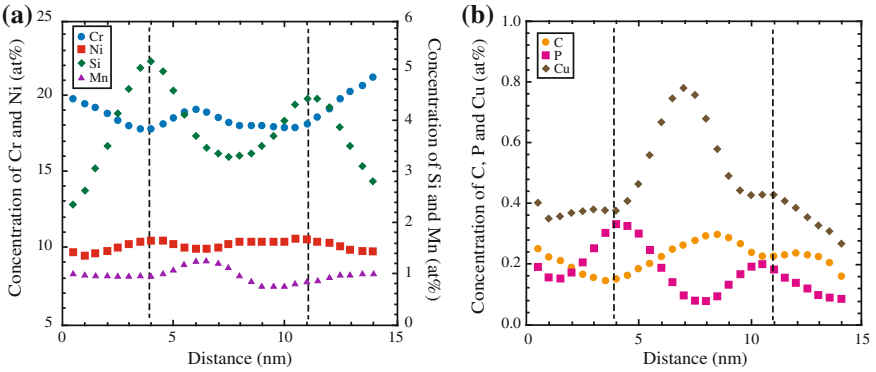

Fig. 6.18 Composition profiles across a dislocation loop in commercial purity alloy 304 stainless steel following irradiation to 5 dpa at 360 °C, (**a**) elements Cr, Ni, Mn, and Si, and (**b**) elements C, P, and Cu (after [23])

the same commercial purity 304 alloy. Note that all three elements were observed to enrich at the grain boundary in the as-received alloy and prior to irradiation (solid symbols). After irradiation, P is observed to enrich, C depletes, and B remains unchanged.

As discussed in Chap. 5, all interfaces are sinks for point defects. While sink strengths vary with sink type, segregation should occur to other sinks to some extent. Figure 6.18(a) shows the segregation of Cr, Ni, Si, and Mn at the core of a dislocation loop. Note that the segregation behavior is identical to that at grain boundaries, Ni and Si enrich, and Cr and Mn deplete. Figure 6.18(b) shows the same for trace elements C, P, and Cu. While grain boundaries are believed to be the stronger sink, Fig. 6.19 shows that the magnitude of RIS at dislocation loops is remarkably similar to that at grain boundaries.

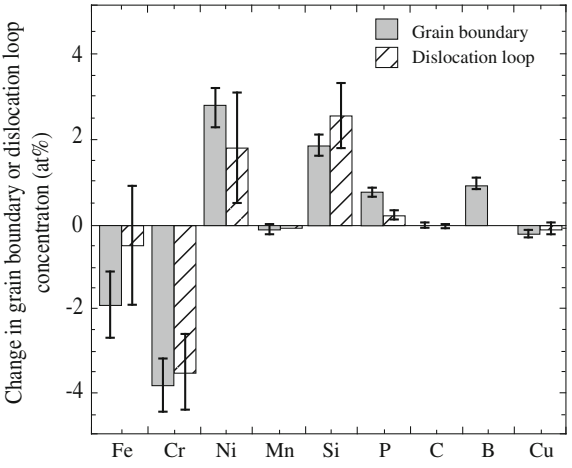

Fig. 6.19 Comparison of the composition change at the grain boundary with that at the dislocation loop in commercial purity 304 stainless steel following irradiation to 5 dpa at 360 °C (after [23])

6.6 RIS in Ferritic Alloys

RIS is also of significance in ferritic steels, particularly pressure vessel steels where the grain boundary segregation of interstitial impurities such as P can have significant consequences for grain boundary embrittlement. Compared to austenitic steels, little work has been done on the segregation of alloying elements in ferritic alloys. Segregation models for interstitial impurities are not as well-developed as for substitutional solutes. Faulkner [24] has reviewed the segregation data and mechanisms and suggests that RIS in ferritic steels is by defect–impurity complexes and that site competition by other elements at the boundary plays a significant role in determining the amount of segregation of a particular impurity. Focusing on the behavior of P, it is assumed that migration by self-interstitial phosphorus complexes is fast such that the concentration remains uniform across the grain boundary plane. The maximum grain boundary concentration of phosphorus is given by:

$$C_{\mathrm{P}}^{\max} = C_g \frac{E_{\mathrm{b}}}{E_{\mathrm{f}}} \left[\frac{C_{\mathrm{g}}^{j} \exp\left(E_{\mathrm{b}}^{j}/kT\right)}{\sum_{j} C_{\mathrm{g}}^{j} \exp\left(E_{\mathrm{b}}^{j}/kT\right)} \right] \left[1 + \frac{\xi K_0 F(\eta)}{ADk^2} \exp\left(E_{\mathrm{f}}^{\mathrm{i}}/kT\right) \right], \tag{6.71}$$

where C_{g} is the total impurity concentration in the grain, E_{b}^{j} is the binding energy between the point defect, the self-interstitial and the impurity atom, E_{f} is the interstitial formation energy, and C_{g}^{j} is the concentration of impurity atom, j, in the grains. The denominator of the first bracket is the sum of point defect binding energy terms for all of the elements entering into the site competition process. In the second bracket, ξ is the defect production efficiency, $F(\eta)$ is a recombination term, K_0 is the defect production rate, A is associated with the vibrational entropy of the atoms surrounding the point defect, D is the defect diffusion coefficient, and k^2 is the sink strength.

Following segregation to the boundary, the impurity concentration will be determined by site competition at the boundary where the concentration of phosphorus is given by:

$$C_{\mathrm{P}}^{*} = C_{\mathrm{P}}^{\max} = \frac{C_{\mathrm{g}}^{\mathrm{P}} \exp(Q_{\mathrm{P}}/kT)}{C_{\mathrm{g}}^{j} \exp\left(Q_j/kT\right) + C_{\mathrm{g}}^{\mathrm{P}} \exp(Q_{\mathrm{P}}/kT)}, \tag{6.72}$$

where $C_{\mathrm{g}}^{\mathrm{P}}$ is the concentration of P and $C_{\mathrm{g}}^{\mathrm{j}}$ is the concentration of the other impurity elements in the grains, and Q_{P} and Q_j are the solute grain boundary binding energies for P and for the other elements, respectively. The value of C_{P}^{*} is the maximum expected segregation at steady state. Before steady state is reached, the grain boundary concentration depends on time according to:

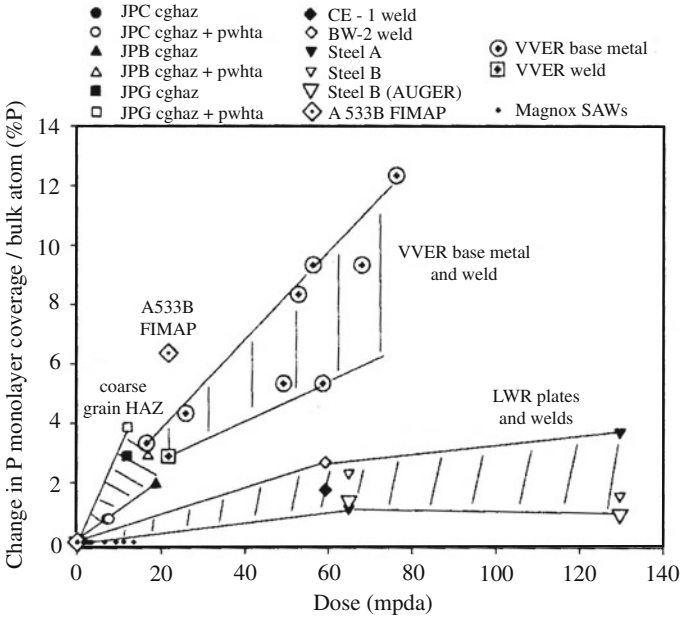

Fig. 6.20 Dose dependence of the irradiation-induced change in grain boundary phosphorus monolayer coverage normalized with respect to the bulk atomic phosphorus concentration for C–Mn SMA LWR plates, welds and coarse HAZ structure and VVER base metal and weld. All irradiation temperatures are 275–290 °C except for the Magnox SAWs, which cover the range 186–311 °C (after [24])

$$\frac{C_P(t) - C_g}{C_P^* - C_g} = 1 - \exp\left(\frac{4D_c t}{\alpha^2 d^2}\right) \operatorname{erfc}\left(\frac{2\sqrt{D_c t}}{\alpha d}\right), \tag{6.73}$$

where D_c is the point defect–impurity complex diffusion coefficient, α is the enrichment ratio, and d is the grain boundary width. Experimental measurements of P segregation in ferritic steels are shown in Fig. 6.20. Note that while the P concentration increases with dose, it varies significantly with the specific alloy. This variation is likely due to site competition with other impurities, most important of which is carbon. The A533 B steel shown has a high grain boundary P level because it has a low C content. Figure 6.21 shows the competition between P and C at the grain boundary and the P segregation is highest when the C level is low.

In higher Cr alloys such as the 9–12 %Cr ferritic–martensitic steels, the behavior of Cr at the grain boundary is of concern because of the potential for the formation of brittle, chromium-rich phases. While it has been shown that Cr depletes in austenitic alloys, it enriches in F–M alloys [25–27]. An example of the segregation behavior in an Fe–9Cr–1Mo alloy (T91) irradiated to 7 dpa at 400 °C with 2 MeV protons is shown in Fig. 6.22. Note that Cr, Ni, Si, and Cu all enrich at the grain

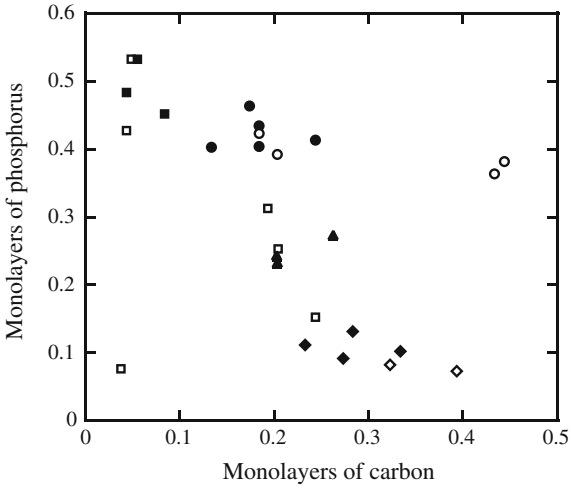

Fig. 6.21 Variation of phosphorus and carbon monolayer coverage at grain boundaries of thermally aged and irradiated ferritic alloys (after [24])

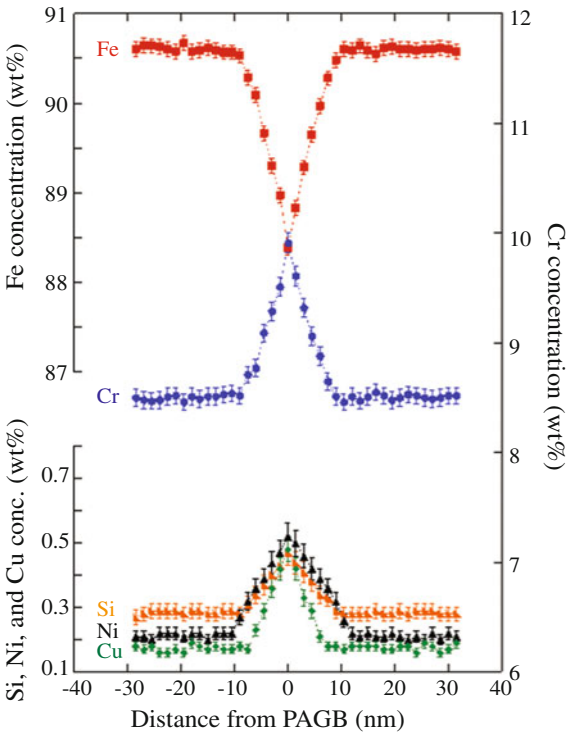

Fig. 6.22 RIS profiles of Fe, Cr, Ni, Si, and Cu in alloy T91 irradiated to 7 dpa at 400 °C (after [26])

boundary with a concomitant depletion of Fe. Figure 6.23 shows the temperature dependence of RIS, peaking between 400 and 450 °C. As the temperature is increased, the enrichment of Cr diminishes and by 700 °C, Cr depletion occurs.

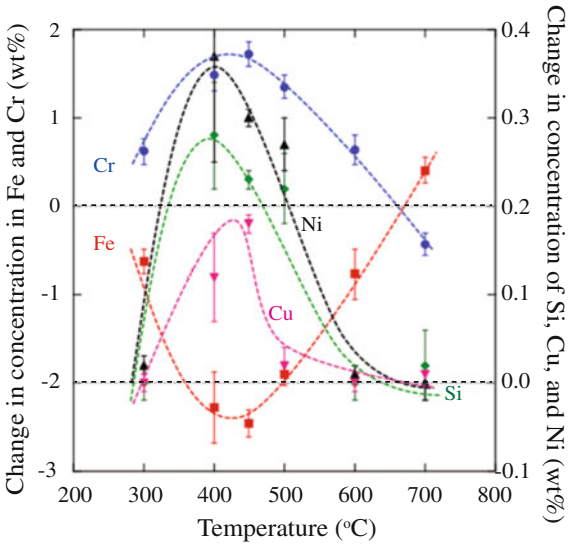

Fig. 6.23 Grain boundary composition as a function of temperature in alloy T91 irradiated to 3 dpa with 2.0 MeV protons (after [26])

This behavior can be understood by referring to the diffusion coefficient ratios of Cr to Fe in bcc Fe–Cr for both vacancies and interstitials, Fig. 6.24. Note that at lower temperatures, the ratio of diffusion coefficients for interstitials exceeds that of vacancies (solid lines for v and i). This means that there are more Cr atoms arriving at the grain boundary (via interstitial flux) than leaving (via vacancy flux), resulting

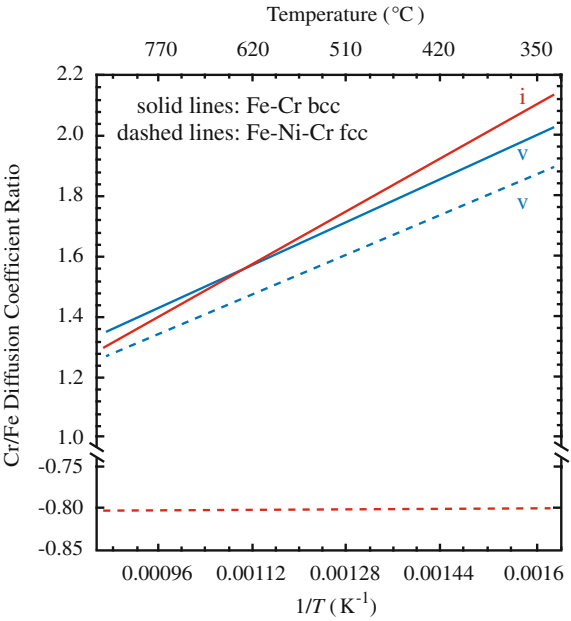

Fig. 6.24 Cr to Fe interstitial diffusion coefficient ratio for bcc Fe–Cr (*solid lines*) compared to that for fcc Fe–Ni–Cr (*dashed lines*) (after [25])

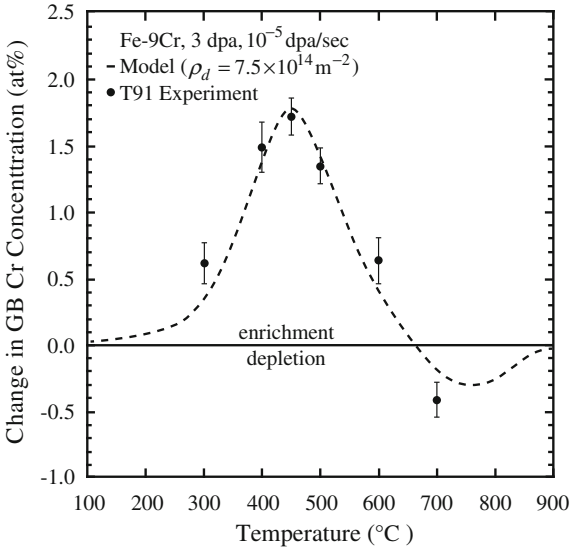

Fig. 6.25 Comparison of grain boundary Cr concentration calculated by the IK model (Fe-9Cr) and with experiment for alloy T91 irradiated at 3 dpa at 10^{-5} dpa/s (after [25])

in a net enrichment of Cr. But at higher temperature, the reverse is true, resulting in depletion of Cr. The crossover occurs because the ratio of the vacancy diffusion coefficient for Cr to that for Fe crosses the ratio for interstitials resulting in a reversal of the segregation direction of Cr. The natural logarithm of the ratio of the diffusion coefficients for Cr to that for Fe is greater than unity for both interstitial and vacancy diffusion, indicating that Cr is a faster diffuser than Fe by both types of point defects. When the interstitial and vacancy diffusion coefficient ratios are equal (i.e., at the crossover temperature), the contribution of Cr enrichment by interstitials is balanced by the contribution of Cr depletion by vacancies. But when the interstitial diffusion coefficient ratio is greater than that for vacancies (i.e., at temperatures below the crossover temperature), Cr enrichment by interstitials dominates Cr depletion by vacancies, resulting in a net Cr enrichment. Conversely, at temperatures above the crossover, Cr depletion by vacancies will dominate Cr enrichment by interstitials, resulting in a net Cr depletion. Figure 6.25 shows the Cr segregation behavior as a function of temperature resulting from the Inverse Kirkendall (IK) mechanism of RIS in bcc Fe–Cr. Note that the IK model of RIS fits the data extremely well and captures the reversal of Cr segregation at 700 °C.

Recall that in austenitic alloys, Cr depletes over the full temperature range. The reason is that the Cr/Fe ratio of diffusion coefficients for interstitials is always below that for vacancies (dashed lines for i and v in Fig. 6.24), so RIS is driven by vacancy diffusion, which means that the Cr will always deplete. This explains why interstitials can be ignored in the IK model for RIS in austenitic stainless steels. ("Ignored" means that the migration energies for interstitials of Fe, Cr, and Ni are set equal to each other, resulting in no net segregation via the interstitial flux).

6.7 Effect of Grain Boundary Structure on RIS

The sink strength of a grain boundary derived in Chap. 5 was for an ideal grain boundary. However, not all boundaries are identical nor ideal and the actual sink strength will vary with the structure of the grain boundary. Because of the complexity and number of possible configurations of grain boundaries, it is not possible to determine the sink strength for specific grain boundary structures. However, the structure can be classified into broad categories [low angle boundaries (LAB), coincident site lattice boundaries (CSL), and high angle boundaries (HAB)] that can be explored for their relative sink strengths [28]. The RIS formalism described in Sect. 6.1 can be used to determine RIS as a function of grain boundary character by treating the grain boundary as a sink with an efficiency that is a function of the grain boundary misorientation angle. A higher general misorientation angle leads to a higher sink strength, while low angles and misorientations near high angle coincident site lattice (CSL) boundaries have a lower sink efficiency. The flux of defects from the first crystal plane into the grain boundary is modeled explicitly by partitioning the defect flux in Eqs. (6.1) and (6.2):

$$\begin{aligned} J_{\mathrm{v}} &= J_{\mathrm{v}}^{0} + J_{\mathrm{v}}^{1} \\ J_{\mathrm{i}} &= J_{\mathrm{i}}^{0} + J_{\mathrm{i}}^{1}, \end{aligned} \tag{6.74}$$

where J_{v}^{0} and J_{i}^{0} are the fluxes of defects within the interaction distance of the grain boundary and J_{v}^{1} and J_{i}^{1} are the fluxes of defects outside the interaction distance of the grain boundary. It is assumed that point defects leaving the region within the interaction distance of a boundary are due to the diffusion of point defects along the grain boundary and the density of annihilation sties at the boundary of interest. The flux of defects near the grain boundary, J_{v}^{0} and J_{i}^{0}, can be related to the flux along a grain boundary, $J_{\mathrm{v}}^{\mathrm{gb}}$ and $J_{\mathrm{i}}^{\mathrm{gb}}$ using [28]:

$$J_{\mathrm{v/i}}^{0} = \frac{2J_{\mathrm{v/i}}^{\mathrm{gb}}\delta}{x_{\mathrm{gb}}} \tag{6.75}$$

for HAB, and:

$$J_{\mathrm{v/i}}^{0} = \frac{J_{\mathrm{v/i}}^{\mathrm{gb}}}{x_{\mathrm{gb}}} \tag{6.76}$$

for LAB where x_{gb} is the distance between grain boundary annihilation sites and δ is the grain boundary thickness. The flux of defects into the grain boundary, $J_{\mathrm{v}}^{\mathrm{gb}}$ and $J_{\mathrm{i}}^{\mathrm{gb}}$, is determined by an approximate defect grain boundary diffusion coefficient defined by the following expression (where k = v or i):

$$D_k^{gb} = g_k a^2 Z f_k^{gb} v_0 \sum_j C_j \exp\left(-\frac{\left(E_a^{z,k} - a^2\gamma_{gb}\right)}{kT}\right), \tag{6.77}$$

where g_k is a dimensionless constant of order one, dependent on the lattice geometry, a is the lattice parameter, Z is the coordination number, f_k^{gb} is the correlation factor for defect type k in the grain boundary, v_0 is the attempt frequency, and γ_{gb} is the specific grain boundary energy. In a multicomponent system, C_j is the fraction of component z near the grain boundary and $E_a^{z,k}$ is the migration energy of component z for defect type k.

From Eq. (6.77), it is clear that as the grain boundary energy, γ_{gb}, increases, the grain boundary diffusion coefficient increases exponentially. For high energy grain boundaries, the flux of defects into the grain boundary is sufficiently fast that the boundary condition approaches ideal sink behavior. The relationship between the grain boundary angle and the grain boundary energy is described using classical grain boundary structure theory [28] for the various classes of grain boundary structures.

Solution of Eqs. (6.29) using the fluxes in Eqs. (6.74) and (6.75) and D_k^{gb} in (6.77) gives the concentration of Cr at the grain boundary of a Fe–Cr (bcc) alloy following irradiation at 400 °C, as a function of the grain boundary misorientation angle, Fig. 6.26. Model results are compared to experimental measurements on LAB and show a general agreement [28]. More broadly, Fig. 6.27 shows the model predictions over a wide range of misorientation angle including both LAB and HAB. This formalism applies not only to grain boundaries, but also to all sinks (dislocations, precipitate interfaces, etc.) that act as less than ideal sinks.

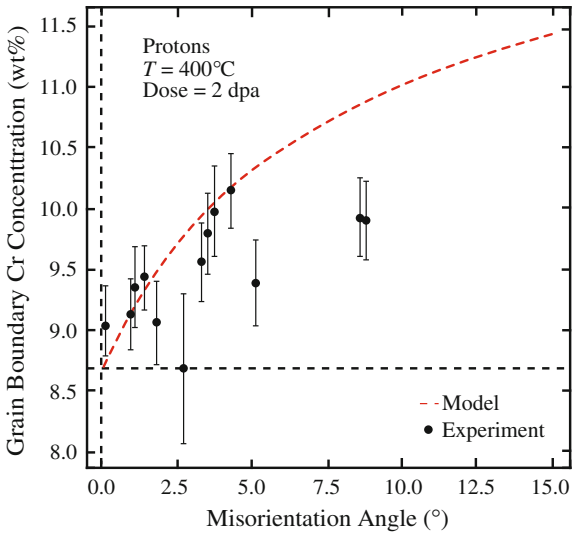

Fig. 6.26 Predicted and observed grain boundary Cr concentration for lath boundaries in bcc Fe–Cr irradiated using protons to a dose of 2 dpa at 400 °C in the low angle grain boundary regime (after [28])

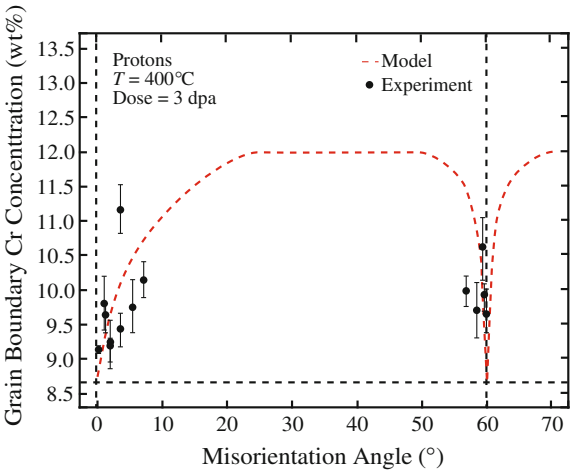

Fig. 6.27 Predicted and experimentally observed grain boundary Cr concentration for all boundaries in bcc Fe–Cr irradiated using protons to a dose of 2 dpa at 400 °C (after [28])

Nomenclature

a	Lattice parameter
A	Term associated with vibrational entropy, see Eq. (6.71)
C_x	Concentration of specie x
C_{P}^{*}	Maximum grain boundary segregation of P at steady state in ferritic steels
d	Grain size
D_k^{gb}	Grain boundary diffusion coefficient for species k
d_{xy}	Partial diffusion coefficient divided by N_y
d_0^x	Pre-exponential term for diffusion of specie x
D	Diffusion coefficient
D_x^y	Partial diffusion coefficient for migration of x via y
$E_{\mathrm{a}}^{\mathrm{z,k}}$	Migration energy of component z for defect type k
E_{eq}^x	Equilibrium energy for specie x
E_{b}^{xz}	Binding energy of specie x to defect z
E_{f}^x	Formation energy of specie x
E_{m}^{xz}	Migration energy of specie x migrating via defect z
E_{xy}	Interaction energy between species x and y
E_{xy}^{ord}	Ordering energy for species x and y
ES_{alloy}^x	Saddle point energy for element x in alloy
F	Correlation coefficient
f_k^{gb}	Correlation factor for defect type k in the grain boundary,
$F(\eta)$	Recombination term in Eq. (6.71)
i	Interstitial designation
k	Boltzmann's constant
k^2	Sink efficiency
v	Vacancy designation

s	Sink designation
J_x	Flux of atom or defect x across a marker plane
K_0	Defect production rate
K_{xy}	Reaction rate constant for x and y
L_{ij}	Onsager coefficients
M_j	Determinant for specie j (defined in Eq. (6.51))
N_x	Atom fraction of specie x
Q_j	Grain boundary binding energy for solute j
r_{xy}	Capture radius for defect x by sink/trap y
R	Recombination rate
S_{m}^{x}	Entropy of migration for specie x
t	Time
T	Temperature
x_{gb}	Distance between grain boundary annihilation sites
X_i	Driving force for diffusion of species i
z	Number of nearest neighbors
Z	Coordination number
α	Enrichment ratio
δ	Grain boundary thickness
χ	Thermodynamic factor defined below Eq. (6.18)
γ_{gb}	Grain boundary energy
γ_x	Activity coefficient of specie x
κ_{xy}	Capture coefficient of defect x by sink/trap y
Λ	Jump distance
μ	Chemical potential
ν_0	Attempt frequency
ω	Jump frequency
Ω	Atomic volume
τ	Time constant
ξ	Defect production efficiency

Subscripts

eq	Equilibrium
f	Formation
g	Impurity
gb	Grain boundary
i, j	Species
l	Trap type
m	Migration
v	Vacancy

Superscripts

j	Specie or defect
k	Solute or defect
Ord	Ordering
t	Trap
z	Alloy component

Acronyms

AES	Auger electron spectroscopy
BWR	Boiling water reactor
F-M	Ferritic–martensitic
IASCC	Irradiation-assisted stress corrosion cracking
IGSCC	Intergranular stress corrosion cracking
IGC	Intergranular corrosion
IK	Inverse Kirkendall
MIK	Modified inverse Kirkendall
MIK-T	Modified inverse Kirkendall-trapping
RIS	Radiation-induced segregation
STEM-EDS	Scanning transmission electron microscopy–energy dispersive spectrometry

Problems

6.1 A sample of Cu–20 %Al is irradiated at 500 °C.

(a) Will aluminum segregate to or from the surface? Explain. (Assume that association of defects with Al and Cu atoms is non-preferential.)
(b) If there is strong binding (a preferential association) of interstitials to the undersized atom, how would your answer to part (a) change? (Assume $E_b^{Cu-i} = 1\,eV$.)
(c) Repeat part (a) for T = 100 °C. (Here, vacancies are immobile.)

6.2 A Ni–18Cr alloy is irradiated at 400 °C.

(a) The chromium concentration is measured at the grain boundary and is found to deplete. What is the sign of the determinant for chromium?
(b) The bulk concentration of nickel decreases from 82 to 70wt%. Assuming nothing else changes, what happens to the determinant of chromium? State your assumptions.
(c) If the diffusion coefficient of chromium vacancies decreases, what happens to the Cr segregation profile?

6.3 An Fe–18Cr–8Ni alloy is irradiated and radiation-induced segregation changes the grain boundary composition. Calculate the Ni and Cr equivalents for the bulk alloy and at the grain boundary assuming $\Delta Cr = -5$ and $\Delta Ni = +3$. In

terms of the Schaeffler diagram, how is the grain boundary area different than the bulk? If an Fe–18Cr–20Ni alloy was irradiated under the same conditions, what changes?

6.4 For the ternary alloy Fe–18Cr–20Ni, determine if iron enriches or depletes during irradiation at 500 °C.

	Fe	Cr	Ni
E_m^v	1.2 eV	1.2 eV	1.32 eV
E_m^i	0.15 eV	0.23 eV	0.16 eV
E_f^v	1.49 eV	1.49 eV	1.49 eV
E_f^i	4.08 eV	4.08 eV	4.93 eV

Use $S_f^v \sim 2.4k$ and neglect S_f^i, S_m^v, S_m^i

References

1. Bruemmer SM, Simonen EP, Scott PM, Andresen PL, Was GS, Nelson LJ (1999) J Nucl Mater 274:299–314
2. Anthony TR (1972) In: Corbett JW, Ianniello LC (eds) Radiation-induced voids in metals and alloys, AEC symposium series, Conf-701601, p 630
3. Okamoto PR, Harkness SD, Laidler JJ (1973) ANS Trans 16:70
4. Wiedersich H, Okamoto PR, Lam NQ (1979) J Nucl Mater 83:98–108
5. Choudhury YS, Barnard L, Tucker JD, Allen TR, Wirth BD, Asta M, Morgan D (2011) J Nucl Mater 411:1
6. Serruys ZY, Brebec G (1982) Phil Mag A46:661
7. Perks JM, Marwick AD, English CA (1986) AERE R 12121 (June)
8. Rehn LE, Okamoto PR, Potter DI, Wiedersich H (1978) J Nucl Mater 74:242–251
9. Rehn LE (1982) In: Picraux ST, Choyke WJ (eds) Metastable materials formation by ion implantation. Elsevier Science, New York, p 17
10. Okamoto PR, Wiedersich H (1974) J Nucl Mater 53:336–345
11. Kornblit L, Ignatiev A (1984) J Nucl Mater 126:77–78
12. Was GS, Allen TR, Busby IT, Gan I, Damcott D, Carter D, Atzmor M, Konik EA (1999) J Nucl Mater 270:96–114
13. Was GS, Allen TR (1993) J Nucl Mater 205:332–338
14. Allen TR, Was GS (1998) Acta Mater 46:3679
15. Lam NQ, Kumar A, Wiedersich H (1982) In: Brager HR, Perrin JS (eds) Effects of radiation on materials, 11th Conference, ASTM STP 782, American Society for Testing and Materials, pp 985–1007
16. Watanabe S, Takahashi H (1994) J Nucl Mater 208:191
17. Grandjean Y, Bellon P, Martin G (1994) Phys Rev B 50:4228
18. Nastar M, Martin G (1999) Mater Sci Forum 294–296:83
19. Mansur LK, Yoo MH (1978) J Nucl Mater 74:228–241
20. Hackett MJ, Was GS, Simonen EP (2005) J ASTM Int 2(7)
21. Fournier L, Sencer BH, Wang Y, Was GS, Gan J, Bruemmer SM, Simonen EP, Allen TR, Cole JI (2002) In: Proceedings of the 10th International conference on environmental degradation of materials in nuclear power systems: Water Reactors. NACE International, Houston

22. Was GS (2004) Recent developments in understanding irradiation assisted stress corrosion cracking. In: Proceedings of the 11th International conference on environmental degradation of materials in nuclear power systems: water reactors, American Nuclear Society, La Grange Park, IL, pp 965–985
23. Jiao Z, Was GS (2011) Acta Mater 59:1120
24. Faulkner RG, Jones RB, Lu Z, Flewitt PEJ (2005) Phil Mag 85(19):2065–2099
25. Wharry JP, Was GS (2014) Acta Mater 65:42
26. Wharry JP, Jiao Z, Was GS (2012) J Nucl Mater 425:117
27. Little E (2006) Mater Sci Technol 22:491
28. Field KG, Barnard LM, Parish CM, Busby JT, Morgan D, Allen TR (2013) J Nucl Mater 435:172–180

Chapter 7
Dislocation Microstructure

One of the most profound consequences of irradiation on the microstructure of materials is the formation of dislocation loops. Dislocation loops have a bias for interstitials and thus have a strong impact on the development of the irradiated microstructure. They also influence the deformation behavior and, consequently, the ductility and hardening of irradiated materials, as will be discussed in Chap. 12. In this chapter, we will review the origin and character of dislocations, their mobility and multiplication and their stresses, strains and energies. The character of dislocation loops will be examined, and models for nucleation and growth will be presented. Finally, the stacking fault tetrahedron (SFT) will be discussed. For a more in-depth treatment of dislocations, the reader is referred to [1–4].

7.1 Dislocation Lines

The discovery of dislocations in crystals has its origin in the discrepancy between the measured and theoretical stress needed to cause shear in a crystal. Consider the stress required to shear a crystal along a given atomic plane. A shear of one atomic distance requires that atoms above the plane all move one lattice spacing relative to those below (Fig. 7.1). To reach the saddle point, each atom must move horizontally a distance of one atom radius, a. Since the separation of two planes is $\sim 2a$, the shear strain at the saddle point is $\gamma \approx a/2a \sim 1/2$. In a perfectly elastic crystal, the ratio of shear stress to shear strain is the shear modulus:

$$\frac{\sigma_s}{\gamma} = \mu. \tag{7.1}$$

For a typical shear modulus of 17 GPa and a shear strain of 1/2, the shear stress from Eq. (7.1) is ~ 8.5 GPa. However, experiments, for example on magnesium, produce deformation at shear stresses of ~ 1 MPa, which is different from theory by

Additional material to this chapter can be downloaded from http://rmsbook2ed.engin.umich.edu/movies/

G.S. Was, *Fundamentals of Radiation Materials Science*,
DOI 10.1007/978-1-4939-3438-6_7

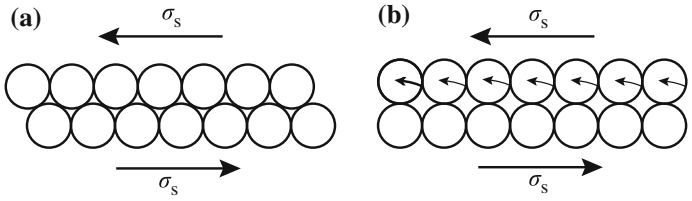

Fig. 7.1 Initial position of atoms above and below a slip plane and the motion of the atoms above the slip plane required to cause slip

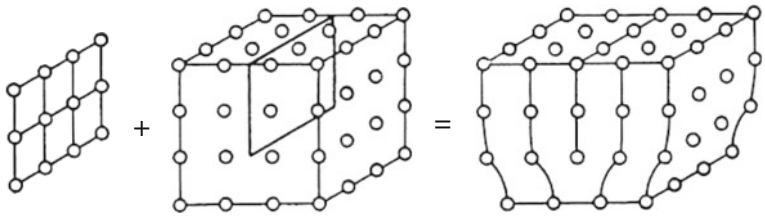

Fig. 7.2 An edge dislocation described as an extra half plane of atoms above the slip plane

a factor of 10^4! The reason is the existence of dislocations that provide for much reduced shear stresses in crystals.

A *dislocation* is a line that forms a boundary between a region of the crystal that has slipped and one that has not. The two basic types of dislocations lines are the edge and the screw. In an *edge dislocation*, atoms over the cut surface are shifted in a direction *perpendicular* to the dislocation line. An edge dislocation can also be thought of as the insertion of an extra half plane of atoms (Fig. 7.2). In a *screw dislocation*, the atoms over the cut surface are shifted in a direction *parallel* to the dislocation line (Fig. 7.3a). The screw dislocation itself is a pole about which a spiral ramp of planes circles (analogous to a parking garage ramp) (Fig. 7.3b). There also exist *mixed dislocations* in which the shift is neither parallel nor perpendicular to the dislocation line, but at some arbitrary angle. Figure 7.4 shows a mixed dislocation in a crystal in which the dislocation line is curved. Note that the boundary separating slipped and unslipped regions is circular. At point A (front face), the dislocation is of pure edge character. At point B (side face), the dislocation is of pure screw character. In between, the dislocation is *mixed* with the proportion of screw character and edge character varying continuously with distance along the line. Figure 7.5 shows the construction of a mixed dislocation.

A dislocation line can also be made in the form of a closed loop rather than a line that terminates at the crystal surface. Following Fig. 7.6, we make a cut along ABCD and shift the atoms parallel to the plane and then rejoin them. Note that segments AB and DC have edge character and segments BC and AD have screw character. Segments AB and DC have opposite sign in that one has a half plane above the cut and one has the half plane below it. The same is true with segments BC and AD. This loop is termed a *perfect* dislocation loop.

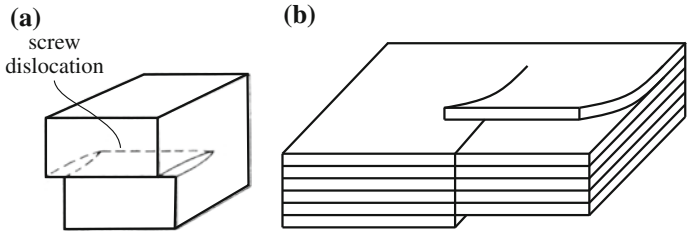

Fig. 7.3 (**a**) A screw dislocation formed by a cut and a shift of atoms in a direction parallel to the *cut line*. (**b**) A schematic showing the "parking ramp" nature of a screw dislocation in which atom planes spiral about the dislocation line

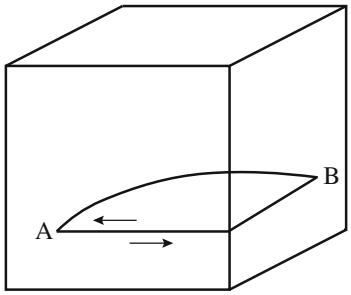

Fig. 7.4 Curved dislocation line with pure edge character at point *A*, pure screw character at point *B*, and mixed character along the length of the dislocation

Now suppose that instead of shifting atoms parallel to the plane as we did in the example of a perfect loop, we fill up the cut with more atoms. The shift of atoms on each side of the cut is *perpendicular* to the surface. Figure 7.7 shows that by insertion of a disk of atoms into the cut, that every segment of the dislocation loop has pure edge character. This is very different from the perfect loop with edge character and screw character. This dislocation loop is called a *prismatic* or *Frank* loop. One variation is to remove a disk of atoms from the cut rather than insert an extra plane of atoms.

7.1.1 Dislocation Motion

Dislocations can move in two modes: glide and climb. Glide is the motion of a dislocation on its slip plane and is a conservative motion in that it requires no long-range mass transport in order to occur. Experiments have shown that the logarithm of the dislocation velocity is proportional to the logarithm of the shear stress causing glide:

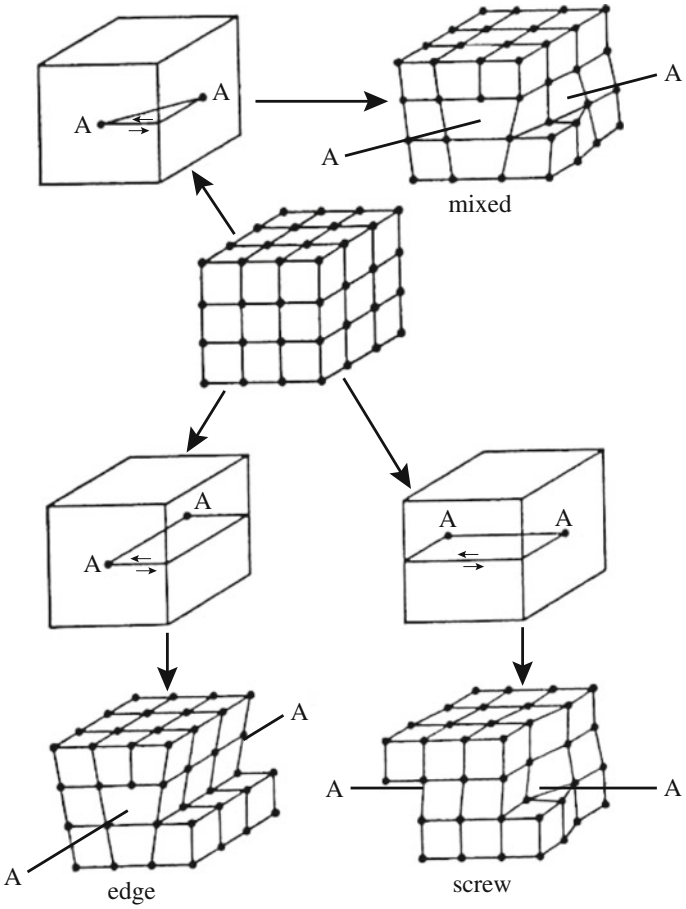

Fig. 7.5 Construction of a dislocation line with mixed character

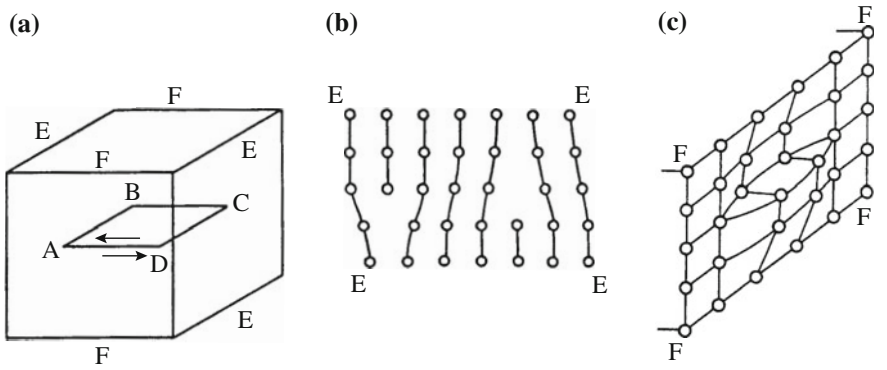

Fig. 7.6 A perfect dislocation loop in a crystal in which the character of the loop varies with position along the loop

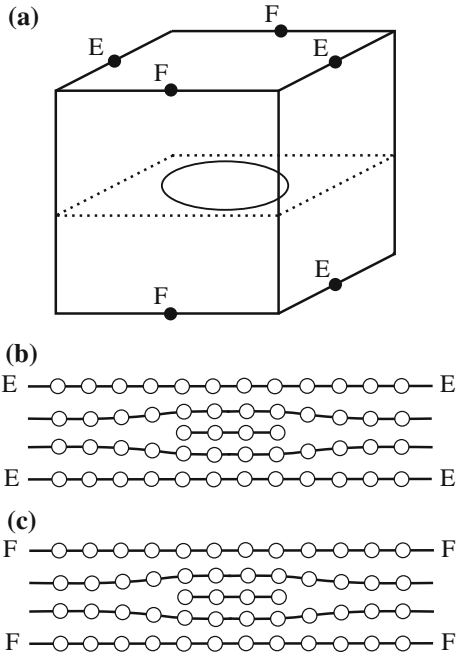

Fig. 7.7 A Frank dislocation loop formed by insertion of a circular plane of atoms between existing planes in the lattice

$$\ln v_g \propto \ln \sigma_s, \tag{7.2}$$

which implies a power law relationship between shear stress and dislocation velocity:

$$v_g = \left(\frac{\sigma_s}{\sigma_D}\right)^m, \tag{7.3}$$

where m is the stress exponent (~ 1.65), and σ_D is the value of the stress that yields a dislocation velocity of 0.01 m/s [5]. Experiments also show that the logarithm of the dislocation velocity is proportional to the reciprocal of the absolute temperature, T:

$$\ln v_g \propto \frac{1}{T}, \tag{7.4}$$

leading to the following description of the velocity of a gliding dislocation in terms of stress and temperature:

$$v_g = f(\sigma) \exp(-E/kT). \tag{7.5}$$

When dislocations glide, they displace the crystal above the slip plane relative to that below. Figure 7.8 shows that if an edge dislocation glides to the surface, the

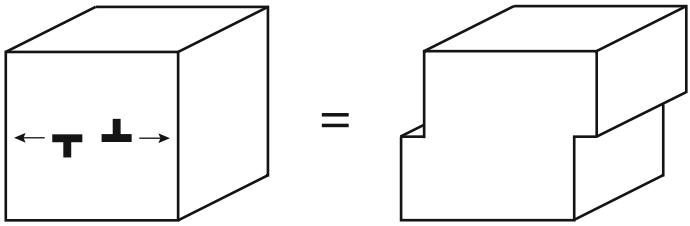

Fig. 7.8 Slip produced by movement of edge dislocations to the surface of a crystal

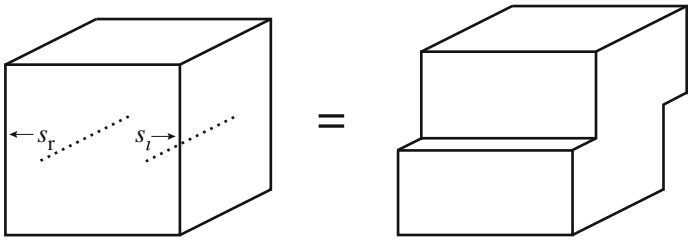

Fig. 7.9 Slip produced by movement of screw dislocations to the surface of a crystal

result is a step on the surface of magnitude equal to the Burgers vector. Screw dislocations will also produce a step on the surface, but on a face that is perpendicular to the dislocation line (Fig. 7.9). The perfect loop described in the last section will also result in displacement of the crystal when it reaches the surface. Figure 7.10 shows the displacement of the crystal above the slip plane relative to that below. Note that the displacements are entirely consistent with the character of the dislocation where it intersects the surface as shown in Figs. 7.8 and 7.9.

A Frank loop is essentially an edge dislocation. The slip plane for this type of loop is defined by the intersection of the loop edge and the adjacent crystal and consists of a cylindrical surface projecting above and below the plane of the loop. Figure 7.11 shows how surface atoms would be displaced if the loop was to glide to the surface. However, this mode of motion is not energetically favorable, and this loop is more likely to move by climb rather than glide.

Dislocations also move by a non-conservative process called *climb*. Climb is an important process for edge dislocations and prismatic loops, since unlike screw dislocations that can glide on *any* plane containing the dislocation, there is only one possible slip plane for an edge dislocation to glide. Climb is the extension or recession of the extra half plane of atoms by absorption or emission of a vacancy, absorption of an interstitial atom, or emission/absorption of clusters of vacancies or single interstitial atoms (SIAs). Figure 7.12 shows the positive climb of an edge dislocation by absorption of a vacancy at the dislocation core. In order for the edge dislocation to move up one lattice spacing, all of the atoms along the edge (into the paper) must absorb a vacancy. Positive climb results in a decrease in the size of the extra half plane, while negative climb results in the increase in the size of the extra

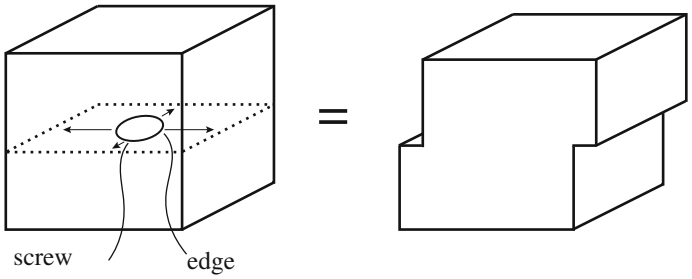

Fig. 7.10 Slip produced by movement of a perfect dislocation loop to the surface of a crystal

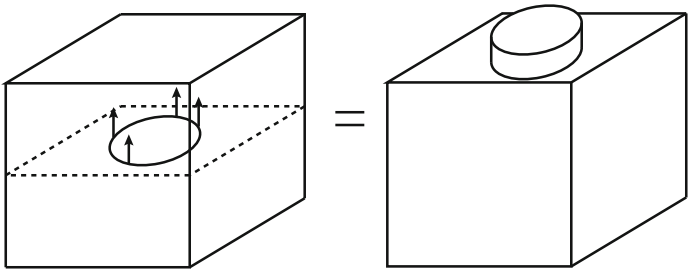

Fig. 7.11 Slip produced by movement of a Frank loop to the surface of a crystal

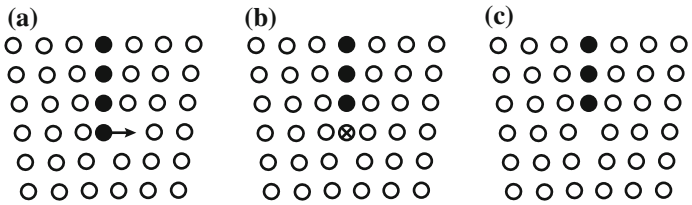

Fig. 7.12 Positive climb of an edge dislocation by absorption of vacancies at its core

half plane. Positive climb is associated with a compressive strain and will be promoted by a compressive stress component perpendicular to the extra plane. Similarly, a tensile stress applied perpendicular to the extra plane promotes growth of the plane and thus negative climb. Since they are essentially edge dislocations, Frank loops climb in the same manner, where positive climb results in loop shrinkage and negative climb results in loop growth. Note that there is a fundamental difference between the nature of the stress that produces slip and that which produces climb. Slip occurs as the result of shear stress, and climb occurs as a result of a normal stress.

Since climb requires that vacancies move through the lattice either to or away from the extra half plane, the rate of climb will be dependent on both the diffusion

coefficient of vacancies and their concentration. In unirradiated solids, this means that climb will be most important at high temperature. However, in irradiated solids, the increased population of vacancies will make climb more important at lower temperatures. Further, the elevated concentration of interstitials means that they too can contribute to climb in a direction that is opposite to that of vacancies.

7.1.2 Description of a Dislocation

A description of a dislocation consists of the specification of the vector defining the line direction, $\boldsymbol{s}$, and the Burgers vector defining the atom shift, $\boldsymbol{b}$. The Burgers vector is defined as follows:

1. Define a positive direction, $\boldsymbol{s}$, along the dislocation line (e.g., into the paper).
2. Construct a plane perpendicular to the dislocation line.
3. Starting in a region of perfect crystal (away from the dislocation core), complete a counterclockwise circuit around the dislocation line (in the plane of the paper)
4. The Burgers vector, $\boldsymbol{b}$, is the vector needed to close the circuit.

The rule is shown schematically in Fig. 7.13 for a screw dislocation. Following this convention, the Burgers vector of an edge dislocation is *perpendicular* to the dislocation line. The Burgers vector of a screw dislocation is *parallel* to the dislocation line.

For an edge dislocation, we can determine the Burgers vector in the following manner. Sighting down the dislocation line (along the positive $\boldsymbol{s}$ direction), we make a counterclockwise circuit around the dislocation. The vector connecting the end point to the origin is the Burgers vector. Figure 7.14 shows an example of the determination of the Burgers vector using the construction rule. (Note that it does not matter which direction is called positive, but we need to adopt a convention in order to determine the orientation of the line and the extra half plane in the crystal. If we sighted in the opposite direction, $\boldsymbol{b}$ will be in the opposite direction. What matters is the specification of $\boldsymbol{s}$ *relative to* $\boldsymbol{b}$.) Following the convention, Fig. 7.15a shows a dislocation with line direction, $\boldsymbol{s}$, pointing into the paper and $\boldsymbol{b}$ pointing to the left. The dislocation in Fig. 7.15b is identical to that in Fig. 7.15a since the

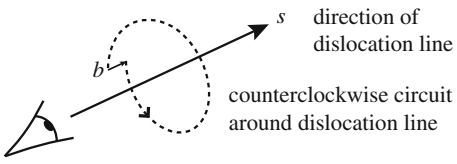

Fig. 7.13 Convention for finding the Burgers vector of a dislocation line characterized by direction $\boldsymbol{s}$

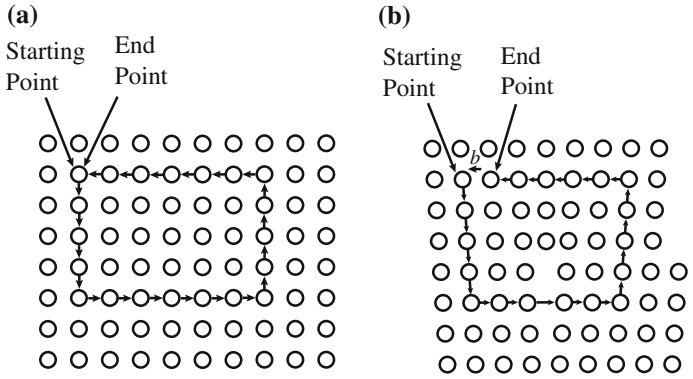

Fig. 7.14 The Burgers circuit for an edge dislocation following the convention shown in Fig. 7.13 for (**a**) a region of perfect crystal, and (**b**) a region containing an edge dislocation

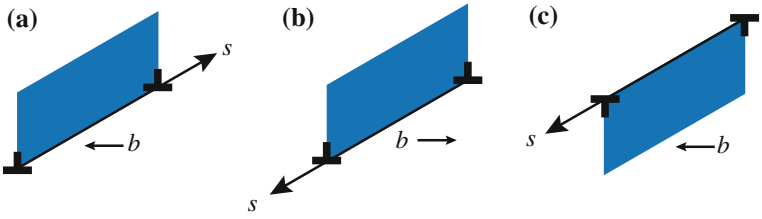

Fig. 7.15 Examples of identical edge dislocations (**a**) and (**b**) and an edge dislocation of opposite sign (**c**)

relationship between $\boldsymbol{s}$ and $\boldsymbol{b}$ is the same. However, the dislocation shown in Fig. 7.15c is of opposite sign.

For a screw dislocation, we consider a left-handed screw (counterclockwise rotation; see Fig. 7.16). With this convention, $\boldsymbol{s}$ and $\boldsymbol{b}$ are in the same direction. Figure 7.17a shows a screw dislocation with Burgers vector in the same direction as $\boldsymbol{s}$. The dislocation shown in Fig. 7.17b is identical to that in Fig. 7.17a, but the dislocation shown in Fig. 7.17c is of opposite sign as the other two.

An edge dislocation glides in the direction of its Burgers vector. A screw dislocation glides in a direction *perpendicular to* its Burgers vector. We adopt the following convention to determine the direction of motion of a dislocation line. *The positive direction of motion is obtained by a counterclockwise rotation on a plane parallel to the slip plane and through* 90° *from the positive direction of the dislocation line itself.* The rule is shown by the illustration in Fig. 7.18a. Figure 7.18b, c shows the positive direction of motion for an edge and screw dislocation, respectively. Figure 7.19 shows the direction of motion for a dislocation loop that is characterized by a single Burgers vector (perfect loop) and changes character along the dislocation line.

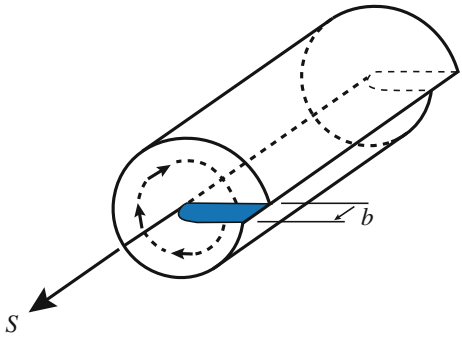

Fig. 7.16 The Burgers circuit for a screw dislocation following the convention shown in Fig. 7.13

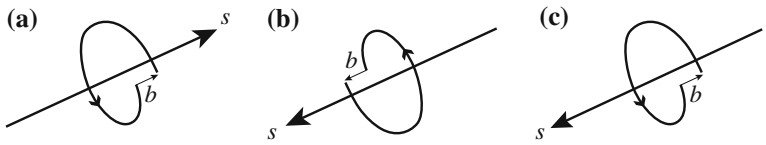

Fig. 7.17 Examples of identical screw dislocations (**a**) and (**b**), and a screw dislocation of opposite sign (**c**)

7.1.3 Displacements, Strains, and Stresses

Dislocations interact with each other and with other microstructure features through their stress fields. Therefore, it is important to establish the stress and strain fields around a dislocation as well as the energy associated with the dislocation line. We will begin with the screw dislocation and then treat the edge dislocation. Recall the orientation of the screw dislocation is one in which the Burgers vector is parallel to the dislocation line, which means that the displacement of atoms is in the direction of the dislocation line. If we describe the dislocation in cylindrical coordinates, Fig. 7.20, then there is no displacement along the r or θ directions so that:

$$u_r = u_\theta = 0. \tag{7.6}$$

In Cartesian coordinates, the displacement in the x–y plane is zero. The only displacement is in the z-direction, and from inspection, we have in cylindrical coordinates:

$$u_z = \frac{b}{2\pi}\theta, \quad u_x = u_y = 0, \tag{7.7}$$

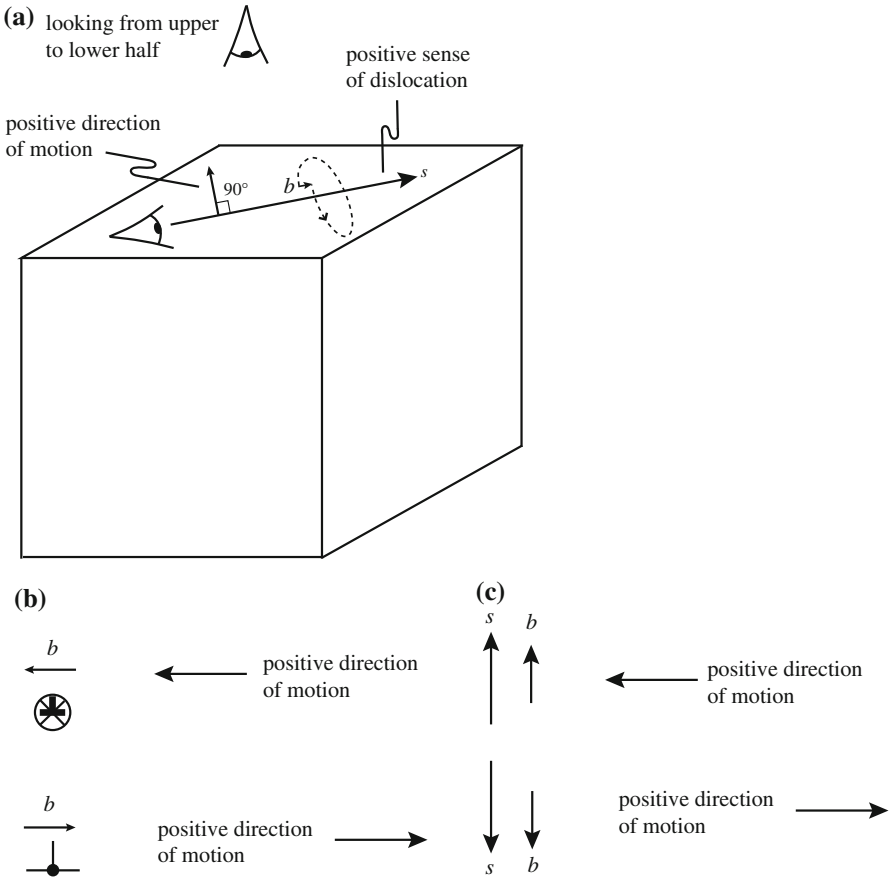

Fig. 7.18 (**a**) Rule for determination of the direction of motion of a dislocation on its slip plane and examples of the positive direction of motion for (**b**) edge and (**c**) screw dislocations

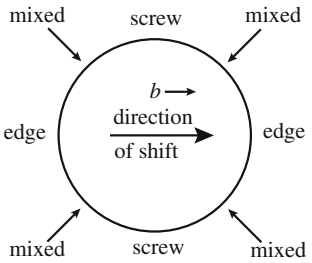

Fig. 7.19 Positive direction of motion of a perfect loop characterized by a single Burgers vector

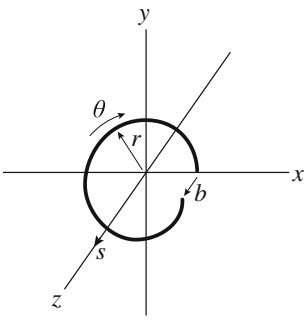

Fig. 7.20 Screw dislocation in the Cartesian coordinate system

and in Cartesian coordinates:

$$u_z = \frac{b}{2\pi}\tan^{-1}\frac{y}{x}, \tag{7.8}$$

where b is the magnitude of the Burgers vector. From elasticity theory, we can calculate the strain from the displacement as:

$$\varepsilon_{\theta z} = \frac{1}{r}\left(\frac{\partial u_z}{\partial \theta}\right) = \frac{b}{2\pi r}, \quad \varepsilon_{rr} = \varepsilon_{\theta\theta} = \varepsilon_{zz} = \varepsilon_{r\theta} = \varepsilon_{rz} = 0, \tag{7.9}$$

and in Cartesian coordinates:

$$\begin{aligned} \varepsilon_{xz} &= \frac{b}{2\pi}\frac{y}{x^2+y^2} = \frac{b}{2\pi r}\sin\theta \\ \varepsilon_{yz} &= -\frac{b}{2\pi}\frac{x}{x^2+y^2} = -\frac{b}{2\pi r}\cos\theta \\ \varepsilon_{xx} &= \varepsilon_{yy} = \varepsilon_{zz} = \varepsilon_{xy} = 0. \end{aligned} \tag{7.10}$$

The stress field of the screw dislocation is determined from the relation between stress and strain:

$$\sigma_{\theta z} = \mu\varepsilon_{\theta z} = \frac{\mu b}{2\pi r}, \quad \sigma_{rr} = \sigma_{\theta\theta} = \sigma_{zz} = \sigma_{r\theta} = \sigma_{rz} = 0, \tag{7.11}$$

and

$$\begin{aligned} \sigma_{xz} &= \frac{\mu b}{2\pi}\frac{y}{x^2+y^2} = \frac{\mu b}{2\pi r}\sin\theta \\ \sigma_{yz} &= -\frac{\mu b}{2\pi}\frac{x}{x^2+y^2} = -\frac{\mu b}{2\pi r}\cos\theta \\ \sigma_{xx} &= \sigma_{yy} = \sigma_{zz} = \sigma_{xy} = 0. \end{aligned} \tag{7.12}$$

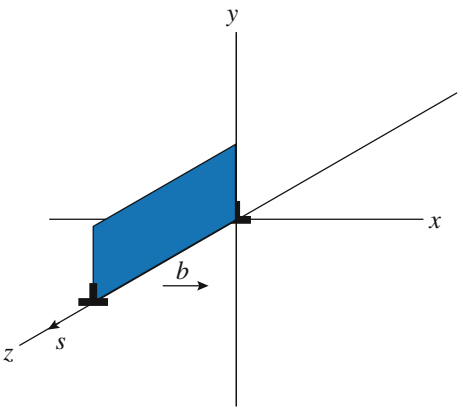

Fig. 7.21 Edge dislocation in the Cartesian coordinate system

For an edge dislocation as shown in Fig. 7.21, the displacement of atoms is in the x-direction. The displacement is not so simple here, but we know that the dislocation will be similar at any point along the z-axis and hence, the stress state is one of plane stress. The displacement field around the edge dislocation in Cartesian coordinates is:

$$\begin{aligned} u_x &= \frac{b}{2\pi}\left[\tan^{-1}\frac{y}{x} + \frac{\lambda+u}{\lambda+2\mu}\frac{xy}{x^2+y^2}\right] \\ u_y &= \frac{b}{2\pi}\left[\frac{-\mu}{2(\lambda+2\mu)}\log\frac{x^2+y^2}{c} + \frac{\lambda+\mu}{\lambda+2\mu}\frac{y^2}{x^2+y^2}\right] \\ u_z &= 0, \end{aligned} \tag{7.13}$$

where the constant c is added to make the log term dimensionless, but is irrelevant since stresses and strains are derivatives of the displacements. The resulting strains are as follows:

$$\begin{aligned} \varepsilon_{xx} &= -\frac{by}{2\pi}\frac{\mu y^2 + (2\lambda+3\mu)x^2}{(\lambda+2\mu)(x^2+y^2)^2} \\ \varepsilon_{yy} &= \frac{by}{2\pi}\frac{(2\lambda+\mu)x^2 - \mu y^2}{(\lambda+2\mu)(x^2+y^2)^2} \\ \varepsilon_{xy} &= \frac{b}{2\pi(1-\nu)}\frac{x(x^2-y^2)}{(x^2+y^2)^2} \\ \varepsilon_{zz} &= \varepsilon_{xz} = \varepsilon_{yz} = 0, \end{aligned} \tag{7.14}$$

where ν is Poisson's ratio, λ is the Lamé constant, and $\nu = \dfrac{\lambda}{2(\lambda+\mu)}$. The stresses around an edge dislocation are then:

$$\begin{aligned}
\sigma_{xx} &= \frac{-\mu b}{2\pi(1-\nu)}\frac{y(3x^2+y^2)}{(x^2+y^2)^2} = \frac{-\mu b}{2\pi(1-\nu)r}\sin\theta(2+\cos 2\theta)\\
\sigma_{yy} &= \frac{\mu b}{2\pi(1-\nu)}\frac{y(x^2-y^2)}{(x^2+y^2)^2} = \frac{\mu b}{2\pi(1-\nu)r}\sin\theta\cos 2\theta\\
\sigma_{xy} &= -\frac{\mu b}{2\pi(1-\nu)}\frac{x(x^2-y^2)}{(x^2+y^2)^2} = \frac{\mu b}{2\pi(1-\nu)r}\cos\theta\cos 2\theta\\
\sigma_{zz} &= \nu(\sigma_{xx}+\sigma_{yy}) = \frac{-\mu\nu by}{\pi(1-\nu)(x^2+y^2)} = \frac{-\mu\nu b}{\pi(1-\nu)r}\sin\theta\\
\sigma_{xz} &= \sigma_{yz} = 0.
\end{aligned} \tag{7.15}$$

The stresses in cylindrical coordinates are as follows:

$$\begin{aligned}
\sigma_{rr} &= \sigma_{\theta\theta} = \frac{\mu b}{2\pi(1-\nu)}\frac{\sin\theta}{r}\\
\sigma_{r\theta} &= \frac{-\mu b}{2\pi(1-\nu)}\frac{\cos\theta}{r}\\
\sigma_{zz} &= \frac{-\mu\nu b}{2\pi(1-\nu)}\frac{\sin\theta}{r}\\
\sigma_{\theta z} &= \sigma_{rz} = 0.
\end{aligned} \tag{7.16}$$

7.1.4 Energy of a Dislocation

Energy is stored in any elastic medium that is stressed. Applying a tensile stress to a rod produces a tensile strain, which is proportional to the stress in an elastic solid. Consider a unit cube within the rod. A stress, σ, is the total force applied across a face of the cube. The strain is the fractional distance the cube elongates in the direction of the stress. So the work done (energy/unit volume) on the cube is the force times the distance, or:

$$W = \int_0^{\varepsilon_{\max}} \sigma \mathrm{d}\varepsilon, \tag{7.17}$$

and from Fig. 7.22, we have:

$$W = 1/2\sigma_{\max}\varepsilon_{\max}. \tag{7.18}$$

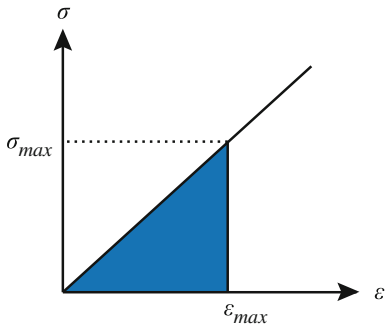

Fig. 7.22 Elastic stress–strain curve showing the stored energy in the strain field

For a generalized stress field, the stored energy per unit volume is as follows:

$$W = 1/2\left(\sigma_{xx}\varepsilon_{xx} + \sigma_{yy}\varepsilon_{yy} + \sigma_{zz}\varepsilon_{zz} + \sigma_{xy}\varepsilon_{xy} + \sigma_{xz}\varepsilon_{xz} + \sigma_{yz}\varepsilon_{yz}\right), \tag{7.19}$$

and in cylindrical coordinates:

$$W = 1/2(\sigma_{rr}\varepsilon_{rr} + \sigma_{\theta\theta}\varepsilon_{\theta\theta} + \sigma_{zz}\varepsilon_{zz} + \sigma_{r\theta}\varepsilon_{r\theta} + \sigma_{rz}\varepsilon_{rz} + \sigma_{\theta z}\varepsilon_{\theta z}), \tag{7.20}$$

where $\sigma_{ij} = \sigma_{ji}$.
Applying Eq. (7.20) to the screw dislocation gives:

$$W = 1/2(\sigma_{\theta z}\varepsilon_{\theta z}) = \frac{\mu b^2}{8\pi^2 r^2}. \tag{7.21}$$

The elastic energy per unit length of the dislocation line is:

$$E_l = \int_{r_c}^{R} W 2\pi r \mathrm{d}r = \frac{\mu b^2}{4\pi}\int_{r_c}^{R}\frac{\mathrm{d}r}{r} = \frac{\mu b^2}{4\pi}\ln\left(\frac{R}{r_c}\right) + \varepsilon_c. \tag{7.22}$$

The limits on the integral are the dislocation core radius, r_c, and R. The dislocation core radius is that distance below which linear elasticity does not hold and is generally taken to be several Burgers vectors in magnitude. R is the outer dimension of the crystal, or for polycrystalline materials, R could be taken to be the grain radius. However, a further constraining condition is the presence of other dislocations, which is the case even in a well-annealed metal in which the dislocation density is still $\sim 10^8$ cm^{-2}. So R is often taken to be the distance midway to the next dislocation. However, the elastic energy is not highly sensitive to R since it appears in the ln term. The term ε_c is the energy of the dislocation core radius, which is not included in the integral since linear continuum elasticity theory breaks down in this region. Assuming that the stress level in the core is $\mu/30$, then for a dislocation core radius of $5b$, the value of ε_c is approximately $\mu b^2/10$, which is about 10–20 % of the value of that in the elastic strain field (ln term).

For an edge dislocation, the elastic energy per unit length determined in the same way as for the screw dislocation is as follows:

$$E_l = \frac{\mu b^2}{4\pi(1-\nu)} \ln\left(\frac{R}{r_c}\right) + \varepsilon_c, \tag{7.23}$$

which is different from the screw dislocation by a factor of $(1 - \nu)$ in the denominator of the first term, or a factor of about 1.6 for $\nu \sim 0\,3$. For typical values of R and r_c, $\frac{\mu b^2}{2} \leq E_l \leq \mu b^2$. The elastic energy per unit length of dislocation line is also called the line tension and is denoted by Γ. Generally, Γ is taken to have the value $\frac{\mu b^2}{2}$.

7.1.5 Line Tension of a Dislocation

Under a uniform applied shear stress, σ_s, an element of dislocation line, ds, is displaced in a direction normal to ds by an amount dl (Fig. 7.23). The area swept out by the dislocation line element, ds, is dsdl. The average displacement of the crystal above the slip plane relative to that below is by an element:

$$\mathrm{d}x = \left(\frac{\mathrm{d}s\mathrm{d}l}{A}\right) b, \tag{7.24}$$

where A is the area of the slip plane. The force creating the shear stress is $\sigma_s A$, and the work done is as follows:

$$\begin{aligned} \mathrm{d}W &= F\mathrm{d}x = \sigma_s A\left(\frac{\mathrm{d}s\mathrm{d}l}{A}\right) b \\ &= \sigma_s \mathrm{d}s\mathrm{d}l b. \end{aligned} \tag{7.25}$$

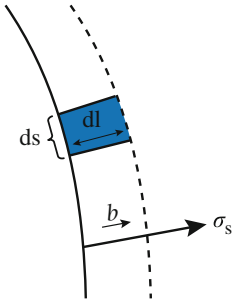

Fig. 7.23 Dislocation line segment ds sweeping out an area dsdl in the direction of the Burgers vector

Since force is work divided by the distance over which it is applied:

$$F = \frac{\mathrm{d}W}{\mathrm{d}l} = \sigma_\mathrm{s}\mathrm{d}sb, \tag{7.26}$$

and the force per unit length is as follows:

$$F_l = \frac{\mathrm{d}W/\mathrm{d}l}{\mathrm{d}s} = \sigma_\mathrm{s}b. \tag{7.27}$$

Consider a curved dislocation line. The line tension produces an inward radial force that tends to straighten out the dislocation line. The dislocation will only remain curved if a shear stress exists to resist the line tension. We wish to determine the shear stress required to maintain the curvature. Consider a segment of a dislocation line as shown in Fig. 7.24. The outward force due to the shear stress is as follows:

$$\sigma_\mathrm{s}b\mathrm{d}s = 2\sigma_\mathrm{s}bR\mathrm{d}\theta. \tag{7.28}$$

The inward restraining force is as follows:

$$2\Gamma\sin(\mathrm{d}\theta) \sim 2\Gamma\mathrm{d}\theta. \tag{7.29}$$

From Eqs. (7.28) and (7.29), we have the force balance:

$$2\Gamma\mathrm{d}\theta = 2\sigma_\mathrm{s}bR\mathrm{d}\theta, \tag{7.30}$$

and solving for σ_s yields the shear stress in terms of the line tension:

$$\sigma_\mathrm{s} = \frac{\Gamma}{bR}. \tag{7.31}$$

For:

$$\Gamma \approx \frac{\mu b^2}{2}, \quad \text{then} \quad \sigma_\mathrm{s} = \frac{\mu b}{2R}, \tag{7.32a}$$

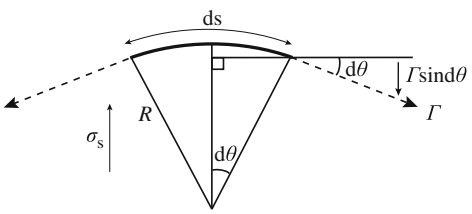

Fig. 7.24 Inward restraining force on a dislocation line segment ds due to a shear stress σ_s

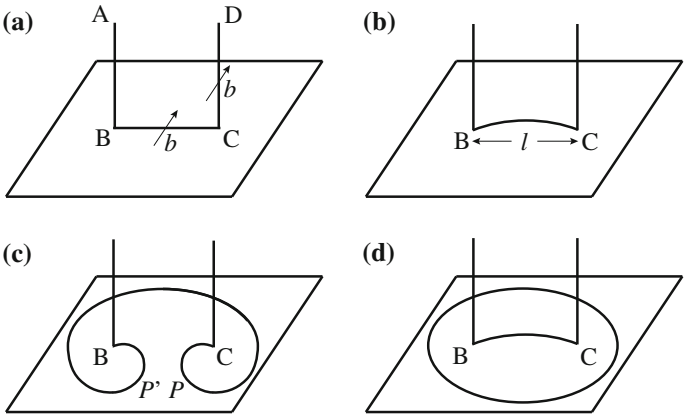

Fig. 7.25 Frank–Read source for the production of dislocations

and for

$$\Gamma \approx \mu b^2, \quad \text{then} \quad \sigma_s = \frac{\mu b}{R}. \tag{7.32b}$$

One mechanism of formation of dislocations in solids is the Frank–Read mechanism. The mechanism is shown in Fig. 7.25 and occurs as follows. A dislocation line segment defined by ABCD and Burgers vector $\boldsymbol{b}$ is such that segments AB and DC are immobile and only segment BC lies in a slip plane. The dislocation segment BC is pinned at the points B and C. The temperature is assumed to be low enough that that climb is not an option. Under an applied stress, the segment BC bows out slightly in response to the stress and adopts the curvature as prescribed by the line tension on the dislocation given in Eq. (7.32a) $\sigma_s = \frac{\mu b}{2R}$, and for $l = 2R$, $\sigma_s \approx \frac{\mu b}{l}$. When the force arising from the curvature of the dislocation line can no longer balance the force produced by the applied stress, the dislocation becomes unstable and bows out to adopt the configuration shown in Fig. 7.25c. Note that at this point, the line segments P and P' have opposite character, and as the dislocation continues to bow out, they come in contact with each other and annihilate, leaving a region of perfect crystal and a perfect loop. The applied shear stress will cause the loop to expand and will also start the process of creating a new loop from the same BC segment. This process can continue to occur, and one such pinned dislocation can produce many loops and will continue as long as the loops are able to expand away from the source. Figure 7.26 shows a micrograph of a Frank–Read source in a silicon crystal. Eventually, the back stress caused by the previous loops will produce a retarding force on the source, and it will shut down. Back stress due to dislocation pileup is discussed in Chap. 12.

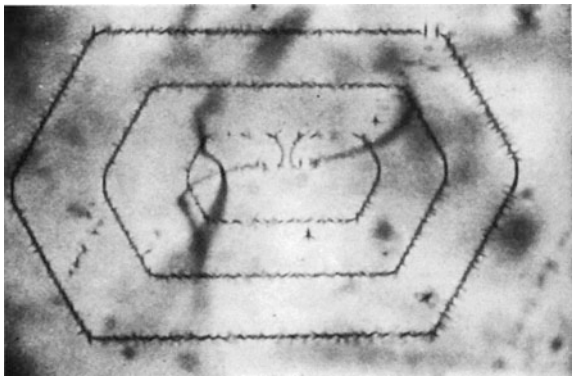

Fig. 7.26 Micrograph of a Frank–Read source in a silicon crystal (from [6])

7.1.6 *Forces on a Dislocation*

We consider here the application of an external stress on a solid containing a dislocation. For example, the application of a shear stress, σ_{xy}, on a solid containing an edge dislocation (Fig. 7.27) produces motion in the $+x$-direction. In moving a dislocation a distance L, the external applied stress will have done an amount of work/unit length of dislocation line equal to $\sigma_{xy}bL$. Then, the force is $F = \sigma_{xy}b$. Note that the force is in the $+x$-direction.

For a screw dislocation, application of a shear stress, σ_{yz}, results in a force $\sigma_{yz}b$, where the force is in the $+x$-direction (Fig. 7.28). Application of a shear stress σ_{xz} produces a force $-\sigma_{xz}b$, where the force is in the $-y$-direction, and motion is perpendicular to the slip plane.

What if we apply a stress to an edge dislocation that produces a force in a direction perpendicular to the slip plane? A tensile stress, σ_{xx}, applied to the edge dislocation in Fig. 7.29 will produce a downward force on the dislocation equal to $-\sigma_{xx}b$. The only way that the dislocation can respond to this stress is to climb.

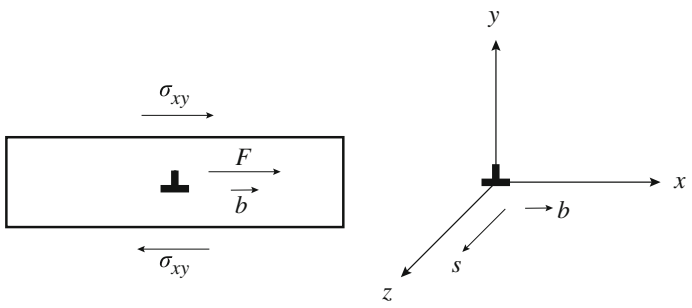

Fig. 7.27 Force on an edge dislocation with character $s|001|$, $b|100|$ due to a shear stress σ_{xy}

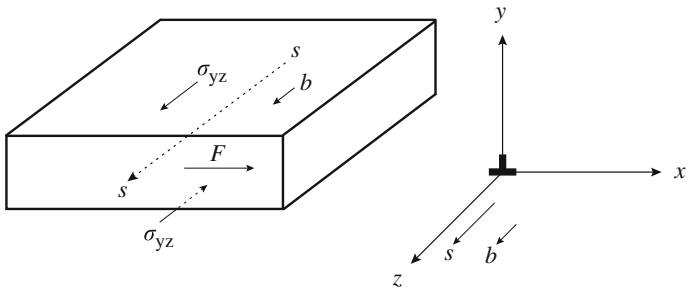

Fig. 7.28 Force on a screw dislocation with character $s|001|$, $b|001|$ due to a shear stress σ_{yz}

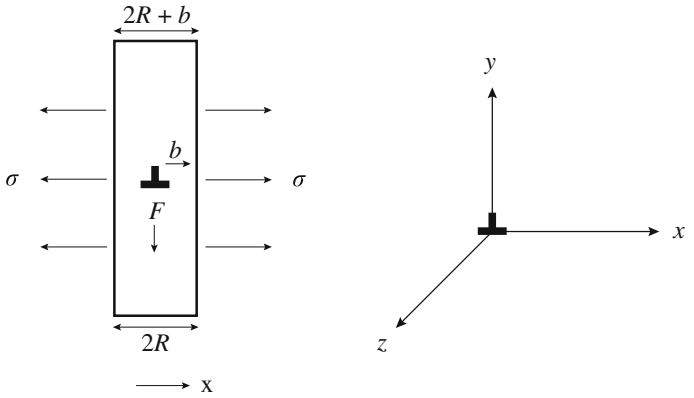

Fig. 7.29 Force on an edge dislocation with character $s|001|$, $b|100|$ due to a normal stress σ_{xx}

Ultimately, we would like to be able to determine the force on any dislocation in a solid subjected to a generalized stress. For example, if we orient a dislocation along the $+z$-direction and its slip plane is perpendicular to the y-axis, then the Burgers vector can be described by:

$$\boldsymbol{b} = b_x\boldsymbol{i} + b_z\boldsymbol{k}, \tag{7.33}$$

where b_x and b_z are edge and screw components of the Burgers vector, and $\boldsymbol{i}$ and $\boldsymbol{k}$ are unit vectors in the x- and z-directions, respectively. This is a mixed dislocation as it's Burgers vector contains components in more than one direction. An external stress placed on the surfaces of a crystal containing a dislocation includes six components: σ_{xx}, σ_{yy}, σ_{zz}, σ_{xy}, $\sigma_{xz,}$ and σ_{yz}. Of these six stress components, only σ_{yz} and σ_{xy} exert a force on an edge dislocation that will cause motion in the slip plane. Stress components σ_{xz} and σ_{xx} cause motion perpendicular to the slip plane. The

term σ_{zz} does no work, nor does σ_{yy}. The total force on a unit length of dislocation line is then:

$$\boldsymbol{F} = \left(\sigma_{xy}b_x + \sigma_{yz}b_z\right)\boldsymbol{i} - \left(\sigma_{xx}b_x + \sigma_{xz}b_z\right)\boldsymbol{j}, \tag{7.34}$$

where the first term is the force component parallel to the slip plane, the second term is the force component normal to the slip plane, and $\boldsymbol{n} = (i, j, k)$ defines the unit vector.

A dislocation of mixed character represents the most general case of a force on a dislocation due to an arbitrary stress field. For a mixed dislocation, the Burgers vector is as follows:

$$\begin{aligned}\boldsymbol{b} &= b_x\boldsymbol{i} + b_y\boldsymbol{j} + b_z\boldsymbol{k} \\ &= b_1\boldsymbol{i} + b_2\boldsymbol{j} + b_3\boldsymbol{k}.\end{aligned} \tag{7.35}$$

Therefore, we write the incremental work done on a dislocation of Burgers vector described by Eq. (7.35) due to an arbitrary stress σ_{ij} as follows:

$$\delta W = \sum_{\substack{i=1 \\ j=1}}^{3} b_i\sigma_{ij}n_j\mathrm{d}A, \tag{7.36}$$

or in matrix notation:

$$\mathrm{d}W = \underline{b}\,\underline{\underline{\sigma}}\,\underline{n}\mathrm{d}A, \tag{7.37}$$

where $\underline{\underline{\sigma}}$ is the stress tensor, $\underline{n}$ is the unit vector perpendicular to the slip plane, and $\underline{b}$ is the Burgers vector. Actually, $\underline{b}$ is a column vector so that Eq. (7.37) is written as follows:

$$\mathrm{d}W = \underline{b}^T\underline{\underline{\sigma}} \cdot \underline{n}\,\mathrm{d}A. \tag{7.38}$$

The term $\underline{n}\ \mathrm{d}A$ can be written as $\mathrm{d}\boldsymbol{A}$ which is just:

$$L(\boldsymbol{s} \times \mathrm{d}\boldsymbol{l}), \tag{7.39}$$

where $\boldsymbol{s}$ is the unit vector in the direction of the dislocation line, L is the length of the dislocation line, and $\mathrm{d}\boldsymbol{l}$ (=$\mathrm{d}x\boldsymbol{i}$ + $\mathrm{d}y\boldsymbol{j}$ + $\mathrm{d}z\boldsymbol{k}$) is the unit vector in the slip plane and is normal to $\boldsymbol{s}$ and $\boldsymbol{n}$ Recall that $\boldsymbol{b} = b_x\boldsymbol{i} + b_y\boldsymbol{j} + b_z\boldsymbol{k}$, so $\boldsymbol{b}$ has a component only in the direction $\mathrm{d}\boldsymbol{l}$. Since $\boldsymbol{A} \cdot \boldsymbol{B} \times \boldsymbol{C} = \boldsymbol{A} \times \boldsymbol{B} \cdot \boldsymbol{C}$, then:

$$\mathrm{d}W = L\underline{b}^T\underline{\underline{\sigma}} \times \underline{s} \cdot \mathrm{d}\boldsymbol{l}, \tag{7.40}$$

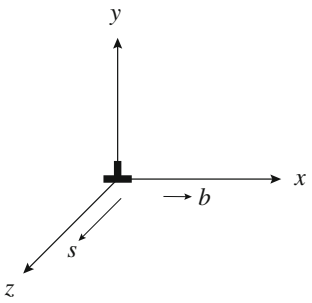

Fig. 7.30 Orientation of an edge dislocation for the determination of the forces due to a generalized stress field

and:

$$\frac{1}{L}\mathrm{d}W = \underline{b}^T\underline{\underline{\sigma}} \times \underline{s} \cdot \mathrm{d}\boldsymbol{l}. \tag{7.41}$$

The term $\underline{b}^T\underline{\underline{\sigma}} \times \underline{s}$ in Eq. (7.41) is the force per unit length on a dislocation due to an external stress that tends to displace the dislocation, and is designated:

$$\boldsymbol{f} = \underline{b}^T\underline{\underline{\sigma}} \times \underline{s}, \tag{7.42}$$

and is known as the *Peach–Koehler* equation.

Let us apply the Peach–Koehler equation to the case of an edge dislocation described by Burgers vector and direction: $b\begin{vmatrix}1\\0\\0\end{vmatrix}$ and $s\begin{vmatrix}0\\0\\1\end{vmatrix}$ and shown in Fig. 7.30. We write the first quantity in Eq. (7.42) as follows:

$$\underline{b}^T\underline{\underline{\sigma}} = b|100|\begin{vmatrix}\sigma_{xx} & \sigma_{xy} & \sigma_{xz}\\ \sigma_{yx} & \sigma_{yy} & \sigma_{yz}\\ \sigma_{zx} & \sigma_{zy} & \sigma_{zz}\end{vmatrix} = b|\,\sigma_{xx} \quad \sigma_{xy} \quad \sigma_{xz}\,|, \tag{7.43}$$

and then taking the cross product with $\boldsymbol{s}$ gives:

$$\underline{b}^T\underline{\underline{\sigma}} \times \underline{s} = b\begin{vmatrix}\boldsymbol{i} & \boldsymbol{j} & \boldsymbol{k}\\ \sigma_{xx} & \sigma_{xy} & \sigma_{xz}\\ 0 & 0 & 1\end{vmatrix}. \tag{7.44}$$

The cross product, or determinant, is $b\sigma_{xy}\boldsymbol{i} - b\sigma_{xx}\boldsymbol{j}$, and the force on the dislocation is as follows:

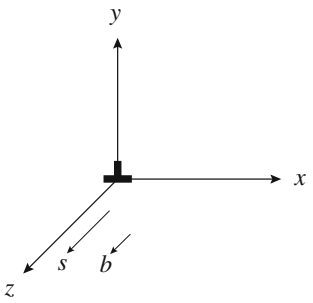

Fig. 7.31 Orientation of a screw dislocation for the determination of the forces due to a generalized stress field

$$\boldsymbol{f} = b\sigma_{xy}\boldsymbol{i} - b\sigma_{xx}\boldsymbol{j}. \tag{7.45}$$

Note that $f_x = b\sigma_{xy}$ is a *glide* force in the $+x$-direction and the force component $f_y = -b\sigma_{xx}$ is the *climb* force in the $-y$-direction. Only σ_{xy} and σ_{xx} can exert forces on a dislocation with Burgers vector and direction defined as in this example.

For a screw dislocation with Burgers vector and direction given by: $b\begin{vmatrix}0\\0\\1\end{vmatrix}$ and $s\begin{vmatrix}0\\0\\1\end{vmatrix}$, and shown in Fig. 7.31, we have:

$$\underline{b}^T\underline{\underline{\sigma}} = b|001|\begin{vmatrix}\sigma_{xx} & \sigma_{xy} & \sigma_{xz}\\ \sigma_{yx} & \sigma_{yy} & \sigma_{yz}\\ \sigma_{zx} & \sigma_{zy} & \sigma_{zz}\end{vmatrix} = b|\,\sigma_{zx} \quad \sigma_{zy} \quad \sigma_{zz}\,|, \tag{7.46}$$

and then taking the cross product with $\boldsymbol{s}$ gives:

$$\boldsymbol{f} = \underline{b}^T\underline{\underline{\sigma}} \times \underline{s} = b\begin{vmatrix}\boldsymbol{i} & \boldsymbol{j} & \boldsymbol{k}\\ \sigma_{zx} & \sigma_{zy} & \sigma_{zz}\\ 0 & 0 & 1\end{vmatrix} = b\sigma_{yz}\boldsymbol{i} - b\sigma_{zx}\boldsymbol{j}, \tag{7.47}$$

and $f_x = b\sigma_{zy}$ and $f_y = -b\sigma_{zx}$. Note that only σ_{zy} and σ_{zx} can exert a force on a dislocation defined in this example.

7.1.7 Interactions Between Dislocations

The *Peach–Koehler* equation can also be used to determine the stress on a dislocation due to that from a second dislocation. The difference is that the stress is due

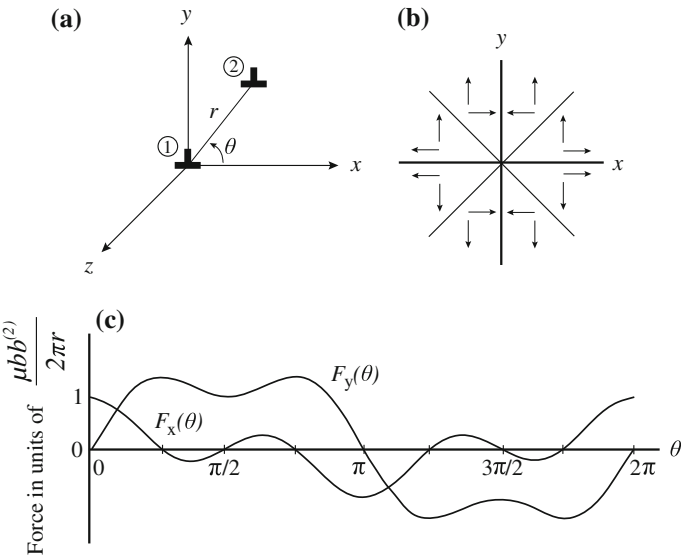

Fig. 7.32 (**a**) Orientation of dislocations to determine the force on edge dislocation (*2*) due to edge dislocation (*1*), and *x*- and *y*-components of the force (**b**) in the *x*–*y* plane, and (**c**) as a function of θ

to the presence of the second dislocation rather than external application. We will examine interactions between dislocations by looking at edge–edge, screw–screw, and edge–screw interactions. We will begin with the edge–edge interaction.

Edge–edge interaction

To find the force on dislocation (2) due to the presence of dislocation (1), we locate dislocation (1) at the origin of our coordinate axes and dislocation (2) at some arbitrary position (Fig. 7.32(a)). According to the Peach–Koehler equation, the force is as follows: $\boldsymbol{f} = \underset{(2)}{\underline{b}^T}\ \underset{(1)}{\underline{\underline{\sigma}}} \times \underset{(2)}{\underline{s}}$, where the Burgers vector and direction are those of dislocation (2), and the stress is due to dislocation (1). The first term in the cross product then becomes:

$$\underline{b}^T\underline{\underline{\sigma}} = \underbrace{b|100|}_{(2)} \underbrace{\begin{vmatrix} \sigma_{xx} & \sigma_{xy} & 0 \\ \sigma_{yx} & \sigma_{yy} & 0 \\ 0 & 0 & \sigma_{zz} \end{vmatrix}}_{(1)} = b|\,\sigma_{xx} \quad \sigma_{xy} \quad 0\,|, \tag{7.48}$$

and

$$\boldsymbol{f} = \underline{b}^T\underline{\underline{\sigma}} \times \underset{(2)}{\underline{s}} = b \begin{vmatrix} \boldsymbol{i} & \boldsymbol{j} & \boldsymbol{k} \\ \sigma_{xx} & \sigma_{xy} & 0 \\ 0 & 0 & 1 \end{vmatrix} = b\sigma_{xy}\boldsymbol{i} - b\sigma_{xx}\boldsymbol{j}. \tag{7.49}$$

The force on dislocation (2) can be written as:

$$\boldsymbol{F} = \underbrace{\frac{\mu b b^{(2)}}{2\mu(1-\nu)r}(\cos\theta\cos 2\theta)\,\boldsymbol{i}}_{F_x(\theta)} - \underbrace{\frac{\mu b b^{(2)}}{2\pi(1-\nu)r}\sin\theta(2+\cos 2\theta)\boldsymbol{j}}_{F_y(\theta)}, \tag{7.50}$$

and the force components in the x–y plane are shown in Fig. 7.32(b), and as a function of θ in Fig. 7.32(c).

Note that if dislocation (2) has the same $\boldsymbol{s}$ but the Burgers vector is in the opposite direction, then the net effect on the resultant force is simply a change in sign of each of the terms in Eq. (7.50) but preservation of the magnitudes. If dislocation (2) has Burgers vector $b\begin{vmatrix}0\\1\\0\end{vmatrix}$, then the preceding analysis becomes:

$$\underline{b}^T\underline{\underline{\sigma}} = \underbrace{b|010|}_{(2)}\underbrace{\begin{vmatrix}\sigma_{xx} & \sigma_{xy} & 0\\ \sigma_{yx} & \sigma_{yy} & 0\\ 0 & 0 & \sigma_{zz}\end{vmatrix}}_{(1)} = b|\,\sigma_{xy} \quad \sigma_{yy} \quad 0\,|, \tag{7.51}$$

$$\boldsymbol{f} = \underline{b}^T\underline{\underline{\sigma}} \times \underset{(2)}{\underline{s}} = b\begin{vmatrix}\boldsymbol{i} & \boldsymbol{j} & \boldsymbol{k}\\ \sigma_{xy} & \sigma_{yy} & 0\\ 0 & 0 & 1\end{vmatrix} = b\sigma_{yy}\boldsymbol{i} - b\sigma_{xy}\boldsymbol{j}. \tag{7.52}$$

In this case, the x-component of the force produces a positive climb force to the right, and the y-component of the force produces a negative (downward) glide force.

Screw–screw interaction

For two screw dislocations as shown in Fig. 7.33(a), the force on dislocation (2) due to dislocation (1) is as follows:

$$\boldsymbol{f} = \underline{b}^T\underline{\underline{\sigma}} \times \underset{(2)}{\underline{s}} = b\begin{vmatrix}\boldsymbol{i} & \boldsymbol{j} & \boldsymbol{k}\\ \sigma_{xz} & \sigma_{yz} & 0\\ 0 & 0 & 1\end{vmatrix} = b\sigma_{yz}\boldsymbol{i} - b\sigma_{xz}\boldsymbol{j}, \tag{7.53}$$

where the x-component of the force, $b\sigma_{yz,}$ is to the right, and the y-component of the force, $-b\sigma_{xz,}$ is downward in Fig. 7.33. The force on dislocation (2) can be written as:

$$\boldsymbol{F} = \frac{\mu b b^{(2)}}{2\pi r}(\cos\theta\boldsymbol{i} + \sin\theta\boldsymbol{j}). \tag{7.54}$$

The force is in a direction that is perpendicular to the dislocation line. It is repulsive if the dislocations are of the same sign and attractive if the dislocations are of

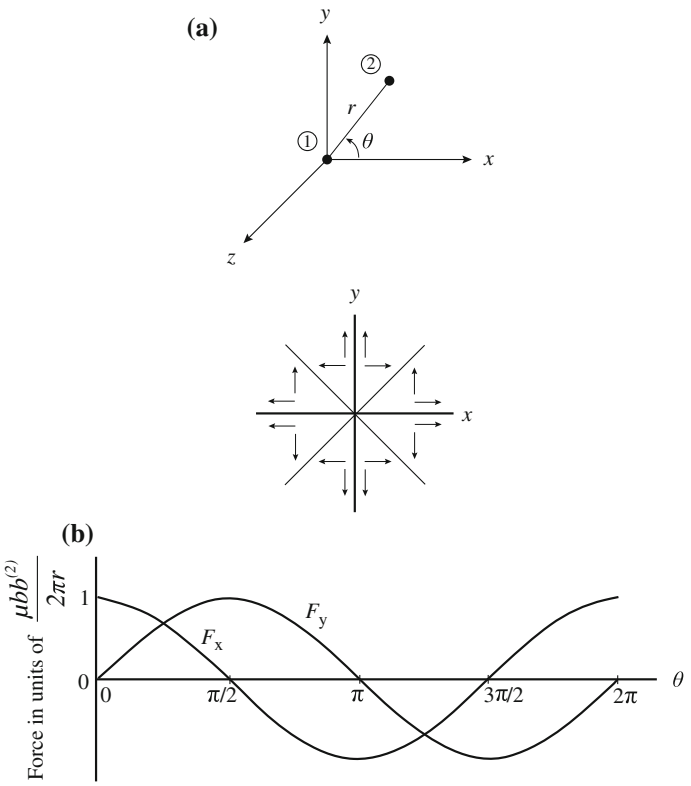

Fig. 7.33 (**a**) Orientation of dislocations to determine the force on screw dislocation (*2*) due to screw dislocation (*1*), and (**b**) the *x*- and *y*-components of the force on a screw dislocation due to another dislocation in the *x*–*y* plane, and (**c**) as a function of θ

opposite sign. The force on the dislocation at the origin due to the dislocation at (r, θ) is equal in magnitude but opposite in sign from the force on the dislocation at (r, θ) due to that at the origin. The force components in the *xy*-plane are shown in Fig. 7.33(b), and the magnitude of the forces as a function of θ are shown in Fig. 7.33(c).

Edge–screw interaction

The last example is the determination of the force between an edge and a screw dislocation as defined in Fig. 7.34. We know that an edge dislocation has no *xz* or *yz* stress components, which are needed to move a screw dislocation. So we can state the following rules: For an edge dislocation with $b\begin{vmatrix}1\\0\\0\end{vmatrix}$ and $s\begin{vmatrix}0\\0\\1\end{vmatrix}$, the only stresses that produce a force on it are σ_{xx} and σ_{xy}. The stress field around the dislocation has

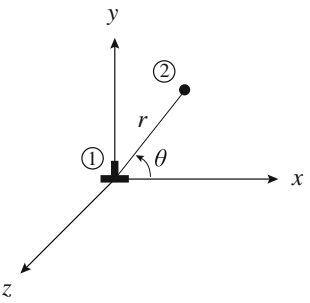

Fig. 7.34 Orientation of dislocations to determine the force on screw dislocation (*2*) due to edge dislocation (*1*)

components σ_{xx}, σ_{yy}, σ_{zz}, and σ_{xy}. For a screw dislocation with $b\begin{vmatrix}0\\0\\1\end{vmatrix}$ and $s\begin{vmatrix}0\\0\\1\end{vmatrix}$, the only stresses that produce a force on it are σ_{xz} and σ_{yz}. The stress field around the dislocation has components σ_{xz} and σ_{yz}.

7.1.8 Extended Dislocations

Slip occurs in the fcc lattice on (111) planes and in the $\langle 110 \rangle$ direction, as shown in Fig. 7.35. The Burgers vector is $a/2[110]$, which is the shortest lattice vector connecting an atom at the cube corner with a neighboring atom at the center of a cube face. However, the atom arrangement on the $\{111\}$ slip plane is such that slip in the [110] direction is not the easiest path. Figure 7.35(b) shows the atom arrangement on a close-packed (111) plane. The $\{111\}$ planes are stacked in the sequence ABCABC…, such that the centers of the A plane of atoms fall on top of each other, and similarly for the B and C planes of atoms. The vector $\boldsymbol{b}_1 = a/2\left[10\overline{1}\right]$ shown in Fig. 7.35(b) is the

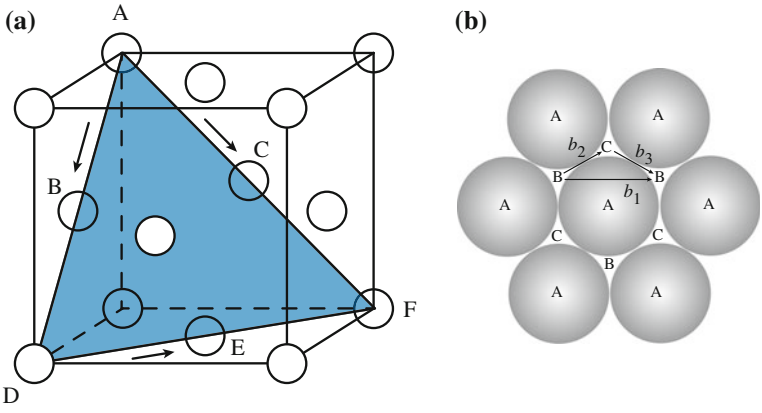

Fig. 7.35 (**a**) Close-packed (111) slip plane in the fcc lattice. (**b**) Slip directions

observed slip direction. However, if atoms are considered as hard spheres, this direction represents a high-energy path as atoms moving from one B site to another must climb over the A atoms. A simpler path is by way of vectors $\boldsymbol{b}_2$ and $\boldsymbol{b}_3$, which is along the "valleys" between the A atoms. This dislocation reaction is given by:

$$\boldsymbol{b}_1 \rightarrow \boldsymbol{b}_2 + \boldsymbol{b}_3, \quad a/2[10\bar{1}] \rightarrow a/6[2\bar{1}\bar{1}] + a/6[11\bar{2}]. \tag{7.55}$$

Essentially, the Burgers vector, $\boldsymbol{b}_1$, of the total dislocation has been dissociated into two *partial dislocations* $\boldsymbol{b}_2$ and $\boldsymbol{b}_3$. Figure 7.36(a) shows the atom arrangement of the partial dislocations on the {111} plane, and Fig. 7.36(b) shows the vector diagram of the dissociation of the total dislocation into two partial dislocations. The partials are often called *Shockley partials*, and the combination of the two partials is termed an *extended dislocation*. Dissociation is independent of dislocation character, and the partial dislocations move as a unit that maintains the equilibrium width between them. The space between the partials is referred to as the faulted region or the *stacking fault*, and its size is determined by the *stacking fault energy*, SFE. The lower the SFE, the greater the separation of the partials, and the higher the

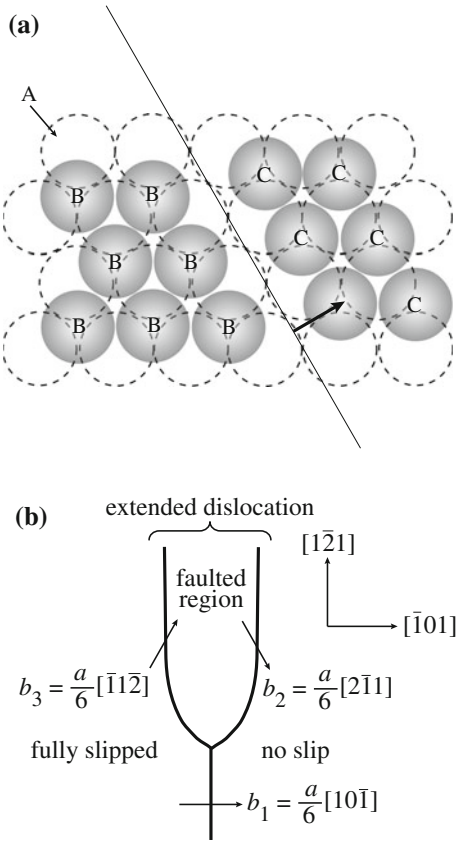

Fig. 7.36 Slip on the close-packed (111) plane in the fcc lattice. (**a**) Location of atoms in a Shockley partial. (**b**) Dislocation dissociation into partial dislocations

energy, the closer they are together. Stacking faults are important in cross-slip as the partials must recombine for cross-slip to occur. Extended dislocations also occur in hcp lattices, but are not commonly observed in bcc metals.

7.1.9 Kinks and Jogs

Both edge and screw dislocations can acquire jogs or steps in the dislocation line by interaction with other dislocations. The jogs are of two types. A jog that lies in the slip plane instead of normal to it is called a kink. Figure 7.37(a) shows an edge dislocation with a kink of screw character that lies in the slip plane of the edge dislocation, and Fig. 7.37(b) shows a screw dislocation with a kink of edge orientation. Kinks are unstable as they can line up and annihilate during glide. A second type of jog is shown in Fig. 7.37(c) in which the jog and the dislocation are of edge orientation. These types of jogs are able to glide since they lie in the slip plane of the dislocation. The only difference between the motion of the jogged edge dislocation and the ordinary edge dislocation is that instead of gliding along a single plane, it glides over a stepped surface. Another type of jog is the most important in plastic deformation and is shown in Fig. 7.37(d). This is a screw dislocation containing a jog with an edge orientation. The only way the screw dislocation can move to a new position and take its jog with it is by climb of the jog. Figure 7.37(e) shows the movement of a jogged screw dislocation as the segments between jogs bow out in the slip plane under an applied stress producing a trail of vacancies left behind the jog as the dislocation moves in its slip plane.

7.2 Faulted Loops and Stacking Fault Tetrahedra

Because of their importance in irradiated materials, we will discuss Frank loops at greater length. Frank loops are important in irradiated materials because they are often nucleated in a displacement cascade. Recall that the cascade consists of a core of vacancies surrounded by a shell of interstitials (Figs. 3.3 and 3.9). If the vacancy core or the interstitial shell collapses (condenses) onto a close-packed plane, Frank loops may be generated. In both cases, a stacking fault results. Vacancy condensation produces an intrinsic fault, and interstitial condensation results in an extrinsic stacking fault. The faults are described as follows.

In regular, close-packed lattices such as fcc and bcc, atom layers follow a regular stacking sequence. In the fcc lattice, the stacking sequence is ABCABCABC…, indicating that every third layer lies over the first layer. Removal of a layer of atoms results in a break or a fault in the stacking sequence. Removal of a plane of atoms produces an intrinsic stacking fault, which is also known as a single fault, and the dislocations attached to the single fault are S-dislocations, giving an S-Frank dislocation (Fig. 7.38(a)). For example, the sequence is modified to

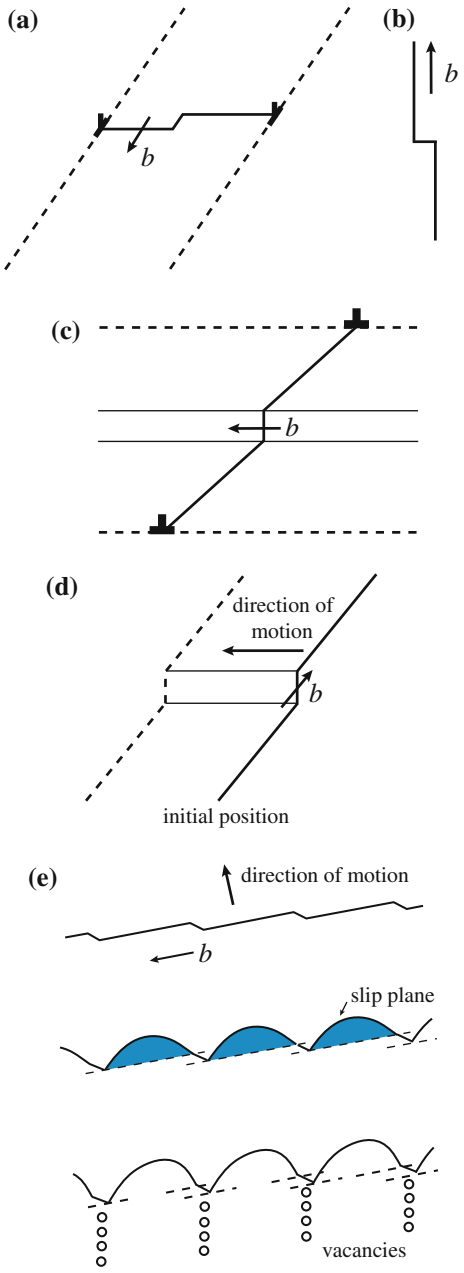

Fig. 7.37 Kinks and jogs in dislocations. (**a**) Edge dislocation with a kink of screw character. (**b**) Screw dislocation with a kink of edge orientation. (**c**) Edge jog in an edge dislocation. (**d**) Edge jog in a screw dislocation and direction of motion of the dislocation. (**e**) Movement of a jogged screw dislocation of part (**d**) showing bowing of the segments between jogs and the trail of vacancies left behind the trail of jogs (after [7])

ABCAB/ABCABC…, where "/" denotes the fault or missing plane of atoms. Insertion of an extra plane of atoms produces a double fault in the stacking sequence: ABCAB/A/CABC… (Fig. 7.38(b)). This is an extrinsic or double fault, and the dislocations are D-dislocations giving a D-Frank loop. The Burgers vector

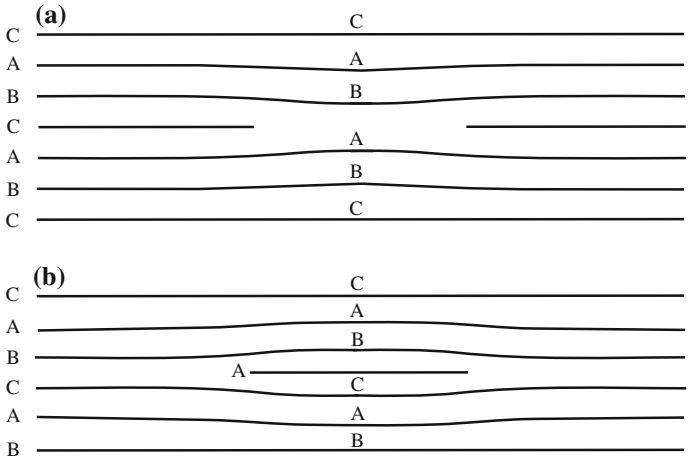

Fig. 7.38 Schematic of (**a**) intrinsic stacking fault and (**b**) extrinsic stacking fault

of the S-Frank and D-Frank loops are identical. Since a Frank loop results from addition or removal of close-packed planes, $\boldsymbol{b}$ must be directed normal to the (111) plane and has a length equal to the spacing between planes, $a/\sqrt{3}$, then the Burgers vector is described by $\boldsymbol{b} = a/3[111]$. Since it is extremely difficult to move on its slip plane (the glide plane is actuallya cylinder defined by the edge of the loop), the Frank loop is considered to be *sessile* or immobile since its glide plane is a *cylinder* defined by the projection of the loop perimeter in a direction perpendicular to, and above or below, the plane of the loop (see Fig. 7.11). A Frank loop can also unfault either autocatalytically or by reaction with a dislocation line to form a perfect loop. This process is described in Chap. 12.

Another dislocation configuration that can form in irradiated metals is the SFT. A SFT is a three-dimensional stacking fault configuration that is in the shape of a tetrahedron. SFTs are believed to evolve directly from vacancy clusters produced in cascades. They are also believed to evolve from Frank loops. A Frank loop will always lie on a (111) plane in an fcc lattice. Figure 7.39(a) shows a loop of triangular shape on a (111) plane with edges parallel to [110] directions. A Frank dislocation that is parallel to a [110] direction can lower its energy by splitting into a Shockley dislocation, $a/6[211]$, and a stair-rod dislocation. The slip plane of the Shockley dislocation is also a (111) plane, but it is different from that containing the Frank loop. Figure 7.39(b) shows two of the three Shockley dislocations formed from the three sides of the Frank loop, moving up (111) planes. Each Shockley has left behind it a stair-rod dislocation, $a/6[110]$, in the position formerly occupied by a side of the Frank dislocation loop (edge of the triangle). The stacking fault contained in the Frank loop now bends at the stair-rod dislocation and extends up onto the close-packed (111) planes of the Shockley dislocations. As the Shockley dislocations move up the planes shown in Fig. 7.39(b), they eventually meet at the intersections of their slip planes and the intersections of Shockley dislocations result

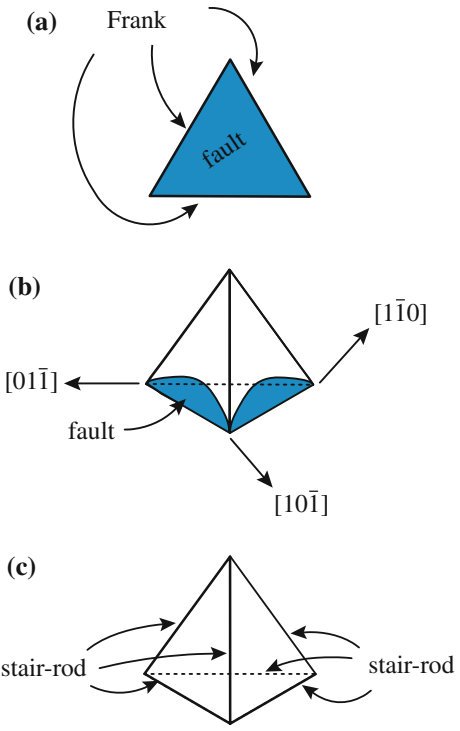

Fig. 7.39 A stacking fault tetrahedron (SFT) formed by faults on each of the faces of the tetrahedron (after [1])

in other stair-rod dislocations along the remaining three edges of the tetrahedron. The final configuration is a tetrahedron whose sides are stacking faults and whose edges are stair-rod dislocations (Fig. 7.39(c)). The Frank dislocation and the Shockley dislocations no longer exist.

Dislocations can also interact with SFTs. MD simulation of the interaction of a dissociated $a/2[110]$ dislocation (into two Shockley partials, $a/6[121]$) on the (111) glide plane shows that several types of interaction are possible [8]. When the SFT is in the slip plane of the dislocation, the SFT may be cut by the dislocation and recovers by a shift of the structure above the glide plane to regain its original shape. The interaction can also create ledges in the SFT that can reduce stability and lead to dissolution. TEM observations show that SFTs can be cut multiple times by dislocations in channels.

7.3 Defect Clusters

As described in Chap. 3, the fraction of defects produced in a cascade is between 20 and 40 % of that predicted by the NRT model due to intracascade recombination. Of these, not all appear as single interstitial atoms or isolated vacancies. A

significant fraction of defects are created in the form of clusters, rather than as single defects. Vacancy clusters may grow to form voids, which are an important microstructure feature that influences both dimensional (Chap. 8) and mechanical (Chap. 12) properties of materials. If the clusters are stable, they may also migrate away from the cascade region and be absorbed at sinks such as dislocations and grain boundaries. Interstitial and vacancy clusters must be treated separately since in general, interstitial clusters are stable and vacancy clusters are not. Their mobilities differ as well with interstitial clusters exhibiting greater mobility than their vacancy counterparts.

7.3.1 *Fraction of Defects Forming Clusters*

In-cascade clustering of defects is important because it promotes nucleation of extended defects. Interstitial clustering can occur in one of two ways. In the first, interstitial clusters are created in the transition between the collisional and thermal spike phases in which atoms that are displaced from the cascade center due to the initial shock wave are pushed into interstitial locations. Alternatively, clusters can occur during the thermal spike phase by short-range diffusion driven by the elastic interaction between neighboring interstitials. The probability of clustering and the size of the clusters tend to increase with increasing PKA energy, and a higher proportion of SIAs form clusters than do vacancies [9]. Figure 7.40 shows the fraction of interstitials that form clusters as a function of the PKA energy in several metals and, at 100 K, as determined by MD simulation [10]. Note that the clustered fraction increases quickly with T as damage transitions from single displacements to cascade morphology. In contrast to the Frenkel pair production efficiency (Fig. 3.21), the clustered fraction varies with the metal, and while there are only 5 metals shown here, the clustering appears to occur according to the crystal structure with the highest

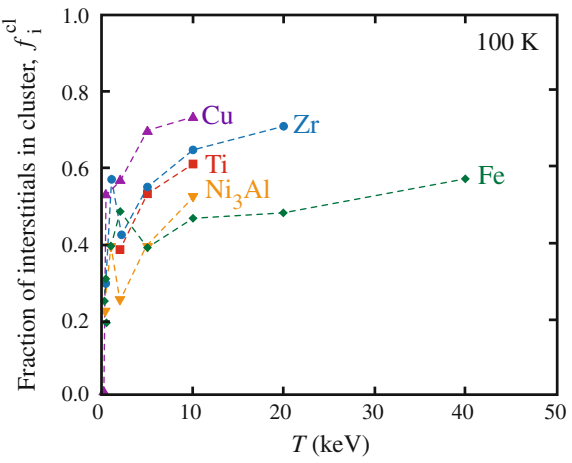

Fig. 7.40 The fraction, f_i^{cl}, of SIAs that survive as clusters containing at least two interstitials in several metals and Ni_3Al at 100 K (after [10])

clustering fraction occurring for the fcc structure and the lowest for the bcc structure with the hcp structure in between.

Note from Fig. 7.40 that with continued increase in T, the cluster fraction saturates. This is likely due to the fact that very high-energy cascades break up into several subcascades that resemble those at lower energy. As such, the surviving defect fraction and the clustering fraction plateau at values representative of the lower energy cascades. An example of subcascade formation is shown in Fig. 7.41 for a 100 keV cascade in 100 K iron where 5 and 10 keV cascades have been superimposed into the same block of atoms for comparison.

While MD results show that the fraction of interstitials in clusters is larger in copper than in α-iron by ∼70–45 % at 100 and 600 K for PKA energies above 5 keV [12], experimental evidence shows that the cluster density in copper is as much as 10^3 higher than that in Fe [13]. While the size of this difference is not understood, it may have its origins in the nature of the cluster as discussed in the next section.

The dependence of in-cascade interstitial clustering on cascade energy is shown in Fig. 7.42 for MD simulation temperatures of 100, 600, and 900 K, where the average number of interstitials in clusters of size two or larger at each energy has been divided by the total number of surviving interstitials in Fig. 7.42(a) and by the number of displaced atoms predicted by the NRT model for that energy in Fig. 7.42(b). Note that

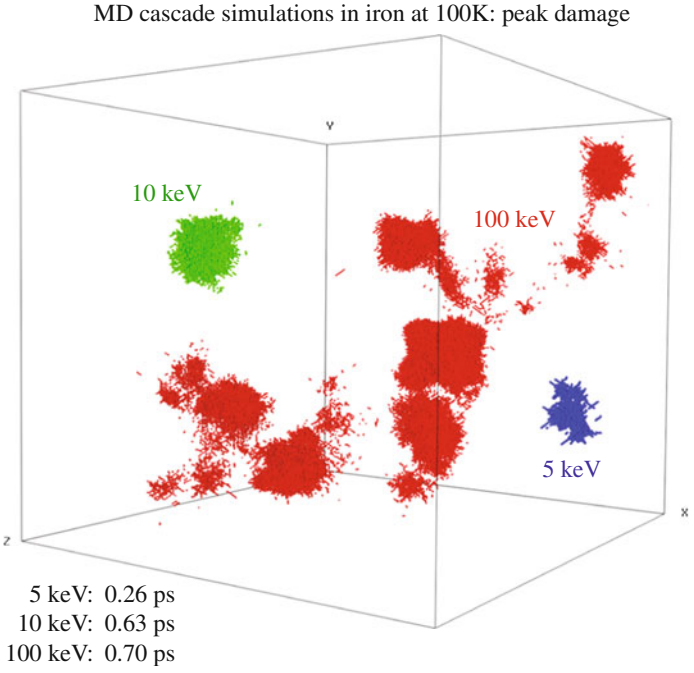

Fig. 7.41 Energy dependence of subcascade formation (after [11])

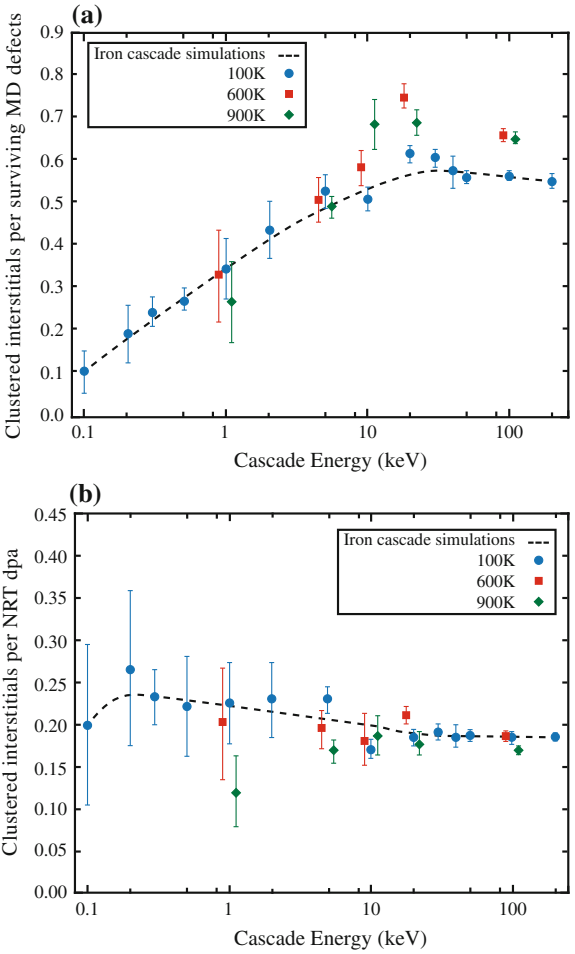

Fig. 7.42 Fraction of surviving interstitials contained in clusters (**a**) relative to the total number of MD defects created and (**b**) relative to the NRT displacements (after [11])

the relative scatter is much higher at lower energies, which is similar to the case of defect survival shown in Fig. 3.17. The average fraction of interstitials in clusters is about 20 % of the NRT displacements above 5 keV, which corresponds to about 60 % of the total surviving interstitials. Although it is not possible to discern a systematic effect of temperature below 10 keV, there is a trend toward greater clustering with increasing temperature at higher energies. This can be more clearly seen in Fig. 7.42a where the ratio of clustered interstitials to surviving interstitials is shown. Interstitial clustering increases at higher temperatures due to the more compact nature and longer lifetime of the cascade at higher temperature, providing more time for interstitials to diffuse and interact. Recall from Sect. 3.6 and Fig. 3.22 that the Frenkel pair production decreases slightly with temperature. Combining these results, the effect of temperature can be described as resulting in an increasing fraction of the decreasing

population of interstitials forming clusters as the temperature increases, yielding a net increase in f_i^{cl}. This effect of temperature on interstitial clustering is consistent with the observations of increasing interstitial clustering fraction with temperature [14].

The clustered fraction can be broken down according to cluster size to reveal the dependence of clustering on cluster size. Figure 7.43 shows the fraction of SIAs in clusters of sizes ≃2, ≃3, and ≃4 in copper as a function of damage energy for an irradiation temperature of 100 K. Note that the cluster fraction is very sensitive to minimum cluster size, especially at lower damage energies, yielding a net decrease in f_i^{cl}.

Clustering of vacancies occurs within the core of the cascade as well, and the extent of clustering varies with the host lattice. Based on the measurements of size and number density of vacancy clusters in irradiated metals, the fraction of vacancies in clusters is estimated to be less than 15 %. The energy and temperature dependence of in-cascade vacancy clustering as a fraction of the NRT displacements is shown in Fig. 7.44 for cascade energies of 10–50 keV. Results are shown for clustering criteria of first, second, and fourth nearest neighbor, NN. A comparison of Figs. 7.42(b) and 7.44 demonstrates that in-cascade vacancy clustering in iron remains lower than that of interstitials even when the fourth NN criterion is used. This is consistent with experimentally observed difficulty of forming visible vacancy clusters in iron and the fact that only relatively small vacancy clusters are found in positron annihilation studies of irradiated ferritic alloys [15]. The true fraction may be larger because of the invisibility of small clusters, but also the fact that vacancy clusters are not nearly as stable as interstitial clusters as will be shown in the next section. The cascade energy dependence of vacancy clustering is similar to that of interstitials; there is essentially zero clustering at the lowest energies, but it rapidly increases with cascade energy and is

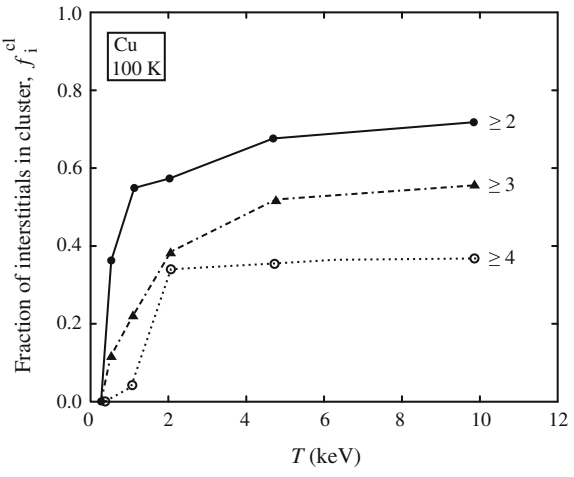

Fig. 7.43 The fraction f_i^{cl}, of SIAs that survive in clusters of two or more, three or more, and four or more in copper at 100 K (after [10])

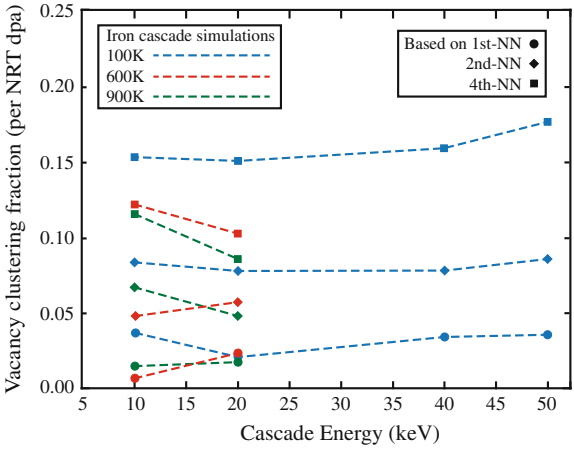

Fig. 7.44 Cascade energy dependence of vacancy clustering described by the number of clustered vacancies divided by NRT displacements (after [11])

relatively independent of energy above ~10 keV. However, vacancy clustering decreases as the temperature increases, which is consistent with vacancy clusters being thermally unstable.

7.3.2 *Types of Clusters*

The structure of the cluster is a strong function of the crystal structure [13, 16]. In α-Fe, MD simulation shows that the most stable configuration of small clusters (<10 SIAs) is a set of ⟨111⟩ crowdions. Next in stability is the ⟨110⟩ crowdion. As the cluster size grows (>7 SIAs), only two configurations are stable, the ⟨111⟩ and ⟨110⟩ crowdions. These crowdions also may act as nuclei for the formation of perfect interstitial dislocation loops with Burgers vector 1/2⟨111⟩ or ⟨100⟩, respectively.

In fcc copper, the ⟨100⟩ dumbbell is the stable configuration of the SIA and the smallest cluster is of the form of two ⟨100⟩ dumbbells. Larger clusters can have two configurations: a set of ⟨100⟩ dumbbells or a set of ⟨110⟩ crowdions, each with {111} as the habit plane. During growth, the clusters transform into faulted Frank loops with Burgers vector 1/3⟨111⟩ and perfect loops with Burgers vector 1/2 ⟨110⟩. The binding energy of SIA loops in Fe and in Cu is shown in Fig. 7.45(a, b), respectively. Note that the binding energy for SIA loops in Cu is slightly higher than for SIA loops in α-Fe, in agreement with the higher clustering fraction predicted by MD modeling. Figure 7.46 shows a micrograph of interstitial clusters and small interstitial loops in a copper foil after irradiation with 30 keV Cu^+ ions. Note that these defect clusters are only a few nanometers in size. Cluster densities can reach very high levels as shown in Fig. 7.47.

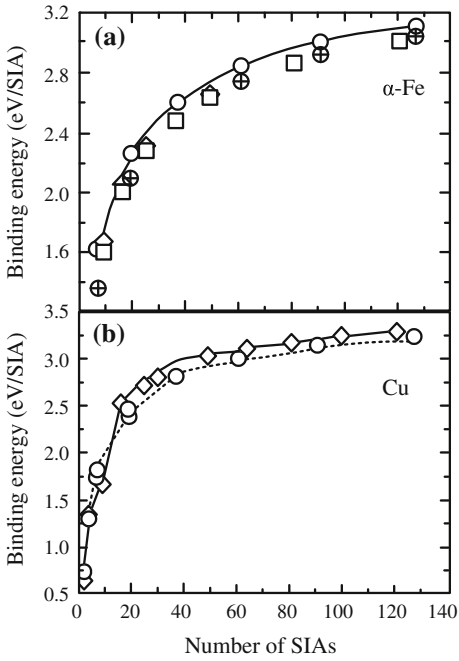

Fig. 7.45 Binding energy for SIA loops of different shapes and Burgers vectors (**a**) in α-Fe and (**b**) in copper (after [13])

The stability of vacancy clusters is low relative to interstitial clusters. The most stable configurations for vacancy clusters in α-Fe are either a set of divacancies concentrated on two adjacent {100} planes, or a set of first nearest neighbor vacancies on a {110} plane. During cluster growth, the first type results in a perfect dislocation loop with Burgers vector ⟨100⟩ and the second unfaults into a perfect loop with Burgers vector 1/2⟨111⟩. Vacancy loops can also exist in the faulted configuration. The loops will generally unfault to form perfect loops when the number of vacancies reaches about 40 [12].

In fcc Cu, the most stable configurations of a vacancy cluster are the SFT and faulted clusters on {111} planes that form Frank loops with Burgers vector 1/3 ⟨111⟩. Binding energies of the various vacancy configurations in α-Fe and Cu are shown in Fig. 7.48(a, b). Note that the binding energy of vacancies in the cluster is much less than that for interstitials shown in Fig. 7.45(a, b). The binding energy per defect for a four-defect cluster is less than 0.4 eV for vacancies, but is about 1.2 eV for interstitials. Observation by transmission electron microscopy [18] reveals that vacancy dislocation loops and SFT a few nanometers in size are formed by cascades in many metals (Fig. 7.49).

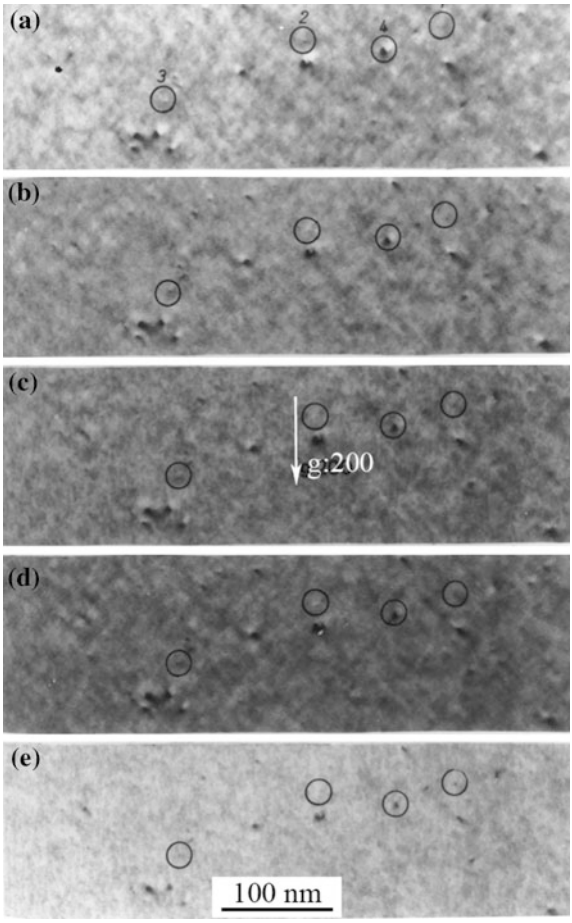

Fig. 7.46 Micrograph of interstitial clusters and small interstitial loops in copper irradiated with 30 keVCu^{+}. Defects are highlighted by the circles on the micrographs (after [17])

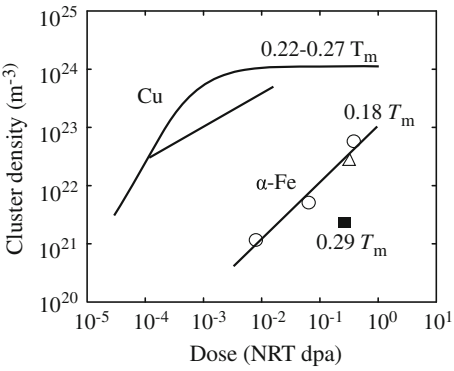

Fig. 7.47 Dose dependence of cluster densities measured in α-iron and copper irradiated with fission neutrons at temperatures below 0.3 T_m (after [13])

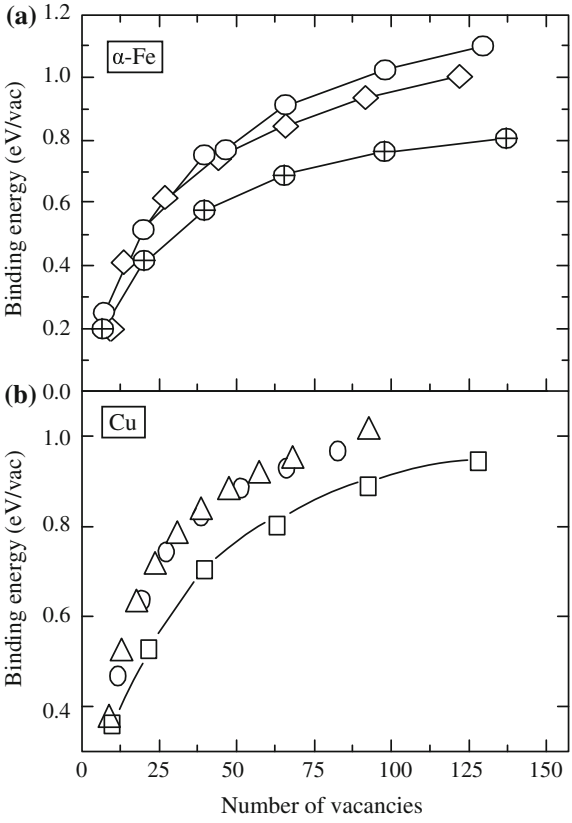

Fig. 7.48 Binding energy of vacancy loops of different shapes and Burgers vectors in (**a**) α-Fe and (**b**) copper (after [13])

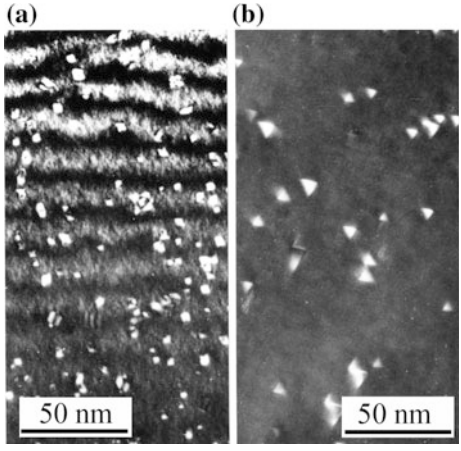

Fig. 7.49 Transmission electron micrograph of (**a**) defect clusters in gold irradiated to 1.1×10^{22} n/m^2 at 200 °C and (**b**) stacking fault tetrahedra in silver irradiated to 4.4×10^{21} n/m^2 at 400 °C (after [18])

7.3.3 *Cluster Mobility*

SIA created in the collision cascades of energetic recoil atoms in metals can form as crowdions and clusters of coupled crowdions along close-packed directions. These crowdions and clusters (essentially small, perfect dislocation loops) can migrate in one-dimensional (1D) random walks by thermally activated glide with a very low activation energy (< 0.1 eV) [19]. Movie 7.1 (http://rmsbook2ed.engin.umich.edu/movies/) shows cluster formation and 1D glide in UHP iron irradiated with 150 keV Fe ions at 400 °C. Clusters are just beginning to nucleate in this real-time recording shown at 2× actual time. Compared to defects migrating in 3D, the SIA and SIA clusters migrating in 1D have a much smaller probability of interacting with other defects within the cascade region. Clusters migrating by 1D glide can change their Burgers vectors by thermal activation or by interaction with another defect and continue their 1D glide along another close-packed direction. The result is a 3D diffusion path that is made up of segments of 1D glide, which is referred to as "mixed 1D/3D" defect migration and shown in Fig. 7.50.

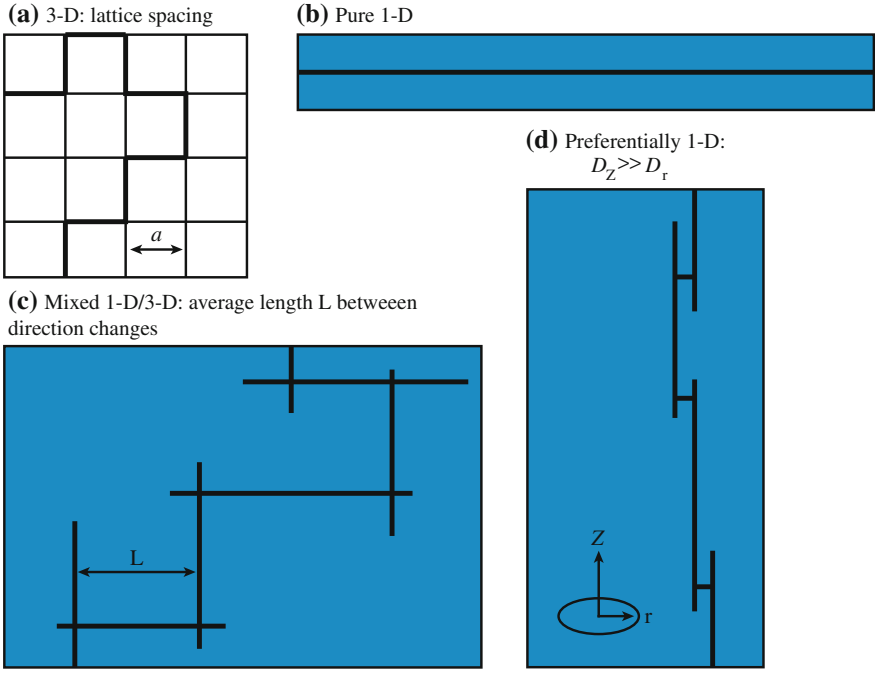

Fig. 7.50 Schematic illustration of defect migration paths by (**a**) 3D random walk on the crystal lattice, (**b**) 1D random walk, (**c**) mixed 1D/3D migration consisting of a 3D path made up of segments of 1D random walks in different random close-packed directions, and (**d**) preferential 1D migration consisting of segments of 1D random walks in the same direction broken by occasional hops to adjacent atom rows (after [20])

However, not all clusters are glissile. Besides stable, faulted Frank loops, SIAs may form metastable arrangement of SIAs that do not reorganize into a stable, glissile form by the end of the thermal spike. They are significant because if they do not migrate away from the cascade, they may act as nucleation sites for the growth of extended defects. Figure 7.42 indicates that the fraction of SIA clusters in a metastable sessile configuration by the end of the thermal spike phase is between 10 and 30 %. The form of these clusters varies with crystal structure. In hcp metals, small sessile clusters form a triangular arrangement of closely packed atoms on the basal plane. In α-iron, three SIAs can form a triangle that is parallel to but displaced from the {111} plane. If clusters form as faulted dislocation loops, such as $\boldsymbol{b} = 1/3\langle 111\rangle$ in fcc, $1/2\langle 110\rangle$ in bcc, and $1/2\langle 0001\rangle$ in hcp, then they are intrinsically sessile and cannot exhibit glide. The ability to move arises from the clustered crowdion form of these extended defects. They have a form best described as small perfect interstitial dislocation loops with Burgers vector $\boldsymbol{b} = 1/2\langle 110\rangle$ in fcc, $1/2\langle 111\rangle$ and $\langle 100\rangle$ in bcc, and $1/3\langle 11\bar{2}0\rangle$ in hcp. Table 7.1 summarizes the Burgers vectors of the glissile and sessile dislocation loops formed by vacancy and interstitial clusters.

Mobile clusters can interact with other clusters or with impurity atoms such as helium. The behavior of small interstitial clusters in the presence of impurity helium atoms and vacancies is illustrated in Movies 7.2–7.4 (http://rmsbook2ed.engin.umich.edu/movies/). In Movie 7.2, a SIA (green spheres) in bcc iron interacts with two substitutional He (light blue spheres) atoms and the interaction leads to recombination and ejection of the He into an interstitial position from which it migrates and traps the other He substitutional atom. Movie 7.3 shows the interaction between a 6-SIA cluster and three substitutional He atoms. In this case, recombination and He ejection occurs with two of the three He atoms resulting in a cluster consisting of 4-SIA and one interstitial He atom, and a cluster consisting of one interstitial He and one substitutional He. Movie 7.4 shows the interaction between a 6-SIA cluster and a 4-He/6-vacancy cluster. Vacancies are denoted by the red spheres. The interaction causes the recombination and rejection of He resulting in a 4-He/1-SIA cluster.

Table 7.1 Summary of Burgers vectors of glissile and sessile loops in fcc, bcc, and hcp lattices (after [10])

Crystal structure	Burgers vector	Cluster mobility
fcc	$\boldsymbol{b} = 1/2\langle 110\rangle$	Glissile
	$\boldsymbol{b} = 1/3\langle 111\rangle$	Sessile
	SFT (vacancy)	Sessile
bcc	$\boldsymbol{b} = 1/2\langle 111\rangle, \langle 100\rangle$	Glissile
	$\boldsymbol{b} = 1/2\langle 110\rangle$	Sessile
hcp	$\boldsymbol{b} = 1/3\langle 11\bar{2}0\rangle$	Glissile
	$\boldsymbol{b} = 1/2\langle 10\bar{1}0\rangle, 1/2\langle 0001\rangle$	Sessile

The majority of SIA clusters are glissile. Di- and tri-interstitial clusters in both α-iron and copper undergo one-dimensional glide along the crowdion direction [13]. In these small clusters, the crowdion can rotate such that glide occurs in an equivalent direction. This rotation results in essentially three-dimensional motion. The rotation frequency is lower for tri-interstitials and increases with temperature for both defects. Larger clusters are essentially perfect dislocation loops with a Burgers vector along the crowdion axis, so that their movement can be considered as thermally assisted glide in one dimension. Figure 7.51 shows 19- and 91-interstitial clusters in α-iron. Both loops extend over six (220) planes as shown in the figures at the right of each cluster. The motion of these clusters is one-dimensional and along ⟨111⟩. A feature of cluster motion is that the effective correlation factor is greater than unity, i.e., a cluster that has moved one step has a high probability of making the next step in the same direction. Movie 7.5 is an MD simulation of a 19-SIA cluster in bcc iron at 287 °C. The cluster exhibits one-dimensional motion in the direction of the Burgers vector.

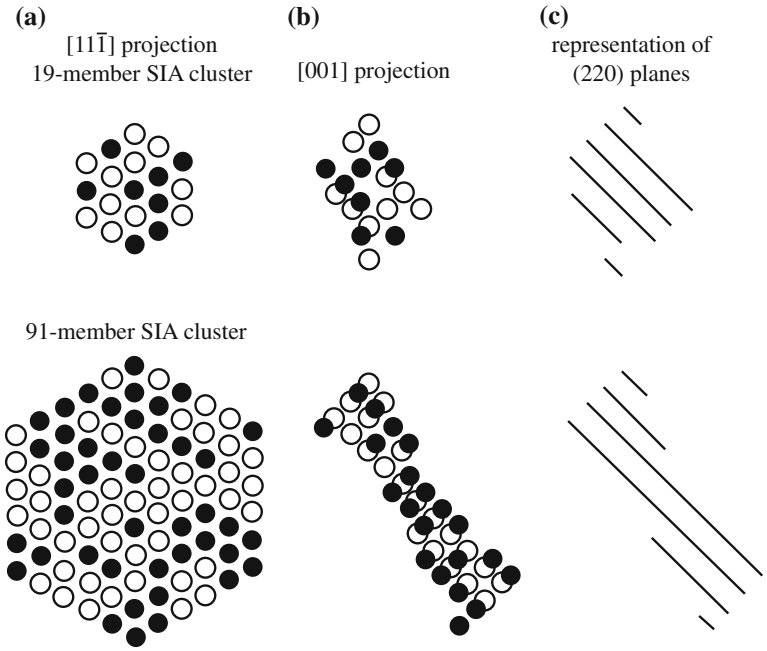

Fig. 7.51 A 19- and 91-interstitial cluster in (**a**) [11$\bar{1}$] and (**b**) [001] projections. Filled and open circles represent the centers of mass of ⟨111⟩ crowdions and split dumbbells, respectively. (**c**) Additional (220) lattice planes occupied by the clusters (after [21])

The activation energy for cluster motion is between 0.022 and 0.026 eV in α-iron and between 0.024 and 0.030 eV in copper [13]. The activation energy is weakly dependent on the size of the cluster, allowing the cluster jump frequency to be expressed as:

$$\nu_n = \nu_0 n^{-s} \exp(-\langle E_\mathrm{m} \rangle / kT), \tag{7.56}$$

where $\langle E_\mathrm{m} \rangle$ is the average effective activation energy, ν_0 is the size-independent, pre-exponential factor, and the term n^{-S} is the cluster size dependence, where a value of ~ 0.65 for s describes the cluster size dependence of the pre-exponential factor for both α-iron and copper. Figure 7.52 shows the total pre-exponential factor as a function of cluster size. This dependence is likely due to enhanced focusing of the crowdion configuration for SIAs in a cluster, which results in increased probability of successive jumps.

Observations have shown that the mobility of clusters depends on the composition. When chromium is added to iron, cluster mobility is significantly reduced. Movie 7.6 shows a comparison of loop hopping in UHP Fe and Fe-8 %Cr under the same irradiation conditions of 150 keV Fe ions at 300 °C. Note that 1D loop motion is evident in pure iron, but relatively rare in Fe-8 %Cr.

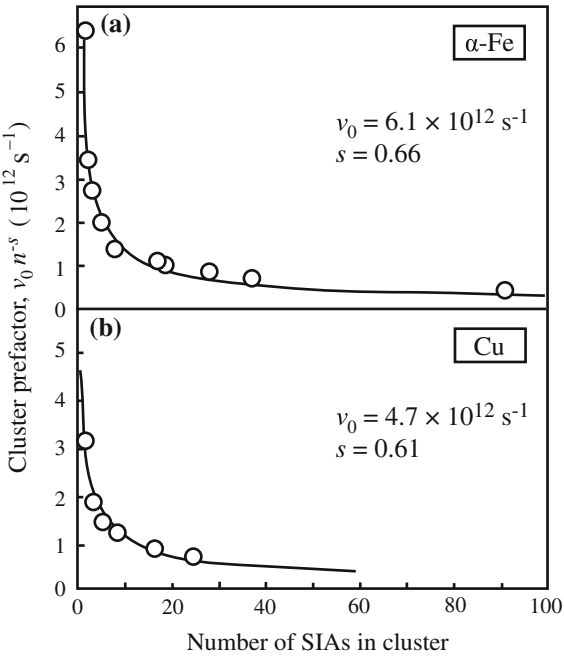

Fig. 7.52 Size dependence of the pre-exponential factor in Eq. (7.56) in (**a**) α-Fe and (**b**) Cu (after [13])

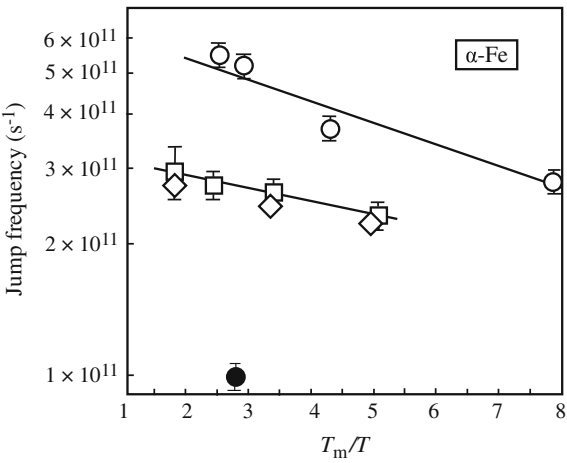

Fig. 7.53 Jump frequency versus reciprocal temperature for vacancy loops (*squares* and *diamonds*) and SIA loops (*circles*) in Fe at 375 °C (after [13])

Vacancy clusters that form perfect dislocation loops are also intrinsically glissile. MD simulation shows that the mobility of perfect vacancy loops with $\boldsymbol{b} = 1/2\langle 110\rangle$ and $1/2\langle 111\rangle$ in Cu and α-iron, respectively, is only slightly lower than that of a cluster of the same number of interstitial crowdions [13]. The result is shown in Fig. 7.53 for a 37-defect cluster. As long as they are in the form of perfect loops, they are mobile. Vacancy clusters that do not collapse to a dislocation structure or that form a Frank loop or SFT are immobile.

7.4 Extended Defects

As described in the previous sections, vacancies and interstitials can cluster to form other types of defects that will be important in defining the effect of irradiation on both physical and mechanical properties of the solid. In principle, a cluster of point defects could be one-dimensional (a line), two-dimensional (a disk), or three-dimensional (a void). Vacancies and interstitials that cluster in numbers greater than those discussed earlier will agglomerate into specific configurations in the crystal lattice. In particular, they will take up the minimum energy configuration, which in three dimensions is a void and in two dimensions is a loop or platelet with a thickness of magnitude equal to one Burgers vector and lying between adjacent close-packed planes.

It may be envisioned that following the radiation damage event, the core of the displacement spike collapses (or the vacancies condense) onto the {111} plane, forming a vacancy disk. The energy of the disk can be written as:

$$E_d = 2\pi r_d^2 \gamma, \tag{7.57}$$

where r_d is the disk radius, and γ is the surface energy of the metal. For a small number of vacancies, the aggregate form with the least energy is the spherical void. The energy of the spherical void of radius r_V is:

$$E_V = 4\pi r_V^2 \gamma. \tag{7.58}$$

If Ω is the atomic volume, then the number of vacancies in the void is as follows:

$$n_v = \frac{4}{3}\frac{\pi r_V^3}{\Omega}. \tag{7.59}$$

The energy of the void written in terms of the number of vacancies, n_v, is as follows:

$$E_V = 4\pi\left(\frac{3n_v\Omega}{4\pi}\right)^{2/3}\gamma = (6n_v\Omega\sqrt{\pi})^{2/3}\gamma. \tag{7.60}$$

For a large number of vacancies, the planar loop is a more stable configuration and this will be discussed shortly.

Another possible configuration of a cluster of vacancies is the SFT as described in Sect. 7.2. The energy of the SFT is given by [4, 22, 23]:

$$E_{SFT} = \frac{\mu L b^2}{6\pi(1-v)}\left[\ln\left(\frac{4L}{a}\right) + 1.017 + 0.97v\right] + \sqrt{3}L^2\gamma_{SFE}, \tag{7.61}$$

where v is Poisson's ratio, a is the lattice parameter, γ_{SFE} is the energy of the stacking fault, and L is the length of the edge of the tetrahedron and $L = a(n_v/3)^{1/2}$.

A similar process involving interstitial condensation may occur around the edges of the depleted zone where high interstitial concentrations may exist. The condensation of interstitials onto a close-packed plane produces an extra layer of atoms and two breaks in the stacking sequence, as described in Sect. 7.2. For a disk of radius r_L, the energy of a faulted loop (vacancy or interstitial) is as follows:

$$E_L = 2\pi r_L \Gamma + \pi r_L^2 \gamma_{SFE}, \tag{7.62}$$

where the first term is the energy of the dislocation line, the second term is the energy associated with the stacking fault, and Γ is the energy per unit length of dislocation line. In the fcc lattice, faulted loops lie on the {111} planes, which have an atom density of $4/\sqrt{3}a^2$, or an area per atom of $\sqrt{3}a^2/4$. So the radius of a loop consisting of n vacancies (or interstitials) is as follows:

$$r_L = \left(\frac{\sqrt{3}a^2 n}{4\pi}\right)^{1/2}. \tag{7.63}$$

Approximating Γ with μb^2, Eq. (7.32b) where μ is the shear modulus and b is the Burgers vector, Eq. (7.62) becomes:

$$E_{\mathrm{L}} = 2\pi\mu b^2\left(\frac{\sqrt{3}a^2 n}{4\pi}\right)^{1/2} + \pi\left(\frac{\sqrt{3}a^2 n}{4\pi}\right)\gamma_{\mathrm{SFE}}. \tag{7.64}$$

More precise expressions for the energy of faulted and perfect loops are given in [4, 6, 22–24], and from [24], the energy of the faulted Frank loop is as follows:

$$E_{\mathrm{F}} = \frac{2}{3}\frac{1}{(1-\nu)}\mu b^2 r_{\mathrm{L}} \ln\left[\frac{4r_{\mathrm{L}}}{r_{\mathrm{c}}} - 2\right] + \pi r_{\mathrm{L}}^2 \gamma_{\mathrm{SFE}}. \tag{7.65}$$

The energy of a perfect loop [18] is as follows:

$$E_{\mathrm{P}} = \frac{2}{3}\frac{1}{(1-\nu)} + \frac{1}{3}\left(\frac{2-\nu}{2(1-\nu)}\right)\mu b^2 r_{\mathrm{L}} \ln\left[\frac{4r_{\mathrm{L}}}{r_{\mathrm{c}}} - 2\right], \tag{7.66}$$

where r_{c} is the dislocation core radius. Equations (7.65) and (7.66) refer to both interstitial and vacancy loops, and from these equations, the difference in energy between a perfect loop and a Frank loop is as follows:

$$\Delta E = \pi r_{\mathrm{L}}^2 \gamma_{\mathrm{SFE}} - \frac{1}{3}\left(\frac{2-\nu}{2(1-\nu)}\right)\mu b^2 r_{\mathrm{L}} \ln\left[\frac{4r_{\mathrm{L}}}{r_{\mathrm{c}}} - 2\right]. \tag{7.67}$$

Therefore, unfaulting is favorable if:

$$\gamma_{\mathrm{SFE}} > \frac{\mu b^2}{3\pi r_{\mathrm{L}}}\left(\frac{2-\nu}{2(1-\nu)}\right) \ln\left[\frac{4r_{\mathrm{L}}}{r_{\mathrm{c}}} - 2\right]. \tag{7.68}$$

Equations for a disk, void, perfect loop, faulted loop, and SFT are plotted in Fig. 7.54(a, b) for 316 stainless steel and zirconium, respectively. The values of the material parameters are provided in the caption. Note that in general faulted defects are more stable in zirconium than in stainless steel, and voids are more stable in stainless steel than in zirconium. In stainless steel, voids are stable to relatively large sizes and the energy of the faulted loop remains below that of the perfect loop to large defect sizes. In zirconium, faulted loops and SFTs are more stable than voids. The high susceptibility to void swelling in stainless steel and the absence of voids in zirconium are in qualitative agreement with the formation energies for these extended defects according to Fig. 7.54.

Since we have just shown that the void is a stable configuration only for small numbers of vacancies, how then can we observe large voids with the number of vacancies exceeding several orders of magnitude? It is well established that for most metals, irradiation at low temperatures ($<0.2T/T_{\mathrm{m}}$) results in aggregation of vacancies and interstitials to form clusters that are bound by dislocations, i.e., loops

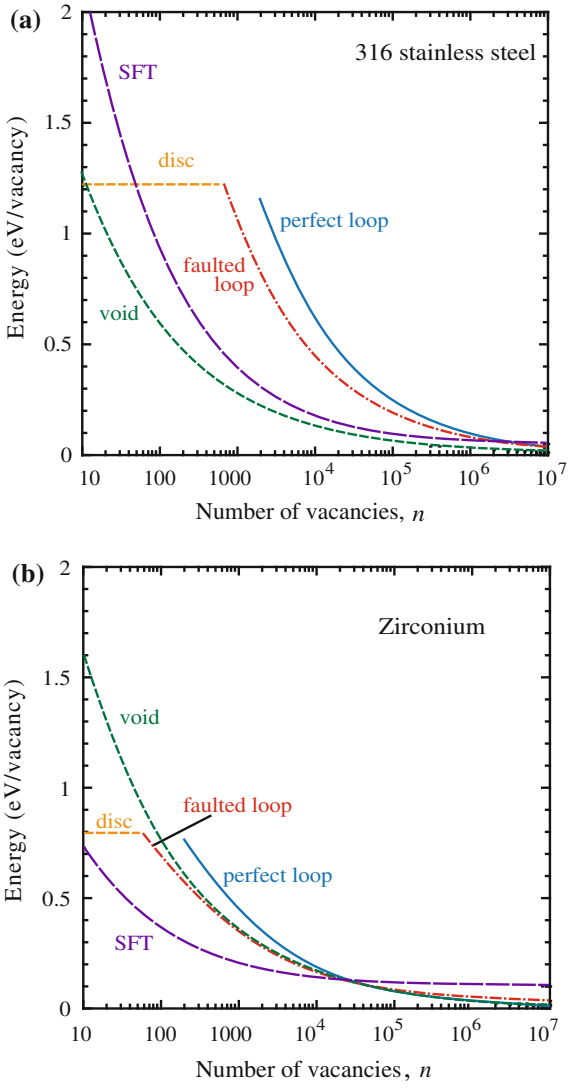

Fig. 7.54 Formation energy for various vacancy cluster defects in (**a**) 316 stainless steel and (**b**) zirconium as a function of the log of the number of vacancies in the cluster. Material parameters for stainless steel are $\gamma_{SFE} = 35$ mJ/m^2, $\gamma = 1.75$ J/m^2, and $\mu = 82$ GPa. Material parameters for zirconium are $\gamma_{SFE} = 102$ mJ/m^2, $\gamma = 1.40$ J/m^2, and $\mu = 33$ GPa

and SFT (in metals with low SFE). At higher temperatures, vacancies can also aggregate to form voids. Voids appear in a band of temperatures ranging from about $1/3 < T/T_m < 1/2$ where insoluble gases such as helium have a strong effect on stabilizing voids. At temperatures less than $1/3T/T_m$, vacancies are not mobile enough to reach the voids before annihilation with migrating interstitials. Also, loops formed by vacancy collapse of cascades are stable against thermal dissociation at low temperatures and hence reduce the number of vacancies available for void growth. At very high temperature, the thermal equilibrium vacancy concentration becomes comparable with the radiation-induced vacancy concentration and

voids tend to shrink by vacancy emission. The subject of void and bubble nucleation and growth will be discussed in more detail in Chap. 8.

7.5 Effective Defect Production

With a better understanding the importance of defect clusters, we can expand and refine our description of defect production. Microstructure evolution is ultimately controlled by the migrating defect fractions of vacancies and interstitials, $MDF_{v,i}$. The most straightforward component of the MDF is the isolated point defect fraction, $IDF_{v,i}$ (discussed in Chap. 3), which is produced directly in the displacement cascade. A second component is the mobile cluster fraction, $MCF_{i,v}$ (discussed in Sect. 7.3.3) and is composed of mobile interstitial defect clusters and mobile vacancy clusters. The third component is defects released from clusters by evaporation, $EDF_{v,i}$, and is most important for vacancies and interstitials at very high temperatures. Taken together, these three sources of isolated defects comprise the migrating defect fraction, $MDF_{v,i}$. Zinkle and Singh [25] constructed a flowchart to show the evolution of the various defect forms (Fig. 7.55), which is an expansion of the more simplistic case shown in Fig. 3.18 by inclusion of the processes in dashed boxes. Zinkle and Singh summarized experiments from which values for $MDF_{v,i}$ could be determined and found that in general $3\ \% < MDF_i < 10\ \%$ and $1\ \% < MDF_v < 10\ \%$ where the percentages refer to the calculated NRT production rate. While there is considerable uncertainty regarding the quantitative values deduced from experiments, the range can be used to bound the expected available defect fraction.

The significance of these processes is that they are not often addressed in traditional rate theory models of microstructure evolution. To create an accurate physical model of defect production and accumulation under cascade damage conditions, the following must be included:

1. The production of a large fraction of defects heterogeneously in the form of vacancy and interstitial clusters with the remainder as isolated vacancies and interstitials
2. The bias for absorption of mobile interstitial clusters and freely migrating interstitials at sinks
3. The fractions of interstitials and vacancies in clustered or isolated forms that are not necessarily equal, which is equivalent to an asymmetric production of freely migrating fractions of vacancies and interstitials
4. Vacancy evaporation from clusters formed during the cascade quench that results in a temperature-dependent contribution to the fraction of freely migrating vacancies

As will be shown in subsequent sections and in the discussion of void formation and growth in Chap. 8, intracascade clustering and the thermal stability of interstitial and vacancy clusters cause an *asymmetry* in the supply of migrating

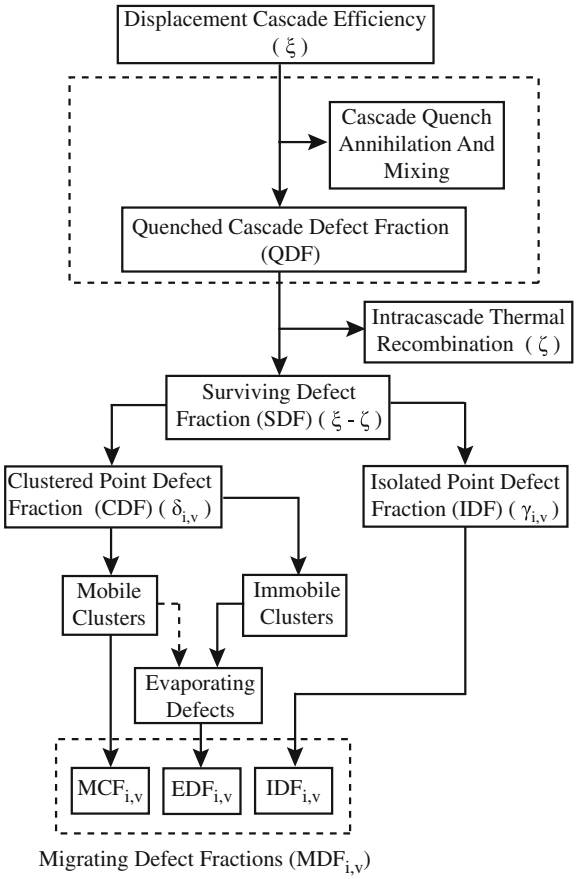

Fig. 7.55 Flowchart giving the contributions to the migrating defect fraction from isolated defects, mobile defect clusters, and evaporating defects (after [25])

vacancies and interstitials, termed the *production bias* and this bias represents a strong driving force for loop and void nucleation and growth.

7.6 Nucleation and Growth of Dislocation Loops

Dislocation loops resulting from vacancy and interstitial condensation are created from clusters of the respective defects and either shrink or grow depending on the flux of defects reaching the embryo. Once they have reached a critical size, the loops become stable and grow until they unfault by interaction with other loops or with the network dislocation density. The following sections describe the processes of loop nucleation, growth, and unfaulting that determine the dislocation microstructure of a metal under irradiation.

7.6.1 Loop Nucleation

Various attempts have been made to determine the nucleation rate of dislocation loops and voids. We will follow a treatment that is based on steady-state concentrations of vacancies and interstitials and assumes dilute solution thermodynamics, as developed by Russell et al. [26]. In this treatment, the effects of cascades are ignored. We will then introduce clustering theory and show how it can be applied to the loop nucleation problem to account for the formation of defect clusters in addition to point defects.

We begin by expressing the nucleation rate of a defect cluster of size n as the flux of clusters between adjacent size classes in a phase space of cluster size. Considering only one type of defect (vacancies, for example), the flux between any two adjacent size classes can be written as follows:

$$J_n = \beta_v(n)\rho(n) - \alpha_v(n+1)\rho(n+1), \tag{7.69}$$

where $\rho(n)$ and $\rho(n+1)$ are the numbers of n-mers (loops containing n vacancies) and $(n+1)$-mers per unit volume. $\beta_v(n)$ is the rate of vacancy capture by a n-mer, and $\alpha_v(n+1)$ is the rate of vacancy loss by a $(n+1)$-mer. The first term in Eq. (7.69) represents an addition to the $n+1$ size class by capture of a vacancy by a n-mer size class. The second term is a loss from the $(n+1)$-mer size class by emission of a vacancy. Figure 7.56 shows the various processes described by Eq. (7.69) in phase space. At steady state, $J_n = 0$ and Eq. (7.69) becomes the following:

$$\sigma_v(n+1) = \beta_v(n)\frac{\rho^0(n)}{\rho^0(n+1)}, \tag{7.70}$$

where $\rho^0(n)$ is the equilibrium concentration of n-mer vacancy loops. Substituting for $\alpha_v(n+1)$ from Eq. (7.69) into the expression for the nucleation rate, Eq. (7.70) yields the following:

$$\begin{aligned} J_n &= \beta_v(n)\left[\rho(n) - \rho(n+1)\frac{\rho^0(n)}{\rho^0(n+1)}\right] \\ &= -\beta_v(n)\rho^0(n)\left[\frac{\rho(n+1)}{\rho^0(n+1)} - \frac{\rho(n)}{\rho^0(n)}\right], \end{aligned} \tag{7.71}$$

and the term in brackets is just the derivative of the ratio $\rho(n)/\rho^0(n)$, or $\dfrac{\partial[\rho(n)/\rho^0(n)]}{\partial n}$. The nucleation rate then becomes:

$$J_n = -\beta_v(n)\rho^0(n)\frac{\partial[\rho(n)/\rho^0(n)]}{\partial n}, \tag{7.72}$$

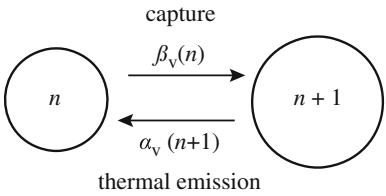

Fig. 7.56 Illustration of the capture and emission processes governing the flux of clusters between adjacent size classes in a phase space of cluster size

where

$$\rho^0(n) = N_0 \exp\left(-\Delta G_n^0/kT\right), \tag{7.73}$$

and N_0 is the number of nucleation sites per unit volume, and ΔG_n^0 is the free energy of forming the n-mer vacancy loop.

The steady-state nucleation rate of vacancy loops (consisting of k vacancies) can also be described as the product of the loop concentration, the jump frequency of the vacancy to the loop, and the jump distance, and is given by:

$$J_k = \rho_k^0 \beta_k Z, \tag{7.74}$$

where ρ_k^0 and β_k are the values of $\rho^0(n)$ and $\beta_v(n)$ at the critical size, k, and Z is the Zeldovich factor that depends on the curvature of ΔG_n^0 near the maximum, at the critical size. If ΔG_n^0 is approximated by a parabola in this region (lower curve in Fig. 7.57), then:

$$Z = \left[-\frac{1}{2\pi kT}\frac{\partial^2 \Delta G_n^0}{\partial n^2}\right]_{n_k}^{1/2}, \tag{7.75}$$

where the derivative is evaluated at the critical loop size, n_k. Its value is the width of ΔG_k^0 at kT units below the maximum and is on the order of 0.05.

Consider now the presence of interstitials in the vacancy loop nucleation formulation. The flux between any two size classes, say n and $n + 1$, now becomes the following:

$$J_n = \beta_v(n)\rho(n) - \alpha_v(n+1)\rho(n+1) - \beta_i(n+1)\rho(n+1), \tag{7.76}$$

where all terms are as previously defined, and $\beta_i(n + 1)$ is the rate of interstitial capture by a $(n + 1)$-mer. Interstitial emission is of low probability and is neglected. Figure 7.58 shows the various processes described by Eq. (7.76) in phase space.

The rate of vacancy emission from a vacancy loop will be governed by temperature, size, and lattice energetics. Since the defect fractions are as high as 10^{-4}, a cluster has a defect in its immediate vicinity only this small fraction of time.

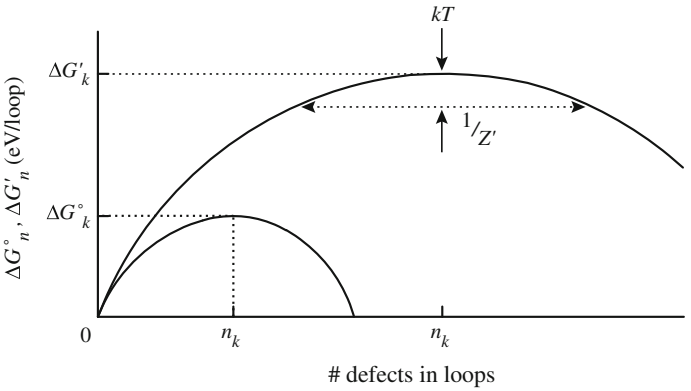

Fig. 7.57 Schematic nucleation curves showing the various parameters which are important in cluster nucleation. ΔG_k^0 is the activation barrier to nucleation if interstitials are not present, while $\Delta G_k'$ is the same quantity if interstitials are present during the vacancy cluster nucleation process (after [26])

The emission probability should be affected only slightly during this time interval and not at all otherwise. Therefore, we conclude that α_v is a value characteristic of a system without interstitials. Setting $J = 0$ in Eq. (7.76) is equivalent to equilibrating the size classes since there is no net flux between size classes. If we neglect interstitials, then from Eq. (7.76) we can write as follows:

$$\alpha_v(n+1) = \frac{\beta_v(n)\rho^0(n)}{\rho^0(n+1)}. \tag{7.77}$$

Combining Eqs. (7.76) and (7.77) gives:

$$J_n = \beta_v(n)\left\{\rho(n) - \rho(n+1)\left[\frac{\rho^0(n)}{\rho^0(n+1)} + \frac{\beta_i(n+1)}{\beta_v(n)}\right]\right\}. \tag{7.78}$$

Since $\rho^0(n) = N_0 \exp(-\Delta G_n^0/kT)$, we note that:

$$\frac{\rho^0(n)}{\rho^0(n+1)} = \exp\left(\frac{\delta G_n^0}{kT}\right), \tag{7.79}$$

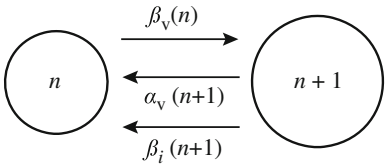

Fig. 7.58 Illustration of the capture and emission processes governing the flux of clusters between adjacent size classes in a phase space of cluster size and including the effect of interstitial capture

where $\delta G_n^0 \equiv \Delta G_{n+1}^0 - \Delta G_n^0$. The term δG_n^0 is the difference between the free energies of creating loops of $j + 1$ and j vacancies from single vacancies at the prevailing supersaturation. We now define new functions of n, $\rho'(n)$, and $\delta G_n'$ such that by analogy with Eq. (7.79):

$$\frac{\rho'(n)}{\rho'(n+1)} = \frac{\rho^0(n)}{\rho^0(n+1)} + \frac{\beta_i(n+1)}{\beta_i(n)} = \exp(\delta G_n'/kT), \tag{7.80}$$

where

$$\delta G_n' = \Delta G_{n+1}' - \Delta G_n', \tag{7.81}$$

and $\Delta G_n'$ is not generally a free energy because of the term $\dfrac{\beta_i(n+1)}{\beta_i(n)}$ in Eq. (7.80). Using the expression in Eq. (7.80), we can rewrite the equation for J_n in terms of $\dfrac{\rho'(n)}{\rho'(n+1)}$ by substituting Eqs. (7.80) into (7.78) to give the following:

$$J_n = \beta_v(n)\left\{\rho(n) - \rho(n+1)\frac{\rho'(n)}{\rho'(n+1)}\right\}. \tag{7.82}$$

Rearranging Eq. (7.82) gives the following:

$$J_n = -\beta_v(n)\rho'(n)\frac{\rho(n+1)}{\rho'(n+1)} - \left[\frac{\rho(n)}{\rho'(n)}\right], \tag{7.83}$$

and noting that:

$$\frac{\left[\dfrac{\rho(n+1)}{\rho'(n+1)} - \dfrac{\rho(n)}{\rho'(n)}\right]}{\Delta n} = \frac{\partial\left(\dfrac{\rho(n)}{\rho'(n)}\right)}{\partial n}, \tag{7.84}$$

gives:

$$J_n = -\beta_v(n)\rho'(n)\frac{\partial[\rho(n)/\rho'(n)]}{\partial n}, \tag{7.85}$$

which is the basic flux equation. Rearranging Eq. (7.85) by taking the natural log of both sides and summing from $j = 0$ to $n - 1$ gives the following:

$$\sum_{j=0}^{n-1} \ln\left(\frac{\rho'(j)}{\rho'(j+1)}\right) = \sum_{j=0}^{n-1}\left\{-\ln\left[\frac{\beta_i(j+1)}{\beta_v(j)} + \exp\left(\frac{\delta G_j^0}{kT}\right)\right]\right\}, \tag{7.86}$$

and

$$\ln\left(\frac{\rho'(n)}{\rho'(0)}\right) = \sum_{j=0}^{n-1}\left\{-\ln\left[\frac{\beta_i(j+1)}{\beta_v(j)} + \exp\left(\frac{\delta G_j^0}{kT}\right)\right]\right\}. \tag{7.87}$$

We can identify two boundary conditions. The first is the quantity $\rho'(0)$, which may be evaluated by noting that as $\beta_i(n)/\beta_v(n) \to 0, \rho'(0) = \rho^0(0)$ and that $\rho^0(0) \to N_0$, is simply the number of nucleation sites per unit volume. Since N_0 (and hence $\rho'(0)$) is independent of loop concentration, we can write the equation as follows:

$$\ln\left(\frac{\rho'(n)}{\rho'(0)}\right) = \sum_{j=0}^{n-1}\left\{-\ln\left[\frac{\beta_i(j+1)}{\beta_v(j)} + \exp\left(\frac{\delta G_j^0}{kT}\right)\right]\right\} = \frac{-\Delta G_n'}{kT}, \tag{7.88}$$

and

$$\Delta G_n' = kT\sum_{j=0}^{n-1}\ln\left[\frac{\beta_i(j+1)}{\beta_v(j)} + \exp\left(\frac{\delta G_j^0}{kT}\right)\right]. \tag{7.89}$$

Since $\beta_i(n)/\beta_v(n) \to 0, \rho'(0) \to \rho^0(0)$ and $\rho^0(0)$ is just N_0, the number of nucleation sites per unit volume, we have then:

$$\rho'(n) = N_0 \exp\left(\frac{-\Delta G_n'}{kT}\right), \tag{7.90}$$

and

$$\Delta G_n^0 = \text{activation barrier without interstitials}$$
$$\Delta G_n' = \text{activation barrier with interstitials.}$$

The upper curve in Fig. 7.57 shows $\Delta G_n'$ as functions of n. Note that $\Delta G_n'$ is larger than ΔG_k^0 and requires a larger loop size due to the hindering effect of interstitials on the loop nucleation process. The maxima in the two curves occur at n_k, ΔG_k^0 and n_k', $\Delta G_k'$.

Now, the steady-state loop nucleation rate may be calculated from the expression for J_n in Eq. (7.85):

$$J_k = Z'\beta_k\rho_k', \tag{7.91}$$

which is the rate at which loops escape over the potential barrier of height $\Delta G'_k$ in units of loops/cm^3 s. The term, β_k, is the rate of single vacancy impingement on a loop of size n'_k The term Z' is:

$$Z' = \left[-\frac{1}{2\pi kT} \frac{\partial^2 \Delta G'_n}{\partial n^2} \right]^{1/2}_{n'_k}. \tag{7.92}$$

The subscript indicates that the second derivative is to be evaluated at $n = n'_k$. As with Z in Eq. (7.75), its value is the width of $\Delta G'_k$ at kT units below the maximum and is of the order of 0.05. The second derivative is found from Eq. (7.69) to be:

$$\frac{1}{kT} \left(\frac{\partial^2 \Delta G'_n}{\partial n^2} \right)_{n'_k} = \left\{ \left[\frac{1}{kT} \frac{\partial^2 \Delta G^0_n}{\partial n^2} \right] \left[\exp\left(\frac{1}{kT} \frac{\partial \Delta G^0}{\partial n} \right) \right] \right\}_{n'_k}, \tag{7.93}$$

giving:

$$\rho'_k = N_0 \exp\left(-\Delta G'_k / kT\right), \tag{7.94}$$

where $\Delta G'_k$ is determined by evaluating Eq. (7.89) at n'_k.

The steady-state nucleation rate will not be established immediately after a sudden change in supersaturation or temperature, but will lag by a characteristic time, τ, known as the incubation time and is given by [26]:

$$\tau = 2(\beta_k Z'^2)^{-1}. \tag{7.95}$$

Equations (7.89) and (7.94) also apply for interstitial loop nucleation except that Z', $\beta_{k,}$ and ρ'_k are for interstitial loops rather than for vacancy loops, and $\Delta G'_n$ for interstitial loops is given as:

$$\Delta G'_n = kT \sum_{j=0}^{n-1} \ln \left[\frac{\beta_v (j+1)}{\beta_i (j)} + \exp\left(\frac{\delta G^0_j}{kT} \right) \right], \tag{7.96}$$

where δG^0_j is now the difference between the free energies of forming dislocation loops of $j+1$ and of j interstitials (in the absence of vacancies), β_k is the gross rate of interstitial capture by the loop of critical size, and $1/Z'$ is the width of $\Delta G'_n$ (for interstitials) a distance kT below the maximum at $\Delta G'_k$, and the net number of interstitials in the critical nucleus is denoted by n'_k. The critical loop size n'_k occurs at the maximum of $\Delta G'_n$ and is determined by solving $\partial \Delta G'_n / \partial n = 0$ for n'_k.

More recent treatments of the nucleation rate call for setting the all the fluxes in Eq. (7.69) equal to the steady-state flux, J_{ss}, leading to a family of equations [27]:

$$J_1 = \beta_v(1)\rho(1) - \alpha(2)\rho(2) = J_{ss} \tag{7.97}$$

$$J_2 = \beta_v(2)\rho(2) - \alpha(3)\rho(3) = J_{ss} \tag{7.98}$$

$$J_3 = \beta_v(3)\rho(3) - \alpha(4)\rho(4) = J_{ss} \tag{7.99}$$

$$\vdots$$

$$J_{n-1} = \beta_v(n-1)\rho(n-1) - \alpha(n)\rho(n), \tag{7.100}$$

where $n = n_v^{max}$. Letting the ratio of shrinkage to growth, $\alpha_k/\beta_v^k = r_k$ for all $k \leq 2$, and letting $r_1 = 1$, the system of equations can be solved by multiplying the equations for J_k by the product of all the r_k with $k \leq i$. That is, Eq. (7.98) is multiplied by r_2, Eq. (7.99) is multiplied by both r_2 and r_3. If the resulting set of equations is summed, all the r_k are eliminated except r_1 and r_n to yield:

$$J_1 = J_{SS} = \frac{\beta_v(1)\rho(1) - \alpha(n)\rho(n)\prod_{j=2}^{n-1} r_j}{1 + \sum_{k=2}^{n-1}\prod_{j=2}^{k} r_j}. \tag{7.101}$$

The product term in the numerator is eliminated by noting that (1) for a nucleation problem, the concentration of the monodefect, ρ (1) will be much greater than ρ (n), and (2) the ratio of the shrinkage to growth terms r_j is less than unity for $n > n_v^*$. Therefore, Eq. (7.101) becomes:

$$J_{SS} = \beta_v(1)\rho(1)\left[1 + \sum_{k=2}^{n-1}\prod_{j=2}^{k} r_j\right]^{-1}. \tag{7.102}$$

The advantage of this method to compute J_{ss} is the elimination of the Zeldovich factor and the approximations that must be made to compute it.

Russell [26] determined that based on vacancy and interstitial parameters and their likely supersaturations in a solid under irradiation, that interstitial loop nucleation is easier than vacancy loop nucleation because interstitial loop nucleation is much less sensitive to vacancy involvement than is vacancy loop nucleation to interstitial involvement. The primary reason is that S_i is expected to be several orders of magnitude greater than S_v during irradiation because of the very low equilibrium concentration of interstitials. Nevertheless, nucleation by this mechanism has been found to be difficult for both vacancy and interstitial loops, in contrast to the observation of stable loop growth after fairly low doses.

7.6.2 Clustering Theory

The nucleation of loops is essentially a clustering process in which enough of one type of defect needs to cluster, in the presence of the other type of defect, to result in a critical size embryo that will survive and grow. The cluster will shrink or grow depending on the net condensation rate of defects on clusters. Generalizing the description of cluster behavior in phase space given in the last section, and taking a vacancy loop as an example, vacancy clusters, v_j consisting of j vacancies will shrink or grow according to the following:

$$\begin{aligned}\frac{\mathrm{d}v_j}{\mathrm{d}t} = K_{0j} &- \sum_{n-1}^{\infty}[\beta_{\mathrm{v}_n}(j)+\beta_{i_n}(j)]v_j - \sum_{n=1}^{J}\alpha_{\mathrm{v}_n}(j)v_j \\ &+ \sum_{n=1}^{j-1}\beta_{\mathrm{v}_n}(j-n)v_{j-n} + \sum_{n=1}^{\infty}\beta_{i_n}(j-n)v_{j+n} \\ &+ \sum_{n=1}^{\infty}\alpha_{\mathrm{v}_n}(j+n)v_{j+n} + \text{additional loss terms},\end{aligned} \tag{7.103}$$

where β_{v_n} and β_{i_n} are the capture rates of migrating defect clusters v_n or i_n by a cluster of size v_j, and α_{v_n} is the corresponding emission or thermal dissolution rate. The first term on the RHS is the direct production of clusters of size j. The second term is the loss of clusters from size class j due to absorption of a vacancy or an interstitial cluster of size n, where $1 \le n < \infty$. The third term is the loss of clusters from size class j due to emission of vacancy clusters of size n. The fourth and fifth terms are the addition of clusters to size class j due to absorption of vacancy clusters by smaller size classes and the absorption of interstitial clusters by larger size classes. The sixth term is the addition of clusters to the size class j by loss of vacancy clusters from larger size classes and the "additional loss terms" allow for other mechanisms of contributing to the number of clusters in size class j.

Equation (7.103) can be solved numerically without further simplification. But for large clusters and long irradiation times, the number of equations required would be extremely large. A major simplification is to require clusters to grow or shrink by only the addition or loss of single point defects, resulting in:

$$\begin{aligned}\frac{\mathrm{d}v_j(t)}{\mathrm{d}t} = K_{0j} &+ \beta(j-1,j)v_{j-1}(t) + \alpha(j+1,j)v_{j+1}(t) \\ &- [\beta(j,j+1)+\alpha(j,j-1)]v_j(t), \quad j \ge 2.\end{aligned} \tag{7.104}$$

If it is assumed that j is a continuous variable and a Taylor series expansion is used in Eq. (7.104) to relate all functions to their values at size j, the simplified

description is a continuum diffusional approximation in size space, known as a *Fokker–Planck equation*:

$$\begin{aligned}\frac{\partial v_j(t)}{\partial t} &= K_{0j}(t) - \frac{\partial}{\partial j}\left\{v_j(t)[\beta(j,j+1) - \alpha(j,j-1)]\right\} \\ &\quad + \frac{1}{2}\frac{\partial^2}{\partial j^2}\left\{v_j(t)[\beta(j,j-1) + \alpha(j,j+1)]\right\},\end{aligned} \tag{7.105}$$

which is further simplified to:

$$\begin{aligned}\frac{\partial v_j(t)}{\partial t} &= K_{0j}(t) - \frac{\partial}{\partial j}F_{\mathrm{v}_j}v_j(t) + \frac{\partial^2}{\partial j^2}D_{\mathrm{v}_j}v_j(t) \\ &= K_{0j}(t) - \frac{\partial}{\partial j}\left(F_{\mathrm{v}_j}v_j(t) - \frac{\partial}{\partial j}D_{\mathrm{v}_j}v_j(t)\right).\end{aligned} \tag{7.106}$$

The first term on the RHS of Eq. (7.106) is the direct production rate of clusters of size j. The second term is the *drift* in size space driven by the excess condensation of one point defect type over another:

$$F_{\mathrm{v}_j} = (z_{\mathrm{v}}D_{\mathrm{v}}C_{\mathrm{v}} - z_iD_iC_i) \tag{7.107}$$

The drift term is responsible for the shift of the cluster size distribution to larger sizes. The drift term ensures that a large cluster will inevitably grow in a radiation field, but due to the evolving microstructure, the drift contribution is not constant with dose. Cluster evolution is also very sensitive to the ratio of the concentration of vacancies and interstitials, as F_{v} contains the difference in their contribution and can change sign. The result is that the sign of F_{v} depends on the overall microstructure.

The third term is the *diffusion* in size space and D_{v_j} is the irradiation-enhanced diffusion coefficient given by:

$$D_{\mathrm{v}_j} = \frac{1}{2}(z_{\mathrm{v}}D_{\mathrm{v}}C_{\mathrm{v}} + z_iD_iC_i). \tag{7.108}$$

The diffusion term causes the cluster size distribution to broaden with dose. The diffusion term accounts for the fact that two different clusters introduced at the same time at the same size may differ in size at a later time due to random encounters with point defects.

Algorithms for the approximate solution of Eq. (7.106) are discussed by Golubov et al. [28]. The features of the Fokker–Planck equation are illustrated in Fig. 7.59 for the development of the interstitial loop size distribution for 316 stainless steel with initial dislocation density of 10^{13} m^{-2}, irradiated at 550 °C at a dose rate of 10^{-6} dpa/s. Note that with increasing dose, the mean loop size increases [drift term in Eq. (7.106)] and the size distribution broadens [diffusion term in Eq. (7.106)]. As small clusters grow and their geometry changes, so does the capture efficiency for freely migrating defects. For very large cluster sizes, the

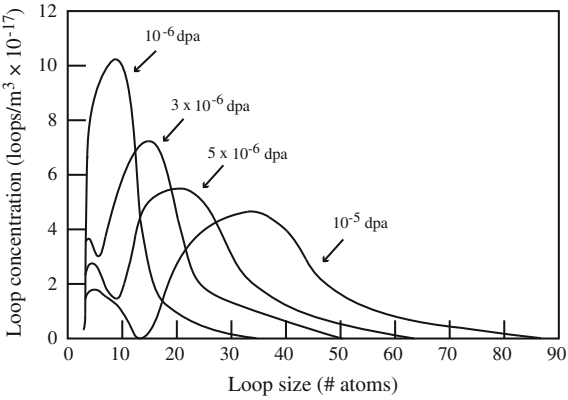

Fig. 7.59 Development of the interstitial loop size distribution with dose in 316 stainless steel irradiated at a dose rate of 10^{-6} dpa/s and a temperature of 550 °C with $\rho_d = 10^{13}$ m^{-2} (after [29])

Fokker–Planck equation is too simple as the defect production and cluster growth depend on the microstructure. The effect of the damage microstructure in the evolution of defect clusters must be accounted for in order to accurately predict their behavior.

7.6.3 Cluster Evolution Via Cluster Dynamics Modeling

The evolution of defect clusters can also be modeled using the cluster dynamics method. Classical rate theory defines a defect cluster by its character, atomic configuration, and size (or number of point defects contained within), but not by its spatial position since the theory assumes that the concentration of each cluster is homogeneous on a mean field basis. In cases such as shallow ion implantations, very thin specimens, or bulk specimens with inhomogeneous microstructure, the accurate treatment of spatially varying damage production or special effects such as surface sinks and dislocation interaction necessitates the inclusion of spatial dependence into rate theory-based models. One such spatially dependent cluster dynamics code is PARASPACE, which incorporates one spatial dimension intended to account for situations where key physical variables depend on position in one primary spatial direction.

As described by [30], PARASPACE treats clusters of intrinsic defects (either self-interstitials or vacancies) and foreign gas atoms (helium, krypton). Since the probability that self-interstitials (I) and vacancies (V) coexist in a single cluster is very low due to their strong tendency for recombination, no mixed I–V clusters are considered. Clusters are defined using just one number (subscript) i, with its absolute value being the number of point defects (I or V) contained and its sign ("−" for I-clusters and "+" for V clusters) indicating the character of the cluster. Two numbers, NI and NV, are chosen as the number of interstitials in the largest I-cluster and the number of vacancies in the largest V cluster, respectively.

Physically, these numbers prescribe the "phase space" within which the clusters can interact with each other, and ensure the conservation of point defects. Numerically, these numbers, together with the number of spatial grids, NX, set the number of equations to be solved. NI and NV are chosen to be large enough so that the computation results are not affected by the prescribed phase space. Since the system may continuously evolve toward larger clusters, the initial values of NI and NV may become limiting at high dose. This is continuously checked within the PARASPACE code through the concentration and its gradient (with respect to i) at the phase boundaries. If certain thresholds are exceeded at the boundaries, the values for NI and NV are increased automatically and the time is reset to the last step prior to the occurrence of this event.

With 1D spatial dependence, the system of ordinary differential equations (ODE) describing defect evolution changes to a system of partial differential equations (PDEs), and the PDEs generally have the following generic form:

$$\frac{\partial C_i^{x_n}}{\partial t} = \phi \times P_i(x_n) + D_i \frac{\partial^2 C_i^{x_n}}{\partial x^2} + \mathrm{GRT} + \mathrm{GRE} + \mathrm{ART} - \mathrm{ARE}, \tag{7.109}$$

where $C_i^{x_n}$ refers to the volumetric concentration (in nm^{-3}) of the ith cluster at the depth position x_n (in nm), ϕ is the particle flux (in $\mathrm{nm}^{-2}\,\mathrm{s}^{-1}$), $P_i(x_n)$ is the production "probability" (in $\mathrm{particle}^{-1}\,\mathrm{nm}^{-1}$) of the ith cluster by irradiation that is obtained through SRIM (combined with MD for intracascade recombination and clustering), D_i is the diffusivity of the ith cluster, GRT is the generation rate of the ith cluster by trapping reactions (A + B $\rightarrow$ i) among other clusters, GRE is the generation rate of the ith cluster by emission processes (C $\rightarrow$ i + B) of other clusters, ART is the annihilation rate of the ith cluster by its trapping reaction with other clusters (i + B $\rightarrow$ C), and ARE is the annihilation rate of the ith cluster by its own emission process (i $\rightarrow$ A + B).

The reaction terms differ slightly among different clusters, and the exact equation for the prescribed phase space (Λ = [−NI, NV]) is given as:

$$\frac{\partial C_i^{x_n}}{\partial t} = \phi \times P_i(x_n) + D_i \frac{\partial^2 C_i^{x_n}}{\partial x^2} + \sum_{\substack{m+p=i \\ m,p\neq 0 \\ m,p\in\Lambda}} k_{m,p}^{+} C_m^{x_n} C_p^{x_n} - \sum_{\substack{m\neq i \\ m\neq 0 \\ m,m+i\in\Lambda}} k_{m,i}^{+} C_m^{x_n} C_i^{x_n} - k_i^{-} C_i^{x_n}, \tag{7.110}$$

for i = NV or −NI, where k^+ is the trapping reaction constant and k^- is the emission reaction constant.

Initially, vacancy and interstitial concentrations are set equal to their thermal equilibrium values and all cluster sizes are set to zero at all depth grids. The PDEs given in Eq. (7.110) are converted to ODEs by introducing the same set of clusters at each depth grid, and thus, the total number of ODEs is equal to the total number of clusters multiplied by the total number of depth grids. Then the diffusion terms in the PDEs are discretized as follows:

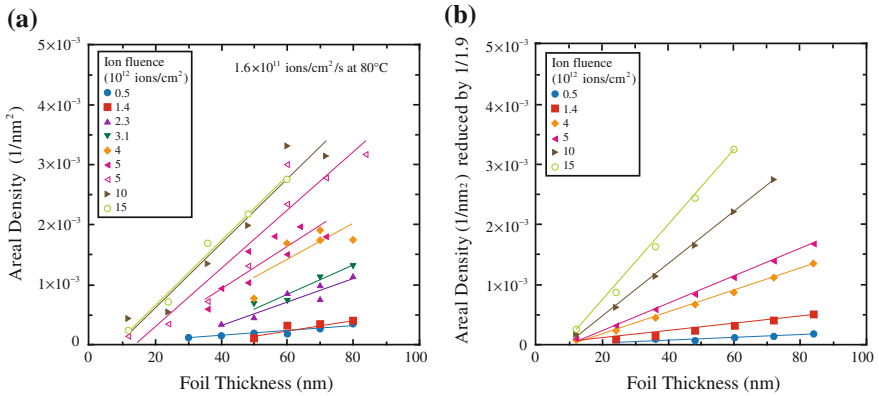

Fig. 7.60 Experimental (**a**) and model-predicted (**b**) areal densities of observable loops (diameter $\geq$ 1.3 nm) in Mo foils of various thicknesses irradiated at an ion flux of 1.6×10^{11} ions cm^{-2} s^{-1} at a temperature of 80 °C. The modeled densities were reduced by a factor of 1.9 to account for loops out of contrast in experiments (after [30])

$$D_i \frac{\partial^2 C_i^{x_n}}{\partial x^2} = D_i \frac{\dfrac{C_i^{x_n+1} - C_i^{x_n}}{x_{n+1} - x_n} - \dfrac{C_i^{x_n} - C_i^{x_n-1}}{x_n - x_{n-1}}}{\dfrac{(x_{n+1} - x_{n-1})}{2}}, \tag{7.111}$$

at all depth grids except the surface(s) where the black-sink boundary condition is enforced.

An example of the application of cluster dynamics modeling is irradiation of a thin foil of Mo with 1 MeV Kr^+ at a dose rate of 1.6×10^{11} ions cm^{-2} s^{-1} at a temperature of 80 °C. Figure 7.60 plots the areal density of observable loops (diameter $\geq$ 1.3 nm) observed experimentally (Fig. 7.60a) and modeled using the PASASPACE cluster dynamics code (Fig. 7.60b). Note that over a large range of doses, there is excellent qualitative agreement in the areal density of loops.

7.7 Dislocation Loop Growth

The growth of loops can also be determined from the Fokker–Planck equations that provide the size distribution of loops of all sizes (see Fig. 7.59). Applying Eq. (7.104) to the case of interstitial loops gives an equation in the form:

$$\frac{di_j}{dt} = K_{0j} + [\beta_v(j+1) + \alpha_i(j+1)]i_{j+1} - [\beta_v(j) + \beta_i(j) + \alpha_i(j)]i_j + \beta_i(j-1)i_{j-1}, \tag{7.112}$$

where i_j is the concentration of interstitial loops of size j and the term on the LHS of Eq. (7.112) is the time rate of change of the population of interstitial loops of size j. The terms $\beta_k(j)$ and $\alpha_k(j)$ are the absorption and emission rates of defects of type k from loops of size j. The first term on the RHS of the equality is the direct production rate of clusters of size j. Practically, this term is different from zero up to the tetrahedral cluster ($j = 4$). The first term in square brackets is the production of clusters of size j by the emission of an interstitial or absorption of a vacancy by clusters of size $j + 1$. The second term in square brackets is the loss of clusters of size j by absorption of a vacancy or an interstitial, or emission of an interstitial. The last term is the addition of clusters of size j by capture of an interstitials by clusters of size $j - 1$. Solution of Eq. (7.112) results in the loop size distribution as a function of time, which describes the evolution of interstitial loops with dose or time.

Pokor et al. [31] used the Fokker–Planck formalism to model the evolution of a population of loops via chemical rate theory in a homogeneous medium. In their treatment, they allowed for production of clusters in the cascade containing up to four defects and solved a set of equations for the concentration of defect clusters consisting of two equations for individual vacancies or interstitials and $2N$ equations for the population of loops up to size N. The physics of the formulation is contained in the expressions for the defect capture rates, β, and emission rates, α, for each defect type, k, as a function of the cluster size, given as [31]:

$$\beta_{\mathrm{k}}(j) = 2\pi r(j) z_{\mathrm{c}}(j) D_{\mathrm{k}} C_{\mathrm{k}}, \tag{7.113}$$

$$\alpha_{\mathrm{k}}(j) = 2\pi r(j) z_{\mathrm{c}}(j) \frac{D_{\mathrm{k}}}{\Omega} \exp(-E_{\mathrm{bk}}(j)/kT), \tag{7.114}$$

where $r(j)$ is the radius of an interstitial loop of size j, D_{k} and C_{k} are the diffusion coefficient and concentration of defect k, $z_{\mathrm{c}}(j)$ is the bias factor for the interstitial loop of size j, and $E_{\mathrm{bk}}(j)$ is the binding energy of for a cluster of j defects of type k. Pokor et al. [31] gives the following expressions for $z_{\mathrm{c}}(j)$ and E_{bi}:

$$z_{\mathrm{c}}(j) = z_i + \left(\sqrt{\frac{b}{8\pi a}} z_{\mathrm{li}} - z_i \right) \frac{1}{j^{a_{\mathrm{li}}/2}}, \tag{7.115}$$

$$E_{\mathrm{b}}^i = E_{\mathrm{f}}^i + \frac{E_{\mathrm{b}}^{2i} - E_{\mathrm{f}}^i}{2^{0.8} - 1} \left(j^{0.8} - (j-1)^{0.8} \right), \tag{7.116}$$

where z_i is the bias factor for a straight dislocation line for interstitials, a is the lattice parameter, and b is the Burgers vector, z_{li} and a_{li} are parameters used to describe the evolution of the bias with cluster size [32]. For the binding energy term, E_{f}^i is the formation energy of an interstitial point defect Eq. (4.16), E_{b}^{2i} is the binding energy of a two-interstitial cluster, and j is the number of defects in a cluster of size j and the expression comes from molecular dynamics simulations [33, 34].

To account for the effect of the annihilation of the network dislocation density with dose, they assumed that the rate of change of the density was proportional to $\rho^{3/2}$, giving $\mathrm{d}\rho/\mathrm{d}t = -Kb^2\rho^{3/2}$, and resulting in a dislocation density that decreases as $1/t^2$ (see next section). The network dislocation density in irradiated metals evolves toward a saturation value with increasing dose. In stainless steel, it has been observed to reach a saturation value of ~6×10^{-14} m^{-2} over a temperature range that spans 400–600 °C [35]. Cluster model results of the loop density and size for three grades of stainless steel irradiated at 330 °C and to doses up to 40 dpa calculated using Eqs. (7.112)–(7.116) are compared against measurements in Fig. 7.61 and show relatively good agreement. Dislocation recovery plays an important role in microstructure evolution as it represents a change in sink density. Failure to account for the recovery of the initial dislocation network would lead to a faster saturation of the loop structure in the 316 alloys. The most sensitive parameters controlling the irradiation microstructure are the temperature, dose, materials constants, and the initial network dislocation density.

Simpler treatments for determining the loop size distribution can be made by neglecting the formation of defect clusters larger than the tetra-interstitial, limiting the number of size classes and simplifying the cluster description. Stoller et al. [36] described the evolution of larger loops by the equation:

$$\frac{\mathrm{d}\rho_j}{\mathrm{d}t} = i_{j-1}\tau_j^{-1} - i_j\tau_{j+1}^{-1}, \tag{7.117}$$

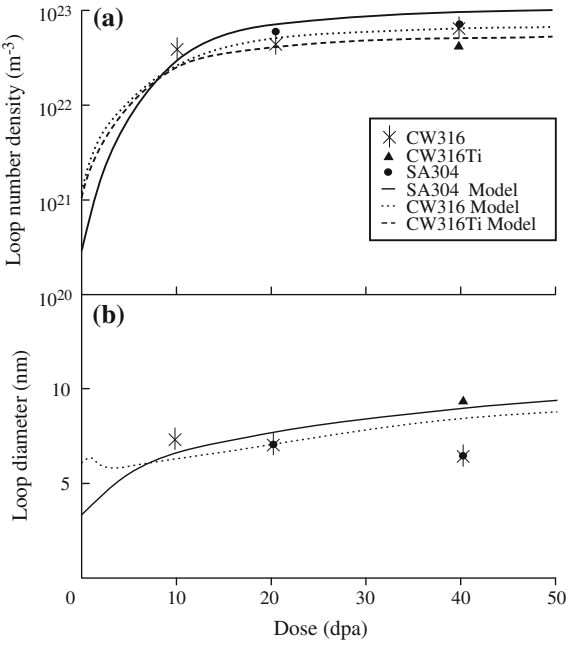

Fig. 7.61 Evolution of the Frank loop (**a**) density and (**b**) size for 330 °C irradiation to high dose according to the cluster dynamics model of Pokor et al. (after [31])

where ρ_j is the number of loops in a given size class with radius r_L, and the τ_j is the lifetime of a loop of size j against growth to the next larger size class:

$$\tau_j = \int_{r_j}^{r_{j+1}} \left(\frac{dr_L}{dt}\right)^{-1} dr_L, \tag{7.118}$$

and

$$\frac{dr_L}{dt} = \frac{\Omega}{b}[z_{iL}(r_L)D_iC_i - z_{vL}(r_L)D_v(C_v - C_{vL})], \tag{7.119}$$

where z_{iL} and z_{vL} are given by Eq. (5.100) and $C_{vL} = C_v^0 \exp(E_F\Omega/kT)$, and E_F is the energy of a faulted loop from Eq. (7.65). Figure 7.62a shows a comparison of the temperature dependence of the calculated maximum faulted loop density and low fluence fast reactor data for 316 stainless steel with initial network dislocation densities of 3×10^{15} m^{-2} (solid line) and 3×10^{13} m^{-2} (dashed line). Figure 7.62b shows the dose dependence of the loop density for solution annealed 316 irradiated at 500 °C.

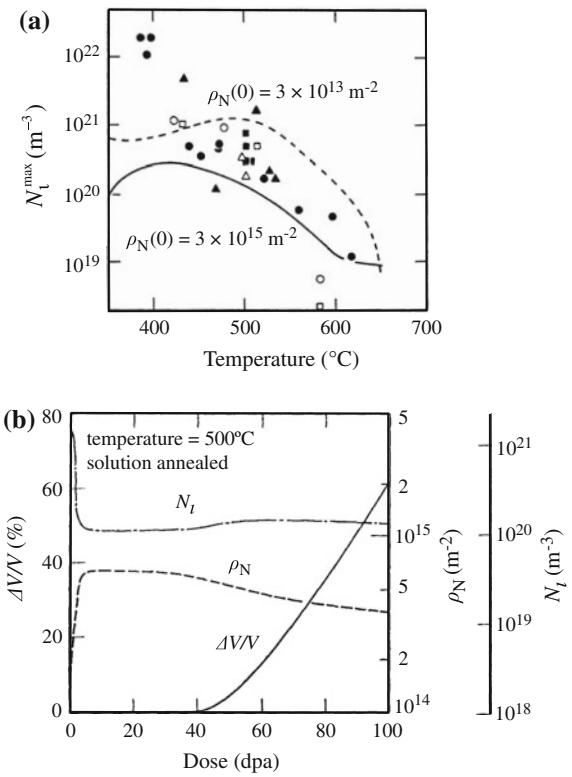

Fig. 7.62 (**a**) Comparison of calculated maximum faulted loop density and low fluence fast reactor data as a function of temperature. (**b**) Dose dependence of faulted loop density for irradiation of solution annealed stainless steel at 500 °C (after [36])

Semenov and Woo [37] accounted for the effect of production bias by writing Eq. (7.119) for the rate of change in loop size to include terms due to interstitial cluster and vacancy cluster absorption:

$$\frac{\mathrm{d}r_\mathrm{L}}{\mathrm{d}t} = \frac{\Omega}{b}\left[J_i - J_\mathrm{v} + J_\mathrm{v}^e + J_i^\mathrm{cl} - J_\mathrm{v}^\mathrm{cl}\right], \tag{7.120}$$

where J_s are the fluxes due to single interstitials, single vacancies, vacancy thermal emission, interstitial clusters, and vacancy clusters, respectively, and τ_d is the lifetime of the dislocation loop. Substituting for the fluxes [36] results in:

$$\frac{\mathrm{d}r_\mathrm{L}}{\mathrm{d}t} = \frac{K_0}{(\rho_\mathrm{N}+\rho_\mathrm{L})b}\left(\frac{k_\mathrm{V}^2\left(\varepsilon_i - \varepsilon_\mathrm{v}'\right) + k_\mathrm{d}^2\bar{z}(1-\varepsilon_i)}{k^2} - \frac{K^e}{K_0}\right), \tag{7.121}$$

where K_0 is the defect production rate, K^e is the vacancy thermal emission rate, ρ_N and ρ_L are the network and loop dislocation densities, $\varepsilon_\mathrm{i,v}$ is the fraction of interstitials and vacancies, respectively, that are immobilized by intracascade clustering, $\varepsilon_\mathrm{v}' = \varepsilon_\mathrm{v} - K^e/K_0$, z_d is the dislocation bias, $k_\mathrm{V,d}^2$ are the sink strengths of voids and dislocations, k^2 is the total sink strength and $\bar{z} = \dfrac{z_\mathrm{d}k_\mathrm{c}^2}{k^2 + z_\mathrm{d}k_\mathrm{d}^2}$. The steady-state interstitial loop growth rate for 316 stainless steel with an effective point defect production rate of 10^{-7} dpa/s is shown as a function of temperature in Fig. 7.63. The growth rate is in units of Burgers vector, b per dpa. Note that the loop growth rate is low at low and high temperatures and peaks at an intermediate temperature of about 500 °C.

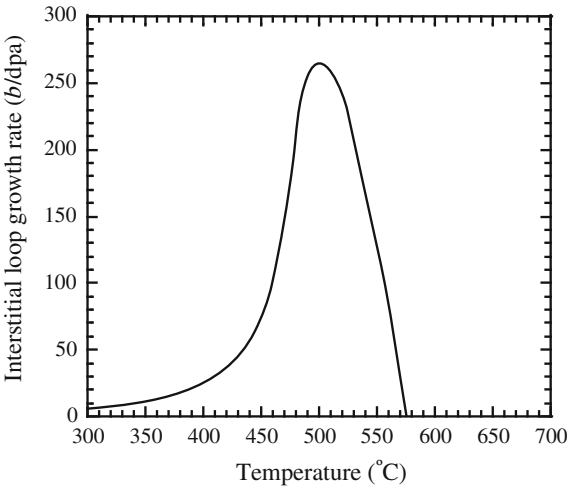

Fig. 7.63 Interstitial loop growth rate in units of Burgers vector, b per dpa as a function of temperature for a 316 stainless steel (after [38])

7.8 Recovery

Growing dislocation loops eventually encounter either network dislocations or each other. The maximum radius to which a loop can grow, $R_{\max}$, is governed by the loop density, ρ_L as given by $\frac{4\pi}{3}\rho_L R_{\max}^3 = 1$. When loops interact, they coalesce and contribute to the network dislocation density. Interaction between individual dislocations and loops results in loop unfaulting that also contributes to the network (discussed in Chap. 12, Sect. 12.3). As the dislocation density increases, the rate of loop interaction with the network increases and the loop radius is further limited by the network dislocation density as described by Eq. (5.85), $\left(\pi R_{\max}^2\right)\rho_N = 1$.

However, observations of irradiated microstructures confirm that the dislocation density saturates, implying that there must also be a process for removal of network dislocations limiting their buildup. The process of recovery can explain the behavior of the dislocation density with irradiation. The rate of change of the dislocation density in a solid under stress at high temperature is assumed to behave according to:

$$\dot{\rho} = B\rho - A\rho^2, \tag{7.122}$$

where ρ is the density of mobile dislocations and A and B are constants [Note that while the rate of dislocation density change given by Eq. (7.122) is phenomenological by nature, a more accurate description of the physical process is provided by Eq. (7.117)]. The first term of Eq. (7.122) is the production rate of dislocations and the second term is the annihilation rate. The loss term is assumed to occur due to mutual annihilation of pairs of dislocations of opposite sign, which implies a reaction rate that is proportional to the square of the number of dislocations present at a given time. Garner and Wolfer [39] showed that the generation rate of dislocations is proportional to $b^2\phi\rho^{1/2}$, so that Eq. (7.122) can be written as:

$$\dot{\rho} = B\rho^{1/2} - A\rho^{3/2}, \tag{7.123}$$

where $B \sim b^2\phi$ and $A \sim v_c$, where v_c is the climb velocity of the dislocation (see Chap. 13). At steady state ($d\rho/dt = 0$), the saturation density is $\rho_s = B/A$. The solution to Eq. (7.122) is given as:

$$\frac{\rho(t)}{\rho_s} = \frac{1 - e^{-x} + \sqrt{\rho_0/\rho_s}(1 + e^{-x})}{1 + e^{-x}\sqrt{\rho_0/\rho_s}(1 - e^{-x})}, \tag{7.124}$$

where ρ_0 is the initial dislocation density and

$$x = A\sqrt{\rho_s}t = \sqrt{\rho_s}v_c t. \tag{7.125}$$

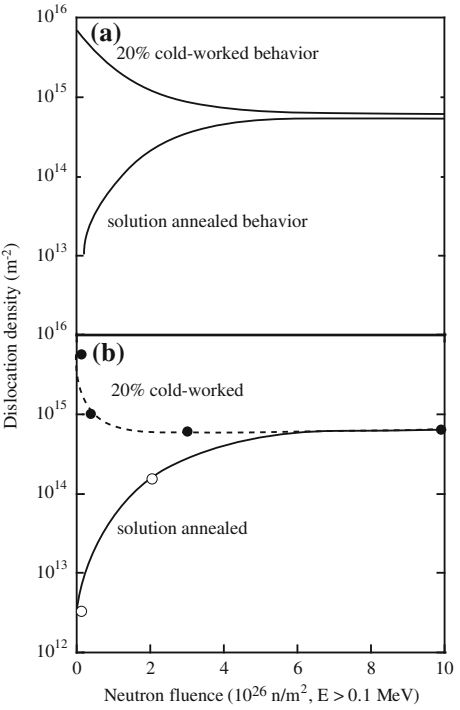

Fig. 7.64 (**a**) Calculated dislocation density evolution in 316 stainless steel at 500 °C using Eq. (7.139), for starting densities of 7×10^{15} m^{-2} and 4×10^{12} m^{-2}, for cold-worked and annealed conditions, respectively (after [34]). (**b**) Measured dislocation density in 20 % cold-worked and annealed 316SS after irradiation in EBR-II at 500 °C (after [40])

Using a saturation density, ρ_s of 6×10^{14} m^{-2}, and initial dislocation densities, ρ_0 of 3×10^{12} m^{-2} for annealed 316 SS and 7×10^{15} m^{-2} for 20 % CW 316 SS, the dislocation densities calculated from Eq. (7.123) are shown in Fig. 7.64a. The relationship between x in Eq. (7.124) and fluence was defined by the case where the dislocation density for annealed 316 SS reached a value of 2×10^{14} m^{-2} at 2×10^{26} n/m^2. Data are plotted in Fig. 7.64b. Note how well the model results of Fig. 7.64a agree with the data. This agreement also establishes that the original dislocations are not different from those produced during the irradiation with regard to their ability to absorb point defects.

7.9 Evolution of the Interstitial Loop Microstructure

The evolution of the interstitial loop population can be described in terms of its response to temperature and dose. The temperature regime that is important for LWR operation is between 270 and 340 °C. Higher temperatures may be reached from gamma heating in certain thick components such as PWR baffle plates. This temperature range represents a transition region between what is commonly termed as low-temperature (50–300 °C) and high-temperature (300–700 °C) behaviors.

Below 300 °C, the dislocation microstructure is characterized by a high density of "black dots" (defect clusters that are too small to resolve in the TEM, <2 nm), network dislocations, and a low density of Frank loops. A very small percentage of the small loops in stainless steels are observed to be SFT, which is much less than the 25–50 % of clusters in nickel or copper [10]. Near 300 °C, the radiation-induced microstructure changes from one dominated by small dislocation loops to one containing larger faulted loops and network dislocations (Fig. 7.65). Figure 7.66 shows large dislocation loops after irradiation at high temperatures. Above 300 °C, the Frank loop population begins to decrease. Figure 7.67 shows the sharp decrease in faulted loop density by a factor of over 1000 between 400 and 600 °C in neutron-irradiated austenitic stainless steels. The increase in loop size with temperature eventually leads to an increase in the loop unfaulting rate which contributes to the reduction in Frank loop population at high temperature.

Loop density increases rapidly to saturation at low irradiation temperatures. Figure 7.68 shows the increase in loop density in austenitic stainless steels irradiated near 300 °C. Loop size is relatively insensitive to fluence below about 300 °C. At these low temperatures, loop sizes and densities become dynamically stable as a population when a balance is reached between new loop formation and the destruction of existing loops. With increasing temperature in the low-temperature regime, the density of fine loops decreases and the loop size increases.

The dislocation microstructure evolves into one composed of Frank loops and network dislocations above about 300 °C. Loop density saturates at a few dpa and the density is maintained (in a dynamic sense) at higher doses. The dislocation network density increases in proportion to the faulted loop density as temperature is increased though the overall dislocation density is expected to stay fairly constant between 300 and 370 °C. In the higher temperature regime (400–600 °C), the population consists of a low density of Frank loops and a dislocation network.

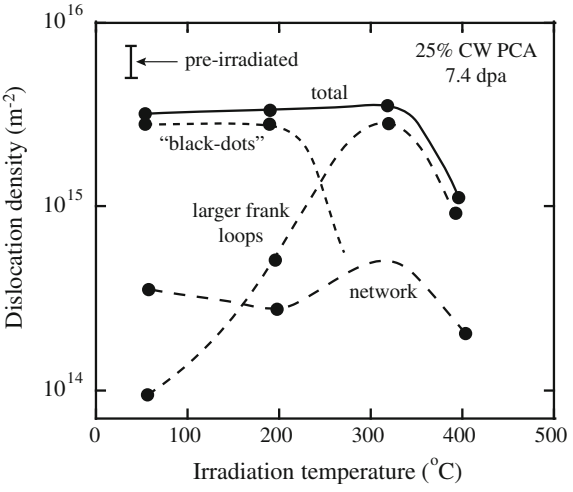

Fig. 7.65 Effect of irradiation temperature in the range 50–400 °C on the components of the dislocation density in neutron-irradiated austenitic stainless steel (after [41])

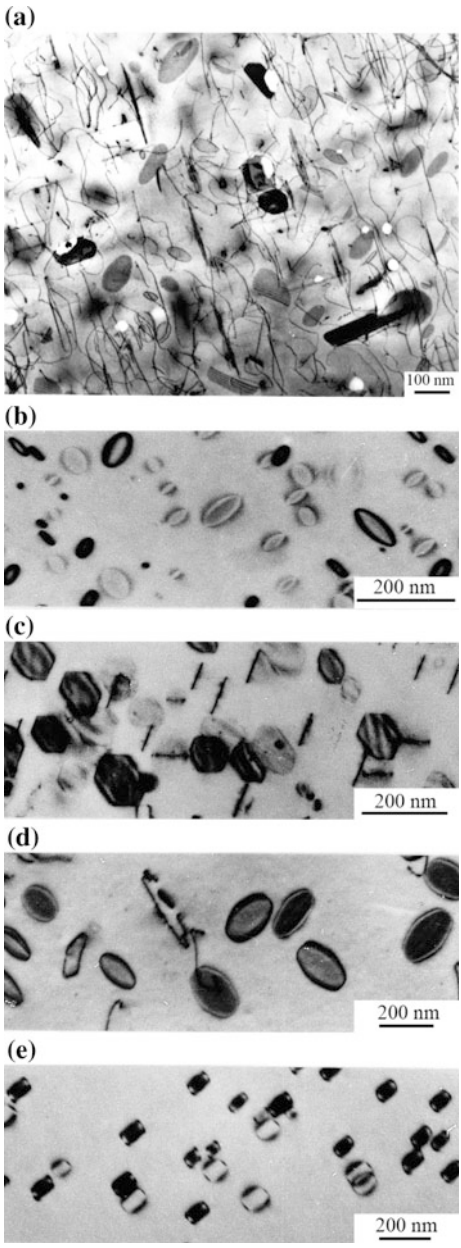

Fig. 7.66 Images of large Frank loops in (**a**) a 300 series stainless steel irradiated at 500 °C to a dose of 10 dpa (from [42]), and (**b**)–(**e**) in irradiated aluminum, copper, nickel, and iron, respectively (after [18])

Evolution may actually occur more slowly if other microstructural processes are also occurring such as void and bubble nucleation and growth.

The description of defect cluster nucleation and evolution provides a backdrop for understanding the phenomenon of void growth discussed in the next chapter. As

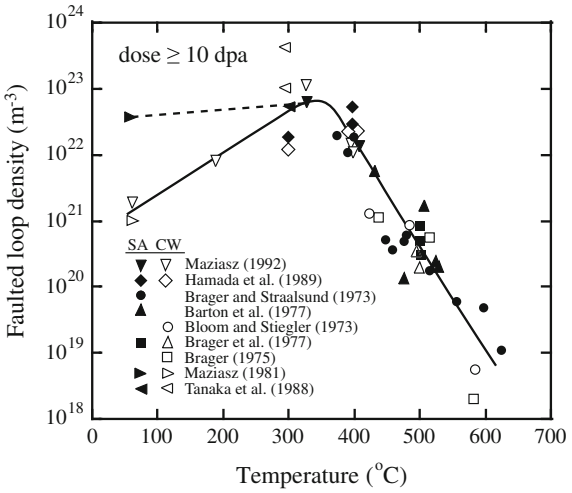

Fig. 7.67 Effect of temperature on the Frank loop density in the intermediate temperature region, 400–600 °C, for neutron-irradiated austenitic stainless steel (after [41])

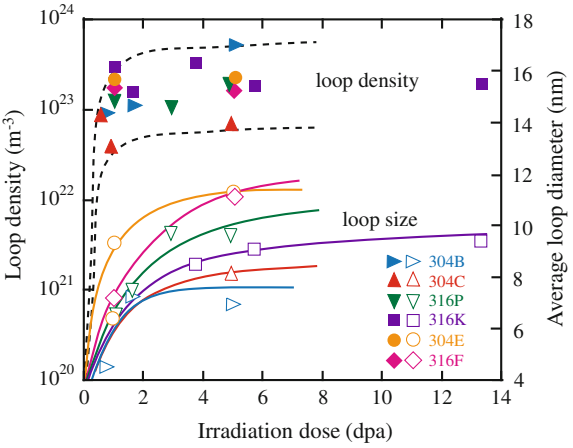

Fig. 7.68 Evolution of the Frank loop density and size in various austenitic stainless steels following irradiation to doses of up to 13 dpa at a temperature near 300 °C (after [43])

will be shown, void formation and growth is intimately linked to the production of defect clusters and their growth into loops, as these microstructures constitute critical sinks that will govern the fate of voids.

Nomenclature

a	Lattice constant
A	Area of slip plane
$\boldsymbol{b}$	Burgers vector
$C_{v,i}$	Concentration of vacancies, interstitials
$C^0_{v,i}$	Thermal equilibrium concentration of vacancies, interstitials

d^x Strength of diffusive spread for clusters by the x process
$D_{\mathrm{v,i}}$ Diffusion coefficient of vacancies, interstitials
D_{k_j} Diffusion term in size space of defect k and cluster size j, Eq. (7.106)
D_l Climb diffusion coefficient
E Energy
E_{b} Binding energy
E_{f} Formation energy
E_l Dislocation loop energy
E_{m} Migration energy
$\langle E_{\mathrm{m}} \rangle$ Effective activation energy for cluster motion
$f_{\mathrm{i}}^{\mathrm{cl}}$ Fraction of interstitials in clusters
F_{k_j} Drift velocity in size space of defect k and cluster size j Eq. (7.106)
G_j Effective Frenkel pair production rate of species j
ΔG Change in free energy
G_0 Standard free energy
i_n Cluster of n interstitials
k Boltzmann's constant
$k^{+/-}$ Rate constant for processes +/− in cluster dynamics Eq. (7.110)
$k^2_{\mathrm{v,i}}$ Total sink strength for vacancies, interstitials
l Length of dislocation line segment
L Length of edge of stacking fault tetrahedron
J Nucleation current. Also flux
K_0 Defect production rate
K^e Vacancy thermal emission rate
m Stress exponent in relation between dislocation velocity and shear stress
$\boldsymbol{n}$ Unit vector
n_k, n'_k Critical cluster size
N_{d} Average number of defects generated in a single cascade
N_{il} Number density of interstitial loop
N_0 Number of lattice sites per unit volume. Also number of nucleation sites
P_{i} Probability of growing an interstitial cluster
P_{m} Loop nucleation probability
r Defect cluster radius
r_{c} Dislocation core radius
r_{L} Loop radius
r_{k} Critical cluster radius
$\boldsymbol{s}$ Positive direction of the dislocation line
T Temperature. Also PKA energy
$S_{\mathrm{v,i}}$ Supersaturation of vacancies, interstitials
u_{ij} Components of the displacement vector
v_{g} Dislocation glide velocity
v_n Cluster of n vacancies
V Volume
W Work

$z_{v,i}$ Vacancy, interstitial bias factor
Z Zeldovich factor Eq. (7.75)
α_j Emission rate of species j
β_j Absorption rate of species j
γ Shear strain. Also surface energy
γ_{SFE} Stacking fault energy
δ Thickness of void shell
ε_c Strain associated with the dislocation core
ε_{ij} Components of strain
ε_{i0} Fraction of interstitials produced in cascades in the form of immobile clusters
Γ Dislocation line tension
λ Lamé constant
λ_d Mean free path between consecutive interstitial cluster coalescing events
μ Shear modulus
ν Poisson's ratio. Also jump frequency
$\rho(n)$ Number density of defect clusters of size n
ν_s Strength of drift term for clusters, by absorption of single defects
Ω Atomic volume
ρ_x Density of entity x
σ, σ_{ij} Stress and components of stress
σ_s Shear stress
σ_D Value of shear stress that yields a dislocation velocity of 0.01 m/s
τ Incubation time Eq. (7.95)
τ_d Lifetime of dislocation loop

Subscripts

c Dislocation core
d Dislocation
i Interstitial
k Critical cluster size
L Loop
F Frank loop
N Dislocation network
P Perfect loop
v Vacancy
0 Initial

Superscripts

c Coalescence
cl Clusters
s Single defects

+ Trapping
− Emission

Acronyms

ARE Cluster annihilation rate by emission
ART Cluster annihilation rate by trapping
EDF Evaporating defect fraction
GRE Cluster generation rate by emission
GRT Cluster generation rate by trapping
IDF Isolated point defect fraction
MCF Mobile cluster fraction
MDF Mobile defect fraction
NI Largest interstitial cluster
NN Nearest neighbor
NV Largest vacancy cluster
PBM Production bias model
PKA Primary knock-on atom
SFE Stacking fault energy
SIA Single interstitial atom
UHP Ultra-high purity

Problems

7.1. Draw billiard ball models of the extra half sheet of atoms which constitute the following dislocations:

(a) The $a/2[110]$ edge dislocation in the (111) plane of the fcc lattice.
(b) The $a/2[111]$ edge dislocation on the (110) plane of the bcc lattice.

7.2. It is found experimentally that a certain material does not change in volume when subjected to an elastic state of stress. What is Poisson's ratio for this material?
7.3. Determine the volume of a 10 cm diameter copper sphere that is subjected to a fluid pressure of 12 MPa.
7.4. Assuming that atoms are hard elastic spheres, show that Poisson's ratio for a close-packed array of spheres is 1/3.
7.5. For a circular shaped disk lying on the (111) plane of an fcc crystal:

(a) Determine the energy as a function of the number of vacancies.
(b) How many vacancies could a spherical void have before it would spontaneously convert to a vacancy disc?

7.6. It is known that the amount of stored energy in a solid can be increased with the addition of dislocations.

(a) Calculate this energy for aluminum with a dislocation density of 10^{12} m^{-2}.
(b) It has also been suggested that this energy can be increased by application of a shear stress, σ_s. Given that the straight edge dislocations in part (a) are in the form of an equally spaced cubic-shaped network, determine the shear stress, σ_s, needed to bow each dislocation segment into a half circle, and calculate the resulting increase in stored energy.

7.7. Calculate the net density of edge dislocations in a thin simple cubic crystal with lattice parameter $a = 2 \times 10^{-8}$ cm if it is bent to have a radius of curvature of 10 cm. (The thickness of the crystal is no greater than 1 mm.)

7.8. In the circular shear loop shown in the figure below, let the x-axis be the direction of the Burgers vector shown in the drawing, the z-axis in the plane of the loop but perpendicular to the direction of the Burgers vector, and the y-axis perpendicular to the plane of the loop. Let θ be the polar angle of the circle measured from point A. At any point θ on the loop, the Burgers vector has an edge component b_e that is perpendicular to the dislocation line at that position and a screw component b_s that is parallel to the line.

(a) Using the fact that the vector $\boldsymbol{b}$ with these components is constant (in magnitude and direction) at all points on the loop, derive expressions for b_e and b_s as functions of θ.
(b) Suppose a shear stress σ_{xy} is applied to the loop. Show that the resultant force on the dislocation line is always radially directed and has a magnitude $\sigma_{xy}b$.

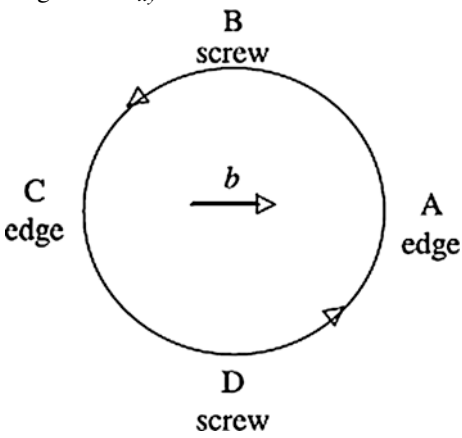

7.9. Plot the stress fields surrounding edge and screw dislocations as a function of θ. Specifically, plot the following:

(a) σ_{xx}, σ_{yy}, and σ_{xy} versus θ for an edge dislocation
(b) σ_{xz} and σ_{yz} versus θ for a screw dislocation

7.10. For the dislocations in the figure below:

(a) Calculate the magnitude of the components of force on dislocation (2) due to dislocation (1).
(b) Repeat part (a) for angles of 0°, 30°, 45°, and 90°.
(c) At $\theta = 30°$, will dislocation (2)

(i) glide toward or away from dislocation (1)?
(ii) tend to climb up or down? Why?

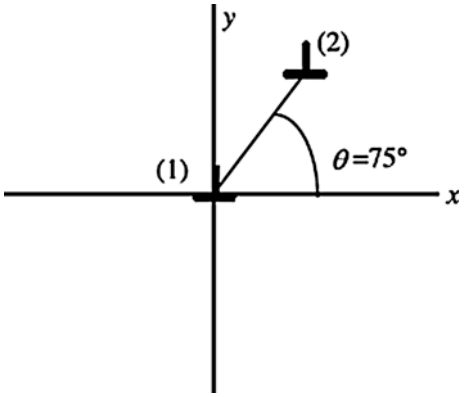

7.11. For the dislocations given in the sketch, find

(a) The force on dislocation (2) due to dislocation (1)
(b) In which direction will dislocation (2) climb and/or glide?
(c) Describe the stress and temperature dependence of these two processes and under what circumstances each will contribute to creep.

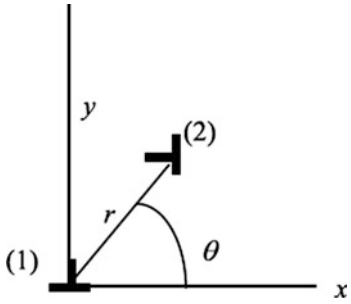

(1) $\boldsymbol{s} = |001|, \boldsymbol{b} = b|100|$
(2) $\boldsymbol{s} = |00\bar{1}|, \boldsymbol{b} = b|0\bar{1}0|$

7.12. An edge dislocation having the properties $\boldsymbol{s} = \boldsymbol{k}$ and $\boldsymbol{b} = b\boldsymbol{j}$ is on a plane $x = X$. Calculate the y-coordinates of the maxima and minima of the glide and

climb forces (separately) that it would experience due to a fixed dislocation at the origin ($\boldsymbol{s} = \boldsymbol{k}$) for the following three cases:

(a) $\boldsymbol{b} = b\boldsymbol{i}$
(b) $\boldsymbol{b} = b\boldsymbol{j}$
(c) $\boldsymbol{b} = b(1/2\boldsymbol{i} + \sqrt{3}/2\boldsymbol{j})$.

7.13. An edge dislocation (1) with $\boldsymbol{s} = [001]$ and $\boldsymbol{b} = b\,[100]$ is located at the origin of a coordinate system. Another edge dislocation (2) with $\boldsymbol{s} = [001]$ and $\boldsymbol{b} = b\left[\sqrt{2}\sqrt{20}\right]$ is located a distance r away from (1) and 45° CCW from the x-axis.

(a) Calculate the glide and climb force on dislocation (2) due to dislocation (1).
(b) Make a graph of the force on dislocation (2) as a function of θ (for a given r) for $0 \le \theta \le 2\pi$.

7.14. Compute the local force on dislocation (2) due to dislocation (1) for the four examples of interaction between two perpendicular dislocations listed below:

$$\boldsymbol{s}_1 = [001] \qquad \boldsymbol{s}_2 = [010]$$
$$\boldsymbol{b}_1 = b\begin{cases}[100]\\[100]\\[100]\\[010]\end{cases} \qquad \boldsymbol{b}_2 = b\begin{cases}[100]\\[010]\\[001]\\[010]\end{cases}$$

where the first dislocation passes through $x = y = 0$ and is parallel to the z-axis, and the second dislocation passes through $x = X$ and $z = 0$ and is parallel to the y-axis.

(a) In which cases does the total force on dislocation (2) vanish?
(b) If dislocation is able to flex, sketch the shape it is likely to assume provided the first dislocation passing through $x = 0$ remains straight.

References

1. Weertman J, Weertman J (1964) Elementary dislocation theory. Macmillian, London
2. Hull D, Bacon DJ (1984) Introduction to dislocations. Pergamon, Oxford
3. Friedel J (1964) Dislocations. Pergamon, New York
4. Hirth JP, Lothe J (1982) Dislocations in crystals, 2nd edn. Wiley Interscience, New York
5. Reed-Hill RE, Abbaschian R (1994) Physical metallurgy principles, 4th edn. PWS, Boston
6. Hull D, Bacon DJ (2001) Introduction to dislocations, 4th edn. Butterworth Heinemann, Philadelphia
7. Dieter GE (1976) Mechanical metallurgy, 2nd edn. McGraw-Hill, New York, p 180
8. Osetsky YN, Stoller RE, Matsukawa Y (2004) J Nucl Mater 329–333:1228–1232
9. Bacon DJ, Osetsky YN, Stoller RE, Voskoboinikov RE (2003) J Nucl Mater 323:152–162
10. Bacon DJ, Gao F, Osetsky YN (2000) J Nucl Mater 276:1–12

11. Stoller RE (2012) Primary radiation damage formation. In: Konings RJM (ed) Comprehensive nuclear materials. Elsevier, Amsterdam, p 293
12. Phythian WJ, Stoller RE, Foreman AJE, Calder AF, Bacon DJ (1995) J Nucl Mater 223:245–261
13. Osetsky YN, Bacon DJ, Serra A, Singh BN, Golubov SI (2000) J Nucl Mater 276:65–77
14. Gao F, Bacon DJ, Flewitt PEJ, Lewis TA (1997) J Nucl Mater 249:77–86
15. Valo M, Krause R, Saarinen K, Hautojarvi P, Hawthorne JR (1992) In: Stoller RE, Kumar AS, Gelles DS (eds) Effects of radiation on materials, ASTM STP, vol 1125. American Society for Testing and Materials, West Conshohocken, pp 172–185
16. Stoller RE (2000) J Nucl Mater 276:22–32
17. Jenkins ML, Kirk MA (2001) Characterization of radiation damage by transmission electron microscopy. Institute of Physics, Philadelphia
18. Kiritani M (1994) J Nucl Mater 216:200–264
19. Osetsky YN, Sera A, Singh BN, Golubov SI (2000) Philos Mag A 80:2131
20. Heinisch HL, Singh BN, Golubov SI (2000) J Nucl Mater 283–287:737
21. Wirth BD, Odette GR, Marondas D, Lucas GE (2000) J Nucl Mater 276:33–40
22. Johnson RA (1967) Phil Mag 16(141):553
23. Jossang T, Hirth JP (1966) Phil Mag 13:657
24. Kelly BT (1966) Irradiation damage to solids. Pergamon, New York
25. Zinkle SJ, Singh BN (1993) J Nucl Mater 199:173–191
26. Russell KC, Powell RW (1973) Acta Meta 21:187
27. Stoller RE, Odette GR (1987) In: Gerner FA, Packan NH, Kumar AS (eds) Radiation-induced changes in microstructure: 13th international symposium (Part I), ASTM STP 955. American Society for Testing and Materials, Philadelphia, pp 358–370
28. Golubov SI, Ovcharenko AM, Barashev AV, Singh BN (2001) Phil Mag A 81(3):643–658
29. Ghoniem NM, Sharafat S (1980) J Nucl Mater 92:121–135
30. Xu D, Wirth BD, Li M, Kirk MA (2012) Acta Mater 60:4286–4302
31. Pokor C, Brecht Y, Dubuisson P, Massoud JP, Barbu A (2004) J Nucl Mater 326:19–29
32. Duparc AH, Moingeon C, Smetniansky-de-Grande N, Barbu A (2002) J Nucl Mater 302:143
33. Soneda N, Diaz de la Rubia T (1998) Phil Mag A 78(5):995
34. Osetsky YN, Serra A, Victoria M, Golubov SI, Priego V (1999) Phil Mag A 79(9):2285
35. Garner FA, Kumar AS (1987) Radiation-induced changes in microstructure: 13th international symposium (Part I), ASTM STP 955. American Society for Testing and Materials, Philadelphia, pp 289–314
36. Stoller RE, Odette GR (1987) In: Garner FA, Packan NH, Kumar AS (eds) Radiation-induced changes in microstructure: 13th international symposium (Part I), ASTM STP 955. American Society for Testing and Materials, Philadelphia, p 371
37. Semenov AA, Woo CH (2003) Phil Mag 813:3765–3782
38. Eyre BL, Bullough R (1965) Phil Mag 12:31
39. Garner FA, Wolfer WG (1982) In: Brager HR, Perrin JS (eds) Effects of radiation on materials: 11th conference, ASTM STP 782. American Society for Testing and Materials, West Conshohocken, p 1073
40. Garner FA (1994) In: Frost BRT (ed) Materials science and technology (chapter 6), vol 10A. VCH, New York, p 419
41. Zinkle SJ, Maziasz PJ, Stoller RE (1993) J Nucl Mater 206:266–286
42. Mansur LK (1994) J Nucl Mater 216:97–123
43. Edwards DJ, Simonen EP, Bruemmer SM (2003) J Nucl Mater 317:13–31

Chapter 8
Irradiation-Induced Voids and Bubbles

The formation and growth of *voids* and *bubbles* is of intense interest for material performance in radiation environments at elevated temperature. The first observation of voids in irradiated metals was published by Cauthorne and Fulton in 1967 [1]. Voids can have a profound influence on material properties because solids undergo *volumetric swelling* when voids form and grow. It has been suggested that the US breeder reactor program experienced a setback of nearly a decade by this surprising observation, as scientists scrambled to understand this phenomenon and the consequences to reactor internals. Since that time, a great deal of effort has been expended toward understanding their formation and growth. Figure 8.1 shows examples of voids in irradiated stainless steel, aluminum, and magnesium. Voids of this size and number density can cause tens of percent increases in volume, translating into significant changes in linear dimensions as well. The challenge of designing a reactor to accommodate swelling of this magnitude quickly becomes monumental.

The formation and growth of voids shares much in common with bubbles. Yet because of their nature—a void is essentially an empty cavity—bubble mechanics are more complicated. It is by virtue of the fact that insoluble gases are formed by transmutation when certain metals are irradiated that drew attention to the subject of bubbles in irradiated metals. Under irradiation, it is possible for large numbers of inert gas bubbles to form, which significantly alter the physical and mechanical properties of metals. Fast and thermal spectrum reactors generate helium via transmutation, and the first wall of a fusion reactor is susceptible to bubble formation due to the high gas loading from reaction products in the plasma. Numerous examples exist in reactor systems where bubbles form and alter material properties, one of the most important being the structural materials of fission reactors. This chapter will address the theory of void and bubble nucleation and growth, along with elucidating the most important factors affecting these processes in reactor systems.

G.S. Was, *Fundamentals of Radiation Materials Science*,
DOI 10.1007/978-1-4939-3438-6_8

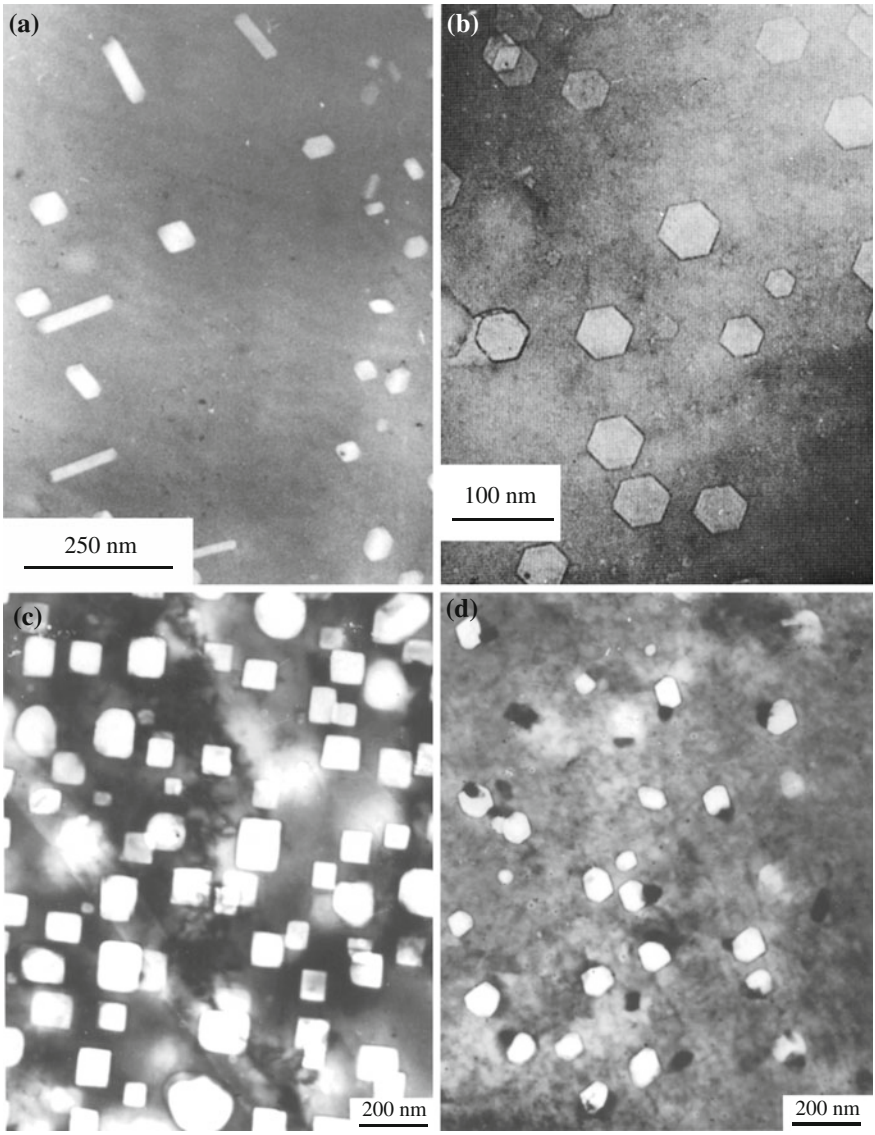

Fig. 8.1 Micrographs of irradiation-induced voids in (**a**) stainless steel, (**b**) aluminum, (**c**) and (**d**) magnesium [2, 3]

8.1 Void Nucleation

The driving force for the formation of voids in solids is the supersaturation of vacancies due to irradiation defined by:

$$S_v = \frac{C_v}{C_v^0}, \tag{8.1}$$

where C_v^0 is the thermal equilibrium concentration of vacancies. During irradiation, defects react to form clusters and the clusters either grow by absorption of defects of the same type, or shrink by absorption of defects of the opposite type. For a cluster of vacancies to grow into a void, there must be a net increase in the number of vacancies absorbed over the number of interstitials absorbed. Thus, we will be interested in the equilibrium void distribution function, $\rho^0(n)$ (where n is the number of vacancies in the void), which is developed by a supersaturation of vacancies in the solid. The distribution function gives the number of vacancy clusters in each size class. Under non-equilibrium conditions, there will be a net flux, J, of voids from one size class to the next larger size class. This is the nucleation current and is the quantity we are interested in finding. The presence of an inert gas in the nucleation process is then considered.

8.1.1 Equilibrium Void Size Distribution

Analogous to the case of point defects (discussed in Chap. 4) and following the derivation in [4], the equilibrium void size distribution is determined from the change in Gibbs free energy of a system containing a distribution $\rho^0(n)$ of vacancy clusters:

$$G = G_0 + \sum_n \rho^0(n) G_n - kT \sum_n \ln w_n, \tag{8.2}$$

where G_0 is the free energy of the perfect lattice, the second term is the work to form a void distribution, and the last term is the entropy contribution to the number of ways that the voids can be distributed in a lattice. The quantity G_n is the Gibbs free energy (reversible work) required to form a void of size n:

$$G_n = H_n - TS_n = E_n + p\upsilon_n - TS_n, \tag{8.3}$$

where

E_n the energy required to form a void of n vacancies
υ_n volume change (= $n\Omega$)
p hydrostatic stress
S_n the excess entropy associated with the process
w_n the number of ways of placing $\rho^0(n)$ voids of size n in the solid.

Neglecting the last two terms on the right, G_n reduces to $G_n \cong E_n$.

For large values of n, the energy of the void can adequately be represented by the surface energy:

$$E_V = 4\pi R_V^2 \gamma, \tag{8.4}$$

where γ is the surface energy of the solid per unit area and R_V is the void radius which is related to the number of vacancies in the void by:

$$n = \frac{4\pi R_V^3}{3\Omega}, \tag{8.5}$$

where Ω is the atomic volume. The reader should note that the expression in Eq. (8.4) is the same as was developed in Eq. (7.58) and for the limiting case of a vacancy, as in Eq. (4.22). Equation (8.4) is, however, an approximation since the energy should properly include terms for the contraction of the surface and for the elastic energy stored in the solid (see Eq. 4.23). Combining Eqs. (8.4) and (8.5) gives:

$$E_n = \left(36\pi\Omega^2\right)^{1/3} \gamma n^{2/3}. \tag{8.6}$$

The last term in Eq. (8.2) is the product of the temperature and the mixing entropy. It can be obtained by calculating the number of ways in which voids can be distributed in a crystal containing N_0 lattice sites per unit volume. The procedure is the same as that used for vacancies in Sect. 4.2 and results in:

$$w_n = \frac{n^{\rho^0(n)}(N_0/n)!}{(N_0/n - \rho^0(n))!(\rho^0(n))!}. \tag{8.7}$$

We now define the chemical potential of a void of size n as μ_n that is related to the Gibbs free energy by:

$$\mu_n = \left.\frac{\partial G}{\partial \rho^0_{(n)}}\right|_{T,p,n}. \tag{8.8}$$

Substituting Eq. (8.7) into Eq. (8.2), using Stirling's approximation for the factorial term in Eq. (8.7), and taking the derivative as required by Eq. (8.8) ($\partial G = \partial \Delta G$ since $\Delta G = G - G_0$) gives:

$$\mu_n = E_n + kT \ln\left[\frac{\rho^0(n)}{N_0}\right]. \tag{8.9}$$

We have neglected $\rho^0(n)$ compared to N_0 because the void concentration is low. For monovacancies ($n = 1$), Eq. (8.9) reduces to:

$$\mu_v = E_v + kT \ln\left(\frac{C_v}{N_0}\right). \tag{8.10}$$

Since the equilibrium concentration of vacancies in a solid is given by:

$$C_v^0 = N_0 \exp\left(\frac{-E_f^v}{kT}\right), \tag{8.11}$$

substituting for N_0 from Eq. (8.11) into Eq. (8.10) gives:

$$\mu_v = kT \ln\left(\frac{C_v}{C_v^0}\right) = kT \ln S_v. \tag{8.12}$$

The criterion for chemical equilibrium is that the chemical potential of reactants and products in the system be the same, i.e.,

$$n\mu_v = \mu_n. \tag{8.13}$$

Substituting Eqs. (8.9) and (8.12) into the criterion for chemical equilibrium, Eq. (8.13) gives:

$$\rho^0(n) = N_0 \exp\left(n \ln S_v - \xi n^{2/3}\right), \tag{8.14}$$

where

$$\xi = \left(36\pi\Omega^2\right)^{1/3} \frac{\gamma}{kT}. \tag{8.15}$$

Substituting Eq. (8.15) into Eq. (8.14) and considering only the term inside the exponent, we have:

$$n \ln S_v - \xi n^{2/3} = n \ln S_v - \frac{\left(36\pi\Omega^2\right)^{1/3} \gamma n^{2/3}}{kT}. \tag{8.16}$$

Expressing Eq. (8.14) as $\rho^0(n) = N_0 \exp(-\Delta G_n^0/kT)$ gives the following expression for ΔG_n^0:

$$\Delta G_n^0 = -nkT \ln S_v + \left(36\pi\Omega^2\right)^{1/3} \gamma n^{2/3}, \tag{8.17}$$

which is just the free energy change in the solid on forming a spherical void consisting of n vacancies on some particular site. A schematic of Eq. (8.17) is shown in Fig. 8.2 in which the free energy is plotted as a function of the number of

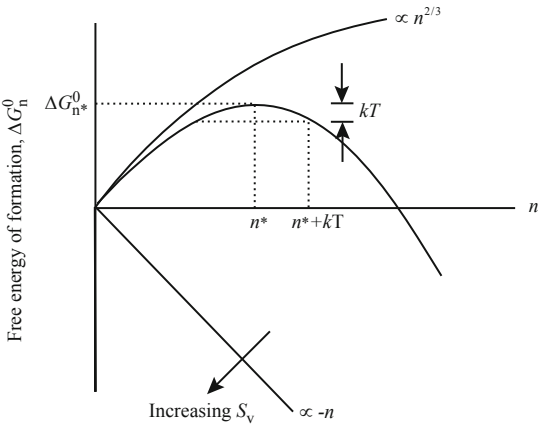

Fig. 8.2 Schematic illustration of ΔG^0_n, the free energy of formation of a spherical void consisting of n vacancies and the effect of thermal fluctuations on the critical size void embryo

vacancies in a void. Note that the first term decreases linearly with n, while the second term increases as $n^{2/3}$. Accounting for the magnitude of the factors in each term, the resulting sum is a curve with a maximum at a value of n^*. This is the critical size of a void embryo which must be achieved in order for the embryo to grow into a void. At the critical point, vacancy addition and removal both cause a reduction in the Gibbs free energy of the system, so this is an unstable point. Above the critical size, addition of vacancies to the embryo causes a decrease in the free energy, which means that void growth is favored, while loss of vacancies causes an increase in the free energy, so this reaction is not favored. Note also that thermal fluctuations add an increment to the embryo size, pushing the critical size to a higher value and thus making it more difficult to nucleate a stable void.

8.1.2 Void Nucleation Rate

The nucleation rate of void embryos (consisting of n vacancies) can be described using the same formalism that was used to describe vacancy loop nucleation in Chap. 7 and developed in [5–7]. However, for the sake of continuity, that derivation will be repeated here for the case of void embryos. Recall from Eq. (7.74) that the nucleation rate of a void embryo of size n is given by:

$$J_n = \rho^0(n)\beta_v(n)Z, \tag{8.18}$$

where $\rho^0(n)$ is the concentration of voids of size n vacancies, $\beta_v(n)$ is the absorption rate, and Z, the Zeldovich factor (defined in Sect. 7.6.1) and the void concentration is given by:

$$\rho^0(n) = N_0 \exp\left(\frac{-\Delta G_n^0}{kT}\right), \tag{8.19}$$

where N_0 is the number of sites on which voids can be formed and ΔG_n^0 is the change in free energy in the solid upon formation of the void and is given in Eq. (8.17). The value of ΔG_n^0 for the critical void embryo size, ΔG_k^0 (for embryo size n_k), is the activation barrier for void formation shown in Fig. 8.3 by the lower curve and is given as:

$$\Delta G_k^0 = -n_k kT \ln S_v + \left(36\pi\Omega^2\right)^{1/3} \gamma n_k^{2/3}. \tag{8.20}$$

The void nucleation rate is the nucleation current given in Eq. (8.18). The void nucleation current, J_n, and activation barrier, ΔG_k^0, apply to the case where only vacancies are present. However, under irradiation, vacancies and interstitials are produced in equal numbers, so the presence of interstitials must be accounted for. We now consider the case where interstitials can also impinge on voids. The analysis is similar to that just presented, but more complicated due to the introduction of another specie that will make void nucleation more difficult.

Consider now the nucleation of vacancy clusters on one particular kind of attractive site [4–6] such as the compressive stress field around a dislocation. The following assumptions are made:

1. The lattice is in thermal and dynamic equilibrium, which are minimally affected by displacement and thermal spikes.
2. Monovacancies and solvent monointerstitials are the only mobile point defects present.
3. The defects obey dilute solution thermodynamics.
4. A steady-state concentration of vacancies and interstitials exists.

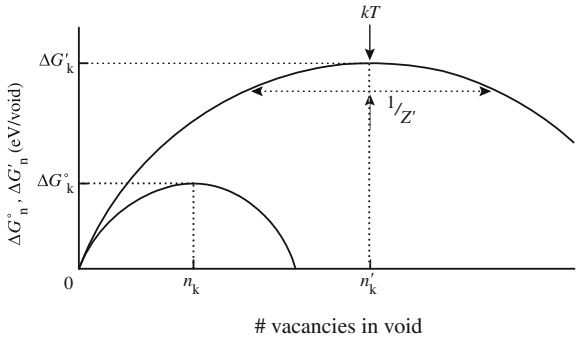

Fig. 8.3 Schematic nucleation curves showing the various parameters which are important in void nucleation. ΔG_k^0 is the activation barrier to nucleation if interstitials are not present, while $\Delta G_k^{'}$ is the same quantity if interstitials are present during the nucleation process (after [6])

Assumption (1) is reasonable as thermal spike lifetimes are very short (10^{-12} s) and dynamical equilibrium should be attained in similar time intervals. Assumption (2) is generally not valid since gas atoms are often present and are known to play an important role in nucleation (treated in Sect. 8.1.3). Assumption (3) should be valid for low defect concentration ($\leq 10^{-4}$ atomic fraction). The final assumption is a gross oversimplification since the microstructure continues to evolve with increasing dose causing sink strength, and therefore defect concentrations, to continually change.

The following derivation of the void nucleation rate from kinetic considerations is similar to that for loops, in which the nucleation rate is expressed as the flux of clusters between adjacent size classes in a phase space of cluster size. A flux is the concentration times velocity or the product of concentration, jump frequency, and jump distance. The flux between any two size classes, say n and $n + 1$, is:

$$J_n = \beta_v(n)\rho(n) - \alpha_v(n+1)\rho(n+1) - \beta_i(n+1)\rho(n+1), \tag{8.21}$$

where $\rho(n)$ and $\rho(n + 1)$ are the number of n-mer (voids containing a net of n vacancies) and $(n + 1)$-mers per unit volume. $\beta_v(n)$ is the rate of vacancy capture by a n-mer, and $\alpha_v(n + 1)$ and $\beta_i(n + 1)$ are the rates of vacancy loss and interstitial capture by a $(n + 1)$-mer, respectively. The first term in Eq. (8.21) represents an addition to the $n + 1$ size class by capture of a vacancy by a void of n-mer size class. The second term is a loss from the $(n + 1)$-mer size class by loss of a vacancy, and the third term is a loss from the $(n + 1)$-mer size class by capture of an interstitial. Interstitial emission is of low probability and is neglected. Figure 8.4 shows the various processes described by Eq. (8.21) in phase space.

Setting $J = 0$ in Eq. (8.21) is equivalent to equilibrating the size classes since there is no net flux between size classes (as we did in Sect. 7.6). If we neglect interstitials, then we can write Eq. (8.21) as:

$$\alpha_v(n+1) = \frac{\beta_v(n)\rho^0(n)}{\rho^0(n+1)}. \tag{8.22}$$

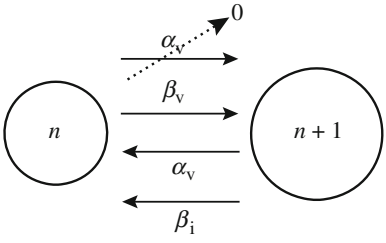

Fig. 8.4 Illustration of the processes governing the flux between adjacent void sizes in a phase space of void size

Combining Eqs. (8.21) and (8.22) gives:

$$J_n = \beta_v(n)\left\{\rho(n) - \rho(n+1)\left[\frac{\rho^0(n)}{\rho^0(n+1)} + \frac{\beta_i(n+1)}{\beta_v(n)}\right]\right\}. \tag{8.23}$$

Since $\rho^0(n) = N_0 \exp(-\Delta G_n^0/kT)$, we note that:

$$\frac{\rho^0(n)}{\rho^0(n+1)} = \exp\left(\frac{\delta G_n^0}{kT}\right), \tag{8.24}$$

where $\delta G_n^0 \equiv \Delta G_{n+1}^0 - \Delta G_n^0$. We now define new functions of n, $\rho'(n)$, and $\delta G_n'$ such that by analogy with Eq. (8.24):

$$\frac{\rho'(n)}{\rho'(n+1)} = \frac{\rho^0(n)}{\rho^0(n+1)} + \frac{\beta_i(n+1)}{\beta_v(n)} = \exp\left(\delta G_n'/kT\right), \tag{8.25}$$

where

$$\delta G_n' = \Delta G_{n+1}' - \Delta G_n', \tag{8.26}$$

and $\Delta G_n'$ is not generally a free energy because of the term $\dfrac{\beta_i(n+1)}{\beta_v(n)}$ in Eq. (8.25). Using the expression in Eq. (8.25), we can rewrite the equation for J_n in terms of $\dfrac{\rho'(n)}{\rho'(n+1)}$ by substituting Eq. (8.25) into Eq. (8.23) to give:

$$J_n = \beta_v(n)\left\{\rho(n) - \rho(n+1)\frac{\rho'(n)}{\rho'(n+1)}\right\}. \tag{8.27}$$

Rearranging Eq. (8.27) gives:

$$J_n = -\beta_v(n)\rho'(n)\left[\frac{\rho(n)}{\rho'(n)} - \frac{\rho(n+1)}{\rho'(n+1)}\right], \tag{8.28}$$

and noting that:

$$\frac{\left[\dfrac{\rho(n)}{\rho'(n)} - \dfrac{\rho(n+1)}{\rho'(n+1)}\right]}{\Delta n} = \frac{\partial\left(\dfrac{\rho(n)}{\rho'(n)}\right)}{\partial n}, \tag{8.29}$$

gives:

$$J_n = -\beta_v(n)\rho'(n)\frac{\partial[\rho(n)/\rho'(n)]}{\partial n}, \tag{8.30}$$

which is the basic flux equation. Rearranging Eq. (8.25) by taking the natural log of both sides and summing from $j = 0$ to $n - 1$ gives:

$$\sum_{j=0}^{n-1} \ln\left(\frac{\rho'(j)}{\rho'(j+1)}\right) = \sum_{j=0}^{n-1} \left\{ -\ln\left[\frac{\beta_i(j+1)}{\beta_v(j)} + \exp\left(\frac{\delta G_j^0}{kT}\right)\right]\right\}, \tag{8.31}$$

and:

$$\ln\left(\frac{\rho'(n)}{\rho'(0)}\right) = \sum_{j=0}^{n-1} \left\{ -\ln\left[\frac{\beta_i(j+1)}{\beta_v(j)} + \exp\left(\frac{\delta G_j^0}{kT}\right)\right]\right\}. \tag{8.32}$$

We can identify two boundary conditions. The first is the quantity $\rho'(0)$, which may be evaluated by noting that as $\beta_i(n)/\beta_v(n) \rightarrow 0$, $\rho'(0) = \rho^0(0)$ and that $\rho^0(0) \rightarrow N_0$, which is simply the number of nucleation sites per unit volume. Since N_0 (and hence $\rho^{'}(0)$) is independent of void concentration, we can write:

$$\begin{aligned} \ln\left(\frac{\rho'(n)}{\rho'(0)}\right) &= \sum_{j=0}^{n-1} \left\{ -\ln\left[\frac{\beta_i(j+1)}{\beta_v(j)} + \exp\left(\frac{\delta G_j^0}{kT}\right)\right]\right\} \\ &= \frac{-\Delta G_n'}{kT}. \end{aligned} \tag{8.33}$$

Since as $\beta_i(n)/\beta_v(n) \rightarrow 0$, $\rho^{'}(0) \rightarrow \rho^0(0)$, and $\rho^0(0)$ is just N_0, the number of nucleation sites per unit volume, we have then:

$$\rho'(n) = N_0 \exp\left(\frac{-\Delta G_n'}{kT}\right), \tag{8.34}$$

and

ΔG_n^0 activation barrier without interstitials,
$\Delta G_n^{'}$ activation barrier with interstitials.

The upper curve in Fig. 8.3 shows $\Delta G_n^{'}$ as functions of n. Note that $\Delta G_n^{'}$ is larger than ΔG_k^0 and requires a larger void size due to the hindering effect of interstitials on the void nucleation process. The maxima in the two curves occur at n_k, ΔG_k^0 and $n_k^{'}$, $\Delta G_k^{'}$.

Now, the steady-state void nucleation rate may be calculated from the expression for J_n in Eq. (8.30):

$$J_k = Z' \beta_k \rho_k', \tag{8.35}$$

which is the rate at which voids escape over the potential barrier of height $\Delta G_k^{'}$ in units of [voids/cm^3 s]. The term β_k is the rate of single vacancy impingement on a void of size $n_k^{'}$. If clusters are assumed to be spherical, then the vacancy impingement rate is expressed by the rate constant for point defect absorption by spherical sinks, as in Eq. (5.84). Since void embryos are small, the capture rate is of

mixed-control type in which both diffusion and reaction rate limitations are of comparable magnitude:

$$\beta_{\mathrm{v}}(n) = \frac{4\pi R_{\mathrm{V}} D_{\mathrm{v}} C_{\mathrm{v}}}{1 + a/R_{\mathrm{V}}}, \tag{8.36}$$

where a is the lattice parameter, assuming that the rate at which vacancies leave a void depends on the size of the void but not on the concentration of vacancies or interstitials or details of the dynamics. Note that for large voids, $a/R_{\mathrm{V}} \rightarrow 0$ and $\beta_{\mathrm{v}}(n)$ has a pure diffusion character.

The term Z', analogous to Z but in the presence of interstitials, is:

$$Z' = \left[-\frac{1}{2\pi kT} \frac{\partial^2 \Delta G'_n}{\partial n^2} \right]^{1/2}_{n'_k}. \tag{8.37}$$

The subscript indicates that the second derivative is to be evaluated at $n = n'_k$. Its value is the width of $\Delta G'_k$ at kT units below the maximum and is in the order of 0.05. The second derivative is found from Eq. (8.25) to be:

$$\frac{1}{kT}\left(\frac{\partial^2 \Delta G'_n}{\partial n^2}\right)_{n'_k} = \left\{ \left[\frac{1}{kT} \frac{\partial^2 \Delta G^0_n}{\partial n^2} \right] \left[\exp\left(\frac{1}{kT} \frac{\partial \Delta G^0}{\partial n} \right) \right] \right\}_{n'_k}, \tag{8.38}$$

giving:

$$\rho'_k = N_0 \exp\left(-\Delta G'_k / kT\right), \tag{8.39}$$

where $\Delta G'_k$ is determined by evaluating Eq. (8.33) at n'_k.

Since the critical void nucleus size is taken as the maximum of the $\Delta G'_n$ curve, differentiating Eq. (8.17) and substituting the result into Eq. (8.33) permit evaluation of $\Delta G'_n$. The maximum in $\Delta G'_n$ is determined by setting $\partial \Delta G'_n / \partial n = 0$:

$$n'_k = \frac{32\pi\gamma^3\Omega^2}{3(k\mathrm{T})^3 \left[\ln\left(\dfrac{\beta_{\mathrm{v}}(n) - \beta_{\mathrm{i}}(n+1)}{\beta^0_{\mathrm{v}}(n)} \right) \right]^3}, \tag{8.40}$$

where $C_{\mathrm{v}}/C^0_{\mathrm{v}} = \beta_{\mathrm{v}}(n)/\beta^0_{\mathrm{v}}(n)$. Since $R_{\mathrm{V}} = \left(\dfrac{3}{4} \dfrac{n\Omega}{\pi} \right)^{1/3}$, the radius corresponding to n'_k is:

$$r'_k = \frac{2\gamma\Omega}{kT \ln\left[\left(\dfrac{\beta_{\mathrm{v}}(n) - \beta_{\mathrm{i}}(n+1)}{\beta^0_{\mathrm{v}}(n)} \right) \right]}. \tag{8.41}$$

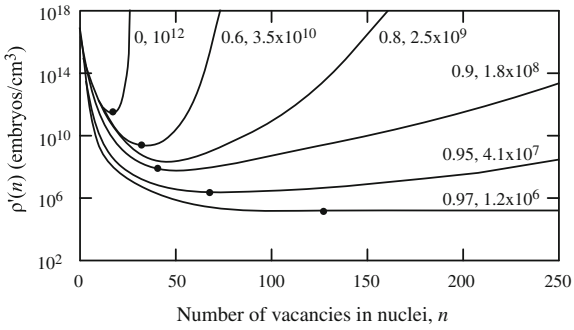

Fig. 8.5 Concentration of void embryos as a function of their size when the net flow of embryos is constrained to be zero. The parameters are the arrival rate ratios β_i/β_v and the nucleation rates (in s^{-1} cm^{-3}) of the unconstrained system. For this example, $T = 627$ °C and $S_v = 430$. *Solid circles* indicate the minima of $n(x)$ (after [8])

Note that as $\beta_i \rightarrow \beta_v$, $r_k' \rightarrow \infty$, which says that if the capture rate for vacancies and interstitials is the same, then the critical void embryo size would need to be ∞.

Figure 8.5 plots $\rho'(n)$ as a function of cluster size n for various values of β_i/β_v for $S_v = 430$ and $T = 627$ °C. Note the effect of increasing the interstitial arrival rate for a fixed vacancy arrival rate. With increasing arrival rate ratio, (β_i/β_v), the slope of the distribution, $d\rho/dn$, decreases everywhere. The reason is that increasing the interstitial flux increases the fraction of embryos of a given size n which actually shrink to the next smallest size $(n - 1)$, whereas to maintain the constrained distribution requires that the increased fraction be balanced by a decreased concentration of nuclei of size n relative to that of size $(n - 1)$.

Increasing the arrival rate ratio also shifts the minimum in the distribution $\rho'(n)$ to larger sizes and to lower concentrations. Since the nucleation rate is proportional to $\rho'(n)$, it decreases tremendously by the deepening and widening of the minimum in $\rho(n)$ as the arrival rate ratio increases. The nucleation rate in Fig. 8.5 decreases about 6 orders of magnitude as the arrival rate ratio is increased from 0 to 0.97.

To obtain void nucleation as β_i/β_v approaches 1 requires higher vacancy supersaturation. The strong dependence of nucleation on vacancy supersaturation is affected only very slightly by the arrival rate ratio. Figure 8.6 shows that a factor of 10 increase in supersaturation causes the nucleation rate to increase from 1 to 10^{15} nuclei/cm^3/s at 627 °C.

The effect of temperature on the vacancy concentration, C^*, required to give a fixed nucleation rate is shown in Fig. 8.7 by the set of curves identified by the arrival rate ratios, β_i/β_v. Over most of the temperature range, C^* increases with

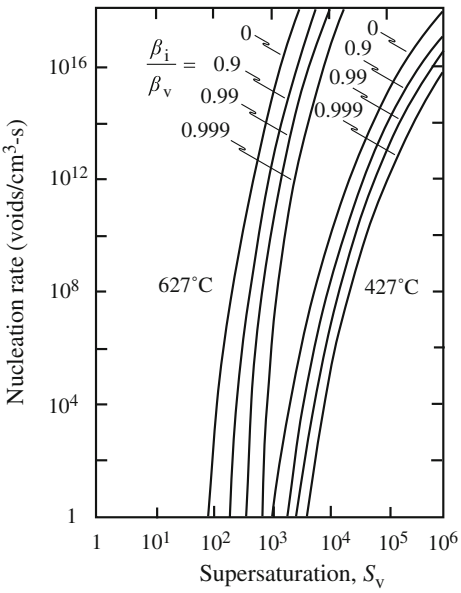

Fig. 8.6 Nucleation rate as a function of the vacancy supersaturation. The parameters are the arrival rate ratios, β_i/β_v, and the temperature (after [8])

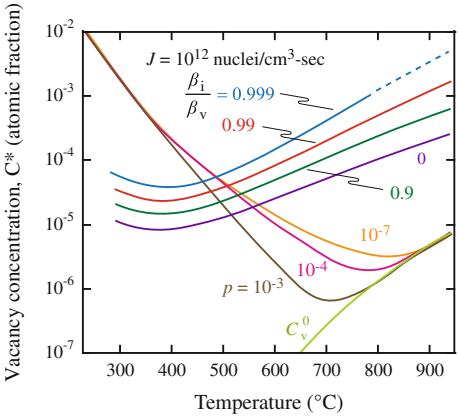

Fig. 8.7 Steady-state vacancy concentration, C^*, caused by a production rate of $K_0 = 10^{-3}$ atom fraction of defect pairs per second. The parameter p on the curves is the probability per jump that a defect is annihilated at existing sinks, such as dislocations. The curve labeled C_v^0 is the thermal equilibrium concentration of vacancies. The set of curves labeled by the arrival rate ratio, β_i/β_v, indicates the vacancy concentration required to give a nucleation rate of 10^{12} void nuclei/cm^{3}s. This nucleation rate is obtained at the temperature and vacancy concentration at the intersection of the curves under the conditions characterized by the curve parameters. The nucleation rate will be higher (*lower*) at temperatures below (*above*) the intersection temperature at fixed values of the parameters (after [8])

temperature even though the supersaturation $S_v = C_v/C_v^0$ decreases. Note that C_v is high at low temperature where the diffusion coefficient is small and there is not much loss. C_v is small at intermediate temperature where annihilation and loss to sinks are great. But C_v is high again at high temperature where $C_v^0 \sim C_v$. The parameter p is the probability per defect jump that the defect is annihilated at a sink. The values of p range from 10^{-7}, typical of an annealed metal to 10^{-3}, which is typical of a heavily cold-worked metal.

Figure 8.8 gives the steady-state vacancy concentrations for several defect production rates K_0 and several nucleation rates J and for a sink-annihilation probability of 10^{-7} and an arrival rate ratio of 0.99. The intersection of the defect production rate and the nucleation rate provides the vacancy concentration at the temperature of the intersection. Higher vacancy production rates promote greater vacancy concentration and a higher nucleation rate.

In summary, the void nucleation rate is a function of the height of the activation barrier. Inclusion of interstitials raises the activation barrier and reduces the nucleation rate. The critical void size radius for survival and growth as a void is a function of the activation barrier height with greater heights requiring larger critical void sizes. Nucleation rate is strongly increased by vacancy supersaturation and a reduced interstitial-to-vacancy arrival rate ratio.

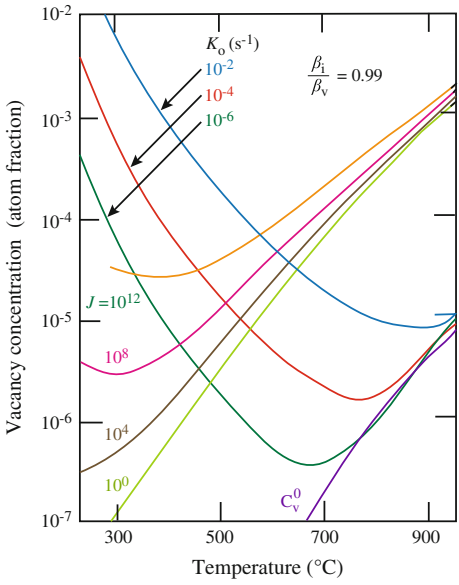

Fig. 8.8 Steady-state vacancy concentrations for several defect production rates and a sink annihilation probability $p = 10^{-7}$ and vacancy concentrations required for several nucleation rates J (in cm^{-3} s^{-1}) at an arrival rate ratio of 0.99. Such nucleation rates are obtained at the indicated defect production rates at the temperature where the curves intersect (after [8])

8.1.3 *Effect of Inert Gas*

Up to this point, we have assumed that a supersaturation of vacancies was sufficient to create a void embryo. It is well known that inert gas atoms may act to stabilize a void embryo and assist in the nucleation process. In fact, there is evidence to suggest that gas atoms are *always* involved in the void nucleation process [6–10]. Hence, several theories have been proposed that involve void nucleation in the presence of inert and non-inert gases [9, 11]. Here, we will consider a simple treatment [4, 9] of an immobile, inert gas, which is just an extension of the theory already developed. We will focus on helium since it is commonly produced by transmutation reactions in core structural materials.

Helium is very immobile compared to vacancies or interstitials in the temperature range of void formation. Once helium is trapped by a void embryo, its return to the matrix is very unlikely. Therefore, nucleation in the presence of helium does not require us to consider the interaction between helium atoms, vacancies, and interstitials in the formation of a void embryo. We may analyze the problem instead, by treating the inert gas atoms as sites for the formation of void embryos by migration of the point defects. In essence, this is a form of heterogeneous void nucleation rather than the homogeneous process described in Sect. 8.1.2.

The phase space description of the gas-containing void behavior is similar to that given in Sect. 8.1.2 and in [6]. The void is assigned coordinates specifying its vacancy content (n) and the number of gas atoms it contains (x) (Fig. 8.9). The void moves in the $+n$ direction by capturing vacancies and in the opposite direction by either thermal emission of vacancies or capture of interstitials:

$$\dot{n} = \beta_{\mathrm{v}}^{0} n^{1/3} - \alpha_{\mathrm{v}} - \beta_{\mathrm{i}}^{0} n^{1/3}, \tag{8.42}$$

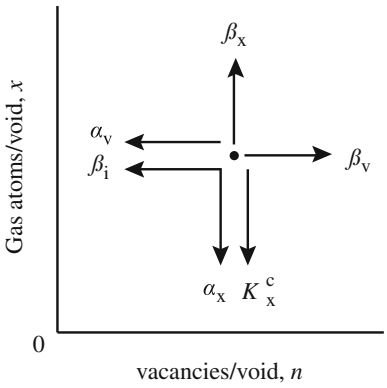

Fig. 8.9 Phase space for void nucleation showing movements of a void following point defect capture (β_i, β_v, β_x) or loss (α_v, α_x, K_x^c) (after [6])

where β_{v}^0 and β_{i}^0 are the arrival rates of vacancies and interstitials to the void, α_{v} is the emission rate of vacancies from the void, and the factor $n^{1/3}$ accounts for the dependence of the capture rate on the void size. Similarly, movement in the positive x-direction occurs by gas atom capture and in the opposite direction by resolution of gas atoms (return of the gas atom to the matrix due to knockout by irradiation) or by thermal emission of gas atoms:

$$\dot{x} = \beta_x^0 n^{1/3} - \alpha_x - xK_x^c, \tag{8.43}$$

where β_{x}^0 is the arrival rate of gas atoms, α_{x} is the emission rate of gas atoms, and $K_{\mathrm{x}}^{\mathrm{c}}$ is the rate of gas atom resolution.

For the case where the voids are in equilibrium with the vacancy and gas atom concentrations, the distribution of gas-filled void embryos containing n vacancies and x gas atoms is:

$$\rho^0(n,x) = N \exp\left(\frac{-\Delta G^0(n,x)}{kT}\right), \tag{8.44}$$

where $\Delta G^0\,(n, x)$ is the free energy of formation of the gas-filled void, also referred to as an (n, x)-mer. For every $(n - 1, x)$-mer capturing a vacancy, a (n, x)-mer will emit a vacancy, and for every $(n, x - 1)$-mer capturing a gas atom, a (n, x)-mer will emit one. Then,

$$\rho^0(n-1,x)\beta_{\mathrm{v}}^0(n-1)^{1/3} = \rho^0(n,x)\alpha_{\mathrm{v}}(n,x), \tag{8.45}$$

and

$$\rho^0(n,x-1)\beta_x^0(x-1)^{1/3} = \rho^0(n,x)\alpha_x(n,x), \tag{8.46}$$

and substituting Eqs. (8.45) and (8.46) into Eq. (8.42) to eliminate $\alpha_{\mathrm{v}}(n, x)$ and $\alpha_x(n, x)$ gives:

$$\dot{n} = \beta_{\mathrm{v}}^0 n^{1/3}\left[1 - \frac{\beta_{\mathrm{i}}^0}{\beta_{\mathrm{v}}^0} - \exp\left(\frac{1}{kT}\frac{\partial \Delta G^0(n,x)}{\partial n}\right)\right] \tag{8.47}$$

$$\dot{x} = \beta_x^0 n^{1/3}\left[1 - \frac{xK_x^c}{\beta_x^0 n^{1/3}} - \exp\left(\frac{1}{kT}\frac{\partial \Delta G^0(n,x)}{\partial x}\right)\right], \tag{8.48}$$

which are the velocities of the void in (n, x) phase space. However, we are interested in the nucleation rate, which requires more development and is described in detail in [4].

We start with a distribution of gas atom clusters, M_x, which is the number of gas atom clusters per unit volume composed of x gas atoms. The total helium concentration in the solid is:

$$M = \sum_{x=1} xM_x, \tag{8.49}$$

and is determined by the helium production rate due to transmutation reactions. We assume that nucleation of voids occurs independently and simultaneously on each of the gas atom clusters characterized by M_x nucleation sites per unit volume. Nucleation is driven by the vacancy and interstitial supersaturation. In addition to heterogeneous nucleation at gas cluster sites, homogenous nucleation is assumed to occur also on the N_0 lattice sites in the solid. The total nucleation rate is the sum of the contributions of the homogeneous and heterogeneous nucleation rates:

$$J = J_{\text{hom}} + \sum_{x=1} J_x, \tag{8.50}$$

where J_{hom} is given by Eq. (8.35). In order to obtain the total nucleation rate, we need to determine the heterogeneous nucleation rate J_x on the M_x gas cluster sites.

The distribution of helium void embryos containing n vacancies and x gas atoms, $\rho^0(n, x)$, is governed by the reaction:

$$n\text{v} = \text{v}_{nx}, \tag{8.51}$$

where v_{nx} denotes a void consisting of n vacancies and x gas atoms. Since helium is immobile, there is no chemical reaction expressing the equilibration of gas atoms between the voids and the bulk. The criterion of chemical equilibrium is then:

$$n\mu_{\text{v}} = \mu_{nx}, \tag{8.52}$$

and the chemical potential of a void with n vacancies and x gas atoms is:

$$\mu_{nx} = \frac{\partial G}{\partial \rho^0(n,x)}. \tag{8.53}$$

The formulation of the total Gibbs free energy for the gas–vacancy cluster is similar to the analysis presented earlier for vacancies alone. Analogous to Eq. (8.2) for voids, the total Gibbs free energy is:

$$G = G_0 + \sum_x \sum_n \left[\rho^0(n,x)G_{nx} - kT \ln w_{nx}\right]. \tag{8.54}$$

As before, w_{nx} *is* the number of ways of arranging ρ^0 $(n\ x)$ voids on M_i sites:

$$w_{nx} = \frac{M_x(M_x-1)\ldots\{M_x-[\rho^0(n,x)-1]\}}{[\rho^0(n,x)]!} = \frac{M_x!}{[M_x-\rho^0(n,x)]![\rho^0(n,x)]!}. \quad (8.55)$$

Using Eq. (8.55) in Eq. (8.54) and using Eq. (8.54) to determine the chemical potential as given in Eq. (8.53) yield:

$$\mu_{nx} = G_{nx} + kT\ln\left[\frac{\rho^0(n,x)}{M_x}\right]. \quad (8.56)$$

The reversible work to form a void embryo from n vacancies and x gas atoms is [4, 12]:

$$G_{nx} = \left(36\pi\Omega^2\right)^{1/3}\gamma n^{2/3} - xkT\ln\left(\frac{MHn\Omega}{xkT}\right). \quad (8.57)$$

The first term is the work to create a gas-free void consisting of n vacancies and is the same as that given in Eq. (8.6) for void formation. The second term is work to move the helium from the solid into the void. H in the second term is the Henry's law constant for the dissolution of helium in the metal. The expression for G_{nx} in Eq. (8.57) is substituted into the expression for the chemical potential of a void with n vacancies and x gas atoms, as in Eq. (8.56). Using the equality in Eq. (8.52) with μ_v given by Eq. (8.12) and solving for ρ^0 (n, x) give:

$$\rho^0(n,x) = M_x\exp\left[n\ln S_v - \xi n^{2/3} + x\ln\left(\frac{MHn\Omega}{xkT}\right)\right], \quad (8.58)$$

which is identical to Eq. (8.14) except for the extra term in the exponent and the pre-exponential factor. In fact, for $x = 0$ and $M_x = N_0$, the result reduces to Eq. (8.14).

Using Eq. (8.44) with M_x substituted for N_0 gives:

$$\Delta G^0(n,x) = -nkT\ln S_v + \left(36\pi\Omega^2\right)^{1/3}\gamma n^{2/3} - xkT\ln\left(\frac{MHn\Omega}{xkT}\right). \quad (8.59)$$

Figure 8.10 shows the free energy of void formation as a function of n and x. The intercept of this surface at $x = 0$ (no gas) corresponds to the $\beta_i/\beta_v = 0$ curve in Fig. 8.5 in which ρ' is plotted as a function of n in Eq. (8.34), $\rho'(n) = N_0\exp(-\Delta G_k'/kT)$, and for $\beta_i/\beta_v = 0$, then $\Delta G_n' = \Delta G(n, x = 0)$. Note that gas atoms in the void reduce the energy barrier for nucleation below that value characteristic of gas-free voids. The saddle point on the surface shown in Fig. 8.10 occurs at $n = 11$ and $x = 6$. The plot, however, does *not* include interstitials (as would a plot of $\Delta G_n'$), which are included in the analysis in exactly the same manner as in the case of homogeneous nucleation.

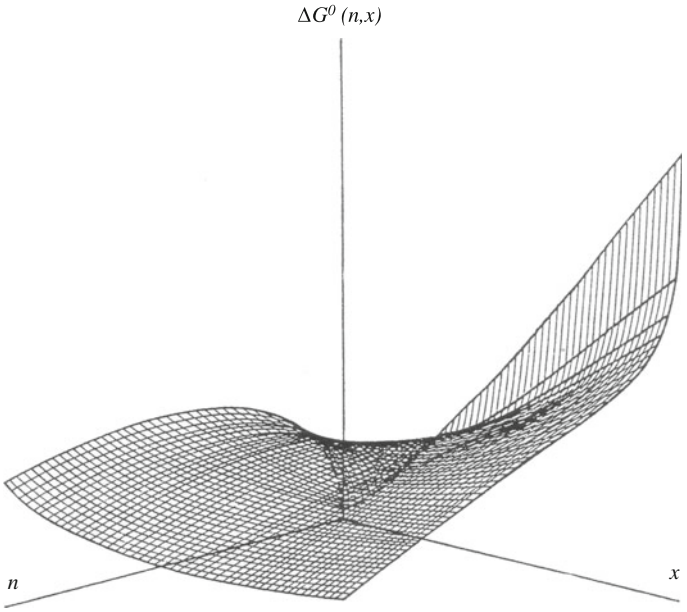

Fig. 8.10 Plot of the free energy of void formation as a function of the number of vacancies (n) and the number of gas atoms (x) in the void. Conditions are as follows: S_v = 600, p_0 = 507 MPa, T = 500 °C, γ = 1 J/m^2 (after [12])

The determination of the nucleation rate is done in the same manner as for homogeneous nucleation, resulting in a nucleation current:

$$J_{k,x} = Z'_x \beta_{kx} \rho'_k(n,x), \tag{8.60}$$

where

$$Z'_x = \left[\frac{-1}{2\pi kT}\frac{\partial^2 \Delta G'(n,x)}{\partial n^2}\right]^{1/2}_{n=n_k}, \tag{8.61}$$

$$\rho'(n,x) = M_x \exp(-\Delta G'(n,x)/kT), \tag{8.62}$$

and

$$\Delta G'(n,x) = kT \sum_{x=0}^{n} \left[\ln\left(\frac{\beta_i^0}{\beta_v^0}\right) + \exp\left(\frac{1}{kT}\frac{\partial \Delta G^0(n,x)}{\partial n}\right)\right], \tag{8.63}$$

and the values of Z'_k and $\rho'(n_k, x)$ are evaluated at the critical void size, n_k, and β_{kx} is the rate of impingement of vacancies on a critical size void.

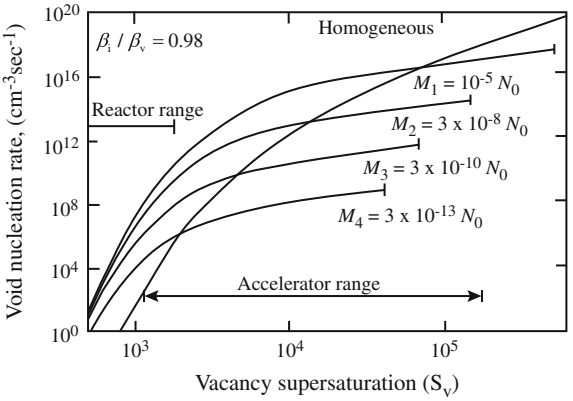

Fig. 8.11 Void nucleation rates (J) on helium atom clusters and the homogeneous nucleation rate (J_{hom}) as functions of vacancy supersaturation at 500 °C. Total helium content of 10 ppm (after [13])

To determine the nucleation rate on the gas atom clusters in the metal, we must estimate the distribution of the available gas (M atoms/cm^3) among the various cluster sizes. For simplicity, the distribution $M_x = M_1^{-(x+1)}$ is assumed. This distribution must satisfy Eq. (8.49). Figure 8.11 shows the results of calculations based on Eqs. (8.60) to (8.62) for M equivalent to 10 ppm helium (equivalent to the amount of helium expected in stainless steel cladding after a fluence of 5×10^{22}n/cm^2). Note that in the regime of vacancy supersaturation expected in a reactor, heterogeneous nucleation on helium atom clusters far outweighs homogeneous nucleation. This behavior constitutes theoretical confirmation of the often-observed enhancement of void nucleation of helium. The relative importance of homogeneous and heterogeneous nucleation shifts according to the helium concentration because $J_{hom}(n)$ is proportional to N_0, whereas $J_x\ (n)$ is proportional to M_x. At low fluence, homogeneous nucleation is dominant because there is not enough helium to drive heterogeneous nucleation. However, since J_{hom} is quite low, no voids are observed until sufficient helium has been generated by transmutation reactions to give the high heterogeneous nucleation rate. This incubation time is physically the relaxation time for the approach to steady state after a step increase in supersaturation. For void formation with or without the presence of gas:

$$\tau = \left(2\beta_k Z_k'\right)^{-1}. \tag{8.64}$$

This value is equivalent to a fluence of 10^{22} n/cm^2 for fast reactor irradiation conditions.

In summary, the effect of gas atoms is to substantially increase the void nucleation rate by lowering the critical radius for a stable void embryo below that for a gas-free void. Therefore, gas atom introduction into the lattice (either by transmutation or by accelerator injection) promotes the formation of voids relative to the pristine lattice.

8.1.4 Void Nucleation with Production Bias

The evolution of dislocation loops under cascade damage conditions was discussed in Sects. 7.5 and 7.6.2 for interstitial clusters. We can use the same treatment to develop a formulation specific to void nucleation [14]. Given that the number of vacancies in a spherical void can be written as:

$$\frac{\mathrm{d}n_\mathrm{v}}{\mathrm{d}t} = \frac{3n_\mathrm{v}^{1/3}}{a^2}\left[D_\mathrm{v}C_\mathrm{v} - D_\mathrm{i}C_\mathrm{i} - D_\mathrm{v}C_\mathrm{v}^0\right] \tag{8.65}$$

$$C_\mathrm{v}^\mathrm{V} = C_\mathrm{v}^0 \exp(2\gamma\Omega/kTR_\mathrm{V}), \tag{8.66}$$

where $a = (3\Omega/4\pi)^{1/3}$, n_v is the number of vacancies in a void, $R_\mathrm{V} = an_\mathrm{v}^{1/3}$, and Ω is the atomic volume, the drift velocity, $F(n)$ (from the Fokker–Planck treatment), is now a single term equal to the RHS of Eq. (8.65). The diffusive spread, described by the term $D(n)$, is a sum of contributions due to single defect jumps, cascades, and vacancy emission as:

$$D(n) = D^s(n) + D^c(n) + D^e(n), \tag{8.67}$$

where

$$D^s(n) = \frac{3n^{1/3}}{2a^2}\left[D_\mathrm{v}\left(C_\mathrm{v} - C_\mathrm{v}^0\right) + D_\mathrm{i}C_\mathrm{i}\right], \tag{8.68}$$

$$D^c(n) = \frac{3n^{2/3}}{4a}\left[\frac{K_\mathrm{v}^\mathrm{eff}\left\langle N_\mathrm{dv}^2\right\rangle}{k_\mathrm{v}N_\mathrm{dv}} + \frac{K_\mathrm{i}^\mathrm{eff}\left\langle N_\mathrm{di}^2\right\rangle}{k_\mathrm{i}N_\mathrm{di}}\right], \tag{8.69}$$

$$D^e(n) = \frac{9D_\mathrm{v}C_\mathrm{v}^0 n^{2/3}}{2a^2}, \tag{8.70}$$

and K_j^eff is the effective generation rate of free point defects, $N_{\mathrm{d}j}$ and $\left\langle N_{\mathrm{d}j}^2\right\rangle$ are the average number and the average square number of free point defects generated in a single cascade, respectively, and k_j^2 is the total sink strength for point defects of the type j. The solution to the general kinetic equation is similar to that for the case of interstitial clusters and is given in [14]. For the case of small critical vacancy size, the void nucleation probability, P_m, is:

$$P_m \cong \left[\frac{\beta}{6\pi R_{\mathrm{cr}} n_{\mathrm{cr}}} \frac{(D_{\mathrm{v}}C_{\mathrm{v}} - D_{\mathrm{i}}C_{\mathrm{i}})}{D_{\mathrm{i}}C_{\mathrm{i}}\left(1 + d n_{\mathrm{cr}}^{1/3}\right)} (n_0 - n_{\mathrm{v0}})\right]^{1/2} \times \exp\left(-\frac{\eta(\beta/R_{\mathrm{cr}}) n_{\mathrm{cr}}^{2/3} - n_0^{2/3}}{1 + 1/\left(d^e n_{\mathrm{cr}}^{1/3}\right) + d^c/d^e}\right), \tag{8.71}$$

where n_0 is the initial void embryo size (generally $\sim$4 vacancies), n_{v0} is a minimum size of a void embryo below which it is no longer a void (generally $\sim$2–3 vacancies), $d = d^{\mathrm{c}} + d^{\mathrm{e}}$, $\beta = 2\gamma\Omega/kT$, and R_{cr} and n_{cr} are the size and vacancy content of the critical size embryo. Assuming that production bias is the main driving force for void growth at elevated temperatures, the ratio $(D_{\mathrm{v}}C_{\mathrm{v}} - D_{\mathrm{i}}C_{\mathrm{i}})/D_{\mathrm{i}}C_{\mathrm{i}}$ is estimated as ε_{i}, the fraction of interstitials produced in cascades in the form of immobile clusters. The term R_{cr} is determined from Eqs. (8.65) and (8.66) under that condition that a void will grow if it receives a net vacancy flux ($D_{\mathrm{v}}C_{\mathrm{v}} > D_{\mathrm{i}}C_{\mathrm{i}}$):

$$R_{\mathrm{cr}} = \frac{\beta D_{\mathrm{v}} C_{\mathrm{v}}^{\mathrm{V}}}{D_{\mathrm{v}}C_{\mathrm{v}} - D_{\mathrm{i}}C_{\mathrm{i}} - D_{\mathrm{v}}C_{\mathrm{v}}^{\mathrm{V}}}, \tag{8.72}$$

and $R(n) = an^{1/3}$. The terms d^{c} and d^{e} are strengths of the diffusive spread for clusters and for vacancy emission relative to single point defects:

$$d^{\mathrm{c}} = \frac{D^{\mathrm{c}}(n_{\mathrm{cr}})}{n_{\mathrm{cr}}^{1/3} D^{\mathrm{s}}(n_{\mathrm{cr}})}, \quad d^{\mathrm{e}} = \frac{D^{\mathrm{e}}(n_{\mathrm{cr}})}{n_{\mathrm{cr}}^{1/3} D^{\mathrm{s}}(n_{\mathrm{cr}})}, \tag{8.73}$$

and the function η has a value between 0.55 and 0.84.

Application of Eq. (8.71) for various values of d^{c} and d^{e} and for a void embryo size of 4 vacancies leads to nucleation probabilities in the range 10^{-6} to 10^{-4} for critical vacancy clusters of size ~100 vacancies (Fig. 8.12). The nucleation rate is then:

$$J \cong \frac{K_{\mathrm{cl}}^{\mathrm{eff}}}{N_{\mathrm{d}}} P_m, \tag{8.74}$$

where $K_{\mathrm{cl}}^{\mathrm{eff}}$ is the effective generation rate of point defects in cluster and free form, N_{d} is the average total number of point defects generated in a single cascade, and ε_{i} is the fraction of interstitials produced in cascades in the form of immobile clusters. Figure 8.13 shows the void nucleation rate calculated for annealed copper compared with experimental data at 250, 300, and 350 °C and different surface energies, γ_{s}, and for different values of d^{e}. In terms of void nuclei created $\mathrm{cm}^{-3}\ \mathrm{s}^{-1}$, the nucleation rate is in the range 10^{15} to 10^{18}, which is larger than what was predicted by conventional nucleation theory. Thus, the effect of production bias is to increase the nucleation rate.

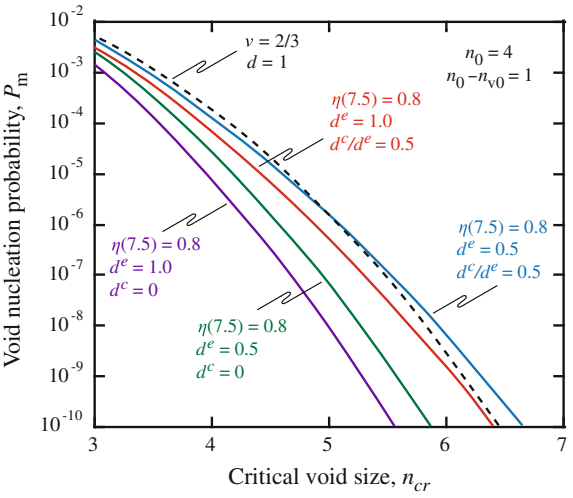

Fig. 8.12 Nucleation probability plotted from Eq. (8.71) for initial void size of four vacancies and minimum size of one vacancy and for different values of d^c and d^e versus the critical void size, n_{cr}. The term $\nu = \frac{(D_v C_v - D_i C_i)[1-\exp(-\beta/R_{cr})]}{D_i C_i}$ (after [14])

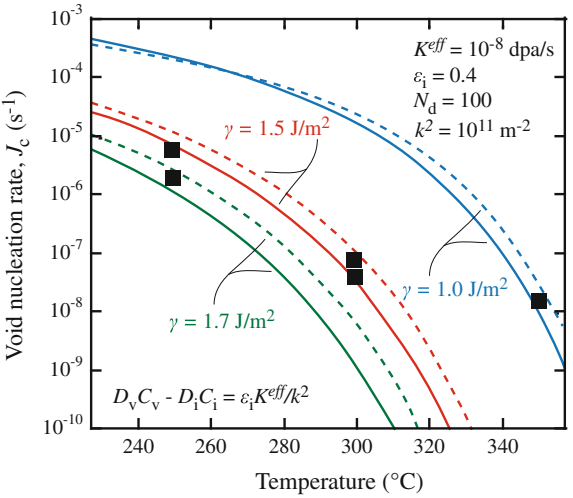

Fig. 8.13 Void nucleation rate versus irradiation temperature for the case of copper under a displacement rate of 10^{-8} dpa/s (after [14])

8.2 Treatment of Defect Sinks in the Growth of Voids

Having determined expressions for the rate at which voids are nucleated in the solid, we now turn to determining the rate at which the void nuclei grow into stable voids. As mentioned earlier, we will assume that the nucleation and growth stages are separated in time and that only after the void embryos are established does growth begin. Of course, this is a simplification of the true in-reactor situation in which the growth of stable nuclei is occurring simultaneously with nucleation.

Void growth is determined by solving the point defect balance equations developed in Chap. 5. These equations provide the vacancy and interstitial supersaturations that drive the nucleation and growth processes. The concentrations of vacancies and interstitials in the solid are determined by equating the rates of defect production and removal by all mechanisms. By doing so, the time derivatives are removed and the resulting solution has the form of a steady-state solution. However, since the defect concentrations are changing with time (dose), the *steady-state* solution is valid over only short time periods and is termed *quasi-steady state*. The quasi-steady-state solution has value because the changes in sink strength due to microstructure evolution are slow compared to the response time of the defect populations. So in essence, the problem can be solved by assuming an initial condition that properly characterizes the sink strengths, solving the point defect balance equations for those sink strengths, then updating the sink strengths, and iterating.

Rates of production and removal are assumed to be uniform throughout the metal. Clearly, strong gradients will exist close to the sink. But they can be neglected by *homogenizing* or *smearing* the sink strengths, that is, by replacing discrete sinks by spatially uniform absorbers of point defects so that the aggregate effect on defect absorption is the same in the homogenized sink case as in the heterogeneous sink case. The sink strengths are those described in Chap. 5. Void growth is then calculated according to rate theory as developed by Brailsford and Bullough [14] subject to the following simplifications:

1. Discrete sinks are replaced by a continuous or *smeared* distribution of sinks.
2. Each sink is given a *strength* so that the current of defects to the *smeared* sink is the same as the current to the actual sinks in the real material.
3. Steps 1 and 2 remove the spatial dependence of C_v and C_i, and the point defect balance equations become:

$$\begin{aligned} \frac{\partial C_v}{\partial t} &= K_0 - \sum_X A_v^X - R_{iv} \\ \frac{\partial C_i}{\partial t} &= K_0 - \sum_X A_i^X - R_{iv}, \end{aligned} \tag{8.75}$$

   where the first term on the right is the production rate of vacancies and interstitials, the second term is the loss rate to all sinks, X, and the last term is the loss rate due to vacancy–interstitial recombination.
4. Vacancy and interstitial concentrations, C_v and C_i, are calculated from Eq. (8.75). The change in sink strength due to the flow of defects to the sink is calculated, and the process, starting with Step 1, is iterated in order to advance in time and dose.

Reaction rate constants for defect–sink reactions and sink strengths for the relevant sinks were determined in Chap. 5 and summarized in Table 5.2. Recall that sinks are classified as neutral (voids, grain boundaries, incoherent precipitates), biased (dislocation network and dislocation loops), or variable biased (coherent precipitates

and over/undersized solutes). For all sink types, the defect absorption rate is proportional to the diffusion coefficient of the point defect and the difference in defect concentration between the bulk and the sink surface. With the exception of dislocation loops, the interstitial concentration at the sink surface is insignificant compared to the bulk value and may be neglected. In the case of vacancies, their concentration at the network dislocation core is maintained at the equilibrium concentration. For voids and loops, the vacancy concentration at the sink surfaces must also be determined. Once the sink strengths and the defect concentrations at the sink surfaces are all known, then we can determine the net absorption rate of defects by void nuclei and use this information to determine the growth rate of the voids.

8.2.1 Defect Absorption Rates and Concentrations at Sink Surfaces

We seek to determine expressions for the absorption rates of defects for each of the relevant sinks, categorized according to sink type. The general form of the absorption rate is:

$$A_j^X = k_X^2 D_j \left(C_j - C_j^X \right) = k_X^2 D_j C_j - L_j^X, \tag{8.76}$$

where A_j^X is the absorption rate of defect j by sink X, k_X^2 is the strength of sink X, D_j is the diffusion coefficient of defect j, C_j and C_j^X are the bulk concentration and sink surface concentration of defect j, respectively, and L_j^X is the thermal emission rate of defect j by sink X. Note that for neutral sinks, the sink strengths are dependent only on the character of the sink and not the defect. This is the advantage of writing the loss terms using sink strengths rather than reaction rate constants.

Neutral Sinks

The loss rate of point defects to voids can be written as:

$$\begin{aligned} A_\mathrm{v}^\mathrm{V} &= k_\mathrm{V}^2 D_\mathrm{v} \left(C_\mathrm{v} - C_\mathrm{v}^\mathrm{V} \right) = k_\mathrm{V}^2 D_\mathrm{v} C_\mathrm{v} - L_\mathrm{v}^\mathrm{V} \\ A_\mathrm{i}^\mathrm{V} &= k_\mathrm{V}^2 D_\mathrm{i} C_\mathrm{i}, \end{aligned} \tag{8.77}$$

where k_V^2 is the sink strength of a void given in Table 5.2, C_v^V is the vacancy concentration at the void surface, L_v^V is the thermal emission rate of vacancies at the sink surface, and all voids are assumed to be the same size. The loss rate of defects to incoherent precipitates is:

$$\begin{aligned} A_\mathrm{v}^\mathrm{IP} &= k_\mathrm{IP}^2 D_\mathrm{v} C_\mathrm{v} \\ A_\mathrm{i}^\mathrm{IP} &= k_\mathrm{IP}^2 D_\mathrm{i} C_\mathrm{i}, \end{aligned} \tag{8.78}$$

and to grain boundaries, the rate is:

$$\begin{aligned} A_{\mathrm{v}}^{\mathrm{gb}} &= k_{\mathrm{gb}}^2 D_{\mathrm{v}} C_{\mathrm{v}} \\ A_{\mathrm{i}}^{\mathrm{gb}} &= k_{\mathrm{gb}}^2 D_{\mathrm{i}} C_{\mathrm{i}}, \end{aligned} \tag{8.79}$$

where the sink strengths are given in Table 5.2, and thermal emission terms have been neglected.

Among Eqs. (8.77), (8.78), and (8.79), the term that is yet to be determined is the vacancy concentration at the void surface, $C_{\mathrm{v}}^{\mathrm{V}}$. This is done as follows. Recall from Eq. (4.15) that the thermal equilibrium concentration of vacancies in a solid is:

$$C_{\mathrm{v}}^0 = \frac{1}{\Omega} \exp\left(\frac{S_{\mathrm{f}}}{k}\right) \exp\left(\frac{-H_{\mathrm{f}}}{kT}\right),$$

where

$$H_{\mathrm{f}} = E_{\mathrm{f}} + p\Omega, \tag{8.80}$$

and the $p\Omega$ term was neglected for single vacancies embedded in the lattice. This simplification does not hold in the solid surrounding a void where forces such as surface tension, pressure due to gas in the void, or an external hydrostatic stress are acting. For example, the existence of a void surface produces a surface tension that can be determined, using Fig. 8.14, as follows:

$$\frac{\text{Force}}{\text{unit area}} = \frac{2\pi r\gamma \sin\theta}{A} \cong \frac{2\pi r\gamma}{\pi r^2}\theta = \frac{2\pi r\gamma}{\pi r^2}\left(\frac{r}{R}\right) = \frac{2\gamma}{R}, \tag{8.81}$$

where the approximation is that sin θ is replaced with θ for small θ. Hence, the p term in Eq. (8.80) becomes:

$$p = -\frac{2\gamma}{R}, \tag{8.82}$$

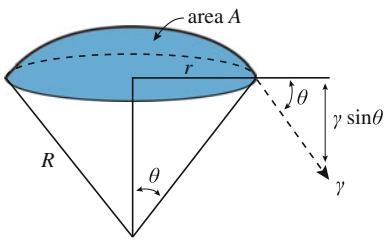

Fig. 8.14 Schematic of the surface tension on a void of radius R

where the minus sign enters because the surface tension acts in an inward direction to shrink the void. The vacancy concentration at the void surface then becomes:

$$C_{\mathrm{v}}^{\mathrm{V}} = \frac{1}{\Omega}\exp\left(\frac{S_{\mathrm{f}}}{k}\right)\exp\left(-\frac{E_{\mathrm{f}}}{kT}\right)\exp\left(-\frac{p\Omega}{kT}\right), \tag{8.83}$$

where

$$C_{\mathrm{v}}^{0} = \frac{1}{\Omega}\exp\left(\frac{S_{\mathrm{f}}}{k}\right)\exp\left(-\frac{E_{\mathrm{f}}}{kT}\right), \tag{8.84}$$

and substituting for $p\Omega$ from Eq. (8.82) gives:

$$C_{\mathrm{v}}^{\mathrm{V}} = C_{\mathrm{v}}^{0}\exp\left(\frac{2\gamma\Omega}{RkT}\right), \tag{8.85}$$

and Eq. (8.77) becomes:

$$A_{\mathrm{v}}^{\mathrm{V}} = k_{\mathrm{V}}^{2}D_{\mathrm{v}}\left[C_{\mathrm{v}} - C_{\mathrm{v}}^{0}\exp\left(\frac{2\gamma\Omega}{RkT}\right)\right]. \tag{8.86}$$

Biased Sinks

The defect loss rate to network dislocations is given by:

$$\begin{aligned} A_{\mathrm{v}}^{N} &= k_{\mathrm{vN}}^{2}D_{\mathrm{v}}\left(C_{\mathrm{v}} - C_{\mathrm{v}}^{0}\right) = k_{\mathrm{vN}}^{2}D_{\mathrm{v}}C_{\mathrm{v}} - L_{\mathrm{v}}^{N} \\ A_{\mathrm{i}}^{N} &= k_{\mathrm{iN}}^{2}D_{\mathrm{i}}C_{\mathrm{i}}, \end{aligned} \tag{8.87}$$

where the sink strengths are given in Table 5.2 and the term C_{v}^{0} is the thermal equilibrium concentration of vacancies. For interstitial dislocation loops, the loss term is:

$$\begin{aligned} A_{\mathrm{v}}^{\mathrm{L}} &= k_{\mathrm{vL}}^{2}D_{\mathrm{v}}\left(C_{\mathrm{v}} - C_{\mathrm{v}}^{\mathrm{L}}\right) = k_{\mathrm{vL}}^{2}D_{\mathrm{v}}C_{\mathrm{v}} - L_{\mathrm{v}}^{\mathrm{L}} \\ A_{\mathrm{i}}^{\mathrm{L}} &= k_{\mathrm{iL}}^{2}D_{\mathrm{i}}\left(C_{\mathrm{i}} - C_{\mathrm{i}}^{\mathrm{L}}\right) = k_{\mathrm{iL}}^{2}D_{\mathrm{i}}C_{\mathrm{i}} - L_{\mathrm{i}}^{\mathrm{L}}, \end{aligned} \tag{8.88}$$

where the sink strengths are the same as for network dislocations since the dislocation core is the same. However, the defect concentration at the sink surface is different from the thermal equilibrium value because addition of a vacancy or an interstitial to the dislocation loop contracts or expands, respectively, the size of the loop and this requires a change in energy. The concentration of vacancies and interstitials in equilibrium with a loop is $C_{\mathrm{v}}^{\mathrm{L}}$ and $C_{\mathrm{i}}^{\mathrm{L}}$, respectively. Following the analysis in [4], the defect concentration in equilibrium with the loop is determined

by considering the Gibbs free energy of a piece of metal containing n_v vacancies and n_i interstitials at concentrations C_v^L and C_i^L, and a single interstitial loop containing m_i interstitials:

$$G = G_0 + E_L(m_i) + n_v\mu_v + n_i\mu_i, \tag{8.89}$$

where G_0 is the free energy of solid without the loop but with C_v and C_i defects, $E_L(m_i)$ is the energy of the loop, and $\mu_{i,v}$ are the chemical potentials of interstitials and vacancies in the solid. For the system to be in chemical equilibrium, the transfer of point defects between the solid and the loop must cause no change in the free energy of the system:

$$\delta G = \left(\frac{dE_L}{dm_i}\right)\delta m_i + \mu_v\delta n_v + \mu_i\delta n_i = 0, \tag{8.90}$$

and

$$\delta m_i = \delta n_v - \delta n_i, \tag{8.91}$$

since the number of interstitials in the loop must come from the bulk. Eliminating δm_i from Eqs. (8.90) and (8.91) gives:

$$\left(\frac{dE_L}{dm_i}\right)\delta n_v - \left(\frac{dE_L}{dm_i}\right)\delta n_i + \mu_v\delta n_v + \mu_i\delta n_i = 0. \tag{8.92}$$

Since changes in vacancy and interstitial concentrations are arbitrary and independent of each other, the coefficients of both changes are set equal to zero, leading to:

$$\begin{aligned} \frac{dE_L}{dm_i} + \mu_v &= 0 \\ \frac{dE_L}{dm_i} - \mu_i &= 0. \end{aligned} \tag{8.93}$$

From Eq. (8.12), the chemical potential of vacancies and interstitials in a solid with concentrations C_v^L and C_i^L is:

$$\begin{aligned} \mu_v &= kT\ln\frac{C_v^L}{C_v^0} \\ \mu_i &= kT\ln\frac{C_i^L}{C_i^0}. \end{aligned} \tag{8.94}$$

For vacancies and interstitials in equilibrium,

$$C_{\mathrm{v}}^{\mathrm{L}} C_{\mathrm{i}}^{\mathrm{L}} = C_{\mathrm{v}}^{0} C_{\mathrm{i}}^{0}, \tag{8.95}$$

or from Eq. (8.93):

$$\mu_{\mathrm{v}} = -\mu_{\mathrm{i}}. \tag{8.96}$$

Combining Eqs. (8.93) and (8.94) for vacancies and then for interstitials yields:

$$\begin{aligned} C_{\mathrm{v}}^{\mathrm{L}} &= C_{\mathrm{v}}^{0} \exp\left(-\frac{\mathrm{d}E_{\mathrm{L}}/\mathrm{d}m_{\mathrm{i}}}{kT}\right) \\ C_{\mathrm{i}}^{\mathrm{L}} &= C_{\mathrm{i}}^{0} \exp\left(\frac{\mathrm{d}E_{\mathrm{L}}/\mathrm{d}m_{\mathrm{i}}}{kT}\right). \end{aligned} \tag{8.97}$$

Using Eq. (7.62) for the energy of a Frank loop:

$$E_{\mathrm{L}} = 2\pi\mu b^2 \left(\frac{\sqrt{3}a^2 m_{\mathrm{i}}}{4\pi}\right)^{1/2} + \pi\left(\frac{\sqrt{3}a^2 m_{\mathrm{i}}}{4\pi}\right)\gamma_{\mathrm{SFE}},$$

and dropping the second term for simplicity, then $\mathrm{d}E_{\mathrm{L}}/\mathrm{d}m_{\mathrm{i}}$ becomes:

$$\frac{\mathrm{d}E_{\mathrm{L}}}{\mathrm{d}m_{\mathrm{i}}} = \frac{\Theta}{2\sqrt{m_{\mathrm{i}}}}, \tag{8.98}$$

where Θ is $2\pi\mu b^2 \left(\frac{\sqrt{3}a^2}{4\pi}\right)^{1/2}$. Substituting into Eq. (8.97) yields:

$$\begin{aligned} C_{\mathrm{v}}^{\mathrm{L}} &= C_{\mathrm{v}}^{0} \exp\left(-\frac{\Theta}{2\sqrt{m_{\mathrm{i}}}kT}\right) \\ C_{\mathrm{i}}^{\mathrm{L}} &= C_{\mathrm{i}}^{0} \exp\left(\frac{\Theta}{2\sqrt{m_{\mathrm{i}}}kT}\right). \end{aligned} \tag{8.99}$$

Note that the vacancy concentration in equilibrium with an interstitial loop is less than the equilibrium vacancy concentration in the solid, while the reverse is true for interstitials. The absorption rates of vacancies and interstitials at loops then become, from Eq. (8.88):

$$\begin{aligned} A_{\mathrm{v}}^{\mathrm{L}} &= z_{\mathrm{v}} D_{\mathrm{v}} \rho_{\mathrm{L}} \left[C_{\mathrm{v}} - C_{\mathrm{v}}^{0} \exp\left(-\frac{\Theta}{2\sqrt{m_{\mathrm{i}}}kT}\right)\right] \\ A_{\mathrm{i}}^{\mathrm{L}} &= z_{\mathrm{i}} D_{\mathrm{i}} \rho_{\mathrm{L}} \left[C_{\mathrm{i}} - C_{\mathrm{i}}^{0} \exp\left(\frac{\Theta}{2\sqrt{m_{\mathrm{i}}}kT}\right)\right]. \end{aligned} \tag{8.100}$$

Variable Biased Sinks

The sink strengths for variable biased sinks are given in Eq. (5.120) and are:

$$k_{\mathrm{vCP}}^2 = 4\pi R_{\mathrm{CP}} \rho_{\mathrm{CP}} Y_{\mathrm{v}}$$
$$k_{\mathrm{iCP}}^2 = 4\pi R_{\mathrm{CP}} \rho_{\mathrm{CP}} Y_{\mathrm{i}},$$

where $Y_{\mathrm{v,i}}$ are sink strengths for coherent precipitates for vacancies and interstitials and the loss rate of point defects to coherent precipitates is:

$$\begin{aligned} A_{\mathrm{v}}^{\mathrm{CP}} &= k_{\mathrm{vCP}}^2 D_{\mathrm{v}} C_{\mathrm{v}} = 4\pi R_{\mathrm{CP}} \rho_{\mathrm{CP}} C_{\mathrm{v}} Y_{\mathrm{v}} \\ A_{\mathrm{i}}^{\mathrm{CP}} &= k_{\mathrm{iCP}}^2 D_{\mathrm{i}} C_{\mathrm{i}} = 4\pi R_{\mathrm{CP}} \rho_{\mathrm{CP}} C_{\mathrm{i}} Y_{\mathrm{i}}. \end{aligned} \tag{8.101}$$

8.2.2 Point Defect Balances

Now that we have expressions for the absorption rates of defects for each type of sink, we can construct the steady-state, point defect balances for the solid under irradiation:

$$\begin{aligned} K_0 - \sum_X A_{\mathrm{v}}^X - R_{\mathrm{iv}} &= 0 \\ K_0 - \sum_X A_{\mathrm{i}}^X - R_{\mathrm{iv}} &= 0, \end{aligned} \tag{8.102}$$

and in the most general form:

$$\begin{aligned} K_0 - k_{\mathrm{v}}^2 D_{\mathrm{v}} \left(C_{\mathrm{v}} - C_{\mathrm{v}}^X \right) - K_{\mathrm{iv}} C_{\mathrm{v}} C_{\mathrm{i}} &= 0 \\ K_0 - k_{\mathrm{i}}^2 D_{\mathrm{i}} \left(C_{\mathrm{i}} - C_{\mathrm{i}}^X \right) - K_{\mathrm{iv}} C_{\mathrm{v}} C_{\mathrm{i}} &= 0, \end{aligned} \tag{8.103}$$

where k_{v}^2 and k_{i}^2 are the total sink strengths for vacancy and interstitial loss:

$$\begin{aligned} k_{\mathrm{v}}^2 &= k_{\mathrm{vV}}^2 + k_{\mathrm{vIP}}^2 + k_{\mathrm{vgb}}^2 + k_{\mathrm{vN}}^2 + k_{\mathrm{vL}}^2 + k_{\mathrm{vCP}}^2 \\ k_{\mathrm{i}}^2 &= k_{\mathrm{iV}}^2 + k_{\mathrm{iIP}}^2 + k_{\mathrm{igb}}^2 + k_{\mathrm{iN}}^2 + k_{\mathrm{iL}}^2 + k_{\mathrm{iCP}}^2, \end{aligned} \tag{8.104}$$

and the C_{v}^X and C_{i}^X are concentrations of vacancies and interstitials at the sink surface. Now, since defect production rates and recombination rates in Eq. (8.103) are equal and there is no net accumulation of point defects at coherent precipitates, then:

$$\sum_X A_{\mathrm{v}}^X = \sum_X A_{\mathrm{i}}^X, \tag{8.105}$$

or

$$A_{\mathrm{v}}^{\mathrm{V}} + A_{\mathrm{v}}^{\mathrm{IP}} + A_{\mathrm{v}}^{\mathrm{gb}} + A_{\mathrm{v}}^{N} + A_{\mathrm{v}}^{\mathrm{L}} + A_{\mathrm{v}}^{\mathrm{CP}} = A_{\mathrm{i}}^{\mathrm{V}} + A_{\mathrm{i}}^{\mathrm{IP}} + A_{\mathrm{i}}^{\mathrm{gb}} + A_{\mathrm{i}}^{N} + A_{\mathrm{i}}^{\mathrm{L}} + A_{i}^{\mathrm{CP}}, \quad (8.106)$$

and therefore,

$$\begin{aligned}&(k_{\mathrm{vV}}^2 + k_{\mathrm{vIP}}^2 + k_{\mathrm{vgb}}^2 + k_{\mathrm{vN}}^2 + k_{\mathrm{vL}}^2 + k_{\mathrm{vCP}}^2) D_{\mathrm{v}} C_{\mathrm{v}} - L_{\mathrm{v}}^{\mathrm{V}} - L_{\mathrm{v}}^{N} - L_{\mathrm{v}}^{\mathrm{L}} \\ &= (k_{\mathrm{iV}}^2 + k_{\mathrm{iIP}}^2 + k_{\mathrm{igb}}^2 + k_{\mathrm{iN}}^2 + k_{\mathrm{iL}}^2 + k_{\mathrm{iCP}}^2) D_{\mathrm{i}} C_{\mathrm{i}} - L_{\mathrm{i}}^{\mathrm{L}}.\end{aligned} \quad (8.107)$$

where the L terms are the thermal emission of the defect from the sink.

Substituting in for the expressions for sink strength and thermal emission from the respective equations in Chaps. 5 and 7 gives:

$$\begin{aligned}4\pi R_{\mathrm{V}} \rho_{\mathrm{V}} D_{\mathrm{v}} &\left[C_{\mathrm{v}} - C_{\mathrm{v}}^0 \exp\left(\frac{2\gamma\Omega}{RkT}\right)\right] + z_{\mathrm{v}} \rho_N D_{\mathrm{v}} (C_{\mathrm{v}} - C_{\mathrm{v}}^0) + 4\pi R_{\mathrm{CP}} \rho_{\mathrm{CP}} D_{\mathrm{v}} C_{\mathrm{v}} Y_{\mathrm{v}} \\ &+ z_{\mathrm{v}} \rho_{\mathrm{L}} D_{\mathrm{v}} \left[C_{\mathrm{v}} - C_{\mathrm{v}}^0 \exp\left(-\frac{\Theta}{2\sqrt{m_{\mathrm{i}} kT}}\right)\right] \\ &= \pi R_{\mathrm{V}} \rho_{\mathrm{V}} D_{\mathrm{i}} C_{\mathrm{i}} + z_{\mathrm{i}} \rho_{\mathrm{N}} D_{\mathrm{i}} C_{\mathrm{i}} + 4\pi R_{\mathrm{CP}} \rho_{\mathrm{CP}} D_i C_i Y_{\mathrm{i}} \\ &+ z_{\mathrm{i}} \rho_{\mathrm{L}} D_{\mathrm{i}} \left[C_{\mathrm{i}} - C_{\mathrm{i}}^0 \exp\left(\frac{\Theta}{2\sqrt{m_{\mathrm{i}} kT}}\right)\right],\end{aligned} \quad (8.108)$$

where terms for grain boundaries and incoherent precipitates are neglected for simplicity. Since the thermal equilibrium interstitial concentration, C_{i}^0, is extremely small, the thermal emission of interstitials from loops can be neglected.

8.3 Void Growth

Now that we have determined the absorption rate of defects for each sink in the solid, we focus on the void with the objective of developing an expression describing its rate of growth. The void growth equation has its origins in the net flux of vacancies to a void embryo. The *net* rate of absorption of vacancies by a void is:

$$A_{\mathrm{net}}^{\mathrm{V}} = A_{\mathrm{v}}^{\mathrm{V}} - A_{\mathrm{i}}^{\mathrm{V}} = 4\pi R D_{\mathrm{v}} (C_{\mathrm{v}} - C_{\mathrm{v}}^{\mathrm{V}}) - 4\pi R D_{\mathrm{i}} C_{\mathrm{i}}, \quad (8.109)$$

where

R is void radius (we have dropped the subscript V for simplicity)
$C_{\mathrm{v,i}}$ is vacancy/interstitial concentration in the solid
$C_{\mathrm{v}}^{\mathrm{V}}$ is vacancy concentration at the void surface, and thermal emission of interstitials from voids is neglected.

The rate of change in volume of the void is just the net absorption rate times the defect volume, Ω:

$$\frac{dV}{dt} = 4\pi R\Omega\left[D_v(C_v - C_v^V) - D_i C_i\right], \tag{8.110}$$

and since

$$V = \frac{4}{3}\pi R^3, \tag{8.111}$$

we obtain the common form of the void growth equation:

$$\frac{dR}{dt} = \dot{R} = \frac{\Omega}{R}\left[D_v(C_v - C_v^V) - D_i C_i\right]. \tag{8.112}$$

Our objective is to determine an expression for the void growth equation, which amounts to determining the values for C_v, C_i, and C_v^V. The general solution procedure is thus to solve the point defect balance equations in Eq. (8.75) for C_v and C_i at some initial value of the void radius, R_0, and then to use those values of C_v and C_i in Eq. (8.112) to increment the void size from R_0 to R'. Since sink strength changes with void size, updated values of C_v and C_i must be obtained for the next void growth increment. The process is then iterated to describe the change in void size with time or dose. This process can be carried out numerically and with small time steps in order to minimize the time increment over which the sink strengths are assumed to be constant. In solving for void size in this way, changes to the microstructure can also be incorporated at the time step boundaries.

While a numerical solution of the void growth equation will produce the most accurate result, it provides no insight into the governing processes during void growth. Brailsford and Bullough [15] inserted the solution of Eq. (8.75) into Eq. (8.112) to obtain an approximate analytical result that provides an excellent tool for understanding the parameters governing void growth. Mansur [5, 16] advanced the analysis to develop expressions for the dependence on critical parameters affecting void growth. We begin by returning to the point defect balance equations at steady state in order to determine the bulk concentrations of vacancies and interstitials, C_v and C_i. Setting the time rate of change of the vacancy and interstitial concentrations equal to zero in Eq. (8.75) gives:

$$\begin{aligned} K_0 - \sum_X A_v^X - R_{iv} &= 0 \\ K_0 - \sum_X A_i^X - R_{iv} &= 0, \end{aligned} \tag{8.113}$$

or

$$\begin{aligned} K_0 - K_{\mathrm{iv}} C_{\mathrm{i}} C_{\mathrm{v}} - K_{\mathrm{vs}} C_{\mathrm{v}} C_{\mathrm{s}} &= 0 \\ K_0 - K_{\mathrm{iv}} C_{\mathrm{i}} C_{\mathrm{v}} - K_{\mathrm{is}} C_{\mathrm{i}} C_{\mathrm{s}} &= 0, \end{aligned} \tag{8.114}$$

with solutions:

$$\begin{aligned} C_{\mathrm{v}} &= \frac{-K_{\mathrm{is}} C_{\mathrm{s}}}{2K_{\mathrm{iv}}} + \left[\frac{K_0 K_{is}}{K_{\mathrm{iv}} K_{\mathrm{vs}}} + \frac{K_{is}^2 C_{\mathrm{s}}^2}{4K_{\mathrm{iv}}} \right]^{1/2} \\ C_{\mathrm{i}} &= \frac{-K_{\mathrm{vs}} C_{\mathrm{s}}}{2K_{\mathrm{iv}}} + \left[\frac{K_0 K_{\mathrm{vs}}}{K_{\mathrm{iv}} K_{is}} + \frac{K_{\mathrm{vs}}^2 C_{\mathrm{s}}^2}{4K_{\mathrm{iv}}} \right]^{1/2}, \end{aligned} \tag{8.115}$$

where C_{s} is the sink concentration. Using Table 5.2 to write the reaction rate constants for vacancies and interstitials at sinks as sink strengths gives:

$$\begin{aligned} C_{\mathrm{v}} &= \frac{-k_{\mathrm{i}}^2 D_{\mathrm{i}}}{2K_{\mathrm{iv}}} + \left[\frac{K_0 k_{\mathrm{i}}^2 D_{\mathrm{i}}}{K_{\mathrm{iv}} k_{\mathrm{v}}^2 D_{\mathrm{v}}} + \frac{(k_{\mathrm{i}}^2)^2 D_{\mathrm{i}}^2}{4K_{\mathrm{iv}}} \right]^{1/2} \\ C_{\mathrm{i}} &= \frac{-k_{\mathrm{v}}^2 D_{\mathrm{v}}}{2K_{\mathrm{iv}}} + \left[\frac{K_0 k_{\mathrm{v}}^2 D_{\mathrm{v}}}{K_{\mathrm{iv}} k_i^2 D_{\mathrm{i}}} + \frac{(k_{\mathrm{v}}^2)^2 D_{\mathrm{i}}^2}{4K_{\mathrm{iv}}} \right]^{1/2}. \end{aligned} \tag{8.116}$$

Defining:

$$\eta = \frac{4K_{\mathrm{iv}} K_0}{D_{\mathrm{i}} D_{\mathrm{v}} k_{\mathrm{v}}^2 k_{\mathrm{i}}^2}, \tag{8.117}$$

and

$$\begin{aligned} k_{\mathrm{v}}^2 &= z_{\mathrm{v}} \rho_{\mathrm{d}} + 4\pi R \rho_{\mathrm{V}} + 4\pi R_{\mathrm{CP}} \rho_{\mathrm{CP}} \\ k_{\mathrm{i}}^2 &= z_{\mathrm{i}} \rho_{\mathrm{d}} + 4\pi R \rho_{\mathrm{V}} + 4\pi R_{\mathrm{CP}} \rho_{\mathrm{CP}}, \end{aligned} \tag{8.118}$$

where, for simplicity, we have neglected grain boundaries, incoherent precipitates and bias factors on voids and coherent precipitates, and the network dislocations and dislocation loops are represented by a single term with density $\rho_{\mathrm{d}} = \rho_{\mathrm{N}} + \rho_{\mathrm{L}}$. Using Eqs. (8.117) and (8.118), then Eq. (8.116) can be written as:

$$\begin{aligned} C_{\mathrm{v}} &= \frac{D_{\mathrm{i}} k_{\mathrm{i}}^2}{2K_{\mathrm{iv}}} \left[(\eta + 1)^{1/2} - 1 \right] \\ C_{\mathrm{i}} &= \frac{D_{\mathrm{v}} k_{\mathrm{v}}^2}{2K_{\mathrm{iv}}} \left[(\eta + 1)^{1/2} - 1 \right]. \end{aligned} \tag{8.119}$$

The void growth rate from Eq. (8.112) can be written in the form:

$$\dot{R} = \dot{R}_0 X(\eta), \tag{8.120}$$

where

$$\dot{R}_0 = \frac{\dfrac{K_0(z_i - z_v)\rho_d \Omega}{R(z_v\rho_d + 4\pi R\rho_V)}}{z_i\rho_d + 4\pi R\rho_V + 4\pi R_{CP}\rho_{CP}\left[1 + \dfrac{(z_i - z_v)\rho_d}{z_v\rho_d + 4\pi R\rho_V}\right]}. \tag{8.121}$$

Equation (8.121) can be simplified by dropping the last term in the square brackets in the denominator, since the difference $(z_i - z_v)$ is small, giving:

$$\dot{R}_0 = \frac{K_0(z_i - z_v)\rho_d \Omega}{R(z_v\rho_d + 4\pi R\rho_V)(z_i\rho_d + 4\pi R\rho_V + 4\pi R_{CP}\rho_{CP})}. \tag{8.122}$$

This growth term is independent of temperature and is proportional to the dislocation bias for interstitials $(z_i - z_v)$ and the defect production rate. Note that $\dot{R}_0$ is:

- Independent of temperature;
- Proportional to the dislocation bias $(z_i - z_v)$;
- Proportional to the defect production rate, K_0.

The term $X(\eta)$ is given by:

$$X(\eta) = F(\eta) - 2\zeta, \tag{8.123}$$

where

$$F(\eta) = \frac{2}{\eta}\left[(\eta + 1)^{1/2} - 1\right], \tag{8.124}$$

and η is a dimensionless parameter defined in Eq. (8.117). Substituting Eq. (8.123) into Eq. (8.120) gives:

$$\dot{R} = \dot{R}_0 F(\eta) - 2\dot{R}_0\zeta. \tag{8.125}$$

The quantity η in the function $F(\eta)$ can be simplified by substituting in for k_v^2 and k_i^2 from Eq. (8.104) (or Table 5.2), giving:

$$\eta = \frac{4K_{iv}K_0}{D_i D_v(z_i\rho_d + 4\pi R\rho_V + 4\pi R_{CP}\rho_{CP})(z_v\rho_d + 4\pi R\rho_V + 4\pi R_{CP}\rho_{CP})}. \tag{8.126}$$

Using the approximation that $z_i \cong z_v$ and eliminating K_{iv} by using Eq. (5.61) gives:

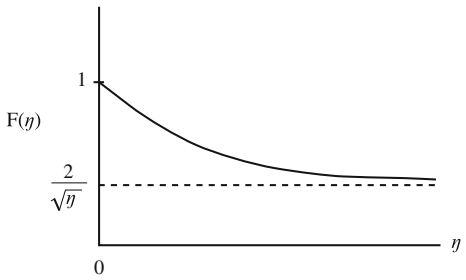

Fig. 8.15 The behavior of $F(\eta)$ in Eq. (8.124) as a function of η

$$\eta = \frac{4z_{iv}K_0\Omega}{D_v a^2(z\rho_d + 4\pi R\rho_V + 4\pi R_{CP}\rho_{CP})^2}. \tag{8.127}$$

The expression for η is substituted into Eq. (8.124) to obtain an expression for $F(\eta)$. This function describes the effect of homogeneous recombination on void growth (Fig. 8.15). When recombination is negligible, $K_{iv} \to 0$ and $\eta \to 0$, and $F \to 1$, or $\lim_{\eta \to 0} F(\eta) = 1$.

Turning now to the second term in Eq. (8.125), we define for simplicity:

$$\dot{R}_{th} = -2\dot{R}_0\zeta, \tag{8.128}$$

so that Eq. (8.125) can now be written as:

$$\dot{R} = \dot{R}_0 F(\eta) + \dot{R}_{th}, \tag{8.129}$$

The term ζ is a function of temperature and is expressed as:

$$\begin{aligned}\zeta = \zeta(T) = {} & \frac{D_v(z_v\rho_d + 4\pi R\rho_v)[z_i\rho_d + 4\pi(R\rho_V + R_{CP}\rho_{CP})]}{2K_0(z_i - z_v)[z_v\rho_d + 4\pi(R\rho_V + R_{CP}\rho_{CP})]} \\ & \times [4\pi R_{CP}\rho_{CP}C_v^V + z_v\{\rho_N(C_v^V - C_v^0) + \rho_L(C_v^V - C_v^L)\}].\end{aligned} \tag{8.130}$$

so that:

$$\begin{aligned}\dot{R}_{th} = -2\dot{R}_0\zeta = {} & \frac{-2D_v(z_v\rho_d + 4\pi R\rho_V)[z_i\rho_d + 4\pi(R\rho_V + R_{CP}\rho_{CP})]}{2K_0(z_i - z_v)\rho_d[z_v\rho_d + 4\pi(R\rho_V + R_{CP}\rho_{CP})]} \\ & \times \frac{\dfrac{K_0(z_i - z_v)\rho_d\Omega}{R(z_v\rho_d + 4\pi R\rho_V)}}{z_i\rho_d + 4\pi R\rho_V + 4\pi R_{CP}\rho_{CP}\left[1 + \dfrac{(z_i - z_v)\rho_d}{z_v\rho_d + 4\pi R\rho_V}\right]} \\ & \times [4\pi R_{CP}\rho_{CP}C_v^V + z_v[\rho_N(C_v^V - C_v^0) + \rho_L(C_v^V - C_v^L)]].\end{aligned} \tag{8.131}$$

By approximating $z_i \cong z_v$, numerous terms in Eq. (8.131) cancel, leaving:

$$\dot{R}_{th} = \frac{-D_v \Omega}{R(z_i \rho_d + 4\pi R \rho_V + 4\pi R_{CP} \rho_{CP})} \times \left[4\pi R_{CP} \rho_{CP} C_v^V + z_v \left[\rho_N (C_v^V - C_v^0) + \rho_L (C_v^V - C_v^L)\right]\right]. \tag{8.132}$$

Substituting in for C_v^V and C_v^L from Eqs. (8.85) and (8.99), respectively, gives:

$$\dot{R}_{th} = \frac{-D_v \Omega}{R(z_i \rho_d + 4\pi R \rho_V + 4\pi R_{CP} \rho_{CP})} \times \left[4\pi R_{CP} \rho_{CP} C_v^0 \exp\left(\frac{2\gamma\Omega}{RkT}\right) + z_v \left[\rho_N \left(C_v^0 \exp\left(\frac{2\gamma\Omega}{RkT}\right) - C_v^0\right) + \rho_L \left(C_v^0 \exp\left(\frac{2\gamma\Omega}{RkT}\right) - C_v^0 \exp\left(-\frac{\Theta}{2\sqrt{m_i kT}}\right)\right)\right]\right]. \tag{8.133}$$

Approximating $\exp(x) \sim x + 1$ for small x in all but the first of the exponential terms of Eq. (8.133) gives:

$$\dot{R}_{th} = \frac{-D_v \Omega}{R(z_i \rho_d + 4\pi R \rho_V + 4\pi R_{CP} \rho_{CP})} \times \left[4\pi R_{CP} \rho_{CP} C_v^0 \exp\left(\frac{2\gamma\Omega}{RkT}\right) + z_v C_v^0 \left[\rho_N \frac{2\gamma\Omega}{RkT} + \rho_L \left(\frac{2\gamma\Omega}{RkT} + \frac{\Theta}{2\sqrt{m_i kT}}\right)\right]\right], \tag{8.134}$$

and pulling the term C_v^0 out into the coefficient yields:

$$\dot{R}_{th} = \frac{-D_v \Omega C_v^0}{R(z_i \rho_d + 4\pi R \rho_V + 4\pi R_{CP} \rho_{CP})} \times \left[4\pi R_{CP} \rho_{CP} \exp\left(\frac{2\gamma\Omega}{RkT}\right) + z_v \rho_N \frac{2\gamma\Omega}{RkT} + z_v \rho_L \left(\frac{2\gamma\Omega}{RkT} + \frac{\theta}{2\sqrt{m_i kT}}\right)\right], \tag{8.135}$$

which is the simplified expression for the thermal emission term. This term represents the thermal emission of defects from sinks. It is independent of defect production rate and is strongly temperature dependent. Note that at very low temperature, $\dot{R}_{th} \to 0$, because of the terms D_v and C_v^0.

The rate of change in the void radius with time, $\dot{R}$, determined from Eq. (8.120), can be used to determine the volumetric swelling rate:

$$\frac{dV}{dt} = 4\pi R^2 \dot{R}. \tag{8.136}$$

Void swelling can be represented in terms of the void size distribution as follows. If $\rho_V(R)\,dR$ is the number of voids/cm^3 with radii between R and $R + dR$, then the total void number density is:

$$\rho_V = \int_0^\infty \rho_V(R)\,dR, \tag{8.137}$$

the average void size is:

$$\bar{R} = \frac{1}{\rho_V}\int_0^\infty R\rho_V(R)dR, \tag{8.138}$$

and the amount of void swelling is defined by the change in volume of the solid:

$$\frac{\Delta V}{V} = \frac{4}{3}\pi \int_0^\infty R^3 \rho_V(R)dR. \tag{8.139}$$

If the void distribution is narrow, then we can approximate the integral in Eq. (8.139) with:

$$\frac{\Delta V}{V} = \frac{4}{3}\pi \bar{R}^3 \rho_V. \tag{8.140}$$

The equations provided in this section allow the determination of the rate of growth of voids in a solid under irradiation and consequently the rate of swelling of that solid. The following sections address the effects of various parameters on void growth.

8.3.1 Temperature Dependence

Figure 8.16 provides a typical plot of void swelling as a function of temperature. Note that swelling is characterized by a peak at intermediate temperature. This behavior should look familiar from the temperature dependence of RIS since the origin is essentially the same. Low defect mobility limits void growth at low temperature, and the approach of the defect concentration to the thermal equilibrium value limits void growth at high temperature due to a loss of supersaturation. In the preceding analysis of the void growth equation, the two highly

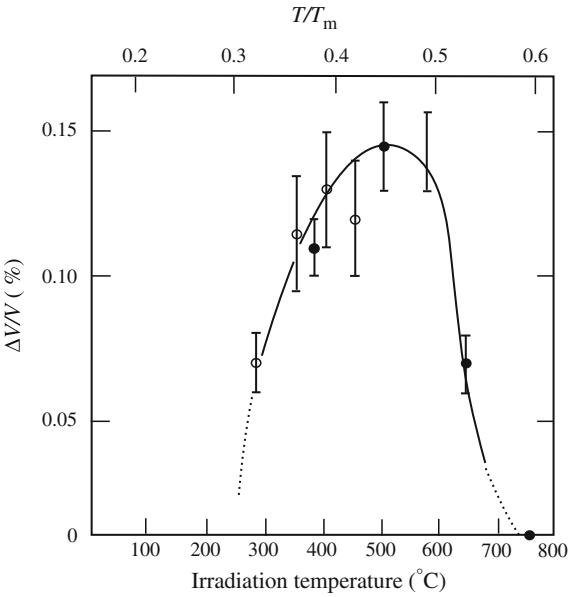

Fig. 8.16 Swelling in nickel as a function of irradiation temperature for a fluence of 5×10^{19} n/cm^2 (after [17])

temperature-sensitive parameters are the vacancy diffusion coefficient D_v and the equilibrium vacancy concentration C_v^0. The temperature dependence of the term $\dot{R}_0 F(\eta)$ is contained in the parameter η, which is controlled by D_v. At low temperatures, swelling is low because vacancies are practically immobile. A low value of D_v makes η large and forces F to become small, resulting in a low value for the term $\dot{R}_0 F(\eta)$. The term $\dot{R}_{th}$ approaches zero since it is proportional to $D_v C_v^0$. Since both $F(\eta)$ and $\dot{R}_{th}$ become small at low temperature, void growth ceases. Under these conditions, the concentration of vacancies builds up and vacancies and interstitials are lost to recombination.

At high temperature, the emission of vacancies by voids counterbalances the net vacancy influx driven by irradiation and suppresses swelling. When in the void growth equation η becomes small and F approaches unity, the term $\dot{R}_{th}$ also increases (but in the negative direction) and dominates at the highest temperatures. Hence, a maximum in the growth rate is predicted at intermediate temperature where both thermal emission and mutual recombination are less important and the net flow of vacancies to voids is maximized. Figure 8.17 shows how the components of the void growth rate combine to result in a peak at intermediate temperature. This is found to be true with all metals.

Figure 8.18(a) shows an example of the sharp dependence of void swelling on temperature in an Fe–Cr–Ni alloy irradiated in the BN-350 reactor as a function of dose and temperature. All the data were for irradiation over a fixed time period, reflecting the variation of dose rates with position in the core. Closed symbols represent samples in which voids were found, and open symbols were samples that

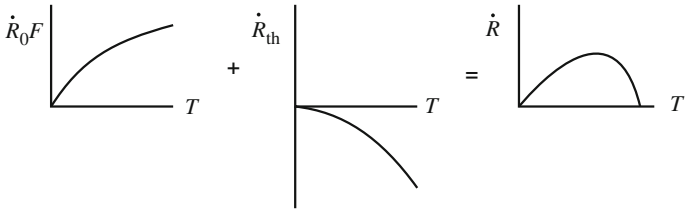

Fig. 8.17 Construction of the total void swelling rate $\dot{R}$ from its components $\dot{R}_0F$ and $\dot{R}_{th}$

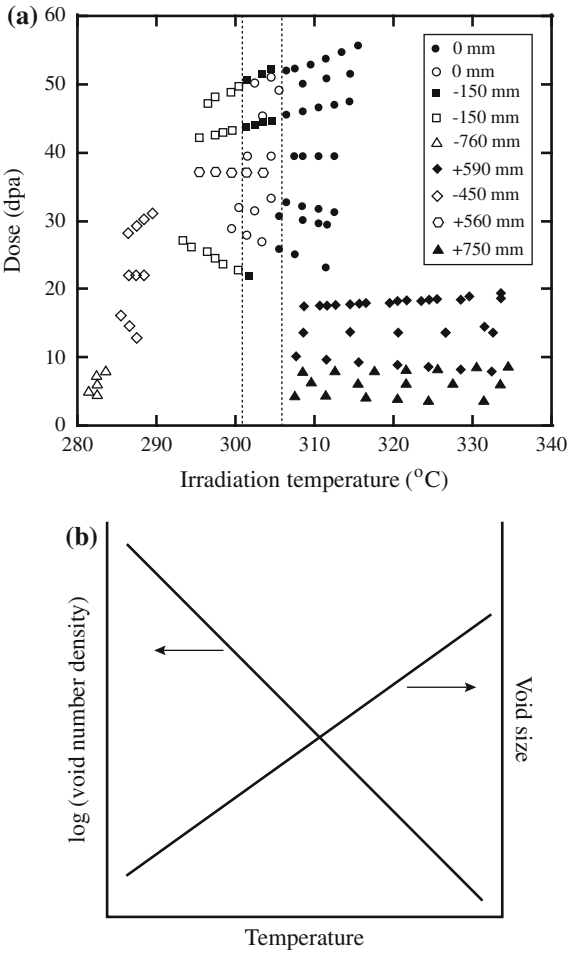

Fig. 8.18 (**a**) Dose–temperature plot of swelling in a Fe–Cr–Ni alloy irradiated in the BN-350 fast reactor showing the sharp temperature threshold for swelling (after [18]). (**b**) Schematic of the temperature dependence of void density and void size

exhibited no voids. Note that despite the differing doses and dose rates, void nucleation occurs with a very sharp temperature threshold at about 302–307 °C, illustrating the high sensitivity of void formation to temperature. The general

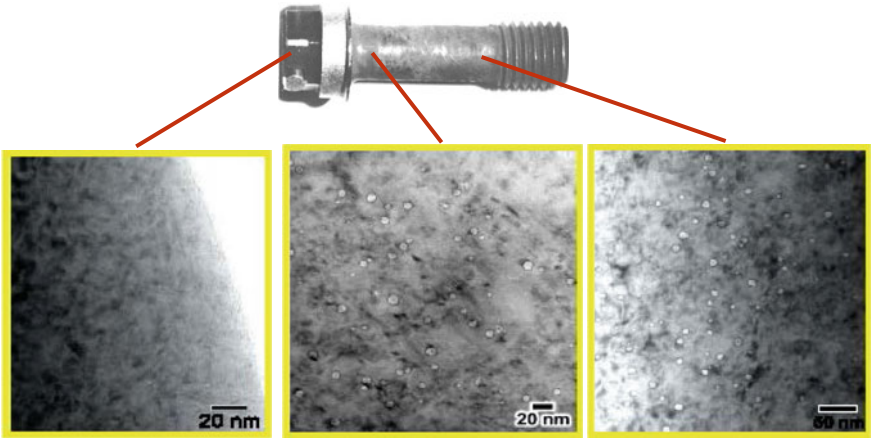

Fig. 8.19 Swelling in a cold-worked 316 SS baffle bolt in a PWR as a function of position along the bolt length. The bolt head was closest to the core, and the temperature distribution is caused by a combination of gamma heating and whether the bolt was exposed to the coolant (*courtesy* S.M. Bruemmer and Garner FA, PNNL)

behavior of the void number density and size with temperature is shown in Fig. 8.18(b). With increasing temperature, the void density falls logarithmically and the size increases, which is the typical behavior for a process that is dominated by nucleation at low temperatures where the void growth is slow and by growth at high temperature where the free energy difference driving void growth is small.

Figure 8.19 shows images of the microstructure in a baffle bolt used to secure baffle–former plates against the baffle in a pressurized water reactor. In this case, the head was closest to the core (received the highest dose) and was exposed to the coolant, hence the lowest temperature. Gamma heating caused the temperature to exceed the coolant temperature ($\sim$320 °C) along the length of the bolt. While the doses differ somewhat, the dominant influence of temperature is noted by both the lack of voids in the lowest temperature location (head) and the largest void size at the highest temperature (top shank).

8.3.2 Dose Dependence

Understanding how swelling depends on dose is critical in the design and operation of components in radiation environments in which voids have the potential to form and grow. From the discussion in the previous section, the dependence is complicated by the occurrence of the defect production rate, K_0, in the terms $\dot{R}_0$ and $F(\eta)$. So we will take a different approach in determining the void growth rate

dependence on dose, following that of Mansur [5]. Recall the expressions for C_v and C_i given in Eq. (8.119):

$$C_v = \frac{D_i k_i^2}{2K_{iv}}\left[(\eta+1)^{1/2}-1\right]$$
$$C_i = \frac{D_v k_v^2}{2K_{iv}}\left[(\eta+1)^{1/2}-1\right],$$

and for η as given in Eq. (8.117):

$$\eta = \frac{4K_{iv}K_0}{D_i D_v k_v^2 k_i^2}.$$

We can write the term in brackets in Eq. (8.119) as:

$$\left[(\eta+1)^{1/2}-1\right] = \left[\left(1+\frac{4K_{iv}K_0}{D_i D_v k_v^2 k_i^2}\right)^{1/2}-1\right]. \tag{8.141}$$

Then, $D_v C_v$ and $D_i C_i$ can be written as:

$$\begin{aligned} D_v C_v &= \frac{D_v D_i k_i^2 z_v}{2K_{iv}}\left[\left(1+\frac{4K_{iv}K_0}{D_i D_v k_v^2 k_i^2}\right)^{1/2}-1\right] \\ D_i C_i &= \frac{D_v D_i k_v^2 z_i}{2K_{iv}}\left[\left(1+\frac{4K_{iv}K_0}{D_i D_v k_v^2 k_i^2}\right)^{1/2}-1\right]. \end{aligned} \tag{8.142}$$

Neglecting thermal emission and substituting into Eq. (8.112) give:

$$\dot{R} = \frac{\Omega D_v D_i}{2RK_{iv}}\left[\left(1+\frac{4K_{iv}K_0}{D_i D_v k_v^2 k_i^2}\right)^{1/2}-1\right]\left(k_v^2 z_v - k_i^2 z_i\right). \tag{8.143}$$

Substituting for k_v^2 and k_i^2 from Eq. (8.104) and considering only coherent precipitates, network dislocations, and loops give:

$$\begin{aligned} \dot{R} = {} & \frac{\Omega D_v D_i}{2RK_{iv}}\left[\left(1+\frac{4K_{iv}K_0}{D_i D_v k_v^2 k_i^2}\right)^{1/2}-1\right] \\ & \times\left[4\pi R_{CP}\rho_{CP}\left(z_i^{CP} z_v - z_v^{CP} z_i\right) + \rho_L\left(z_i^{L} z_v - z_v^{L} z_i\right) + \rho_N\left(z_i^{N} z_v - z_v^{N} z_i\right)\right]. \end{aligned} \tag{8.144}$$

Simplifying Eq. (8.144) for the case of voids and total dislocation density only, we have:

$$\dot{R} = \frac{\Omega D_v D_i}{2RK_{iv}} \left[\left(1 + \frac{4K_{iv}K_0}{D_i D_v k_v^2 k_i^2} \right)^{1/2} - 1 \right] \rho_d \left(z_i^d z_v - z_v^d z_i \right). \tag{8.145}$$

The term $\left(z_i^d z_v - z_v^d z_i\right)$ is the bias of dislocations versus that for voids and is the determinant of the propensity for a void to grow or shrink. Growth will occur if $z_i^d z_v > z_v^d z_i$, or stated as ratios, $\frac{z_i^d}{z_v^d} > \frac{z_i}{z_v}$, and shrinkage will occur if the inequality is in the other direction. The presence of other sinks will affect swelling through their inclusion in the terms k_v^2 and k_i^2. The larger the sink strengths, the lower will be the void growth rate due to the loss of defects to those sinks.

The limiting behaviors of Eq. (8.145) are the cases in which recombination dominates $\frac{4K_{iv}K_0}{D_i D_v k_v^2 k_i^2} \gg 1$ (loss of defects to recombination is much larger than that lost to sinks) and loss to sinks dominates $\frac{4K_{iv}K_0}{D_i D_v k_v^2 k_i^2} \ll 1$[5]. Assuming that the only sinks besides voids are network dislocations, we have:

$$\dot{R} = \frac{\Omega}{R} \left(\frac{D_i D_v K_0}{z_i^N z_v^N K_{iv}} \right)^{1/2} \frac{Q_i^{1/2} Q_v^{1/2} \left(z_i^N z_v - z_v^N z_i \right)}{(1+Q_v)^{1/2}(1+Q_i)^{1/2}} : \text{ recombination dominant} \tag{8.146}$$

$$\dot{R} = \frac{\Omega K_0 Q_i Q_v}{R\rho_N (1+Q_v)(1+Q_i)} \left(z_i^N z_v - z_v^N z_i \right) : \text{sink dominant}, \tag{8.147}$$

where

$$Q_{i,v} = \frac{z_{i,v}^N \rho_N}{4\pi R \rho_V z_{i,v}} \tag{8.148}$$

is the ratio of dislocation sink strength to void sink strength. Note that the growth rate is dependent on $K_0^{1/2}$ when recombination is dominant, as in Eq. (8.146). However, when sinks are dominant, Eq. (8.147) shows that the growth rate is proportional to K_0. Multiplying Eq. (8.147) by $4\pi R^2 \rho_V$ and given that $\Omega = 1/N_0$, the site density gives the volume swelling rate:

$$\frac{d(\Delta V/V)}{dt} = K_0 \left(\frac{z_i - z_v}{z_v} \right) \frac{Q}{(1+Q)^2}. \tag{8.149}$$

This is the same expression that can be obtained from Eq. (8.122) by neglecting the effect of coherent precipitates. For $Q = 1$ and $z_i - z_v = 0.01$, we have:

$$\frac{\Delta V}{V}\% \cong 1/4 \times (\text{dose in dpa}). \tag{8.150}$$

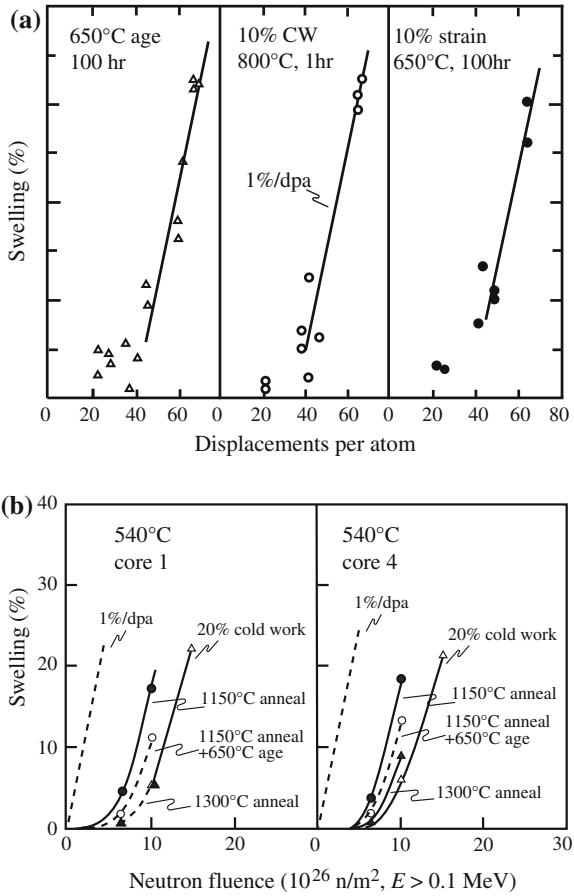

Fig. 8.20 (**a**) Early development of 1 %/dpa swelling rates in aged OKH16N15M3B steel during irradiation in the BOR-60 reactor at 400–500 °C (after [20]). (**b**) Variations in swelling at 540 °C in EBR-II for two nominally similar heats of 316 stainless steel as a function of starting condition (after [21])

Garner [19] has shown that over a wide dose range, the steady-state swelling rate in austenitic stainless steels is of the order of ~ 1 %/dpa (Fig. 8.20). The linear dependence is consistent with a sink-dominated process, but the magnitude of the coefficient is a factor of four greater than that predicted by Eq. (8.150). The discrepancy is likely due to the effect of clusters that is not accounted for in the rate theory model. A closer look at the behavior of vacancies and interstitials in the cascade shows that the fraction of vacancies and interstitials that form clusters is larger than has been accounted for thus far. Vacancy clusters form near the cascade core, and interstitial clusters form near the cascade periphery. Mobile interstitial clusters can reach sinks by migration of the cluster as a whole. Vacancies emitted by vacancy clusters by thermal emission are also free to reach sinks. Since the fraction of interstitials and vacancies in clusters is not the same, nor is their thermal stability, the difference between vacancy and interstitial clusters results in a difference in the effective production rates of vacancies compared to that of interstitials, termed the *production bias*, and can influence void swelling. The net result is

that the sink strength of the clusters is much greater than that of the measurable dislocation loops, resulting in a much greater driving force for void swelling than is accounted for by the rate equation formulation. This is one of the reasons that the observed steady-state swelling dependence on dose is greater than that predicted by the rate equation formulation.

8.3.3 Role of Dislocations as Biased Sinks

The dislocation structure of an alloy can exert a profound effect on the swelling behavior. Equation (8.122) demonstrates that both a biased sink (e.g., dislocations) and a neutral sink are necessary for void growth. If the bias is removed, $z_i = z_v$, then $\dot{R}_0 = 0$ and swelling will not occur as defects will flow equally to each sink.

The Q-dependence of $\dot{R}_0$ is shown in Fig. 8.21. Note that $\dot{R}_0$ is a maximum at $Q = 1$, or when the flow of vacancies to voids and dislocations is equal. The regime $Q > 1$ is representative of the low-dose regime in which both R and ρ_V are small, so vacancy loss to the existing dislocation network dominates. This is why cold-worked alloys swell less. When $Q \sim 1$, then the flow of vacancies to voids and dislocations is approximately equal. This is the regime where bias exerts its greatest influence. If the flow of vacancies and interstitials to sinks is equal, and more interstitials go to dislocations, then more vacancies must flow to voids. At $Q \sim 1$, the flows are equal, so the bias is most effective in promoting void growth. When $Q < 1$, defect flow to voids dominates the loss terms, and since few defects flow to dislocations, the bias is not very effective in creating an imbalance in point defect fluxes, so the flow of vacancies and interstitials to voids is similar in magnitude and void growth slows or ceases. Although dislocations exhibit a slight preference for interstitials $\left(\frac{\beta_d}{\beta_V} \geq 1\right)$, in a cold-worked material, the dislocations provide so many sinks for vacancies that the effect of a vacancy supersaturation is essentially multiplied, resulting in low void nucleation and growth rates. By the same mechanism, grain boundaries provide *unbiased* sinks for point defects and will keep the vacancy supersaturation too low for growth, provided that the grain boundary area is large enough (i.e., very small grains). Figure 8.22(a) shows a plot

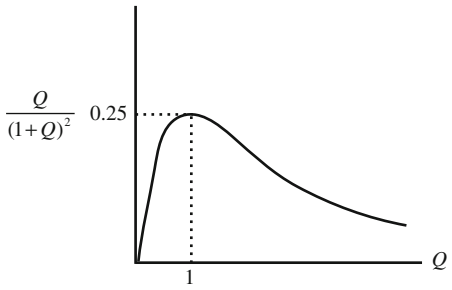

Fig. 8.21 Dependence of swelling on the dislocation/void sink strength ratio, Q, in Eq. (8.149)

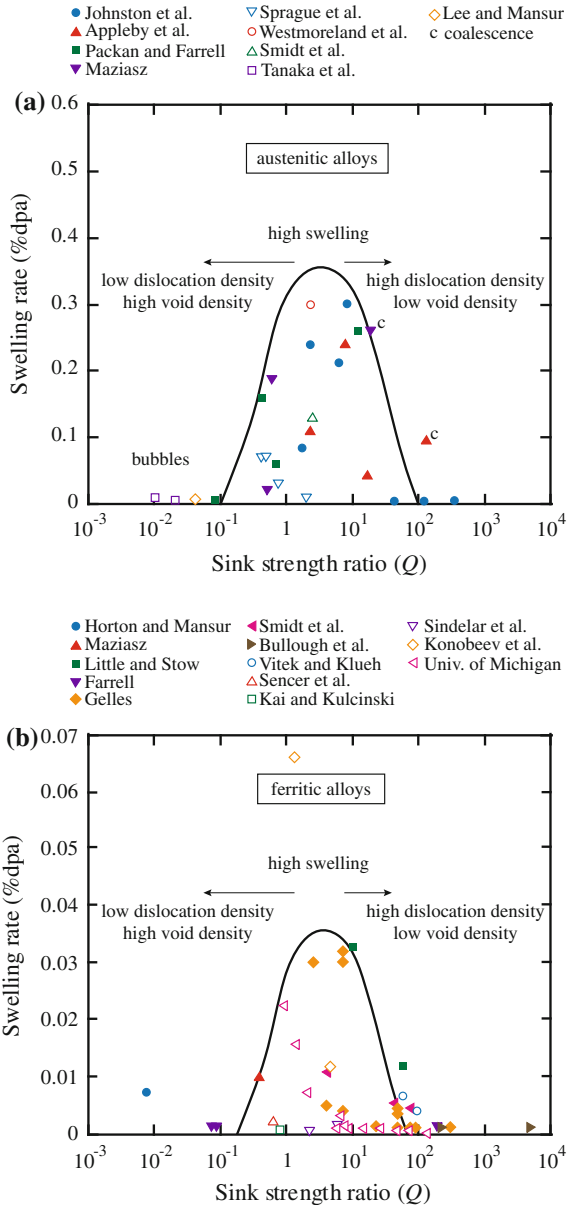

Fig. 8.22 Experimentally observed swelling rates as a function of Q for (**a**) austenitic stainless steels (after [5]) and (**b**) ferritic–martensitic steels

of swelling rate versus the sink strength ratio, Q, for several austenitic stainless steels, and Fig. 8.22(b) shows the same for ferritic–martensitic alloys. Indeed, the dependence shown in Fig. 8.21 is obeyed in practice.

The effect of cold-work on swelling in reactor exposures is shown in Fig. 8.23. Figure 8.23(a) shows the effect of cold-work on swelling in 316 stainless steel

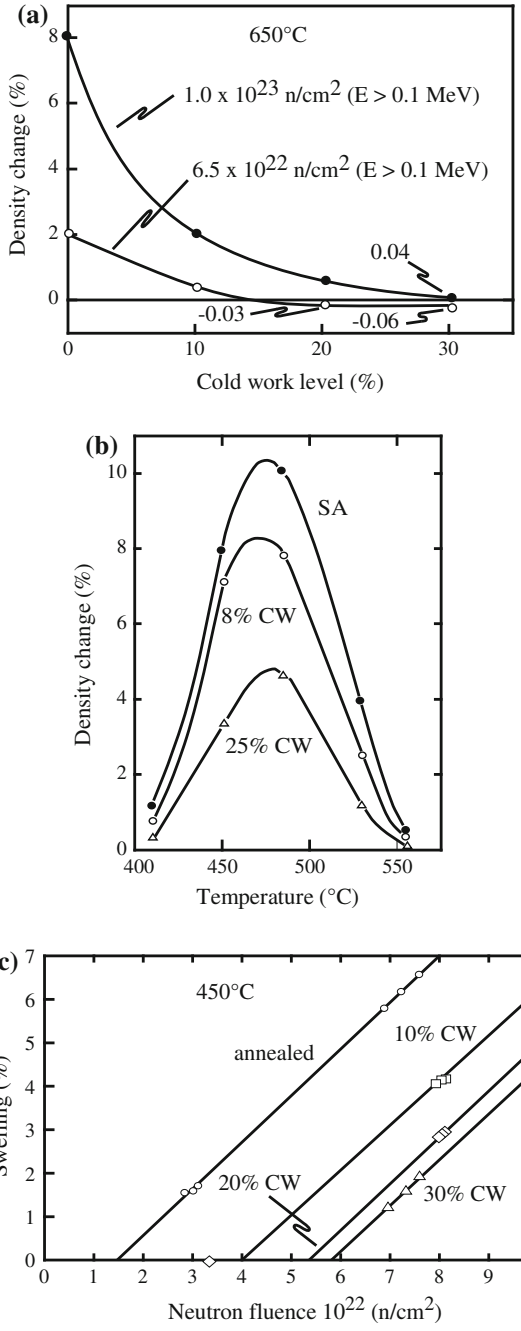

Fig. 8.23 (**a**) Effect of cold-work level on the swelling of 316 stainless steel irradiated at 650 °C in EBR-II to 33 and 50 dpa (after [22]). (**b**) Dependence of swelling on cold-work for various temperatures for 316 stainless steel irradiated in the RAPSODIE reactor to doses of 20–71 dpa (after [23]). (**c**) Effect of cold-work on swelling in 304 stainless steel at 450 °C in EBR-II (after [24])

irradiated in EBR-II at 650 °C to levels of 33 and 50 dpa. Note that for both cases, the amount of swelling decreases with increasing cold-work. Figure 8.23(b) shows that cold-work affects the temperature dependence of swelling by suppressing the magnitude of the swelling peak with increasing levels of cold-work. The data are taken from a stainless steel irradiated to doses of 20–61 dpa in the RAPSODIE reactor. Figure 8.23(c) shows the effect of cold-work on the dose dependence of swelling in 304 stainless steel and that increasing cold-work decreases the amount of swelling, but at reduced rates as the amount of cold-work increases. Note also that these data show that the primary effect of cold-work is to extend the transient swelling regime, rather than to alter the steady-state swelling rate.

8.3.4 Dose Rate Dependence

The location of the peak swelling temperature depends on the dose rate, sink strength, and the predominant mode of defect loss. When the dose rate increases, more point defects are created, but their migration velocities are unchanged. To remove defects at the higher dose rate at steady state requires point defect concentrations to be higher, resulting in greater recombination and a reduction in the net absorption of vacancies by voids and hence a reduction in the void growth rate. As a result, the *bell-shaped* swelling curve is displaced to higher temperatures with increasing dose rate. Figure 8.24 is a plot of the temperature dependence of the term $F(\eta)$ in Eq. (8.125) and illustrates the shift of the swelling peak with dose rate, K_0, similar to that for RIS shown in Fig. 6.9. Alternatively, at a given temperature, the void growth rate decreases for increasing dose rate. At temperatures where thermal emission is non-negligible, the void growth rate is a complicated function of dose rate. Nevertheless, the experimental data substantiate the effect of dose rate on swelling. Figure 8.25 shows swelling in annealed and cold-worked 316 stainless

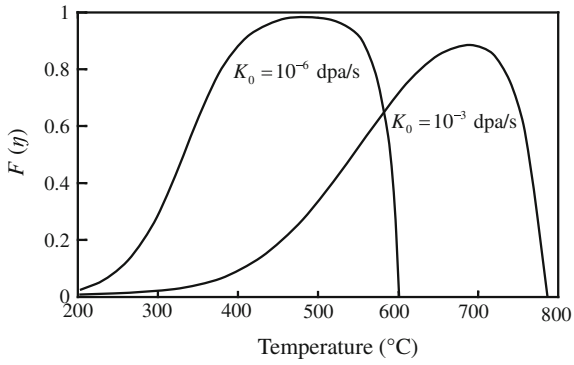

Fig. 8.24 Variation of the function $F(\eta)$ in Eq. (8.124) with temperature, illustrating the shift of the peak with dose rate, K_0. Parameters used to construct the curves are as follows: $\rho_d = 10^9$ cm^{-2}, $E_f^v = 1.6$ eV, $z_i - z_v = 0.01$, $z_v = 1$, $4\pi R\rho_V = 10^{-11}$ cm^{-2}, $D_v = \exp(-1.4\text{ eV}/kT)$ cm^2 s^{-1} (after [15])

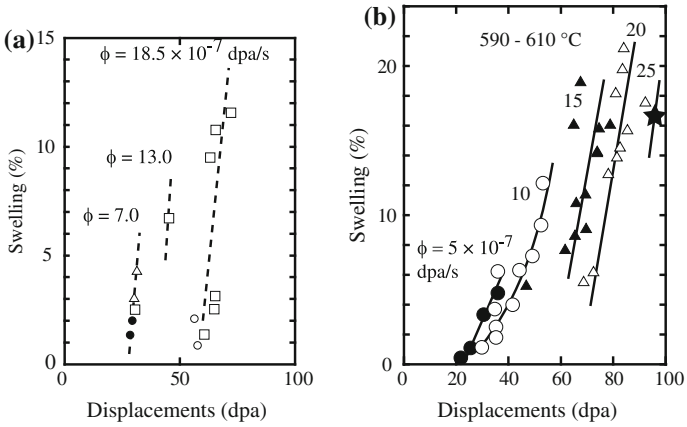

Fig. 8.25 (**a**) Effect of displacement rate on swelling of annealed 316 stainless steel in the RAPSODIE reactor fuel pin cladding at 562 °C. (**b**) Swelling in cold-worked 316 stainless steel in the PHENIX reactor fuel pin cladding at 590–610 °C (after [25, 26])

steel at temperatures between 562 and 610 °C over a range of dose rates. Note that increasing dose rate has the effect of reducing the swelling rate at a given dose, but that at steady state, all data have a similar slope, indicating that the primary effect of dose rate is on the duration of the swelling transition period.

If we move up the temperature scale, we can restore the same relative ratio of recombination rate to absorption rate at sinks. In fact, by requiring that this ratio be invariant, we can obtain a relationship between temperature and dose rate, termed the *temperature shift*.

8.3.5 Irradiation Variable Shifts

The concept of variable shifts was developed to provide a better understanding of the relationship between variables in swelling [16]. The idea is that when one irradiation variable is changed, a shift in other variables can be determined that will preserve a physical quantity describing the behavior of defects during irradiation. There are two such quantities that pertain to the limiting case where recombination dominates defect loss. The number of defects per unit volume that have *recombined* up to a time τ is:

$$N_{\mathrm{R}} = K_{\mathrm{iv}} \int_0^{\tau} C_{\mathrm{i}} C_{\mathrm{v}} \, \mathrm{d}t. \tag{8.151}$$

When the solid is at steady state and defect concentrations are controlled by recombination, Eq. (8.116) gives:

$$C_{\mathrm{v}} = \left(\frac{K_0}{K_{\mathrm{iv}}}\frac{z_{\mathrm{i}}D_{\mathrm{i}}}{z_{\mathrm{v}}D_{\mathrm{v}}}\right)^{1/2}$$
$$C_{\mathrm{i}} = \left(\frac{K_0}{K_{\mathrm{iv}}}\frac{z_{\mathrm{v}}D_{\mathrm{v}}}{z_{\mathrm{i}}D_{\mathrm{i}}}\right)^{1/2}, \tag{8.152}$$

and substituting into Eq. (8.151) yields:

$$N_{\mathrm{R}} = K_0\tau. \tag{8.153}$$

The number of defects *lost to sinks* per unit volume up to a time τ is:

$$N_{\mathrm{Sj}} = \int_0^{\tau} K_j C_j \mathrm{d}t, \tag{8.154}$$

where K is the loss rate and C is the defect concentration and the subscript j denotes the defect type. Substituting Eq. (8.152) into Eq. (8.154) gives for vacancies:

$$N_{\mathrm{Sv}} = \frac{K_{\mathrm{v}}}{(K_0K_{\mathrm{iv}})^{1/2}}\left(\frac{z_{\mathrm{i}}D_{\mathrm{i}}}{z_{\mathrm{v}}D_{\mathrm{v}}}\right)^{1/2}\Phi, \tag{8.155}$$

where Φ is the dose and the expression for interstitials is identical.

These definitions can be used to determine relationships between any two of the three variables: temperature, dose, and dose rate, taking the third to be constant. For example, in the steady-state recombination-dominated regime, we may require N_{s} to be equal for dose 1 and dose rate 1 to that for dose 2 and dose rate 2 at a *fixed temperature*:

$$\frac{K_{\mathrm{v}}}{(K_{0_1}K_{\mathrm{iv}})^{1/2}}\left(\frac{z_{\mathrm{i}}D_{\mathrm{i}}}{z_{\mathrm{v}}D_{\mathrm{v}}}\right)^{1/2}\Phi_1 = \frac{K_{\mathrm{v}}}{(K_{0_2}K_{\mathrm{iv}})^{1/2}}\left(\frac{z_{\mathrm{i}}D_{\mathrm{i}}}{z_{\mathrm{v}}D_{\mathrm{v}}}\right)^{1/2}\Phi_2,$$

and canceling terms in the equality gives:

$$\frac{\Phi_2}{\Phi_1} = \left(\frac{K_{0_1}}{K_{0_2}}\right)^{1/2}. \tag{8.156}$$

For a given change in dose rate, the shift in temperature required at constant dose to keep N_{s} invariant is determined by equating the same terms, but with *fixed dose* resulting in:

$$\left(\frac{D_{\mathrm{v}}}{K_0}\right)_1^{1/2} = \left(\frac{D_{\mathrm{v}}}{K_0}\right)_2^{1/2}, \tag{8.157}$$

or substituting in for D_v from Eq. (4.55), $D_v = D_0 \exp\left(-E_m^v/kT\right)$:

$$T_2 - T_1 = \frac{\dfrac{kT_1^2}{E_m^v}\ln\left(\dfrac{K_{0_2}}{K_{0_1}}\right)}{1 - \dfrac{kT_1}{E_m^v}\ln\left(\dfrac{K_{0_2}}{K_{0_1}}\right)}. \tag{8.158}$$

For a change in dose, the shift in temperature required to maintain N_s invariant at *fixed dose rate* is:

$$\left(D_v^{1/2}\Phi\right)_1 = \left(D_v^{1/2}\Phi\right)_2, \tag{8.159}$$

and substituting in for D_v:

$$\frac{\Phi_2}{\Phi_1} = \exp\left[\frac{E_m^v}{2k}\left(\frac{1}{T_2} - \frac{1}{T_1}\right)\right], \tag{8.160}$$

and rearranging gives:

$$T_2 - T_1 = \frac{\dfrac{-2kT_1^2}{E_m^v}\ln\dfrac{\Phi_2}{\Phi_1}}{1 + \dfrac{2kT_1}{E_m^v}\ln\dfrac{\Phi_2}{\Phi_1}}. \tag{8.161}$$

There is another important temperature shift that, instead of requiring that N_s be invariant, requires the net flux of vacancies over interstitials to a particular type of sink (voids in this case) to be invariant, where the net flux is relevant to void swelling. The temperature shift derived in this way for the recombination-dominated regime to keep swelling rate (N_R) invariant is [16]:

$$T_2 - T_1 = \frac{\dfrac{kT_1^2}{E_m^v + 2E_f^v}\ln\dfrac{K_{0_2}}{K_{0_1}}}{1 - \dfrac{kT_1}{E_m^v + 2E_f^v}\ln\dfrac{K_{0_2}}{K_{0_1}}}. \tag{8.162}$$

where E_f^v is the vacancy formation energy.

The various variable shifts described in this section are shown in the following figures. Figure 8.26 shows the relationship between dose versus dose rate dependence at a reference temperature of 200 °C for the case of N_s invariant, as in Eq. (8.156). Figure 8.27 shows the temperature shift as a function of dose rate at constant dose for three values of vacancy migration energy for N_s invariant, as in Eq. (8.158), and Fig. 8.28 shows the same relationship for the constant dose rate case, as in Eq. (8.161). Figure 8.29 shows the temperature shift as a function of dose for constant dose rate to keep the swelling rate, N_R, invariant, as in

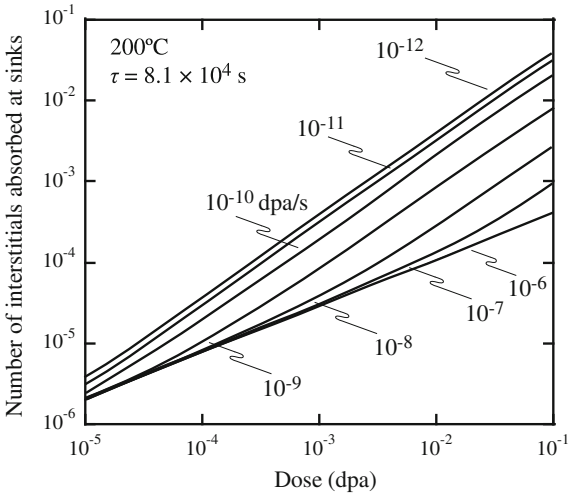

Fig. 8.26 Number of interstitials absorbed at sinks as a function of dose at 200 °C for different dose rates (after [27])

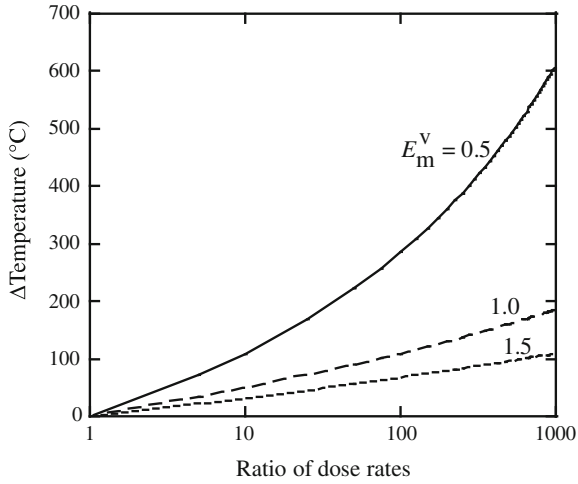

Fig. 8.27 Temperature shift from the reference 200 °C required at constant dose in order to maintain the same point defect absorption at sinks as a function of dose rate, normalized to initial dose rate. Results are shown for three different vacancy migration energies (after [27])

Eq. (8.162). Figure 8.30 shows that the temperature shift concept works well in describing the shift in the peak in the swelling versus temperature curve in nickel over more than five orders of magnitude in the dose rate as given by Eq. (8.162).

The general form of the temperature shift equation is [28, 29]:

$$T_2 - T_1 = \frac{\dfrac{kT_1^2}{E_m^v + n(E_f^v + E_*^v)}M}{1 - \dfrac{kT_1}{E_m^v + n(E_f^v + E_*^v)}M}, \tag{8.163}$$

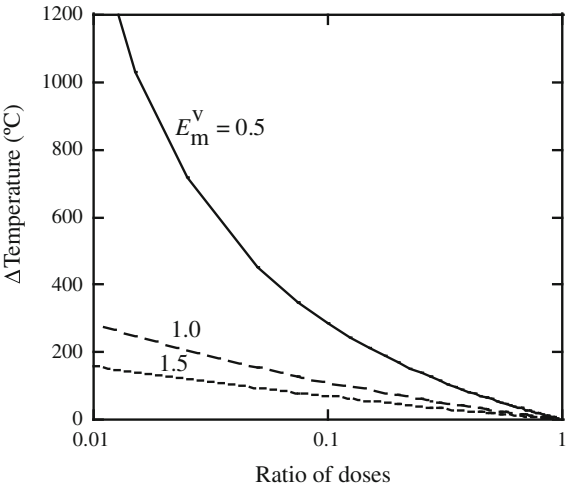

Fig. 8.28 Temperature shift from the reference 200 °C required at constant dose rate in order to maintain the same point defect absorption at sinks as a function of dose, normalized to initial dose. Results are shown for three different vacancy migration energies (after [27])

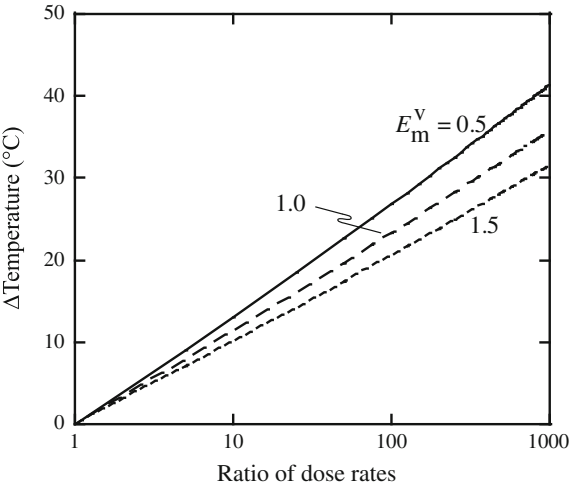

Fig. 8.29 Temperature shift from the reference 200 °C required at constant dose in order to maintain swelling invariance as a function of dose rate, normalized to initial dose rate. Results are shown for three different vacancy migration energies and a formation energy of 1.5 eV

where

$$M = \left[\ln \frac{K_{0_2} k_{i_1}^2 k_{v_1}^2}{K_{0_1} k_{i_2}^2 k_{v_2}^2} + \ln B \right], \tag{8.164}$$

and

$$B = \left[\frac{k_{i_2}^2 \exp(-E_*^v/kT_2) - k_{v_2}^2 \exp(-E_*^i/kT_2)}{k_{i_1}^2 \exp(-E_*^v/kT_1) - k_{v_1}^2 \exp(-E_*^i/kT_1)} \right]^2. \tag{8.165}$$

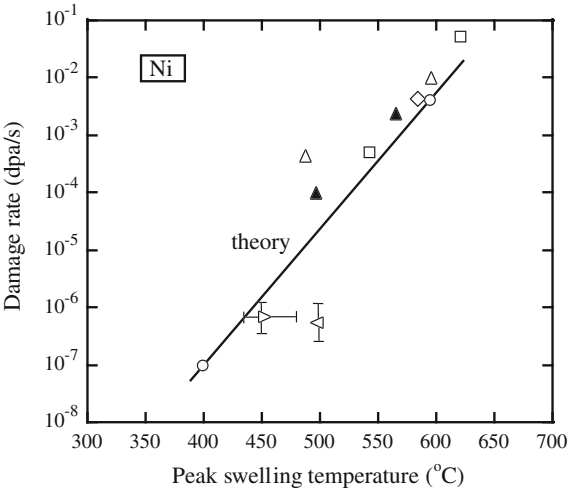

Fig. 8.30 Temperature shift of peak swelling as a function of dose rate. *Points* are experimental data, and the *line* is from theory (after [5])

The value of n is determined by the dominant process responsible for point defect removal, $n = 1$ for sink-dominated cases and $n = 2$ for recombination-dominated cases, while the value of B is determined both by the dominant process and by the mode of void growth. In the case where both interstitials and vacancies are diffusion controlled:

$$B = \frac{\rho_{d_2}}{\rho_{d_1}}, \quad \text{for} \quad n = 1, \tag{8.166}$$

$$B = \frac{r_{c_1}}{r_{c_2}} \left[\frac{\rho_{d_2}}{\rho_{d_1}}\right]^2, \quad \text{for} \quad n = 2, \tag{8.167}$$

where r_c is the radius of the recombination volume and ρ_d is the dislocation density. The term $E_*^{\mathrm{v,i}}$ represents the additional energy above the normal lattice migration energy that the point defect must overcome on diffusing to the void and is nonzero only for the case of reaction rate control. For interstitial and vacancy reaction rate control:

$$B = \frac{\rho_{d_2}}{\rho_{d_1}} \left[\frac{z_i^d \exp(-E_*^{\mathrm{v}}/kT_2) - z_{\mathrm{v}}^d \exp(-E_*^i/kT_2)}{z_i^d \exp(-E_*^{\mathrm{v}}/kT_1) - z_{\mathrm{v}}^d \exp(-E_*^i/kT_1)}\right], \quad \text{for} \quad n = 1, \tag{8.168}$$

$$B = \frac{r_{c_1}}{r_{c_2}} \left[\frac{k_{i_2}^2 \exp(-E_*^{\mathrm{v}}/kT_2) - k_{\mathrm{v}_2}^2 \exp(-E_*^i/kT_2)}{k_{i_1}^2 \exp(-E_*^{\mathrm{v}}/kT_1) - k_{\mathrm{v}_1}^2 \exp(-E_*^i/kT_1)}\right], \quad \text{for} \quad n = 2. \tag{8.169}$$

For interstitial reaction rate control and vacancy diffusion control,

$$B = \frac{\rho_{d_2}}{\rho_{d_1}} \left[\frac{bz_i^d - z_v^d R_v \exp(-E_*^i/kT_2)}{bz_i^d - z_v^d R_v \exp(-E_*^i/kT_1)} \right], \quad \text{for} \quad n = 1, \tag{8.170}$$

$$B = \frac{r_{c_1}}{r_{c_2}} \left[\frac{bk_{i_2}^2 - k_{v_2}^2 R_v \exp(-E_*^i/kT_2)}{bk_{i_1}^2 - k_{v_1}^2 R_v \exp(-E_*^i/kT_1)} \right]^2, \quad \text{for} \quad n = 2, \tag{8.171}$$

where R_v is the void radius and b is the Burgers vector. The dominant process of point defect loss as well as the mode of void growth affects the form of the temperature shift expression. When recombination dominates, the temperature shift is smaller since $2E_f^v$ occurs in the denominator. But when sinks dominate, the value is E_f^v. The reason for this is that the radiation-induced void growth rate is proportional to generation rate when sinks dominate, while it is proportional to the square root of the generation rate if recombination dominates (see Eqs. 8.146 and 8.147), However, the thermal emission rate depends on the same exponential in temperature in both cases. Thus, a given initial ratio of thermal emission rate to radiation-induced growth rate of voids may be recovered after a given increase in dose rate by a smaller increase in temperature where recombination dominates.

8.3.6 *Effect of Production Bias*

We now must consider the case of cascade formation in which both vacancy and interstitial clusters and loops are formed during the damage process. The vacancy clusters, however, are not stable and will emit vacancies that become freely migrating vacancies and are available to various sinks, including voids. Due to their high formation energies, immobilization of interstitials in clusters is permanent. So there is a bias between vacancy and interstitial production in cascade damage. Recall the point defect balance equations Eq. (5.1) that account for the incorporation of both vacancies and interstitials into clusters and the emission of vacancies from vacancy clusters. The following [30] point defect balance equations are rewritten using sink strengths instead of reaction rate constants yielding:

$$\begin{aligned} \frac{dC_v}{dt} &= K_0(1-\varepsilon_r)(1-\varepsilon_v) - k_v^2 D_v C_v - K_{iv} D_i C_i C_v + L_v \\ \frac{dC_i}{dt} &= K_0(1-\varepsilon_r)(1-\varepsilon_i) - k_i^2 D_i C_i - K_{iv} D_i C_i C_v, \end{aligned} \tag{8.172}$$

where ε_r is the fraction of defects that recombine in the cascade and ε_v and ε_i are the fraction of clustered vacancies and interstitials, respectively, and k_v^2 and k_i^2 are the total sink strengths for vacancies and interstitials, respectively, where:

$$k^2 = k_{\mathrm{V}}^2 + k_{\mathrm{N}}^2 + k_{\mathrm{vcl}}^2 + k_{\mathrm{icl}}^2 \tag{8.173}$$

where subscripts "V" and "N" refer to voids and network dislocations, respectively, and subscripts "vcl" and "icl" represent vacancy and interstitial loops or clusters, respectively, K_{iv} is the recombination coefficient, and L_{v} is the thermal emission term given by:

$$L_{\mathrm{v}} = L_{\mathrm{v}}^{V} + L_{\mathrm{v}}^{N} + L_{\mathrm{v}}^{\mathrm{icl}} + L_{\mathrm{v}}^{\mathrm{vcl}}. \tag{8.174}$$

The swelling rate is given in Eq. (8.110) as:

$$\frac{\mathrm{d}(\Delta V/V)}{\mathrm{d}t} = 4\pi R\Omega[D_{\mathrm{v}}(C_{\mathrm{v}} - C_{\mathrm{v}}^0) - D_{\mathrm{i}}C_{\mathrm{i}}],$$

and accounting for production bias caused by the formation of clusters, we can determine the steady-state swelling rate from Eqs. (8.172) and (8.174), neglecting recombination, to give [30]:

$$\frac{\mathrm{d}(\Delta V/V)}{\mathrm{d}t} = \frac{z_{\mathrm{i}}k_{\mathrm{V}}^2k_{\mathrm{d}}^2(1-\varepsilon_{\mathrm{v}})K}{k_{\mathrm{v}}^2k_{\mathrm{i}}^2} + \frac{k_{\mathrm{V}}^2(\varepsilon_{\mathrm{i}} - \varepsilon_{\mathrm{v}})K}{k_{\mathrm{i}}^2} + \frac{k_{\mathrm{V}}^2L_{\mathrm{v}}}{k_{\mathrm{v}}^2} - k_{\mathrm{V}}^2D_{\mathrm{v}}C_{\mathrm{v}}^{V}, \tag{8.175}$$

where z_{-i} is the dislocation bias, $K = (1 - \varepsilon_{\mathrm{r}})K_0$, and $C_{\mathrm{v}}^{\mathrm{V}}$ is the vacancy concentration at the void surface. The swelling rate in Eq. (8.175) can be rewritten as a sum of two contributions: a dislocation bias–driven contribution and a production bias–driven contribution, i.e.,

$$\frac{\mathrm{d}(\Delta V/V)}{\mathrm{d}t} = \left.\frac{\mathrm{d}(\Delta V/V)}{\mathrm{d}t}\right|_{\mathrm{db}} + \left.\frac{\mathrm{d}(\Delta V/V)}{\mathrm{d}t}\right|_{\mathrm{pb}}$$

or

$$\left.\frac{\mathrm{d}(\Delta V/V)}{\mathrm{d}t}\right|_{\mathrm{db}} = \frac{z_{\mathrm{i}}k_{\mathrm{V}}^2k_{\mathrm{d}}^2(1-\varepsilon_{\mathrm{v}})K}{k_{\mathrm{v}}^2k_{\mathrm{i}}^2} + \frac{k_{\mathrm{V}}^2}{k_{\mathrm{v}}^2}\left[L_{\mathrm{v}}^{\mathrm{V}} + L_{\mathrm{v}}^{\mathrm{N}} - (k_{\mathrm{V}}^2 + k_{\mathrm{N}}^2)D_{\mathrm{v}}C_{\mathrm{v}}^{\mathrm{V}}\right] \tag{8.176}$$

$$\left.\frac{\mathrm{d}(\Delta V/V)}{\mathrm{d}t}\right|_{\mathrm{pb}} = \frac{k_{\mathrm{V}}^2(\varepsilon_{\mathrm{i}} - \varepsilon_{\mathrm{v}})K}{k_{\mathrm{i}}^2} + \frac{k_{\mathrm{V}}^2}{k_{\mathrm{v}}^2}\left[L_{\mathrm{v}}^{\mathrm{vcl}} + L_{\mathrm{v}}^{\mathrm{icl}} - (k_{\mathrm{vcl}}^2 + k_{\mathrm{icl}}^2)D_{\mathrm{v}}C_{\mathrm{v}}^{\mathrm{V}}\right]. \tag{8.177}$$

In Eq. (8.176), the first term corresponds to swelling due to the biased arrival (caused by the usual dislocation bias) of mobile vacancies at the voids. The second term corresponds to effects caused by the emission of vacancies from the voids (that tends to anneal the voids) and from the dislocation network (that increases swelling). The swelling rate in Eq. (8.176) does not contain effects due to the interstitial and vacancy clusters formed during cascade damage. In Eq. (8.177), the first term represents the reduction of the interstitial flux to voids due to interstitial clustering

(which would help swelling). The second term represents the flux to the voids of vacancies evaporating under the line tension from the vacancy loops. The line tension of the interstitial loops, on the other hand, favors the absorption of vacancies that are otherwise available to the voids.

Where interstitials are assumed not to cluster, i.e., $\varepsilon_i = 0$, and the lifetimes of the vacancy loops are limited to those due to thermal and bias-driven annealing, the second term in Eq. (8.177) can then be shown to cancel the first term and the ε_v contribution in Eq. (8.176). The collapse of a cascade into vacancy loops then does not produce any appreciable effects on the swelling rate. With the immobilization of the interstitials in interstitial loops and their subsequent destruction by dislocation sweep and cascade collapse, the re-emission of vacancies from the vacancy loops essentially produces a production bias that drives the swelling according to Eq. (8.177), as discussed earlier in this section.

Under electron irradiation, there is no cascade effect, i.e., $\varepsilon_i = \varepsilon_v = 0$ and $K = K_0$. Therefore, in this case, the swelling is purely dislocation bias driven and $\left.\frac{d(\Delta V/V)}{dt}\right|_{db}$ is the only contribution. In the case of cascade damage, however, neither ε_i nor ε_v are likely to be zero. For simplicity, we may use a previously obtained result [30] that the vacancy loop contribution in Eq. (8.177) vanishes due to mutual cancelation. Then, $\left.\frac{d(\Delta V/V)}{dt}\right|_{pb}$ is given by:

$$\frac{d(\Delta V/V)_{pb}}{dt} = \frac{k_V^2}{k_i^2}\varepsilon_i K. \tag{8.178}$$

Note that ε_i need not be very large, just a few percent is enough to make a significant contribution to the total steady-state swelling rate of the order of 1 % K.

As described in the preceding paragraphs, the origin of the "production bias" lies in the special features of damage production in the form of cascades. The physical reason for this bias is the immobilization of a certain fraction of interstitials in the form of thermally stable clusters in the cascade zone. During irradiation at elevated temperatures, the vacancies would evaporate from the collapsed or uncollapsed cascade and would diffuse not only to the interstitial clusters but also to the cavities. Thus, the number of interstitials tied up in the clusters represents approximately the number of vacancies available for the cavity growth. This is basically the strength of the production bias.

The net result of the production bias is precisely the same as that of the dislocation bias, namely the production of an excess of vacancies. However, it is also quite apparent that the physical processes involved in the two mechanisms are very different. In the case of dislocation bias, the interstitial atoms are expected to migrate to dislocations where they are preferentially annihilated due to the strain–field interaction. In the cascade damage situation, this mechanism would not operate effectively since a large number of interstitials are immobilized in the form

of interstitial clusters. In the case of production bias, it is the interstitial–interstitial interaction (and not the interstitial–dislocation interaction) that determines the bias.

However, as noted in Chap. 5, Sect. 5.1.7, and discussed in Chap. 7, Sect. 7.3.3, more recent work has shown that interstitial clusters can have very high 1D mobility. This high mobility allows them to escape to annihilate at sinks such as grain boundaries, thus creating a production bias without the need for dislocation motion. Then, SIA clusters are composed of glissile (g) and sessile (s) components, or $\varepsilon_\mathrm{i} = \varepsilon_\mathrm{i}^\mathrm{g} + \varepsilon_\mathrm{i}^\mathrm{s}$. In the case of glissile SIA clusters, an additional equation is needed in the point defect balance equations of Eq. (8.172) to account for the glissile interstitial clusters [31]:

$$\begin{aligned}
\frac{\mathrm{d}C_\mathrm{v}}{\mathrm{d}t} &= K_0(1-\varepsilon_\mathrm{r})(1-\varepsilon_\mathrm{v}) - k_\mathrm{v}^2 D_\mathrm{v} C_\mathrm{v} - K_\mathrm{iv} D_i C_i C_\mathrm{v} + L_\mathrm{v} \\
\frac{\mathrm{d}C_\mathrm{i}}{\mathrm{d}t} &= K_0(1-\varepsilon_\mathrm{r})(1-\varepsilon_\mathrm{i}) - k_\mathrm{i}^2 D_\mathrm{i} C_\mathrm{i} - K_\mathrm{iv} D_\mathrm{i} C_\mathrm{i} C_\mathrm{v} \\
\frac{\mathrm{d}C_\mathrm{gicl}(x)}{\mathrm{d}t} &= K_\mathrm{gicl}(x) - k_\mathrm{g}^2 D_\mathrm{gicl} C_\mathrm{gicl}(x),
\end{aligned} \tag{8.179}$$

where $C_\mathrm{gicl}(x)$ is the concentration, $K_\mathrm{gicl}(x)$ is the production rate, k_g^2 is the sink strength, and D_gicl is the diffusion coefficient of glissile SIA clusters of size x. The sink strength of the glissile cluster can be written as:

$$k_\mathrm{g}^2 = 2\left(\frac{\pi r_\mathrm{d} \rho_\mathrm{d}}{2} + \pi r_\mathrm{V}^2 \rho_\mathrm{V} + \sigma_\mathrm{vcl}\rho_\mathrm{vcl} + \sigma_\mathrm{icl}\rho_\mathrm{icl}\right)^2, \tag{8.180}$$

where σ_vcl and σ_icl are the interaction cross sections and ρ_vcl and ρ_icl the number densities of the sessile vacancy and mobile SIA clusters, respectively. Note that σ_vcl and σ_icl are proportional to the product of the loop circumference and the corresponding capture radius, similar to r_d for dislocations.

Swelling can be calculated from the solutions of Eqs. (8.179) and (8.110). Writing Eqs. (8.179) to include the individual sink strengths from Eqs. (8.173) yields:

$$\begin{aligned}
\frac{\mathrm{d}C_\mathrm{v}}{\mathrm{d}t} &= K_0(1-\varepsilon_\mathrm{r})(1-\varepsilon_\mathrm{v}) - (k_\mathrm{V}^2 + z_\mathrm{v}^\mathrm{d}\rho_d + z_\mathrm{v}^\mathrm{icl} k_\mathrm{icl}^2 + z_\mathrm{v}^\mathrm{vcl} k_\mathrm{vcl}^2) D_\mathrm{v} C_\mathrm{v} - K_\mathrm{iv} D_\mathrm{i} C_\mathrm{i} C_\mathrm{v} + L_\mathrm{v} \\
\frac{\mathrm{d}C_\mathrm{i}}{\mathrm{d}t} &= K_0(1-\varepsilon_\mathrm{r})(1-\varepsilon_\mathrm{i}) - (k_\mathrm{V}^2 + z_\mathrm{v}^\mathrm{d}\rho_\mathrm{d} + z_\mathrm{i}^\mathrm{icl} k_\mathrm{icl}^2 + z_\mathrm{i}^\mathrm{vcl} k_\mathrm{vcl}^2) D_\mathrm{i} C_\mathrm{i} - K_\mathrm{iv} D_\mathrm{i} C_\mathrm{i} C_\mathrm{v} \\
\frac{\mathrm{d}C_\mathrm{gicl}}{\mathrm{d}t} &= K_\mathrm{gicl} - D_\mathrm{gicl} C_\mathrm{gicl} k_\mathrm{g}^2 = K_\mathrm{gicl} - 2 D_\mathrm{gicl} C_\mathrm{gicl} \left(\frac{\pi r_\mathrm{d} \rho_\mathrm{d}}{2} + \pi r_\mathrm{V}^2 \rho_\mathrm{V} + \sigma_\mathrm{vcl}\rho_\mathrm{vcl} + \sigma_\mathrm{icl}\rho_\mathrm{icl}\right)^2,
\end{aligned} \tag{8.181}$$

At steady state and neglecting recombination, Eqs. (8.181) becomes:

$$\begin{aligned} K_{\mathrm{v}} &= D_{\mathrm{v}}C_{\mathrm{v}}(k_{\mathrm{V}}^2 + z_{\mathrm{v}}^{\mathrm{d}}\rho_{\mathrm{d}}) + D_{\mathrm{v}}C_{\mathrm{v}}z_{\mathrm{v}}^{\mathrm{icl}}k_{\mathrm{icl}}^2 + D_{\mathrm{v}}C_{\mathrm{v}}z_{\mathrm{v}}^{\mathrm{vcl}}k_{\mathrm{vcl}}^2 + 2D_{\mathrm{v}}C_{\mathrm{v}}\Lambda x_{\mathrm{g}}\sigma_{\mathrm{icl}}\rho_{\mathrm{icl}} \\ K_{\mathrm{i}} &= D_{\mathrm{i}}C_{\mathrm{i}}(k_{\mathrm{V}}^2 + z_{\mathrm{v}}^{\mathrm{d}}\rho_{\mathrm{d}}) + D_{\mathrm{v}}C_{\mathrm{v}}z_{\mathrm{v}}^{\mathrm{icl}}k_{\mathrm{icl}}^2 + D_{\mathrm{i}}C_{\mathrm{i}}z_{\mathrm{v}}^{\mathrm{vcl}}k_{\mathrm{vcl}}^2 - 2D_{\mathrm{v}}C_{\mathrm{v}}\Lambda x_{\mathrm{g}}\sigma_{\mathrm{icl}}\rho_{\mathrm{icl}} \\ K_{\mathrm{gicl}} &= D_{\mathrm{gicl}}C_{\mathrm{gicl}}k_{\mathrm{g}}^2, \end{aligned} \tag{8.182}$$

where

$$\begin{aligned} K_{\mathrm{v}} &= K_0(1-\varepsilon_{\mathrm{r}})(1-\varepsilon_{\mathrm{v}}) \\ K_{\mathrm{i}} &= K_0(1-\varepsilon_{\mathrm{r}})(1-\varepsilon_{\mathrm{i}}), \end{aligned} \tag{8.183}$$

and $\Lambda = \sqrt{k_{\mathrm{g}}^2/2}$.

The vacancy supersaturation is obtained from the difference between $D_{\mathrm{v}}C_{\mathrm{v}}$ and $D_{\mathrm{i}}C_{\mathrm{i}}$ using the first two equations in Eqs. (8.182):

$$D_{\mathrm{v}}C_{\mathrm{v}} - D_{\mathrm{i}}C_{\mathrm{i}} = B_{\mathrm{d}}\frac{z_{\mathrm{v}}^{\mathrm{d}}\rho_{\mathrm{d}}}{k_{\mathrm{V}}^2 + z_{\mathrm{v}}^{\mathrm{d}}\rho_{\mathrm{d}}}D_{\mathrm{v}}C_{\mathrm{v}} + \frac{\varepsilon_{\mathrm{i}}^{g}K_0(1-\varepsilon_{\mathrm{r}})}{k_{\mathrm{V}}^2 + z_{\mathrm{v}}^{\mathrm{d}}\rho_{\mathrm{d}}}\left(1 - \frac{\sigma_{\mathrm{vcl}}\rho_{\mathrm{vcl}} + \sigma_{\mathrm{icl}}\rho_{\mathrm{icl}}}{\Lambda}\right), \tag{8.184}$$

where $\varepsilon_{\mathrm{i}}^{\mathrm{g}}$ is the fraction of interstitials in glissile clusters and B_{d} is the dislocation bias term given by $B_{\mathrm{d}} = (z_{\mathrm{i}}^{\mathrm{d}} - z_{\mathrm{v}}^{\mathrm{d}})/z_{\mathrm{v}}^{\mathrm{d}}$. The swelling rate is given by:

$$\frac{\mathrm{d}(\Delta V/V)_{\mathrm{pb}}}{\mathrm{d}t} = k_{\mathrm{V}}^2(D_{\mathrm{v}}C_{\mathrm{v}} - D_{\mathrm{i}}C_{\mathrm{i}}) - 2D_{\mathrm{icl}}^{\mathrm{g}}C_{\mathrm{icl}}^{\mathrm{g}}x_{\mathrm{g}}\Lambda\pi r_{\mathrm{V}}^2\rho_{\mathrm{V}}, \tag{8.185}$$

and substituting Eq. (8.184) into Eq. (8.185), the swelling rate becomes:

$$\begin{aligned} \frac{\mathrm{d}(\Delta V/V)_{\mathrm{pb}}}{\mathrm{d}t} = K_0(1-\varepsilon_{\mathrm{r}})\Bigg\{ & B_{\mathrm{d}}\frac{k_{\mathrm{V}}^2 z_{\mathrm{v}}^{\mathrm{d}}\rho_{\mathrm{d}}}{(k_{\mathrm{V}}^2 + z_{\mathrm{v}}^{\mathrm{d}}\rho_{\mathrm{d}})(k_{\mathrm{V}}^2 + z_{\mathrm{v}}^{\mathrm{d}}\rho_{\mathrm{d}} + z_{\mathrm{v}}^{\mathrm{icl}}k_{\mathrm{icl}}^2 + z_{\mathrm{v}}^{\mathrm{vcl}}k_{\mathrm{vcl}}^2)} \\ & + \varepsilon_{\mathrm{i}}^{g}\left[\frac{k_{\mathrm{V}}^2}{k_{\mathrm{V}}^2 + z_{\mathrm{v}}^{\mathrm{d}}\rho_{\mathrm{d}}}\left(1 - \frac{\sigma_{\mathrm{vcl}}\rho_{\mathrm{vcl}} + \sigma_{\mathrm{icl}}\rho_{\mathrm{icl}}}{\Lambda}\right) - \frac{\pi r_V^2\rho_V}{\Lambda}\right]\Bigg\}. \end{aligned} \tag{8.186}$$

The first term in brackets on the right-hand side of Eq. (8.186) represents the influence of the dislocation bias, and the second one describes the production bias. The factor $(1 - \varepsilon_{\mathrm{r}})$ accounts for the intracascade recombination of defects, which is a function of the recoil energy and reduces the rate of defect production compared to the NRT value, K_0. Swelling rate is also a function of recoil energy by virtue of the dependence on $\varepsilon_{\mathrm{i}}^{\mathrm{g}}$, which increases with PKA energy up to about 10–20 keV.

The effect of the two biases, dislocation and production, are quite different. The dislocation bias depends only on the microstructure and predicts continued void growth. The production bias can be positive or negative, depending on the

microstructure. The first term in Eq. (8.186) decreases the effect of production bias due to recombination of the SIA clusters at sessile vacancy and SIA clusters, while the second term arises from the capture of SIA clusters by voids. The latter term may become equal to zero or even negative; hence, the combination of the two bias factors does not necessarily lead to a higher swelling rate.

Considering only Frenkel pair production, the swelling rate given by Eq. (8.122) predicts that the swelling rate will be small at a low dislocation density. If this is the case, then the swelling rate in well-annealed metals at low doses should be small. Experiments have shown that the void swelling rate in fully annealed pure copper irradiated with fission neutrons up to about 0.01 dpa is ~ 1 %/dpa [32], which is similar to the maximum swelling rate found in materials at high doses. Referring to Eq. (8.186), in annealed materials, the dislocation bias term is negligible. At low doses, the void size is small, and therefore, the void cross section for the interaction with SIA glissile clusters ($\pi r_V^2 \rho_V / \Lambda$) is small. (Also, at low dose, the cluster density will be small, so the term in parentheses in the second line of Eq. (8.186) ~ 1). Thus, the swelling rate is driven by the production bias:

$$\frac{\mathrm{d}(\Delta V/V)}{\mathrm{d}t} \approx K_0(1-\varepsilon_\mathrm{r})\varepsilon_\mathrm{i}^\mathrm{g} \frac{k_V^2}{k_V^2 + z_\mathrm{v}^\mathrm{d}\rho_\mathrm{d}}. \tag{8.187}$$

When $z_\mathrm{v}^\mathrm{d}\rho_\mathrm{d} \ll k_V^2$, the swelling rate is determined by the cascade parameters:

$$\frac{\mathrm{d}(\Delta V/V)}{\mathrm{d}t} \approx K_0(1-\varepsilon_\mathrm{r})\varepsilon_\mathrm{i}^\mathrm{g}. \tag{8.188}$$

Note that the swelling rate given in Eq. (8.188) is the maximum swelling rate that can be achieved by production bias. Referring to Eq. (8.187) and assuming that there is no interaction of mobile SIA clusters with voids and sessile clusters, the swelling rate is given by:

$$\frac{\mathrm{d}(\Delta V/V)}{\mathrm{d}t} \approx 1/2 K_0(1-\varepsilon_\mathrm{r})\varepsilon_\mathrm{i}^\mathrm{g}, \tag{8.189}$$

where the sink strength ratio, $\frac{k_V^2}{k_V^2 + z_\mathrm{v}^\mathrm{d}\rho_\mathrm{d}} = ½$, the value achieved when $Q = 1$ in Eq. (8.148). Data have shown that $1 - \varepsilon_\mathrm{r} = 0.01$ and $\varepsilon_\mathrm{i}^\mathrm{g}$ in good agreement with MD simulations of cascades, yielding a maximum swelling rate of ~ 1 %/dpa.

Production bias helps to explain some additional observations. Golubov et al. [31] and Singh et al. [34] compared the microstructure of annealed copper irradiated with 2.5 MeV electrons, 3 MeV protons, and fission neutrons at ~ 520 K. For all irradiations, the damage rate was $\sim 10^{-8}$ dpa/s. The average recoil energies were estimated to be about 0.05, 1, and 60 keV, respectively, and the primary damage form was Frenkel pairs for electrons, small cascades for protons, and large cascades for neutrons. Thus, the cascade efficiency $(1 - \varepsilon_\mathrm{r})$ was highest for electrons and lowest for neutrons. If dislocation bias is responsible for swelling, then the swelling rate is

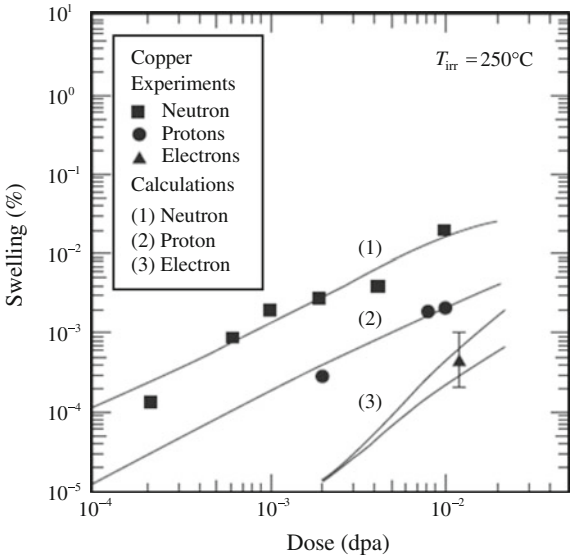

Fig. 8.31 Experimentally measured and calculated void swelling in pure copper after irradiation with 2.5 MeV electrons, 3 MeV protons, and fission neutrons. The calculations were performed in the framework of the Frenkel pair 3D model (PF3DM) for electron irradiation and using the production bias model (PBM) for irradiation with protons and fission neutrons (after [31])

proportional to the damage rate and must be highest for electron irradiation and lowest for neutron irradiation. Figure 8.31 shows just the opposite with a swelling rate for neutron irradiation of about 50 times that for electrons, with protons in between. These results can be understood from Eq. (8.186). Under electron irradiation, only the first term on the right-hand side operates as $\varepsilon_i^{\mathrm{g}} = 0$. The swelling rate is low in this case because of the low dislocation density. Under cascade damage conditions, the damage rate is smaller because of the low cascade efficiency. But in this case, $\varepsilon_{\mathrm{i}}^{\mathrm{g}} \neq 0$ and the second term on the right-hand side of Eq. (8.186) is dominant.

Cascade production of SIA clusters can also affect the nucleation of voids through damage accumulation. The sink strengths of the clusters, k_{vcl}^2 and k_{icl}^2, at steady state are given by [31]:

$$k_{\mathrm{vcl}}^2 = \frac{\varepsilon_{\mathrm{v}}^{\mathrm{s}} K_{\mathrm{v}}}{D_{\mathrm{v}} \exp(-E_{\mathrm{vcl}}/kT)(k_V^2 + z_{\mathrm{v}}^{\mathrm{d}}\rho_{\mathrm{d}}) - \varepsilon_{\mathrm{i}}^{\mathrm{g}} K_{\mathrm{v}}} (k_V^2 + z_{\mathrm{v}}^{\mathrm{d}}\rho_{\mathrm{d}}) \left(1 - \frac{1}{x_{\mathrm{vcl}}^{\mathrm{s}}}\right) \tag{8.190}$$

$$k_{\mathrm{icl}}^2 = \frac{\varepsilon_{\mathrm{i}}^{\mathrm{s}}}{\varepsilon_{\mathrm{i}}^{\mathrm{g}}} (k_{\mathrm{V}}^2 + z_{\mathrm{v}}^{\mathrm{d}}\rho_{\mathrm{d}}) \left(1 - \frac{1}{x_{\mathrm{icl}}^{\mathrm{s}}}\right), \tag{8.191}$$

where E_{vcl} is an effective binding energy of vacancies with the vacancy clusters, $x_{\mathrm{vcl,\,icl}}$ are the mean sizes of the vacancy and SIA glissile clusters, and $\varepsilon_{\mathrm{i}}^{\mathrm{s,g}}$ are the fraction of interstitials in sessile (s) and glissile (g) clusters. From Eq. (8.191), the

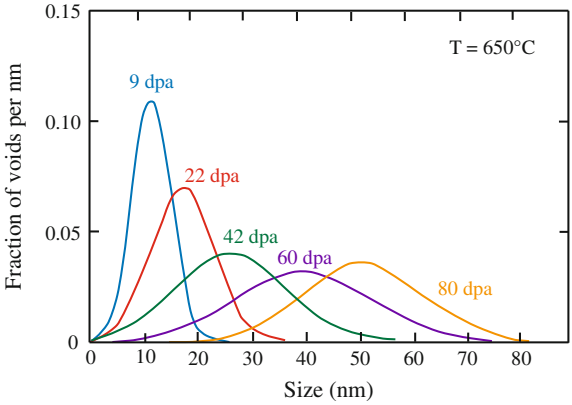

Fig. 8.32 Experimentally measured void size distribution in a Fe–Cr–Ni alloy irradiated at 650 °C (after [33])

steady-state sink strength of sessile SIA clusters is inversely proportional to the fraction of SIAs produced in cascades in the form of mobile SIA clusters, and thus, $k_{\mathrm{icl}}^2 \rightarrow \infty$ when $\varepsilon_{\mathrm{i}}^{\mathrm{g}} \rightarrow 0$, or as the fraction of interstitials in glissile clusters goes to zero, the sink strength of the (sessile) clusters approaches infinity. Such a case may be reached in large cascades as produced from neutron irradiation combined with impurities that may provide cluster immobilization. The "incubation period" of swelling observed in many alloys may be due to this process. A possible scenario may be that during the incubation period, the material is purified by RIS on SIA clusters because of their high density. At high enough doses, the high number density of SIA clusters decreases via the absorption of excess vacancies, restoring conditions for damage accumulation and consequent void growth.

As presented in the description of clusters using the Fokker–Planck formulation (Sect. 7.6), it was noted that the cluster size distribution is broadened by the parameter D and shifted by the parameter F. Thus, with increasing dose, the solution to the Fokker–Planck equation describes the broadening of the void size distribution and the increase in the mean void size of the distribution with dose. This general behavior can be compared with experimental swelling results for Fe–Cr–Ni irradiated at 650 °C. Figure 8.32 shows that the mean size of the distribution increases from about 11 nm at 9 dpa to over 50 nm by 80 dpa with a corresponding broadening of the distribution. Since swelling is mainly sensitive to the shift of the mean size of the distribution, linear swelling ($\Delta V/V \propto$ dose) is obtained when the growth rate is large compared to the diffusional broadening, in which case the swelling rate is then given by the drift force alone.

8.3.7 Stress Dependence

Equation (8.125) shows that the void growth rate consists of two components. $\dot{R}_{\mathrm{th}}$ is the thermal emission term and hence is the only part affected by the state of stress or

internal gas pressure. Consequently, the internal gas pressure and stress begin to affect the growth rate only when $\dot{R}_{\text{th}}$ becomes significant, i.e., for temperatures greater than the peak swelling temperature. When the solid is under a hydrostatic stress and when voids contain gas that exerts a pressure on the void surface, the equilibrium vacancy concentration at voids and dislocations will be different from that in the stress-free, gas-free state. Brailsford and Bullough showed that the pressure, but not the external stress, will affect the concentration of vacancies in equilibrium with the void. Hence, the force balance for the gas-containing void in mechanical equilibrium, as in Eq. (8.82), becomes:

$$\sigma = p - \frac{2\gamma}{R}, \tag{8.192}$$

where σ is the hydrostatic stress and p is the gas pressure in the void. (In the case of a non-equilibrium bubble, the appropriate stress is the radial component of the stress tensor, σ_{r}.) The vacancy concentration at the surface of the void, given by Eq. (8.85) in the gas-free case, becomes:

$$C_{\text{v}}^{\text{V}} = C_{\text{v}}^{0} \exp\left[-\frac{\Omega}{kT}\left(p - \frac{2\gamma}{R}\right)\right]. \tag{8.193}$$

Similarly, the equilibrium vacancy concentration adjacent to the network dislocations becomes:

$$C_{\text{v}}^{\text{N}} = C_{\text{v}}^{0} \exp\left[-\frac{\sigma\Omega}{kT}\right]. \tag{8.194}$$

Repeating the solution to the void growth equation using the equilibrium vacancy concentration at the void surface given by Eq. (8.193) and the equilibrium vacancy concentration at the network dislocations given by Eq. (8.194) revises the thermal emission term, R_{th}, in Eq. (8.135) (with $\rho_{\text{CP}} = \rho_{\text{L}} = 0$) as follows:

$$\dot{R}_{\text{th}} = \frac{D_{\text{v}} C_{\text{v}}^{0} \Omega^2 z_{\text{v}} \rho_{\text{d}} \left(\sigma + p - \frac{2\gamma}{R}\right)}{RkT(z_{\text{v}}\rho_{\text{d}} + 4\pi R \rho_{\text{V}})}. \tag{8.195}$$

Note that shrinkage due to thermal emission becomes instead stress-enhanced growth when the sum of the external stress and gas pressure exceeds the stress due to surface tension:

$$\sigma + p > \frac{2\gamma}{R}. \tag{8.196}$$

Note that for a stressed solid containing no gas, stress-enhanced growth will occur when $\sigma > \frac{2\gamma}{R}$. For a void containing x gas atoms, Eq. (8.196) becomes:

$$\sigma = \frac{2\gamma}{R} - \left(\frac{3xkT}{4\pi R^3}\right). \tag{8.197}$$

The void radius at which $\frac{d\sigma}{dR} = 0$ is called the critical void radius and is given by:

$$R_{cr} = \left(\frac{9xkT}{8\pi\gamma}\right)^{1/2}, \tag{8.198}$$

and substituting into Eq. (8.197) gives the stress at the critical void size, which is the critical stress for unlimited void growth:

$$\sigma_{cr} = \frac{4\gamma}{3}\left(\frac{8\pi\gamma}{9xkT}\right)^{1/2}. \tag{8.199}$$

The effect of stress on void growth in steel is given in Fig. 8.33. Note that there is little effect of stress out to high dose when the stress is low. But when stress is increased, the swelling increases rapidly at relatively lower doses. Figure 8.34 also accounts for the presence of helium in the growth of voids under stress.

However, this formulation predicts that the void growth rate is proportional to stress, which is counter to the 1 %/dpa observations. Also, as shown in Fig. 8.34, the effect of stress is only significant at very high temperatures. Experimental data have since shown that the prime role of stress is on shortening the transient swelling regime, rather than increasing the swelling rate in the steady-state regime. Figure 8.35 shows the effect of stress on swelling in modified 316 stainless steel alloys irradiated in the PHENIX reactor. Note that with increasing stress, the swelling rate (slope) approaches a constant value at lower doses. Stress can also

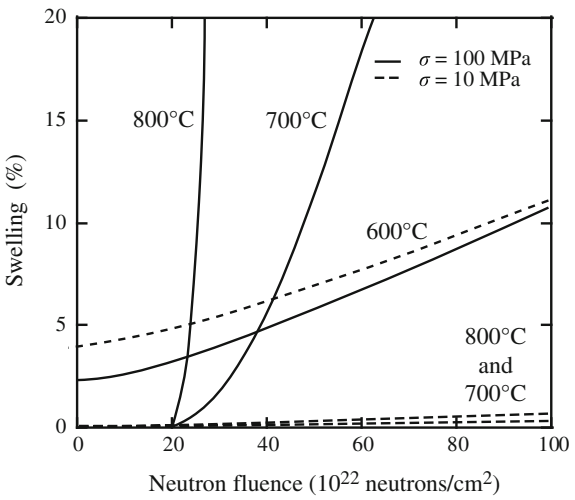

Fig. 8.33 Stress-enhanced swelling for various stress levels and temperatures as a function of fluence (after [35])

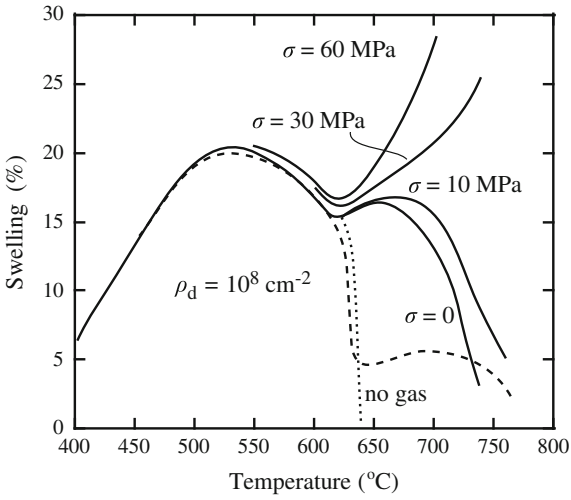

Fig. 8.34 Temperature dependence of stress-enhanced void growth in steel. The *solid curves* apply to a dislocation density of 10^8 cm^{-2} and a helium production rate of 10^{-6} appm/s (after [36])

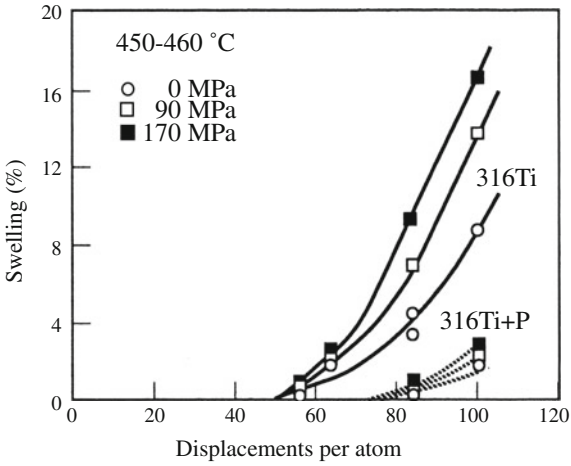

Fig. 8.35 Effect of stress on swelling of two modified 316 stainless steels irradiated in the form of pressurized tubes in the PHENIX reactor (after [37])

affect the stability of void nuclei, which would explain the observation of more rapid nucleation.

In the development of the nucleation rate of voids, the nucleation current and number density of voids of size n were described by Eqs. (8.18) and (8.19), respectively, for the case of vacancy condensation excluding interstitials:

$$J_n = Z\beta N_0 \exp\left(\frac{-\Delta G_n^0}{kT}\right), \quad \text{and} \quad \rho^0(n) = N_0 \exp\left(\frac{-\Delta G_n^0}{kT}\right).$$

with the free energy of formation of void of size n given by Eq. (8.17):

$$\Delta G_n^0 = -nkT \ln S_v + \left(36\pi\Omega^2\right)^{1/3} \gamma n^{2/3}.$$

Accounting for the application of an external hydrostatic stress, σ_h, gives:

$$\Delta G_n^0(\sigma_h) = -nkT \ln S_v + \left(36\pi\Omega^2\right)^{1/3} \gamma n^{2/3} - n\sigma_h \Omega, \tag{8.200}$$

and

$$\Delta G_n^0(\sigma_h) = \Delta G_n^0(0) + n\sigma_h \Omega. \tag{8.201}$$

Note that the effect of gas pressure, p, in the void can also be accounted for by the addition of a term, $np\Omega$.

When interstitials are present, the free energy is given by Eq. (8.33):

$$\Delta G_n' = kT \sum_{j=0}^{n-1} \ln \left[\frac{\beta_i(j+1)}{\beta_v(j)} + \exp\left(\frac{\delta G_j^0}{kT} \right) \right],$$

where δG_j^0 is the increment in free energy of a void in going from j vacancies to $j + 1$ vacancies if no interstitials are present. By assuming that stress affects only the free energy barrier (and not the critical nucleus size) and that the stress contribution of the energy per atom is not dependent on the number of atoms in the cluster, then we can approximate the free energy in Eq. (8.33) in a manner similar to that done in Eq. (8.201) [38]:

$$\Delta G_n'(\sigma_h) = \Delta G_n'(0) + n\sigma_h \Omega. \tag{8.202}$$

Then, from Eq. (8.35), the ratio of stressed to unstressed steady-state nucleation rates in a homogeneous, coprecipitation environment is:

$$\frac{J_n(\sigma_h)}{J_n(0)} = \frac{\exp\left[-\left(\Delta G_n' - n\sigma_h \Omega\right)/kT\right]}{\exp\left[-\Delta G_n'/kT\right]}. \tag{8.203}$$

Using Eqs. (8.22) and (8.23) to write the ratio of nucleation currents in terms of the ratio of void number densities in the stressed and unstressed states gives:

$$\frac{J_n(\sigma_h)}{J_n(0)} = \frac{Z'(\sigma_h)\beta_n(\sigma_h)\rho_n(\sigma_h)}{Z'(0)\beta_n(0)\rho_n(0)} = \frac{Z'(\sigma_h)\beta_n(\sigma_h)\exp\left[-\left(\Delta G_n'(\sigma_h)\right)\right]}{Z'(0)\beta_n(0)\exp\left[-\Delta G_n'(0)\right]}, \tag{8.204}$$

and provided that neither the arrival rate ratio, $\beta_n(\sigma_h)/\beta_n(0)$, nor Z' is sensitive to the stress level [39], then Eq. (8.204) becomes:

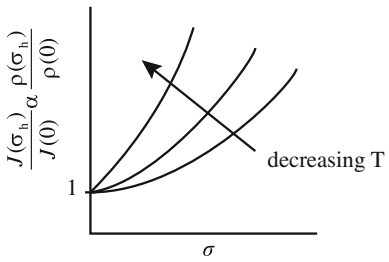

Fig. 8.36 Variation of the void nucleation rate and the void number density as a function of stress and temperature, as described by Eq. (8.205)

$$\frac{\rho_n(\sigma_h)}{\rho_n(0)} \approx \exp(n\sigma_h \Omega/kT). \tag{8.205}$$

Example 8.1 Effect of stress on void density

Assuming an external stress of 100 MPa and a void cluster size of ~15 at a temperature of 450 °C, Eq. (8.205) gives an increase in the void number density by a factor of ~6. However, for a stress of 200 MPa, the increase is 34, and for 300 MPa, the factor becomes ~200. Since both stress and temperature appear in the exponent, the factor rises rapidly with an increase in stress and with a decrease in temperature (Fig. 8.36). Referring back to Fig. 8.35, the decreasing time to reach the steady-state swelling rate as stress is increased is explainable by stress-enhanced nucleation, which will be more important at lower temperatures, contrary to the effect of stress on the steady-state swelling rate.

8.3.8 *Effect of RIS*

Recall from Chap. 6, Sect. 6.4, that RIS (radiation-induced segregation) of alloying elements occurs at sinks, which can include voids. The result is a *coated void* in which the void develops a shell of composition that is different from that in the matrix. As we have seen, for austenitic stainless steels, the void coating is enriched in nickel and depleted in chromium relative to the matrix. A primary effect of the composition change is a change in diffusion coefficient leading to a change in the void capture efficiency. The capture efficiency for the vacancy in the shell is [16, 40]:

$$z_v^V(r_V) = \frac{1 + \delta/r_V}{1 + D_v \delta / D_v^S r_V}, \tag{8.206}$$

where r_V is the void radius, δ is the thickness of the shell, and D_v^S is the vacancy diffusion coefficient in the shell. Recall that an expression for the composition dependence of D_v in the shell, D_v^S, was determined in Sect. 6.4 of Chap. 6. Using the expression for the capture efficiency in the void growth equations results in a reduction in void growth if $D_v^S < D_v$ and $D_i^S \sim D_i$.

A more important effect of the coating is the elastic interaction between a point defect and a void surrounded with a coating that has different elastic constants than the matrix. The result is a change in capture efficiency of the void for defects. The capture efficiency due to a difference in elastic constants is given as:

$$z_{i,v}^V(r_V) = \left[\frac{r_V}{r_c} + \frac{r_V}{(r_c+\delta)^2}\frac{D_{i,v}}{w_{i,v}}\right]^{-1}, \tag{8.207}$$

where r_c is the void plus coating radius and the transfer velocity, $w_{i,v}$, is

$$w_{i,v} = \frac{D_{i,v}\exp\left(-E_{i,v}^*/kT\right)}{a}, \tag{8.208}$$

where a is the lattice parameter and E^* is the repulsive interaction energy at its largest positive value. The sign of E^* is positive (repulsion) if the matrix of the shell is stiffer than that of the matrix. Since E^* is proportional to the square of the point defect relaxation volume, the sink efficiency is much smaller for the interstitial than for the vacancy due to the larger repulsion for the interstitial. So the stiffer shell results in a repulsion that is greater for the interstitial than for the vacancy, making void nucleation and growth more rapid in the case of a coated void (Fig. 8.37).

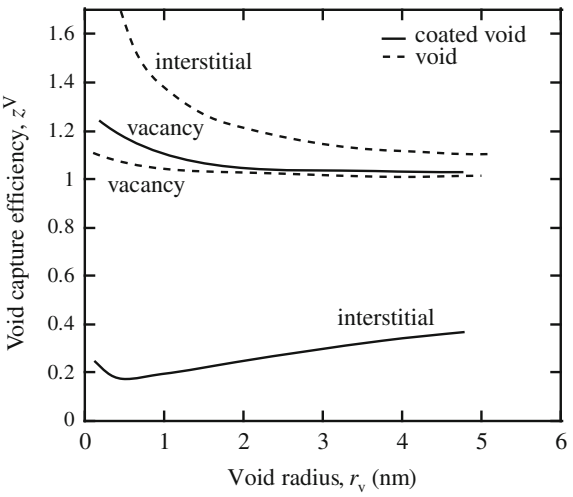

Fig. 8.37 Capture efficiencies for point defect diffusion to a void and a coated void as a function of void radius, r_V. The void prefers interstitials, especially at small void sizes. The preference is reversed for the coated void (after [16])

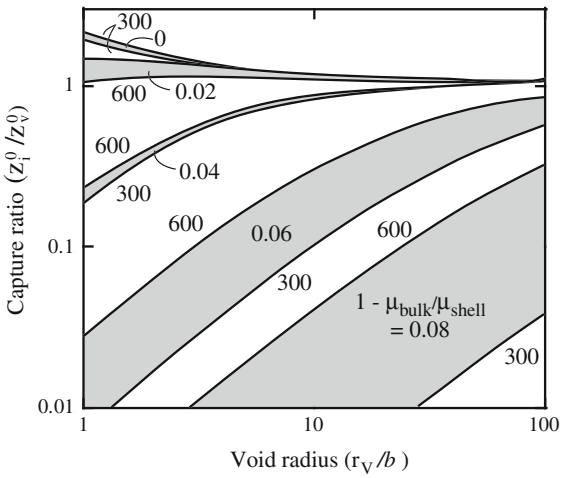

Fig. 8.38 Capture ratio z_i^0/z_v^0 for coated voids with a shell thickness of two atomic layers and zero surface stress (after [41])

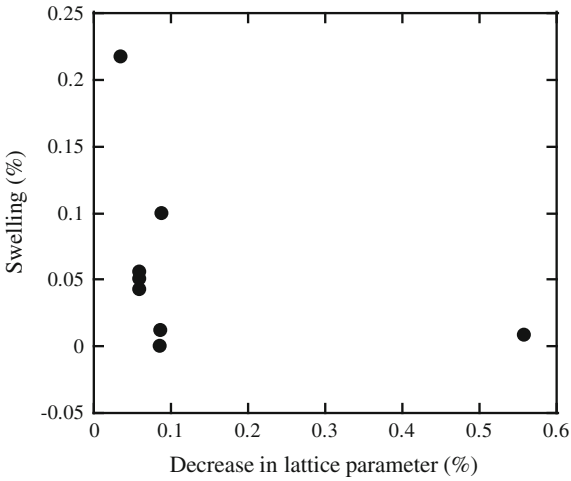

Fig. 8.39 Decrease in swelling as a function of changing lattice parameter. Swelling decreases with decreasing lattice parameter, which is caused by RIS at the void surface (after [42])

A change in the shear modulus or lattice parameter in the shell can also alter the preference of the void for vacancies and interstitials [41] by creating a barrier to defect diffusion through the shell due to a change in the strain energy. When segregation leads to a shell with a shear modulus or lattice parameter only slightly higher than in the surrounding matrix, the void becomes a highly preferential sink for vacancies and swelling is increased. Conversely, a reduction in the shear modulus and lattice parameter should result in reduced void swelling. Figure 8.38 shows the effect of the shear modulus ($1 - \mu_{bulk}/\mu_{shell}$) on the interstitial/vacancy capture ratio. For small voids, a few percent change in the shear modulus can result in orders of magnitude change in the capture ratio. Allen et al. [42] compared the

swelling and RIS behavior of a range of alloys with different nickel content. Calculation of the lattice parameter for the void shell composition shows that the swelling behavior can be explained by a decrease in lattice parameter at the void surface (Fig. 8.39). In fact, segregation leads to a smaller lattice parameter with a lower shear modulus, and the *softer* shell reduces void swelling.

8.3.9 Void Lattices

Voids have also been found to organize themselves in periodic arrays or lattices in a metal under irradiation and also in periodic walls of defect clusters. Figure 8.40(a) shows a void lattice in bcc Nb following irradiation with 8.5 MeV Ta^+ to a dose of 300 dpa at 800 °C, and Fig. 8.40(b) shows a periodic array of planar {001} walls of defects in Cu at 3 dpa. The lattices are much easier to form in bcc metals than in fcc metals, though lattices have been observed in Ni, Al, and stainless steel. Their formation is independent of the type of irradiating particle as long as cascades are produced. Void lattices are a form of self-organization that occurs as responses of complex systems to external stimuli. It is believed that self-organization results from the collective interaction between system components under external forces that drive the system far from equilibrium. In irradiated solids, the void patterns are believed to be linked to the collective action of the point defects on the lattice structure. Wall formation is restricted to a temperature range between 0.2 and 0.4 T_m, while void lattice formation occurs at somewhat higher temperatures. Characteristic is the partial or complete isomorphy of the ordered defect structure with the host lattice [44].

A full understanding of the formation of void lattices is still lacking, but the theory is able to account for many of the parametric effects in lattice formation. Kinetic rate theory and the determination of an instability threshold can explain many of the observations to date. Transport and reactions of defects during bombardment have been modeled by nonlinear diffusion–reaction equations for the cases of periodic defect walls and of void lattices. The isotropic diffusion–reaction models can describe conditions for the destabilization of the homogeneous defect cluster distributions and predict characteristic periodicity lengths but have to be modified substantially to account for the structural and orientation relationships between ordered defect arrangements and crystal structure. Possible reasons for these properties are (1) elastic interactions between defects that are probably important in wall formation and (2) low-dimensional defect transport that is probably important for void and bubble lattice formation. In general, ordered defect structures form when the following general conditions are satisfied [43]:

1. Agglomeration of vacancies into clusters during the collisional phase of cascade cooling.
2. A bias for dislocations toward preferential absorption of interstitials over vacancies.

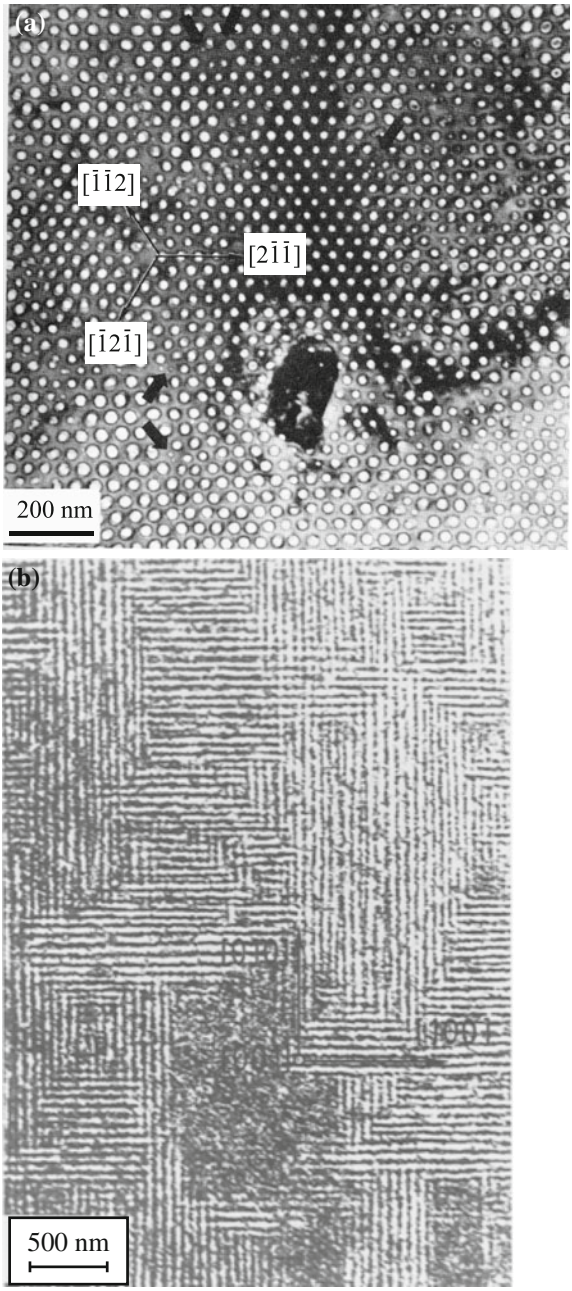

Fig. 8.40 Void lattice in (**a**) Nb irradiated with 8.5 MeV Ta^+ at 800 °C to 300 dpa (after [43]) and (**b**) periodic arrays of planar {001} walls of defects in Cu irradiated to 0.65 dpa (after [44])

3. An asymmetry in the production and diffusion of mobile point defects (production bias).
4. Some degree of anisotropy during the evolution of clustered defects. This could be triggered either by diffusional anisotropies of point defects, or by anisotropic elastic interaction between defect clusters during the latter stages of their evolution.

Two features of void ordering are as follows: (1) The symmetry and crystallographic orientation of a void lattice are always the same as those of the host lattice and (2) the void lattices are formed under neutron and heavy ion but not electron irradiation. The occurrence of void lattice formation under cascade damage conditions (neutron or ion irradiation) and its absence under single Frenkel pair production (electron irradiation) are strong evidence for a key role of the 1D motion of thermally stable SIA clusters directly produced in cascades. In cubic metals, void ordering is probably due to one-dimensional SIA loop glide. This mechanism would also provide an explanation for the enhanced swelling adjacent to grain boundaries. The role of crowdions is unclear because of their limited effective diffusion range [44]. However, it has been shown that when there is anisotropic transport of self-interstitial atoms by the crowdion mechanism (i.e., transport in which some crystal directions are preferred over others), voids occupying spatial positions that form a regular lattice grow faster, on average, than the randomly distributed voids [45]. However, for the void lattice to form, randomly distributed voids have to disappear. This can occur through stochastic void coarsening. Since void evolution in this case is sensitive to the spatial variations in the void growth rate, even a small fraction of interstitials moving as crowdions can significantly affect the spatial behavior of the void ensemble, resulting in the dissolution of randomly distributed voids with lower growth rates by stochastic fluctuations, and the nucleation and growth of voids forming a regular lattice. A general result of all models proposed to explain void lattice formation is that the existence of fundamental asymmetries in the behavior of v-type and SIA-type defects (production, diffusion, and annihilation), in spite of their principle particle–antiparticle relation, is a necessary prerequisite for the formation of ordered defect structures in metals under particle bombardment [44].

8.3.10 Effect of Microstructure and Composition

The alloy microstructure can exert significant effects on void nucleation and growth. Microstructure features such as composition, solute addition, and precipitate structure are among the most important in influencing void behavior.

Major Element Composition

In simple Fe–Cr–Ni austenitic alloys, swelling drops dramatically with increasing nickel content, reaching a minimum at about 50 at.%. Figure 8.41 shows that the

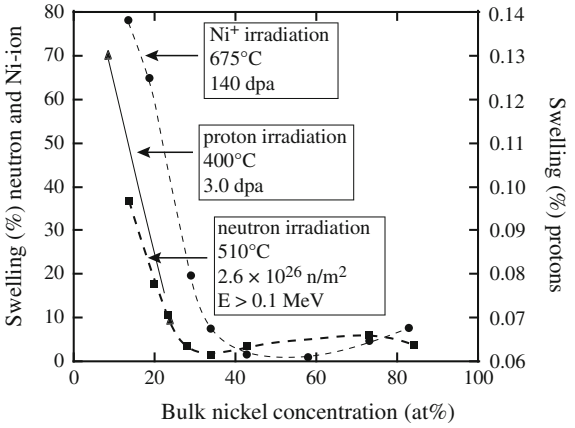

Fig. 8.41 The effect of bulk nickel concentration on swelling resulting from irradiation with different particles: neutrons, nickel ions, and protons (after [42])

swelling dependence of nickel holds for various particle irradiations. The effect of Ni content on swelling is primarily due to the change in incubation dose as shown in Fig. 8.42. In fact, the data in Fig. 8.43 show that at steady state, the swelling rate is the same over a wide range of nickel content.

Chromium content also affects swelling of austenitic alloys. Figure 8.44 shows that increasing chromium over the range 15 to 30 % results in greater swelling. Less data are available on the systematic effect of Cr than for Ni, but the available data suggest that swelling increases monotonically with Cr content. Swelling is much less of a problem in ferritic alloys, but reaches a maximum with a chromium content of about 15 at.%. Figure 8.45 summarizes the effect of Ni and Cr on swelling in Fe–Cr–Ni alloys at 675 °C.

Solute Additions

Void swelling should be inhibited by additions of minor elements that bind either vacancies or interstitials with sufficient strength to reduce the effective mobility, thus preventing defects from reaching sinks and promoting recombination. The effect of solutes on the point defect balance equations was presented in Chap. 6, Sect. 6.4. The effect of solute addition on void swelling behavior can be determined by solving Eq. (6.66) through Eq. (6.70) and the nucleation rate, as in Eq. (8.35), and the void swelling rate, as in Eq. (8.112). Results of numerical methods solution [47] show that with increasing values of binding energy, the activation energy for void nucleation increases (Fig. 8.46). The void swelling rate decreases with increasing binding energy as shown in Fig. 8.47. The net effect of solute addition on void swelling is shown in Fig. 8.48, which indicates that for increased solute concentration and binding energy, void swelling decreases. Data on the role of solutes in swelling are in general agreement with the model. Figure 8.49 shows that Si and P strongly influence the swelling of austenitic stainless steels. In fact, Si is a fast diffuser and is known to alter the ratio of diffusivities of the solvent atoms. As shown in Fig. 8.50, the effect of P on swelling is indeed in extending the incubation period

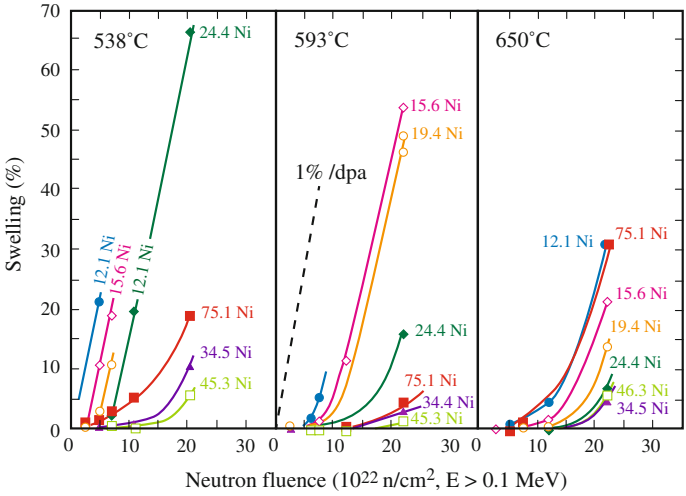

Fig. 8.42 The influence of temperature and nickel content on swelling of ternary Fe–15Cr–*x*Ni alloys in EBR-II (after [46])

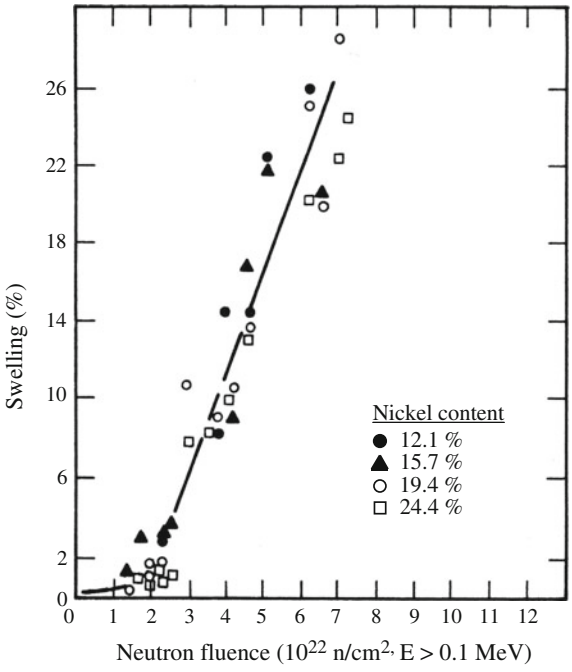

Fig. 8.43 Swelling of Fe–15Cr–xNi ternary alloys in EBR-II at temperatures between 400 and 510 °C for nickel levels between 12.1 and 24.4 wt% (after [46])

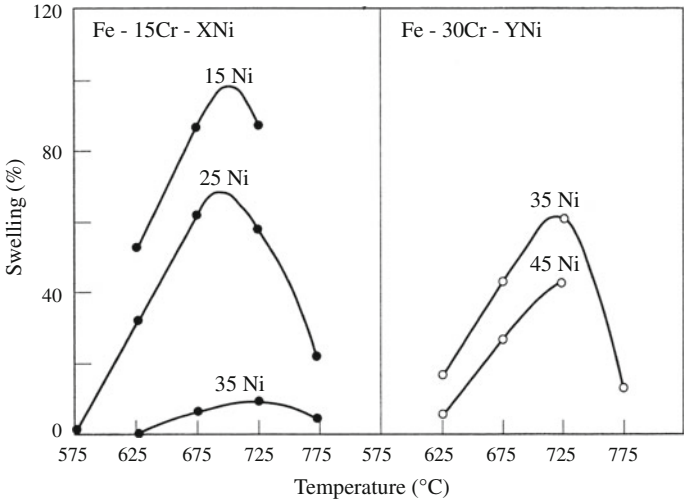

Fig. 8.44 Effect of chromium content on swelling in Fe–Cr–Ni alloys following 5 MeV Ni^+ ion irradiations to a dose of 140 dpa (after [19])

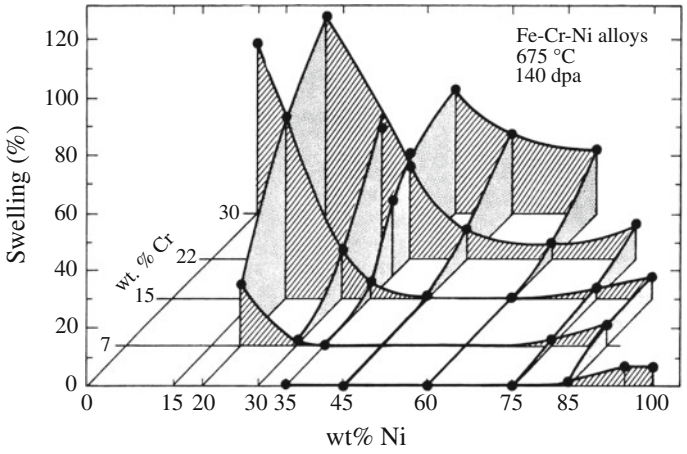

Fig. 8.45 Two-dimensional plot of the nickel and chromium dependence of swelling in Fe–Cr–Ni alloys irradiated with 5 MeV Ni^+ ions at 675 °C to a dose of 140 dpa. Swelling was measured by the step-height technique (after [19])

to larger doses. Oversize solutes such as Hf have a similar effect in suppressing the nucleation of voids in stainless steels irradiated at ~300 °C. While other factors are important, Fig. 8.51 shows that the addition of ~1 wt% Hf to 316 stainless steel results in the suppression of void formation during Ni^{++} ion irradiation at 500 °C through a dose of 50 dpa, compared to an incubation dose of only 2 dpa for the reference 316 stainless steel alloy.

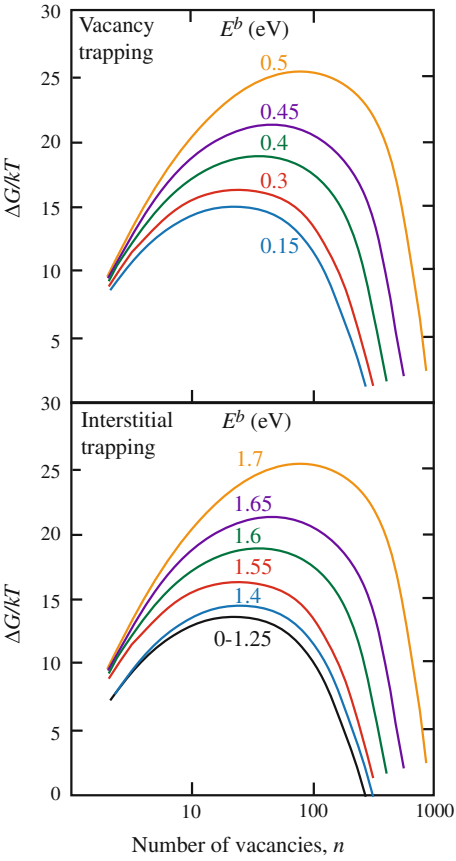

Fig. 8.46 The effect of impurity trapping on the free energy of void nucleation. Upper curves are for vacancy trapping and lower curves for interstitial trapping. The nucleation rates calculated from the curves are given as a function of binding energy in eV (after [47])

Precipitates

Precipitates can act as recombination sites for vacancy–interstitial annihilation to reduce void swelling. Precipitates can also inhibit dislocation climb necessary for dislocations to act as a preferential sink for interstitials and hence retard void growth.

In fact, precipitates can affect cavity growth in three ways [51]. The first is a direct effect in which voids that are attached to precipitates can undergo large growth rates because the precipitate acts as a collector of point defects. Precipitates can indirectly affect void growth by changing the overall sink strength of the solid or by changing the characteristics of the matrix.

As discussed in Sect. 5.8, the coherent precipitate is considered to be a site where constrained recombination of defects occurs due to the distribution of saturable traps that acquire a steady-state occupation probability as a result of a balance between defect capture, defect thermal release, and extrinsic recombination with the anti-defect. However, incoherent precipitates accept any excess point defect flux that

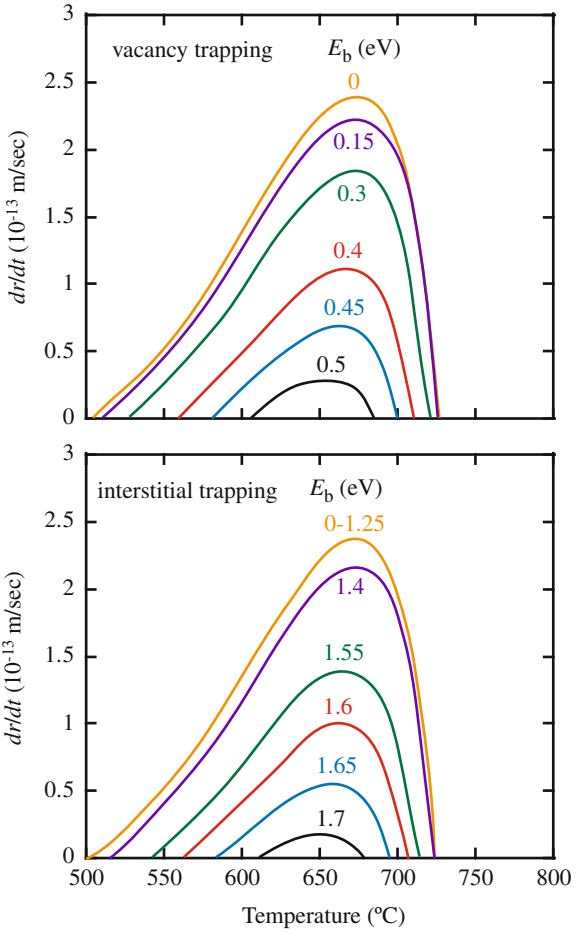

Fig. 8.47 The effect of impurity trapping on void growth rates. *Upper curves* are for vacancy trapping, and *lower curves* are for interstitial trapping (after [47])

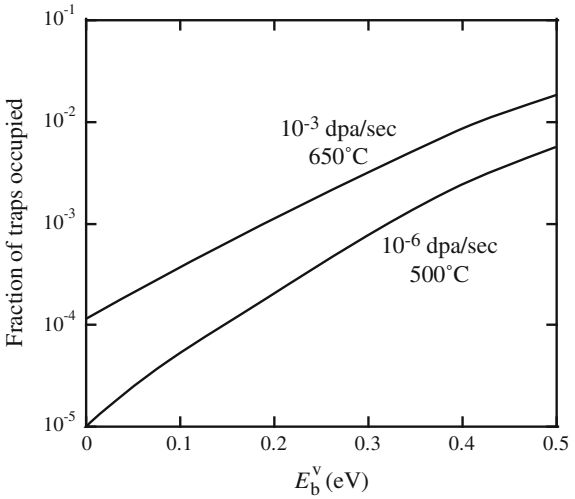

Fig. 8.48 The fraction of traps occupied for vacancy trapping at typical charged particle and fast reactor dose rates and temperatures versus binding energy. Under these conditions, the fraction of traps occupied is small even at high vacancy binding energies (after [47])

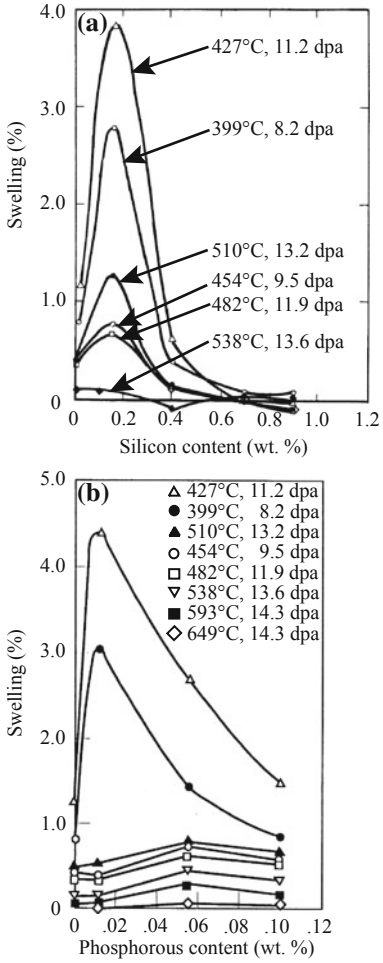

Fig. 8.49 Influence of (**a**) silicon and (**b**) phosphorus on the swelling in EBR-II of annealed Fe–25Ni–15Cr at various combinations of temperature and fluence (after [48])

happens to impinge on it. These precipitates can accumulate defects and may act as sites for rapid transport of defects, similar to grain boundaries. In fact, they can serve as sites for the collection of defects which are then channeled to voids.

While the potential exists for precipitates to strongly influence void growth through their action as sinks or recombination sites, measurements of the effect of precipitation on void growth have failed to show that they play a significant role.

Grain Boundaries

In polycrystalline materials, voids are not homogeneously distributed throughout a grain. A common observation is that a region adjacent to the grain boundaries is absent of voids. This region extends to a roughly fixed distance into the grain from the grain boundary and is referred to as the void-denuded zone, shown in Fig. 8.52

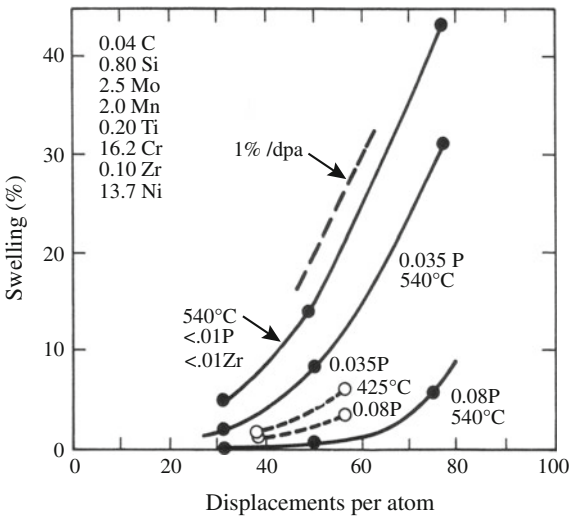

Fig. 8.50 Influence of phosphorus level on swelling in EBR-II for a titanium-modified 316 steel at 425 and 540 °C (after [49])

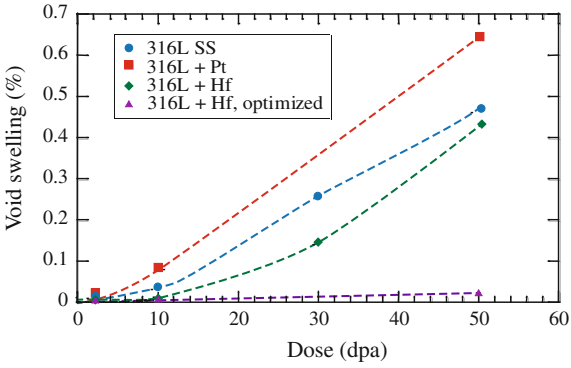

Fig. 8.51 Suppression of swelling to at least 50 dpa in 316 SS doped with ~1 wt% Hf after irradiation with 5 MeV Ni^{++}ions at 500 °C (after [50])

for ion-irradiated Ni and for lath boundaries in ferritic–martensitic alloy HT9. Considering only Frenkel pair production, e.g., electron irradiation, these denuded zones occur because of the diffusion of vacancies to the grain boundary sink that reduces the vacancy supersaturation near the grain boundary below the level needed to sustain void nucleation. Note in Fig. 8.53 that denuded zone occurrence is dependent on the sink strength of the grain boundary. In the same sample, a random high-angle grain boundary (RHGB) exhibits a clear denuded zone (Fig. 8.53(a)), but a coincident site lattice boundary (CSLB) shows no such zone (Figure 8.53(b)). The difference is likely due to the low energy of the CSLB, resulting in a low sink strength. Figure 8.53(c) is an extreme example of a heterogeneous void distribution in ferritic–martensitic alloy HT9 that is, perhaps, due to the many void-denuded zones next to grain boundaries.

Figure 8.54 shows the normalized vacancy supersaturation (S/S_0) profiles as a function of distance from the grain boundary, represented as a fraction of the grain

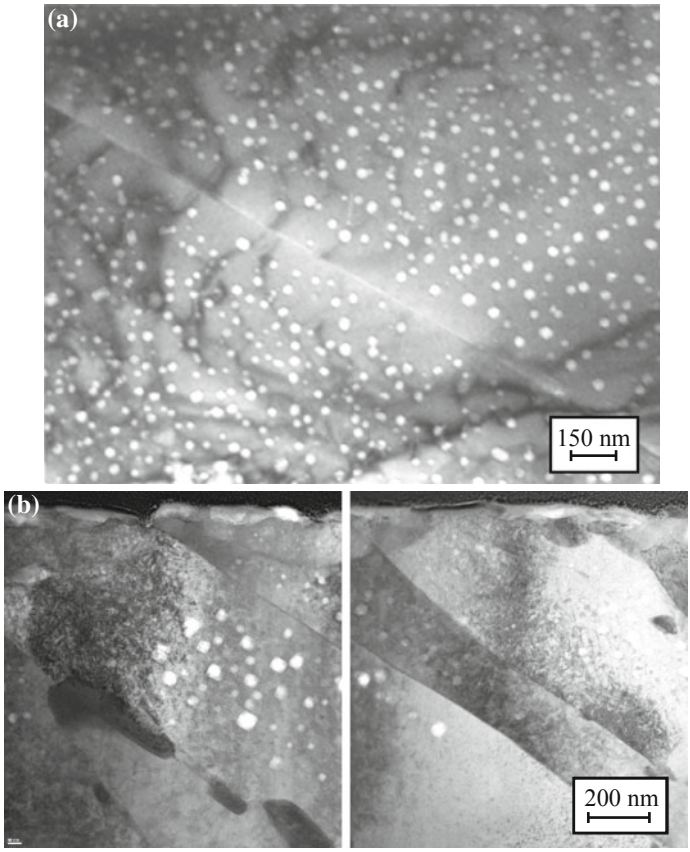

Fig. 8.52 Transmission electron micrographs of the void denuded zone (**a**) in ion-irradiated nickel (after [52]) and (**b**) near lath boundaries in alloy HT9 irradiated with 5 MeV Fe^{++} ions at 460 °C to 375 dpa after preimplantation with 1 appm He (*courtesy* A. Monterrosa)

diameter, d_g. Two features are of significance. First, regardless of grain size, the vacancy concentration drops to nearly zero at the grain boundary, greatly reducing the vacancy supersaturation in its vicinity. Second, with increasing grain size, the depth-dependent portion of the vacancy supersaturation profile extends deeper into the grain interior and its peak value becomes smaller as the grain size gets smaller. Figure 8.55 shows the calculated grain size–dependent supersaturation and experimentally measured swelling as a function of grain size. With decreasing grain size, more and more vacancies produced in the grain interior manage to diffuse to and annihilate at the grain boundaries. Thus, the volume of solid in which the vacancy supersaturation can support void nucleation decreases with decreasing grain size. The implication is that void swelling can be suppressed by reducing the grain size below some critical size.

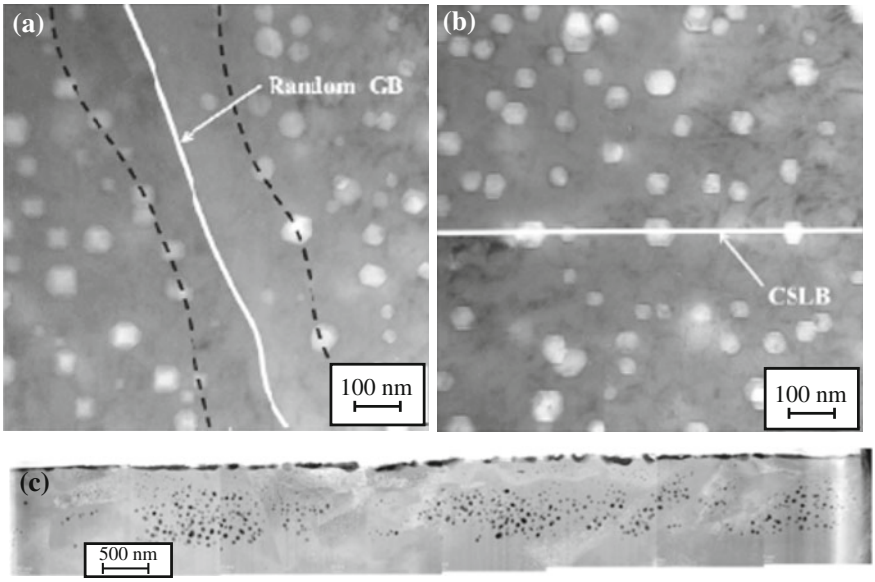

Fig. 8.53 Denuded zone (**a**) at a random grain boundary, (**b**) at a CSLB in Fe–15Cr–15Ni following neutron irradiation at 476 °C to 18 dpa (after [53]), and (**c**) in HT9 irradiated at 460 °C to 375 dpa (*courtesy* K. Sun)

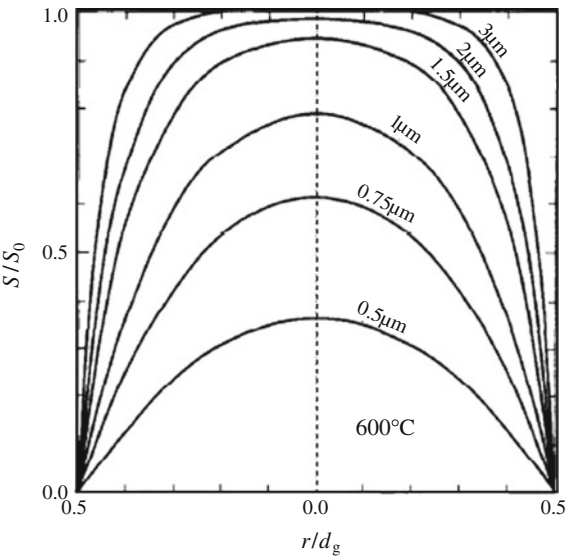

Fig. 8.54 Normalized vacancy supersaturation (S/S_0) profiles calculated for different grain sizes (d_g) in an austenitic stainless steel under 1 MeV electron irradiation at 873 K; $r/d_g = 0$ refers to the grain center, and $r/d_g = 0.5$ refers to the position of the grain boundaries (after [54])

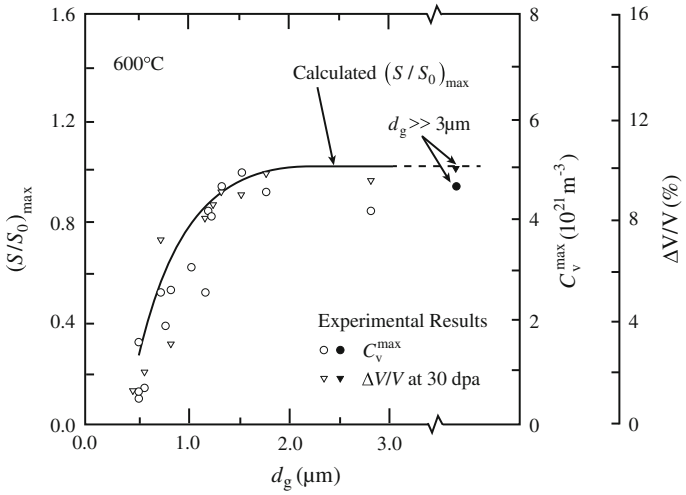

Fig. 8.55 Variation of the maximum vacancy supersaturation $(S/S_0)_{max}$ (i.e., at $r/d_g = 0$) with grain size (d_g) in an austenitic stainless steel irradiated with 1 MeV electron at 873 K. For comparison, the measured values of void density (C_v^{max}) and swelling are also plotted for different grain sizes (after [54])

The data shown in Fig. 8.55 come from 1 MeV electron irradiation that produces isolated Frenkel pairs distributed homogeneously in the solid. In this case, damage accumulation can be understood in terms of random, three-dimensional diffusion and biased attraction of monointerstitials to dislocations using conventional rate theory. Conversely, under cascade damage conditions, the nucleation and growth of cavities are significantly enhanced in the zone immediately adjacent to the void-denuded zone along the grain boundaries, referred to as the peak zone, as in Fig. 8.56. This peak zone is believed to be a consequence of the production bias. One-dimensional glide of small interstitial clusters will remove SIAs from the grain interior to grain boundaries over distances up to several microns. The result is the generation of a high vacancy supersaturation in the peak zone adjacent to the denuded zone in cases where cascades are formed. Thus, the observation of the peak zone formation under cascade damage conditions and its absence during single-displacement conditions likely arise because of differences in recoil energy. The consequence is that under cascade damage conditions, void swelling would first increase with increasing grain size, reaching a maximum at a grain size when the peak zone maxima overlap. Swelling would then decrease with grain size, becoming independent of the grain size at sizes greater than the peak zone width.

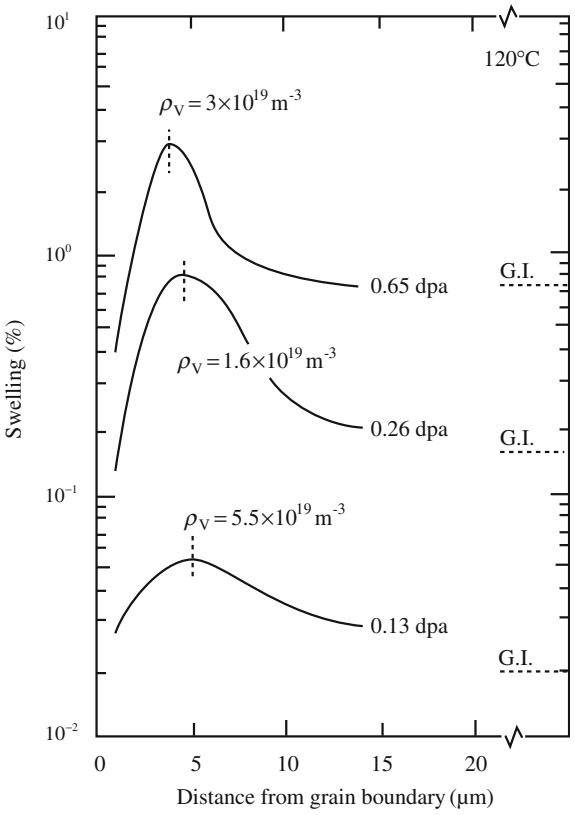

Fig. 8.56 Variation of void swelling with the distance from the grain boundary in aluminum irradiated with fission neutrons at 393 K. The cavity density (ρ_V) in the peak swelling zone is also indicated. The levels of the void swelling in the grain interior (G.I.) are also marked (after [54])

8.3.11 Effect of Reactor Operating History

Much of our understanding of void behavior in metals comes from irradiation in reactors. The experimental data are used to validate models and to provide material parameters to benchmark the models. Given that most models assume that reactor parameters (temperature, dose rate, stress) are constant over time, it is often true that in both commercial and test reactors these parameters can vary considerably during operation and due to the shutdown–start-up cycle. It is not unusual for irradiation experiments to experience numerous power (and hence temperatures) reductions over the course of a six-month to one-year irradiation. Garner [55] cites one instance in which a 600 °C, three-year irradiation, experienced 237 temperature setbacks in the first year, during which the temperature fell to as low as 50 °C. While the dose accumulated at these lower-than-target temperatures is low (0.12 dpa in the 3.5 dpa accumulated in year 1), they can have a profound effect on the microstructure.

Figure 8.57(a) shows the difference of dislocation loop size and number density in Ni–2.0Si samples irradiated in JMTR at 400 °C for the case of "conventional"

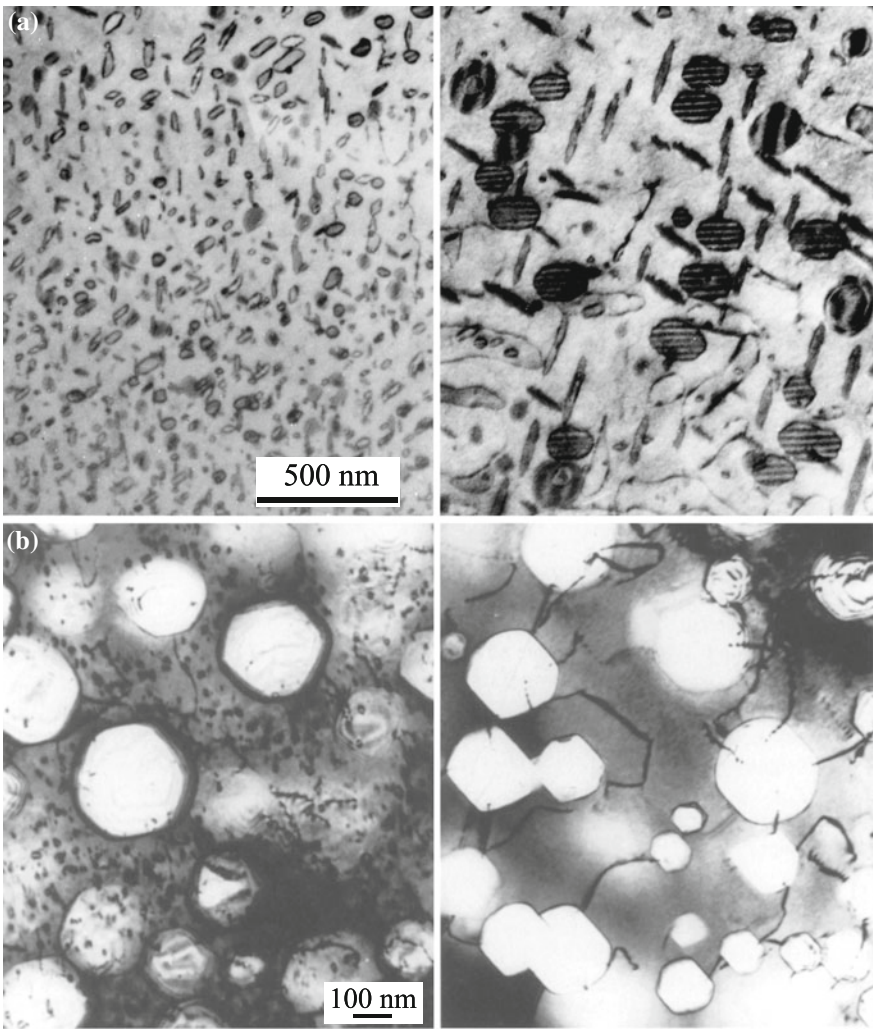

Fig. 8.57 (**a**) Effect of temperature control on dislocation loop formation and growth in Ni–2 %Si irradiated at 400 °C in the Japan Materials Test Reactor (JMTR) to a dose of $\sim 10^{24}$ n/m^2. LHS is conventional control (0.92×10^{24} n/m^2, $E > 1.0$ MeV), and RHS is improved control (0.96×10^{24} n/m^2). (**b**) Effect of shutdown rate on the formation of small dislocation loops in Fe–15Cr–16Ni irradiated at in FFTF at 600 °C. The image *on the left* underwent a slow temperature decrease during power shutdowns compared to a very rapid reduction in temperature at shutdown for the sample *on the right* (after [55])

temperature control versus one where the temperature control was considerably improved. The smaller mean loop size and larger density are likely the result of additional loop nucleation during the periods where temperature was low, but the neutron flux was nonzero. This low-temperature microstructure persisted at the

nominal irradiation temperature and resulted in an alteration of the loop size distribution as compared to the case in which temperature was controlled. Low-temperature loop nucleation in a high-temperature microstructure can also affect the evolution of the void microstructure.

Figure 8.57(b) shows the microstructure of a Fe–15Cr–16Ni alloy irradiated at 600 °C in the Materials Open Test Assembly (MOTA) in the Fast Flux Test Facility (FFTF) to comparable doses. The sample on the left was in an assembly, and reactor shutdown occurred over a six-hour period during which the temperature was reduced by 50–100 °C and then to gradually over the six-hour period during which the flux was also decreased. Irradiation during cooling is responsible for the formation of the fine dislocation loop structure. Following rapid shutdown during which the neutron flux and temperature are decreased over a several minute period, no fine loop structure is observed. The fast drop in temperature does not provide an opportunity to accumulate enough dose in this intermediate-temperature regime to cause loop nucleation.

The significance of these observations is twofold. First, that a low-temperature dislocation microstructure introduced into a high-temperature microstructure can alter the further development of that microstructure, affecting both loop and void evolution. Second, only very small doses (<0.1 dpa) are required to nucleate the fine loop structure that remains stable during the continuation of the irradiation at high temperature. These data also provide additional information on the loop nucleation rate, indicating that it is perhaps higher than current models can explain.

8.4 Bubbles

Up to this point, we have been treating voids as essentially empty cavities that grow and shrink by the absorption of vacancies. We have accounted for the effect of gas atoms on the nucleation of voids and also on the equilibrium vacancy concentration at the void surface. But we have not discussed the magnitude of the pressure in the void due to the gas and the effect this may have on the growth of the void. We also have made no distinction between a void and a bubble. One question that we would like to answer is how much gas must a void have in order to be considered a bubble? In a practical sense, the distinction is largely one of degree and character. A cavity is considered to be a bubble if the effect of the gas (on the surface energy and due to the pressure) causes the cavity to become spherical. This is essentially how voids and bubbles are distinguished in transmission electron microscopy. Due to the periodicity of the lattice, cavities will be faceted with the facets lying on the close-packed planes. But if the surface energy is changed by the gas, or if the gas pressure is high enough, then the cavity will become spherical in shape. Of course, very large voids will approach a spherical shape as the contribution of the facets diminishes with increasing void radius.

Because insoluble gases are often formed by transmutation when certain elements are irradiated, inert gas bubbles form, which alter the mechanical and

physical properties of an alloy. Bubble formation depends on the mobility of the gas (in the form of either individual atoms or complexes), the minimum number of gas atoms which are able to form a stable nucleus and the rate at which lattice vacancies can be supplied to enhance the stability of a nucleated core.

Bubbles nucleate under irradiation and then grow or redissolve. The criterion is that nucleation ceases when a gas atom diffusing at random is most likely to encounter a pre-existing nucleus rather than take part in creating a new one. The resulting bubble density varies inversely as the square root of the gas atom diffusion coefficient and thus increases with decreasing temperature.

The following assumptions about bubble nucleation under irradiation are made. Homogeneous nucleation is predicated on the premise that bubbles grow by the interaction of gas atoms from a background atomic population on a random basis. Thus, no account is taken of local effects such as cascade processes or precipitation on lattice defects or impurity agglomerates. Concerning stable nuclei, we assume that a pair of gas atoms is stable against thermal dissociation and that its activation energy is such that its motion may be ignored with respect to that of single gas atoms.

In this section, we will first consider the mechanics of bubbles followed by the development of bubble growth models that will closely parallel void growth.

8.4.1 Bubble Mechanics

For a bubble of radius R, embedded in a solid medium, the change in the free energy of the solid due to the bubble is:

$$\mathrm{d}G = V\,\mathrm{d}p + \gamma \mathrm{d}A. \tag{8.209}$$

Since

$$V\,\mathrm{d}p = \mathrm{d}(pV) - p\,\mathrm{d}V, \tag{8.210}$$

and for an ideal gas, pV = constant and $V = 4/3\pi R^3$, then:

$$\frac{\mathrm{d}G}{\mathrm{d}r} = -4\pi R^2\left(p - \frac{2\gamma}{R}\right). \tag{8.211}$$

Setting $\mathrm{d}G/\,\mathrm{d}r = 0$ yields:

$$p = 2\gamma/R. \tag{8.212}$$

Thus, the equilibrium condition for a bubble is expressed by the force balance $p = 2\gamma/R$, in which the force due to the outward pressure of the gas, p, is balanced by

the inward-acting force due to the surface tension, $2\gamma/R$. In the presence of a stress, the force balance becomes:

$$p = \frac{2\gamma}{R} - \sigma. \tag{8.213}$$

where positive stress is tension.

All bubble models require a specific relation between the number of gas atoms in a bubble and its radius. The van der Waals equation of state is used to describe the thermodynamic state of inert gas in bubbles. Let n_x be the number of gas atoms in a spherical bubble of radius R and the gas density is ρ_g. Then,

$$n_x = (4/3\pi R^3)\rho_g. \tag{8.214}$$

From the ideal gas law ($pV = nkT$), we have:

$$p\frac{V}{n} = kT \quad \text{or} \quad \frac{p}{\rho_g} = kT \quad \text{or} \quad p = \frac{3nkT}{4\pi R^3}. \tag{8.215}$$

Using Eq. (8.212) for mechanical equilibrium to eliminate ρ_g and p in Eqs. (8.214) and (8.215) gives:

$$\begin{aligned} n_x &= 4/3\pi R^3 \frac{2\gamma}{RkT} \\ &= \frac{8\pi R^2\gamma}{3kT}. \end{aligned} \tag{8.216}$$

For small R, $1/\rho_g$ is not proportional to R and we must account for the volume occupied by the gas atoms themselves. We do this by modifying Eq. (8.215) to include a term B which is a function of temperature and pressure. This gives us van der Waals equation of state:

$$p\left(\frac{1}{\rho_g} - B\right) = kT \quad \text{or} \quad \frac{1}{\rho_g} = B + \left(\frac{kT}{2\gamma}\right)R, \tag{8.217}$$

and Eq. (8.216) becomes:

$$n_x = \frac{8\pi R^2\gamma}{3(kT + 2B\gamma/R)} = \frac{4/3\pi R^3}{B + (kT/2\gamma)R}. \tag{8.218}$$

For large R, the perfect gas approximation applies, and for very small R, the dense gas limit applies. Physically, there is a minimum volume occupied by each atom, B, and as R decreases, the volume per atom approaches this limit. The result is:

$$\frac{1}{\rho_g} = B\frac{\text{nm}^3}{\text{atom}} : \text{dense gas limit}, \tag{8.219}$$

and

$$\frac{1}{\rho_g} \cong \left(\frac{kT}{2\gamma}\right)R : \text{ideal gas limit}. \tag{8.220}$$

Note that for stainless steel at 500 °C, where $\gamma \sim 1.75$ J/m^2, $2\gamma/kT \sim 328$ nm^{-2}, then $\frac{1}{\rho_g} \cong 3 \times 10^{-4} R\frac{\text{nm}^3}{\text{atom}}$.

The limiting cases corresponding to Eqs. (8.219) and (8.220) are:

$$n_x = \left(\frac{4\pi R^3}{3B}\right) \text{for small } R \tag{8.221}$$

$$= \left(\frac{4\pi R^2}{3}\right)\left(\frac{2\gamma}{kT}\right) \text{for large } R. \tag{8.222}$$

If Eq. (8.212) is not satisfied, then the bubble is described as a non-equilibrium bubble. That is, the bubble is not in equilibrium with the solid. Mechanical equilibrium is usually maintained by a flow of vacancies to the bubble to provide the additional volume needed to accommodate the influx of gas atoms. Whether Eq. (8.212) is satisfied depends on the relative absorption rate of vacancies and gas atoms by the bubble. A bubble of radius R can be considered as the absence of $(4/3\pi R^3)/\Omega$ matrix atoms where Ω is the atomic volume. The empty sphere of radius R can be thought of as consisting of n_v vacancies given by:

$$n_v = \frac{4/3\pi R^3}{\Omega}. \tag{8.223}$$

The number of gas atoms in a sphere of radius R in mechanical equilibrium is given by Eq. (8.218). The number of vacancies per gas atom in an equilibrium bubble is then:

$$\frac{n_v}{n_x} = \left(\frac{kT}{2\gamma}\right)\frac{R}{\Omega} + \frac{B}{\Omega}. \tag{8.224}$$

Note that n_x increases as R^2, but n_v increases as R^3, so increasing numbers of vacancies are needed per gas atom in order to maintain equilibrium.

Stress is accounted for by taking Eq. (8.213) and substituting for p from Eq. (8.215) to give:

$$\sigma = \frac{2\gamma}{R} - \frac{3n_x kT}{4\pi R^3}, \tag{8.225}$$

where σ is the hydrostatic tensile stress. The critical bubble radius for unstable bubble growth is determined by setting $d\sigma/dr = 0$ and solving for R, yielding:

$$R_c = \left(\frac{9n_x kT}{8\pi\gamma}\right)^{1/2}. \tag{8.226}$$

Substituting for R_c in Eq. (8.226) into Eq. (8.225) gives:

$$\sigma_c = \left(\frac{128n\gamma^3}{81n_x kT}\right)^{1/2}, \quad \text{or} \quad n_x = \frac{128n\gamma^3}{81\sigma_c^2 kT}. \tag{8.227}$$

The critical bubble radius, R_c, is related to the equilibrium bubble radius, R_0, by expressing Eqs. (8.216) and (8.226) in terms of the number of gas atoms in the bubble, n_x, and eliminating n_x, giving:

$$R_c = \sqrt{3}R_0, \tag{8.228}$$

and the critical stress in terms of R_0 is:

$$\sigma_c = \frac{4\sqrt{3}\gamma}{9R_0}. \tag{8.229}$$

Substituting for Eq. (8.222) into Eq. (8.225) to eliminate n_x gives a relation between the applied stress, the initial bubble size, and the critical bubble size:

$$\sigma_c = \frac{2\gamma}{R_c}\left(1 - \frac{R_0^2}{R_c^2}\right). \tag{8.230}$$

Equations (8.229) and (8.230) provide the bubble stability criterion in terms of the applied stress and the bubble size. For bubbles of size R_0, Eq. (8.229) gives the critical stress for stability. For a solid with bubbles of size $R_0 < R_c$, application of a tensile stress σ_c will cause the bubble to grow to size R_c specified by Eq. (8.230). If $R_0 > R_c$ or if σ_c is greater than the right-hand side of Eq. (8.229), then the bubble will grow without bound. Or, for a given applied stress, Eq. (8.229) gives the critical bubble radius for stability. Equation (8.226) can be compared to the stability equation for a gas-free void in a solid subject to a stress, σ. For $p = 0$ in Eq. (8.213), we have that $\sigma = 2\gamma/R$. The numerical coefficient in Eq. (8.229) is about 0.77, which is less by about a factor of 3 than the coefficient for the void. The difference is due to the effect of the gas pressure in the bubble that assists the stress.

8.4.2 Growth Law

Analogous to void growth, the time rate of change of the volume of a bubble is equal to the difference in the rates at which vacancies and interstitials are absorbed and to the volume carried by each of these point defects:

$$\frac{\mathrm{d}}{\mathrm{d}t}\left(\frac{4}{3}\pi R^3\right) = \Omega\left[4\pi R D_\mathrm{v}(C_\mathrm{v} - C_\mathrm{v}^\mathrm{v}) - 4\pi R D_\mathrm{i}(C_\mathrm{i} - C_\mathrm{i}^\mathrm{v})\right], \tag{8.231}$$

and so the growth law is:

$$\frac{\mathrm{d}R}{\mathrm{d}t} \equiv \dot{R} = \frac{\Omega}{R}\left[D_\mathrm{v}(C_\mathrm{v} - C_\mathrm{v}^\mathrm{V}) - D_\mathrm{i}(C_\mathrm{i} - C_\mathrm{i}^\mathrm{V})\right], \tag{8.232}$$

where C_v^V and C_i^V are the concentrations of vacancies and interstitials at the bubble surface and C_v and C_i are the point defect concentrations in the bulk solid. The thermodynamic vacancy concentration at the bubble surface given by Eq. (8.85) is modified to include the effect of gas pressure in the bubble:

$$C_\mathrm{v}^\mathrm{V} = C_\mathrm{v}^0 \exp\left[\frac{-\Omega}{kT}\left(p - \frac{2\gamma}{R}\right)\right], \tag{8.233}$$

and for interstitials

$$C_\mathrm{i}^\mathrm{V} = C_\mathrm{i}^0 \exp\left[\frac{\Omega}{kT}\left(p - \frac{2\gamma}{R}\right)\right], \tag{8.234}$$

where C_v^0 and C_i^0 are the thermodynamic equilibrium concentrations of vacancies and interstitials, respectively, for a stress-free solid and the exponential terms reflect the presence of a mechanical stress acting on the solid equal in magnitude to $p - 2\gamma/R$. Because C_i^0 is so small, the interstitial term, as in Eq. (8.234), can be neglected.

Setting $\mathrm{d}R/\mathrm{d}t = 0$ in Eq. (8.232) and substituting Eq. (8.233) for C_v^V into the resulting expression, taking logarithms and rearranging gives [56, 57]:

$$R_\mathrm{c} = \frac{2\gamma}{p + \dfrac{kT}{\Omega}\ln S_\mathrm{v}}, \tag{8.235}$$

where S_v is the effective vacancy supersaturation given by:

$$S_\mathrm{v} = \frac{D_\mathrm{v}C_\mathrm{v} - D_\mathrm{i}C_\mathrm{i}}{D_\mathrm{v}C_\mathrm{v}^0}. \tag{8.236}$$

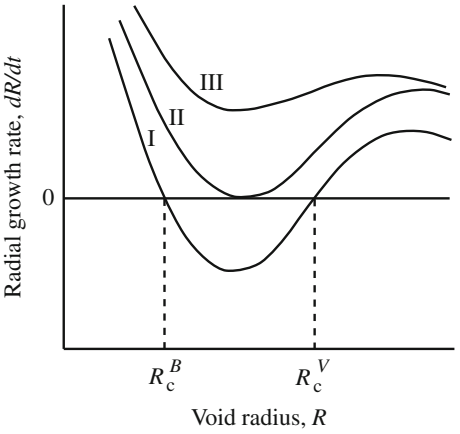

Fig. 8.58 Schematic plot of cavity growth rate as a function of cavity radius for increasing amount of helium gas in the void or S_v (after [56])

Now, substituting Eq. (8.215) for p into Eq. (8.235) and rearranging gives:

$$g(R_c) = R_c^3 - \frac{2\gamma\Omega}{kT \ln S_v} R_c^2 + \frac{3n_x\Omega}{4\pi \ln S_v} = 0, \tag{8.237}$$

where the expression denoted by the function $g(R_c)$ is zero when R_c is a root. The growth rate is plotted as a function of void radius in Fig. 8.58 for three conditions. The lower curve is the case where Eq. (8.237) has three real roots, the middle curve shows the case in which at least two of the roots are equal, and the upper curve has one real root [57]. In case I, the roots are denoted R_c^B and R_c^V. A void containing enough gas atoms that it is between R_c^B and R_c^V will shrink back to R_c^B. A void with the same number of gas atoms but with radius below R_c^B will grow to R_c^B and stop. Finally, a void with the same number of gas atoms and with radius above R_c^V will grow without limit by bias-driven growth. As the number of gas atoms increases, Eq. (8.237) is represented by curves that progress from I to II to III. In the case of curve III, the number of gas atoms is large enough that there will be no intersections with the $dR/dt = 0$ axis and these cavities will only grow by bias-driven growth. At some critical number of gas atoms, there is just one intersection of the function dR/dt with the $dR/dt = 0$ axis. This case is represented by curve II. In this case, the corresponding number of gas atoms is denoted as n_x^* and the corresponding minimum critical radius where R_c^B and R_c^V coincide is denoted as R_c^*. The quantity, n_x^*, is the maximum number of gas atoms that may be contained in a cavity for there to still exist a critical radius, with a minimum value of R_c^*.

The minimum critical radius, R_c^*. can be found by taking the derivative of Eq. (8.237) with respect to R_c, giving:

$$\frac{dg(R_c)}{dR_c} = 3R_c^2 - \frac{4\gamma\Omega}{kT \ln S_v} R_c. \tag{8.238}$$

Setting Eqs. (8.237) and (8.238) to zero simultaneously yields the minimum critical radius:

$$R_c^* = \frac{4\gamma\Omega}{3kT\ln S_v}, \tag{8.239}$$

and from Eq. (8.226):

$$n_x^* = \frac{128\pi\gamma^3\Omega^2}{81(kT)^3(\ln S_v)^2}. \tag{8.240}$$

Stoller et al. [57] noted that Eq. (8.240) can be written for non-spherical cavities using a shape factor, F_V, such that:

$$n_x^* = \frac{32F_V\gamma^3\Omega^2}{27(kT)^3(\ln S_v)^2}, \tag{8.241}$$

where $F_V = 4\pi/3$ for a spherical void. He also notes that more physically reasonable solutions are obtained using a hard sphere equation of state rather than the ideal gas law, which tends to overpredict swelling incubation times.

It should also be noted that Eqs. (8.240) and (8.228) are the same when σ is replaced with $\Omega/\ln S$, indicating that the stability criterion is the same regardless of whether the solid is acted on by an actual stress or an effective stress defined by the irradiation-induced vacancy supersaturation. A bubble is stable for negative vacancy supersaturation and can be stable or metastable for positive vacancy supersaturation, depending on the magnitude of the supersaturation, the gas content, and the bubble size according to Fig. 8.58. For a constant stress or irradiation-induced vacancy supersaturation, when the stability limit is reached by gas absorption, a bubble starts to grow by vacancy absorption and is transformed into a cavity. Equations (8.239) and (8.226) describe the bubble-to-void conversion criterion.

Equation (8.232) can be used to calculate the swelling rate due to bubble swelling by assuming all gas to be in the bubbles, resolution to be insignificant, and the gas to be ideal such that:

$$p = \frac{n_x kT}{4/3\pi R^3\rho_B}, \tag{8.242}$$

where ρ_B is the total bubble density and $n_x = \dot{x}t$ is the gas concentration in the solid being produced by transmutation at a rate of $\dot{x}$ The swelling rate due to bubble growth is:

$$\mathrm{d}(\Delta V/V)/\mathrm{d}t = (4\pi R^2\rho_B/\Omega)\mathrm{d}R/\mathrm{d}t. \tag{8.243}$$

8.4.3 Bubble Growth by Dislocation Loop Punching

While vacancy diffusion is the prime mechanism contributing to bubble growth on a fine scale, an additional mechanism for bubble growth in the case of high gas pressure is dislocation loop punching. If the pressure in the bubble is large enough, the stress in the solid nearby may reach a level where dislocation sources can be activated, resulting in the growth of the bubble by *punching out* a dislocation loop (Fig. 8.59). Recall that the stress required to operate a Frank–Read source is $\sim \mu b/l$, where l is the spacing between pinning points. Dislocation sources that are easiest to activate will be those with $l \sim r_0$, where r_0 is the radius of the bubble. So the excess pressure required for the bubble to generate dislocations is then $\sim \mu b/r_0$. The magnitude of the excess pressure required to generate prismatic dislocations can be determined by comparing the free energy change of the bubble upon creation of a dislocation loop of size equal to the bubble, to the energy of the loop itself [59]. The work to increase the bubble size is:

$$\Delta F = -pdV = -\left(p - \frac{2\gamma}{r_0}\right)\pi r_0^2 b, \tag{8.244}$$

where p is the pressure in the bubble, V is the bubble volume, γ is the surface energy, and b is the Burgers vector magnitude. Neglecting the stacking fault energy contribution, the energy of the prismatic dislocation loop of radius r_0 given by Eq. (7.64) is approximated as:

$$E_{\mathrm{L}} = \frac{\mu b^2 r_0}{2(1-\nu)} \ln \frac{4r_0}{r_{\mathrm{c}}}, \tag{8.245}$$

where r_{c} is the dislocation core radius. For dislocation loop formation to be energetically possible,

$$\left(p - \frac{2\gamma}{r}\right)\pi r_0^2 b > \frac{\mu b^2 r_0}{2(1-\nu)} \ln \frac{4r_0}{r_{\mathrm{c}}}, \tag{8.246}$$

or approximating E_{L} as $\pi \mu b^2 r_0$:

$$p > (2\gamma + \mu b)/r_0. \tag{8.247}$$

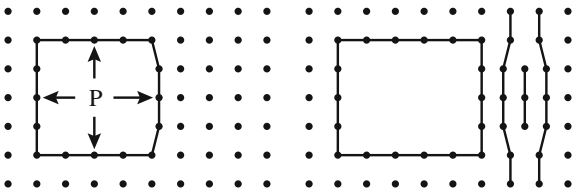

Fig. 8.59 Schematic illustration of the growth of a bubble by dislocation loop punching (after [58])

For typical values of γ and μ, the gas pressure in the bubble must be about an order of magnitude greater than $2\gamma/r_0$ before dislocations can be generated and allow the bubble to expand.

8.4.4 Bubble Lattices

Similar to void lattices described earlier, high levels of He can result in the organization of gas bubble lattices. In fact, gas bubble lattice formation has been observed in bcc, fcc, and hcp metals following He injection at temperatures $<0.3T_m$ [60]. Helium bubbles in Cu are aligned with dense-packed rows parallel to matrix {111} directions. Johnson et al. [60] measured the lattice constant of the He bubble superlattice in Cu to be a_{He} = 7.6 nm, corresponding to a bubble density of 10^{25} bubbles/m^3. Figure 8.60 shows a bright-field transmission electron micrograph of a helium gas bubble lattice in molybdenum following 40 keV He^+ irradiation to a dose of 5×10^{21} He^+/m^2 at 500 °C. While the same forces driving the formation of void lattices are expected to apply to bubble lattices, additional interactions may arise due to the close spacing of overpressurized bubbles, such as bubble growth by dislocation loop punching.

8.4.5 Helium Production

An important ingredient in bubble formation and growth is the production of helium. In a reactor, He production is governed by the boron and nickel contents of the alloy through the reactions:

$$^{10}\mathrm{B}(n,\alpha)^{7}\mathrm{Li}\,, \tag{8.248}$$

Fig. 8.60 He gas bubble superlattice formed in molybdenum following 40 keV He^+ irradiation to a dose of 5×10^{21} He^+/m^2 at 500 °C (after [43])

and the two-step reaction:

$$^{58}\mathrm{Ni}(n,\gamma)^{59}\mathrm{Ni}(n,\alpha)^{56}\mathrm{Fe}\,. \tag{8.249}$$

The thermal neutron (n, α) cross section for ^{10}B is very large, about 3837b, while the thermal neutron cross sections for the reactions in Eq. (8.249) are 4.6b and 12.3b, respectively. For thermal reactors then, a large amount of helium is produced early in life from transmutation of boron, but this source burns out by about 1 dpa ($\sim 10^{21}$ n/cm^2).

The presence of nickel in stainless steels provides a smaller but sustained source of helium at higher dose. ^{59}Ni is not a naturally occurring isotope and is produced from ^{58}Ni. Thus, this helium contribution involves a delay relative to that of single-step threshold (n, α) reactions [61]. Since both steps of the sequence involve cross sections that increase with decreasing energy and the second step exhibits a resonance at 203 eV, the generation rate per dpa in fast reactors increases near the core boundaries and out-of-core areas.

Nickel has five naturally occurring stable isotopes with ^{58}Ni comprising 67.8 % natural abundance, ^{60}Ni comprising 26.2, and ~6.1 % total of ^{61}Ni, ^{62}Ni, and ^{64}Ni. There is no natural ^{59}Ni or ^{63}Ni at the beginning of radiation. During irradiation in a highly thermalized neutron spectrum, all nickel isotopes are strongly transmuted, primarily to the next higher isotopic number of nickel. ^{59}Ni has a half-life of 76,000 years and is progressively transmuted to ^{60}Ni, while ^{58}Ni is continuously reduced in concentration. Therefore, the ^{59}Ni concentration rises to a peak at a thermal neutron fluence of 4×10^{22} n cm^{-2} where the 59/58 ratio peaks at ~0.04 and then declines, as shown in Fig. 8.61.

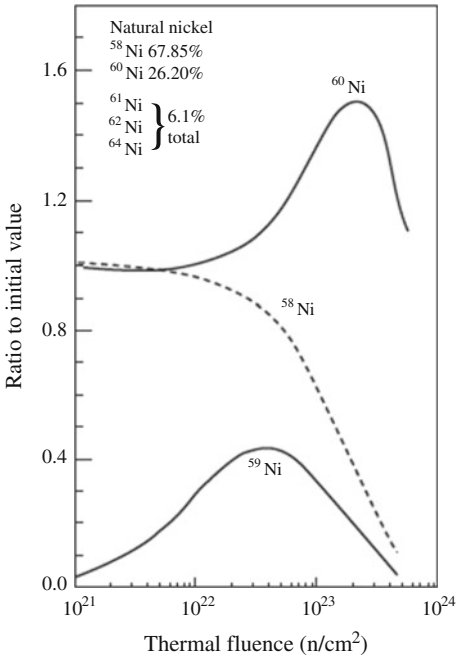

Fig. 8.61 Transmutation-induced evolution of three nickel isotopes during irradiation in thermalized neutron spectrum (after [62])

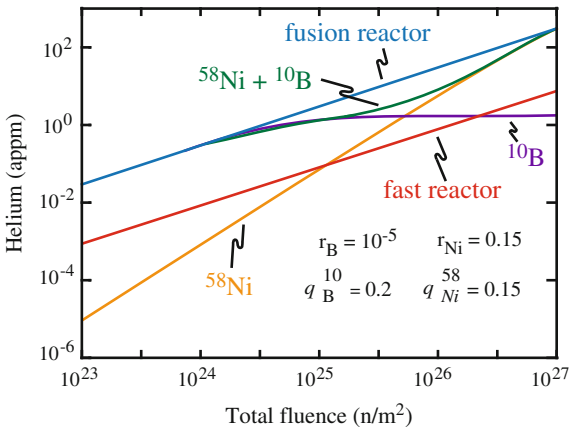

Fig. 8.62 Helium buildup versus fluence for stainless steel in HFIR (thermal reactor), a fusion reactor spectrum, and a fast reactor spectrum. In the figure, r is the atom fraction of boron or nickel in the alloy and q is the initial fraction of the isotope listed in the figure (after [27])

In this regard, thermal reactors produce greater amounts of helium at low-dose and in a lower-dose-rate environment, making low-dose helium-induced swelling a potentially greater problem in a thermal reactor than in a fast reactor. Figure 8.62 shows the production rate of helium from an alloy containing ^{58}Ni and ^{10}B in the HFIR (thermal) reactor. Note that the production rate of helium is dominated at low fluence by the contribution from ^{10}B and at higher fluence by ^{58}Ni. Helium buildup for the same alloy in a fast reactor and a fusion reactor is shown for comparison. Note that the helium buildup in a fusion reactor matches that in HFIR, and both are higher than that in a fast reactor.

The reaction in Eq. (8.249) has another important consequence. The recoil of the ^{59}Ni upon emission of the gamma ray produces only about five displacements per event and usually is not a significant addition to the displacement dose. However, the isotope ^{59}Ni undergoes three strong reactions with thermal and resonance ($\sim$0.2 keV) neutrons, two of which are highly exothermic and can significantly add to the dpa level. These reactions, in order of highest-to-lowest thermal cross section, are (n, γ) to produce ^{60}Ni, followed by (n, α) and (n, p) to produce helium and hydrogen, respectively.

Even at relatively low thermal-to-fast neutron ratios, the reaction sequence can produce significant amounts of helium. For example, He/dpa ratios in the order of $\sim$3–8 appm dpa^{-1} can be experienced along the length of a 316 stainless baffle bolt in the baffle–former assembly of a pressurized water reactor [61], while comparable rates in fast reactors are in the order of 0.1–0.2 appm dpa^{-1}. In thermalized spectra, the latter two reactions can quickly overwhelm the gas production produced by nickel at high neutron energies. The ^{59}Ni(n, α) reaction releases 5.1 MeV in the form of a 4.8 MeV alpha particle, which loses most of its energy by electronic losses that results in the deposition of significant thermal energy but the production

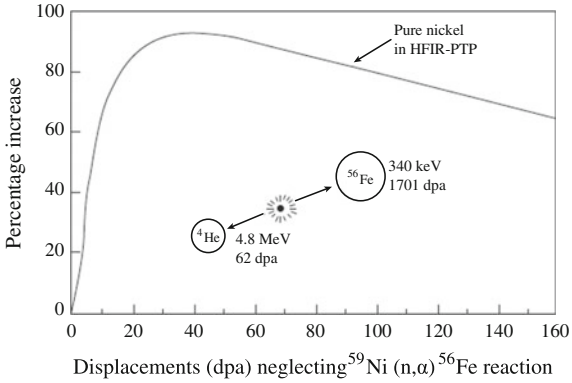

Fig. 8.63 Increase in dpa arising from the effect of ^{59}Ni to produce helium when pure nickel is irradiated in the HFIR test reactor in the peripheral target position where the thermal-to-fast ratio is 2.0 (after [62])

of only ~62 atomic displacements per each event, and a recoiling ^{56} Fe carrying 340 keV, which is very large compared to most primary knock-on energies, and produces ~1700 displacements per event.

An example of the time-dependent increase in dpa rate in highly thermalized light water spectra is shown for pure nickel in Fig. 8.63 for a thermal-to-fast ratio of 2.0. Note that the calculated increase in this figure addresses only the ^{59}Ni(n, α) reaction. Additional increases occur as a result of the ^{59}Ni(n, p) and ^{59}Ni(n, γ) reactions, resulting in roughly doubling the dpa due to the three ^{59}Ni reactions before a calculated dose of ~40 dpa is attained.

An even stronger example of the linkage of the ^{59}Ni transmutation effect and the displacement process has been observed [62]. In-core thermal-to-fast ratios in heavy water-moderated reactors such as CANDUs are on the order of ~10, but far from the core, the ratio can be near ~1000. Compression-loaded springs constructed of high nickel alloy X-750 were examined after 18.5 years of operation far from the core and were found to be completely relaxed. Calculating the ^{59}Ni contribution, it was deduced that full relaxation occurred in ~3–4 years rather than the 650–700 years one would predict based on dpa calculated without taking into account the ^{59}Ni contribution. Therefore, in this case, ^{59}Ni contributed ~95 % of the dpa damage. Additionally, 1100 appm of helium was calculated to have been produced at the midsection of the spring in ~3 years, with ~20,000 appm helium having been produced when the spring was examined after 18.5 years of exposure. Figure 8.64 shows calculations of H, He, and displacement damage in alloy X-750 garter springs used in CANDU reactors as a function of fluence. Note that at end of life (~4.5×10^{23} n/cm^2), the damage level is ~65 dpa of which ~62 dpa comes from the recoil of ^{59}Ni, the He level is 22,000 appm (338 appm He/dpa), and the H level is ~4500 appm (69 appm H/dpa). Such levels of He and potentially H will cause significant bubble formation and swelling in the alloy.

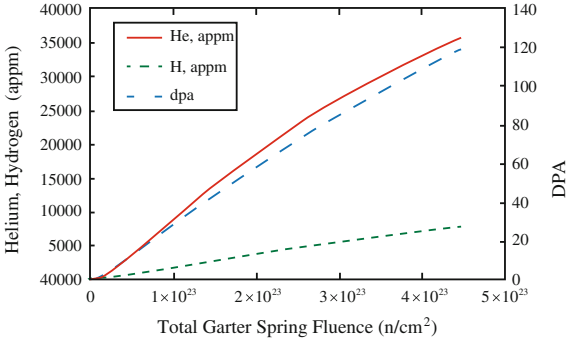

Fig. 8.64 He, H, and dpa production as a function of fluence for X-750 garter springs in a CANDU reactor (*courtesy* CANDU Owners Group)

Another consequence of the ^{59}Ni sequence is the inducement of temperature increases due to gamma heating. At the peak ^{59}Ni level reached at 4×10^{22} n cm^{-2} (Fig. 8.61), the nuclear heating rates from the energetic (n, α) and (n, p) reactions are 0.377 and 0.023 Wg^{-1} of nickel, significantly larger than the neutron heating level of $\sim$0.03 Wg^{-1} of natural nickel. Thus, an increase in nuclear heating of $\sim$0.4 Wg^{-1} of nickel must be added to the gamma heating rate at the peak ^{59}Ni level. Depending on the nickel level of the steel and the level of gamma heating, which is the primary cause of temperature increases in the interior of thick plates, this additional heating contribution may or may not be significant.

Gamma heating is also a strong function of the thermal-to-fast (T/F) neutron ratio and the neutron flux, being $\sim$54 Wg^{-1} in the center of the HFIR test reactor where the T/F ratio is $\sim$2.0. In pressurized water reactors in austenitic core internals, however, the T/F ratios are lower by a factor of 2–10, depending on location, and the gamma heating rates in the baffle–former assembly are $\sim$1–3 Wg^{-1}. In this case, an additional 0.4 Wg^{-1} of nuclear heating can be a significant but time-dependent addition to total heating, especially for high-nickel alloys.

Nomenclature

a	Lattice constant
$A^{X}_{v,i}$	Absorption rate of vacancies, interstitials by sink X
B	Volume occupied by a gas atom in a bubble
B_d	Dislocation bias term defined below Eq. (8.184) as $B_d = (z^d_i - z^d_v)/z^d_v$
C_{giL}	Concentration of glissile SIA loops
C_j	Concentration of species j
C^0_j	Thermal equilibrium concentration of species j
C^L_v	Vacancy concentration in equilibrium with a dislocation loop
C^V_v	Vacancy concentration at the void surface
D_j	Diffusion coefficient of species j
D^c	Diffusive spread due to cascades
D^e	Diffusive spread due to vacancy emission
D^s	Diffusive spread due to single defect jumps
E	Energy

E_{b}^{j} Binding energy of specie j
E_{f}^{J} Formation energy of specie j
E_{m}^{j} Migration energy of specie j
E_{vL} Effective binding energy of vacancies with vacancy clusters
$E_{*}^{\mathrm{v,i}}$ See definition after Eq. (8.167)
F_{V} Shape factor (= $4\pi/3$ for spherical void)
$g(R_{\mathrm{c}})$ Void growth rate factor, defined in Eq. (8.216)
G Free energy
G_0 Free energy of perfect lattice
ΔG Change in free energy
ΔG_n^0 Activation barrier for void nucleation without interstitials
$\Delta G_n^{'}$ Activation barrier for void nucleation with interstitials
H Enthalpy, also Henry's law constant, as in Eq. (8.57)
J Nucleation current
k Boltzmann's constant
k_{g}^2 Sink strength for 1D diffusing SIA clusters
k_X^2 Sink strength of sink X
k_j^2 Total sink strength species j
$k_{\mathrm{cl}}^{\mathrm{eff}}$ Effective production rate of defects in clusters and free form
K_j Loss rate of species j
K_{iv} Vacancy–interstitial recombination rate
k_j^{eff} Effective production rate of free defects of type j
K_0 Defect production rate
k_x^{c} Rate of gas atom resolution
l Distance of cluster to a grain boundary
L_j Thermal emission rate of species j
m_{i} Number of interstitial in an interstitial loop
M Helium concentration
M_x Helium cluster of x gas atoms
n Number of vacancies in a void
n_{cr} Number of vacancies in a void of critical size
$n_{\mathrm{k}}, n_{\mathrm{k}}'$ Critical void nucleus cluster size
n_{vi} Number of vacancies and interstitials
$N_{\mathrm{d}j}$ Average number of defects of type j generated in a single cascade
N_0 Number of lattice sites per unit volume
N_{R} Number of defects per unit volume that have recombined
N_{S} Number of defects per unit volume lost to sinks
p Gas pressure
P_m Probability of nucleating a void embryo of size m
Q Sink strength ratio
R Radius
r_{c} Recombination volume radius, or dislocation core radius (Eq. 8.245)
r_0 Prismatic dislocation loop radius

R	Void or bubble radius
R_g	Grain radius
R_c	Critical bubble radius
R_cr	Critical void radius
R_iv	Vacancy–interstitial recombination rate
R_max	Saturation void size
R_0	Equilibrium bubble radius
$\dot{R}$	Rate of change of radius, growth rate
r_k, $r_k^{'}$	Critical void nucleus radius
S	Entropy
S_j	Supersaturation of species j
T	Temperature
V	Volume
$\Delta V/V$	Fractional volume
w_n	Number of ways of removing $\rho^0(n)$ voids of size n from a solid
x	Number of gas atoms in a void
$x_\mathrm{vcl,icl}$	Mean sizes of vacancy and SIA glissile clusters
z_v	Vacancy bias factor
z_i	Interstitial bias factor
z_iv	Combinatorial factor for vacancy–interstitial recombination
Z	Zeldovich factor
Z'	Zeldovich factor in the presence of interstitials or in a stressed solid
α_j	Emission rate of species j
β	$2\gamma\Omega/kT$ defined in Eq. (8.71)
β_j	Absorption rate of species j
δ	Thickness of void shell
$\varepsilon_\mathrm{i}^\mathrm{g}$	Fraction of interstitials in glissile clusters
ε_j	Fraction of defect j that is lost to clusters
ε_r	Fraction of Frenkel pairs that recombine during cascade cooling
Φ	Fluence or dose
γ	Surface energy
γ_{SFE}	Stacking fault energy
Λ	Defined in Eq. (8.182) as $\sqrt{k_\mathrm{g}^2/2}$
η	Defined in Eq. (8.117)
μ	Shear modulus
μ_x	Chemical potential of species x
ν	Poisson's ratio
θ	Angle between surface and tangent to void, as in Eq. (8.81)
Θ	Defined in Eq. (8.98)
ρ	Void size distribution
ρ_x	Density of entity x
σ_icl	Interaction cross section for SIA loops
σ_vcl	Interaction cross section for vacancy loops

σ_h Hydrostatic stress
Σ_s Macroscopic neutron scattering cross section
τ Time Constant
Ω Atomic volume
ξ Defined in Eq. (8.15)
ζ Defined in Eq. (8.130)

Subscripts

B Bubbles
cr Critical size
CP Coherent precipitates
d Dislocations
db Dislocation bias
g Glissile clusters or gas
gb Grain boundary
g Glissile SIA loops
hom Homogeneous
i Interstitials
icl SIA loops
j Defect specie representation
IP Incoherent precipitates
L Dislocation loops
N Network dislocations
pb Production bias
s Sinks
v Vacancy
V Void
vcl Vacancy loops
0 Equilibrium

Superscripts

c Cascades
E Vacancy emission
g Glissile
L Loops
m Number of vacancies in a void embryo of size m
s Single defects, sessile
V Voids
0 Equilibrium
* Minimum critical value
′ In the presence of interstitials

Problems

8.1 In a solid where the effect of interstitials is neglected (i.e., where $\beta_i/\beta_v = 0$),

(a) Determine the critical void embryo size (in terms of the number of vacancies *and* void radius).
(b) Show schematically how the number of vacancies in the critical size void embryo varies with:

(i) Temperature
(ii) Degree of vacancy supersaturation
(iii) Void surface energy
(iv) The presence of interstitials.

(c) How do your answers to parts (a) *and* (b) change when an inert gas is present?

8.2 Determine the critical void embryo size for 316 stainless steel ($a = 0.3$ nm, $\gamma = 1.75$ J/m^2) irradiated at 500 °C so as to produce a vacancy supersaturation of 10^3.

8.3 Derive Eq. (8.40).

8.4 Calculate and plot the relative void growth rate $\dot{R}/\dot{R}_o$ for stainless steel ($T_m = 1823$ K) as a function of T/T_m, given that

$$
\begin{aligned}
Q_f^v &= 1.4\,\text{eV} \\
Q_m^v &= 1.09\,\text{eV} \\
\rho_d &= 10^{10}\,\text{cm}^{-2} \\
\Sigma s &= 0.3\,\text{cm}^{-1} \\
\phi &= 10^{14}\,\text{n/cm}^2\text{s} \\
\nu &= \#\ \text{displacements/neutron} = 100 \\
z_{iv} &= 30 \\
z_i &= 1.02 \\
z_v &= 1.00 \\
a^3 &= \Omega = 0.011\,\text{nm}^3 \\
kT/2\gamma &= 0.01\,\text{nm}^2 \\
\nu &= 10^{13}\,\text{s}^{-1}
\end{aligned}
$$

Neglect voids as sinks ($\rho_V \simeq 0$) and precipitates ($\rho_{CP} \simeq 0$) and loops as sinks ($\rho_L \simeq 0$). Assume the vacancy diffusion coefficient is given by

$$D_v = va^2 \exp(-Q_m^v/kT)$$

and the equilibrium vacancy concentration is given by

$$C_v^0 = \Omega^{-1} \exp(-Q_f^v/kT)\,.$$

Assume the void diameter is 50 nm.

8.5 The equation for growth of a cavity is given by:

$$\frac{dR}{dt} = \frac{\Omega}{R}[D_v(C_v - C_v^V) - D_i C_i]\,.$$

Explain what happens to the cavity growth rate if the radiation dose rate doubles. Assume low sink strength and low temperature. Explain what happens if the radiation stops, but the sample is held at the same temperature at which it was irradiated.

8.6 A solid is subjected to a neutron flux, resulting in void formation and growth. At time t_1, a condition is reached where the dislocation density is 10^9 cm^{-2}, the voids are all 100 nm in diameter at a density of 10^{14} cm^{-3}, and the void growth rate is zero. In the absence of thermal emission, however, $\dot{R} = 10^{-2}$ nm/s. The metal is instantaneously strained such that the dislocation density increases by a factor of 10 and the void growth rate in the absence of thermal emission increases to 8×10^{-2} nm/s. Determine the direction and magnitude of the hydrostatic stress needed to suppress void growth. Assume that the solid contains no dislocation loops or precipitates and that the voids are gas free.

8.7 Pure nickel has been found to be highly susceptible to void formation when irradiated in a fast neutron spectrum. Along with voids, perfect dislocation loops are found in nickel. In comparison, Fe–18Cr–8Ni stainless steel is less susceptible to void formation and faulted Frank loops are found, but voids are also present.

As the nickel content in the stainless steel is increased, two other observations are made. The susceptibility to void formation decreases, and voids that are present are surrounded by a nickel-rich shell.

Given the following information, explain each of these observations.

$$\gamma/\gamma_{SFE}|_{Ni} < \gamma/\gamma_{SFE}|_{Fe}, \quad R_{Ni} < R_{Fe}$$

Element	Cr	Fe	Ni
$\sigma_{eff}(n, \alpha)$	0.20	0.23	4.20

8.8 (a) Explain the reason for the characteristic bell-shaped plot of swelling versus irradiation temperature.
(b) How and why is the shape changed by:

(i) Cold-work prior to irradiation
(ii) The addition of impurities
(iii) Grain size

(c) Explain why swelling and creep can affect each other.

8.9 You are designing the stainless steel fuel cladding for the advanced breeder reactor. Your objective is to delay void nucleation *and* minimize void growth. Concerning cladding fabrication, you can control:

(a) Grain size
(b) Degree of cold-work
(c) Precipitate density
(d) Impurity content of the steel.

From a design standpoint, you can control the normal operating temperature of the cladding over a window of 100 °C.
Using void nucleation and growth theory, how can you utilize these *five* parameters to reach this goal? Be quantitative where possible.

8.10 Annealing is a means of removing radiation damage from an alloy. For stainless steel with both dislocation loop and void populations, explain what will occur when the steel is annealed at 600 °C for several hours. In describing the changes during annealing, indicate relative rates and end points.

8.11 In the absence of gas atoms, we wish to eliminate voids in Cu by thermal treatment at 400 °C. Calculate the length of time needed to accomplish this for initial void radii of 5 and 30 nm. The surface free energy of copper is 1.73 J/m^2.

8.12 Given that the number of gas atoms in a bubble can be described as

$$m = (4/3\pi R^3)\rho_g$$

and that the gas atom density, ρ_g, can be described by

$$1/\rho_g = B + (kT/2\gamma)R$$

where B is the dense gas limit:

(a) Show that the volume increase that accompanies coalescence of equal-sized gas bubbles is

$$(\Delta V/V)_{\text{final}}/((\Delta V/V)_{\text{initial}} = /\sqrt{2}.$$

(b) Assuming that the overall gas balance in UO_2 can be given as

$$YF't = mN$$

where

Y noble gas yield of a fission event
F' fission rate density
m gas atoms per bubble
N bubble density,

and all the gas remains in bubbles, develop an expression for the volumetric swelling rate and indicate the dependence on burnup.

(c) How would you account for

(i) Gas remaining in the matrix?
(ii) Resolution?

References

1. Cauthorne C, Fulton E (1967) Nature 216:575
2. Jenkins ML, Kirk MA (2001) Characterization of radiation damage by transmission electron microscopy. Institute of Physics Publishing, Philadelphia
3. Adda U (1972) In: Corbett JW, Ianiello LC (eds) Proceedings of radiation-induced voids in metals, CONF-710601, USAEC Technical Information Center, Oak Ridge, TN, 1972, p 31
4. Olander DR (1976) Fundamental aspects of nuclear reactor fuel elements, TID-26711-P1. Technical Information Center, USERDA, Washington, DC
5. Mansur LK (1994) J Nucl Mater 216:97–123
6. Russell KC (1971) Acta Met 19:753
7. Powell RW, Russell KC (1972) Rad Eff 12:127
8. Katz JL, Wiedersich H (1972) In: Corbett JW, Ianiello LC (eds) Proceedings of radiation-induced voids in metals, CONF-710601, USAEC Technical Information Center, Oak Ridge, TN, 1972, p 825
9. Russell KC (1979) Acta Met 26:1615
10. Packan NH, Farrell K, Stregler JO (1978) J Nucl Mater 78:143
11. Wiedersich H, Katy JL (1979) Adv Colloid Interface Sci 10:33
12. Russell KC (1972) Acta Met 20:899
13. Katz JL, Wiedersich H (1973) J Nucl Mater 46:41
14. Semenov AA, Woo CH (2002) Phys Rev B 66:024118
15. Brailsford AD, Bullough R (1972) J Nucl Mater 44:121–135
16. Mansur LK (1978) Nucl Technol 40:5–34
17. Brimhall JL, Kissinger HE, Kulcinski GL (1972) In: Corbett JW, Ianiello LC (eds) Proceedings of radiation-induced voids in metals, CONF-710601, USAEC Technical Information Center, Oak Ridge, TN, 1972, p 338

18. Garner FA, Porollo SI, Vorobjev AN, Konobeev YuV, Dvoriashin AM (1999) In: Ford FP, Bruemmer SM, Was GS (eds) Proceedings of the 9th international symposium on environmental degradation of materials in nuclear power systems: water reactors, the minerals, metals and materials society, Warrendale, PA, p 1051
19. Garner FA (1984) Irradiation performance of cladding and structural steels in liquid metal reactors, chap 6. In: Frost BRT (ed) Materials science and technology, vol 10A, nuclear materials, part I. VCH, New York
20. Krasnoselov VA, Prokhorov VI, Koleskikov AN, Ostrovskii ZA (1983) Atomnaya Energiya 54(2):111–114
21. Garner FA, Bates JF, Mitchell MA (1992) J Nucl Mater 189:201–209
22. Brager HR, Garner FA (1979) Effects of radiation on structural materials the 9th international symposium, STP 683. America Society for Testing and Materials, Philadelphia, PA, 1979, pp 207–232
23. Dupouy JM, Lehmann J, Boutard JL (1978) In: Proceedings of the conference on reactor materials science, vol. 5, Alushta, USSR. Moscow, USSR Government, pp 280–296
24. Busboom HJ, McClelland GC, Bell WL, Appleby WK (1975) Swelling of types 304 and 316 stainless steel irradiated to 8 × 1022 n/cm^2, general electric company report GEAP-14062. General Electric Co., Sunnyvale
25. Seran LJ, Dupouy JM (1982) In: Effects of radiation on materials the 11th international symposium, STP 782. American Society for Testing and Materials, Philadelphia, PA, 1982, pp 5–16
26. Seran LJ, Dupouy JM (1983) In: Proceedings of the conference on dimensional stability and mechanical behavior of irradiated metals and alloys, vol 1, Brighton. British Nuclear Energy Society, London, 1983, pp 22–28
27. Mansur LK (1993) J Nucl Mater 206:306–323
28. Mansur LK (1978) J Nucl Mater 78:156–160
29. Mansur LK (1978) Nucl Technol 40:5–34
30. Woo CH, Singh BN (1990) Phys Stat Sol (b) 159:609
31. Golubov SI, Barashev AV, Stoller RE (2012) In: Konings RJM (ed) Comprehensive Nuclear Materials, 1.13. Elsevier, Amsterdam
32. Singh BN, Foreman AJE (1992) Philos Mag A 1992(66):975
33. Abromeit C (1994) J Nucl Mater 216:78–96
34. Singh BN, Eldrup M, Horsewell A, Earhart P, Dworschak F (2000) Philos Mag 80:2629
35. Brailsford AD, Bullough R (1973) J Nucl Mater 48:87
36. Brailsford AD, Bullough R (1972) British Rep AERE-TB-542
37. Dubuisson P, Maillard A, Delalande C, Gilbon D, Seran JL (1992) Effects of Radiation on materials the 15th international symposium, STP 1125. American Society for Testing and Materials, Philadelphia, PA, 1992, pp 995–1014
38. Brager HR, Garner FA, Guthrie GL (1977) J Nucl Mater 66:301–321
39. Wolfer WG, Foster JP, Garner FA (1972) Nucl Technol 16:55
40. Brailsford AD (1975) J Nucl Mater 56:7
41. Wolfer WG, Mansur LK (1980) J Nucl Mater 91:265
42. Allen TR, Cole JI, Gan J, Was GS, Dropek R, Kenik EA (2005) J Nucl Mater 341:90–100
43. Ghoniem NM, Walgraef DJ, Zinkle S (2002) Comput Aided Mater Des 8:1–38
44. Jager W, Trinkaus H (1993) J Nucl Mater 205:394–410
45. Woo CH, Frank W (1985) J Nucl Mater 137:7
46. Garner FA (1984) J Nucl Mater 122–123:459–471
47. Mansur LK, Yoo MH (1978) J Nucl Mater 74:228–241
48. Garner FA, Kumar AS (1987) Radiation-Induced Changes in Microstructure the 13th International Symposium, STP 955 (Part 1). American Society for Testing and Materials, Philadelphia, PA, 1987, pp 289–314
49. Garner FA, Brager HR (1985) J Nucl Mater 133–134:511–514
50. Gan J, Simonen EP, Bruemmer SM, Fournier L, Sencer BH, Was GS (2004) J Nucl Mater 325:94–106

51. Brailsford AD, Mansur LK (1981) J Nucl Mater 103–104:1403–1408
52. Shiakh MA (1992) J Nucl Mater 187:303–306
53. Sekio Y, Yamashita S, Sakaguchi N, Takahashi H (2014) J Nucl Mater 458:355–360
54. Singh BN, Zinkle SJ (1994) J Nucl Mater 217:161–171
55. Garner FA, Sekimura N, Grossbeck ML, Ermi AM, Newkirk JW, Watanabe H, Kiritani M (1993) J Nucl Mater 205:206–218
56. Mansur LK, Coghlan WA (1983) J Nucl Mater 119:1–25
57. Stoller RE, Odette GR (1985) J Nucl Mater 131:118–125
58. Evans JH (1978) J Nucl Mater 76–77:228–234
59. Trinkaus H (1983) Rad Eff 78:189–211
60. Johnson PB, Mazey DJ, Evans JH (1983) Rad Eff 78:147–156
61. Garner FA (2012) Radiation damage in austenitic steels. In: Konings RJM (ed) Comprehensive Nuclear Materials, 4.02:33. Elsevier, Amsterdam
62. Garner FA, Griffiths M, Greenwood LR, Gilbert ER (2010) In: Proceedings of the 14th international conference on environmental degradation of materials in nuclear power systems—water reactors. American Nuclear Society, 1344–1354

Chapter 9
Phase Stability Under Irradiation

Irradiation can have profound effects on the formation or dissolution of phases by alteration of the stability of those phases. The most direct way in which irradiation can alter phase stability is by causing local enrichment or depletion of solute such that the solubility limit is crossed. But irradiation can also dissolve phases by recoil dissolution, cause disordering by creating anti-site defects, and lead to nucleation and growth of distinct phases. Under specific conditions, irradiation can also lead to the formation of metastable phases including amorphization. Because the phase structure of an alloy can significantly affect the physical and mechanical properties of the material, understanding how irradiation affects phase stability is of great importance for engineering materials.

9.1 Radiation-Induced Segregation and Radiation-Induced Precipitation

Radiation-enhanced diffusion (RED), discussed in Chap. 4, and radiation-induced segregation (RIS), presented in Chap. 6, explain how irradiation can increase the transport of atoms in the alloy, and how the coupling between the vacancy and interstitial fluxes and the solute and solvent atoms can lead to enrichment or depletion of solute atoms at defect sinks such as the free surface, grain boundaries, dislocations, precipitate interfaces, etc. Enrichment or depletion of solute can lead directly to precipitate formation if the local solute concentration exceeds the solubility limit, or precipitate dissolution if the solute content is driven below the solubility limit. Recall that the temperature dependence of RIS is such that at low temperatures, RIS is minimal due to low defect mobility and the high recombination rate of vacancies and interstitials, limiting the number available to annihilate at sinks.

Additional material to this chapter can be downloaded from http://rmsbook2ed.engin.umich.edu/movies/

G.S. Was, *Fundamentals of Radiation Materials Science*,
DOI 10.1007/978-1-4939-3438-6_9

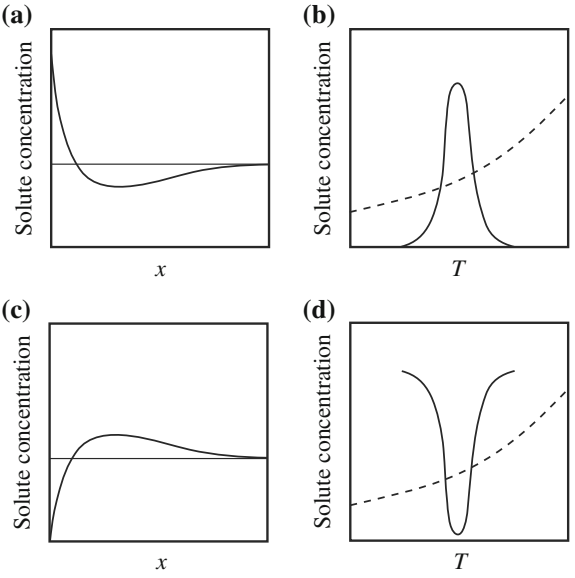

Fig. 9.1 Schematic illustration showing (**a**) enrichment of solute at a sink and (**b**) its corresponding elevation above the solubility limit, and (**c**) depletion of a solute at a sink and (**d**) its corresponding suppression below the solubility limit

At high temperature, the high equilibrium vacancy concentration leads to faster back diffusion, limiting the degree of RIS. However, at intermediate temperatures, significant participation of the solute in the defect fluxes results in pronounced segregation at sinks. Figure 9.1 shows how RIS can lead to precipitate formation or dissolution at a sink. Enrichment of a solute at a sink (Fig. 9.1(a)) can raise the local concentration above the solubility limit (shown as a dashed line in Fig. 9.1(b)) locally. The excess solute can then precipitate as a second phase. If a second phase is already present, then depletion of the solute (Fig. 9.1(c)) can lead to dissolution of that phase locally (Fig. 9.1(d)).

A classic example of radiation-induced precipitate formation and dissolution is described in Sect. 6.1.2 and Figs. 9.2 and 9.3 for the case of RIS in solid solution Ni–Si and Ni–Al alloys. The consequence of a large amount of solute enrichment at sinks is precipitation of a second phase. In the Ni–Si system, Si is undersized relative to Ni and enriches at sinks during irradiation (Fig. 9.2). RIS causes segregation to levels that are well above the solubility of Si in Ni, resulting in formation of a Ni_3Si, γ' precipitate. Ni_3Si precipitates at the surface, grain boundaries and dislocation loops. Conversely, in the case of Ni–Al, Al is oversized with respect to Ni and depletes at sinks under irradiation as shown in Fig. 9.3. The result is the dissolution of existing precipitates at those locations. Since the Ni–Al alloy is an initially homogeneous alloy and the Al content is below the solubility limit for Al, no precipitates are present before irradiation. However, as shown in Fig. 9.3, the region *behind* the depleted zone is enriched in Al and this amount of enrichment exceeds the solubility level at locations that are displaced from the sink interface, resulting in precipitation of Ni_3Al in a subsurface layer a small distance away from

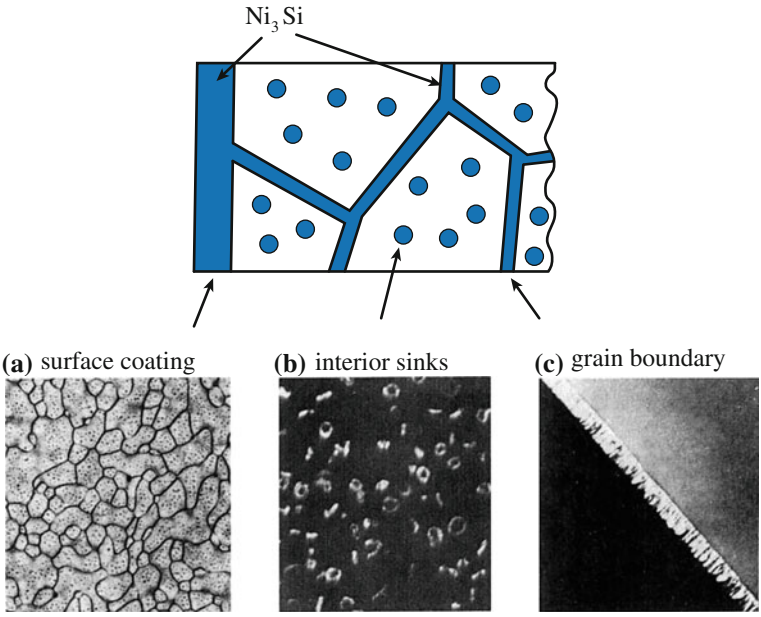

Fig. 9.2 Formation of γ'-Ni_3Si on defect sinks in a solid solution of Ni–6 at.% Si alloy showing (**a**) a surface coating of Ni_3Si, (**b**) toroidal γ' precipitates at dislocation loops and (**c**) a grain boundary coated with Ni_3Si (from [1])

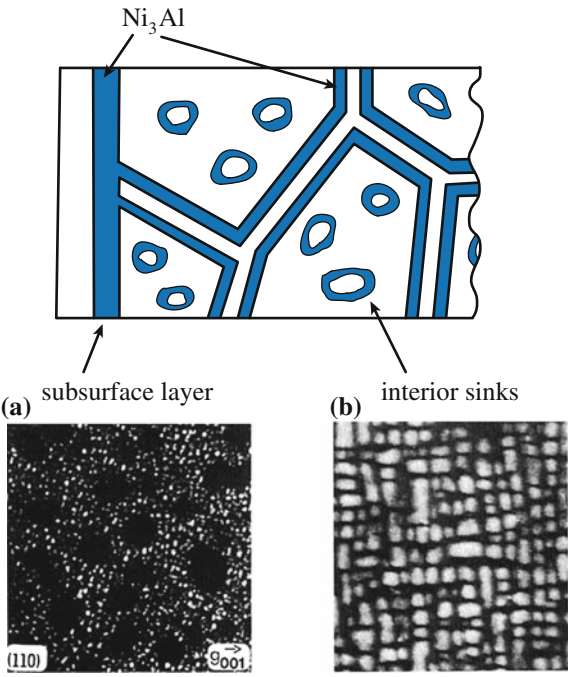

Fig. 9.3 Formation of γ'-Ni_3Al away from defect sinks in a solid solution of Ni–12.8 at.% Al showing (**a**) a subsurface layer of γ'-Ni_3Al, and (**b**) formation of Ni_3Al away from dislocation loops (from [1])

the grain boundary and dislocation loops. Both of these examples are consequences of crossing the solubility line for an element in solution by solute enrichment or depletion due to RIS and constitute a primary mechanism of phase instability under irradiation.

9.2 Recoil Dissolution

Atom displacements created within collision cascades can cause the atoms in a precipitate to be ballistically driven into the surrounding matrix, thus contributing to the dissolution of the precipitate. Nelson et al. [2] developed a model (NHM) for recoil dissolution of precipitates that will be summarized here. For a displacement rate in the solid of K_0 dpa/s, the flux of atoms (atoms per unit area per second) from the precipitate surface can be written as ζK_0. For a spherical precipitate of radius r_p, the dissolution rate expressed as the rate of volume shrinkage is given by:

$$\frac{dV}{dt} = -4\pi r_p^2 \zeta K_0 \Omega, \tag{9.1}$$

where Ω is the atomic volume.

Dissolution by recoil re-solution of the solute is balanced by growth of the precipitate due to diffusion of the solute atoms to the precipitate. Even though the solute is being redistributed between the precipitate and the matrix, the total concentration of solute, C, is fixed and can be expressed as:

$$C = 4/3\pi r_p^3 \rho\, C_p + C_s, \tag{9.2}$$

where ρ is the precipitate density and C_p is the concentration of solute in the precipitates and C_s is the concentration of solute in solution. The growth rate of precipitates due to the solute flux is given by:

$$\frac{dV}{dt} = \frac{3DC_s r_p}{C_p}, \tag{9.3}$$

where D is the solute diffusion coefficient.

The net growth rate of the precipitate is then the sum of terms due to recoil dissolution, Eq. (9.1) and precipitate growth due to diffusion of solute from solution, Eq. (9.3) and can be written as:

$$\frac{dV}{dt} = -4\pi r_p^2 \zeta K_0 \Omega + \frac{3DC_s r_p}{C_p}. \tag{9.4}$$

Substituting for C_s from Eq. (9.2) gives:

$$\frac{dV}{dt} = -4\pi r_p^2 \zeta K_0 \Omega + \frac{3DCr_p}{C_p} - 4\pi r_p^4 D\rho, \tag{9.5}$$

and writing Eq. (9.5) as a radial growth law gives:

$$\frac{dr_p}{dt} = -\zeta K_0 \Omega + \frac{3DC}{4\pi r_p C_p} - r_p^2 D\rho. \tag{9.6}$$

Equation (9.6) is plotted in Fig. 9.4 and shows that for small precipitate sizes, the growth rate is positive, but at larger sizes where the surface area becomes large, precipitates will dissolve. At the size dictated by zero growth rate, dissolution is balanced by reprecipitation. Note that the effect of irradiation is to result in a type of *inverse* coarsening in which smaller particles are more stable than larger ones, which is opposite that which occurs by Ostwald ripening.

The solute concentration profile can be determined with the use of a cell model in which all precipitates are of the same size and each is in a matrix cell of radius, L, with $4/3\pi L^3\rho = 1$. In the Wilkes model [3], re-solution deposits the solute atoms homogeneously throughout the cell and constitutes a *source* term in the steady-state solution of the diffusion equation. Figure 9.5 shows the solute source term in the matrix surrounding the precipitate. The diffusion equation is $\frac{\partial C}{\partial t} = D\nabla^2 C + \zeta K_0$, and subject to the boundary conditions: $\left.\frac{\partial C}{\partial r}\right|_{r=L} = 0$ at the cell boundary ($r = L$), and the solute concentration at the precipitate surface equals the equilibrium concentration, $C(r_p) = C_e$, the concentration is then:

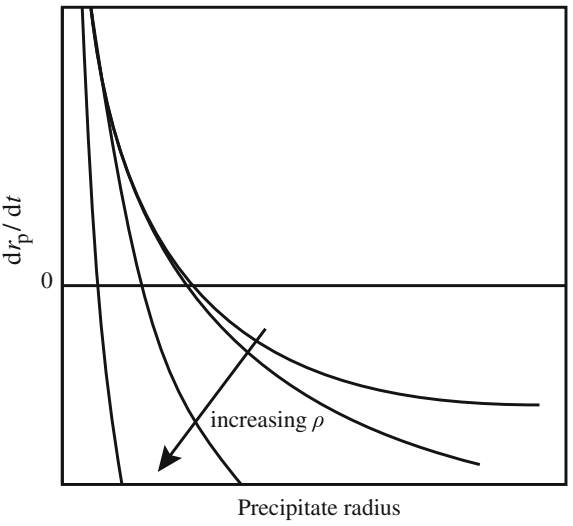

Fig. 9.4 Growth rates for precipitates undergoing irradiation-induced dissolution (from [2])

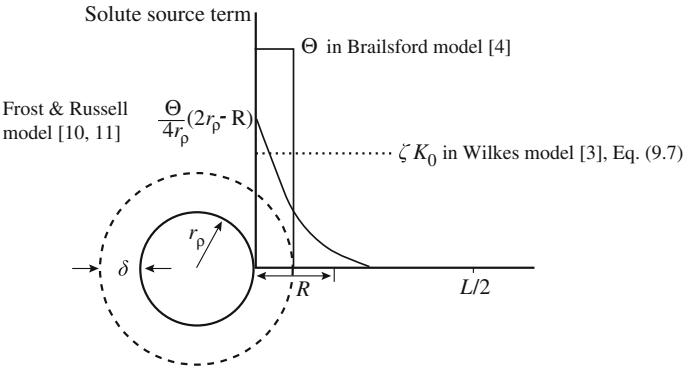

Fig. 9.5 Source terms for irradiation-induced re-solution of solute from the precipitate, according to various models. The term r_p is the precipitate radius, L is the precipitate spacing, R is the recoil radius in the Frost–Russell model [10, 11], and δ is the shell about r_p in the Brailsford model [4]

$$C(r) = C_e + \frac{\zeta K_0 r_p^2}{2\Omega D(L^3 - r_p^3)}\left[\frac{2L^3(r - r_p)}{r r_p} - r^2 + r_p^2\right]. \tag{9.7}$$

The concentration profile of Eq. (9.7) is plotted in Fig. 9.6(a) and shows that the solute concentration rises from the precipitate boundary, r_p, and levels out as it approaches the cell boundary, L. The steady-state cell boundary concentration, $C(L)$ can be written as an excess concentration:

$$\begin{aligned}\chi &= \frac{2D\Omega}{\zeta K_0}(C(L) - C_e) \\ &= L\frac{2(r_p/L) - 3(r_p/L)^2 + (r_p/L)^4}{1 - (r_p/L)^2},\end{aligned} \tag{9.8}$$

and is shown in Fig. 9.6(b) as a function of precipitate-to-cell radius ratio (r_p/L). Note that for a fixed cell size, the cell boundary concentration initially increases since the steady-state solute supersaturation is increasing with precipitate surface area. When the precipitate is large, the precipitate surface is close to the cell wall and back diffusion becomes significant, thus causing a reduction in the concentration. For most practical situations, the volume fraction of precipitate is small so that the precipitate size distribution is to the left of the peak in Fig. 9.6(b). As a result, small precipitates will experience a net loss of solute until steady state is reached.

An improvement in the treatment of the source term in the simple NHM model is obtained by assuming that particles are spaced infinitely far from each other (dissolution–reprecipitation at one particle is unaffected by others) and that

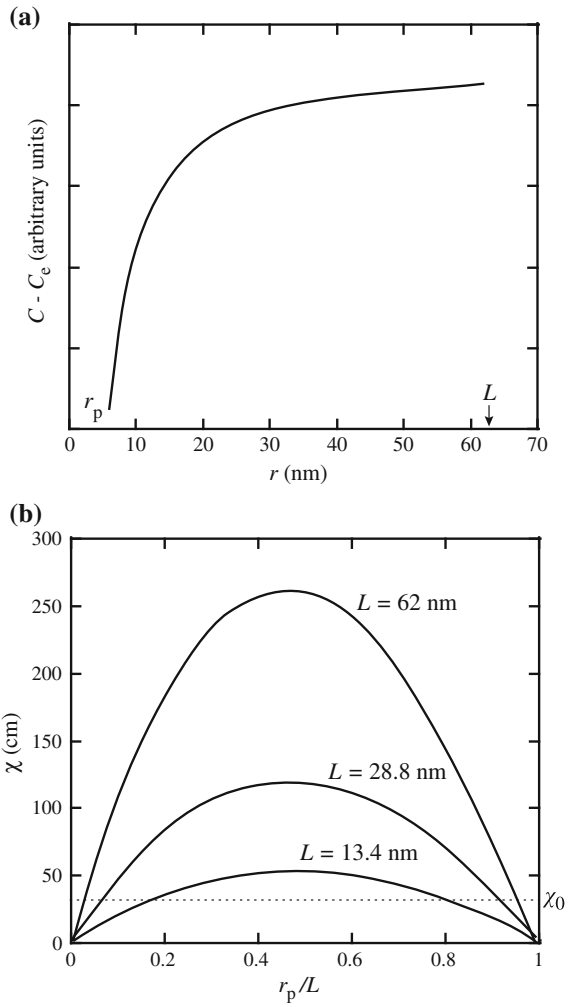

Fig. 9.6 (**a**) Steady-state solute concentration in the matrix from Eq. (9.7), and (**b**) steady-state boundary concentration from Eq. (9.8) (from [3])

resolution occurs at a uniform rate in a shell of thickness δ around the particle of radius, r_p (Fig. 9.5) [4]. For an initial precipitate size of r_0, the resulting size was found to be:

$$r_0^3 - r_p^3 = \frac{3\delta^2 r_p(3r_p + 2\delta)}{8\pi D\rho_p\left[(r_p+\delta)^3 - r_p^3\right]}\left(-\frac{\Theta}{4\pi r_p^2}\right), \tag{9.9}$$

where Θ is the re-solution-induced rate of precipitate volume change. The effect of irradiation in this model is to reduce the precipitate size from its original dimension by up to a factor of 2 [3]. Note that for the case where $\delta \rightarrow \infty$, the result reduces to that given in Eq. (9.6).

This result can be compared to the well-known thermal coarsening behavior of precipitates described by Wagner [5] and Lifshitz and Slyosov [6]:

$$\bar{r}_{\mathrm{p}}^3 - \bar{r}_0^3 = \frac{8DC_{\mathrm{e}}\gamma V_{\mathrm{m}}^2 t}{9\mathcal{R}T}, \tag{9.10}$$

where r_0 is the initial average precipitate radius, C_{e} is the solubility of the precipitate of infinite radius, V_{m} is the molar volume, γ is the particle-matrix interface energy, and $\mathcal{R}$ is the gas constant. Accounting for irradiation-induced re-solution and irradiation-enhanced diffusion, the maximum stable particle size [7–9] is shown to be:

$$r_{\max} = \left(\frac{3aD}{lfK_0}\right)^{1/2}, \tag{9.11}$$

where a is the lattice spacing, l is the linear dimension of the cascade, f is the fraction of solute atoms dissolved, and the product $l\,f$ is the shrinkage by re-solution [2]. When particles are initially larger than the maximum stable size, the maximum size decreases according to:

$$r_{\max}(K_0 t) - r_{\max}(K_0 t_0) = -lfK_0(t - t_0), \tag{9.12a}$$

and when the initial particle sizes are much smaller than that given by the equilibrium size distribution, then the particle size increases according to:

$$r_{\max}^3(K_0 t) - r_{\max}^3(K_0 t_0) = 9aD(t - t_0). \tag{9.12b}$$

Note that Eq. (9.12b) is similar to Eq. (9.10) for thermal coarsening.

A modification to the Wilkes's cell model is to provide a source term for the redeposited solute that is more realistic than having it deposited uniformly in the cell (Wilkes [3]) or uniformly in a shell (Brailsford [4]). Frost and Russell [10, 11] model the rate of solute redeposition in the matrix using the rate at which recoils originate in the matrix, which depends on the distance from the precipitate center, r, according to:

$$G(r) = \frac{\Theta}{4rR}\left[r_{\mathrm{p}}^2 - (r - R)^2\right], \tag{9.13}$$

where Θ is the re-solution rate per atom and R is the recoil distance (Fig. 9.5). Solving the diffusion equation with the spatially dependent source term, $G(r)$:

$$\frac{\partial C}{\partial t} = D\nabla^2 C + G, \tag{9.14}$$

gives:

$$C(r) = C_0 + \frac{\Theta}{48RD}[r^3 - r_p^3 - 4R(r^2 - r_p^2) - 6(r_p^2 - R^2)(r - r_p) - (3r_p - R)(r_p + R)^3]\left(\frac{1}{r} - \frac{1}{r_p}\right), \tag{9.15}$$

where C_0 is the initial solute concentration and the maximum concentration is given by:

$$C_{max} = C_0 + \frac{\Theta R^2}{12D}\left(1 - \frac{R}{4r_p}\right). \tag{9.16}$$

The maximum solute concentration is proportional to the re-solution rate and weakly dependent on the precipitate size.

The inverse coarsening rate of particles that are not of the same size can be determined by calculating the diffusion near each particle [10, 11]. The calculation assumes that the concentration at the edge of its cell is an average matrix concentration and that there is no net flux to or away from a precipitate of some radius, r_m, giving:

$$\frac{dr_p}{dt} = \left(1 - \frac{r_p}{r_m}\right)\frac{1}{r_p^2}\frac{L}{(L - r_p)}\frac{\Theta R^3}{48}, \tag{9.17}$$

for which solutions exist depending on the value of r_m. Assuming that $r_p \ll L$ and the initial precipitate size is r_0, then:

$$\frac{r_p^3(t)}{r_0^3} = 1 + \frac{t}{\tau_A}, \quad \text{for } r_p \ll r_m \text{ and } \tau_A = \frac{48r_0^3}{\Theta R^3}, \tag{9.18}$$

$$\frac{r_p^2(t)}{r_0^2} = 1 - \frac{t}{\tau_B}, \quad \text{for } r_p \gg r_m \text{ and } \tau_B = \frac{24r_m r_0^2}{\Theta R^3}, \tag{9.19}$$

$$r_p - r_m = (r_0 - r_m)\exp(-t/\tau_C), \quad \text{for } r \cong r_m \text{ and } \tau_C = \frac{48r_m^3}{\Theta R^3}. \tag{9.20}$$

Note that the relation between the particle size and time is $r_p^3 \propto t$ when the size is below r_m and $r_p^2 \propto t$ when the size is greater than r_m. For all cases, when R, r_0, and r_m are of the order of 10 nm, τ is between $10/\Theta$ and $100/\Theta$. For the case of fast reactor conditions, $\Theta \sim 10^{-7}$ s^{-1}, so 10^8 s $\le \tau \le 10^9$ s, which is equivalent to 3–30 years. In heavy ion irradiation, $\Theta \sim 10^{-3}$ s^{-1} so that 10^4 s $\le \tau \le 10^5$ s. Since the incubation time varies with r^3, larger precipitates would require even longer for inverse coarsening to occur. Consequently, irradiation-induced inverse coarsening by recoil re-solution is expected only after very long-term exposures.

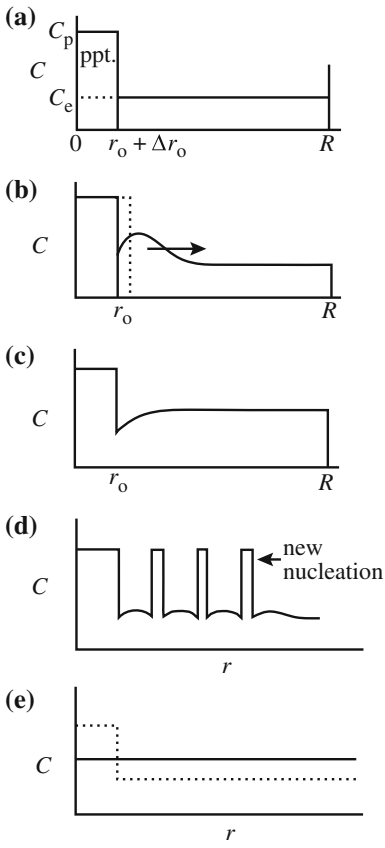

Fig. 9.7 Schematic illustration of radiation-induced precipitate dissolution and precipitation as a function of dose. (**a**) Unirradiated state, (**b**) surface dissolution at low dose, (**c**) steady state, and either (**d**) nucleation of new precipitates due to local solute supersaturation in the matrix, or (**e**) continued dissolution of the precipitate due to low precipitate density (from [12])

The effect of irradiation on precipitate stability is shown schematically in Fig. 9.7 as a series of illustrations with increasing dose. Prior to irradiation, the precipitate is in equilibrium with the matrix solute concentration, C_e (Fig. 9.7(a)). Irradiation causes dissolution of the precipitate surface and an increase in the solute content near the interface that begins to diffuse away (Fig. 9.7(b)). Re-solution is balanced by reprecipitation and results in a steady-state concentration profile (Fig. 9.7(c)). Local supersaturation of solute may lead to the nucleation of new precipitates in the matrix (Fig. 9.7(d)) or if the precipitates are very widely spaced, the matrix solute may not reach a value that results in steady state and the precipitate will continue to dissolve (Fig. 9.7(e)).

Determining the stability of a phase under irradiation is complicated by the influence of multiple parameters such as the displacement rate, temperature, and sink strength. An estimate for the stability of a precipitate can be obtained by considering two opposing processes: ballistic mixing and radiation-enhanced interdiffusion. This problem was analyzed by Abromeit et al. [13] and the analysis

is summarized here. Precipitates are assumed to be dissolved by ballistic mixing at a rate approximated by:

$$R_{\mathrm{m}} = \beta K_0 \Omega, \tag{9.21}$$

where $K_0\Omega$ is the displacement rate in dpa/s, and β is a factor that links displacement rate to solute loss from the precipitate. Similarly, the rate of formation or growth of a precipitate due to radiation-enhanced diffusion is given by:

$$R_{\mathrm{g}} = \alpha \tilde{D}, \tag{9.22}$$

where α is a constant and $\tilde{D}$ is the interdiffusion coefficient. The solubility limit may be determined by equating the two processes, yielding:

$$\alpha \tilde{D} = \beta K_0 \Omega. \tag{9.23}$$

The steady-state point defect balance equations Chap. 5:

$$\begin{aligned} K_0 - K_{\mathrm{iv}} C_{\mathrm{i}} C_{\mathrm{v}} - D_{\mathrm{v}} k_{\mathrm{s}}^2 C_{\mathrm{v}} &= 0 \\ K_0 - K_{\mathrm{iv}} C_{\mathrm{i}} C_{\mathrm{v}} - D_{\mathrm{i}} k_{\mathrm{s}}^2 C_{\mathrm{i}} &= 0, \end{aligned} \tag{9.24}$$

and the variables are as defined in Chap. 5, where $K_{\mathrm{iv}} = 4\pi r_{\mathrm{iv}} D_{\mathrm{i}}/\Omega$, and $k_{\mathrm{s}}^2 = 4\pi r_{\mathrm{s}} C_{\mathrm{s}}/\Omega$ is the sink strength. Note that in this analysis, no distinction is made in the sink strength for vacancies and interstitials.

When recombination dominates defect loss:

$$\tilde{D} = A K_0^{1/2} D_i^{1/2} (\Omega/4\pi r_{iv})^{1/2}, \tag{9.25}$$

and when defect annihilation at sinks dominates, $\tilde{D}$ is temperature independent and can be described as:

$$\tilde{D} = A K_0 / k_{\mathrm{s}}^2 \tag{9.26}$$

and A is a constant describing the transport efficiencies of the atoms via vacancies and interstitials. Eliminating $\tilde{D}$ from Eqs. (9.25) and (9.26) defines the boundary between the regimes where recombination is dominant and where annihilation at sinks is dominant and gives:

$$K_0 = k_{\mathrm{s}}^4 D_{\mathrm{i}} (\Omega/4\pi r_{\mathrm{iv}}). \tag{9.27}$$

Equation (9.27) is shown by the plane, P_1, in Fig. 9.8 that plots the solubility as a function of damage rate, temperature, and sink strength. Eliminating $\tilde{D}$ between Eqs. (9.23) and (9.26) yields the critical sink strength:

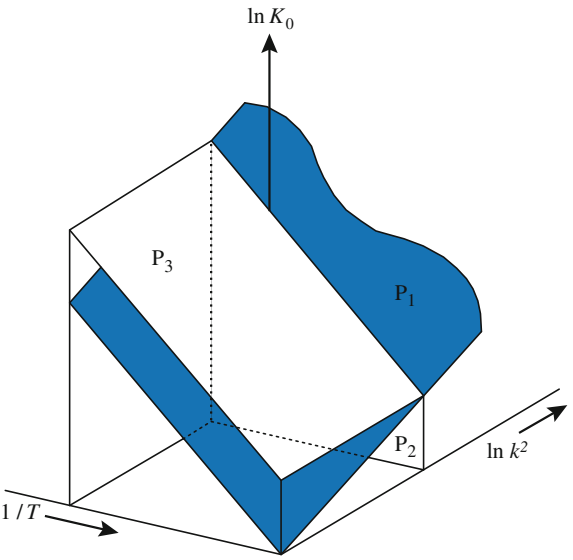

Fig. 9.8 Stability diagram for precipitates under irradiation in displacement rate–temperature–sink strength space. The plane P_1 separates recombination and annihilation regimes, and precipitates are stable below the plane P_3 and to the left of the plane P_2 (after [13])

$$k_c^2 = A\alpha/\beta\Omega. \tag{9.28}$$

Equation (9.28) is shown as the plane, P_2, in Fig. 9.8. Finally, according to Eqs. (9.23) and (9.26), a temperature-dependent boundary separates the two-phase from the one-phase regimes and is given as:

$$K_0 = (A\alpha/\beta)^2 D_i/4\pi r_{iv}\Omega, \tag{9.29}$$

and is shown as plane P_3 in Fig. 9.8. Precipitates are stable below P_3 and to the left of P_2. The region representing stability of the two-phase structure increases in size with increasing temperature due to increasing diffusivity and with increasing values of the critical sink strength, k_c^2.

The term β in Eq. (9.21) is approximated by $\beta = \beta_1 V_c/\Omega$, where β_1 is a constant and V_c is the volume of the collision cascade and is therefore proportional to the cube of the cascade radius, r_c [13]. Reprecipitation of the solute dissolved into the matrix by the cascade is controlled by interdiffusion with the rate constant given by Fick's law as $\alpha = 4\alpha_1/r_c^2$, where α_1 is a constant. Inserting these expressions for α and β into Eqs. (9.28) and (9.29) gives:

$$k_c^2 = \frac{3\pi A\alpha_1}{\beta_1}\frac{1}{r_c^5}, \tag{9.30}$$

$$K_0 = \left(\frac{A\alpha_1}{\beta_1}\right)^2 \frac{3D_i\Omega}{4\pi^3 r_{iv}}\frac{1}{r_c^{10}}. \tag{9.31}$$

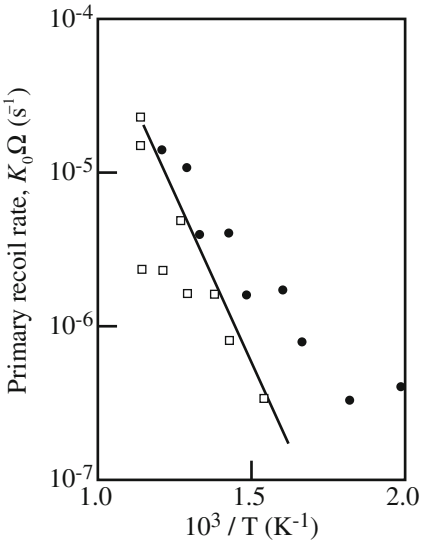

Fig. 9.9 Stability of the two-phase structure in Cu–48 %Ni–8 %Fe irradiated with 300 keV Cu^{++}. *Filled symbols* denote irradiation-induced disordering of the two-phase structure and *open symbols* denote no irradiation effect. The *line* is the best fit of Eq. (9.31) (after [13])

Note that both the critical sink strength and the production rate/temperature relationship exhibit a very strong dependence on the cascade size. The model was applied to the case of a Cu–48 %Ni–8 %Fe alloy irradiated with 300 keV Cu^+ ions over a range of temperatures and displacement rates. Figure 9.9 plots the primary recoil rate versus $1/T$ with the open symbols denoting irradiation-induced dissolution of the two-phase structure. Note that there is a critical displacement rate for irradiation-induced dissolution that increases with temperature. The line in the graph is the optimal fit of Eq. (9.31) to the data, from which the cascade radius was determined to be ~ 2.7 nm.

In summary, radiation-induced dissolution is a key process affecting the stability of precipitates. Radiation results in re-solution of the precipitate outer surface, and the evolution of the phase microstructure is then determined by the relative rates of re-solution and reprecipitation. In essence, phase stability is controlled by kinetic processes in the solid. Besides dissolution, precipitate stability is also affected by radiation-induced disordering, described in the next section.

9.3 Radiation Disordering

The NHM model described in the last section was originally developed for both recoil dissolution and disordering dissolution. Disordering involves the loss of long-range order due to irradiation. Irradiation-induced disordering is shown in Movie 9.1 (http://rmsbook2ed.engin.umich.edu/movies/) for a 10 keV Au ion bombarding an ordered Cu_3Au structure. In the case of disordering, displacement is assumed to occur in a shell of thickness, l, at the precipitate surface and result in the loss of solute atoms by diffusion to the matrix. It is also assumed that only a fraction, f, of these solute atoms

actually become dissolved. Defining $\xi = l\,f$ as the dissolution parameter, then the dissolution rate given in Eq. (9.1) becomes:

$$\frac{\mathrm{d}V}{\mathrm{d}t} = -4\pi r_\mathrm{p}^2 \xi K_0, \tag{9.32}$$

and the rate of change of the precipitate size due to disordering dissolution is:

$$\frac{\mathrm{d}r_\mathrm{p}}{\mathrm{d}t} = -\xi K_0 + \frac{3DC}{4\pi r_\mathrm{p} C_\mathrm{p}} - r_\mathrm{p}^2 D\rho, \tag{9.33}$$

which is identical to Eq. (9.6) except for the first term. Russell [14] points out that since $l \sim 10$ nm, then for $f \sim 1$, $\xi = l\,f \sim 10$ nm. Comparing this value to the corresponding term in Eq. (9.6) for recoil dissolution, where $\zeta\Omega \sim 10^{-4}$ nm, shows that the disordering dissolution rate is much higher than that due to recoil dissolution, so disordering dissolution is expected to be a much more effective process. Referring back to Fig. 9.4 shows that the stable precipitate size will be lower for disordering dissolution due to its greater efficiency.

Irradiation is known to disorder alloys by the creation of vacancies and interstitials and anti-site defects, in which the atoms are relocated to the complementary site, disrupting the order in the alloy. But disordered alloys will return to their equilibrium state as long as diffusion can occur. In fact, the high concentration of vacancies and interstitials produced by irradiation can enhance the ordering process by radiation-enhanced diffusion. Therefore, irradiation causes two opposing processes to occur: disordering and reordering. Liou and Wilkes [15] describe the rate of change of order in an alloy due to irradiation starting from the Bragg–Williams definition of long-range order for a binary alloy with atoms arranged on two sublattices, α and β, where the long-range order parameter is defined as:

$$S = \frac{(f_{\mathrm{A}\alpha} - X_\mathrm{A})}{(1 - X_\mathrm{A})}, \tag{9.34}$$

where $f_{\mathrm{A}\alpha}$ is the probability of an A atom being on an α lattice site, and X_A is the atomic fraction of A atoms. When $S = 1$, the alloy is completely ordered and when $S = 0$, the alloy is completely disordered.

Under irradiation, the rate of ordering can be written as a competition between radiation-induced disordering and thermal reordering:

$$\frac{\mathrm{d}S}{\mathrm{d}t} = \left(\frac{\mathrm{d}S}{\mathrm{d}t}\right)_\mathrm{irr} + \left(\frac{\mathrm{d}S}{\mathrm{d}t}\right)_\mathrm{th}. \tag{9.35}$$

The disordering rate due to irradiation can be written as:

$$\left(\frac{\mathrm{d}S}{\mathrm{d}t}\right)_\mathrm{irr} = -\varepsilon K_0 S, \tag{9.36}$$

where ε is the disordering *efficiency*, or the ratio of replacements to displacements, and is of the order 10–100 under neutron irradiation.

The thermal order–disorder transition can be written as a chemical reaction in which A and B atoms on the wrong lattice sites are interchanged so that the A–B pair is on the correct sites:

$$(\mathrm{A}-\mathrm{B})_{\text{wrong}} \underset{K_{\mathrm{w}}}{\overset{K_{\mathrm{c}}}{\rightleftharpoons}} (\mathrm{A}-\mathrm{B})_{\text{correct}}, \tag{9.37}$$

where the rate constants, K_{c} and K_{w}, are given by:

$$K_{\mathrm{c}} = v_{\mathrm{c}} \exp(-U/kT), \tag{9.38a}$$

$$K_{\mathrm{w}} = v_{\mathrm{w}} \exp[(-U+V_{\mathrm{T}})/kT], \tag{9.38b}$$

where U is the energy barrier for the reaction and the activation energy, V_{T} is the energy reduction when the wrong A–B pair transforms to the correct A–B pair and the $v_{\mathrm{c,w}}$ are the frequency factors for the *correct* and *wrong* pairs, respectively. The solution of the chemical rate equations gives the following relation for the order parameter in terms of the equilibrium order parameter, S_{e} and the time, t:

$$\frac{(1-S)}{(1-S_{\mathrm{e}})} = \cot h(k_{\mathrm{O}}t + y), \tag{9.39}$$

where y is a constant and k_{O} is the rate constant defined as:

$$k_{\mathrm{O}} = \left[v_{\mathrm{v}}C_{\mathrm{v}} \exp(-E^{\mathrm{v}}_{\mathrm{mO}}/kT)(Z_\alpha + Z_\beta - 2) + v_{\mathrm{i}}\sigma C_{\mathrm{i}} \exp(-E^{\mathrm{i}}_{\mathrm{mO}}/kT)\right](X_{\mathrm{A}}/X_{\mathrm{B}})^{1/2} \times Z_\beta \exp(-V_{\mathrm{O}}/2kT), \tag{9.40}$$

where $2v_{\mathrm{v}} = (v_{\mathrm{c}}v_{\mathrm{w}})^{1/2}_{\mathrm{v}}$ and $3v_{\mathrm{i}} = (v_{\mathrm{c}}v_{\mathrm{w}})^{1/2}_{\mathrm{i}}$ are the frequency factors for exchange by vacancies and interstitials, respectively, $E^{\mathrm{v}}_{\mathrm{mO}}$ and $E^{\mathrm{i}}_{\mathrm{mO}}$ are the vacancy and interstitial migration energies for ordering, $Z_{\alpha,}$ is the number of α sites that are nearest neighbor to a β site and Z_β is the reverse, where α and β refer to the two sublattices, σ is a parameter accounting for the number of reaction paths and their probabilities, and X_{A} and X_{B} are the atom fractions of A and B atoms, respectively. V_{O} is the activation energy for ordering, $V_{\mathrm{O}} = AV$, where A is crystal structure dependent (A = 6 for fcc and A = 14 for bcc) and $V = V_{\mathrm{AB}} - (V_{\mathrm{AA}} + V_{\mathrm{BB}})/2$, where the V_{XY} terms are the energies of the respective atom pairs. The time derivative of the thermal order parameter can be written as follows [15]:

$$\left(\frac{\mathrm{d}S}{\mathrm{d}t}\right)_{\mathrm{th}} = \frac{k_{\mathrm{O}}(1-S)^2}{(1-S_{\mathrm{e}})} - (1-S_{\mathrm{e}})k_{\mathrm{O}}. \tag{9.41}$$

The steady-state solution to Eq. (9.35), where the terms are given in Eqs. (9.36) and (9.41), is:

$$S = 1 + \varepsilon K_0 - \frac{(1 - S_e)}{2k_O}\left(\varepsilon^2 K_0^2 + 4k_O^2 + \frac{4k_O \varepsilon K_0}{(1 - S_e)}\right)^{1/2}. \tag{9.42}$$

Liou and Wilkes applied this formalism to the $AuCu_3$ system as a function of temperature and dose rate. Figure 9.10 shows that at any given temperature, the effect of increasing dose rate is a reduction in the order, as expected. Also, for a given dose rate, increasing temperatures results in greater order. Another way of showing the competing effects of irradiation and temperature on the alloy order is given in Fig. 9.11(a). Here, the equilibrium value of S_e is 1.0, but the alloy is in a state where the order, $S_{observed}$ is less than S_e. At low temperature, where defect motion is restricted, the effect of irradiation is to disorder the alloy. At high temperature, the effect of irradiation is to increase defect mobility so that the order parameter approaches equilibrium, which lies above the original, incompletely equilibrated state. That is, irradiation assists ordering at high temperatures. This behavior is further illustrated by the example shown in Fig. 9.11(b), which is a first-order transition of a solid solution alloy in the disordered α phase to an ordered α' phase. Under irradiation, the ordered phase becomes disordered at low temperatures, reverting to the α phase as shown in Fig. 9.11(c). Since the degree of disordering is dependent on the dose rate, the shape of the phase fields shown in Fig. 9.11(c) will change at higher dose rate. The dependence of the phase fields on dose rate is shown schematically in Fig. 9.11(d), in which the ordered region continues to shrink with increasing dose rate.

The change in the phase diagram caused by irradiation-induced disordering constitutes an irradiation-modified phase transition as disordering can change the alloy phase structure. Recall that the ordered state is the arrangement of atoms that minimizes the free energy of the solid. Consequently, radiation-induced disorder increases the free energy of the solid above the equilibrium value. Hence, under

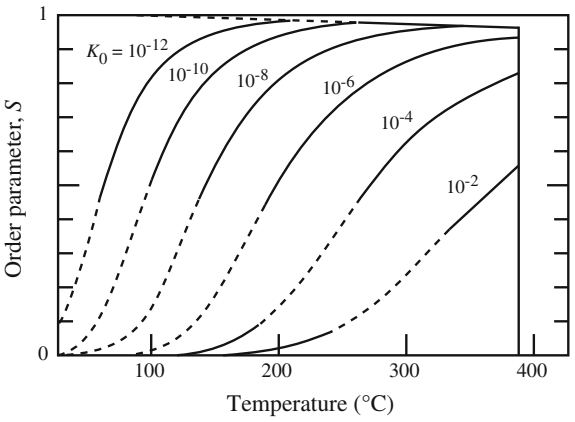

Fig. 9.10 Steady-state long-range order parameter for Cu_3Au under irradiation for various dose rates (after [15])

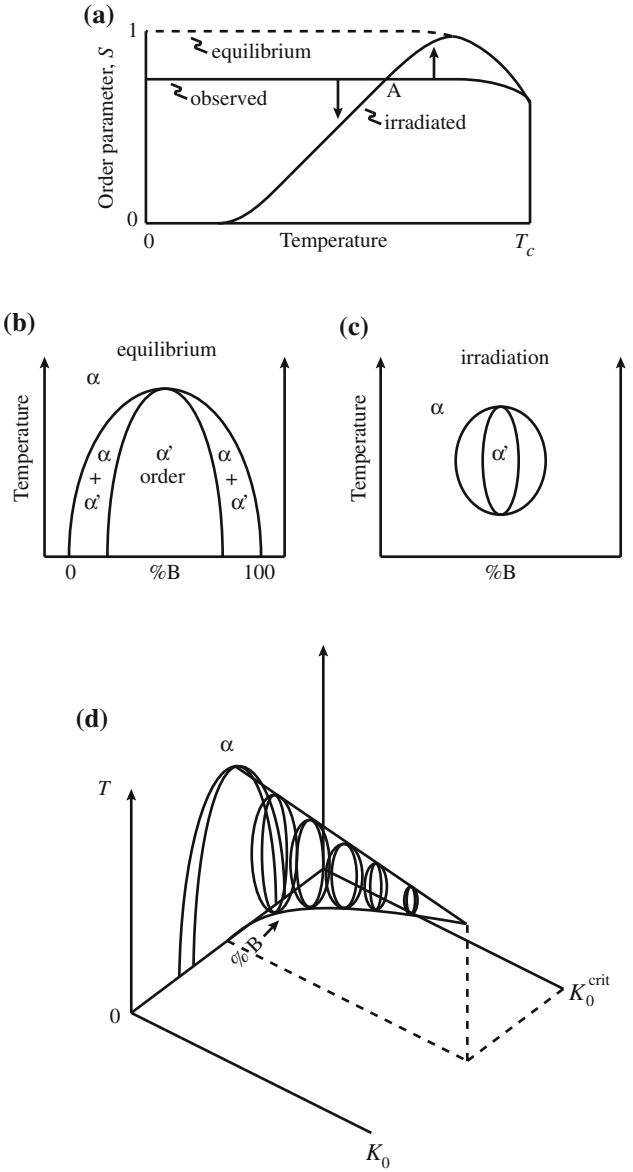

Fig. 9.11 (**a**) Effect of irradiation on the temperature dependence of the order parameter for a phase structure that is not at the equilibrium order, S_e. (**b**) Equilibrium phase diagram showing a first-order phase transformation of the disordered α phase to the ordered α'-phase. (**c**) Modification of the phase diagram by irradiation reflecting the change in order as given in (**a**). (**d**) Dependence on the irradiation-modified phase diagram with dose rate (after [3])

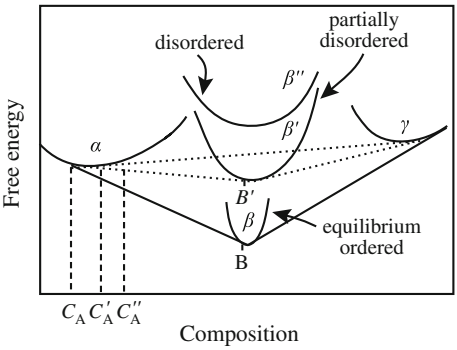

Fig. 9.12 Schematic illustration of a phase diagram for an alloy with an ordered intermetallic compound, β, showing partial disordering to β', and complete disordering to β'' due to the increase in free energy caused by irradiation (after [14])

irradiation, a new free energy balance may be achieved between adjacent phases in the alloy. Figure 9.12 shows how the compositions of the α and γ phases determined by the common tangent of free energy curves can be changed when irradiation induces an increase in the free energy of the intermetallic β phase, resulting in a partially disordered phase, β'. Note that while the ordered β phase is in equilibrium with the α phase at a composition C_A, partial disordering by irradiation raises the free energy of the β phase to β' and the concentration of A in equilibrium with α and β' phases is now C'_A. Further irradiation can lead to complete disordering, β'' phase, such that the phase does not form. Note that order–disorder transformation energies are generally in the range of 0.1–0.6 eV/atom [16].

The effect of irradiation on ordering can also be understood with the aid of the thermal spike model of the cascade, discussed in Sects. 3.3 and 10.2.4. Recall that the energy density in the core of the cascade can reach values such that the region resembles a liquid-like structure. Wollenberger [12] determined the time dependence of the temperature in the cascade as a function of the distance from the center of the spike, where temperature is normalized to the disordering temperature, T_c, and the result is shown in Fig. 9.13 for nickel. In this figure, r_c is the value of the cascade radius at which the temperature just reaches the disordering temperature at any time during the thermal spike, which in this case is 2.6 nm. As such, the temperature of the region inside this radius can be assumed to exceed T_c, resulting in disordering of the center of the cascade. Presumably, in the outer regions of the cascade where the temperature is below T_c but where the vacancy density is high, reordering will occur. In fact, when the reordered shell of a new cascade overlaps the disordered zone from an old cascade, the remaining disorder will be reduced, causing a reduction in the disordering efficiency per cascade with increasing fluence. The consequence of this overlap process is that the long-range order parameter will not completely vanish, even at high fluences.

At low temperatures where vacancies are immobile, irradiation-induced disordering can occur very quickly in some systems. For example, the $NiAl_3$ phase ($D0_{11}$) is extremely unstable under irradiation [17], becoming disordered following irradiation with 500 keV Kr at RT to a dose of 2×10^{14} i/cm^2 [18]. On the other hand, Fe_3Al (bcc) and FeAl (bcc-B2) undergo only partial disordering after 40 dpa of 2.5 MeV Ni^+ irradiation [19]. Hence, factors besides dose play a role in the order–disorder transformation reaction in alloys.

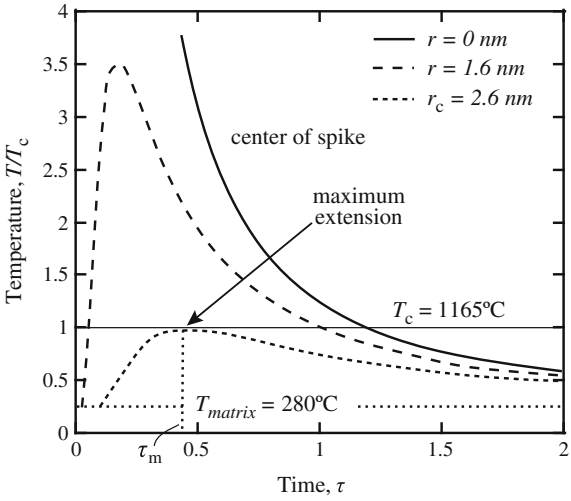

Fig. 9.13 Time dependence of the temperature of a thermal spike for different radial locations within the spike (after [12])

9.4 Incoherent Precipitate Nucleation

Irradiation can induce the formation of precipitates in an alloy. Precipitate growth and nucleation can be expressed as a *chemical* effect of vacancies and interstitials due to high levels of solute supersaturation under irradiation. The supersaturation provides the driving force for the reaction. Maydet and Russell [20] developed a model for the growth of spherical, incoherent precipitates under irradiation and that model is described here.

The precipitate is characterized by two variables: the number of solute atoms, x, and the number of excess vacancies, n, which is the difference in the number of matrix atoms displaced by the precipitate and x. Precipitates with greater atomic volume than the matrix must have $n > 0$ to relieve the strain energy, and undersized precipitates must have $n < 0$. The precipitate behavior is described by its movement in a phase space of coordinates n and x, much as was done with dislocation loops and voids in Chaps. 7 and 8. Figure 9.14 shows how the precipitate can move in phase space by capture of solute atoms, β_x, vacancies, β_v, or interstitials, β_i, or the emission of solute atoms, α_x, or vacancies, α_v. The particle moves in phase space with a velocity equal to the frequency of addition of solute or defect times the jump distance:

$$\dot{x} = \beta_x(n,x) - \alpha_x(n,x), \tag{9.43}$$

$$\dot{n} = \beta_v(n,x) - \alpha_v(n,x) - \beta_i(n,x). \tag{9.44}$$

The βs are determined from concentrations and diffusivities of the defects and solute and the αs are determined as follows:

As with void nucleation, there exists an energy barrier to the growth of the precipitate above some size, such that precipitates below this size equilibrate with

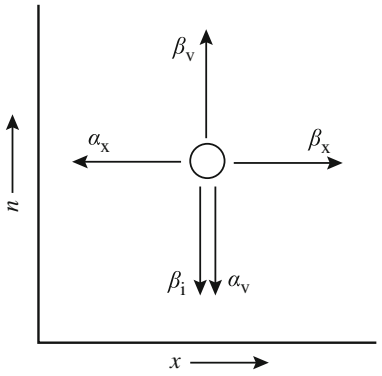

Fig. 9.14 Precipitate trajectories in (n, x) phase space showing the processes giving rise to its motion (after [20])

each other and growth and shrinkage occur at the same rate. That is, the excess number of $(n, x-1)$-mer gaining a solute atom to become a (n, x)-mer is balanced by the reverse process. The same holds for the number of $(n-1, x)$-mer gaining a vacancy to become a (n, x)-mer. The equilibrium number of (n, x)-mer is then:

$$\rho_p^0(n,x) = \frac{1}{\Omega_m}\exp\left(-\frac{\Delta G_p^0(n,x)}{kT}\right), \tag{9.45}$$

where Ω_m is the atomic volume of the matrix phase and $\Delta G_p^0(n,x)$ is the free energy of formation of a precipitate from n matrix vacancies and x solute atoms. The balance between $(n, x-1)$-mer and (n, x)-mer can be written as:

$$\beta_v(n-1,x)\rho_p^0(n-1,x) = \alpha_v(n,x)\rho_p^0(n,x), \tag{9.46}$$

$$\beta_x(n,x-1)\rho_p^0(n,x-1) = \alpha_x(n,x)\rho_p^0(n,x). \tag{9.47}$$

Substituting Eq. (9.45) into Eqs. (9.46) and (9.47) and replacing differences in $\Delta G_p^0(n,x)$ by derivatives, gives:

$$\alpha_v(n,x) \approx \beta_v(n,x)\exp\left(\frac{1}{kT}\frac{\partial \Delta G_p^0(n,x)}{\partial n}\right), \tag{9.48}$$

$$\alpha_x(n,x) \approx \beta_x(n,x)\exp\left(\frac{1}{kT}\frac{\partial \Delta G_p^0(n,x)}{\partial x}\right), \tag{9.49}$$

where $\beta_v(n-1, x)$ and $\beta_x(n, x-1)$ in Eqs. (9.46) and (9.47) vary slowly with n and x and have been replaced with their values at (n, x).

The free energy change upon formation of a precipitate from a solid solution that contains a supersaturation of solute and vacancies is given as:

$$\Delta G_{\mathrm{p}}^{0} = -nkT \ln S_{\mathrm{v}} + (36\pi\Omega^2)^{1/3}\gamma x^{2/3} - xkT \ln S_x + \frac{\Omega E x(\delta - n/x)^2}{9(1-\nu)}, \quad (9.50)$$

where S_{v} is the vacancy supersaturation, S_x is the solute supersaturation, Ω is the atomic volume of the precipitate, $\delta = (\Omega - \Omega_{\mathrm{m}})/\Omega_{\mathrm{m}}$, γ is the matrix–precipitate surface energy, E is Young's modulus, ν is Poisson's ratio, and the remaining variables are as previously defined. The first two terms are the same as in the formation of a void from a supersaturation of vacancies given in Eq. (8.17) in which the first term is due to the vacancy supersaturation and the second term is the contribution of surface energy (with the number of solute atoms substituted for the number of vacancies in the aggregate). The third term reflects the effect of solute supersaturation, analogous to vacancy supersaturation, and the last term accounts for the elastic (volume) strain energy due to either an excess or deficit of vacancies from the stress-free condition (given by $\delta = n/x$). Substituting Eqs. (9.48) and (9.49) for $\alpha_{\mathrm{v}}(n, x)$ and $\alpha_x(n, x)$ into Eqs. (9.43) and (9.44) gives:

$$\dot{x} = \beta_x(n,x) - \alpha_x(n,x) = \beta_x\left[1 - \exp\left(\frac{1}{kT}\frac{\partial \Delta G_{\mathrm{p}}^{0}}{\partial x}\right)\right], \quad (9.51)$$

$$\dot{n} = \beta_{\mathrm{v}}(n,x) - \alpha_{\mathrm{v}}(n,x) - \beta_{\mathrm{i}}(n,x) = \beta_{\mathrm{v}}\left[1 - \frac{\beta_{\mathrm{i}}}{\beta_{\mathrm{v}}} - \exp\left(\frac{1}{kT}\frac{\partial \Delta G_{\mathrm{p}}^{0}}{\partial n}\right)\right], \quad (9.52)$$

where from Eq. (9.50), the arguments of the exponents are determined to be:

$$\frac{1}{kT}\frac{\partial \Delta G_{\mathrm{p}}^{0}}{\partial x} = -\ln S_x + \frac{2Ax^{-1/3}}{3} + B(\delta^2 - n^2/x^2), \quad (9.53)$$

$$\frac{1}{kT}\frac{\partial \Delta G_{\mathrm{p}}^{0}}{\partial n} = -\ln S_{\mathrm{v}} - 2B(\delta - n/x), \quad (9.54)$$

with $A = \dfrac{(36\pi\Omega^2)^{1/3}\gamma}{kT}$ and $B = \dfrac{\Omega \mathrm{E}}{9kT(1-\nu)}$.

The behavior of the precipitate in (n, x) space may be described by constructing nodal lines in (n, x) space along which $\dot{x}$ and $\dot{n}$ individually are set equal to zero as follows:

$$n = x\left[\delta + \frac{1}{2B}\ln\left\{S_{\mathrm{v}}\left(1 - \frac{\beta_{\mathrm{i}}}{\beta_{\mathrm{v}}}\right)\right\}\right], \quad \text{for } \dot{n} = 0, \quad (9.55)$$

$$n = x\delta\left[1 + \frac{2A}{3B\delta^2 x^{1/3}} - \frac{1}{\delta^2 B}\ln S_x\right]^{1/2}, \quad \text{for } \dot{x} = 0. \quad (9.56)$$

Figure 9.15 shows that the nodal lines in (n, x) space converge and cross at a critical point, beyond which they diverge. The critical point (n^*, x^*) is found by solving Eqs. (9.55) and (9.56) simultaneously to obtain:

$$x^* = -\frac{32\pi\gamma^3\Omega^2}{3(\Delta\phi)^3}, \quad \text{or} \quad r_p^* = -\frac{2\gamma\Omega}{\Delta\phi} \tag{9.57}$$

$$n^* = x^*\left[\delta + \frac{1}{2B}\ln\left\{S_v\left(1 - \frac{\beta_i}{\beta_v}\right)\right\}\right], \tag{9.58}$$

where x^* and r_p^* are related by $x^* = \dfrac{4/3\pi r_p^2}{\Omega}$, and the irradiation-modified free energy is given by:

$$\Delta\phi = -kT\ln\left[S_x[S_v(1-\beta_i/\beta_v)]^\delta\right] - \frac{kT}{4B}[\ln(S_v(1-\beta_i/\beta_v))]^2. \tag{9.59}$$

Figure 9.15 is constructed for the case where $\delta > 0$, that is an excess of vacancies relative to solute. Under this condition, the region above the $\dot{n} = 0$ line contains an excess of vacancies and has a greater tendency for emission than capture, giving $\dot{n} < 0$, or shrinkage. The opposite is true for the $\dot{x} = 0$ nodal line in that the vacancy rich precipitate will decrease its strain energy by solute capture, causing $\dot{x} > 0$ and supporting growth. As shown, particle growth is determined by the quadrants defined by the critical point. Precipitates grow in quadrant 1 and decay in quadrant 3 and behavior in quadrants 2 and 4 depend on the values of the capture terms. Precipitates that are between the nodal lines cannot escape. When $x > x^*$, precipitates will grow and when $x < x^*$, they will decay. In general, irradiation will tend to stabilize a precipitate with $\delta > 0$ and destabilize ones with $\delta < 0$. Note that the unstable case of $\delta < 0$ means that $\Delta\phi > 0$, which can only occur if the first term in Eq. (9.59) is positive since the second term is always negative as long as $\beta_i/\beta_v < 1$.

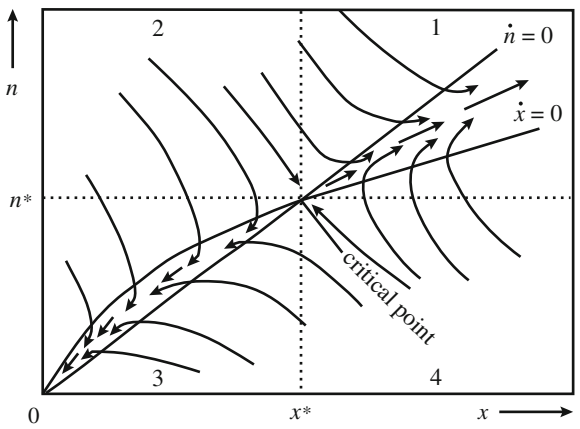

Fig. 9.15 Nodal lines, critical points, and precipitate trajectories in (n, x) phase space for growth of an oversized, incoherent precipitate under irradiation (after [20])

Physically, this means that since there is a *net* arrival of vacancies to the precipitate, those precipitates that need the vacancies to grow (e.g., an oversized precipitate, $\delta > 0$) will be stabilized by irradiation.

For an undersized precipitate phase ($\delta < 0$) to grow from a slightly supersaturated solid solution without prohibitive strain energy, the particle must emit vacancies into the matrix. In the absence of excess vacancies, this is easily done, as vacancies arrive at and leave the interface at the same rate (in the absence of growth or decay), and there is no trouble in establishing a net flux out to allow growth. Under irradiation, the vacancy emission rate is not altered, but the arrival rate is increased by several orders of magnitude. It is then almost impossible to achieve a net emission of vacancies. There will instead tend to be a net gain of solute atoms in the face of the slight solute supersaturation. The excess vacancies thus destabilize the undersized precipitate phase. The same arguments may be used to understand stabilization of an oversized precipitate.

The potential function given in Eq. (9.59) has some of the properties of a free energy. It predicts whether precipitates of a given size will be stable under irradiation and provides the minimum stable precipitate size. In the absence of excess vacancies due to irradiation, $\Delta\phi$ in Eq. (9.59) becomes $\Delta\phi = -kT \ln S_x$, which is the Gibbs–Thompson equation. The effect of irradiation is to shift the effective free energy curve for the precipitate vertically by the amount $\delta kT \ln[S_v(1 - \beta_i/\beta_v)]$. If $\Delta\phi < 0$, precipitates larger than x^* will be stable, and if $\Delta\phi > 0$, all precipitates will decay. This is shown schematically in Fig. 9.16. For this alloy, the θ phase is thermally stable and the ψ phase is not. The effect of irradiation is to destabilize the θ phase ($\delta < 0$) and stabilize the ψ phase ($\delta > 0$), by virtue of the sign of δ. Note that the order of stability is reversed by irradiation so that the θ phase would dissolve and the ψ phase would precipitate. The precipitation of the ψ phase under irradiation is an example of irradiation-induced precipitation in an undersaturated solid solution.

The nucleation rate of precipitates due to irradiation can also be estimated. The nucleation rate is the number of precipitate nuclei growing past a certain value of

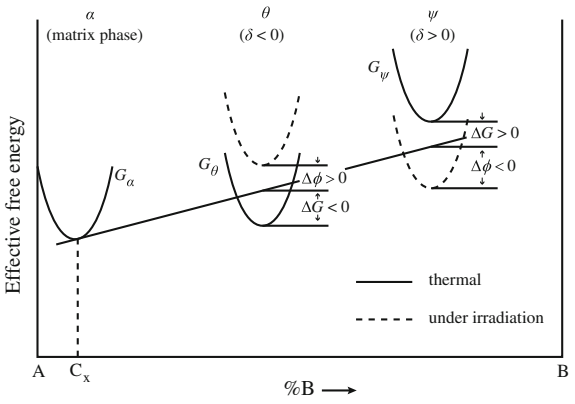

Fig. 9.16 Schematic phase diagram showing the effect of irradiation on the stability of incoherent precipitates in the case where the precipitate is thermally stable (θ) and thermally unstable (ψ) (after [21])

x per unit time and volume [22]. At steady state, the nucleation flux is independent of x, and the nucleation rate can be given at an arbitrary value of x as:

$$J_{\mathrm{p}}(x) = \sum_{n=-\infty}^{\infty} [\beta_x(x)\rho_{\mathrm{p}}(n,x) - \alpha_x(n,x)\rho_{\mathrm{p}}(n,x+1)], \tag{9.60}$$

and the summation converges rapidly for large values of n due to the effect of strain energy. Figure 9.17 shows how the nucleation rate varies with supersaturation of vacancies and solute in the Al–2 %Ge system under irradiation. As expected, the nucleation rate increases with both S_x and S_v, but is more sensitive to S_x. Figure 9.17(a)

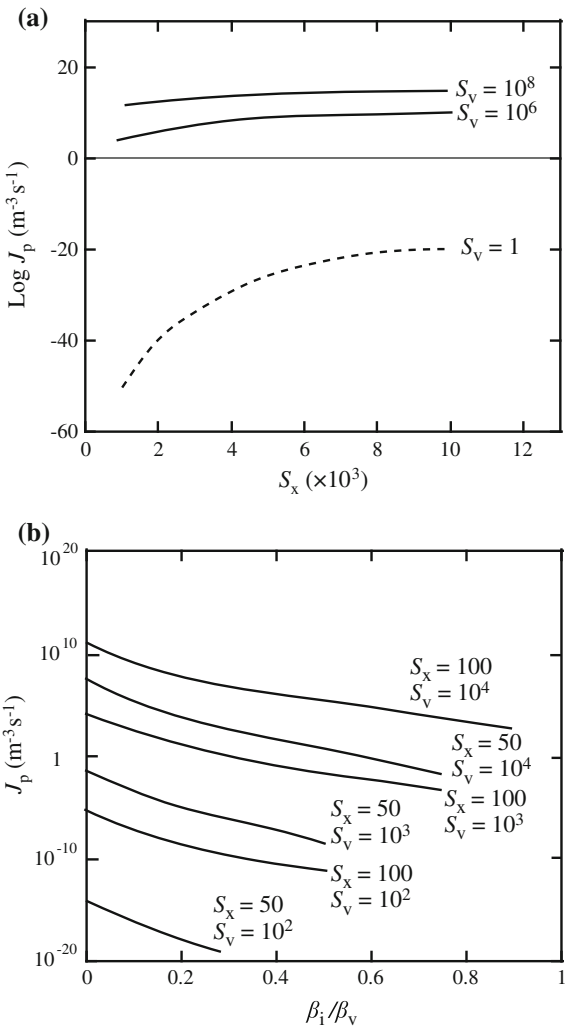

Fig. 9.17 (**a**) Dependence of nucleation rate on solute supersaturation for various vacancy supersaturation levels, based on a solid solution of Ge in Al at 27 °C. (**b**) Effect of interstitial–vacancy arrival rate ratio on the nucleation rate for several solute and vacancy supersaturation levels, based on a solid solution of Ge in Al at 127 °C (after [21])

shows the huge effect of excess vacancies alone on precipitate nucleation. Excess vacancies elevate the nucleation rate from infinitesimal to a high value giving a high precipitate density. Figure 9.17(b) shows that the effect of excess interstitials is to reduce the nucleation rate somewhat, but by factors small compared to the huge enhancements due to the vacancies. Irradiation is thus a tool for creating phases which otherwise might be impossible to obtain, and also for preventing the formation of phases that are otherwise stable.

9.5 Coherent Precipitate Nucleation

The preceding analysis applies for the precipitation of incoherent precipitates from a solid solution due to irradiation. We consider here the precipitation of *coherent* precipitates due to irradiation. The distinction between these two cases lies in the behavior of point defects at the precipitate surface. As shown in Chap. 8, incoherent precipitates behave like voids in that defects can be absorbed and emitted. However, the coherent precipitate interface acts as a defect trap such that the defect retains its identity. This feature has the result of reducing the problem of determining the energy change due to precipitation from a two-dimensional (n, x) problem to a one-dimensional (x) problem. Cauvin and Martin [23], as summarized by Russell [14], described the pseudo-equilibrium precipitate size distribution under irradiation, $\rho'(x)$, as:

$$\frac{\rho'(x)}{\rho'(x+1)} = \frac{\rho^0(x)}{\rho^0(x+1)} B(x), \tag{9.61}$$

where $\rho^0(x)$ is the equilibrium size distribution in the absence of irradiation produced defects, and $B(x)$ is defined by:

$$B(x) = \frac{\beta_v(x)[\rho_v(x) + \rho_n(x)] + \beta_i(x)[\rho_i(x) + \rho_n(x)]}{[\beta_v(x) + \beta_i(x)]\rho_t(x)}, \tag{9.62}$$

where

$\rho_i(x)$ is number of clusters with trapped interstitials,
$\rho_v(x)$ is number of clusters with trapped vacancies,
$\rho_n(x)$ is number of clusters with no trapped defects, and
$\rho_t(x) = \rho_i(x) + \rho_v(x) + \rho_n(x)$.

The quantity $B(x)$ is the fraction of solute arriving at the precipitate that does *not* result in defect annihilation. The thermal and irradiation-modified solubilities are related by: $C_{irr} = C_0 B(\infty)$. In parallel with the equilibrium free energy, the pseudo-free energy, $\Delta G'(x)$, is given in terms of the pseudo-equilibrium precipitate size distribution, $\rho'(x)$, as:

$$\frac{\rho'(x)}{\rho'(x+1)} = \exp\left(\frac{1}{kT}\frac{\partial \Delta G'}{\partial x}\right). \tag{9.63}$$

As with an unirradiated solid solution in which a metastable condition exists if $G(x)$ has a maximum in x, then $G'(x)$ must have a maximum in x for metastability in the irradiated state. Recalling that $\rho^0(x) = \exp(-G^0(x)/kT)$, then Eq. (9.61) can be rewritten using Eq. (9.63) as:

$$\frac{\partial G'(x)}{\partial x} = \frac{\partial \Delta G^0(x)}{\partial x} + kT \ln B(x), \tag{9.64}$$

and $B(x)$ has one of two forms depending on the sign of the term, σ defined as:

$$\sigma = \frac{(1 - p_i/p_v)}{(1 - \beta_i/\beta_v)}. \tag{9.65}$$

where $p_{i,v}$ is the probability of a particular trapping site being occupied by an interstitial or a vacancy. For either case, the value of B approaches a constant with increasing values of x, and in similar fashion for large x:

$$\frac{\partial \Delta G^0(x)}{\partial x} = -kT \ln S_x, \tag{9.66}$$

and Eq. (9.64) can be written as:

$$\frac{\partial G'(x)}{\partial x} = -kT \ln S_x + kT \ln B(x). \tag{9.67}$$

Figure 9.18 shows the terms of the expression in Eq. (9.64) for the pseudo-free energy of the solid solution under irradiation for various values of σ. When $\sigma < 0$, if $-kT \ln B(\infty) > -kT \ln S_x$, then the solution will be metastable, as in Fig. 9.18(a). If $\sigma > 0$, then the solution to $\dfrac{\partial G'(x)}{\partial x} = 0$ may have 0, 1, or 2 roots. The solid solution is stable if there are zero roots. With one root, the solution is metastable (Fig. 9.18(b)). But in the case of 2 roots (Fig. 9.18(c)), the solution is metastable below the value x^{**}, and the precipitate could never grow to large size. Note that in this model, irradiation will always decrease solid solubility.

A compilation of precipitates formed in undersaturated solid solutions due to irradiation is shown in Table 9.1. Note that precipitation can occur with many particle types and over large ranges of temperature and dose rate. The relation between these latter two variables is important and is highlighted in Fig. 9.18(d) and (e). Figure 9.18(d) is constructed from 1 MeV irradiation of several undersaturated Ni–Si solid solution alloys and delineates the region of Ni_3Si, γ' precipitation from the solid solution, as shown by the filled circles. Figure 9.18(e) shows the dose dependence of solubility in Al–Zn. With increasing dose rate, formation of Guinier–Preston (GP) zones (Zn-rich

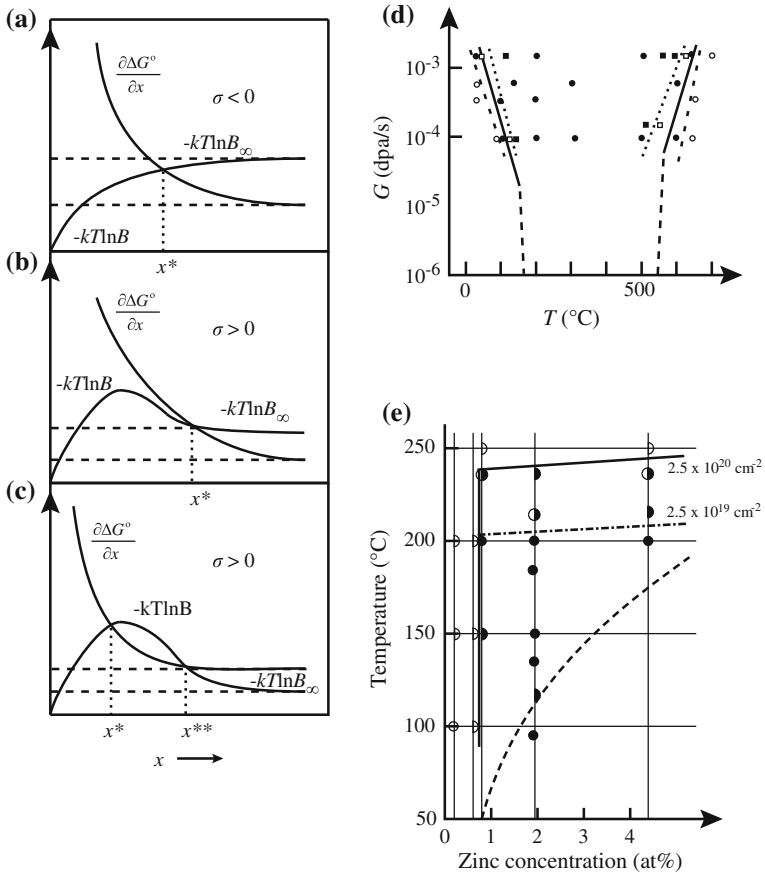

Fig. 9.18 Schematic illustration of stability altered by defect recombination at the particle–matrix interface. (**a**) $\sigma < 0$, 1 root. (**b**) $\sigma > 0$, 1 root. (**c**) $\sigma > 0$, 2 roots (from [23]). (**d**) Dose rate–temperature dependence of precipitation of Ni_3Si, γ' from undersaturated Ni–Si solid solution alloys irradiated with 1 MeV electrons, - - - Ni–6at.%Si, — Ni–4at.%Si, ····· Ni–2at.%Si. (**e**) Increase in temperature at which Zn-rich clusters, or GP zones are stable with increasing irradiation dose rate by 1 MeV electrons over a range of Zn concentration in the Al–Zn phase diagram. *Half circles* to the right (left) indicate data at high (low) irradiation flux. *Full* (*open*) *symbols* indicated occurrence (absence) of irradiation-induced precipitation. *Dashed line* is the stability limit in the absence of irradiation (after [24])

clusters) in Al–Zn occurs at higher temperatures compared to the stability limit in the absence of irradiation (dashed line). Both of these examples show that irradiation of an undersaturated solid solution can lead to precipitation under irradiation at temperatures where the precipitate would not be thermally stable. They also underscore the strong coupling between temperature and dose rate in irradiation-induced precipitation.

Table 9.1 Irradiation-induced precipitation in undersaturated binary alloys (after [24])

Alloy	Projectile	Precipitate	Morphology
MgCd	e^-	Mg_3Cd	–
AlZn	n	β Zn	Homogeneous precipitation
	e^-	GP zones and β Zn	Homogeneous precipitation
AlAg	e^-	(100) Ag-rich platelets	Homogeneous precipitation
NiBe	Ni^+	β NiBe	At interstitial dislocation loops
	e^-	β NiBe	Homogeneous precipitation and at interstitial dislocation loops
NiSi	n	γ' Ni_3Si	At interstitial dislocation loops
	Ni^+	γ' Ni_3Si	At interstitial dislocation loops
	e^-	γ' Ni_3Si	At interstitial dislocation loops
	H^+	γ' Ni_3Si	Coherent, triggered by inhomogeneity of defect production
NiGe	e^-	γ' Ni_3Ge	At cavities and dislocation lines
CuBe	e^-	GP zones	Homogeneous precipitation
	Cu^+	γ	At cascades
PdMo	Cu^+	Mo	At dislocation loops
PdFe	H^+	γ' Pd_3Fe	At dislocation loops
PdW	H^+, N^+, e^-	bcc W	At dislocation loops
WRe	n	WRe_3, W-Re	Homogeneous precipitation
FeV	e^-	Unidentified	Homogeneous precipitation
FeCr	e^-	Unidentified	Homogeneous precipitation
Various ternaries	n, ions, e^-	Changes of composition	–

In summary, irradiation can affect phase stability by numerous processes: solute enrichment or depletion, precipitate re-solution, precipitate disordering, and irradiation-induced nucleation of both incoherent and coherent precipitates. Irradiation can also induce the formation of phases that are not stable under equilibrium conditions or metastable phases. Metastable phase formation is discussed in the next section.

9.6 Examples of Radiation-Induced Precipitation

The following sections contain examples of radiation-induced precipitation in ferritic–martensitic steels and austenitic stainless steels. The bulk of the examples are from atom probe tomography (APT), which provides information on the local composition but not the crystal structure. Precipitation of distinct phases generally occurs once the local composition exceeds a phase boundary, so the early stages of

precipitation are more accurately described as solute clustering in which the local composition is enriched in solute but not to the point where a distinct phase has formed. Therefore, in the following sections, such regions will be referred to generally as solute clusters unless distinct phases were positively identified.

9.6.1 Ferritic–Martensitic Steels

Ferritic–martensitic (FM) steels are candidates for both fast reactor cladding and ducts and replacement core structural components in light water reactors. They contain 9–12 wt% Cr, and several minor alloying elements designed for resistance to creep at high temperatures. Precipitates that form under irradiation are very sensitive to the alloy content as shown in Fig. 9.19, which contains images of clusters in atom probe tips formed following irradiation to 7 dpa at 400 °C with 2 MeV protons. Note that in alloy T91, Cu-rich and Ni/Si-rich clusters form, but there is no evidence of Cr-rich phases due to the low Cr content of the steel. In both HCM12A and HT9, which contain higher levels of Cr, Cr-rich clusters were observed to form. Cu-rich clusters/precipitates form in HCM12A containing 1.02 % Cu, but not in HT9, which contains only 0.04 wt% Cu. However, Ni/Si-rich clusters form in all three alloys because the Ni and Si contents are similar.

Clusters tend to nucleate heterogeneously on existing defects in the microstructure, which act as point defect sinks and thus, sites for radiation-induced segregation. Figure 9.20 shows examples of Ni/Si cluster nucleation on grain boundaries in HT9 (Fig. 9.20(a)), dislocation loops and lines in HCM12A

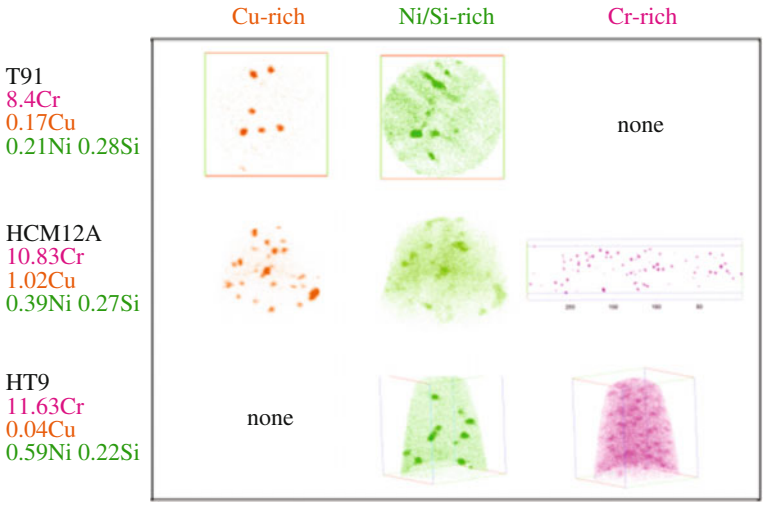

Fig. 9.19 Radiation-induced Cu-rich, Ni/Si and Cr-rich clusters in T91, HCM12A, and HT9 irradiated with 2 MeV protons to 7 dpa at 400 °C (after [25])

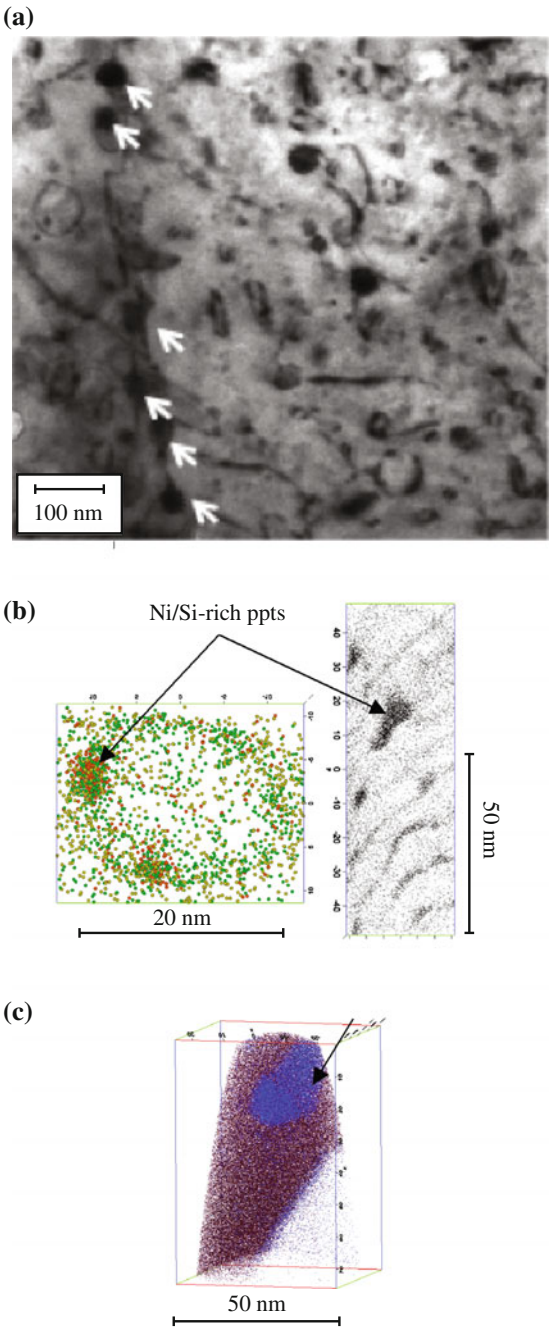

Fig. 9.20 Association of Ni/Si clusters or precipitates with various microstructure sinks; (**a**) on grain boundaries in alloy HT9 following irradiation with Fe^{++} to 188 dpa at 460 °C (after [26]), (**b**) on dislocation loops and lines in HCM12A irradiated with protons to 7 dpa at 400 °C, and (**c**) on a $Cr_{23}C_6$ chromium carbide in HT9 irradiated with Fe^{++} to 250 dpa at 500 °C

(Fig. 9.20(b)) and on existing chromium carbides in HT9 (Fig. 9.20(c)). In alloy HCM12A, clusters begin to form at relatively low dose—by 3.5 dpa for Cu and Ni/Si following irradiation at 400 °C with 5 MeV Fe^{++} (Fig. 9.21). This is a bit surprising since void formation in these same alloys requires in excess of 100 dpa to produce observable (by TEM) voids. A close inspection of Fig. 9.21 reveals that the locations of Ni/Si-rich clusters and Cu-rich clusters are correlated, as shown in Fig. 9.22. In fact, Ni/Si-rich clusters appear to be forming on previously formed Cu-rich clusters. Cr-rich clusters are slower to form and result in much lower density and smaller sizes.

With increasing dose, the density and size of clusters increase initially, followed by a decrease in density while size continues to increase. This coarsening process is

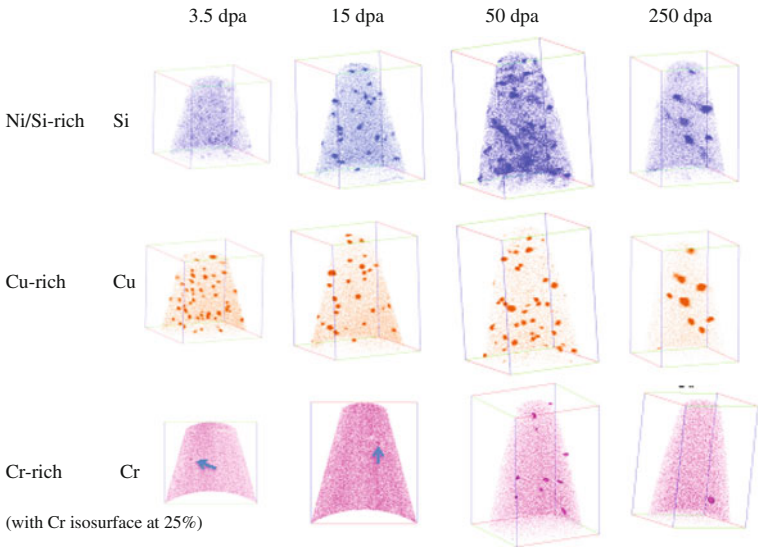

Fig. 9.21 Dose dependence of cluster/precipitate evolution (Ni/Si, Cu-rich and Cr-rich) in HCM12A irradiated with 5 MeV Fe^{++} from 3.5 to 250 dpa at 400 °C

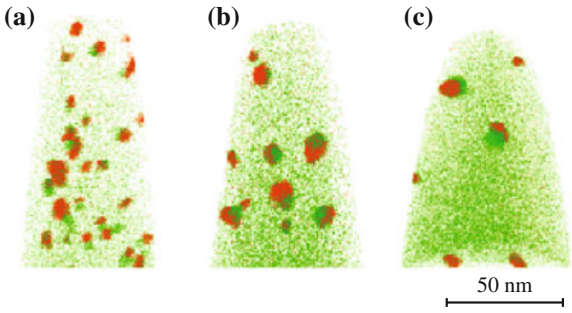

Fig. 9.22 Ni/Si/Mn-rich (*green*) and Cu-rich (*red*) clusters/precipitates in HCM12A following 2 MeV proton irradiation to (**a**) 7 dpa at 400 °C and (**b**) 7 dpa at 500 °C, and (**c**) following Fe^{++} irradiation to 50 dpa at 500 °C (after [27])

shown for T91 in Fig. 9.23(a) and for HCM12A in Fig. 9.23(b) during irradiation at 400 °C. Increasing the temperature to 500 °C results in a lower density of larger clusters, Fig. 9.23(b), as expected. Clusters continue to evolve up through 250 dpa. In fact, not only do the size and density change, but so do the composition and structure. Figure 9.24 shows examples of Ni/Si/Mn-rich clusters in alloy T91 following irradiation at 400 °C to 15 and 250 dpa. Note that at 15 dpa, the cluster is rather *dilute* in that the composition at the core of the cluster reaches only ~20 % Ni-20 %Si with minimal Mn. Given the composition, it is likely a Ni/Si-rich cluster rather than a separate phase. However, by 250 dpa, the composition of the cluster is 18Mn-52Ni-24Si, which is very close to the composition of G-phase ($Mn_6Ni_{16}Si_7$) confirmed by electron diffraction in TEM. Thus, RIS at point defect sinks results in solute enriched clusters, which later evolve into distinct phases.

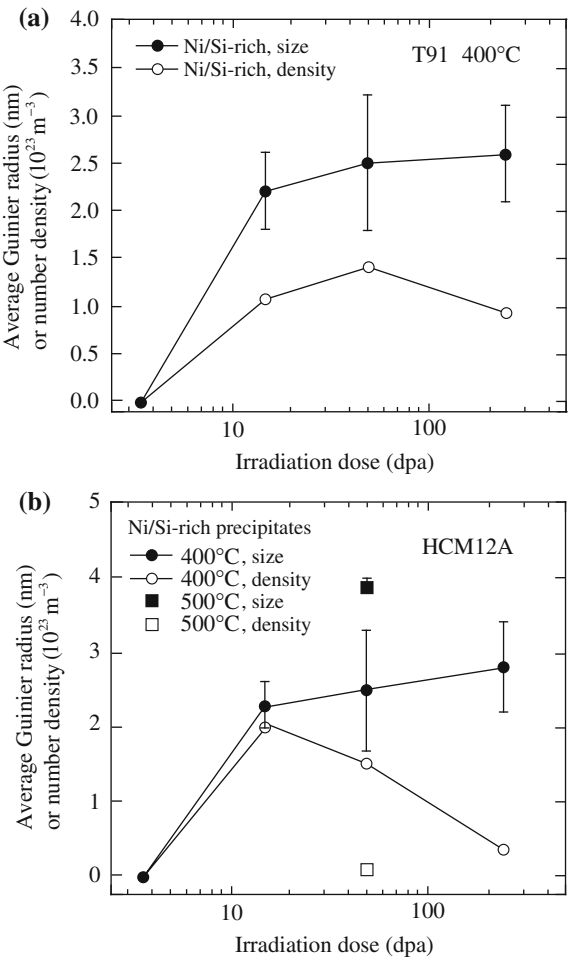

Fig. 9.23 Evolution of Ni/Si-rich cluster size and number density with irradiation dose for 5 MeV Fe^{++} irradiations up to 250 dpa (**a**) in T91 at 400 °C, and (**b**) in HCM12A at 400 and 500 °C

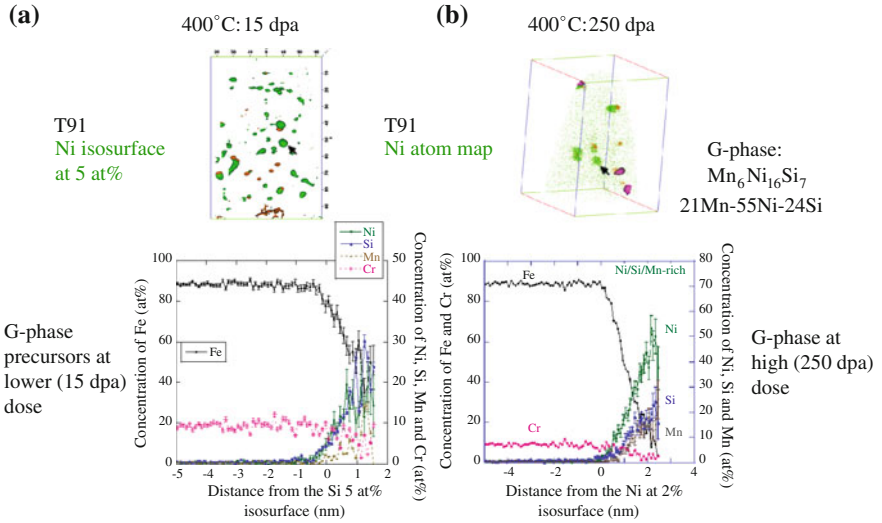

Fig. 9.24 Evolution of the composition of Ni/Si-rich clusters in alloy T91 irradiated with 5 MeV Fe^{++} irradiations at 400 °C to (**a**) 15 dpa, and (**b**) 250 dpa

At very high doses (≥250 dpa), irradiation induces the formation of a chromium-rich phase. Figure 9.25 shows the emergence of Cr-rich M_2X precipitates that are aligned along crystallographic directions.

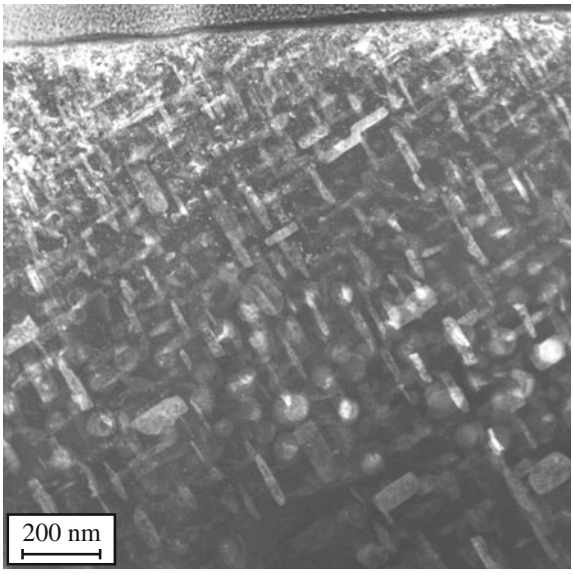

Fig. 9.25 Bright-field TEM image of chromium-rich M_2X precipitates formed in HT9 following 5 MeV Fe^{++} irradiation to 450 dpa at 460 °C

9.6.2 *Austenitic Stainless Steels*

Radiation-induced precipitation in austenitic stainless steels is in many ways, very similar to that in FM steels. Common precipitates formed are G-phase ($Mn_6Ni_{16}Si_7$), γ' (Ni_3Si), and Cu-rich clusters. Figure 9.26 shows that irradiation of a commercial purity 304 SS to 10 dpa at 360 °C with 2 MeV protons resulted in the segregation of Ni, Si, P, and Cu to larger clusters such as dislocation loops. High number densities of Ni/Si and Cu clusters were observed to form at existing dislocation loops. At this low dose, the clusters are regions of enhanced solute concentration, but are not separate phases because the concentration is still rather dilute. Irradiation to higher dose (46 dpa) results in much higher Ni and Si concentrations and formation of G-phase as confirmed by electron diffraction in TEM [29]. Cu clusters first observed by Jiao and Was [30], were unexpected, and likely were the result of a higher level of Cu (0.42 wt%) in this alloy heat.

Similar to the case for voids described in Sect. 8.3.10, the presence of defect sinks produces strong gradients in both vacancy and interstitial concentration

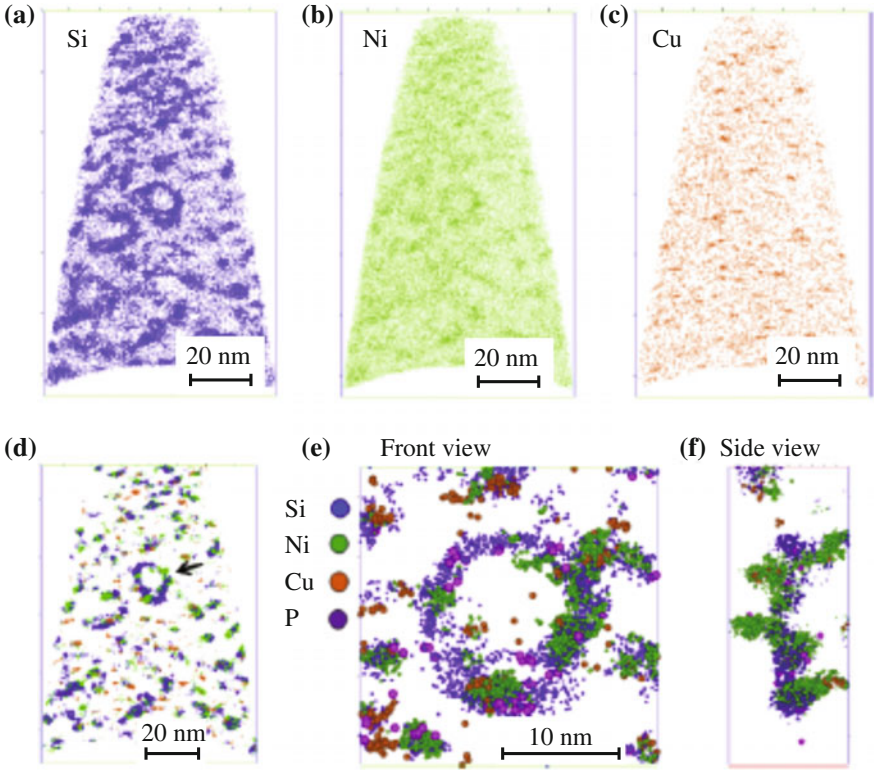

Fig. 9.26 Atom maps of (**a**) Si, (**b**) Ni, and (**c**) Cu in APT tips of commercial purity 304 SS irradiated with 2 MeV protons to 10 dpa at 360 °C. (**d**)–(**f**) Filtered atom maps showing Si atoms over 6.3 at.% Si, Ni atoms over 23 at.% Ni, Cu atoms over 3 at.% Cu and P atoms over 2 at.% P (after [28])

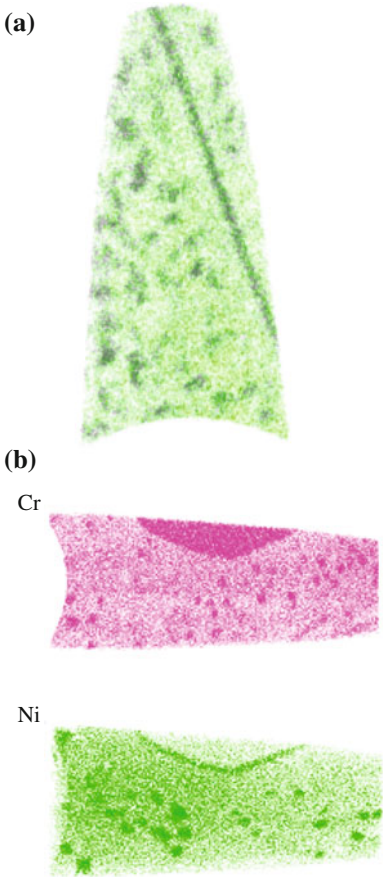

Fig. 9.27 Denuded zone for Ni/Si-rich clusters about (**a**) grain boundary in high-purity 304 SS + Si irradiated with 2 MeV protons to 5 dpa at 360 °C (after [30]), and (**b**) chromium carbide–matrix phase boundary in HCM12A irradiated with 2 MeV protons to 7 dpa at 400 °C (after [25])

profiles, reducing the degrees of supersaturation as the sink is approached. Hence, the driving force for precipitation is reduced and denuded zones form around these sinks. Figure 9.27(a) shows a grain boundary in HP304+Si irradiated to 5 dpa at 360 °C denuded of Ni/Si-rich clusters. Figure 9.27(b) shows a denuded region around a chromium carbide in HCM12A irradiated to 7 dpa at 400 °C. Note that in this case, both Ni/Si-rich precipitates and Cr-rich precipitates are denuded near the phase boundary.

9.7 Metastable Phases

Since the term *metastable* implies a phase with a free energy higher than that of the stable phase under the prevailing conditions of temperature and pressure, it is natural to look to thermodynamics to explain their formation under irradiation.

Experimental results seem to indicate a strong role of thermodynamics in the tendency to form metastable phases. Intermetallic compounds with small ranges of solubility and complex crystal structures are prime candidates for transformation to a metastable phase [19]. Also, the change in the free energy of the solid due to irradiation-induced defect buildup argues for a thermodynamic explanation [31]. However, not all transformations can be explained on a purely thermodynamic basis as solids under irradiation are generally far from equilibrium. Irradiation can be considered as similar to a quench process in which the atom configurations are essentially determined during the relaxation period following the collision events. At low temperatures, kinetics are restricted and the formation of complex crystalline structures is unlikely. Irradiation will usually result in solid solution, simple cubic structures, or amorphous structures. The structure of the metastable system is, however, influenced by the equilibrium nature of the system. Those systems with many intermetallic compounds will form amorphous phases, while those with no intermetallic alloys show a tendency to form solid solutions. At high temperature where atom mobility is significant, equilibrium phases will usually form.

Metastable phases can be formed by neutron irradiation or by ion irradiation, ion implantation, and ion beam mixing. Differences in the transformation process between ion irradiation techniques can provide insight into the mechanism governing metastable phase formation. For example, in ion irradiation experiments, the main result of the radiation is imparting damage to the lattice. However, in ion implantation the implanted species provides a chemical alteration to the target as well. Ion beam mixing experiments are designed to follow the transformation by rapidly (far from equilibrium) altering the bulk content of the film. Metastable phases formed by irradiation usually occur by one of four types of transformations [32]:

order $\rightarrow$ disorder,
crystal structure transformation: A $\rightarrow$ B,
crystal structure A $\rightarrow$ quasicrystal structure, and
crystal structure A $\rightarrow$ amorphous structure.

The first three transformations will be briefly discussed and amorphization will be discussed in Sect. 9.8. For a more complete discussion of metastable phase formation, the reader is referred to [33].

9.7.1 Order–Disorder Transformations

The order–disorder transformation and its role in phase stability were discussed in Sect. 9.3. However, radiation-induced disorder has been linked to metastable phase formation. In fact, many compounds are believed to undergo chemical disordering prior to amorphization under electron irradiation. Luzzi and Meshii [34] showed

that of 32 compounds irradiated, all underwent chemical disordering and 15 amorphized. They concluded that irradiation-induced chemical disordering provided the driving force for amorphization and cited the difficulty in forming the amorphous structure in pure metals as support for this argument. The linkage between disordering and amorphization also depends on the irradiation conditions, in particular the mass of the particle and whether damage is introduced via Frenkel pairs (electron irradiation) or in cascades (heavy ion irradiation). Comparison of the enthalpy for the order–disorder transformation to that for the crystalline-to-amorphous transformation shows that $\Delta H_{\text{O-D}} \sim 5\Delta H_{\text{c-a}}$ [16]. So in fact, the enthalpy change for disordering may be sufficient to induce amorphization. The role of disordering in the onset of amorphization will be discussed in Sect. 9.8.

9.7.2 Crystal Structure Transformations

Numerous examples exist on the transformation from one crystal structure to another upon ion irradiation. One of the simplest examples is the transformation of pure nickel metal from fcc to hcp under irradiation. This transformation has been found to occur during irradiation with a variety of species including neutrons, chemically inert elements such as He and Ar, the metalloids P and As, as well as self-irradiation [35]. Observations on P-implanted high-purity Ni [36] revealed an orientation relationship between the new hcp phase and the fcc matrix similar to that observed for martensitic fcc $\rightarrow$ hcp transformations. The transformation in Ni is thus believed to be martensitic. TEM examination of Sb-implanted Ni showed hcp particles extending 20 nm beyond the implanted depth, but dechanneling is present up to 130 nm, suggesting that the defect distribution is playing a role in the structure transformation.

Ion irradiation has also been found to induce phase transformations between bcc and fcc phases in iron-based austenitic alloys [37]. The most prominent example is the fcc-to-bcc transformation of 304 stainless steel following implantation with $3 \times 10^{16}\text{Fe}^{+}/\text{cm}^2$ at 160 keV. Although this dose amounted to an increase in the Fe alloy composition by only $\sim$1 at.% (67 at.% Fe nominal), the structure transformed from fcc $\rightarrow$ bcc. The orientation relationship was neither the Kurdjumov–Sachs nor the Nishijima–Wasserman relationships typically found in ion-irradiated steels [37], but instead obeyed the following relationship:

$$(100)_{\text{bcc}} \parallel (100)_{\text{fcc}} \quad \text{and} \quad [010]_{\text{bcc}} \parallel [011]_{\text{fcc}}. \tag{9.68}$$

Follstaedt [38] suggested that the transformation need not be occurring martensitically, but that the increased defect concentration and hence, diffusivity, may be responsible for the transformation. It should also be noted that this transformation is fundamentally different from that of nickel under irradiation in that the

transformation is from the metastable state to the equilibrium structure, whereas in the case of Ni, the transformation is from the equilibrium fcc structure to a metastable hcp structure.

The heat of formation of an alloy can have a strong influence on whether a metastable phase forms. Figure 9.28 shows the irradiation-induced solubilities for several binary metal systems as a function of the heat of formation, ΔH_f. The samples were in the form of multilayers and were bombarded at 77 K by 400 keV Kr^+ ions. All systems had positive values of ΔH_f, meaning that in thermal equilibrium there is no or only a limited miscibility of the components of the considered system. Note that the data points of the systems whose components have the same structures and of systems with components of different structure follow smooth curves. Both curves exhibit a rapid decrease from complete solubility to levels below 15 at.% in a range of ΔH_f of about 12 kJ/mol. However, even at large values of ΔH_f, the solubility still has not disappeared.

Metastable solid solutions can also form by displacement mixing at temperatures at which radiation-enhanced diffusion is sufficiently slow to maintain the supersaturated solid solution phase. Ion beam mixing of multilayered Ag–Cu targets form a continuous series of metastable solid solutions across the phase diagram. Although the phase diagram of the Cu–Ag system is a simple eutectic one with rather small solubilities of Ag in Cu and Cu in Ag, irradiation produced a single phase, metastable solid solution with the fcc structure across the entire Cu–Ag system [40]. Since ion beam mixing takes place mainly in the solid state, extended solid solutions can be achieved in nearly immiscible systems such as Ag–Ni. Even in the binary Au–Fe and Au–V systems which have more complex phase diagrams exhibiting a large solubility gap and several intermetallic compounds, respectively,

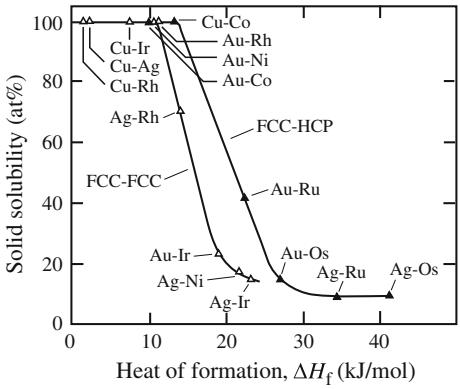

Fig. 9.28 Irradiation-induced solid solubilities for binary metal systems of positive heats of formation (after [39])

and the bcc structure at the Fe- and V-rich terminal solid solutions, metastable solid solutions form across both systems during ion beam mixing [41]. In all cases, the lattice parameters of the solid solutions vary smoothly with composition and show small or moderate deviations from Vegard's law between the appropriate end-members.

9.7.3 Quasicrystal Formation

The most novel metastable phases are the quasicrystalline phases, produced by ion irradiation of specific Al alloys. These phases show long-range order, but possess forbidden crystalline symmetries such as five- or sixfold symmetry. The phase was discovered by Shectman et al. [42] at the National Bureau of Standards. Quasicrystals have positional order, but are neither periodically nor randomly spaced; instead, they are quasi-periodically spaced. This means that, given the position of one unit cell, the positions of the other unit cells are determined according to a predictable but subtle sequence that never quite repeats. Because these structures are highly ordered like crystals but are quasi-periodic instead of periodic, they have been called quasi-periodic crystals, or quasicrystals for short.

The first quasicrystals formed by ion irradiation were in the Al–Mn system and examples extend into ternary and quaternary systems as well. In these initial experiments, the quasicrystal phase was formed by irradiating alternating layers of Al and Mn in the composition $Al_{84}Mn_{16}$ with 400 keV Xe ions to doses of 2–10×10^{15}Xe/cm^2 at 80 °C [43, 44]. Results showed that the icosahedral phase forms without a separate thermal treatment at or above 80 °C, while the amorphous phase forms at 60 °C. The icosahedron is a regular polyhedron possessing twenty identical triangular faces, thirty edges, and twelve vertices. The black pentagons on the surface of a soccer ball are centered on the vertices of an icosahedron. This observed dependence on sample temperature suggests that the icosahedral phase does not form within the dense ion cascade, but rather during subsequent defect evolution. Similar results have been achieved with freestanding Al–Fe multilayered samples [45], indicating that both multilayered and amorphous samples can be transformed to the quasicrystalline phase. In addition to temperature, the composition of the samples has an important effect on quasicrystal formation, establishing that quasicrystals are formed within a well-defined composition and temperature region.

9.8 Amorphization

Irradiation can induce the formation of amorphous phases in alloys. Although the phase space available to an alloy is extremely large, only one point corresponds to an absolute minimum in free energy. This point represents the equilibrium phase.

Given sufficient time, at any temperature greater than zero, the system will find that point and settle into the equilibrium phase. Nonetheless, there are generally other minima in the free energy phase space, which are of varying depths. These other minima correspond to metastable phases. Certain of these phases exhibit compositional short-range order (CSRO) very similar to that of the equilibrium phase but with different compositional long-range order. Similarly, the spatial arrangements of the atoms on a small scale (topological short-range order, TSRO) can be very similar to the equilibrium phase but with different long-range order (such as fcc vs. hcp phases). In general, there may exist many phases with CSRO and TSRO that are nearly identical to the equilibrium phase. Common examples of such metastable phases include glasses and crystalline solids with a slightly different unit cell than the equilibrium.

It has been suggested that in alloys with large negative heats of formation, disruption of chemical short-range order will lead to lattice destabilization and the formation of an amorphous phase [46]. In fact, the data on ion irradiation of intermetallic compounds supports just this sort of conclusion [22, 46]. Contradicting these observations are results of electron irradiation that show that complete long-range disordering often precedes the formation of an amorphous phase [32, 47]. For intermetallic compounds such as NiAl or FeTi, electron irradiation disorders but does not amorphize the compounds [48]. Irradiation with light ions produces much the same result as electron irradiation in that the amorphous phase is difficult to form, suggesting that disruption of CSRO is not adequate for lattice destabilization and that another mechanism must be responsible for amorphization such as topological disorder [48–52]. In fact, self-ion irradiation of Ni that induces a phase change from stable fcc to metastable hcp as discussed in Sect. 9.7 clearly has no chemical component and must be a result of the topological disorder introduced into the system by the Ni^+ beam. The next two sections discuss the roles of heat of compound formation, crystal structure differences, solubility range of intermetallic compounds and the critical defect density on the formation of the amorphous phase.

9.8.1 Heat of Compound Formation and Crystal Structure Differences

A good correlation exists between the heat of formation of a compound and the formation of amorphous phases in metal–metal systems [53], with large negative heats of formation tending to amorphize under irradiation. A plot of the ratio of the atomic radii versus the heat of formation calculated using the Miedema model [54] shows where amorphization will occur (Fig. 9.29). In fact, alloys do not become amorphous if the heat of formation is greater than about +10 kJ/mol. However, the

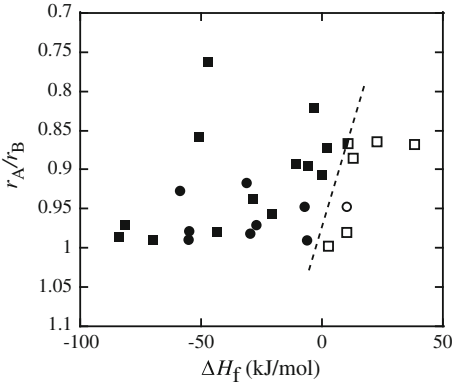

Fig. 9.29 Ratio of atomic radii versus the heat of formation of an equi-atomic compound (*square* metal–metal crystalline, *filled square* metal–metal amorphous, *circle* metal–metalloid crystalline, *filled circle* metalmetalloid amorphous) (after [53])

amorphous structure can be formed by ion mixing if the heat of formation is higher, e.g., Cr/Ag, Co/Cu, Fe/Cu, and Co/Au. Specific compositions in the Au–Ir, Au–Ru, and Au–Os systems, whose heats of formation range from +19 to +27 kJ/mol, were made amorphous by irradiation [39].

It has also been observed that crystalline phases of simple structures such as solid solutions or simple cubic structures form under irradiation, while amorphous phases are formed from more complex structures. This is explained by the short duration of the relaxation stage following the thermal spike. During the relaxation period, atoms attempt to rearrange themselves. If the relaxation time is sufficient for precipitates to nucleate, crystalline phase formation may be achieved. The time required for nucleation is strongly influenced by the temperature, the crystalline structure of nuclei and the composition of the films that have been homogenized with thermal treatments or ion beams. If the overall composition is not close to a simple crystal structure in the equilibrium phase diagram and there is not a strong chemical driving force (as well as mobility) to promote significant atomic motion, then crystalline phase formation may be inhibited.

The role of structure difference in the propensity for irradiation-induced amorphization can be understood with the aid of a binary constitution diagram of an A–B alloy (Fig. 9.30(a)), a schematic free energy diagram for this alloy (Fig. 9.30(b)) and the corresponding polymorphic phase diagram (Fig. 9.30(c)) [55]. Note that the T_0 curves in Fig. 9.30(c) are obtained from the crossing of the solid free energy curve with that of the liquid (or amorphous) curve at a given temperature. The T_0^{α} line defines the thermodynamic composition limits of the α-solution. When the concentration profile induced by mixing falls locally outside these limits, the α-solution is superheated with respect to the liquid (amorphous) phase and is not stable. Since melting is a local phenomenon not involving long-range diffusion, and

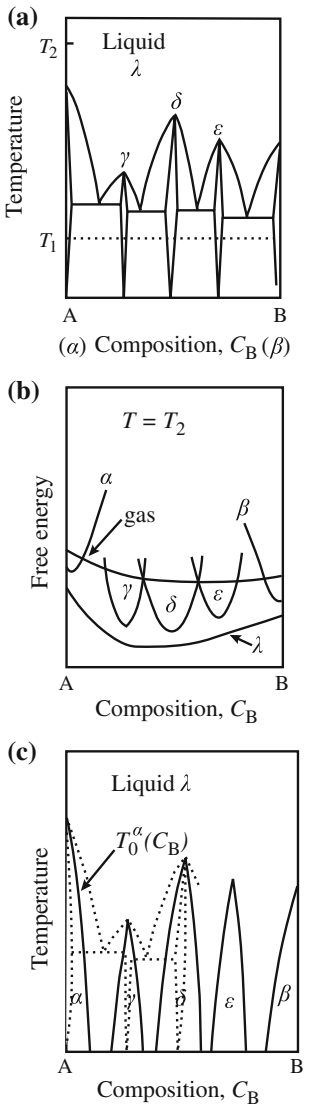

Fig. 9.30 (**a**) Binary constitution diagram of an A–B alloy. (**b**) Schematic free energy diagram for the alloy at temperature T_2. (**c**) Polymorphic phase diagram corresponding to the equilibrium phase diagram in part (**a**). The *dashed lines* show part of the original equilibrium diagram. *Solid lines* are representative T_0 lines of each phase. The T_0 lines define regions of polymorphic solid formation from the liquid state. Regions outside correspond to liquid or amorphous (polymorphic) states (after [55])

since solids are not observed to withstand extensive superheating, it follows that observation of an α-phase outside these composition limits represents an unstable state. Such a state will likely melt or amorphize before thermal spike evolution is complete. This leads to the first fundamental rule for solid-phase formation.

Johnson et al. [55] suggest that terminal solid solutions α and β can be formed up to the limits of the T_0^α and T_0^β curves (i.e., within the polymorphic phase diagram

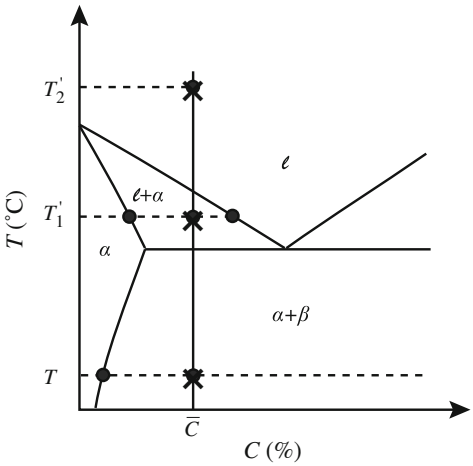

Fig. 9.31 Possible configurations of an equilibrium, two-phase alloy under irradiation at temperature T. Irradiation to an effective temperature, T_1' gives amorphous and crystalline phases of different composition, while more intense irradiation to an effective temperature, T_2' gives a single uniform amorphous phase (after [55])

limits of α and β). Solutions formed outside these limits are superheated and unstable against amorphization or melting. Secondly, intermetallic compounds with broad equilibrium homogeneity ranges (wide polymorphic limits in Fig. 9.30), and low-energy interfaces with α-solution or β-solution phases may form in the prompt cascade, provided that their respective growth kinetics allow high growth velocities. Compounds with narrow homogeneity range and complex chemically ordered unit cells should not form. Finally, amorphous phases are expected whenever the ion-induced composition profile $C_B(z)$ lies outside the polymorphic limits of crystalline phases. Amorphization may occur in addition when polymorphic limits permit compound formation but kinetics of compound formation or growth are slow.

Martin [56] proposed a theory for amorphization that is similar in nature to that of Johnson. In this model, he adds the ballistic radiation recoil re-solution displacement jumps to thermally activated jumps to obtain an irradiation-altered diffusion equation. The practical effect of irradiation is then to cause the system to assume the configuration at temperature T that would be stable at a temperature T' in the absence of irradiation: $T' = T\,(1 + D_B/D')$, where D' is the thermally activated diffusion coefficient and D_B is the diffusion coefficient including ballistic effects (Fig. 9.31). The theory predicts that irradiation of an equilibrium alloy of two solid phases at temperature T could raise the *effective* temperature to T_1', or under sufficiently intense irradiation to T_2'. At T_1' the irradiated alloy would at steady state be composed of amorphous and crystalline phases of different compositions. Irradiation intense enough to raise the effective temperature to T_2' would produce a uniform amorphous alloy.

9.8.2 Solubility Range of Compounds and Critical Defect Density

The tendency toward amorphization of the intermetallic compounds by irradiation correlates reasonably well with the degree of solubility within the phases. That is, alloys with limited solubility or a narrow compositional range show greater tendency for amorphous transformation. This correlation is also consistent with the concept that a critical energy or defect density must be created before the amorphous transformation can occur. If the total free energy of the defect crystalline state becomes greater than that of the amorphous state, a spontaneous transformation should occur. Associated with this critical free energy is a critical defect concentration. If this critical defect concentration can be reached under irradiation, then the crystal should relax into the lower free energy (amorphous) state. This critical defect concentration has been estimated at 0.02 for silicon and germanium [57]. An estimate of the defect concentration required for amorphization can be made based on the increase in energy of lattice upon formation of a stable Frenkel pair. Each Frenkel pair will raise the energy of the alloy by an amount equal to the enthalpy of defect formation, $\Delta H_{\mathrm{i-v}}$. The concentration of vacancy–interstitial pairs, $C_{\mathrm{i-v}}$, needed to increase the energy of the alloy by $\Delta H_{\mathrm{c\text{-}a}}$ can be estimated from the relationship:

$$\Delta H_{\mathrm{c-a}} = C_{\mathrm{i-v}} \Delta H_{\mathrm{i-v}}. \tag{9.69}$$

The magnitude of $\Delta H_{\mathrm{i-v}}$ for an fcc metal is approximately 5 eV, and $\Delta H_{\mathrm{c\text{-}a}}$ is approximately 0.06 eV/atom [16], giving the critical vacancy–interstitial concentration for amorphization as ~ 0.01. However, while such levels are not possible at reactor core component temperatures, they may be achievable in laboratory experiments conducted at temperatures where vacancies are immobile.

The link between defect density and degree of solubility can be understood by referring to the free energy diagram in Fig. 9.32. Compounds with no or limited compositional range will undergo a greater increase in free energy than those with wide compositional range. The greater increase in free energy is due to the inability of the compound to exist in equilibrium outside the designated composition range. This is manifest in the narrow and steeply rising free energy versus composition curves. For ordered phases (intermetallics), the increase is not only due to point defects, but anti-site defects in regions of localized non-stoichiometry. This proposed solubility rule is very consistent with Johnson's thermodynamic analysis [55]. Note that for $NiAl_3$, only a slight deviation from stoichiometry is needed to result in a very large rise in the free energy. Therefore, the critical anti-site defect density would be low for $NiAl_3$ as compared to NiAl.

Anti-site defects may play a critical role in the amorphization process since calculations have shown that the critical defect density may be difficult to reach

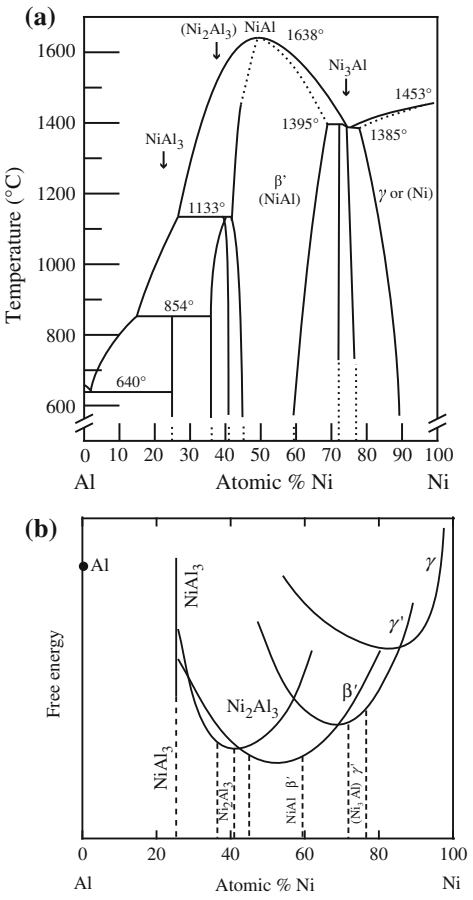

Fig. 9.32 Ni–Al phase diagram (**a**) with hypothetical free energy diagram (**b**) at the irradiation temperature (after [19])

accounting for only point defects. However, since the defect concentration is strongly dependent on atom mobility and this is largely unknown in intermetallic compounds, accurate estimates of defect concentration are difficult to determine. Further, the critical defect density will be strongly temperature dependent with higher concentrations required at higher temperatures.

Further support for the existence of a critical defect density is provided by the observation that compounds that become amorphous during irradiation do not show evidence of prior dislocation loop formation [31, 58]. Although it has been assumed that the attainment of a critical defect concentration will cause an amorphous transformation, the high free energy associated with the point defects can also be relieved through the formation of a dislocation structure through the collapse of interstitial or vacancy clusters into small loops. However, observations show that a material either transforms directly to the amorphous state or forms dislocation loops.

Since greater mobility is required for the formation of dislocation loops, and the maximum defect concentration associated with the nucleation of loops in irradiated metals is $\sim 10^{-4}$ [59], almost two orders of magnitude less than that for amorphization indicate that defect mobility is a key factor in the amorphization process. This observation is consistent with the ease of amorphization in intermetallics where defect mobility is low, and the preferential formation of dislocation loops in pure metals and solid solution alloys where the mobility is high.

9.8.3 Thermodynamics and Kinetics of Amorphization

In many respects, the C → A (crystalline-to-amorphous) transformation can be understood by relating it to melting by virtue of the similarity of these transformations. For example, amorphization is known to occur in a heterogeneous manner, similar to the first-order nucleation and growth process characteristic of melting. Also, Brillouin scattering studies have shown that intermetallics undergo a softening in the shear modulus, analogous to that observed at the onset of melting of many metals. As such, the C → A transformation can be considered to be a type of melting transformation. Okamoto et al. [60] wrote a comprehensive review of the physics of the crystalline-to-amorphous phase transformation. The role of irradiation in this transformation as presented in their paper is followed here.

The liquid-to-glass transition is characterized by a temperature called the glass transition temperature, T_g. The glass transition is not a thermodynamic phase transition, but rather the point in the relaxation process where configurational equilibrium can no longer be achieved during the experiment. In this regard, it is more of a kinetic parameter that depends on the timescale of observation. Free energy plots of the glass transition for perfect and defected crystals are shown in Fig. 9.33. The perfect crystal is shown by the bottom line, and the defected crystals, denoted by the dashed lines, have higher free energies. The melting temperatures are given by T_m^0 and T_m^d, respectively. Also shown are two glass transition temperatures, T_g corresponding to an unrelaxed glassy state and T_k corresponding to the ideal glass transition temperature. Since the glass transition temperature is dependent on time, it is postulated that there exists some temperature, T_k, below which the transition will never occur, and is known as the ideal glass temperature. Note that these points lie at a higher free energy than that of either the perfect crystal or the defected crystal.

As described by Okamoto et al. [60], one of the simplest models of melting is due to Lindemann [61] who proposed that crystals melt when the root-mean-square (rms) thermal displacement $\langle \delta_{vib}^2 \rangle^{1/2}$ of atoms from their equilibrium sites becomes large enough to encroach on nearest neighbors, or when the vibrational amplitude is about 50 % of the interatomic spacing. Thus, melting occurs when $\langle \delta_{vib}^2 \rangle^{1/2} / r_{nn}$ reaches a critical value equal to some fraction $\langle \delta_{crit}^2 \rangle^{1/2} / r_{nn}$ of the nearest-neighbor spacing, r_{nn}. In the harmonic Debye model of crystal lattices, the mean-square

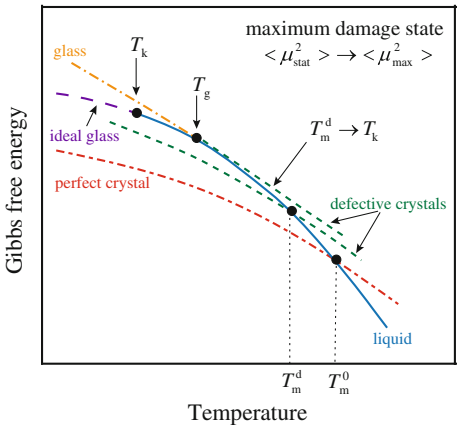

Fig. 9.33 Schematic plot of the Gibbs free energy as a function of temperature for a perfect crystal, the liquid phase and two defective crystalline states. T_m^0 and T_m^d are the thermodynamic melting temperatures of the perfect and defective crystals, respectively, T_g is the kinetic glass transition temperature for the unrelaxed glassy phase and T_k is the ideal glass transition temperature (after [60])

thermal displacement for a perfect crystal at a temperature T above the Debye temperature, Θ_0, is:

$$\langle \delta^2_{vib} \rangle = \frac{36\pi^2\hbar^2 T}{Mk\Theta_0^2}, \tag{9.70}$$

where $\hbar$ is Planck's constant, k is Boltzmann's constant, and M is the atomic mass. Since melting occurs when $\langle \delta^2_{vib} \rangle$ reaches some critical value. Then from Eq. (9.70), the melting temperature of the perfect crystal is:

$$T_m^0 = \frac{Mk\Theta_0^2}{36\pi^2\hbar^2} \langle \delta^2_{crit} \rangle. \tag{9.71}$$

The total mean-square atomic displacement is composed of thermal $\langle \delta^2_{vib} \rangle$ and static $\langle \delta^2_{stat} \rangle$ components, where the latter is due to defect structures such as point defects, anti-site defects, size mismatch between solute, solvent atoms in solid solution, defect clusters, and impurities. The generalized form of the Lindemann melting criterion then becomes:

$$\langle \delta^2_{crit} \rangle = \langle \delta^2_{stat} \rangle + \langle \delta^2_{vib} \rangle, \tag{9.72}$$

where $\langle \delta^2_{crit} \rangle$ is a constant. Referring back to Fig. 9.33, this criterion shows that the crystal can be melted either by heating it to the melting point, $T_m^0 \left(\langle \delta^2_{vib} \rangle = \langle \delta^2_{crit} \rangle \right)$ or by increasing the amount of static disorder, $\langle \delta^2_{stat} \rangle$ in the crystal until the free

energy is equal to that of the liquid. As the damage level increases, the melting temperature of the defective crystal, T_m^d defined by the intersection of the free energy curve with that of the supercooled liquid, decreases, as shown in Fig. 9.33. The maximum damage state will occur when the free energy curve of the defective crystal is tangent to that of the supercooled liquid, shown as the upper most dashed line in Fig. 9.33.

The state of maximum damage, $\langle \delta^2_{stat} \rangle = \langle \delta^2_{crit} \rangle$, or where $T_m^d = 0$, is the theoretical upper limit for damage accumulation in a defective crystal. Figure 9.34 shows a polymorphous melting curve for a defective crystal in which $\langle \delta^2_{stat} \rangle$ represents the sum total of the effect of all defects in the crystal. The linear region follows from Eq. (9.72). Along the melting curve, where $T = T_m^d$, Eq. (9.72) becomes:

$$\langle \delta^2_{crit} \rangle = \langle \delta^2_{stat} \rangle + \frac{36\pi^2\hbar^2 T_m^d}{Mk\Theta_0^2}, \tag{9.73}$$

which is written in the form of Eq. (9.71) as:

$$T_m^d = \frac{Mk\Theta_d^2}{36\pi^2\hbar^2} \langle \delta^2_{crit} \rangle, \tag{9.74}$$

where the Debye temperature of the defective crystal, Θ_d, is given as:

$$\Theta_d^2 = \Theta_0^2 \left(1 - \frac{\langle \delta^2_{stat} \rangle}{\langle \delta^2_{crit} \rangle} \right). \tag{9.75}$$

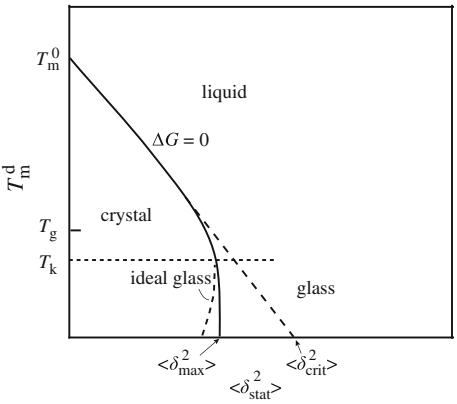

Fig. 9.34 Generalized T_0 curve showing schematically the effects of static atomic disorder as measured by $\langle \delta^2_{stat} \rangle$, on the melting temperature of the defective crystal, T_m^d . $\langle \delta^2_{max} \rangle$ and $\langle \delta^2_{crit} \rangle$ are the critical values of $\langle \delta^2_{stat} \rangle$ for thermodynamic and mechanical melting (after [60])

In a perfect crystal, $\langle \delta^2_{\text{stat}} \rangle \rightarrow 0$, $\Theta^2_{\text{d}} \rightarrow \Theta^2_0$, and $T^{\text{d}}_{\text{m}} \rightarrow T^{\text{d}}_0$. Note that Eq. (9.74) shows that the proportionality between the melting temperature and $\langle \delta^2_{\text{stat}} \rangle$, Fig. 9.34, is related to the Debye temperature given in Eq. (9.75). Also, since Θ^2_{d} is proportional to the shear modulus, μ_{d}, the linear decrease in melting temperature also means that disorder-induced reduction of the shear modulus is occurring with the same functional dependence on $\langle \delta^2_{\text{stat}} \rangle$. From these proportionalities, we can write:

$$\frac{T^{\text{d}}_{\text{m}}}{T^0_{\text{m}}} = \frac{\mu_{\text{d}}}{\mu_0} = \frac{\Theta^2_{\text{d}}}{\Theta^2_0} = \left(1 - \frac{\langle \delta^2_{\text{stat}} \rangle}{\langle \delta^2_{\text{crit}} \rangle}\right). \tag{9.76}$$

If it were possible to relate the defects created by irradiation to the mean-square displacement in the solid, then we could use Eq. (9.76) to determine the amorphization criterion directly. Since this is not possible, there are two alternative ways of determining the amorphization criteria. One is through disordering and another is through free energy change.

9.8.3.1 Radiation-Induced Amorphization Driven by Disordering

Recall that in Sect. 9.7, we determined that the disordering energy should be sufficient to drive the C → A transformation. In fact, the chemical rate theory of radiation-induced order–disorder transformation can be used to determine the cutoff temperature, below which amorphization can occur. In this model [62], the rate of change in the long-range order parameter consists of a disordering term due to irradiation and a thermal reordering term, similar to that in Sect. 9.3,

$$\begin{aligned} \frac{\text{d}S}{\text{d}t} = &-\varepsilon K_0 S + \nu \exp\left(\frac{-U}{kT}\right)[C_{\text{A}}(1 - C_{\text{A}})(1 - S)^2 \\ &- \exp\left(\frac{-V}{kT}\right)(S + C_{\text{A}}(1 - C_{\text{A}})(1 - S)^2)], \end{aligned} \tag{9.77}$$

where U is the energy barrier for the A–B pair interchange, V is the ordering energy such that $V = V_{\text{AB}} - 1/2\ (V_{\text{AA}} + V_{\text{BB}})$ where V_{AB}, V_{AA}, and V_{BB} are the bond energies for A–B, A–A, and B–B pairs, respectively, and the remaining terms were defined in Sect. 9.3. The first term is the irradiation-induced disordering rate, and the second and third terms are the thermal reordering and disordering rates. An example of the variation of long-range order with temperature in the CuTi system is shown in Fig. 9.35 along with the variation of amorphization dose with temperature. Note that below about −53 °C, the order parameter drops to zero. This is the cutoff temperature, T_{C}, which coincides with the onset of amorphization, $T_{\text{c-a}}$. Just above the cutoff temperature, dS/dt is $\sim$ 0 and the relationship between the cutoff temperature and the damage rate, K_0, can be written by setting dS/dt in Eq. (9.77) to zero:

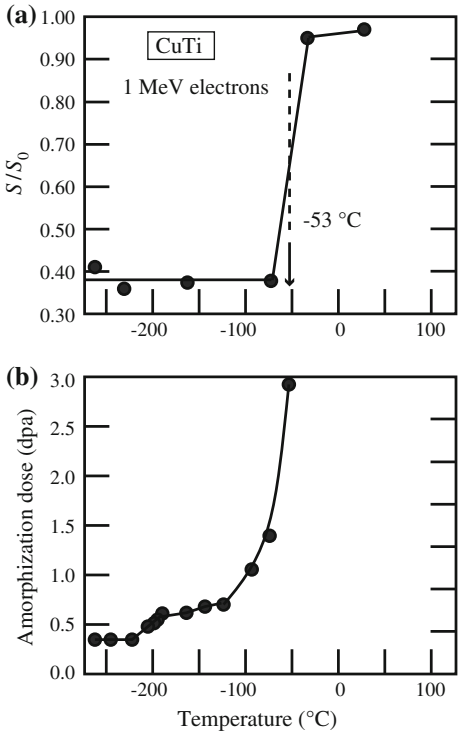

Fig. 9.35 Temperature dependence of (**a**) the long-range order parameter S/S_0, and (**b**) the critical amorphization dose for CuTi, irradiated with 1 MeV electrons (after [60])

$$\varepsilon K_0 S_0 = \nu \exp\left(\frac{-U}{kT_C}\right)\Big[C_A(1-C_A)(1-S_0)^2 - \exp\left(\frac{-VS_0}{kT_C}\right)(S_0 + C_A(1-C_A)(1-S_0)^2)\Big], \tag{9.78}$$

where S_0 is the steady-state value of the long-range order parameter. For typical values of V, the exponent inside the square brackets is of the order 10^{-5} to 10^{-21} and so the second term can be neglected, and the expression in Eq. (9.78) can be solved for T_C:

$$T_C = U\left[k \ln\left(\frac{\nu C_A(1-C_A)(1-S_0)^2}{\varepsilon K_0 S_0}\right)\right]^{-1}. \tag{9.79}$$

Equation (9.79) gives an estimation of the cutoff temperature, or the $T_{c\text{-}a}$ temperature for a solid under irradiation. Note that it depends on the displacement rate and also on the number of replacements per displacement, ε. As such, the temperature at which amorphization will occur will depend on the irradiating particle and the dose rate. Figure 9.36 shows a schematic illustration of the temperature dependence of the critical dose for amorphization for various types of charged particles. $T_{c\text{-}a}$ is the

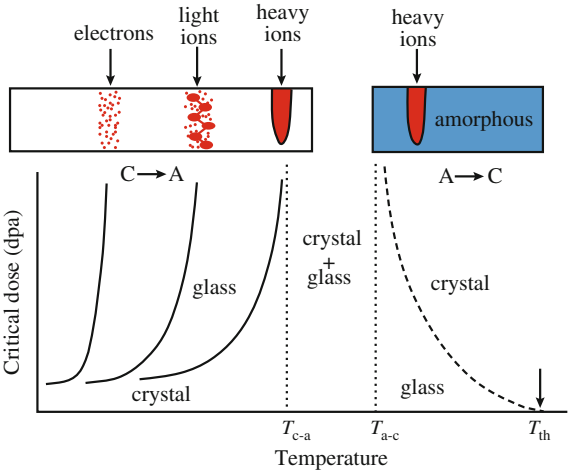

Fig. 9.36 Schematic illustration of the temperature dependence of the critical dose for amorphization for irradiation by various types of particles (after [60])

temperature below which complete amorphization can be achieved. $T_{a\text{-}c}$ is the temperature beyond which the crystalline compound cannot be amorphized and is independent of irradiation conditions, and T_{th} is the thermal recrystallization temperature. Okamoto et al. [60] describe the main kinetic features of irradiation-induced amorphization as follows:

- For a specified particle and dose rate, there is a temperature at which the two competing processes of damage production and recovery just balance. Below that temperature, damage production dominates recover and the crystal can be completely amorphized.
- Amorphization occurs homogeneously at low temperature, far from the critical dose rate and temperature. Heterogeneous amorphization occurs near the cutoff temperature.
- For fixed dose rate, $T_{c\text{–}a}$ increases with increasing particle mass.
- $T_{c\text{–}a}$ is a kinetic parameter that depends on the irradiation variables such as dose rate. Higher dose rates shift $T_{c\text{–}a}$ to higher values.
- There is a temperature, $T_{a\text{–}c}$ above which amorphization is impossible. $T_{a\text{–}c}$ depends on the target temperature but not irradiation variables.
- Between $T_{a\text{–}c}$ and T_{th}, irradiation can induce the A → C transformation and the dose required for the transformation is temperature dependent.

Figure 9.37(a) and (b) shows two examples of the temperature dependence of irradiation-induced amorphization in NiAl and NiTi, respectively. Figure 9.38 shows how $T_{c\text{–}a}$ varies with particle type at nearly equal dose rates. Clearly, irradiation with heavy ions can induce amorphization over a much larger temperature range than is possible by irradiation with electrons because the ions can transfer much more energy in a much smaller volume than can electrons. While electron irradiation in the ∼ MeV range produces isolated displacements (single Frenkel pairs), heavy ion

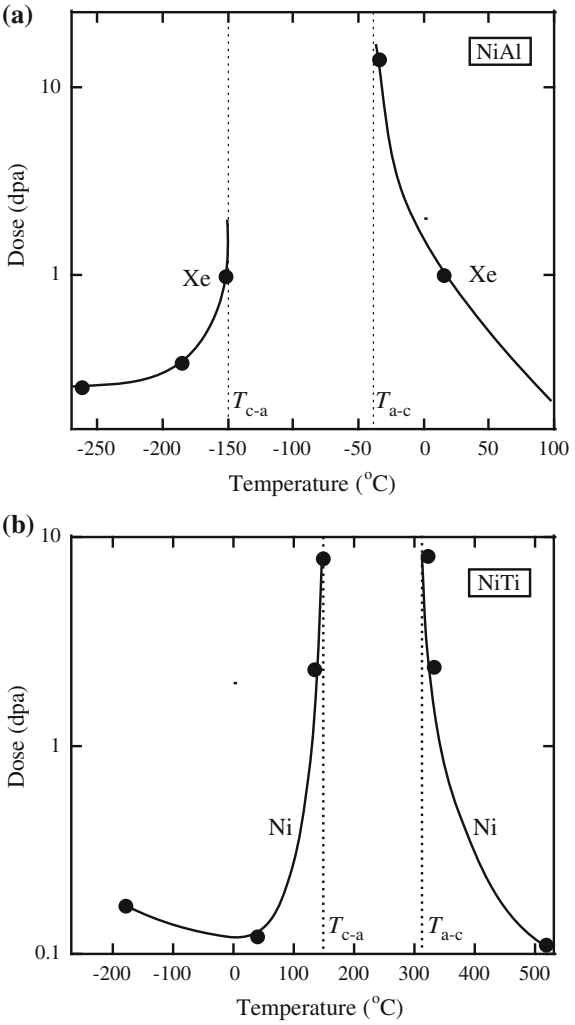

Fig. 9.37 Temperature dependence of the total displacement dose for ion-induced amorphization and crystallization of (**a**) crystalline and amorphous NiAl, and (**b**) crystalline and amorphous NiTi (after [60])

irradiation results in cascades in which the effective displacement rate is high such that the damage rate outweighs the recovery rate.

Relating the ordering process to the mean-square static displacement, Okamoto et al. [60, 63] show that

$$\langle \delta^2_{\text{stat}} \rangle \propto (1 - S^2), \tag{9.80}$$

and since from Eq. (9.76), $\langle \delta^2_{\text{stat}} \rangle$ is proportional to the shear modulus, μ, then $\mu \propto (1 - S^2)$. Figure 9.39 shows that amorphization of Zr_3Al occurs very near to the point where the straight line fit through data crosses the horizontal line for the

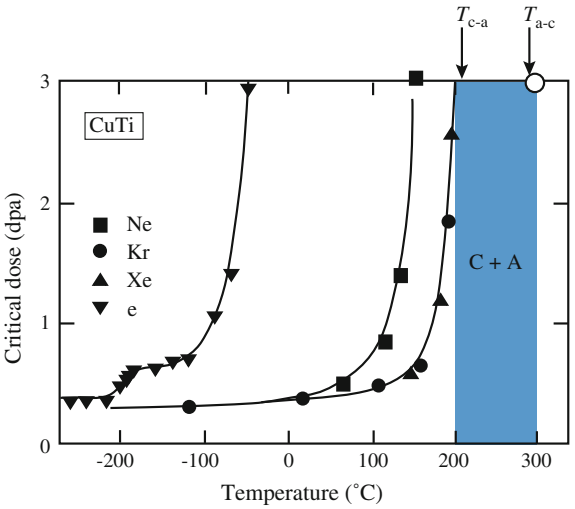

Fig. 9.38 Temperature dependence of the critical amorphization dose for CuTi during irradiation with 1 MeV electrons and 1 MeV Ne, Kr, and Xe ions, all at a dose rate of 10^{-3} dpa/s (after [60])

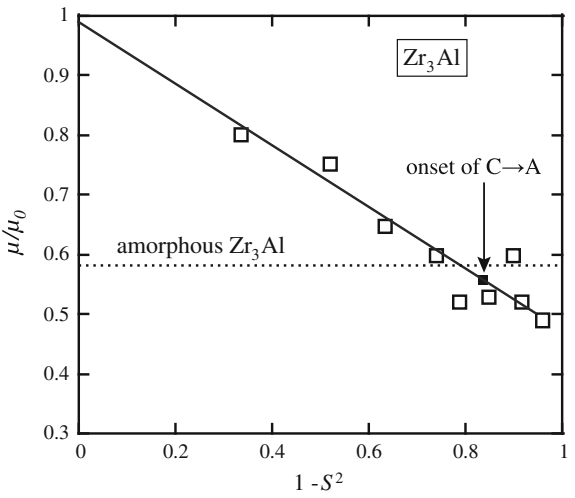

Fig. 9.39 Relative change in the shear modulus with increasing degree of disorder $(1 - S^2)$ in 1 MeV Kr^+-irradiated Zr_3Al. The *dashed line* represents the relative shear modulus in the amorphous phase, and the *vertical arrow* indicates the onset of amorphization (after [60])

amorphous alloy, showing that the onset of amorphization is related to a critical value of the mean-square chemical disorder $(1 - S^2)$ and from Eq. (9.80), the mean-square static displacement. Another example of the role of disorder in amorphization is shown in Fig. 9.40 which gives the dose dependence of S for Zr_3Al during irradiation with 1 MeV electrons at two temperatures, and ions at 22 °C. The onset of amorphization is shown by the arrows, and although it occurs at different doses for the different particles and irradiation temperatures, the value of the order parameter is about the same. The significance of this observation is that while disordering kinetics differ between particles and temperatures, amorphization

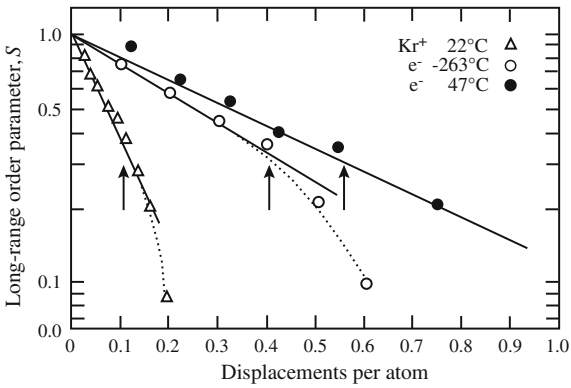

Fig. 9.40 Damage–dose dependence of the long-range order parameter, S in Zr_3Al during irradiation with 1 MeV electrons at −263 and 47 °C and with 1 MeV Kr at 22 °C (after [60])

depends only on the magnitude of S and not how it is reached. Figure 9.41 [60, 63] shows an additional example of the correlation between the onset of amorphization and the *rms* static displacement for case of B implantation into Nb. When the mean-square static displacement reaches a critical value, amorphization occurs.

9.8.3.2 Radiation-Induced Amorphization Driven by Free Energy

Amorphization can also be explained by considering the free energy of the transformation, as explained by Motta et al. [64, 65] and summarized here. The criterion for amorphization is that the free energy change upon irradiation, ΔG_{irr}, must be greater than that for the C → A transformation, ΔG_{ca}:

$$\Delta G_{\text{irr}} \geq \Delta G_{\text{ca}}. \tag{9.81}$$

The term ΔG_{irr} includes all of the defects created by irradiation and can be written as the sum of terms representing chemical disordering, ΔG_{dis}, and all other defects, ΔG_{def}:

$$\Delta G_{\text{irr}} = \Delta G_{\text{def}} + \Delta G_{\text{dis}} = \sum_j (C_j E_j - T\Delta S_j) + \Delta C_{\text{AB}} NV - T\Delta S_{\text{dis}}, \tag{9.82}$$

where C_j is the concentration of defect j, E_j is the formation energy, V is the ordering energy (defined earlier), and ΔS_j and ΔS_{dis} are the configuration entropy changes due to point defects and anti-site defects, respectively. The term ΔC_{AB} is the change in the number of A–B pairs and is determined from the long-range order parameter, S, as:

$$\Delta C_{\text{AB}} = N[A(1 - S^2) + B(1 - S)], \tag{9.83}$$

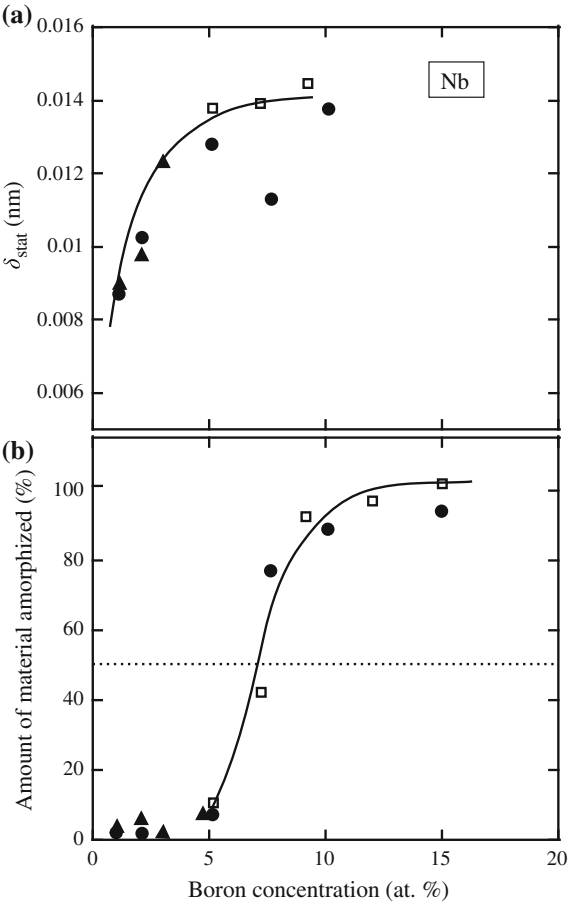

Fig. 9.41 Correlation between (**a**) average static displacement, δ_{stat}, and (**b**) volume fraction of the amorphous phase versus the concentration of B atoms implanted into Nb (after [38])

where N is the number of lattice sites per mole and A and B are the fractions of atoms on the respective lattice sites in the ordered phase. The concentrations of defects are given by the defect balance equations given in Eq. (5.1). Equations (9.81), (9.82), and (9.83), and (5.1) can be used to determine a relationship between the dose to amorphization, the damage rate, and the temperature. Motta determined this relationship for electron irradiation of Zr_3Fe to be:

$$\Phi_a K_0^{1/2} = B \exp(-E_m^i/2kT) \,, \tag{9.84}$$

where Φ_a is the dose to amorphization, K_0 is the damage rate, E_m^i is the interstitial migration energy, and B is a constant, and the results shown in Fig. 9.42 are found to be in good agreement with observations, shown in Fig. 9.43.

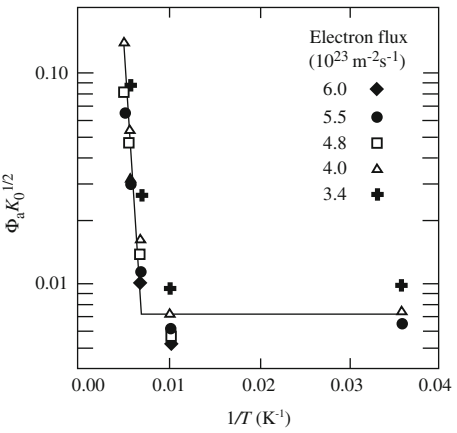

Fig. 9.42 Plot of the dose to amorphization × square root of damage rate versus 1/*T*. The *lines* are fit to the data and indicate that there are two regimes, an athermal regime at low temperature and a thermally activated regime at higher temperature (after [64])

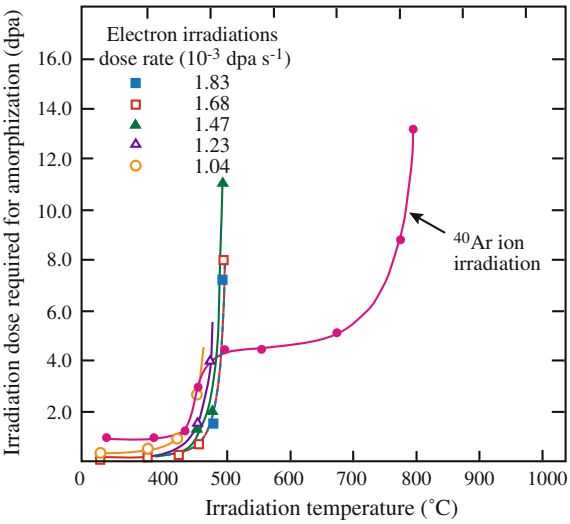

Fig. 9.43 Dose to amorphization for Zr_3Fe during electron and Ar^+ irradiation (after [64])

9.9 Phase Stability in Reactor Core Component Alloys

The stability of phases in engineering alloys under irradiation is of great technological importance. Stainless steels are widely used in the cores of current and advanced reactor systems and have also been studied most comprehensively. Some 10 phases are observed to be affected by irradiation of austenitic stainless steels [66–68]. These phases can be grouped into three categories [66]: *radiation-induced*, *radiation-modified*, and *radiation-enhanced*. Table 9.2 gives the phases belonging to each category along with a crystallographic and morphological description of the phases. The radiation-induced phases include γ', G, and M_xP phases and appear only under irradiation, but not under thermal conditions. The radiation-modified

Table 9.2 Phases observed in austenitic stainless steel alloys after neutron irradiation (after [66, 67])

Radiation	Phase	Crystal structure	Lattice parameter (nm)	Morphology	Orientation in γ matrix	Volume misfit
– Induced	γ' (Ni_3Si)	Cubic, A1 Fm3m	0.35	Spherical	Cube on cube	−0.1
	G ($M_6Ni_{16}Si_7$)	Cubic, A1 Fm3m	1.12	Small rod	Random	0.05
	M_2P (FeTiP)	Hexagonal, C22, P321	0.6 (c/a = 0.6)	Thin lath	$(1210)_{ppt} \parallel (001)_{\gamma}$	−0.4
	Cr_3P	Tetragonal, S_4^2 14	0.92 (c/a = 0.5)	–	–	~0
– Modified	η (M_6C)	Cubic, E9, Fd3M	1.08	Rhombohedral	Cube on cube or twin	0.1
	Laves (A_2B)	Hexagonal, C14 $P6_3/mmc$	0.47 (c/a = 0.77)	Faulted lath	Various	−0.05
	M_2P (FeTiP)	Same	Same	Same	Same	Same
– Enhanced	MC	Cubic, B1 Fm3m	0.43	Spherical	Spherical	0.7
	η (M_6C)	Same	Same	Same	Same	Same
	τ ($M_{23}C_6$)	Cubic, $D8_4$ Fm3m	1.06	Rhombohedral platelet	Cube on cube or twin	0.1
	Laves (A_2B)	Same	Same	Same	Same	Same
	σ	Tetragonal, $D8_b$ p4/mnm	0.88 (c/a = 0.52)	Various	Various	~0
	χ	Cubic, A12 143m	0.89	Various	Various	0.05

group consists of phases that occur during both irradiation and thermal aging and includes η (M_6C), Laves and M_2P (FeTiP). The radiation-enhanced category consists of phases that regularly occur during thermal processing, but are either produced more rapidly or more abundantly at lower temperatures during reactor irradiation. Phases in this category include M_6C, $M_{23}C_6$, and MC carbides and σ and χ intermetallic phases.

Figure 9.44 provides a temperature–dose map in which the various phases listed in Table 9.2 are found to form. Note that while fluences of approximately 10 dpa are required for these phases to appear, the more important variable is temperature. In solution-annealed and cold-worked 316 SS, there is little evidence of significant radiation-induced precipitation below 370 °C. The only phase found to form in this regime is γ'-Ni_3Si, and it has been observed in both light water reactor core components and following proton irradiation at 360 °C [69]. The γ' phase has also been detected in 316 stainless steel irradiated in a fast reactor as low as 270 °C [66]. Between 400 and 550 °C, γ'-Ni_3Si readily forms during fast reactor irradiations and is greatest in steels with higher Si and Ti contents. In mixed spectrum reactors in this temperature range, fine Cr-rich phases such as $M_{23}C_6$ and M_6C form in 316 SS and Ti-rich MC forms in Ti-modified steels [66]. In the 500–600 °C temperature range, both radiation-induced and radiation-modified phases form, including the G-phase ($M_6Ni_{16}Si_7$), M_6C, laves and phosphides and silicides. The G-phase volume fraction is a function of the Si, Ti, and Nb content of the steel with volume fraction increasing with alloy composition.

The appearance of these phases can be related to the effects of irradiation on phase stability. By far, the greatest effect of irradiation on precipitation in stainless steels is due to solute enrichment via radiation-induced segregation. Recall from Chap. 6 that irradiation of austenitic stainless steels causes the enrichment of Si and Ni at sinks and many of the phases appearing under irradiation are rich in one or

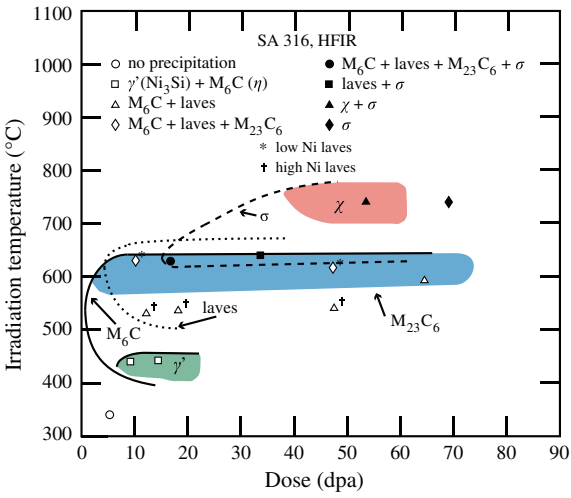

Fig. 9.44 Dose and temperature dependence of precipitate phase formation in solution-annealed 316 stainless steel irradiated in HFIR (after [67])

both of these elements. Radiation-enhanced diffusion affects MC precipitation by enhancing its growth compared to that under thermal conditions. While it is expected that oversized phases are more stable under irradiation and undersized phases are less stable, of the phases given in Table 9.2, three have positive misfits of at least 10 % and of those, only M_6C is stable under a wide range of irradiation conditions. Both MC and $M_{23}C_6$ are oversized and will benefit from vacancy supersaturation, but also from the depletion of their main constituent, Cr, due to RIS. Conversely, several of the phases that are undersized are induced or enhanced by irradiation: Laves, M_2P, γ'. Clearly, the effect of solute segregation and other material and irradiation parameters play a large role in the phases that are stable under irradiation.

Nomenclature

a	Lattice spacing
A	Term relating to crystal structure dependence on ordering energy
C_e	Matrix solute concentration
C_i	Concentration of species i
C_p	Concentration of solute in the precipitate
D	Diffusion coefficient
$\tilde{D}$	Interdiffusion coefficient
E	Young's modulus
E^j_{mO}	Migration energy for ordering of defect j
G	Solute source term
ΔG_p	Free energy of formation of a precipitate
$\Delta G'$	Pseudo-free energy of formation of a precipitate
ΔG_{ac}	Free energy change due to amorphization
ΔG_{irr}	Free energy change due to irradiation
ΔG_{def}	Free energy change due to defects
ΔG_{dis}	Free energy change due to chemical disordering
$\hbar$	Planck's constant
ΔH_f	Heat of formation
ΔH_{i-v}	Enthalpy of defect formation
$\Delta H_{c\text{-}a}$	Enthalpy for the crystalline-to-amorphous transition
J_p	Precipitate nucleation rate
k	Boltzmann's constant
k_O	Rate constant for the ordering reaction
k_s^2	Sink strength
K_{iv}	Recombination rate constant
K_0	Defect production rate
L	Cell size
M	Atomic mass
n	Excess number of vacancies in a precipitate
N	Atom number density

p_x	Probability that a trap site is occupied by species x
Q	Activation energy for ordering
r_c	Cascade radius
r_p	Precipitate radius
r_j	Recombination radius of species j
r_{nn}	Nearest-neighbor atom spacing
R	Metal–metalloid size ratio
R_m	Precipitate dissolution rate by ballistic mixing
R_s	Precipitate growth rate due to radiation-enhanced diffusion
S	Long-range order parameter
S_e	Equilibrium value of order parameter
S_j	Supersaturation of species j
$S_{observed}$	Observed long-range ordering parameter
S_0	Steady-state value of order parameter
S_v	Vacancy supersaturation
S_x	Solute supersaturation
ΔS_{dis}	Configurational entropy change due to anti-site defects
ΔS_j	Configurational entropy change due to point defects
t	Time
T	Temperature
T_C	Cutoff temperature
T_{a-c}	Temperature above which crystal cannot be amorphized
T_{c-a}	Temperature below which complete amorphization can be achieved
T_g	Glass transition temperature
T_k	Ideal glass transition temperature
T_m	Melting temperature
U	Energy barrier for ordering reaction
V	Volume; also ordering parameter
V_0	Activation energy when the long-range order parameter, $S = 1$
V_T	Energy reduction when a wrong A–B pair transforms to a correct A–B pair
V_c	Cascade volume
V_m	Molar volume
V_{ij}	Bond energy for species i and j
x	Number of solute atoms in a precipitate
X_j	Atom fraction of species j
Z_α	Number of α sites that are nearest neighbor to a β site
Z_β	Number of β sites that are nearest neighbor to a α site
α	Constant in Eq. (9.22)
α_j	Emission rate of species j
β	Constant in Eq. (9.21)
β_j	Capture rate of species j
δ	Fractional difference in volume of the precipitate relative to the matrix

$\langle \delta^2_{\text{crit}} \rangle^{1/2}$	Critical value of means square displacement
$\langle \delta^2_{\text{stat}} \rangle^{1/2}$	Amount of static disorder in the solid
$\langle \delta^2_{\text{vib}} \rangle^{1/2}$	Root-mean-square thermal displacement
ε	Disordering efficiency
γ	Particle–matrix interface energy; also surface energy
μ	Shear modulus
ν	Poisson's ratio
ν_j	Frequency factor for defect j
ν_{c}	Frequency factor for correct A–B pair
ν_{w}	Frequency factor for wrong A–B pair
Θ	Re-solution rate of precipitate volume
Θ_0	Debye temperature
ρ	Density
ρ_{p}	Precipitate number density
ρ^0_{p}	Equilibrium precipitate number density
ρ'	Pseudo-equilibrium precipitate number density
σ	Parameter in Eq. (9.40)
σ_{D}	Displacement cross section
τ	Time constant
Ω	Atomic volume
ξ	Dissolution parameter in Eq. (9.32)
ζ	Constant in Eq. (9.1)

Superscripts

i	Interstitial
v	Vacancy

Subscripts

d	Defective
def	Defects
dis	Disordered
e	Solubility
i	Interstitials
irr	Irradiation
m	Matrix
max	Maximum
O	Ordering
p	Precipitate
s	Solute
th	Thermal

v Vacancies
x Solute atom
0 Initial

Acronyms

APT Atom probe tomography
CSRO Compositional short-range order
HFIR High Flux Isotope Reactor (Oak Ridge National Laboratory)
NHM Nelson–Hudson–Mazey
RED Radiation-enhanced diffusion
RIS Radiation-induced segregation
rms Root mean square
TEM Transmission electron microscopy
TSRO Topological short-range order

Problems

9.1 A spherical precipitate grows via a random nucleation process at temperature T. The same precipitate grows under irradiation at the same temperature T. Under irradiation, the time to obtain the same volume fraction of precipitate is half that during pure thermal aging. Calculate the difference in the activation energy at this temperature between thermal and irradiated conditions for this transformation process. State key assumptions.

9.2 What phase is 304 stainless steel? Does radiation-induced segregation in 304 stainless steel tend to stabilize or destabilize this phase? Explain why.

9.3 For 316 SS under irradiation with a vacancy supersaturation, $S_v = 10^4$ and a solute supersaturation, $S_x = 10^2$, find the interstitial to vacancy arrival rate ratio (β_i/β_v) that will stabilize a precipitate phase that is oversized by 5 % ($\delta = 0.05$). Plot your results as a function of temperature from 573 to 873 K. Neglect the temperature dependence of Young's modulus. Use $E = 200$ MPa and $\nu = 0.3$.

9.4 For γ' in a Ni–5 %Al alloy undergoing shrinkage by recoil dissolution and growth by diffusion of the solute from solution:

(a) Determine the critical γ' precipitate radius, below which growth occurs and above which shrinkage will occur.
(b) Compare your result to that expected when the precipitate size is governed by dissolution disordering.
Use the following irradiation parameters:

$\phi_f = 10^{15}$ n/cm^2 s ($E \sim 0.5$ MeV)
$\rho = 10^{15}$ cm^{-3}
$\zeta\Omega = 10^{-4}$ nm

$\xi = 10$ nm
$D = 10^{-15}$ cm^2/s

9.5 For the same alloy as in the last problem, plot the dependence of the maximum stable particle size on f, the fraction of atoms dissolved by a cascade for precipitates undergoing irradiation-induced re-solution. Make the plot for the range $0 < f < 1$ and $l = 10$ nm.

9.6 Estimate the disordering rate due to irradiation for Ni–25Al (γ') irradiated with 5 MeV Ni^{++} ions at a displacement rate of 10^{-3} dpa/s and with a disordering efficiency of 30.

9.7 A recent paper reports the discovery of a new microstructural defect aggregate, termed a black hole because of its affinity for vacancies $\left(z_v^{BH} > z_i^{BH}\right)$. Describe how the presence of these black holes along with the usual array of defect sinks will affect:

(a) Void nucleation rate,
(b) Critical void size,
(c) Void growth rate,
(d) Incoherent precipitate ($\delta > 0$) stability, and
(e) Incoherent precipitate nucleation rate.

9.8 In the nickel-rich end of the Ni–Al system, a solid solution of Al in Ni, known as the γ phase, has an fcc crystal structure. Near a composition of Ni–50Al, the β phase (bcc) is the stable structure. Given the information below, determine the window on S_v and β_i/β_v needed to form the NiAl (β) phase from:

(a) A saturated solution of Al in Ni,
(b) A supersaturated solution, $S_x = 2.0$,
(c) An undersaturated solution, $S_x = 0.5$.
Irradiation temperature = 500 °C

$\nu = 0.35$,
$E = 150$ GPa,
$a_\beta = 0.3574$ nm,
$a_\gamma = 0.490$ nm.

9.9 Using the rules for amorphous phase formation, describe the relative ease of forming an amorphous phase in each single- and two-phase region of the Ni–Al phase diagram. Explain your reasoning.

9.10 One of the theories of the formation of irradiation-induced amorphization requires that the vacancy and interstitial defect concentrations reach a level of 2 %, at which point the affected volume will become amorphized. Determine whether this is possible in NiAl (β'—bcc) by determining the migration enthalpy for interstitials at 300 K, which would allow the point defect concentrations to reach the critical concentration. Assume a low sink concentration and a displacement rate of 10^{-4} dpa/s.

9.11 Estimate the crystalline-to-amorphous temperature for $NiAl_3$ for the following irradiation and material parameters under 5 MeV Ni^{++} ion irradiation:

$K_0 = 10^{-3}$ dpa/s,
$U = 0.1$ eV,
$\nu = 10^{13}$ s^{-1},
$\varepsilon = 30$

References

1. Rehn LE (1982) In: Picraux ST, Choyke WJ (eds) Metastable materials formation by ion implantation. Elsevier Science, New York, pp 17–33
2. Nelson RS, Hudson JA, Mazey DJ (1972) M Nucl Mater 44:318–330
3. Wilkes P (1979) J Nucl Mater 83:166–175
4. Brailsford AD (1980) J Nucl Mater 91:221–222
5. Wagner C (1961) Z Elektrochem 65:581–591
6. Lifshitz IM, Slyozov VV (1961) Phys Chem Solids 19:35–50
7. Frost HJ, Russell KC (1983) In: Nolfi FV (ed) Phase transformations during irradiation. Applied Science, New York, p 75
8. Baron M, Chang H, Bleiberg ML (1977) In: Bleiberg ML, Bennett JW (eds) Radiation effects in breeder reactor structural materials. TMS-AIME, New York, pp 395–404
9. Bilsby CF (1975) J Nucl Mater 55:125–133
10. Frost HJ, Russell KC (1982) Acta Metal 30:953–960
11. Frost HJ, Russell KC (1981) J Nucl Mater 103–104:1427–1432
12. Wollenberger H (1994) J Nucl Mater 2116:63–77
13. Abromeit C, Naundorf V, Wollenberger H (1988) J Nucl Mater 155–157:1174–1178
14. Russell KC (1984) Prog Mater Sci 28:229–434
15. Liou K-Y, Wilkes P (1979) J Nucl Mater 87:317–330
16. Nastasi M, Mayer JW, Hirvonen JK (1966) Ion-solid interactions: fundamentals and applications. Cambridge University Press, Cambridge, p 342
17. Potter DI (1983) In: Nolfi FV (ed) Phase transformations during irradiation. Applied Science, New York, p 213
18. Eridon J, Rehn L, Was G (1987) Nucl Instr Meth B 19/20:626
19. Brimhall JL, Kissinger HE, Charlot LA (1983) Rad Eff 77:273
20. Maydet SI, Russell KC (1977) J Nucl Mater 64:101–114
21. Russell KC (1979) J Nucl Mater 83:176–185
22. Mruzik MR, Russell KC (1978) J Nucl Mater 78:343–353
23. Cauvin R, Martin G (1981) Phys Rev B 32(7):3322–3332
24. Martin G, Bellon P (1997) In: Ehrenreich H, Spaepen F (eds) Solid state physics: advances in research and applications, vol 50. Academic, New York, pp 189–332
25. Jiao Z, Shankar V, Was GS (2011) J Nucl Mater 419:52–62
26. Was GS, Jiao Z, Getto E, Sun K, Monterrosa AM, Maloy SA, Anderoglu O, Sencer BH, Hackett M (2014) Scripta Mater 88:33–36
27. Jiao Z, Was GS (2012) J Nucl Mater 425:105–111
28. Chen Y, Chou PH, Marquis EA (2014) J Nucl Mater 451:130–136
29. Jiao Z, Was GS (2014) J Nucl Mater 449:200–206
30. Jiao Z, Was GS (2011) Acta Mater 59:1220–1238
31. Brimhall JL, Simonen EP (1986) Nucl Instr Meth B 16:187
32. Was GS, Eridon JM (1987) Nucl Instr Meth B 24/25:557

33. Was GS (1989) Prog Surf Sci 32(3/4):211
34. Luzzi DE, Meshii M (1986) Scr Metal 20:943
35. Johnson E, Wohlenberg T, Grant WA (1970) Phase Transitions 1:23
36. Grant WA (1981) Nucl Instr Meth 182/183:809
37. Johnson E, Littmark U, Johnson A, Christodoulides C (1982) Phil Mag A 45:803
38. Follstaedt DM (1985) Nucl Instr Meth B 78:11
39. Peiner E, Kopitzki K (1988) Nucl Instr Meth B 34:173
40. Tsaur BY, Lau SS, Mayer JW (1980) Appl Phys Lett 36:823
41. Tsaur BY, Lau SS, Hung LS, Mayer JW (1981) Nucl Instr Meth 182/813:1
42. Shectman D, Blech I, Gratias D, Cahn JW (1984) Phys Rev Lett 53:1951
43. Knapp JA, Follstaedt DM (1985) Phys Rev Lett 55(15):1591
44. Lilienfield DA, Nastasi M, Johnson HH, Ast AG, Mayer JW (1985) Phys Rev Lett 55 (15):1587
45. Lilienfield DA, Mayer JW (1987) Mat Res Soc Symp 74. Materials Research Society, Pittsburgh, p 339
46. Ossi PM (1977) Mater Sci Eng 90:55
47. Luzzi DE, Mori H, Fujita H, Meshii M (1984) Scr Metal 18:957
48. Pedraza DF (1987) Mater Sci Eng 90:69
49. Pedraza DF (1990) Rad Eff 112:11
50. Pedraza DF, Mansur LK (1986) Nucl Instr Meth B 16:203
51. Pedraza DF (1986) J Mater Res 1:425
52. Simonen EP (1986) Nucl Instr Meth B 16:198
53. Alonso JA, Somoza S (1983) Solid State Comm 48:765
54. Miedema AR (1973) J Less Comm Metals 32:117
55. Johnson WL, Cheng Y-T, Van Rossum M, Nicolet M-A (1985) Nucl Instr Meth B 7/8:657
56. Martin G (1984) Phys Rev B 30:1424
57. Swanson ML, Parsons JR, Hoelke CW (1971) Rad Eff 9:249
58. Brimhall JL, Kissinger HE, Pelton AR (1985) Rad Eff 90:241
59. Brimhall JL, Simonen EP, Kissinger HE (1973) J Nucl Mater 48:339
60. Okamoto PR, Lam NQ, Rehn LE (1999) In: Ehrenreich H, Spaepen F (eds) Solid state physics: advances in research and applications, vol 52. Academic, New York, pp 2–137
61. Lindemann FA (1910) Z Phys 11:609
62. Dienes GJ (1955) Acta Metal 3:549
63. Lam NQ, Okamoto PR, Li M (1997) J Nucl Mater 251:89–07
64. Motta AT, Howe LM, Okamoto PR (1999) J Nucl Mater 270:174–186
65. Motta AT (1997) J Nucl Mater 244:227–250
66. Mansur LK (1987) In: Freeman GR (ed) Kinetics of nonhomogeneous processes. Wiley, New York, pp 377–463
67. Maziasz PJ, McHargue CJ (1987) Int Mater Rev 32(4):190–218
68. Maziasz P (1993) J Nucl Mater 205:118–145
69. Was GS (2004) In: Proceedings of the 11th international conference on environmental degradation of materials in nuclear power systems: water reactors. American Nuclear Society, La Grange Park, IL, pp 965–985

Chapter 10
Unique Effects of Ion Irradiation

This chapter will focus on processes that are unique to ion bombardment of metals and alloys. Ion bombardment is important in fusion reactor systems in which the reaction products consist of energetic helium and hydrogen (deuterium or tritium) ions that impact the first wall and other components. In laboratory experiments, ion implantation, ion beam mixing (IBM), and ion beam-assisted deposition are used to study ion–solid interactions and to create new phases and unique microstructures. The topic of ion beam modification of materials or ion–solid interactions in general is a broad subject, and a comprehensive treatment is beyond the scope of this text. (The reader is referred to several excellent texts and review articles on the subject, see e.g., [1–5].) Rather, we will focus on processes that occur during ion–solid interactions and that result in unique microstructures or phases in the target, such as displacement mixing, preferential sputtering, Gibbsian adsorption, and grain growth, and the combination of these processes that together alter the target from its original state. Recall that ions not only create damage, but they contribute to a chemical change in the target by virtue of their presence. Processes affecting the surface structure and composition that are negligible under neutron irradiation (sputtering, recoil mixing, and Gibbsian adsorption) can be very significant under ion irradiation.

We will start with a brief introduction of ion irradiation techniques to set the stage for understanding the effects to be described later. The effects of ion irradiation on composition, microstructure, and phase formation will then be presented, followed by the effects due to bombardment by gases at high doses and high temperature as will be experienced in the first wall of a fusion reactor, or at low temperature in a laboratory. A final topic is the unique processes that occur in film formation by ion beam-assisted deposition (IBAD).

Additional material to this chapter can be downloaded from http://rmsbook2ed.engin.umich.edu/movies/

G.S. Was, *Fundamentals of Radiation Materials Science*,
DOI 10.1007/978-1-4939-3438-6_10

10.1 Ion Irradiation Techniques

The modification of metal surfaces by ion beams can be accomplished by a variety of methods, each with its own advantages for particular situations. The principal methods include ion implantation, IBM, ion beam-assisted deposition, and plasma source ion implantation and are shown schematically in Fig. 10.1(a–d). Each of these techniques will be briefly described and considered for their capacity to alter the composition of the target.

Ion implantation (II) is the bombardment of a target with a beam of ions in the energy range from a few hundred keV to several MeV. The beam is usually monoenergetic, contains a single charge state and is generally (but not always) mass analyzed. Due to the stochastic nature of the elastic collision process, the ions come to rest in a Gaussian distribution with the mean of the Gaussian centered about R_p, the projected range, and the FWHM $\sim 2.35\Delta R_p$, where ΔR_p is the standard deviation from the mean.

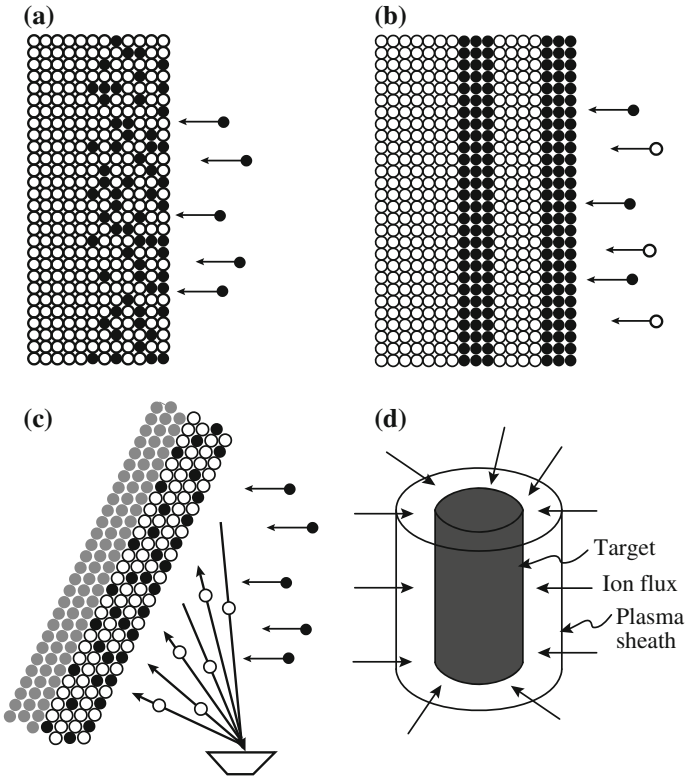

Fig. 10.1 Ion beam surface modification by (**a**) direct ion implantation, (**b**) ion beam mixing, (**c**) ion beam-assisted deposition, and (**d**) plasma source ion implantation (after [3])

Although it is a simple process, this technique has several disadvantages from the standpoint of modifying the surface composition. First, since the depth of the implanted distribution varies as $E^{1/2}$, energies in the several hundred keV range that are achievable in the most common implanters will result in projected ranges of less than 100 nm for most heavy ions. Energies in the MeV range are required to penetrate into the micrometer range. Second, sputtering will limit the concentration of the implanted specie to a value that is the reciprocal of the sputtering yield (see Sect. 10.2.1). Since sputtering yields of metals at these energies range from 2 to 5, the maximum concentration of implanted specie is 50–20 %, respectively. The shape and location of the distribution can also be a drawback. In corrosion, where the composition of the top few monolayers is most important, the bulk of the modification occurs at considerably greater depths, leaving the surface lean in the implanted specie. When implantation induces a phase transformation, the effectiveness or efficiency of direct implantation is lesser still. Finally, it is often desirable to implant metal ions into pure metals or alloys to achieve a particular surface composition. As a practical matter, most commercial implanters can produce large currents of inert gases, but more elaborate measures are needed to produce metal ions at currents that are practical. IBM provides an alternative to the shortcomings of direct ion implantation.

IBM refers to the homogenization of bilayers or multilayers of elements deposited onto the surface of a target prior to bombardment. The idea behind IBM is to create a surface alloy by homogenizing alternate layers of the alloy constituents deposited in a thickness ratio so as to result in the desired final composition following mixing. IBM overcomes several of the shortcomings of ion implantation. First, the requirement of producing a metal ion beam is eliminated since noble gases can be used for mixing. Noble gases will not contribute a chemical effect in the solid and yet can be made into high-current beams in most commercial implanters. Second, there is no restriction on the composition range since the final composition is controlled by the ratio of layer thicknesses. This also removes two other shortfalls of ion implantation, that of uniformity and surface deficiency of the implanted specie. IBM results in a very uniform composition throughout the depth of penetration of the ion, including the very near-surface region that is problematical for ion implantation. Finally, if the elemental layers are made thin enough, the dose needed to achieve complete mixing can be orders of magnitude lower than that needed to produce concentrated alloys by direct implantation.

If the process is carried out at low temperature, the result is often a metastable alloy in the form of either a supersaturated solid solution or an amorphous structure. The microstructure can then be controlled by subsequent annealing treatments. However, despite its many advantages, IBM still suffers from the same disadvantage of limited depth of penetration. The thickness of the surface is still governed by the projected range of the ion, which is in the 100 nm range for heavy ions of a few hundred keV. A solution to this problem lies in the technique of ion beam-assisted deposition.

Ion beam-assisted/ion beam-enhanced deposition (IBAD/IBED) refers to the growth of a film with the assistance of an ion beam. In this technique, a film is

grown onto a substrate by physical vapor deposition concurrently with the bombardment by an ion beam of low ($\sim$1 keV) energy. The advantages of this method are numerous. First, there is virtually no limit to the thickness of film that can be modified since bombardment occurs during growth. Second, ion bombardment concurrent with vapor deposition provides for an atomically mixed interface, resulting in greater adherence. The composition gradient at the interface can be controlled by the deposition rate and the ion flux. Third, the enhanced mobility of the surface during growth allows for the control of grain size and morphology, texture, density, composition, and residual stress state. These properties are determined principally by controlling the atom deposition rate in conjunction with the ion flux (ion-to-atom arrival rate ratio), ion energy, fluence, and species. Hence, pure metals, solid solution alloys, intermetallic compounds, and a host of metal-based compounds can be grown by this technique.

A final technique is plasma source ion implantation (PSII). In this technique, the target is placed directly in the plasma source and is then pulse biased to a high negative potential (–40 to –100 keV). A plasma sheath forms around the target and ions are accelerated normal to the target surface across the plasma sheath. PSII has several potential advantages relative to conventional line-of-sight implantation including elimination of the need for target manipulation and beam rastering, elimination of target masking (retained dose problem), operation of the ion source hardware and controls are near ground potential, and easier scaling to large and/or heavy targets.

All of these techniques involve energetic ion–solid interaction and the physical processes that constitute this interaction such as sputtering, Gibbsian adsorption, recoil implantation, displacement mixing, radiation-enhanced diffusion, and radiation-induced segregation. These processes affect composition, microstructure, and phase structure and form the basis for the observed changes in the physical and mechanical properties of the metal or alloy. Chapters 7, 8, and 9 described the microstructure and phase changes due to irradiation, and this chapter will focus on the composition effects and some additional effects unique to ion irradiation, such as grain growth, texture modification, and surface morphology during high gas loading.

10.2 Composition Changes

Under ion bombardment, a variety of processes occur, some of which are much more pronounced than in the case of neutron irradiation and some that are the same. Bombardment by heavy ions results in sputtering of atoms from the surface, inducing compositional changes in the near-surface region of the target. At temperatures between 0.3 and 0.5 T_m, Gibbsian adsorption causes changes in the composition of the first two atom layers, which can impact the sputtering process. The primary disordering mechanism is collisional or ballistic mixing which can be qualitatively classified into recoil implantation and cascade (isotropic) mixing.

Recoil implantation refers to the direct displacement of a target atom by a bombarding ion. Indirect processes involving other target atoms are collectively called cascade mixing. Referring to experiments involving the implantation into a bilayer or a thin marker layer embedded in a monatomic solid, recoil implantation produces a shift and a broadening of a given initial profile while cascade mixing produces broadening. But in addition to collisional mixing, thermal processes may become important, leading to radiation-enhanced diffusion (Chap. 5). When the flux of defects to sinks becomes coupled to the flux of host atoms, radiation-induced segregation can occur, resulting in the accumulation or depletion of an alloy component at defect sinks (Chap. 6). The following subsections provide a development of the physical processes of sputtering, Gibbsian adsorption, recoil implantation, and cascade mixing. Radiation-enhanced diffusion and radiation-induced segregation were described in earlier chapters and will be included only in combination with other processes to present a complete picture of composition changes under ion bombardment.

10.2.1 Sputtering

Sputtering is a key element in determining surface composition under ion bombardment, primarily through the action of preferential sputtering. Different elements sputter with different probabilities, and the surface composition is a function of these probabilities. This section will briefly describe the process of physical sputtering, followed by a discussion of preferential sputtering as it affects surface compositional changes in alloys.

Basic Model

Surfaces of solids erode under ion bombardment. The erosion rate is characterized by the sputtering yield, Y, which is defined as the mean number of emitted atoms per incident particle. Y depends on the structure and composition of the target, parameters of the incident beam and the experimental geometry. For medium mass ions and keV energies, $0.5 \leq Y < 20$.

In the sputtering process, atoms are ejected from the outer surface layers (Fig. 10.2). The bombarding ion transfers energy in collisions to the target atoms that recoil with enough energy to generate other recoils. Some of the backward-directed recoils will intersect the surface with enough energy to escape the solid. It is these recoils that make up most of the sputtered yield, which is proportional to the number of displaced or recoil atoms. In the linear cascade regime, the number of recoils is proportional to the energy deposited per unit depth in nuclear energy loss [6–9]. A collision cascade is linear if only a minor fraction of the target atoms within the cascade volume is set in motion. For a bulk cascade, this implies a low density of point defects generated. As applied to sputtering, it means that the sputter yield must be small compared to the number of target atoms located within the surface area affected by a bombarding particle. In practice, cascades in

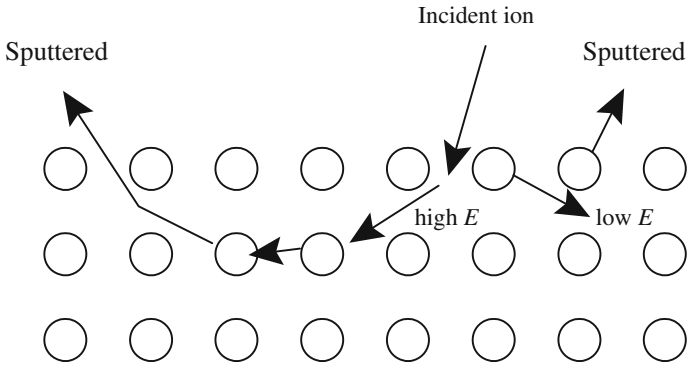

Fig. 10.2 Schematic illustration of the redirection of momentum from an incident ion to the backward direction resulting in sputtering

metals are close to linear except those generated by rather heavy ions bombarding heavy targets in the energy range from ~10 to ~1 MeV. The sputtering yield for particles incident on the surface can be expressed as follows:

$$Y = \Lambda F_D(E_0), \tag{10.1}$$

where Y is the number of atoms emitted per incident particle, E_0 is the incident particle energy, Λ contains all the material properties such as surface binding energies and incident ion angular dependence, and F_D is the density of deposited energy per unit depth at the surface and depends on the type, energy, and direction of the incident ion and the target parameters Z_2, M_2, and N. The derivation of Λ involves a description of the number of recoil atoms that can overcome the surface barrier and escape from the solid. Sigmund [6] has derived an expression for Λ using the Thomas–Fermi screening function:

$$\Lambda = 0.042/NU_0, \tag{10.2}$$

where N is the atomic number density and U_0 is the surface binding energy and can be estimated from the heat of sublimation. The deposited energy, F_D is given as follows:

$$F_\mathrm{D}(E_0) = \alpha \, \mathrm{d}E/\mathrm{d}x|_\mathrm{n}, \tag{10.3}$$

where $\mathrm{d}E/\mathrm{d}x|_\mathrm{n}$ is the energy loss rate due to nuclear stopping and α is a correction factor that accounts for the angle of incidence of the beam to the surface and contributions due to large angle scattering events. The factor α increases with the angle of incidence due to increased energy deposition in the surface, and α also increases with M_2/M_1, again, due to greater energy deposition in the surface. Using the inverse square potential (see Eq. (1.59)), $\mathrm{d}E/\mathrm{d}x|_\mathrm{n}$ is evaluated to be:

$$\mathrm{d}E/\mathrm{d}x|_{\mathrm{n}} = NS_{\mathrm{n}} = N\frac{\pi^2}{2}Z_1Z_2\varepsilon^2 a\frac{M_1}{M_1+M_2}, \tag{10.4}$$

where N is the atom number density, S_{n} is the nuclear stopping power, a is the screening radius, ε is the unit charge, Z and M are atomic number and atomic mass, respectively, and the subscripts 1 and 2 refer to incident and target atoms, respectively. The nuclear stopping power calculated using a Thomas–Fermi cross section [10] is as follows:

$$S_{\mathrm{n}}(E) = 4\pi a Z_1Z_2\varepsilon^2\frac{M_1}{M_1+M_2}S_{\mathrm{n}}(\in), \tag{10.5}$$

where $S_{\mathrm{n}}(\in)$ is the reduced stopping power (from Eq. (1.148)), and the reduced energy, $\in$ (from Eq. (1.139)) is as follows:

$$\in = \frac{M_2}{M_1+M_2}\frac{a}{Z_1Z_2\varepsilon^2}E. \tag{10.6}$$

For 1 keV Ar incident on Cu, a = 0.0103 nm and $\in$ = 0.008, and for 10 keV O incident on Cu, a = 0.0115 nm and $\in$ = 0.27. For ion energies between 1 and 10 keV, values of $\in$ are in the range 0.01–0.3, or just below the plateau in $\mathrm{d}E/\mathrm{d}x|_{\mathrm{n}}$. Using the energy-independent value of $S_{\mathrm{n}}(\in)$ of $\sim$0.327 (from Eq. (1.150)) gives $\mathrm{d}E/\mathrm{d}x|_{\mathrm{n}} \sim$ 1240 eV/nm for Ar incident on C, and $\mathrm{d}E/\mathrm{d}x|_{\mathrm{n}} \sim$ 320 eV/nm for O incident on Cu. Using the expression for Λ in Eq. (10.2), the sputtering yield in Eq. (10.1) becomes

$$Y = 0.528\alpha Z_1Z_2\frac{M_1}{U_0(M_1+M_2)}S_{\mathrm{n}}(\in). \tag{10.7}$$

For Ar incident on Cu, NS_{n} = $\mathrm{d}E/\mathrm{d}x|_{\mathrm{n}}$ = 1240 eV/nm, $U_0 \sim$ 3 eV, $\alpha \sim$ 0.25, Λ = 0.0165 nm/eV and N = 85 atoms/nm^3, giving $Y \sim$ 5.1. Figure 10.3 shows the variation of the sputter yield with angle, atomic number of the ion, target atom–incident ion mass ratio, and ion energy. Sputtering increases with departure from normal incidence because more of the ion energy is deposited close to the surface. The same is true for the dependence on Z of the ion for a fixed energy. Sputter yield is low at low energies because of the small amount of energy deposited in the surface. Similarly, since the elastic scattering cross section decreases with energy, the energy deposited in the surface region drops at high energies and the sputter yield falls. The result is a peak at intermediate energies where the energy deposition in the near-surface region is high.

The sputtering yield can be used to determine the steady-state concentration of the implanted specie [1] as follows. We assume that we are implanting an ion of element A into a target of element B, where $N_{\mathrm{A,B}}$ is the atomic concentration and $S_{\mathrm{A,B}}$ is the sputtered flux of elements A and B. Then at any time, we have that:

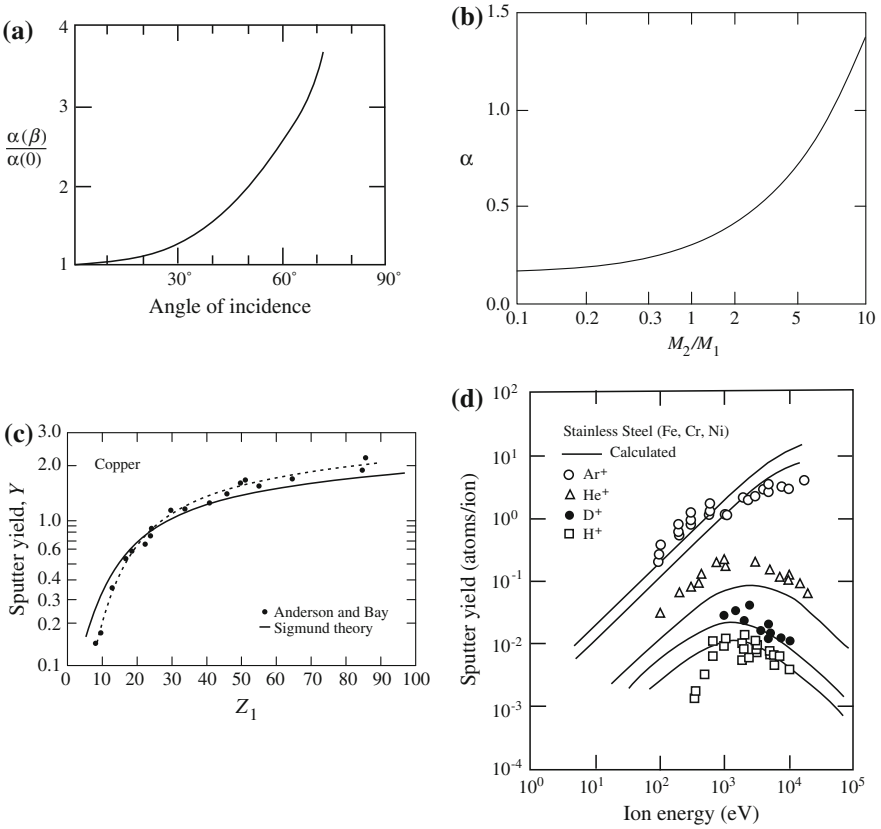

Fig. 10.3 Dependence of sputter yield on (**a**) angle of incidence, β, where β is measured from the surface normal (after [8]), (**b**) atomic number of the incident (after [9]), (**c**) target atom: incident ion mass ratio through the factor α in Eq. (10.3) (after [8]), and (**d**) incident ion energy (after [7])

$$S_B/S_A = \chi(N_B/N_A), \tag{10.8}$$

where χ is the ratio of probabilities for sputtering a B atom off the surface to that for an A atom. The flux of incident A atoms, ϕ_A, is related to the total sputtered flux by the sputtering yield:

$$\phi_A Y = S_A + S_B. \tag{10.9}$$

At steady state, the addition of A atoms by implantation equals that lost by sputtering, so there is no net change in the total number of A atoms in the target and $\phi_A = S_A$. Substituting for S_A into Eq. (10.9) yields $S_B = (Y - 1)\phi_A$. Substituting for S_A and S_B into Eq. (10.8) gives the steady-state surface composition:

$$N_A/N_B = \chi(Y-1)^{-1}. \tag{10.10}$$

For the case where $\chi = 1$, Eq. (10.10) becomes:

$$N_A/(N_A + N_B) = 1/Y, \tag{10.11}$$

which indicates that the concentration of the implanted specie is determined directly by the sputter yield.

Preferential Sputtering

When energetic ions strike a target consisting of an alloy, not all of the elements of the target will be sputtered with the same yield. The yield of A atoms of an alloy per incident ion in the flux of sputtered atoms [11] is as follows:

$$Y_A = \int_0^\infty \sigma_A(x)(C_A(x)/\Omega)\,dx, \tag{10.12}$$

where $\sigma_A(x)$ is the cross section for A atoms at a depth $x \geq 0$ to be ejected from the surface, $x = 0$, into the region $x < 0$ per incoming ion, $C_A(x)$ is the atomic fraction of A in the alloy at depth x, and Ω is the mean atomic volume. We can also define the probability per unit depth, $p_A(x)$, that an A atom present at depth x is ejected by an incoming ion:

$$p_A(x) \equiv \sigma_A(x)/\Omega. \tag{10.13}$$

The yield of A atoms then takes the form:

$$Y_A = \int_0^\infty C_A(x)p_A(x)dx. \tag{10.14}$$

The primary effects in alloy sputtering are those related to the individual sputtering events and the physical variables contributing to the sputter yield and are all contained in the sputter probability, p_A, which depends on the type and energy of the incoming ion, the type of the sputtered atom and its surface binding energy, etc. Since the values of the sputter probabilities, p_i, will differ for differing atomic species, preferential sputtering will occur.

The secondary effects in alloy sputtering enter into Eq. (10.14) via the atomic concentration, C_A, which gives the probability that a site is occupied by an A atom. As a consequence, the sputter yields of the alloying components will be affected through the factor $C_A(x)$ in Eq. (10.14). Practically, sputtered atoms come from a shallow layer (Fig. 10.1) with the contribution falling off exponentially with depth. The decay length is of the order of two atomic layers. Therefore, the integral in Eq. (10.14) can be replaced [6, 7, 12] by the following:

$$Y_A \bar{p}_A C_A^s, \tag{10.15}$$

where $\bar{p}_A$ is the average total probability for an A atom present in the surface layer to be sputtered off per incident ion and C_A^s is the average atomic concentration of A in the surface layer, denoted by the superscript s. The thickness of this layer is not well-defined but should be taken as one or two atomic layers for determining C_A^s since the origin of sputtered ions is heavily weighted toward the first atomic layer.

Differences in the sputter probabilities for component atoms in an alloy are caused by differences in the amounts of energy and momentum transferred to atoms of different masses, and surface binding energies. However, continued sputtering of a semi-infinite alloy target of uniform bulk composition must eventually lead to a steady state in which the composition of the flux of sputtered atoms leaving the surface equals the composition of the bulk alloy. Wiedersich et al. [11] have shown that bombardment of a binary alloy AB with a flux of ions ϕ (ions/cm^{2}s) leads to an atom removal rate given by the following:

$$\frac{dN}{dt} = \phi(Y_A + Y_B). \tag{10.16}$$

Therefore, the rate at which the sputtered surface recedes can be calculated from the total rate of atom loss per unit area:

$$\dot{\delta} = d\delta/dt = \phi\Omega dN/dt = \phi\Omega(\bar{p}_A C_A^s + \bar{p}_B C_B^s), \tag{10.17}$$

where δ is the thickness of the surface layer removed by sputtering.

They also showed that the net accumulation rate of species, i in a slab of solid at the surface of the sample, $0 \le x < x_0$ is

$$\frac{dN_i}{dt} = \phi\left[C_i^b(\alpha/\Omega^b) - Y_i\right], \tag{10.18}$$

where C_i^b is the atomic concentration of component i of the bulk alloy, denoted by the superscript b, α is the volume removed per incident ion, and Ω^b is the average atomic volume of the bulk alloy. The net rate of accumulation of implanted ions is

$$\frac{dN_0}{dt} = \phi[1 - Y_0]. \tag{10.19}$$

At steady state, the terms in the square brackets of Eqs. (10.18) and (10.19) must equal zero, giving

$$Y_1 : Y_2 : Y_3 \ldots = C_1^b : C_2^b : C_3^b \ldots, \tag{10.20}$$

and

$$Y_0 = 1. \tag{10.21}$$

That is, the ratios of the alloy components in the sputtered flux are the same as those of the bulk alloy and their concentrations are just uniformly *diluted* by the re-emitted sputter ions. Note that the steady-state flux of sputtered atoms contains *no information* on preferential sputtering. Information about preferential sputtering can be obtained from the steady-state concentrations in the near-surface region via the approximation given in Eq. (10.15). Substituting Eq. (10.15) into Eq. (10.20) yields:

$$\frac{p_1}{p_2} = \frac{C_1^{\mathrm{b}}}{C_1^{\mathrm{s}}} \frac{C_2^{\mathrm{s}}}{C_2^{\mathrm{b}}}, \quad \text{or} \quad \frac{C_1^{\mathrm{s}}}{C_2^{\mathrm{s}}} = \frac{C_1^{\mathrm{b}}}{C_2^{\mathrm{b}}} \frac{p_2}{p_1}. \tag{10.22}$$

That is, after steady state is attained, the sputter probabilities are proportional to the ratio of the bulk and surface concentrations of the element in question. The sputter probability of the sputter ions can be obtained from the surface concentration:

$$p_0 \cong \frac{1}{C_0^{\mathrm{s}}}. \tag{10.23}$$

Lam and Wiedersich [13] have described the time evolution of preferential sputtering, PS on the near-surface composition for a binary alloy AB with $p_{\mathrm{A}}^{\mathrm{s}} > p_{\mathrm{B}}^{\mathrm{s}}$, i.e., for the case where PS of A atoms occurs (see Fig. 10.4). Note that initially, the concentration of A atoms in the sputtered flux (top dashed line) is larger than in the bulk. However, as the surface composition changes (bottom dashed line) and the near-surface layer composition is altered, a steady state will be achieved after a

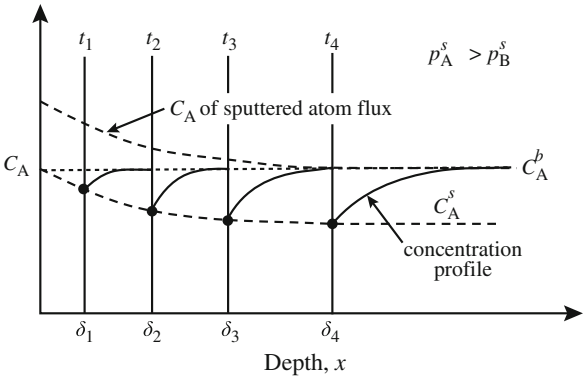

Fig. 10.4 Schematic description of the effect of preferential sputtering on the time evolution of the composition of the near-surface region of the sample and of the sputtered atom flux (after [13])

certain bombardment time, when the composition of the sputtered atom flux becomes equal to the bulk composition, as dictated by the law of conservation of matter. That is, the surface concentration of A atoms will evolve to a steady state at which the higher sputtering probability of element A relative to element B is offset by a lower A atom concentration.

Consider a binary alloy, A:B such that $C_A^b = C_B^b = 0.5$. Then from Eq. (10.22), we have:

$$\frac{C_A^s}{C_B^s} = \frac{\bar{p}_B}{\bar{p}_A}. \tag{10.24}$$

If the surface concentrations are measured to be $C_A^s = 0.33$ and $C_B^s = 0.67$, then we know that $\bar{p}_A : \bar{p}_B = 2.0$. Conversely, if we measure a steady-state sputtered atom flux of A atoms to B atoms of 1.0 (Y_A: Y_B = 1.0), then all this tells us is that S_A: S_B = 1.0. That is, measuring the sputtered atom flux tells us nothing about the surface composition. We must make surface composition measurements directly and independently.

10.2.2 Gibbsian Adsorption

Gibbsian adsorption (or thermal surface segregation) is the process by which the surface of an alloy readjusts itself to a composition different from that of the bulk in order to lower the free energy of the alloy [14]. In metallic systems, the change can be quite substantial, but the effect is confined to one or two atomic layers. The bulk composition is essentially unaffected because of the large bulk-to-surface volume ratio. The readjustment occurs spontaneously at temperatures sufficiently high for diffusion to proceed at reasonable speed. Consider a surface layer of composition C_A^s and C_B^s that differs from the bulk composition C_A^b and C_B^b. At equilibrium, the surface composition is related to the bulk composition [14] by:

$$\frac{C_A^s}{C_B^s} = \frac{C_A^b}{C_B^b} \exp\left(-\frac{\Delta H_A}{kT}\right), \tag{10.25}$$

where ΔH_A is the heat of adsorption, defined as the enthalpy change associated with the exchange of an A atom in the bulk with a B atom at the surface. At elevated temperature, equilibrium is approached by a net flux, J_A of A atoms described by:

$$J_A \Omega = \left[\left(v_A^{b \to s} C_A^b C_B^s \right) - \left(v_A^{s \to b} C_A^s C_B^b \right) \right] \xi, \tag{10.26}$$

where ξ is the atomic layer thickness, $v_A^{b \to s}$ is the bulk-to-surface jump frequency and $v_A^{s \to b}$ is the surface-to-bulk jump frequency for atom A. The first term on the

right is the flux of A atoms from the bulk to the surface and the second term is the flux of A atoms from the surface to the bulk. At equilibrium ($J_A = 0$), or:

$$\frac{\nu_A^{b\to s}}{\nu_A^{s\to b}} = \frac{C_A^s}{C_A^b}\frac{C_B^b}{C_B^s}, \tag{10.27}$$

and substituting into Eq. (10.25) gives:

$$\nu_A^{s\to b} = \nu_A^{b\to s}\exp\left(-\frac{\Delta H_A}{kT}\right). \tag{10.28}$$

This says that the activation enthalpy for a surface segregating element (one that must have $\Delta H_A < 0$) for the jump back into the bulk is effectively increased by the heat of adsorption relative to the migration enthalpy in the bulk. The difference in concentration between the surface layer and the bulk is established and maintained by the reduced probability of thermally activated jumps of A atoms from the surface into the bulk. The enhanced surface concentration due to Gibbsian adsorption, GA will result in an increased loss of the segregated elements due to sputtering. Continued preferential loss of an element by GA requires that diffusion be high ($T \geq 0.5T_m$), but because sputtering enhances thermal diffusion, the effect of GA becomes significant at $T \cong 0.3T_m$. However, the athermal displacement mixing process will oppose GA. The effect of GA at steady state is to suppress the concentration in the alloy just below the surface layer to a value that maintains the surface layer concentration at the value dictated by preferential sputtering. Hence, under ion bombardment, the surface composition will be affected by both of these processes. Lam and Wiedersich [13] provided a schematic description of the dynamic behavior of the surface composition during ion bombardment resulting from the simultaneous effects of GA and PS. In the example shown in Fig. 10.5, Gibbsian adsorption results in a surface concentration of A atoms that is initially greater than the bulk level, shown by the step change in A atom concentration at the

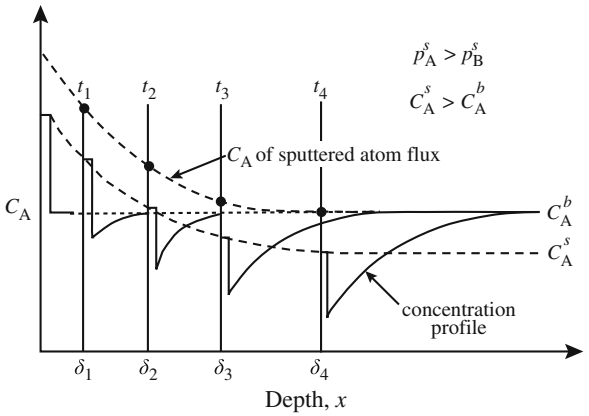

Fig. 10.5 Schematic description of the simultaneous effects of GA and PS on the time evolution of the near-surface composition and of the sputtered atom flux (after [13])

surface. This leads to enhanced preferential sputtering of A atoms since the sputtered atom flux is primarily from the first atom layer. Consequently, the concentration of A atoms in the subsurface layer will be reduced in an effort to re-establish thermodynamic equilibrium. After a time, t_1, the A atom concentration profile resembles the original in that there is a stepwise enrichment of A at the surface, but the surface concentration is reduced relative to the original and the concentration behind the step is reduced as well. With increasing bombardment time, the surface concentration of A continues to drop and the zone depleted in atom A increases in depth and width. Steady state is reached when the composition of the sputtered atom flux is equal to the bulk composition of the alloy.

10.2.3 Recoil Implantation

The incoming ion beam imparts its momentum to the atoms (and electrons) of the solid. Hence, the momentum distribution of atoms during the displacement process is not isotropic and atoms will be relocated preferentially in the beam direction. This does *not* lead to any significant net atom transport in the beam direction because the solid will relax to approximately its normal density, i.e., the flux of recoiling atoms in the beam direction is compensated by a uniform flux of atoms due to relaxation in the opposite direction. In alloys, the relocation cross section and the range of the recoiling atoms depend on the charge and mass of the nucleus in such a way that generally the lighter component atoms will be transported relative to the heavier components in the beam direction. This can be described as a flux of atoms of some of the alloy components toward deeper regions in the target, compensated by an opposite flux of the remainder of components to maintain atomic density at the proper value, i.e., the net flux of atoms is approximately zero across any plane parallel to the surface inside the target. The expression "recoil implantation" is used to describe the net transport parallel to the beam direction of some types of atoms relative to other types. The mechanics of recoil implantation have been developed by Sigmund et al. [15–17] and are summarized here.

Consider the average implantation effect of a single ion (M_0, Z_0) slowing down along a straight line to a well-defined range, R in a homogeneous binary alloy of components 1 and 2 characterized by M_i, Z_i, and concentration C_i with $i = 1, 2$, and $C_1 + C_2 = 1$. The number of i recoils created with energy (T, dT) in element (x, dx) along its path is:

$$NC_i \mathrm{d}x \sigma_{0i}(E(x), T), \tag{10.29}$$

where $E(x)$ is the ion energy at depth x and σ_{0i} is the elastic scattering cross section between the incoming ion, 0, and atom i. From LSS theory, the projected range of a recoil, R_p, is:

$$R_{\mathrm{p}} = R_i(T)\left(\frac{T}{\gamma_{0i}E(x)}\right)^{1/2}, \tag{10.30}$$

where R_i is the path length and recoils are assumed to slow down on a straight line to a well-defined range, and $\gamma_{ij} = 4M_iM_j/(M_i + M_j)^2$. Then, the total *effect*, P_i, of the knock-on implantation is the integral of the *number* of recoils and their *range*:

$$P_i = NC_i \int_0^R \mathrm{d}x \int_0^{\gamma_{0i}E(x)} \sigma_{0i}(E(x), T)R_i(T)\left(\frac{T}{\gamma_{0i}E(x)}\right)^{1/2} \mathrm{d}T. \tag{10.31}$$

Equation (10.31) is evaluated on the basis of power law scattering:

$$\begin{aligned} \sigma_{ij}(E,T) &= C_{ij}E^{-m}T^{-1-m}, \quad i,j = 0,1,2 \quad 0<m<1 \\ C_{ij} &= B_1 a_{ij}^{2(1-m)}\left(\frac{M_i}{M_j}\right)^m (Z_iZ_j)^{2m} \\ a_{ij} &= B_2(Z_i^{2/3}Z_j^{2/3})^{-1/2}, \end{aligned} \tag{10.32}$$

where B_1 and B_2 are constants. The range $R_i(T)$ is determined, as in Chap. 1, from the partial stopping cross section:

$$S_{ij}(E) = \int T'\mathrm{d}\sigma_{ij}(E,T'). \tag{10.33}$$

Performing the integration in Eqs. (10.31) and (10.33) and dividing by the projected range yields:

$$Q_i = \frac{P_i}{R_{\mathrm{p}}} = \frac{1-m}{m(1+2m)}\gamma_{01}^{2m-1}\frac{C_i}{(A_{i1}+A_{i2})}, \tag{10.34}$$

where

$$A_{ij} = C_j\left(\frac{\gamma_{ij}}{\gamma_{0i}}\right)^{1-m}\left(\frac{a_{ij}}{a_{0i}}\right)^{2(1-m)}\left(\frac{M_i^2}{M_0M_j}\right)^m\left(\frac{Z_j}{Z_0}\right)^{2m}, \tag{10.35}$$

where 0 is the incoming ion, i is the atom struck by the ion, and j is the subsequent atoms struck by the ith atom.

Q_i is the *equivalent* number of i atoms recoil implanted over the depth R_{p} (i.e., the ion range) in the direction of the ion beam, per incident ion. The dominating term in Q_i with regard to its dependence on i is the factor M_i^{2m} in Eq. (10.35). It shows that recoil implantation prefers the *lighter* species since the number of i recoils at a given energy (T, dT) is proportional to $M_i^{-m}Z_i^{2m}$, so it is greatest for the heavy component. But the *range* of i recoils at a given T is proportional to

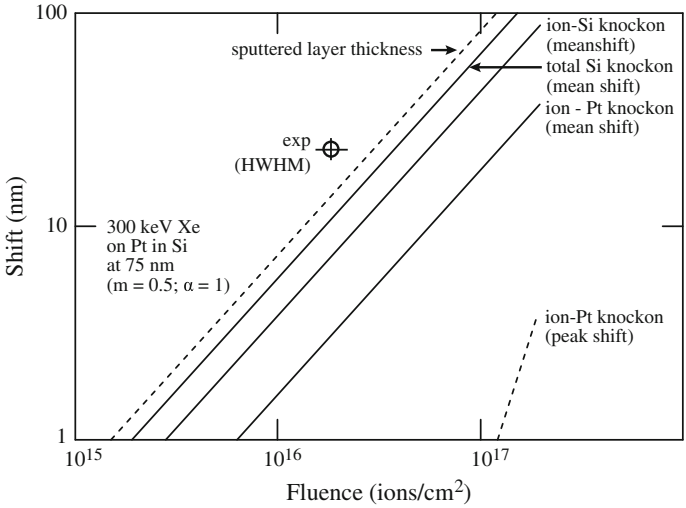

Fig. 10.6 Marker layer shift for 300 keV Xe ions incident on a thin Pt layer at 75 nm in Si, calculated using Sigmund's recoil implantation model (after [16])

$M_i^{-m} Z_i^{-2m}$, so it is greatest for the light component. Hence, the combined effect, or the number × range, is proportional to M_i^{-2m}.

As an example, consider Ar^+ bombardment of PtSi. The resulting values for the equivalent number of each atom-type recoil implanted over the range of the ion [15] are

$$Q_{Pt} = 0.034, \quad Q_{Si} = 0.37 \quad \text{for } m = 0.5$$
$$Q_{Pt} = 0.019, \quad Q_{Si} = 0.94 \quad \text{for } m = 0.33.$$

In both cases, there is a net transport of Si relative to that of Pt. Results for a similar experiment in which Si containing a marker layer of Pt was bombarded with 300 keV Xe^+ are shown in Fig. 10.6. Note that the shift of the ion-Si knock-on is greater than that for the ion–Pt knock-on, resulting in a net transport of Si away from the surface, relative to that for Pt. The significance of this result is that preferential transport of a specie in a target based on its mass can contribute to mixing of the solid.

10.2.4 Cascade (Isotropic, Displacement) Mixing

The rapid transfer of energy from recoiling atoms of the solid to other atoms leads to an efficient randomization of recoil directions within cascades. As a consequence, most of the relocation events of atoms in energetic cascades lead to *isotropic*

mixing rather than to recoil implantation. Molecular dynamics calculations indicate that the number of replacements in a displacement event results in a mean square diffusion distance of atoms, $\langle x^2 \rangle \sim 30\, a^2$ per defect pair produced (where a is the nearest neighbor distance). Thus, an atomically sharp interface is broadened by $\langle x^2 \rangle^{1/2}$, or about 5 atom planes for a dose of one dpa. Broadening increases proportionally to the square root of dose, so IBM of multilayer targets is an efficient means of homogenizing the solid.

As with neutron irradiation, ion irradiation of a target results in the production of a collision cascade. Depending on the ion mass and its energy, the energy density in the cascade can range from 10^{-3} to 10 eV/atom. The cascade propagation time is of the order 10^{-14} s and the quench time, is 10^{-12} s. It is important to distinguish between individual cascades and cascade overlap. In a target undergoing ion bombardment at a current density (proportional to dose rate) of 1 μA/cm^2 (~6×10^{12}ions/cm^{2}s for singly charged ions), successive cascades will occur in a given region of material at roughly 1 s intervals for cascade diameters of ~ 4 nm. That is, each volume of material will experience a cascade once each second. In order for cascade overlap to be avoided, the total dose must be kept below $\sim 10^{13}$ ions/cm^2. Realize that even in the cascade overlap regime, the cascade lifetime is $\sim 10^{-12}$ s, so there is no temporal communication between cascades unless there is some thermal diffusion. Within a single cascade, the mean displacement distance is always insignificantly small. For example, if each Frenkel pair is displaced, an average of ~ 1 nm (R_{recoil}), because the ratio of the number of displaced atoms, N_{d} to the total number of atoms within the central core of the cascade, N_{cas}, is much less than unity, the mean atomic displacement within the cascade ($R_{\text{recoil}} \times N_{\text{d}}/N_{\text{cas}}$) is negligible. Only with the aid of radiation-enhanced diffusion after the cascade has ended, could significant mixing occur. At doses of ~10^{16} ions/cm^2, the implanted region receives over 10^3 successive overlapping cascades and the cumulative effect of ballistic mixing is no longer negligible.

Ballistic Mixing

Recall that the atomic model of thermal diffusion resulted in a diffusion coefficient of the form, Eq. (4.44):

$$D = 1/6\lambda^2 \Gamma, \tag{10.36}$$

where Γ is the total jump frequency and λ is the jump length. If we assume that the distribution of momentum transfers in cascade mixing is isotropic, then the result is a cumulative random walk-like displacement process. We can characterize the transport process by introducing an *effective diffusion coefficient*, D^* [18, 19] where:

$$D^* = 1/6R^2 F, \tag{10.37}$$

where R is the root-mean-square displacement of an atom in the collision cascade and $F(x)$ is the atomic displacement rate in dpa/s due to an incoming particle flux ϕ.

F can be estimated from the K–P displacement model as follows. Recall from Chap. 2 Eqs. (2.1) and (2.2) that:

$$\frac{R_d}{N} = F = \int \phi(E)\sigma_D(E_i)dE_i, \tag{10.38}$$

and

$$\sigma_D(E_i) = \int \sigma_s(E_i, T)\nu(T)dT. \tag{10.39}$$

Assuming a monoenergetic particle flux and isotropic elastic scattering gives:

$$\nu = \bar{T}/2E_d, \tag{10.40}$$

and

$$\sigma_D = \frac{\bar{T}}{2E_d}\sigma_s, \tag{10.41}$$

giving

$$F = \phi\sigma_s\frac{\bar{T}}{2E_d}. \tag{10.42}$$

By the definition of average energy loss, $dE/dx|_n = \frac{\bar{T}}{\lambda} = N\sigma_s\bar{T}$, and substituting for $\bar{T}$ into Eq. (10.42) gives:

$$F = \frac{\phi\ dE/dx|_n}{2E_dN}, \tag{10.43}$$

where $dE/dx|_n$ is the ion energy deposited per unit depth into atomic processes and E_d is the displacement energy. Substituting the expression for F in Eq. (10.43) into Eq. (10.37) for D^* gives:

$$D^* \cong \frac{R^2\phi\, dE/dx|_n}{12E_dN}. \tag{10.44}$$

As mentioned earlier, the effect of cascade mixing is to smear out an originally sharp interface or to broaden a delta function to a Gaussian distribution. Let us consider the effect of cascade mixing on three different composition profiles in a target. Recall that Fick's second law states that:

$$\frac{\partial C}{\partial t} = -\nabla \cdot D\nabla C = -D\nabla^2 C, \quad \text{for} \quad D \neq f(C). \tag{10.45}$$

Case 1: Thin film

For the geometry shown in Fig. 10.7(a), the boundary conditions are as follows:

$$C \to 0 \quad \text{as} \quad t \to 0 \quad \text{for } |x| > 0$$
$$C \to 1 \quad \text{as} \quad t \to 0 \quad \text{for } x = 0$$

$\int_{-\infty}^{\infty} C(x.t)\, dx = \alpha$, where α is the total amount of solute in the target. Assuming that the layer is infinitely thin, the solution to Fick's second law is:

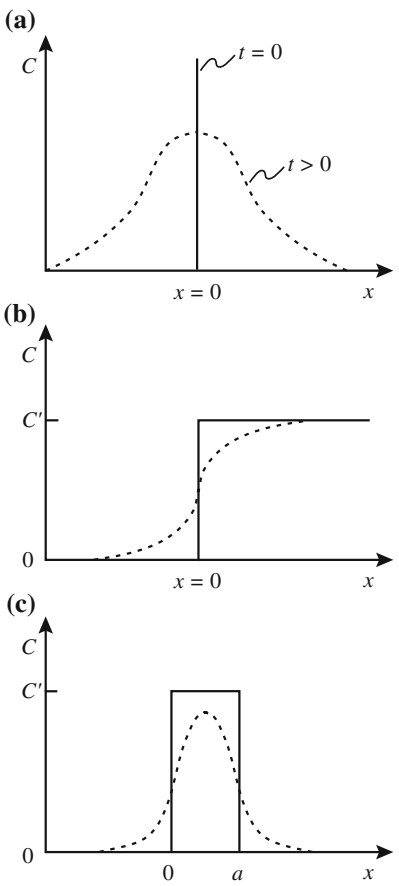

Fig. 10.7 Schematic illustration of the effect of ion beam mixing on (**a**) a thin film, (**b**) a pair of semi-infinite solids (bilayer), and (**c**) a thin film of finite thickness (multilayer)

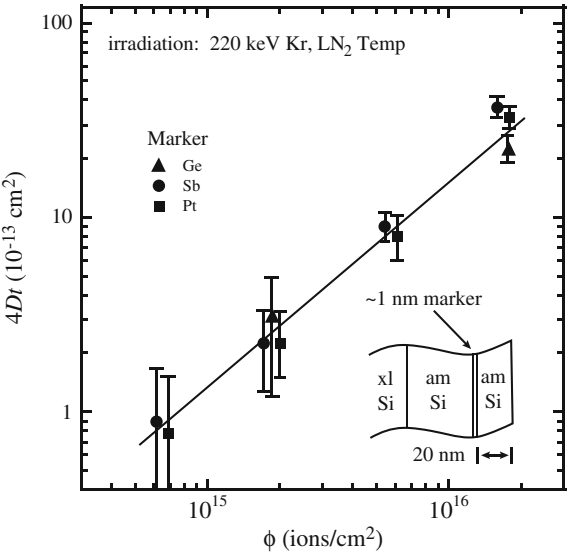

Fig. 10.8 Marker mixing data for several different markers in amorphous Si showing the relationship between the effective ion mixing diffusion coefficient, $4Dt$, and the dose, ϕt (after [1])

$$C(x,t) = \frac{\alpha}{\sqrt{4\pi Dt}} \exp\left(\frac{-x^2}{4Dt}\right), \tag{10.46}$$

where the variance, $\sigma^2 = 4Dt$; the standard deviation, $\sigma = \sqrt{4Dt}$; and the full width at half maximum, FWHM = 2.35σ. From Eq. (10.44), the increment of FWHM due to cascade mixing is then:

$$\Delta\text{FWHM} = 2.35\sqrt{4D^*t} \cong R\left[\frac{2\mathrm{d}E/\mathrm{d}x|_n \phi t}{E_d N}\right]^{1/2}. \tag{10.47}$$

Note that the broadening of the thin film as described by ΔFWHM is proportional to $(\phi t)^{1/2}$, or the effective ion mixing coefficient, $4Dt$ is proportional to ϕt. Figure 10.8 shows that as predicted by Eq. (10.47), mixing given by $4Dt$ is proportional to the dose.

Taking the example of 150 keV Kr^+ bombardment of a Ni sample containing a thin film as in Fig. 10.7(a), the dose needed to produce a ΔFWHM of 10 nm is:

$$\Delta\text{FWHM} = 10\text{ nm} \cong R\left[\frac{2\mathrm{d}E/\mathrm{d}x|_n \phi t}{E_d N}\right]^{1/2}. \tag{10.48}$$

For $\mathrm{d}E/\mathrm{d}x|_n = N\sigma_s\bar{T}$ then Eq. (10.48) becomes:

$$\Delta\text{FWHM} = 10\ \text{nm} \cong R\left[\frac{2\sigma_s \bar{T}\phi t}{E_d}\right]^{1/2}. \tag{10.49}$$

For $\sigma_s \sim 10^{16}$ cm^2, $\bar{T} \sim E_i = 150$ keV, $E_d \sim 15$ eV and $R \sim 1.5$ nm, and the dose to cause a ΔFWHM of 10 nm is 8.5×10^{14} i/cm^2. If He^+ is used instead of Kr^+, then the required dose is 3.5×10^{15} i/cm^2.

Case 2: Pair of semi-infinite solids (bilayer)

For a bilayer as shown in Fig. 10.7b, the boundary conditions are:

$$\begin{aligned} C &= 0 \quad \text{for } x<0 \text{ at } t = 0, \\ C &= C' \quad \text{for } x > 0 \text{ at } t = 0. \end{aligned}$$

The solution to Fick's second law subject to the boundary conditions is:

$$C(x,t) = \frac{C'}{2}\left[1 + \text{erf}\left(\frac{x}{\sqrt{4Dt}}\right)\right]. \tag{10.50}$$

Figure 10.9 shows that as predicted by Eq. (10.50), mixing across a bilayer interface as described by $4Dt$ is, indeed, linear with dose for several bilayers systems, although the proportionality constant is system-dependent, as will be discussed later.

Case 3: Thin film of finite thickness (multilayer)

For a layer of finite thickness, as shown in Fig. 10.7c, the boundary conditions are:

$$\begin{aligned} C &= C' \quad \text{for } 0<x<a \quad \text{and} \quad t = 0, \\ C &= 0 \quad \text{for } x<0, x > a \quad \text{and} \quad t = 0. \end{aligned}$$

The solution is:

$$C(x,t) = \frac{C'}{2}\left[\text{erf}\left(\frac{x}{\sqrt{4Dt}}\right) - \text{erf}\left(\frac{x-a}{\sqrt{4Dt}}\right)\right]. \tag{10.51}$$

Chemical Effects on Ion Beam Mixing

Observations of mixing in binary systems reveal large differences in the amount of mixing that cannot be explained by ballistic effects. For example, mixing in the Cu–Au system is an order of magnitude higher than that in the Cu–W system [21, 22] and mixing of marker layers in Si and Ge varies significantly for elements of similar mass [23]. These systems are *collisionally similar* systems in that the ratio of the masses of the constituents is similar and so in a ballistic mixing model,

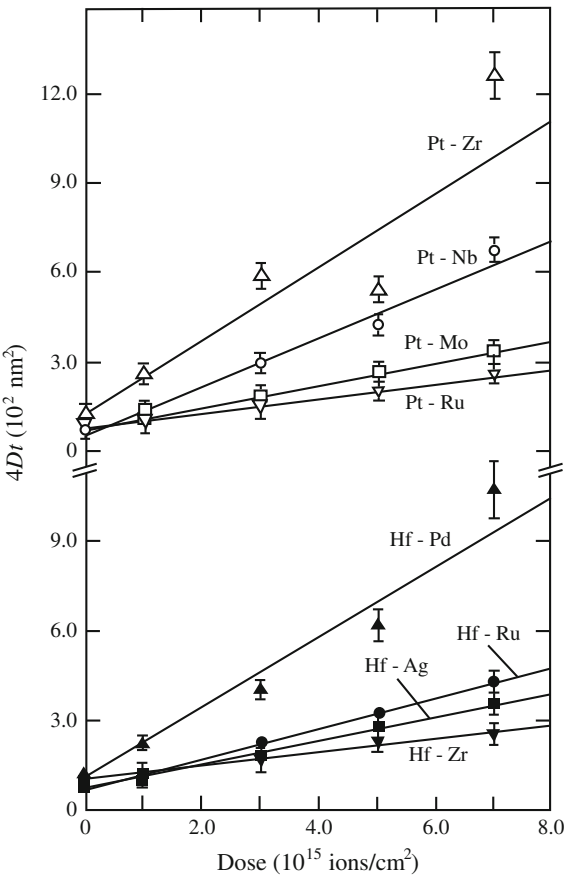

Fig. 10.9 Mixing of the interface versus dose for several bilayer samples irradiated with 600 keV Xe^{++} ions at 77 K (after [20])

they should behave similarly. Quite to the contrary, Fig. 10.9 showed that collisionally similar binary systems exhibited very different mixing rates. Further, mixing was occurring at 77 K where radiation-enhanced diffusion is suppressed.

Johnson [24–29] accounted for the chemical nature of the binary alloy components by first realizing that fundamentally, diffusion is driven by a chemical potential gradient, $\nabla\mu(x)$, and only for ideal solutions does Fick's law apply. More generally, for interdiffusion of two metals which form non-ideal solutions, one must relate $\nabla\mu(x)$ to $\nabla C(x)$. This can be accomplished by replacing D by a modified D' that accounts for the Kirkendall effect and describes diffusional intermixing the following:

$$\begin{aligned} D' &= \left[D_A^0 C_B + D_B^0 C_A\right]\left[1 + \frac{\partial \ln \gamma(C_A)}{\partial \ln C_A}\right] \\ &= D\left[1 - \frac{2\Delta H_{mix}}{kT}\right]. \end{aligned} \tag{10.52}$$

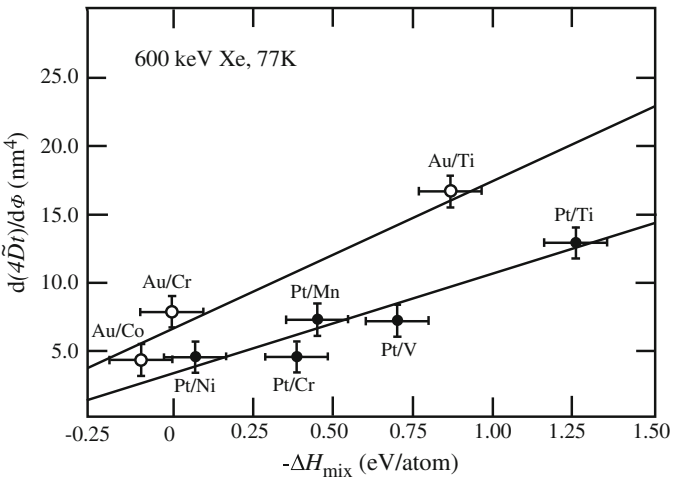

Fig. 10.10 Effect of the heat of mixing on the observed mixing rates for several binary metal systems following irradiation with 600 keV Xe^{++} ions at 77 K (after [24])

where D is the rate coefficient of unbiased mixing, γ is the activity coefficient, and ΔH_{mix} is the enthalpy of mixing given by:

$$\begin{aligned} \Delta H_{\text{mix}} &= 2\delta C_{\text{A}} C_{\text{B}}, \\ \delta &= z[H_{\text{AB}} - (H_{\text{AA}} + H_{\text{BB}})/2], \end{aligned} \tag{10.53}$$

where z is the coordination number (number of nearest neighbors) and H_{ij} is the potential between atom pairs, or pair enthalpies. Recall from Sect. 6.1 that the second term in square brackets in Eq. (10.52) is also referred to as the thermodynamic factor, χ. Equation (10.52) simply says that random walk will be *biased* when the potential energy depends on the configuration. So mixing rates depend not only on the number of random walk steps per unit time, but also on the degree of Darken biasing. Figure 10.10 highlights the effect of ΔH_{mix} on mixing rates for several bilayer systems. Equation Eq. (10.52) can be used to obtain a value of kT_{eff}, the effective temperature at which diffusion occurs. [28] In the Pt–Au system, the value for kT_{eff} is 1–2 eV. This means that the dominant contribution to ion mixing occurs when particle kinetic energies are of the order 1 eV!

If mixing depends on the thermodynamic properties of the solid, then it should depend on the cohesive energy, ΔH_{coh}, which is a measure of how tightly bound atoms are in a solid. Indeed, if we plot $\text{d}(4Dt)/\text{d}\phi$ versus ΔH_{coh}, we note a strong correlation (Fig. 10.11). The energy range of interest, ~1 eV, correlates with the thermalized regime of a displacement cascade, which can be depicted as a thermal spike. The effect of thermal spikes on diffusion was treated by Rossi and Nastasi [30] starting with Vineyard's thermal spike model [31] in which the nonlinear

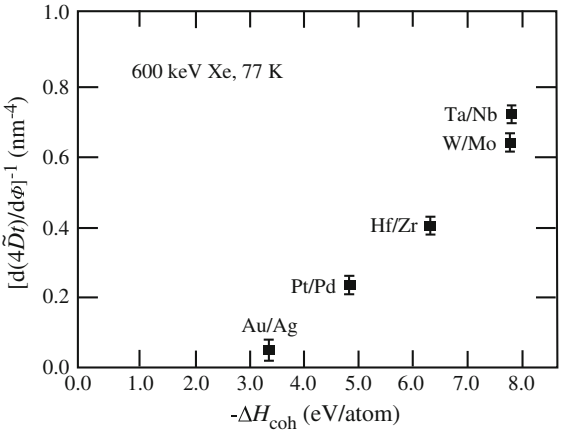

Fig. 10.11 Effect of the average cohesive energy on ion mixing in several binary metal systems following irradiation with 600 keV Xe^{++} at 77 K (after [29])

Fourier equation for heat conduction in an isotropic and uniform medium is given as follows:

$$\nabla\kappa \cdot \nabla T = c\frac{\partial T}{\partial t}, \tag{10.54}$$

where $\kappa = \kappa_0 T^{n-1}$ is the thermal diffusivity, $c = c_0 T^{n-1}$ is the specific heat capacity, κ_0 and c_0 are constants and $n \geq 1$. At time $t = 0$, a cylindrical spike is introduced along an infinite straight line at constant energy density, ε, where the distance perpendicular to the axis of the cylinder is r. The initial condition for the temperature distribution is given by:

$$Q = \int c\mathrm{d}T = (c_0/n)T^n(r,0). \tag{10.55}$$

For zero initial ambient temperature, solution of Eq. (10.54) subject to the boundary condition in Eq. (10.55) gives the temperature distribution in space and time:

$$T(r,t) = \left[\frac{n\varepsilon}{4\pi\kappa_0 t}\right]^{1/n} \exp(-c_0 r^2/4\pi\kappa_0 t). \tag{10.56}$$

Defining η as the total number of atom jumps in one spike per unit length of the spike, then analogous to thermal diffusion, we assume Arrhenius behavior for the jump rate, R such that $R = A\ \exp(-Q/kT)$, then η is:

$$\eta = \int 2\pi r\mathrm{d}r \int A\ \exp(-Q/T(r,t))\mathrm{d}t. \tag{10.57}$$

Integration of Eq. (10.57) yields:

$$\eta = \frac{n^3 \Gamma(2n) A\varepsilon^2}{8\pi\kappa_0 c_0 Q^{2n}}, \tag{10.58}$$

where $\Gamma(2n)$ is the gamma function with argument $2n$. For moderate temperatures, $n = 1$ and Eq. (10.58) becomes:

$$\eta = \frac{A\varepsilon^2}{8\pi\kappa c Q^2}. \tag{10.59}$$

Referring back to Eq. (10.52) for a binary system with $|\Delta H_{\text{mix}}| > 0$, the *effective* jump rate at temperature T can be written as:

$$R_{\text{eff}} = A \exp(-Q/kT)[1 - 2\Delta H_{\text{mix}}/kT], \tag{10.60}$$

and Eq. (10.57) becomes:

$$\eta_c = \int 2\pi r \mathrm{d}r \int A \exp(-Q/kT(r,t))[1 - 2\Delta H_{\text{mix}}/kT(r,t)]\mathrm{d}t, \tag{10.61}$$

where the subscript on η denotes chemical biasing. Taking $n = 1$ and carrying out the integral over the size and lifetime of the spike yields:

$$\eta_c = \frac{A\varepsilon^2}{8\pi\kappa c Q^2}(1 - 4\Delta H_{\text{mix}}/Q). \tag{10.62}$$

Since the activation energy scales with the cohesive energy, we take $Q = -s_2 \Delta H_{\text{coh}}$, where s_2 is a constant. After a dose Φ (i/cm^2), the total number of jumps in the solid is equal to $\eta_c \Phi/\rho$, where ρ is the atomic density. The mixing rate is then given by:

$$\frac{\mathrm{d}(4Dt)}{\mathrm{d}\Phi} = \eta_c r_c^2/\rho, \tag{10.63}$$

where r_c is a characteristic jump distance. Assuming that r_c scales with the interatomic distance as $r_c = s_1 \rho^{-1/3}$, we obtain the following:

$$\frac{\mathrm{d}(4Dt)}{\mathrm{d}\Phi} = \frac{K_1 \varepsilon^2}{\rho^{5/3}(\Delta H_{\text{coh}})^2}(1 + K_2 \Delta H_{\text{mix}}/\Delta H_{\text{coh}}), \tag{10.64}$$

where K_1 depends on κ, c and A, and $K_2 = 4/s_2$. Equation (10.64) is plotted in Fig. 10.12 as the mixing versus the ratio of $\Delta H_{\text{mix}}/\Delta H_{\text{coh}}$ for a large number of binary systems and shows excellent correlation, indicating that the chemical effect on beam mixing is indeed, strong even at temperatures where RED does not occur. With increasing temperature, RED contributes to mixing as well.

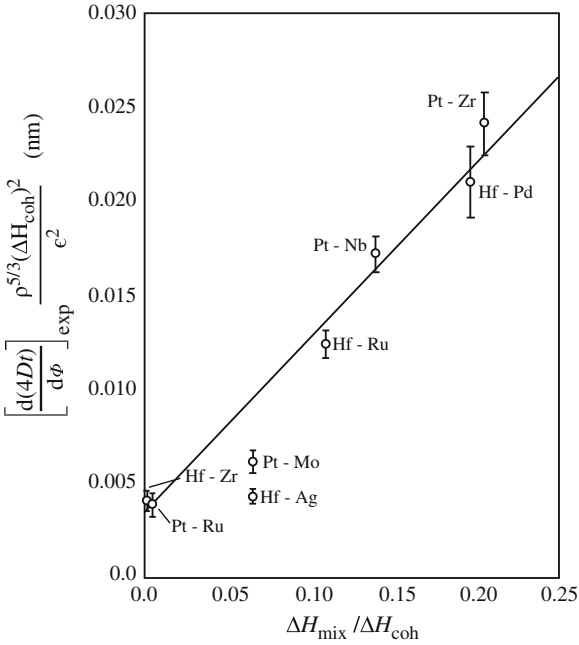

Fig. 10.12 Correlation between mixing and the ratio of $\Delta H_{mix}/\Delta H_{coh}$ for several metal bilayers irradiated with 600 keV Xe^{++} at 77 K (after [20])

Figure 10.13 shows the amount of intermixed silicon in a Si–Nb bilayer sample that was irradiated with Si^+ ions [32]. At high temperature, the data follow an Arrhenius-type behavior with an activation energy of 0.9 eV. As the temperature is lowered, the amount of intermixing does not continue to drop, but levels out at a value that is determined by the ballistic mixing of the elements, which is temperature dependent. Mixing induced only by temperature (thermal mixing) is shown by the solid curve on the left with an activation energy of 2.7 eV. The effect of radiation-enhanced diffusion is then the difference between the two plots that display Arrhenius behavior. Note that the low-temperature mixing is not due to an enhancement of diffusion by radiation, but rather to ballistic mixing. The total amount of mixing can be described by an effective diffusion coefficient [25] of the form

$$D = D_{\text{ballistic}} + D_{\text{rad}} \exp(-Q/kT), \tag{10.65}$$

where the first term on the right-hand side is due to ballistic mixing and is temperature independent, and the second term is due to radiation-enhanced diffusion and has an Arrhenius-type temperature dependence, where Q is an apparent activation energy. The temperature at which the two terms contribute equally to diffusion can be determined from Eq. (10.65) to be:

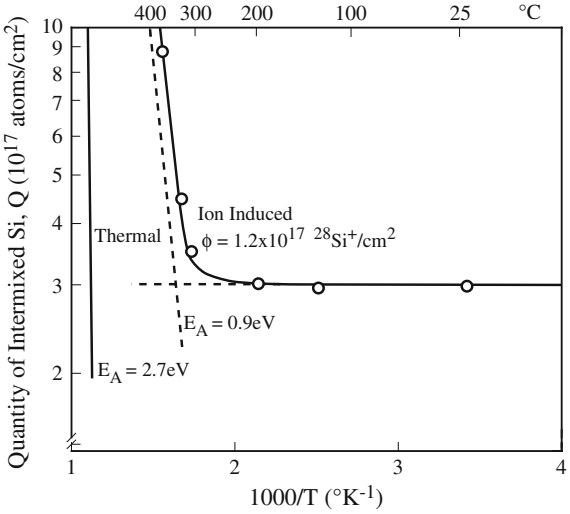

Fig. 10.13 Logarithm of the quantity of intermixed silicon versus reciprocal temperature for an Nb–Si bilayer sample after a fluence of 1.2×10^{17} $^{28}Si^+/cm^2$. The solid line is fit to the data points of the sum of a temperature-independent part (nearly horizontal dotted line) and a thermally activated part (high slope dotted line) with an activation energy $E_A \sim 0.9$ eV (after [32])

$$T_c = \frac{Q}{k[\ln(D_{rad}/D_{ballistic})]}. \tag{10.66}$$

Assuming that there is a scaling relationship between the apparent activation energy and the cohesive energy of the matrix, ΔH_{coh}, i.e., $Q = S\Delta H_{coh}$, where S is a scaling factor, then we obtain

$$T_c = \frac{S\Delta H_{coh}}{k[\ln(D_{rad}/D_{ballistic})]}. \tag{10.67}$$

Figure 10.14 shows the critical temperature as a function of the average cohesive energy for several bilayer systems using a scaling factor, $S = 0.1$ [33]. Note that the critical temperature is linear with the cohesive energy, as predicted by Eq. (10.67). That the vacancy migration energy also scales with the cohesive energy means that radiation-enhanced diffusion is due to vacancy migration.

In addition to homogenization of a target, displacement mixing is a very effective tool to study phase transformations under irradiation. Phase stability under irradiation was covered in Chap. 9, but IBM provides a unique opportunity to study ion-induced phase formation. Figure 10.15 shows how bilayer wedge samples can be made to cover the full range of composition in the Ni–Al binary system and how the phases develop as a function of composition. Figure 10.16 also shows that in

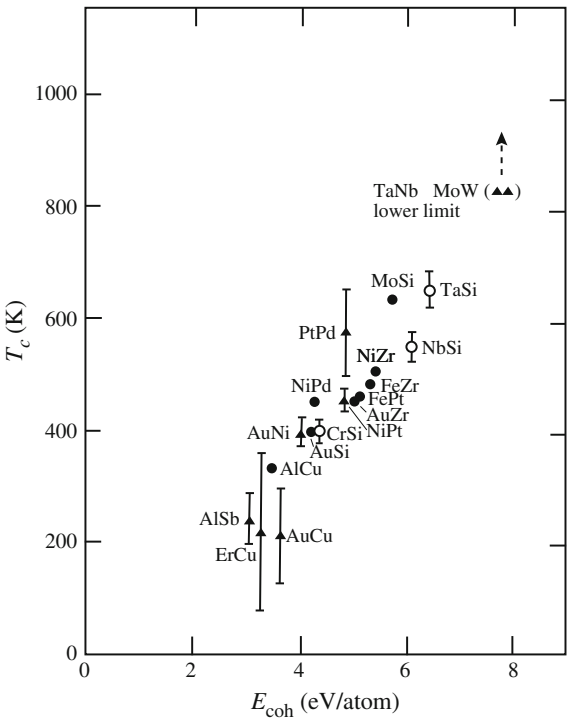

Fig. 10.14 Correlation between the average cohesive energy and the critical temperature, T_c, at which mixing by radiation-enhanced diffusion equals that due to ballistic processes (after [33])

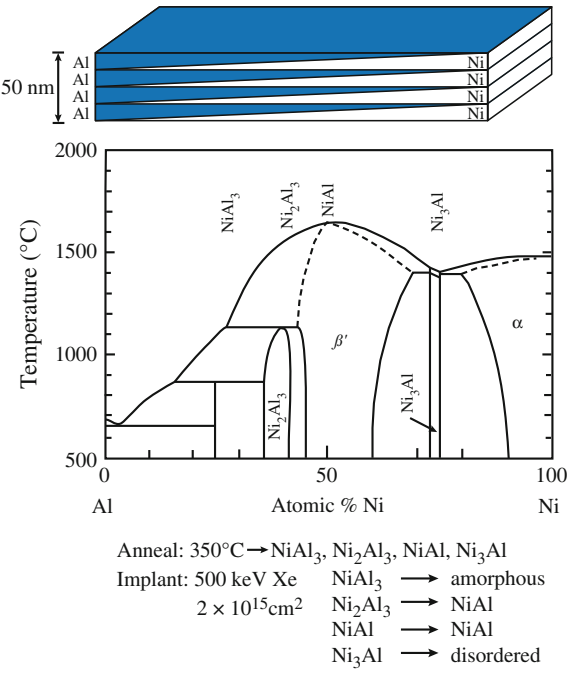

Fig. 10.15 Sample configuration, equilibrium phase diagram of Ni–Al and results of multilayered samples preannealed at 350 °C followed by irradiation with 500 keV Xe^+ to a dose of 2×10^{15} cm^{-2} (after [34])

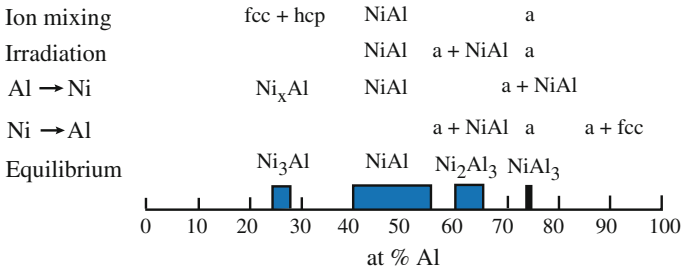

Fig. 10.16 Summary of microstructures in the Ni–Al system prepared by various ion beam treatments (after [35])

most cases the phases formed are independent of whether the irradiation is by IBM, direct ion implantation of an inert element, or direct implantation of A into B or B into A.

10.2.5 Combination of Processes Affecting Surface Compositional Changes

Accounting for the effects of all the processes described in the previous sections, Lam and Wiedersich [13] constructed a phenomenological model for bombardment-induced composition modification by formulating a set of coupled partial differential equations describing the temporal and spatial evolution of defect and atom concentrations during ion bombardment of a binary alloy. The formulation was based on the set of diffusion and reaction rate equations, i.e., Fick's second law with source and sink terms, describing the time rate of change of the alloy composition and defect concentrations:

$$\frac{\partial C_{\mathrm{v}}}{\partial t} = -\nabla \cdot (\Omega J_{\mathrm{v}}) + K_0 - R, \tag{10.68}$$

$$\frac{\partial C_{\mathrm{i}}}{\partial t} = -\nabla \cdot (\Omega J_{\mathrm{i}}) + K_0 - R, \tag{10.69}$$

$$\frac{\partial C_{\mathrm{A}}}{\partial t} = -\nabla \cdot [(\Omega J_{\mathrm{A}}) - D_{\mathrm{A}}^{\mathrm{disp}} \nabla C_{\mathrm{A}}], \tag{10.70}$$

where K_0 and R are the locally and spatially dependent rates of production and recombination of vacancies and interstitials and $D_{\mathrm{A}}^{\mathrm{disp}}$ is the diffusion coefficient caused solely by the displacement process. The time-dependent atom and defect concentration distributions can be determined by solving Eqs. (10.68) through (10.70) numerically for a semi-infinite target using appropriate starting and boundary conditions as described by Lam. [13, 36–38] This formulation covers the

processes of DM, RED, and RIS. Gibbsian adsorption and preferential sputtering can be accommodated in the model by treating the surface layer as a separate phase. Because of the structure of the phenomenological model, calculations can be made to determine the dependence of surface and subsurface compositional changes on material and irradiation variables as well as isolating the contributions of individual processes. However, because many of the parameters needed in the models are unknown, quantitative comparisons with experiment are difficult. Nevertheless, semiquantitative modeling of bombardment-induced compositional redistribution in several binary alloys has been made.

Wiedersich et al. [11, 34] provided a concise description of the effects of the different processes that occur during bombardment of an alloy and how those processes affect the surface composition. The calculations were performed with various combinations of preferential sputtering, displacement mixing, radiation-enhanced diffusion, Gibbsian adsorption, and radiation-induced segregation included. Figure 10.17 shows the time evolution of the Cu concentration profiles and the location of the sample surface in Cu–40 at.%Ni bombarded with 5 keV Ar ions at 400 °C. Gibbsian adsorption causes an initial enrichment in the surface concentration of Cu (1 s). After 10^2 s, sputtering has preferentially removed Cu from the surface, resulting in a depletion of surface Cu relative to the bulk. After 4×10^3 s, steady state is achieved and the Cu concentration is depleted at the surface, but the depth profile continues to reflect the effect of GA. Note also the recession of the surface with increasing dose due to sputtering.

Figure 10.18 shows the time dependence of the Cu concentration at the alloy surface. Note that in the absence of irradiation (curve 1), GA leads to a strong Cu enrichment in the first atom layer. Accounting only for PS and RED during irradiation (2) causes a monotonic decrease in C^s_{Cu} to the steady-state value, defined by the sputtering probability ratio and the bulk composition. If GA is included (3), C^s_{Cu} increases rapidly at short times owing to radiation-enhanced adsorption and then decreases slowly to the steady-state value. The inclusion of DM reduces the effect of GA (4). Considering only PS, RED, and RIS (5), C^s_{Cu} decreases rapidly to the steady-state value due to the dominant effect of segregation. If GA is added (6), then the effect of RIS is masked. Finally, with the addition of DM (7), or when all processes are included, C^s_{Cu} increases initially and then decreases toward the steady-state value. The effect of different combinations of processes on the steady-state Cu concentration profile is illustrated in Fig. 10.19.

10.2.6 Implant Redistribution During Ion Implantation

The implantation example given in Figs. 10.17, 10.18, and 10.19 was for bombardment of an alloy with an inert gas ion that plays no role as a chemical constituent of the alloy. In ion implantation, the concentration of the implanted ion is important to track, in addition to the effects of the various surfaces processes.

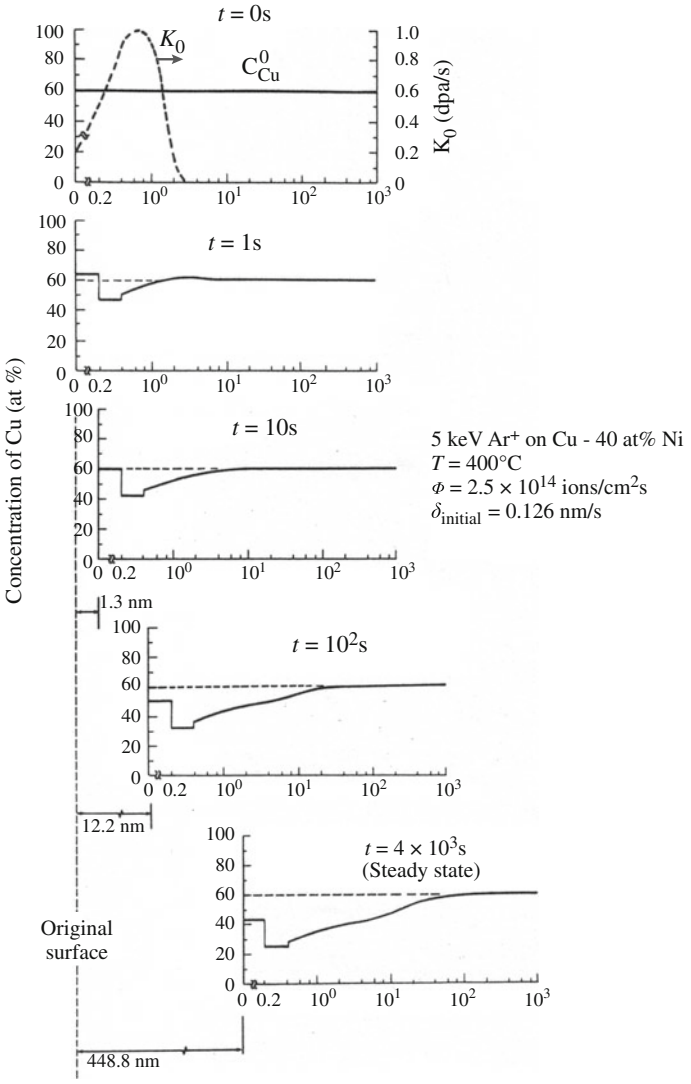

Fig. 10.17 Time evolution of Cu concentration and the location of the surface in a Cu-40 at.%Ni alloy bombarded with 5 keV Ar^+ at 400 °C (after [11])

A kinetic model was developed by Lam and Leaf [39] to describe the effects of these kinetic processes on the spatial redistribution of implanted atoms during the implantation process. The effects of spatially non-uniform rates of damage and ion deposition, as well as the movement of the bombarded surface as a result of sputtering and introduction of foreign atoms into the system, were taken into account. The evolution of the implant concentration profile in time and space was

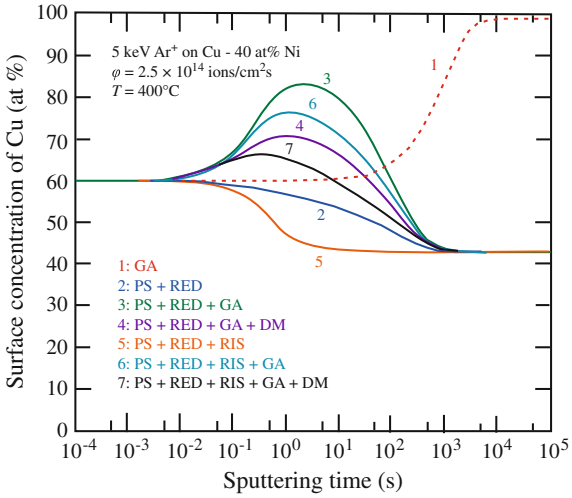

Fig. 10.18 Effects of various combinations of Gibbsian adsorption (GA), preferential sputtering (PS), radiation-enhanced diffusion (RED), displacement mixing (DM), and radiation-induced segregation (RIS) on the time evolution of the surface concentration of Cu in Cu-40 at.%Ni described in Fig. 10.17 (after [11])

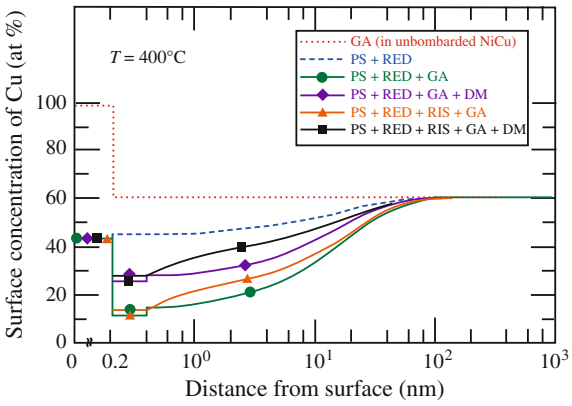

Fig. 10.19 Effects of various combinations of the same five processes described in Fig. 10.16 on the steady-state Cu concentration profiles (after [11])

calculated for various temperatures, ion energies, and ion–target combinations for a metal substrate B into which A atoms are implanted at a flux ϕ. The local concentrations of vacancies, B interstitials, A interstitials, A–vacancy complexes and free substitutional (A) solutes change with implantation time according to a system of kinetic equations [39] similar to those of Eqs. (10.68) through (10.70). Concurrently with the buildup of solute concentration in the host matrix, the surface is subjected to displacements both from sputtering and the introduction of foreign atoms into the system. Sputtering causes a recession of the surface, while

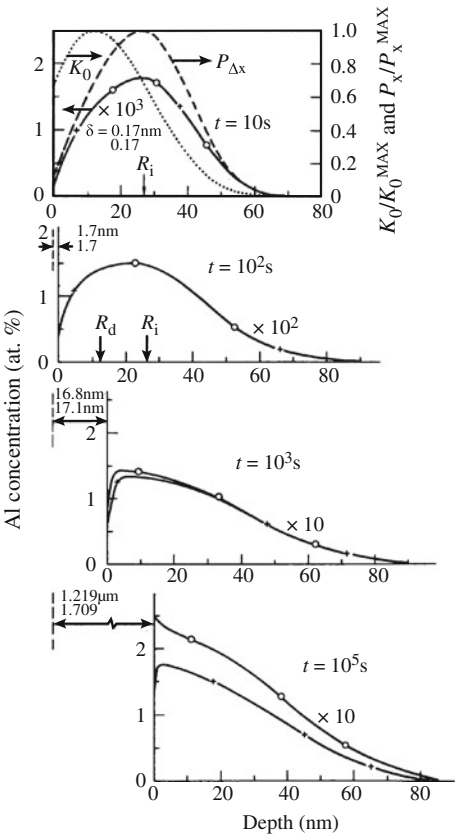

Fig. 10.20 Development of Al concentration profiles during 50 keV implantation into Ni at 500 °C. The normalized damage rate, K_0, and ion deposition rate, P, are shown in the top plot, and the surface displacements resulting from sputtering are indicated. Note that the concentration profiles are multiplied by factors shown in each plot (after [13])

implantation causes an expansion. The net surface displacement rate is controlled by the competition between the rates of ion collection and sputtering.

The temporal and spatial evolution of the surface and subsurface alloy composition is obtained by solving this set of equations for a semi-infinite medium, starting from the thermodynamic equilibrium conditions. Sample calculations were performed for low and high-energy Al^+ and Si^+ implantations into Ni, since it is known from earlier studies that in irradiated Ni, Si segregates in the same direction as the defect fluxes, whereas Al opposes the defect fluxes [40]. Redistributions of Al and Si solutes in Ni during 50 keV implantation at 500 °C are shown in Figs. 10.20 and 10.21, respectively.

In the Al-implantation case, C_{Al}^s increases with time to a steady-state value of ~50 at.%, which is governed by the partial sputtering yield of the implant. This value is substantially larger than that obtained in very-high-energy implantation, where sputtering is negligible and C_{Al}^s is controlled by RIS. However, the total implant concentration remaining in the sample is significantly smaller because of

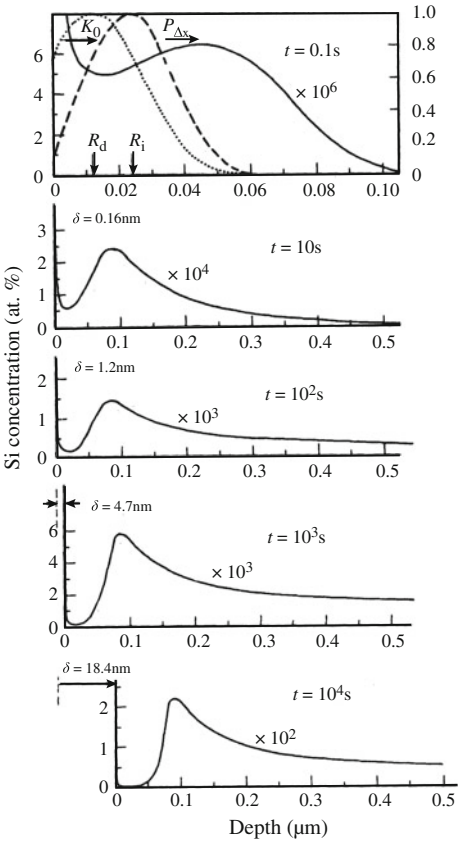

Fig. 10.21 Time evolution of the Si concentration profile during 50 keV implantation into Ni at 500 °C. The normalized damage rate, K_0, and ion deposition rate, P, are shown in the top plot. Surface displacements resulting from sputtering are indicated (after [13])

sputtering. Furthermore, the shape of the steady-state implant profile is dictated by PS, which controls the boundary condition at the surface, and by RED and RIS.

The evolution of the Si profile is rather different from that of Al, because of the different RIS behaviors. After a short implantation time, Si enrichment occurs at the surface because of RIS, and the Si distribution peak starts moving into the sample interior (Fig. 10.21). With increasing time, C^s_{Si} increases monotonically, attaining a steady-state value of ~ 100 at.% at $t \geq 2 \times 10^4$ s. Unlike the Al case, the Si profile shows a significant shift of the implant distribution into the beyond-range region. This predicted translation of the Si distribution peak into the sample interior was consistent with experimental measurements by Mayer et al. [41] in Si-implanted Ni at elevated temperatures.

10.3 Other Effects of Ion Implantation

In addition to those described thus far, several other processes must be considered during ion–solid interaction. For example, ion bombardment in which the displacement cascade intersects the surface can produce a crater on the surface. Movie 10.1 (http://rmsbook2ed.engin.umich.edu/movies/) shows an MD simulation of a 100 keV Xe ion impinging on a gold target. With the absence of constraint at the surface, the damage zone expansion intersects the surface and subsequent cooling results in a surface crater that can alter various other properties of the target. Additional processes such as grain growth, texture development, dislocation microstructure formation, gas bubble formation, and displacements due to electronic excitation will be discussed, with IBAD presented last.

10.3.1 Grain Growth

Ion-induced grain growth has been observed during irradiation of pure metals and multilayers. Liu and Mayer [42] observed the growth of grains of pure nickel films upon irradiation with inert gas ions, Ar, Kr, and Xe, in the energy range 150–580 keV. In their experiments, the grain size increased with dose until saturation at about 1×10^{16} i/cm^2. They found a nearly homogeneous grain size in the irradiated samples as compared to a wide spread in the grain size of thermally annealed samples. They also observed a dependence of the saturated grain size on ion species and only a weak dependence of grain size on ion dose at high doses (Fig. 10.22). The localized damage caused by the displacement spike in the vicinity of the grain boundary is the likely driving force for grain growth. The observed grain growth is explained by the reordering or growth of heavily damaged grains into neighboring, undamaged grains. The reduction in energy at a localized growing grain is equivalent to the difference between the energy released from the consumed region and the energy required to expand the grain boundary. The initially rapid grain growth can be explained by a larger probability of damaging an entire grain when the grains are small. As the irradiation process continues, the large grains consume the small ones and the average grain size increases. When the average diameter of the growing grains approaches the dimension of the damaged volume, the probability of highly damaging an entire grain by a single collision cascade is reduced, as is the chance of growing certain grains at the expense of others. Therefore, the grain growth rate gradually decreases with the increase of grain size.

The grain growth rate during mixing of multilayered Ni–Al films is enhanced over that due to bombardment of codeposited Ni–Al films of the same average composition by a factor of 2.2 (Fig. 10.23). This enhancement can be understood using the concept of the heat of mixing, using Johnson's expression for the total number of atom jumps induced in a spike per unit length of a cylindrical thermal spike, η. Assuming that this value is proportional to grain boundary mobility, the

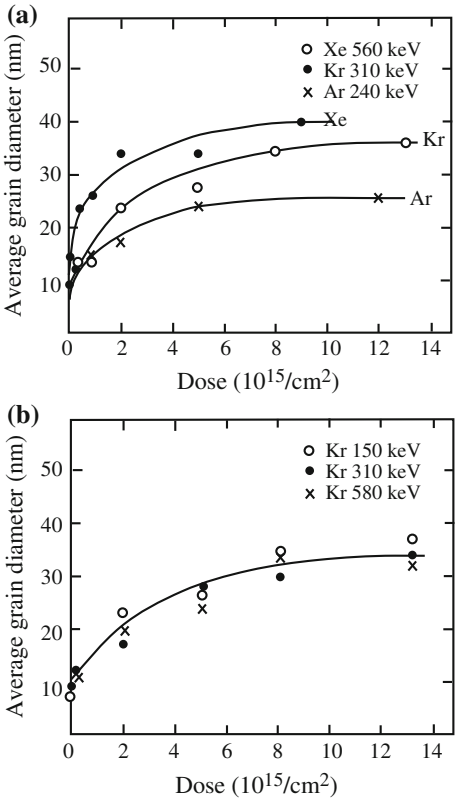

Fig. 10.22 Average grain diameter versus dose for (**a**) 240 keV Ar, 310 keV Kr, and 560 keV Xe ion irradiations of polycrystalline nickel films, and (**b**) 150, 310, and 580 keV Kr ion irradiations of polycrystalline nickel films (after [42])

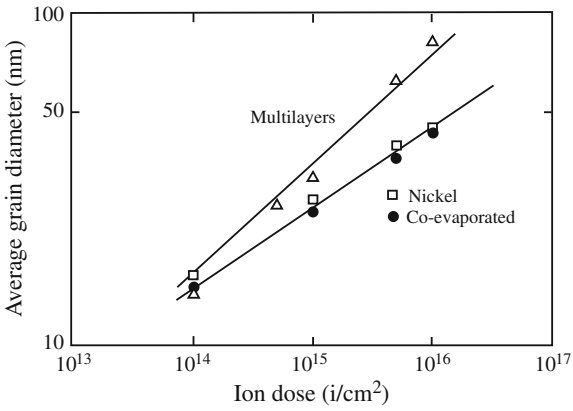

Fig. 10.23 Ion-induced grain growth observed in 40-nm-thick nickel, Ni-20 at. %Al multilayers and Ni-20 at. %Al coevaporated films irradiated with 700 keV Xe^{++} ions (after [43])

grain size, d, can be related to the initial grain size, d_0, and η in Eq. (10.64) as follows:

$$(d^3 - d_0^3)/\phi\alpha\varepsilon^2\Delta H_{\text{coh}}^2[1 + K_2(\Delta H_{\text{mix}}/\Delta H_{\text{coh}})]. \tag{10.71}$$

Since $\Delta H_{\text{mix}} = 0$ for the irradiated coevaporated films, the ratio of measured values of mobilities should be:

$$\frac{(d^3 - d_0^3)|_{\text{ML}}/\phi|_{\text{ML}}}{(d^3 - d_0^3)|_{\text{CO}}/\phi|_{\text{CO}}} = 1 + K_2(\Delta H_{\text{mix}}/\Delta H_{\text{coh}}). \tag{10.72}$$

Given the cohesive energy and heat of mixing of a Ni–20 at.%Al alloy, the ratio in Eq. (10.72) is 3.0, as compared to the measured value of 2.2. These results indicate that the heat of mixing appears to play a role in ion-induced grain growth as well as IBM.

10.3.2 Texture

There have been many reports of texture effects in ion beam-mixed or ion beam-assisted deposition of films. Alexander et al. [43] and Eridon et al. [44] found that mixing multilayers of Ni and Al in the composition Ni–20 %Al resulted in the formation of the hcp [45, 46] and fcc (γ) phases. The γ phase had a strong $\langle 111 \rangle$ texture and the hcp phase had a $\langle 001 \rangle$ texture. The textures were such that the close-packed planes of both phases were parallel to the film surface. These textures formed regardless of the angle of the ion irradiation with respect to the film. The formation of the texture seemed to be driven by the matching of the close-packed planes. Ahmed and Potter [47] found that irradiation of Ni with Al to $1.2 \times 10^{18}/\text{cm}^2$ resulted in 350 nm grains of β' phase oriented with respect to the underlying fcc nickel in accord with the Nishiyama relationship [48]. The development of texture during ion beam-assisted deposition is discussed in Sect. 10.7.

10.3.3 Dislocation Microstructure

Ion implantation can induce the formation of a high dislocation density well beyond the implanted layer in response to high surface stresses caused by high doses of the implanted element [49]. Figure 10.24 shows the depth profile of the dislocation density in α-Fe resulting from implantation of various ions (C, Fe, W, Ar) at energies between 40 and 110 keV and to doses up to 10^{18} cm^{-2}. Note that while the projected ion range is less than 50 nm in all cases, the induced dislocation density peaks at between 5 and 10 μm and extends out to over 100 μm or more. The substructure is characterized by a dense dislocation network in which the

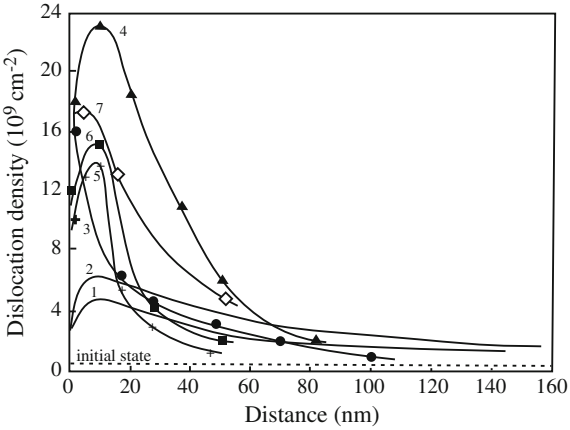

Fig. 10.24 Dislocation density versus depth in α-Fe irradiated with (*1*) C: 40 keV, 1×10^{16} cm^{-2}, (*2*) C: 40 keV, 1×10^{18} cm^{-2}, (*3*) Fe: 68 keV, 1×10^{18} cm^{-2}, (*4*) W: 110 keV, 2×10^{17} cm^{-2}, (*5*) Ar: 50 keV, 2×10^{16} cm^{-2}, (*6*) Ar: 50 keV, 5×10^{16} cm^{-2}, and (*7*) Ar: 50 keV, 1×10^{17} cm^{-2}. Irradiations 1–4 were pulsed and irradiations 5–7 were continuous (after [49])

dislocation density increases with dose and with the radius of the implanted ion. *X*-ray diffraction measurements show that the stresses exceed the yield stress and cause plastic strains in the range of 10 %.

The high-density dislocation network created by ion implantation can induce recrystallization which can then affect the distribution of the implanted specie. Ahmed and Potter [47] performed a study of 180 keV Al implantation into pure Ni at 25 °C and at elevated temperatures (300–600 °C). At elevated temperatures, individual dislocation loops dominate the microstructure at the lowest fluences ($\sim 10^{15}$ cm^{-2}). These loops bound collections of interstitial atoms or vacancies, defects caused by the energetic Al ions penetrating the nickel structure and displacing atoms from their lattice sites. The loops climb with further implantation, intersect and react with other loops, and form complex dislocation networks after a dose of 2.1×10^{17} Al/cm^2. By a dose of 3×10^{17} Al/cm^2, three-dimensional aggregates of vacancies are present.

The composition profile of Al implanted into Ni is relatively independent of temperature between 23 and 600 °C and for doses less than 10^{18} cm^{-2}. However, at higher doses, gross changes in the implanted distribution occur with the profile flattening and a considerable amount of Al transported to greater depths (Fig. 10.25). The same occurs following aging of room temperature implantations at 600 °C for 15 min. The microstructures developed at depths greater than the range of the 180keVAl^+ ions, ~100 nm, play an important role in determining the stability of the implanted concentration profiles.

Dislocation loops are present at depths near 300 nm following room temperature implantation. These loops are faulted Frank loops, 5–10 nm in diameter and their number density increases with fluence, reaching $\sim 4 \times 10^{16}$ cm^{-2} at 3×10^{18} cm^{-2}.

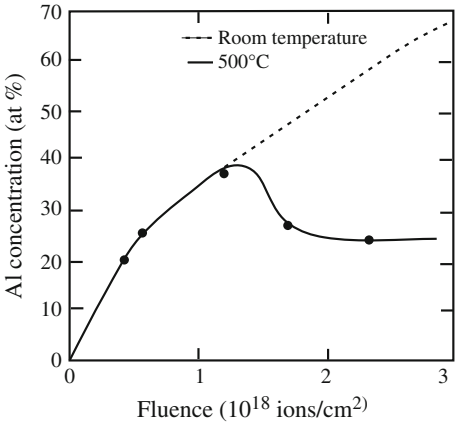

Fig. 10.25 Peak aluminum concentration plotted versus fluence for implantation of aluminum into nickel at 500 °C (after [47])

However, the dislocations behind the implanted layer are removed when the material is heated to 600 °C. This occurs by recrystallization, which is also responsible for the redistribution of implanted Al. The following describes the processes occurring.

Following room temperature implantation, an amorphous phase extends to a depth of ~160 nm. Small crystals of β' and γ extend from 160 to ~300 nm and from ~300 to ~400 nm, respectively. Dislocations and dislocation loops extend beyond this to depths of >800 nm. Aging at 600 °C, following room temperature implantation or implanting at high temperatures causes recrystallization of the fine grain structure to depths of ~800 to ~1000 nm. In both instances, aluminum atoms must move through relatively pure nickel to accomplish the redistribution, which is only possible if some fast diffusion process occurs. This is afforded by the small grains which form upon recrystallization of the heavily dislocated region beyond the implanted layer and provide high-angle grain boundaries for abnormally fast diffusion. The composition reaches a plateau by virtue of the limited extent of the recrystallization. Figure 10.26 shows that the redistribution only occurs above a threshold dose indicating the role of the radiation damage in the recrystallization process. This example serves to tie together the roles of the implanted specie, the character of the radiation damage and the processes (recrystallization and abnormally fast diffusion) that can be affected by implantation fields.

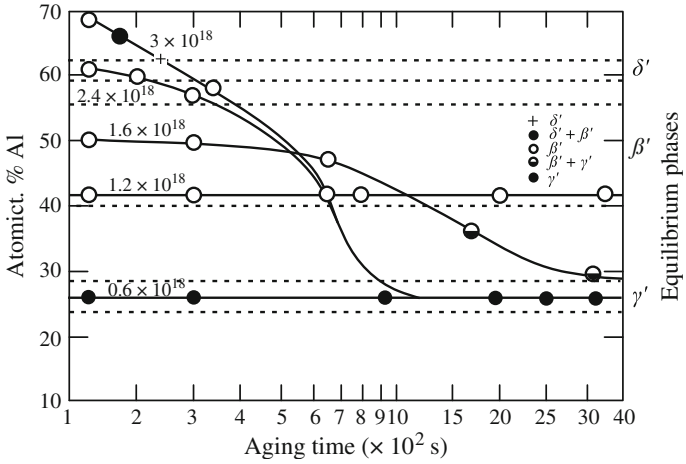

Fig. 10.26 Aluminum concentration versus time at 600 °C for fluences between 0.6 and 3.0 × 10^{18} i/cm^2. The phases observed in the implanted layers, symbols on curves, and those expected based on the equilibrium phase diagram (right side ordinate) are shown (after [47])

10.4 High-Dose Gas Loading: Blistering and Exfoliation

The first wall and divertor of a fusion reactor are expected to be subject to high fluxes of moderate-to-low-energy deuterium and helium ions created as fusion reaction products. Below 1 MeV, helium comes to rest approximately 1 μm below the surface and extended exposure at high flux can lead to very high levels of helium. At the expected temperatures (400–700 °C) and aided by the high defect concentration due to radiation damage, He will be mobile and will form bubbles as discussed in Chap. 8. The growth and coalescence of bubbles lead to the formation of blisters resulting in exfoliation of the surface as shown in Fig. 10.27. Figure 10.28(a) illustrates the result of high He loading a short distance beneath the surface of a metal. The bubbles are constrained to a narrow band of solid beneath the surface. There, they may grow and either coalesce to form larger bubbles or cause interbubble fracture due to the stresses between the bubbles (Fig. 10.28(a)). A cross-sectional image of the subsurface region of a nickel sample bombarded with a high dose of He (Fig. 10.28(b)) shows that the bubble microstructure is confined to the near-surface region. Stresses arise because the bubbles are not in equilibrium. That is, pressure due to the gas in the bubble is not balanced by the stress due to the surface tension, resulting in a radially directed stress, σ_{rr}, on the bubble:

$$\sigma_{rr} = p - (2\gamma/r). \tag{10.73}$$

Wolfer [52] developed an expression for the average stress field between bubbles:

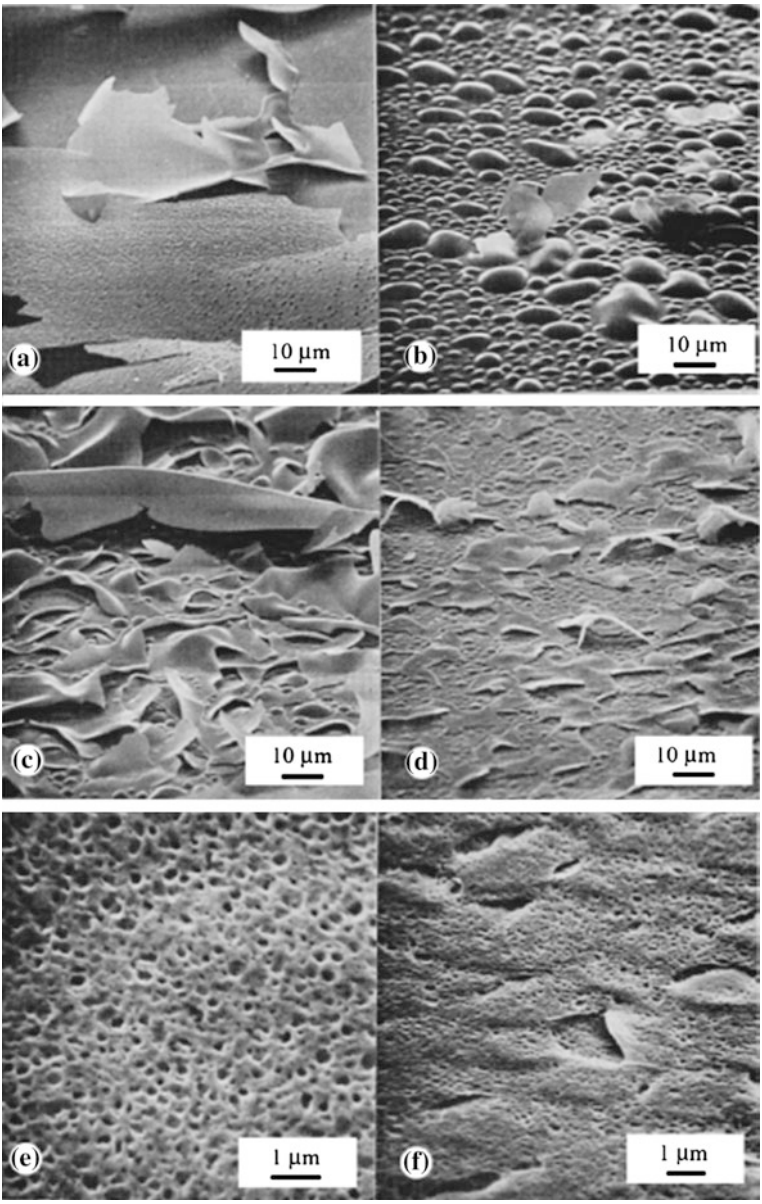

Fig. 10.27 Surface topography of polycrystalline nickel irradiated with different doses of 100 keV He^+ ions: (**a**) 2×10^{18} $^4He/cm^2$ at normal incidence, (**b**) 2×10^{18} $^3He/cm^2$ at normal incidence, (**c**) 1×10^{19} $^3He/cm^2$ at normal incidence, (**d**) 2×10^{19} $^3He/cm^2$ at 60° from normal, (**e**) 1.2×10^{20} $^4He/cm^2$ at normal, and (**f**) 3.4×10^{19} $^3He/cm^2$ at 60° from normal (after [50])

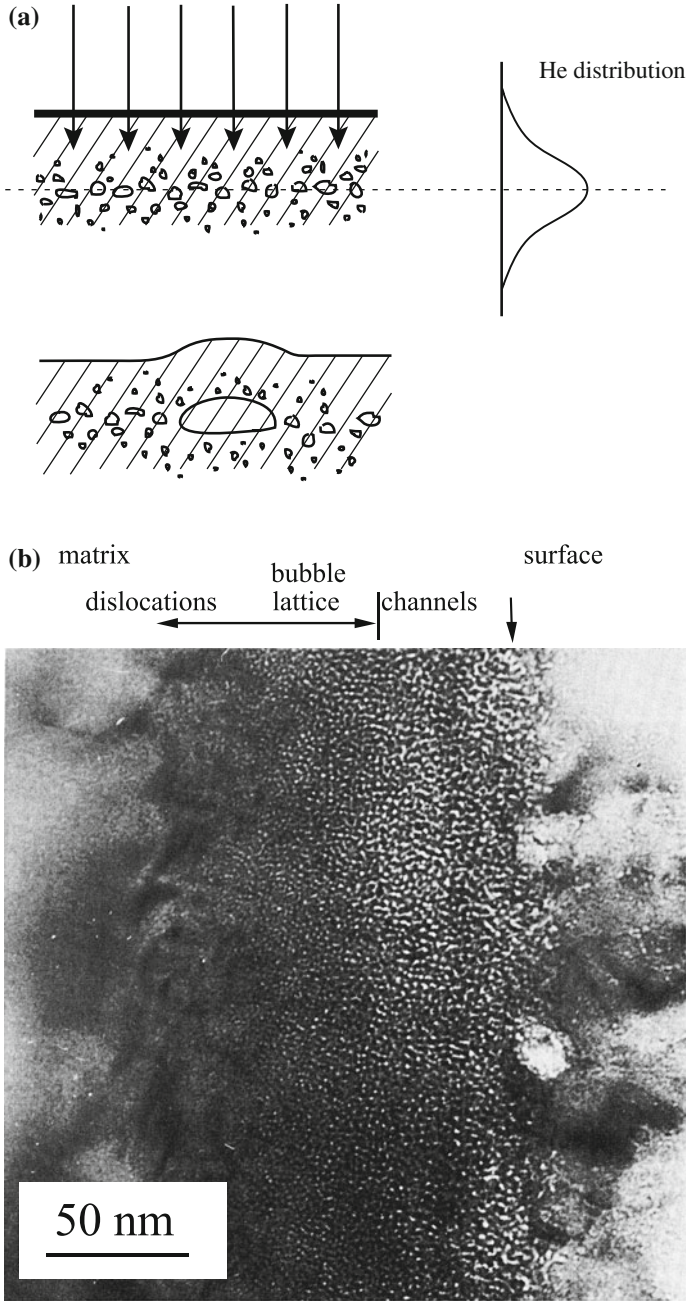

Fig. 10.28 (**a**) Coalescence of bubbles below the surface of a sample loaded with a high dose of helium. (**b**) Cross section of a high-dose, He-implanted surface layer of nickel showing the dislocations (*deep*), bubble lattice (*middle*), and connected channels (*near-surface*) (after [51])

$$\frac{\bar{\sigma}}{\mu} = \left[f_{\mathrm{He}} \frac{p}{\mu\rho\Omega} - \frac{2\gamma}{\mu\Omega} \left(\frac{4\pi\rho_{\mathrm{B}}}{3} \right)^{1/3} S^{2/3} \right] F(S), \tag{10.74}$$

where μ is the shear modulus, $f_{\mathrm{He}} = m\rho_{\mathrm{B}}\Omega$, m is the number of gas atoms in a bubble, ρ_{B} is the bubble density, Ω is the atomic volume of the metal atoms, ρ is the helium density in the bubbles, γ is the surface energy, and $S = f_{\mathrm{He}}/\rho$. The function $F(S)$ is defined for a random array of bubbles and for $\rho \sim 1.0$ as:

$$F(S) = (0.827S^{1/3} - S)^{-1}. \tag{10.75}$$

Since the ultimate tensile strength determines both the ductile, transgranular fracture of fcc metals and the transgranular cleavage fracture of bcc and hcp metals and is about 0.003 μ for fcc metals and roughly 0.01 μ for bcc metals, then $\bar{\sigma} \sim 0.01$ μ. The corresponding helium concentrations needed to reach the stress to cause fracture between bubbles due to the stress are shown in Fig. 10.29, and for $\rho = 1$, the critical helium concentration is ~20–40 %. Wolfer also identifies another stress, the lateral stress, σ_{L}, that is in the plane of the bubbles parallel to the surface (Fig. 10.30). The lateral stress depends on the swelling rate, $\dot{S}$ according to

$$\sigma_{\mathrm{L}} = \frac{-\dot{S}E}{(1-v)}, \tag{10.76}$$

where E is the elastic modulus and v is Poisson's ratio. Blister formation is then a two-step process. Fracture starts at the depth, t_{B}, below the surface where $\bar{\sigma}$ is a maximum by growth of the bubbles to a point where the local stresses are sufficient to crack open the plane adjoining the bubbles. The penny-shaped crack then spreads

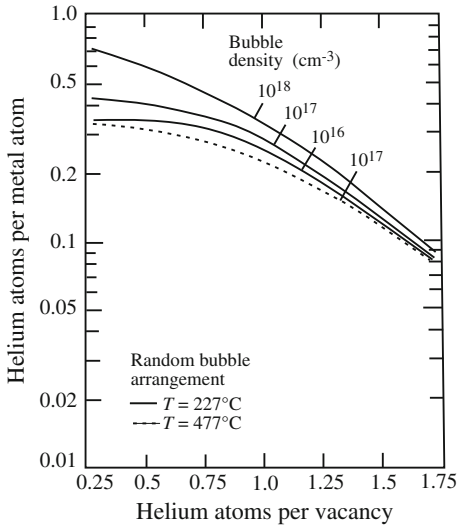

Fig. 10.29 Critical implanted He concentration versus He concentration in the bubbles for the case of random bubbles (after [52])

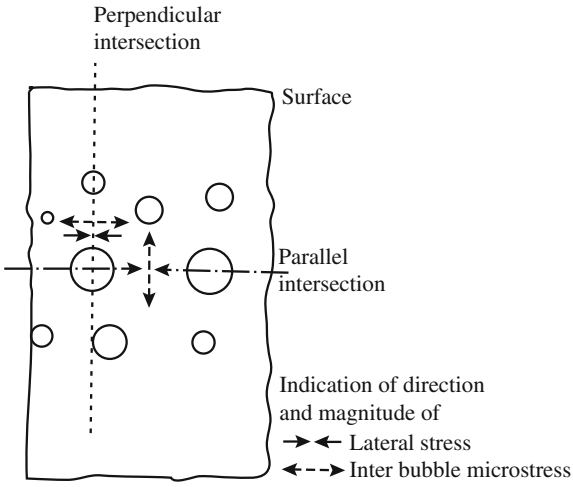

Fig. 10.30 Schematic cross section of the He-implanted layer with gas bubbles and definitions of the lateral stress and the interbubble stress (after [52])

until a diameter, D_B, is reached where the buckling condition is satisfied by the existing lateral load:

$$D_B = 1.55\left[\frac{\mu}{(1-v)P}\right]^{1/2} t_B^{3/2}, \tag{10.77}$$

where

$$P = -\int_0^{t_B} \sigma_L \mathrm{d}t_B \tag{10.78}$$

Note that experiment has identified the relationship between the blister base diameter and its thickness to be $D_B \sim t_B^m$, where $0.85 < m < 1.5$, and this relation supports the lateral stress as the cause of blister formation [52]. Alternatively, the penny-shaped crack can continue to extend until detachment occurs, resulting in flaking and exfoliation as shown in Fig. 10.27.

Very high doses of helium or implantation at high temperature often result in a *sponge*-type structure in which the surface consists of a series of pits as shown in Fig. 10.31. At very high temperature where bubbles are mobile, the pits may be the result of bubble intersection with the surface. However, high-dose ion implantation can led to severe topological surface changes and this is the subject of much investigation.

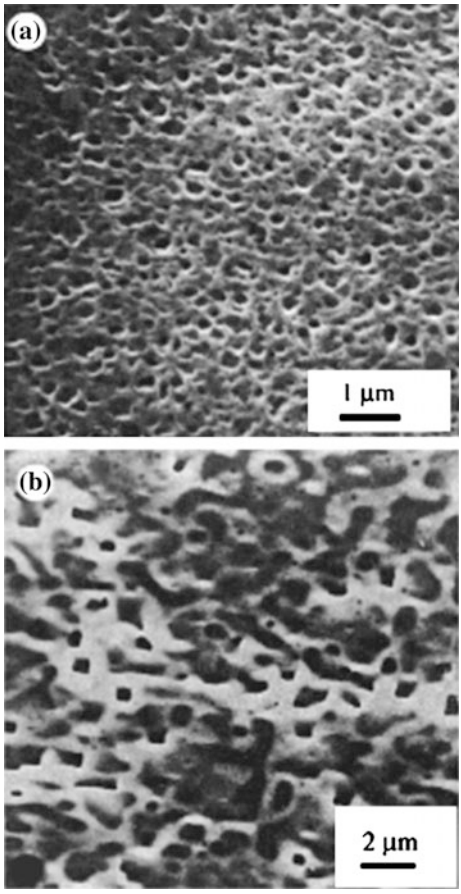

Fig. 10.31 Holes in the surface of Nb irradiated with (**a**) 1.2×10^{20} He/cm^2 at 23 °C and (**b**) 3×10^{17} He/cm^2 at 823 °C (after [53])

10.5 Solid Phases and Inert Gas Bubble Lattices

Implantation of noble gases to high doses at room temperature can lead to a different phenomenon: solid bubbles. Ar, Kr, and Xe implanted into a variety of host metals have been observed to form solid bubbles consisting of crystals of the implanted noble gas. In Ni and Al, gases precipitate as solids with the same crystal structure as the host lattice and epitaxially aligned with the matrix. The solid-phase forms at doses in the range of 10^{20} m^{-2} and the precipitate size is about 1.5 nm in Ni and up to 4.7 nm in Al [54, 55]. The lattice parameter of the precipitates is larger than that of the host and increases with the atomic mass of the inert gas. The lattice parameter increases with dose and tends toward a saturation value as shown in Fig. 10.32. Precipitate densities can be very high, in the range of 10^{24} m^{-3}. The average pressure of the solid gas can be determined from the average gas density, the lattice constant, and the equation of state for the gas and is estimated to reach

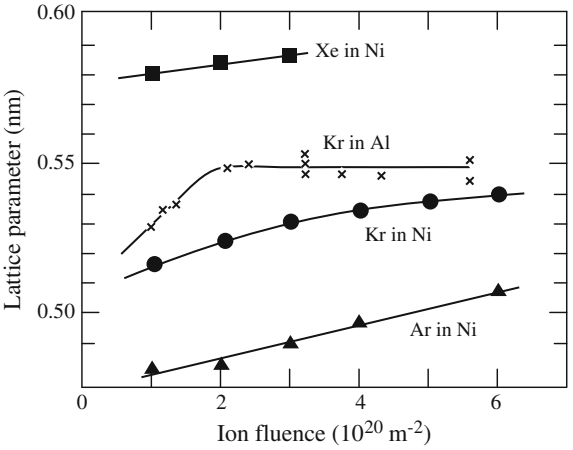

Fig. 10.32 Lattice parameter of solid noble gas precipitates of Xe, Kr, and Ar in nickel and of Kr in aluminum, as a function of fluence and implanted at room temperature (after [54] and [55])

values in excess of 40kbar. While the pressure required to solidify the gas at room temperature depends on the gas (8kbar for Kr and 11.5kbar for Ar), the calculated values are in excess of these amounts by several times. The inert gas is held in the solid state by the interatomic forces between the Kr–Kr and the Kr–Ni atoms, for the case of Kr in Ni. As the precipitate size increases, the average spacing between the gas atoms increases, decreasing the magnitude of the Kr–Kr interaction. Eventually, the decrease in gas pressure allows melting of the solid Kr. Implantation of high doses of Kr into amorphous TiCr resulted in the precipitation of crystalline Kr as in the case of crystalline metal hosts, but in this case, the solid Kr precipitates induced local crystallization of the host as a bcc structure.

High-dose implantation at room temperature can also lead to bubble lattice formation similar to the void lattices described in Chap. 8. Bubble lattices have been observed in Cu, Ni, Au, Ti, and stainless steel irradiated with He or Kr. In fcc lattices, the bubbles form in densely packed rows parallel to the matrix {111} trace directions [56] and can be described by a lattice constant of order 7.6 nm, corresponding to a bubble density of $\sim 10^{25} m^{-3}$. In hcp lattices, the bubble alignment is parallel to the basal plane, similar to that found for void ordering [57]. The formation of a bubble lattice is independent of the inert gas used and whether the gas atoms are present in bubbles in a gaseous or solid form.

10.6 Displacements Due to Electronic Excitation

In energetic particle irradiation of solids, the kinetic energy of irradiating particles is transferred to lattice and electronic systems in solids through elastic collision and electronic excitation, respectively. The transferred energy to the lattice system induces atomic displacements directly. In the electronic excitation process, on the other hand, atomic displacements can be caused as a result of indirect energy

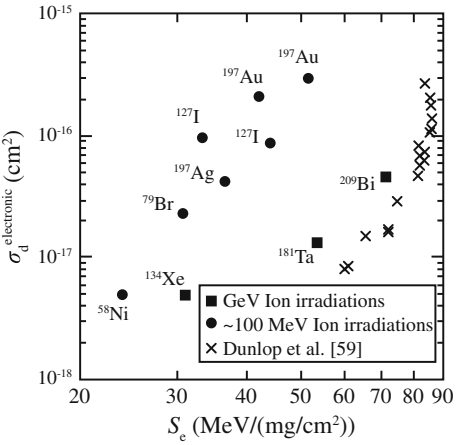

Fig. 10.33 Defect production cross section through electronic excitation, σ_d^e, plotted against electronic stopping power, S_e, for irradiation in the high-S_e regime (after [60])

transfer from irradiating particles. In metals, however, atomic displacements through electronic excitation had been considered to hardly occur because of rapid energy dissipation by a large number of conduction electrons. In the last decade, nevertheless, atomic displacements induced by high-density electronic excitation have been found even in metallic targets [58, 59].

In describing atomic displacements through electronic excitation process, the thermal spike model and the Coulomb explosion model have been proposed. In the thermal spike model, the energy of target electrons excited by incident ions is transferred to the lattice system through electron–lattice interaction after rapid energy diffusion in the electronic system. In the Coulomb explosion model, adjacent target atoms ionized via electronic excitation along the incident ion trajectory gain outward momentum due to the mutual Coulomb repulsion, and then atomic displacements are induced.

According to careful consideration of the contribution of elastic collision and electronic excitation to the defect production and annihilation, the defect production cross section through electronic excitation, σ_d^e, can be extracted from the total defect production cross section in the high-S_e regime ($S_e > \sim 20$ MeV/(mg/cm^2)). Figure 10.33 shows σ_d^e for irradiation in this regime plotted against S_e for 100 MeV and GeV ion irradiation of iron [60] along with previous results also conducted with GeV ions [59]. As shown in the figure, σ_d^e for 100 MeV ion irradiations is larger than that for GeV ion irradiations even at the same S_e value. Since the ion velocity at ~ 100 MeV is much lower than that at GeV, the difference in σ_d^e even at the same value of S_e is termed "the velocity effect." The data in Fig. 10.33 can be replotted using the primary ionization rate as a scaling factor:

$$\frac{dJ}{dx} = \frac{Z^{*2}\alpha}{I_0 v^2} \ln\left(\frac{2m_e v^2}{0.048\, I_0}\right), \tag{10.79}$$

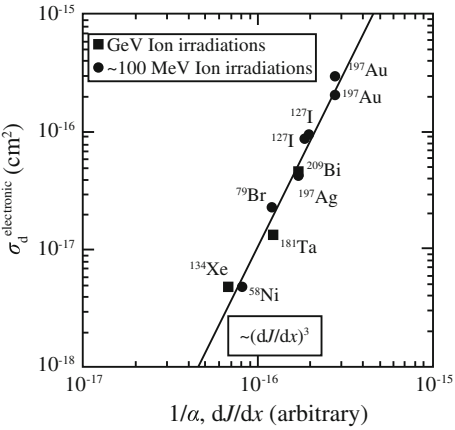

Fig. 10.34 Defect production cross section through electronic excitation, σ_d^e, as a function of primary ionization rate, dJ/dx, for irradiation in the high-S_e regime (after [60])

where dJ/dx is the number of iron atoms ionized by an incident ion per unit path length, Z^* is ion effective charge, I_0 is the ionization potential of the most loosely bound electron, υ is the ion velocity, α is a constant depending on the target material (7.87 eV for iron), and m_e is the electron mass. The data for σ_d^e in Fig. 10.33 is replotted in Fig. 10.34 against dJ/dx in the high-S_e regime. The correlation between σ_d^e and dJ/dx is excellent and all of the data collapse onto a single line. The good correlation between the cross section for defect production by electronic interaction (σ_d^e) and the ionization rate (dJ/dx) rather than the transferred energy (S_e) indicates that atomic displacements in iron via electronic excitation can be triggered by the Coulomb explosion mechanism [60].

10.7 Ion Beam-Assisted Deposition

The bombardment of a growing film with energetic particles has been observed to change a number of characteristics and properties, critical to the performance of thin films and coatings, such as adhesion, densification, residual stress, crystallographic texture, grain size and morphology, optical, electrical and transport properties, and hardness and ductility. The process of simultaneous thin-film deposition and directed ion bombardment from an ion source is generically termed IBAD, but goes by a number of variants and different terms, including ion-assisted coating (IAC), ion-assisted deposition (IAD), ion vapor deposition (IVD), ion beam-enhanced deposition (IBED), and dynamic recoil mixing (DRM).

The interest in ion-assisted deposition is the increased control of film microstructure and properties through alteration of the surface processes occurring during film synthesis. As shown in Fig. 10.35, these properties are controlled by the microstructure, and microstructure is controlled by the processes occurring during deposition, such as condensation, re-evaporation, mobility, clustering, sputtering,

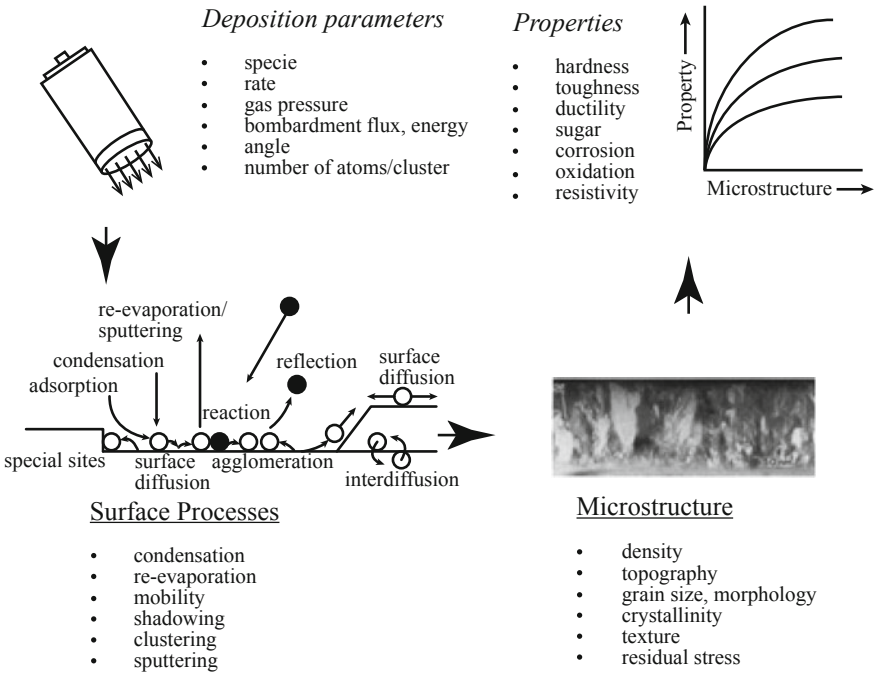

Fig. 10.35 Coupling between film deposition parameters, surface processes, microstructure, and properties

and shadowing. During (physical or reactive) deposition, the process variables that can be used to control the deposition are limited to deposition rate, substrate temperature, substrate orientation, and chamber pressure. The attractiveness of IBAD is that the ion beam provides additional "knobs" to control surface processes and therefore microstructure and properties. These include the type of ion, ion energy, ion flux, ion angle, and ion-to-atom arrival rate ratio. This section will focus on the processes that control microstructure features such as density, grain size and morphology, residual stress and crystallographic texture. More details on materials modification by IBAD can be found in refs [1, 4, 5, 61].

10.7.1 Microstructure

The microstructure of a deposited film is determined by nucleation and growth processes. Atomic processes that occur on the surface of a crystal are illustrated in the lower left-hand image of Fig. 10.35. Atoms of mass M impinge from the vapor (of pressure p) at a rate given by:

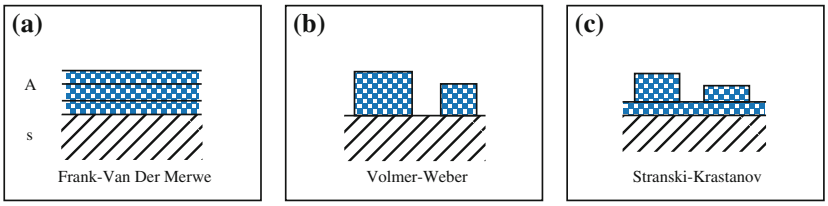

Fig. 10.36 The three common modes of thin-film growth, (**a**) Frank–van der Merwe, (**b**) Volmer–Weber, and (**c**) Stranski–Krastanov or mixed mode (after [4])

$$R = p(2\pi MkT)^{-1/2}, \tag{10.80}$$

where k is Boltzmann's constant and T is the temperature in Kelvin. Single atoms striking the surface diffuse over the surface until lost by processes such as evaporation, formation of a critical size nucleus, capture by an existing cluster, or trapping at a special site. Each process is characterized by a time constant. Real surfaces are highly defected, consisting of ledges, kinks, dislocations, and point defects that can modify the binding energy of an adatom or cluster to the surface, and hence, the energetics of the processes. Rearrangement of small clusters can occur by interdiffusion and with the substrate, surface diffusion to form a more stable shape, and annealing of defects.

Several distinct modes of thin-film growth are observed [4] as shown in Fig. 10.36. Layer or Frank–van der Merwe mode describes the layer-by-layer growth of the film that completely covers the surface. Island or Volmer–Weber growth results in the formation and growth of islands several layers thick before complete surface coverage occurs. Finally, a mixed mode called Stranski–Krastanov is an intermediate case in which a monolayer first forms followed by the growth of islands. Growth mode is controlled by the film–substrate interactions, producing island growth when the condensing atoms are bound more strongly to each other than the substrate, and layer-by-layer growth when the interaction with the substrate is stronger and monotonically decreases as each layer is added. Stranski–Krastanov growth occurs when the monotonic decrease in binding energy is disrupted by some factor such as lattice mismatch or orientation and island formation becomes more favorable.

Film nucleation and growth are strongly affected by the substrate temperature. The grain structure for vapor-deposited metal films is strongly dependent on the substrate homologous temperature (T/T_m) and can be described by a zone model [62], Fig. 10.37. According to this model, deposition in zone I ($T/T_m < 0.15$) is characterized by restricted surface mobility of deposited atoms, resulting in small (5–20 nm) equiaxed crystallites. In zone II ($< 0.3T/T_m < 0.5$), deposited atoms have sufficient mobility such that grains can grow to larger sizes prior to deposition of the next layers of material. The grain structure in this zone is columnar with column diameters smaller than the film thickness. In between zones I and II is zone T, a transition zone between equiaxed and columnar grains. Finally, at $T/T_m > 0.5$, the

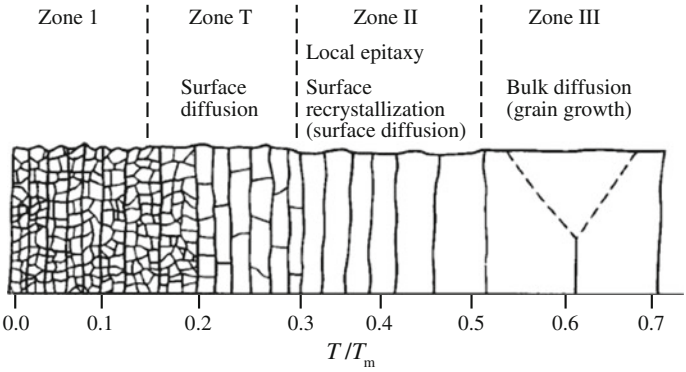

Fig. 10.37 Zone model for the grain structure of vapor-deposited metal films (after [62])

high surface mobility enables the growth of large columnar grains with diameters larger than the film thickness.

As noted earlier, the effect of an ion beam on film growth will depend on the ion type, energy and the relative flux ratio of ions to deposited atoms. The effect of ion bombardment on film growth is described by either the ratio of the ion flux to the atom flux, or the ion-to-atom arrival rate ratio, R, or as the average energy deposited per atom, E_a, which is the product of R and the ion energy, E_{ion}. Thus:

$$R = \frac{J_i}{J_a}, \tag{10.81}$$

where J_i is the ion flux and J_a is the atom flux, and

$$E_a = E_{ion} R = E_{ion} \frac{J_i}{J_a}. \tag{10.82}$$

These parameters will be used in the following sections to describe the effect of ion bombardment on the evolution of deposited thin films.

The effect of ion bombardment on the evolution of the film microstructure is shown in Fig. 10.38 for the case of Ar sputtering during deposition. Note that the higher the sputtering gas pressure, the greater the density of possible collision centers, and the greater the probability of the reflected neutral atoms losing energy through a collision event while traveling toward the substrate. Thus, there is an inverse relationship between the energy of the bombarding particle (reflected neutral) at the growing film surface and the sputtering gas pressure, making the sputtering process directly comparable with the average ion energy, E_a, applied in the IBAD process. Zone 1 is characterized by columnar grains with pipes along the grain boundaries and poor mechanical strength. The presence of high Ar pressure increases the temperature at which zone 1 structures are stable, possibly due to

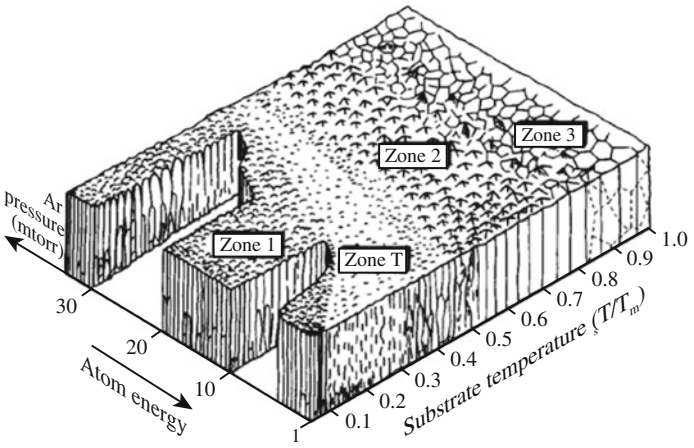

Fig. 10.38 Schematic representation of the film structure as a function of sputtering gas pressure/IBAD energy and substrate temperature, T_s, normalized to the melting temperature, T_m (after [63, 64])

trapping of the gas at the boundary. The zone 1 structure results when adatom diffusion is too limited to overcome the effects of shadowing. Shadowing produces open boundaries, particularly under conditions of oblique flux, because the high points receive more flux than the low points. Surface roughness may develop because of substrate roughness, preferential nucleation on inhomogeneities, or from the shape of the initial nuclei. Zone T or transition microstructures are also dominated by shadowing effects but have finer features, which appear fibrous and have better mechanical integrity. Zone 2 microstructures form at $T/T_m = 0.3–0.5$ and are dominated by adatom surface diffusion processes. The structure has columnar grains with good mechanical integrity at the boundaries, smooth surface facets, and there is little sensitivity to the inert gas pressure. Zone 3 structures form at $T/T_m \sim 0.5$ and are dominated by bulk diffusion processes. Recovery and recrystallization processes typically occur in this temperature regime, driven by the minimization of strain energy and surface energy of the grains. Columnar grains recrystallize to form equiaxed grains in zone 3.

Densification

One of the major consequences of ion bombardments during film growth is densification. IBAD can produce significant increases in the density of deposited oxide or nitride compounds such as ZrO_2 [65] or TiN [66], but it can also produce increases in the density of metal films [4]. Under low adatom mobility, a columnar microstructure with voids develops and leads to shadowing in zone 1 [67]. A transition from low packing density films (0.7) to fully dense films occurs as a function of temperature and deposition rate [68]. A hard sphere model was used in which the depositing spheres intersect the surface at random points and are assumed to stick in place except for relaxation into nearby “pockets” where they make

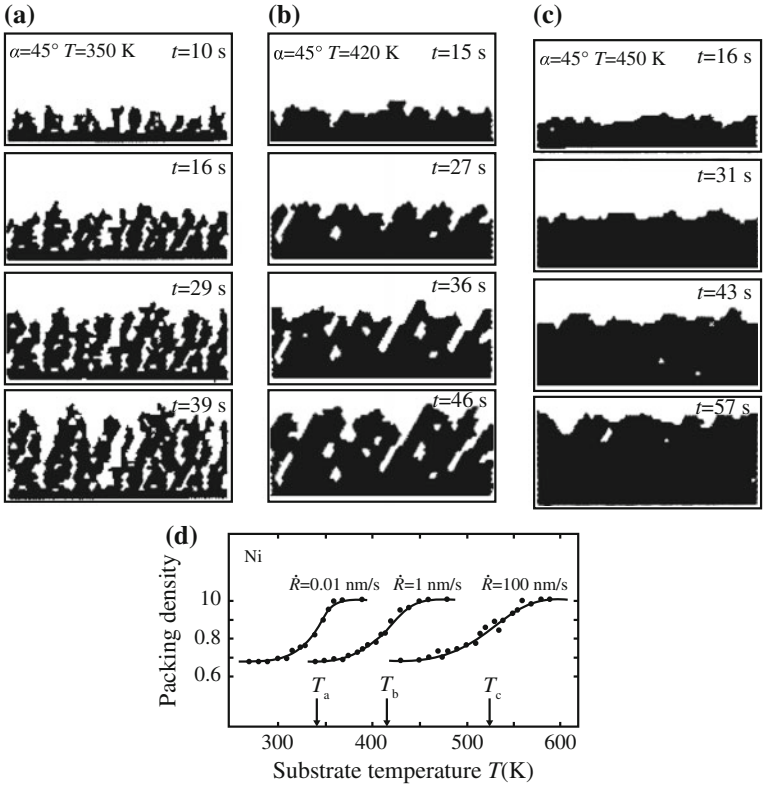

Fig. 10.39 A model of film growth using a 2D hard sphere growth model showing the effect of temperature on packing density of films (**a**–**c**) and a summary of multiple simulations showing that temperature influences packing density while deposition rate changes transition temperature and sharpness of transition (**d**) (after [68])

contact with two other spheres. This generates columns inclined along the angle of incidence with "pipes" between the columns. A schematic of the film structure and density changes is shown in Fig. 10.39. When a thermal activation process is added to simulate temperature-dependent diffusion processes, a dense microstructure forms at the equivalent of 0.3 T_m. Simulation of a thermal spike was examined by depositing energy in a region below the surface corresponding to the proper ion range, dissipating the energy by thermal conductivity, and allowing thermally activated jumps between adjacent lattice sites. The calculations showed some bridging of columns occurred near the surface but generally densification of the film did not occur.

A collision cascade simulation was considered next in which momentum was transferred via forward recoils and sputtering [69]. Mass transport and incorporation distributions were calculated using the TRIM.SP code and the results applied to a 2D model. Densification of a zone 1 microstructure was observed to a depth 3 nm

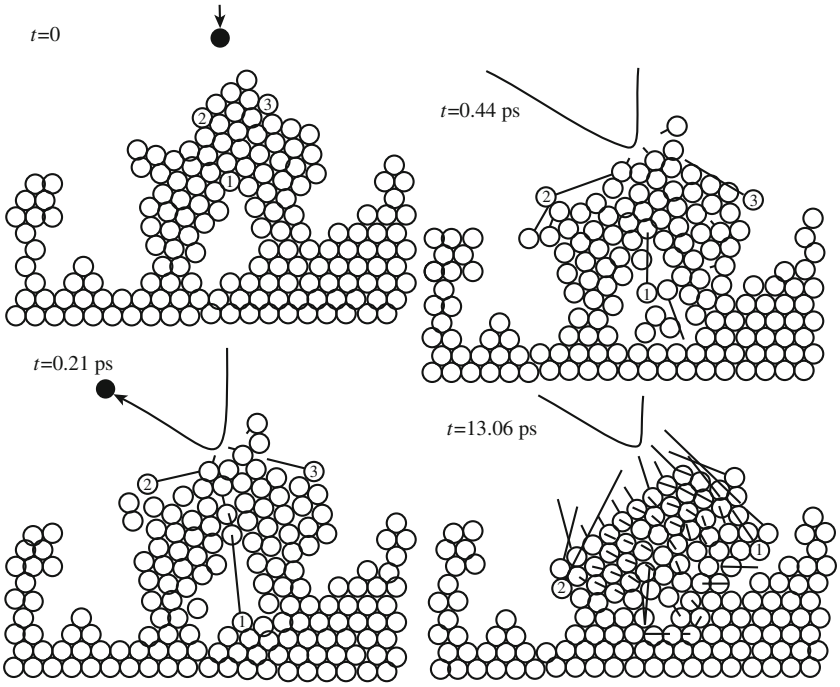

Fig. 10.40 2D molecular dynamics simulation of atomic rearrangements produced by impact of 100 eV Ar^+ on a Ni film with a porous structure. Effects include forward recoils, lateral displacements, and collapse of the lattice to a more densely packed configuration (after [71])

below the surface as a result of knock-on atoms filling the voids. Experimental results for ZrO_2 and CeO_2 were reproduced by the model. A further refinement of the model used experimentally determined sputtering rates and the thickness of the layer damaged by O_2^+ ion beam etching rates where sputtering exceeded the deposition rate [70]. The model incorporated sputtering, ion implantation, recoil implantation, and diffusion of atoms from non-stoichiometric regions. Good agreement with experimental results was found by allowing a slightly greater diffusion of excess atoms toward the surface than toward the bulk.

Using a Lennard–Jones potential for atom interactions and a zero substrate temperature to examine microstructure, 2D molecular dynamics simulation can be used to examine microstructure, average density, and epitaxy using deposited atoms with low energies in the vapor deposition and sputtering ranges. Densification increases with energy and exceeds a relative density of 0.9 for energies typical of sputtered particles. Figure 10.40 shows that IBAD of Ni using 100 eV Ar^+ produces atomic rearrangements in a collision sequence that results in both a collapse of voids in the structure and transport of atoms on the surface. The effect of ion bombardment on microstructure development for a sequence of ion impacts at a 30° angle of incidence and R value of 0.16 is shown in Fig. 10.41(a). Packing density

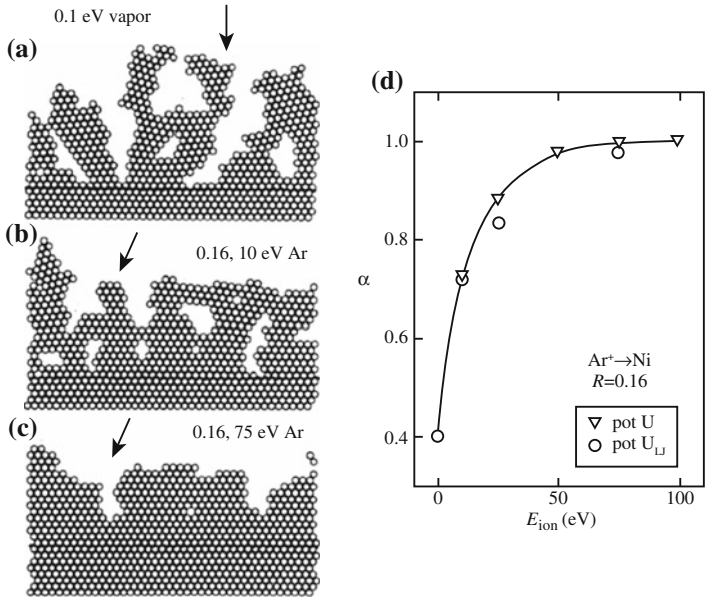

Fig. 10.41 Evolution of the film microstructure during deposition: (**a**) 0.1 eV vapor atoms at normal incidence, (**b**) with bombardment by 10 keV Ar^+ ions at $R = 0.16$ and angle of 30° to normal, (**c**) with bombardment by 75 eV Ar^+ ions at $R = 0.16$ and angle of 30° to normal, and (**d**) influence of ion energy, E_{ion}, on the degree of epitaxy, α, for Ar^+ ions on a Ni film with $R = 0.16$ (after [72])

increases with arrival rate ratio for a given energy in agreement with experimental observations of a critical current density. The degree of epitaxy at the interface also increases with both arrival rate ratio and energy as shown in Fig. 10.41(b). These molecular dynamics simulations show that forward recoils of film atoms either fill voids or keep them open until filled by the vapor flux. This process and the mobility of surface atoms are the primary mechanisms by which ion bombardment promotes densification of films deposited under conditions of low adatom mobility.

The effect of ion bombardment on the void fraction in amorphous Ge is shown in Fig. 10.42. Note the linear dependence up to about 5 eV/atom, beyond which saturation density is reached. The results indicate that the important factors that determine the film microstructure in ion-assisted deposition is the particle flux-energy product. As will be shown in the section on residual stress, the microstructure determines the nature of the stress.

Grain size and morphology

Grain size and grain morphology of PVD films is a strong function of substrate temperature, or more specifically, the dominant nucleation and growth process in a particular temperature regime. Since IBAD has been shown to modify the nucleation and early growth stages of film deposition, it should also affect grain size and morphology. As shown in the last section, ion bombardment disrupts the columnar

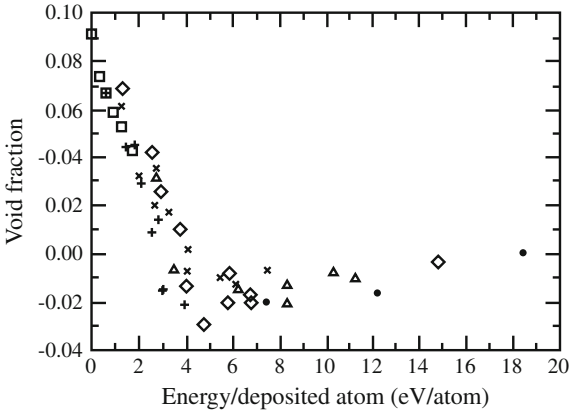

Fig. 10.42 Void fraction variation in amorphous Ge as a function of energy per deposited atom, E_a (after [73])

structure and open boundaries in zone 1, and if the substrate is heated, it can produce grain growth. An example is TiN film grown on high-speed steel (HSS) by magnetron sputtering [74]. The film has a bimodal grain size distribution that was a result of epitaxial nucleation on carbides. Films grown without bias show substantial grain growth between 550 and 650 °C. Addition of substrate bias produces bombardment of the growing film with 300 eV ions at an arrival rate ratio of 0.6. The ion bombardment disrupts the bimodal grain growth in HSS, producing a dense structure with no voids at the boundaries, and reducing the grain size to 50 nm. The microstructures observed are typical zone T microstructures attributed to a shift of the transition temperature to lower homologous temperatures because film growth in TiN appears to depend on Ti adatom mobility. The addition of substrate bias reduces the grain size by causing continual renucleation of the grains. A modified structure diagram using an energy scale instead of gas pressure is shown in Fig. 10.43 and indicates that the widening of zone T is the principal effect of decreasing the energy of the bombarding particles.

Figure 10.44 shows the effect of E_a on the grain size in Ag deposited by dual ion beam sputtering. E_a is the calculated energy/film atom which also includes the energy deposited from the sputtered flux. Note that the size decreases with increasing energy/atom and saturates at about 50 eV/atom, as shown in Fig. 10.44(a). In Fig. 10.44(b), Cu films were deposited under IBAD at various R values and for ion energies of 62, and 600 eV. IBAD produced no change in size for 62 eV, but a marked decrease in crystallite size for the higher energies at R values up to 0.02. Above the critical R value, the crystallite size saturates, with the highest energy producing the largest reduction in grain size [30 nm for 600 eV, 70 nm for 125 eV (not shown)]. Substrate temperatures of 62–103 °C resulted in the same saturation size for the 600 eV bombardment, but a 230 °C temperature resulted in a slightly larger size (40 nm).

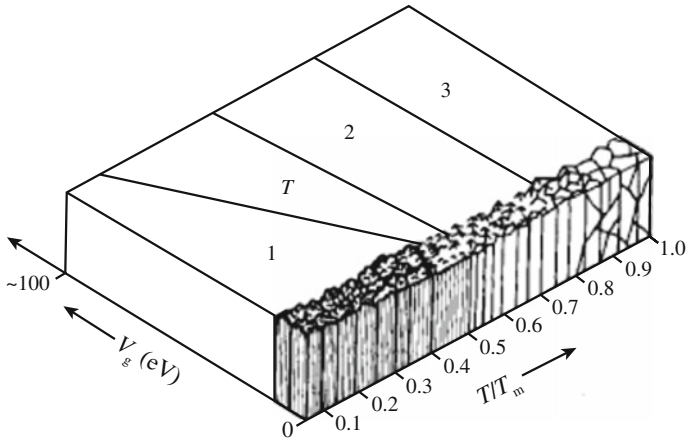

Fig. 10.43 Alternative to the film structure diagram in Fig. 10.38 showing more directly the effects of ion energy on film structure (after [64])

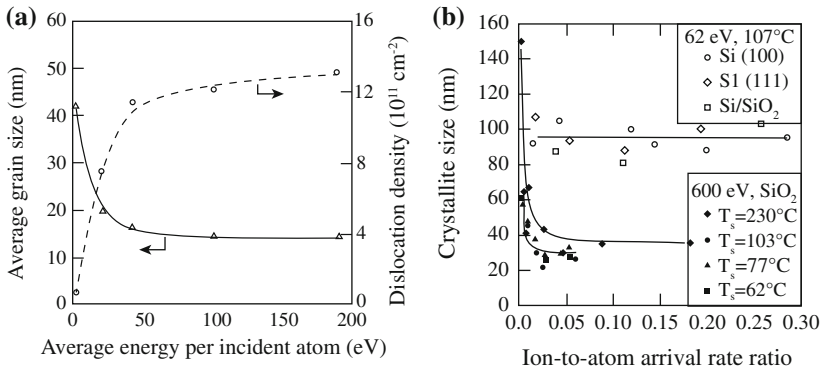

Fig. 10.44 (**a**) Variation of grain size and dislocation density with E_a in Ag films deposited by dual ion beam sputtering (after [75]), and (**b**) variation in grain size of Cu films deposited under a range of IBAD process parameters including R ratio, ion energy, and substrate temperature (after [76])

Films grown under conditions of biased sputtering or IBAD generally show a decrease in grain size in both zone 1 and zone T temperature regimes and a disruption of columnar grain structures. This reflects the influence of ion bombardment on nucleation of grains. Occasional observations of an increase in grain size indicate other factors which might promote grain growth, such as a higher temperature or high strain energy, are present and may dominate in certain materials or under certain deposition conditions.

10.7.2 Residual Stress

While IBAD has been shown to produce significant changes in both the magnitude and sign of residual stresses in deposited films, the mechanism(s) of residual stress generation are poorly understood. Residual tensile stresses can result from densification or grain growth when structural relaxation lags the deposition rate. Structural relaxation occurs to minimize the free energy of the system and results in a reduction of the specific volume of the film as long as the film is unconstrained. If geometrically constrained by the substrate, volumetric relaxation is inhibited and a residual stress (and strain) is produced in the film and substrate. Phase changes resulting in a different specific volume also produce tensile or compressive stresses depending on the sign of the volume change. Mechanisms for compressive residual stress formation include thermal spikes, recoil implantation, and trapped bombardment gases. A common feature of residual stress formation in films is that they generally occur subsequent to the deposition process.

Sources of stress in vapor-deposited films

One source of residual stress is the thermal expansion mismatch between the film and substrate. This mismatch leads to stresses when the temperature changes. The resulting residual stress, σ^{R}, is that which would be induced in a thin film attached to an infinite substrate:

$$\sigma^{R} = E_f \Delta\alpha \frac{T_R - T}{(1 - \nu_f)}, \tag{10.83}$$

where E_f and ν_f are the elastic modulus and Poisson's ratio of the film, T is the temperature, T_R is the reference temperature at which the stress is zero, and $\Delta\alpha = \alpha_f - \alpha_s$, where subscript f refers to the film and s to the substrate. Residual stress due to thermal expansion mismatch often occurs upon cool-down following deposition. Aside from thermal expansion differences, when a polycrystalline film is grown on a substrate having an incoherent interface, there is no obvious mechanism for generating stress in the surface layer *as* it deposits. Surface diffusion allows atom displacement to relax strains as they attempt to develop. This situation differs from that for coherent, single-crystal films that incur coherency strains. Intrinsic stresses will develop as a consequence of *subsequent* diffusional effects that occur in the deposited film. Such stress formation involves mechanisms that eliminate those defects present in the film, which have an associated free volume [77, 78].

If point defects are trapped in the film as it grows, they contribute a free volume to the film. Their subsequent elimination at either grain boundaries or dislocations will induce intrinsic residual stresses, as shown in Fig. 10.45(a). The chemical potential of a solid is given by:

$$\mu = \mu_0 + \sigma_n \Omega + kT \ln C/C_0, \tag{10.84}$$

where C/C_0 is the excess point defect concentration, μ_0 is the reference chemical potential, and σ_n is the stress normal to the dislocation or grain boundary. The equilibrium, intrinsic stress, is obtained when $\mu = \mu_0$ and is given by:

$$\sigma_{eq}^{R} = \left(\frac{kT}{\Omega}\right) \ln \frac{C}{C_0}. \tag{10.85}$$

Note that this stress develops with time at temperature as it requires lattice diffusion and thus occurs post-deposition. It can also be either tensile (vacancy elimination) or compressive (interstitial elimination).

As described in the section on microstructure evolution, deposited films often contain free volume at grain boundaries in the form of small voids, Fig. 10.45(b). Subsequent diffusion or sintering will eliminate the voids and induce a residual tensile stress. The maximum value of stress is a function of the radius of curvature, r, of the as-deposited voids and is given as:

$$\sigma_{eq}^{R} = 2\gamma_s / r, \tag{10.86}$$

where γ_s is the surface energy.

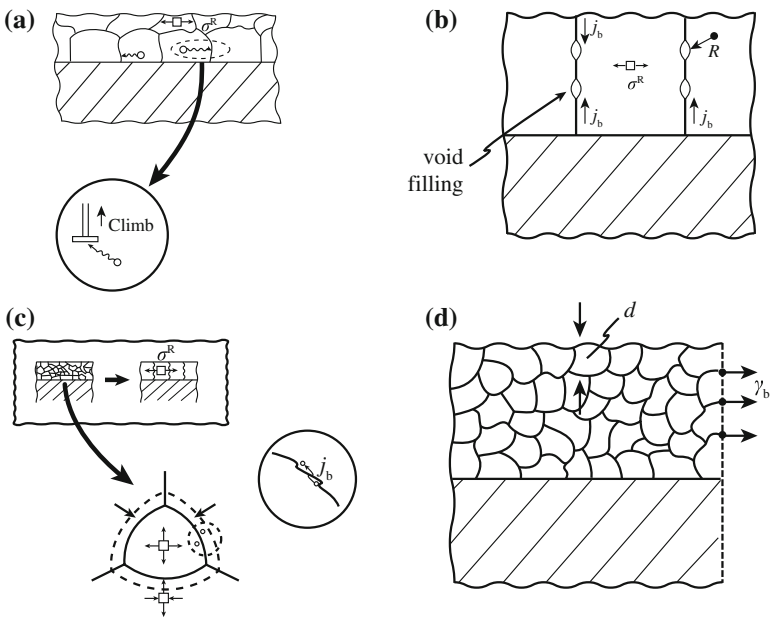

Fig. 10.45 Sources of residual tensile stress in thin films: (**a**) point defect annihilation at edge dislocations or grain boundaries, (**b**) removal of voids at the grain boundaries by sintering, (**c**) grain growth, and (**d**) grain boundaries (after [77])

Free volume in the grain boundary can also be eliminated by grain growth, as shown in Fig. 10.45(c). As small grains disappear, stresses develop and provide a strain energy contribution to the chemical potential of the atoms on the two sides of a grain boundary. The strain associated with the process is:

$$\varepsilon = 6\left(\frac{1}{d} - \frac{t}{d_0}\right)\Delta a, \tag{10.87}$$

where d is the final grain size, d_0 is the initial value as the film deposits, and Δa is the grain boundary free volume per unit area. The contribution of the strain energy to the chemical potential difference is:

$$\Delta\mu_s = 1/2E\Omega\varepsilon^2, \tag{10.88}$$

where Ω is the atomic volume and E is Young's modulus. This potential adds to that from the grain boundary curvature given by:

$$\Delta\mu_b = (2\gamma_b/d)\Omega, \tag{10.89}$$

where γ_b is the grain boundary energy. The equilibrium residual stress is obtained by setting the potential difference to zero. Equating $\Delta\mu_s$ and $\Delta\mu_b$ gives:

$$\sigma_{eq}^R = 3\gamma_b/2\Delta a, \tag{10.90}$$

which occurs at an equilibrium grain size:

$$d_{eq} = \frac{3(1-v)d_0^2\gamma_b}{4E(\Delta a)^2}. \tag{10.91}$$

Again, the stresses develop with time at temperature by grain boundary diffusion and the stresses are always tensile in nature.

Finally, it should be noted that there is a stress associated with the grain boundaries, Fig. 10.45(d). This stress is given by:

$$\sigma^R \approx \gamma_b/d. \tag{10.92}$$

Additional sources of stress include the incorporation of impurities during deposition and their subsequent diffusion, and phase transformations post-deposition. Both result in volume changes that can induce residual stresses (either tensile or compressive) with time after the film has formed.

Sources of stress in ion beam-assisted deposition

Compressive residual stresses are less common in PVD films but are frequently observed in films formed by IBAD. Explanations proposed for their origin include thermal spikes, recoil implantation, and trapped bombardment gas. For magnetron sputter-deposited thin films, it was found that there exists a transition pressure

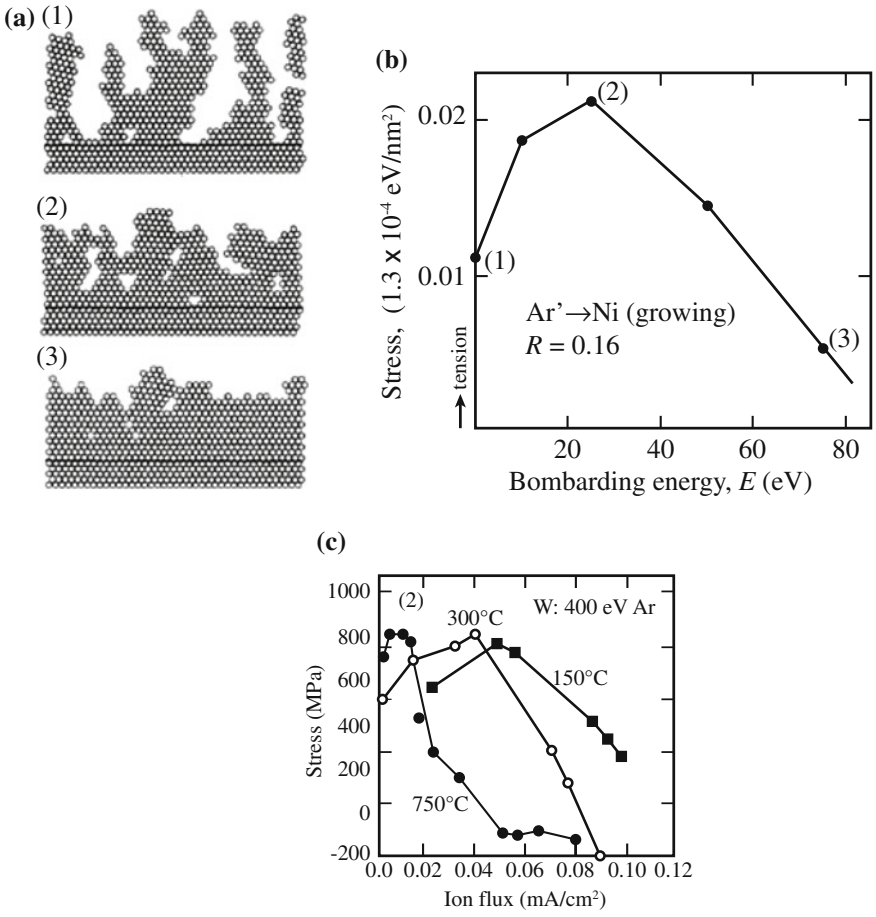

Fig. 10.46 (**a**) Microstructure evolution with increase incident kinetic energy of adatoms (after [79]), (**b**) MD simulation of Ar-ion-assisted, vapor-deposited Ni film (after [79]), and (**c**) W films evaporated concurrent with 400 eV Ar ion bombardment for case (2) in part (**b**) (after [1])

below which the films are in compression, while above the pressure the films are in tension. Following the effect of ion bombardment on film densification and grain morphology, energetic particle bombardment is believed to suppress the formation of the under-dense zone 1 structure and leads to reduction in the tensile stress, and eventually, at low enough pressure, to compressive internal stress [79]. Figure 10.46 shows the evolution of the film microstructure as a function of adatom kinetic energy. At very low adatom kinetic energies (case (1) in Fig. 10.46(a, b)), the structure is rich in defects such as large micropores, open voids, and the onset of microcolumns. At intermediate energies (case (2) in Fig. 10.46(a, b)), the pores become smaller and the atomic network is more interconnected. The tensile stress in

such a compact but still porous network is at a maximum as the short-range attractive interatomic forces across small defects can act most effectively. At larger kinetic energies (case (3) in Fig. 10.46(a, b)), the defects gradually disappear and well-layered crystal structure evolves, resulting in almost zero stress. Note that the residual stress in W films formed with 400 eV Ar bombardment (Fig. 10.46(c)) follow the same dependence described by the model shown in Figs. 10.46(a, b).

Cascade collision model

The ratio of the ion current to the evaporant flux to produce a zero-stress state is termed the critical ion-to-atom arrival rate ratio. The value of the critical arrival rate ratio for the annealing of stress in a vapor-deposited film can be determined using cascade collision simulations by postulating that stress annealing requires each atom in the growing film to be involved in at least one collision cascade [1]. If the average volume affected by a cascade is V_{cas}, and the average atomic density in the film is N, then the average number of atoms affected per cascade is NV_{cas}. A lower limit for the critical ion-to-atom flux ratio, $(J_i/J_a)_c$, (ignoring cascade overlap) is then:

$$(J_i/J_a)_c = (NV_{cas})^{-1}. \tag{10.93}$$

The cascade volume can be related to the ion energy through the range of the ion in the solid [1] resulting in the following, energy-dependent expressions for the critical ion-to-atom arrival rate ratio:

$$(J_i/J_a)_c = \begin{cases} 150E^{-1.59} & (0.2\text{keV} < E_{ion} < 2\,\text{keV}) \\ 4760E^{-2.04} & (2\text{keV} < E_{ion} < 5\,\text{keV}) \end{cases}. \tag{10.94}$$

A plot of the critical ion-to-atom arrival rate ratio as a function of ion energy as given in Eq. (10.94) (shown as open circles (o)) is compared with experimental data (×) on stress relief in Fig. 10.47. Note that the experimental data obeys an $E^{-3/2}$ energy dependence, which is close that of the model based on collision cascades.

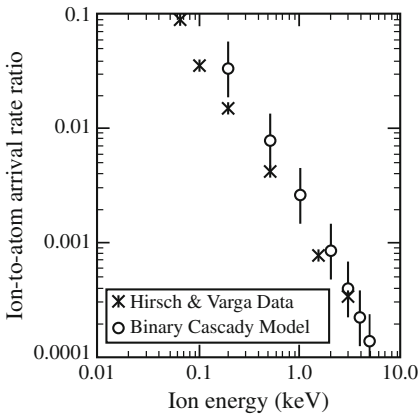

Fig. 10.47 Calculated and experimentally observed critical ion-to-atom arrival rate ratio for stress annealing in Ge IBAD films as a function of Ar ion energy (after [80])

Forward recoil model

Another mechanism by which residual stress can develop in films formed using energetic particle bombardment is based on the concept of shot peeing or forward recoil [73]. In this mechanism, atoms are displaced from their equilibrium positions through a series of primary and recoil collisions, producing a volumetric distortion. At low deposition temperatures ($T/T_m < 0.25$), mass transport and defect mobility are sufficiently low to freeze the volumetric distortion in place. The relative volumetric distortion (strain), ε, is proportional to the fractional number of atoms n/N displaced from equilibrium sites, so that:

$$\varepsilon = \frac{Kn}{N}, \tag{10.95}$$

where K is a proportionality factor and N is the atomic number density. Applying Sigmund's concept of forward sputtering [81] to a growing film (see Sect. 10.2.1), n is given by the product of the forward yield, Y (atoms/ion), and the ion flux, ϕ, as:

$$n = Y\phi. \tag{10.96}$$

For polycrystalline targets, the yield is given by:

$$Y = GF, \tag{10.97}$$

where F is the deposited energy density per unit depth, and G is a term that contains the target material properties, which for low-energy collisions (≤ keV) is given by:

$$G = \frac{0.042}{NU_{coh}}, \tag{10.98}$$

where U_{coh} is the cohesive energy. Low-energy Born–Mayer interatomic potentials are assumed to represent the interaction. The deposited energy is given by:

$$F = \alpha(M_2/M_1)S_n(E_{ion}, Z, M)N, \tag{10.99}$$

where α is an energy-independent function, S_n is the reduced nuclear stopping cross-sectional function, and E_{ion} the ion energy. Over the range $0.675 < M_2/M_1 < 4.8$, α can be approximated by an energy-independent expression:

$$\alpha = 0.07(1 + M_2/M_1), \tag{10.100}$$

where M_1 and M_2 are the projectile and target mass, respectively. For low projectile energy $(E/E_c \ll 1)$, where E_c is the Coulombic energy, which is of the order 50–100 keV), the reduced stopping power, S_n, can be approximated by:

$$S_n \simeq 3.33(E_{ion}/E_c)^{1/2}. \tag{10.101}$$

The expression for strain is then given by:

$$\varepsilon = \frac{K'\phi\sqrt{E_{ion}}}{N}, \tag{10.102}$$

where K' is a constant. The stress, σ, in the film is obtained by substituting ε into Hooke's law, resulting in:

$$\sigma^R = \frac{K'\phi\sqrt{E_{ion}}EM_2}{N_0(1-v)\rho}, \tag{10.103}$$

where E is the elastic modulus, v is Poisson's ratio, N_0 is Avogadro's number, and ρ is the density. The elastic and physical properties of the target in Eq. (10.102) can be combined into the quantity:

$$Q = \frac{EM_2}{(1-v)\rho}, \tag{10.104}$$

which represents the stored elastic energy per mole. A simplified expression for the compressive residual stress is:

$$\sigma^R = k\phi\sqrt{E_p}Q, \tag{10.105}$$

where the factor, k contains N_0 and other numerical constants.

The stress dependence on the molar volume, $M_2\rho$, indicates that the interaction between the energetic particles and the film target produces a strain that is not constant but is related to the atomic arrangement. The square root dependence on the particle energy is a direct consequence of the energy dependence of the nuclear stopping power, suggesting that the atomic peening mechanism is momentum driven. In addition, the model predicts a dependence on the elastic properties, modified by the molar volume, indicating an atomic volume dependence of the strain. The linear dependence of the residual stress on Q is shown in Fig. 10.48 for deposition by various ion beam techniques and for various materials [73].

Residual stress from trapped gas

The incorporation of the bombardment gas into the film either in the matrix or in the form of gas-filled voids can induce a residual stress in the film. IBAD is often conducted using inert gas (Ne, Ar, Kr, Xe) to impart momentum to the adatoms, and gas incorporation can result. As the gas is essentially insoluble in metals, the gas atoms will precipitate into small bubbles that can exert a stress against the substrate, Fig. 10.49. Modeling the film as an equivalent sphere in which the void and sphere radii are chosen so as to maintain the proper void volume, the governing equation for the displacement, u, of the sphere boundary is:

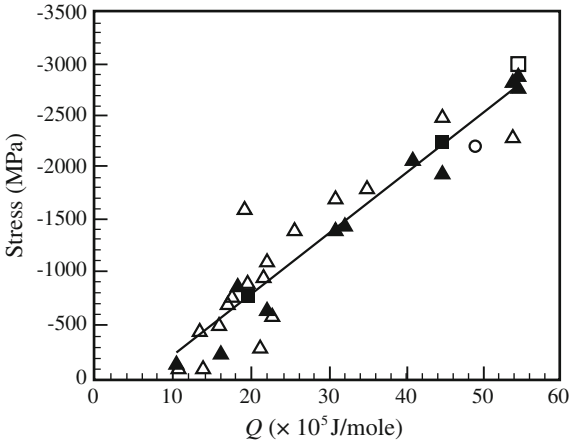

Fig. 10.48 Variation of intrinsic stress with Q, the elastic energy/mole, for films prepared by a variety of deposition techniques (after [73])

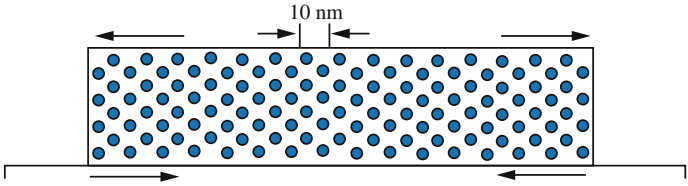

Fig. 10.49 Schematic illustration of the source of stress in an IBAD film due to gas trapped in bubbles

$$\frac{\mathrm{d}^2u}{\mathrm{d}r^2} + \frac{2}{r}\cdot\frac{\mathrm{d}u}{\mathrm{d}r} - \frac{2u}{r^2} = 0. \tag{10.106}$$

The solution to the equation is:

$$u = A/r^2 + Br, \tag{10.107}$$

with

$$\begin{aligned} \varepsilon_{rr} &= \frac{\mathrm{d}u}{\mathrm{d}r} = -\frac{2A}{r^3} + B, \\ \varepsilon_{\theta\theta} &= \varepsilon_{\phi\phi} = u/r = A/r^3 + B, \end{aligned} \tag{10.108}$$

and

$$\begin{aligned}\sigma_{rr} &= 2\mu\varepsilon_{rr} + \lambda(\varepsilon_{rr} + 2\varepsilon_{\theta\theta}),\\ \sigma_{\phi\phi} &= \sigma_{\theta\theta} = 2\mu\varepsilon_{\theta\theta} + \lambda(\varepsilon_{rr} + 2\varepsilon_{\theta\theta}),\end{aligned} \tag{10.109}$$

where ε is strain, σ is stress, μ is the shear modulus, and λ is the Lame coefficient, and A and B are constants. Applying boundary conditions of:

- zero displacement of the surface of the equivalent sphere, $u = 0$ at $r = r_0$, to account for the constraint of the film by the substrate which gives rise to a biaxial stress state, and
- equivalence of gas pressure and stress at the void surface, $\sigma_{rr}(r = r_0) = -p$, gives:

$$\begin{aligned}B &= \frac{-p}{\left\{2\mu[2(1/f)^3 + 1] + 3\lambda\right\}},\\ A &= -Br_0^3,\end{aligned} \tag{10.110}$$

and

$$\sigma_{rr} = \frac{3p(2\mu + \lambda)}{[4\mu(1/f) + (2\mu + 3\lambda)]}, \tag{10.111}$$

where $f = (r_i/r_0)^3$, is the volume fraction of void. Using a void volume fraction, $f = 0.3$, $\nu = 0.3$, and $E = 150$ MPa gives $\mu = 67$ MPa and $\lambda = 101$ MPa for amorphous alumina and yields $\sigma_{rr} \simeq -0.53p$. Fig. 10.50 shows the residual stress resulting from formation of an IBAD film using different types of bombardment gases (Table 10.1).

10.7.3 Film Texture

Thin films of PVD-deposited materials normally grow with the planes of highest atomic density parallel to the substrate, so fcc films have a ⟨111⟩ texture, bcc films have a ⟨110⟩ texture, and hcp films have a ⟨0002⟩ texture (for ideal *c/a* ratios). The easiest channeling directions in each structure are as follows:

fcc ⟨110⟩, ⟨100⟩, ⟨111⟩
bcc ⟨111⟩, ⟨100⟩, ⟨110⟩
hcp ⟨1120⟩, ⟨0002⟩

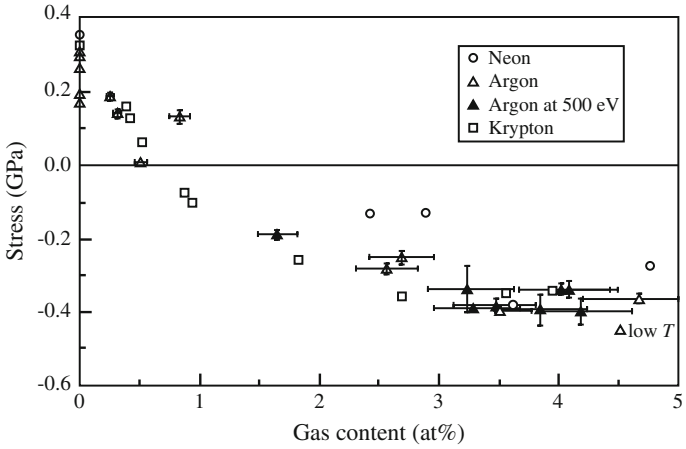

Fig. 10.50 Residual film stress as a function of gas pressure and type of gas for amorphous alumina films (after [82])

Table 10.1 Sources of residual stress in deposited films

Source of stress	Equation	Tension (+)/compression (−)
Thermal expansion	$\sigma^{\mathrm{R}} = E_{\mathrm{f}}\Delta\alpha\dfrac{T_{\mathrm{R}} - T}{(1-\nu_{\mathrm{f}})}$ (10.83)	Either
Point defect elimination	$\sigma^{\mathrm{R}}_{\mathrm{eq}} = \left(\dfrac{kT}{\Omega}\right)\ln\dfrac{C}{C_0}$ (10.85)	Tension
Grain boundary porosity elimination	$\sigma^{\mathrm{R}}_{\mathrm{eq}} = 2\gamma_{\mathrm{s}}/r$ (10.86)	Tension
Grain growth in film	$\sigma^{\mathrm{R}}_{\mathrm{eq}} = 3\gamma_{\mathrm{b}}/2\Delta a$ (10.90)	Tension
Grain boundary	$\sigma^{\mathrm{R}} \approx \gamma_{\mathrm{b}}/d$ (10.92)	Tension
Precipitation	–	Either
Impurities	–	Either
Cascade collision	$(J_{\mathrm{i}}/J_{\mathrm{a}})_{\mathrm{c}} = \begin{cases} 150E^{-1.59} & (0.2\,\mathrm{keV} < E_{\mathrm{ion}} < 2\,\mathrm{keV}) \\ 4760E^{-2.04} & (2\,\mathrm{keV} < E_{\mathrm{ion}} < 5\,\mathrm{keV}) \end{cases}$ (10.94)	Compression
Forward recoil	$\sigma^{\mathrm{R}} = k\phi\sqrt{E_{\mathrm{p}}Q}$ (10.105)	Compression
Trapped gas	$\sigma_{rr} = \dfrac{3p(2\mu+\lambda)}{[4\mu(1/f)+(2\mu+3\lambda)]}$ (10.111)	Compression

The development of crystallographic texture during IBAD can be correlated with the channeling directions of ions in the crystal lattice and the density of energy deposition would be inversely related to the depth of channeling. Thus, in an fcc crystal, the ease of channeling is in the order ⟨110⟩, ⟨200⟩, ⟨111⟩.

Ion bombardment causes a shift in the preferred orientation to alignment of the easiest channeling direction along the ion beam axis. Thus, an ion beam at normal incidence on a fcc film will cause a shift in orientation from ⟨111⟩ to ⟨110⟩ texture. A beam incident at an angle will produce a different texture depending on the crystallography. The texturing effect appears to be most sensitive to high-energy beams because of the larger volume affected per ion and the deeper penetration. Experiments on ion bombardment during deposition of an Al film show that while Al forms a very strong ⟨111⟩ texture during physical vapor deposition, bombardment during deposition can induce an equally strong ⟨110⟩ texture that is driven by ion channeling [83].

It is believed that the preferential growth of grains with the channeling direction aligned with the ion beam due to reduced sputtering is responsible for the crystallographic texture during IBAD [84, 85]. The difference in sputtering yields between aligned and unaligned grains can be as high as a factor of 5 in some materials [86]. This difference leads to a larger net growth rate for aligned grains than for unaligned grains. The newly deposited layer grows epitaxially on grains with low sputter yield orientation, and these grains will eventually dominate the film. This same process is also expected to control the surface roughness evolution, especially under deposition conditions where the surface diffusion is very limited.

The concepts of ion channeling and preferential sputtering are shown in the schematic diagram in Fig. 10.51. An ion impinging on a crystal in a direction aligned with the open channels in that crystal will become trapped in the channel and lose energy slowly by electronic energy transfer rather than by making high-angle nuclear collisions. The net result is transport of the atom deep into the crystal and deposition of energy away from the surface. The deposition of energy deep in the crystal also means that the sputtering yield will be low for channeled ions. This is contrasted with the interaction of an ion with a crystal in an unaligned orientation. In this case, the ion has a higher probability of causing a high-angle collision near the surface, resulting in energy deposition by elastic interactions near the surface and a higher sputtering yield. Hence, an observable difference between

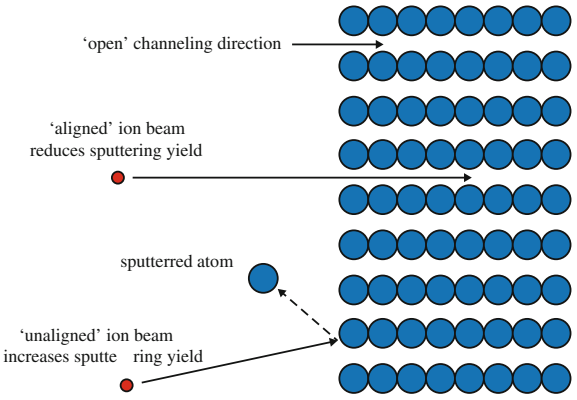

Fig. 10.51 Schematic diagram of ion channeling and preferential sputtering during ion bombardment

channeled and non-channeled ions is a lower sputtering yield in the case of channeling.

During film deposition, crystallites are formed on the substrate with a number of different orientations. If an ion beam were directed onto the surface during film growth and the ion energy exceeded the channeling energy, the crystallites with open channels in the beam direction will have a lower sputtering yield than those with channels that are not aligned with the beam. The result is a lower sputtering rate for the aligned crystallites. Crystallites whose channeling directions are aligned with the beam will have a higher survival probability based on a reduced sputtering yield. The reduced sputtering yield also means an increased growth rate for aligned grains. This concept for texture development can be applied to control both out-of-plane and in-plane textures.

Figure 10.52 shows a schematic of the control of film texture during IBAD. In fcc metals, Fig. 10.52(a), the growth plane is (111) due to its high packing density and low energy. That is, this plane is thermodynamically preferred. The easiest channeling direction in the fcc lattice is [110]. Hence, if an ion beam is directed normal to the surface, then crystallites with their [110] directions in the beam direction will be favored, and a (110) out-of-plane texture is favored. By virtue of the higher survival probability of [110]-aligned grains versus [111]-aligned grains, the (110) texture should be preferred. The result is a strong (110) texture in which the grains nucleate and grow faster than the (111) grains by virtue of the lower sputtering rate and reduced surface mobility. Since this texture is highly non-equilibrium, atom mobility (film temperature) is an important factor in retaining the ion-induced (110) texture.

The control of in-plane texture occurs in much the same manner as control of out-of-plane texture and is shown in the schematic in Fig. 10.52(b). The example is the growth of a bcc (e.g., Nb) film under ion bombardment. Niobium displays a (110) growth texture when deposited by physical vapor deposition. The easiest channeling direction in the bcc lattice is [100]. However, the aim here is to control the in-plane texture, not the out-of-plane texture. The Nb crystal has a (110) growth texture in which the [110] direction is normal to the substrate surface. The [100] direction makes an angle of 45° with [110]. Hence, ion bombardment at an angle of

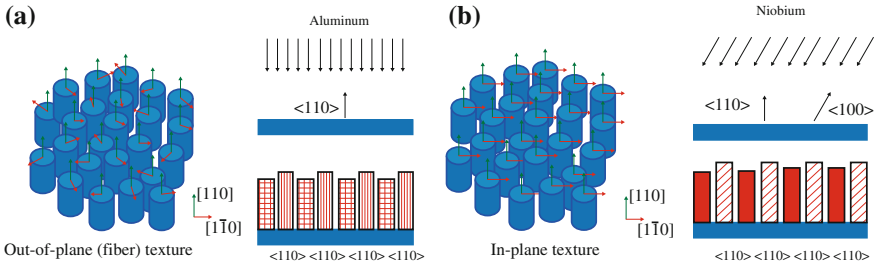

Fig. 10.52 Examples of formation of (**a**) (110) fiber texture in fcc Al, and (**b**) in-plane texture in bcc Nb by IBAD

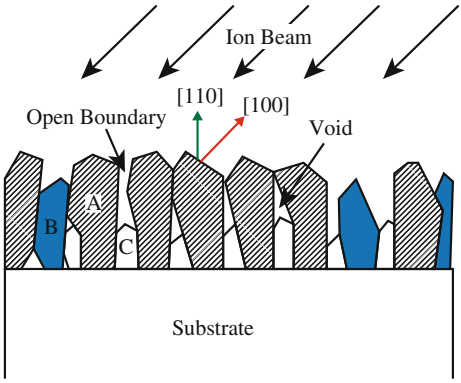

Fig. 10.53 Growth of aligned grains at the expense of unaligned grains during IBAD

45° will result in the alignment of the [100] direction with the ion beam. This forces the $[1\bar{1}0]$ in-plane direction to be parallel with the projection of the ion beam on the film surface, resulting in an in-plane $[1\bar{1}0]$ texture. Ion bombardment does not disturb the out-of-plane texture. Thus, the film formed under an ion assist grows with a {110} out-of-plane texture and a {110}) in-plane texture.

In both cases, subsequent film growth is governed by the differences in sputtering rate between aligned and unaligned grains. The schematic in Fig. 10.53 shows that as growth proceeds, aligned grains grow at a faster rate than do unaligned grains. The aligned grains eventually "bridge-over" and coalesce, resulting in saturation of the film texture. The difference in growth rates and the occurrence of bridge-over also explain the development of the surface roughness in textured films [87, 88].

In summary, ion irradiation combined with film deposition can provide substantially enhanced control of the film microstructure and properties. The changes to deposited films brought about by IBAD are summarized in Fig. 10.54, in which the numbers refer to specific experiments. Those highlighted in red (1–4) are control of residual stress, in blue (1, 15) are changes in adhesion, in green (7) is texture, and in purple (16) is hardness. Note that most phenomena occur between an average energy deposition of 1 and 100 eV/atom.

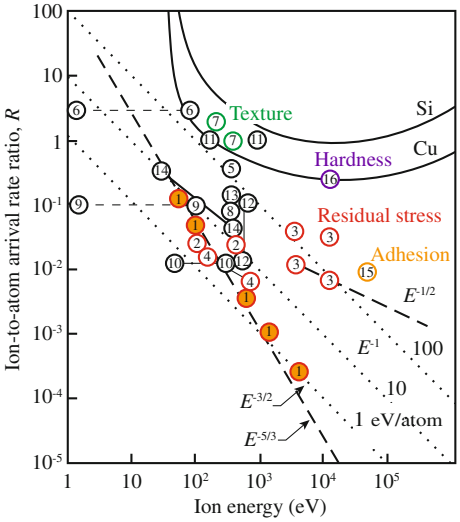

Fig. 10.54 Map of the parameter space for arrival rate ratio and ion energy showing regions where ion beam-activated phenomena have been observed. Delineated regions in upper right corner represent complete removal of Si and Cu by sputtering and blank spaces in lower left corner are region where normal thermally activated processes would be found (after [89])

Nomenclature

a	Screening radius; also nearest neighbor distance
c	Specific heat capacity
C	Concentration
$\mathrm{d}E/\mathrm{d}x\|_\mathrm{n}$	Energy loss rate due to nuclear stopping
d	Grain size
D	Diffusion coefficient
D_B	Blister diameter
D^*	Effective diffusion coefficient
D'	Modified diffusion coefficient accounting for diffusional intermixing
E	Energy; also Young's modulus
E_a	Energy per deposited atom
E_c	Columbic energy
E_coh	Cohesive energy
E_d	Displacement energy
E_ion	Ion energy
E_mix	Energy of mixing
F	Displacement rate in dpa/s; also deposited energy density per unit depth
F_D	Deposited energy
H_{ij}	Potential energy between atom pairs of type i and j
ΔH_coh	Cohesive energy

ΔH_A	Heat of adsorption
ΔH_{mix}	Heat of mixing
I_0	Ionization potential
J	Ionization rate defined in Eq. (10.79)
J_a	Flux of atoms in vapor deposition
J_i	Flux of atoms of type i; also flux of ions in IBAD
k	Boltzmann's constant
K_0	Defect production rate
m	Number of gas atoms in a bubble
m_e	Mass of electron
M	Atomic mass
n	Number of atoms
N	Atom number density
p	Gas pressure in a bubble or vapor pressure
p_i	Sputter probability of atom of type i
$\bar{p}_i$	Average total sputter probability of atom of type i
P	Load
P_i	Total effect of recoil implantation, Eq. (10.31)
Q	Activation energy; also stored elastic energy per mole
Q_i	Equivalent number of i atoms recoil implanted over a depth R_p
r_c	Characteristic jump distance in a thermal spike
r	Radius of curvature of void
R	Ion range; also root mean square of an atom in a collision cascade; also vacancy–interstitial recombination rate; also ion-to-atom arrival rate ratio; also jump rate in thermal spikes; and also atom impingement rate in vacuum
R_d	Displacement rate in #/cm^{3}s
R_p	Projected range
R_{recoil}	Recoil range
ΔR_p	Standard deviation of the projected range
S	Scaling factor
S_e	Electronic stopping power
S_i	Sputtered flux of atom of type i
S_n	Nuclear stopping power
S_X	Sputtered flux of element X
t	Time
t_B	Blister shell thickness
T	Temperature; also energy transferred in a collision event
T_{eff}	Effective temperature at which diffusion occurs
u	Displacement
U_{coh}	Cohesive energy
U_0	Surface binding energy
v	Ion velocity
V	Volume

Y	Sputter yield
z	Coordination number
Z	Atomic number
α	Constant in Eq. (10.3) and defined differently in Eq. (10.79); also degree of epitaxy in IBAD; and also thermal expansion coefficient
χ	Ratio of probability of sputtering a B atom to that for an A atom
δ	Thickness of surface layer removed by sputtering
$\Delta\alpha$	Difference in thermal expansion coefficients
ε	Unit charge; also the energy density in the cascade; and also strain
$\in$	Reduced energy
λ	Lame coefficient: also jump length
μ	Chemical potential
ϕ	Flux of ions or atoms
γ	Activity coefficient; also surface energy
γ_b	Grain boundary energy
Γ	Total jump frequency
η	Number of atom jumps in a thermal spike per unit length of the spike
κ	Thermal diffusivity
Λ	Factor in sputtering yield Eq. (10.2) containing material parameters
μ	Shear modulus; also chemical potential
ν	Number of displacement per primary knock-on atom; also Poisson's ratio
$\nu_i^{s\to b}$	Surface-to-bulk jump frequency for atom i
$\nu_i^{b\to s}$	Bulk-to-surface jump frequency for atom i
Ω	Atomic volume
ρ	Atom density
ρ_B	Gas bubble density
σ_d	Displacement cross section
σ_d^e	Displacement cross section by electronic excitation
σ^R	Residual stress in a deposited film
σ_s	Scattering cross section
$\sigma_{0,i}$	Elastic scattering cross section between ions and i atoms
σ_i	Surface ejection cross section for atoms of type i
σ_L	Lateral stress in the solid
$\bar{\sigma}$	Average stress
Ω	Atomic volume
ξ	Atomic layer thickness

Superscripts

B Bulk
R Residual stress
s Surface

Subscripts

A Adsorption
B Bubble or blister
cas Cascade
d Displaced
D Displacement
eq Equilibrium
f Film
i Incoming ion
P Projected
s Scattering; also substrate

Acronyms

CO	Coevaporated
DM	Displacement mixing
GA	Gibbsian adsorption
FWHM	Full width at half maximum
IBAD	Ion beam-assisted deposition
IBED	Ion beam-enhanced deposition
IBM	Ion beam mixing
II	Ion implantation
ML	Multilayered
PS	Preferential sputtering
PSII	Plasma source ion implantation
RED	Radiation-enhanced diffusion
RIS	Radiation-induced segregation

Problems

10.1 Use the description of how a delta function distribution of particles spreads by diffusion to calculate the width of an initially sharply peaked distribution of:

(a) Vacancies,
(b) Interstitials, and
(c) Self-tracer diffusing by vacancy mechanism,

in Pt, after a time $t = 1$ min, for temperatures of 20 and 800 °C.

10.2 Consider a thin foil of a binary alloy in which the surface is the only defect sink. The foil is at thermal equilibrium at low temperature and is then heated instantaneously to near its melting point. Describe qualitatively the evolution of:

(a) The vacancy concentration and
(b) The composition profile.

10.3 A bilayer of 50 nm Pd on top of 50 nm Ni is deposited on a silicon substrate. The layer is mixed with 300 keV Kr^+ at a current of 40μA/cm^2 for 40 s.

(a) Plot the concentration profile of the Pd after mixing.
(b) If the sputtering yield of the Pd is 13 and Kr is half as likely as Pd to be sputtered, what is the maximum amount of Kr that can be implanted into this sample?

10.4 A Ni–1 %Si alloy is heated to a temperature of 500 °C during irradiation with 500 keV Kr ions at a current density of 1 μA/cm^2.

(a) What physical processes will be important in determining the surface concentration?
(b) If each process occurs independently of the others, what would be the effect of *each* on the surface composition?
(c) Estimate the *combined* effect of these processes on the surface composition and provide an argument to support your answer for the case where:

(i) Thermal processes dominate pure collisional processes and
(ii) Pure collisional processes dominate thermal processes.

Draw the composition versus depth profile for cases (i) and (ii).

$$C_{\mathrm{Si}}^{\mathrm{B}} = 0.01$$
$$C_{\mathrm{Ni}}^{\mathrm{B}} = 0.99$$
$$\Delta H_{\mathrm{A}}^{\mathrm{Si}} = -0.1\,\mathrm{eV}$$
$$\bar{p}_{\mathrm{Si}}/\bar{p}_{\mathrm{Ni}} = 2.0$$
$$\Delta H_{\mathrm{m}}^{\mathrm{Ni,v}} = 0.77\,\mathrm{eV}$$

$$\Delta H_{\mathrm{m}}^{\mathrm{Ni,i}} = 0.1\,\mathrm{eV}$$
$$\Delta H_{\mathrm{m}}^{\mathrm{Si,v}} = 0.28\,\mathrm{eV}$$
$$\Delta H_{\mathrm{m}}^{\mathrm{Si,i}} = 0.15\,\mathrm{eV}$$
$$R_{\mathrm{S}_i} = 0.1176\,\mathrm{nm}$$
$$R_{\mathrm{Ni}} = 0.1245\,\mathrm{nm}$$

$$\frac{C_A^{surface}}{C_B^{surface}} = \frac{C_A^{bulk}}{C_B^{bulk}} \exp\left(\frac{-\Delta H_A}{kT}\right)$$

$$\frac{\bar{p}_A}{\bar{p}_A} = \frac{C_A^{bulk}}{C_B^{surface}} \frac{C_B^{bulk}}{C_A^{surface}}$$

10.5 A homogeneous A–B alloy of composition A–50 at.%B is bombarded with 5 keV Ar ions at 400 °C. Given that the surface concentration following bombardment is 30 % A and 70 % B, describe what processes or combinations of processes could give rise to such behavior and which processes are dominant?

$\Delta H^v_{m,A}$ = migration enthalpy for A atoms by vacancies = 0.7 eV
$\Delta H^v_{m,B}$ = migration enthalpy for B atoms by vacancies = 0.9 eV
$\Delta H^i_{m,A} = \Delta H^i_{m,B}$ = migration enthalpy for A and B atoms via interstitials = 0.1 eV
ΔH_A = enthalpy of adsorption of A in B = − 0.3 eV
p^s_A = sputtering probability for A atoms = 3 atoms/ion
p^s_B = sputtering probability for B atoms = 4 atoms/ion
C_A = constant × $(d_{Av}/d_{Bv} – d_{Ai}/d_{Bi})C_v$
$d_{Av} \propto \exp(-\Delta H_{m,A}/kT)$
$C^s_A/C^s_B = (C^b_A/C^b_B)\exp(-\Delta H_A/kT)$

10.6 Explain why ion beam mixing experiments often do not agree with the predictions from the ballistic theory of mixing. How would the temperature of the sample affect your answer?

10.7 A sample of polycrystalline Si is bombarded with 500 keV Al^+ ions to a dose of 5×10^{15} i/cm^2. Given that R_p = 260 nm and ΔR_p = 94 nm and that the damage profile has the same shape but peaks at $0.8R_p$, calculate the peak damage in the material using reasonable assumptions.
The distribution of ions is given by $N(x) = N_p \exp(-X^2/2)$ where $X = (x - R_p)/\Delta R_p$ and $N_p = 0.4N_s/\Delta R_p$.
Assume that electronic stopping varies with energy as $kE^{1/2}$ where $k = 1.5 \times 10^{-16}$ eV$^{1/2}$cm^2.
Energy transfer cross section based on inverse square law

$$\sigma(E,T) = \frac{\pi^2 a^2 E_a \gamma^{1/2}}{8E^{1/2}T^{3/2}}$$

Energy transfer cross section based on Rutherford scattering

$$\sigma(E,T) = \frac{\pi b_0^2 E\gamma}{4T^2}$$

$$N = 3 \times 10^{22}\, a/cm^3$$

$$E_c = 28\,\text{keV}$$

$$E_a = 14\,\text{keV}$$

$$E_b = 14\,\text{keV}$$

$$E_d = 30\,\text{eV}$$

$$a = a_B/(z_1 z_2)^{1/6}$$

$$a_B = 0.053\,nm$$

$$b_0 = z_1 z_2 \varepsilon^2/\eta E$$

$$\varepsilon^2 = 2a_B E_R$$

10.8 Explain cohesive energy and heat of mixing. What are the approximate magnitudes of these energies? How can they influence ion beam mixing?

10.9 A Cu–40 %Ni target is irradiated with 100 keV Ar^+ at a current density of 40μA/cm^2

(a) Determine which element will segregate to the surface under irradiation at 500 °C.

b) On a single graph, draw the surface concentration as a function of time at 400 °C for the following processes:

(i) GA only,
(ii) PS + RED,
(iii) PS + RED + GA, and
(iv) PS + RED + RIS.

GA = Gibbsian adsorption,
PS = Preferential sputtering,
RED = Radiation-enhanced diffusion, and
RIS = Radiation-induced segregation.

$$\Delta H_{\text{m,v}}^{\text{Cu}} = 0.77\,\text{eV}$$

$$\Delta H_{\text{m,v}}^{\text{Ni}} = 0.82\,\text{eV}$$

$$\Delta H_{\text{m,i}}^{\text{Cu,Ni}} = 0.12\,\text{eV}$$

$$\Delta H_{\text{A}}^{\text{Cu}} = -0.25\,\text{eV}$$

P_{Cu} = 5.5, P_{Ni} = 2.75 atoms/ion per unit concentration.

10.10 Determine the lateral load at which helium bubbles cause blistering in 316 stainless steel under the condition that the blister diameter $\sim 2t_B$ where t_B is the blister cap thickness.

References

1. Nastasi M, Mayer JW, Hirvonen JK (1996) Ion-solid interactions: fundamentals and applications. Cambridge University Press, Cambridge
2. Komarov F (1992) Ion beam modification of materials. Gordon and Breach, Philadelphia
3. Was GS (1989) Prog Surf Sci 32(3/4):211–312
4. Smidt F (1990) Int Mater Rev 35(2):61–128
5. Hirvonen JK (1991) Mater Sci Rep 6:251–274
6. Sigmund P (1969) Phys Rev 184:383
7. Smith DL (1978) J Nucl Mater 75:20–31
8. Sigmund P (1981) Sputtering by particle bombardment I. Springer, Berlin, p 9
9. Winters HF (1976) In: Kaminsky M (ed) Radiation effects in solid surfaces. American Chemical Society, Washington, DC, p 1
10. Lindhard J, Nielsen V, Scharff M (1968) Kgl Danske Videnskab Selskab Mat Fys Medd 36 (10):1
11. Wiedersich H, Andersen HH, Lam NQ, Rehn LE, Pickering HW (1983) In: Poate JM, Foti G, Jacobson DC (eds) Surface modification and alloying, NATO series on materials science. Plenum, New York, p 261
12. Falcone G, Sigmund P (1981) Appl Phys 25:307
13. Lam NQ, Wiedersich H (1987) Nucl Instr Meth B 18:471
14. Wynblatt P, Ku RC (1979) In: Johnson WC, Blakely JM (eds) Interfacial segregation. American Society for Metals, Metals Park, OH, p 115
15. Sigmund P (1979) J Appl Phys 50(11):7261
16. Sigmund P, Gras-Marti A (1981) Nucl Instr Meth 182/183:25
17. Gras-Marti A, Sigmund P (1981) Nucl Instr Meth 180:211
18. Myers SM (1980) Nucl Instr Meth 168:265
19. Anderson HH (1979) Appl Phys (Germany) 18:131
20. Workman TW, Cheng YT, Johnson WL, Nicolet MA (1987) Appl Phys Lett 50(21):1485
21. Westendorp H, Wang ZL, Saris FW (1982) Nucl Instr Meth 194:453
22. Wang ZL, Westendorp JFM, Doorn S, Saris FW (1982) In: Picraux ST, Choyke WJ (eds) Metastable materials formation by ion implantation. Elsevier, New York, p 59
23. Paine BM, Averback RS (1985) Nucl Instr Meth B 7(8):666
24. Johnson WL, Cheng Y-T, Van Rossum M, Nicolet M-A (1985) Nucl Instr Meth B 7(8):657
25. Van Rossum M, Cheng Y-T (1988) Defect Diffusion. Forum 57(58):1
26. Cheng Y-T, Workman TW, Nicolet M-A, Johnson WL (1987) Beam-solid interactions and transient processes, vol 74. Materials Research Society, Pittsburgh, p 419
27. Ma E, Workman TW, Johnson WL, Nicolet M-A (1989) Appl Phys Lett 54(5):413
28. Cheng Y-T, Van Rossum M, Nicolet M-A, Johnson WL (1984) Appl Phys Lett 45(2):185
29. Van Rossum M, Cheng Y-T, Nicolet M-A, Johnson WL (1985) Appl Phys Lett 46(6):610
30. Rossi F, Nastasi M (1991) J Appl Phys 69(3):1310
31. Vineyard GH (1976) Rad Eff 29:245
32. Matteson S, Roth J, Nicolet M (1979) Rad Eff 42:217–226
33. Cheng Y-T (1989) Phys Rev B 40(10):7403–7405
34. Hung LS, Mayer JW (1985) Nucl Instr Meth B 7(8):676
35. Was GS, Eridon JM (1987) Nucl Instr Meth B 24(25):557

36. Lam NQ, Leaf GK, Wiedersich H (1980) J Nucl Mater 88:289
37. Lam NQ, Wiedersich H (1982) In: Picraux ST, Choyke WJ (eds) Metastable materials formation by ion implantation. Elsevier, New York, p 35
38. Lam NQ, Wiedersich H (1981) J Nucl Mater 103(104):433
39. Lam NQ, Leaf GK (1986) J Mater Res 1:251
40. Rehn LE, Okamoto PR (1983) In: Nolfi FV (ed) Phase transformations during irradiation. Applied Science, New York, p 247
41. Mayer SGB, Milillo FF, Potter DI (1985) In: Koch CC, Liu CT, Stoloff NS (eds) High-temperature ordered intermetallic alloys, vol 39. Materials Research Society, Pittsburgh, p 521
42. Liu JC, Mayer JW (1987) Nucl Instr Meth B 19(29):538
43. Alexander D, Was G, Rehn LE (1990) Materials research symposium, vol 157. Materials Research Society, Pittsburgh, PA, p 155
44. Eridon J, Rehn L, Was GS (1987) Nucl Instr Meth B 19(20):626
45. Eridon J, Was GS, Rehn L (1987) J Appl Phys 62(5):2145
46. Johnson E, Wohlenberg T, Grant WA (1979) Phase Trans 1:23
47. Ahmed M, Potter DI (1987) Acta Metal 35(9):2341
48. Nishiyama Z (1978) In: Fine ME, Meshii M, Wayman CM (eds) Martensitic transformations, vol 7. Academic, New York
49. Didenko AN, Kozlov EV (1993) Sharkeev YuN, Tailashev AS, Rajabchikov AI, Pranjavichus L, Augulis L. Surf Coat Technol 56:97–104
50. Behrisch R, Risch M, Roth J, Scherzer BMU (1976) Proceedings of the 9th symposium on fusion technology. Pergamon, New York, pp 531–539
51. Ullmaier H (1983) Rad Eff 78:1–10
52. Wolfer WG (1980) J Nucl Mater 93(94):713–720
53. Behrisch R, Scherzer BMU (1983) Rad Eff 78:393–403
54. Birtcher RC, Jäger W (1987) Ultramicroscopy 22:267–280
55. Liu AS, Birtcher RC (1989) Materials research society symposium, vol 128. Materials Research Society, Pittsburgh, pp 303–308
56. Johnson PR (1983) Rad Eff 78:147–156
57. Mazey DJ, Evans JH (1986) J Nucl Mater 138:16–18
58. Iwase A, Iwata T (1994) Nucl Instr Meth Phys Res B 90:322
59. Dunlop A, Lesueur D, Legrand P, Dammak H, Dural J (1994) Nucl Instr and Meth Phys Res B 90:330
60. Chimi Y, Iwase A, Ishikawa N, Kambara T (2002) Nucl Instr Meth Phys Res B 193:248–252
61. Auciello O, Kelly R (eds) (1984) Ion bombardment modification of surfaces fundamentals and applications. Elsevier, New York
62. Grovenor CRM, Hentzell HTG, Smith DA (1984) Acta Metall 32:773
63. Thornton JA (1982) Coating deposition by sputtering, in deposition technologies for film and coatings. In: Bunshah RF (ed) Noyes Publications, Park Ridge, Chap 5
64. Messier R, Giri AP, Roy RA (1984) J Vac Sci Technol, A 2:500
65. Martin PH, Netterfield RP, Sainty WG (1984) J Appl Phys 55:235
66. Smidt FA (1988) In: Proceedings of DOE workshop on "coatings for advanced heat engines" Conference 870762, V-29, US Department of Energy, Washington, DC
67. Yamada I (1977) In: Proceedings of Int Ion Engin Cong, Kyoto, p 1177
68. Muller K-H (1985) J Appl Phys 58:2573
69. Muller K-H (1986) J Appl Phys 59:2803
70. Muller K-H, Netterfield RP, Martin PJ (1987) Phys Rev B 35:527
71. Netterfield RP, Muller K-H, McKenzie DR, Goodman MJ, Margin PF (1988) J Appl Phys 63:760
72. Muller K-H (1987) Phys Rev B 35:7906
73. Windischmann (1992) Crit Rev Solid States Mater Sci 17:547–596
74. Hibbs MK, Johannsson BO, Sundgren JE (1984) Helmersson. Thin Solid Films 122:115

75. Greene JE, Motocka T, Sundgren J-E, Lubben D, Gorbatkin S, Barnett SA (1987) Nucl Instrum Meth Phys Res B27:226
76. Roy RA, Cuomo JJ, Yee DS (1988) J Vac Sci Technol, A 6:1621
77. Evans AG, Hutchinson JW (1995) Acta Metall Mater 43:2507–2530
78. Doerner MF, Nix WD (1983) CRC Crit Rev Solid States Mater Sci 14:224
79. Muller KH (1987) J Appl Phys 62:1796
80. Brighton DR, Hubler GK (1987) Nucl Instrm Meth Phys Res B28:527
81. Sigmund P (1981) Sputtering by particle bombardment I. Springer, Berlin, p 1
82. Parfitt L, Goldner M, Jones JW, Was GS (1995) J Appl Phys 77:3029
83. Ma Z, Was GS (1999) J Mater Res 14(10):4051–4061
84. Bradley RM, Harper JME, Smith DA (1986) J Appl Phys 60:4160–4164
85. Bradley RM, Harper JME, Smith DA (1987) J Vac Sci Technol A5:1792–1793
86. Roosendaal HE (1981) Sputtering by particle bombardment I. Springer, Berlin, p 217
87. Ji H, Was GS (1999) Nucl Instr Meth In Phys Res B 148:880–885
88. Ji H, Was GS (1999) J Mater Res 14:2524
89. Harper JME, Cuomo JJ, Gambino RJ, Kaufman HE (1984) In ion bombardment modification of surfaces: fundamentals and applications. Elsevier Science, Amsterdam, pp 127–162, Chap 4

Chapter 11
Emulating Neutron Irradiation Effects with Ions

Radiation effects research is conducted with a variety of energetic particles: neutrons, electrons, light ions, and heavy ions. Energetic ions can be used to understand the effects of neutron irradiation in reactor components, and interest in this application of ion irradiation has grown in recent years for several reasons that include the avoidance of high residual radioactivity and a decline in the availability of test reactors for materials irradiation. The damage state and microstructure resulting from ion irradiation, and thus the degree to which ion irradiation emulates neutron irradiation, depend principally on the particle type and the damage rate. This chapter will begin with a brief review of the damage function, primary recoil spectrum, and efficiency of defect production for various particle types. Effects of particle type on both microstructure and microchemistry will be discussed, followed by the effects of the irradiated microstructure on mechanical properties. The roles of dose, dose rate, and temperature parameters and the constraints on parameter space by each particle source will be discussed and compared against the effects of neutron irradiation.

11.1 Motivation for Using Ion Irradiation as a Surrogate for Neutron Irradiation

In the 1960s and 1970s, heavy ion irradiation was developed for the purpose of simulating neutron damage in support of the fast breeder reactor program [1–3]. Ion irradiation and simultaneous He injection have also been used to simulate the effects of 14 MeV neutron damage in conjunction with the fusion reactor engineering program. The application of ion irradiation (defined here as any charged particle, including electrons) to the study of neutron irradiation damage is of interest to the light water reactor community to address issues such as stress corrosion cracking (SCC) of core materials that are affected by irradiation [4–6]. Ion irradiation is also being used to understand the irradiated microstructure of reactor pressure vessel steels, Zircaloy fuel cladding, and materials for advanced reactor concepts.

G.S. Was, *Fundamentals of Radiation Materials Science*,
DOI 10.1007/978-1-4939-3438-6_11

There is significant incentive to use ion irradiation to study neutron damage as this technique has the potential for yielding answers on basic processes in addition to the potential for enormous savings in time and money. Neutron irradiation experiments are not amenable to studies involving a wide range of conditions, which is precisely what is required for investigations of the basic damage processes. Radiation damage experiments using ion irradiation allow for easy variation of the irradiation parameters such as dose, dose rate, and temperature over a wide range of values.

Typical neutron irradiation experiments in test reactors require years of incore exposure to reach appreciable fluence levels for accelerated post-irradiation testing. This is accompanied by at least another year of capsule design and preparation as well as disassembly and cooling. Analysis of microchemical changes using techniques such as Auger electron spectroscopy (AES) and atom probe tomography (APT), microstructural changes by energy dispersive spectroscopy via scanning transmission electron microscopy (STEM-EDS), and mechanical property or SCC evaluation can take several additional years because of the precautions, special facilities, and instrumentation required for handling radioactive samples. The result is that a single cycle from irradiation through microanalysis and mechanical property/SCC testing may take between three and five years. Such a long cycle length does not permit for iteration on irradiation or material conditions that is critical in any experimental research program. The long lead time required for design and irradiation also reduces flexibility in altering irradiation programs as new data become available. Because of the long cycle time, the requirement of special facilities and special sample handling, the costs for neutron irradiation experiments are very high.

In contrast to neutron irradiation, ion irradiation enjoys considerable advantages in both cycle length and cost. Ion irradiations of any type rarely require more than several tens of hours to reach damage levels in the 1–10 dpa range. Ion irradiation produces little or no residual radioactivity, allowing handling of samples without the need for special precautions. These features translate into significantly reduced cycle length and cost. The challenge is then to verify the equivalency of the results of neutron and ion irradiation.

The key question that needs to be answered is how do results from neutron and charged particle irradiation experiments compare? How, for example is one to compare the results of a component irradiated in-core at 288 °C to a fluence of 1×10^{21} n/cm^2 ($E > 1$ MeV) over a period of 8.5 months, with an ion irradiation experiment using 3 MeV protons at 400 °C to 1 dpa (displacements per atom) at a dose rate of 10^{-5} dpa/s ($\sim$1 day), or 5 MeV Ni^{++} at 500 °C to 10 dpa at a dose rate of 5×10^{-3} dpa/s ($\sim$1 h)? The first question to resolve is the measure of radiation effect. In the irradiation-assisted stress corrosion cracking (IASCC) problem in LWRs, concern has centered on two effects of irradiation: *segregation* of major alloying elements or impurities to grain boundaries, which then cause embrittlement or enhance the intergranular stress corrosion cracking (IGSCC) process, and *hardening* of the matrix that results in localized deformation and embrittlement. The appropriate *measure* of the radiation effect in the former case would then be the

alloy concentration at the grain boundary or the amount of impurity segregated to the grain boundary. This quantity is measurable by analytical techniques such as AES or STEM-EDS. For the latter case, the *measure* of the radiation effect would be the nature, size, density, and distribution of dislocation loops, black dots, and the total dislocation network, and how they impact the deformation of the alloy. Hence, specific and measurable effects of irradiation can be determined for both neutron and ion irradiation experiments.

The next concern is determining how ion irradiation translates into the environment describing neutron irradiation. That is, what are the irradiation conditions required for ion irradiation to yield the same *measure* of radiation effect as that for neutron irradiation? This is the key question; for in a post-irradiation test program, it is only the *final state* of the material that is important in the determination of equivalence, and not the path taken. Therefore, if one could devise ion irradiation experiments that yielded the same *measures* of irradiation effects as observed in neutron irradiation experiments, then the data obtained in post-irradiation experiments will be equivalent. In such a case, ion irradiation experiments can provide a direct substitute for neutron irradiation. While neutron irradiation will likely be required to qualify materials for reactor application, ion irradiation provides a low cost and rapid means of elucidating mechanisms and screening materials for the most important variables.

11.2 Review of Aspects of Radiation Damage Relevant to Ion Irradiation

The first challenge in determining the equivalence between the measure of radiation effect in charged particle and neutron irradiation is the use of a common dose unit. Recall from the introduction that irradiated material properties can be more successfully compared using dpa as a measure of exposure. The basic (measurable) dose unit for neutron irradiation is the fluence in (n/cm^2) above some energy ($E > x$ MeV), where x is the energy threshold. For charged particles, it is the integrated current or charge in units of Q/cm^2. Both of these measures can be converted to dose in units of dpa and dose rate as dpa/s using one of several models for the determination of dpa, as described in Chap. 2. A fundamental difference between ion and neutron irradiation effects is the particle energy spectrum that arises due to the difference in how the particles are produced. Ions are produced in accelerators and emerge in monoenergetic beams with vary narrow energy widths. However, the neutron energy spectrum in a reactor extends over several orders of magnitude in energy, thus presenting a much more complicated source term for radiation damage. Figure 11.1 shows the considerable difference in neutron and ion energy spectra and also between neutron spectra in different reactors and at different locations within the reactor vessel.

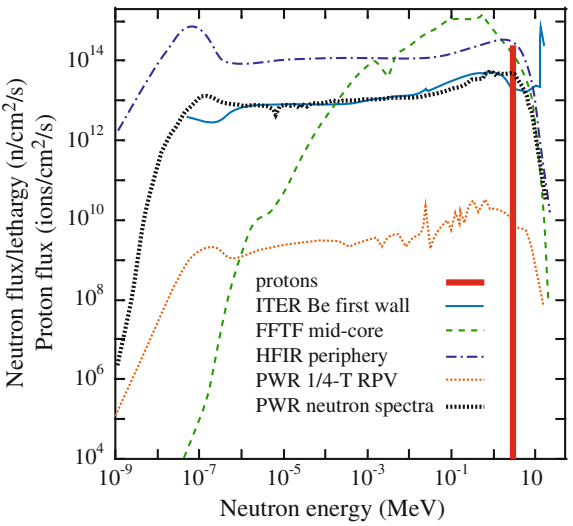

Fig. 11.1 Energy spectra of incident ions in a monoenergetic ion beam, and neutrons from a variety of reactor types (after [7])

Another major difference in the characteristics of ions and neutrons is their depth of penetration. As shown in Fig. 2.25 of Chap. 2, ions lose energy quickly because of high electronic energy loss, giving rise to a spatially non-uniform energy deposition profile caused by the varying importance of electronic and nuclear energy loss during the slowing down process. Their penetration distances range between 0.1 and 100 μm for ion energies that can practically be achieved by laboratory-scale accelerators or implanters. By virtue of their electrical neutrality, neutrons can penetrate very large distances and produce spatially flat damage profiles over many millimeters of material.

As discussed in Chap. 2, the total number of displacements per atom is given by the K–P [8] or NRT [9] models. This quantity provides an adequate measure of the number of displacements created by the incoming particle irrespective of the mass of the particle. In addition to dpa, the primary recoil spectrum describes the relative number of collisions in which an energy between T and $T + \mathrm{d}T$ is transferred from the primary recoil atom to other target atoms. The fraction of recoils between the displacement energy E_d, and T is given as, from Eq. (3.11):

$$P(E_\mathrm{i}, T) = \frac{1}{N} \int_{E_\mathrm{d}}^{T} \sigma(E_\mathrm{i}, T')\, \mathrm{d}T' \tag{11.1}$$

where N is the total number of primary recoils and $\sigma(E_\mathrm{i}, T')$ is the differential cross section for a particle of energy E_i to create a recoil of energy T', and E_d is the displacement energy. The recoil fraction is shown in Fig. 3.5, which reveals only a small difference between ions of very different masses.

But there is a substantial difference in the damage morphology between particles of different mass. Light ions such as electrons and protons will produce damage as

isolated Frenkel pairs or in small clusters while heavy ions and neutrons produce damage in large clusters (see Fig. 3.7). For 1 MeV particle irradiation of copper, half of the recoils for protons are produced with energies less than ~60 eV while the same number for Kr occurs at about 150 eV. Recoils are weighted toward lower energies because of the screened Coulomb potential that controls the interactions of charged particles. For an unscreened Coulomb interaction, the probability of creating a recoil of energy T varies as $1/T^2$. However, neutrons interact as hard spheres and the probability of creating a recoil of energy T is independent of recoil energy. In fact, a more important parameter describing the distribution of damage over the energy range is a combination of the fraction of defects of a particular energy and the damage energy. As described in Chap. 3, the *weighted average* recoil spectrum, $W(E_i, T)$, weights the primary recoil spectrum by the number of defects or the damage energy produced in each recoil:

$$W(E_i, T) = \frac{1}{E_D(E_i)} \int_{E_d}^{T} \sigma(E_i, T') E_D(T') \mathrm{d}T' , \tag{11.2}$$

$$E_D(E_i) = \int_{E_d}^{\hat{T}} \sigma(E_i, T') E_D(T') \mathrm{d}T' , \tag{11.3}$$

where $\hat{T}$ is the maximum recoil energy given by $\hat{T} = \gamma E_i = 4E_i M_1 M_2/(M_1 + M_2)^2$. As described in Chap. 3, for the extremes of Coulomb and hard sphere interactions, the weighted average recoil spectrum for each type of interaction is given as follows:

$$W_{\mathrm{Coul}}(E_i, T) = \frac{\ln T - \ln E_d}{\ln \hat{T} - \ln E_d} \tag{11.4a}$$

$$W_{\mathrm{HS}}(E_i, T) = \frac{T^2 - E_d^2}{\hat{T}^2} . \tag{11.4b}$$

Equations (11.4a) and (11.4b) are graphed in Fig. 3.6 for 1 MeV particle irradiations of copper. The Coulomb forces extend to infinity and slowly increase as the particle approaches the target, hence the slow increase with energy. In a hard sphere interaction, the particles and target do not *feel* each other until their separation reaches the hard sphere radius at which point the repulsive force goes to infinity. A screened Coulomb potential is most appropriate for heavy ion irradiation. Note the large difference in $W(E_i, T)$ between the various types of irradiations. While heavy ions come closer to reproducing the energy distribution of recoils of neutrons than do light ions, neither is accurate in the *tails* of the distribution. This does not mean that ions are poor simulations of radiation damage, but it does mean that damage is produced differently and this difference will need to be considered when designing an irradiation program that is intended to produce microchemical and microstructural changes that match those from neutron irradiation.

The actual number of defects that survive the displacement cascade and their spatial distribution in the solid will determine the effect on the irradiated microstructure. This topic was covered in Chaps. 3 and 7 by classification of defects according to their behavior in the solid. Figure 11.2 summarizes the effect of damage morphology from the viewpoint of the grain boundary and how the defect flow affects radiation-induced grain boundary segregation. Despite the equivalence in energy among the four particle types described in Fig. 3.7, the average energy transferred and the defect production efficiencies vary by almost two orders of magnitude! This is explained by the differences in the cascade morphology among the different particle types. Neutrons and heavy ions produce dense cascades that result in substantial recombination during the cooling or quenching phase. However, electrons are just capable of producing a few widely spaced Frenkel pairs that have a low probability of recombination. Protons produce small widely spaced cascades and many isolated FPs due to the Coulomb interaction, and therefore, fall between the extremes in displacement efficiency as defined by electrons and neutrons.

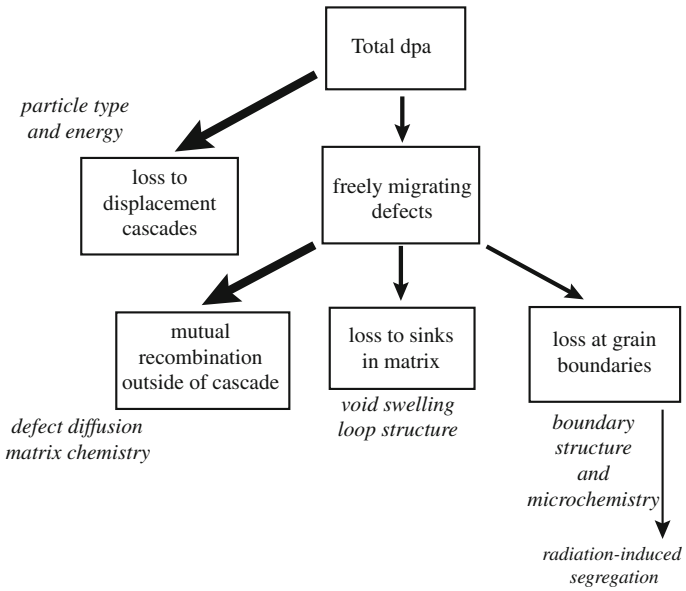

Fig. 11.2 History of point defects after creation in the displacement cascade

11.3 Particle-Type Dependence of RIS

We will focus on the comparison between four types of particle irradiation in order to outline a methodology for establishing equivalence between neutron and charged particle irradiation. We will further focus on radiation-induced segregation as the *measure* of the effect of irradiation in order to compare the particles. RIS is selected because it depends only on the action of point defects, and not on their agglomeration. The irradiation parameters for the four particle types are given in Table 11.1. Each experiment is characterized by the particle type, energy and irradiation temperature, reported dose rate, and reported total dose. The last column is the dose to reach a steady-state RIS profile using the Perk's model [11]. The columns labeled *reported* and *corrected* refer to RIS calculations using the nominal (*reported* value) and the efficiency-corrected (*corrected* value) dose rate, respectively. The displacement efficiency is calculated using Naundorf's model, described in Chap. 3.

A quantity of interest in RIS for LWR core materials is the amount of chromium depleted from the grain boundary, or the area inside the Cr concentration profile (Fig. 11.3). In non-LWR reactor systems, other elements may be of interest due to the potential for in-reactor precipitation. The appropriate measure of depletion is somewhat questionable. One could use the grain boundary chromium value as the measure of the extent of chromium depletion. Alternatively, the FWHM of the depletion profile has been used. In fact, both of these quantities are useful and can be obtained from measured depletion profiles. However, the area inside the Cr concentration profile represents changes to a volume of material and is more sensitive to changes in the profile shape than either the grain boundary value or the FWHM alone. The amount of Cr depletion is determined by integrating the concentration profile for that element with distance from the grain boundary:

$$M = \int_0^{l(t)} \left[C_A^0 - C_A(x,t)\right] \mathrm{d}x\,, \tag{11.5}$$

where M is the segregated area, C_A^0 is the bulk atom concentration, $C_A(x, t)$ is the atom concentration near the surface, and $l(t)$ is the half width of the depleted zone.

Figure 11.4(a, b) shows the amount of grain boundary chromium depletion as a function of irradiation dose (Fig. 11.4(a)) and time (Fig. 11.4(b)) for each of the four particles described in Table 11.1. The calculated values of Cr depletion for each of the particle types using *reported* and *corrected* dose rates, according to the freely migrating defect production efficiencies, are shown by the open and closed symbols, respectively. Since electrons are assumed to be 100 % efficient in producing defects available to affect segregation, there is no change in the segregated area after accounting for efficiency. However, there is a difference with protons, heavy ions, and neutrons, which amounts to a reduction in the amount of segregation. The difference is largest for neutrons and smallest for protons. The difference is a function of not only the displacement efficiency, but also the slope of the

Table 11.1 Comparison of irradiation parameters and RIS for different particle types (from [10])

Particle type	Energy (MeV)	Temp (°C)	Efficiency	Dose rate (dpa/s)		Total dose (dpa)		Dose to steady state[b] (dpa)	
				Reported	Corrected[a]	Reported	Corrected	Reported	Corrected
Electrons	1.0	450	1.0	2×10^{-3}	2×10^{-3}	10	10	28	28
Protons	3.4	360	0.2	7×10^{-6}	1×10^{-6}	1	0.2	7	3
Ni ions	5.0	500	0.04	5×10^{-3}	2×10^{-4}	10	0.4	25	7
Neutrons	Fission reactor	288	0.02	$\sim 5 \times 10^{-8}$	1×10^{-9}	1	0.02	4	1.4

[a]Efficiency-corrected value
[b]As calculated by the Perks model [11] for RIS

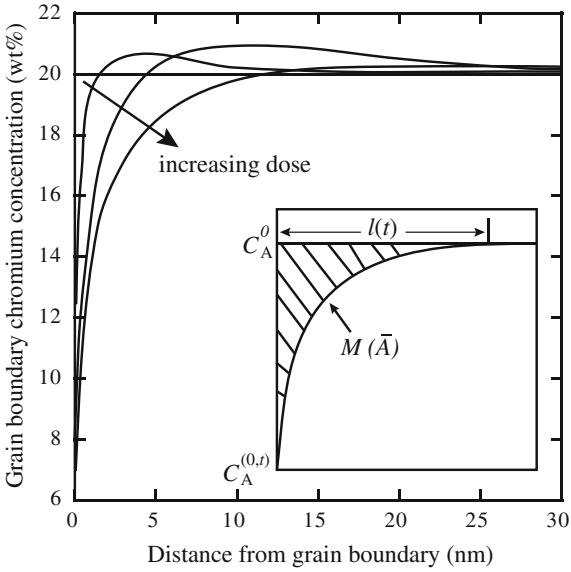

Fig. 11.3 Definition of the segregated area, M in a quantitative assessment of RIS

dose rate curves. Nevertheless, substantial differences result in the expected amounts of grain boundary segregation when the displacement efficiency is taken into account.

Figure 11.5(a) shows the calculated amount of Cr depletion as a function of temperature for several displacement rates at *steady state*. Steady state is reached at different dose levels for each experiment. At a given displacement rate, the segregated area peaks at some intermediate temperature and falls off at both higher and lower temperatures. This is due to the dominance of recombination at low temperatures and back diffusion at high temperatures [10]. Also note that the effect of a decreasing displacement rate is to shift the curves to higher maxima at lower temperatures. For a given dose, a lower displacement rate yields lower steady-state defect concentrations, reducing the number of defects lost to recombination, and shifting the curve to lower temperatures while increasing the degree of segregation. Figure 11.5(a) also shows the effect of three of the four parameters defining an experiment: particle type, temperature, and dose rate. It does not show the effect of dose since this is a steady-state result that is achieved at different doses for each of the experiments described in Table 11.1.

Figure 11.5(b) shows the dose required to reach steady state as a function of temperature and dose rate. Each of the experiments is plotted for both the reported and the corrected displacement rates. Note the large difference in the dose to reach steady state between electrons and neutrons. In general, irradiation at a lower dpa rate will result in a lower dose to reach steady state and the difference is greatest for this comparison. Correspondingly, proton and heavy ion irradiation fall between neutrons and electrons for the experiments described in Table 11.1. This can be

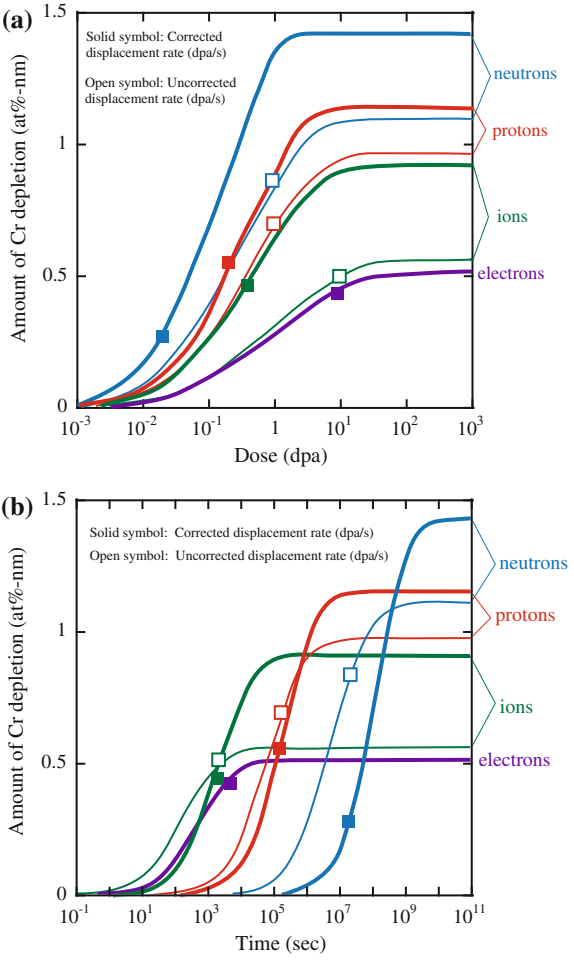

Fig. 11.4 Chromium depletion versus (**a**) dose and (**b**) irradiation time, for several particle types (thin line) and the effect of correcting for particle efficiency (heavy line) (after [10]). Symbols refer to conditions in Table 11.1

understood by considering the chemical rate equations given in Eq. (5.1), where the first term is the production rate, the second is the loss by mutual recombination, and the third is the loss by annihilation of defects at sinks. At steady state, $C_{i,v} \propto K_0^{1/2}$ at low temperature and $C_{i,v} \propto K_0$ at high temperature (see Chap. 5). So, the resulting point defect concentrations are strong functions of the production rate.

Figure 11.6 shows a plot of segregation as a function of temperature for particles with displacement rates characteristic of their sources. Note that the temperature at which segregation is a maximum (concentration is a minimum) shifts to higher values with increasing dose rate. This is due to the trade-off between temperature and dose rate. The temperature-dose rate interdependence for stainless steel over a wide range of temperatures and dose rates is shown in Fig. 11.7. Also noted are the regions in which reactor irradiation by neutrons, and where proton and Ni ion

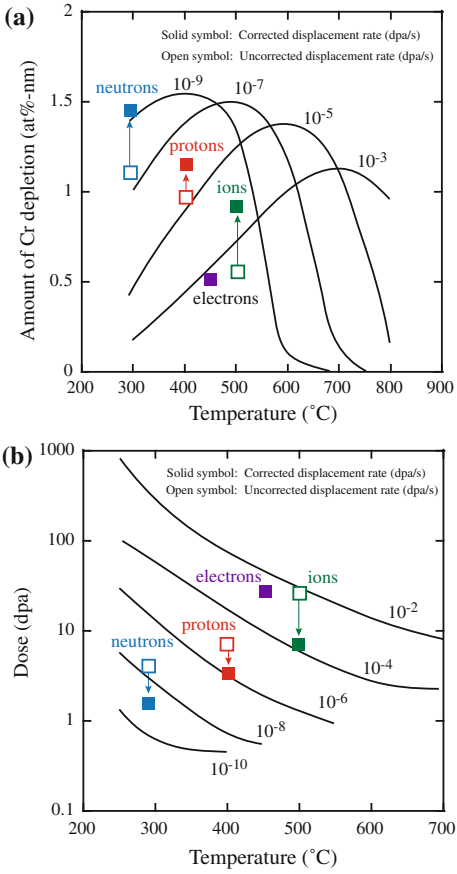

Fig. 11.5 (**a**) Chromium depletion and (**b**) dose to reach steady state as a function of temperature, dose rate, and particle efficiency (after [10]). Symbols refer to conditions in Table 11.1

irradiations occur. This graph explains why the experiments conducted at the highest dose rates are also conducted at the highest temperatures.

A simple method for examining the trade-off between dose rate and temperature in comparing irradiation effects from different particle types is found in the invariance requirements discussed in Chap. 8. For a given change in dose rate, we would like to know what change in temperature (at the same dose) is required to cause the same number of defects to be absorbed at sinks. The number of defects per unit volume that are lost to sinks up to time τ is given as:

$$N_{Sj} = \int_0^{\tau} k_{Sj}^2 C_j \mathrm{d}t, \tag{11.6}$$

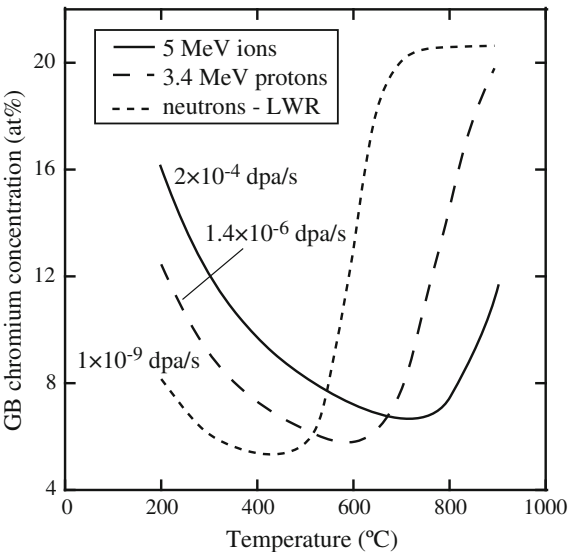

Fig. 11.6 Dependence of grain boundary chromium concentration on temperature for particles with various dose rates and defect generation efficiencies (after [10])

and the ratio of vacancy loss to interstitial loss is given as:

$$R_S = \frac{N_{Sv}}{N_{Si}}, \tag{11.7}$$

where j = v or i, and k_S^2 is the sink strength. The quantity N_S is important in describing microstructure development involving total point defect flux to sinks (e.g., RIS). The number of defects per unit volume that have recombined up to time τ is given by:

$$N_R = K_{iv} \int_0^{\tau} C_i C_v dt, \tag{11.8}$$

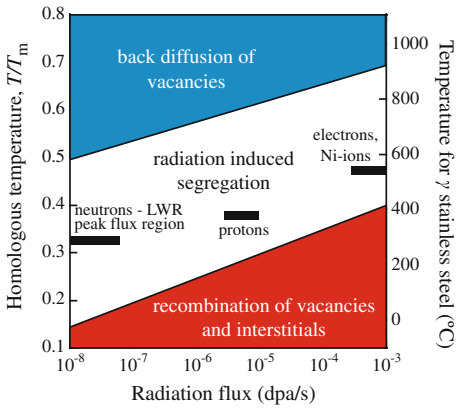

Fig. 11.7 Relation between temperature and dose rate in the context of radiation-induced segregation, and the locations of neutron, proton, and nickel ion irradiations

where K_{iv} is the vacancy–interstitial recombination coefficient. N_R is the relevant quantity for the growth of defect aggregates such as voids and loops that require partitioning of point defects to allow growth.

The invariance requirements can be used to prescribe an ion irradiation temperature-dose rate combination that simulates neutron radiation. We take the example of irradiation of stainless steel under typical boiling water reactor (BWR) core irradiation conditions of $\sim 4.5 \times 10^{-8}$ dpa/s at 288 °C. If we were to conduct a proton irradiation with a characteristic dose rate of 7.0×10^{-6} dpa/s, then using Eq. (8.158) with a vacancy formation energy of 1.9 eV and a vacancy migration energy of 1.3 eV, the experiment will be invariant in N_S with the BWR core irradiation (e.g., RIS), for a proton irradiation at 400 °C. Similarly, using Eq. (8.162), an irradiation temperature of 300 °C will result in an invariant N_R (e.g., swelling or loop growth). For a Ni^{++} ion irradiation at a dose rate of 10^{-3} dpa/s, the respective temperatures are 675 °C (N_S invariant) and 340 °C (N_R invariant). In other words, the temperature "shift" due to the higher dose rate is dependent on the microstructure feature of interest. Also, with increasing difference in dose rate, the ΔT between proton and ion irradiation increases substantially. The nominal irradiation temperatures selected for proton irradiation, 360 °C and for Ni^{++} irradiation, 500 °C represent compromises between the extremes for invariant N_S and N_R.

11.4 Advantages and Disadvantages of the Various Particle Types

Each particle type has its advantages and disadvantages for use in the study or emulation of radiation effects. Common disadvantages of charged particle beams are the lack of transmutation reactions and the need to use a raster-scanned beam. With the exception of some minor transmutation reactions that can occur with light ion irradiation, charged particles do not reproduce the types of transmutation reactions that occur in reactor core materials due to interaction with neutrons. The most important of these is the production of He by transmutation of Ni or B (See Sect. 8.4.5). But a second consideration is that of a raster-scanned beam in which any volume element of the target is exposed to the beam for only a fraction of the raster-scan cycle. For a typical beam scanner and beam parameters, the fraction of time that any particular volume element in the solid is being bombarded is ~ 0.025. Thus, the instantaneous dose rate during the *beam-on* portion of the cycle is 40 times that of the average (Fig. 11.8). The result is that the defect production rate is very high and defects can anneal out in the remaining 0.975 portion of the cycle before the beam again passes through the volume element. As such, the effective defect production rate in raster-scanned systems will be less and must be accounted for.

While one objective of ion irradiation is to emulate the effect of neutrons, a second is to understand basic physical radiation damage processes, for which neutron irradiation is often less well suited. While ion irradiation can be conducted

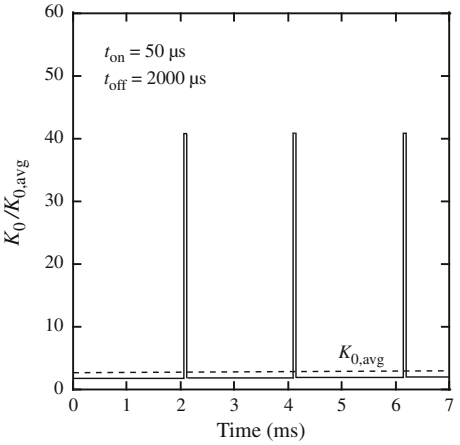

Fig. 11.8 The effect of a raster-scanned beam on the instantaneous production rate of point defects with the same time averaged rate as a continuous source (after [12])

with excellent control over temperature, dose rate, and total dose, such control is a challenge to reactor irradiations. For example, instrumented tubes with active temperature control are expensive to design, build, and operate. Even so, frequent power changes can be difficult to handle as the flux–temperature relationship will change and this can result in artifacts in the irradiated microstructure (see Sect. 8.3.11 and Fig. 8.57). On the other hand, cheaper "rabbit" tube irradiations use passive gamma heating and temperatures are not known with any certainty. Similarly, doses and dose rates are most often determined by neutronic models of the core locations and are not verifiable. As such, ion irradiations enjoy the advantage of better control and verification of irradiation conditions as compared to neutron irradiation. Table 11.2 provides a list of advantages and disadvantages for each of three particle types: electrons, heavy ions, and light ions (protons), and they are discussed in detail in the following sections.

11.4.1 Electrons

Electron irradiation is easily conducted in a high-voltage transmission electron microscope and as such, it uses a rather simple ion source, that being either a hot filament or a field emission gun. An advantage is that the same instrument used for irradiation damage can be used to image the damage. Another advantage is that the high dose rate requires very short irradiation time, but this will also require a large temperature shift as explained in the previous section.

There are several disadvantages to electron irradiation using a TEM. First, energies are generally limited to 1 MeV. This energy is sufficient to produce an isolated Frenkel pair in transition metals, but not cascades. The high dose rate requires high temperatures that must be closely monitored and controlled, which is difficult to do precisely in a typical TEM sample stage. Another drawback is that

Table 11.2 Advantages and disadvantages of irradiations with various particle types (after [12])

Advantages	Disadvantages
Electrons	
Relatively "simple" source—TEM	Energy limited to ~1 MeV
Uses standard TEM sample	No cascades
High dose rate—short irradiation times	Very high beam current (high dpa rate) leading to large temperature shift relative to neutrons
	Poor control of sample temperature
	Strong "Gaussian" shape (non-uniform intensity profile) to beam
	No transmutation
Heavy Ions	
High dose rate—short irradiation times	Very limited depth of penetration
High T_{avg}	Strongly peaked damage profile
Cascade production	Very high beam current (high dpa rate) leading to large temperature shift relative to neutrons
	No transmutation
	Potential for composition changes at high dose via implanted ion
Protons	
Accelerated dose rate—moderate irradiation times	Minor sample activation
Modest ΔT required	Smaller, widely separated cascades
Good depth of penetration	No transmutation
Flat damage profile over tens of μm	Damage rate limited by heat removal

since irradiations are often conducted on thin foils, defects are created in close proximity to the surface and their behavior may be affected by the presence of the surface. Perhaps, the most serious drawback is the Gaussian shape to the electron beam that can give rise to strong dose rate gradients across the irradiated region. Figure 11.9 shows the composition profile of copper around a grain boundary in Ni–39 %Cu following electron irradiation. Note that while there is local depletion at the grain boundary (as expected), the region adjacent to the minimum is strongly enriched in copper due to the strong defect flux *out* of the irradiated zone defined by the horizontal line below the spectrum. This outward-directed defect flux causes a reversal in the direction of segregation from that caused by a defect flux *to* the sink. Another often observed artifact in electron irradiation is very broad grain boundary enrichment and depletion profiles. Figure 11.10 shows that the enrichment profile for Ni and the depletion profiles for Fe and Cr in stainless steel have widths on the order of 75–100 nm, which is much greater than the 5–10 nm widths observed following neutron irradiation under similar conditions and all model simulations of

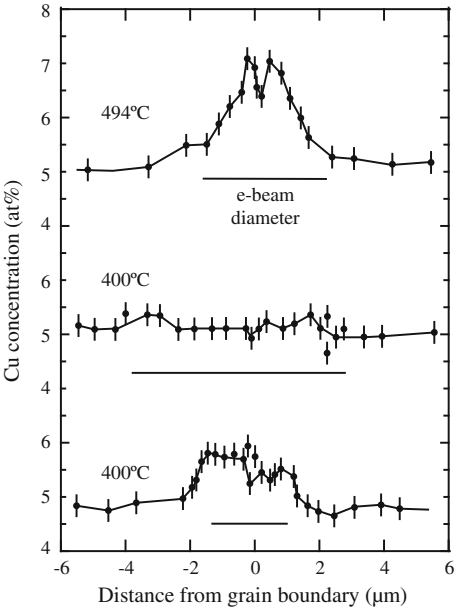

Fig. 11.9 Enrichment of copper at the grain boundary in Ni-39 %Cu. The enrichment is caused by the high-defect flux away from the irradiated region defined by the horizontal line (after [13])

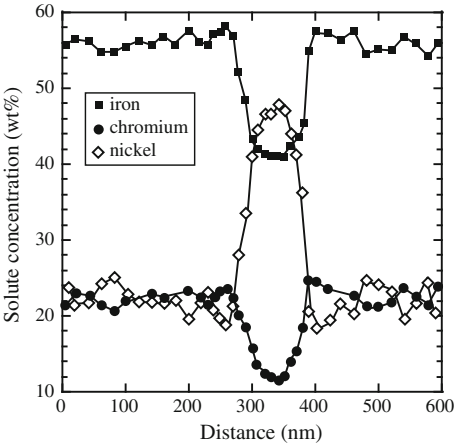

Fig. 11.10 Broad grain boundary enrichment and depletion profiles in Fe–20Cr–25Ni–0.75Nb–0.5Si following irradiation with electrons at 420 °C to 7.2 dpa (after [14])

radiation-induced segregation. A similar effect was noted by Wakai [15] in electron and D^+ irradiation of the same alloy in which it was observed that the segregation was much greater and narrower around the grain boundary in the deuteron-irradiated sample as compared to the electron irradiation (Fig. 11.11).

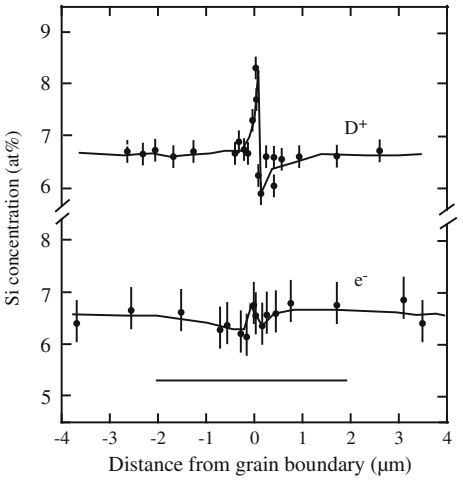

Fig. 11.11 Comparison of deuteron and electron irradiation showing the greater amount of Si segregation and the narrower profile for the deuteron irradiation (after [15])

11.4.2 Heavy Ions

Heavy ions enjoy the benefit of high dose rates resulting in the accumulation of high doses in short times. Also, because they are typically produced in the energy range of a few MeV, they are very efficient at producing dense cascades, similar to those produced by neutrons (Fig. 3.7). The disadvantage is that as with electrons, the high dose rates require large temperature shifts so that irradiations must be conducted at temperatures of order ~500 °C in order to create similar effects as neutron irradiation at ~300 °C. Clearly, there is not much temperature margin for studying neutron irradiations at high temperature since higher ion irradiation temperatures will cause annealing. Another drawback is the short penetration depth and the continuously varying dose rate over the penetration depth. Figure 11.12 shows

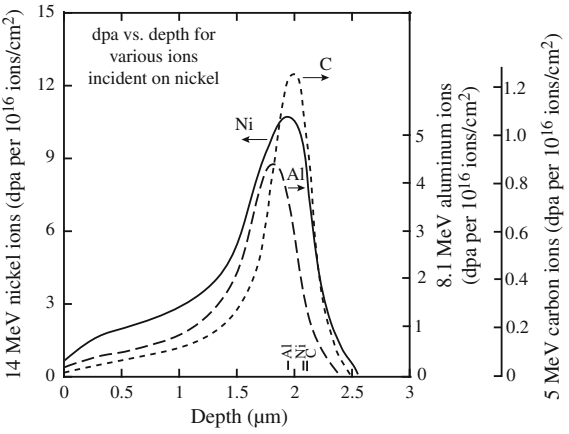

Fig. 11.12 Damage profiles for C, Al, and Ni irradiation of a nickel target at energies selected to result in the same penetration depth (after [16])

the damage profile for several heavy ions incident on nickel. Note that the damage rate varies continuously and peaks sharply at only 2 μm below the surface. As a result, regions at well-defined depths from the surface must be able to be reproducibly sampled in order to avoid dose or dose rate variations. Small errors (500 nm) made in locating the volume to be characterized can result in a dose that varies by a factor of two from the target value.

A problem that is rather unique to nickel ion irradiation of stainless steel or nickel-base alloys is that in addition to the damage they create, each bombarding Ni ion constitutes an interstitial. Figure 11.13(a) shows that 5 MeV Ni^{++} irradiation of a Fe–15Cr–35Ni alloy resulted in high swelling in the immediate subsurface region compared to that near the damage peak. As shown in Fig. 11.13(b), the Ni^{++} ions come to rest at a position just beyond the peak damage range. So even though the peak damage rate is about 3× that at the surface, swelling at that location is suppressed by about a factor of 5 compared to the surface [17]. The reason is that the bombarding Ni^{++} ions constitute interstitials and the surplus of interstitials near the damage peak results in a reduction of the void growth rate [18, 19]. In the dose rate-temperature regime where recombination is the dominant point defect loss mechanism, interstitials injected by Ni^{++} ion bombardment may never recombine

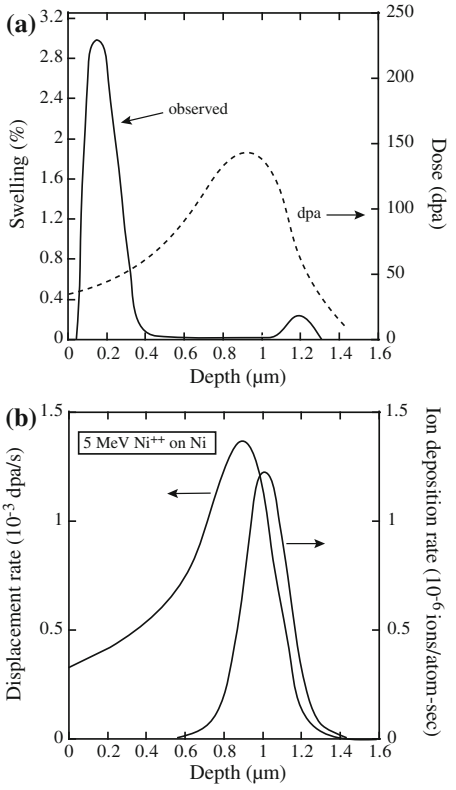

Fig. 11.13 (**a**) Subsurface swelling resulting from 5 MeV Ni^{++} ion irradiation of Fe–15Cr–35Ni at 625 °C (after [17]). (**b**) Displacement rate and ion deposition rate calculated for 5 MeV Ni^{++} on nickel (after [18])

since there is no corresponding vacancy production. Therefore, injected interstitials comprise a larger fraction of the point defects absorbed at sinks whenever the fraction of point defects recombining is large, such as in the peak swelling regime.

11.4.3 Protons

In many ways, proton irradiation overcomes the drawbacks of electron and neutron irradiation. At only a few MeV, the penetration depth can exceed 40 μm and the damage profile is relatively flat such that the dose rate varies by less than a factor of 2 over several tens of μm. Further, the depth of penetration is sufficient to assess such properties as irradiation hardening through microhardness measurements and SCC through crack initiation tests such as the slow strain rate test. Figure 11.14 (and Fig. 2.25) shows schematics of 3.2 MeV proton and 5 MeV Ni^{++} damage profiles in stainless steel. Superimposed on the depth scale is a grain structure with a grain size of 10 μm. Note that with this grain size, there are numerous grain boundaries and a significant irradiated volume over which the proton damage rate is flat. The dose rate for proton irradiations is 2–3 orders of magnitude lower than that for electrons or ions, thus requiring only a modest temperature shift, but since it is still 10^2 to 10^3 times higher than neutron irradiation, modest doses can be achieved in a reasonably short irradiation time.

The advantages are that because of the small mass of the proton compared to heavy ions, the recoil energy is smaller and the resulting damage morphology is characterized by smaller, more widely spaced cascades than with ions or neutrons (see Fig. 3.7). Also, since only a few MeV are required to surmount the Coulomb barrier for light ions, there is also a minor amount of sample activation that increases with proton energy.

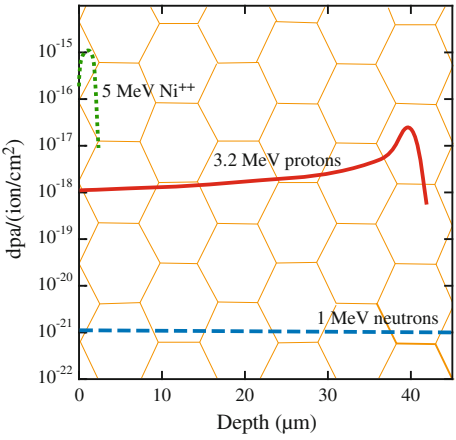

Fig. 11.14 Damage profiles for 3.2 MeV protons and 5 MeV Ni^{++} ions in stainless steel (after [12])

11.5 Irradiation Parameters for Particle Irradiations

In the process of setting up an ion irradiation experiment, a number of parameters that involve beam characteristics (energy, current/dose) and beam–target interaction must be considered. One of the most important considerations is the depth of penetration. Figure 11.15 shows the range versus particle energy for protons, helium ions, and nickel ions in stainless steel as calculated by SRIM [20]. The difference in penetration depth between light and heavy ions is over an order of magnitude in this energy range. Figure 11.16 shows how several other parameters describing the target behavior during proton irradiation vary with energy: dose rate, the time to reach 1 dpa, deposited energy, and the maximum permissible beam current (which will determine the dose rate and total dose) given a temperature limitation of 360 °C. With increasing energy, the dose rate at the surface decreases due to the drop in the elastic scattering cross section (Fig. 11.16(a)). Consequently, the time to reach a target dose level, and hence the length of an irradiation, increases rapidly (Fig. 11.16(b)). Energy deposition scales linearly with the beam energy, raising the burden of removing the added heat in order to control the temperature of the irradiated region (Fig. 11.16(c)). The need to remove the heat due to higher energies will limit the beam current for a specific target temperature (Fig. 11.16(d)) and a limit on the beam current (or dose rate) will result in a longer irradiation to achieve the specified dose. Figure 11.17 summarizes how competing features of an irradiation vary with beam energy, creating trade-offs in the beam parameters. For example, while greater depth is generally favored in order to increase the volume of irradiated material, the higher energy required leads to lower dose rates near the surface and higher residual radioactivity. For proton irradiation, the optimum energy range, achieved by balancing these factors, lies between 2 and 5 MeV as shown by the shaded region.

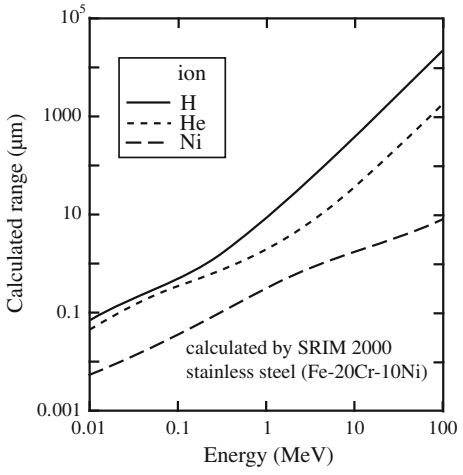

Fig. 11.15 Range of protons, helium atoms, and nickel ions in stainless steel as a function of ion energy (after [12])

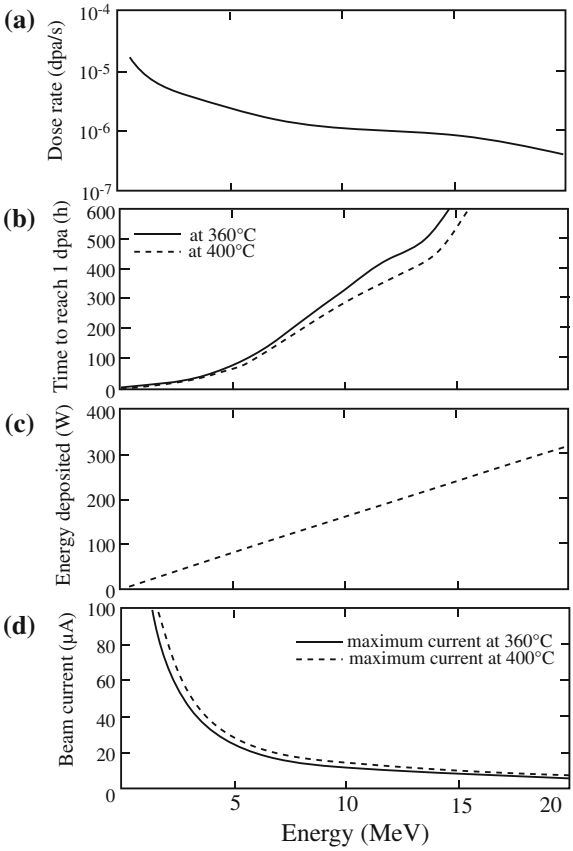

Fig. 11.16 Behavior of beam–target parameters as a function of beam energy for proton irradiation at 360 °C. (**a**) Dose rate, (**b**) time to reach 1 dpa, (**c**) energy deposition, and (**d**) beam current limit to maintain a sample temperature of 360 °C (after [12])

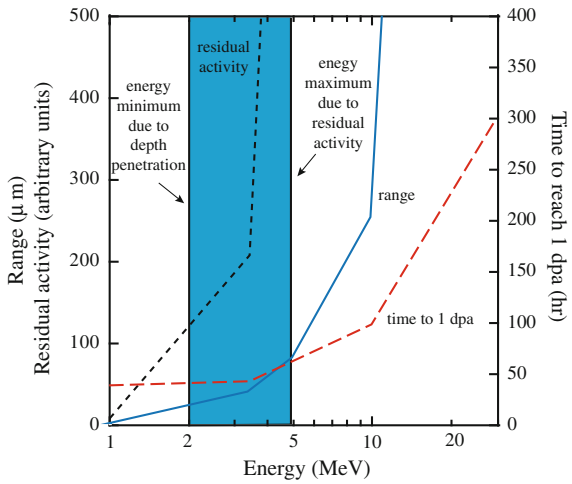

Fig. 11.17 Variation of ion range, residual activity, and time to reach 1 dpa as a function of proton energy (after [12])

11.6 Emulation of Neutron Irradiation Damage with Proton Irradiation

Proton irradiation has undergone considerable refinement as a radiation damage tool. Numerous experiments have been conducted and compared to equivalent neutron irradiation experiments in order to determine if proton irradiation can capture the effects of neutron irradiation on microstructure, microchemistry and hardening. In some cases, benchmarking exercises were conducted on the same native heat as neutron irradiation in order to eliminate heat-to-heat variations that may obscure comparison of the effects of the two types of irradiating particles. The following examples cover a number of irradiation effects on several alloys in an effort to demonstrate the capability of proton irradiation to capture the critical effects of neutron irradiation.

Figures 11.18, 11.19, 11.20, and 11.21 show direct comparisons of the *same* irradiation feature on the *same* alloy heats (commercial purity (CP) 304 and 316 stainless steels) following either neutron irradiation at 275 °C or proton irradiation at 360 °C to similar doses. Figure 11.18 compares the RIS behavior of Cr, Ni, and Si in a 316 stainless steel alloy following irradiation to approximately 1 dpa. Neutron irradiation results are in open symbols and proton irradiation results are in solid symbols. This dose range was chosen as an extreme test of proton irradiation to capture the "W"-shaped chromium depletion profile caused by irradiation of a microstructure-containing grain boundary chromium enrichment prior to irradiation. Note that the two profiles trace each other extremely closely both in magnitude and in spatial extent. The agreement extends across all three elements.

Figure 11.19 shows the agreement in the dislocation microstructure as measured by the dislocation loop size distribution (Fig. 11.19(a)) and the size and number density of dislocation loops (Fig. 11.19(b)) for 304 SS and 316 SS. Note that the main features of the loop size distributions are captured by both irradiations; sharply peaked distribution in the case of 304 SS and a flatter distribution with a tail for the

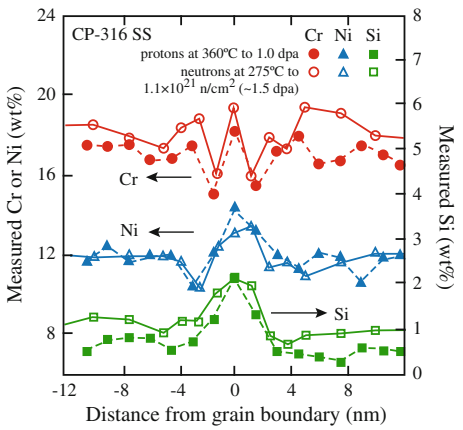

Fig. 11.18 Comparison of grain boundary segregation of Cr, Ni, and Si in commercial purity 316 stainless steel following irradiation with either protons or neutrons to similar doses (after [21])

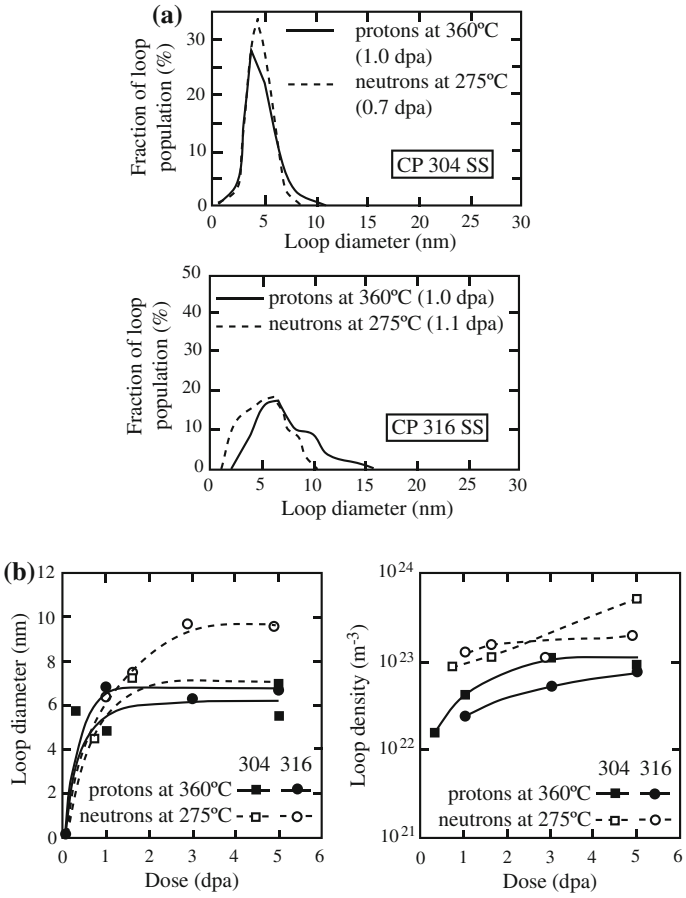

Fig. 11.19 Comparison of (**a**) loop size distributions and (**b**) loop diameter and loop number density for commercial purity 304 and 316 stainless steels irradiated with neutrons or protons to similar doses (after [21])

case of 316 SS. The agreement in loop size is good for the 304 SS alloy, while loops are smaller for the proton-irradiated 316 alloy. The loop density is about a factor of 3 less for the proton-irradiated case than for the neutron-irradiated case, which is expected since the proton irradiation temperature was optimized to track RIS (higher temperature) rather than the dislocation loop microstructure. That the loop sizes and densities are this close is somewhat remarkable considering that loop density is driven by in-cascade clustering, and cascades from proton irradiation are much smaller than those from neutron irradiation. However, the surviving fraction of interstitial loops is greater for proton irradiation, partially compensating the greater loop formation rate under neutron irradiation and resulting in loop densities that are within a factor of 3 [22].

Figure 11.20 shows the comparison of irradiation hardening between the two types of irradiation. The results are close, with proton irradiation resulting in slightly lower hardness. Figure 11.21 shows the IASCC susceptibility of CP 304 SS as measured by the %IG on the fracture surface following constant load testing (neutron-irradiated samples) and constant extension rate testing (proton-irradiated samples) in BWR normal water chemistry. Despite the significantly different testing mode, the results are in excellent agreement with that both proton and neutron irradiation result in the onset of IASCC at about 1 dpa (see Chap. 16).

In a study covering 11 solute addition alloys and 3 commercial alloys as part of the Cooperative IASCC Research (CIR) Program [23], the microstructure and properties of both proton and neutron irradiation were analyzed in which the latter was conducted in the BOR-60 reactor to doses between 4 and 47 dpa. Solute addition alloys consisted of controlled-purity heats of Fe–18Cr–12Ni to which single solute additions were made to test their effect on IASCC. Within this program, the grain boundary RIS of 6 solute addition alloys and 3 commercial alloys was measured following proton irradiation to 5.5 dpa (360 °C) or neutron

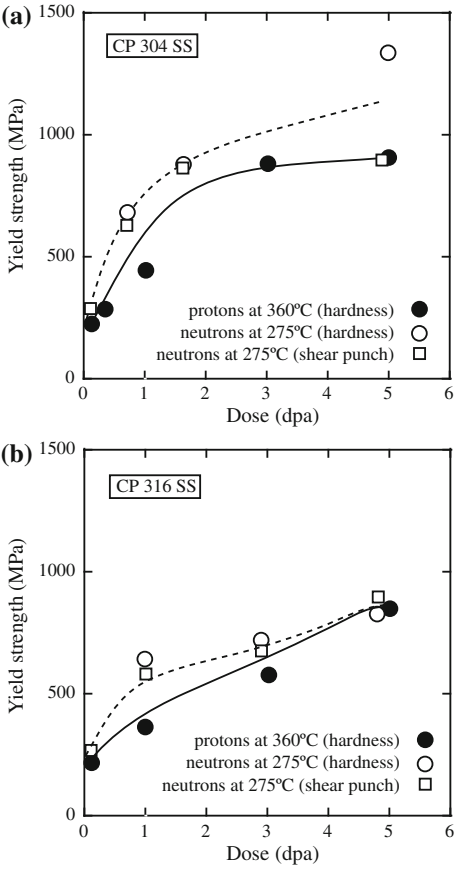

Fig. 11.20 Comparison of hardening in commercial purity (**a**) 304, and (**b**) 316 stainless steel irradiated with neutrons or protons to similar doses (after [21])

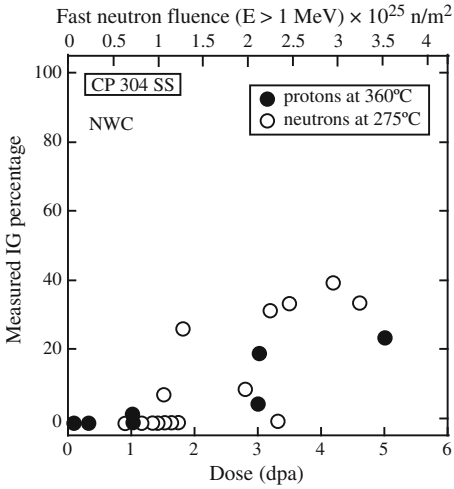

Fig. 11.21 Comparison of the extent of intergranular stress corrosion cracking in commercial purity 304 stainless steel following similar SCC tests of either neutron- or proton-irradiated samples from the same heat (after [21])

irradiation to between 5.4 and 11.8 dpa (320 °C). Figure 11.22 shows the agreement in grain boundary enrichment or depletion of Cr, Ni, Fe, Si, and Mo for these alloys. Proton and neutron irradiation under the selected conditions resulted in nearly identical elemental segregation behavior at grain boundaries [24]. The slightly higher temperature during proton irradiation was sufficient to increase diffusion kinetics and compensate for the increased damage rate.

The %IG cracking on the fracture surfaces was measured on both sample sets and results are shown in Fig. 11.23 as %IG relative to the reference Fe–18Cr–12Ni alloy without solute addition. As shown in the figure, the agreement is remarkable. Relative to the reference heat, the addition of either Ni, or Ni and Cr completely suppressed cracking in both neutron- and proton-irradiated samples. The addition of Mo produced no discernable effect on IG cracking in either of the irradiated samples. Finally, the addition of Si resulted in a substantial increase in %IG for both

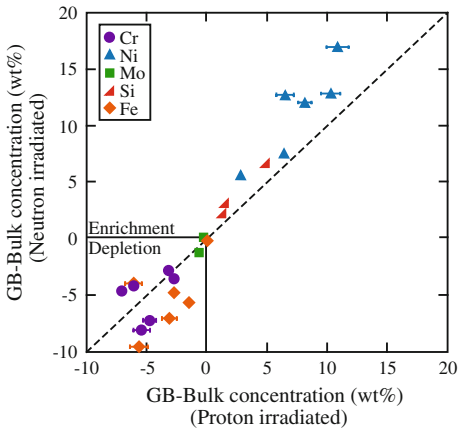

Fig. 11.22 Comparison of elemental enrichment and depletion from the bulk composition as a result of neutron and proton irradiation [24]

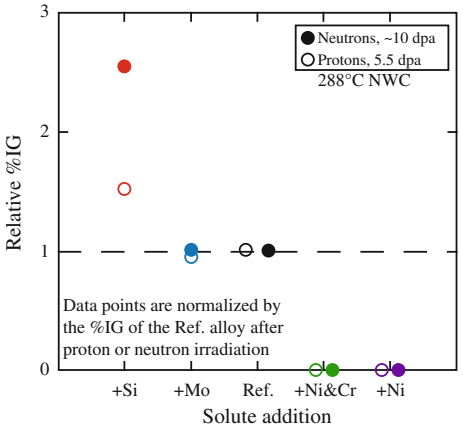

Fig. 11.23 Comparison of % IG after CERT testing of neutron- and proton-irradiated high-purity solute addition alloys tested in simulated BWR NWC [24]

irradiations. This agreement was perhaps the most notable of all of the existing data in that IASCC incorporates so many features in the irradiated microstructure. It also emphasized the importance of conducting experiments on the same heat of material to obtain a valid comparison by eliminating heat-to-heat variations.

Residual stresses are observed to relax under irradiation. Experiments were conducted on Inconel 718 following proton irradiation using 17 MeV protons at 300 °C [25] and on shot peened 304 followed by irradiation at 288 °C using 3.2 MeV protons to a dose of 2.0 dpa [26] and compared to respective results in reactor. In Inconel 718, the creep rate showed the expected linear dependence for applied shear stresses between 150 and 450 MPa. Stress relaxation amounted to about 30 % after a dose of 0.35 dpa, in good agreement with in-pile irradiation at 315 °C, Fig. 11.24(a) [27]. Results on 304 SS showed that the compressive stress

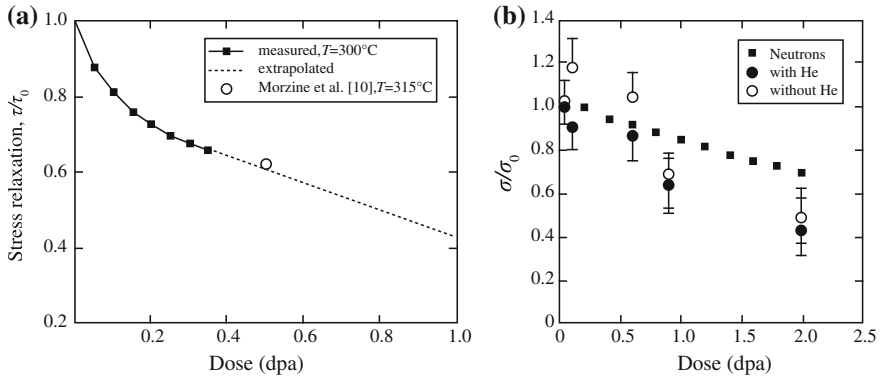

Fig. 11.24 Stress relaxation for (**a**) Inconel 718 after proton irradiation using 17 MeV protons at 300 °C [25] and compared with in-pile measurements at 315 °C [27], and (**b**) 304 SS irradiated with 3.2 MeV protons at 288 °C [26] and compared with neutron irradiation predictions [28]

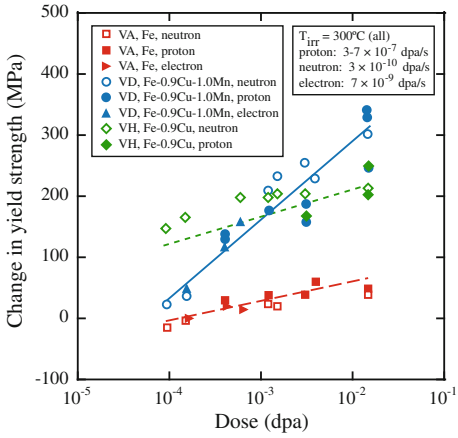

Fig. 11.25 Irradiation hardening in model reactor pressure vessel steels following neutron, proton, and electron irradiation at about 300 °C (after [29])

state was progressively relaxed throughout the dose range and that preinjection of helium did not significantly affect the relaxation, Fig. 11.24(b). A comparison of the results from proton irradiation and predictions based on neutron-induced relaxation of externally applied stresses [28] showed good agreement.

The next examples are from reactor pressure vessel steel, Zircaloy, and graphite. Figure 11.25 shows an experiment on model reactor pressure vessel alloys, in which the same heats were irradiated with neutrons, electrons, or protons at around 300 °C to doses spanning two orders of magnitude. The alloys include a high-purity Fe heat (VA) that hardens very little under irradiation, an Fe–0.9Cu (VH) heat that hardens rapidly initially, followed by a slower hardening rate above 0.1 mpda, and a Fe–0.9Ce–1.0Mn alloy (VD) in which the hardening rate is greatest over the dose range studied. Despite the very different compositions and hardening rates, the results of the three types of irradiation agree remarkably well.

Figure 11.26 shows hardening for Zircaloy-2 and Zircaloy-4 irradiated with either neutrons or protons. Although the irradiations were not conducted on the

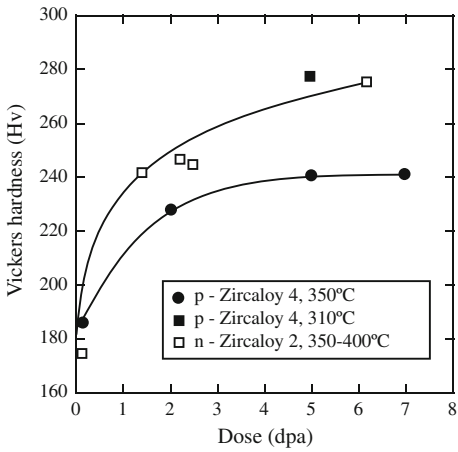

Fig. 11.26 Hardening of Zircaloy-4 irradiated with 3 MeV protons at 310 and 350 °C and comparison to neutron-irradiated Zircaloy-2 (after [30])

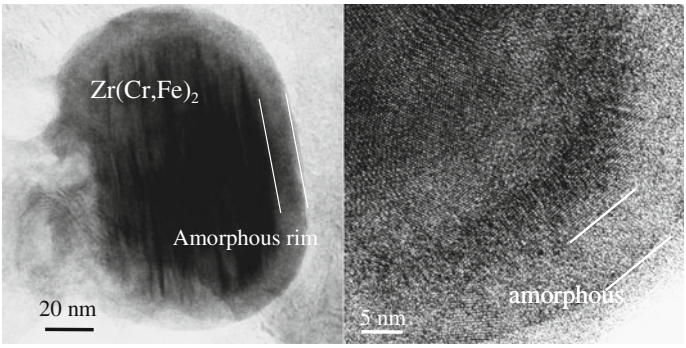

Fig. 11.27 Conventional (*left*) and high-resolution (*right*) image of a $Zr(Cr, Fe)_2$ precipitate after proton irradiation to 5 dpa at 310 °C, showing amorphization of the precipitate (after [30])

same heats of material, nor using similar irradiation parameters, there is good agreement in the magnitude and dose dependence of hardening. Figure 11.27 also shows proton-induced amorphization of a $Zr(Fe, Cr)_2$ precipitate after irradiation to 5 dpa at 310 °C, similar to that observed in reactor.

The corrosion kinetics of Zircaloy-4, both in-pile and out-of-pile, has been studied extensively to understand the role of irradiation on corrosion. Figure 11.28 shows oxide thickness data from the in situ irradiation–corrosion experiment [31] compared with in-pile data generated from MATPRO [32]. The unirradiated oxide growth rate of the reference sample (solid circles in red) was in good agreement with out-of-pile data. The proton irradiation data are also shown (solid squares in green) and the growth rate was about a factor of 10 higher than in the unirradiated case. Note that the growth rate was similar to that for in-pile behavior in the post-transition regime. In this regime, the oxide growth rate should be proportional to the dose rate. Therefore, equating the ratio of oxide growth rate to dose rate for

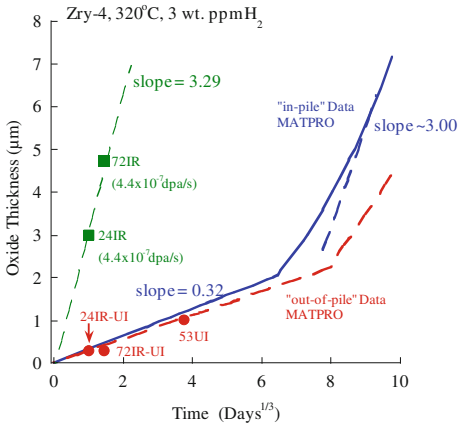

Fig. 11.28 Plot of oxide thickness as a function of corrosion time for in situ proton irradiation–corrosion data [31], and for in-pile and out-of-pile data [32]

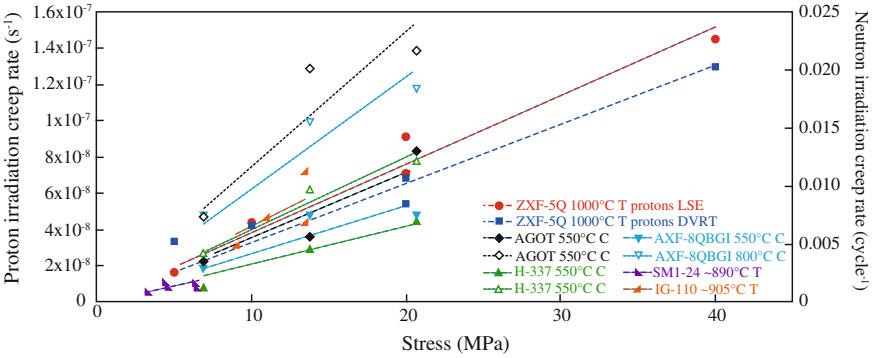

Fig. 11.29 Stress dependence of proton irradiation creep in ultra-fine grain graphite [33]

protons to that for neutrons yields a neutron damage rate of $\sim 4.4 \times 10^{-8}$ dpa/s, in good agreement with the range of values in the literature; $3.2–6.5 \times 10^{-8}$ dpa/s. This relationship suggested that oxidation under proton irradiation follows post-transition growth kinetics.

As discussed in Chap. 13, irradiation of samples under constant load can result in significant irradiation-induced creep. Proton irradiation creep experiments on ultra-fine grain graphite in the temperature range 900–1200 °C with stresses between 5 and 20 MPa and to a maximum dose of 1.0 dpa exhibited a linear dependence on the applied tensile stress, the dose rate and the temperature, and no dependence on the dose up to 1.0 dpa. Results were in excellent agreement with reactor creep experiments in the stress dependence of irradiation creep in graphite, Fig. 11.29. Both proton and neutron irradiation data show little dependence on temperature and dose rate, but the creep rates for proton irradiation were higher than those for reactor data by about an order of magnitude. Changes in the lattice parameters compared favorably with those after neutron irradiation at similar temperature and dose.

These examples represent a comprehensive collection of comparison data between proton and neutron irradiation and taken together, serve as a good example of the capability for charged particles to emulate the effect of neutron irradiation on the alloy microstructure. A more severe test of ion–neutron emulation is heavy ion irradiation at significantly higher dose rates as discussed next.

11.7 Emulation of Neutron Irradiation Damage with Self-Ion Irradiation

The challenge in using heavy- or self-ions to emulate neutron irradiation is greater than that for protons because of the issues listed in Sect. 11.4.2. However, the benefit is great since damage rates in the 10^{-4} to 10^{-2} dpa/s range can be achieved,

compressing the timescale to achieve several hundred dpa from decades (even in fast reactors) to hours. Very few experiments have been performed in which the microstructure or properties of heavy- or self-ion irradiations have been benchmarked against those from reactor irradiation. One such study [34] compared the full extent of the entire irradiated microstructure created in-reactor to that produced by self-ion irradiation designed to emulate that microstructure. Ferritic–martensitic alloy HT9 (Fe–12Cr–1Mo) heat 84425 was used in the hexagonal fuel bundle duct labeled ACO-3, in the Fast Flux Test Facility (FFTF). It was heat treated at 1065 °C/30 min/air cooled followed by 750 °C/60 min/air cooled. The fuel bundle was irradiated in several locations in FFTF over the time period 1985–1992 during which it accumulated a total damage of about 155 dpa at an average temperature of 443 °C [35]. Pieces from an archival section of this same duct were irradiated in a 1.7 MV tandem accelerator with self-ions (Fe^{++}) at 5 MeV at a temperature of 460 °C and to a dose of 188 dpa determined using SRIM [36] in the Kinchin-Pease mode [37]. At this energy, Fe^{++} ions come to rest at a depth of approximately 1.6 μm below the surface. The ion irradiation temperature represents a 17 °C increment above the neutron irradiation temperature, as predicted by invariance theory [38]. To emulate transmutation in reactor, helium was implanted prior to ion irradiation to a concentration of 1 appm over a depth range of 300–1000 nm by varying the implantation energy over five different values. This amount of He was set below that generated in reactor to compensate for the initially high He/dpa ratio in the ion irradiation experiment.

Figure 11.30(a–d) shows the pairs of images of each microstructure feature (dislocation loops, precipitates, and voids) characterized in both ion- and reactor-irradiated samples of HT9 heat 84425. Qualitatively, the microstructures

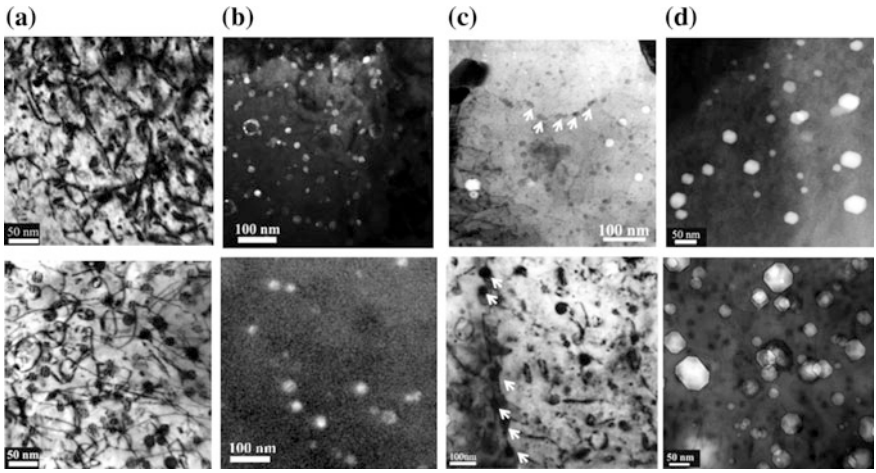

Fig. 11.30 Comparison of irradiation microstructure in HT9 following Fe^{++} irradiation (460 °C:188 dpa with 1 appm helium, *top images*) and following reactor irradiation in FFTF (443 °C:155 dpa, *bottom images*): (**a**) bright field TEM images of line dislocations and loops, (**b**) dark field TEM images of G-phase precipitates in the matrix, (**c**) bright field images of G-phase precipitates along grain boundaries, and (**d**) voids (after [34])

showed all the same radiation-produced features. In both cases, the dislocation microstructure consists of dislocation line segments ($a\langle 100\rangle$ and $(a/2)\langle 111\rangle$) and loops, predominantly $a\langle 100\rangle$ type, of similar diameter ($\sim$20 nm) and number density ($5–9 \times 10^{20}$ m^{-3}) (Fig. 11.30(a)). Radiation-induced precipitates were primarily the G-phase as shown in the dark field TEM image (Fig. 11.30(b)) and a Cr-rich phase (not shown). The composition of the G-phase was confirmed by APT to be close to $Mn_6Ni_{16}Si_7$. G-phase precipitates also appeared along grain boundaries in both cases, as shown in the TEM bright field images in Fig. 11.30(c). The Cr-rich phases under reactor irradiation contained only Cr, and those irradiated with Fe^{++} consisted of Cr with a few percent carbon. Void formation was very heterogeneous in both reactor and Fe^{++}-irradiated samples, with large variations between grains and laths. However, the size and the number density were similar (Fig. 11.30(d)).

A quantitative comparison of defect size and number density as a ratio of ion irradiation to reactor irradiation is shown in Fig. 11.31. The void swelling was nearly identical between the two irradiations, and the size and the density of precipitates and loops following ion irradiation were within a factor of two of those for reactor irradiation. Results indicated that as predicted by invariance theory, the reactor-irradiated microstructure can be emulated by ion irradiation with only a modest temperature increment (17 °C). The damage increment (33 dpa) over the reactor irradiation was also small. These results indicate that an Fe^{++} irradiation at 460 °C with preinjection of 1 appm He emulates the irradiated microstructure, both qualitatively and quantitatively (within a factor of two), created by fast reactor irradiation at an average temperature of 443 °C and to a similar damage level.

A set of experiments similar to that for F-M steel was conducted on solution annealed 304L SS from a core shroud, and cold worked 316 SS from a baffle bolt [39]. Both steels were irradiated in the BOR-60 reactor to doses of 5.4, 10.3, and 46 dpa. Archive material from both heats was irradiated with 5 MeV Ni^{++} ions at temperatures and doses of 380 °C:46 and 260 dpa, 500 °C:46 dpa, and 600 °C:46 dpa. Ni^{++} ion irradiation at 380 °C produced a dislocation loop microstructure close to that by neutron irradiation at 320 °C in terms of loop size

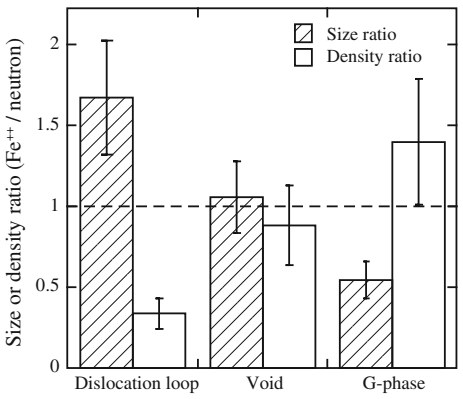

Fig. 11.31 Comparison of size and number density ratios of defect clusters for ion and neutron irradiation under similar conditions (after [34])

and density for the 304L SS. For the 316L SS, the dislocation loop density was a factor of 4 lower that that in reactor and no SFTs were observed.

Ni/Si-rich clusters were observed in self-ion-irradiated 304L SS (5 MeV Fe^{++}) at 380 °C:46 dpa and they were likely precursors of G-phase. Some of the Ni/Si-rich clusters reached the composition of G-phase at 260 dpa [40]. However, the precipitate size was smaller and the density was lower compared to neutron irradiations at 320 °C to 46 dpa, indicating that a temperature shift larger than 60 °C may be needed for SA 304L SS to exhibit a comparable G-phase morphology. G-phase precipitates were observed in cold worked 316 SS following self-ion irradiation to 46 dpa at 380 °C, although most of the Ni/Si-rich clusters were still in the precursor stage. Considering only the G-phase particles, the average size was ~4 nm and the number density is estimated to be 0.1×10^{23} m^{-3}. The average size of precipitates by self-ion irradiations at 380 °C:46 dpa was slightly smaller than those found in neutron irradiated same heat of samples at 320 °C:46 dpa (~5 nm) but at higher density (number density in neutron-irradiated samples was reported to be $<0.1 \times 10^{23}$ m^{-3}). The temperature shift for cold worked 316 SS appeared to be smaller than that of solution annealed 304L SS probably due to the high density of dislocations, which served as defect sinks and mitigated the effect of high dose rate.

Radiation-induced segregation in cold worked 316 SS by heavy ion irradiation at 380 °C was comparable to that by neutrons at 320 °C. The modest temperature shift for RIS in this alloy may be due to the highly deformed microstructures, which consist of high density of defect sinks. There was substantial difference in the magnitude of segregation between ion and neutron irradiation to similar doses in the SA 304L SS alloy with less segregation in ion irradiation than in neutron irradiation. Increasing the temperature to 500 °C increased the magnitude of segregation but the widths of the enriched or depleted zones were much larger at the higher temperature. Results appear to follow the invariance relations, which predict that larger temperature shifts are required to match RIS than the loop or void microstructure.

Nomenclature

C_i	Concentration of atom of type i
E_d	Displacement energy
k_S^2	Sink strength
$l(t)$	Half width of the chromium-depleted zone
M	Amount of grain boundary chromium depletion defined by Eq. (11.5)
N_S	Number of defects per unit volume lost to sinks
N_R	Number of defects per unit volume lost to recombination
R_S	Ratio of vacancy loss to interstitial loss
T	Energy transferred
$P(T)$	Fraction of recoils between E_d and T
$W(E_i, T)$	Weighted average recoil spectrum
$\sigma(E_i, T)$	Scattering cross section for the transfer of energy in $T + dT$
$\sigma_D(E_i)$	Displacement cross section

Acronyms

AES	Auger electron spectroscopy
APT	Atom probe tomography
CP	Commercial purity
IASCC	Irradiation-assisted stress corrosion cracking
IGSCC	Intergranular stress corrosion cracking
K–P	Kinchen–Pease
NRT	Norgett, Robinson, Torrens
SCC	Stress corrosion cracking
SRIM	Stopping power and ranges of ions in matter
STEM-EDS	Scanning transmission electron microscopy-energy dispersive spectroscopy

Problems

11.1 Radiation effects experiments can be conducted with a variety of energetic particles. However, the result is sometimes dependent on the nature of the irradiating particle and the conditions under which the irradiation occurs.

(a) Explain (as quantitatively as possible) the differences in the effects of irradiation for a 1 MeV particle of the following types: electron, proton, neutron, and Ni ion. In your answer, make sure you address the following:

(i) The recoil spectrum
(ii) The damage function
(iii) The spatial distribution of defects and the form of the defects
(iv) The subsequent behavior of freely migrating defects and defect clusters.

(b) Unfortunately, irradiations with the various types of particles do not occur under identical conditions. The following are typical temperatures and dose rates for irradiation with each particle type, as dictated by the facility needed to produce such particles:

Electrons: 500 °C, 10^{-3} dpa/s
Protons: 400 °C, 10^{-5} dpa/s
Ni ions: 500 °C, 10^{-3} dpa/s
Neutrons: 300 °C, 10^{-8} dpa/s
Answer part (a) again given these irradiation conditions.

11.2 Three separate particles travel through a pure iron slab, specifically 1 MeV neutrons, 1 MeV gammas, and 1 MeV electrons. For each:

(a) Calculate the maximum possible energy transfer to an Fe atom from each particle.
(b) State any assumptions you made in part (a).
(c) Explain the relative damage consequences for each particle.
(d) To minimize damage to the iron, would it be a good idea to place shielding between the radiation source and the iron slab?

11.3 Calculate and graph the weighted recoil spectra for 1 MeV protons and 1 MeV neutrons incident on copper.

11.4 Using the invariance requirements, determine the temperature at which proton irradiations should be conducted in order to produce:

(a) The same amount of RIS
(b) The same dislocation microstructure as irradiation in a fast reactor at a temperature of 500 °C, given that the proton damage rate is 10^{-5} dpa/s and the damage rate in a fast reactor is 8×10^{-8} dpa/s. Use $E_m^v = 1.3$eV; $E_f^m = 1.9$eV.

11.5 Determine the optimum ion irradiation technique for the following objectives:

(a) High-dose (100 dpa) microstructure investigation of stainless steel at high (500 °C) temperature
(b) Investigation of the effect of irradiation on SCC of a zirconium alloy in water
(c) Tracking the evolution of amorphization with dose.

References

1. Abromeit C (1994) J Nucl Mater 216:78–96
2. Mazey DJ (1990) J Nucl Mater 174:196
3. Active Standard (1989) Standard practice for neutron irradiation damage simulation by charged particle irradiation, designation E521-89. American Standards for Testing and Materials, Philadelphia, p D-9
4. Was GS, Andresen PL (1992) JOM 44(4):8
5. Andresen PL, Ford FP, Murphy SM, Perks JM (1990) In: Proceedings of the 4th international symposium on environmental degradation of materials in nuclear power systems: water reactors. National Association of Corrosion Engineers, Houston, pp 1–83
6. Andresen PL (1992) In: Jones RH (ed) Stress corrosion cracking, materials performance and evaluation. ASM International, Metals Park, p 181
7. Sterbentz JW (2004) Neutronic evaluation of a 21 × 21 supercritical water reactor fuel assembly design with water rods and SiC clad/duct materials, INEEL/EXT-04-02096, Idaho National Engineering and Environmental Laboratory. Bechtel BWXT Idaho, LLC, Idaho Fall, ID

8. Kinchin GH, Pease RS (1955) Prog Phys 18:1
9. Norgett MJ, Robinson MT, Torrens IM (1974) Nucl Eng Des 33:50
10. Was GS, Allen T (1993) J Nucl Mater 205:332–338
11. Perks JM, Marwick AD, English CA (1986) AERE R 12121 June
12. Was GS, Allen TR (2007): In: Sickefus KE, Kotomin EA, Obervaga BP (eds) Radiation effects in solids, NATO science series II: mathematics, physics and chemistry, vol 235. Springer, Berlin, pp 65–98
13. Ezawa T, Wakai E (1991) Ultramicroscopy 39:187
14. Ashworth JA, Norris DIR, Jones IP (1992) JNM 189:289
15. Wakai E (1992) Trans JIM 33(10):884
16. Whitley JB (1978) Dissertation. Nuclear engineering, University of Wisconsin-Madison
17. Garner FA (1983) J Nucl Mater 117:177–197
18. Lee EH, Mansur LK, Yoo MH (1979) J Nucl Mater 85(86):577–581
19. Brailsford AD, Mansur LK (1977) J Nucl Mater 71:110–116
20. Ziegler JF, Biersack JP, Littmark U (1996) The stopping and range of ions in matter. Pergamon, New York
21. Was GS, Busby JT, Allen T, Kenik EA, Jenssen A, Bruemmer SM, Gan J, Edwards AD, Scott P, Andresen PL (2002) J Nucl Mater 300:198–216
22. Gan J, Was GS, Stoller R (2001) J Nucl Mater 299:53–67
23. Scott P (2003) Materials reliability program: a review of the cooperative irradiation assisted stress corrosion cracking research program (MRP-98), 1002807, Palo Alto, CA
24. Stephenson KJ, Was GS (2015) J Nucl Mater. 456:85–98
25. Scholz R, Matera R (2000) J Nucl Mater 414:283–287
26. Sencer BH, Was GS, Yuya H, Isobe Y, Sagasaka M, Garner FA (2005) J Nucl Mater 336:314–322
27. Baicry J, Mardon JP, Morize P (1987) In: Adamson RB, van Swam LFP (eds) Proceedings on seventh international symposium on Zirconium in the nuclear industry, STM STP 939, American Society for Testing and Materials, West Conshohocken, PA, p. 101
28. Garner FA (1994) Irradiation performance of cladding and structural steels in liquid metal reactors. In: Frost BRT (ed) Materials science and technology: a comprehensive treatment (Chapter 6), vol 10A. VCH, New York, p 419
29. Was GS, Hash M, Odette GR (2005) Phil Mag 85(4–7):703–722
30. Zu XT, Sun K, Atzmon M, Wang LM, You LP, Wan FR, Busby JT, Was GS, Adamson RB (2005) Phil Mag 85(4–7):649–659
31. Wang P, Was GS (2015) J Mater Res 30(9):1335–1348
32. Allison CM et al, MATPRO-A library of materials properties for light-water-reactor accident analysis, NUREG/CR-6150, EGG-2720, vol 4, pp 4–234
33. Campbell A, Campbell KB, Was GS (2013) Carbon 60:410
34. Was GS, Jiao Z, Getto E, Sun K, Monterrosa AM, Maloy SA, Anderoglu O, Sencer BH, Hackett M (2014) Scr Mater 88:33
35. Sencer BH, Kennedy JR, Cole JI, Maloy SA, Garner FA (2009) J Nucl Mater 393:235
36. Ziegler JF, Ziegler MD, Biersak JP (2010) Nucl Instr Meth Phys Res B 268:1818
37. Stoller RE, Toloczko MB, Was GS, Certain AG, Dwaraknath S, Garner FA (2013) Nucl Instr Meth Phys Res B 310:75
38. Mansur LK (1978) Nucl Technol 40:5
39. Was GS, Jiao Z, Van der ven A, Buremmer S, Edwards D (2012) Aging and embrittlement of high fluence stainless steels, final report, NEUP project CFP-09-767, December 2012
40. Jiao Z, Was GS (2014) J Nucl Mater 449:200

Part III
Mechanical and Environmental Effects of Radiation Damage

Chapter 12
Irradiation Hardening and Deformation

Exposure of metals to irradiation results in an increase in the yield strength over a wide temperature range and is most pronounced at $T_{irr} < 0.3T_m$. Typical engineering stress–stress curves for fcc and bcc steelsare shown in Fig. 12.1. Note that for both crystal structures, in addition to increasing the yield strength, the ductility (measured either by total elongation or by uniform elongation) is reduced. Irradiation also increases the yield strength, σ_y much more than it does the ultimate tensile strength (σ_{UTS} or UTS) for both fcc and bcc metals. The approach of σ_y to σ_{UTS} results in a loss of ductility to the limit where $\sigma_y = \sigma_{UTS}$ and uniform elongation is zero. In bcc metals tested at low temperature, high fluences may even result in the disappearance of necking deformation with fracture occurring on the elastic line, rendering them totally brittle.

Irradiation-induced hardening in both fcc and bcc metals is caused by the production of the various defects discussed in Chaps. 3, and 7–9:

- Defect clusters
- Impurity–defect cluster complexes
- Dislocation loops (faulted or unfaulted, vacancy or interstitial type)
- Dislocation lines (dislocation loops that have unfaulted and joined the dislocation network of the original microstructure)
- Voids and bubbles
- Precipitates

This chapter will focus on the mechanisms of irradiation hardening in metals due to the various irradiation-produced defects. Before beginning a discussion of hardening, it is helpful to briefly review the basic elements of elasticity and plasticity theory [1], which will serve as a basis for understanding the effect of irradiation on hardening.

Additional material to this chapter can be downloaded from http://rmsbook2ed.engin.umich.edu/movies/

G.S. Was, *Fundamentals of Radiation Materials Science*,
DOI 10.1007/978-1-4939-3438-6_12

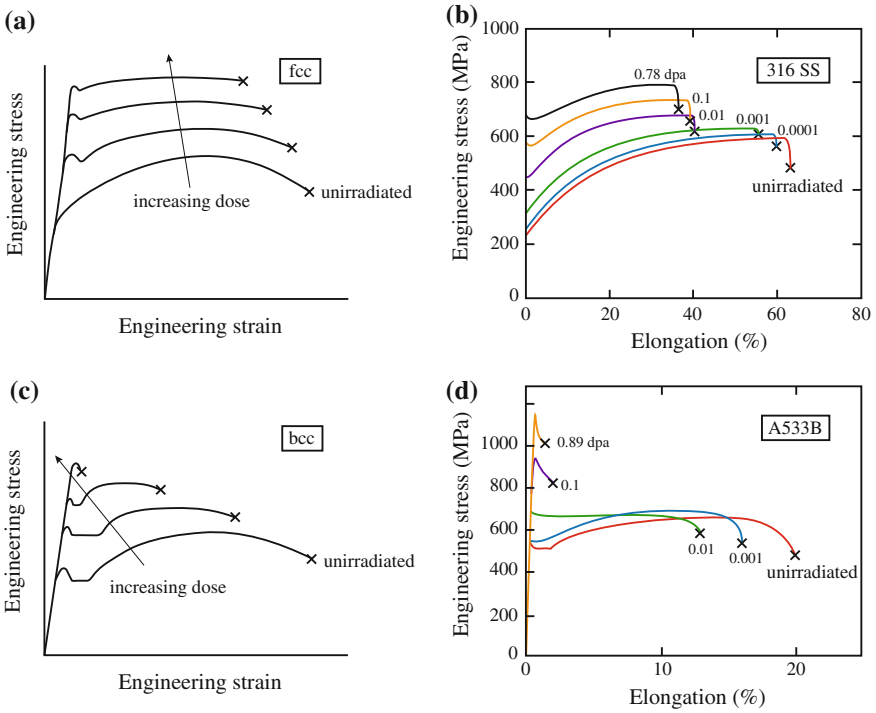

Fig. 12.1 Effect of irradiation on the stress–strain behavior (**a**) schematic and (**b**) example in an austenitic (fcc) stainless steel, and (**c**) schematic and (**d**) example in a ferritic (bcc) steel

12.1 Elastic and Plastic Deformation

12.1.1 Elasticity

In the elastic region, deformation is proportional to load, and the relation is known as Hooke's law:

$$\sigma = E\varepsilon, \tag{12.1}$$

where σ is stress, ε is strain, and E is the modulus of elasticity in tension or compression. While a tensile force in the x-direction produces extension along the x-axis, it also produces a contraction along the transverse y- and z-directions. The transverse strain is a constant fraction of the longitudinal strain:

$$\varepsilon_{yy} = \varepsilon_{zz} = -\nu\varepsilon_{xx} = \frac{-\nu\sigma_{xx}}{E}, \tag{12.2}$$

where v is the Poisson's ratio and has a value of 0.25 for perfectly isotropic elastic materials, but is approximately 0.33 for most metals. For a three-dimensional state of stress, the resulting strains are as follows:

Stress	x-Strain	y-Strain	z-Strain
σ_{xx}	$\varepsilon_{xx} = \frac{\sigma_{xx}}{E}$	$\varepsilon_{yy} = \frac{-v\sigma_{xx}}{E}$	$\varepsilon_{zz} = \frac{-v\sigma_{xx}}{E}$
σ_{yy}	$\varepsilon_{xx} = \frac{-v\sigma_{yy}}{E}$	$\varepsilon_{yy} = \frac{\sigma_{yy}}{E}$	$\varepsilon_{zz} = \frac{-v\sigma_{yy}}{E}$
σ_{zz}	$\varepsilon_{xx} = \frac{-v\sigma_{zz}}{E}$	$\varepsilon_{yy} = \frac{-v\sigma_{zz}}{E}$	$\varepsilon_{zz} = \frac{\sigma_{zz}}{E}$

Superposition of strain components yields:

$$\begin{aligned}
\varepsilon_{xx} &= \frac{1}{E}[\sigma_{xx} - v(\sigma_{yy} + \sigma_{zz})] \\
\varepsilon_{yy} &= \frac{1}{E}[\sigma_{yy} - v(\sigma_{xx} + \sigma_{zz})] \\
\varepsilon_{zz} &= \frac{1}{E}[\sigma_{zz} - v(\sigma_{xx} + \sigma_{yy})].
\end{aligned} \tag{12.3}$$

Adding the strain components gives the following:

$$\varepsilon_{xx} + \varepsilon_{yy} + \varepsilon_{zz} = \frac{1-2v}{E}(\sigma_{xx} + \sigma_{yy} + \sigma_{zz}), \tag{12.4}$$

and

$$\sigma_m = 1/3(\sigma_{xx} + \sigma_{yy} + \sigma_{zz}) \tag{12.5}$$

is the hydrostatic or mean stress, and

$$\Delta = \varepsilon_{xx} + \varepsilon_{yy} + \varepsilon_{zz} \tag{12.6}$$

is the volume strain. Shear stresses produce shear strains according to the following relations:

$$\varepsilon_{xy} = \frac{\sigma_{xy}}{\mu}, \quad \varepsilon_{yz} = \frac{\sigma_{yz}}{\mu}, \quad \varepsilon_{xz} = \frac{\sigma_{xz}}{\mu}, \tag{12.7}$$

where μ is the shear modulus.

The stress–strain relations for an isotropic solid involve three elastic constants, v, E, and μ, that are related as follows:

$$\mu = \frac{E}{2(1+v)}. \tag{12.8}$$

In a general anisotropic linear elastic solid, there are up to 21 independent elastic constants. Since the constants must obey various geometrical constraints for a given crystal structure, the number of independent elastic constants is reduced considerably in structures possessing a high degree of symmetry.

For small elastic strains, there is no coupling between the expressions for normal stress and strain and the equations for shear stress and shear strain and we can solve for stress in terms of strain. Writing Eq. (12.4) in terms of stress:

$$\sigma_{xx} + \sigma_{yy} + \sigma_{zz} = \frac{E}{1-2v}(\varepsilon_{xx} + \varepsilon_{yy} + \varepsilon_{zz}), \tag{12.9}$$

subtracting σ_{xx} from both sides of Eq. (12.9) and substituting for (σ_{yy} + σ_{zz}) into the first equation in Eq. (12.3) gives the following:

$$\varepsilon_{xx} = \frac{1+v}{E}\sigma_{xx} - \frac{v}{E}(\varepsilon_{xx} + \varepsilon_{yy} + \varepsilon_{zz}), \tag{12.10}$$

and solving for σ_{xx} gives the following:

$$\sigma_{xx} = \frac{E}{1+v}\varepsilon_{xx} + \frac{vE}{(1+v)(1-2v)}(\varepsilon_{xx} + \varepsilon_{yy} + \varepsilon_{zz}), \tag{12.11}$$

or in tensor notation:

$$\sigma_{ij} = \frac{E}{1+v}\varepsilon_{ij} + \frac{vE}{(1+v)(1-2v)}\varepsilon_{ij}\delta_{ij}, \tag{12.12}$$

where δ_{ij} is the Kronecker delta with values δ_{ij} = 1 for $i = j$, and δ_{ij} = 0 for $i \neq j$. (Note that the terms $\varepsilon_{ij}\delta_{ij}$ imply the use of Einstein notation.) Upon expansion, this expression yields three equations for normal stress and six equations for shear stress. Equation (12.12) is often written in briefer notation using the Lamé constant, defined as follows:

$$\lambda = \frac{vE}{(1+v)(1-2v)}. \tag{12.13}$$

Substituting for Eqs. (12.6), (12.8) and (12.13) for Δ, μ, and λ, respectively, into Eq. (12.11) gives the following:

$$\sigma_{xx} = 2\mu\varepsilon_{xx} + \lambda\Delta. \tag{12.14}$$

The stresses and strains can be broken into hydrostatic and deviatoric components. Hydrostatic stress involves only pure tension and compression while deviatoric stress represents the shear stresses in the total state of stress. The distortion is related to the stress deviator by:

$$\sigma'_{ij} = \frac{E}{1+v}\varepsilon'_{ij} = 2\mu\varepsilon'_{ij}, \tag{12.15}$$

while the relationship between hydrostatic stress and mean strain is given as:

$$\sigma_{ii} = \frac{E}{1-2v}\varepsilon_{ii} = 3K\varepsilon_{ii}, \tag{12.16}$$

where $K = \dfrac{E}{3(1-2v)}$ is the bulk modulus or volumetric modulus of elasticity. The bulk modulus is the ratio of the hydrostatic pressure to the dilatation that it produces:

$$K = \frac{\sigma_m}{\Delta} = \frac{-p}{\Delta} = \frac{1}{\beta}, \tag{12.17}$$

where $-p$ is the hydrostatic pressure and β is the compressibility of the solid. Note that the hydrostatic component of the stress tensor produces only elastic volume changes and does not cause plastic deformation. So the yield stress of a solid is independent of the hydrostatic stress. The stress deviator involves shear stress and is responsible for plastic deformation.

Two special cases of engineering importance are plane stress and plane strain. The plane stress state occurs when one of the principal stresses is zero, such as in a thin sheet loaded in the plane of the sheet (Fig. 12.2(a)) or an internally pressurized, thin-walled tube. In this case, the principal stresses are given as:

$$\begin{aligned} \sigma_1 &= \frac{E}{1-v^2}(\varepsilon_1 + v\varepsilon_2), \\ \sigma_2 &= \frac{E}{1-v^2}(\varepsilon_2 + v\varepsilon_1), \\ \sigma_3 &= 0. \end{aligned} \tag{12.18}$$

The plane strain state is one in which one of the principal strains is zero such as occurs when one dimension is much greater than the other two (Fig. 12.2(b)). In this case, we have $\varepsilon_3 = \dfrac{1}{E}[\sigma_3 - v(\sigma_1 + \sigma_2)]$, and combining with $\sigma_3 = v(\sigma_1 + \sigma_2)$ gives:

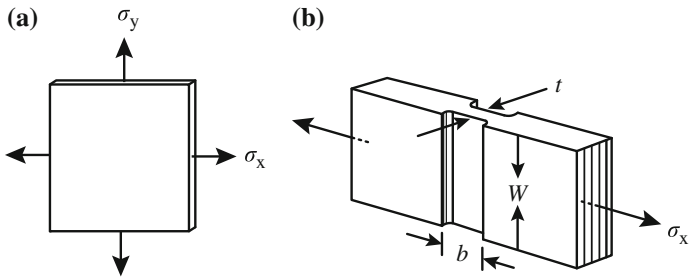

Fig. 12.2 Examples of (**a**) plane stress state and (**b**) plane strain state

$$\begin{aligned}\varepsilon_1 &= \frac{1}{E}[(1-\nu^2)\sigma_1 - \nu(1+\nu)\sigma_2],\\ \varepsilon_2 &= \frac{1}{E}[(1-\nu^2)\sigma_2 - \nu(1+\nu)\sigma_1],\\ \varepsilon_3 &= 0.\end{aligned} \tag{12.19}$$

Note that the expressions in Eqs. (12.18) and (12.19) are written in terms of principal stresses and principal strains, which act normal to the principal planes. Principal planes are those on which the maximum normal stresses act, and on which no shearing stresses act.

The strain energy, *U,* is the energy expended by the action of external forces in deforming an elastic body. The work performed during elastic deformation is stored as elastic energy and is recovered upon release of the applied forces. Energy is the product of force, *F,* through the distance, δ, over which it acts. In deformation of an elastic solid, the force and deformation increase linearly from zero to a value of $1/2F\delta$. This quantity is the area under the elastic portion of the stress–strain curve that was presented in Chap. 7 (Fig. 7.22). If we subject a cube to a tensile stress in the *x*-direction, then we can write an expression for the change in strain energy of the solid:

$$\begin{aligned}\mathrm{d}U &= 1/2F\,\mathrm{d}\delta\\ &= 1/2(\sigma_{xx}A)(\varepsilon_{xx}\mathrm{d}x)\\ &= 1/2(\sigma_{xx}\varepsilon_{xx})(A\mathrm{d}x).\end{aligned} \tag{12.20}$$

Since $A\ \mathrm{d}x$ is the volume increment, the strain energy per unit volume or strain energy density is:

$$\begin{aligned}u &= 1/2\sigma_{xx}\varepsilon_{xx}\\ &= 1/2\frac{\sigma_{xx}^2}{E}\\ &= 1/2\varepsilon_{xx}^2 E.\end{aligned} \tag{12.21}$$

For pure shear stress:

$$\begin{aligned}u &= 1/2\sigma_{xy}\varepsilon_{xy}\\ &= 1/2\frac{\sigma_{xy}^2}{\mu}\\ &= 1/2\varepsilon_{xy}^2\mu.\end{aligned} \tag{12.22}$$

Elastic strain energy for a three-dimensional stress state is obtained by superposition of Eqs. (12.21) and (12.22):

$$\begin{aligned} u &= 1/2(\sigma_{xx}\varepsilon_{xx} + \sigma_{yy}\varepsilon_{yy} + \sigma_{zz}\varepsilon_{zz} + \sigma_{xy}\varepsilon_{xy} + \sigma_{yz}\varepsilon_{yz} + \sigma_{xz}\varepsilon_{xz}) \\ &= 1/2\sigma_{ij}\varepsilon_{ij}. \end{aligned} \tag{12.23}$$

Substituting expressions for strains from Eqs. (12.3) and (12.7) gives the following:

$$\begin{aligned} u = \frac{1}{2E}\left(\sigma_{xx}^2 + \sigma_{yy}^2 + \sigma_{zz}^2\right) - \frac{v}{E}(\sigma_{xx}\sigma_{yy} + \sigma_{yy}\sigma_{zz} + \sigma_{xx}\sigma_{zz}) \\ + \frac{1}{2\mu}\left(\sigma_{xy}^2 + \sigma_{yz}^2 + \sigma_{xz}^2\right), \end{aligned} \tag{12.24}$$

and substituting Eq. (12.12) into Eq. (12.24) gives the following:

$$u = 1/2\lambda\,\Delta^2 + \mu(\varepsilon_{xx}^2 + \varepsilon_{yy}^2 + \varepsilon_{zz}^2) + 1/2\mu(\varepsilon_{xy}^2 + \varepsilon_{yz}^2 + \varepsilon_{xz}^2). \tag{12.25}$$

Note that the derivative of u with respect to any strain component gives the corresponding stress component:

$$\frac{\partial u}{\partial \varepsilon_{xx}} = \lambda\,\Delta + 2\mu\varepsilon_{xx} = \sigma_{xx} \quad \text{and} \quad \frac{\partial u}{\partial \sigma_{xx}} = \varepsilon_{xx}. \tag{12.26}$$

12.1.2 Plasticity

Elastic deformation depends only on the initial and final states of stress and strain, while plastic strain depends on the loading path by which the final state is achieved. The stress required to cause metal to flow plastically to any given strain describes the flow curve, which is given by the power law hardening relationship:

$$\sigma = K\varepsilon_{\mathrm{p}}^{n}, \tag{12.27}$$

where ε_{p} is the plastic strain, K is the stress at $\varepsilon_{\mathrm{p}} = 1.0$, and n is the strain hardening exponent. Note that $n = 0$ for perfectly plastic behavior and $n = 1$ for elastic behavior. Typically, n is between 0.1 and 0.5. The shape of the power law hardening curve for various values of n is shown in Fig. 12.3. The yield strength is easy to find in a tension test. We would like to develop mathematical relations for predicting the conditions under which plastic yielding begins when a material is subject to any possible combination of stresses. However, there is currently no way of calculating the relationship between the stress components to correlate yield in a three-dimensional state of stress with yield in uniaxial tension. All yielding criteria are empirical.

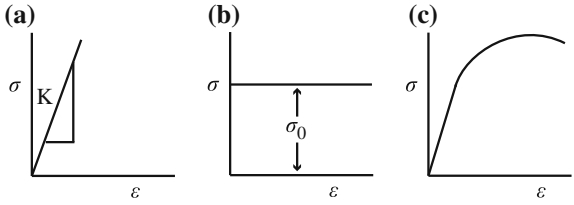

Fig. 12.3 Flow curves drawn from Eq. (12.27) for the cases (**a**) elastic behavior, $n = 1$, (**b**) perfectly plastic behavior, $n = 0$, (**c**) plastic behavior with intermediate value of n

Von Mises proposed that yielding will occur when the second invariant of the stress deviator (see for example [1]) exceeded some critical value, k^2, where:

$$k^2 = 1/6\left[(\sigma_1 - \sigma_2)^2 + (\sigma_2 - \sigma_3)^2 + (\sigma_3 - \sigma_1)^2\right]. \tag{12.28}$$

The value of k is determined by applying this expression to a uniaxial tension test in which $\sigma_1 = \sigma_y$, $\sigma_2 = \sigma_3 = 0$, (σ_y is the yield stress) giving:

$$\sigma_y^2 + \sigma_y^2 = 6k^2, \quad \text{or} \quad \sigma_y = \sqrt{3}k. \tag{12.29}$$

Substituting Eq. (12.29) into Eq. (12.28) gives the familiar form of the von Mises yield criterion:

$$\sigma_y = 1/\sqrt{2}\left[(\sigma_1 - \sigma_2)^2 + (\sigma_2 - \sigma_3)^2 + (\sigma_3 - \sigma_1)^2\right]^{1/2}, \tag{12.30}$$

and if shear stresses are present:

$$\sigma_y = 1/\sqrt{2}[(\sigma_{xx} - \sigma_{yy})^2 + (\sigma_{yy} - \sigma_{zz})^2 + (\sigma_{zz} - \sigma_{xx})^2 + 6(\sigma_{xy} + \sigma_{yz} + \sigma_{xz})]^{1/2}. \tag{12.31}$$

Yielding will occur when the differences in stresses on the right side of the equation exceed the yield stress in uniaxial tension, σ_y. For a pure shear stress state (as in a torsion test), the shear stress, σ_s, is related to the principal stresses by:

$$\sigma_1 = -\sigma_3 = \sigma_s, \quad \sigma_2 = 0, \tag{12.32}$$

and at yield:

$$\sigma_1^2 + \sigma_1^2 + 4\sigma_1^2 = 6k^2, \quad \text{and} \quad \sigma_1 = k, \tag{12.33}$$

so k is the yield stress in pure shear. The von Mises criterion predicts that the yield stress in torsion will be less than that in uniaxial tension by:

$$k = \frac{1}{\sqrt{3}}\sigma_y = 0.577\sigma_y. \tag{12.34}$$

Another criterion used for yielding due to a multiaxial stress state is the Tresca (or maximum shear stress) criterion, which says that yielding occurs when the maximum shear stress reaches the value of the shear stress in the uniaxial tension test:

$$\sigma_s^{max} = \frac{\sigma_1 - \sigma_3}{2}, \tag{12.35}$$

where σ_1 is the algebraically largest principal stress and σ_3 is the algebraically smallest principal stress. For uniaxial tension, $\sigma_1 = \sigma_y$, $\sigma_2 = \sigma_3 = 0$, and the shearing yield stress, σ_{sy}, is equal to $\sigma_y/2$, and (12.35) becomes:

$$\sigma_s^{max} = \frac{\sigma_1 - \sigma_3}{2} = \frac{\sigma_y}{2} = \sigma_{sy}, \tag{12.36}$$

so the maximum shear stress criterion is then given by:

$$\sigma_1 - \sigma_3 = \sigma_y. \tag{12.37}$$

For a pure shear stress state, $\sigma_1 = -\sigma_3 = k$, and $\sigma_2 = 0$; so the maximum shear stress criterion states that yielding will occur when:

$$\sigma_1 - \sigma_3 = 2k = \sigma_y, \quad \text{or} \quad k = \frac{\sigma_y}{2}. \tag{12.38}$$

The Tresca yield criterion has been observed to hold fairly well in alloys that exhibit a yield drop [2]. Alloys that yield by homogeneous plastic flow generally obey the von Mises criterion or deviate from it only slightly. In fact, in many real materials, the yield surface is "between" the Tresca and von Mises criteria [2].

12.1.3 Tension Test

The tension test is perhaps the best way to demonstrate the elastic and plastic behavior of metals. In a tension test, a specimen is subjected to a continually increasing uniaxial tensile force, while simultaneous observations are made of the elongation of the specimen. Data are plotted in a stress–strain diagram from load-elongation measurements, resulting in an engineering stress–engineering strain curve. The parameters used to describe the stress–strain curve are as follows:

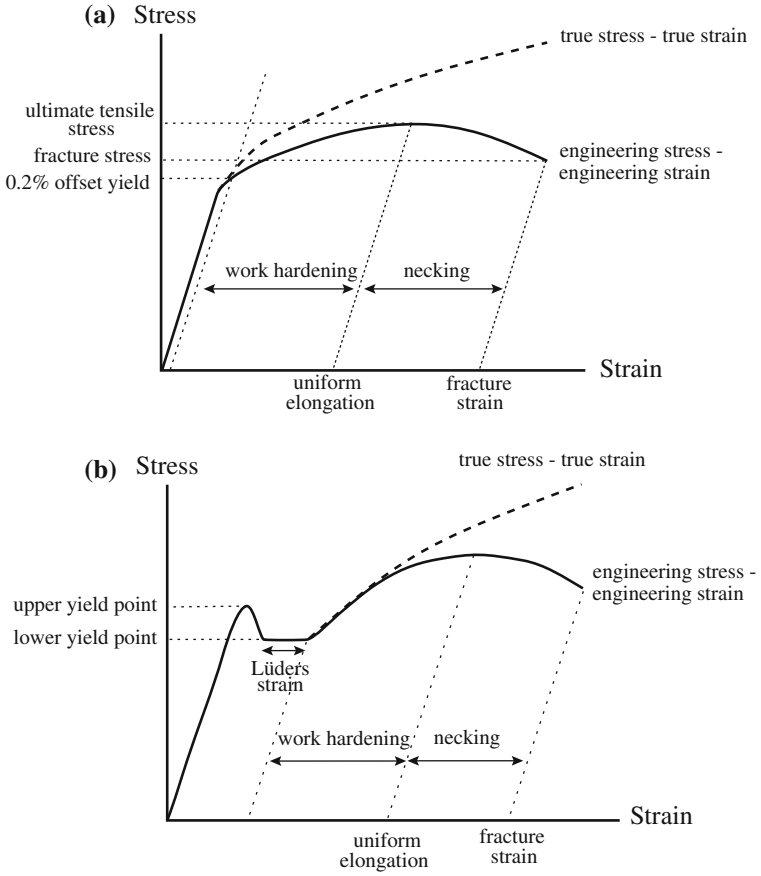

Fig. 12.4 Engineering stress–engineering strain and true stress–true strain curves resulting from a uniaxial tensile test and key parameters defining the curves for (**a**) fcc metals and (**b**) bcc metals

- Yield strength
- Tensile strength
- Fracture strength
- Uniform strain
- Fracture strain
- Reduction in area

Figure 12.4 illustrates the engineering stress–engineering strain curve and the parameters used to describe the behavior of the sample. The average longitudinal stress S is the load P divided by the *original* area, A_0:

$$S = \frac{P}{A_0}. \tag{12.39}$$

The average linear strain, e is the ratio of the change in length, δ to the original length, L_0:

$$e = \frac{\delta}{L_0} = \frac{\Delta L}{L_0} = \frac{L - L_0}{L_0}. \tag{12.40}$$

The engineering stress–engineering strain curve is not a true indication of the deformation characteristics of a material because it is based entirely on the original dimensions of the specimen that change continuously during a test.

The true stress, σ, and true strain, ε, are based on the instantaneous values of cross-sectional area and length and are given by:

$$\sigma = \frac{P}{A} = S\frac{A_0}{A}, \tag{12.41}$$

$$\begin{aligned} \varepsilon &= \int_{L_0}^{L_f} \frac{\mathrm{d}L}{L} \\ &= \ln\frac{L_f}{L_0} = \ln(e+1). \end{aligned} \tag{12.42}$$

While the true strain and engineering strain are close at small values of strain (<0.2), they diverge significantly at large values of strain. The relationship between true and engineering stress is determined by invoking conservation of volume:

$$\frac{A_0}{A} = \frac{L}{L_0} = e + 1, \quad \text{and} \quad \sigma = \frac{P}{A} = S(e+1). \tag{12.43}$$

Up to a certain limiting load, a solid will recover its original dimensions when the load is removed. The load beyond which the material no longer behaves elastically is the *elastic limit*. If the elastic limit is exceeded, the body will retain a permanent set upon removal of the load. The stress at which plasticity begins is called the *yield stress*, σ_y or YS. Various definitions exist for the yield stress but the commonly accepted one is the offset yield strength, determined by the stress corresponding to the intersection of the stress–strain curve and a line parallel to the elastic part of the curve and offset by a strain of 0.2 %. The yield strength is written as follows:

$$\sigma_y = \frac{P_{(\text{strain offset}=0.2\%)}}{A_0}. \tag{12.44}$$

The *tensile strength* or *ultimate tensile strength* (UTS) is the maximum load divided by the original cross-sectional area of the sample:

$$S_u = \frac{P_{\max}}{A_0}. \tag{12.45}$$

The true stress at maximum load is the true tensile strength and is given by the maximum load divided by the sample cross-sectional area at maximum load:

$$\sigma_{\mathrm{u}} = \frac{P_{\max}}{A_{\mathrm{u}}}, \quad \varepsilon_{\mathrm{u}} = \ln\frac{A_0}{A_{\mathrm{u}}}. \tag{12.46}$$

Eliminating $P_{\max}$ from Eqs. (12.45) and (12.46) gives:

$$\begin{aligned} \sigma_{\mathrm{u}} &= S_{\mathrm{u}}\frac{A_0}{A_{\mathrm{u}}} \\ &= S_{\mathrm{u}}\exp(\varepsilon_{\mathrm{u}}). \end{aligned} \tag{12.47}$$

The *fracture stress* is the stress at the point of failure and is given by:

$$\begin{aligned} S_{\mathrm{f}} &= \frac{P_{\mathrm{f}}}{A_0}, \quad e_{\mathrm{f}} = \frac{L_{\mathrm{f}} - L_0}{L_0} \\ \sigma_{\mathrm{f}} &= \frac{P_{\mathrm{f}}}{A_{\mathrm{f}}}, \quad \varepsilon_{\mathrm{f}} = \ln\frac{A_0}{A_{\mathrm{f}}}. \end{aligned} \tag{12.48}$$

Strain occurs uniformly in the gage section of the sample up to the UTS, which is when necking or localized deformation begins to occur. The true uniform strain, ε_{u}, is given by the strain at maximum load:

$$\varepsilon_{\mathrm{u}} = \ln\frac{A_0}{A_{\mathrm{u}}}. \tag{12.49}$$

The true fracture strain, ε_{f} is the true strain based on the original area and the area after fracture, A_{f}:

$$\varepsilon_{\mathrm{f}} = \ln\frac{A_0}{A_{\mathrm{f}}} = \ln\frac{1}{1 - RA}, \tag{12.50}$$

where RA is the reduction in area at fracture:

$$RA = \frac{A_0 - A_{\mathrm{f}}}{A_0}. \tag{12.51}$$

Finally, the local necking strain, ε_n, is the strain required to deform the specimen from the maximum load to fracture:

$$\varepsilon_n = \ln \frac{A_u}{A_f}. \tag{12.52}$$

A final quantity of importance in the tensile test is the onset of plastic instability, which occurs when the increase in stress due to the decreasing cross-sectional area becomes greater than the load-carrying ability of the metal. This necking or localized deformation begins at the point of maximum load and is defined by the condition that $dP = 0$:

$$\begin{aligned} P &= \sigma A \\ dP &= \sigma dA + A d\sigma = 0, \quad \text{and} \quad -\frac{dA}{A} = \frac{d\sigma}{\sigma} \end{aligned} \tag{12.53}$$

and from conservation of volume:

$$\frac{dL}{L} = -\frac{dA}{A} = d\varepsilon, \tag{12.54}$$

so that at the point of tensile instability:

$$\sigma = \frac{d\sigma}{d\varepsilon}. \tag{12.55}$$

That is, the point of necking at maximum load is obtained from the true stress–true strain curve by finding the point on the curve where the rate of strain hardening equals the stress. Referring back to the flow curve relation given in Eq. (12.27), the strain hardening exponent is defined by:

$$n = \frac{d \ln \sigma}{d \ln \varepsilon} = \frac{\varepsilon \, d\sigma}{\sigma \, d\varepsilon}, \quad \text{and} \quad \frac{d\sigma}{d\varepsilon} = n \frac{\sigma}{\varepsilon}. \tag{12.56}$$

Substituting Eq. (12.55) into Eq. (12.56) gives a simple expression for the true uniform strain:

$$\varepsilon_u = n. \tag{12.57}$$

That is, the true uniform strain is equal to the strain hardening exponent in the power law hardening expression, Eq. (12.27).

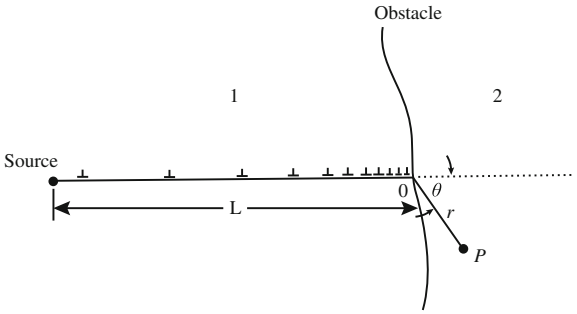

Fig. 12.5 Dislocation pileup at an obstacle in a solid

12.1.4 Yield Strength

The yield strength represents the onset of plasticity and hence is a key parameter in determining the mechanical behavior of metals. Yielding can be understood by examining the behavior of dislocations in a metal under stress. Dislocations formed by sources such as the Frank–Read source, frequently pile up on slip planes at barriers such as grain boundaries, precipitates, or sessile dislocations. The leading dislocation is acted on not only by the applied shear stress, but also by the interaction with other dislocations on the slip plane, leading to a high stress concentration on the lead dislocation in the pileup. The pileup of dislocations also exerts a back stress on dislocations further from the barrier, opposing their motion on the slip plane (Fig. 12.5). The high stress at the head of the pileup can initiate yielding on the other side of the barrier (or it may nucleate a crack at the barrier, see Chap. 14).

The number of dislocations in the pileup can be estimated by summing the x-direction forces between each dislocation in the pileup under the condition of mechanical equilibrium. The number of dislocations in a pileup of length L under a shear stress σ_s on the slip plane [3] is:

$$n = \frac{\pi(1-\nu)L\sigma_s}{\mu b}. \tag{12.58}$$

At large distances from the pileup, the array of n dislocations can be considered to act like a single dislocation with Burgers vector nb with a force equal to $nb\sigma_s$. A more complete analysis of the stress at the head of the pileup was made by Stroh [4] who showed that the tensile stress normal to the line OP in the neighboring grain is:

$$\sigma = \frac{3}{2}\left(\frac{L}{r}\right)^{1/2}\sigma_s \sin\theta\cos\theta/2. \tag{12.59}$$

The maximum value of σ occurs at $\theta = 70.5°$ and yields:

$$\sigma = \frac{2}{\sqrt{3}}\left(\frac{L}{r}\right)^{1/2}\sigma_s, \tag{12.60}$$

and the shear stress acting in the plane OP is given by:

$$\sigma_P = \beta\sigma_s\left(\frac{L}{r}\right)^{1/2}, \tag{12.61}$$

and β is a factor dependent on orientation with a value approximately equal to unity.

If the obstacle is a grain boundary, and the distance from the head of the pileup in grain 1 to the nearest dislocation source in grain 2 in Fig. 12.5 is r, and the length of the pileup, L, is taken to be equal to the grain diameter, d, then yielding will occur when the shear stress in the pileup, σ_s, reaches the shear stress to cause yielding, σ_{sy} or $\sigma_s = \sigma_{sy}$. If σ_{sd} is the stress required to nucleate slip in grain 2, then the shear stress causing yielding can be written as follows:

$$(\sigma_{sy} - \sigma_{si})\left(\frac{d}{r}\right)^{1/2} = \sigma_{sd}, \tag{12.62}$$

where σ_{si} is the friction stress, or the stress opposing dislocation motion in the slip plane. Equation (12.62) can be written in terms of the normal stress where $\sigma = M\sigma_s$ and M is the Taylor factor defined as the ratio of the axial stress to the resolved shear stress:

$$\begin{aligned}\sigma_y &= \sigma_i + M\sigma_{sd}\left(\frac{r}{d}\right)^{1/2} \\ &= \sigma_i + k_y d^{-1/2}.\end{aligned} \tag{12.63}$$

Equation (12.63) is the Hall–Petch equation, which describes the grain size dependence of the yield stress. Note that the yield strength increases with decreasing grain size. Yield behavior in metals is generally found to follow this relation for nominal grain sizes (few to hundreds of micrometers), but fails at very low grain sizes in the nanometer range.

12.2 Irradiation Hardening

Irradiation of a metal causes strengthening by *source hardening* and *friction hardening*. Source hardening is the increase in stress required to start a dislocation moving on its glide plane. The applied stress required to release a dislocation into its slip plane is called the *unpinning* or unlocking stress. Once moving, the

dislocation can be impeded by natural- or radiation-produced obstacles lying close to or in the slip plane. The resistance to motion caused by these obstacles is referred to as friction hardening. Both of these concepts will be discussed and then applied to describe the hardening resulting from each of the radiation-induced defects listed earlier. It should be noted, however, that the true distinction between source and friction hardening is unclear, as lattice hardening produces all the characteristics of the deformation that has been attributed to source hardening. The loss of distinction is due to the fact that the distance between defect clusters is less than the source length that would produce the observed critical shear stress. Therefore, the *source* cannot operate without interference from the lattice clusters [5]. Nevertheless, we will treat them separately in the following sections. Hardening mechanisms will first be discussed for single crystals containing an obstacle of a single type. The superposition of hardening from different origins in a single crystal will be treated next followed by an extension of theory to the polycrystalline solid.

12.2.1 Source Hardening

Source hardening is found in irradiated fcc, and both unirradiated and irradiated bcc metals. In unirradiated bcc metals, source hardening is manifested by the upper and lower yield points in the stress–strain curves (Fig. 12.4(b)) and is thought to be caused by the pinning or locking of dislocation lines by impurity atoms. Before a Frank–Read source can operate under an applied stress, the dislocation line must be unpinned from the impurities. This requires a larger stress than that to move the dislocation, causing a drop in the yield stress. Yield then continues at a constant *flow stress* (*Lüders* strain region) until the onset of work hardening which progresses in the same manner as in fcc metals.

Source hardening is found in irradiated fcc metals in which irradiation-produced defect clusters in the vicinity of Frank–Read sources raise the stress required to expand the loops and to permit source multiplication. Once the stress level is sufficient to release the source, the moving dislocations can destroy the small clusters and reduce the stress needed to continue the deformation.

In unirradiated fcc metals, the stress required to initiate dislocation motion is the unpinning stress of the Frank–Read sources in the metal and is given by Eq. (7.32a) as $\sigma_{\mathrm{FR}} = \frac{\mu b}{l}$, where μ is the shear modulus, b is the Burgers vector, and $l(=2R)$ is the distance between pinning points shown in Fig. 7.25. Note that the stress is inversely proportional to the distance between pinning points. The gradual onset of yielding characteristic in fcc metals is generally explained by a distribution of stresses required to operate the sources. At low applied stress, dislocation sources easiest to operate (with large separation between pinning points) begin to generate dislocations. As dislocations are generated and move through the lattice, they begin to pile up and exert a back stress on the dislocation source, ceasing its operation and hence

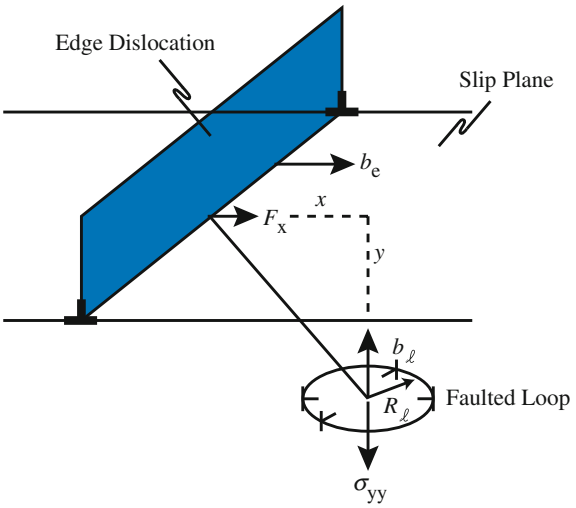

Fig. 12.6 Hardening by faulted loops caused by the interaction of stress fields between an edge dislocation moving on its slip plane located parallel to and displaced a distance y from the plane of the loop (after [3])

the plastic strain. With increasing applied stress, more dislocation sources are activated and dislocation multiplication increases.

Source hardening requires the dislocation line segment to bow out between the pinning points, which requires strong pinning. However, release of the dislocation will occur at lower values of applied stress if the dislocation segment is able to unlock itself before bowing occurs. That is, applied stresses below that required to operate a Frank–Read source are able to push the dislocation line segment past the pinning points. This process could occur, for example, if the pinning points consisted of small dislocation loops or defect clusters. The stress necessary to unlock a dislocation line segment from a small loop can be estimated using the analysis in [3].

Consider a group of edge character loops arranged in a row, each having Burgers vector b_ℓ, radius r, and spacing l, and are at a stand-off distance y from the straight edge dislocation of Burgers vector b_e, as shown in Fig. 12.6. Referring to the interaction between edge dislocations presented in Sect. 7.1.7, only the σ_{yy} term exerts a stress on the loop that acts to expand or contract it. The force on the loop due to the σ_{yy} component of stress from the straight edge dislocation is $2\pi r\sigma_{yy}b_\ell$, and the work to expand the loop is given as:

$$\begin{aligned} \frac{dW}{dr} &= 2\pi r\sigma_{yy}b_\ell \\ W &= \pi r^2\sigma_{yy}b_\ell. \end{aligned} \tag{12.64}$$

Substituting for the stress, σ_{yy}, given by Eq. (7.15), into Eq. (12.64) and differentiating with respect to x gives the force between the loop and the edge segment in the x-direction:

$$F_x = \frac{-\partial W}{\partial x} = -\frac{\mu b_\ell b_e r^2}{1-\nu}\frac{xy(3y^2 - x^2)}{(x^2+y^2)^3}. \tag{12.65}$$

Singh et al. [6] noted that the force is a maximum at an angle of about 40° between the distance vector and the glide plane of the dislocation and the value of the force can be written as a function of r/y:

$$F_x^{\max} \approx \frac{0.28\mu b^2}{(1-\nu)}\left(\frac{r}{y}\right)^2 \approx 0.4\mu b^2\left(\frac{r}{y}\right)^2, \tag{12.66}$$

for $\nu = 1/3$ and $b_\ell = b_e$. Given that $F = \sigma_s bl$, then:

$$\sigma_s = \frac{0.4\mu b}{l}\left(\frac{r}{y}\right)^2. \tag{12.67}$$

Singh suggests that $y = 1.5r$ is consistent with the observed microstructure, yielding a relation for the shear stress in terms of the loop spacing as:

$$\sigma_s = \frac{0.18\mu b}{l}. \tag{12.68}$$

Note that this value of shear stress is considerably less than that to initiate a Frank–Read source by bowing of the dislocation segment of $\sigma_{FR} = \frac{\mu b}{l}$.

Singh et al. also postulated that the unlocking process occurred by interaction between an edge segment and a network of loops that are no longer well separated, but have lost their individuality and act as a network. For this case, the yield stress can be estimated by the stress necessary to overcome the interaction between dislocation dipoles. This problem is treated in more detail in Chap. 13, in which the shear stress is provided in Eq. (13.23) as:

$$\sigma_s = \frac{\mu b}{8\pi(1-\nu)y} \approx \frac{0.06\mu b}{y}, \tag{12.69}$$

for $\nu = 1/3$.

12.2.2 Friction Hardening

Friction hardening refers to the stress required to sustain plastic deformation, which is often termed the flow stress, or friction stress. The forces responsible for resisting dislocation motion through a crystal lattice arise from the dislocation network and obstacles such as defect clusters, loops, precipitates, voids. These sources of

hardening are characterized as either long range or short range. Long-range stresses are caused by dislocation–dislocation interaction by virtue of their stress fields. Short-range stresses have their origin in the interaction between the moving dislocation and the discrete obstacles in the slip plane. The total applied shear stress necessary to overcome both long-range and short-range forces in order to move the dislocation is given as:

$$\sigma_{\mathrm{F}} = \sigma_{\mathrm{LR}} + \sigma_{\mathrm{SR}}, \tag{12.70}$$

where σ_{F} is the friction stress and the subscripts LR and SR represent long- and short-range contributions, respectively, and σ_{SR} is given by:

$$\sigma_{\mathrm{SR}} = \sigma_{\mathrm{ppt}} + \sigma_{\mathrm{void}} + \sigma_{\mathrm{loops}}, \tag{12.71}$$

where the terms on the right-hand side of the equality correspond to precipitates, voids, and loops, respectively.

Long-Range Stresses

Long-range forces arise from the repulsive interaction between a moving dislocation and components of the dislocation network of the solid. Dislocations on parallel glide planes exert forces on each other due to their stress fields, which constitute the long-range stress fields. Referring back to Eq. (7.50) describing the force between edge dislocations, the maximum force occurs at an angle $\theta = 0°$, which yields a value of:

$$F_x(0°) = F_{\mathrm{LR}} = \frac{\mu b^2}{2\pi(1-\nu)r}. \tag{12.72}$$

Taking ν = 1/3, and the distance between dislocations, r from Eq. (5.85) as $1/\sqrt{\pi\rho_{\mathrm{d}}}$, where ρ_{d} is the dislocation density gives:

$$F_{\mathrm{LR}} = \frac{\mu b^2\sqrt{\pi\rho_{\mathrm{d}}}}{4/3\pi} \approx \frac{\sqrt{\pi}\mu b^2\sqrt{\rho_{\mathrm{d}}}}{4} \approx \alpha\mu b^2\sqrt{\rho_{\mathrm{d}}}, \tag{12.73}$$

where α is a constant. The stress needed to overcome this force is $\sigma_{\mathrm{LR}} = F_{\mathrm{LR}}/b$, giving:

$$\sigma_{\mathrm{LR}} = \alpha\mu b\sqrt{\rho_{\mathrm{d}}}. \tag{12.74}$$

Note that if the long-range stress is equated to the unpinning stress given as the grain size-dependent term in Eq. (12.63), then the yield strength can be written as:

$$\sigma_{\mathrm{y}} = \sigma_{\mathrm{i}} + \alpha M\mu b\rho_{\mathrm{d}}^{1/2}. \tag{12.75}$$

Equation (12.75) actually represents a different way of obtaining the grain size dependence of the yield stress, since the dislocation density has been observed to vary with grain size, d as $\rho_d = 1/d$.

Short-Range Stresses

Short-range forces are due to the interaction between a moving dislocation and an obstacle that lies in its slip plane. Short-range forces arise only when the dislocation contacts the obstacle. Short-range forces can be classified into athermal and thermally activated interactions. An athermal stress interaction is independent of temperature and results in the dislocation bowing around the obstacle. In thermally activated processes, the dislocation will overcome the obstacle either by cutting through, or climbing over it. Both processes require the addition of energy through an increase in temperature. We will discuss dislocation bowing around the obstacle and obstacle cutting in this section, and the process of climb will be described in detail in Chap. 13 on creep.

The friction stress due to a dispersion of barriers depends on the average separation between the obstacles in the slip plane of the moving dislocation. Figure 12.7 shows a unit area of a slip plane that is intersected by portions of spherical objects of diameter d, which are randomly distributed throughout the solid at a concentration of N cm^{-3}. Any sphere that has its center within the slab of volume d centered on the slip plane intersects the slip plane. The number of obstacles in this volume element is Nd, which is also the number of intersections per unit area on the slip plane. The product of the number of intersections per unit area, Nd, and the square of the distance between obstacles, l^2, is unity, yielding the distance between obstacles:

$$l = (Nd)^{-1/2}. \tag{12.76}$$

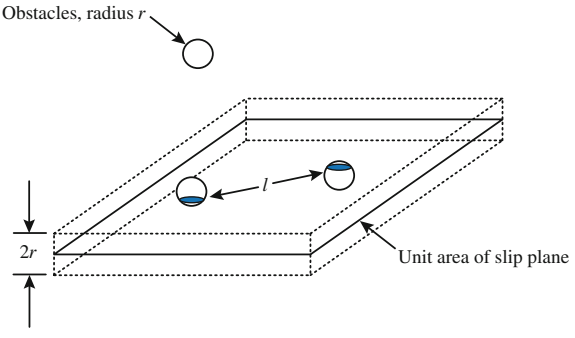

Fig. 12.7 Schematic showing the intersection of spherical obstacles of radius r and spacing l with a unit area of slip plane (after [3])

Precipitates

When a dislocation encounters an obstacle such as an incoherent precipitate, the short-range interaction occurs when it physically contacts the obstacle. For strong obstacles, an applied stress will cause the dislocation to bow out between the obstacles. Bowing will continue until adjacent segments touch and annihilate each other. This "pinch-off" process is exactly the same as occurs in a Frank–Read source. Following pinch-off, the dislocation is free to continue along its glide plane until it encounters the next obstacle and the process repeats itself. The obstacles are left with a dislocation loop surrounding them, which presents a stronger obstacle to the next dislocation that comes along (Fig. 12.8(a)). The short-range stress due to an array of obstacles of density N and size d is determined as follows. The line tension of an edge dislocation was given in Eq. (7.22) as $\Gamma \approx \frac{\mu b^2}{4\pi} \ln\left(\frac{R}{r_c}\right)$, where R is equated to the grain radius and r_c is the dislocation core radius and the dislocation

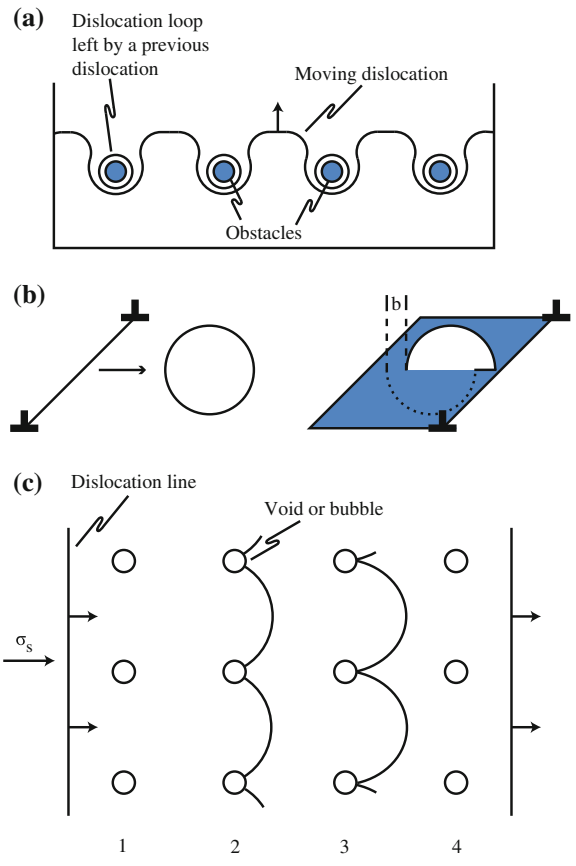

Fig. 12.8 (**a**) Dislocation bowing around hard obstacles such as precipitates. (**b**) Dislocation cutting of an obstacle such as a precipitate. (**c**) Dislocation interaction with voids

core energy is neglected. From Eq. (7.31), the shear stress is related to the line tension by $\sigma_s = \Gamma/bR$. Substituting for Γ from Eq. (7.22) and setting $R = l/2$ where l is the obstacle spacing gives:

$$\sigma_s \approx \frac{\mu b}{l}\frac{1}{2\pi}\ln\left(\frac{l}{2r_c}\right). \tag{12.77}$$

Substituting for l from Eq. (12.76) gives:

$$\sigma_s \approx \alpha\mu b\sqrt{Nd}, \tag{12.78}$$

where $\alpha \approx \frac{1}{2\pi}\ln\left(\frac{l}{2r_c}\right)$. The applied stress at yield, σ_y, is related to the resolved shear stress, σ_s, by the Taylor factor, M such that $\sigma_y = M\sigma_s$, and Eq. (12.77) can be written in terms of the applied stress as:

$$\sigma_y \approx \alpha M\mu b\sqrt{Nd}. \tag{12.79}$$

Stoller and Zinkle [7] have shown that M is actually an upper limit for the ratio of uniaxial yield strength to resolved shear strength and has the value of 3.06 for both fcc and bcc lattices. Equation (12.79) is generally written as:

$$\Delta\sigma_y = \alpha M\mu b\sqrt{Nd}, \tag{12.80}$$

where $\Delta\sigma_y$ represents the *increment* in the yield strength due to the obstacles of size d, number density N, and strength α. In fact, the term α represents the strength of the specific barrier in terms of the Orowan hardening model. A perfectly hard barrier would have a value of $\alpha = 1$. Hardening according to Eq. (12.80) is often termed *dispersed barrier* hardening after the original formulation of Seeger [8].

Dislocation bowing provides the greatest strengthening by obstacles. However, obstacle cutting can also provide strengthening. Obstacle cutting results in hardening by a variety of mechanisms, summarized by Dieter [1] as follows:

1. Shearing of the particle creates a step of width b on either side of the particle and the increase in surface area requires additional work be done to shear the particle.
2. If the particles are ordered structures, such as intermetallic compounds, then the shearing will also produce a new interface within the particle that will require extra energy.
3. Hardening also arises from the difference between the elastic moduli of the matrix and particle, which affects the line tension of the dislocation requiring additional stress to cut the particle.
4. Strengthening also occurs due to the difference in Peierls stress between the particle and matrix.

Figure 12.8(b) shows the result of a dislocation cutting an obstacle. The resulting obstacle is sheared and the top and bottom halves are displaced along the glide plane by an amount equal to the magnitude of the Burgers vector of the dislocation. Successive shearing of the obstacle on the same plane can result in complete separation of the two parts resulting in two smaller obstacles.

Molecular dynamic (MD) simulation of dislocation–obstacle interaction provides a means of visualizing complicated microstructural processes as shown in the following sections. It is important to note, however, that simulations are only as good as the interatomic potentials that define them and they may be influenced by other factors such as the size of the simulated volume and the strain rate. Hence, their value is largely in their qualitative description rather than as a strict quantitative interpretation.

Movies 12.1–12.3 (http://rmsbook2ed.engin.umich.edu/movies/) show molecular dynamic simulations of the interaction between a dissociated edge dislocation and a cobalt precipitate in copper as a function of precipitate size at a temperature of 10 K and under an applied stress of 100 MPa. The precipitate diameter in Movie 12.1 is 1.5 nm and it is sheared by both partials of the edge dislocation. Movies 12.2 and 12.3 are for 3 and 5 nm diameter precipitates, respectively, and show that while the first partial shears the precipitate, the trailing partial undergoes Orowan bowing and pinch-off, leaving a ring around the precipitate as shown in the schematic illustration in Fig. 12.8(a). Movie 12.4 shows the shearing of a 2-nm copper precipitate. The first part of the movie shows the behavior of the dislocation line in the shearing process, and the second part shows the shearing of the precipitate to result in an offset of the part of the precipitate above the slip plane relative to that below, as illustrated in Fig. 12.8(b).

For the case where hardening results from the difference in moduli between the precipitate and the matrix, such as for large vacancy clusters or copper-rich precipitates in ferritic pressure vessel steels, the Russell and Brown model [9] has been found to best describe hardening. They showed that the yield stress in shear is a function of the obstacle spacing in the slip plane, l, and the critical angle at which the dislocation can cut an obstacle, ϕ:

$$\begin{aligned} \sigma_{sy} &= 0.8\frac{\mu b}{l}\cos\frac{\phi}{2} \quad \text{for } \phi \leq 100^\circ \\ \sigma_{sy} &= 0.8\frac{\mu b}{l}\left(\cos\frac{\phi}{2}\right)^{3/2} \quad \text{for } \phi > 100^\circ \end{aligned} \tag{12.81}$$

and when $\phi = 0$, the stress is the Orowan stress. They showed that if a dislocation crosses an interface and has energy E_1 per unit length on one side and energy E_2 per unit length on the other, then the equilibrium of the dislocation requires that $E_1 \sin \theta_1 = E_2 \sin \theta_2$, where θ_1 and θ_2 are the angles between the dislocation and the normal to the interface. When the energy of the dislocation is lower in the precipitate than it is in the matrix ($E_1 < E_2$), then the angle ϕ has a minimum value

when the dislocation is about to break away, given by $\phi_{\min} = 2\sin^{-1}(E_1/E_2)$, and the strength from Eq. (12.81) is given by:

$$\begin{aligned} \sigma_{sy} &= 0.8\frac{\mu b}{l}\left[1-\frac{E_1^2}{E_2^2}\right]^{1/2} \quad \text{for } \sin^{-1}\frac{E_1}{E_2} < 50^\circ \\ \sigma_{sy} &= 0.8\frac{\mu b}{l}\left[1-\frac{E_1^2}{E_2^2}\right]^{3/4} \quad \text{for } \sin^{-1}\frac{E_1}{E_2} \geq 50^\circ, \end{aligned} \tag{12.82}$$

where:

$$\frac{E_1}{E_2} = \frac{E_1^\infty \log\frac{r}{r_c}}{E_2^\infty \log\frac{R}{r_c}} + \frac{\log\frac{R}{r}}{\log\frac{R}{r_c}}, \tag{12.83}$$

and E^∞ is the energy per unit length of dislocation in the infinite media, R is an outer cut-off radius (taken as half the distance to the next obstacle) and r_c is the dislocation core radius. The stresses in Eq. (12.82) depend inversely on the particle spacing, l, and therefore decrease as the particle radius increases (for constant volume fraction of precipitate). However, combining Eq. (12.83) with Eq. (12.82) yields a maximum in the relation between strength and precipitate size. For voids or for precipitates in pressure vessel steels, the maximum is at about $2r_c$ ($\sim$5a) or $\sim$1.5 nm.

Voids

Dislocations can also cut through voids, although the structure of the void is the same before and after the cut. Precipitates and voids are generally considered to be hard barriers with $\alpha \sim 1$. The only difference between passage of a mobile dislocation through precipitates and voids is that in the case of voids, the dislocation segments always meet the void surface at right angles and leave no dislocation ring after passage through the void (Fig. 12.8(c)). As described by Olander [3], the force to cut through a void is given by:

$$F = \frac{U_V}{R} = \sigma_s b l, \tag{12.84}$$

where U_V is the elastic strain energy in a volume of solid equal to the cavity, R is the radius of the cavity, and l is the void spacing on the slip plane. From Eq. (7.21), the elastic energy per unit volume for a screw dislocation is given as $W = \frac{\mu b^2}{8\pi^2 r^2}$. The elastic energy of the void–dislocation interaction energy can be approximated by the elastic energy in the volume of the void:

$$\begin{aligned} U_{\mathrm{v}} &= \int_{r_{\mathrm{c}}}^{R} 4\pi r^2 W \,\mathrm{d}r \\ &= 4\pi \int_{r_{\mathrm{c}}}^{R} \frac{\mu b^2}{8\pi^2} \mathrm{d}r \\ &= \frac{\mu b^2}{2\pi}(R - r_{\mathrm{c}}) \approx \frac{\mu b^2 R}{2\pi}. \end{aligned} \tag{12.85}$$

Substituting into Eq. (12.84) and solving for σ_{s} gives:

$$\sigma_{\mathrm{s}} = \frac{1}{2\pi}\frac{\mu b}{l}, \tag{12.86}$$

which is smaller than the Orowan stress, Eq. (7.32a) by a factor of $1/2\pi$ indicating that cutting of voids requires less energy than bowing around them. Written in the form of Eq. (12.80) gives:

$$\Delta\sigma_{\mathrm{y}} = \alpha M \mu b \sqrt{Nd}, \quad \alpha \approx 0.16 \tag{12.87}$$

A more complete treatment of dislocation–void interaction accounts for image stresses, dislocation self-interaction, and elastic anisotropy of the crystal. The image stress must be added to the dislocation stress in order to make the void surfaces traction free. Dislocation self-interaction refers to the dipole-like attractive forces between the dislocation branches terminating at a void, which can aid in pulling the branches together around the void, thus diminishing strengthening effects. Finally, elastic anisotropy of the crystal containing the void row must be accounted for in the dislocation stress field calculation. Inclusion of these factors in the calculation of the stress necessary for a dislocation to cut a void shows that the void is a very strong obstacle, approaching the Orowan stress value for impenetrable obstacles. A detailed treatment of these effects is given in [10].

The interaction between dislocations and voids is illustrated in Movies 12.5–12.7 (http://rmsbook2ed.engin.umich.edu/movies/). Movie 12.5 shows the interaction of leading and trailing partials of a dissociated edge dislocation with a 3 nm void in copper at 0 K. Note that the dislocation lines maintain a right angle with the void surface throughout the interaction. Movie 12.6 shows the shearing of a 1 nm void in iron by a dislocation and the resulting stress–strain behavior due to the dislocation–void interaction. In these three perspectives, the displacement of the top half of the void relative to the bottom half is evident. Finally, Movie 12.7 shows the repeated shearing by multiple dislocations of a 2.6 nm He bubble under an applied shear stress of 100 MPa. Note that the bubble appears to elongate in the direction of the applied stress, due to the offset of the half above the slip plane relative to that below, similar to that shown in Fig. 12.8(b).

Loops

The interaction between a mobile dislocation and a loop was described in Sect. 12.2.1 where it was shown that the stress in Eq. (12.68) is of the order $\sigma_s \sim \dfrac{0.2\mu b}{l}$ and for l given by Eq. (12.76) the stress becomes:

$$\sigma_s = 0.2\mu b\sqrt{Nd}, \tag{12.88}$$

which is well below the Orowan stress. Written in the form of Eq. (12.80), the yield strength increment due to loops is given as:

$$\Delta\sigma_y = \alpha M\mu b\sqrt{Nd}, \quad \text{with } \alpha \approx 0.2. \tag{12.89}$$

The types of interactions between dislocation lines and loops described in this chapter are illustrated in Movies 12.8–12.12 (http://rmsbook2ed.engin.umich.edu/movies/). In Movies 12.8 and 12.9, the interaction between the dislocation and the loop is through the stress fields. Movie 12.8 shows an edge dislocation in copper (edge on: red spheres are the partials), interacting with a 37 SIA perfect loop (green spheres) a distance 2 loop diameters from the dislocation. Both have Burgers vector 1/2[110]. Note that as the dislocation moves, the interacting strain fields drag the loop in the direction of the moving dislocation. Movie 12.9 shows an edge dislocation bypassing a 153 SIA Frank loop at 100 K under an applied stress of 300 MPa in copper. The blue spheres are atoms in the fcc crystal and the yellow spheres are atoms in the stacking fault. During the non-intersecting interaction, the Frank loop rotates to become a mobile perfect loop and glides to annihilation at the free surface.

Movies 12.10–12.12 illustrate interactions in which the dislocation contacts the loop. Movie 12.10 shows a dissociated screw dislocation shearing the same Frank loop under the same conditions as that shown in Movie 12.9. Note that the sheared loop is absorbed into the screw dislocation core. Movie 12.11 is another example of a screw dislocation interacting with a perfect loop (same Burgers vector) in which the loop is absorbed and then re-emitted a distance away from the original absorption point, and the dislocation cross slips onto a different glide plane. Movie 12.12 shows an edge dislocation interacting with and unfaulting a Frank loop (5 nm, 331 SIA) in iron at 300 K, resulting in near destruction of the loop.

Another type of faulted defect, the stacking-fault tetrahedron, described in Chap. 7, also interacts with dislocations and can contribute to hardening. Movie 12.13 shows the interaction of successive edge dislocations with a 153-vacancy SFT at 100 K under an applied stress of 100 MPa in copper. The SFT is sheared into a smaller SFT and a truncated base and subsequent interactions result in absorption of the truncated base into the dislocation. Movie 12.14 shows the details of the interaction between edge partials shown in Movie 12.13 but at a slower rate and with a 45-vacancy SFT.

Movies 12.15–12.17 show the interaction of a screw dislocation with an SFT in Cu. In Movie 12.15, the 45-vacancy SFT is sheared and in Movie 12.16, the 98-vacancy SFT is absorbed and then re-emitted. Movie 12.17 shows a 78-vacancy SFT being absorbed and re-emitted as a smaller SFT and a separate truncated base. A real-time movie of a dislocation–SFT interaction in copper was conducted on a sample under dynamic loading in the stage of a transmission electron microscope at room temperature, Movie 12.18. The SFTs were introduced by quenching the copper specimen in iced brine after a 2 h anneal at 1073 K. The weak-beam dark-field movie shows a dislocation being pinned by a stacking-fault tetrahedron. The result of the interaction is the formation of a perfect loop. Finally, Movies 12.19 and 12.20 show the interaction of a screw dislocation in copper with multiple defects: a 78-vacancy SFT and a perfect loop consisting of 61 interstitials in Movie 12.19 and 91 interstitials in Movie 12.20.

Effect of Temperature

As described in the preceding section, obstacle strength and density determine the velocity of dislocations in a polycrystal. If the Gibbs free energy of activation for cutting or bypassing an obstacle is $\Delta G(\sigma_s)$, then the mean velocity of a dislocation segment, $\bar{v}$, is given by [11]:

$$\bar{v} = \beta b v \exp\left(-\frac{\Delta G(\sigma_s)}{kT}\right), \tag{12.90}$$

where β is a dimensionless parameter, b is the magnitude of the Burgers vector, v is the ground frequency of the dislocation, and σ_s is the shear stress. The term $\Delta G(\sigma_s)$ is a function of the internal stress and the distribution of obstacles and for a regular array of obstacles, it can be expressed as:

$$\Delta G(\sigma_s) = \Delta F\left(1 - \frac{\sigma_s}{\sigma_s^0}\right), \tag{12.91}$$

where ΔF is the total free energy (activation energy) required to overcome the obstacle without aid from an external stress. The term σ_s^0 is the stress at which a dislocation can move through the obstacle with no help from thermal energy, or essentially, the flow stress at 0 K where $\Delta G = 0$.

Generalizing to a random array of obstacles [11], Eq. (12.91) becomes the following:

$$\Delta G(\sigma_s) = \Delta F\left[1 - \left(\frac{\sigma_s}{\sigma_s^0}\right)^p\right]^q, \tag{12.92}$$

Table 12.1 Strength of various obstacle types causing source and friction hardening in irradiated metals

Type of strengthening	Obstacle classification	Obstacle type	Stress increment	Value of α
Source		Loops	$\sigma_s = \frac{0.18\mu b}{l}$ isolated loops $\sigma_s \approx \frac{0.06\mu b}{y}$ loop network	
Friction	Long range	Dislocation network	$\sigma_{LR} = \alpha\mu b\sqrt{\rho d}$	<0.2
	Short range	Precipitates and voids	$\Delta\sigma_y = \alpha M\mu b\sqrt{Nd}$	1.0 bowing 0.3–0.5 cutting
		Dislocation loops		0.25–0.5
		Black dots		< 0.2

where $0 \le p \le 1$ and $1 \le q \le 2$, and where σ_s^0 is given phenomenologically by:

$$\frac{\sigma_s}{\sigma_s^0} = \left[1 - \left(\frac{T}{T_0}\right)^p\right]^q, \tag{12.93}$$

where reasonable limiting behavior is found with $p = 2/3$ and $q = 3/2$ [12]. Since the strain rate is proportional to the average dislocation velocity (see Sect. 13.1), the rate equation for discrete obstacle controlled plasticity is given by:

$$\dot{\varepsilon} = \dot{\varepsilon}_0 \exp\left\{-\frac{\Delta F}{kT}\left[1 - \left(\frac{\sigma_s}{\sigma_s^0}\right)^p\right]^q\right\}, \tag{12.94}$$

which captures both the stress and the temperature dependence of dislocation passage through a random array of obstacles.

Hardening due to long-range and short-range obstacles is summarized in Table 12.1 using Eq. (12.80) to describe short-range obstacles. Note that the values of α can vary by a significant amount depending on obstacle type. Much work has been done to determine the value of α experimentally, and column 5 in Table 12.1 gives the generally accepted values for α based on experimental work.

12.2.3 Superposition of Hardening Mechanisms

As discussed in Chaps. 7–9, the microstructure of an irradiated metal can be quite complicated. At very low dose, it consists of defect clusters and small loops. With increasing dose, the loop microstructure saturates at a particular number density and

loop size, and as loops unfault and become part of the dislocation line network, the dislocation density rises. At higher temperatures, voids and bubbles contribute to the microstructure, and irradiation-induced precipitation can also contribute. Each of these features presents a different type of obstacle to the moving dislocation. In order to assess the hardening of a true irradiated microstructure, we must have some way of accounting for obstacles of different types, sizes, and number densities. Below, we treat several special cases of various combinations of short-range and long-range obstacles as originally described by Bement [13].

Long-Range Stresses and Short-Range Obstacles

If long-range internal stresses exist in the lattice, as caused for example by groups of dislocations of predominantly the same sign of Burgers vector, and if in addition, dispersed barriers with a short-range interaction and an average distance, l_{SR} smaller than the average "wavelength" of the long-range stresses, are present, on average the effective stress available for pushing the dislocation over the short-range obstacles (σ_{SR}) is the difference between the applied stress σ_{a} and the stress σ_{LR} necessary for moving the dislocations through the long-range stress field:

$$\sigma_{\mathrm{a}} = \sigma_{\mathrm{LR}} + \sigma_{\mathrm{SR}}, \quad l_{\mathrm{SR}} < l_{\mathrm{LR}}. \tag{12.95}$$

Thus, the total stress is composed of the stress due to the two types of hardening as if each acted independently. Such is not the case if two types of short-range obstacles are present.

Two Types of Short-Range Obstacles

In an irradiated microstructure consisting of two types of short-range obstacles, the superposition depends sensitively on the strengths and relative concentrations of the two types of obstacles.

Two Strong Obstacles If both types of obstacles are strong such that dislocations interact by means of the Orowan mechanism, the moving dislocation cannot distinguish between them, and the sum of the area densities, *N,* of the two obstacles in the glide plane determines the effective obstacle distance:

$$l = \frac{1}{\sqrt{N_1 + N_2}}, \tag{12.96}$$

$$\text{and} \quad \frac{1}{l^2} = \frac{1}{l_1^2} + \frac{1}{l_2^2}, \tag{12.97}$$

$$\text{giving} \quad \sigma_{\mathrm{a}}^2 = \sigma_1^2 + \sigma_2^2, \tag{12.98}$$

where σ_1 and σ_2 are the critical (short-range) stresses of the obstacles of type 1 or 2 with average distances l_1 and l_2, respectively, would act separately. This root-sum-square (RSS) model was shown by Foreman and Makin [14] to apply for a population of obstacles with similar strengths. However, the behavior of the dislocation differs depending on the strength of the obstacle. Figure 12.9 shows the final configuration of a dislocation line just prior to yielding for obstacle strength, α, of 0.1, 0.5, and 0.8 [15]. If there are types of obstacles in the lattice which can be surmounted with the help of thermal activation and for which the forces (F_1 and F_2) are nearly the same, Eq. (12.98) holds for the same reasons given above.

Two Obstacles with Different Strengths There exist several subcases for combinations of weak and strong particles. Kocks [16] considered the case of many weak and a few strong obstacles giving the conditions:

$$F_1 \ll F_2 \quad \text{with} \quad l_1 \ll l_2. \tag{12.99}$$

If a dislocation segment bows out under the applied stress between two strong obstacles, it cuts through many weak ones in its path. The more it bows out the larger the angle becomes between neighboring branches of the dislocation at the weak obstacles and the smaller (at a given stress) the force is with which the dislocation is pressed against the weak obstacles. Simultaneously, the angle

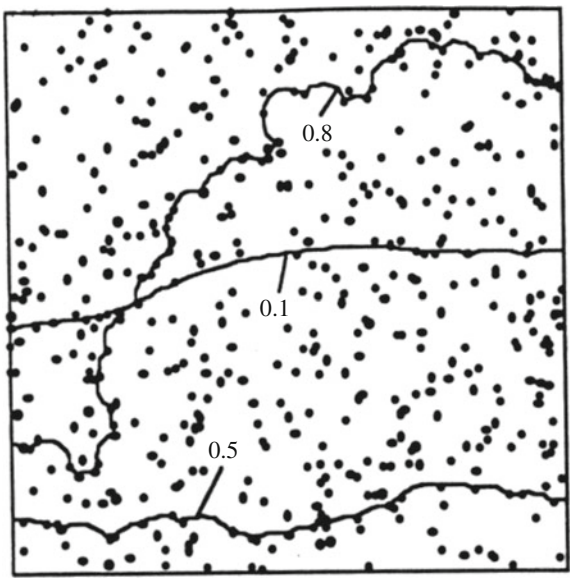

Fig. 12.9 Result of computer simulation of the shape of a dislocation line just prior to yielding for various fixed values of a (0.1, 0.5, 0.8) (after [15])

between the neighboring branches of the dislocation at the strong obstacles becomes smaller and the force acting on them increases (Fig. 12.10). The critical situation is reached when the dislocation can break through weak and strong obstacles simultaneously.

The applied stress required to push the dislocation through this critical configuration is given as:

$$\sigma_a = \sigma_1 + \sigma_2. \tag{12.100}$$

Movie 12.21 (http://rmsbook2ed.engin.umich.edu/movies/) is a real-time movie of dislocation–defect interaction during the straining of an irradiated copper sample. The sample was irradiated with 200 keV Kr^+ to a dose of about 10^{12} i/cm^2 at room temperature in the IVEM at Argonne National Laboratory. The defects consist predominantly of Frank loops with Burgers vector $a/3\langle 111\rangle$ and a smaller density (~ 10 %) of stacking-fault tetrahedra. As shown, the dislocation moves in a jerky manner with small segments breaking free from individual pining points and no observable defect absorption.

If no extreme condition exists as in Eq. (12.99), the thermally activated surmounting of the two types of obstacles must be treated in terms of so-called dependent processes. For such processes, the waiting time t_s (average time during which a dislocation is pressed against an obstacle of type s until it gets enough thermal energy to overcome it) enters the theoretical treatment additively, so that the time a dislocation needs for moving over a given area is proportional to $N_1t_1 + N_2t_2$. If $N_1t_1 \gg N_2t_2$, the effective flow stress is determined almost

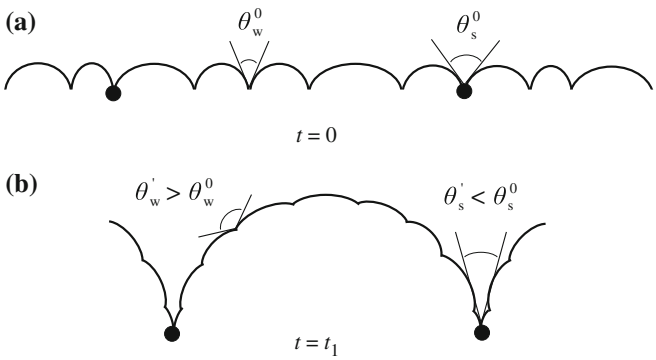

Fig. 12.10 Movement of a dislocation in an obstacle field consisting of many weak and a few strong obstacles (**a**) before application of a stress and (**b**) after the dislocation has moved past many of the weak barriers

exclusively by the obstacles of type 1; type 2 is "transparent" for the dislocation under the stress necessary to overcome type 1:

$$\sigma_a \approx \sigma_1 \quad \text{for } N_1 t_1 \gg N_2 t_2;\ \sigma_1 \gg \sigma_2 \tag{12.101a}$$

$$\sigma_a \approx \sigma_2 \quad \text{for } N_1 t_1 \ll N_2 t_2;\ \sigma_1 \ll \sigma_2. \tag{12.101b}$$

This means that if type 2 obstacles are added to a constant concentration of type 1 obstacles, Eq. (12.101a) holds for small concentration and Eq. (12.101b) for high concentrations of type 2 obstacles so that a transition occurs in the effective flow stress from σ_1 to σ_2. In extreme cases of very low or very high concentrations of type 2 obstacles, the stresses that the two types of obstacles would demand separately determine the effective flow stress.

In summary, the RSS superposition law, $\Delta\sigma_{yr} = \sqrt{\sum_i \left(\Delta\sigma_{yi}\right)^2}$ works well when obstacles have similar strengths, and the linear sum, or superposition law, $\Delta\sigma_{yl} = \sum_i \Delta\sigma_{yi}$ is better as the strengths become more dissimilar. Odette [16] has shown that hardening in a microstructure consisting of a wide range of obstacle strength is best fit by a combination of the root-square-sum and linear sum models, with the following weighting parameter, S:

$$\left(\Delta\sigma_y - \Delta\sigma_{yr}\right) = S\left(\Delta\sigma_{yl} - \Delta\sigma_{yr}\right) \tag{12.102}$$

and S can be related to the obstacle strengths by:

$$S \approx \alpha_s - 5\alpha_w + 3.3\alpha_s\alpha_w, \tag{12.103}$$

such that $S = 1$ for the linear sum law and $S = 0$ for the RSS law. According to Eq. (12.103), S decreases with increasing α_w (stronger weak obstacles) and decreasing α_s (weaker strong obstacles). The superposition rules for different hardening mechanisms are summarized in Table 12.2.

Using Eqs. (12.80) and (12.75), observed trends in the dose and temperature dependence for ρ_d and $\sqrt{Nd}$, and the obstacle strengths ($\alpha_{voids} = 1.0$) listed in Table 12.1, Lucas [17] estimated the hardening as a function of dose for three temperatures, as shown in Fig. 12.11. While these are only predictions, they serve to illustrate the relative contributions to hardening of the various microstructure features. In stainless steels, low-temperature (100 °C) hardening is dominated by black dot damage and small loops at low doses and the network density at higher doses. Above about 400 °C, voids and bubbles begin to make a contribution to the hardening. Intermediate to these temperatures, hardening is a maximum (near 300 °C) due to the combination of black dots, loops, and He bubbles. At lower doses, voids and loops contribute the majority of hardening, but at higher doses, the dislocation microstructure and voids become the major source of hardening [18]. These predictions differ somewhat from LWR data at ~300 °C [19] and even up to 400 °C [20, 21] in that the peak in hardness is not observed. This is likely due to the stability

Table 12.2 Superposition rules for hardening

I. Long-range stresses and short-range obstacles
$\sigma_a = \sigma_{LR} + \sigma_{SR}$
II. Two types of short-range obstacles
A. Both types strong
$l = \dfrac{l}{\sqrt{N_1 + N_2}}$
$\sigma_a^2 = \sigma_1^2 + \sigma_2^2$
B. Many weak and few strong
$F_1 < F_2;$ with $l_1 < l_2$
$\sigma_a = \sigma_1 + \sigma_2$
C. Thermally activated motion over barrier
$\sigma_a \approx \sigma_1$ for $N_1 t_1 \gg N_2 t_2; \tau_1 \gg \tau_2$
$\sigma_a \approx \sigma_1$ for $N_1 t_1 \ll N_2 t_2; \tau_1 \ll \tau_2$
III. Wide range of obstacle strength
$(\sigma_y - \sigma_{yr}) = S(\sigma_{yl} - \sigma_{yr})$
$S \approx \alpha_s - 5\alpha_w + 3.3\alpha_s\alpha_w$

of the loop microstructure to high doses at temperatures below 400 °C. At high temperature (600 °C), hardening is dominated by network dislocations. The contribution from voids can be significant at very high doses.

12.2.4 Hardening in Polycrystals

Up to this point, we have considered hardening only in single crystals and have not accounted for the effect of grain boundaries in polycrystalline metals. In polycrystals [13], the flow stress is increased by the influence of the different grain orientations and of the grain boundaries. As described by Eq. (12.63), the *tensile* yield stress depends on the grain size d according to the Hall–Petch relation given by $\sigma_y = \sigma_i + k_y d^{-1/2}$, where σ_i is the friction stress and k_y is the unpinning stress. The term k_y is based on the premise that a slip band is a stress concentration and that plastic flow between grains, and therefore, throughout the polycrystalline solid occurs when the stress concentration due to a dislocation pileup at a boundary is sufficient to activate a dislocation source in the neighboring grain. In the case of iron, steel, and molybdenum, the effect of irradiation on the Hall–Petch relationship is to increase the friction stress σ_i, with little effect on k_y for small grain sizes. For larger grain sizes, samples undergo a greater increase in yield strength which reduces k_y to almost zero (Fig. 12.12).

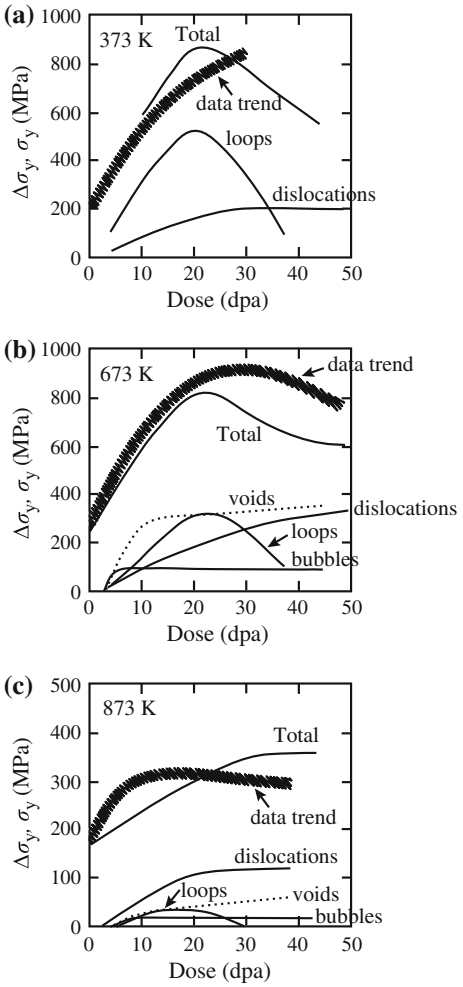

Fig. 12.11 Comparison of model predictions of the contribution to hardening from various microstructure features to data trends at (**a**) 100 °C, (**b**) 400 °C, and (**c**) 600 °C (after [17])

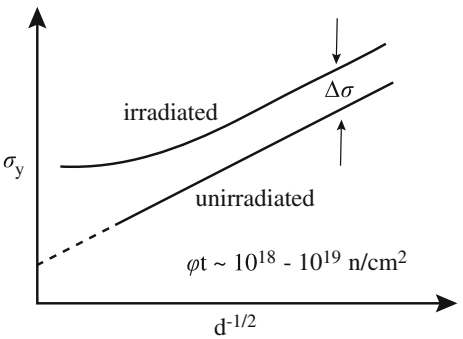

Fig. 12.12 Effects of irradiation on the Hall–Petch relationship for ferritic steel (after [13])

The dislocation density in a solid undergoing plastic deformation increases linearly with strain, ε according to:

$$\rho = \rho_0 + A\varepsilon, \tag{12.104}$$

and

$$A = \beta/d, \tag{12.105}$$

where β is a constant and d is the grain diameter. Recall from Eq. (12.75) that the yield strength is related to the dislocation density by: $\sigma_y = \sigma_i + \mu b \rho_d^{1/2}$, and using Eqs. (12.104) and (12.105) and assuming that $\rho_0 \ll A\varepsilon$, the yield strength can be written as:

$$\sigma_y = \sigma_i + \mu b \left(\frac{\beta\varepsilon}{d}\right)^{1/2}, \tag{12.106}$$

which is equivalent to the Hall–Petch equation with:

$$k_y = \mu b(\beta\varepsilon)^{1/2}. \tag{12.107}$$

In this work hardening model, β is a measure of work hardenability due to dislocation channeling. As β approaches zero in irradiated material because of loss of strain hardenability due to dislocation channeling, the term $\beta\varepsilon/d$ becomes very small and k_y approaches zero.

Data from a low alloy Fe–Mn–C steel was used to chronicle the development of radiation hardening using the Hall–Petch parameters, as well as the strength coefficient K and the strain hardening exponent, n from the power law hardening equation given in Eq. (12.27). Four stages of radiation hardening of a Fe–Cr–Mn steel with progressively increasing dose are shown in Fig. 12.13. Stage A occurs for very low dose (10^{15}–10^{16} n/cm^2) and involves an increase in k_y with negligible increase in stress σ_i, and no change in n and K. The result is an increase in the upper yield point and the Lüder's strain. Stage B occurs around 10^{18} n/cm^2 and represents an increase in σ_i but little change in k_y. In this stage, both n and K decrease, resulting in a reduced slope of the stress–strain curve and an increase in the Lüder's strain. Stage C appears at fluences of about 3×10^{18} n/cm^2 and is characterized by a continued increase in σ_i and a decrease in k_y. The strain hardening exponent, n, continues to decrease but K increases slightly, resulting in a small change in the slope of the stress–strain curve and a small decrease in Lüder's strain. In stage D, σ_i continues to increase and k_y falls nearly to zero. Also both n and K decrease, resulting in a further decrease in the slope of the stress–strain curve and the near disappearance of Lüder's strain. Although this description of the effects of irradiation on stress–strain behavior is specific to the iron alloy system, the changes in the parameters σ_i and k_y are consistent with the current understanding of barrier–hardening interactions, dislocation channeling, and grain size effects, and highlight

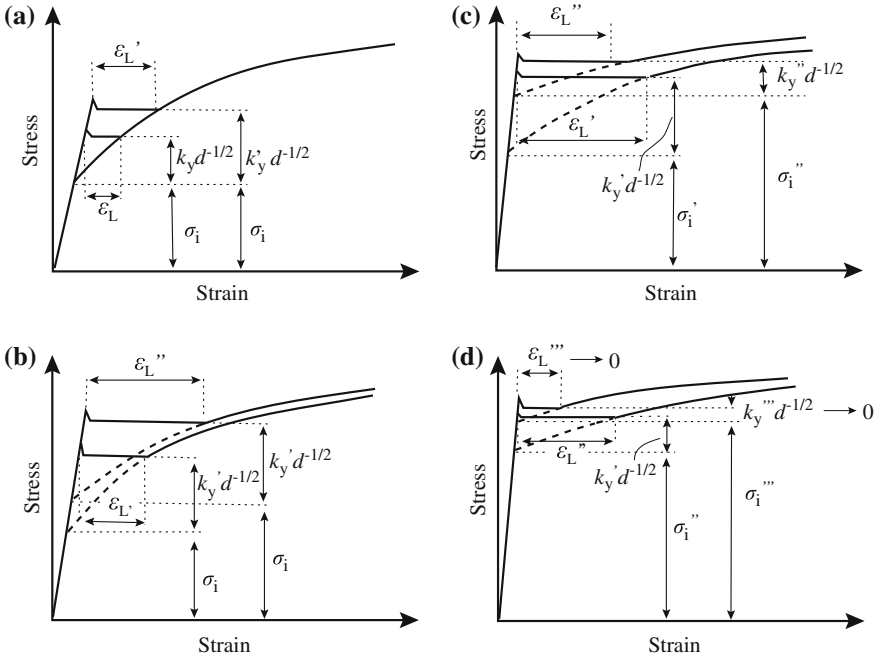

Fig. 12.13 Changes in the stress–strain curves for Fe–Cr–Mn steel irradiated at 80–100 °C to neutron doses of (**a**) 10^{16} n/cm^2, (**b**) 10^{18} n/cm^2, (**c**) 3×10^{18} n/cm^2, (**d**) $>5 \times 10^{18}$ n/cm^2 (after [13])

the changing nature of the fluence dependence of irradiation hardening in polycrystals. However, experimentally, k_y has been observed to either increase or decrease [22] suggesting that the grain size effect is not as well-established as suggested in Fig. 12.12.

12.2.5 Saturation of Irradiation Hardening

According to the dispersed barrier hardening model, Eq. (12.80), the increment in yield strength, $\Delta\sigma_y$ increases as $N^{1/2}$. In the absence of mechanisms for the destruction of obstacles, N is proportional to the total fluence and hence irradiation hardening should be proportional to $(\phi t)^{1/2}$:

$$\Delta\sigma_S \propto (\phi t)^{1/2}. \tag{12.108}$$

That is, the number of obstacles continues to increase with fluence without bound. This is clearly counter to observations of the dislocation microstructure evolution at

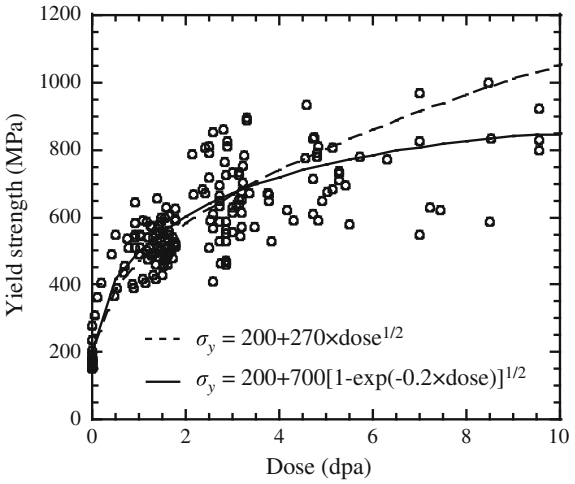

Fig. 12.14 Effect of irradiation dose on measured tensile yield strength for several 300 series stainless steels irradiated and tested at a temperature of about 300 °C (after [19])

LWR temperatures, Chap. 7, in which the dislocation loop density and size are observed to saturate by several dpa. However, at low doses, the hardening described by Eq. (12.108) is reasonably accurate. Figure 12.14 shows the irradiation hardening in 300 series stainless steels irradiated at about 300 °C and tested at about that same temperature. Note that the hardening can be fit with a $(\phi t)^{1/2}$ dependence quite well through about 5 dpa. However, the model described by Eq. (12.108) will clearly overestimate the hardening once saturation of the dislocation microstructure occurs.

In trying to account for saturation of hardening at higher doses, Makin and Minter [23] postulated that if a displacement cascade occurs in the neighborhood of an existing zone or cluster, no new zone is formed. This "prohibited" zone has a volume V. According to this model, as the concentration increases, it becomes harder to form new zones because of the reduced volume available for new zone formation. The time rate of change of the density of zones, N, is then given by:

$$\frac{dN}{dt} = \zeta \Sigma_s \phi (1 - VN), \tag{12.109}$$

where ζ is the number of zones created per neutron collision (~ 1), Σ_s is the macroscopic scattering cross section, and ϕ is the fast neutron flux. The term in parenthesis represents the fraction of solid volume available for the creation of new zones. Integration of Eq. (12.109) gives the following:

$$N = \frac{1}{V}[1 - \exp(-\zeta V \Sigma_s \phi t)], \tag{12.110}$$

and substitution of Eq. (12.110) into Eq. (12.80) yields

$$\Delta\sigma_y = A[1 - \exp(-B\phi t)]^{1/2}. \tag{12.111}$$

where $A = \alpha M \mu b \left(\frac{d}{V}\right)^{1/2}$, and $B = \zeta V \Sigma_s$. Higgy and Hammad [24] found that for 304 SS, 316 SS, and 347 SS above fluences of about 5×10^{19} n/cm^2, the irradiation hardening increment can be described by Eq. (12.111) with $B = 2$–3×10^{-21} cm^2/n. Odette and Lucas [25] found that this same equation fit the data for hardening in 300 series stainless steels irradiated and tested at about 300 °C, with $A \approx 670$ MPa and $B \approx 0.5$ dpa^{-1} with ϕt in units of dpa or $B \approx 7 \times 10^{-22}$ cm^2/n with ϕt in units of n/cm^2 and assuming that 1 dpa $\approx 7 \times 10^{20}$ n/cm^2. Note that application of Eq. (12.111) with similar values of A and B produces a good fit to the data in Fig. 12.14. Bement [26] found that for Zircaloy-2, $B = 2.99 \times 10^{-21}$ cm^2/n at 280 °C.

Fluence exponents of less than 0.5 are commonly observed. Eason [27] found in analyzing a sizable database consisting of several stainless steels that the yield strength increment at 288 °C followed a fluence dependence of the form:

$$\Delta\sigma_y = a\left(\phi t / 10^{20}\right)^b, \tag{12.112}$$

where

- for type 304 and 304L stainless steel, $a \sim 2.05$ and $b = 0.124$,
- for type 316 stainless steel $a = 0.595$ and $b = 0.491$,
- for type 316L stainless steel $a = 0.517$ and $b = 0.562$, and
- for type 347 stainless steel $a = 1.627$ and $b = 0.124$.

Williams and Hunter [21] used a modified form of Eq. (12.111):

$$\Delta\sigma_y = A[1 - \exp(-B\phi t)], \tag{12.113}$$

to fit hardening in an A533-B steel plate using $A = 22$ ksi (152 MPa) and $B = 2 \times 10^{-19}$ cm^2/n (Fig. 12.15).

Saturation occurs when a balance is reached between the creation and the destruction of obstacles. Interstitial and vacancy loops are created from defect clusters. Interstitial loops grow in size as their numbers increase. However, vacancy loops are generally unstable and shrink due to vacancy emission. Interstitial loops are removed by unfaulting. So an alternative formulation for the number of obstacles is to associate a lifetime, τ to these defects, [29] in which case, their density should develop according to:

$$\frac{dN}{dt} = \zeta \Sigma_s \phi - \frac{N}{\tau}, \tag{12.114}$$

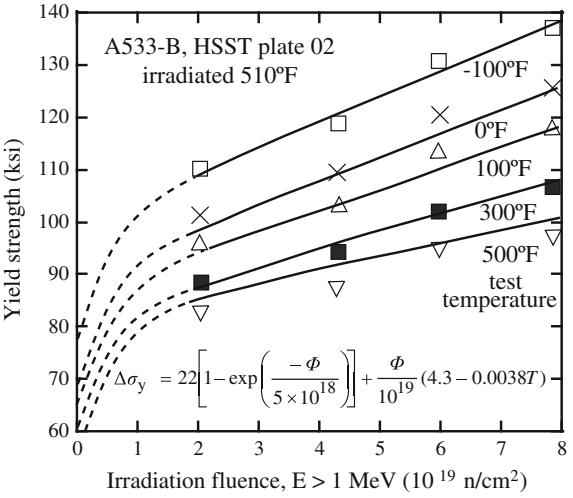

Fig. 12.15 Effect of irradiation fluence on the yield strength of A533-B steel for different test temperatures. Curves are the fits to the yield strength increment given by Eq. (12.113) (after [28])

with a solution of the form:

$$N = \zeta \Sigma_s \phi \tau [1 - \exp(-t/\tau)]. \tag{12.115}$$

12.2.6 Comparison of Measured and Predicted Hardening

The dispersed barrier hardening model has been applied to irradiation hardening of alloys in several systems. The most successful application is in the case of austenitic stainless steels and for irradiated microstructures that are dominated by loops. Figure 12.16 shows the correlation between measured and calculated yield strength for a set of solid solution alloys, which were all derived from a base alloy of composition Fe–18Cr–12Ni–1Mn, and differ in the single element added to the alloy. The alloys were irradiated with 3.2 MeV protons at 360 °C to a dose of 5.5 dpa and the microstructure was characterized by TEM. Loop and void size and density were determined for each alloy. Only the base 316 stainless steel alloy, 316 + Mo, and 316 + Ni/Cr contained voids. The measurements of yield strength in Fig. 12.16 actually come from microhardness indentations (discussed in Sect. 12.2.8) and the calculated hardness values are determined from the dispersed barrier hardening model, Eq. (12.80). In this case, $\alpha = 0.25$ for loops and $\alpha = 0.5$ for voids produced the best fit with the data.

The loop strength of 0.25 is consistent with, although on the low side, of what has been observed in the literature [3, 13, 17, 31–34]. Values of α for loops as high as 0.5 have been deduced from strengthening data [35]. The value of α for voids (0.5) is half that of the theoretical value for Orowan strengthening. However, Ando et al. [36] have shown that cavity shearing is more likely than Orowan pinning,

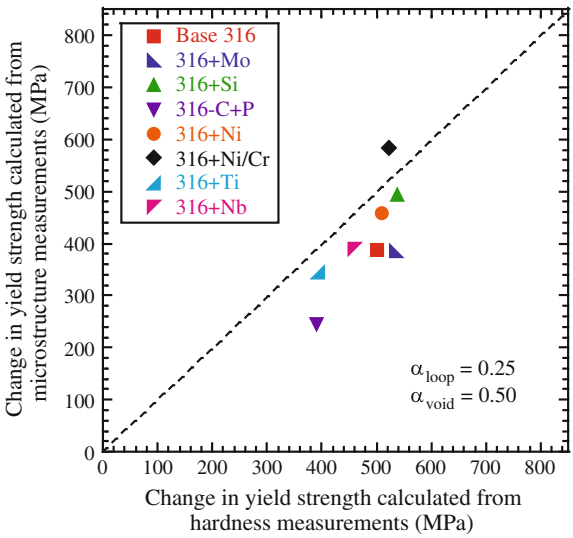

Fig. 12.16 Correlation between measured and calculated yield strength using Eq. (12.80) (after [30])

resulting in a value of $\alpha = 0.5$ rather than 1.0. They concluded that the high value of α observed in some experiments is likely due to cavity–precipitate association. Electron microscopy has revealed that bubbles and MC precipitates nucleate and grow together in austenitic stainless steels [37]. Kelly [38] considered the hardening to be due to two spheres in contact rather than a single obstacle and derived the following relation for the bubble–precipitate pair:

$$\Delta\sigma_{\text{bubble-ppt}} = \frac{0.16M\mu b\sqrt{Nd}}{1 - \frac{\sqrt{6}}{3}\sqrt{Nd}} \ln\left(\frac{\sqrt{6d}}{3b}\right). \tag{12.116}$$

Hardening in ferritic steels used in reactor pressure vessels can be very complicated due to the role of solutes such as copper, nickel, and manganese, and the roles of temperature and irradiation flux. Hardening in RPV steels is controlled by the evolution of two primary classes of ultra-fine scale features: copper-rich precipitates (CRP) and matrix features (MF) [39]. The latter class can be subdivided into unstable matrix features (UMF) and stable matrix features (SMF), such that MF = UMF + SMF. CRPs form from a supersaturated solid solution as a consequence of radiation-enhanced diffusion. These precipitates are extremely small and are best described as nanoscale defects and contribute the largest amount to hardening (Fig. 12.17). They are the dominant feature in irradiated RPV steels that have Cu contents greater than about 1 %. Their size and volume fraction increase with Cu content above about 1 %, but the number density is relatively insensitive to copper in the range 0.2–0.4 %. As such, their significance in hardening increases up to about 0.25–0.35 % Cu [16]. CRPs can also become enhanced in Ni and Mn depending on the amount of these solutes in the steel.

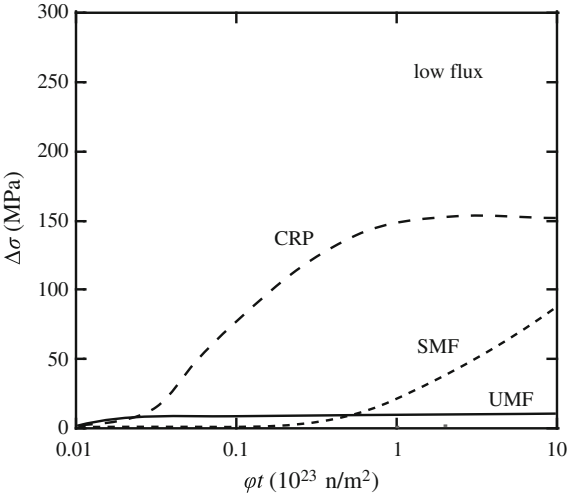

Fig. 12.17 Components of the microstructure contributing to hardening of a ferritic pressure vessel steel (after [40])

SMFs are not completely understood, but likely consist of a range of defect cluster–solute complexes whose exact natures depend on the metallurgical variables and irradiation conditions. Phosphides, carbonitrides, manganese-rich phases, large vacancy clusters, and immobile interstitial loops are all likely candidates for the SMFs. SMFs account for the residual hardening in low Cu steels. UMFs undergo recovery during irradiation and likely consist of small vacancy and interstitial clusters produced directly in displacement cascades.

The increase in yield strength in RPV steels due to irradiation can be described by the following [41]:

$$\Delta\sigma_{\mathrm{y}} = \Delta\sigma_{\mathrm{yp}} + B\sqrt{\phi t}, \tag{12.117}$$

where $\Delta\sigma_{\mathrm{yp}}$ is the contribution from CRPs and $B\sqrt{\phi t}$ is due to SMFs. The parameter B in the second term contains the composition dependence of hardening due to SMFs and will vary between steels. Odette et al. [41] have identified the composition dependence of B for low Cu steels (<0.1 %) to be:

$$B = 681\mathrm{P} + 460\mathrm{Cu} + 10.4\mathrm{Ni} + 10.7\mathrm{Mn} - 10\,[\mathrm{MPa}]. \tag{12.118}$$

Figure 12.18 shows the very strong dependence of hardening on copper content, which has a profound impact on RPV steels and welds.

Dose rate affects the yield strength increment through the term $\Delta\sigma_{\mathrm{yp}}$. Odette [41] has shown that higher dose rates shift the yield strength to higher fluences (Fig. 12.19(a)) in the preplateau region. The CRP term can be written as follows:

$$\Delta\sigma_{\mathrm{yp}}(\phi t_{\mathrm{e}}) = \Delta\sigma_{\mathrm{ypm}}\sqrt{X}, \tag{12.119}$$

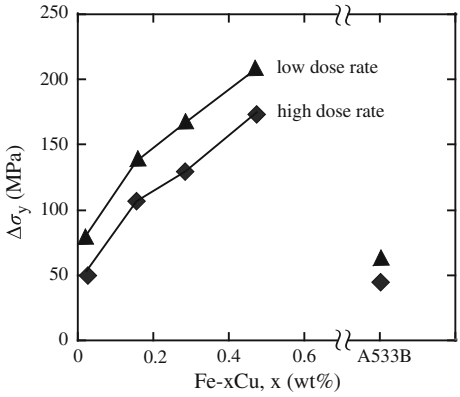

Fig. 12.18 Effect of copper on the hardening of ferritic steel alloys (after [42])

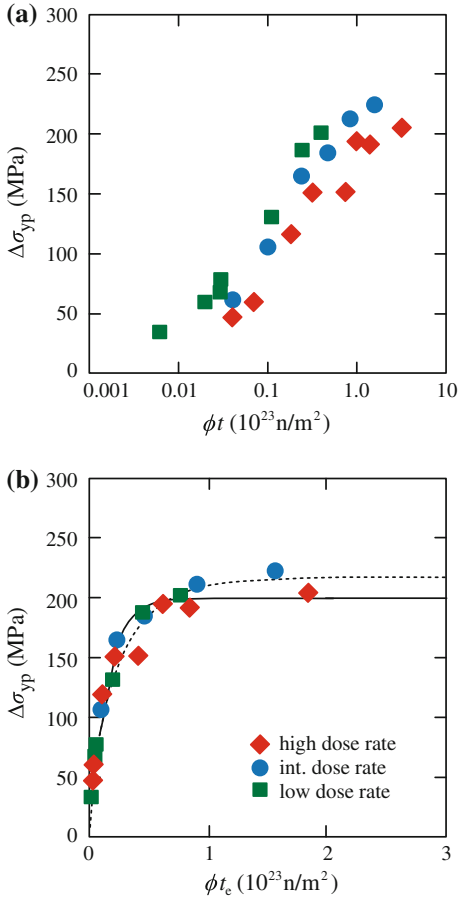

Fig. 12.19 Hardening of an A533B-type bainitic steel containing 0.4 % Cu and 1.25 % Ni following irradiation at 290 °C (**a**) due to copper-rich precipitates versus fluence, and (**b**) due to copper-rich precipitates versus *effective* fluence (after [41])

where $\Delta\sigma_{ypm}$ is the plateau value of hardening (relatively insensitive to dose rate), ϕt_e is an effective fluence defined by $\phi t_e \approx \phi t(\phi_r/\phi)^{1/2}$, and ϕ_r is a reference flux.

The term X is given by:

$$X = \left\{1 - \exp\left[-(F\phi t_e)^{\beta}\right]\right\}, \tag{12.120}$$

where F and β are the fitting parameters. The result is that the CRP contribution to yield strength can be expressed as a function of ϕt_e (Fig. 12.19(b)) which shows that the CRP increment can be accounted for by using the effective fluence.

Attempts to apply the dispersed barrier hardening model to predict hardening in irradiated ferritic-martensitic steels have met with less success as the result is generally less than the measured value by a significant amount [43, 44].

12.2.7 Radiation Anneal Hardening

An additional hardening mechanism occurs upon annealing of bcc metals following irradiation and is known as radiation anneal hardening (RAH) [45]. Figure 12.20 shows the yield strength as a function of annealing temperature following irradiation of niobium containing 35 wppm C and 41 wppm O to a fluence of 2×10^{18} n/cm^2. Note that hardening begins at a temperature of about 120 °C and increases to a maximum at about 180 °C before decreasing. However, a second peak in hardening appears at a temperature of 300 °C before the yield strength drops due to recovery. These peaks in the hardness are attributed to the oxygen and carbon impurities in the metal. It is well known that interstitial impurities increase the yield strength of bcc metals. In the irradiated state, the radiation-produced defects serve as trapping centers for interstitial impurities. Annealing enables the migration of the interstitials to defect clusters resulting in the formation of

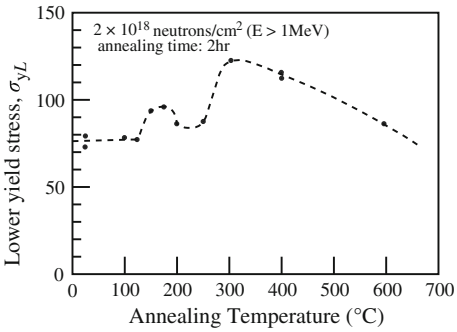

Fig. 12.20 Radiation anneal hardening in niobium containing 35 wppm C, 41 wppm O, and 5 wppm N following irradiation to 2×10^{18} n/cm^2 and annealing for 2 h. Unirradiated yield strength is ~40 MPa (after [46])

impurity–defect complexes or the strengthening of existing defect clusters, both of which act as barriers to slip dislocation motion.

In the example shown in Fig. 12.20, the first peak is due to the migration of oxygen to defect clusters and the second peak is due to the migration of carbon. Measurements of the change in resistivity with time at temperature can be used to determine the activation energy for resistivity change, which can then be compared with the activation energy for diffusion of the impurities to determine their identity. In niobium, vanadium, and iron alloys, the primary agents responsible for RAH are oxygen, carbon, and nitrogen.

12.2.8 The Correlation Between Hardness and Yield Strength

Much data on hardening come from indentation or shear punch measurements of irradiated samples. Indentation techniques include Vickers microhardness and ball indentation. The Vickers microhardness technique uses a diamond pyramid-shaped indenter tip that is pressed against the sample with a predetermined load (Fig. 12.21(a)). The shape of the indent and the magnitude of the load determine the

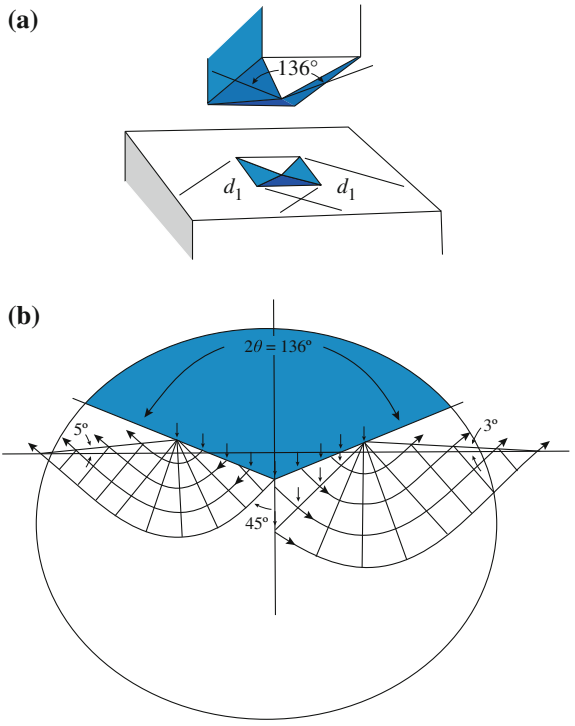

Fig. 12.21 Illustration of (**a**) the diamond pyramid tip used in Vickers microhardness measurement and the tip impression in the sample, and (**b**) flow pattern during Vickers indentation of a metal (after [47])

value of hardness, which is a measure of the resistance of the solid to deformation. The shear punch test is essentially a blanking operation in which a flat punch is driven at a constant rate through a TEM-sized disk. The disk is constrained along both its upper and lower surfaces in a test fixture, which also guides the punch. The load on the punch is measured as a function of specimen displacement, which is taken to be equivalent to the crosshead displacement. The yield and maximum loads are taken from a plot of punch load versus punch displacement. All of these techniques enjoy advantages over tensile testing in that they are relatively simple and quick, require much smaller volumes of irradiated materials, and in the case of microhardness indentation, are compatible with ion irradiation in which the damage is confined to the surface region. However, as hardening is generally defined as the increment in the yield strength due to the irradiated microstructure, there is much interest in relating hardness measurements to yield strength in order to increase its utility.

As originally described by Tabor [48], the indentations made during hardness tests are discernible as permanent impressions in the metal, so that the indentation is primarily a measure of the plastic properties of the metal. While it is true that some changes in shape and size occur when the indenter is removed, the overriding effect is the plastic flow of the metal around the indenter tip, implying that the mean pressure over the indenter is connected to the plastic rather than elastic properties of the metal. Tabor [48] showed that this is indeed the case for a variety of different hardness and scratch tests, based on the work of Prandtl [49] and Hencky [50] and that the hardness measurement can also be used as a measure of the yield stress of the metal.

During indentation, stress is applied to the metal surface through the indenter tip. However, since the tip surface is not parallel to the sample surface, the stress state during indentation is not simply compressive. Instead, the stresses must be examined in two dimensions (along and perpendicular to the axis of the indenter tip). Plastic deformation during indentation occurs when the Huber–Mises criterion is satisfied, which in the two-dimensional case occurs when the maximum shear stress reaches a critical value, k:

$$2k = 1.15\sigma_{\mathrm{y}}, \tag{12.121}$$

where σ_{y} is the yield stress.

The pyramidal shape of the indenter tip can be treated as a wedge during indentation. The pattern of plastic flow around the indenter tip during indentation can be determined using the Prandtl solution [49]. The flow pattern is shown schematically in Fig. 12.21(b) for a Vickers indentation. The pressure normal to the surface of the indenter tip P can be calculated as:

$$P = 2k(1 + \pi/2). \tag{12.122}$$

Equations (12.121) and (12.122) can be combined to yield:

$$P = 2k(1 + \pi/2) = 1.15\sigma_y(1 + \pi/2) = 2.96\sigma_y. \tag{12.123}$$

For a Vickers indenter:

$$H_v \equiv \frac{\text{load}}{\text{contact area}} = 0.927P, \tag{12.124}$$

where 0.927 is the ratio of the area of the base of the pyramid (the projected area) to the area of the sides of the pyramid (contact area). Combining Eqs. (12.123) and (12.124) gives the following:

$$H_v = 0.927P = 0.927 \times 2.96\sigma_y = 2.74\sigma_y. \tag{12.125}$$

Writing this expression in terms of yield strength gives the correlation:

$$\sigma_y = CH_v, \quad \text{with} \tag{12.126}$$

$C = 0.364$ for σ_y and H_v in units of kg/mm^2, and
$C = 3.55$ for σ_y in MPa and H_v in kg/mm^2

Tabor found the same result experimentally for a variety of metals (aluminum, copper, and mild steel). More recently, Larsson [51] studied indentation tests both theoretically and numerically. Specifically, he used finite element analysis to examine elastic–plastic material behavior under sharp contact situations (nanoindenters, Vickers or cone indenters, or even gear contact). Larsson's finite element results were in good agreement with the results of Tabor, validating the assertion that yield stress can, indeed, be determined from Vickers hardness measurements.

Busby et al. [52] reviewed existing correlations and compiled hardness data on austenitic stainless steels and ferritic steels to empirically determine the correlation between hardness and yield strength. In general, austenitic stainless steels follow a relation of the form:

$$\Delta\sigma_y = 3.03\Delta H_v, \tag{12.127}$$

and ferritic steels obey a correlation of the form:

$$\Delta\sigma_y = 3.06\Delta H_v. \tag{12.128}$$

Figure 12.22(a, b) shows these correlations for the two classes of steels. The correlations are extremely close and can be taken to be equivalent given the confidence interval used. While the dataset is best fit with a linear relation, the authors noted

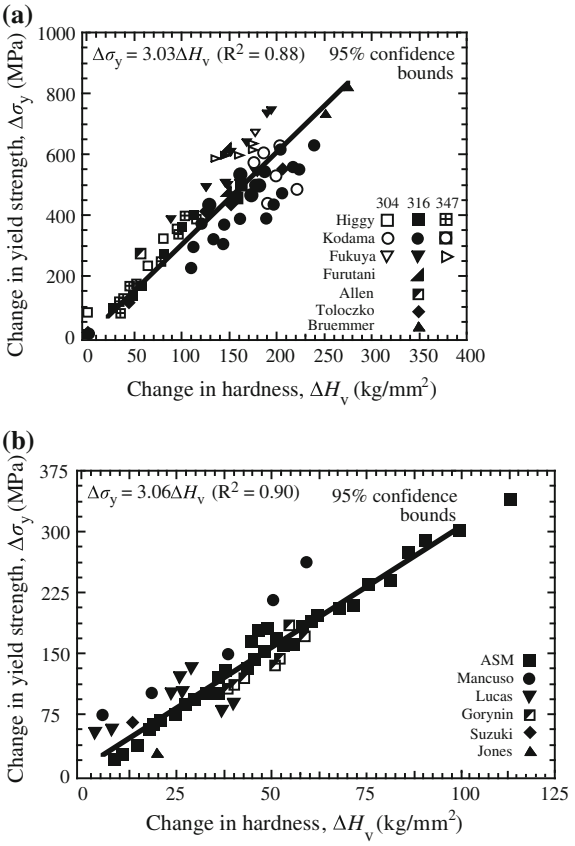

Fig. 12.22 Experimental data plotted as a change in yield stress versus change in hardness for (**a**) austenitic stainless steels and (**b**) ferritic steels. The hardness-yield stress correlation is also plotted along with 95 % confidence bounds (after [52])

that for austenitic stainless steels, there is some indication of a reduction in slope with increasing values of hardness. A two-slope fit resulted in:

$$\begin{aligned} \Delta\sigma_y &= 3.63\Delta H_v \qquad \Delta H_v < 100 \text{ kg/mm}^2 \\ \Delta\sigma_y &= 2.13\Delta H_v + 155 \quad \Delta H_v > 100 \text{ kg/mm}^2. \end{aligned} \tag{12.129}$$

The slope of the correlation in the low-load regime is close to Tabor's theoretical value of 3.55 with the difference attributed to scatter in the database. The lower value of the slope at higher loads may reflect the differences between a hardness test and a tensile test. While the yield stress is measured at approximately 0.2 % strain, the hardness test involves much higher strains, estimated to be between 8 and 18 % [48, 51]. Thus, the nature of deformation of the irradiated metal will influence the correlation between hardness and yield strength at the higher hardness levels.

A correlation coefficient of 3.5 has been shown to fit a wide range of RPV steel data [53]. It should also be noted that this data is best fit with a simple linear regression that intersects the ordinate at about 30 MPa at a ΔH_v of zero, which

could be a consequence of the fact that ΔH_v values correspond to a flow stress of several percent plastic strain. At low levels of hardening, σ_y may increase due to dislocation cutting of small defects, without a measurable increase in ΔH_v. At the higher levels of hardening reached when defects are harder, the flow stress rises in proportion to the yield stress.

12.3 Deformation in Irradiated Metals

In addition to undergoing hardening, irradiated metals experience a loss of ductility and a loss of work hardening. The loss of ductility with dose in austenitic steels irradiated and tested at ~300 °C is shown in Fig. 12.23. Note that ductility drops from some 20–30 % to values of less than 1 % by ~4 dpa. The decrease in work hardening is evident by the decrease in the difference between σ_{UTS} and σ_y with increasing irradiation dose as shown in Fig. 12.1(a–d). If the stress–strain behavior of the metal follows the power law hardening model given in Eq. (12.27), $\sigma = K\varepsilon^n$, then, as shown in Eq. (12.57), the true uniform elongation ε_u is equal to n. So to first order, variations in ε_u with irradiation follow the changes that occur to the work hardening behavior described by n. The behavior of ε_u versus dose for stainless steel over the temperature range 300–500 °C can be described by the curves in Fig. 12.24(a). The uniform elongation decreases significantly and approaches a minimum at a dose that decreases with temperature down to 300 °C. The temperature dependence of the loss of ductility is shown more clearly in Fig. 12.24(b). As core components in light water reactors are generally at temperatures around 300 °C, the minimum in ductility at that temperature is a major concern.

The loss of uniform ductility and work hardening are due to the same cause: the interaction between dislocations and the irradiated microstructure. Up to this point, we have only discussed how irradiation can lead to hardening by pinning of

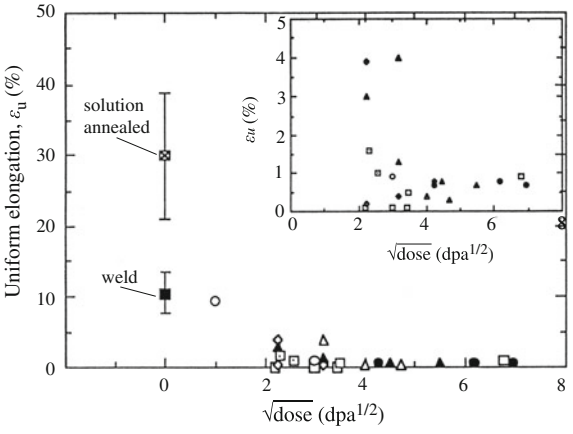

Fig. 12.23 Uniform elongation as a function of the square root of dose for 300 series austenitic stainless steels irradiated and tested at ~300 °C (after [25])

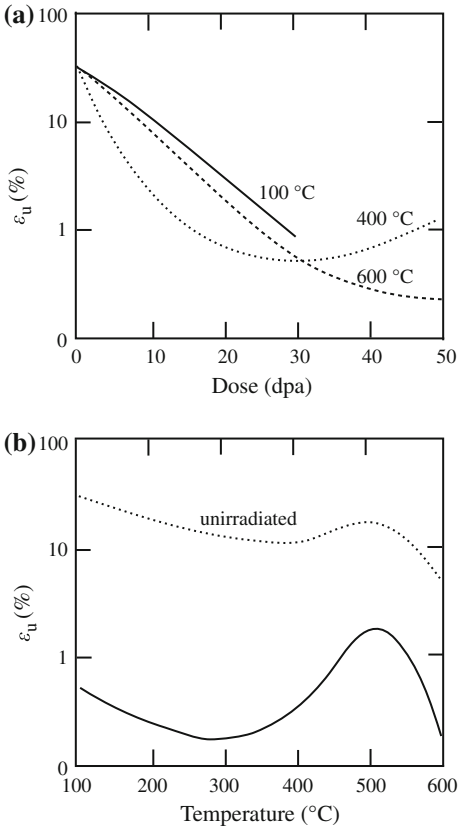

Fig. 12.24 Variation of uniform ductility in austenitic stainless steel with (**a**) dose and temperature, and (**b**) temperature (after [17])

dislocations by obstacles. However, dislocation–loop interaction can result in unfaulting of the loop and incorporation into the dislocation network. In fcc metals, unfaulting of a Frank loop can occur by several mechanisms. In one such mechanism [54], a mobile dislocation with Burgers vector $a/2[\bar{1}01]$ (shown as *DB* in Fig. 12.25(a)) intersects a small Frank loop with Burgers vector $a/3[\bar{1}11]$ ($D\delta$ in Fig. 12.25(a)) to form a Shockley partial on the loop plane with Burgers vector $a/6[\bar{1}\bar{2}1]$ (δB in Fig. 12.25(a)). The interaction of the Shockley partial with the faulted loop generates a helical segment on the original dislocation with Burgers vector $DB = D\delta + \delta B$, and eliminates the loop.

A second type of reaction occurs when a glissile, perfect dislocation, $a/2[\bar{1}\bar{1}2]$ interacts with a sessile $a/3[111]$ Frank loop creating an $a/6[\bar{1}\bar{1}2]$ dislocation according to $a/2[\bar{1}\bar{1}0] + a/3[111] = a/6[\bar{1}\bar{1}2]$[55]. The Shockley partial created by the interaction can sweep across the Frank loop, removing the stacking fault and reacting with the opposite side of the Frank loop according to $a/6[\bar{1}\bar{1}2] + a/3[\bar{1}\bar{1}\bar{1}] = a/2[\bar{1}\bar{1}0]$. Figure 12.25(b) shows the process by which the Frank loop lying in the plane of the figure interacts with a perfect dislocation moving on some other plane. The Frank loop is annihilated and the only remnant is a coil in the $a/2[\bar{1}\bar{1}0]$

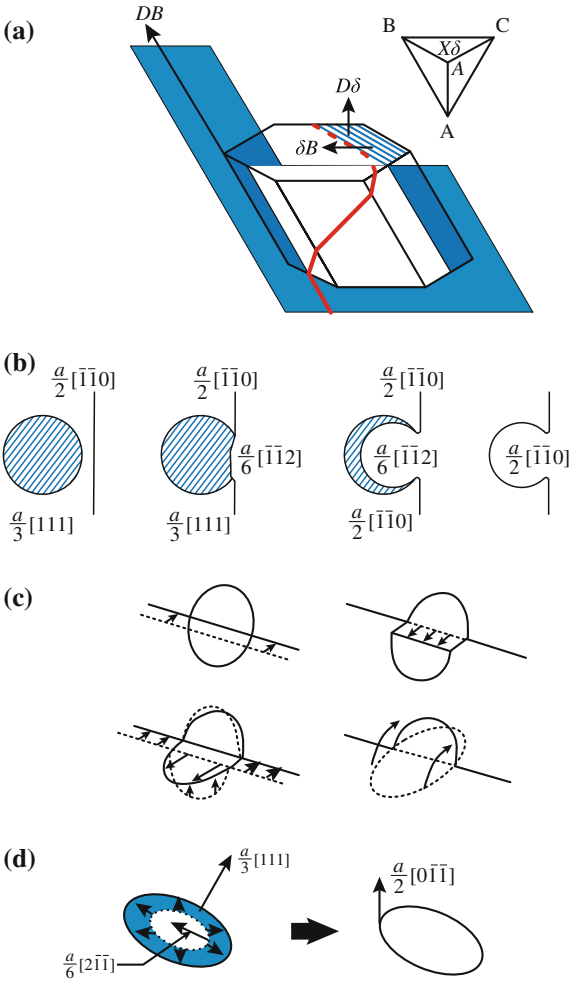

Fig. 12.25 Loop unfaulting mechanisms proposed by (**a**) Strudel and Washburn [54]. (**b**) Gelles [55]. (**c**) Foreman and Sharp [56], and (**d**) Tanigawa [57]

dislocation approximately on the Frank loop {111} plane. The result is that the unfaulting product of a perfect dislocation–Frank loop interaction immediately becomes part of the perfect dislocation network.

A third mechanism [56] involves intersection of a mobile dislocation with a loop in which the loop glides on itself and becomes part of the glide dislocation as shown in Fig. 12.25(c). Finally, unfaulting can be triggered by the formation of a Shockley partial loop inside a Frank loop [57]. Reaction between the Shockley partial loop of the type $a/6[11\bar{2}]$ and the Frank loop proceeds according to: $a/6[11\bar{2}] + a/3[111] = a/2[110]$ and is shown in Fig. 12.25(d).

In bcc metals, faulted loops are rarely observed because of the high stacking-fault energy that causes unfaulting at very small loop sizes. The Frank loop is of the form $a/2[110]$, and the stacking fault can be removed by two possible

unfaulting reactions [58]: $a/2[110] + a/2[00\bar{1}] \rightarrow a/2[11\bar{1}]$, or $a/2[110] + a/2[\bar{1}10] \rightarrow a/2[010]$, with the result being a perfect loop in either case. The result of each of these unfaulting reactions is the removal of the dislocation loop from the microstructure and the growth of the dislocation network density.

12.3.1 Localized Deformation

Multiple shearing can eliminate defect clusters and coherent precipitates in the dislocation glide plane. So in fact, passage of an initial group of dislocations down a particular slip plane can result in the clearing of the obstacles in that slip plane so that subsequent dislocations can pass relatively unimpeded. First observed in the 1960s in bcc metals [59, 60], this process is referred to as *dislocation channeling*, which occurs in fcc, bcc, and hcp crystal lattices. As a result of channeling, work hardening in channels drops to nearly zero along with the macroscopic uniform strain, as the deformation becomes highly localized within the channels. Byun et al. [61] have pointed out that channel deformation occurs in unirradiated metals at high stress, and that the common feature between channel deformation in irradiated and unirradiated metals is the high stress.

Dislocation channels are characterized by width, spacing, and the amount of strain in the channel. Figure 12.26 shows TEM images of dislocation channels in Fe–18Cr–12Ni irradiated to 5.5 dpa at 360 °C with 3 MeV protons and strained to 7 % at 288 °C. Note in Fig. 12.26(b) the contrast difference between the channel and the matrix, indicating that the channel has been cleared of most of the obstacles. Channel width is generally on the order of 0.1 μm and channels are typically spaced 1–3 μm apart. Channels propagate across grains, initiating and terminating at grain boundaries. In a tensile sample, the channels of surface grains produce a step on the surface. Figure 12.27 shows an SEM image of the surface of irradiated stainless

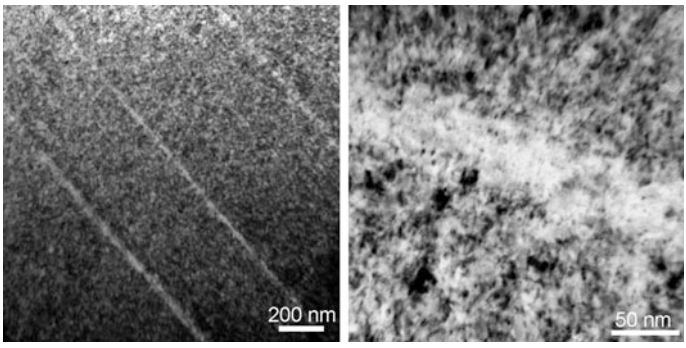

Fig. 12.26 Transmission electron micrographs of dislocation channels in Fe–18Cr–12Ni irradiated to 5.5 dpa at 360 °C with 3 MeV protons and strained to 7 % at 288 °C (courtesy of Z Jiao, University of Michigan)

Fig. 12.27 Scanning electron micrograph of dislocation channels intersecting the surface of austenitic stainless steels irradiated to 5.5 dpa with 3.2 MeV protons at 360 °C followed by straining at 3×10^{-7} s^{-1} to 7 % plastic strain in 288 °C argon (courtesy of Z Jiao, University of Michigan)

steel samples strained to 7 %, from which the magnitude of the surface step can be characterized using Atomic-force microscopy (AFM). Figure 12.28 shows how the intersection of a channel with the surface produces a step of height, h due to the passage of dislocations down the channel. For a step height, h, and a width, w, the channel strain, γ, is simply:

$$\gamma = h/w. \tag{12.130}$$

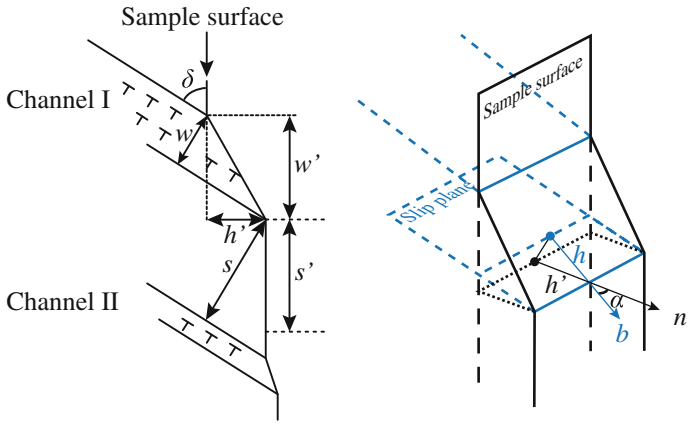

Fig. 12.28 Intersection of dislocation channels with a surface creating a step on the surface. Primed quantities are *apparent* values of height, h', width, w', and spacing, s', that are measured directly and must be converted to true height, h, true width, w, and spacing, s, to determine the strain in the channel (after [62])

However, measurement of the channels on the surface will provide apparent values of height, h', width, w', and spacing, s', that must be converted to true values using [62]:

$$\begin{aligned} w &= w' \sin(\delta) - h' \cos(\delta) \\ h &= h' / \cos(\alpha), \end{aligned} \tag{12.131}$$

where δ is the angle between dislocation slip plane and the sample surface and α is the angle between the dislocation slip direction and the surface normal.

The number of dislocations in a channel, n, can be related to the step height by $n = h/b$, where b is the Burgers vector. Was et al. [62] have shown that straining 316L stainless steel to about 7 % applied strain following irradiation to 5.5 dpa at 360 °C resulted in an average channel strain of close to 100 % caused by the passage of over 1000 dislocations down the channels. The great majority (>90 %) of total strain in the solid occurs in the channels, meaning that irradiated materials act like a multilayered solid (such as a metal-ceramic multilayered material) in which all strain occurs in the softer layer. Observations and model calculations indicate that many fewer dislocations (a few to 50) remain in the channels [62, 63]. Two possible reasons for the low number of residual dislocations in the channels are slip transfer to neighboring grains in cases where the slip planes are closely aligned between grains, or reaction of the dislocation with the grain boundary. When a dislocation channel intersects a grain boundary, dislocations in the channel either transfer to an adjoining grain or pile up at the grain boundary. When a dislocation transfers, it leaves a residual dislocation in the grain boundary. The reaction of dislocations involving grain boundaries can be expressed as: $\boldsymbol{b}_r = \boldsymbol{b}_1 - \boldsymbol{b}_2$, where $\boldsymbol{b}_r$ is the Burgers vector of the residual dislocation left behind in the grain boundary, and $\boldsymbol{b}_1$ and $\boldsymbol{b}_2$ are the Burgers vectors of dislocations in grains 1 and 2, respectively. The number of residual dislocations in a grain boundary is likely proportional to the channel height or channel strain as the portion of dislocations piled up at a grain boundary is relatively small.

An example of dislocation interaction with precipitates is shown in Fig. 12.29. This is an APT image of a dislocation channel in a field of radiation-induced

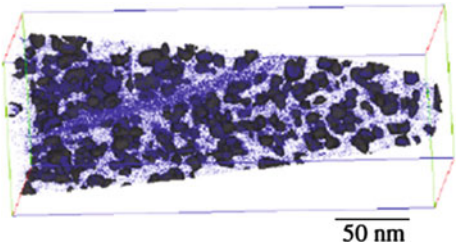

Fig. 12.29 Atom map of Si in a dislocation channel in a 304 SS alloy containing 1 % Si after irradiation to 5 dpa at 360 °C and straining to 6 % at 288 °C (after [64])

Ni-/Si-rich precipitates in a high-purity 304 stainless steel alloy containing ~1 at.% Si irradiated to 5 dpa at 360 °C with 2 MeV protons, and followed by straining to 6 % at 288 °C [64]. The image shows an atom map of Si. Precipitates are identified by regions with Si concentration ≥5 at.% and appear as dark clusters, while Si atoms appear as small purple dots. Quantitative chemical analysis, represented by the density of dots, indicate that the concentration of Si in the channel is greater than that in the bulk and much greater than that between precipitates. These observations indicate that the passage of dislocations induced dissolution of the precipitates in the channel, providing a path of lower resistance for subsequent dislocations.

A second example shows that dislocation cutting of voids does not result in their removal [65]. Figure 12.30 shows two images of a dislocation channel in a high-purity Fe–18Cr–12Ni alloy irradiated with 2 MeV protons to 5 dpa at 360 °C and strained to 7 % at 288 °C. Note in the left-hand image that the dislocation channel appears to be relatively free of dislocation loops, discernable from the reduction in contrast in the channel verses that outside the channel. The same region imaged in a slightly underfocused condition shows that voids are still present in the channel, and at a density that is similar to that outside the channel. These observations indicate that voids can survive in channels when deformation occurs at temperature.

In addition to channeling caused by gliding dislocations, deformation twinning is also observed to occur. Deformation twinning or mechanical twinning is a localized deformation mechanism caused by partial dislocations. In fcc metals with low stacking-fault energy (SFE), deformation twins are formed by the glide of Shockley partial dislocations of the same sign on successive {111} planes. In these twins, the shear strain is 70.7 % and the defects are cleared by glide of the partial

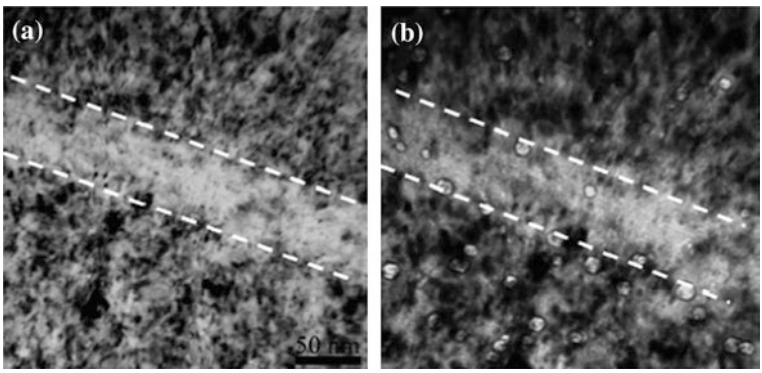

Fig. 12.30 TEM image of a dislocation channel in an Fe–18Cr–12Ni alloy irradiated to 5 dpa at 360 °C and strained to 7 % at 288 °C showing (**a**) the cleared channel, and (**b**) voids in the channel visible in the underfocused condition (after [65])

dislocations [66]. The Shockley partials are formed from dissociation of the ordinary dislocation with Burgers vector 1/2 ⟨110⟩ into leading and trailing partial dislocations with Burgers vector of the type 1/6 ⟨112⟩. The separation of the partials or the width of the stacking fault, d, is given by:

$$d \approx \frac{\mu b^2}{4\pi\gamma_{\mathrm{SFE}}}, \tag{12.132}$$

where γ_{SFE} is the stacking-fault energy. In low stacking-fault energy metals, the separation of partials is large. Was et al. [62] have observed the formation of twins at the intersection of dislocation channels with grain boundaries where the stress and strain is the greatest. Whether by channeling or twinning, localized deformation increases strongly with dose. Twinning is also favored at low temperatures.

12.3.2 Deformation Mechanism Maps

As described in Chap. 7, plastic deformation is characterized by the shear stress, strain or strain rate, and temperature. Frost and Ashby [67] classified deformation mechanisms into five groups:

1. Flow above the ideal shear strength
2. Low-temperature plasticity by dislocation glide
3. Low-temperature plasticity by twinning
4. Power law creep by dislocation glide or climb and glide
5. Diffusional creep

Each of these mechanisms can be subdivided into additional mechanisms. When stress and temperature are the independent variables, then the response of the metal is the strain rate and strain. Alternatively, the temperature and strain rate could be selected as the independent variables and the stress constitutes the response of the metal.

If strain rate is selected as the dependent variable, a convenient method of relating the strain rate of a metal to the independent variables of shear stress and temperature is the deformation mechanism map. A deformation mechanism map is a representation of the mechanism of deformation in stress-temperature space where shear stress, σ_s, is represented by the normalized stress, σ_s/μ, where μ is the shear modulus, and temperature is represented by the homologous temperature, T/T_m, where T_m is the melting temperature. The map provides a relationship between the two independent variables σ_s and T and the dependent variable, $\dot{\varepsilon}$. An example of such a map for 316 stainless steel is given in Fig. 12.31(a), in which the normalized stress is plotted on the ordinate and the homologous temperature is plotted on the

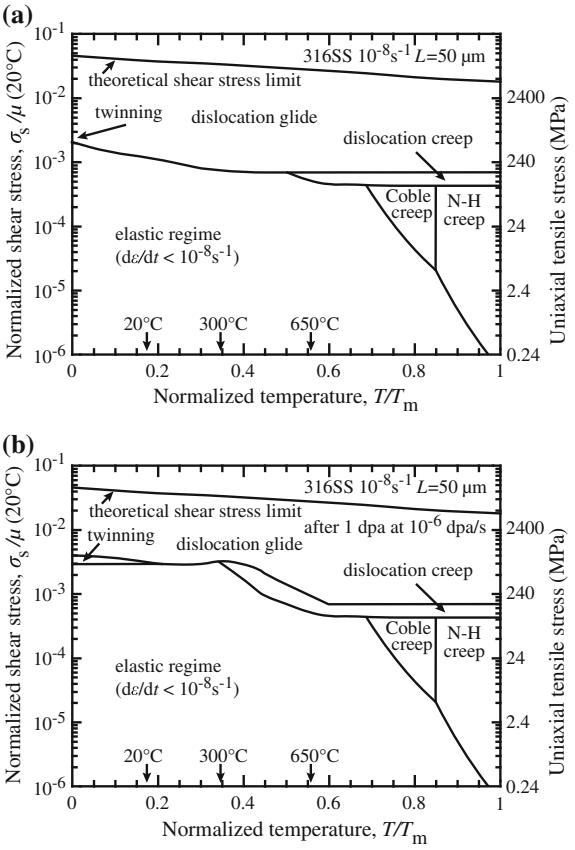

Fig. 12.31 Deformation mechanism map for 316 stainless steel with a grain size of 50 μm and deformed at a strain rate of 10^{-8} s^{-1} for (**a**) unirradiated condition, and (**b**) irradiated to 1 dpa at 10^{-6} dpa/s (after [68])

abscissa. The various deformation mechanisms are denoted by labeled regions in the map, and the strain rate response of the metal to the stress/temperature combinations is given by contours of equistrain rate. Essentially, the strain rate contours provide the constitutive law in the form of a single equation:

$$\dot{\varepsilon} = f(\sigma_s, T). \tag{12.133}$$

Figure 12.31(a) shows that above the ideal shear strength, plastic collapse occurs and the strain rate approaches infinity:

$$\begin{aligned} \dot{\varepsilon} &= \infty \quad \text{for } \sigma_s \geq \alpha\mu \\ \dot{\varepsilon} &= 0 \quad \text{for } \sigma_s < \alpha\mu, \end{aligned} \tag{12.134}$$

where α depends on the crystal structure and instability criterion but is generally between 0.05 and 0.1. Below the ideal shear strength, flow can occur by glide of dislocations that is generally limited by obstacles. Ashby gives the strain rate in the discrete obstacle controlled plasticity regime as:

$$\dot{\varepsilon} = \dot{\varepsilon}_0 \exp\left[-\frac{Q}{kT}\left(1 - \frac{\sigma_s}{\sigma_s^0}\right)\right], \tag{12.135}$$

where Q is the activation energy required to overcome the obstacle without aid from external stress, and σ_s^0 is the athermal component of the flow stress. At low-temperature and high normalized stress, twinning is observed to occur. Byun et al. [63] have characterized the deformation in terms of the stress and strain, and have determined that the twinning stress σ_t in polycrystalline metals could be defined by the critical stress for infinite separation of partials:

$$\sigma_t = 6.14\frac{\gamma_{SFE}}{b}, \tag{12.136}$$

where b is the Burgers vector of the partial dislocation. The strain rate equation for twinning [67] is given as:

$$\dot{\varepsilon} = \dot{\varepsilon}_t \exp\left[-\frac{Q_t}{kT}\left(1 - \frac{\sigma_s}{\sigma_t}\right)\right], \tag{12.137}$$

where Q_t is the activation free energy to nucleate a twin without the aid of external stress, σ_t is the stress required to nucleate twinning in the absence of thermal activation, and $\dot{\varepsilon}_t$ is a constant. The balance of the deformation map refers to creep mechanisms and these are discussed in detail in Chap. 13.

The effect of irradiation at a strain rate of 10^{-8} s^{-1} is shown in Fig. 12.31(b). Due to irradiation hardening at temperatures below about $0.5T/T_m$, the stress for dislocation glide is increased, reducing the dislocation glide regime. Above this temperature, irradiation-enhanced softening can occur, causing a reduction in the stress for dislocation glide and an expansion of the glide regime at high temperature. At low temperatures and high stresses, twinning can occur.

Byun and Hashimoto [69], and Farrell et al. [70] have constructed deformation mode maps for irradiated alloys that describe the mode of deformation as a function of applied strain. The stress-based map is shown in Fig. 12.32(a) and the strain-based map is shown in Fig. 12.32(b) for 316 austenitic stainless steel. In the stress-based map, higher dose leads to an increase in yield strength and an increase in the elastic deformation regime.

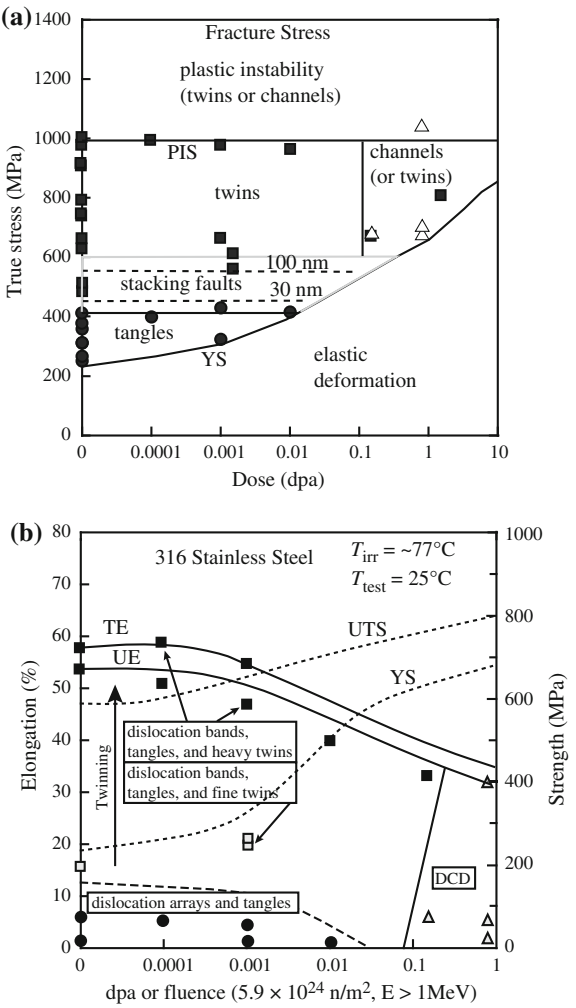

Fig. 12.32 (**a**) Stress-based deformation mode map for 316 stainless steel in true stress-dose space (PIS plastic instability stress) (after [69]). (**b**) Strain-based deformation mode map for 316 stainless steel neutron irradiated at 65–100 °C and tested at room temperature (TE total elongation, UE uniform elongation, DCD dislocation channeling deformation) (after [70])

Nomenclature

A	Area of slip plane or dislocation loop or cross-sectional area of a tensile sample after straining
A_0	Original cross-sectional area in a tensile sample
$\boldsymbol{b}$	Burgers vector
d	Grain size or obstacle diameter or separation distance of partial dislocations
e	Elastic strain
E	Elastic modulus
F	Force
h	Dislocation channel height
H_v	Vickers hardness

K Bulk modulus or constant in power law hardening equation
k Square root of second invariant of the stress deviator used for the von Mises yield criterion
k_y Unpinning stress
L_0 Original length of a tensile sample
L Deformed length of tensile sample. Also length of dislocation pileup on a slip plane
l Distance between obstacles on the slip plane
m Schmidt factor
M Taylor factor
N Number density of obstacles on a slip plane
n Number of dislocations in a pileup
p Hydrostatic pressure
P Load
r Distance from obstacle to Frank–Read source
r_d Dislocation core radius
R Radius of an obstacle
S Engineering stress, or weighting parameter from Eq. (12.103)
t Time
T Temperature
u Elastic strain energy density
U Elastic strain energy
U_V Elastic strain energy of volume of a void
V Volume
w Dislocation channel width
W Work
α Obstacle hardness
β Compressibility, work hardenability
ϕ Neutron flux
Φ Neutron fluence
ϕt_e Effective neutron fluence
Δ Volume strain
δ Increment of distance
ε, ε_{ij} Strain and components of strain
γ Dislocation channel strain
γ_{SFE} Stacking-fault energy
Γ Dislocation line tension
λ Lamé coefficient
μ Shear modulus
ν Poisson's ratio
ρ_d Dislocation density
σ Tensile stress
σ_i Friction stress
σ_m Mean stress

σ_s	Shear stress
σ_s^0	Athermal component of flow stress
σ_y	Yield stress
σ_{yp}	CRP contribution to yield stress
σ_{ypm}	Yield strength plateau
τ	Defect lifetime
ζ	Number of damage zones created per neutron collision

Subscripts

d	Dislocation
f	Fracture
i, j or x, y, z	Stress and strain components
loop	Loops
LR	Long range
n	Necking
ppt	Precipitates
s	Shear or strong
SR	Short range
u	Uniform
void	Voids
V	Void
w	Weak
y	Yield
yr	Root-sum-square
yl	Linear sum

Superscripts

n	Strain hardening exponent

Acronyms

AFM	Atomic-force microscope
APT	Atom probe tomography
CRP	Copper-rich precipitates
MF	Matrix features
RA	Reduction in area
RAH	Radiation anneal hardening
RPV	Reactor pressure vessel
RSS	Root-sum-square
SEM	Scanning electron microscopy
SFE	Stacking-fault energy
SMF	Stable matrix features
TEM	Transmission electron microscope

UMF Unstable matrix features
UTS Ultimatetensile strength
YS Yield strength

Problems

12.1 The irradiated microstructure will determine the extent of hardening in an alloy. Your goal is to limit the radiation hardening in a metal. Assume that all hardening comes from voids and that no transmutation gas is present. For a fixed number of vacancies trapped in cavities, would you prefer a large density of small voids or a small density of large voids? Explain your reasoning.

12.2 If an alloy swells by an increase in the radii of voids at constant density, by how much does a doubling of the swelling harden the alloy? For this scenario, is the swelling or the hardening from voids more of a concern?

12.3 Electron microscopic examination of a 316 stainless steel specimen that has been irradiated at 400 °C in a fast neutron fluence of 1×10^{22} n/cm^2 ($E > 0.1$ MeV) reveals voids with an average diameter of 40 nm and a number density of 2.2×10^{15} cm^{-3}. In addition, faulted loops of a diameter 16 nm are present at a number density of 1.8×10^{15} cm^{-3}. The incremental increase in the shear stress caused by a barrier can be expressed as:

$$\Delta\tau = \alpha\mu b/l\left(\mu = 80\,\text{GPa}, b = 2.5 \times 10^{-10}\,\text{m}\right)$$

Assuming that both types of defects act as hard barriers ($\alpha = 1$ for voids, $\alpha = 1/2$ for faulted loops) and are distributed in regular, square arrays:

(a) Calculate the change in the critical resolved shear stress ($\Delta\tau$) due to irradiation.
(b) What is the interparticle spacing of the square arrays?
(c) Which causes greater hardening, voids, or loops?

12.4 For 316 stainless steel irradiated at 400 °C to a fast neutron fluence of 1×10^{22} n/cm^2 ($E > 0.1$ MeV), determine the dislocation loop size and density required to produce the same hardening as the void population given in Problem 12.3.

12.5 A pressure vessel steel is irradiated at 300 °C to a fluence of 10^{20} n/cm^2. We wish to determine the change in NDT due to such an irradiation. NDT is defined by the condition that $\sigma_f = \sigma_y$ or $\sigma_y k_y = 4\mu\gamma d^{-1/2}$. The effect of irradiation on source hardening can be determined as follows:

$$d\left(\sigma_y k_y\right) = \sigma_y dk_y + k_y d\sigma_y = 0,$$

since the term $4\mu\gamma d^{-1/2}$ is essentially constant during irradiation.

The changes in k_y and σ_y due to the variables T and ϕt (where ϕt is manifest by radiation hardening or an increase in the friction stress σ_i) are given as:

$$dk_y = \frac{\partial k_y}{\partial T} dT + \frac{\partial k_y}{\partial \sigma_i} d\sigma_i$$
$$d\sigma_y = \frac{\partial \sigma_y}{\partial T} dT + \frac{\partial \sigma_y}{\partial \sigma_i} d\sigma_i.$$

Combining these expressions and neglecting the effect of radiation on source hardening ($\partial k_y/\partial \sigma_i = 0$ and $\partial \sigma_y/\partial \sigma_i = 1$), we obtain an increase in transition temperature dT_D;

$$\frac{dT_D}{d\sigma_i} = -\left(\frac{\sigma_y}{k_y}\frac{\partial k_y}{\partial T} + \frac{\partial \sigma_y}{\partial T}\right)^{-1}.$$

To find the increase in transition temperature dT_D as a function of fluence, we need the dependence of friction stress σ_i on ϕt. This will give us:

$$dT_D = \frac{dT_D}{d\sigma_i}\frac{d\sigma_i}{d(\phi t)} d(\phi t).$$

Using Makin's theory for hardening by depleted zones,

$$\sigma_i = \sigma_i^0 [1 - \exp(-\alpha V \Sigma_s \phi t)]^{1/2}$$

and that

$$\sigma_i^0 = 6.64\,\text{GPa}$$
$$\alpha = 1$$
$$\Sigma_s = 0.26\,\text{cm}^{-1}$$

and a cluster size of 6 nm, calculate the increase in transition temperature dT_D after a fluence increment of 10^{20} n/cm^2, given that $dT_D/d\sigma_i \sim 0.3$ °C/MPa.

12.6 The work hardening region of the stress–strain curve can be represented by the relation $\sigma = k\varepsilon^n$, where n is the work hardening coefficient. By increasing the yield stress more than the ultimate tensile stress, irradiation effectively reduces the work hardening coefficient. Using the criterion for plastic instability, $d\sigma/d\varepsilon = \sigma$, calculate the reduction in uniform elongation due to an irradiation that decreases n by an amount Δn.

12.7 A specimen of Ni–1Al is irradiated at 550 °C with 3.5 MeV nickel ions to a dose of 9 dpa. The resulting structure contains a void distribution consisting of 3×10^{14} voids/cm^3 at an average diameter of 50 nm.

(a) What is the required stress for a dislocation to cut through an array of these barriers and what fraction is this of the full Orowan stress?
(b) Assuming a constant total void volume, what is the stress if void growth causes the average void size to double?

Use the elastic constants for pure nickel and assume a grain size of 10 μm.

12.8 Consider a dislocation line in a solid containing N bubbles of radius R per cubic centimeter. A shear stress, τ_{xy}, is applied to the solid, which causes the dislocation to glide along its slip plane. Under what conditions will the bubbles be swept along by the dislocation rather than be bypassed by it?

12.9 You have 3 tensile samples of 316 stainless steel. Two were irradiated in a reactor to 10^{21} n/cm^2 at 300 °C and one was left unirradiated. The three samples are tested in a tensile test in the laboratory in the following manner: One irradiated sample is tested at room temperature, another at 300 °C, and the unirradiated sample is tested at 300 °C, all at the same strain rate. On a single graph, draw the engineering stress–engineering strain curves that would result, labeling the points σ_y, σ_{UTS}, σ_f, ε_u, ε_f. Provide a brief explanation justifying the relative positions of the curves.

12.10 Draw the engineering stress–engineering strain curves that would result from a tensile test in the laboratory on the samples in Problem 12.9 following irradiation to 10^{21} n/cm^2 at 300 °C and 700 °C. Label the points σ_y, σ_{UTS}, σ_f, ε_u, ε_f.

References

1. Dieter GE (1976) Mechanical metallurgy, 2nd edn. McGraw-Hill, New York
2. Kocks UF (1970) Metal Trans 1:1121–1143
3. Olander DR (1976) Fundamental aspects of nuclear reactor fuel elements, Chap 18. TLD-26711-Pl. Technical Information Center, ERDA, Washington, DC
4. Stroh AN (1954) Proc Roy Soc Vol London 223:404–414
5. Makin MJ, Sharp JV (1965) Phys Stat Sol 9:109
6. Singh BN, Foreman AJE, Trinkaus H (1997) J Nucl Mater 249:103–115
7. Stoller RE (2000) SJ Zinkle. J Nucl Mater 283–287:349–352
8. Seeger A (1958) Proceedings of 2nd United Nations international conference on the peaceful uses of atomic energy, Geneva, vol 6. United Nations, NY, p 250
9. Russell KC, Brown LM (1972) Acta Metal 20:969–974
10. Scattergood RO, Bacon DJ (1982) Acta Metal 30:1665–1677
11. Kocks UF, Arbon AS, Ashby MF (1975) Prog Mater Sci 19:1
12. Kocks UF (1977) Mater Sci Eng 27:291–298
13. Bement AL (1972) Rev Roum Phys 17(3):361–380
14. Foreman AJE, Makin MJ (1967) Can J Physics 45:511
15. Kocks UF (1969) Physics of strength and plasticity. MIT Press, Cambridge, p 13
16. Odette GR, Lucas GE (1998) Rad Eff Defects Solid 44:189
17. Lucas GE (1993) J Nucl Mater 206:287–305
18. Was GS, Busby JT, Andresen PL (2006) Corrosion in the Nuclear Power Industry, ASM handbook, vol 13C. ASM International, pp 386–414

19. Was GS, Andresen PL (2007) Effect of irradiation and corrosion on SCC in LWRs, Corrosion in the Nuclear Power Industry, vol 13 B, Chap 5-A3. American Society for Metals, Metals Park, OH (in press)
20. Zinkle SJ, Maziasz PJ, Stoller RE (1993) J Nucl Mater 206:266–286
21. Garner FA (1993) J Nucl Mater 205:98–117
22. Kojima S, Zinkle SJ, Heinisch HL (1989) Grain size effect on radiation hardening in neutron-irradiated polycrystalline copper, fusion reactor materials semiannual progress report for period ending March 31, 1989, DOE/ER-0313/6: 43–49
23. Makin MJ, Minter FJ (1957) J Inst Metals 24:399
24. Higgy HR, Hammad FH (1975) J Nucl Mater 55:177–186
25. Odette GR, Lucas GE (1991) J Nucl Mater 179–181:572–576
26. Bement AL (1963) HW-74955, p 181
27. Eason ED (1998) Development, evaluation and analysis of the initial CIR-IASCC database, EPRI Report TR-108749, Oct 1998, pp 3–7 to 3–10
28. Williams JA, Hunter CW (1972) Effects of radiation on substructure and mechanical properties of metals and alloys, STM STP 529. American Society for Testing and Materials, Philadelphia, PA, p 13
29. Pettersson K (1992) Radiation effects on mechanical properties of light water reactor structural materials, TR1TA-MAC-0461. Materials Research Center, The Royal Institute of Technology, Stockholm
30. Was GS, Busby JT (2003) Use of proton irradiation to determine IASCC mechanisms in light water reactors: solute addition alloys, final report, project EP-P3038/C1434, Report #1007440. Electric Power Research Institute, Palo Alto, CA, April, 2003
31. Garner FA, Hamilton ML, Panayotou NF, Johnson GD (1981) J Nucl Mater 103(104): 803–808
32. Grossbeck ML, Maziasz PJ, Rowcliffe AF (1992) J Nucl Mater 191–194:808–812
33. Zinkle SJ (1992) In: Stoller RE, Kumar AS, Gelles DS (eds) Effects of radiation on materials the 15th international symposium, ASTM STP 1125. American Society for Testing and Materials, Philadelphia, PA, 1992, pp 813–834
34. Bloom EE (1976) Irradiation strengthening and embrittlement. Radiation damage in metals. American Society for Metals, Metals Park, pp 295–329
35. Hashimoto N, Wakai E, Robertson JP (1999) J Nucl Mater 273:95–101
36. Ando M, Katoh Y, Tanigawa H, Kohyama A, Iwai T (2000) J Nucl Mater 283–287:423–427
37. Maziasz PJ (1993) J Nucl Mater 205:118–145
38. Kelly PM (1972) Scr Metal 6:647
39. Odette GR, Lucas GE, Klingensmith RD, Stoller RE (1996) In: Gelles DS, Nanstad RK, Kumar AS, Little EA (eds) Effects of radiation on materials the 17th international symposium, STM STP 1270. American Society for Testing and Materials, Philadelphia, PA, 1996, pp 606–636
40. Odette GR, Mader EV, Lucas GE, Phythian W, English CA (1993) In: Kumar AS, Gelles DS, Nanstad RK, Little EA (eds) Effects of radiation on materials the 16th international symposium, ASTM STP 1175. American Society for Testing and Materials, Philadelphia, PA, 1993, p 373
41. Odette GR, Yamamoto T, Klingensmith D (2005) Phil Mag 85(4–7):779–797
42. Kasada R, Kitao T, Morishita K, Matsui H, Kimura A (2001) In: Rosinski ST, Grossbeck ML, Allen TR, Kumar AS (eds) Effects of radiation on materials the 20th international symposium, ASTM STP 1405. American Society for Testing and Materials, West Conshohocken, PA, 2001, p 237
43. Schaeublin R, Gelles D, Victoria M (2002) J Nucl Mater 307–311:197–202
44. Gupta G, Jiao Z, Ham AN, Busby JT, Was GS (2006) Microstructural evolution of proton irradiated T91. J Nucl Mater 351(1–3):162–173
45. Wechsler MS, Murty KL (1989) Metal Trans A 20A:2637–2649
46. Ohr SM, Tucker RP, Wechsler MS (1970) Phys Status Solidi A 2:559–569

47. McClintock FA, Argon AS (1966) Mechanical metallurgy of materials. Addison-Wesley, New York
48. Tabor D (1956) The physical meaning of indentation and scratch hardness. Brit J App Phy 7:159
49. Prandtl L (1920) Nachr Ges Wiss, Gottingen, p 74
50. Hencky H, Agnew Z (1923) Math Mech 3:250
51. Larsson PL (2001) Investigation of sharp contact at rigid-plastic conditions. Int J Mech Sci 43:895–920
52. Busby JT, Hash MC, Was GS (2005) J Nucl Mater 336:267–278
53. Lucas GE, Odette GR, Maiti R (1987) Sheckherd JW (1987). In: Garner FA, Henagar CH, Igata N (eds) Influence of radiation on materials properties the 13th international symposium (Part II), STM STP 956. American Society for Testing and Materials, Philadelphia, PA, pp 379–394
54. Strudel JL, Washburn J (1964) Phil Mag 9:491
55. Gelles DS (1981) In: Ashby MF, Bullough R, Hartley CS, Hirth JP (eds) Proceedings of dislocation modeling of physical systems. Pergamon, Oxford, p 158
56. Foreman AJE, Sharp JV (1969) Phil Mag 19:931
57. Tanigawa H, Kohyama A, Katoh Y (1996) J Nucl Mater 239:80
58. Eyre BL, Bullough R (1965) Phil Mag 12:31
59. Eyre BL (1962) Phil Mag 7:2107
60. Tucker RP, Wechsler MS, Ohr SM (1969) J Appl Phys 40(1):400–408
61. Byun TS, Farrell K (2004) Acta Mater 52:1597–1608
62. Was GS, Jiao Z, Busby JT (2006) In: Gdoutos EE (ed) Proceedings of the 16th European conference of fracture. Springer, Berlin
63. Byun TS, Hashimoto N (2006) J Nucl Mater 354:123–130
64. Jiao Z, McMurtrey M, Was GS (2011) Scr Mater 65:159–162
65. Jiao Z, Was GS (2010) J Nucl Mater 407:34–43
66. Byun TS, Hashimoto N, Farrell K, Lee EH (2006) J Nucl Mater 354:251–264
67. Frost HJ, Ashby MJ (1982) Deformation-mechanism maps: the plasticity and creep of metals and ceramics. Pergamon, New York
68. Zinkle SJ, Lucas GE (2003) Deformation and fracture mechanisms in irradiated fcc and bcc metals. US Department of Energy, Semi-Annual Report, DOE-ER-0313/34, p 117
69. Byun TS, Hashimoto N, Farrell K (2006) J Nucl Mater 351:303–315
70. Farrell K, Byun TS, Hashimoto N (2004) J Nucl Mater 335:471–486

Chapter 13
Irradiation Creep and Growth

Creep is the time-dependent deformation of a metal under constant load and at high temperature ($T/T_m > 0.3$). The metal responds by elongating with a strain defined either as the nominal strain, e, calculated from the original length of the sample:

$$e = \int_{l_0}^{l} \frac{dl}{l_0} = \frac{l - l_0}{l_0}, \tag{13.1}$$

or as the true strain, ε, determined from the instantaneous length of the sample:

$$\varepsilon = \int_{l_0}^{l} \frac{dl}{l} = \ln \frac{l}{l_0} = \ln(1 + e). \tag{13.2}$$

The nominal or engineering strain is related to the nominal or engineering stress corresponding to the initial cross section of the sample, while the true strain is related to the true stress corresponding to the instantaneous cross section. The components of strain are elastic, anelastic, and plastic. Elastic strain is instantaneous, time-independent, and reversible upon release of the stress. Anelastic strain is also reversible but depends on strain rate. Plastic strain is time-dependent and irreversible and is characterized by a volume conservative change in shape or distortion of the sample. Creep refers to the time-dependent component of plastic strain.

In general, creep is a temperature-dependent process, requiring the thermal formation of vacancies and the motion of vacancies by volume or grain boundary diffusion, or the climb of dislocations over obstacles and glide along slip planes. The probability of vacancy formation and of vacancy or dislocation motion is proportional to $\exp(-Q/kT)$, where Q is the activation energy for the rate-limiting process. Increased temperature provides the thermal energy required to overcome

G.S. Was, *Fundamentals of Radiation Materials Science*,
DOI 10.1007/978-1-4939-3438-6_13

obstacles and barriers to dislocation motion. Creep is also dependent on the stress, and the nature of the stress dependence provides information about the mechanism by which it occurs. Due to the production of excess defects, irradiation can accelerate creep. Irradiation creep is not strongly dependent on temperature, primarily because the formation of vacancies and self-interstitials is provided by energetic atomic displacement rather than by thermal processes. Creep is most important in reactor applications in regions of intermediate temperature, high neutron/ion flux, and low stress. However, before we attempt to understand the role of irradiation in creep, we will review the main thermal creep mechanisms, as they will constitute the foundation for understanding irradiation creep.

13.1 Thermal Creep

In most alloys, thermal creep proceeds through a sequence of stages as shown in Fig. 13.1. In stage I, the metal undergoes strain hardening leading to a decrease in strain rate with time. At long times, necking occurs due to localized deformation resulting in an increase in the strain rate, stage III. Between these two stages is stage II, during which the creep rate is either constant or a minimum. In this region, strain hardening is balanced by recovery so that the creep rate is relatively constant. Creep in this regime is designated as steady-state or secondary creep. This is also the region of most technological importance and in which the majority of service life is spent. The variables describing plastic deformation are the shear stress, σ_s, temperature T, strain rate $\dot{\varepsilon}$, and strain ε, or time, t. The key-independent variables governing creep in metals in practical applications are temperature and stress, and the deformation mechanisms can be characterized according to these variables. As discussed in Chap. 12, Sect. 12.3, the Ashby-type deformation mechanism map can be used to describe the various deformation processes as a function of normalized stress and homologous temperature. In that chapter, we focused on the regions

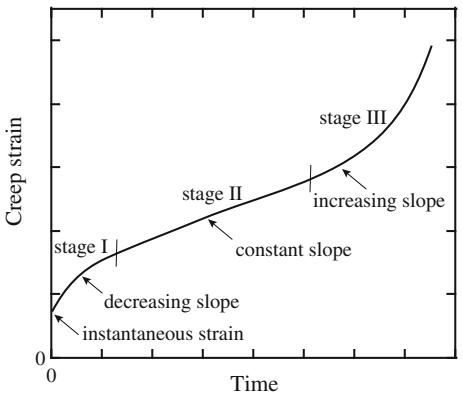

Fig. 13.1 Creep curve of a metal exhibiting the classical three stages of creep

described by plastic collapse and dislocation glide. Here, we will focus on the regions that exhibit rate-dependent plasticity, or creep.

Figure 13.2 shows a deformation mechanism map of pure nickel, for which we can develop the equations for the strain rate. The strain rate in the region of dislocation glide is given by the Orowan equation, which is a relationship between the strain rate and dislocation velocity and is determined as follows. When an edge dislocation moves completely across a slip plane, the upper half of the crystal is sheared relative to the lower half by an amount equal to one Burgers vector, b (Figs. 13.3(a)–(b)). If the dislocation moves only part way across the crystal, or a distance Δx, then the top surface is translated by an amount $b\Delta x/x$ relative to the bottom surface (Fig. 13.3(c)). So the displacement of the top half of the crystal relative to the bottom half is in relation to the fraction of the length the crystal has slipped. If the area of the slip plane is A, then $b\Delta A/A$ is the equivalent expression. The shear strain, $\varepsilon_{s,}$ is the displacement divided by the height, z, of the crystal and is given by:

$$\varepsilon_s = \frac{b\Delta A}{A}\frac{1}{z}. \tag{13.3}$$

The term zA is the volume of the crystal, V. For n dislocations of length, l, moving an average distance, $\overline{\Delta x}$, on the slip plane, the area swept out by the dislocation, ΔA, can be written as $nl\overline{\Delta x}$ giving:

$$\varepsilon_s = \frac{nbl\overline{\Delta x}}{V}. \tag{13.4}$$

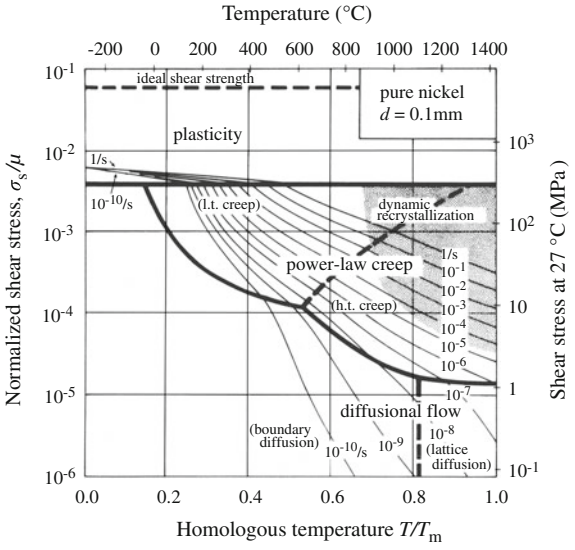

Fig. 13.2 Deformation mechanism map for pure nickel in which the strain rates and deformation mechanisms are given as a function of the normalized shear stress and the homologous temperature (after [1])

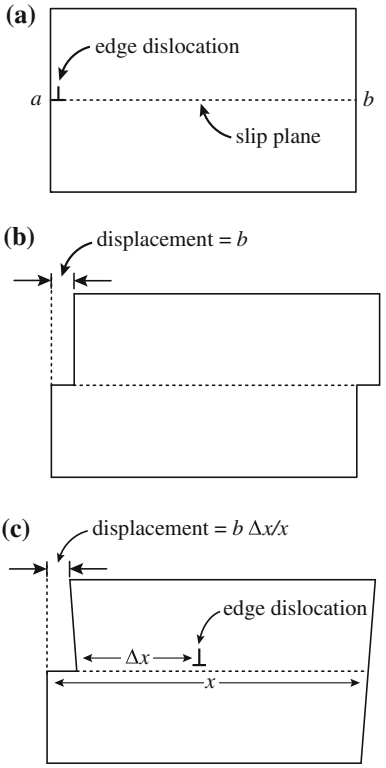

Fig. 13.3 Displacement of halves of a crystal due to passage of a dislocation along its slip plane

The term nl/V is the mobile dislocation density, ρ_m, and if the dislocations move over the distance in a time interval Δt, Eq. (13.4) can be written as a strain rate:

$$\dot{\varepsilon}_s = \rho_m b v_d, \tag{13.5}$$

where v_d is the average dislocation velocity. Equation (13.5) can be expressed in terms of the tensile strain rate, $\dot{\varepsilon}$, as

$$\dot{\varepsilon} = 1/2\rho_m b v_d, \tag{13.6}$$

where 1/2 is an approximate Schmid orientation factor.

At steady state, ρ_m is a function of stress and temperature only. As given in Eq. (7.32b), the shear stress $\sigma_s = \mu b/R$, where μ is the shear modulus and R is half the distance to the next dislocation. Since R is proportional to $\rho^{-1/2}$, then Eq. (7.32b) becomes:

$$\rho_m = \alpha\left(\frac{\sigma_s}{\mu b}\right)^2, \tag{13.7}$$

where α is a constant of order unity. The form of Eq. (13.7) depends on the process limiting plasticity at low temperature, discrete obstacles, lattice resistance, or phonon/electron drag [1].

High-temperature plasticity is described by the following:

$$\dot{\varepsilon} = c\left(\frac{\sigma_s}{\mu}\right)^n, \tag{13.8}$$

where n varies between 3 and 10 and is termed power law creep. Power law creep can occur by glide, climb-enabled glide, or Harper–Dorn creep, each process characterized by a different dependence on the stress. At very high stresses (above $10^{-3}\mu$), the strain rate is higher than predicted by power law creep and this regime is termed power law breakdown where the creep rate is given in the following form:

$$\dot{\varepsilon} = B\exp(A\sigma_s)\exp\left(\frac{-Q}{kT}\right), \tag{13.9}$$

where the activation energy, Q, often exceeds the values for self-diffusion.

At high temperatures and low stress (lower right portion of the map in Fig. 13.2), diffusional flow can drive creep. For creep controlled by lattice diffusion, the creep rate is described by:

$$\dot{\varepsilon} = \frac{A\sigma_s\Omega D_{vol}}{kTd^2}, \tag{13.10}$$

where D_{vol} is the volume diffusion coefficient and d is the grain size. When grain boundary diffusion dominates, then the creep rate varies as d^{-3}:

$$\dot{\varepsilon} = \frac{A\pi\delta_{gb}\sigma_s\Omega D_{gb}}{kTd^3}, \tag{13.11}$$

where D_{gb} is the grain boundary diffusivity and δ_{gb} is the effective thickness of the grain boundary. Equations (13.10) and (13.11) can be combined into a single equation describing creep as:

$$\dot{\varepsilon} = \frac{A\sigma_s\Omega D_{eff}}{kTd^2}, \tag{13.12}$$

where the effective diffusion coefficient, $D_{eff,}$ is given by:

$$D_{eff} = D_{vol}\left[1 + \frac{\pi\delta_{gb}}{d}\frac{D_{gb}}{D_{vol}}\right]. \tag{13.13}$$

A more complete discussion of diffusional creep will be given in Sect. 13.1.2. We will focus first on dislocation creep as this is the mechanism of primary relevance to irradiation creep.

13.1.1 Dislocation Creep

Climb and Glide

In the climb and glide model, creep is controlled by the time required for a dislocation and blocked by an obstacle, such as a void or loop, to climb to a slip plane that does not intersect the obstacle so it is free to glide. The obstacle blocking the slip of a dislocation on its glide plane causes additional dislocations generated by a nearby source to pile up behind it, as shown in Fig. 13.4. The stress fields of the dislocations overlap and create an increasing stress on the dislocation at the head of the pileup. For a solid with a mobile dislocation density, ρ_m, each dislocation, driven by a stress σ, travels a mean distance, l, by glide, resulting in a strain:

$$\varepsilon = \rho_m b l. \tag{13.14}$$

The strain rate is as follows:

$$\dot{\varepsilon} = b\frac{d}{dt}(\rho_m l) = b\rho_m \frac{dl}{dt} + bl\frac{d\rho_m}{dt}, \tag{13.15}$$

where $\bar{\upsilon} = \frac{dl}{dt}$ is the mean glide velocity, and $\frac{d\rho_m}{dt}$ is the generation rate of dislocations. We will assume that $\rho_m \bar{\upsilon} \gg l\frac{d\rho_m}{dt}$, so that creep is controlled by dislocation velocity and not dislocation generation and then the creep rate is the same as that given in Eq. (13.5), $\dot{\varepsilon} = \rho_m b \bar{\upsilon}$. However, if the moving dislocation encounters obstacles along its path, which it must overcome, then the velocity must account for the time that the dislocation is held up by the obstacle and not just its motion on the glide plane. The effective velocity can be written as:

$$\bar{\upsilon} = \frac{l}{t} = \frac{l}{t_c + t_g}, \tag{13.16}$$

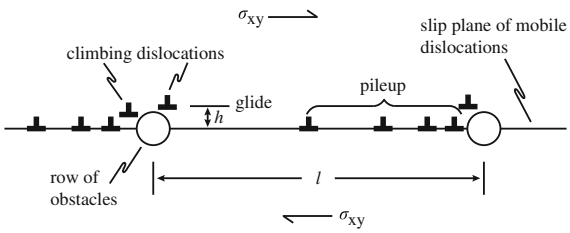

Fig. 13.4 Schematic showing the pileup of dislocations behind an obstacle on the glide plane of the dislocations

where t_g is the time spent in glide, t_c is the time spent pinned at the obstacle, and l is the distance between obstacles. As will be discussed in the next section, the dislocation overcomes the obstacle by climbing to a slip plane that bypasses the obstacle. The time required for climb is much greater than that for glide, so that Eq. (13.16) reduces to:

$$\bar{v} \approx \frac{l}{t_c}. \tag{13.17}$$

For an obstacle of height h, the time that the dislocation spends climbing to a slip plane that bypasses the obstacle can be written as:

$$t_c = \frac{h}{v_c}, \tag{13.18}$$

where v_c is the climb velocity. Substituting Eqs. (13.17) and (13.18) into Eq. (13.5) gives:

$$\dot{\varepsilon} = \rho_m b l \frac{v_c}{h}. \tag{13.19}$$

Equation (13.19) shows that determination of the creep rate amounts to determining the obstacle height and the climb velocity of the dislocation. The obstacle height is determined in the next section.

Obstacle Height

Obstacles to dislocations are often other dislocations. Equation (7.50) described the force on a moving edge dislocation due to a stationary edge dislocation. That force has two components, one in the x-direction (along the glide plane) and one in the y-direction (perpendicular to the glide plane). From Eq. (7.50), those forces are as follows:

$$F_x = \frac{\mu b^2}{2\pi(1-\nu)r}(\cos\theta\cos 2\theta) \tag{13.20a}$$

$$F_y = -\frac{\mu b^2}{2\pi(1-\nu)r}\sin\theta(2+\cos 2\theta), \tag{13.20b}$$

where we have dropped the individual designations on the Burgers vectors. Substituting for r using $y = r\cos\theta$ gives:

$$F_x = \frac{G}{y}\sin\theta\cos\theta\cos 2\theta = \frac{G}{y}g_x(\theta) \tag{13.21a}$$

$$F_y = -\frac{G}{y}\sin^2\theta(2+\cos 2\theta) = -\frac{G}{y}g_y(\theta). \tag{13.21b}$$

where $G = \dfrac{\mu b^2}{2\pi(1-\nu)}$ and $g_{x,y}(\theta)$ are functions of θ in Eqs. (13.21a) and (13.21b). The force on the moving dislocation due to the applied shear stress is $F = \sigma_{xy} b$ This force is balanced by that due to the repulsion from the stationary dislocation, Eq. (13.21a) giving:

$$\sigma_{xy} b = F_x = \frac{G}{y} g_x(\theta). \tag{13.22}$$

The blocked dislocation is also subjected to a climb force provided by Fy in Eq. (13.21b). Under this force, the dislocation will climb in a direction perpendicular to its slip plane until it reaches the point where the glide plane no longer intersects the obstacle. During its climb, the angle between the two dislocations increases starting from a value near $\theta = 0$. Referring back to the variation in force between the two dislocations as a function of angle and separation distance, r, shown in Fig. 7.32, we replot the angular dependence of the forces in Fig. 13.5 over the range $0 \le \theta \le \pi$ for a separation given by y, where the angular dependence is given by $g_{x,y}(\theta)$ in Eqs. (13.21a) and (13.21b) and $y = r\sin\theta$. Note that the restraining force between the two dislocations increases with θ initially. Once the angle reaches $\pi/8$, the restraining force is at a maximum. If the force due to the applied stress has remained in balance with the restraining force, then for values of θ above $\pi/8$, the applied stress will exceed the restraining force and the dislocation will be free to move beyond the obstacle. Setting $g_x(\theta)$ to its maximum value in Eq. (13.22) and designating the value of y at this point as the height of the obstacle, h, that must be overcome for the dislocation to be able to continue to glide yield an expression for h:

$$\begin{aligned} h = y &= \frac{G}{4\sigma_{xy} b} \\ &= \frac{\mu b}{8\pi(1-\nu)\sigma_{xy}} \sim \frac{\mu b}{16\sigma_{xy}} \quad \text{for} \quad \nu \sim 1/3. \end{aligned} \tag{13.23}$$

When there are n dislocations in a pileup against the obstacle, the stress in Eq. (13.23) is multiplied by n.

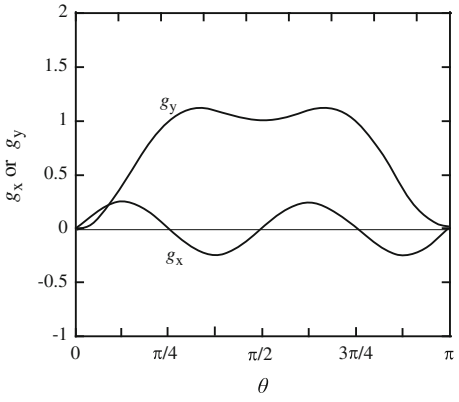

Fig. 13.5 Plot of the angular components, $g_x(\theta)$ and $g_y(\theta)$, of the force on an edge dislocation due to a stationary edge dislocation where y is the vertical separation distance between the two

Climb Velocity

An edge dislocation of Burgers vector, b, subjected to a normal stress, σ, perpendicular to the extra plane of atoms climbs in the direction normal to the slip plane. Climb occurs by absorption or emission of vacancies at the dislocation core. We will assume that this process occurs along the entire length of the dislocation line. When the solid is under an applied stress, σ (tensile is positive), the vacancy concentration in equilibrium with the dislocation is given by:

$$C(R) = C_{\mathrm{v}}^{0} \exp\left(\frac{\sigma\Omega}{kT}\right), \tag{13.24}$$

where Ω is the atomic volume and C_{v}^{0} is the equilibrium vacancy concentration in the solid, a distance R away, where R is the distance between dislocations in the solid and is given by $R = 1/\sqrt{\pi\rho_{\mathrm{d}}}$, where ρ_{d} is the dislocation density such that $\pi R^2\rho_{\mathrm{d}} = 1$ (area per dislocation × dislocations per unity area = 1). The distance R also defines the *unit cell* that reproduces, on average, the collection of ρ_{d} dislocations in the solid.

Driven by the difference in vacancy concentration between the dislocation core and the radius of the cylinder of the unit cell, defined by R, the vacancy flux to the dislocation is as follows:

$$J = 2\pi r D_{\mathrm{v}} \frac{\mathrm{d}C_{\mathrm{v}}}{\mathrm{d}r}, \tag{13.25}$$

where C_{v} is the vacancy concentration in the region $r_{\mathrm{c}} < r < R$, (r_{c} is the dislocation core radius), and is described by the diffusion equation in cylindrical coordinates:

$$\frac{1}{r}\frac{\mathrm{d}}{\mathrm{d}r}\left(r\frac{\mathrm{d}C_{\mathrm{v}}}{\mathrm{d}r}\right) = 0, \tag{13.26}$$

with boundary conditions:

$$\begin{aligned} C_{\mathrm{v}}(R) &= C_{\mathrm{v}}^{0} \exp\left(\frac{\sigma\Omega}{kT}\right) \\ C_{\mathrm{v}}(r_{\mathrm{c}}) &= C_{\mathrm{v}}^{0}. \end{aligned} \tag{13.27}$$

The solution to Eq. (13.26) subject to boundary conditions in Eq. (13.27) is as follows:

$$C_{\mathrm{v}} = C_{\mathrm{v}}^{0} - C_{\mathrm{v}}^{0}\left[1 - \exp\left(\frac{\sigma\Omega}{kT}\right)\right]\frac{\ln R/r}{\ln R/r_{c}}. \tag{13.28}$$

For $\frac{\sigma\Omega}{kT}$ small, we can approximate the exponent by $e^x \sim x + 1$, and Eq. (13.28) becomes:

$$C_v = C_v^0\left(1 + \frac{\sigma\Omega}{kT}\right)\frac{\ln R/r}{\ln R/r_c}. \tag{13.29}$$

Evaluating the gradient of the concentration profile at $r = r_c$ gives:

$$\frac{dC_v}{dr} = C_v^0\frac{\sigma\Omega}{kT}\frac{1}{\ln R/r_c}\frac{1}{r_c}, \tag{13.30}$$

and the flux, as in Eq. (13.25), becomes:

$$J_v = \frac{2\pi D_v C_v^0 \sigma\Omega}{kT\ln R/r_c}. \tag{13.31}$$

The flow of vacancies to the dislocation per unit length is $J\Omega$, or Jb^3, where $\Omega \sim b^3$. The sheet of atoms has a thickness of b so dividing by b gives the flow of volume per unit length per unit thickness, or the flow per unit distance perpendicular to the glide plane, which is just the climb velocity:

$$\begin{aligned} v_c &= \frac{2\pi D_v C_v^0 \sigma\Omega b^2}{kT\ln R/r_c} \\ &= \frac{2\pi D_{vol}\sigma b^2}{kT\ln R/r_c}, \end{aligned} \tag{13.32}$$

for $D_v C_v^0\Omega = D_{vol}$.

We now have all the elements required to derive the creep rate due to dislocation climb and glide over obstacles. Recall that the creep rate is given by Eq. (13.19) as $\dot{\varepsilon} = \rho_m bl\frac{v_c}{h}$. For the case where the dislocations are being created by Frank–Read sources, the creep rate can be expressed as the product of the Frank–Read source density, ρ_{FR}, the area swept out by the source times the Burgers vector, Ab, and the inverse of the waiting time, v_c/h or:

$$\dot{\varepsilon} = \rho_{FR}Ab\frac{v_c}{h}. \tag{13.33}$$

Substituting in for h from Eq. (13.23) and v_c from Eq. (13.32) gives:

$$\dot{\varepsilon} = \frac{16\pi^2\rho_{FR}Ab^3D_{vol}\sigma(1-\nu)n\sigma_{xy}}{\mu bkT\ln R/r_c}. \tag{13.34}$$

The number of dislocations, n, in a pileup is given by [2]:

$$n = \frac{\pi(1-\nu)l\sigma_{xy}}{\mu b}, \tag{13.35}$$

where l is the length of the pileup, and the stress $\sigma = n\sigma_{xy}$ [2]. Substituting into Eq. (13.34) gives:

$$\dot{\varepsilon} = \frac{16\pi^2\rho_{\mathrm{FR}}AD_{\mathrm{vol}}(1-\nu)^3 l^2\sigma_{xy}^4}{\mu^3 kT\ln R/r_{\mathrm{c}}}. \tag{13.36}$$

Weertman [3, 4] suggests that the quantity $\rho_{\mathrm{FR}}Al^2$ is proportional to σ_{xy}^{-1}, yielding:

$$\dot{\varepsilon} = \frac{\mathrm{C}\pi^2 D_{\mathrm{vol}}(1-\nu)^3\sigma_{xy}^3}{\mu^3 kT\ln R/r_{\mathrm{c}}}, \tag{13.37}$$

where C is a constant. According to Eq. (13.37), the creep rate due to climb and glide is proportional to the self-diffusion coefficient and the stress to the power 3.

Climb and Annihilation

Climbing dislocations can also encounter other dislocations of opposite sign, creating an attractive force between them that drives the climb and results in mutual annihilation of the dislocations [5]. Figure 13.6 shows dislocation loops spaced apart from each other and on different slip planes. Dislocations of opposite sign will experience an attractive force that will cause them to climb toward each other and to annihilate. This is an important mechanism in that it provides a means for limiting the dislocation density in the solid. The creep rate is determined using the same

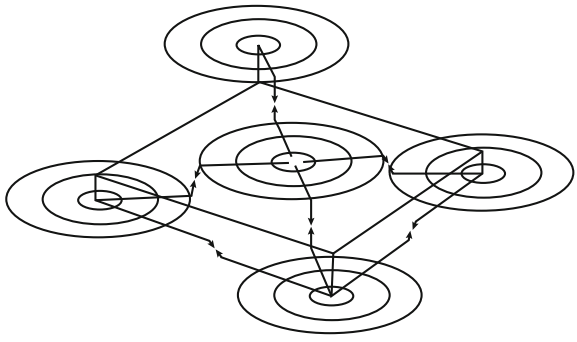

Fig. 13.6 Dislocations climbing toward each other to mutual annihilation

equation as for climb over obstacles and is caused by glide of dislocations, and piled up behind the lead dislocation, once annihilation has occurred (Fig. 13.7). That is,

$$\dot{\varepsilon} = \rho_{\mathrm{FR}} A b \frac{\upsilon_{\mathrm{c}}}{h} = \frac{\rho_{\mathrm{FR}} A b}{t_{\mathrm{c}}}, \tag{13.38}$$

where t_{c} is the waiting time defined by υ_{c}/h. The climb velocity is the same as determined in Eq. (13.32), but the height is now the distance between two dislocations that are climbing toward each other. Referring back to the climb force caused by a normal stress, Eq. (13.22) showed that:

$$\sigma = \frac{F_y}{b} \cong -\frac{G}{by}. \tag{13.39}$$

The rate of approach of the two dislocations of opposite sign is 2 υ_c, and combining Eq. (13.32) for υ_c and Eq. (13.39) for σ gives

$$\mathrm{d}y/\mathrm{d}t = 2\upsilon_c = -2\left(\frac{2\pi b D_{\mathrm{vol}} G}{kT \ln R/r_{\mathrm{c}} y}\right), \tag{13.40}$$

and integrating Eq. (13.40) between the limits $y = h$ at $t = 0$ and $y = 0$ at $t = t_{\mathrm{c}}$ gives:

$$t_{\mathrm{c}} = \frac{kT \ln R/r_{\mathrm{c}} h^2}{8\pi b D_{\mathrm{vol}} G}. \tag{13.41}$$

For n dislocations produced by each Frank–Read source, the waiting time per dislocation is t_{c}/n, where n is approximated by l/h [3]. Substituting Eq. (13.41) into Eq. (13.38) gives:

$$\dot{\varepsilon} = \frac{\rho_{\mathrm{FR}} A b^2 8\pi l D_{\mathrm{vol}} G}{kT \ln R/r_{\mathrm{c}} h^3}. \tag{13.42}$$

In Eq. (13.42), A is the area swept out by the dislocation and can be approximated by πl^2, where the distance l between sources on a slip plane is given as $(h\,\rho_{\mathrm{FR}})^{-1/2}$,

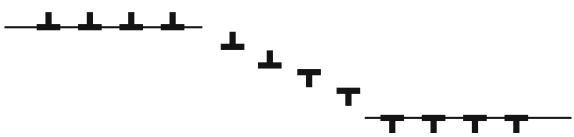

Fig. 13.7 Arrangement of a network of Frank–Read sources that produce dislocations that climb to annihilation (after [5])

where ρ_{FR} is the source density and h is the separation between sources normal to their slip planes. Substituting the expressions for A and l in Eq. (13.42) gives:

$$\dot{\varepsilon} = \frac{8\pi^2 b^2 D_{vol} G}{kT\rho_{FR}^{0.5} \ln R/r_c h^{4.5}}. \tag{13.43}$$

Substituting for h Eq. (13.23), and G (line below Eq. (13.21b)) gives:

$$\dot{\varepsilon} = \frac{C\pi^{5.5}(1-\nu)^{3.5} D_{vol} \sigma_{xy}^{4.5}}{kT\rho_{FR}^{0.5} b^{0.5} \mu^{3.5} \ln R/r_c}, \tag{13.44}$$

where C is a constant that contains the numerical terms. Note that the stress is raised to the power 4.5 rather than 3.0 in the climb to glide mode. In both climb models, the creep rate is proportional to D_{vol} or $\exp(-E_{vol}/kT)$.

13.1.2 Diffusional Creep

In the high-temperature low-stress regime of the deformation mechanism map, if we ignore the role of dislocations, then atom diffusion by way of vacancies controls creep. Consider the case of an idealized, cuboidal grain of edge length d on which a stress is applied as shown in Fig. 13.8(a). The faces will act as the sources and sinks for vacancies. Under the applied stress, vacancies will follow the paths described by the dashed lines and atoms will move in the opposite direction (solid lines). Note

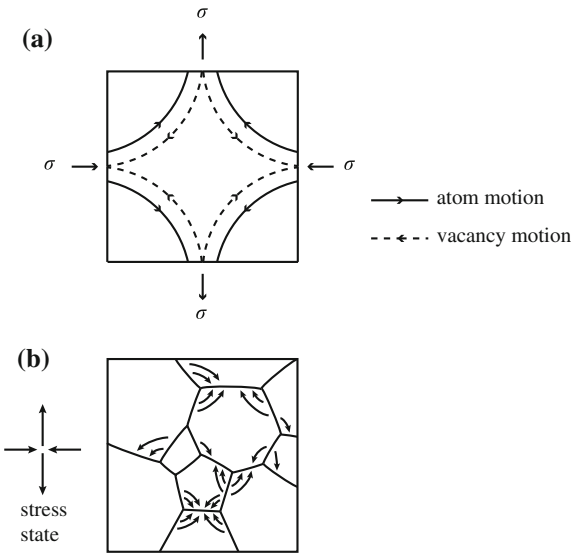

Fig. 13.8 Idealization (**a**) of a more realistic picture of vacancy and atom flow between grain faces (**b**) aligned with tensile or compressive directions of the applied stresses

that the vacancy flow is from the faces acted on by the tensile stress to those acted on by the compressive stress. The atom flow is in the opposite direction, from the faces acted on by a compressive stress to those acted on by a tensile stress. A more realistic picture of the process is shown in Fig. 13.8(b). The creation of a vacancy on the face acted on by a compressive stress, σ, due to thermal activation requires that the free energy of vacancy creation be increased by, $\sigma\Omega$, the work expended on transferring a volume Ω. A vacancy created on the face acted on by the tensile stress, σ, means that the free energy will be lowered by the same amount, $\sigma\Omega$. Therefore, at equilibrium, the vacancy concentration at the respective faces is as follows:

$$\begin{aligned} C_{\mathrm{v}}^{\mathrm{t}} &= C_{\mathrm{v}}^{0} \exp\left(\frac{\sigma\Omega}{kT}\right) \\ C_{\mathrm{v}}^{\mathrm{c}} &= C_{\mathrm{v}}^{0} \exp\left(\frac{-\sigma\Omega}{kT}\right), \end{aligned} \tag{13.45}$$

where σ is the magnitude of the stress, and the superscripts t and c refer to tensile and compressive, respectively. The vacancy flow rate, A across the area d^2 acted on by the stress is as follows:

$$A = J_{\mathrm{v}} d^2. \tag{13.46}$$

The magnitude of the vacancy flux, J_{v}, is given by Fick's law:

$$\begin{aligned} J_{\mathrm{v}} &= D_{\mathrm{v}} \frac{\mathrm{d}C}{\mathrm{d}x} \\ &\approx \kappa D_{\mathrm{v}} \frac{C_{\mathrm{v}}^{\mathrm{t}} - C_{\mathrm{v}}^{\mathrm{c}}}{d}, \end{aligned} \tag{13.47}$$

where D_{v} is the vacancy diffusion coefficient, and κ is a coefficient of proportionality between the mean vacancy diffusion path and the cube edge d. Substituting Eqs. (13.45) and (13.47) into Eq. (13.46) gives:

$$A = D_{\mathrm{v}} C_{\mathrm{v}}^{0} \kappa d \left[\exp\left(\frac{\sigma\Omega}{kT}\right) - \exp\left(\frac{-\sigma\Omega}{kT}\right)\right]. \tag{13.48}$$

Recognizing that $D_{\mathrm{vol}} = D_{\mathrm{v}} C_{\mathrm{v}}^{0} \Omega$ and that the difference in exponentials can be written using the hyperbolic sine function, Eq. (13.48) becomes:

$$A = \frac{2\kappa d D_{\mathrm{vol}}}{\Omega} \sinh(\sigma\Omega/kT). \tag{13.49}$$

The strain is just the atom volume, Ω, transferred to the compressive faces per unit area (d^2) divided by the dimension, d:

$$\varepsilon = \frac{\Omega}{d^2}\frac{1}{d}. \tag{13.50}$$

Since the flow rate of vacancies to the boundary is A, then the strain rate becomes:

$$\dot{\varepsilon} = A\frac{\Omega}{d^3} = \frac{2\kappa D_{\text{vol}}}{d^2}\sinh(\sigma\Omega/kT), \tag{13.51}$$

and for $\sigma\Omega/kT$ small (~ 1), the sinh term can be approximated by its argument, yielding:

$$\dot{\varepsilon} = B_{\text{vol}}\frac{D_{\text{vol}}\sigma\Omega}{d^2kT}, \tag{13.52}$$

where B_{vol} is the constant 2κ. Note that the creep rate is controlled by stress to the power $n = 1$ and is inversely proportional to the square of the grain diameter. The temperature dependence is governed by the volume diffusion coefficient D_{vol} exp ($-E_{\text{vol}}/kT$) and is identical to that due to dislocation creep described in the last section. Extension of this mechanism to polycrystals [6] results in the exact same expression. Diffusional creep due to volume or lattice diffusion of atoms by way of vacancies is termed Nabarro–Herring (N–H) creep after the individuals who first derived the creep expression [7, 8].

At temperatures below the range where Nabarro–Herring creep occurs, grain boundary diffusion dominates mass transport. Coble [9] first derived an expression for grain boundary-dominated diffusion assuming spherical grains, yielding the following expression:

$$\dot{\varepsilon} = B_{\text{gb}}\frac{D_{\text{gb}}\delta_{\text{gb}}\sigma\Omega}{\pi d^3kT}. \tag{13.53}$$

In this expression, D_{gb} is the grain boundary diffusion coefficient, δ_{gb} is the grain boundary width, and the constant $B_{\text{gb}} \sim 148$ [6]. Note that while the stress dependence is the same as for N–H creep, the grain size dependence is d^{-3} rather than d^{-2}. Due to the nature of grain boundary diffusion versus volume diffusion, Coble creep will dominate at lower temperatures and N–H creep will dominate at higher temperatures, and both will contribute in the intermediate temperature range. The diffusional creep rate can therefore be described by a common equation:

$$\dot{\varepsilon} = B\frac{\sigma\Omega}{d^2kT}D_{\text{eff}}, \tag{13.54}$$

and as was shown earlier, D_{eff} is the effective diffusion coefficient given by:

$$D_{\text{eff}} = D_{\text{vol}}\left(1 + \frac{\pi}{d}\frac{D_{\text{gb}}\delta_{\text{gb}}}{D_{\text{vol}}}\right), \tag{13.55}$$

and the constant $B = 14$ [6]. It follows then that grain boundary diffusion will contribute to the creep rate at larger values of $D_{\text{gb}}/D_{\text{vol}}$ and for smaller grain sizes d.

13.2 Irradiation Creep

Irradiation significantly increases the creep rate over that due to thermal creep or induces creep in temperature regimes where thermal creep is negligible. Both stainless steels and zirconium alloys exhibit irradiation creep rates that are significantly larger than thermal creep rates at the same temperature. In fact, at light water reactor core temperatures, thermal creep is negligible, but the irradiation creep rate can exceed $10^{-6}\ \text{s}^{-1}$. Irradiation increases the numbers of interstitials and vacancies in the solid, but the effect of this increase is not merely to accelerate thermal creep. In fact, as will be shown, irradiation does not accelerate diffusional creep rates. Rather, irradiation creep needs to be understood in the context of enhanced defect production, the application of a stress, and the developing irradiation microstructure. The formation and growth of loops and voids play important roles in the creep process. As will be shown, the stress-induced nucleation of dislocation loops and the bowing of dislocation lines by stress-assisted preferential absorption of interstitials can account for the transient portion of the creep behavior, but climb and glide are required to explain steady-state creep. The following sections present the mechanisms responsible for creep in metals under irradiation and their dependencies on the independent variables of dose rate, temperature, and stress as well as the developing microstructure.

13.2.1 Stress-Induced Preferential Nucleation of Loops (SIPN)

The application of an external stress can enhance the probability of interstitial loops nucleating on planes with a preferred orientation. Interstitial loops will be more likely to nucleate on planes perpendicular to an applied tensile stress than parallel to the stress. Vacancy loops will be less likely to nucleate on planes perpendicular (non-aligned) to the tensile stress and more likely to nucleate on planes parallel (aligned) to the stress. In either case, such preferential loop nucleation will cause the solid to increase in length in the direction of the applied tensile stress (Fig. 13.9). This process is termed the *stress-induced preferential nucleation*, SIPN mechanism

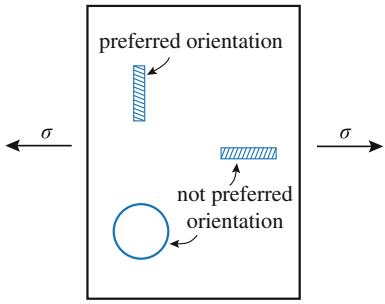

Fig. 13.9 Schematic of the influence of stress on the nucleation of dislocation loops

of irradiation creep [10]. If f is the excess fraction of aligned interstitial loops, then the concentration of aligned loops, N_{AL}, [11] is as follows:

$$N_{\mathrm{AL}} = 1/3(1-f)N_{\mathrm{L}} + fN_{\mathrm{L}}, \tag{13.56}$$

and the concentration of non-aligned loops, N_{NL}, is as follows:

$$N_{\mathrm{NL}} = 2/3(1-f)N_{\mathrm{L}}, \tag{13.57}$$

where N_{L} is the total loop concentration. The excess fraction of aligned interstitial loops is determined as follows.

If n interstitials are required before the interstitial aggregate is able to form an interstitial loop, then the probability that such an aggregate will form, p, in response to a normal stress is as follows:

$$p_i = \exp\frac{\sigma_i n\Omega}{kT} \Bigg/ \sum_{j=1}^{n_0} \exp\frac{\sigma_j n\Omega}{kT}, \tag{13.58}$$

where the subscript i refers to the ith orientation of n_0 possible loop orientations, and the number of loops in the ith orientation is as follows:

$$N_{\mathrm{L}}^{i} = p_i N_{\mathrm{L}}. \tag{13.59}$$

Defining f_i as the excess fraction of interstitial loops in the ith orientation, then:

$$p_i N_{\mathrm{L}} = \frac{1}{n_0}\left(1 - \sum_{j=1}^{n_0} f_j\right) N_{\mathrm{L}} + f_i N_{\mathrm{L}}, \quad i = 1\ldots n_0, \tag{13.60}$$

giving:

$$f_i = \left(\exp\frac{\sigma_i n\Omega}{kT} - 1\right) \Bigg/ \sum_{j=1}^{n_0} \exp\frac{\sigma_j n\Omega}{kT}. \tag{13.61}$$

We can simplify the description by reducing the n_0 possible orientations to the three orthogonal directions. Then, for a uniaxial tensile stress orthogonal to the $i = 1$ orientation, the other two orthogonal orientations ($i = 2, 3$) will have $p_2 = p_3 = 0$, and:

$$f_1 = \left(\exp\frac{\sigma_1 n\Omega}{kT} - 1\right) \Big/ \left(\exp\frac{\sigma_1 n\Omega}{kT} + 2\right), \tag{13.62}$$

and $f_2 = f_3 = 0$.

Using the result from Eq. (13.62), the creep strain due to the asymmetry in the loop population is as follows:

$$\varepsilon = 2/3\left[\pi r_L^2 b N_{AL} - 1/2\pi r_L^2 b N_{NL}\right]. \tag{13.63}$$

Substituting for N_{AL} and N_{NL} from Eqs. (13.56) and (13.57) gives:

$$\varepsilon = 2/3 f \pi r_L^2 b N_L, \tag{13.64}$$

where b is the Burgers vector, and r_L is the average loop radius. The creep rate is obtained by taking the time derivative of the creep strain given in Eq. (13.64), yielding:

$$\dot{\varepsilon} = 4/3 f b \pi r_L N_L \dot{r}_L, \tag{13.65}$$

and defining $\rho_L = 2\pi r_L N_L$ as the loop line length per unit volume gives:

$$\dot{\varepsilon} = 2/3 f b \rho_L \dot{r}_L. \tag{13.66}$$

If the argument of the exponential term in the expression for f in Eq. (13.62) is small compared to 1, then the exponent can be replaced by $\exp(x) \sim x + 1$, yielding:

$$f = \frac{\sigma n\Omega}{3kT}, \tag{13.67}$$

where the subscript on the stress is dropped, and Eq. (13.66) becomes:

$$\dot{\varepsilon} = \frac{2}{9}\frac{\sigma n b\Omega}{kT}\rho_L \dot{r}_L. \tag{13.68}$$

Note that the creep rate is proportional to stress and the loop growth rate, $\dot{r}_L$. Brailsford and Bullough [10] have shown that the creep rate can be related to swelling if the irradiated microstructure consists of only loops and voids as sinks and the absorption rate of vacancies by voids equals the absorption rate of interstitials by loops. In Eq. (13.65), the product of $2\pi r_L b$ (edge area of loop of thickness b) and $\dot{r}_L$ is the interstitial volume added to the loop. Multiplying by N_L loop/unit

volume gives the volume fraction increase of the loop due to the net absorption of interstitials. If this is balanced by a corresponding and equal net absorption of vacancies to voids to produce a fractional swelling rate, $\dot{S}$, then Eq. (13.65) becomes:

$$\dot{\varepsilon} = 2/3 f \dot{S}. \tag{13.69}$$

Substituting for f using Eq. (13.67) for the case where n is small yields:

$$\dot{\varepsilon} = \frac{2}{9}\frac{\sigma n b \Omega}{kT}\dot{S}, \tag{13.70}$$

and generalizing for the case where the total dislocation density is $\rho = \rho_L + \rho_N$ gives:

$$\dot{\varepsilon} = \frac{2}{9}\frac{\sigma n \Omega}{kT}\frac{\rho_L}{\rho}\dot{S}. \tag{13.71}$$

A more general treatment [12] of strain due to an anisotropic distribution of loops describes the strain in a volume due to a continuous distribution of dislocation loops [13] using the strain tensor:

$$\varepsilon_{ij} = \sum_{k=1}^{M} \frac{\rho^k A^k n_i^k b_j^k}{\Delta V}, \tag{13.72}$$

The equation describes the strain ε caused by M groups of loops in a volume ΔV, where the k^{th} group of loops all have the same Burgers vector b, area A, normal vector n, and number density ρ. The subscript i denotes x-, y-, z-directions of the loop normal vector, and subscript j denotes the contribution of loop Burgers vectors to the x-, y-, z-directions. M represents individual grains within a polycrystal. For a single grain:

$$\varepsilon_{ij}^k = \frac{N^k \pi \left(\frac{d}{2}\right)^2 n_i^k b_j^k}{\Delta V}, \tag{13.73}$$

where N^k is the total number of the k^{th} loop in the volume ΔV, and d is the measured loop diameter. Solution of Eq. (13.73) requires an expression for N^k. Taking as an example, irradiation of T91 at 500 °C to 1 dpa during application of a tensile stress of 180 MPa, the $a\langle 100\rangle$ loop distribution is shown in Fig. 13.10(a) and plotted in Fig. 13.10(b). Note that loops form preferentially with their normal in the direction of the tensile stress according to the following equation:

$$N^k/N = \alpha - \beta\theta^k, \tag{13.74}$$

where the constants α and β are fitting constants, and θ is defined as the angle between the loop normal and the tensile axis as shown in Fig. 13.11. Substituting

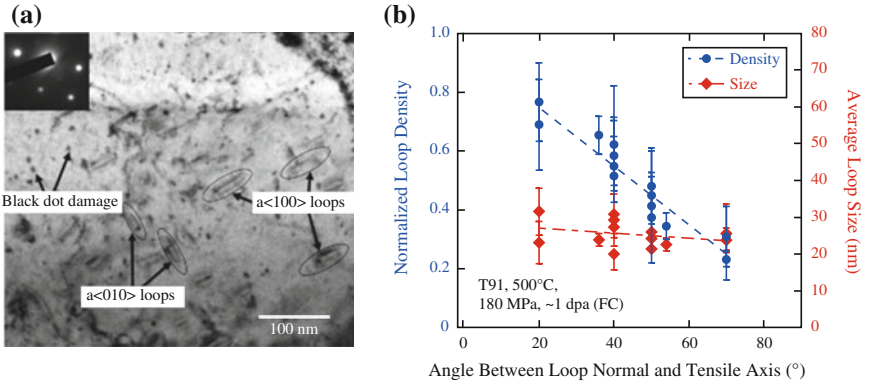

Fig. 13.10 (**a**) TEM image of $a\langle 100\rangle$ edge-on loops with $g = \langle 110\rangle$ on the $\langle 100\rangle$ zone axis and (**b**) loop anisotropy plot of the loop density and size following irradiation at 500 °C with a tensile stress of 180 MPa (after [12])

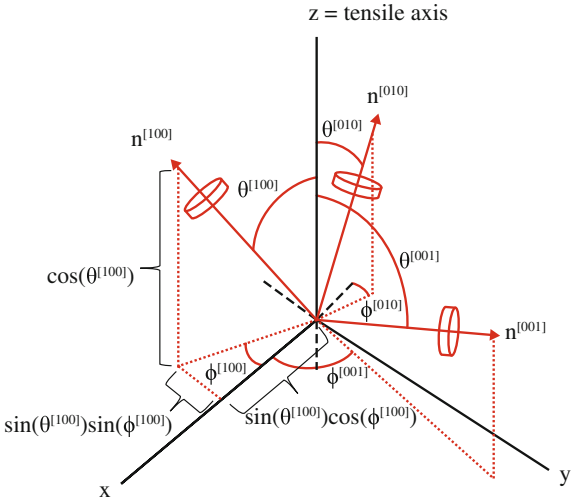

Fig. 13.11 Schematic of the normal vectors n^k of three sets of dislocation loops, where k = [100], [010], and [001]. The components of the $n^{[100]}$ are defined in the Cartesian coordinate system where the z-axis is the tensile axis (after [12])

the expression for N^k in Eq. (13.74) into Eq. (13.73) and simplifying [12] yields the strain in direction i:

$$\varepsilon_i = b\rho\pi\left(\frac{d}{2}\right)^2 \frac{\int_{\phi=0}^{\pi/2}\int_{\theta=0}^{\pi/2} n_i(\alpha-\beta\theta)\mathrm{d}\phi\mathrm{d}\theta}{\int_{\phi=0}^{\pi/2}\int_{\theta=0}^{\pi/2}(\alpha-\beta\theta)\mathrm{d}\phi\mathrm{d}\theta} - \frac{1}{3}\varepsilon_{\mathrm{vol}}. \tag{13.75}$$

The last term in Eq. (13.75) ensures volume conservation of creep by subtracting one-third of the volumetric expansion caused by dislocation loops from the strain of the three primary directions.

In the example provided, the creep strain due to anisotropy of the dislocation loops observed in the samples was found to account for only about 4.4 % of the total strain measured in the sample. This observation was consistent with previous works that claimed that strain due to anisotropy in the dislocation loops was much lower than the total measured strain [14], suggesting that another deformation mechanism must be driving the irradiation creep behavior.

Whether SIPN can accurately account for the observed creep strains is a matter of considerable debate. Matthews and Finnis [14] reviewed the arguments for and against SIPN and noted that while observations have supported an increase in preferred loop orientation with tensile stress, the magnitude of the measured creep strain is higher than can be accounted for by preferred orientation by a factor of 2–4, even if n is assumed to be large (10–30). The greatest limitation of the model is that once a loop is nucleated, the strain rate is determined by the irradiation dose, but is independent of stress. Thus, creep should continue if the stress is removed once nucleation has been completed. Also, if nucleation occurs before the stress is applied, then creep should not occur. Clearly, SIPN cannot account for all of the observed creep, but it may be a viable mechanism for a portion of the observed creep strain rate. A compliment to loop nucleation is preferential absorption of defects by loops caused by the applied stress, discussed in the next section.

13.2.2 Stress-Induced Preferential Absorption (SIPA)

At steady state, there are several distinct processes that may result in creep of a solid under irradiation and stress. They are (1) the transfer of atoms from planes parallel to the applied stress to those perpendicular to the applied stress, (2) the glide of dislocations on planes inclined to the stress direction, and (3) the climb and glide of dislocations due to the interstitial bias of the dislocation. The first is termed *stress-induced preferential absorption* (SIPA), and the second process is termed *preferred absorption glide* (PAG) [15]. PAG results from preferred absorption (SIPA) but is an additional component to the creep strain since it describes the glide contribution to the creep strain, whereas SIPA describes only the climb contribution to creep strain. The third mechanism is creep strain from the climb and glide process due to the net absorption of interstitials on dislocations of all orientations (i.e., unassisted by stress) and is essentially the same process as the climb and glide model described in Sect. 13.1 but for the case where the defect source is the excess interstitials. Note that this process is tied to swelling as the corresponding net excess of vacancies accumulates at cavities causing swelling.

The origin of the preferred absorption is the interaction between the dislocation and defects. In conventional SIPA, the origin is the elastic interaction between the

long-range stress field of the dislocation and that of the defect. Other origins for SIPA are anisotropic diffusion and elastodiffusion. While differing in the details of the origin of the interaction, all of these mechanisms result in a preferred absorption of interstitials by dislocations.

The flux of excess interstitials absorbed by dislocations with orientation described by j and density ρ_{j} is as follows:

$$J_j = \rho_j \Omega \left(z_{\mathrm{i}}^{\mathrm{d}j} D_{\mathrm{i}} C_{\mathrm{i}} - z_{\mathrm{v}}^{\mathrm{d}j} D_{\mathrm{v}} C_{\mathrm{v}} + z_{\mathrm{v}}^{\mathrm{d}j} D_{\mathrm{v}} C_{\mathrm{v}}^{\mathrm{d}j} \right), \tag{13.76}$$

where $z_{\mathrm{i,v}}^{\mathrm{d}j}$ are the capture efficiencies of dislocations of orientation, j, D_{iv} are the diffusion coefficients, and C_{iv} are the bulk concentrations of interstitials and vacancies. The variable, $C_{\mathrm{v}}^{\mathrm{d}j}$, is the vacancy concentration in equilibrium with a dislocation of orientation j. For a uniaxial tensile stress where $j = 1$:

$$C_{\mathrm{v}}^{\mathrm{d}1} = C_{\mathrm{v}}^{0} \exp\left(\frac{\sigma \Omega}{kT} \right) \tag{13.77}$$

$$C_{\mathrm{v}}^{\mathrm{d}2} = C_{\mathrm{v}}^{\mathrm{d}3} = C_{\mathrm{v}}^{0}. \tag{13.78}$$

The interstitial flux, J_j, can also be related to the climb velocity as follows:

$$J_j = b \rho_j \upsilon_j, \tag{13.79}$$

where ρ_j is the density of dislocations with their planes perpendicular to j. Substituting for J_j from Eq. (13.79) into Eq. (13.76) and solving for υ_{j} gives:

$$\upsilon_j = \frac{\Omega}{b} \left(z_{\mathrm{i}}^{\mathrm{d}j} D_{\mathrm{i}} C_{\mathrm{i}} - z_{\mathrm{v}}^{\mathrm{d}j} D_{\mathrm{v}} C_{\mathrm{v}} + z_{\mathrm{v}}^{\mathrm{d}j} D_{\mathrm{v}} C_{\mathrm{v}}^{\mathrm{d}j} \right). \tag{13.80}$$

Substituting Eq. (13.80) into Eq. (13.5) gives the total creep rate as:

$$\dot{\varepsilon}_{\mathrm{j}} = \Omega \left(z_{\mathrm{i}}^{\mathrm{d}j} D_{\mathrm{i}} C_{\mathrm{i}} - z_{\mathrm{v}}^{\mathrm{d}j} D_{\mathrm{v}} C_{\mathrm{v}} + z_{\mathrm{v}}^{\mathrm{d}j} D_{\mathrm{v}} C_{\mathrm{v}}^{\mathrm{d}j} \right) \rho_j. \tag{13.81}$$

But Eq. (13.81) also includes contributions due to void swelling. That component of the strain is just one-third of the volumetric swelling, or $\varepsilon = 1/3(\varepsilon_1 + \varepsilon_2 + \varepsilon_3)$, and the swelling strain rate, $\dot{\varepsilon}_{\mathrm{S}}$, is as follows:

$$\dot{\varepsilon}_{\mathrm{S}} = \frac{\Omega}{3} \sum_{n=1}^{3} \left(z_{\mathrm{i}}^{\mathrm{d}n} D_{\mathrm{i}} C_{\mathrm{i}} - z_{\mathrm{v}}^{\mathrm{d}n} D_{\mathrm{v}} C_{\mathrm{v}} + z_{\mathrm{v}}^{\mathrm{d}n} D_{\mathrm{v}} C_{\mathrm{v}}^{\mathrm{d}n} \right) \rho_n. \tag{13.82}$$

The creep by climb due to preferential absorption of interstitials at dislocations is then:

$$\begin{aligned}\dot{\varepsilon}_j = {} & \Omega(z_{\mathrm{i}}^{\mathrm{d}j} D_{\mathrm{i}} C_{\mathrm{i}} - z_{\mathrm{v}}^{\mathrm{d}j} D_{\mathrm{v}} C_{\mathrm{v}} + z_{\mathrm{v}}^{\mathrm{d}j} D_{\mathrm{v}} C_{\mathrm{v}}^{\mathrm{d}j})\rho_j \\ & - \frac{\Omega}{3} \sum_{n=1}^{3} \left(z_{\mathrm{i}}^{\mathrm{d}n} D_{\mathrm{i}} C_{\mathrm{i}} - z_{\mathrm{v}}^{\mathrm{d}n} D_{\mathrm{v}} C_{\mathrm{v}} + z_{\mathrm{v}}^{\mathrm{d}n} D_{\mathrm{v}} C_{\mathrm{v}}^{\mathrm{d}n} \right) \rho_n .\end{aligned} \tag{13.83}$$

For dislocations distributed isotropically among the three orthogonal directions:

$$\rho_1 = \rho_2 = \rho_3 = \rho/3. \tag{13.84}$$

Substituting Eqs. (13.77) and (13.78) for the equilibrium vacancy concentration and Eq. (13.84) for the dislocation density into Eq. (13.83) for the stress direction $j = 1 = A$ (aligned dislocations) gives:

$$\dot{\varepsilon}_{\mathrm{climb}} = \frac{2}{9}\Omega\rho \left\{ \underbrace{\left[\Delta z_{\mathrm{i}}^{\mathrm{d}} D_{\mathrm{i}} C_{\mathrm{i}} - \Delta z_{\mathrm{v}}^{\mathrm{d}} D_{\mathrm{v}} C_{\mathrm{v}} \right]}_{\mathrm{SIPA}} + \underbrace{D_{\mathrm{v}} C_{\mathrm{v}}^{0} \left[z_{\mathrm{v}}^{\mathrm{dA}} \exp\left(\frac{\sigma\Omega}{kT} \right) - z_{\mathrm{v}}^{\mathrm{dN}} \right]}_{\mathrm{PE}} \right\}, \tag{13.85}$$

where $\Delta z_{\mathrm{i,v}}^{\mathrm{d}} = z_{\mathrm{i,v}}^{\mathrm{dA}} - z_{\mathrm{i,v}}^{\mathrm{dN}}$, and $z_{\mathrm{i,v}}^{\mathrm{dA}}$ denotes the capture efficiency of aligned dislocations, and $z_{\mathrm{i,v}}^{\mathrm{dN}}$ denotes the capture efficiency of non-aligned dislocations ($j = 2$). The first term in square brackets is the dislocation climb creep rate due to preferential absorption of interstitials, or SIPA:

$$\dot{\varepsilon}_{\mathrm{SIPA}} = \frac{2}{9}\Omega\rho \left[\Delta z_{\mathrm{i}}^{\mathrm{d}} D_{\mathrm{i}} C_{\mathrm{i}} - \Delta z_{\mathrm{v}}^{\mathrm{d}} D_{\mathrm{v}} C_{\mathrm{v}} \right]. \tag{13.86}$$

The second term in square brackets is the dislocation climb creep rate due to preferred emission, PE [15], of vacancies:

$$\dot{\varepsilon}_{\mathrm{PE}} = \frac{2}{9}\Omega\rho D_{\mathrm{v}} C_{\mathrm{v}}^{0} \left[z_{\mathrm{v}}^{\mathrm{dA}} \exp\left(\frac{\sigma\Omega}{kT} \right) - z_{\mathrm{v}}^{\mathrm{dN}} \right]. \tag{13.87}$$

If the differences in capture efficiencies (preference) of the dislocations in different orientations were removed, i.e., $\Delta z_{\mathrm{i}}^{\mathrm{d}} = \Delta z_{\mathrm{v}}^{\mathrm{d}} = 0$, then the first term disappears and the creep rate is then due solely to thermal processes.

13.2.3 Climb and Glide Due to Preferential Absorption Glide (PAG)

While SIPA provides a mechanism for creep by dislocation climb, dislocations can also contribute to creep by glide if they are able to overcome obstacles in their slip plane by the climb process [15]. Under an applied stress, pinned dislocations will glide until they reach a configuration where the restoring force due to line tension is balanced by the applied stress. Since dislocations are pinned, creep is limited to the elastic stress given by $\varepsilon = \sigma/E$. Climb enables the dislocation to overcome the initial pinning points. The released segments bow out between new pinning points until, again, the line tension balances the applied stress. Figure 13.12 shows the process by which dislocation segments bow out between pinning points, are released from the pinning points, and are then pinned again. Each cycle of climb and glide to pinning results in an elastic deflection in addition to the strain due to climb, which together, account for the total creep strain in the solid, all the while, the dislocation network maintains its configuration. This mechanism has also been referred to as "transient creep" because of its occurrence at low dose. However, since the dislocation lines can continue to bow out after climbing over pinning points, it can also account for steady-state creep.

Similar to Eq. (13.19), the creep rate due to climb and glide can be written as:

$$\dot{\varepsilon}_{\mathrm{CG}} = \varepsilon \frac{\upsilon_{\mathrm{c}}}{l}, \tag{13.88}$$

where ε is the strain due to elastic deflection, υ_{c} is the climb velocity, and l is the distance between pinning points. When pinning is caused by the network dislocation density, l is given by $l = 1/\sqrt{\pi\rho_{\mathrm{d}}}$, and ρ_{d} is the dislocation density. Equation (13.88) then becomes:

$$\dot{\varepsilon}_{\mathrm{CG}} = \varepsilon(\pi\rho_{\mathrm{d}})^{1/2}\upsilon_{\mathrm{c}}. \tag{13.89}$$

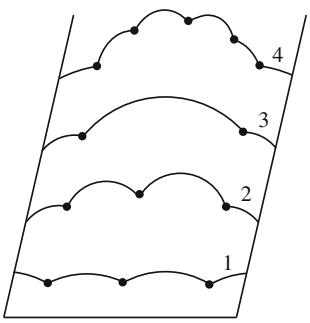

Fig. 13.12 Schematic of glide by dislocation bowing and the pinning and unpinning of dislocation segments

The climb velocity can be determined from Eq. (13.80) by adding and subtracting the velocity component due to volumetric swelling:

$$\begin{aligned} v_j = \frac{\Omega}{b}\Bigg[&\left(z_{\mathrm{i}}^{\mathrm{d}j} D_{\mathrm{i}} C_{\mathrm{i}} - z_{\mathrm{v}}^{\mathrm{d}j} D_{\mathrm{v}} C_{\mathrm{v}} + z_{\mathrm{v}}^{\mathrm{d}j} D_{\mathrm{v}} C_{\mathrm{v}}^{\mathrm{d}j}\right) \\ &- \frac{1}{3\rho_j} \sum_{n=1}^{3} \left(z_{\mathrm{i}}^{\mathrm{d}n} D_{\mathrm{i}} C_{\mathrm{i}} - z_{\mathrm{v}}^{\mathrm{d}n} D_{\mathrm{v}} C_{\mathrm{v}} + z_{\mathrm{v}}^{\mathrm{d}n} D_{\mathrm{v}} C_{\mathrm{v}}^{\mathrm{d}n}\right) \rho_n \Bigg] \\ &+ \frac{\Omega}{3b\rho_j} \sum_{n=1}^{3} \left(z_{\mathrm{i}}^{\mathrm{d}n} D_{\mathrm{i}} C_{\mathrm{i}} - z_{\mathrm{v}}^{\mathrm{d}n} D_{\mathrm{v}} C_{\mathrm{v}} + z_{\mathrm{v}}^{\mathrm{d}n} D_{\mathrm{v}} C_{\mathrm{v}}^{\mathrm{d}n}\right) \rho_n . \end{aligned} \tag{13.90}$$

The physical meanings of the terms in Eq. (13.90) are as follows. The first term in square brackets is the climb velocity due to all processes contributing to vacancy and interstitial absorption and vacancy emission. The second term in the square brackets is the climb due to net point defect absorption and emission at dislocations attributable only to swelling. Subtracting this term from the first term yields the net result, enclosed in square brackets, being the climb velocity due only to the volume-conserving processes of stress-induced preferential absorption and to preferred vacancy emission. The last term in Eq. (13.90) is the dislocation climb velocity due to isotropic swelling. It is the terms in square brackets that are responsible for the climb and glide process in the absence of swelling. Using Eq. (13.84) and the average velocity of the dislocations given by:

$$v = \frac{|v_1| + |v_2| + |v_3|}{3}, \tag{13.91}$$

equation (13.90) becomes:

$$v = \frac{\Omega}{3b}\left\{\left|z_{\mathrm{i}}^{\mathrm{d}1} D_{\mathrm{i}} C_{\mathrm{i}} - z_{\mathrm{v}}^{\mathrm{d}1} D_{\mathrm{v}} C_{\mathrm{v}} + z_{\mathrm{v}}^{\mathrm{d}1} D_{\mathrm{v}} C_{\mathrm{v}}^{\mathrm{d}1}\right| + 2\left|z_{\mathrm{i}}^{\mathrm{d}2} D_{\mathrm{i}} C_{\mathrm{i}} - z_{\mathrm{v}}^{\mathrm{d}2} D_{\mathrm{v}} C_{\mathrm{v}} + z_{\mathrm{v}}^{\mathrm{d}2} D_{\mathrm{v}} C_{\mathrm{v}}^{\mathrm{d}2}\right|\right\}. \tag{13.92}$$

When preferential absorption and preferential emission occur without swelling, the number of interstitials absorbed must be balanced by the number of vacancies absorbed, so:

$$\left(z_{\mathrm{i}}^{\mathrm{d}1} D_{\mathrm{i}} C_{\mathrm{i}} - z_{\mathrm{v}}^{\mathrm{d}1} D_{\mathrm{v}} C_{\mathrm{v}} + z_{\mathrm{v}}^{\mathrm{d}1} D_{\mathrm{v}} C_{\mathrm{v}}^{\mathrm{d}1}\right) = 2\left(z_{\mathrm{i}}^{\mathrm{d}2} D_{\mathrm{i}} C_{\mathrm{i}} - z_{\mathrm{v}}^{\mathrm{d}2} D_{\mathrm{v}} C_{\mathrm{v}} + z_{\mathrm{v}}^{\mathrm{d}2} D_{\mathrm{v}} C_{\mathrm{v}}^{\mathrm{d}2}\right), \tag{13.93}$$

and Eq. (13.92) becomes:

$$v = \frac{2}{3}\frac{\Omega}{b}\left(z_{\mathrm{i}}^{\mathrm{d}1} D_{\mathrm{i}} C_{\mathrm{i}} - z_{\mathrm{v}}^{\mathrm{d}1} D_{\mathrm{v}} C_{\mathrm{v}} + z_{\mathrm{v}}^{\mathrm{d}1} D_{\mathrm{v}} C_{\mathrm{v}}^{\mathrm{d}1}\right). \tag{13.94}$$

Substituting the climb velocity given in Eq. (13.94) into the creep equation for climb and glide, Eq. (13.89) gives:

$$\dot{\varepsilon}_{\mathrm{CG}} = \frac{2}{3}\frac{\varepsilon}{b}\Omega(\pi\rho_{\mathrm{d}})^{1/2}\left(z_{\mathrm{i}}^{\mathrm{d1}}D_{\mathrm{i}}C_{\mathrm{i}} - z_{\mathrm{v}}^{\mathrm{d1}}D_{\mathrm{v}}C_{\mathrm{v}} + z_{\mathrm{v}}^{\mathrm{d1}}D_{\mathrm{v}}C_{\mathrm{v}}^{\mathrm{d1}}\right). \tag{13.95}$$

After some manipulation of Eq. (13.95), Mansur [15] showed that the climb and glide creep rate can be written as:

$$\dot{\varepsilon}_{\mathrm{CG}} = \frac{4}{9}\frac{\varepsilon\Omega}{b}\Omega(\pi\rho_{\mathrm{d}})^{1/2}D_{\mathrm{i}}C_{\mathrm{i}}\Delta z_{\mathrm{i}}^{\mathrm{d}}, \tag{13.96}$$

where $\Delta z_{\mathrm{i}}^{\mathrm{d}}$ is defined after Eq. (13.85). Note that in both Eqs. (13.86) and (13.96), the term $\Delta z_{\mathrm{i}}^{\mathrm{d}}$ appears, which represents the difference in capture efficiencies between aligned and non-aligned dislocations, and is therefore dependent on stress. Mansur writes $\Delta z_{\mathrm{i}}^{\mathrm{d}} = \Delta z_{\mathrm{i}}'\varepsilon$ (where $\Delta z_{\mathrm{i}}'$ is independent of stress) so that $\dot{\varepsilon}_{\mathrm{SIPA}} \propto \varepsilon$ and $\dot{\varepsilon}_{\mathrm{CG}} \propto \varepsilon^2$, and since $\varepsilon = \sigma/E$,we have $\dot{\varepsilon}_{\mathrm{SIPA}} \propto \sigma$ and $\dot{\varepsilon}_{\mathrm{CG}} \propto \sigma^2$. Also, as shown in Sect. 5.1.3, the term C_{i} is proportional to the defect production rate, K_0, for sink-dominated cases and to $K_0^{1/2}$ for recombination-dominated cases. It should also be noted that since there is no need for a net preferential absorption of interstitials at all edge dislocations, creep can proceed in the absence of swelling.

13.2.4 Climb and Glide Driven by Dislocation Bias

The preceding analysis describes creep that is driven by stress-induced preferential absorption of interstitials at dislocations. The creep rate has both climb and glide components, and the creep process is governed by dislocation segment bowing following climb to free the segment from the pinning points. Here, we consider creep that is driven by the dislocation bias rather than preferential absorption. Clearly in order for there to be a net absorption of interstitials by dislocations requires that there is an equivalent net absorption of vacancies by other sinks in the solid. These sinks are assumed to be voids. Creep due to the excess absorption of interstitials at dislocations is equivalent to the thermal creep climb and glide mechanisms discussed in Sect. 13.2, but with interstitial absorption replacing vacancy absorption. For this case, we return to Eq. (13.19), which expresses the creep rate in terms of the climb velocity, υ_{c}, and the obstacle height, h. Equation (13.79) gives the climb velocity in terms of the absorption flux of interstitials at dislocations. For climb due solely to dislocation bias, Eq. (13.76) for the interstitial flux becomes:

$$J = \rho_{\mathrm{m}}\Omega\left[z_{\mathrm{i}}^{\mathrm{d}}D_{\mathrm{i}}C_{\mathrm{i}} - z_{\mathrm{v}}^{\mathrm{d}}D_{\mathrm{v}}C_{\mathrm{v}}^{\mathrm{d}}\right], \tag{13.97}$$

and substituting the expression for J in Eq. (13.97) into Eq. (13.79) and solving for υ_c gives:

$$\upsilon_c = \frac{\Omega}{b}\left[z_i^d D_i C_i - z_v^d D_v C_v^d\right]. \tag{13.98}$$

Equation (13.98) also can be obtained directly from Eq. (13.90) by neglecting thermal emission, $C_v^{dj} \sim 0$, and requiring that the zs for dislocations do not have an orientation dependence, so that $z_v^{dj} = z_v^d$ *and* $z_i^{dj} = z_i^d$. The obstacle height is given in Eq. (13.23), and in the case of a dislocation pileup against an obstacle, the stress σ_{xy} is replaced by $n\sigma_{xy}$ where n is the number of dislocations in the pileup and is given by Eq. (13.35). Substituting Eq. (13.98) for υ_c, Eq. (13.23) for h, and Eq. (13.35) for n into Eq. (13.19) gives:

$$\dot{\varepsilon} = \frac{\rho_m l^2 \Omega 8\pi^2 (1-\nu)^2 \sigma_{xy}^2}{(\mu b)^2}\left[z_i^d D_i C_i - z_v^d D_v C_v^d\right]. \tag{13.99}$$

When creep is driven by swelling, the absorption rate of interstitials at dislocations is balanced by the same absorption rate of vacancies by voids:

$$\rho_m (J_i^d - J_v^d) = A_v^V - A_i^V = \frac{1}{\Omega}\frac{\Delta \dot{V}}{V}. \tag{13.100}$$

Substituting Eq. (13.100) into Eq. (13.99) gives:

$$\dot{\varepsilon} = \frac{\rho_m}{\rho_d}\frac{8\pi^2 l^2 (1-\nu)^2 \sigma_{xy}^2}{(\mu b)^2}\frac{\Delta \dot{V}}{V}, \tag{13.101}$$

where the term ρ_m/ρ_d is the fraction of the dislocation density that is mobile and can contribute to creep. It should also be noted that irradiated metals often do not exhibit pileups at obstacles. In this case, the number of dislocations in a pileup, n, is set equal to 1 and the creep rate is proportional to the stress. Wolfer et al. [16] showed that when Frank loops are the obstacles, the creep rate is proportional to stress to the power $n = 1$.

13.2.5 Transient Creep

Creep can occur prior to the achievement of steady state by the vacancy and interstitial concentrations. Such creep is referred to as *transient creep*. Three transient creep processes are of greatest importance: *glide-induced transient absorption, start-up-induced transient absorption*, and *cascade creep*.

Glide-Induced Transient Absorption

In climb and glide creep, the climb process is the limiting step as glide occurs extremely rapidly. In fact, the glide process is so rapid that steady-state concentrations of point defects cannot be maintained at the dislocation. As a result, the dislocation absorbs both vacancies and interstitials rapidly in an effort to re-establish the steady-state point defect diffusion profiles at its new location [17]. However, vacancies and interstitials are not absorbed in equal numbers, and the imbalance in absorption rate gives rise to a form of transient creep termed glide-induced transient absorption. Figure 5.3 in Chap. 5 shows that at steady state, the bulk vacancy concentration exceeds the interstitial concentration by orders of magnitude. Consequently, the flow of vacancies to the dislocation causes an increment of positive climb, releasing the dislocation from an obstacle and producing creep by glide. Figure 13.13 shows the increment of climb caused by excess vacancy absorption prior to achievement of steady-state diffusion profiles. The initial climb shown in the positive direction is the transient vacancy climb, and the negative climb at longer times ($Dt = 10^8$ nm^2) is the bias-driven interstitial climb. If the transient positive climb is large enough to escape the barrier, the dislocation glides to the next barrier. If the transient climb is inadequate, the steady-state climb eventually reverses the dislocation motion, and escape occurs in the negative direction. Once steady state has been achieved, then climb is controlled by the small net excess of interstitials due to stress-induced preferential absorption described in the preceding section. This form of transient climb can cause high creep rates at low temperatures, where the steady-state vacancy concentration is high, as long as the temperature is not too low so that vacancy diffusion is limiting.

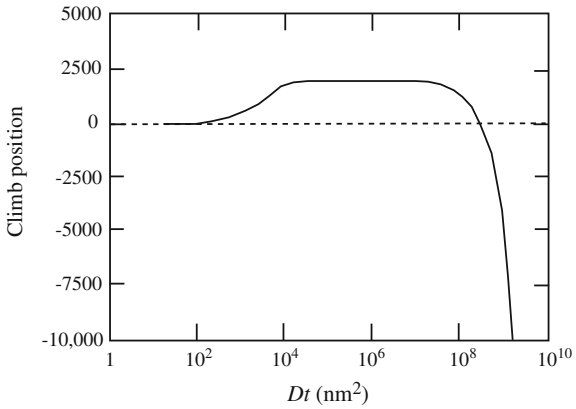

Fig. 13.13 Dislocation climb for a unit length of dislocation in units normalized to the steady-state vacancy concentration divided by 10^{18}. The diffusion coefficients are in units of nm^2/s, and a steady-state climb rate corresponding to 1 % of the total interstitial flux is assumed (after [17])

Start-Up-Induced Transient Absorption

Significant creep can also occur at low temperatures coincident with the start of the irradiation. This creep process, referred to as start-up-induced transient absorption, occurs by the absorption of interstitials prior to steady state when interstitials are mobile, but vacancy diffusion is too slow for them to interact with the dislocations [18]. Referring again to Fig. 5.3, at the start of irradiation at low temperature, the concentrations of both vacancies and interstitials increase linearly with time until interstitials begin to be absorbed at sinks. At this point in time, defined by the time constant τ_2, the interstitial concentration reaches a quasi-steady state, while the vacancy concentration continues to climb. The continued buildup of vacancies causes recombination to occur, resulting in a decrease in the interstitial concentration and a slower rate of vacancy buildup with time. With additional increase in the vacancy concentration, recombination dominates the loss process (at $t = \tau_4$) causing a steeper decline in the interstitial loss rate and a smaller rate of vacancy buildup. Eventually, steady state is reached when the vacancy concentration is high enough that vacancies interact with sinks.

The contribution of interstitials to creep during this start-up transient can be estimated by determining the number of excess interstitials, N_i, that are absorbed by the dislocations in each time interval in Fig. 5.3. For example, in the time interval τ_4–τ_2, the number of interstitials produced is K_0 (τ_4–τ_2), and the number remaining is $K_0/K_{is}C_s$, so the number absorbed by the dislocation is as follows:

$$N_i = K_0(\tau_4 - \tau_2) - K_0/K_{is}C_s. \tag{13.102}$$

Using the same analysis, estimates can be made for the number of interstitials absorbed during the time interval τ_3–τ_4, or until steady state is reached, at which point the transient ends. Interstitial absorption results in climb-enabled glide as described by Eq. (13.96), with N_i substituted for C_i. Figure 13.14 shows that the

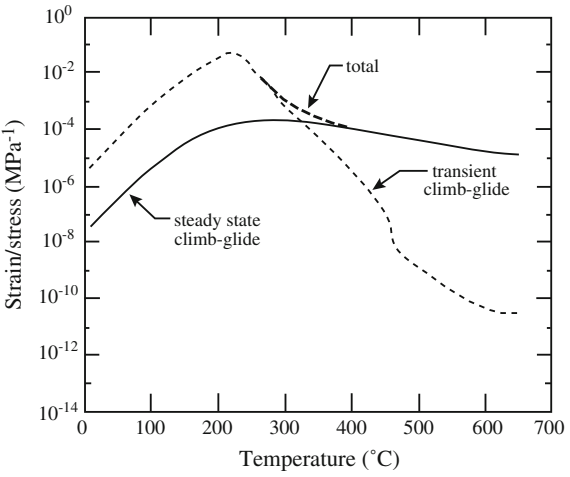

Fig. 13.14 Creep deformation per unit stress as a function of temperature for austenitic alloys using the conventional climb-enabled glide model (steady-state condition) and the start-up-induced transient absorption model (from [18])

total creep strain in austenitic stainless steels can be dominated by start-up-induced transient absorption at temperatures into the 300 °C range and near the 200 °C range for ferritic alloys. As such, it is an important mechanism of creep at low temperature and during the start-up phase of an irradiation.

Cascade Creep

One of the simplest transient creep models is based on the effect of stress on the displacement spike volume. As described by Brinkman and Wiedersich [19], if a load is applied to a solid during the occurrence of a displacement spike, then elastic strain in the spike region is relaxed locally and frozen in. The strain rate from this process is given by:

$$\dot{\varepsilon}_{\text{cas}} = \varepsilon_{\text{e}} V_{\text{cas}} \alpha N \sigma_{\text{s}} \phi, \tag{13.103}$$

where the elastic strain $\varepsilon_{\text{e}} = \sigma/E$, V_{cas} is the volume of the cascade, α is the number of spikes per neutron scattering event, N is the atom number density in the solid, σ_{s} is the neutron scattering cross section, and ϕ is the fast neutron flux. Matthews and Finnis [14] noted that this creep rate underestimates the observed irradiation creep in neutron-irradiated structural materials. However, since defect generation does not occur continuously over space and time, and not all defects escape the damage region, strain caused by cascade effects may be important to consider. A dislocation segment will make climb excursions in response to fluctuations in the local vacancy concentration caused by a nearby cascade. During an excursion, there is a probability that the segment will be unpinned. Mansur [20] accounted for cascade effects in the climb-enabled glide model by replacing υ_{c}/h in Eq. (13.19) by the release frequency of pinned dislocation segments, ω:

$$\dot{\varepsilon} = \rho b l \omega, \tag{13.104}$$

where:

$$\omega = \sum_{j-1}^{h} R_j F_j, \tag{13.105}$$

and F_j is the frequency with which a dislocation segment climbs to a height of at least h:

$$F_j = 4\pi N \sigma_{\text{s}} \phi \int_0^{\infty} \rho^2 P_j \mathrm{d}r, \tag{13.106}$$

and P_j is the probability of climb of j or greater. The term, $R_{j,}$ is the probability of finding a dislocation a distance jb from the unpinning point and is given by:

$$R_j = \rho_j/\rho. \tag{13.107}$$

The release frequencies and hence the creep rates determined using this model are comparable to those from preferred absorption-driven climb or swelling-driven climb [20].

13.2.6 Loop Unfaulting

Another possible interaction between an applied stress and interstitial loops that could produce creep strain is loop unfaulting. As discussed in Chap. 7, dislocation loops grow in size and eventually become unstable and unfault to become part of the dislocation network. This process is equivalent to the production of mobile dislocations which may then participate in the creep process by SIPA, PAG, or climb and glide driven by interstitial bias. The maximum radius to which a loop can grow, $R_{\max}$, is governed by the loop density and is given by:

$$\frac{4\pi}{3}\rho_{\mathrm{L}}R_{\max}^{3}=1. \tag{13.108}$$

When loops interact, they coalesce and contribute to the network dislocation density. Interaction between individual dislocations and loops results in loop unfaulting that also contributes to the network (see Chap. 12, Sect. 12.3). As the dislocation density increases, the rate of loop interaction with the network increases and the loop radius is limited to a value of the order of the network mesh length, $\rho_{\mathrm{N}}^{-1/2}$, where ρ_{N} is the network dislocation density. Loop unfaulting can contribute to irradiation creep strain since the presence of a stress will assist the nucleation of the unfaulting dislocations with favorable orientations resulting in an increased probability of unfaulting. The application of a shear stress in the plane of the loops will induce a greater number of loops to shear in the direction favored by the stress to produce a net shear of the crystal, which will appear as creep. If ρ is the total dislocation density and ρ_{s} is the number of dislocation loops lying on a plane for which the shear stress is a maximum, then the number of loops shearing in that direction is given by Lewthwaite [21] as follows:

$$\rho_1=\frac{\rho_{\mathrm{s}}\exp\left(\dfrac{\pi R_{\mathrm{c}}^{2}b\sigma}{kT}\right)}{\exp\left(\dfrac{\pi R_{\mathrm{c}}^{2}b\sigma}{kT}\right)+\exp\left(-\dfrac{\pi R_{\mathrm{c}}^{2}b\sigma}{kT}\right)}, \tag{13.109}$$

where R_{c} is the critical loop size for unfaulting [the maximum value is given by Eq. (13.108)], and σ is the stress. The number of loops shearing in the opposite direction is $\rho_2 = \rho_{\mathrm{s}}-\rho_1$, and the strain due to the loop unfaulting is then:

$$\varepsilon=\bar{A}b_{\mathrm{s}}(\rho_1-\rho_2), \tag{13.110}$$

where $\bar{A}$ is the average loop area, and b_s is the magnitude of the Burgers vector of the reaction producing the strain. Substituting in for ρ_1 and ρ_2 in Eq. (13.110) and averaging the strain over all possible loop orientations (which gives a factor of 1/30) yields:

$$\varepsilon = \frac{\rho \bar{A} b_s}{30}\left[\frac{\exp\left(\frac{\pi R_c^2 b\sigma}{kT}\right) - \exp\left(-\frac{\pi R_c^2 b\sigma}{kT}\right)}{\exp\left(\frac{\pi R_c^2 b\sigma}{kT}\right) + \exp\left(-\frac{\pi R_c^2 b\sigma}{kT}\right)}\right]. \tag{13.111}$$

The term in brackets can be written as the hyperbolic tangent of the argument, giving:

$$\varepsilon = \frac{\rho \bar{A} b_s}{30}\tanh\left(\pi R_c^2 b\sigma/kT\right). \tag{13.112}$$

If the argument is small compared to 1, then $\tanh x \sim x$ and Eq. (13.112) becomes:

$$\varepsilon = \frac{\rho \bar{A} b_s}{30}\pi R_c^2 b\sigma/kT. \tag{13.113}$$

If loop growth is driven by swelling, then $\rho \bar{A} b_s$ is replaced with $\Delta \dot{V}/V$, the loop volume $\pi R_c^2 b$ is equated with the volume of the defects in the loop, $n_c \Omega$, and the term $\frac{k_L^2}{k_L^2 + k_N^2}$ is added to account for the network dislocation density as well, to yield the creep rate in terms of the swelling rate:

$$\dot{\varepsilon} = \frac{\Delta \dot{V}}{V}\frac{k_L^2}{k_L^2 + k_N^2}\frac{\pi R_c^2 b\sigma/kT}{30}. \tag{13.114}$$

Matthews and Finnis [14] noted that the unfaulting radius is large in austenitic alloys and the creep rate can be significant, but because of the small critical loop size in bcc metals, the contribution will be small.

13.2.7 Recovery Creep

All of the irradiation creep mechanisms discussed thus far allow for or contribute to the growth of the dislocation density, but do not account for the removal of dislocations, as must occur during creep. Matthews and Finnis [14] expressed the rate of change in dislocation density in terms of the creep rate as follows:

$$\dot{\rho} = \frac{\dot{\varepsilon}}{bl} - 2\rho^{3/2} v_c, \tag{13.115}$$

where l is the mean dislocation glide length, and v_c is the climb velocity. The first term is the production rate of dislocations due to creep, obtained from Eq. (13.14), and the second term is the loss due to annihilation. Taking the steady-state limit of $\dot{\rho} = 0$, the steady-state creep rate is expressed in terms of the dislocation density as follows:

$$\dot{\varepsilon} = 2bl\rho^{3/2}v_c. \tag{13.116}$$

The stress dependence is determined by the dislocation density, the climb velocity, and the slip length. The dislocation density varies with stress according to Eq. (13.7) (in which the term, α, appears in the denominator inside the brackets) $\rho = \dfrac{\sigma^2}{\alpha^2\mu^2b^2}$ and contributes a σ^3 term to the creep rate given in Eq. (13.116). For stress-induced preferential absorption, we have from Eq. (13.86):

$$v_{\mathrm{SIPA}} = \frac{2}{9}\frac{\Omega}{b}\left(z_i^d D_i C_i - z_v^d D_v C_v + z_v^d D_v C_v^d\right), \tag{13.117}$$

substituting into Eq. (13.116) and equating $\Omega = b^3$ gives:

$$\dot{\varepsilon} = \frac{4}{9}\frac{\sigma^3 l}{\alpha^3\mu^3}\left(z_i^d D_i C_i - z_v^d D_v C_v + z_v^d D_v C_v^d\right). \tag{13.118}$$

If l is fixed by impenetrable obstacles and is therefore independent of stress, then the stress dependence of the creep rate is σ^3. However, if l is determined by the dislocation density, then substituting for l from Eq. (13.88) and expressing the dislocation density in terms of stress, Eq. (13.7) gives:

$$\dot{\varepsilon} = \frac{4}{9}\frac{\sigma^2 b}{\sqrt{\pi}\alpha^2\mu^2}\left(z_i^d D_i C_i - z_v^d D_v C_v + z_v^d D_v C_v^d\right), \tag{13.119}$$

where the stress dependence is σ^2, which is the same stress dependence as in preferential absorption climb and glide given by Eq. (13.99).

13.2.8 *Diffusional Creep: Why There Is No Effect of Irradiation*

All of the mechanisms of irradiation creep discussed thus far are based on the actions of dislocations. The reason is that while diffusional creep is a viable thermal creep mechanism, it is unaffected by irradiation and can be understood as follows. Consider the discussion of Nabarro–Herring creep in Sect. 13.1.2. There it was shown that creep is driven by a difference in the equilibrium vacancy concentrations at the grain boundaries oriented parallel to the tensile and compressive stress directions, Eq. (13.45). Under irradiation, Eq. (13.47) is modified to include interstitials:

$$J_v = D_v \frac{dC_v}{dx} - D_i \frac{dC_i}{dx} \approx \kappa D_v \frac{C_v^t - C_v^c}{d} - \kappa D_i \frac{C_i^t - C_i^c}{d}. \tag{13.120}$$

Substituting in for C_v^t and C_v^c from Eq. (13.45) and for C_i^t and for C_i^c using the same equations but with the signs on the arguments of the exponential terms reversed because of the opposite effect of stress on interstitials gives:

$$\begin{aligned} J_v = \kappa D_v & \frac{C_v^0 \exp\left(\frac{\sigma\Omega}{kT}\right) - C_v^0 \exp\left(-\frac{\sigma\Omega}{kT}\right)}{d} \\ - \kappa D_i & \frac{C_i^0 \exp\left(-\frac{\sigma\Omega}{kT}\right) - C_i^0 \exp\left(\frac{\sigma\Omega}{kT}\right)}{d}. \end{aligned} \tag{13.121}$$

Applying the approximation that the term $\frac{\sigma\Omega}{kT}$ is small compared to 1 yields:

$$J_v = \frac{2\kappa\sigma\Omega}{dkT}(D_v C_v^0 + D_i C_i^0) \approx \frac{2\kappa\sigma\Omega}{dkT} D_v C_v^0, \tag{13.122}$$

where the approximation is due to the fact that although D_i is greater than D_v, C_v^0 is much greater than C_i^0 The vacancy flux given in Eq. (13.122) is the same as that in Eq. (13.47), and thus, there is no effect of irradiation on Nabarro–Herring creep. The reason is that the creep rate is driven by the *difference* in the equilibrium values of defects at the grain boundaries, and these values do not depend on the concentration of vacancies or interstitials in the matrix. Irradiation simply serves to increase the flow of defects to each boundary equally without a change in the net amount. The same argument applies to Coble creep. As such, diffusional creep is unaffected by irradiation and does not contribute to irradiation creep.

13.2.9 Comparison of Theory with Creep Data

Much like thermal creep, irradiation creep is characterized by an initially high creep rate that declines with irradiation dose or fluence and transitions into steady-state or secondary creep that is generally linear with dose. The difference between irradiation creep and thermal creep is in the magnitudes. A general equation for irradiation creep is as follows:

$$\varepsilon = A\left[1 - \exp\left(-\frac{\phi t}{C}\right)\right]\sigma + B_0 \sigma^n \phi^m t, \tag{13.123}$$

where the first term is transient creep, and the second term is steady-state creep. A typical irradiation creep curve exhibiting transient and steady-state regimes

is shown in Fig. 13.15 for 20 % CW 316 stainless steel. Irradiation creep rates are much larger than those due solely to thermal processes. Of the mechanisms discussed, SIPN accounts best for the transitory nature of the primary creep regime, but cannot explain steady-state creep. In the absence of swelling, steady-state irradiation creep can be described by the second term in Eq. (13.123). Data show that the creep strain rate is proportional to neutron fluence ($m = 1$), Fig. 13.16, and also proportional to stress ($n = 1$). The creep strain is then often written as the effective strain per unit of effective stress per dpa:

$$\dot{\bar{\varepsilon}}/\bar{\sigma} = B_0, \tag{13.124}$$

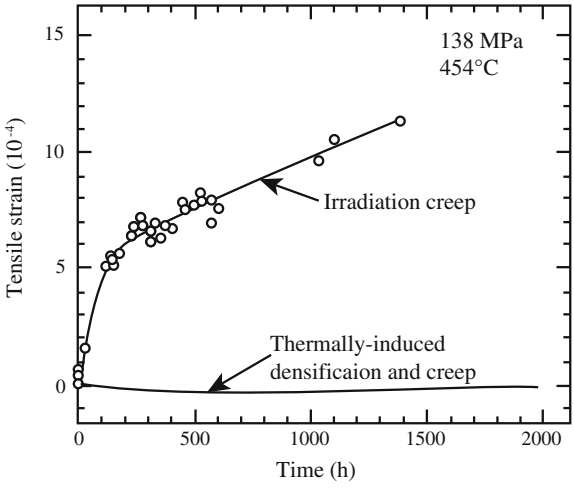

Fig. 13.15 Irradiation creep in 20 % cold-worked 316 stainless steel irradiated in EBR-II (after [22])

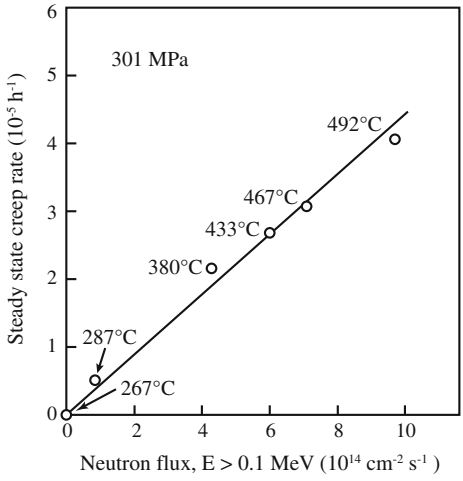

Fig. 13.16 Creep rate as a function of neutron flux in annealed 09Kh16NM3B irradiated in BR-10 (after [22])

where $\dot{\bar{\varepsilon}}$ is the effective strain rate, $\bar{\sigma}$ is the effective stress, and B_0 is the creep compliance. Note that the "rate" implied by the dot over $\bar{\varepsilon}$ is per dpa, not time. The creep compliance, B_0, is independent of composition, starting state, dpa rate, and temperature over the range of reactor relevant conditions.

There are significant data to support the irradiation creep rate behavior described by Eq. (13.124), and some of the most convincing data provided in Fig. 13.17 gives a value of B_0 of $\sim 3\times10^{-6}$ MPa^{-1} dpa^{-1}. The dependence of creep rate on stress to the power $n = 1$ provides support for the SIPA mechanism of creep. Note also that the strains appear to be independent of temperature over the range studied, supporting irradiation creep as the mechanism behind the strain rate rather than thermal creep, which has a very steep temperature dependence. The creep rate has also been observed to vary as $\phi^{1/2}$ at low temperature, yielding a B_0 dependence on flux of (dpa rate)$^{-1/2}$. In ferritic–martensitic alloy T91, the creep rate is found to follow an approximately linear stress dependence in the low-stress regime, and a transition to a strong dependence on stress ($n \sim 14$) in the high-stress regime, Fig. 13.18, indicative of a transition from irradiation-induced creep by either SIPA or PAG at low stress, to power law breakdown at high stress [23].

When void swelling occurs during creep, the steady-state creep rate is proportional to the swelling rate and the relationship is described by the following empirical equation [22]:

$$\dot{\bar{\varepsilon}}/\bar{\sigma} = B_0 + D\dot{S}, \tag{13.125}$$

where D is the creep-swelling coupling coefficient and $\dot{S}$ is the instantaneous volumetric swelling rate per dpa. While Eq. (13.125) is empirical, the relationship can also be determined from theory as well. Recall Eq. (8.122) for swelling in which

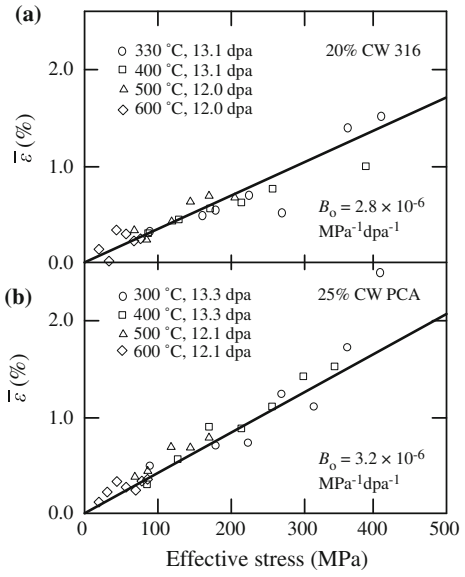

Fig. 13.17 Dependence of the normalized creep strain on effective stress in (**a**) 20 % CW and (**b**) 25 % CW PCA, over a range of temperatures and within a narrow dose range of 12.0–13 3 dpa [22]

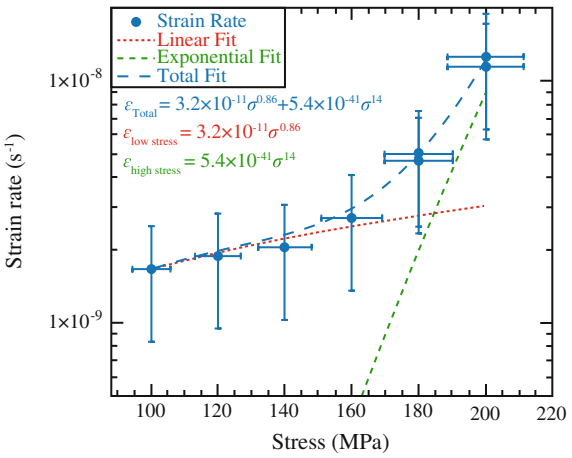

Fig. 13.18 Stress dependence of irradiation creep rate of T91 at 450 °C, 1.7×10^{-6} dpa/s and fits to the data in the low and high-stress regimes (after [23])

thermal emission of vacancies is negligible and recombination is negligible. Assuming that the only point defect sinks are voids and dislocations and that the dislocation sink strength is much greater than the void sink strength, then Eq. (8.122) becomes:

$$\dot{R} = \frac{K_0(z_i - z_v)\Omega}{R z_i z_v \rho_d}, \tag{13.126}$$

and the void swelling rate is as follows:

$$\dot{S} = 4\pi R^2 \dot{R}\rho_v = \frac{4\pi R K_0 \rho_v \Omega\left(z_i^d - z_v^d\right)}{z_i^d z_v^d \rho_d}. \tag{13.127}$$

Substituting the expression for C_i from Eqs. (5.31) and (5.67) into Eq. (13.86) for SIPA creep, where only the first term is retained, the creep rate can be written as:

$$\dot{\varepsilon}_{SIPA} = \frac{2}{9}\frac{\Omega\rho_d \Delta z_i^d K_0}{z_i^d \rho_d}, \tag{13.128}$$

and the ratio of the creep rate to the swelling rate is as follows:

$$\frac{\dot{\varepsilon}_{SIPA}}{\dot{S}} = \frac{2}{9}\delta\frac{z_v^d \rho_d}{4\pi R_V \rho_V}, \tag{13.129}$$

where $\delta = \dfrac{\Delta z_i^d}{\left(z_i^d - z_v^d\right)}$. The linear dependence of creep rate on void swelling applies as well to climb–glide creep.

Some of the earliest and most convincing results supporting this coupling between creep and swelling are shown in Fig. 13.19 for annealed 304 SS irradiated in EBRII. The coupling was further supported by the strong correlation between creep and swelling in pressurized tube experiments in the PHENIX reactor (Fig. 13.20). Typical values for D are $\sim 10^{-2}$ MPa^{-1}. Garner [22] presents a more complete description of the dependencies of B_0 and D on the various parameters affecting creep. While the creep compliance and the coupling term are not strict constants, the relation between creep, stress, flux, and swelling is well described by

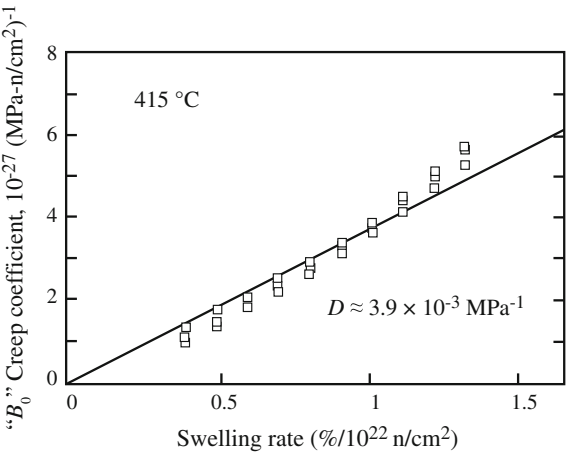

Fig. 13.19 Correlation of irradiation creep coefficients with swelling rates for annealed 304L stainless steel irradiated in EBR-II (after [22])

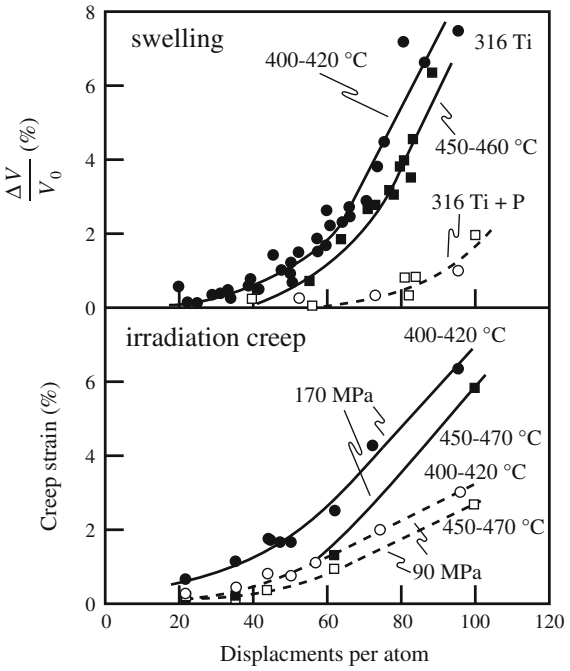

Fig. 13.20 Swelling and creep strains in two French steels irradiated as pressurized tubes in the PHENIX reactor (after [22])

Eq. (13.125).The complexity of irradiation creep and its strong dependence on the irradiated microstructure is illustrated by the observation by Garner et al. [24] that at high levels of irradiation dose, the irradiation creep rate can drop to zero. This phenomenon is illustrated in Fig. 13.21 in which instantaneous creep coefficient in a stainless steel irradiated in EBR-II at 550 °C is observed to increase to a maximum and then drop to zero at high dose. Note that deformation has not stopped, rather at the point where the creep compliance goes to zero, the deformation can be totally accounted for by the strain due to swelling, $\varepsilon_{linear} = \varepsilon_{swelling}/3$. This occurrence has its origin in the development of the dislocation network and loop microstructure. Under irradiation and an applied stress, creep is sensitive to the anisotropy of the dislocation microstructure and accounts for processes such as SIPA and PAG, in addition to SIPN. In the absence of swelling, the degree of anisotropy increases with dose. When voids begin to form, they consume vacancies and the matching interstitial flux to dislocations overwhelms that in the void-free, dislocation-dominated case, causing an increase in the creep rate that is coincident with the onset of swelling. When voids become the dominant sink, they absorb both vacancies and interstitials in large numbers. The consequence is twofold: a reduction in the creep rate caused by the small excess interstitial flux to dislocations and a saturation in swelling due to low excess vacancy absorption. The dependence of creep on composition and metallurgical condition is largely determined by the response of swelling to those factors in the regime where creep is driven by swelling.

13.2.10 Irradiation-Modified Deformation Mechanism Map

The deformation mechanism map for 316 stainless steel can be modified to account for irradiation creep. Figure 13.22 shows the deformation map for 316 SS constructed in a manner identical to that for Fig. 12.31, but at a strain rate of 10^{-10} s^{-1} [25]. At this strain rate, irradiation creep is observable in the intermediate

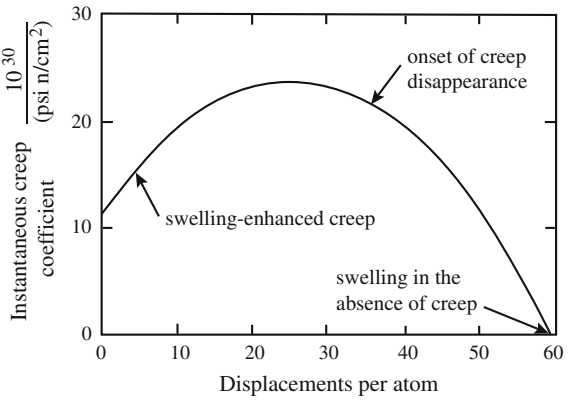

Fig. 13.21 The instantaneous creep coefficient determined from strain measurements of pressurized tubes of stainless steel, irradiated in the EBR-II reactor at 550 °C (after [22])

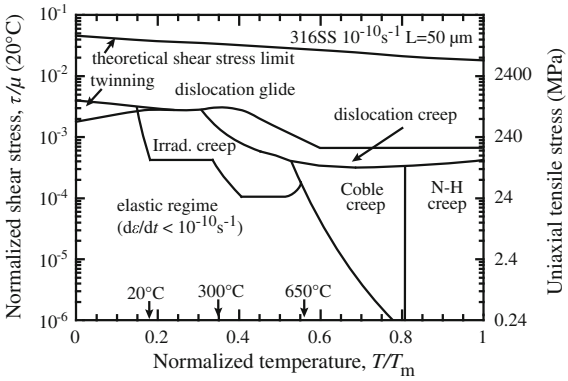

Fig. 13.22 Deformation mechanism map for 316 stainless steel irradiated to 1 dpa for a plastic strain rate of 10^{-10} s^{-1} (after [25])

temperature regime. Below 20 °C, interstitial mobility drops and so does the irradiation creep rate. Above about 600 °C, Coble creep is the dominant creep mechanism. The irradiation creep regime, therefore, lies at intermediate temperature and intermediate stresses and can be described by the constitutive equation for irradiation creep strain given by Eq. (13.125) in which the first term is due to dislocation creep (lower temperature portion of irradiation creep regime) and the second term is due to swelling-driven creep (higher temperature portion). The net effect of irradiation is to extend rate-dependent deformation to lower stresses.

13.3 Irradiation Growth and Creep in Zirconium Alloys

In addition to swelling and creep, there is another phenomenon that leads to strains in some solids under irradiation. This phenomenon is termed *growth. Swelling* is the isotropic volume expansion of a solid without an external stress. *Creep* is the volume conservative distortion of a solid under an applied stress. *Growth* is the volume conservative distortion of a solid without an applied stress. Growth is only observed in non-cubic systems as it is highly dependent on anisotropy of the crystal structure. For this reason, irradiation growth can be significant in hcp metals such as zirconium and magnesium. Zirconium is stable in the α phase (hcp) below 863 °C and in the β phase (bcc) between 863 °C and T_m. Alpha-Zr has an ideal c/a ratio of 1.589. Three types of planes play key roles in the deformation and growth behavior of α-zirconium and its alloys:

- Prism I $(10\bar{1}0)$ and prism II $(11\bar{2}0)$
- Pyramidal $(11\bar{2}1), (11\bar{2}2), (10\bar{1}2)$
- Basal (0001)

Also of importance are the $(10\bar{1}2)$ and $(11\bar{2}2)$ planes. The prism, pyramidal, and basal planes are shown in Fig. 13.23.

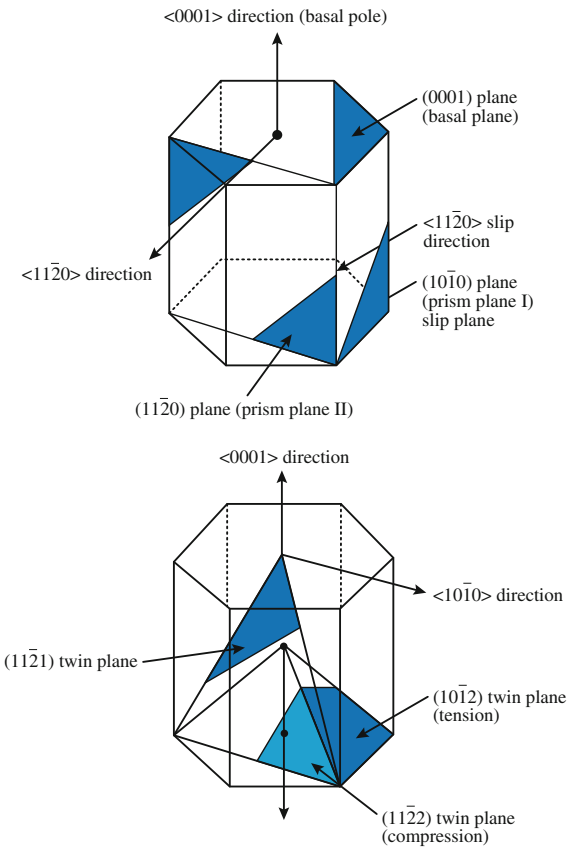

Fig. 13.23 Prism, pyramidal, and basal planes in an hcp structure (after [26])

Deformation in hcp metals occurs by both slip and twinning. For stresses along the *a*-axis, slip occurs primarily on the $(10\bar{1}0)$ prism I plane in the $\langle 11\bar{2}0\rangle$ direction. At higher stress, slip occurs on the $(10\bar{1}1)$ and $(11\bar{2}1)$ pyramidal planes and in a $\langle c + a\rangle$ direction, or along $\langle 11\bar{2}3\rangle$ At high temperatures, slip can occur on the (0001) basal plane in the *a*-direction, $\langle 1\bar{2}10\rangle$. Twinning is also a common deformation mode in hcp metals. Twinning will occur for stresses that have a component in the *c*-direction on one of the four pyramidal planes. The slip systems for deformation along the *c*-direction and as a function of temperature are given in Table 13.1. Note that different levels of stress are required to activate different deformation mechanisms. Hence, the stress needed to cause plastic deformation is a

Table 13.1 Slip systems for deformation in zirconium

	Tension (*c*-axis)		Compression (*c*-axis)	
Temp	Plane	Direction	Plane	Direction
Low	$(11\bar{2}1)$	$\langle\bar{1}\bar{1}21\rangle$	$(11\bar{2}1)$	$\langle\bar{1}\bar{1}23\rangle$
High	$(10\bar{1}2)$	$\langle\bar{1}011\rangle$	$(10\bar{1}1)$	$\langle\bar{1}012\rangle$

function of direction. A crystal possessing properties that are directionally dependent are called anisotropic.

Commercial production techniques result in Zr components in which the grains are aligned along preferential directions of the crystal. The preferential orientation of crystal directions is known as texture. The implication of texture in Zr components is that the anisotropic nature of the single crystal is exhibited in the polycrystalline material. Further, the texture changes with deformation, and this is known as texture rotation. The texture is quantified by the f_i number or the fraction of basal poles in the ith direction, where $i = L, T,$ or N for longitudinal, transverse, and normal, respectively. Note that $f_L + f_T + f_N = 1$ always.

13.3.1 Microstructure of Irradiated Zirconium Alloys

To understand growth and creep in an anisotropic solid, we must have an understanding of the nature of the irradiated microstructure. One of the prime consequences of the crystal structure of zirconium and its alloys is anisotropic diffusion [27]. Another is that the dilatational strain of the self-interstitial is smaller in Zr than in most cubic solids, resulting in smaller elastic interaction between dislocations and interstitials, which gives rise to vacancy loop stability. In fact, this small dilatational misfit may also explain the ease of Zr in accommodating interstitial gas atoms. The irradiation microstructure of Zr alloys can be summarized as follows.

Vacancy and interstitial $\langle a \rangle$-type 1/3 $\langle 1120 \rangle$ (prism plane) loops nucleate and grow during neutron irradiation. Both are present in approximately equal numbers between temperatures of 300 and 450 °C, but vacancy loops are unstable above this range due to thermal emission. The relative numbers of vacancy and interstitial loops are dependent on the proximity of biased sinks for either interstitials or vacancies. The $\langle a \rangle$-type dislocation loops arrange themselves in layers parallel to the basal plane, as shown in Fig. 13.24.

At doses above about 2.5×10^{25} n/m^2, in the temperature range 300–500 °C, $\langle c \rangle$-component dislocations start to develop on both the pyramidal and basal planes. The latter consist of vacancy loops having Burgers vector $1/6\langle 20\bar{2}3 \rangle$. The basal vacancy loops are believed to nucleate in collision cascades and owe their stability to solutes that lower the stacking fault energy and stabilize them at small size. Impurity segregation at dislocations near the loops or anisotropic diffusion is likely to be the most important factors governing loop growth. Additional factors that are important in $\langle c \rangle$-component loops are stress and the magnitude of the Burgers vector.

At all temperatures, dislocation loop growth contributes to the network during irradiation, and recovery of the dislocation network is not significant below 400 °C. The $\langle c \rangle$-component vacancy sinks are likely net vacancy sinks and $\langle c \rangle$-type dislocations are probably net interstitial sinks. The fact that $\langle c \rangle$-component loops on

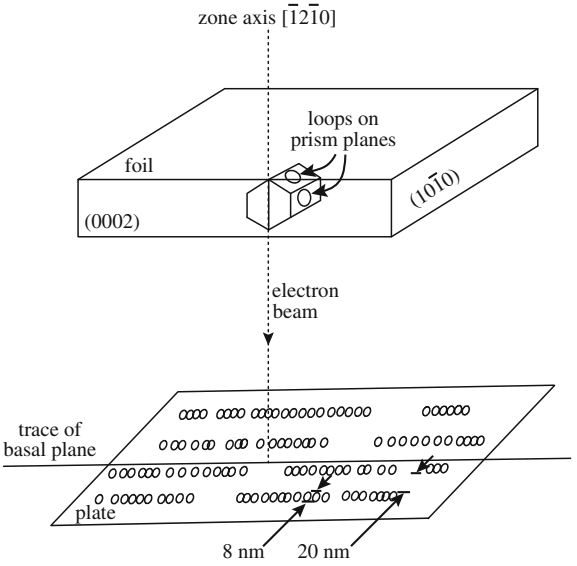

Fig. 13.24 Schematic diagram of the arrangement of dislocation loops on prism planes in irradiated zirconium (after [28])

basal planes are generally of vacancy character also indicates that the ⟨*c*⟩-component network dislocations are also vacancy sinks since they climb in a similar manner.

Grain boundaries serve as sinks for interstitial defects during irradiation of annealed Zr. The bias is dependent on the grain boundary orientation and is a minimum for boundary planes that are parallel to the basal plane (0001). Voids can form in Zr at temperatures between 350 and 500 °C, and their formation is a strong function of impurities and the presence of insoluble gases. When they form, they also tend to be located at second phase particles. In fact, the lack of insoluble gases is likely one of the reasons for the instability of voids and the stability of ⟨*c*⟩-component loops instead. As in cubic metals, insoluble gases play an important role in stabilizing small vacancy clusters against collapse to vacancy loops.

Lastly, radiation induces the formation (of ZrSn or ZrNb) or the dissolution or redistribution and reprecipitation of intermetallic phases containing Zr and Fe, Cr or Ni depending on temperature, solute content, and dose. The rebalancing of solute in the matrix can have an impact on the processes of creep and growth.

13.3.2 Irradiation Growth

Growth is easiest to understand first in single crystal zirconium. Measurements of growth of single crystal zirconium were first reported by Buckley in 1962 [29]. The shape change that occurred involved an expansion along the *a*-axis and a contraction along the *c*-axis, with magnitudes that resulted in zero net volume change,

consistent with the concept of growth as a volume conservative distortion process. Results of these observations led to one of the first models of irradiation growth which held that interstitials condensed as dislocation loops lying on the prism planes and vacancies from depleted zones collapsed to form vacancy loops lying on the basal planes. This process is equivalent to a transfer of atoms from basal planes to prism planes via the irradiation-induced point defects, as shown schematically in Fig. 13.25. The growth strains of single crystal zirconium as a function of neutron fluence are shown in Fig. 13.26 in which there is a large positive growth strain in the $\langle a \rangle$-direction, a negative growth strain in the $\langle c \rangle$-direction, and near zero strain in the $\langle c + a \rangle$-direction. But subsequent, detailed TEM observations [27, 28] of the dislocation loop structure of Zr that had undergone irradiation growth showed that all of the irradiation-induced dislocation loops had Burgers vectors of the type, $b = 1/3\langle 11\bar{2}0 \rangle$, or $\langle a \rangle$-type loops and no indication of $\langle c \rangle$-component loops. While the loops with $\langle a \rangle$-type Burgers vector could account for the a-axis expansion, they

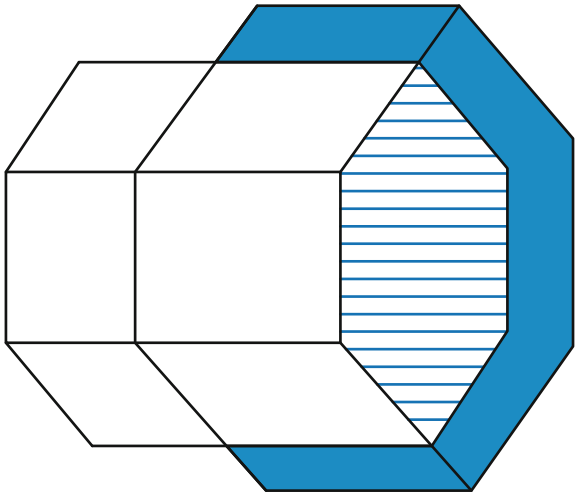

Fig. 13.25 Schematic of the change in shape of single crystal of α-zirconium produced by interstitial condensation on prism planes and vacancy-depleted zone collapse on basal planes

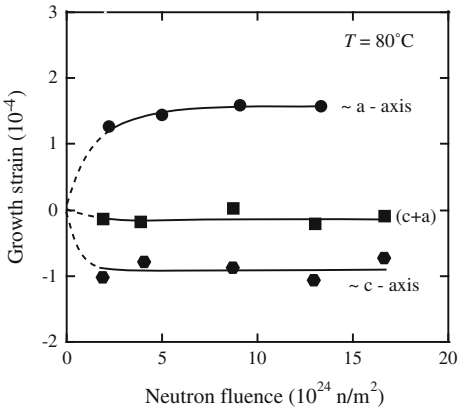

Fig. 13.26 Growth strains of annealed single crystals of zirconium as a function of neutron fluence at 80 °C (after [30])

do not account for the *c*-axis contraction. In fact, after an initial strain of about 10^{-4}, the growth quickly saturated. Irradiation to much higher doses showed that the saturation was in fact temporary and that the growth strain exhibited a *breakaway* behavior above $\sim 2.5 \times 10^{25}$ n/m^2 (Fig. 13.27). Breakaway growth has been ascribed to the nucleation and growth of $\langle c \rangle$-component vacancy loops [29]. The current evidence supports the nucleation of a low density of loops with $1/6\langle 20\bar{2}3 \rangle$ Burgers vectors that grow to relatively large sizes (>100 nm). In fact, much of the growth strain in Zircaloy-2 at high fluence can be accounted for by excess interstitial annihilation at $\langle a \rangle$-type loops and network dislocations with the corresponding vacancies annihilating at the $\langle c \rangle$-component loops [33].

In polycrystalline zirconium alloys, irradiation growth consists of three components: (1) a short-term transient due to irradiation-induced microstructure changes such as defect clusters or loops, (2) a crystallographic texture-dependent steady-state growth component, and (3) a texture-dependent long-term transient arising from breakaway growth [32]. The growth strain in a given direction of a polycrystal, ***d,*** can be related to its crystallographic texture by the *f* numbers and is proportional to the growth anisotropy factor, G_d:

$$G_d = 1 - 3f_d^b \,, \tag{13.130}$$

where f_d^b is the resolved fraction of basal poles in the direction *d*. The values of f_d^b are determined from basal pole figures obtained by X-ray diffraction using the relationship:

$$f_d^b = \sum_q V_q \cos^2 q \,, \tag{13.131}$$

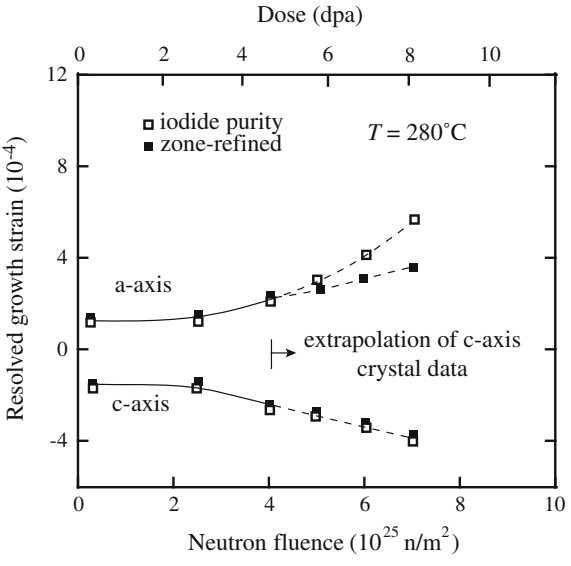

Fig. 13.27 Growth at high fluence for annealed zirconium single crystals at 273 °C showing the onset of breakaway growth at a fluence of 2.5×10^{25} n/m^2 (after [30])

where V_q is the volume fraction of grains with their basal poles at an angle q from the direction d. If the resolved fraction of basal poles in a given direction is equal to 1/3, then according to Eq. (13.130), the growth in that direction should be zero. The growth strain in the longitudinal, transverse, and thickness directions of recrystallized and cold-worked Zircaloy-2 irradiated at 287 °C and 327 °C fit the behavior rather well [35]. Figure 13.28 shows that the growth behavior of recrystallized Zircaloy-2 at 57 °C also follows Eq. (13.130).

Irradiation growth is weakly dependent on grain size with smaller grains giving rise to larger growth. It is also dependent on cold-work with higher cold-work resulting in a greater growth strain (Fig. 13.29). Growth appears to be dependent on fluence, but there is not much evidence to support a flux dependence. Finally, growth is observed to increase with temperature, with a rapid increase above about 400 °C due in part to an increase in volume. It has also been proposed that impurity elements, such as Fe, can stabilize $\langle c \rangle$-component loop embryos and enable their growth. Irradiation has been observed to amorphize Fe- and Cr-rich precipitates

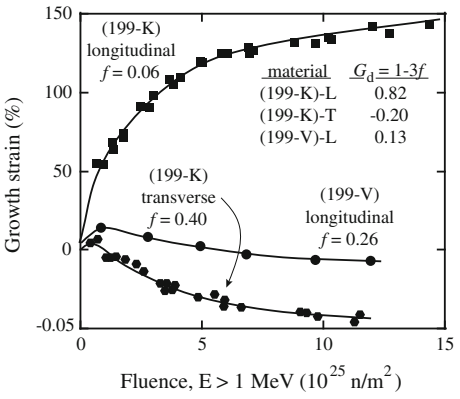

Fig. 13.28 Texture dependence of irradiation growth of Zircaloy-2 sheet at 57 °C (after [36])

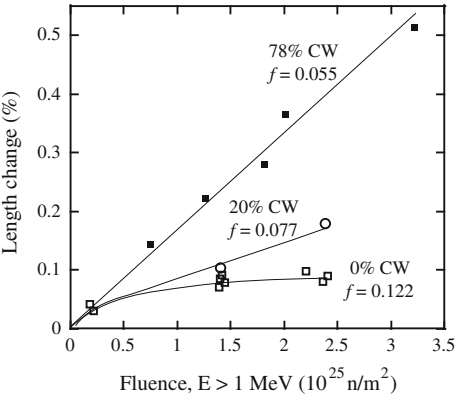

Fig. 13.29 Effect of cold-work on irradiation growth in Zircaloy-4 irradiated near 282 °C (after [34])

[37] causing the redistribution of iron into the matrix [38]. This dissolution process may be a source of iron for $\langle c \rangle$-component loop stabilization at high fluences.

A model [39] has been developed that attempts to capture the sensitivity of the growth rate to the microstructure by estimating the annihilation probabilities for interstitials and for vacancies at the various microstructural sinks. It holds that growth is driven by the difference in the anisotropy of interstitial and vacancy migration in which (1–3*f*) growth can occur in cold-worked microstructures by vacancy partitioning to the $\langle c + a \rangle$-network dislocations and interstitial partitioning to the *a*-type dislocations. The linear dependence of the growth rate of cold-worked and stress-relieved Zircaloy-2 is controlled by fast vacancy migration with a low migration energy of 0.7 eV. The breakaway growth at high fluences is due to the appearance of basal plane loops which act as strong vacancy sinks.

13.3.3 Irradiation Creep

Time-dependent deformation in zirconium alloys is a combination of thermal creep, irradiation creep, and growth. While the thermal creep component at reactor temperatures is generally small if not negligible, irradiation creep and growth components are not easily separable. The dependence of unirradiated zirconium tensile and creep properties on temperature can be subdivided into three regions as shown in Fig. 13.30. Below about 175 °C, the yield stress decreases with temperature, but creep below the yield stress does not depend strongly on temperature. Region II is the *athermal* region of creep and extends between about 175 and 523 °C in which mechanical recovery balances strain aging and the net effect is that creep is independent of temperature but does not readily reach steady-state creep. Above 523 °C, the strong dependence of yield strength on temperature and the increased recovery leads to steady-state creep rates at constant stress.

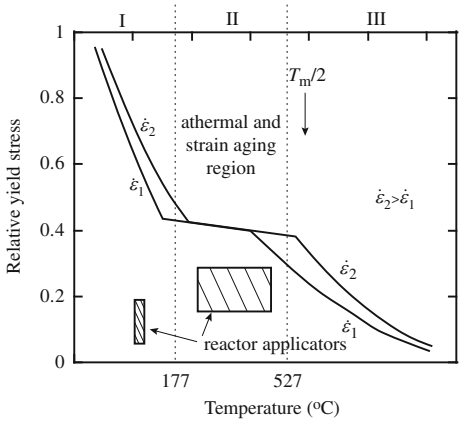

Fig. 13.30 Temperature dependence of the yield strength of zirconium alloys (after [34])

In reactor, creep follows the phenomenological equation:

$$\dot{\varepsilon} = A\sigma^n \phi^m G_d \exp(-Q/kT)[f(t) \text{ or } g(\varepsilon)] , \tag{13.132}$$

where *f(t)* and $g(\varepsilon)$ are functions of time and strain, respectively, and other terms are as previously defined. While the flux dependence is generally taken to be linear, correlations show that the value of m varies between 0.25 and 0.85 at low fluxes (10^{16} n/m^{2}s) and rises to an asymptotic value of 1.0 at high fluxes (10^{18} n/m^{2}s) [34]. The flux exponent also was found to decrease with temperature and become negligible above 523 °C (region III) [40]. The fluence dependence is generally linear, but data exist to show that at high fluence ($> \sim 2 \times 10^{25}$ n/m^2), there is an upturn in the creep rate (Fig. 13.31).

Creep of zirconium alloys is highly dependent on the stress. At 300 °C and low stress ($<1/3\sigma_y$), $n = 1$. With increasing stress to values between 200 and 400 MPa, n rises to a value of 2 and then increases rapidly at higher stresses and can reach a value of 100 at a stress of 600 MPa (Fig. 13.32). Below about 300 °C, the temperature dependence of creep is weak and the activation energy is between 16 and 40 kJ/mol (Fig. 13.33). The temperature dependence increases rapidly with temperature, and Q can exceed 200 kJ/mol. However, the transition temperature for Q is dependent on alloy content, metallurgical condition, and stress [34]. As with growth, creep is highly dependent on the texture, which is included as the anisotropy coefficient in Eq. (13.132). However, as shown in Fig. 13.34, the texture dependence is greatest in the primary creep range. Creep in zirconium alloys is believed to be due to slip of $\langle a \rangle$-type dislocations on prism planes with secondary slip of $\langle c + a \rangle$-type dislocations on pyramidal planes. In Zircaloy-2 and Zr–2.5 % Nb, slip of $\langle a \rangle$-type dislocations contributed over 90 % of the total strain [41]. The most likely mechanism to explain creep at low stress is the SIPA mechanism. As discussed earlier, this mechanism has an $n = 1$ stress dependence, which is consistent with creep at low stress. The elastodiffusion origin of SIPA [42] in which

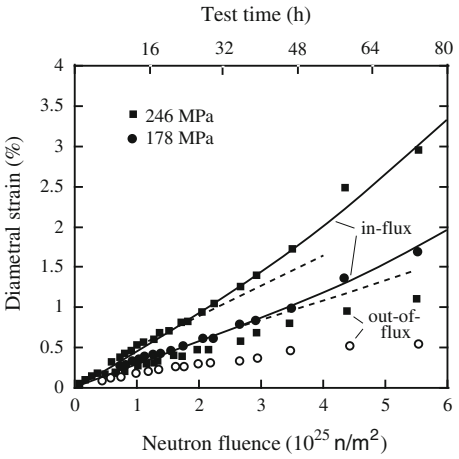

Fig. 13.31 Diametral creep strain in cold-worked Zr–1.5Nb tubes irradiated at 297 °C and a fast neutron flux of 2.1×10^{17} n/m^{2}s (after [34])

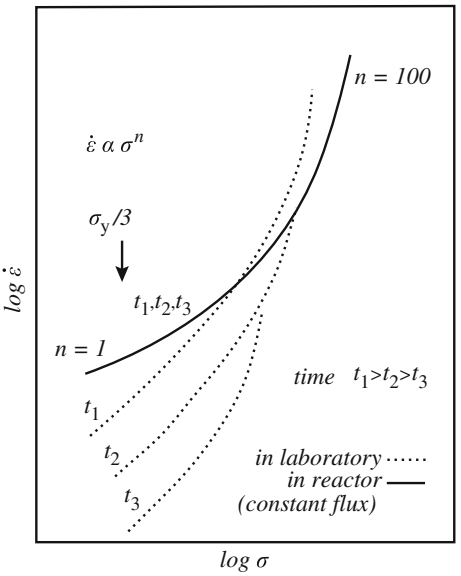

Fig. 13.32 Schematic of the stress dependence of in-reactor creep in zirconium alloys at about 300 °C (after [34])

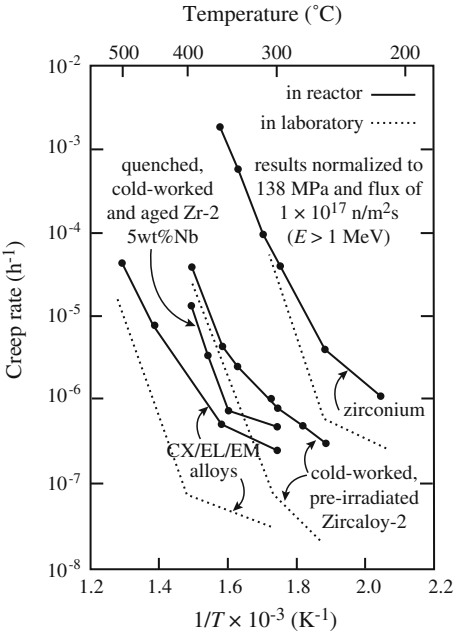

Fig. 13.33 Temperature dependence of in-reactor creep in zirconium alloys (after [34])

diffusion of interstitials is anisotropic in an applied stress field is consistent with the partitioning of interstitials to $\langle a \rangle$-type loops, facilitating their climb and glide.

A deformation-mechanism map for unirradiated Zircaloy-4 calculated assuming a grain size of 150 μm [43] is shown in Fig. 13.35. The map was drawn as contours

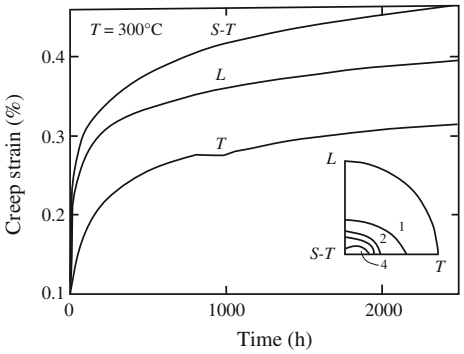

Fig. 13.34 Creep of cold-worked Zircaloy-2 at 207 MPa and 300 °C after [34]

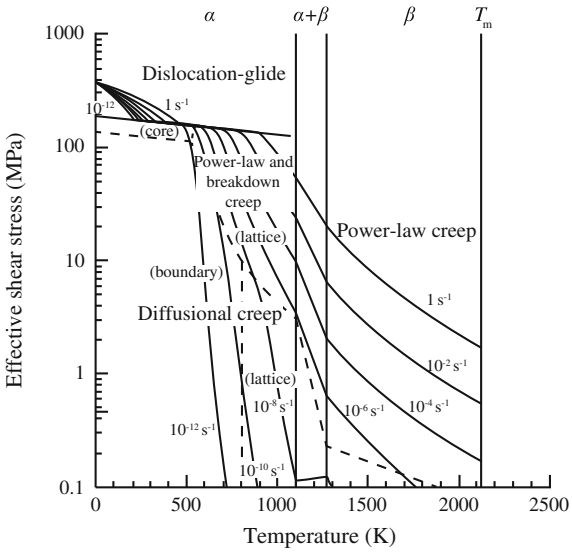

Fig. 13.35 Deformation-mechanism map for unirradiated Zircaloy-4 with a grain size of 150 μm (after [43])

of constant strain rate in a stress–temperature space. All mechanisms were assumed to act simultaneously, and the boundaries between the different mechanisms were set to where the dominant mechanisms switched. An exception to this rule was the transition to dislocation glide. For consistency between the strain rates in the different regimes, a transition stress of $\tilde{\tau}/G = 4.8 \times 10^{-3}$ was set below which dislocation glide was not active. This is equivalent to a narrow region in which the flow rate of the alloy is independent of temperature.

Nomenclature

A	Area of slip plane or dislocation loop
$\bar{A}$	Average loop area
a	Lattice constant
$\boldsymbol{b}$	Burgers vector
B_0	Creep compliance
$C_{\mathrm{v,i}}$	Concentration of vacancies, interstitials
$C^0_{\mathrm{v,i}}$	Thermal equilibrium concentration of vacancies, interstitials
d	Grain size
D	Creep-swelling coupling coefficient
D_{eff}	Effective diffusion coefficient
D_{gb}	Grain boundary diffusion coefficient
$D_{\mathrm{i,v}}$	Interstitial, vacancy diffusion coefficient
D_{vol}	Volume diffusion coefficient
e	Engineering strain
E	Energy or elastic modulus
E_{vol}	Activation energy for volume diffusion
$f^{\mathrm{b}}_{\mathrm{d}}$	Resolved fraction of basal poles in the d direction
f_{i}	Fraction of interstitial loops aligned in direction i. Also resolved fraction of basal poles of hcp unit cells in the i direction
F_{i}	Component of force in the ith direction
F_j	Frequency with which a dislocation climbs a height, h
G_{d}	Anisotropy factor
h	Obstacle height on glide plane
k	Boltzmann's constant
$k^2_{\mathrm{v,i}}$	Total sink strength for vacancies, interstitials
$k^2_{\mathrm{L,N}}$	Sink strengths for loops, networks
l	Glide length on the slip plane
J	Flux
n	The number of interstitials is required to form an interstitial loop also, number of dislocations in a pileup
n_0	Number of possible loop orientations
N	Atom number density
N_{L}	Number density of dislocation loops
P_j	Probability of a dislocation climb of j or greater
r_{c}	Dislocation core radius
r_{L}	Dislocation loop radius
R_{c}	Critical loop size for survival
R_j	Probability of finding a dislocation a distance j from unpinning point
R_{max}	Maximum dislocation loop radius
S	Loop number density
$\dot{S}$	Swelling rate
t	Time
T	Temperature
T_{m}	Melting temperature

υ_c	Dislocation climb velocity
υ_d	Average dislocation velocity
V	Volume
V_{cas}	Volume of cascade
V_q	Volume fraction of grains with their basal poles at an angle q with respect to a direction, d
$\frac{\Delta \dot{V}}{V}$	Swelling rate
$z_{i,v}^{dj}$	Capture efficiencies of dislocation of orientation j
$\Delta z_{i,v}^{d}$	Difference in capture efficiencies between aligned and non-aligned loops
α	Number of spikes per neutron scattering event, constant in Eq. (13.74)
β	Constant in Eq. (13.74)
ϕ	Neutron flux
δ	Effective thickness of the grain boundary
ε_s	Shear strain
$\dot{\varepsilon}$	Strain rate
$\dot{\bar{\varepsilon}}$	Effective strain (or creep) rate
$\dot{\varepsilon}_m$	Swelling strain
ε, ε_{ij}	Strain and components of strain
ε_e	Elastic strain
ε_{vol}	Volume strain
μ	Shear modulus
ν	Poisson's ratio
ω	Release frequency of pinned dislocation segments
Ω	Atomic volume
ρ	Total dislocation density
$\rho_{m,L,N}$	Mobile, loop, and network components of dislocation density
ρ_{FR}	Frank–Read source density
σ, σ_{ij}	Stress and components of stress
σ_s	Neutron scattering cross section. Also shear stress
$\bar{\sigma}$	Effective stress
θ	Angle between loop normal and tensile axis in (Eq. 13.74)

Subscripts

AL	Aligned loops
c	Climb
d	Dislocation
eff	Effective
FR	Frank–Read
g	Glide
gb	Grain boundary
i, v	Interstitial, vacancy
NL	Non-aligned loop
L	Loop

m	Mobile
N	Network
s	Shear
S	Swelling
vol	Volume

Superscripts

c	Compressive
dA	Aligned dislocation loops
dN	Non-aligned dislocation loops
D	Dislocation
L	Loops
V	Void
n	Stress exponent
m	Flux exponent
t	Tensile

Acronyms

GC	Glide and climb
FR	Frank–Read
N-H	Nabarro–Herring
PA	Preferential absorption
PAG	Preferential absorption glide
PE	Preferential emission
SIPA	Stress-induced preferential absorption
SIPN	Stress-induced preferential nucleation

Problems

13.1 Referring back to the void growth rate calculation in Problem 8.4 of Chap. 8:

(a) Calculate the irradiation creep rate for stainless steel as a function of temperature and applied shear stress. Assume a void number density of 2×10^{15} cm^{-3} for the creep rate calculation.

(b) Identify the window in stress–temperature space in which the creep rate remains below 0.01 %/h.

13.2 In the Hesketh model of irradiation creep by stress-enhanced vacancy–loop collapse, depleted zones with less than $m_c \sim 200$ vacancies remain in the solid as vacancy platelets. For $m < m_c$, the volume per platelet of size m is $m\Omega$. Using the inverse square distribution function for vacancy platelet (or depleted zone) size produced by a neutron collision, compute the swelling due to uncollapsed platelets in the absence of applied stress at a fast fluence

of 10^{20} neutrons/cm^2. Assume $\Sigma_s = 0.2$ cm^{-1}, $\Omega = 0.012$ nm^3, and $\nu = 500$ Frenkel pairs per fast neutron collision.

13.3 An Inconel 718 bolt is used to hold a reactor mechanical component in place. The lifetime of the bolt is determined by the stress relaxation (due to irradiation creep). The bolt must be replaced if the load drops to 10 % of the initial load. For the small irradiation dose received by the bolt, assume the creep strain rate $(\dot{\varepsilon})$ during irradiation is proportional to the displacement-damage rate $(\dot{\phi})$ and the effective stress (σ) as given in Eq. (13.124):

$$\dot{\varepsilon} = -B\dot{\phi}\,\sigma$$

(a) Calculate the radiation damage (in dpa) when the bolt stress drops to 10 % of the initial value. Assume the elastic modulus E is a constant value of 7.6×10^{10} Pa and the creep coefficient B is a constant value of 1.6×10^{-6}MPa^{-1} dpa^{-1}.

(b) Due to changes in fuel loading patterns, the dpa rate at the bolt decreases by 50 % after 5 dpa. Recalculate the total dose to reach 10 % of the initial preload. Does this change the time to replace the bolt?

13.4 A dislocation that absorbs vacancies and interstitials at different rates will exhibit climb. The climb velocity v_c is given by $v_c = (J_i^d - J_v^d)b^2$ where J_i^d is the flux of interstitials to a unit length of dislocation line and b is the Burgers vector. If the average obstacle size is 100 nm, calculate the mean time needed for dislocations to climb over obstacles in fcc aluminum at 200 °C in a monoenergetic neutron flux of 10^{14} n/cm^2 s (E = 1 MeV). Assume that the obstacles are *not* sinks for point defects and that kinetics are diffusion-limited.

$$\begin{aligned}
T_m &= 660\ ^\circ\text{C}\\
a &= 0.405\ \text{nm}\\
Q_f^v &= 3.2\ \text{eV}\\
Q_m^v &= 0.62\ \text{eV}\\
Q_f^i &= 0.66\ \text{eV}\\
Q_m^i &= 0.12\ \text{eV}\\
S_{th}^v &= 0.7k\\
S_{th}^i &= 8k\\
S_m^v &= S_m^i = 0\\
\nu &= 10^{13}\ \text{s}^{-1}\\
\rho_d &= 10^9\ \text{cm}^{-2}\\
b &= 0.2\ \text{nm}\\
z_{id} &= 1.02\\
z_{vd} &= 1.0
\end{aligned}$$

13.5 A creep experiment is performed on unirradiated 316 stainless steel (T_m = 1750 K) samples at 300 °C and 700 °C in the laboratory at low stress. Comparison experiments are performed on a second pair of 316 SS samples at the same temperatures, but *during* irradiation in a neutron flux of 1×10^{14} n/cm^{2}s ($E > 1$ MeV). A third pair of samples is tested in the laboratory at the same temperatures but after being irradiated to a fluence of 10^{21} n/cm^2 at the test temperatures.

(a) Make two plots, one for each temperature. Draw, label, and explain the expected creep curves for each of these experiments.
(b) What mechanisms would you expect to control creep in each of these experiments?

13.6 The 316 stainless steel sample irradiated at 700 °C in Problem 13.5 fails at 1 % strain in a creep test. The failure is attributed to helium embrittlement, and calculations show that the total helium content in the metal was 10^{17} at/cm^3, the grain size was 20 μm, and the swelling at failure was 30 %. What is the stress at failure?

13.7 The generalized equation for thermal creep is as follows:

$$\dot{\varepsilon} = \frac{ADb\mu}{kT}\left(\frac{\sigma}{\mu}\right)^n \left(\frac{b}{d}\right)^p, \quad \text{where} \quad D = D_0 \exp(-Q/kT)$$

D Diffusion coefficient
d Grain size
b Burgers vector
k Boltzmann's constant
T Temperature (K)
μ Shear modulus
σ Applied stress
n Stress exponent
p Inverse grain size exponent
A Dimensionless parameter

(a) Are any of the variables that describe the creep affected by irradiation?
(b) If so, how would increasing the displacement rate during an irradiation by an order of magnitude change the creep rate in a pure alloy with very low sink density?

13.8 The generalized correlation between creep and swelling given in Eq. (13.125) is as follows:

$$\dot{\bar{\varepsilon}}/\bar{\sigma} = B_0 + D\dot{S}$$

Comparing this equation to the generalized creep equation in Problem 13.7 implies that the stress exponent is 1. What does that tell you about the likely mechanisms of creep?

References

1. Frost HJ, Ashby MJ (1982) Deformation mechanism maps: the plasticity and creep of metals and ceramics. Pergamon, New York
2. Olander DR (1976) Fundamental aspects of nuclear reactor fuel elements, TLD-26711-Pl. Technical Information Center, ERDA, Washington Chap. 19
3. Weertman J (1955) J Appl Phys 26(10):1213
4. Weertman J (1968) Trans ASM 61:681
5. Weertman J (1957) J Appl Phys 28(3):362
6. Cadek J (1988) Creep in metallic materials. Elsevier, New York
7. Nabarro FRN (1948) Report on Conference on Strength of Solids. Physical Society, London, p 75
8. Herring C (1950) J Appl Phys 21:437
9. Coble RL (1963) J Appl Phys 34:1679
10. Brailsford AD, Bullough R (1973) Phil Mag 27:49
11. Bullough R (1985) Dislocations and properties of real materials. In: Proceedings of royal society, London, The Institute of Metals, London, p 283
12. Cheng X, Was GS (2014). J Nucl Mater 454:255–264
13. Kroupa (1966) In: Gruber B (ed) Theory of crystal defects. Adacemic Press, New York, pp 308–311
14. Matthews JR, Finnis MW (1988) J Nucl Mater 159:257–285
15. Mansur LK (1979) Phil Mag A 39(4):497
16. Wolfer WG, Foster JP, Garner FA (1972) Nucl Technol 16:55
17. Mansur LK (1992) Mater Sci Forum 97–99:489–498
18. Grossbeck ML, Mansur LK (1991) JNM 179–181:130–134
19. Brinkman JA, Wiedersich H (1964) In: Proceedings of the symposium on flow and fracture of metals and alloys in nuclear environment, STP 380. American Society for Testing and Materials, West Conshohocken, p 3
20. Mansur LK, Coghlan WA, Reiley TC, Wolfer WG (1981) J Nucl Mater 103/104:1257
21. Lewthwaite GW (1973) Scr Metal 7:75
22. Garner FA (1994) In: Frost BRT (ed) Materials science and technology, Chap. 6, vol 10A. VCH, New York, p 419
23. Cheng X, Was GS (2015) J Nucl Mater 459:183
24. Garner FA, Grossbeck ML (1994) Fusion materials semi-annual progress report DE/ER-0313/16. US DOE, Oak Ridge, TN, Mar 1994
25. Zinkle S, Lucas GE (2003) Deformation and fracture mechanisms in irradiated FCC and BCC metals, US department of energy, semi-annual report, DOE-ER-0313/34. US DOE, Washington, DC
26. Klepfer HH (ed) (1962) Proceedings of the USAEC symposium on zirconium alloy development, US Atomic Energy Commission, GEAP4089, vol II, p 13–11
27. Griffiths M (1988) J Nucl Mater 159:190
28. Northwood DO (1977) At Energy Rev 15(4):547
29. Buckley SN (1962) Uranium and graphite. Institute of Metals, London, p 445
30. Carpenter GJC, Zee RH, Rogerson A (1988) J Nucl Mater 159:86
31. Fidleris V (1975) At Energy Rev 13:51
32. Northwood DO, Fidleris V, Gilbert RW, Carpenter GJC (1976) J Nucl Mater 61:123
33. Griffiths M, Gilbert RW (1987) J Nucl Mater 150:169
34. Fidleris V (1988) J Nucl Mater 159:22
35. Adamson RB, Tucker RP, Fidleris V (1982) Zirconium in the nuclear industry the 5th symposium, STP 754. American Society for Testing and Materials, West Conshohocken, p 208
36. Fidleris V, Tucker RP, Adamson RB (1987) Zirconium in the nuclear industry the 7th symposium, STP 939. American Society for Testing and Materials, West Conshohocken, p 49
37. Lemaignan C, Motta AT (1994) In: Frost BRT (ed) Materials science and technology, vol 10B. VCH, New York, p 1 Chap. 7

38. Zu XT, Sun K, Atzmon M, Wang LM, You LP, Wan FR, Busby JT, Was GS, Adamson RB (2005) Phil Mag 85(4–7):649–659
39. Holt RA (1988) J Nucl Mater 159:310
40. Nichols FA (1969) J Nucl Mater 20:249
41. Christodoulou N, Causey AR, Woo CH, Tome CN, Klassen RJ, Holt RA (1993) In: Kumar AS, Gelles DS, Nanstad RK, Little EA (eds) Proceedings of the 16th international symposium on effects of radiation on materials, ASTM STP 1175. American Society for Testing and Materials, West Conshohocken, pp 1111–1128
42. Woo CH (1984) J Nucl Mater 120:55
43. Wang H, Hu Z, Lu W, Thouless MD (2013) J Nucl Mater 433:188

Chapter 14
Fracture and Embrittlement

Embrittlement of a metal is measured by the amount of plastic or creep deformation that occurs before fracture. Irradiation invariably renders a metal less ductile than the unirradiated condition. Fracture can be of the brittle type in which a small crack rapidly propagates across an entire component, or it can occur after long times at stress and after appreciable plastic deformation. Failure by stress rupture takes place by linkage of small intergranular cracks or cavities that have developed throughout the interior of the metal.

The fracture behavior of irradiated structural materials is of vital interest not only for reasons of public safety in the case of pressure containment systems but also for reasons of economy, in the case of fuel performance and plant reliability. Consequently, major efforts have been made to determine the mechanics and engineering limits for fracture of pressure vessel steels and reactor core component alloys under various metallurgical and operational conditions. Although considerable properties data have been compiled to provide guidance for design and safeguards analysis, the effects of irradiation on basic fracture initiation and propagation mechanisms is still under investigation.

In this chapter, we will first develop the formulation for the theoretical cohesive strength of metals, followed by an introduction to fracture mechanics. Using these tools we will address the theory of brittle fracture and merge this theory with the theory of yielding in metals to describe the fracture behavior of metals spanning the elastic-plastic transition. The influence of irradiation combined with other embrittling effects on the fracture behavior of pressure vessel steels will be treated, followed by an application of fracture mechanics to crack propagation and fatigue crack growth. Finally, high-temperature embrittlement and fracture mechanisms will be discussed.

14.1 Types of Fracture

Metals can exhibit different types of fracture depending on the alloy, temperature, state of stress and rate of loading. Fracture can be classified into two general categories: *ductile fracture* and *brittle fracture*. Ductile fracture is characterized by

G.S. Was, *Fundamentals of Radiation Materials Science*,
DOI 10.1007/978-1-4939-3438-6_14

appreciable plastic deformation prior to and during the propagation of a crack. Brittle fracture in metals is characterized by a rapid rate of crack propagation, with no gross deformation and very little microdeformation. Actually, the boundary between a ductile and brittle fracture is arbitrary and depends on the situation being considered.

Brittle fracture often occurs by cleavage, or separation along a crystallographic plane of low index. The cleavage mode of fracture is controlled by tensile stresses acting normal to a crystallographic cleavage plane. Brittle fractures have been observed in bcc and hcp metals, but not in fcc metals except by grain boundary embrittlement. In polycrystalline samples, fractures are classified as either *transgranular*, in which the crack propagates through the grains, or *intergranular*, in which the crack propagates along the grain boundaries.

14.2 The Cohesive Strength of Metals

In most basic terms, the strength of metals is due to the cohesive forces between atoms. Figure 1.8 in Chap. 1 showed the variation in the potential function for an atom about its equilibrium site. Figure 14.1 shows the corresponding variation in cohesive force between two atoms as a function of the separation between theses atoms. This curve results from the attractive and repulsive forces between atoms. The interatomic spacing of the atoms in the unstrained condition is indicated by the length increment, a. If the crystal is subjected to a tensile load, the separation between atoms increases. The repulsive force decreases more rapidly with increased separation than does the attractive force, so that a net force between atoms balances the tensile load. As the tensile load is increased still further, the repulsive force is negligible and the attractive force begins to decrease because of the increased separation of the atoms. This point corresponds to the maximum in the curve, which is equal to the theoretical cohesive strength of the material.

A good approximation to the theoretical cohesive strength can be obtained if it is assumed that the cohesive force curve can be represented by a sine curve [1]:

$$\sigma = \sigma_{\text{th}} \sin \frac{2\pi x}{\lambda} \tag{14.1}$$

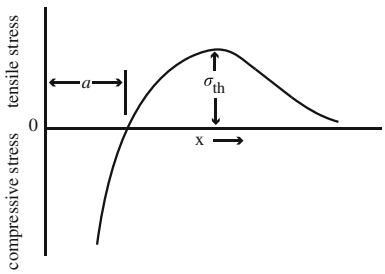

Fig. 14.1 Cohesive force on an atom relative to the separation distance between atoms (after [1])

where σ_{th} is the theoretical cohesive strength and x is the displacement in atomic spacing in a lattice with wavelength λ. For small displacements $\sin x \approx x$, and:

$$\sigma = \sigma_{th} \frac{2\pi x}{\lambda}. \tag{14.2}$$

Limiting consideration to a brittle elastic solid, from Hooke's law we have:

$$\sigma = E\varepsilon = \frac{Ex}{a}. \tag{14.3}$$

Eliminating x from Eqs. (14.2) and (14.3) gives:

$$\sigma_{th} = \frac{\lambda}{2\pi}\frac{E}{a}. \tag{14.4}$$

When fracture occurs in a brittle solid, all of the work expended in producing the fracture goes into the creation of two new surfaces. Each of these surfaces has a *surface energy* of γ in units of energy/unit area. The work done per unit area of surface in creating the fracture, U_f is the area under the stress-displacement curve of Fig. 14.1:

$$U_f = \int_0^{\lambda/2} \sigma_{th} \sin\frac{2\pi x}{\lambda} dx = \frac{\lambda\sigma_{th}}{\pi}, \tag{14.5}$$

where λ is the wavelength. This energy is that required to create the two new fracture surfaces:

$$\frac{\lambda\sigma_{th}}{\pi} = 2\gamma, \quad \text{or} \quad \lambda = \frac{2\pi\gamma}{\sigma_{th}}, \tag{14.6}$$

and substituting into Eq. (14.4) gives:

$$\sigma_{th} = \left(\frac{E\gamma}{a}\right)^{1/2}. \tag{14.7}$$

Equation (14.6) provides an estimate of the theoretical stress required to create two new surfaces with surface energy, γ. Taking typical values for the parameters in Eq. (14.7) yields values for the theoretical fracture strength that are 10–1000 times that found in engineering materials. To resolve this discrepancy, Griffith [2] proposed that a brittle material contains a population of fine cracks that produce a stress concentration of sufficient magnitude so that the theoretical cohesive strength is reached in localized regions at a nominal stress, which is well below the theoretical value.

When a crack increases its length in the process of brittle fracture, it produces an increase in the surface area of the sides of the crack. Energy is required to overcome the cohesive force of the atoms, or expressed in another way, crack growth requires an increase in surface energy. The source of the increased surface energy is the elastic strain energy which is released as the crack spreads. Griffith established the following criterion for the propagation of a crack: "A crack will propagate when the decrease in elastic strain energy is at least equal to the energy required to create the new crack surface." This criterion can be used to determine the magnitude of the tensile stress, which will just cause a crack of a certain size to propagate as a brittle fracture.

If we consider an elliptical crack of length $2c$ in a flat plate of unit thickness under an applied stress, σ acting normal to the crack plane, then the presence of a crack reduces the total strain energy by the amount [3]:

$$U_{\mathrm{E}} = -\frac{\pi c^2 \sigma^2}{E}. \tag{14.8}$$

The decrease in strain energy is available for creation of the two crack surfaces that requires the energy:

$$U_{\mathrm{S}} = 4\gamma c. \tag{14.9}$$

According to Griffith's criterion, the crack will propagate under a constant applied stress, σ if an incremental increase in crack length produces no change in the total energy of the system, i.e., the increased surface energy is compensated by a decrease in elastic strain energy. Using Eqs. (14.8) and (14.9), this criterion can be expressed by the following:

$$\frac{\partial}{\partial c}\left(4\gamma c - \frac{\pi \sigma^2 c^2}{E}\right) = 0, \tag{14.10}$$

and solving for the stress gives:

$$\sigma_{\mathrm{f}} = \left(\frac{2E\gamma}{\pi c}\right)^{1/2}. \tag{14.11a}$$

For the plane strain condition, E is replaced by $E/(1-\nu)^2$ giving:

$$\sigma_{\mathrm{f}} = \left(\frac{2E\gamma}{(1-\nu)^2 \pi c}\right)^{1/2}. \tag{14.11b}$$

Equations (14.11a, 14.11b) give the stress, σ_{f} required to propagate a crack in a brittle material as a function of the size of the microcrack.

It is well established that even metals that fail in a completely brittle manner have undergone some plastic deformation prior to fracture. Therefore, in the strictest sense,

Grittith's equation for the fracture stress does not apply for metals. Orowan [4] suggested that the Griffith equation would be made more compatible with brittle fracture in metals by the inclusion of a term expressing the plastic work required to extend the crack wall, γ_p. In this case, Eq. (14.11a) is modified as follows:

$$\sigma_f = \left[\frac{2E(\gamma + \gamma_p)}{\pi c}\right]^{1/2} \approx \left(\frac{E\gamma_p}{c}\right)^{1/2}. \tag{14.12}$$

The surface energy term can be neglected since estimates of the plastic-work term are about 10^2–10^3 J/m^2 compared with values of about 1 J/m^2 for γ.

14.3 Fracture Mechanics

Fracture mechanics seeks to describe the resistance to cracking, or the toughness, of engineering materials under conditions similar to those encountered in engineering practice. In considering this subject we shall use the approach of Irwin [5] as described by Reed-Hill [6], who considers the work done in moving a crack a small distance, Δx, in order to determine the effective force resisting its movement. In computing this work, he assumes, for ease of presentation, that the crack moves backward and closes rather than opens. Thus, we assume that Fig. 14.2a represents one end of a crack that extends through the thickness of an infinitely wide plate of unit thickness, and that the plate is loaded by a uniform tensile stress. As indicated in Fig. 14.2b, the tensile stress is applied in the y-direction on the upper and lower surfaces of the crack over a distance, Δx measured from the crack tip. This stress will close up the crack over the distance Δx if σ_{yy} is increased at all points to the same value that it had when the crack was originally at point a. The extension of the crack from point a to point b is shown in Fig. 14.2c.

Considering a small element, dx of the interval Δx, as shown in Fig. 14.2c, the opposite sides of this element move through a distance $2Y$ as the crack closes. Elasticity theory assumes that the displacement of the crack surfaces varies linearly with the hypothetical stress σ_{yy} applied to the crack surfaces. The work done on the small element dx, as σ_{yy} is raised to the value that closes the crack, is then:

$$dW = \frac{2Y}{2}\sigma_{yy}dx = Y\sigma_{yy}dx, \tag{14.13}$$

and the work required to close the crack over the distance Δx is:

$$\Delta W = \int_0^{\Delta x} Y\sigma_{yy}dx. \tag{14.14}$$

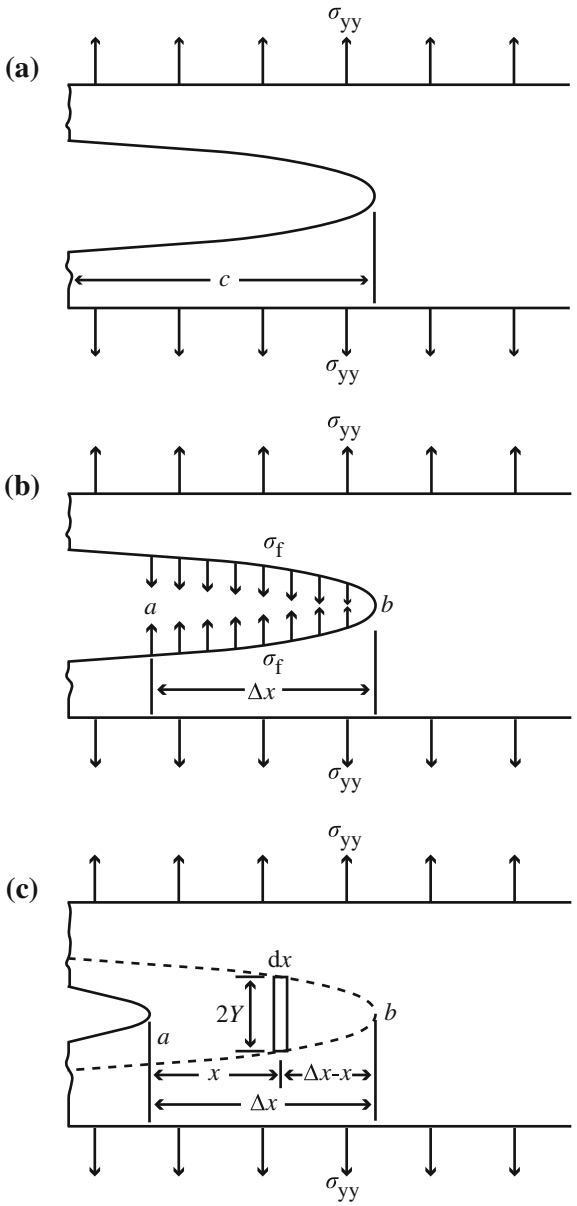

Fig. 14.2 Illustration of the Irwin method for determining the conditions for fracture (after [6])

We further assume that the material ahead of the crack is subjected to a condition of plane stress. As discussed in Sect. 12.1, this means that the stress component, σ_{zz}, parallel to the edge of the crack is zero so that all the stress components lie in the plane of the plate. With this condition, elasticity theory predicts that:

$$\sigma_{yy} = \frac{\sigma\sqrt{c}}{\sqrt{2x}}, \tag{14.15}$$

and

$$Y = \frac{2\sigma\sqrt{c}}{E}\sqrt{2(\Delta x - x)}, \tag{14.16}$$

where x is the distance measured from point a in Fig. 14.2(c), c is the half-crack length, and σ is the applied external stress. Evaluation of ΔW in Eq. (14.14) gives:

$$\Delta W = \frac{\sigma^2 c\pi\Delta x}{E}. \tag{14.17}$$

Since the derivative of the work with respect to the distance corresponds to a force, Irwin defines a *crack extension force* (actually a force per unit length) as:

$$G = \frac{\Delta W}{\Delta x} = \sigma_{\mathrm{f}}^2 \frac{c\pi}{E}, \tag{14.18}$$

where σ_{f} is the applied stress at fracture. This force may be considered as that necessary to move the crack through the metal. Note that if this expression is compared to the Griffith relationship given in Eq. (14.11a), we have:

$$G = \frac{\sigma_{\mathrm{f}}^2 c\pi}{E} = 2\gamma, \tag{14.19}$$

which suggests that the force per unit length exerted on the crack front as it advances is equal to twice the specific surface energy, γ. This result is expected since, according to the Griffith concept, the work expended in advancing the crack is converted into the surface energy of the two crack surfaces.

In this example, the Irwin analysis has been applied to a crack in a brittle elastic solid where its movement does not involve plastic deformation ahead of the crack. However, the Irwin approach can also be applied to problems where crack advance involves plastic deformation, in which Eq. (14.19) becomes:

$$G = 2\left(\gamma_{\mathrm{p}} + \gamma\right), \tag{14.20}$$

where γ is the true surface energy and γ_{p} is the plastic work per unit area involved in the creation of the surface. However, as described earlier, in most practical examples, $\gamma_{\mathrm{p}} \gg \gamma$, and γ can be neglected in comparison to γ_{p}, so that:

$$G \approx 2\gamma_{\mathrm{p}}. \tag{14.21}$$

In Eq. (14.21), the right hand side of the equation represents the energy per unit plate thickness to make a crack grow in an elastic solid. Accordingly it is called the

crack resistance force and is designated by R. So, crack growth begins when the critical energy release rate, G_c equals the crack resistance force R. Since R represents the rate at which energy is expended in growing a crack, then:

$$R = \mathrm{d}W/\mathrm{d}c = 2\gamma. \tag{14.22}$$

As indicated above for fracture in a brittle elastic plate, the vertical component of the stress ahead of the crack is given by the expression:

$$\sigma_{yy} = \frac{\sigma\sqrt{c}}{\sqrt{2x}}, \tag{14.23}$$

where x is the distance ahead of the crack. Note that in the numerator of the term on the RHS of the equation we have the product of the applied stress, σ, and the square root of c, the half-crack length. These two factors determine the general level of the stress at points ahead of the crack. The larger the applied stress or the greater the crack length, the more severe will be the stress at any point in front of the crack. Because of this, it is common practice in fracture analysis to use a parameter known as the *stress intensity factor*, which contains the product $\sigma\sqrt{c}$. In the case of a crack in a brittle elastic plate where the stress components ahead of the crack correspond to a condition of plane stress, the stress intensity factor K is defined as:

$$K = \sigma\sqrt{c\pi}. \tag{14.24}$$

At this point, it is convenient to define the three basic modes of fracture, as shown in Fig. 14.3. Mode I corresponds to fracture where the crack surfaces are displaced normal to themselves. This is a typical tensile type of fracture. In the second mode, Mode II, the crack surfaces are sheared relative to each other in a direction normal to the crack front; while in Mode III, the shearing action is parallel to the crack front.

The stress field around a crack in a solid depends on the mode. In the case of Mode I fracture in a plate with a center crack of length $2c$, the equations are expressed in terms of polar coordinate, r and θ, where r is the distance in the xy-plane from the crack tip to an element in space, and θ is the angle between r and the x-axis (as shown in Fig. 14.4):

$$\begin{aligned}
\sigma_{xx} &= \sigma(c/2r)^{1/2}\cos\frac{\theta}{2}\left[1 - \sin\frac{\theta}{2}\cos\frac{3\theta}{2}\right] \\
\sigma_{yy} &= \sigma(c/2r)^{1/2}\cos\frac{\theta}{2}\left[1 + \sin\frac{\theta}{2}\cos\frac{3\theta}{2}\right] \\
\sigma_{zz} &= 0, \quad \text{for plane stress crack growth} \\
\sigma_{zz} &= v(\sigma_{xx} + \sigma_{yy}), \quad \text{for plane strain crack growth} \\
\sigma_{xy} &= \sigma(c/2r)^{1/2}\sin\frac{\theta}{2}\cos\frac{\theta}{2}\cos\frac{3\theta}{2} \\
\sigma_{yz} &= \sigma_{xz} = 0.
\end{aligned} \tag{14.25}$$

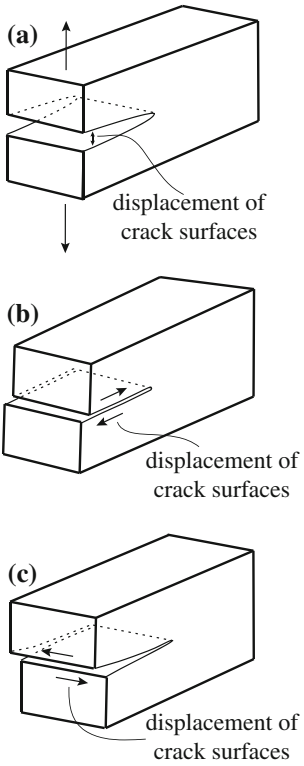

Fig. 14.3 The three basic modes of fracture (**a**) Mode I, tensile, (**b**) Mode II, shear in the direction normal to the crack front, and (**c**) Mode III, shear in the direction parallel to the crack front

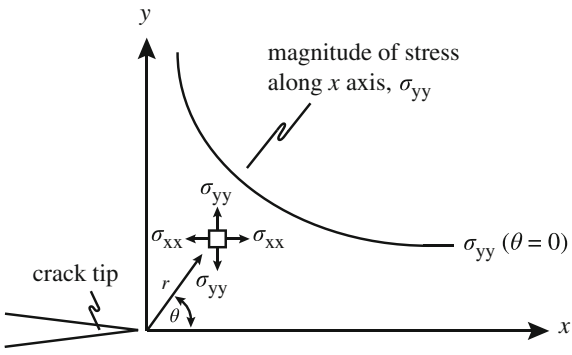

Fig. 14.4 Coordinate system for description of the stress field ahead of the crack as given by Eq. (14.25)

These equations are valid within a limited region around the crack tip. The stress field can be written in terms of the stress intensity factor using Eq. (14.24). For Mode I, the stress field around a crack tip is written as follows:

$$\begin{aligned}\sigma_{xx} &= K_{\mathrm{I}}/(2\pi r)^{1/2}\cos\frac{\theta}{2}\left[1-\sin\frac{\theta}{2}\cos\frac{3\theta}{2}\right]\\ \sigma_{yy} &= K_{\mathrm{I}}/(2\pi r)^{1/2}\cos\frac{\theta}{2}\left[1+\sin\frac{\theta}{2}\cos\frac{3\theta}{2}\right]\\ \sigma_{xy} &= K_{\mathrm{I}}/(2\pi r)^{1/2}\sin\frac{\theta}{2}\cos\frac{\theta}{2}\cos\frac{3\theta}{2}.\end{aligned} \tag{14.26}$$

When the applied stress is raised to the point where the crack is able to move rapidly, a critical value of the stress intensity factor is obtained above which unstable crack propagation occurs. This condition is written:

$$K_{\mathrm{c}} = \sigma_{\mathrm{f}}\sqrt{c\pi}. \tag{14.27}$$

The quantity K_{c} is called the *fracture toughness* and is rather simply related to the crack extension force:

$$G_{\mathrm{c}} = \frac{\sigma_{\mathrm{f}}^2 c\pi}{E} = \frac{K_{\mathrm{c}}^2}{E}, \tag{14.28}$$

for the case of plane stress, and for plane strain, Eq. (14.28) becomes:

$$G_{\mathrm{c}} = \frac{\sigma_{\mathrm{f}}^2 c\pi(1-\nu^2)}{E} = \frac{K_c^2(1-\nu^2)}{E}. \tag{14.29}$$

Both G_{c} and K_{c} may be considered to be parameters that measure the resistance of a metal to crack extension. It is important to note, however, that the relations between G_{c} and K_{c} refer specifically to a particular set of fracture conditions: where the crack advances elastically in a plate under the action of a simple tensile stress, and the stress components in front of the crack correspond to a condition of either plane stress or plane strain. For other fracture conditions, the relationship between G_{c} and K_{c} will normally be different. In fact, from Eq. (14.21), we can write:

$$G_{\mathrm{c}} = \frac{\sigma_{\mathrm{f}}^2 c\pi(1-\nu^2)}{E} = 2\gamma_{\mathrm{p}} = R\,. \tag{14.30}$$

For fracture in Mode I loading, it is normal practice to add the subscript I to the symbols K_{c} and G_{c}. The relationship given earlier is, accordingly, more properly written:

$$G_{\mathrm{Ic}} = \frac{\sigma_{\mathrm{f}}^2 c\pi}{E} = \frac{K_{\mathrm{Ic}}^2}{E} \quad \text{or} \quad G_{\mathrm{Ic}} = \frac{K_{\mathrm{Ic}}^2(1-\nu^2)}{E}. \tag{14.31}$$

The crack tip stresses due to an applied stress can result in plastic flow at the tip of the crack. The plastic zone ahead of the crack tip is kidney-shaped with lobes extending above and below the plane of fracture. A cross section through the plastic zone in the *xy*-plane is shown in Fig. 14.5. The extent of the zone in the crack plane (*xz*-plane in Fig. 14.5) is often used as an estimate of the plastic zone size. Using the expression for σ_{yy} in Eq. (14.26) and evaluating it at $\theta = 0$ gives $\sigma_{yy} = K_{\mathrm{I}}/(2\pi r_{\mathrm{p}})^{1/2}$. Solving for r_{p} and using $\sigma_{yy} = \sigma_{\mathrm{y}}$ for plane stress and $\sigma_{yy} = \sqrt{3}\sigma_{\mathrm{y}}$ for plane strain, where σ_{y} is the yield stress, gives:

$$r_{\mathrm{p}} = K_{\mathrm{I}}^2/2\pi\sigma_{\mathrm{y}}^2; \quad \text{plane stress} \tag{14.32}$$

$$r_{\mathrm{p}} = K_{\mathrm{I}}^2/6\pi\sigma_{\mathrm{y}}^2; \quad \text{plane strain}\ . \tag{14.33}$$

Figures 14.6 shows the stress distributions ahead of the crack in plane stress (a), and plane strain (b), assuming that the stress σ_{yy} does not exceed the yield stress, σ_{y}. Note that the plastic zone size in the case of plane strain is about a factor of 3 less than that in plane stress as dictated by Eqs. (14.32) and (14.33).

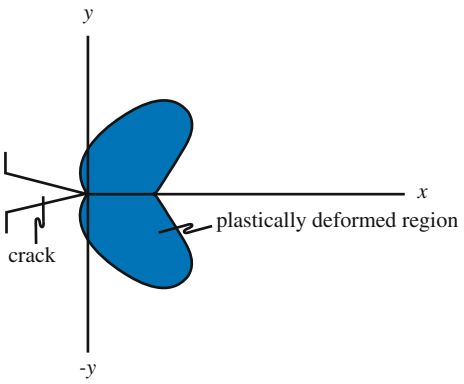

Fig. 14.5 Cross section (in the *xy*-plane) of the plastic zone in front of a crack tip

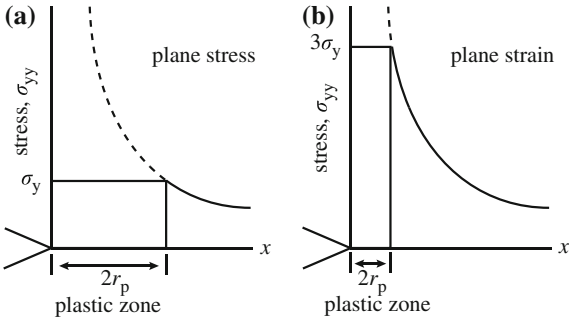

Fig. 14.6 Stress distribution ahead of a crack assuming that σ_{yy} cannot exceed σ_{y} for the cases of (**a**) plane stress and (**b**) plane strain

14.4 Fracture Mechanics Tests

The objective of a fracture mechanics test is to determine the fracture parameters describing the resistance of the metal to crack advance. The Mode I fracture toughness is such a parameter and standard sample design and test methods have been developed to determine the plane strain fracture toughness of a metal. This standardized method is described by ASTM standard E399 [7] and applies to two sample designs, the 3-point loaded notched beam specimen and the compact tension specimen. The compact tension specimen is a common sample design and is shown in Fig. 14.7. Plane strain fracture toughness measurements rely on the validity of *linear elastic fracture mechanics* (LEFM). That is, Eq. (14.26) are assumed to be valid during plane strain fracture as they were derived using elasticity theory and do not account for plasticity. Therefore, for LEFM to hold, the size of the plastic zone, as given by Eq. (14.33) ahead of the crack tip must be small. Since, $r_p \propto 1/\sigma_y^2$, the yield strength plays a large role in the size of the plastic zone, and hence, the validity of the test. ASTM standard E399 requires that the thickness of the sample be of a minimum size in order to ensure plane strain fracture. That size is given as:

$$B \geq 2.5\left(K_{Ic}/\sigma_y\right)^2, \tag{14.34}$$

where B is the specimen thickness. In addition, the size of the ligament, which is the length of uncracked material in the sample defined by $(W - a)$ in Fig. 14.7, must also be larger than the plastic zone size by the same amount as the sample thickness, B and the crack length, resulting in the following size requirements:

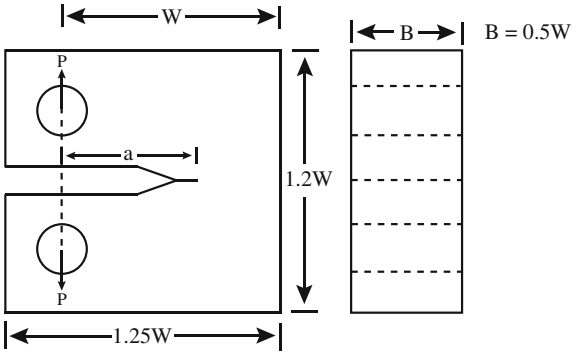

Fig. 14.7 ASTM compact tension sample design for plane strain fracture toughness measurements

$$\begin{aligned} a &\geq 2.5(K_{\mathrm{Ic}}/\sigma_{\mathrm{y}})^2 \\ B &\geq 2.5(K_{\mathrm{Ic}}/\sigma_{\mathrm{y}})^2 \\ W &\geq 5.0(K_{\mathrm{Ic}}/\sigma_{\mathrm{y}})^2, \end{aligned} \tag{14.35}$$

where a is used here to denote crack length. Note that Eq. (14.35) require a value for K_{Ic} in order to determine validity of the sample that will be used to measure K_{Ic}. So in practice, the magnitude of K_{Ic} is estimated in order to determine if the sample made from the metal to be tested will meet the requirements of Eq. (14.35). For a compact tension specimen, the stress intensity factor can be written in terms of the applied load, P, the sample dimensions, B and W and the ratio of crack length to sample width, a/W, and has the following form:

$$K = \frac{P}{BW^{1/2}} \times \frac{\left(2+\frac{a}{W}\right)\left[0.886+4.64\left(\frac{a}{W}\right)-13.32\left(\frac{a}{W}\right)^2+14.72\left(\frac{a}{W}\right)^3-5.6\left(\frac{a}{W}\right)^4\right]}{\left(1-\frac{a}{W}\right)^{3/2}}, \tag{14.36}$$

where the first term on the RHS is essentially the applied stress, and the second term reflects the effect of crack length.

14.5 Elastic-Plastic Fracture Mechanics

The determination of plane strain fracture toughness depends on the validity of LEFM for the particular test. If the yield strength is very high and the sample thickness is great enough, LEFM is satisfied. However, the low strength and high toughness for most metals (even in the irradiated state) requires thicknesses that could approach a meter in order to satisfy LEFM. When the plastic zone size in a sample is large enough to distort the elastic stress field, determination of fracture toughness using K_{Ic} is impractical. To obtain a measure of the resistance of a metal to fracture when significant plasticity is involved, other methods have been developed. The *J integral* and *crack opening displacement* methods as described by Reed-Hill [8], are two such methods that will be briefly reviewed.

The J integral proposed by Rice is a method for characterizing the stress-strain field at the tip of a crack by an integration path taken sufficiently far from the crack tip to be substituted for a path close to the crack tip region. Formally, the J integral is defined for either elastic or elastic-plastic behavior as:

$$J = \int_{\zeta} W\mathrm{d}y - T\left(\frac{\partial u}{\partial x}\right)\mathrm{d}x, \tag{14.37}$$

where ζ is a contour around the crack tip, taken in a counterclockwise direction, W is the strain energy density $\left(\int_0^{\varepsilon} \sigma \mathrm{d}\varepsilon\right)$, T is the traction vector normal to an element ds of the path $\zeta(T_i = \sigma_{ij} n_{ij})$ and u is the displacement vector, Fig. 14.8(a).

From a more physical viewpoint, J is the potential energy difference between two identically loaded bodies having slightly different crack lengths, or:

$$J = -\mathrm{d}V/\mathrm{d}c, \tag{14.38}$$

where V is the potential energy of the system, J is the negative of the rate of change of the potential energy with respect to the change in crack length. In experiments, dV/dc is determined by plotting the load-displacement curves of two specimens with different initial crack lengths. As shown in Fig. 14.8(b), loading to a constant load results in crack growth of the crack of initial length c to c + dc, that produces an increment in the displacement, δ. The area between the two $P - \delta$ curves is the energy difference dV and when divided by dc, gives J.

The crack opening displacement approach assumes that crack growth occurs when the magnitude of the plastic strain at the tip of a crack reaches a critical value

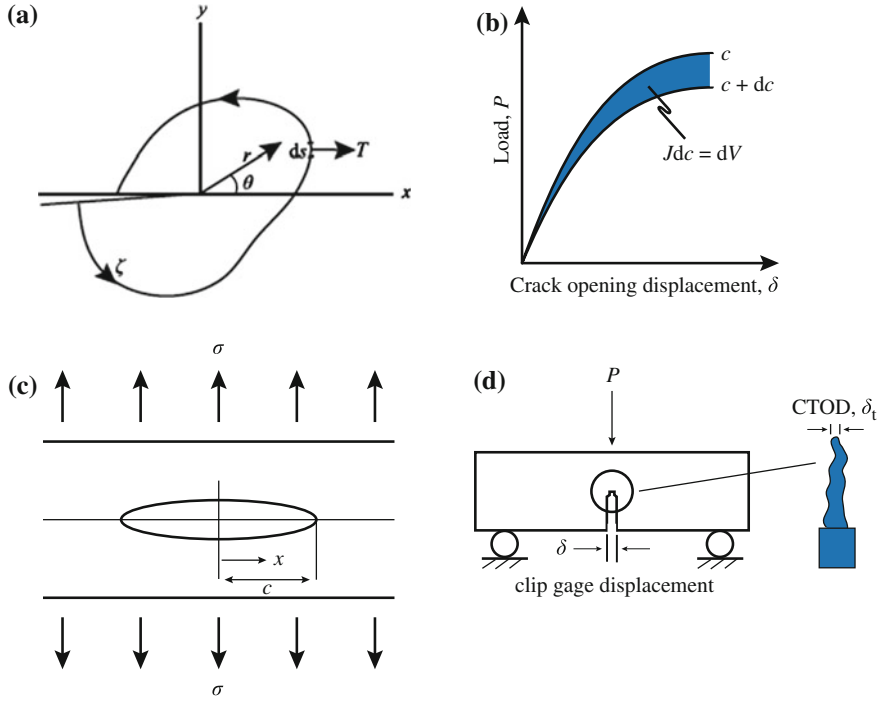

Fig. 14.8 (**a**) Crack-tip geometry and line integral contour. (**b**) Load-displacement curves for a constant displacement test on a plate containing cracks with slightly different initial lengths used to determine the J integral. (**c**) Crack geometry for COD analysis. (**d**) COD test setup in which displacement is measured using a clip gage

that depends on the specific metal or alloy. This critical strain can also be used as a failure criterion. The crack tip opening displacement for a crack of length $2c$ in an infinite thin plate subjected to uniform tensile stress, σ in a metal where plastic deformation occurs at the crack tip, Fig. 14.8(c), was determined by Dugdale [9] as:

$$\delta_t = \frac{\pi c \sigma^2}{E \sigma_y}. \tag{14.39}$$

Re-writing the expression for the crack extension force, Eq. (14.31) by dividing both sides by σ_y gives:

$$\frac{G}{\sigma_y} = \frac{\pi c \sigma_f^2}{E \sigma_y}, \tag{14.40}$$

and substituting Eq. (14.39) into Eq. (14.40) gives:

$$G = \sigma_y \delta_t, \tag{14.41}$$

resulting in the following expression for the stress in terms of the critical crack tip opening displacement, δ_{ct} for fracture:

$$\sigma_f = \left(\frac{E}{\pi c} \sigma_y \delta_{ct} \right)^{1/2}. \tag{14.42}$$

The *crack opening displacement* (COD), δ at a distance x from the center of the crack is related to the crack tip opening displacement, δ_t by:

$$\delta = \frac{4\sigma}{E} \sqrt{c^2 - x^2 + E^2 \delta_t^2 / 16\sigma^2}, \tag{14.43}$$

and can be measured by a clip gage attached to the faces of the sample, as shown in Fig. 14.8(d), resulting in the load-displacement curve shown in Fig. 14.8(b). Note that $x = 0$ when the measurement is taken on the surface of the sample shown in Fig. 14.8(c).

For linear elastic behavior, the J integral is identical to G. Therefore, a J failure criterion for the linear elastic case is identical to the K_{Ic} failure criterion, so that for linear elastic plane strain conditions:

$$J_{Ic} = G_{Ic} = \frac{(1 - \nu^2) K_{Ic}^2}{E}. \tag{14.44}$$

With increasing toughness, many materials do not fail catastrophically at a particular value of J or δ. Rather, they exhibit a gradual increase in J and δ with increasing crack length. A plot of J versus crack length, c, is termed the *R curve*. Figure 14.9 illustrates a typical R curve for a ductile metal. Initially, the slope is

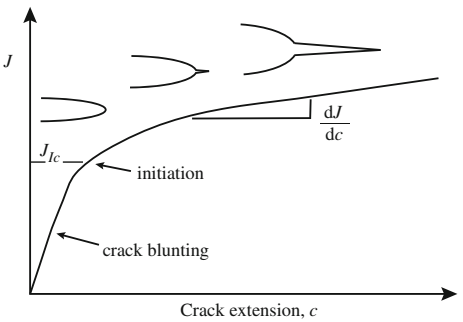

Fig. 14.9 Schematic *R* curve for a ductile metal (after [10])

very steep and there is a small amount of apparent crack growth due to tip blunting. As J increases, the material at the tip fails locally and crack advance occurs. A measure of the fracture toughness for elastic-plastic deformation is J_{Ic}, defined as the initiation of stable crack growth. From Fig. 14.9, J_{Ic} occurs when the crack begins to grow, but the precise point where this occurs is often poorly defined, resulting in a somewhat arbitrary definition.

14.6 Brittle Fracture

The greatest success of the application of the concept of fracture mechanics has been in the case of brittle fracture. Three basic factors contribute to cleavage-type fracture that is characteristic of brittle fracture: (1) a triaxial state of stress, (2) a low temperature, and (3) a high strain rate. All three of these factors do not have to be present at the same time to produce brittle fracture. A triaxial state of stress, such as exists at a notch, and low temperature are responsible for most service failures of the brittle type. However, since these effects are accentuated at a high rate of loading, many types of tests have been used to determine the susceptibility of materials to brittle fracture.

The process of brittle fracture consists of three stages:

1. Plastic deformation involving the pile-up of dislocations along their slip planes at an obstacle
2. The buildup of shear stress at the head of the pile-up to nucleate a microcrack
3. In some cases the stored elastic strain energy drives the microcrack to complete fracture without further dislocation movement in the pile-up. More typically in metals, a distinct growth stage is observed in which an increased stress is required to propagate the microcrack.

Plastic deformation by dislocation pile-up is treated in the theory of yielding in metals proposed by Cottrell [11]. This theory applies to metals exhibiting a distinct yield point and can be used to determine the fracture stress. Knowledge of both the yield stress and fracture strength permits the conditions for brittle fracture to be deduced.

The lower yield point in bcc metals or in irradiated fcc metals contains contributions due to source hardening and friction hardening. Cottrell assumes that dislocations in a few isolated grains have been unlocked either because the orientation of these grains relative to the load is such as to produce the maximum resolved shear stress on active slip planes or because a few sources in these grains have particularly low unpinning stresses. In either case, the dislocations produced in the prematurely yielded grains pile up against the grain boundary. The enhanced shear stress in the neighborhood of the pile-up triggers the sources in the adjacent grain. As such, yielding propagates across the entire specimen as the material flows.

The shear stress exerted on the slip plane in a grain next to one that has yielded and released an avalanche of dislocations which are stopped by the grain boundary is shown in Fig. 12.5. The shear stress acting on the sources in grain 2 consists of two components, the applied shear stress σ_a and the shear stress due to the proximity of the pile-up in grain 1. The latter is given in Eq. (12.62), which is re-written as:

$$\sigma_2 = \left(\frac{d}{r}\right)^{1/2} (\sigma_a - \sigma_i) \tag{14.45}$$

where σ_a is reduced by σ_i to account for the friction stress experienced by dislocations in the pile-up in grain 1. Writing Eq. (14.45) in terms of the applied stress and grouping terms containing $d^{-1/2}$ yields the Hall–Petch equation for the effect of grain size on yielding, Eq. (12.63), $\sigma_y = \sigma_i + k_y d^{-1/2}$, where the second term on the right gives the source-hardening contribution to the yield stress.

Zener first proposed the idea that the high stresses produced at the head of a dislocation pile-up could produce fracture [12]. The model is shown in Fig. 14.10. The shear stress acting on the slip plan squeezes the dislocations together. At some critical value of stress the dislocations at the head of the pile-up are pushed so close together that they coalesce into a wedge crack or cavity dislocation of height nb and length $2c$. Stroh [13] has shown that provided the stress concentration at the head of the pile-up is not relieved by plastic deformation, then the tensile stress at the pile-up is given by:

$$\sigma = (\sigma_a - \sigma_i)\left(\frac{L}{r}\right)^{1/2}, \tag{14.46}$$

where σ_a is the applied shear stress, L is the length of the blocked slip band and r is the distance in the slip plane from the lead dislocation. Equation (14.46) (similar to Eq. (14.45)) can be equated with the theoretical cohesive strength, Eq. (14.7):

$$(\sigma_a - \sigma_i)\left(\frac{L}{r}\right)^{1/2} = \left(\frac{E\gamma}{a}\right)^{1/2}, \tag{14.47}$$

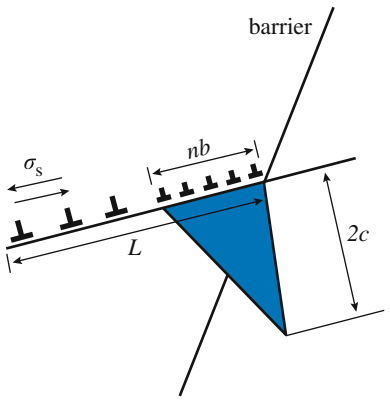

Fig. 14.10 Schematic of the formation of a microcrack at a pile-up of edge dislocations against a barrier

such that microcrack nucleation occurs at:

$$\sigma_a - \sigma_i = \left(\frac{Er\gamma}{La}\right)^{1/2}. \tag{14.48}$$

If we let $r \approx a$ and $E \approx 2\mu$ then Eq. (14.48) becomes:

$$\sigma_a - \sigma_i = \left(\frac{2\mu\gamma}{L}\right)^{1/2}. \tag{14.49}$$

But from Eq. (12.58), the number of dislocations in the slip band can be expressed as:

$$n \approx 2(\sigma_a - \sigma_i)\frac{L}{\mu b}, \tag{14.50}$$

so eliminating L from Eqs. (14.49) and (14.50) gives:

$$(\sigma_a - \sigma_i)nb \approx 2\gamma. \tag{14.51}$$

This form of the equation for microcrack nucleation was proposed by Cottrell [11]. It has the direct physical significance that a crack will form when the work done by the applied shear stress in producing a displacement nb equals the work done in moving the dislocations against the friction stress plus the work in producing the new fracture surfaces. In terms of the normal stress:

$$\sigma(nb) \approx 4\gamma. \tag{14.52}$$

Assuming that the dislocation source is at the center of a grain of diameter d, so that $L = d/2$, and substituting Eq. (14.50) into Eq. (14.52) gives:

$$\sigma(\sigma_a - \sigma_i) = \frac{4\mu\gamma}{d}. \tag{14.53}$$

But since at the yield stress, σ_y is identified with σ_a and $(\sigma_y - \sigma_i) = k_y d^{-1/2}$ (see Eq. (12.63)), then from Eq. (14.32) we have the Cottrell–Petch equation:

$$\sigma = \sigma_f = \frac{4\mu\gamma}{k_y} d^{-1/2}. \tag{14.54}$$

This equation represents the stress required to propagate a microcrack of length d in brittle fracture.

The wedge crack in Fig. 14.10 arises due to the coalescence of nb dislocations, so the fractional elongation of the grain (strain) is nb/d. Using Eq. (14.52), the strain to initiate a wedge crack of size nb is $\varepsilon_f = nb/d = 4\gamma/\sigma d$, which is the fracture strain in the case of brittle fracture when the elastic stored energy drives the microcrack to complete failure.

The dependence of yield stress and fracture stress on grain size typical of a low-carbon steel are plotted in Fig. 14.11. Note that the two lines cross at a particular value of d and σ, and this intersection is the ductile-to-brittle transition. To the left of the transition, fracture and yielding occur simultaneously. However, fracture occurs at the yield stress since in our model, yielding must occur first. To the right of the transition, yielding occurs first and the incremental strain between σ_f and σ_y is due to work hardening of the metal. During this process, the metal is deforming plastically and the fracture stress increases with decreasing d. The parameter, k_y determines the number of dislocations that are released into a pile-up when a source is unlocked. Materials with a high value of k_y (e.g., ferritic steels and molybdenum) are more prone to brittle fracture than materials with lower values (e.g., niobium and tantalum). In bcc metals, the frictional resistance increases rapidly as the temperature falls below room temperature and thus leads to a ductile-to-brittle transition.

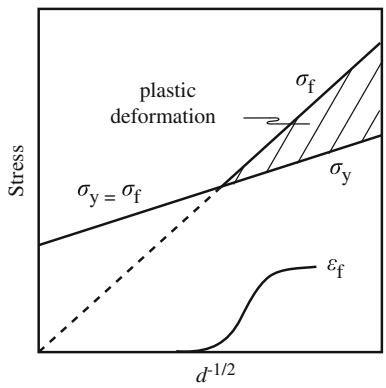

Fig. 14.11 Effect of grain size on yield and fracture stress of a typical low-carbon steel tested at low temperature

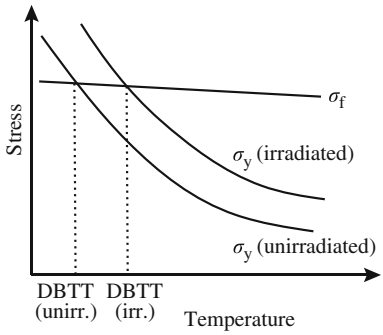

Fig. 14.12 The relationship between temperature dependence of yield stress and fracture strength and the ductile-to-brittle transition temperature

The Cottrell–Petch theory provides an explanation of why irradiation embrittles steels. The irradiation-induced defects and defect clusters raise the frictional component to the yield stress, σ_i by increasing the resistance to dislocation motion. However, in unirradiated bcc metals, the sources are strongly pinned by impurity atoms in the absence of neutron-produced point defects (resulting in the upper and lower-yield point phenomenon), so irradiation has only a small effect on k_y. The net effect of these different dependencies on irradiation is that the yield strength is increased much more than the fracture strength. Figure 14.12 shows the effect of irradiation on the temperature dependence of the yield and fracture strengths. Note that the increase in the yield strength due to irradiation displaces the temperature at which brittle fracture occurs to higher temperatures. The drastic loss in ductility at low temperature results from the different sensitivities of σ_y and σ_f to neutron damage. The *ductile-brittle transition temperature* (DBTT) or the *nil-ductility temperature* (NDT) is defined by the condition that $\sigma_f = \sigma_y$, which from Eq. (14.54) is:

$$\sigma_y k_y = 4\mu\gamma d^{-1/2}. \tag{14.55}$$

Bement [14] has written the Cottrell–Petch equation for the fracture stress as:

$$\sigma_f = \frac{\beta\mu\gamma_e}{k_S} d^{-1/2}, \tag{14.56}$$

where β is a constant related to the degree of triaxiality of the applied stress, γ_e ($= \gamma + \gamma_p$) is the effective surface energy of the crack, and $k_S = M^{-1}k_y$, where M is the Taylor orientation factor.

From the Cottrell–Petch equation an irradiation-induced increase in yield strength, increase in k_S, or decrease in the effective surface energy, γ_e can promote embrittlement. Since the fracture stress, σ_f is not greatly affected by irradiation and is much less dependent upon temperature than is σ_y, these irradiation-induced

property changes can also cause a significant increase in the DBTT (under the criteria $\sigma_y = \sigma_f$) [15] as expressed by:

$$T_c = C^{-1}\left[\ln Bk_s d^{1/2}/(\beta\mu\gamma - k_y k_s)\right], \tag{14.57}$$

where B and C are constants for expressing the temperature dependence of σ_i (neglecting long-range stresses) given by:

$$\sigma_i = B\exp(-CT), \tag{14.58}$$

with T as the absolute temperature.

The expected effects of irradiation on the individual parameters of the Cottrell–Petch equation are given by Bement in Table 14.1. Although σ_y definitely increases with irradiation, which alone accounts for a substantial shift in the ductile-brittle transition temperature for steel, the effects of residual elements and dislocation channeling on σ_i and k_S are not as well-established.

Investigations of the effects of irradiation on the Hall–Petch relationship for iron, steel, and molybdenum have given varying results; however, the trend indicates that there is little effect of irradiation on k_y at relatively small grain size ($d^{-1/2} > 4$ mm$^{-1/2}$) and a reduction of k_y to small values at larger grain sizes. Irradiation of Armco-iron (50 μm grain size) to a dose of 3×10^{18}n/cm^2 ($E > 1$ MeV) at 50 °C results in a decrease in k_y from 396 to 305 MPa(μm)$^{1/2}$ [16]. The significant reduction in k_y for large grain size occurs at neutron fluences greater than $\sim 10^{18}$ n/cm^2, which is the threshold for large increases in yield strength and correspondingly large increases in the ductile-brittle transition temperature. At these neutron exposures well-defined defect clusters and dislocation channels are observed in the electron microscope.

Contrary to observations, dislocation channeling might be expected to increase the value of k_y by restricting dislocation cross slip and by restricting the number of operating slip systems required to maintain continuity across grain boundaries. It is

Table 14.1 Effect of irradiation on parameters in the Cottrell–Petch equation (14.56) after [14]

Term	Description	Effect of irradiation
σ_y	Yield stress	Increase
$\Delta\sigma = \sigma_f - \sigma_y$	Stress increment for fracture	Decrease
β	Triaxiality of applied stress	-
μ	Shear modulus	-
γ_e	Effective surface energy ($\gamma + \gamma_p$)	Decrease
d	Grain size	-
k_y	Petch slope	Decrease (d large) little change (d small)
M	Taylor orientation factor	Increase (?) due to channeling
σ_c	Source operating stress	Increase
r	Distance from source to pile-up	Decrease (?) due to channeling

possible that in fine-grained material radiation defect clusters offer little additional impedance to forced slip near the boundaries in accordance with Johnson's model for k_y [17] and that in coarse-grained material the contributions of long-range stresses due to dislocation pile-ups at channel intersections or other barriers (such as carbides) override back stresses due to boundaries. That is, the flow stress becomes grain-size independent of k_y on post-yield strain and the amount of dislocation multiplication that occurs during channel formation is not known, so that grain size effects on the yielding and fracture of irradiated bcc metals are still uncertain.

From the preceding analysis, not only the assumption for the number of coalesced dislocations, nb in the wedge crack but also the surface energy term is important to the application of fracture models. The surface energy is also a critical parameter in the analysis of the propagation of existing cracks as described by the theories of Griffith [2], Orowan [4], and Irwin [5]. Reduction in the plane strain fracture toughness, K_{Ic}, for irradiated steel [18] would result partly from reduction in the critical crack extension force, $G_c = K_{Ic}^2/E$ which would result from reduction in effective surface energy ($G_c = 2\gamma_e$ when $\sigma = \sigma_f$).

The effective surface energy, γ_e for polycrystalline metals consists of the intrinsic surface energy, γ for a given cleavage plane and a term, γ_p which represents plastic relaxation at the tip of a flaw. Plastic relaxation at a crack tip can occur by either source multiplication or by extensive cross slip and both processes are strongly restricted by radiation damage in the early stages of plastic strain. Therefore, the effective surface energy at yielding should approach the intrinsic surface energy with increasing neutron fluence. However, measurements of γ_e have not been made for irradiated metals.

An extension of fracture theory relative to contributions of the intrinsic surface energy, γ and the plastic work energy, γ_p on cleavage fracture in bcc metals is the work of Stein reported by Bement [14]. It was found that the cleavage plane along which cracks propagate is the one for which the plastic work is the least and is not the one determined by differences in the intrinsic surface energy. If one were to consider two potential fracture planes before irradiation, the cleavage plane having the lowest work energy, γ_p would be the operating plane in cleavage fracture, even though its intrinsic energy, γ might be higher. After irradiation, however, if γ_p approaches a very low value, the intrinsic surface energy might then assume a controlling role in cleavage fracture, and the order of preference between the two (or more) potential cleavage planes might be reversed. As yet this possibility is unexplored.

14.7 Irradiation-Induced Embrittlement in Ferritic Steels

Most reactor pressure vessel steels have in common the characteristic of undergoing a transition from ductile to brittle fracture as the temperature is reduced. This transition usually occurs in a temperature range of only about 80 °C [19]. Over this range, the micro- and macroscopic nature of the fracture gradually changes from

ductile dimpled rupture to cleavage along crystallographic boundaries with a broad range of mixed fracture modes in between. An important element of assessing the fracture characteristics of irradiated pressure vessel steels is the notched bar impact test. This test and the interpretation of its outcome in terms of the fracture mechanisms are discussed next.

14.7.1 Notched Bar Impact Testing

Despite the development of well-designed fracture mechanics methodology and test samples, the simple Charpy impact test has historically served as the primary basis for defining radiation effects on ductility. However, the results obtained from notched bar tests, such as the Charpy test, are not readily expressed in terms of design requirements, since it is not possible to measure the components of the triaxial stress condition at the notch. Nevertheless, the Charpy impact test has become widely used throughout the world as a severe test for brittle fracture.

The Charpy specimen has a square cross section (10 × 10 mm) and contains a 45° V-notch, 2 mm deep with a 0.25 mm root radius (Fig. 14.13). The specimen is supported in a horizontal position and loaded behind the notch by the impact of a heavy swinging pendulum (with impact velocity of approximately 5 m/s). The specimen is forced to bend and fracture at a high strain rate on the order of 10^3 s^{-1}.

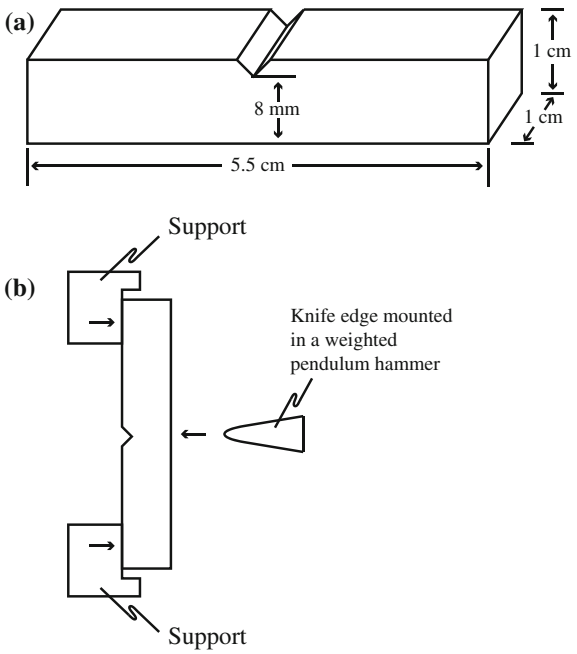

Fig. 14.13 (**a**) The Charpy V-notch impact test specimen. (**b**) Method of applying the impact load to the specimen

The principal measurement from the impact test is the energy absorbed in fracturing the specimen. After breaking the test bar, the pendulum continues on to a height, which decreases as the energy absorbed in fracture increases. The energy absorbed in fracture, usually expressed in J or ft-lbs, is read directly from a calibrated dial on the impact tester. If the fracture is completely ductile, the energy expended will be high; when it is completely brittle, the energy expended will be low. The energy required for fracture of a Charpy specimen is often designated C_V followed by the value, for example, C_V 41 J or C_{41}. Since the energy-absorbing capacity of the steel varies with temperature, the impact test provides a simple method of following the change in the fracture mode of a steel as a function of temperature. A representative curve, showing the transition from ductile to brittle behavior, is given in Fig. 14.14. One of its important features is that the transition is not sharp but occurs over a range of temperatures. Examination of the fracture surfaces yields a reasonable correlation between the amount of the cross section that has broken in a ductile fashion and the energy expended in breaking the specimen. Completely ductile specimens exhibit surfaces that are rough or fibrous, while those of brittle specimens contain an irregular array of small bright facets, each corresponding to the surface of a cleaved crystal. In those specimens where the fracture is part ductile and part brittle, the brittle, or bright area is found at the center of the cross section. Two measures of the transition from brittle to ductile behavior are the percent shear fracture and the lateral expansion, and both follow the same dependence on temperature as does the absorbed energy plot given in Fig. 14.14. Therefore, the shift from ductile to brittle behavior can also be followed by examining the fracture surfaces of impact specimens.

The Charpy impact test has been widely used to measure the effect of a number of variables on the brittle-to-ductile transition. The lack of a sharp transition in absorbed energy to mark the separation of ductile and brittle behavior poses a difficulty in interpretation of the Charpy test result. Still, as a matter of convenience, it is common practice to speak of the transition temperature of a metal. This term, however, needs to be carefully defined as there are a number of different ways of

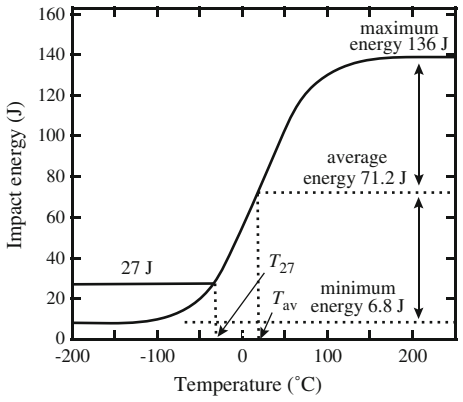

Fig. 14.14 Illustration of the effect of irradiation on the Charpy impact curve for a reactor pressure vessel steel, showing a shift in DBTT and a decrease in the upper shelf energy

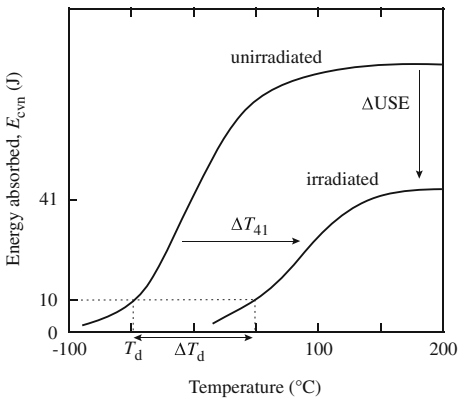

Fig. 14.15 Transition temperature shift as a function of yield stress resulting from irradiation

expressing it. One is to take the temperature at which an impact specimen fractures with a half-brittle and half-ductile fracture surface. A second way of defining the transition temperature uses the average energy criterion: the temperature at which the energy absorbed falls to one-half the difference between that needed to fracture a completely ductile specimen, and that needed to fracture a completely brittle specimen. The temperature at which a Charpy specimen breaks with a fixed amount of energy, e.g., 41 J, is also a widely employed basis for the transition temperature. Another metric, the nil-ductility temperature, is defined as the temperature at which fracture initiates with essentially no prior plastic deformation. The true NDT temperature is determined from drop weight tests as prescribed by ASTM E208-95a. From this temperature, the reference temperature, RT_{NDT}, is given by $RT_{NDT} = T_{NDT} - 60$ °F [20].

Figure 14.15 illustrates the effect of irradiation on a Charpy curve for a typical pressure vessel steel. Note that irradiation causes a shift of the curve to higher temperatures and a reduction in the upper shelf energy (USE). Further, the slope of the curve is reduced with irradiation. All three of these features change with increasing fluence and hardening.

14.7.2 DBTT and Reduction in the Upper Shelf Energy

The shift from ductile to brittle fracture was discussed earlier with the aid of the Hall–Petch relationship. It was shown that the yield strength decreases with temperature and the fracture stress is roughly temperature-independent, so the intersection of the fracture stress curve and the flow stress curve is taken as the ductile-to-brittle transition temperature (DBTT). Irradiation causes an increase in the yield stress, shifting the point at which the fracture stress and yield stress curves intersect to higher temperature, thus increasing the DBTT as was shown in Fig. 14.12. The transition from ductile to brittle behavior is most commonly characterized by the intersection of the Charpy curve with the 41 J line, denoted

C_{41}, and the corresponding temperature shift between unirradiated and irradiated condition is designated ΔT_{41}. Odette [21] noted that ΔT_{41} is a non-linear function of $\Delta\sigma_y$, with $\Delta T_{41}/\Delta\sigma_y$ increasing with $\Delta\sigma_y$ and T^*, where T^* is the temperature at which the fracture and flow stress curves intersect. Thus the DBTT increases faster than linear with increases in hardening due to irradiation.

Irradiation-induced segregation of embrittling elements such as phosphorus can lead to a drop in the fracture stress, causing an additional shift in the DBTT. Phosphorus segregates to grain boundaries during irradiation as described in Chap. 6, where it is believed to reduce grain boundary cohesion, resulting in an increase in the DBTT or a decrease in the lower shelf toughness. The additional increase in the DBTT is shown as ΔT_2 in Fig. 14.16. If both mechanisms are operative, the combined shift of ΔT occurs where the two components are combined by linear addition as in Fig. 14.16.

Irradiation not only increases the DBTT but also reduces the energy absorption for fracture at the ductile shelf of the transition curve (Fig. 14.15). The change in upper shelf energy also appears to result from the increase in yield stress due to irradiation. Figure 14.17 shows the fractional change in upper shelf energy, f with the change in yield stress and is described by:

$$\begin{aligned} f &= 9\times10^{-4}\Delta\sigma_y \quad \text{for } 0<\Delta\sigma_y<40\,\text{MPa} \\ &= 9\times10^{-4}\Delta\sigma_y + 0.02\sqrt{\Delta\sigma_y - 40} \quad \text{for } \Delta\sigma_y > 40\,\text{MPa}. \end{aligned} \tag{14.59}$$

In addition to shifting the yield stress curve to higher temperatures, irradiation also reduces the slope of the curve, and represents an additional contribution to the temperature shift. Odette [21] showed that the energy-temperature slope change can be related to the decrease in the upper shelf energy (E_U), and that the ratio of irradiated to unirradiated upper shelf energy ($f_{Eu} = E_{U,i}/E_U$) empirically correlates with $\Delta\sigma_y$:

$$\Delta T_s(^\circ\text{C}) \approx \frac{3720}{E_u}\left(\frac{1-f_{E_u}}{f_{E_u}}\right). \tag{14.60}$$

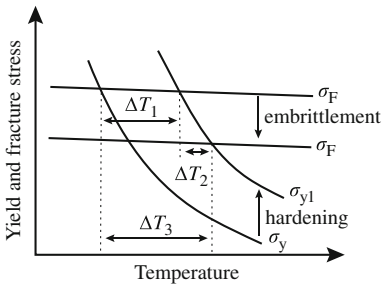

Fig. 14.16 Variation of the yield stress and fracture stress with temperature and irradiation, resulting in independent contributions to the transition temperature shift (after [22])

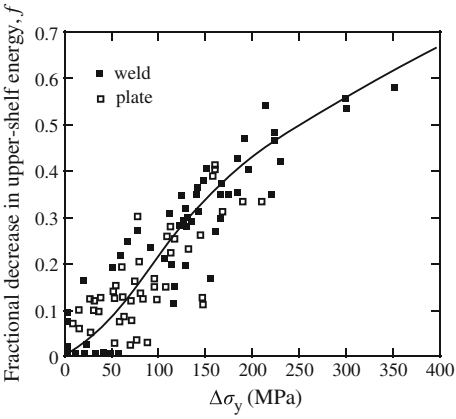

Fig. 14.17 Fractional decrease in the Charpy upper shelf energy as a function of yield strength increase due to irradiation (after [21])

The resulting transition temperature can be expressed as:

$$\Delta T = \Delta T_1 + \Delta T_2 + \Delta T_s. \tag{14.61}$$

Decreases in the upper shelf energy have been linked to an increase in the amount of shear fracture on the fracture surface [23]. Nevertheless, the effect of irradiation on the upper shelf energy is believed to be due to a reduction in strain hardening and flow localization leading to lower ductility and an increased triaxial stress state due to strength increases [21]. As discussed in Chap. 12, flow localization in the form of dislocation channeling occurs in irradiated ferritic steels and may contribute to the reduced ductility in the ductile fracture regime.

14.7.3 Master Curve Approach

Of greatest importance in ensuring the integrity of reactor pressure vessel steels under irradiation is to be able to quantitatively determine how the fracture toughness of the steel is affected by irradiation. Irradiation shifts the fracture toughness curve to higher temperatures. Figure 14.18 shows that the effect of irradiation is to displace the fracture toughness curve to the right on the temperature scale. Interestingly, the shape of the curve is similar before and after irradiation. In fact, it has been observed that over a range of ferritic steels, the fracture toughness transition curves have a characteristic shape. The fixed shape implies that the fracture toughness for these materials can be described by a series of curves that differ only in their location on the temperature scale. This is the basis for the *Master Curve* concept. According to this concept a fracture toughness curve can be determined by a single parameter that fixes the position of the Master Curve on the temperature scale. This parameter is termed, T_0 and is defined as the temperature at which the

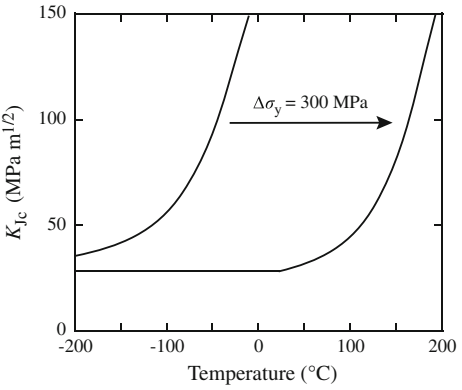

Fig. 14.18 Displacement of the fracture toughness curve with irradiation

median fracture toughness for a 1 T (25.4 mm thick) fracture toughness specimen equals 100 MPa m$^{1/2}$ (91 ksi in$^{1/2}$). The Master Curve is given as:

$$K_{Jc(med)} = 30 + 70\exp(0.019(T - T_0)) \tag{14.62}$$

where T is the test temperature, T_0 is the reference temperature defined above, and $K_{Jc(med)}$ is the median fracture toughness in MPa m$^{1/2}$. The median fracture toughness is defined as:

$$K_{Jc(med)} = \sqrt{\frac{J_c E}{(1 - \nu^2)}}, \tag{14.63}$$

where E is Young's Modulus, ν is Poisson's ratio and J_c is the value of the J integral at the onset of cleavage fracture and is determined from the area under the load-displacement curve.

Reactor surveillance programs have historically used Charpy V-notch specimens rather than fracture toughness specimens. These specimens are exposed in surveillance capsules, after which they are tested, and the shift in impact energy due to irradiation is calculated. These temperature shifts are all that is available to determine the shift in fracture toughness due to irradiation. Figure 14.19 shows that in principle, the change in DBTT measured in a Charpy test should be relatable to the shift of the fracture toughness curve.

Charpy curves taken before and after irradiation of weld material containing high Cu, Ni and Mn contents and irradiated at 288 °C to 0.74 × 10^{19} n/cm^2 ($E > 1$ MeV) [25] exhibit an increase in the ΔT_{41} by 169 °C and a substantial reduction in the upper shelf energy of some 40 J, Fig. 14.20. Fracture toughness experiments were conducted on 0.5 T and 1 T CT specimens made from the same alloy and irradiated under the same conditions. The unloading compliance method was used to determine the J integral versus crack extension, from which a value of J_c was determined. That was converted to the critical value of the stress intensity factor using Eq. (14.63), and replicate tests were used to determine $K_{Jc(med)}$. The median fracture

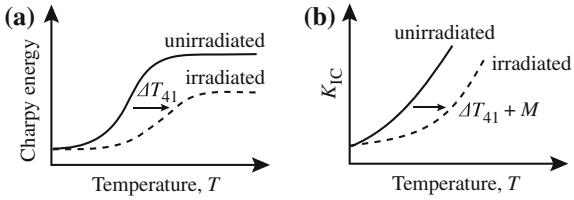

Fig. 14.19 Application of the transition temperature shift in a Charpy test to the fracture toughness test. (**a**) Charpy impact energy, and (**b**) fracture toughness (after [24])

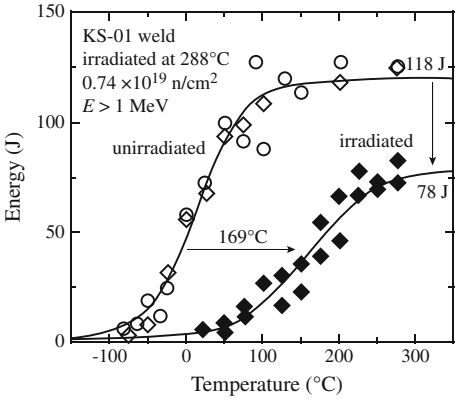

Fig. 14.20 Charpy impact energy versus test temperature for weld metal in the unirradiated condition and following irradiation to 0.74×10^{19} n/cm^2 ($E > 1.0$ MeV) at 288 °C (after [25])

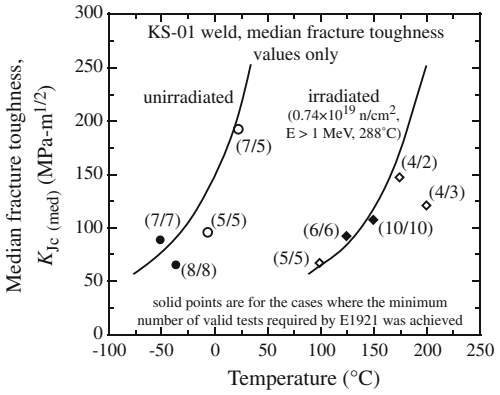

Fig. 14.21 Median fracture toughness of the same weld metal in the unirradiated condition and following irradiation under the same conditions as for the Charpy test in Fig. 14.20 (after [25])

toughness is plotted in Fig. 14.21 and from the Master Curve definition, the shift of the value of T_0 is determined at 100 MPa m$^{1/2}$ to be 165 °C, which is in excellent agreement with the Charpy ΔT_{41} value of 169 °C.

The approach of estimating fracture toughness based on a reference temperature employs what is termed the *adjusted reference temperature* (ART) [26], which is a function of the Charpy temperature shift as follows:

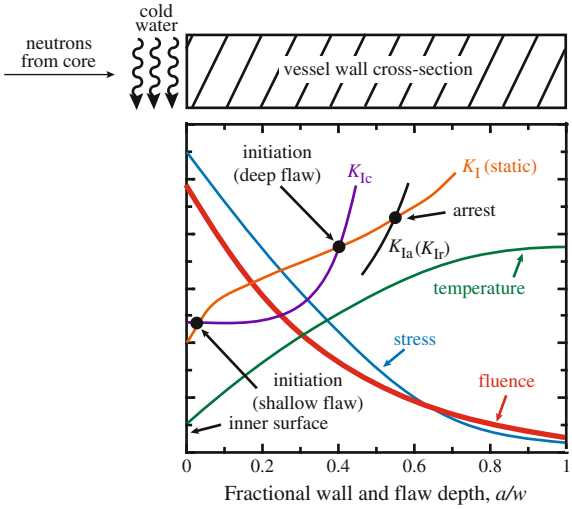

Fig. 14.22 Temperature, fluence, stress and resulting toughness gradient through the thickness of a reactor pressure vessel wall (courtesy of ST Rosinski, EPRI)

$$ART = RT_{\mathrm{NDT}} + \Delta T_{41} + M, \tag{14.64}$$

where RT_{NDT} is a reference nil-ductility temperature for the unirradiated material, ΔT_{41} is the Charpy temperature shift at $C_{\mathrm{V}} = 41$ J, and M is a margin-of-safety term that has a value of 36 °C for welds to account for uncertainties in RT_{NDT} and ΔT_{41}. In this way, the large amount of surveillance data collected on Charpy samples can be used to determine the fracture toughness of the irradiated steel, which is crucial for ensuring the integrity of the pressure vessel as it ages.

An additional consideration in assessing the integrity of the pressure vessel is the establishment of gradients due to its thickness. Since the pressure vessel wall thickness can exceed 200 mm, neutron fluence, temperature and stress will all vary through the thickness of the vessel wall. Variation in the temperature and neutron fluence will cause the microstructure to differ as a function of position in the vessel. Since fluence is at a maximum and temperature is at a minimum at the inner diameter of the vessel, the hardening and embrittlement will be greatest there. That stress is a maximum at the surface means that the fracture toughness will be lowest at the vessel inner surface (Fig. 14.22). Flaws initiating at the inner surface will be growing into material with increasing toughness, providing an additional margin of safety against through-wall cracking.

14.7.4 Factors Affecting the Degree of Embrittlement

Because irradiation hardening is the principal factor affecting embrittlement, the same factors that influence hardening will influence embrittlement. These include:

– Steel composition and microstructure
– Exposure temperature
– Neutron environment.

14.7.4.1 Effects of Microstructure and Composition

Of considerable importance to the improvement of the ductile-brittle transition temperature of pressure vessel steel is the influence of the microstructure on the fracture stress. The critical fracture stress can be increased by decreasing the mean dislocation path length (λ) in steel, which can be accomplished by reducing the grain size ($d = 2\lambda$) in pearlitic steels or by reducing the interparticle spacing ($l = \lambda$) among dispersed carbides (hard barriers) in tempered steels [26, 27]. Although refinements in grain size and carbide dispersion can increase the fracture stress to a greater extent than yield stress, thereby reducing both the static and dynamic transition temperatures, irradiation hardening can reverse these beneficial effects.

It has also been suggested that the abundance of grain boundaries in fine-grain steel act as a more efficient trap for defects. This role is thought to be especially important where free interstitial (and embrittling) elements such as nitrogen may be more homogeneously trapped, thereby lessening the effects on macroscopic properties of the irradiated steel. However, as discussed earlier, grain boundary segregation of elements such as phosphorus can result in embrittlement of the grain boundary.

As in the case of hardening, the presence of substitutional elements, such as copper, nickel, manganese and phosphorus, controls the level of embrittlement in the Mn–Mo steels used in the USA for reactor pressure vessels. The dominant hardening and hence, embrittling feature is the copper-rich precipitate (CRP), which consists of very small (1–3 nm) coherent precipitates with high Cu content that can form at number densities exceeding 10^{23} m^{-3}. CRPs are enriched in Mn and Ni as well as smaller amounts of P and Si. Both Ni and Mn form strong bonds with Cu in the precipitate and increase the volume of the precipitate. As such, increasing amounts of Ni and Mn amplify the hardening effect of Cu. The effect of Cu on the embrittlement of A533B steel is shown in Fig. 14.23. As a result of a large NRL study on the role of residuals in radiation embrittlement, it was concluded some time ago that clean steels (low residuals P, S, Cu, Sn, As, Sb, etc.) mean low radiation sensitivity [28]. In fact, it is possible to develop steels with low residual content that show very low response to irradiation to end-of-life fluences (Fig. 14.24).

Notwithstanding the influence of residual elements on radiation defect stabilization, there are other intrinsic effects of these elements on impact behavior, which may prove to be important in radiation embrittlement sensitivity. Those residual elements which restrict cross slip, cause significant matrix strengthening, and reduce fracture surface energy are primarily suspect. Phosphorus contributes strongly to all three processes, copper is a potent solid solution hardener while silicon, vanadium, aluminum and cobalt diminish the ease of cross slip.

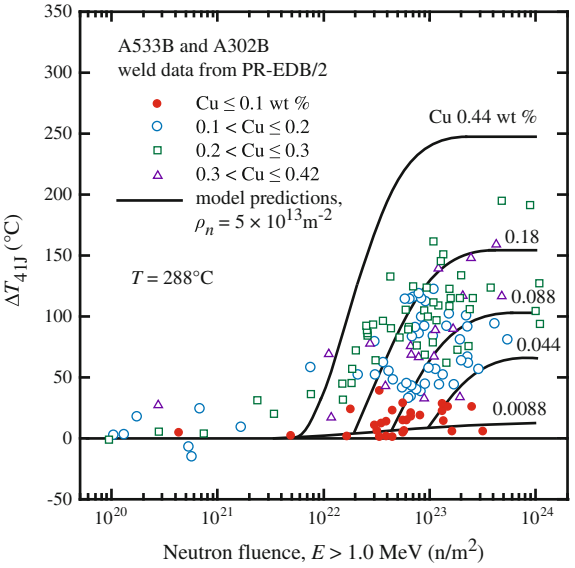

Fig. 14.23 Effect of copper content on the temperature shift of A533-B and A302-B welds irradiated at 288 °C (after [28])

14.7.4.2 Effect of Temperature

As shown by both Charpy and fracture toughness curves, the level of embrittlement is progressively reduced with higher irradiation temperature. This effect is a manifestation of the annealing process that is accelerated at higher temperatures. The mechanisms responsible for affecting the strength of pressure vessel steels (dislocation impedance by irradiation-induced precipitates, defect-solute clusters) are essentially low-temperature processes and are annealed out at temperatures approaching 400 °C in steel. Figure 14.25 shows the drop in the transition temperature increase for a given fluence as the irradiation temperature is raised. The implication is that irradiation at higher temperature will result in less embrittlement than at low temperature.

14.7.4.3 Effect of Neutron Environment

It is well established that the magnitude of embrittlement is a strong function of the neutron fluence as the transition temperature increases rapidly with fluence. Attempts have been made to characterize the transition temperature shift as a function of neutron fluence. A simple model is:

$$\Delta T_{41} = A(\phi t)^n, \tag{14.65}$$

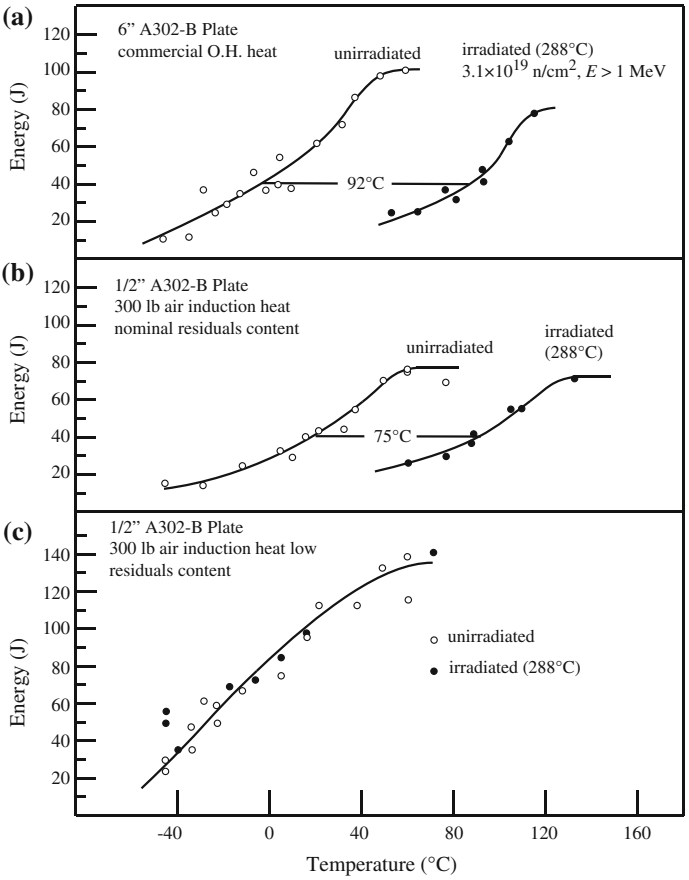

Fig. 14.24 Comparison of radiation embrittlement sensitivity in A302-B plate. (**a**) Commercial heat. (**b**) Air-induction heat with nominal residuals. (**c**) Air-induction heat with low residuals (after [29])

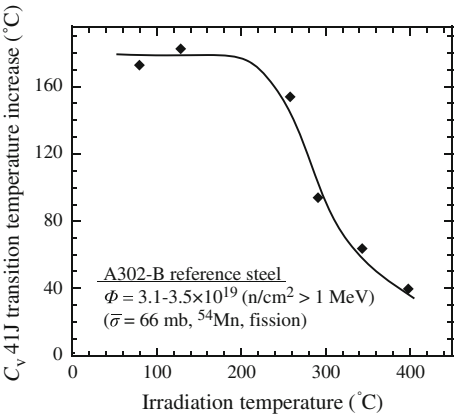

Fig. 14.25 Effect of irradiation temperature on transition temperature increase for an A302-B steel (after [19])

where ΔT_{41} is the transition temperature shift of Charpy energy at 41 J or the fracture toughness at 100 MPa $m^{1/2}$ and ϕt is the neutron fluence in units of n/cm^2 ($E > 1.0$ MeV). The value of the exponent, n will vary depending on the type of steel. The average value of n for advanced US steels is 0.5 [30], but the value is closer to 0.33 for Russian steels [31]. The US Nuclear Regulatory Commission (NRC) Regulatory Guide 1.99 (RG 1.99), Rev. 2 [32] provides the following relation:

$$\Delta T_{41} = A\Phi^{(0.28-0.1\log\Phi)}, \tag{14.66}$$

where Φ is neutron fluence in units of 10^{19} n/cm^2 ($E > 1$ MeV). An example of the behavior of the transition temperature with fluence is shown in Fig. 14.26 for a 0.24 % Cu–1.6 % Ni weld irradiated at 290 °C [33] and compared to the NRC Regulatory Guide 1.99 specification [32]. Unfortunately the response of different steels, and the influence of other factors is reflected in the value of A and causes a large scatter. Further, there does appear to be a tendency towards saturation, which is also strongly influenced by many factors. As shown in Figs. 12.17 and 14.27, the effect of CRPs on hardening and embrittlement saturates at high doses due to depletion of copper from the matrix.

Of greater importance is the role of flux or dose rate on embrittlement. At very low fluxes ($<10^{14}$ n/m^2 s), CRP growth is increased due to enhanced copper diffusion due mainly to thermal processes. At very high fluxes ($\gg 10^{16}$ n/m^2s), a high density of unstable matrix defects becomes significant. These defects increase vacancy and interstitial loss, reducing radiation-enhanced diffusion and slowing the growth of CRPs. In the intermediate flux regime (10^{15}–10^{16} n/m^2s), there is a significant influence of flux on embrittlement in which hardening and embrittlement vary as $\phi^{-1/2}$ (see Fig. 12.19(a)). The mechanism for this effect is believed to involve enhanced solute trapping as well as enhanced recombination and a high efficiency for radiation-enhanced diffusion.

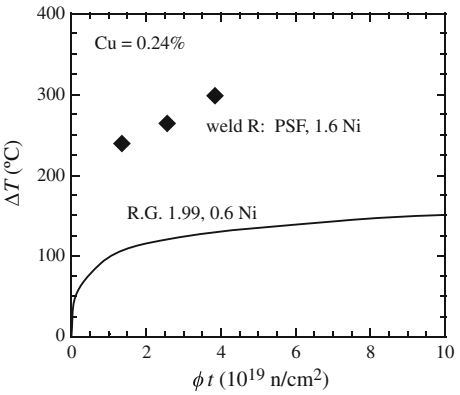

Fig. 14.26 Effect of neutron fluence ($E > 1.0$ MeV) on the transition temperature in a 0.24Cu–1.6Ni weld metal irradiated at 290 °C (after [33])

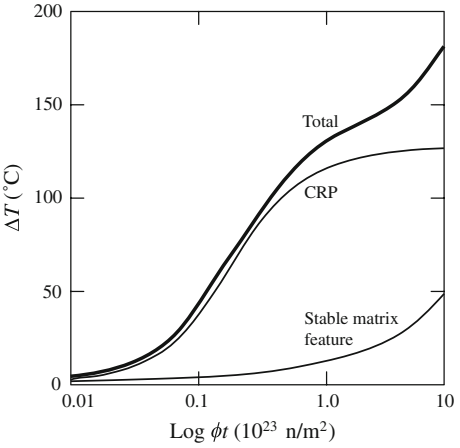

Fig. 14.27 Effect of copper-rich precipitates (CRP) on the fluence dependence of the transition temperature (after [34])

14.7.5 Embrittlement of Ferritic-Martensitic Steels

Ferritic-martensitic steels have been considered for use in both fusion and advanced fission reactor systems because of their resistance to swelling and helium embrittlement, and the potential for low activation. The steels are used in the two-phase, ferritic-martensitic structure, and can be heat treated to optimize toughness and high-temperature strength. The standard heat treatment consists of a solution anneal to completely austenitize the microstructure and to dissolve the carbides, followed by a tempering treatment to relieve the stresses and enhance toughness. The resulting microstructure consists of tempered martensitic laths forming subgrains in a ferrite matrix with a high dislocation density.

However, as with low alloy steels used for thermal reactor pressure vessels, these steels are also susceptible to brittle fracture. Figure 14.28 shows a set of Charpy curves for three F-M steels: modified 9Cr–1Mo, NF616 (12Cr–2W), and HCM12A

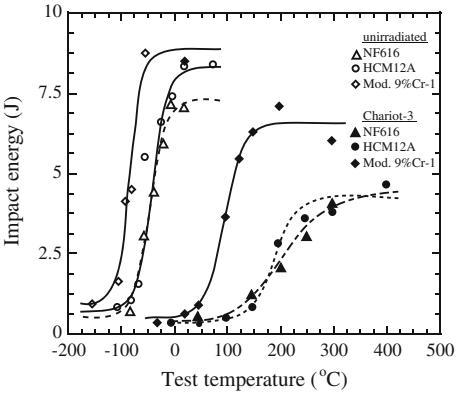

Fig. 14.28 Transition temperature curves for different F-M steels measured using miniaturized Charpy specimens (after [35])

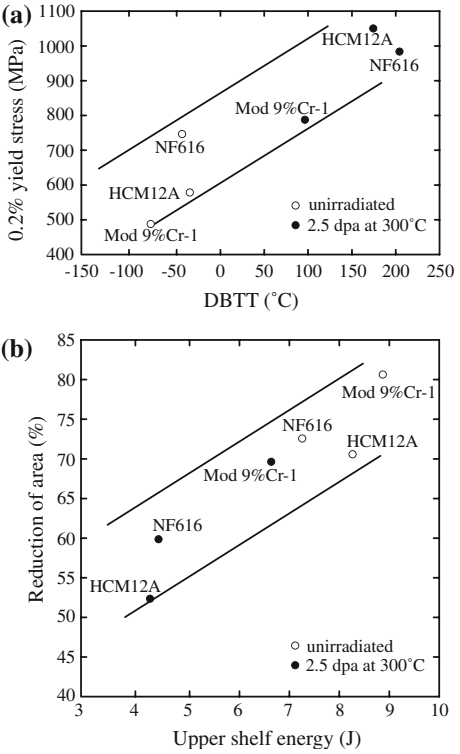

Fig. 14.29 Relationship between (**a**) yield strength and DBTT and (**b**) reduction in area and upper shelf energy (after [35])

(12Cr–2W–1Cu) before and after irradiation in the high flux reactor in Petten (Netherlands) to 2.5 dpa at 300 °C. Note that all three alloys show substantial transition temperature shifts. The shift for the modified 9Cr–1Mo steel was 175 °C, compared to 225 °C for HCM12A and 249 °C for NF616. All steels exhibited reductions in the upper shelf energy of between 2.2 and 4.0 J. As with the low alloy steels, the yield strength can be correlated with DBTT as shown in Fig. 14.29(a). However, the drop in upper shelf energy can also be correlated with the reduction in area as shown in Fig. 14.29(b).

14.7.6 Annealing and Re-Irradiation

One way of reversing the embrittling effects of irradiation is to thermally anneal out the defects to restore the toughness properties that were degraded by neutron irradiation. However, the success of annealing depends on the rate of embrittlement upon re-irradiation of the steel. Annealing of irradiated pressure vessel steels at temperatures near 450 °C for 70–150 h will provide nearly complete recovery of the transition temperature, even after irradiation to very high fluences ($>1\times10^{20}$ n/cm^2) [30].

Annealing under these conditions produces a significant drop in the density and volume fraction of copper-rich precipitates. The annealing treatment also coarsens the remaining precipitates and results in an overall reduction of Cu in solution [31]. The lower amount of Cu in solution makes the annealed alloy less susceptible to embrittlement and it exhibits a lower re-embrittlement rate than in the unirradiated condition. Figure 14.30(a)–(c) show the effect of annealing and re-irradiation on the

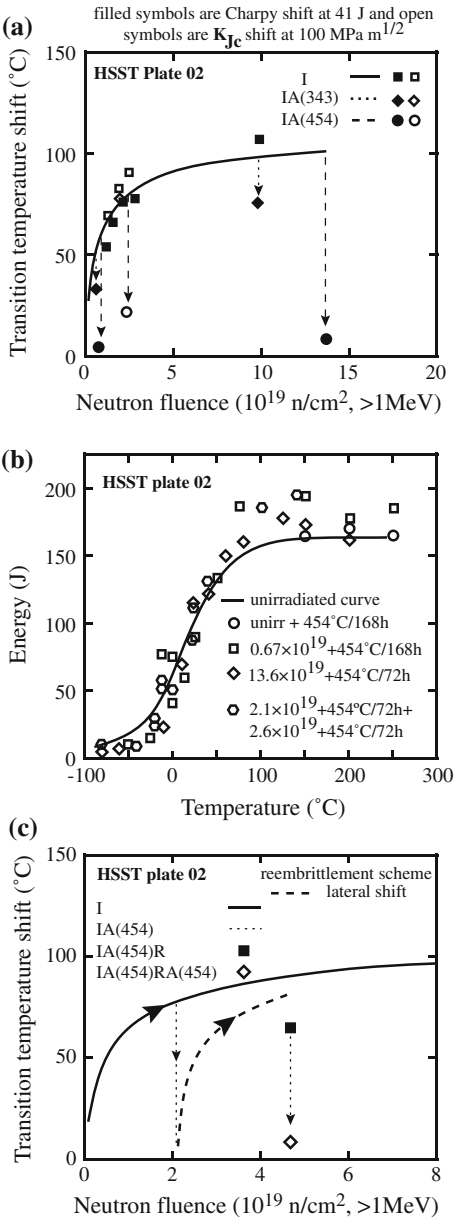

Fig. 14.30 Effect of irradiation and annealing in an A533B steel plate on (**a**) transition temperature shift, (**b**) Charpy curve, and (**c**) transition temperature shift following re-irradiation (after [31])

embrittlement of an A533B, class 1 plate. Figure 14.30(a) shows the increase in ΔT_{41} with fluence. Annealing at 454 °C for times between 72 and 168 h (Fig. 14.30(b)) results in Charpy curves that are indistinguishable from that of the unirradiated curve. Re-irradiation to 4.7×10^{19} n/cm^2 of a sample initially irradiated to 2×10^{19} n/cm^2 and then annealed at 454 °C for 72 h produced less hardening that the original irradiation. The measured transition temperature shift is shown in Fig. 14.30(c) by the solid symbol, which is well below the re-embrittlement *lateral shift* (dotted line) predicted by NRC Regulatory Guide 1.162.

14.7.7 Fatigue

Basic structural changes occur in a metal when it is subjected to cyclic stress. These changes divide the fatigue process into stages:

1. *Crack initiation* is the early development of fatigue damage that can be removed by suitable thermal annealing.
2. *Slip band crack growth* involves the deepening of the initial crack on planes of high shear stress, frequently referred to as *stage* I *crack growth*.
3. *Crack growth on planes of high tensile stress* involves growth of a well-defined crack in a direction normal to the maximum tensile stress, called *stage* II *crack growth*.
4. *Ultimate ductile failure* occurs when the crack reaches sufficient length that the remaining cross section cannot support the applied load, *stage* III.

Fatigue life is measured by the S-N curve in which the number of cycles to failure is plotted versus the stress (maximum or average). S-N curves generally apply to fatigue failure at a high number of cycles ($N > 10^5$) and at these lives, the stress is generally elastic, though plastic deformation occurs on a microscale. At higher stresses, deformation is characterized by gross plasticity and strain-controlled, low cycle fatigue tests are most appropriate for assessing fatigue life in this regime. While the stress amplitude is fixed in a high cycle fatigue test, the stress intensity factor will increase as the crack length increases with the number of cycles, as prescribed by Eq. (14.27). The increase in crack length is therefore related to the change in ΔK by:

$$\Delta K = K_{\max} - K_{\min} = (\sigma_{\max} - \sigma_{\min})\sqrt{\pi c}. \tag{14.67}$$

The fatigue crack growth process is divided into stages that depend on the magnitude of ΔK. The rate of crack propagation in fatigue is denoted as $\mathrm{d}a/\mathrm{d}N$ and varies with ΔK in an inert environment as shown in Fig. 14.31(a). The stage I crack propagates initially along the persistent slip bands. In polycrystalline metal, the crack may extend for only a few grain diameters before the crack propagation changes to stage II. The rate of crack propagation in stage I is generally very low,

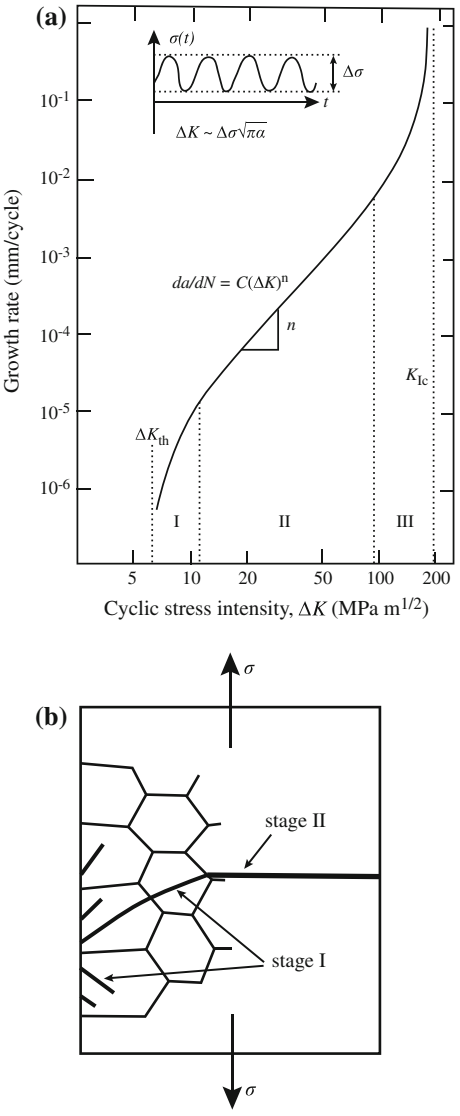

Fig. 14.31 (**a**) Schematic illustration of fatigue crack growth behavior in an inert environment as a function of the stress intensity factor range, ΔK, and (**b**) schematic representation of stages I and II in fatigue crack propagation in a metal (after [36])

on the order of nanometers per cycle. The fracture surface of stage I fracture is highly faceted. Figure 14.31(b) shows a schematic illustration of stages I and II during fatigue crack propagation in metals.

Stage II crack propagation occurs by a plastic blunting process [37] that is illustrated in Fig. 14.32. At the start of the loading cycle the crack tip is sharp (Fig. 14.32(a)). As the tensile load is applied the small double notch at the crack tip concentrates the slip along planes at 45° to the plane of the crack (Fig. 14.32(b)).

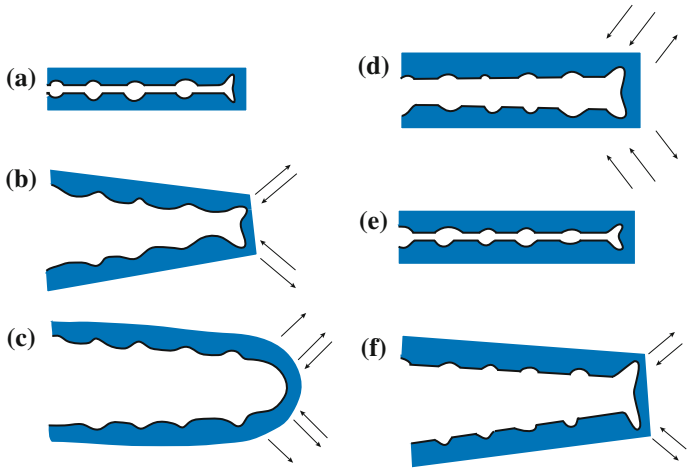

Fig. 14.32 Plastic blunting process for growth of stage II fatigue cracks (after [37])

As the crack widens to its maximum extension (Fig. 14.32(c)) it grows longer by plastic shearing and at the same time its tip becomes blunter. When the load is changed to compression the slip direction in the end zones is reversed (Fig. 14.32(d)). The crack faces are pressed together and the new crack surface created in tension is forced into the plane of the crack (Fig. 14.32(e)) where it partly folds by buckling to form a re-sharpened crack tip. The re-sharpened crack is then ready to advance and be blunted in the next stress cycle (Fig. 14.32(f)).

Considerable research has gone into determining the laws of fatigue crack propagation for stage II growth. In general, the aim in fatigue crack growth rate testing is to maintain a predominantly elastic condition in the test specimen, thereby allowing results to be interpreted in terms of the crack tip stress intensity defined by linear elastic fracture mechanics. The crack propagation rate in stage II is described by the *Paris equation*:

$$\frac{\mathrm{d}a}{\mathrm{d}N} = C(\Delta K)^n \tag{14.68}$$

where $\mathrm{d}a/\mathrm{d}N$ is the incremental increase in the crack length per cycle, C and n are constants and ΔK is the stress intensity factor range given in Eq. (14.67). (Note that it is common to represent the crack growth per cycle as $\mathrm{d}a/\mathrm{d}N$ and the crack growth rate as $\mathrm{d}a/\mathrm{d}t$, where a is the crack length). In addition to the specification of ΔK, the ratio of $K_{\max}$ to $K_{\min}$ is an important parameter describing the mean stress during cyclic loading and is designated as the R ratio, such that $\Delta K = K_{\max}\,(1 - R)$. Note that stage III fatigue crack growth is limited by the static fracture toughness, K_{Ic}. The initiation of fatigue crack growth is defined by the threshold value of the stress

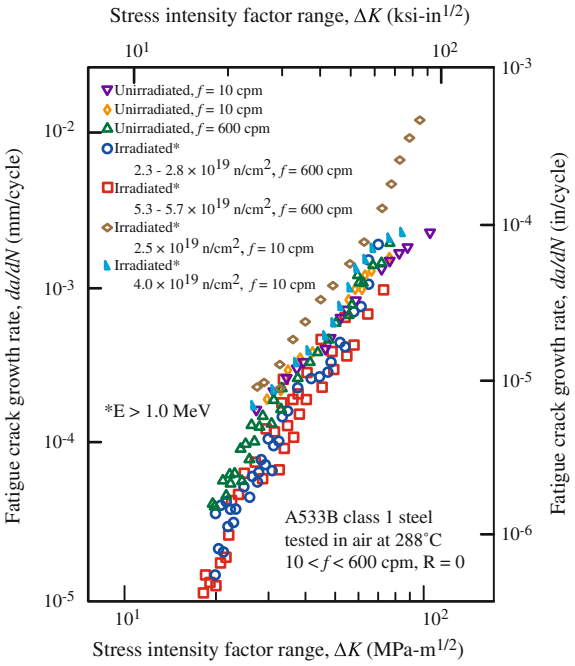

Fig. 14.33 Fatigue crack growth behavior of irradiated and unirradiated A533-B class 1 steel tested in air at 288 °C (after [38])

intensity increment, ΔK_{th}, below which a fatigue crack cannot propagate. Fracture toughness behavior is closely related to the concepts of fatigue crack growth, since the fracture toughness provides the "end-of-life" criteria for terminating fatigue crack growth. One of the more profound changes induced by neutron irradiation is the decrease in fracture toughness. Hence, the effect of neutron irradiation on the fatigue crack growth of pressure vessel steels is of considerable importance.

Considerable progress has been made in using LEFM techniques to characterize the effect of neutron irradiation on the fatigue crack propagation behavior of reactor pressure vessel steels. The general observation is that neutron irradiation, in most cases, does not have a significant detrimental effect on the fatigue crack growth behavior of pressure vessel steels in an air environment (Fig. 14.33). In pressurized water environments, irradiation has not been found to increase the growth rates beyond those, which are due to the environment itself (Fig. 14.34).

Thus, after considerable testing, there is no detectable effect of irradiation on the fatigue crack growth rate of pressure vessel steels. However, a wider range of external variables, such as waveform, temperatures, load ratios, and especially the environment, may well combine to synergistically worsen the situation. The role of the environment in crack growth will be discussed in Chap. 16.

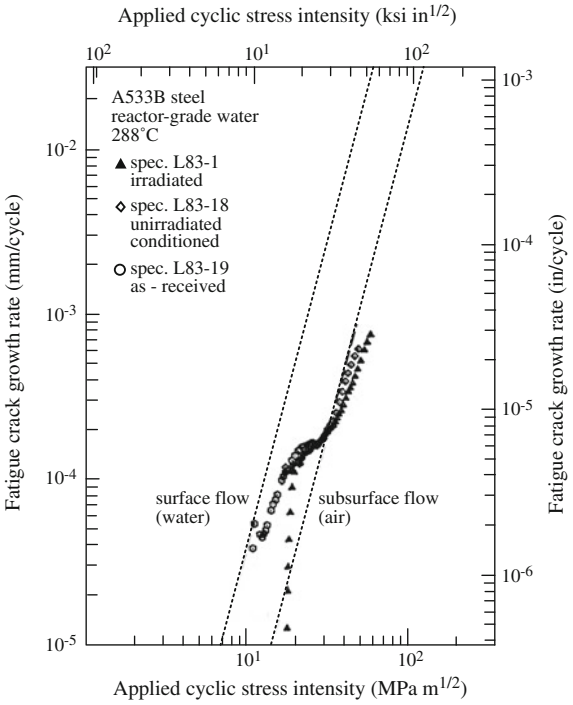

Fig. 14.34 Fatigue crack growth rates for unirradiated and irradiated A533-B steel in high temperature, pressurized reactor grade water (after [39])

14.8 Fracture and Fatigue of Austenitic Alloys at Low to Intermediate Temperatures

Austenitic stainless steels are used in numerous core structures in light water reactors that operate in the low to intermediate temperature range (<400 °C). As shown in Chap. 12, in this temperature range significant increases in yield strength occur (up to a factor of 5) that are accompanied by a drastic loss of ductility (from ~30 to <1 %). The implication of these mechanical property changes on fracture and fatigue are discussed next.

14.8.1 Effect of Irradiation on Fracture Toughness

The fracture toughness of irradiated stainless steels in the intermediate temperature range decreases sharply with irradiation dose [40]. Figure 14.35(a) shows the fracture toughness as a function crack extension for 304 stainless steel irradiated to various neutron doses at 288 °C, where J_{Ic} is given by Eq. (14.44). Figure 14.35(b) shows the drop in J_{Ic} as a function of neutron exposure up to 25 dpa in austenitic stainless steels irradiated in LWRs and tested in the temperature range 250–320 °C. In fact, the value

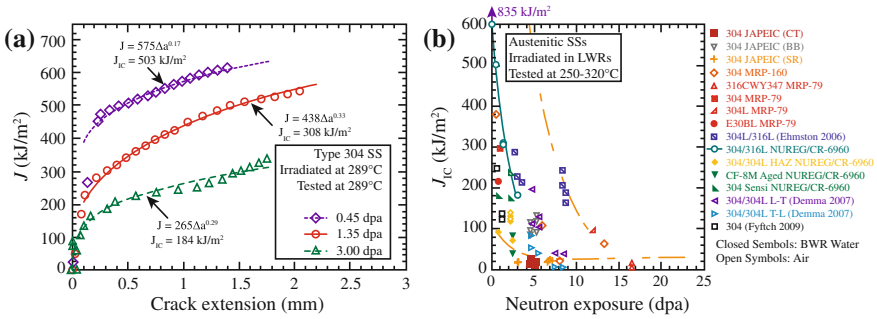

Fig. 14.35 (**a**) Fracture toughness versus crack extension of 304 SS for various doses irradiated and tested at 289 °C, and (**b**) fracture toughness as a function of neutron dose for austenitic stainless steels irradiated in LWRs (after [41])

of J_{Ic} drops from values between 600 and 835 kJ/m^2 in the unirradiated condition to values as low as 20 kJ/m^2 at ~5 dpa [41]. In elastic-plastic fracture, the resistance to crack growth is also described by the tearing modulus, T_m defined as:

$$T_m = \frac{dJ}{da}\frac{E}{\sigma_0^2}, \tag{14.69}$$

where dJ/da is the slope of the resistance curve of J versus increase in crack length, a and σ_0 is the flow stress which is approximated by the average of the yield and ultimate strengths. The tearing modulus also decreases significantly as a result of neutron irradiation in this temperature range.

Odette and Lucas [42] used a scaling relationship to describe the dependence of fracture toughness on irradiation:

$$\frac{K_{Ic}^{irr}}{K_{Ic}^{unirr}} = \sqrt{\frac{e_u^{irr}}{e_u^{unirr}}\frac{\sigma_0^{irr}}{\sigma_0^{unirr}}}, \tag{14.70}$$

where e_u is the uniform engineering strain. While this equation has been fit to fracture toughness data for several austenitic stainless steels, it does not provide a physical basis for the reduction in toughness. Instead, it has been proposed that the loss of fracture toughness with irradiation is due to a change in fracture mode.

In the unirradiated condition, ductile metals such as stainless steels fracture by ductile-dimple rupture in which voids nucleate and grow in the plastic region ahead of the crack tip until they eventually linkup with the crack tip by necking of the remaining ligament (Fig. 14.36(a)) [43]. At low dose, irradiation may accelerate void linkage by work softening and localized deformation. Coalescence can occur by diffuse necking (DN) when the microvoid height is approximately equal to the distance from its edge to the blunted crack tip. Coalescence may also occur at lower strain by localized necking (LN) between the void and the crack tip. In either case, the fracture toughness can be related to deformation parameters by:

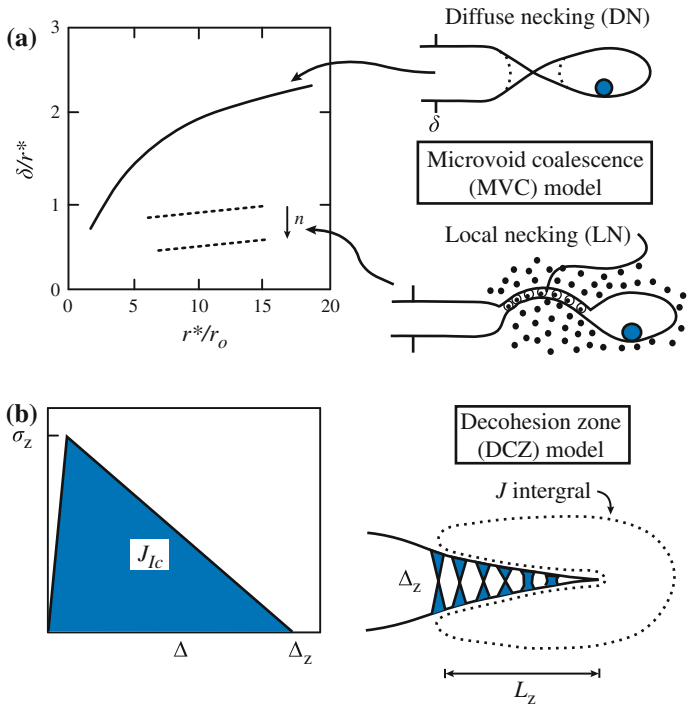

Fig. 14.36 Models of ductile fracture. (**a**) Microvoid coalescence model: ratio of crack opening, δ to distance to next void at point of crack linkage, r^* versus the latter quantity normalized by the initial inclusion radius, r_0. (**b**) Decohesion zone model: crack growth by the failure of plastic ligaments bridging the faces of a virtual crack (after [43])

$$K_{\mathrm{Jc}} = \sqrt{1.5\beta r^* \sigma_0 E'}, \tag{14.71}$$

where β is the ratio of crack opening to the distance to the next void at the point of crack-void linkage ($\beta = \delta/r^*$), and $E' = E/(1 - \nu^2)$. The value of β decreases as deformation becomes increasingly localized. At high doses, crack advance is more likely controlled by heterogeneous deformation in the zone ahead of the crack due to intense dislocation channeling in the solid. In this case, fracture occurs by a decohesion process in which deformation is concentrated into a series of plastic ligaments behind the crack tip (Fig. 14.36(b)) and extending over a process zone of length, L_z. Crack growth occurs when the displacement capacity of the last ligament, Δ_z is reached under a local stress σ_z:

$$K_{\mathrm{Jc}} = \sqrt{0.5\Delta_z \sigma_z E'}. \tag{14.72}$$

While these models are consistent with the role of the increased localization of plastic flow with irradiation dose, confirming experiments have yet to be conducted.

In addition to altering the ductile fracture process, irradiation may also result in a change in fracture mode from ductile-dimple rupture to cleavage. It is well-known that plasticity can induce martensite formation in austenitic stainless steels that may fracture by a quasi-cleavage mechanism. However, such processes are unlikely when deformation occurs at temperatures >300 °C.

14.8.2 Effect of Irradiation on Fatigue

Due to the reduced uniform strain and increasing localization of plastic deformation resulting from irradiation, it may be expected that fatigue crack growth should respond accordingly. In particular, in stage III fatigue crack growth, where the growth rate is limited by the fracture toughness, Fig. 14.31(a), reduction in fracture toughness due to irradiation will result in an increase in crack growth rate. In stage I, the threshold stress intensity range ΔK_{th} is sensitive to the chemical environment, the R ratio, grain boundary impurity segregation and to the tendency for high strength materials to undergo flow localization. This latter sensitivity is supported by empirical data that show that ΔK_{th} decreases with increasing yield strength in unirradiated 316 SS [44]. Consequently, the severe localization of plasticity caused by irradiation may be expected to lead to decreases in the threshold stress intensity.

However, the data on the effect of irradiation on fatigue in austenitic stainless steels in the low to intermediate temperature range is mostly in stage II that is described by the Paris equation. In this regime, crack propagation is primarily dependent on the elastic properties of the solid, and less so on the microstructure and on plastic deformation processes. Limited data shows that the crack growth rate is, in fact, relatively insensitive to irradiation to doses of up to about 30 dpa. Figure 14.37 shows that the crack growth rate of 316 stainless steel irradiated to 2.03×10^{21} n/cm^2 at 380 °C is bounded on the high side by crack growth in mill-annealed plate and on the low side by 20 % cold-worked plate, both in the unirradiated condition. For types 304 and 316 SS irradiated at 405–410 °C up to 6.0 dpa, the CGRs are up to a factor of two higher than those for non-irradiated material [41]. As such, irradiation of austenitic stainless steels to low or intermediate doses does not result in significant increases in fatigue crack growth. However, with increasing temperature, the generation and accumulation of helium into bubbles can affect the fatigue crack propagation, as will be discussed in the next section.

Nevertheless, it may be expected that under irradiation, low cycle fatigue life should decrease due to decreased ductility, and high cycle fatigue life should increase due to increased strength. This behavior was indeed measured for 304 stainless steel at both room temperature and 325°C following irradiation to 8×10^{22}n/cm^2 ($E > 0.1$ MeV) at a temperature of 400 °C [46]. The beneficial effect of irradiation in HCF is likely due to the fact that despite significant hardening, and a reduction in work hardening coefficient by a factor of 2.7, the alloy retained ductility to 4–5 % elongation.

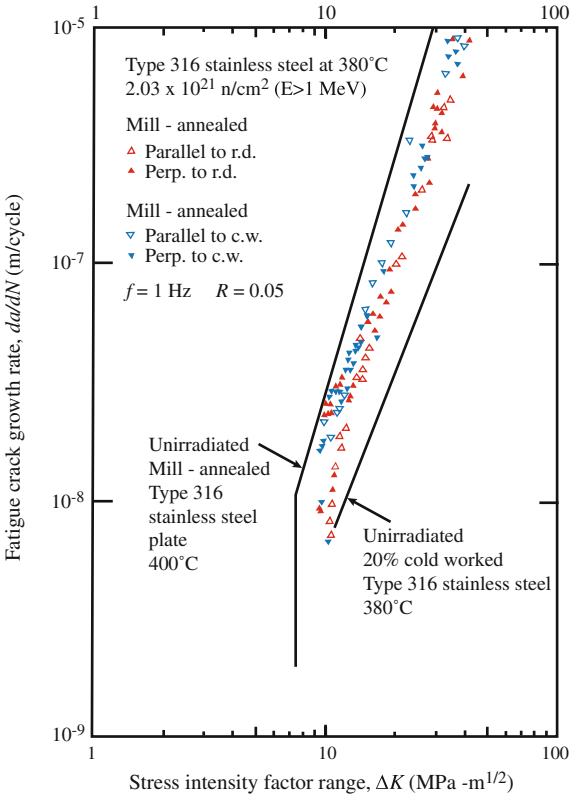

Fig. 14.37 Effect of irradiation to 2.03×10^{21} n/cm^2 ($E > 1$ MeV) at 380 °C on fatigue crack propagation rate in mill-annealed and 20 % cold-worked type 316 SS (after [45])

14.9 High-Temperature Embrittlement

Nuclear systems that operate in the high-temperature regime include fast reactors, advanced fission reactors, fusion reactors, and systems for accelerator-based transmutation of wastes. Among these systems, three alloy classes, austenitic stainless steels, ferritic-martensitic steels and vanadium alloys, are among the primary candidate alloys for core components. These alloys are selected based on their high-temperature strength. However, degradation mechanisms unique to the high-temperature regime can limit their usefulness.

The nature of fracture at high temperatures is quite different from the mode of fracture exhibited by metals and alloys at low temperatures. At low temperatures fracture tends to result from shearing through grains of the metal (i.e., transgranular fracture) and often occurs only after appreciable deformation. The fracture mode that terminates the third stage of high-temperature creep or the deformation in a high-temperature tensile test is usually of the intergranular type. As the temperature increases (above 0.3 T/T_m), the grain boundary loses strength relative to the matrix.

At these temperatures, grain boundary sliding is prevalent and intergranular fracture can occur by Zener wedge cracking at grain boundary junctures (higher stresses and lower temperatures), by the fracture of continuous, brittle boundary phases, by grain boundary void formation (lower stresses and higher temperatures), or by helium embrittlement via grain boundary bubbles.

The effect of irradiation on the high-temperature embrittlement of alloys is measured in a creep rupture test. Creep rupture refers to the failure of a specimen that has been subject to stresses well below the yield stress for long periods of time. Deformation occurs by creep (Chap. 13) rather than by rapid plastic deformation characteristic of a tensile test. In a creep rupture test, the time to failure, or the *rupture life*, t_f, and the *elongation at failure*, ε_f, are measured. Provided that steady state creep prevails for the major portion of the test, these two quantities are related by:

$$t_f = \frac{\varepsilon_f}{\dot{\varepsilon}} \tag{14.73}$$

were $\dot{\varepsilon}$ is the steady state creep rate. The creep rupture properties depend on the extent of irradiation, the irradiation and testing temperatures and on the degree of cold-work of the specimens. These variables directly control the creep rate and the elongation at fracture ε_f. The rupture life, t_f, is indirectly affected by the same variables because it is the ratio of ε_f to $\dot{\varepsilon}$. Fig. 14.38 shows the effect of fast neutron fluence on the creep rupture properties of an austenitic stainless steel. The data indicate that both the creep rate $\dot{\varepsilon}$ and the elongation to fracture ε_f are reduced in the irradiated specimens. Those processes which affect the former were discussed in Chap. 13 (Irradiation Creep), while the mechanisms that reduce the elongation to fracture ε_f, i.e., grain boundary voids, grain boundary sliding and helium embrittlement, are the subject of this section.

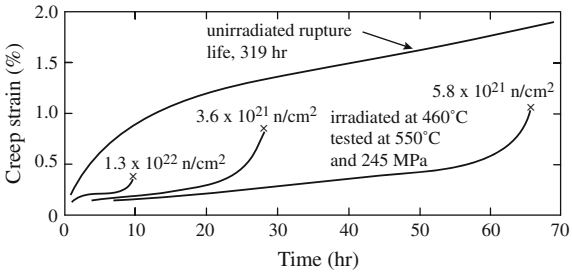

Fig. 14.38 Effect of irradiation on the creep rupture of annealed 304 stainless steel irradiated at 370–460 °C and tested at 550 °C and 241 MPa (after [47])

14.9.1 Grain Boundary Voids and Bubbles

At high temperature, diffusion is rapid and the application of a stress can result in the nucleation and growth of voids on grain boundaries that are aligned perpendicular to the applied stress. Void nucleation and growth are aided by creep that is important at temperatures above about 0.3 T_m. Stresses well below those required for the formation of wedge cracks can lead to formation and growth of grain boundary voids. Once formed, the voids grow by rapid diffusion along grain boundaries until the remaining cross sectional area is too low to support the load and fracture occurs either by linkage of bubbles, or more likely, crack propagation through the grain boundary void array. If helium is present, it can accelerate void growth through the effect of pressure on the void surfaces, resulting in a reduction in the time to failure.

In analyzing embrittlement due to void or bubble growth on the grain boundaries, we will first consider purely diffusive growth of the voids. However, the presence of a tensile stress at high temperature will produce creep, which can couple with diffusion to accelerate growth of the voids. In the limit, void growth is controlled by the overall creep rate. Finally, we will consider grain boundary cavity growth by grain boundary sliding, a process that becomes more favorable at higher temperatures where grain boundary strength drops.

14.9.1.1 Diffuse Growth of Voids and Bubbles

Diffusive growth of voids on grain boundaries was first analyzed by Hull and Rimmer [48] and was based on the assumptions that:

- Diffusion through the cavity surface is sufficiently fast for the cavity to remain spherical in shape.
- Grain boundary diffusion dominates volume diffusion.
- The grains themselves are rigid and their movement in the direction normal to the boundary is not constrained.
- Vacancies are supplied by the grain boundary and the void is in equilibrium with the applied stress; $\sigma = 2\gamma/R$.

Voids are assumed to be arranged on a square grid in the grain boundary plane where the spacing between the neighboring voids is $2b$. The grain boundary is considered to have a thickness designated as δ_{gb}, and vacancies created in the annulus around the grain boundary diffuse to and are absorbed by the void causing it to grow. From the preceding assumptions, the vacancy concentration at the void surface is given, with $p = 0$, by;

$$C_v(R) = C_v^0 \exp\left(\frac{2\gamma}{R}\frac{\Omega}{kT}\right). \tag{14.74}$$

The flux of vacancies to the void is:

$$J_{\text{gb}} = \frac{D_{\text{gb}} \nabla \mu}{kT\Omega}, \tag{14.75}$$

where $\nabla\mu$ is the gradient of the chemical potential and D_{gb} is the grain boundary diffusion coefficient. For a void of radius R, the chemical potential is $\mu = \sigma\Omega$ and the gradient is:

$$\nabla \mu = \frac{\Omega}{b}\left(\sigma - \frac{2\gamma}{R}\right), \tag{14.76}$$

and the vacancy flux to the void is:

$$J_{\text{gb}} = \frac{D_{\text{gb}}}{kTb}\left(\sigma - \frac{2\gamma}{R}\right). \tag{14.77}$$

Assuming the void remains spherical, the time rate of change of the void volume is:

$$\begin{aligned} \frac{\mathrm{d}V}{\mathrm{d}t} &= \left(2\pi R \delta_{\text{gb}}\right) J_{\text{gb}} \Omega \\ &= \frac{2\pi D_{\text{gb}} \delta_{\text{gb}} \Omega R}{kTb}\left(\sigma - \frac{2\gamma}{R}\right), \end{aligned} \tag{14.78}$$

and the rate of growth of the void size is:

$$\frac{\mathrm{d}R}{\mathrm{d}t} = \dot{R} = \frac{D_{\text{gb}} \delta_{\text{gb}} \Omega}{kTRb}\left(\sigma - \frac{2\gamma}{R}\right). \tag{14.79}$$

This diffusive cavity growth model assumes that diffusion at the cavity surface is much faster than along the grain boundary, allowing the void to maintain its spherical shape. However, if this is not true, then the void will assume a *lens* shape and growth depends more strongly on the stress. It can be shown [49] that for low stresses:

$$\dot{R} = \frac{D_{\text{s}} \delta_{\text{s}} \Omega \sigma^3}{2kT\gamma^2}, \text{ for } 3.5\frac{\sigma b}{\gamma} X \ll 1, \tag{14.80}$$

and

$$\dot{R} = \frac{\left(D_{\text{gb}} \delta_{\text{gb}}\right)^{3/2}}{2\left(D_{\text{s}} \delta_{\text{s}}\right)^{1/2}} \frac{\Omega \sigma^{3/2}}{kTb^{3/2}\gamma^{1/2}}, \text{ for } 3.5\frac{\sigma b}{\gamma} X \gg 1, \tag{14.81}$$

where $X = D_s\delta_s/D_{gb}\delta_{gb}$, D_s is the surface diffusion coefficient and δ_s is the surface thickness, or the depth over which surface diffusion occurs.

If helium accumulates in the voids, then it can assist in void growth by virtue of the internal pressure. In this case, Eq. (14.74) is modified to account for the pressure in the void:

$$C_v(R) = C_v^0 \exp\frac{\Omega}{kT}\left[\left(\frac{2\gamma}{R} - p\right)\right], \tag{14.82}$$

and the growth law for helium filled bubbles becomes:

$$\dot{R} = \frac{D_{gb}\delta_{gb}\Omega}{kTRb}\left(\sigma - \frac{2\gamma}{R} + p\right). \tag{14.83}$$

14.9.1.2 Power-Law Creep-Controlled Void Growth

Cadek [50] reviewed the role of creep in grain boundary void growth and that treatment will be summarized here. Void growth on an isolated grain boundary can only occur if the displacements of the grain in response to cavity growth are accommodated by creep flow in the surrounding grain. In the temperature range of interest for materials in nuclear systems, dislocation creep is the dominant creep mode as discussed in Chap. 13. Nevertheless, if void growth is occurring faster than can be accommodated by the creep rate, load is shed by the voids to the surroundings until the stress on the cavities is reduced to a value that is compatible with the flow of the solid by creep. The net effect is a reduction in the void growth rate such that the void growth rate is controlled by the creep rate. In this case [46], constrained cavity growth occurs according to the following rate:

$$\dot{R} = \frac{1}{2.5}\left(\frac{b}{R}\right)^2 d_f\dot{\varepsilon}, \tag{14.84}$$

where $\dot{\varepsilon}$ is the creep rate and d_f is the grain facet diameter. Compared to the linear stress dependence for diffusional growth of cavities, power-law creep constrained growth is proportional to σ^n through the power-law creep relation: $\dot{\varepsilon} = A(\sigma/B)^n$, giving:

$$\dot{R} = \frac{A}{2.5}\left(\frac{b}{R}\right)^2\left(\frac{\sigma}{B}\right)^n d_f, \tag{14.85}$$

where n is typically between 2 and 3.

14.9.1.3 Coupled Diffusion and Power-Law Creep

Intermediate to purely diffusive and power-law constrained cavity growth is coupled diffusive and power-law creep-driven growth. In this mode, diffusive cavity growth can be affected by power-law creep of the surrounding matrix such that the diffusion distance in the boundary is reduced and growth is accelerated. In this regime, the volumetric cavity growth rate is:

$$\dot{V} = 2\pi R^3 A \left(\frac{\sigma b^2}{B(b^2 - R^2)} \right)^n, \tag{14.86}$$

and the growth law becomes:

$$\dot{R} = \frac{RA}{2} \left(\frac{\sigma b^2}{B(b^2 - R^2)} \right)^n. \tag{14.87}$$

From the power-law creep relation, Eq. (14.87) can be written in terms of the creep rate, $\dot{\varepsilon}$ as:

$$\dot{R} = \frac{R}{2} \dot{\varepsilon} \left(\frac{b^2}{b^2 - R^2} \right)^n. \tag{14.88}$$

Equations (14.87) and (14.88) apply at high stresses where creep deformation dominates. At low stresses, the rate of growth is controlled by diffusion and the void growth rate is described by Eqs. (14.84) and (14.85).

14.9.1.4 Failure Strain and Time to Rupture

The time to failure is obtained by integration of the growth law from $R = R_0$, the initial void size to $R = R_f$, where R_f is the void size at failure:

$$t_f = \int_{R_0}^{R_f} \frac{dR}{\dot{R}}. \tag{14.89}$$

Alternatively, Eq. (14.89) can be written in terms of the area fraction of cavities as:

$$t_f = \int_{f_0}^{f_f} \frac{df}{f}, \tag{14.90}$$

where $f = R^2/b^2$ is the area fraction of cavities assuming a one-dimensional representation of voids on the boundary. Using a square lattice geometry, the fractional area occupied by the voids at the point where the voids touch is shown in Fig. 14.39. When voids touch, the separation distance, $b = 2R$, and the fraction of the grain boundary covered by the voids is given by the shaded area. The cross sectional area of the voids on the grain boundary is $4 \times (\pi R^2/4)$, and the grain boundary area is $b^2 = (2R)^2$, so the ratio is $f = \pi R^2/(2R)^2 = \pi/4$. However, rupture will occur sooner as the remaining cross sectional area cannot support the increasing stress. The fracture criterion $f_f = 0.25$ is typically adopted [51]. The strain at failure is determined as follows. For a void of volume $4/3\pi R^3$ at a grain boundary of area $\pi b^2 - \pi R^2$, the relative displacement of the grains is $u = \dfrac{4/3\pi R^3}{\pi b^2}$, and the strain at failure is u/d, where d is the mean grain diameter, giving:

$$\varepsilon_f = 4/3 f_f^{3/2} \frac{b}{d}, \tag{14.91}$$

and applying the fracture criterion $f_f = 0.25$ gives:

$$\varepsilon_f \cong 0.17 \frac{b}{d}. \tag{14.92}$$

Similar to the concept of capture volume or unit cell for voids distributed through the volume of the solid (Eq. 5.68), the capture volume for N_{gb} voids on grain boundaries is:

$$\pi b^2 N_{gb} = 1, \tag{14.93}$$

where the capture radius = b. Substituting for b from Eq. (14.93) and $f = \pi/4$ into the expression for fracture strain given in Eq. (14.91) yields:

$$\varepsilon_f = \frac{\pi}{6 d N_{gb}^{1/2}}. \tag{14.94}$$

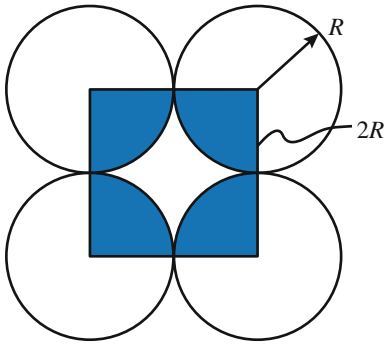

Fig. 14.39 Illustration of grain boundary voids at the point in time where the void surfaces touch

Assuming voids lie on the faces of cube-shaped grains with sides of length d, there are $Nd^3/6d^2 = Nd/6$ voids per unit grain boundary area. Since each void is shared by two grain boundaries, $N_{gb} = Nd/3$. Substituting for N_{gb} into Eq. (14.94) gives:

$$\varepsilon_f = \left(\frac{\pi^2}{12Nd^3}\right)^{1/2}. \tag{14.95}$$

Cocks and Ashby [47] have determined expressions for the failure time for each of the growth mechanisms described in this section. For purely diffusional void growth, the failure time is:

$$t_f \cong t_n + \frac{0.17}{\phi_0 A}\left(\frac{B}{\sigma}\right), \tag{14.96}$$

$$\text{where } \phi_0 = \frac{2D_{gb}\delta_{gb}\Omega}{kTb^3}\frac{B}{A}, \tag{14.97}$$

and t_n is the void nucleation time. For the power-law creep regime or due to coupled grain boundary diffusion and power-law creep, the failure strain is given by the strain due to creep in the specimen as a whole plus that due specifically to the voids [47]:

$$\varepsilon_f = t_f\dot{\varepsilon} + 0.17\frac{b}{d}, \text{ and} \tag{14.98}$$

$$t_f = t_n + \frac{1}{n\dot{\varepsilon}}. \tag{14.99}$$

14.9.2 Grain Boundary Sliding

As the temperature of a metal is increased, fracture under applied stress changes from transgranular to intergranular. Figure 14.40 shows the relationship between strength of the grain matrix and grain boundaries as a function of temperature and strain rate. The intersection between the strength of the grains and that of the grain boundaries is termed the *equicohesive temperature* (ECT) denoting the temperature at which they have equal strength. Above the ECT, grain boundary facture is more likely, while below it, transgranular fracture is preferred. Also shown in Fig. 14.40 is the role of strain rate on the ECT. Decreasing strain rate moves the ECT to lower temperatures, reflecting the increasing importance of grain boundary processes in determining the fracture strength of the metal.

At temperatures in the creep regime, low stresses or strain rates cause fracture to be dominated by wedge cracks leading to fracture across the grain facet and possibly interaction and linkage to final fracture. At still lower stresses, intergranular

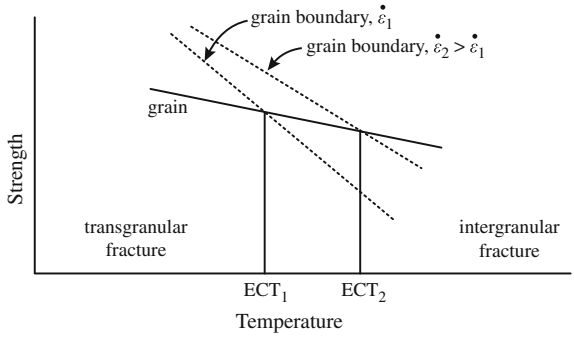

Fig. 14.40 Equicohesive temperature delineating transgranular fracture from intergranular fracture as a function of temperature, and the role of strain rate on the ECT

creep fracture is dominated by the formation, growth and coalescence of grain boundary cavities, as discussed in the previous section. The low to intermediate stress regime is where grain boundary sliding (GBS) can lead to cracking and fracture. Under these conditions, grains are able to slide along grain boundaries resulting in the formation of voids or cracks at triple points as shown in Fig. 14.41. This process is similar to wedge crack formation in brittle fracture discussed in Sect. 14.6, but at high temperature, the source of strain is in the grain boundary rather than in a slip band in the matrix. Grain boundary void formation relieves the

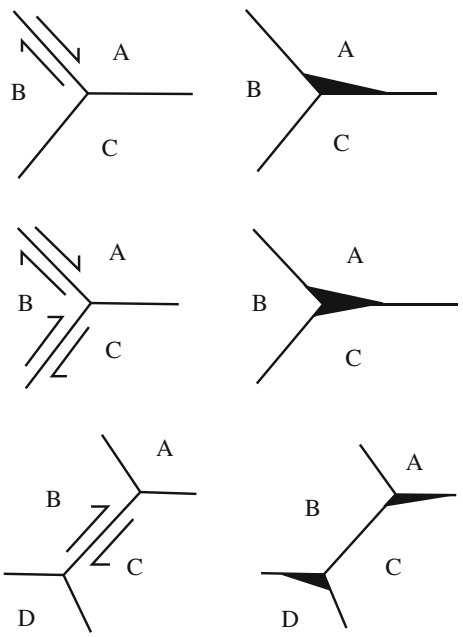

Fig. 14.41 Intergranular cracking due to grain boundary sliding

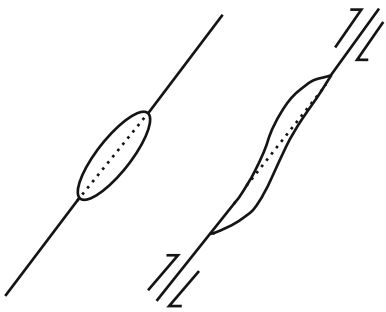

Fig. 14.42 The effect of grain boundary sliding on the shape of the grain boundary cavities

localized high stresses at triple points. In fact, GBS is responsible for both grain boundary void formation and growth.

Grain boundary sliding has its origin in the dislocation creep process. Dislocations generated in a neighboring grain due to power-law creep may be incorporated into a grain boundary by glide. These dislocations can move by a combination of glide and climb along the grain boundary. Sliding is accommodated by the opening up of grain boundary voids and the rate of GBS is proportional to the Burgers vector component parallel to the grain boundary plane and controlled by climb [50]. Since GBS is caused by the glide of the same dislocations that cause grain deformation, there is a linear relationship between the strain due to GBS, ε_{gbs}, and the total creep strain, ε. The strain rate due to GBS was determined by Langdon [52] to be:

$$\dot{\varepsilon}_{\text{gbs}} = AD_{\text{vol}} \frac{b^2\sigma^2}{\mu \text{d}kT}, \tag{14.100}$$

where D_{vol} is the volume diffusion coefficient and d is the mean grain diameter.

Grain boundary sliding can result in crack-like growth of cavities due to distortion and sharpening of the shape of the cavity such that surface diffusion is stimulated. As shown in Fig. 14.42, sliding of the grain boundary produces a more distinct acicular shape to the cavity in which surface diffusion plays a larger role in growth. As such, the rate of cavity growth is linked to the rate of grain boundary sliding. The net effect of GBS is to enhance the transport of matter along the grain boundary, in effect, enhancing the grain boundary diffusion coefficient and accelerating void growth.

14.9.3 Grain Boundary Crack Growth

While link-up of cavities on grain boundary facets results in fracture of the grain boundary, cavity growth and coalescence occur at very different rates due to their non-uniform distribution on grain boundaries. Therefore, local link-up and the formation of a crack that propagates to adjacent grain boundaries is a likely mechanism for intergranular creep crack growth. The cracks propagate by either

diffusion of vacancies to the crack tip and deposition of atoms in the grain boundary facet, plastic flow or plastic flow-enhanced diffusion. In either of these cases, the cracks grow in steps by nucleation and growth of cavities that successively link-up with the crack.

Figure 14.43 shows the propagation of a crack along a cavitated grain boundary. As shown in Sect. 14.3, the stress field ahead of the crack tip of a stressed solid is amplified by the presence of the crack, and this stress will enhance growth of cavities closest to the tip. Figure 14.44(a) shows the stress distributions ahead of grain boundary cracks, cavities and the intermediate case of crack-like cavities leading to subcritical crack growth by cavity growth and coalescence ahead of the crack tip (Fig. 14.44(b)). When helium is present, the growth of cracks and bubbles is driven by gas absorption and the supply of helium becomes a key factor in

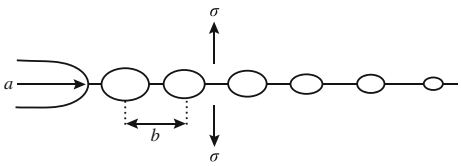

Fig. 14.43 Propagation of a crack by the growth of cavities ahead of the crack tip

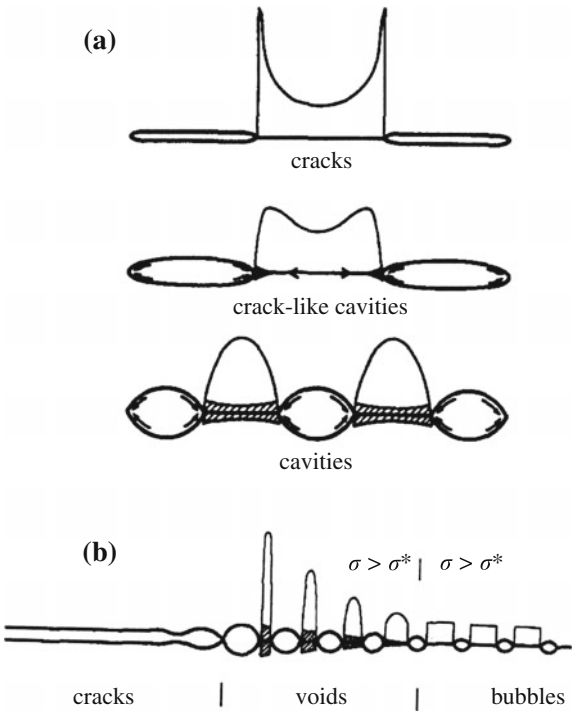

Fig. 14.44 Schematic illustration of (**a**) the stress distribution between cracks, cavities and crack-like cavities, and (**b**) the growth of a crack by unstable void growth and coalescence ahead of the crack tip (after [53])

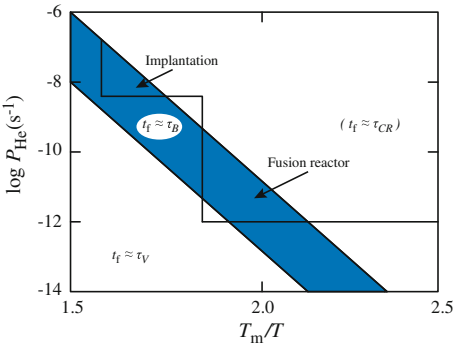

Fig. 14.45 Mechanisms controlling the lifetime, t_f of a sample under stress, gas-driven stable bubble growth, τ_B, stress-driven unstable void growth, τ_V and subcritical crack growth by void coalescence, τ_{CR} (after [53])

limiting their growth. Trinkhaus [53] has shown that subcritical crack growth by void coalescence is favored at high He pressure and low temperatures, while stress-driven void growth dominates at high temperature and low He content, with gas-driven bubble growth becoming important at higher helium contents in the solid (Fig. 14.45).

The mechanisms of high-temperature embrittlement and fracture discussed in the preceding sections apply to unirradiated as well as irradiated solids. So it is appropriate to reiterate the mechanisms by which irradiation can accelerate the embrittlement and fracture processes. First, the nucleation of voids in a solid under stress occurs more easily by virtue of irradiation-induced void growth. As shown earlier, helium produced by transmutation reduces the critical void size for stability and thus enhances void and bubble growth. Both of these processes will accelerate the growth of grain boundary cavities, reducing the time to rupture. At high temperature, where grain boundary strength is reduced relative to the matrix, irradiation hardening can accentuate that difference, favoring fracture along grain boundaries. The occurrence of dislocation channeling results in localized deformation and the efficient transmission of plasticity to the grain boundary that can accelerate grain boundary sliding and contribute to grain boundary void formation and growth. Finally, the incorporation of transmutation helium into grain boundary voids can assist in grain boundary crack growth by link-up of voids. So in summary, while high-temperature grain boundary embrittlement is characteristic of deformation and fracture in unirradiated metals, irradiation during deformation can significantly enhances these processes and shorten the time to failure.

14.9.4 Fracture Mechanism Maps

Similar to deformation mechanism maps described in Chap. 12, Ashby-type maps of fracture mechanisms can be constructed to show the regimes for the different

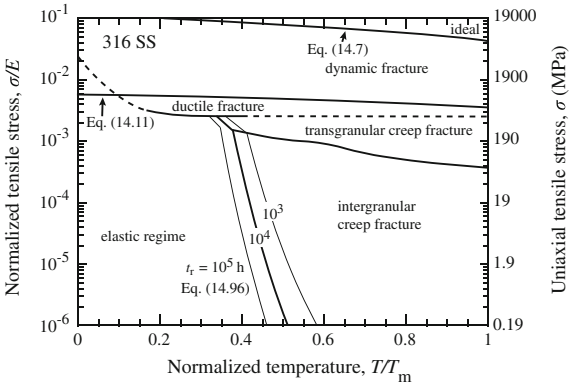

Fig. 14.46 Fracture mechanism map for 316 stainless steel (after [55])

types of fracture as a function of normalized stress and homologous temperature [54]. In these maps, the rupture time is used to determine the boundaries between various fracture mechanisms. Unfortunately, the constitutive equations describing fracture are not as well-established for the various fracture mechanisms. A fracture map for stainless steel constructed by Zinkle [55] is shown in Fig. 14.46. The upper most line describes the ideal fracture strength of the alloy as given by Eq. (14.7). The fracture stress separating the elastic regime from cleavage is given by Eq. (14.11(a), 14.11(b)). The boundary between the elastic regime and the intergranular creep fracture regime is described by Eq. (14.96). The effect of irradiation on the fracture mechanism map is through changes in time to rupture defining the regime boundaries. In fcc metals, the primary effect of irradiation is on the intergranular creep fracture regime due to high-temperature helium embrittlement. In bcc metals, radiation hardening will increase the cleavage regime.

Nomenclature

a	Lattice parameter. Also crack length
B	Compact tension sample thickness
b	Half spacing between voids on a grain boundary
c	Half-crack length
C_v	Energy absorbed in a Charpy V-notch test. Also vacancy concentration
d	Grain size or obstacle diameter or separation distance of partial dislocations
d_f	Grain facet diameter
D	Diffusion coefficient
e_u	Engineering uniform elongation strain
E	Elastic modulus
E_U	Charpy upper shelf energy
f	Fractional change in upper shelf energy. Also area fraction of cavities on grain boundaries

f_f	Fracture criterion for area fraction of grain boundaries
F	Work done by an external force
G	Crack extension force
G_c	Crack extension force corresponding to fracture toughness
J	Value of the J integral, defined in Eq. (14.37)
k	Boltzmann's constant
K	Stress intensity factor
K_c	Fracture toughness
K_{Jc}	Fracture toughness equivalent to J_c
$K_{Jc(med)}$	Median fracture toughness
k_s	Irradiation-induced increase in yield stress
k_y	Unpinning parameter or source hardening contribution to the yield stress
L	Length of dislocation pile-up on a slip plane
M	Taylor factor
n	Number of dislocations in a pile-up
P	Load
r_p	Plastic zone size
RT_{NDT}	Reference nil-ductility temperature
R	Void radius
t	Time
t_f	Creep rupture life
t_n	Void nucleation time
T	Temperature
T^*	Temperature at which flow stress and fracture stress curves intersect
T_m	Tearing modulus
T_0	Reference temperature for Master curve
ΔT_x	Charpy transition temperature shift at a C_V value of x
U_E	Elastic strain energy
U_f	Work to create a surface by fracture
U_S	Decrease in strain energy due to formation of crack surfaces
V	Volume. Also potential energy of the system
W	Work. Also width parameter for the compact tension sample
β	Constant related to the degree of triaxiality of the applied stress Also ratio of crack opening to void spacing, Eq. (14.71)
ε	Strain
ε_f	Fracture strain
$\dot{\varepsilon}$	Creep strain
ϕ	Neutron flux
Φ	Neutron fluence
Δ_z	Displacement of last ligament at a crack tip
δ	Crack opening displacement, COD
δ_t	Crack tip opening displacement, CTOD
γ	Surface energy

γ_e	Effective surface energy
γ_p	Plastic work term
λ	Lattice wavelength spacing
μ	Shear modulus. Also chemical potential
ν	Poisson's ratio
Ω	Atomic volume
σ	Tensile stress
σ_a	Applied stress
σ_f	Fracture stress
σ_i	Friction stress
σ_0	Flow stress
σ_{th}	Theoretical cohesive strength
σ_y	Yield stress
τ	Defect lifetime

Subscripts

c	Critical value of K, G or J for onset of fracture
f	Fracture. Also final condition
gb	Grain boundary
gbs	Grain boundary sliding
I, II, III,	Fracture mode
R	Rupture
S	Surface
u	Uniform, also displacement
v	Vacancy
V	Void
vol	Volume
0	Initial

Superscripts

n	Exponent on stress in the creep equation. Also exponent on ΔK in the crack growth rate equation Eq. (14.68)

Acronyms

COD	Crack opening displacement
CRP	Copper-rich precipitates
DBTT	Ductile-to-brittle transition temperature
ECT	Equicohesive temperature
GBS	Grain boundary sliding
LEFM	Linear elastic fracture mechanics

NDT Nil-ductility temperature
RPV Reactor pressure vessel
USE Upper shelf energy

Problems

14.1 In an AISI 4340 steel, γ_e, the effective surface energy that takes into account the work done in expanding the crack, is about 1.5×10^3 Pa-m. Assuming a grain size of ASTM 8:

(a) Compute the stress to propagate a crack equal in length to an average grain diameter. Take $E = 200$ GPa.
(b) Using the value computed in part (a), calculate the crack length for unstable fracture in AISI 4340 given that $K_{IC} = 58$ MPa-m$^{1/2}$.

14.2 A fracture toughness measurement conducted at −40 °C yielded a value for the crack extension force G_{IC} of 7.08 N/m for a low-carbon steel of grain size 23 μm and $E = 207$ GPa. Compute the effective surface energy $\gamma_e = \gamma_s + \gamma_p$, in (Pa-m) associated with the crack propagation.

14.3 From the knowledge that the yield strength of a pressure vessel steel can be described by the Hall–Petch relation, Eq. (12.63), and that the fracture strength can be described by the Cottrell–Petch relation, Eq. (14.54), and the temperature dependence of each of these terms, explain:

(a) Why the fracture toughness increases with increasing temperature while the yield strength decreases.
(b) How the fracture toughness and yield strength curves plotted as a function of temperature would change if the sample were irradiated.

14.4 A steel plate 305 mm wide and 6.35 mm thick contains a 25.4 mm long crack along each edge.

(a) Calculate the force required to propagate the crack the remaining 254 mm across the width of the plane.
(b) Calculate the force required to break the plate in tension if there were no crack. Assume the fracture strength is 700 MPa (10^5 psi).
(c) Calculate the force required to break the plate in tension at the theoretical cohesive strength.

For steel, use:

$$E = 100\text{GPa}\,(14.5 \times 10^6\,\text{psi})$$
$$\gamma_s = 1\,\text{J/m}^2$$
$$a = 3 \times 10^{-10}\,\text{m}$$

14.5 Draw a Charpy impact energy curve for a carbon steel before and after irradiation at 300 °C to 2×10^{19} n/cm^2.

(a) Explain the behavior of irradiation in terms of σ_y and σ_f.
(b) List the factors that may influence the NDT and ductile shelf energy. Explain the mechanism and the direction of change.

14.6 Consider helium bubbles 100 nm in radius located on a grain boundary.

(a) To what size do the bubbles grow under the influence of a tensile stress one-half the critical value for instability?
(b) Two of the bubbles coalesce. What is the equilibrium size of the new bubble?

14.7 A fusion first wall made of austenitic stainless steel is subjected to a fast neutron flux of 5×10^{14} n/cm^{2}s ($E > 1$ MeV) and a stress of one-half of the unirradiated yield strength. After 300 days, the wall is removed and analyzed by transmission electron microscopy (TEM). It is revealed that 30 % of the grain boundary is covered with either voids or bubbles with an average size of 50 nm. Given the following information, make a prediction of the time to rupture and the failure mechanism:

$$\sigma_y = 280\,\text{MPa}$$
$$d = 20\,\mu\text{m}$$
$$\gamma = 5\,\text{J/m}^2$$
$$\dot{\varepsilon} = C\sigma\phi = \text{steady state creep rate}$$
$$C = 1.3 \times 10^{-27}\,\text{cm}^2/\text{MPa}$$

14.8 At 300 °C, 2 % of the volume of a solid is occupied by equilibrium bubbles, all of which have radius R_i. The number of gas atoms is assumed to remain unchanged for all cases described below. Ideal gas behavior is assumed, so that the number of gas atoms in an equilibrium bubble is $m = \frac{4\pi R^2}{3}\frac{2\gamma}{kT}$.

(a) Impurity atoms segregate to the bubble surfaces, leading to a 30 % reduction in the surface energy, γ. Calculate the volume fraction occupied by bubbles after equilibrium is re-established.
(b) The temperature is then raised to T = 800 °C, which leads to diffusion of the impurities into the bulk, restoring the original value of γ. Calculate the volume fraction occupied by bubbles after equilibrium is re-established.
(c) For the same initial conditions (2 % at 300 °C), bubbles coalesce in groups of ten and reach equilibrium. What is the resulting volume fraction occupied by bubbles?

14.9 An austenitic stainless steel fuel pin under an applied stress of 140 MPa fails, owing to helium embrittlement at a strain of 1 %. What concentration (in atomic ppm) of helium in the metal is necessary to cause fracture at this value of strain? The irradiation temperature is 700 °C.

References

1. Dieter GE (1976) Mechanical metallurgy, 2nd edn. McGraw-Hill, New York
2. Griffith AA (1968) Trans Am Soc Met 61:871–906
3. Inglis CE (1913) Trans Inst Nav Archit 55(1):219–230
4. Orowan E (1950) Fatigue and fracture of metals. Wiley, New York
5. Irwin GR (1958) Encyclopedia of physics, IV. Springer, Berlin
6. Reed-Hill RE (1973) Physical metallurgy principles, 2nd edn. D Van Nostrandm New York
7. ASTM (2005) E399-05 standard test method for linear-elastic plane-strain fracture toughness K_{Ic} of metallic materials. ASTM International, West Conshohocken, PA
8. Reed-Hill RE (1992) Physical metallurgy principles, 3rd edn. PWS, Boston
9. Dugdale DS (1960) J Mech Phys Solids 8:100
10. Anderson TL (1995) Fracture mechanics, 2nd edn. CRC, New York, p 142
11. Cottrell AH (1958) Trans AIME 212:192
12. Zener C (1948) Fracturing of metals. American Society for Metals, Metals Park, Ohio
13. Stroh AH (1957) Adv Phys 6:418
14. Bement AL (1972) Rev Roum Phys 17(4):505
15. Petch NJ (1957) Fracture. Wiley, New York, p 54
16. Murty KL (1999) J Nucl Mater 270:115–128
17. Johnson AA (1962) Phil Mag 7:177
18. Mager TR, Hazelton WS (1969) Radiation damage in reactor materials, vol I. IAEA, Vienna, p 317
19. Steele LE (1975) Neutron irradiation embrittlement of reactor pressure vessel steels. IAEA, Vienna
20. ASTM (2000) E 208-95, standard test method for conducting drop-weight test to determine nil-ductility transition temperature of ferritic steels. ASTM International, West Conshohocken, PA
21. Odette GR, Lambrozo PM, Wullaert RA (1985) In: Garner FA, Perrin JS (eds) Effects of irradiation on materials the 12th international symposium, ASTM STP 870. America Society for Testing and Materials, Philadelphia, PA, pp 840–850
22. English CA, Ortner SR, Cage G, Server WL, Rosinski ST (2001) In: Rosinski ST, Gross-beck ML, Allen TR, Kumar AS (eds) Effects of radiation on materials the 20th international symposium, ASTM STP 1405. American Society for Testing and Materials, West Conshohocken, PA, 2001, pp 151–173
23. Hausild P, Kyta M, Karlik M, Pesck P (2005) JNM 341:184–188
24. Odette GR, Lucas GE (1996) J Non Destr Eval 15:137
25. Sokolov MA, Nanstad RK, Miller MK (2004) J ASTM Int 1(9):123–137
26. Lott RG, Rosinski ST, Server WL (2004) J ASTM Int 1(5):300–310
27. Hahn GT, Rosenfield AR (1966) Acta Metal 14:1815
28. Stoller RE (2004) J ASTM Int 1(4):326–337 Paper ID JAI11355
29. Steele LE, Hawthorne JR (1967) ASTM STP-426, effects of irradiation on structural materials. American Society for Testing and Materials, Philadelphia, PA, p 534
30. Steele LE, Davies LM, Ingham T, Brumovsky M (1985) Garner FA, Perrin JS (eds) Effects of irradiation on materials the 12th international symposium. American Society for Testing and Materials, Philadelphia, PA, pp 863–899
31. Sokolov MA, Chernobaeva AA, Nanstad RK, Nikolaev YA, Korolev YN (2000) In: Hamilton ML, Kumar AS, Rosinski ST, Grossbeck ML (eds) Effects of radiation on materials the 19th international symposium, ASTM STP 1366. American Society for Testing and Materials, West Conshohocken, PA, pp 415–434
32. US Nuclear Regulatory Commission (1998) Regulatory Guide 199, Radiation Embrittlement of Reactor Vessel Materials, Revision 2. US Nuclear Regulatory Commission, Washington, DC, May 1998
33. Odette GR, Lucas GE (1998) Rad Eff Defects Solid 44:189

34. Odette GR, Lucas GE (2001) JOM July:18–22
35. Horsten MG, van Osch EV, Gelles DS, Hamilton ML (2000) In: Hamilton ML, Kumar AS, Rosinski ST, Grossbeck ML (eds) Effects of radiation on materials the 19th international symposium, ASTM STP 1366. American Society for Testing and Materials, West Conshohocken, PA, pp 579–593
36. Callister WD (1991) Materials science and engineering, an introduction. Wiley, New York
37. Laird C (1967) Fatigue crack propagation, ASTM STP-415. American Society for Testing and Materials, Philadelphia, PA, p 131
38. James LA (1977) Nucl Safety 18(6):791
39. Cullen WH, Watson HE, Taylor RE, Loss FJ (1981) J Nucl Mater 96:261
40. US Nuclear Regulatory Commission (2003) Fracture toughness and crack growth rates of irradiated austenitic stainless steels, NUREG/CR-6826. US Nuclear Regulatory Commission, Washington, DC, p 21
41. Chopra OK, Rao AS (2011) J Nucl Mater 412:195
42. Odette GR, Lucas GE (1991) J Nucl Mater 179–181:572
43. Odette GR, Lucas GE (1992) J Nucl Mater 191–194:50–57
44. Wolfer WG, Jones RH (1981) J Nucl Mater 103(104):1305–1314
45. Lloyd G (1982) J Nucl Mater 110:20–27
46. Murty KL, Holland FR (1982) Nucl Technol 58:530–537
47. Bloom EE (1976) Irradiation strengthening and embrittlement. Radiation damage in metals. American Society for Metals, Metals Park, OH, pp 295–329
48. Hull D, Rimmer DE (1959) Phil Mag 4:673
49. Nix WD, Yu KS, Wang JS (1983) Metal Trans 14A:563
50. Cadek J (1988) Creep in metallic materials, materials science monographs 48. Elsevier, New York
51. Cocks ACF, Ashby MF (1982) Prog Int Mat Sci 27:189–244
52. Langdon TG, Vastava RB (1982) In: Rhode RW, Swearengen JC (eds) Mechanical testing for deformation model development, ASTM STP 765. American Society for Testing and Materials, Philadelphia, PA, 1982, p 435
53. Trinkaus H, Ullmaier H (1994) J Nucl Mater 212–215:303–309
54. Teirlinck D, Zok F, Embury JD, Ashby MF (1988) Acta Metal 36:1213–1228
55. Li M, Zinkle SJ (2007) J Nucl Mater 361(2–3):192–205

Chapter 15
Corrosion and Stress Corrosion Cracking Fundamentals

Corrosion can be broadly described as the destruction or deterioration of a metal or alloy by way of a chemical or electrochemical reaction with its environment. It can be considered as extractive metallurgy in reverse, or the process by which a metal is returned to its natural state—an oxide. Corrosion can occur in wet (aqueous) environments and also in dry (gaseous) environments, and can occur at a high rate or a very slow rate. It can also take many forms, as discussed in the next section.

Nearly, all metallic corrosion processes involve the transfer of electronic charge in aqueous solutions. Consider the corrosion of zinc in hydrochloric (HCl) acid. Zinc reacts with the acid to form soluble zinc chloride and liberates hydrogen bubbles at the surface. It occurs by two reactions. The first is the oxidation of Zn to Zn^{++} and the liberation of 2 electrons, and the second is the combination of the two electrons with 2 hydrogen ions to yield 2 hydrogen atoms or H_2. The reactions are as follows:

$$Zn \rightarrow Zn^{++} + 2e^{-} \tag{15.1}$$

$$2H^{+} + 2e^{-} \rightarrow H_2, \tag{15.2}$$

for a total reaction described by:

$$Zn + 2HCl \rightarrow ZnCl_2 + H_2 \tag{15.3}$$

or in ionic form:

$$Zn + 2H^{+} + 2Cl^{-} \rightarrow Zn^{++} + 2Cl^{-} + H_2. \tag{15.4}$$

The reaction in Eq. (15.1) is the anodic, or oxidation reaction in which the valence of Zn increases from 0 to +2 and liberates electrons. The reaction in Eq. (15.2) is the cathodic, or reduction reaction in which the oxidation state of H decreases from +1 to 0 by consuming electrons. Water is the carrier of ions, or the electrolyte. Note that the reactions shown in Eqs. (15.1) and (15.2) can occur simultaneously on the surface of a piece of Zn immersed in HCl. These reactions involve the transfer of charge or current. The relationship between current and mass of the reacting metal, *M*, is given by Faraday's law:

G.S. Was, *Fundamentals of Radiation Materials Science*,
DOI 10.1007/978-1-4939-3438-6_15

$$M = kIt, \tag{15.5}$$

where I is the current (amperes, A), t is the time (s), and k is the electrochemical equivalent (g/Coulomb or g/C) given by:

$$k = A/nF, \tag{15.6}$$

where A is the atomic weight, n is the number of equivalents exchanged, and F is Faraday's constant (96,500 C/eq). Recall that a Coulomb is the amount of charge transferred by a current of one ampere for 1 s. Hence, the corrosion rate of a metal is directly related to its reaction rate with the environment.

This chapter will focus on the fundamentals of aqueous corrosion by virtue of its importance in water reactor systems, and provide a foundation for understanding the interplay between corrosion and irradiation in the degradation of metals and alloys treated in Chap. 16. It begins with a description of the various forms of corrosion followed by the thermodynamics of corrosion including the use of potential–pH or Pourbaix diagrams, kinetics of corrosion, passivity, crevice corrosion, and then stress corrosion cracking. The latter two topics provide a basis for understanding the processes of irradiation accelerated corrosion (IAC) and irradiation-assisted stress corrosion cracking (IASCC).

15.1 Forms of Corrosion

While corrosion is most often envisioned as the loss of metal from a surface exposed to the electrolyte, corrosion can take many forms as summarized in Fig. 15.1. The eight forms of corrosion include uniform corrosion, crevice corrosion, pitting, intergranular attack, selective leaching or dealloying, erosion corrosion, stress corrosion cracking, and hydrogen damage.

Uniform corrosion

Uniform corrosion is characterized by a reaction that proceeds uniformly over the entire surface of the component, e.g., rusting of iron or tarnishing of silver. Various units are used to describe the uniform removal of metal, such as the thinning rate in mm/yr or the mass loss per unit area in g/m^{2}yr. Uniform corrosion is not really uniform on a microscopic level. In fact, the orientation of grain faces on the surface will determine which corrodes the fastest. As grains dissolve away, preferential sites for attack will alternate. All other forms of corrosion can be broadly classified as localized corrosion.

Crevice corrosion

Crevice corrosion is characterized by intense localized corrosion that occurs most frequently within crevices or shielded areas on metal surfaces exposed to corrosives. The attack is usually associated with small volumes of stagnant solution.

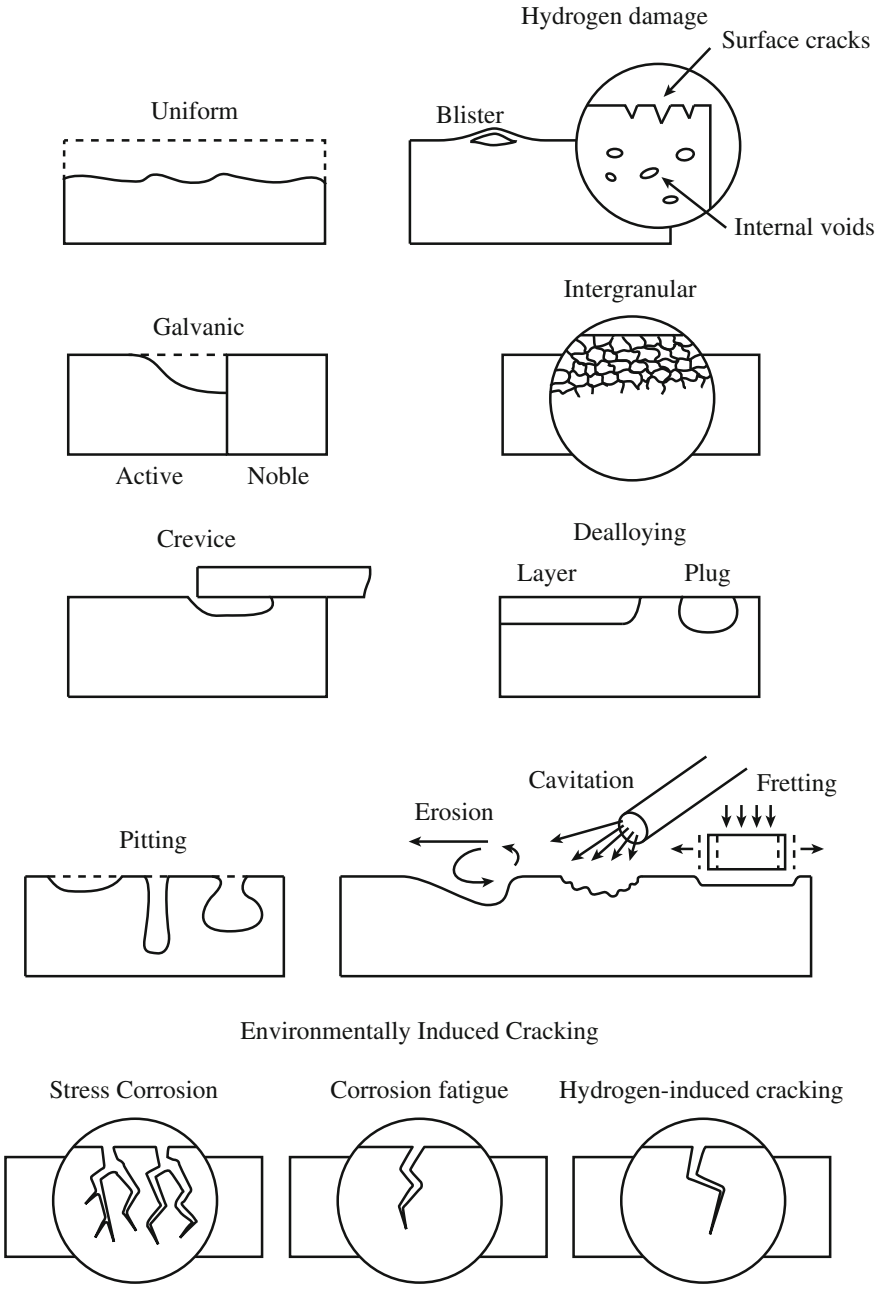

Fig. 15.1 Eight forms of corrosion (after [2])

To function as a corrosion site, a crevice must be wide enough to permit liquid entry, but sufficiently narrow to maintain a stagnant zone. For this reason, crevice corrosion usually occurs in openings of width $\leq$0.1 mm. In tight cracks, the gap may be as small as 10–100 nm.

Although crevice corrosion can result from a difference in metal ion and oxygen concentration between the crevice and the outside (oxygen cell), more processes are involved. Initially, oxidation and reduction occur uniformly over the entire metal surface, and charge is conserved. But after a short time, oxygen in the crevice is depleted because of restricted access, so the reduction reaction cannot occur in the crevice. Corrosion can continue if the reduction reaction occurs on the external surface. After awhile, the excess positive charge in the crevice due to continued metal dissolution will drive Cl^- migration into the crevice to balance the overall charge. The increased metal chloride concentration hydrolyzes the water producing an insoluble hydroxide (MOH) and a free acid. The pH in the crevice drops and metal dissolution is accelerated, thus increasing Cl^- migration into the crevice. The process is autocatalytic and rapidly accelerating.

Pitting corrosion

Pitting is a form of extremely localized corrosion that results in holes in the metal. Pits are often very small in diameter ($\sim$ 10–1000 μm) and can be either high or low density. The surface of a component undergoing pitting may show little or no attack away from the pits themselves.

Pitting is autocatalytic in nature in that the corrosion processes within a pit produce conditions that are both stimulating and necessary for continued pit activity. Say, for example, that a metal M is undergoing pitting in an aerated NaCl solution. Metal dissolution occurs within the pit, while oxygen reduction occurs outside the pit on adjacent surfaces. The excess positive charge in the pit induces Cl^- migration into the pit producing a high concentration of metal chlorides, MCl, and hydrogen ions as a result of the hydrolysis of water. Since both hydrogen ions (low pH) and Cl^- stimulate the dissolution of metal, the process accelerates with time. Since the solubility of oxygen in concentrated solutions is very small, no oxygen reduction occurs in the pit. Instead, oxygen is reduced on adjacent surfaces, and this tends to suppress corrosion on the exposed surface by a sort of cathodic protection. Further, since the pit area is much smaller than the unpitted area, to maintain charge conservation ($I_{\text{oxidation}} = I_{\text{reduction}}$), then $i_{\text{anode}} \gg i_{\text{cathode}}$, where I is current and i is current density.

The pitting process resembles quite closely that of crevice corrosion. In fact, practically all systems that show pitting attack are susceptible to crevice corrosion. However, the reverse is not always true. It is the self-initiating characteristic of pitting that makes it unique. Unfortunately, the mechanism of pit initiation is not well understood. It is believed that pits probably nucleate at weak points in the surface film that can be attacked by ions such as Cl^-, causing a defect and initiating the localized corrosion process.

Intergranular corrosion

Localized attack of grain boundary regions can result in a loss of strength and/or disintegration of the region. The grain boundary itself is only slightly more reactive than the matrix and generally will not cause problems. However, in cases where there is a change in composition or phase, then severe intergranular corrosion can occur. Some examples are the segregation or depletion of alloying elements. Fe in Al will segregate to the grain boundary and cause intergranular corrosion (IGC), as does depletion of Cr at the grain boundaries in stainless steel and nickel-base austenitic alloys.

Selective leaching or dealloying

Selective leaching or dealloying is the preferential removal of one element from a solid alloy by corrosion. The most common example is the selective removal of zinc in brass. The overall dimension of the part does not change, but it becomes considerably weaker and permeable due to its porous nature. The color also changes to a red or copper color. This mechanism is known to occur in other systems such as Cu–Ni alloys and is also referred to as "dezincification." The process occurs by either a layer-type or plug-type mechanism. In the case of brass, both Zn and Cu dissolve into solution, but while the Zn ions stay in solution, the Cu plates back onto the structure. When oxygen is present, the copper often appears as a copper oxide on the surface.

Erosion corrosion

Erosion corrosion is the acceleration or increase in the rate of deterioration or attack of a metal because of the relative movement between a corrosive fluid and the metal surface. The metal is removed as the dissolved ions or solid corrosion products are swept away. Mechanical wear and abrasion are often involved in the process.

Corrosion is characterized by a grooved, scalloped, or scooped out appearance of the surface. Metals that depend on a surface film (passive layer) for protection are damaged when the protective layer is worn away. Soft metals such as copper or lead are readily damaged or worn mechanically. If the flow rate over the metal surface is high enough, cavitation can occur. Cavitation is damage to the metal caused by collapse of bubbles on the metal surface (tube wall). The pounding causes cavity formation. Examples of cavitation damage include ship propellers and pump impellers.

Stress corrosion cracking

Stress corrosion cracking (including stress-assisted corrosion and corrosion fatigue) is the premature failure of an alloy or metal in the presence of a tensile stress and an aggressive environment. Examples include stainless steels in Cl^- and OH^-, aluminum alloys in halides (Cl^-, Br^-, etc.), carbon steel in OH^- and NO_3^-, α-brass in NH_4^+, and stainless steels and nickel-base alloys in high-temperature water. In stress corrosion cracking, the metal or alloy is virtually unattacked over most of its

surface, while fine cracks pass through it. Cracks can be either transgranular or intergranular. In the past, it was believed that only alloys were susceptible to SCC, but recent evidence shows that pure metals can also fail by this process.

Hydrogen (embrittlement) damage

Hydrogen damage can take many forms. One is blistering in which penetration of hydrogen results in the formation of high-pressure bubbles which then deform the surface and can lead to exfoliation if the metal between the bubble and the surface is thin enough. Hydrogen attack involves the reaction of hydrogen with a component of the alloy. For example, the reaction of hydrogen with carbon in steel to form methane can cause damage to the metal. Hydrogen also causes embrittlement by either directly affecting the strength of atom bonds in the matrix or grain boundary, or by enhancing localized plasticity, resulting in failure that resembles brittle fracture.

Understanding the various forms of corrosion requires an understanding of the driving force for corrosion described by thermodynamics, as well as the kinetics of corrosion. Combined, they provide the foundation for understanding the various ways in which metals and alloys behave in aqueous environments and exposed to ionizing radiation.

15.2 Thermodynamics of Corrosion

15.2.1 The Driving Force for Corrosion

The tendency for corrosion to occur is determined by thermodynamics. The corrosion reaction can be written as follows:

$$(-v_A)A + (-v_B)B + (-v_C)C + \cdots = v_M M + v_N N + v_O O + \cdots, \tag{15.7}$$

where v_i are stoichiometric coefficients for substances, *A, B, C*, etc., and their sign is positive for products and negative for reactants. Equation (15.7) states that $(-v_A)$ particles (molecules, atoms, ions) of substance *A*, $(-v_B)$ particles of substance *B*, etc., react to form v_M particles of *M*, v_N particles of *N*, etc. The electrochemical potential, $\tilde{\mu}_k$, of a species *k* can be defined as the partial molar Gibbs energy of this species:

$$\tilde{\mu}_k \equiv \left(\frac{\partial G}{\partial n_k}\right)_{P,T,n_{j\neq k}}, \tag{15.8}$$

where $\tilde{\mu}_k$ denotes the change in the Gibbs energy of the system, *G*, upon addition of a differential amount of the species *k* normalized to a one mole change in *k*. The change in Gibbs energy for this reaction is as follows:

$$\Delta G = v_M \tilde{\mu}_M + v_N \tilde{\mu}_N + \cdots - [(-v_A)\tilde{\mu}_A + (-v_B)\tilde{\mu}_B + \cdots] = \sum_k v_k \tilde{\mu}_k. \quad (15.9)$$

Actually, the electrochemical potential is composed of "chemical" and "electrical" parts such that:

$$(\tilde{\mu}_k)_x = (\mu_k)_x + nFE_x \quad (15.10)$$

$(\tilde{\mu}_k)_x$ is the electrochemical potential of the kth particle type in phase x, and $(\mu_k)_x$ is the chemical potential of the kth particle type in phase x. The term nFE_x is the work to transfer n charges from infinite separation to the inside of the phase, E_x, and is the Galvani or electrochemical potential in the phase under consideration. For example, consider the reaction of pure metallic zinc in HCl:

$$(\mathrm{Zn})_\mathrm{m} + 2(\mathrm{H}^+)_\mathrm{l} \rightarrow (\mathrm{Zn}^{2+})_\mathrm{l} + (\mathrm{H}_2)_\mathrm{g}, \quad (15.11)$$

where subscripts m, l, and g denote metal, liquid, and gas, respectively. From the above, the Gibbs energy of the reaction is as follows:

$$\Delta G = (\tilde{\mu}_{\mathrm{Zn}^{2+}})_\mathrm{l} + \left(\mu_{\mathrm{H}_2}\right)_\mathrm{g} - 2(\tilde{\mu}_{\mathrm{H}^+})_\mathrm{l} - (\mu_{\mathrm{Zn}})_\mathrm{m}, \quad (15.12)$$

and using Eq. (15.10), we can write:

$$\Delta G = (\mu_{\mathrm{Zn}^{2+}})_\mathrm{l} + \left(\mu_{\mathrm{H}_2}\right)_\mathrm{g} - 2(\mu_{\mathrm{H}^+})_\mathrm{l} - (\mu_{\mathrm{Zn}})_\mathrm{m} + 2FE_\mathrm{l} - 2FE_\mathrm{l}. \quad (15.13)$$

However, since the electrical work terms always exactly cancel, the Gibbs energy of the reaction is determined solely by the chemical potentials:

$$\Delta G = \sum_k v_k (\mu_k)_x. \quad (15.14)$$

The chemical potential of each species can be written as follows:

$$\mu_k = \mu_k^0 + RT \ln a_k, \quad (15.15)$$

where μ_k^0 is the standard chemical potential and the activity is $a_k = \gamma_k C_k$, where γ_k is the activity coefficient and C_k is the concentration of species k. Substituting into Eq. (15.14) gives:

$$\Delta G = \sum v_k \mu_k^0 + RT \ln \Pi a_k^{v_k}, \quad (15.16)$$

where $\sum v_k \mu_k^0 = \Delta G^0$ is the standard Gibbs reaction energy, yielding:

$$\Delta G - \Delta G^0 = RT \ln \Pi a_k^{v_k} = RT \ln \frac{a_M^{v_M} . a_N^{v_N} \ldots}{a_A^{-v_A} \cdot a_B^{-v_B} \ldots} = RT \ln \frac{a_{\text{product}}}{a_{\text{reactant}}}. \tag{15.17}$$

If an electrochemical cell is operated under reversible conditions, the charge, nF, passed reversibly at equilibrium through a potential E corresponds to the free energy change, ΔG. That is, $|\Delta G|$ = charge passed · potential difference = work (energy) to transfer n charges from infinite separation to the inside of the phase:

$$|\Delta G| = nF.|E|, \tag{15.18}$$

where n is the number of electrons involved in the reaction and E is the cell potential. According to sign convention:

$$\Delta G = -nFE, \quad \text{and} \quad \Delta G^0 = -nFE^0. \tag{15.19}$$

Substituting into Eq. (15.17) gives:

$$E - E^0 = -\frac{RT}{nF} \ln \left[\frac{a_{\text{prod}}}{a_{\text{react}}}\right] = -\frac{2.3RT}{nF} \log \left[\frac{a_{\text{prod}}}{a_{\text{react}}}\right]. \tag{15.20}$$

This is the Nernst equation, which expresses the exact electromotive force (EMF) of a cell in terms of the activities of products and reactants of the cell. The equation applies equally well to a single electrode or the total reaction. For Zn immersed in water at 25 °C (298 K):

Anodic reaction: $Zn \rightarrow Zn^{++} + 2e^-$

$$E_{Zn} = E^0_{Zn} - \frac{0.0257}{2} \ln \left[\frac{a_{Zn^{++}}}{a_{Zn}}\right] = E^0_{Zn} - \frac{0.0257}{2} \ln a_{Zn^{++}}, \quad \text{since } a_{Zn} = 1.$$

Cathodic reaction: $2H^+ + 2e^- \rightarrow H_2$

$$E_{H_2} = E^0_{H_2} - \frac{0.0257}{2} \ln \left[\frac{p_{H_2}}{a^2_{H_2}}\right],$$

where p_{H_2} is the hydrogen gas pressure. The total reaction is as follows: $Zn + 2H^+ \rightarrow Zn^{++} + H_2$, and the EMF of the cell is as follows:

$$E_{\text{cell}} = E_{Zn} + E_{H_2} = E^0_{Zn} + E^0_{H_2} - \frac{0.0257}{2} \ln [a_{Zn^{++}}] - \frac{0.0257}{2} \ln \left[\frac{p_{H_2}}{a^2_{H^+}}\right].$$

E_0 is the standard potential or *standard single electrode potential* (SSEP). This refers to the reactants and products in the standard state. E is the single electrode potential, or *equilibrium standard electrode potential* (ESEP), and refers to the reactants and products in any state.

We now pose a fundamental question: What is the tendency for metals to corrode? The real measure of whether a metal will corrode is whether its actual single electrode potential is above or below its equilibrium single electrode potential (ESEP). For example, the reaction $M = M^{n+} + ne^-$ will proceed to the right if the measured single electrode potential (MSEP) is greater than the equilibrium single electrode potential, MSEP > ESEP. However, if MSEP < ESEP, the reaction will proceed to the left. The problem is that we cannot measure potentials or voltages of a single electrode without another electrode being present. But we may try to build separate cells to physically separate the anode from the cathode.

In the cell shown in Fig. 15.2, the Pt electrode serves only as a site for the reduction of hydrogen and is physically separated from the Zn electrode. Pt does not participate in the reaction. As before:

$$E_{\mathrm{Zn}} = E^0_{\mathrm{Zn}} - \frac{0.0257}{2} \ln a_{\mathrm{Zn}^{++}},$$

and

$$E_{\mathrm{H_2}} = E^0_{\mathrm{H_2}} - \frac{0.0257}{2} \ln \left[\frac{p_{\mathrm{H_2}}}{a^2_{\mathrm{H_2}}} \right].$$

To measure E^0_{Zn}, we must establish a reference. We arbitrarily let this reference be $E^0_{\mathrm{H_2}} \equiv 0$. This is the SSEP for the reduction of hydrogen. Fixing $p_{\mathrm{H_2}} = 1$ atm and $a_{\mathrm{H}^+} = 1$, then $E_{\mathrm{H_2}} = 0$. Therefore:

$$E_{\mathrm{cell}} = E_{\mathrm{Zn}} = E^0_{\mathrm{Zn}} - \frac{RT}{2F} \ln a_{\mathrm{Zn}^{++}}.$$

If we want to find the value of E^0_{Zn}, then setting $a_{\mathrm{Zn}^{++}} = 1$ gives $E_{\mathrm{cell}} = E^0_{\mathrm{Zn}}$. Hence, the half-cell potential for any electrode is equal to the EMF of a cell with the standard hydrogen electrode (SHE) as the other electrode.

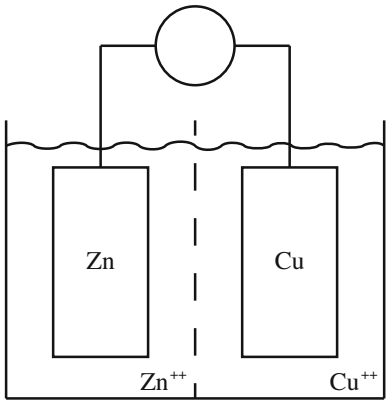

Fig. 15.2 A Zn–Cu electrochemical cell

15.2.2 EMF Series and Sign Conventions

Since the equilibrium cell voltage of a cell consisting of an electrode X and the normal hydrogen electrode is the equilibrium electrode potential, E_X of the X electrode, an orderly arrangement can be constructed of the standard potentials of all metals. This arrangement is termed the EMF series or potential series and is shown in Table 15.1. The position in the EMF series is determined by the equilibrium potential of a metal in contact with its ions at a concentration equal to unit activity. Notice that the equilibrium potential (by definition) for H_2/H^+ is 0. Metals with positive potentials are more noble than hydrogen, while those with negative values are less noble, or active with respect to hydrogen. Thus, the direction of increasingly positive values is the noble direction, whereas the direction of increasingly negative values is the active direction.

Table 15.1 Standard electromotive force potentials (reduction potentials) (after [2])

	Reaction	Standard potential, E^0 (volts vs. SHE)
Noble	$Au^{3+} + 3e^- = Au$	+1.498
↑	$Cl_2 + 2e^- = 2Cl^-$	+1.358
	$O_2 + 4H^+ + 4e^- = 2H_2O$ (pH 0)	+1.229
	$Pt^{3+} + 3e^- = Pt$	+1.2
	$O_2 + 2H_2 + 4e^- = 4OH^-$ (pH 7)[a]	+0.82
	$Ag^+ + e^- = Ag$	+0.799
	$Hg_2^{2+} + 4e^- = 2Hg$	+0.788
	$Fe^{3+} + e^- = Fe^{2+}$	+0.771
	$O_2 + 2H_2O + 4e^- = 4OH^-$ (pH 14)	+0.401
	$Cu^{2+} + 2e^- = Cu$	+0.337
	$Sn^4 + 2e^- = Sn^{2+}$	+0.15
	$2H^+ + 2e^- = H_2$	0.000
	$Pb^{2+} + 2e^- = Pb$	−0.126
	$Sn^{2+} + 2e^- = Sn$	–0.136
	$Ni^{2+} + 2e^- = Ni$	–0.250
	$Co^{2+} + 2e^- = Co$	−0.277
	$Cd^{2+} + 2e^- = Cd$	−0.403
	$Fe^{2+} + 2e^- = Fe$	–0.440
	$Cr^{3+} + 3e^- = Cr$	−0.744
	$Zn^{2+} + 2e^- = Zn$	−0.763
	$2H_2O + 2e^- = H_2 + 2OH^-$	−0.828
↓	$Al^{3+} + 3e^- = Al$	−1.662
	$Mg^{2+} + 2e^- = Mg$	–2.363
	$Na^+ + e^- = Na$	–2.714
Active	$K^+ + e^- = K$	–2.925

[a]Not a standard state

Unfortunately, a problem arises with differences in convention for the sign of the E^0 values. In one convention we have zinc-minus, copper-plus such that the values of E^0 for the Zn/Zn^{++} and the Cu/Cu^{++} electrodes are -0.76 and $+0.34$ V, respectively, for a Zn electrode in a solution of unit activity of Zn^{++} and a Cu electrode in a solution of unit activity of Cu^{++}. The other convention is zinc-plus and copper-minus. The proper convention is determined as follows:

1. Set up a cell consisting of an SHE on the left side and another electrode on the right side.
2. Measure the open-circuit potential of the cell by applying a potential difference exactly equal and opposite in sign to that produced by the cell itself. This is done by adjusting a potentiometer until the reading on the galvanometer is zero (no current flowing).
3. The potentiometer reading gives the magnitude of the potential difference across the cell as well as the sign of the charge on the electrode.

For example, the following cell
$Pt/H_2[1\ \text{atm}],\ H^+[a_{H^+} = 1]//Zn^{++}[a_{Zn^{++}} = 1]/Zn$ gives:

1. A magnitude of $E^0_{Zn/Zn^{++}}$ of 0.76 V,
2. The zinc electrode is negative.

For Pt/H_2 [1 atm], $H^+[a_{H^+} = 1]//Cu^{++}[a_{Cu^{++}} = 1]/Cu$ we have:

1. The magnitude of $E^0_{Cu/Cu^{++}}$ is 0.34 V,
2. The copper electrode is positive.

By affixing to the measured magnitude of $E^0_{Zn/Zn^{++}}$ for a Zn/Zn^{++} electrode the same sign as the observed polarity of the zinc electrode, we have: $E^0_{Zn/Zn^{++}} = -0.76$ V and $E^0_{Cu/Cu^{++}} = 0.34$ V. As a rule, if charge transfer reactions are written as reductions (electronations), e.g., $Zn^{++} + 2e^- \rightarrow Zn$, the sign of the electrode potential as derived from the free energy change comes out in agreement with that indicated by the observed polarity of the electrode: $\Delta G = -nFE$ or $E = -\Delta G/nF$.

Based on a 1953 meeting of the International Union of Pure and Applied Chemistry (IUPAC) in Stockholm, the following decisions were made that reinforce the rule given above:

1. The cell implicit in the measurement of a standard electrode potential should be arranged so that the hydrogen electrode is on the left:

$$Pt/H_2[1\ \text{atm}],\ H^+[a_{H^+} = 1]//M^{++}/M.$$

2. The measured potential difference across such a cell furnishes the magnitude of the standard electrode potential.
3. The polarity of the electrode on the right, i.e., the sign of the charge on the M electrode, serves to define the sign that is affixed to the E^0 value.
4. The charge transfer reaction implicit in the statement of a standard potential of an M/M^+ electrode is a reduction reaction $M^{n+} + ne^- \rightarrow M$.

For a cell with two electrodes, neither of which are H_2, how does one determine which is the anode (where oxidation occurs) and which is the cathode (where reduction occurs)? There are two conventions for making this determination: the American (or sign bivariant) convention and the European (or sign invariant) convention.

American (sign bivariant) convention

Write the reaction as either an oxidation reaction or a reduction reaction:

$$\text{Oxidation:} \quad \text{Zn} \rightarrow \text{Zn}^{++} + 2\text{e}^- \quad E^0 = +0.76 \text{ V}$$
$$\text{Reduction:} \quad \text{Zn}^{++} + 2\text{e}^- \rightarrow \text{Zn} \quad E^0 = -0.76 \text{ V}$$

Using the Nernst equation for these two equations:

$$E = E^0 - \frac{RT}{nF} \ln \frac{a_\text{p}}{a_\text{r}}, \tag{15.21}$$

Oxidation:

$$E_\text{Zn} = E^0_\text{Zn} - \frac{RT}{nF} \ln a_{\text{Zn}^{++}} = 0.76 - \frac{RT}{2F} \ln a_{\text{Zn}^{++}}$$

Reduction:

$$E_\text{Zn} = E^0_\text{Zn} - \frac{RT}{2F} \ln \frac{1}{a_{\text{Zn}^{++}}} = 0.76 - \frac{RT}{2F} \ln a_{\text{Zn}^{++}}$$

1. Write the reaction as either an oxidation or reduction reaction.
2. Use the corresponding oxidation or reduction potentials.
3. Identify the products and reactants from the reaction.

In the American convention, the sign on the EMF is an indication of the thermodynamic tendency for the reaction to proceed as written.

$E_\text{Zn} = +0.76$ V(oxidation) $\Rightarrow \Delta G < 0$: reaction proceeds spontaneously
$E_\text{Zn} = -0.76$ V(reduction) $\Rightarrow \Delta G > 0$: reaction won't go

Notice that $E^{\text{oxidation}}_\text{Zn} = -E^{\text{reduction}}_\text{Zn}$.

European (sign invariant) convention

Write the reaction as a reduction reaction:

$$Zn^{++} + 2e^{-} \rightarrow Zn$$

The Nernst equation is written as follows:

$$E = E^0 + \frac{RT}{nF} \ln \frac{a_A}{a_D}, \tag{15.22}$$

where A = electron acceptor or the oxidized specie (ion) and D = electron donor or the reduced specie (metal), giving:

$$E_{Zn} = E^0_{Zn} + \frac{RT}{2F} \ln a_{Zn^{++}} = -0.76 + \frac{RT}{2F} \ln a_{Zn^{++}}.$$

The sign on the EMF in the European convention arises because negatively charged electrons are liberated at the zinc electrode. This convention is implemented as follows:

1. Subtract the standard potential of the electrode on the left from that on the right.
2. The sign of the potential difference across the cell corresponds to the polarity of the electrode on the right.

For an electrochemical cell in which two different metals are coupled, the rules are then applied as follows:

American convention

- Guess at reactions (oxidation/reduction).
- Adjust the sign on E^0 according to the direction of the reaction.
- Use $E = E^0 - \frac{RT}{nF} \ln \frac{a_p}{a_r}$.
- Compare the sign on E_{cell} to determine the direction in which the reaction will go.

$$\begin{pmatrix} E_{cell} < 0 \rightarrow \Delta G > 0, \text{ no} \\ E_{cell} > 0 \rightarrow \Delta G < 0, \text{ yes} \end{pmatrix}$$

European convention

- Fix the electrode locations.
- Write both reactions as either oxidation or reduction.
- Use $E = E^0 + \frac{RT}{nF} \ln \frac{a_A}{a_D}$.
- $E_{cell} = E_{RHS} - E_{LHS}$.

- Sign applies to RHS. If $<0 \rightarrow$ anode
  If $>0 \rightarrow$ cathode

The two conventions can be used to determine the EMF of the cell shown in Fig. 15.2. Under the American convention, we guess at the reactions and write:

$$\mathrm{Zn} \rightarrow \mathrm{Zn}^{++} + 2\mathrm{e}^- \quad E_{\mathrm{Zn}} = E^0_{\mathrm{Zn}} - \frac{RT}{2F} \ln a_{\mathrm{Zn}^{++}}$$

$$\mathrm{Cu}^{++} + 2\mathrm{e}^- \rightarrow \mathrm{Cu} \quad E_{\mathrm{Cu}} = E^0_{\mathrm{Cu}} - \frac{RT}{2F} \ln \frac{1}{a_{\mathrm{Cu}^{++}}}$$

$$\text{Adding gives: } E_{\mathrm{cell}} = E_{\mathrm{Zn}} + E_{\mathrm{Cu}} = 0.76\ \mathrm{V} + 0.34\ \mathrm{V} - \frac{RT}{2F} \ln \frac{a_{\mathrm{Zn}^{++}}}{a_{\mathrm{Cu}^{++}}}.$$

For unit activities, $a_{\mathrm{Cu}^{++}} = a_{\mathrm{Zn}^{++}} = 1$, giving $E_{\mathrm{cell}} = 1.1$ V, $\Delta G < 0$, and the reaction proceeds as written. Note that if it was assumed instead that Cu was the anode and Zn the cathode, then the following would occur:

$$\text{Anode :} \quad \mathrm{Cu} \rightarrow \mathrm{Cu}^{++} + 2\mathrm{e}^- \quad E_{\mathrm{Cu}} = E^0_{\mathrm{Cu}} - \frac{RT}{2F} \ln a_{\mathrm{Cu}^{++}}$$

$$\text{Cathode :} \quad \mathrm{Zn}^{++} + 2\mathrm{e}^- \rightarrow \mathrm{Zn} \quad E_{\mathrm{Zn}} = E^0_{\mathrm{Zn}} - \frac{RT}{2F} \ln \frac{1}{a_{\mathrm{Zn}^{++}}}$$

Adding gives: $E_{\mathrm{cell}} = E_{\mathrm{Zn}} + E_{\mathrm{Cu}} = -0.34\ \mathrm{V} - 0.76\ \mathrm{V} = -1.1\ \mathrm{V}$, $E_{\mathrm{cell}} < 0$, $\Delta G > 0$, and the reaction as written would not go. Rather it will proceed in the opposite direction.

Following the European convention, both reactions are written as reduction reactions:

$$\mathrm{Zn}^{++} + 2\mathrm{e}^- \rightarrow \mathrm{Zn} \quad \text{and} \quad \mathrm{Cu}^{++} + 2\mathrm{e}^- \rightarrow \mathrm{Cu}$$

Subtract the RHS from the LHS to give:

$$\begin{aligned} \mathrm{E}_{\mathrm{cell}} = \mathrm{E}_{\mathrm{Zn}} - \mathrm{E}_{\mathrm{Cu}} = E_{\mathrm{Zn}} &= E^0_{\mathrm{Zn}} + \frac{RT}{2F} \ln a_{\mathrm{Zn}^{++}} - E^0_{\mathrm{Cu}} - \frac{RT}{2F} \ln a_{\mathrm{Cu}^{++}} \\ &= E^0_{\mathrm{Zn}} - E^0_{\mathrm{Cu}} + \frac{RT}{2F} \ln \frac{a_{\mathrm{Zn}^{++}}}{a_{\mathrm{Cu}^{++}}}. \end{aligned}$$

For unit activities, $E_{\mathrm{cell}} = -1.1$ V, which says that the zinc electrode is negative with respect to the Cu electrode, so zinc is the anode and Cu is the cathode.

Of two metals composing a cell, the anode is the more active in the EMF series provided that the ion activities in equilibrium are both unity. Since unit activity corresponds in some cases to impossible concentrations of metal ions because of restricted solubility of metal salts, it is obvious that the EMF series has only limited utility for predicting which metal is anodic to another. In practice, the actual activities of ions in equilibrium with a given metal vary greatly with the environment. So two approaches are taken. One is to use a more reasonable activity of, say,

Table 15.2 Galvanic series in seawater

Cathodic (noble)
↑
platinum
gold
graphite
titanium
silver
zirconium
AISI Type 316, 317 stainless steels (passive)
AISI Type 304 stainless steel (passive)
AISI Type 430 stainless steel (passive)
nickel (passive)
copper-nickel (70-30)
bronzes
copper
brasses
nickel (active)
naval brass
tin
lead
AISI Type 316, 317 stainless steels (active)
AISI Type 304 stainless steel (active)
cast iron
steel or iron
aluminum alloy 2024
cadmium
aluminum alloy 1100
zinc
magnesium and magnesium alloys
↓
Anodic (active)

10^{-6} mol/kg such that $a_{M^{2+}} \simeq C_{M^{2+}}$. This is the approach followed in the discussion of stability (Pourbaix) diagrams in Sect. 15.2.3. The second is to arrange the metals and alloys in accord with their actual measured potentials in a given environment, such as seawater. An example is shown in Table 15.2.

15.2.3 Stability (Pourbaix) Diagrams

The stability of a metal in an aqueous solution can be represented by an E-pH, or Pourbaix diagram [1]. These diagrams are graphical representations of the domains of stability of metals, metal ions, oxides, and other species in solution. The diagrams are based on thermodynamic computations for a number of selected chemical species and the possible equilibria between them. It is possible to predict from an E-pH diagram if a metal will corrode or not. It is *not* possible to determine how fast it will corrode.

The stability diagram is analogous to the equilibrium phase diagram in that it portrays phase equilibria between metal, metal ions, and metal oxide all at 25 °C in aqueous solutions, much as the equilibrium phase diagram portrays phase equilibrium in a binary alloy as in Fig. 15.3(a). We can write equations for phases of iron that might form in aqueous solutions and then do tests to find regions of validity or applicability. For example, consider the line labeled ① in Fig. 15.3(a):

$$e^- + Fe^{3+} = Fe^{2+} \quad E_{Fe^{3+}/Fe^{2+}} = E^0_{Fe^{3+}/Fe^{2+}} + \frac{RT}{F}\ln\left[\frac{a_{Fe^{3+}}}{a_{Fe^{2+}}}\right]$$
$$= 0.77 + 0.0257\ln\left[\frac{a_{Fe^{3+}}}{a_{Fe^{2+}}}\right].$$

Choosing a metal ion activity of 10^{-6} mol/kg, then $a_{Fe^{3+}} = a_{Fe^{2+}} = 10^{-6}$, so $E = 0.77$ V.

Consider next, line ② in Fig. 15.3(a):

$$2e^- + Fe^{2+} = Fe \quad E_{Fe^{2+}/Fe} = E^0_{Fe^{2+}/Fe} + \frac{RT}{F}\ln a_{Fe^{2+}},$$

and for an activity of 10^{-6},

$$E_{Fe^{2+}/Fe} = -0.44 + \frac{0.059}{2}(-6)$$
$$= -0.62 \text{ V}.$$

These are examples of a particular type of reaction known as pure charge transfer reactions. These electrochemical reactions involve only electrons and the reduced and oxidized species. They do not have protons (H^+) as reacting particles and so are not influenced by pH; hence, they represent horizontal lines in the stability diagram. In our example, we selected a single activity for the reaction. However, stability

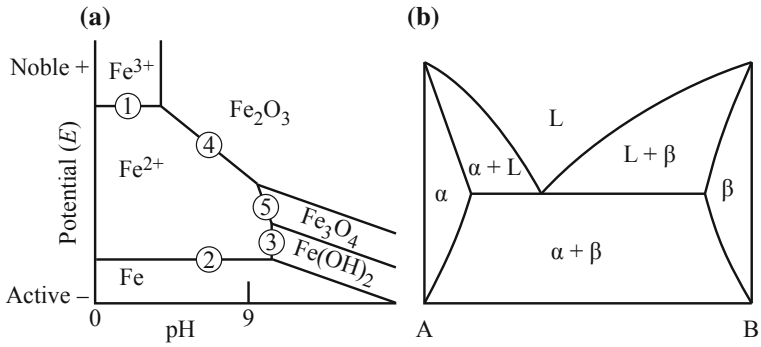

Fig. 15.3 Comparison of (**a**) a Pourbaix diagram with (**b**) a phase diagram. Both diagrams describe regions in which the various phases are thermodynamically stable

diagrams are often drawn for several activities. In the case of line ② in the iron stability diagram:

$$\begin{aligned} E_{Fe^{2+}/Fe} &= -0.44 \text{ V}, a = 1 \text{ mol/kg} \\ &= -0.50 \text{ V}, a = 10^{-2} \text{ mol/kg} \\ &= -0.56 \text{ V}, a = 10^{-4} \text{ mol/kg} \\ &= -0.62 \text{ V}, a = 10^{-6} \text{ mol/kg} \end{aligned}$$

as shown in Fig. 15.4. For any activity of Fe^{2+} in the solution, a horizontal line represents the equilibrium potential, that is, the potential at which Fe^{2+} ion and Fe metal can coexist. Above the line is the region of stability of Fe^{2+}; iron metal at these potentials will tend to corrode and produce Fe^{2+} as the stable species. Below the line, Fe metal is stable, and iron in these conditions will not corrode.

Consider next, line ③, which is a vertical line described by the reaction:

$$Fe^{2+} + 2H_2O = Fe(OH)_2 + 2H^+, \text{ or equivalently, } Fe^{2+} + 2OH^- = Fe(OH)_2.$$

Note that there is no charge transfer in this reaction. Iron is in the +2 valence state on both sides, and there is no change in the oxidation state. This is called an acid–base reaction. Since no charge is transferred, the reaction is independent of potential, hence a vertical line in the stability diagram. The pH is found as follows. Recall that:

$$\Delta G^0 = \sum \nu_p \mu_p^0 - \sum \nu_r \mu_r^0 = -RT \ln \frac{a_p}{a_r} \sum \nu_r \mu_r^0 = -2.3RT \log \frac{a_p}{a_r}. \quad (15.23)$$

Applying this equation to the reaction describing line ③ gives:

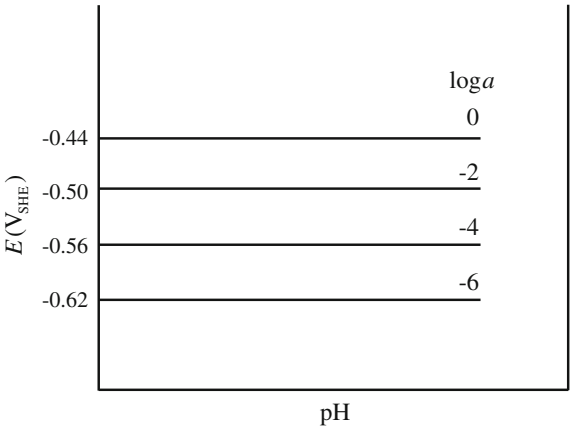

Fig. 15.4 Potential–pH diagram showing the equilibrium for the reaction $Fe = Fe^{++} + 2e^-$ at Fe^{++} activities from 10^{-6} to 1.0

$$\frac{\mu^0_{Fe^{2+}} + 2\mu^0_{H_2O} - \mu^0_{Fe(OH)_2} - 2\mu^0_{H^+}}{2.3RT} = \log \frac{a_{Fe(OH)_2} a^2_{H^+}}{a_{Fe^{2+}} a^2_{H_2O}}. \tag{15.24}$$

Note that there is no acceptor/donor or oxidized/reduced species in this reaction, so we use product/reactant. But since this appears on both sides of the equation, the choice is arbitrary. From the Atlas of Electrochemical Equilibria [1], we find that:

$$\begin{aligned} \mu^0_{H^+} &= 0 \\ \mu^0_{H_2O} &= -56{,}690\,\text{cal/mol} \\ \mu^0_{Fe^{2+}} &= -20{,}310\,\text{cal/mol} \\ \mu^0_{Fe(OH)_2} &= -115{,}586\,\text{cal/mol} \end{aligned}$$

R = 1.986 cal/mole K (8.31 J/mole K). For an iron ion activity, $a_{Fe^{2+}} = 10^{-6}$ mol/kg, substitution of the values for the chemical potentials in Eq. (15.24) into Eq. (15.23) yields pH = 9.65.

A third type of reaction involves both electrons and H^+ and is represented by sloping lines as, for example, lines ④ and ⑤ in Fig. 15.3(a). The reaction for line ④ is given by:

$$Fe_2O_3 + 6H^+ + 2e^- = 2Fe^{2+} + 3H_2O.$$

The sloping line indicates both pH and potential dependence. The potential for line ④ is written as follows:

$$E_{Fe_2O_3/Fe^{2+}} = E^0_{Fe_2O_3/Fe^{2+}} + \frac{RT}{2F} \ln \frac{a_{Fe_2O_3} a^6_{H^+}}{a^2_{Fe^{2+}} a^3_{H_2O}}.$$

Taking $a_{Fe_2O_3} = a_{H_2O} = 1$ mol/kg, we have:

$$\begin{aligned} E_{Fe_2O_3/Fe^{2+}} &= 0.73 - \frac{RT}{2F} \ln a^2_{Fe^{2+}} + \frac{RT}{2F} \ln a^6_{H^+} \\ &= 0.73 - \frac{RT}{F} \ln a_{Fe^{2+}} + \frac{3RT}{F} \ln a_{H^+} \\ &= 0.73 - 0.059 \ln a_{Fe^{2+}} + 3(0.059) \ln a_{H^+} \\ &= 0.73 - 0.059 \ln a_{Fe^{2+}} - 0.177\text{pH}. \end{aligned}$$

Note that the slope of the line is −0.177.

The reaction for line ⑤ is written as follows:

$$Fe_3O_4 + 8H^+ + 2e^- = 3Fe^{2+} + 4H_2O.$$

Assuming unit activities, the potential for line ⑤ is written as follows:

$$E_{Fe_3O_4/Fe^{2+}} = E^0_{Fe_3O_4/Fe^{2+}} + \frac{0.059}{2}\log\frac{a^8_{H^+}}{a^3_{Fe^{2+}}}$$
$$= 0.98 - 0.236\text{pH} - 0.88 \log a_{Fe^{2+}}.$$

Note that the factor in front of the pH term is larger than for line ④ and is reflected in the steeper slope of line ⑤.

We still need to determine E^0. Recall from Eq. (15.19) that:

$$\Delta G^0 = -nFE^0, \quad \text{or} \quad E^0 = -\frac{\Delta G^0}{nF}, \tag{15.25}$$

and from Eq. (15.16):

$$E^0 = \frac{\sum \nu_{ox}\mu^0_{ox} - \sum \nu_{red}\mu^0_{red}}{nF}. \tag{15.26}$$

Applying Eq. (15.26) to reaction ⑤ gives:

$$E^0_{Fe_3O_4/Fe^{2+}} = \frac{\left[\mu^0_{Fe_3O_4} + 8\mu^0_{H^+}\right] - \left[3\mu^0_{Fe^{2+}} - 4\mu^0_{H_2O}\right]}{2F}$$

By convention, $\mu^0_{H^+} = \mu^0_{H_2} = 0$, and

$$\mu^0_{Fe^{2+}} = -20{,}310 \text{ cal/mole},$$
$$\mu^0_{H_2O} = -56{,}690 \text{ cal/mole},$$
$$\mu^0_{Fe_3O_4} = -242{,}400 \text{ cal/mole},$$

and substituting in for F = 96,500 C/eq = 23,060 cal/eq yields $E^0_{Fe_3O_4/Fe^{2+}} = 0.98$ V.

Our diagram so far represents only the anodic half-cell of iron in water. We have not yet considered the cathodic half-cell. Consider the reaction between hydrogen gas and an acid solution:

$$2H^+ + 2e^- = H_2.$$

An equivalent reaction in neutral or alkaline solutions is as follows:

$$2H_2O + 2e^- = H_2 + 2OH^-.$$

Thus, at higher pH where OH^- is predominant over H^+, the second equation is the more appropriate reaction. However, because the two are equivalent (add OH^- to both sides), then:

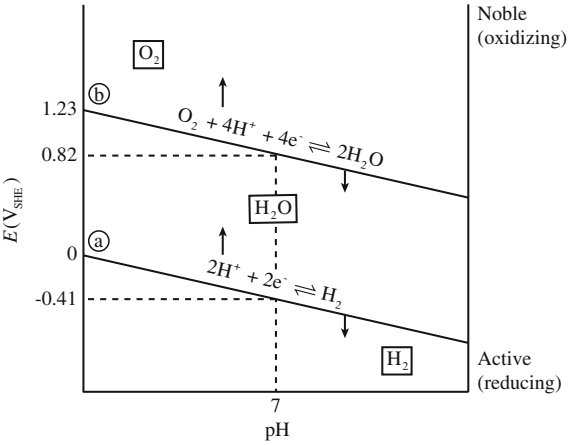

Fig. 15.5 E-pH diagram for water

$$2H^+ + 2e^- = H_2 \qquad ⓐ$$

represents the pH dependence of the half-cell electrode for both. Plotted on a potential–pH diagram shows that $E_{H^+/H_2} = 0$ at pH = 0 ($a_{H^+} = 1$) with a slope of −0.059 V as in Fig. 15.5. For a potential more active than E_{H^+/H_2}, hydrogen is evolved and water is thermodynamically unstable and will decompose. Below the ⓐ line, water is unstable and will decompose to H_2 gas. Above the ⓐ line, water is stable and H_2 (if present) is oxidized to H^+ or H_2O.

As the potential becomes more noble (positive), the oxidation of water becomes thermodynamically feasible:

$$O_2 + 4H^+ + 4e^- = 2H_2O \,(\text{acid})$$

or

$$O_2 + H_2O + 4e^- = 4OH^- (\text{neutral, alkaline})$$

and

$$O_2 + 4H^+ + 4e^- = 2H_2O, \quad \text{or} \quad O_2 + 2H_2O + 4e^- = 4OH^- \qquad ⓑ$$

$$E_{O_2/H_2O} = E^0_{O_2/H_2O} + \frac{0.059}{4}\log\frac{[H^+]^4 p_{O_2}}{a^2_{H_2O}} = 1.23 - 0.059\,\text{pH}. \qquad (15.27)$$

For $p_{O_2} = 1$ atm, $E_{O_2/H_2O} = E^0 - 0.059\,\text{pH}$. For pH = 0, $E = E^0 = 1.226$ V (for unit activity of OH^-). For pH = 14, $E = 0.401$ V. At potentials noble to E_{O_2/H_2O} at any pH, water is unstable and is oxidized to O_2. Below E_{O_2/H_2O}, water is stable and

dissolved oxygen is reduced to water. Note that the two equations are represented by the lines ⓐ and ⓑ, respectively, on the E-pH diagram for water and have the same slope as in Fig. 15.5. Below line ⓐ, the reaction $2H^+ + 2e^- = H_2$ proceeds to the right reducing hydrogen to form hydrogen gas. Above line ⓑ, water is oxidized to form gaseous oxygen and the reaction described by line ⓑ proceeds to the left. Between the lines, the stable form of water is H_2O. So the potential–pH diagram is divided into three regions:

Top: Water is oxidized to form O_2 gas.
Middle: Water is stable and cannot be electrolyzed.
Bottom: H^+ is reduced to form H_2 gas.

The potential–pH diagram in Fig. 15.6 shows the conditions under which corrosion will cause H_2 evolution or will reduce dissolved O_2. Note that when pressure is increased, line ⓑ moves up and line ⓐ moves down, expanding the domain over which water is stable. The superposition of the water E-pH diagram onto the E-pH diagram for iron is shown in Fig. 15.7.

The E-pH diagram can be divided into corrosion, immunity, and passivation domains as in Fig. 15.8. The immunity domain is that in which iron metal is stable in water. The passivation domain is one in which an oxide, hydroxide, hydride, or salt is the solid stable form, but not the metal. The corrosion domain is the one in which the metal ion is the stable form. Consider the anodic and cathodic reactions occurring at points ①, ②, and ③ along the vertical dotted line in Fig. 15.7. Fe^{2+} is stable at point ①, and only one reduction reaction (reduction of oxygen) is possible. Given this situation, some specific corrosion control strategies are implied. First, if the cell is deaerated, thus removing oxygen, then the reduction reaction is suppressed and the anodic reaction cannot proceed. A second strategy is anodic protection in which the potential is increased into the passive region in which the

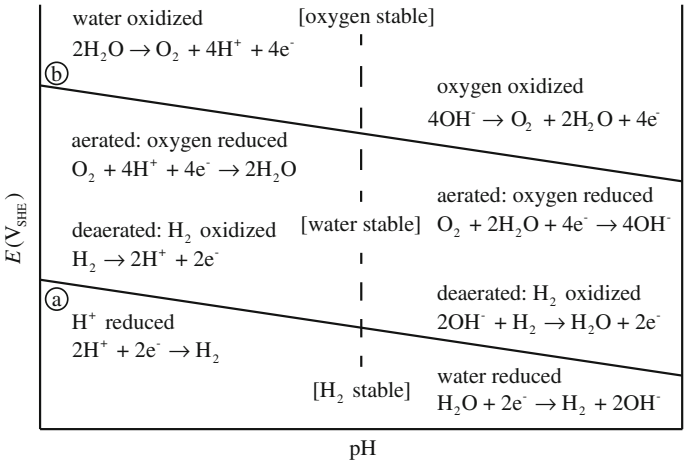

Fig. 15.6 Reactions in the various regions of E-pH diagram for water

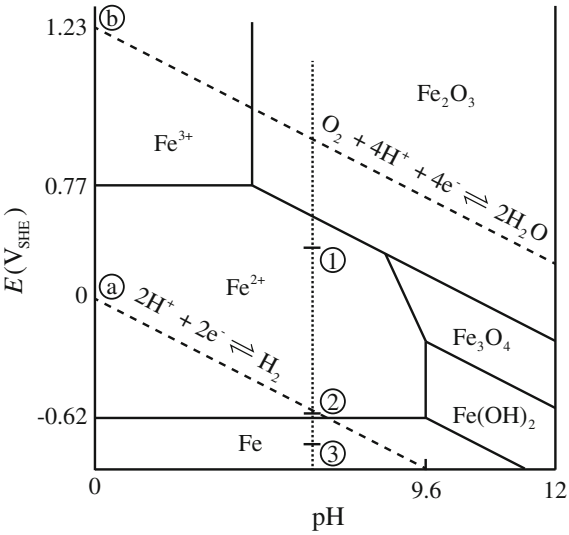

Fig. 15.7 Superposition of E-pH diagram for water onto that for iron

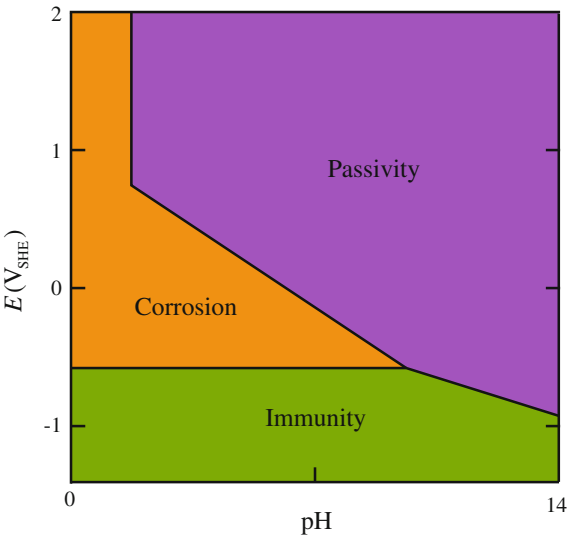

Fig. 15.8 Division of E-pH diagram into domains

passive film will suppress the dissolution of Fe to Fe^{2+}. A third option is to raise the pH into the passive region, achieving the same result as option 2. For point ②, there are two possible reduction reactions, so deaeration would not work in this case. Corrosion control strategies for point ② include increasing the pH, increasing the potential (anodic protection), and decreasing the potential (cathodic protection). Note that decreasing the potential is the better strategy since the magnitude of the decrease is small, compared to a very large increase required to achieve anodic protection. Point ③ is in the stable Fe region so no control measures need to be taken to prevent corrosion of Fe.

While E-pH diagrams are extremely useful for determining the stability of metals in aqueous solutions, they have limitations. These include the following:

- E-pH diagrams are *equilibrium* diagrams, so they tell us nothing about the kinetics of corrosion.
- They are constructed for pure metals. (However, they can be superimposed for approximation of the behavior of alloys.)
- They are dependent on temperature and are useful only at the temperature at which they are constructed.
- It is not always true that when a film forms, it is protective. A protective film must be a poor ionic conductor. So the passive region does not guarantee protection of the underlying metal.
- Most practical corrosion problems involve not only water, but anions such as Cl^- and $SO_4^=$. These must be accounted for separately.
- The pH value indicated in the diagram is that of the solution in direct contact with the metal and is not necessarily that of the bulk solution.

15.3 Kinetics of Corrosion

Imagine the immersion of a metal electrode M into an electrolyte containing M^+ ions, e.g., a Ag electrode in a silver nitrate solution, $AgNO_3$. At the instant of immersion, the metal is electroneutral (uncharged), $q_m = 0$. Since the interface region must then be electroneutral, there must be no net charge on the solution side, $|q_m| = |q_s| = 0$. There is zero potential difference and zero electric field in the interphase region, so there are no electrical effects and no electrochemistry.

Consider the one-step reduction reaction consisting of electron acceptance by an electron acceptor ion, A^+:

$$A^+ + e^- \rightarrow D.$$

Whether this will occur spontaneously will be determined by thermodynamics, in particular,

$$\tilde{\mu}_{A^+} + \mu_{A^+} + FE. \tag{15.28}$$

Since there is no field, FE is zero so $\tilde{\mu}_{A^+} = \mu_{A^+}$, and the interface is at equilibrium only if the chemical potential of A^+ is the same on both sides of the interface. If not, then the gradient of chemical potential acts as the driving force for diffusion.

Consider the movement of the positive ion A^+ from the solution side of the interface to the metal surface (a few tenths of a nm away). As the ion moves from solution to electrode, its potential energy changes. The positive ion must have a certain activation energy for the charge transfer reaction to occur. The process of an ion jumping from solution site to metal site is similar to lattice diffusion where

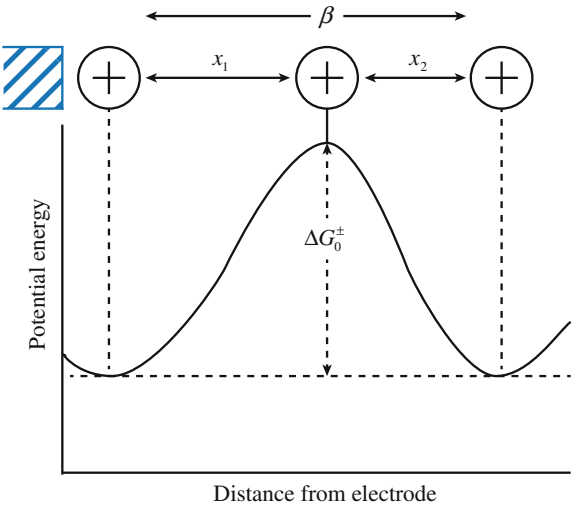

Fig. 15.9 Variation of potential energy with distance from the electrode surface

potential energy barriers must also be overcome as in Fig. 15.9. The frequency with which an ion successfully jumps the energy barrier for diffusion (jump frequency) is as follows:

$$k_c^r = \frac{kT}{h} e^{-\frac{\Delta G_{cr}^{0\pm}}{RT}}, \tag{15.29}$$

where subscript, c, refers to the chemical driving force (no electric field) and the superscript, *r*, refers to the reduction reaction. The pre-exponential term is the vibrational frequency, where k is Boltzmann's constant, h is Planck's constant, and T is temperature. The exponential term is the probability, and $\Delta G_{cr}^{0\pm}$ is the standard free energy of activation, or the change in free energy required to climb to the top of the barrier ($\pm$) when there is zero electric field acting on the ion. The rate of the reduction reaction under zero electric field is the product of the jump frequency and the concentration of electron-acceptor ions, A^+, on the solution side of the interface:

$$v_c^r = k_c^r C_{A^+}. \tag{15.30}$$

Hence, under zero-field conditions, the electron transfer reaction is given by purely chemical kinetics considerations.

The transfer of an electron from the electrode to the electron acceptor has left the metal positively charged (poorer in negative charges) and the solution negatively charged (poorer in positive charges). Charge separation at the interface has created an electrified interface, an electrical field, and a potential difference across the

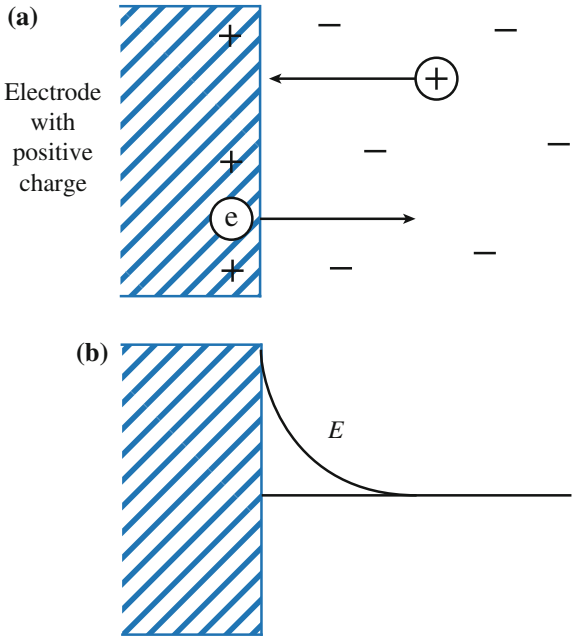

Fig. 15.10 The buildup of positive charge on the electrode surface (**a**) reduces an electric field (**b**) which generates a potential that makes addition of positive charge or removal of electrons more difficult (**c**)

interface. How is the rate of subsequent electron transfer affected by the creation of the electric field? The next electron and next ion must move against the field to react as in Fig. 15.10(a). Clearly, work must be done by the positive ion in order to climb the potential energy barrier as in Fig. 15.10(b). Thus, the reduction reaction consists of moving the ion from its initial state *across* the interface to its final position on the metal. The work in activating this ion is the charge times the potential difference through which the ion is moved to reach the top of the barrier. The total potential difference through which the ion passes is E, but of the contribution of electrostatic work to the standard free energy of activation for the reduction reaction, only a part of E is important. It is that part through which the ion passes to reach the peak of the energy barrier and is described by the symmetry factor, β:

$$\beta = \frac{\text{distance across the double layer to the summit}}{\text{distance across the whole double layer}} \equiv \text{symmetry factor} \qquad (15.31)$$

The electrical contribution to the free energy of activation for the reduction reaction is $+\beta FE$ as shown in Fig. 15.11(a). In a field, the total free energy of activation for reduction is the chemical free energy of activation, $\Delta G_{cr}^{0\pm}$, plus the electrical contribution βFE, yielding:

$$\Delta G_{r}^{0\pm} = \Delta G_{cr}^{0\pm} + \beta FE. \qquad (15.32)$$

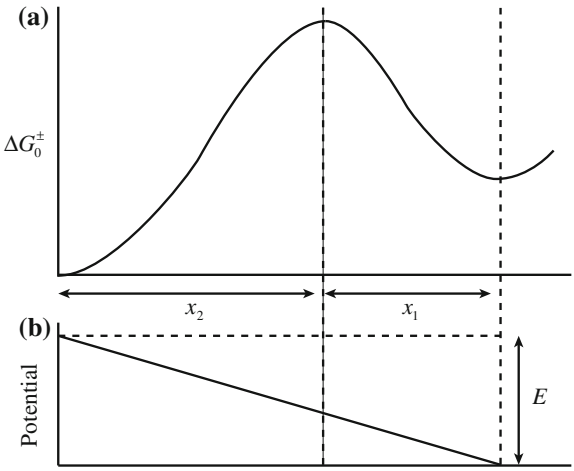

Fig. 15.11 (**a**) Variation of free energy change with distance from the electrode and (**b**) the contribution of the potential at the surface to the magnitude of the energy barrier

The rate of the reduction reaction under an electric field is then as follows:

$$\begin{aligned} v_e^r &= C_{A^+} \frac{kT}{h} e^{-\Delta G_r^{0\pm}/RT} \\ &= C_{A^+} \frac{kT}{h} e^{-\Delta G_{cr}^{0\pm}/RT} e^{-\beta FE/RT} \\ &= k_c^r C_{A^+} e^{-\beta FE/RT}. \end{aligned} \tag{15.33}$$

v_e^r has units of moles of positive ions reacting per second by crossing a unit area of the interface, and the subscript, e, denotes the reaction under an electric field. Multiplying by charge per mole, F, gives the current density:

$$\begin{aligned} i_r &= F v_e^r \\ &= F k_c^r C_{A^+} e^{-\beta FE/RT}, \end{aligned} \tag{15.34}$$

in units of A/cm^2. Equation (15.34) shows the link between the electric field and the rate of electron transfer across the interface. Small changes in E produce large changes in i. For example, for $\beta \sim 1/2$, a potential change of 0.12 V produces a change in i by a factor of 10. Thus, if a metal is not connected to any other source of charge, every reduction of A^+ ions:

- Charges the metal more positively and the solution more negatively,
- Increases the potential difference and the field across the interface,
- Increases the electrical work of activating an ion to the top of the barrier,
- Decreases the electrical factor $e^{-\beta FE/RT}$, and
- Reduces the rate of the reduction reaction.

According to this picture, charge leakage should stop after some time due to the buildup of such a large potential difference. But this does not happen. We have not considered the reverse reaction, oxidation:

$$D \rightarrow A^{+} + e^{-}.$$

If the directed field hinders the ion transfer from solution to electrode because the ion is moving against the field, then it helps the reverse reaction because the positive ion moves with the field which acts to reduce the work required to move it. If the positive ion has to be activated through a potential difference of βE in the forward direction (solution to metal) (Fig. 15.12(a)), it has to be activated through the remainder $(1 - \beta)E$ in the oxidation reaction as in Fig. 15.12(b). So the electrical work of activation for oxidation is $F[(1 - \beta)E]$, and the rate of oxidation is as follows:

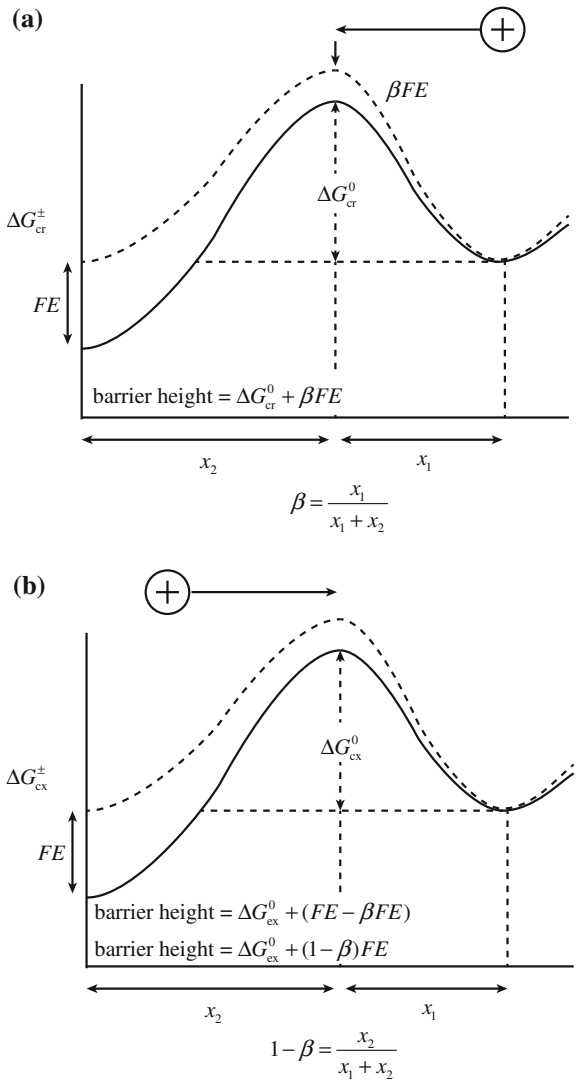

Fig. 15.12 Contribution of the potential to the energy barrier for (**a**) reduction and (**b**) oxidation

$$v_{\mathrm{e}}^{\mathrm{x}} = k_{\mathrm{c}}^{\mathrm{x}} C_{\mathrm{D}} \mathrm{e}^{(1-\beta)FE/RT}, \tag{15.35}$$

and the current density is as follows:

$$\begin{aligned} i_{\mathrm{x}} &= F v_{\mathrm{e}}^{\mathrm{x}} \\ &= F k_{\mathrm{c}}^{\mathrm{x}} C_D \mathrm{e}^{(1-\beta)FE/RT}. \end{aligned} \tag{15.36}$$

So, as the excess positive charge on the metal builds up and decreases the reduction rate, the reverse reaction rate increases by pumping electrons into the metal, decreasing the positive charge, and negating the tendency to stop the reduction reaction. If no external current source is applied, the reactions will just balance. The potential at which the currents become equal and the charges on the metal and in solution become constant (as well as the electric field) is the equilibrium (reversible) potential, E^{e}. At equilibrium, the oxidation and reduction reactions continue to occur, but at the same rate, the currents are equal in magnitude and opposite in direction:

$$i_{\mathrm{r}} = F k_{\mathrm{c}}^{\mathrm{r}} C_{\mathrm{A}^+} \mathrm{e}^{-\beta FE^{\mathrm{e}}/RT} = i_{\mathrm{x}} = F k_{\mathrm{c}}^{\mathrm{x}} C_{\mathrm{D}} \mathrm{e}^{(1-\beta)FE^{\mathrm{e}}/RT}. \tag{15.37}$$

Since the oxidation and reduction rates are equal, the magnitude can be designated by a single term, the *equilibrium exchange current density*, i_0, such that:

$$i_0 = i_{\mathrm{r}} = F k_{\mathrm{c}}^{\mathrm{r}} C_{\mathrm{A}^+} \mathrm{e}^{-\beta FE^{\mathrm{e}}/RT} = i_{\mathrm{x}} = F k_{\mathrm{c}}^{\mathrm{x}} C_{\mathrm{D}} \mathrm{e}^{(1-\beta)FE^{\mathrm{e}}/RT}. \tag{15.38}$$

The exchange current density reflects the kinetic properties of the particular interfacial system and can vary from one reaction to another and from one electrode to another by orders of magnitude. It cannot be measured directly because there is no *net* current to measure. A net flow (or drift) of electrons is produced only when the interface is no longer at equilibrium. The non-equilibrium drift current density is the difference between reduction and oxidation currents:

$$i = i_{\mathrm{x}} - i_{\mathrm{r}} = F k_{\mathrm{c}}^{\mathrm{x}} C_{\mathrm{D}} \mathrm{e}^{(1-\beta)FE/RT} - F k_{\mathrm{c}}^{\mathrm{r}} C_{\mathrm{A}^+} \mathrm{e}^{-\beta FE/RT}, \tag{15.39}$$

where $E \neq E^{\mathrm{e}}$ and is the potential difference across the interface. We can write E as follows:

$$E = E_{\mathrm{e}} + \Delta E = E^{\mathrm{e}} + \eta, \tag{15.40}$$

where η is the overpotential, which is a measure of the departure from equilibrium potential. For an externally driven electrochemical cell, the overpotential is the potential difference that drives the current; it is the current-producing potential. But if the system is a self-driven cell, then the current driven through the external load generates an excess potential; this is the current-produced potential. The term overpotential is used to refer to both the current-producing potential in a driven

system and to the current-produced potential in a self-driving cell. The net current density is then as follows:

$$i = \left\{ Fk_c^x C_D e^{(1-\beta)FE^e/RT} \right\} e^{(1-\beta)F\eta/RT} - \left\{ Fk_c^r C_{A^+} e^{-\beta FE^e/RT} \right\} e^{-\beta F\eta/RT} \quad (15.41)$$

But the terms inside the brackets are the expressions for the equilibrium exchange current density, i_0. Therefore:

$$i = i_0 \left[e^{(1-\beta)F\eta/RT} - e^{-\beta F\eta/RT} \right]. \quad (15.42)$$

This is the Butler–Volmer equation. It shows how the current density across a metal–solution interface depends on the difference η between the actual non-equilibrium and equilibrium potentials as in Fig. 15.13. Note that small changes in η produce large changes in i.

There are several special cases that result in more simplified forms of this equation. If we let the symmetry factor $\beta = 1/2$, then Eq. (15.42) becomes:

$$i = i_0 \left[e^{F\eta/2RT} - e^{-F\eta/2RT} \right], \quad (15.43)$$

and since $\frac{e^x - e^{-x}}{2} = \sinh x$ then $i = i_0 \sinh \frac{F\eta}{2RT}$ and a plot of i versus η yields a symmetric curve as in Fig. 15.14(a), where oxidation and reduction reactions proceed at equal rates (currents) for equal overpotentials. The practical significance

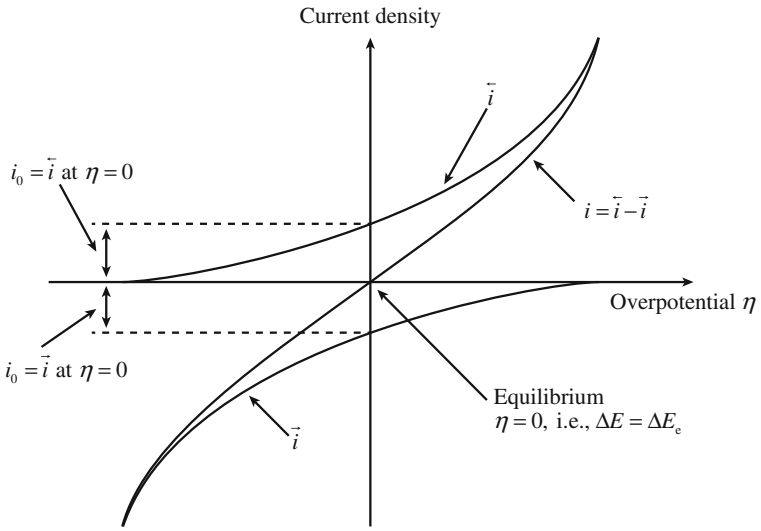

Fig. 15.13 Current density versus overpotential showing that the point of zero overpotential corresponds to zero current and occurs when the surface electrode is at equilibrium (after [2])

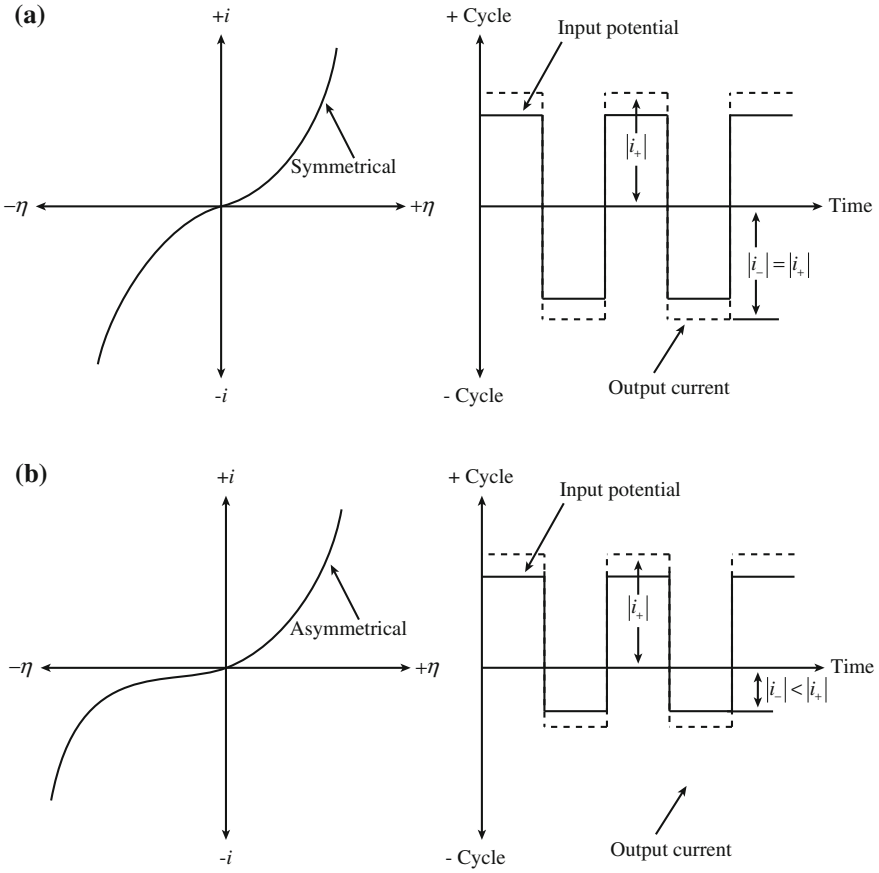

Fig. 15.14 (**a**) When the i versus η relation is perfectly symmetrical ($\beta = 1/2$), the interface cannot rectify the current responding to a periodically varying potential. (**b**) When the symmetry factor $\beta \neq 1/2$, the i versus η curve is asymmetrical and there is a Faradaic rectification effect or a periodically varying potential (after [2])

of this behavior is that the interface can only be rectifying if the symmetry factor $\beta \neq ½$ as in Fig. 15.14(b).

We now consider two limiting cases of the Butler–Volmer equation; one in which the overpotential is large and one in which the overpotential is small. When η is large positive, $e^{(1-\beta)F\eta/RT} \gg e^{-\beta F\eta/RT}$ and the corrosion current, i, is as follows:

$$i \simeq i_x = i_0 e^{(1-\beta)F\eta/RT}. \tag{15.44}$$

Taking the natural log of both sides yields:

$$\eta = -\frac{RT}{(1-\beta)F}\ln i_0 + \frac{RT}{(1-\beta)F}\ln\, i. \tag{15.45}$$

If η is large negative:

$$i \simeq i_{\mathrm{r}} = -i_0 \mathrm{e}^{-\beta F\eta/RT}, \quad \text{and} \quad \eta = \frac{RT}{\beta F}\ln i_0 - \frac{RT}{\beta F}\ln i. \tag{15.46}$$

The case with $\eta > 0$ is termed anodic polarization, and η is the anodic overpotential, η_{A}. The case with $\eta < 0$ is cathodic polarization, and η is the cathodic overpotential, η_{C}. We can write the anodic and cathodic overpotentials as Tafel equations:

$$\begin{aligned} \eta_{\mathrm{A}} &= A + B\ln i_A \\ \eta_{\mathrm{C}} &= A' + B'\ln i_{\mathrm{C}}, \end{aligned} \tag{15.47}$$

where

$$\begin{aligned} A &= \frac{-RT}{(1-\beta)F}\ln i_0; \quad & B &= \frac{RT}{(1-\beta)F} \\ A' &= \frac{RT}{\beta F}\ln i_0; & B' &= \frac{-RT}{\beta F}. \end{aligned} \tag{15.48}$$

Hence, at large $|\eta|$ ($\geq$ 0.12 V), the overpotential is proportional to ln i as in Fig. 15.15. Note also that back extrapolation of the Tafel equations yields the exchange current density, i_0. The Tafel equations are central kinetic expressions in electrochemistry.

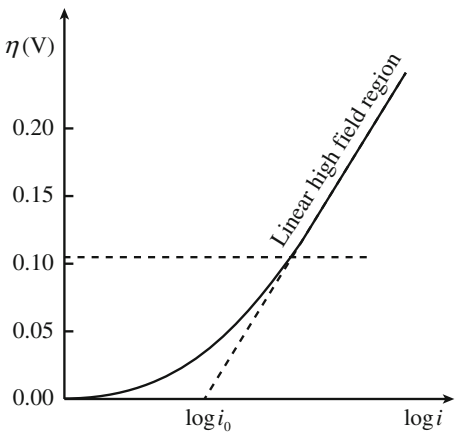

Fig. 15.15 Tafel line showing the exponential relationship at high overpotentials, yielding a linear relationship between η and log i linear (after [2])

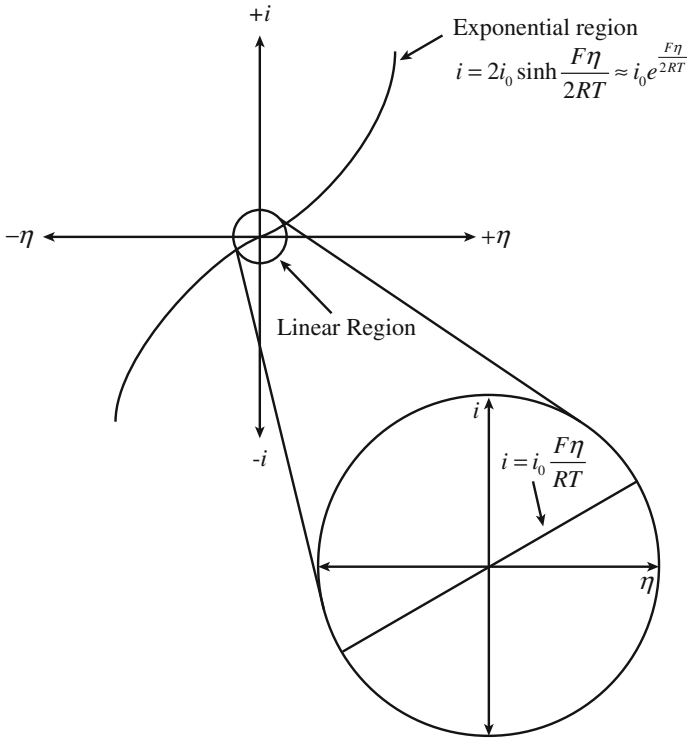

Fig. 15.16 At small overpotentials, the i versus η relationship is linear (after [2])

The second case is for very small η, in which the exponentials in Eq. (15.42) are small and expanding them and retaining only the first two terms of each exponential term yields:

$$\begin{aligned} i &\simeq i_0 \left[1 + \frac{(1-\beta)F\eta}{RT} - 1 + \frac{\beta F\eta}{RT} \right] \\ &\simeq i_0 \frac{F\eta}{RT}. \end{aligned} \tag{15.49}$$

This simplified expression is valid for $\eta \leq 0.01$ V. Note also that i is greater than zero for $\eta = \eta_A > 0$ and i is less than zero for $\eta = \eta_C < 0$. Note also that the current density is proportional to the overpotential as in Fig. 15.16; this is termed the linear region. Equation (15.49) can be written as follows:

$$i = \sigma_{m/s}\eta, \tag{15.50}$$

where $\sigma_{m/s}$ is the conductivity of the metal–solution interface.

15.4 Polarization

As described in Sect. 15.3, the potential of the electrode must be different from the equilibrium value for a net current to flow. The potential difference is the overpotential, η, and the relationship between the values of the net current density resulting from application of η constitutes a polarization curve. Activation polarization refers to the case in which the reaction at the electrode surface requires an activation energy in order to go. Activation polarization of any kind increases with current density, i, in accord with the Tafel equation. This is to be distinguished from other types of polarization such as concentration polarization and resistance polarization.

If we only consider a single electrode and large overpotentials, then the overpotential is related to the current by the Tafel equations (15.47). For anodic polarization using log rather than ln:

$$\begin{aligned} \eta_A &= A_A + B_A \log i_A \\ A_A &= -\frac{2.3RT}{(1-\beta)F}\log\, i_0; \quad B_A = \frac{2.3RT}{(1-\beta)F}, \end{aligned} \tag{15.51}$$

and for cathodic polarization:

$$\begin{aligned} \eta_C &= A_C + B_C \log i_C \\ A_C &= \frac{2.3RT}{\beta F}\log\, i_0; \quad B_C = -\frac{2.3RT}{\beta F}, \end{aligned} \tag{15.52}$$

as shown in Fig. 15.17. The situation describing single electrode kinetics is clear and uncomplicated. However, what happens when we consider anodic and cathodic processes occurring simultaneously. This is the subject of mixed potential theory.

15.4.1 Mixed Potential Theory

Mixed potential theory consists of two hypotheses:

1. Any electrochemical reaction can be divided into two or more partial oxidation and reduction reactions.
2. There can be no net accumulation of charge during an electrochemical reaction.

From this, it follows that the total rate of oxidation must equal the total rate of reduction. Consider the immersion of Zn in an HCl solution as in Fig. 15.18. Zinc corrodes rapidly with evolution of hydrogen gas. If a piece of zinc is immersed in HCl containing Zn ions, the electrode potential cannot simultaneously be at two reversible potentials (Zn and H_2). The only point in the entire system where the oxidation rate equals the reduction rate is at the intersection point, E_{corr}, as in

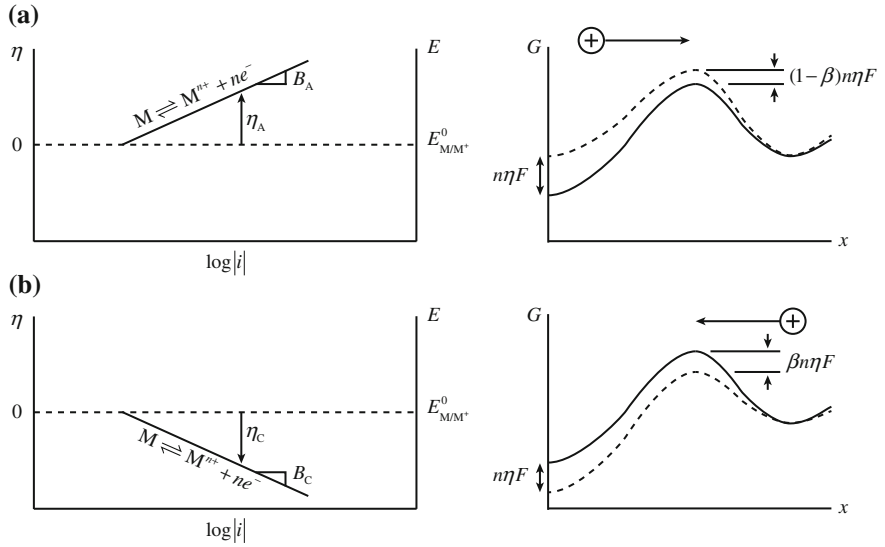

Fig. 15.17 Single electrode polarization curves and accompanying activation energy model for (**a**) anodic and (**b**) cathodic reactions

Fig. 15.18 Corrosion of zinc in HCl

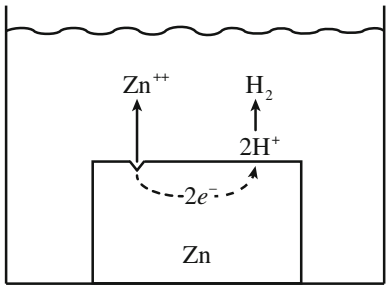

Fig. 15.19(a). Why must this be the potential of the cell? Because (1) charge must be conserved and (2) the entire Zn surface must be at a constant potential. Since it is an excellent conductor and since the H^+ reduction reaction occurs on the surface, it must be occurring at the same potential. The current density at this point corresponds to the rate of zinc dissolution as well as the rate of H_2 evolution. The reactions polarize each electrode in the direction of the other; zinc is polarized anodically and H is polarized cathodically.

If we put Fe into HCl, will it corrode faster or slower than Zn? Compare the polarization plot for Zn (Fig. 15.19(a)) to that for Fe (Fig. 15.19(b)). Note the exchange current densities for Fe/Fe^{++} and H/Fe compared to Zn/Zn^{++} and H/Zn. Although Zn has a higher tendency to corrode in acid due to its higher driving force (lower equilibrium potential compared to iron), Zn is a poor catalyst for H reduction. Thus, the corrosion rate of Fe is greater than Zn. This illustrates the fact

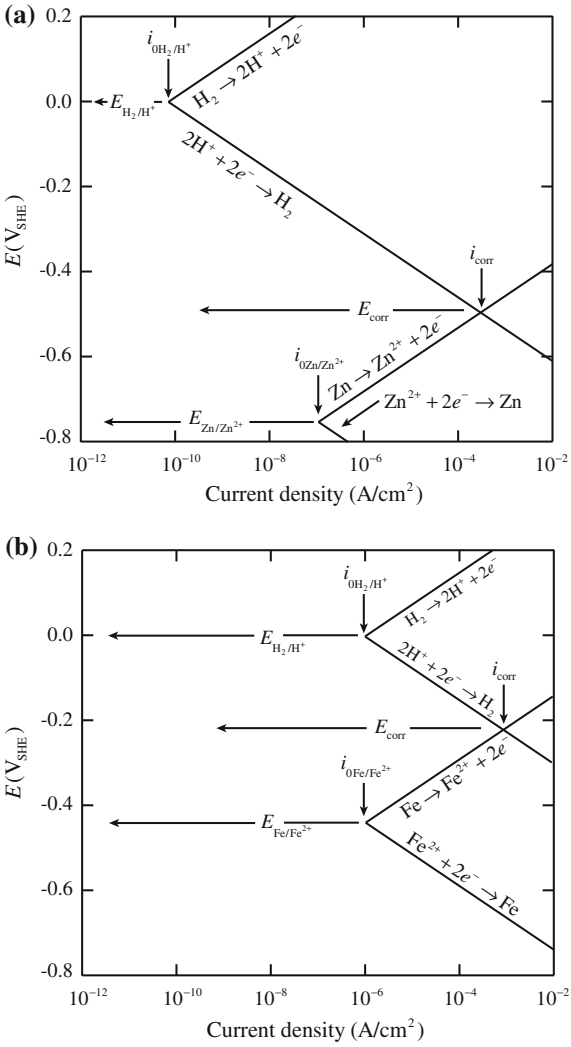

Fig. 15.19 Anodic and cathodic half-cell reactions present simultaneously on (**a**) a corroding zinc surface and (**b**) a corroding Fe surface (after [3])

that kinetics does not necessarily follow thermodynamics. That is, the corrosion rate of the system with a higher driving force is actually smaller. The variation in exchange current densities on various metal surfaces is illustrated in Fig. 15.20.

15.4.2 Galvanic Couples

Consider the coupling of an active metal to a noble metal, e.g., Zn and Pt as in Fig. 15.21. Pt cannot be oxidized, and there is no Pt^+ in solution to be reduced. With

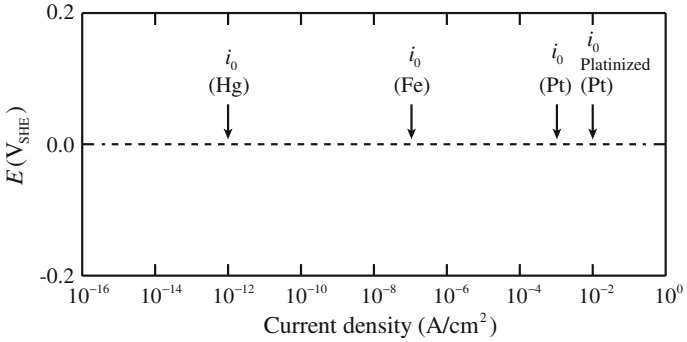

Fig. 15.20 Effect of the metal surface on the hydrogen–hydrogen ion exchange current density (after [3])

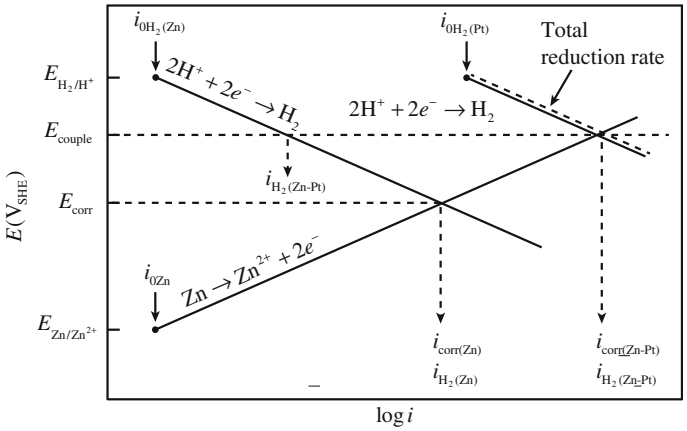

Fig. 15.21 Polarization diagram for a galvanic couple between an active and noble metal (after [3])

Zn and Pt uncoupled, $i_{0_{Zn/Zn^{++}}} = 10^{-6}$ A/cm^2 and $i_{0_{H/Zn}} = 10^{-6}$ A/cm^2. But coupling Zn to Pt results in a much larger value of $i_{cathodic}$ or hydrogen evolution. Why? Pt is a much better catalyst for H_2 evolution so electrons are delivered to the Pt surface where $i_{0_{H/Pt}} 10^{-3}$ A/cm^2. There is one oxidation reaction, $Zn \rightarrow Zn^{++} + 2e^-$, and one reduction reaction, $2H^+ + 2e^- \rightarrow H_2$, but at *two* locations. So there are two exchange current densities, $i_{0_{H/Zn}}$ and $i_{0_{H/Pt}}$ and $i_{0_{total}} = i_{0_{H/Zn}} + i_{0_{H/Pt}}$.

Note that the increase in the corrosion rate of Zn observed when this metal is coupled to Pt is the result of the higher exchange current density for hydrogen evolution on the Pt surface. It is not due to the more noble reversible potential of the Pt/Pt^+ electrode. To test this idea, compare a Zn/Au couple to a Zn/Pt couple. Figure 15.22 shows that since $i_{0_{H/Au}} \ll i_{0_{H/Pt}}$, the corrosion rate increase upon

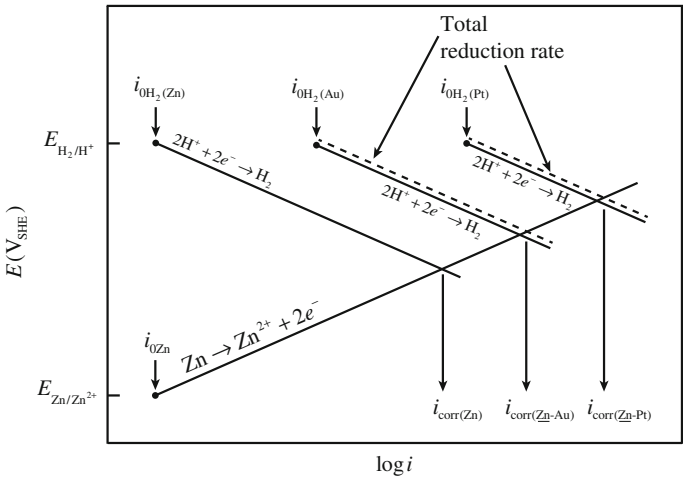

Fig. 15.22 Effects of platinum and gold galvanically coupled to zinc in dilute acid (after [3])

coupling to Au is less than that when coupling to Pt; $i_{corr(Zn)} < i_{corr(Zn-Au)} < i_{corr(Zn-Pt)}$. The reason why gold produces a less severe galvanic effect is not related to its reversible potential, but rather to the fact that it has a lower hydrogen exchange current density than does platinum.

Now, consider the coupling of two active metals: Zn and Fe as in Fig. 15.23(a). The polarization diagram is shown in Fig. 15.23(b). Upon coupling Zn to Fe, the following occurs as in Fig. 15.23(c):

(a) i_{Zn} increases (point a' → point a),
(b) i_{Fe} decreases (point b' → point b),
(c) $i_{H/Zn}$ decreases (point c' → point c), and
(d) $i_{H/Fe}$ increases (point d' → point d).

The Zn electrode is no longer at equilibrium since $i_{anodic} > i_{cathodic}$ (point a > point c) as in Fig. 15.24(a). For the Fe electrode, the reverse is true since $i_{anodic} < i_{cathodic}$ (point b < point d) as in Fig. 15.24(b). Fe is cathodically protected by making it act as the cathode. Since H^+ reduction on the surface of Fe is the main reaction, the corrosion of Fe is reduced. In this case, Zn is acting as a sacrificial anode. In general, in a couple of two active metals, the more active metal becomes the anode and cathodically protects the less active metal.

Finally, consider the corrosion reaction described in Fig. 15.23 when an oxidizer such as Fe^{3+} is added to the solution, as shown in Fig. 15.25. Note that there are now three redox systems: metal–metal ion, hydrogen ion–hydrogen gas, and ferric–ferrous ions. The basic principles of mixed potential theory still apply. At steady state, the total rate of oxidation must equal the total rate of reduction to satisfy the charge conservation principle, and E_{corr} is determined where the two are equal. Starting at the most noble half-cell electrode potential, $E_{Fe^{3+}/Fe^{2+}}$, and proceeding in the

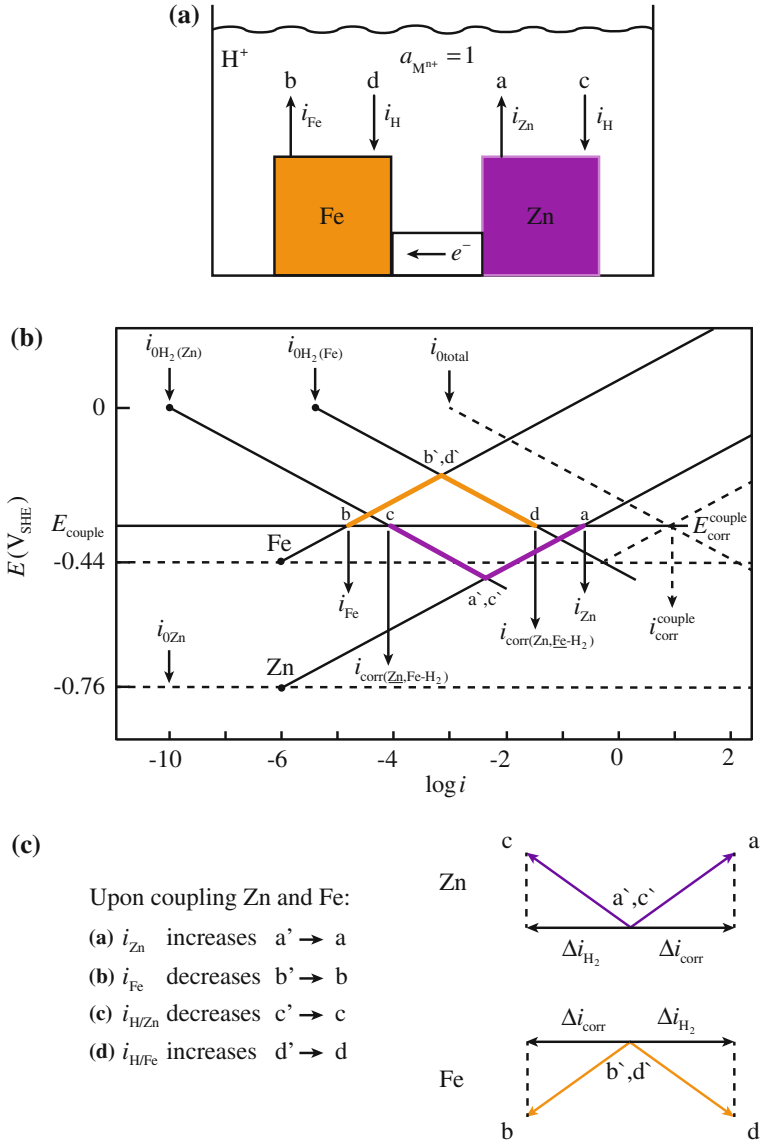

Fig. 15.23 Galvanic coupling of two active metals: (**a**) Fe and Zn in acid, (**b**) polarization diagram, (**c**) exchange current densities (after [2])

negative (active) direction, the total reduction current density for hydrogen reduction E_{H_2/H^+} is reached, at which point the reduction current density for hydrogen must be added. The total reduction current density then follows the parallel dashed line marked "total reduction" until the half-cell electrode potential for metal oxidation is reached, when another increase occurs due to reduction of M^+ to M.

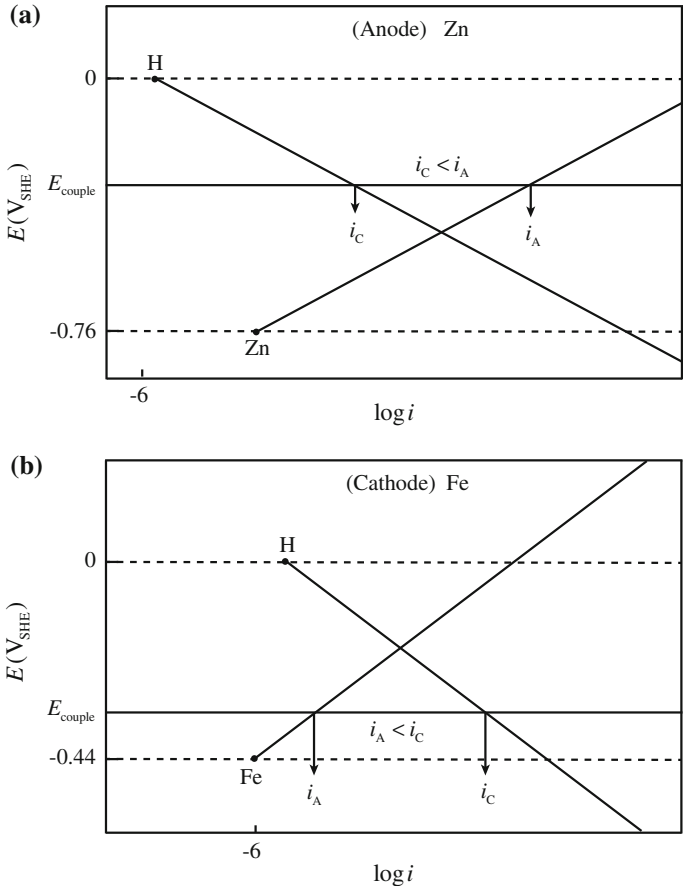

Fig. 15.24 Single electrode polarization diagrams for (**a**) Zn and (**b**) Fe in Fig. 15.23

The total oxidation current is determined in a similar manner, starting with the most active half-cell electrode potential in the system, E_{M/M^+}. The total oxidation current density follows the line to more positive potentials for oxidation of M to M^+ until E_{H_2/H^+} is reached, at which point a current density for oxidation of H_2 to H^+ must be included. The total current density for oxidation follows the parallel line marked "total oxidation" until $E_{Fe^{3+}/Fe^{2+}}$ is reached and another addition is included for oxidation of Fe^{2+} to Fe^{3+}.

The corrosion potential, E_{corr}, is defined in Fig. 15.25 by the intersection of the total oxidation and total reduction lines where the two are equal, fulfilling the charge conservation principle. Because $M \rightarrow M^+ + e^-$ is the only oxidation reaction present, the total oxidation current density is also the corrosion rate, i_{corr}. However,

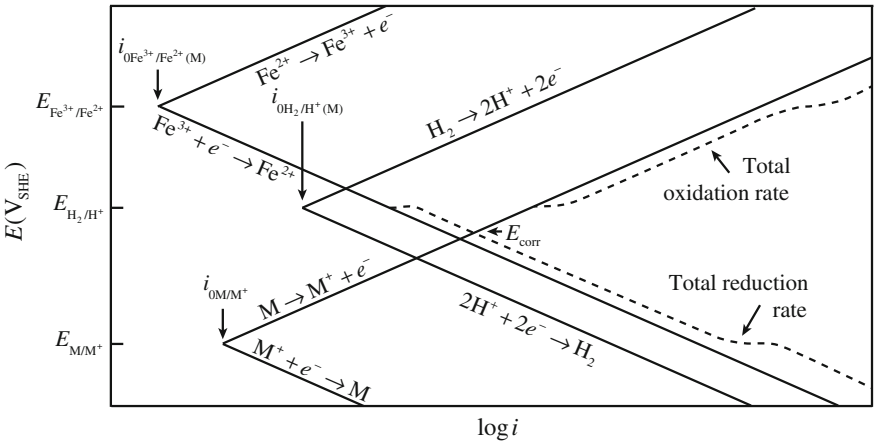

Fig. 15.25 Determination of the corrosion potential for a corroding metal M exposed to an acid solution with a second oxidizer, Fe^{3+}/Fe^{2+} (after [2])

both Fe^{3+} and H^+ are being reduced in this system, and the sum of their rates, $i_{Fe^{3+}\rightarrow Fe^{2+}} + i_{H^+\rightarrow H_2}$, is equal to total reduction, which is in turn equal to total oxidation, or i_{corr}:

$$i_{corr} = i_{Fe^{3+}\rightarrow Fe^{2+}} + i_{H^+\rightarrow H_2}.$$

The two reduction rates are defined in Fig. 15.25 by the intersection of the horizontal equipotential line at E_{corr} with the polarization curves for the reduction rates of each half-cell reaction.

15.4.3 Anode/Cathode Area Ratio

Until now, it has been assumed that anodic and cathodic areas were equal. But what if the areas are unequal? The issue of anode and cathode areas for three different cases is shown in Fig. 15.26. In the polarization diagram, E is plotted versus the logarithm of the current, log I, not the current density, log i. Although the exchange current density may remain the same, the exchange current changes. As the cathode area increases relative to the anode, the cathodic current will drive the anodic current higher so more oxidation must occur at the anode. Increasing the area, A, of the cathode displaces the H_2/Pt curve to the right, increasing the corrosion of Zn. Since:

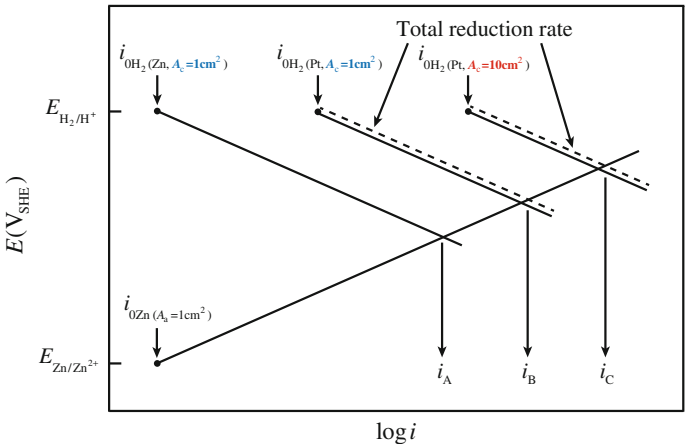

Fig. 15.26 Effect of cathode surface area on the galvanic interaction between zinc and platinum in dilute acid solution (after [2])

$$i_A A_A = i_C A_C, \tag{15.53}$$

then

$$i_A = i_C \frac{A_C}{A_A}. \tag{15.54}$$

Also, since $I_A = I_C$ always, then $|I_A| = |I_C|$ is greater when $A_C/A_A > 1$. So if we increase A_C/A_A, we increase i_A. An extreme case of this process is pitting corrosion.

15.4.4 Multiple Cathodic Reactions

Consider the association between the Pourbaix and polarization diagrams as shown for Fe in Fig. 15.27. This picture is correct for a deaerated electrolyte because in this case, the only reduction reaction possible is that of H^+. But suppose the solution is aerated. Depending upon the potential, oxygen gas may need to be considered. In addition to the reduction reaction $2H^+ + 2e^- = H_2$, we may have $1/2O_2 + 2H^+ + 2e^- = H_2O$. Figure 15.28 shows the effect of addition of oxygen to the solution containing Fe on E_{corr} and i_{corr}. Note that both E_{corr} and i_{corr} increase as a result of aeration.

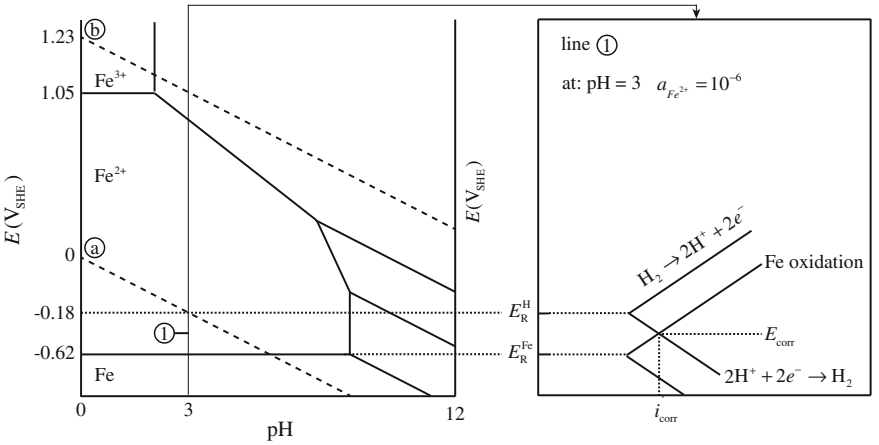

Fig. 15.27 Association between Pourbaix and polarization diagrams in the active region for iron

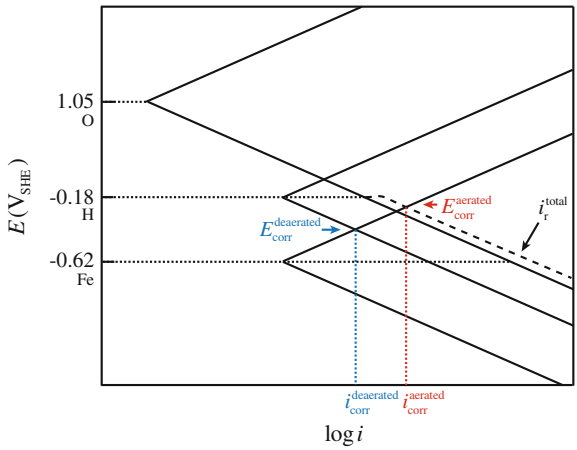

Fig. 15.28 Effect of multiple reduction reactions on the corrosion of iron in acid

15.4.5 Other Types of Polarization

Two other types of polarization of importance in alloys used in reactor systems are concentration polarization and resistance polarization. Consider the evolution of hydrogen at an electrode. At low reduction rates, the distribution of hydrogen ions in the solution adjacent to the electrode surface is relatively uniform. But at very high reduction rates, the region adjacent to the electrode surface will become depleted of H^+ ions. Further increases in the reduction rate will be limited by the diffusion rate of hydrogen ions to the electrode surface. The limiting rate is the limiting diffusion current density, i_L. The same can be true for anodic dissolution where the rate of removal of anodic products (dissolved cations) does not increase

proportionally with the dissolution current and a disproportionate anodic overpotential is required to further increase the rate of dissolution.

The situation is one where the charge transfer reaction is in virtual equilibrium, but the interfacial concentration, C, of the electron acceptor M^{n+} is not the bulk value, C_0, but $C < C_0$. If a current is passing through the interfaces, what is the potential difference across the interface? For solutions near equilibrium (no activation polarization), the current is zero and the potential difference across the interface is given by the Nernst equation:

$$E_e = E^0 + \frac{RT}{nF} \ln\, C_0. \tag{15.55}$$

What concentration should be used in Eq. (15.55) for the potential corresponding to a current density of i? It cannot be C_0 because we know that $C < C_0$, so:

$$E = E^0 + \frac{RT}{nF} \ln\, C. \tag{15.56}$$

This says that the passage of current has made the potential depart from the zero current value, E_e. Thus, $E - E_e$ is a potential difference produced by a *concentration change* at the interface and is known as the concentration overpotential, η_{conc}. The rate of dissolution is i/nF and, from Fick's second law, is equal to $(D[C - C_0])/\delta$, where D is the diffusion coefficient, C and C_0 are the ionic concentrations in the electrode surface and in the bulk, respectively, and δ is the thickness of the diffusion layer. From the Nernst equation, the overpotential, or polarization arising from concentration effects, η_{conc}, is as follows:

$$\eta_{conc} = E - E_e = \frac{RT}{nF} \ln \frac{C}{C_0}, \tag{15.57}$$

and since:

$$C = C_0 - \frac{i\delta}{DnF}, \tag{15.58}$$

then:

$$\eta_{conc} = \frac{RT}{nF} \ln \left(1 - i \frac{\delta}{DC_0 nF}\right). \tag{15.59}$$

As $\eta \longrightarrow \infty$, the critical limiting or diffusion current density is given by:

$$i_L = \frac{DC_0 nF}{\delta}. \tag{15.60}$$

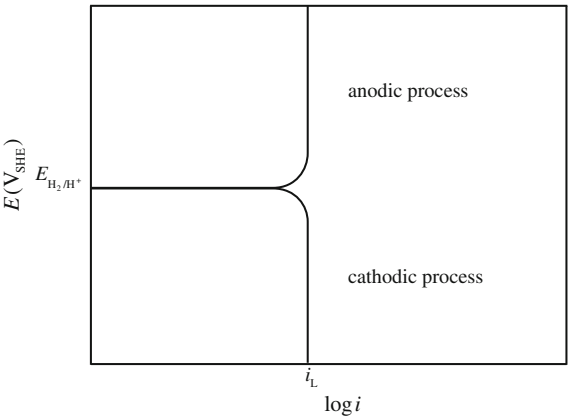

Fig. 15.29 Concentration polarization diagram in the absence of activation polarization

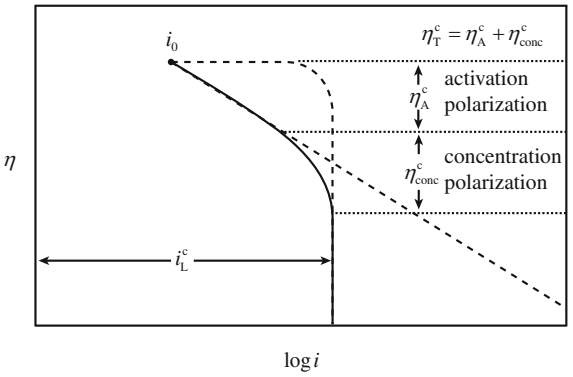

Fig. 15.30 Polarization diagram with combined activation and concentration polarization (after [3])

The potential change resulting from concentration polarization can be expressed as follows:

$$\eta_{conc} = \frac{2.3\,RT}{nF} \log \frac{i_L - i_A}{i_L}, \tag{15.61}$$

where i_A is the externally applied current density. The limiting current density is shown in Fig. 15.29 in the absence of activation polarization. Note that when $i_A = i_L$, $\eta \rightarrow \infty$, and when $i_C = i_L$, $\eta \rightarrow -\infty$. Usually, activation and concentration polarization both occur at an electrode. At low reaction rates, activation polarization controls, while at high reaction rates, concentration polarization becomes controlling. The total polarization of the electrolyte is the sum of the contributions of activation and concentration polarization, as shown in Fig. 15.30. The total anodic and cathodic polarization is then the sum of Eq. (15.61) and either Eq. (15.51) or Eq. (15.52):

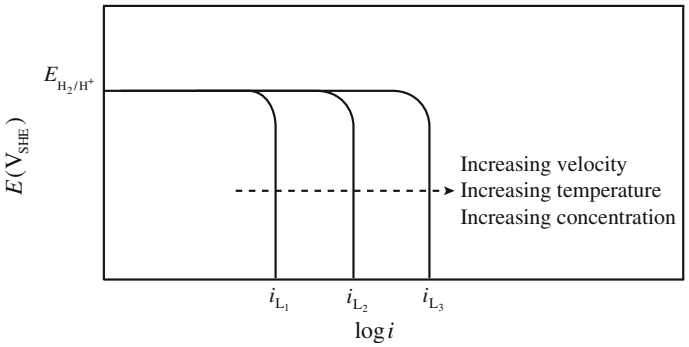

Fig. 15.31 Effect of different solution conditions on the limiting current density in concentration polarization (after [3])

$$\eta_A^T = \frac{2.3\,RT}{(1-\beta)nF}\log\frac{i}{i_0} + \frac{2.3\,RT}{nF}\log\frac{i_L^A - i}{i_L^A}$$
$$\eta_C^T = -\frac{2.3\,RT}{\beta nF}\log\frac{i}{i_0} - \frac{2.3\,RT}{nF}\log\frac{i_L^C - i}{i_L^C}. \tag{15.62}$$

The limiting current density is a function of agitation, temperature, concentration, and position of the anode, as shown in Fig. 15.31. Consider a metal immersed in a corrosive system in which the reduction process is under diffusion control as illustrated in Fig. 15.32(a). Note that with increasing solution velocity (agitation), the corrosion rate increases up to point D. However, as velocity is increased further, the reduction reaction becomes activation-controlled. As a consequence, the corrosion rate becomes independent of velocity at very high velocities as in Fig. 15.32(b).

Resistance polarization is the third type of polarization that can occur on electrodes in aqueous solution. An electrolyte through which a current is passing will contribute to the overpotential by a factor:

$$\eta_R = i_A \times R, \tag{15.63}$$

where i_A is the current density, R is the resistance of the path travelled by the current ($\rho L/A$), ρ is the solution resistivity, L the path length, A the area, and η_R is the resistance polarization, otherwise known as the *IR* drop as in Fig. 15.33. The IR drop may be high in poorly conducting electrolytes or in cases where a film forms. Bubbles and cavities also add to resistance. The total overpotential is then as follows:

$$\eta_T = \eta_A + \eta_{conc} + \eta_{R.} \tag{15.64}$$

The shape of the polarization curve is then more complicated as it is composed of three separate effects: activation energy requirements, concentration effects, and

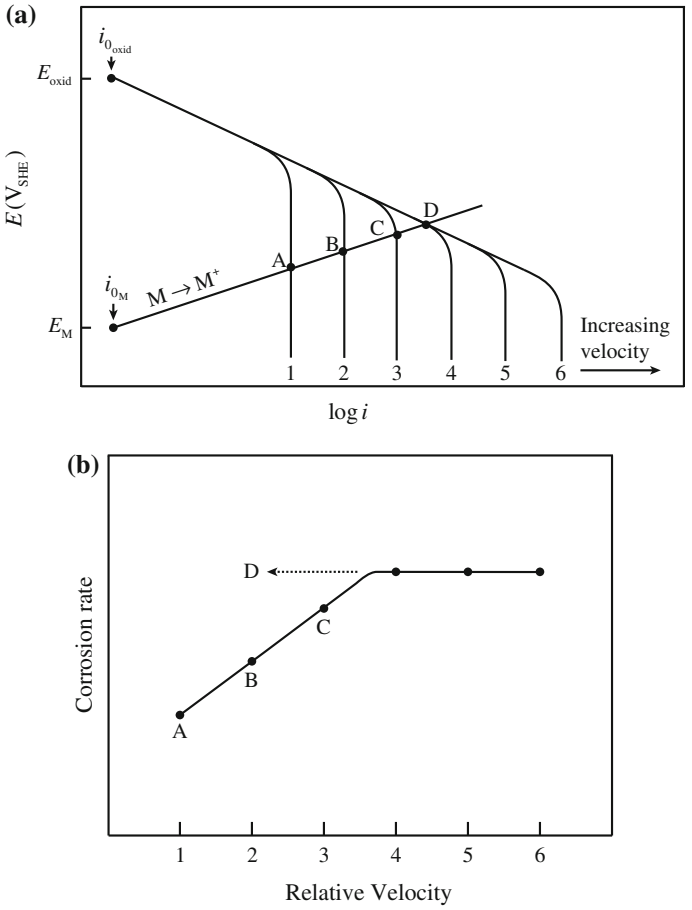

Fig. 15.32 Effect of solution velocity on (**a**) electrochemical behavior and (**b**) corrosion rate of an *active* metal corroding with a diffusion-controlled cathodic process (after [3])

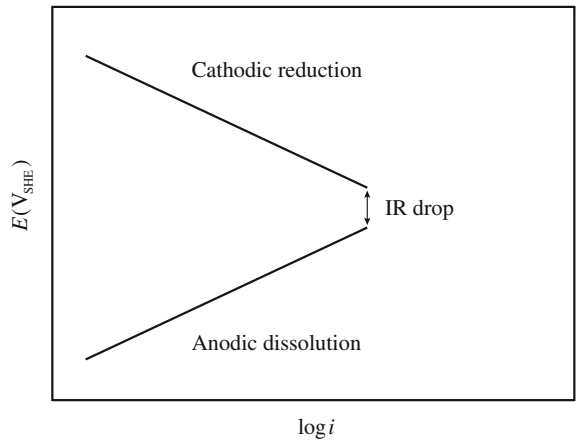

Fig. 15.33 IR drop between sites of cathodic and anodic reactions

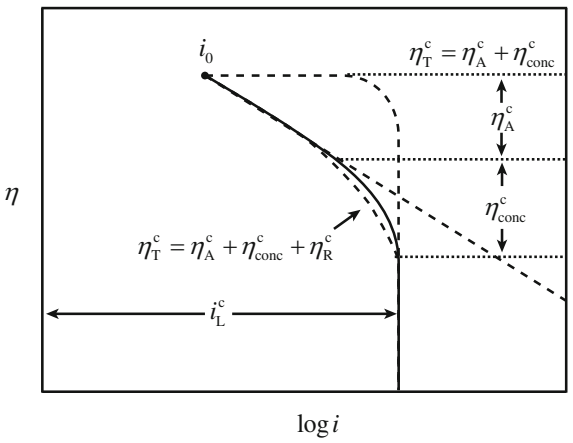

Fig. 15.34 Polarization diagram with combined activation, concentration, and resistance polarization

resistance effects. Figure 15.34 shows the makeup of the total overpotential by the three contributions.

Both resistance of the electrolyte and polarization of the electrodes limit the magnitude of current produced by a galvanic cell. When polarization occurs mostly at the anode, the corrosion reaction is anodically polarized as in Fig. 15.35(a). When polarization occurs mostly at the cathode, the corrosion rate is cathodically controlled as in Fig. 15.35(b). Resistance polarization controls the total polarization when the electrolyte resistance is so high that the resultant current is not sufficient to polarize either the anode or cathode. Figure 15.35(c) shows the case in which the corrosion current is controlled by the IR drop through the electrolyte. However, mixed control occurs when polarization occurs to some degree at both the anode and cathode as in Fig. 15.35(d). If the anodic area of the corroding metal is small (say due to a porous film), there may be considerable anodic polarization accompanying corrosion even though measurement shows that the unit area of bare anode polarizes only slightly at a given current density. Figure 15.36 shows the case where the area of the anode is half that of the cathode.

In corrosion of zinc amalgam (Zn + Hg) in acid chloride, Hg is polarized to nearly the corrosion potential of Zn. Mercury atoms act as cathodes, and Zn atoms act as anodes. The corrosion reaction is controlled almost entirely by the rate of hydrogen evolution at the cathodic areas resulting in a polarization diagram shown in Fig. 15.37. So the high hydrogen overvoltage of Hg limits the corrosion rate of amalgams in non-oxidizing acids.

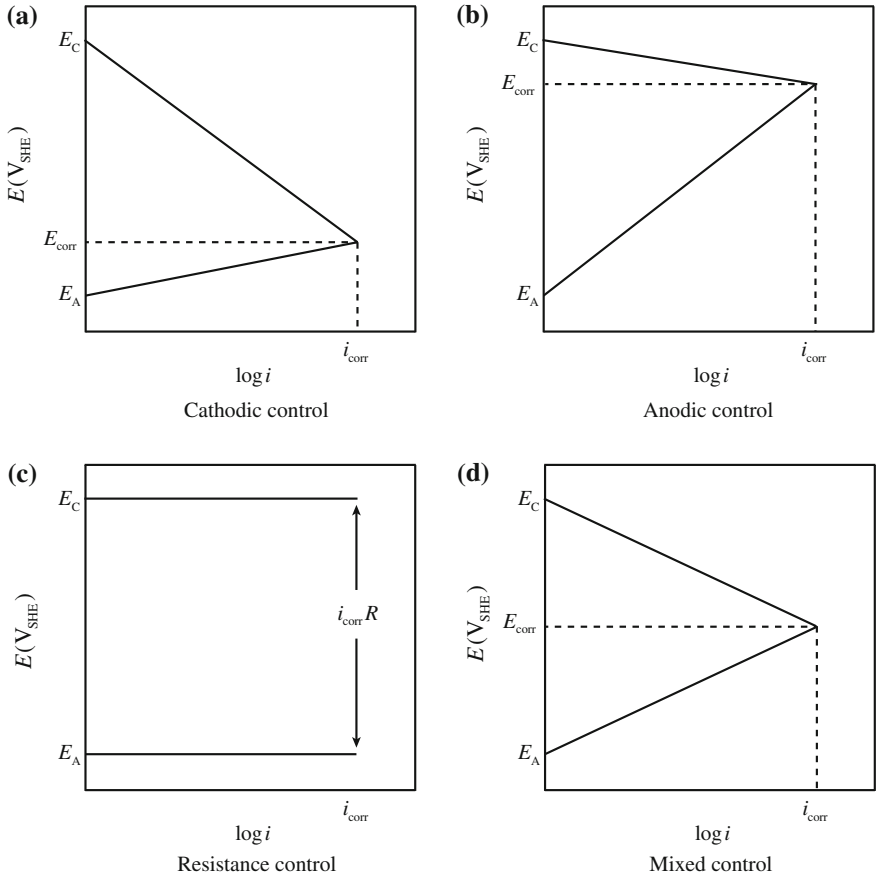

Fig. 15.35 Polarization of Zn in dilute acid occurring (**a**) predominantly at the anode, (**b**) predominantly at the cathode, (**c**) by resistance control, and (**d**) by mixed control (after [4])

15.5 Passivity

A strict definition of passivity does not exist. In an engineering sense, passivity is a state in which the metal is covered with a surface film and the corrosion rate is very low. A metal is considered to be passive if it substantially resists corrosion in a given environment resulting from marked anodic dissolution. A metal is also considered to be passive if it substantially resists corrosion in a given environment despite a marked thermodynamic tendency to react. The polarization diagram for a passivating metal is much different than that for an active metal. Figure 15.38 shows the polarization diagram for a passive metal. As the potential increases above E_{corr}, the rate of metal dissolution increases. The highest rate of corrosion is denoted the critical current density, i_{crit}. The lower portion of the anodic curve exhibits a Tafel relationship up to i_{crit}, which is the current required to generate a sufficiently high

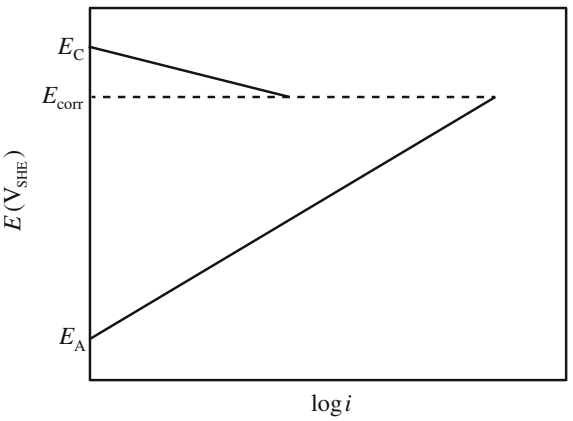

Fig. 15.36 Polarization diagram for the case where the anode area equals one-half of the cathode area (after [4])

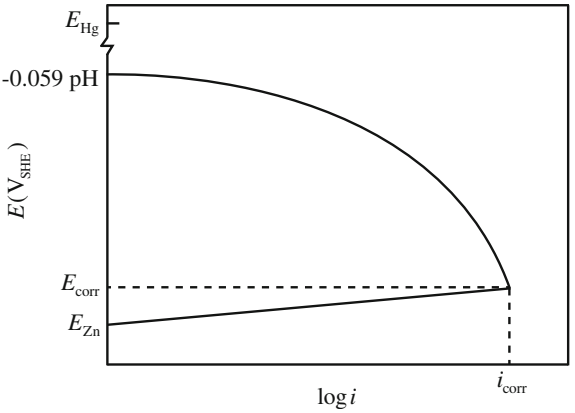

Fig. 15.37 Polarization diagram for zinc amalgam in deaerated HCl (after [4])

concentration of metal ions such that the nucleation and growth of a surface film can proceed. The potential corresponding to i_{crit} is called the primary passive potential (E_{pp}), and it represents the transition of a metal from an active state to a passive state.

Due to the onset of passivity, log i starts to decrease sharply beyond E_{pp} due to the film formation on the metal surface. Log i can drop several orders of magnitude below log i_{crit}. The potential at which the current becomes virtually independent of potential and remains virtually stationary is called the Flade potential (E_F). It represents the onset of full passivity on the metal surface. Actually, it is defined as the potential at which the metal changes from a passive to an active state and is normally not much different from E_{pp} in value.

Flade potential

If a metal is anodically passivated and the applied potential is removed, the potential of the specimen becomes active again. The potential corresponding

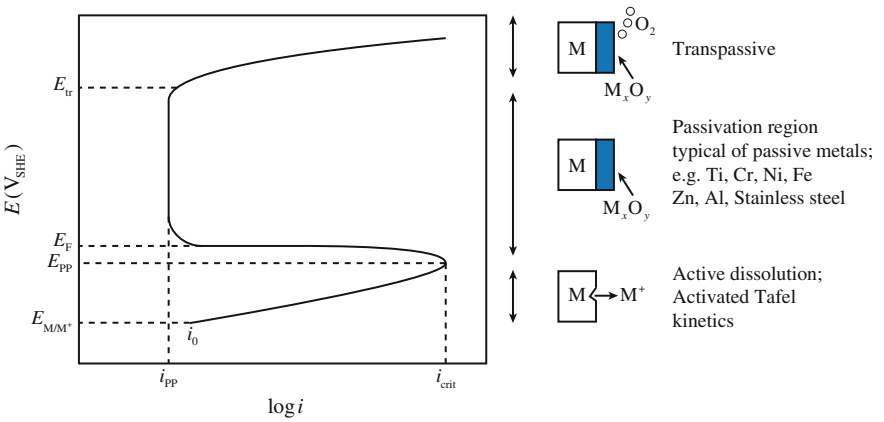

Fig. 15.38 Schematic of active–passive polarization behavior

to the re-establishment of active conditions is called the Flade potential. It is pH dependent:

$$E_F = E_F^0 - 0.059\text{pH},$$

where E_F^0 is the Flade potential at pH = 0. The potential is associated with the dissolution of the protective passive film. The stability of passivity is related to the Flade potential assuming the following anodic reaction:

$$M + H_2O \rightarrow OM + 2H^+ + 2e^-,$$

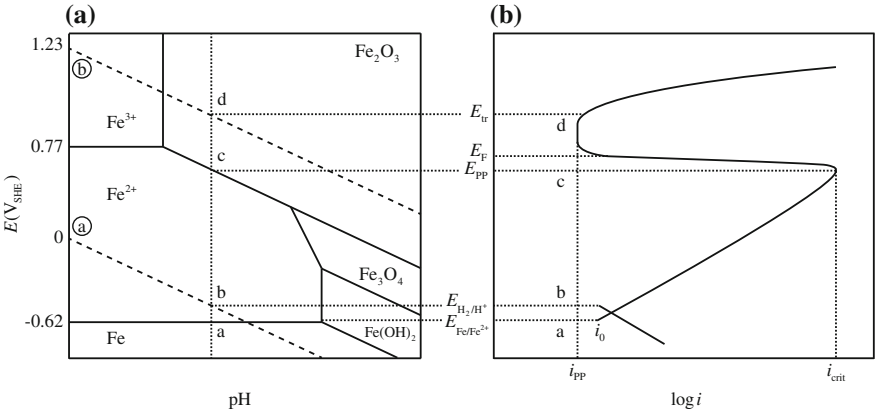

Fig. 15.39 Relationship between (**a**) E-pH diagram and (**b**) polarization diagram for Fe in the passive region

where E_F is the potential for the reaction. Note that for Fe, E_F^0 corresponds closely to the line separating Fe^{++} and Fe_2O_3 in Fig. 15.39. $E_F^0 = 0.63$ V for iron versus −0.20 V for Cr indicating a greater stability of the passive film on Cr.

The minimum current density required to maintain the metal in a passive state is called the passive current density (i_{pp}). At i_{pp}, the metal dissolution occurs at a constant rate. As the potential is increased in the noble direction, the film begins to thicken. According to electric field theory, dissolution proceeds by transport of ionic species through the film under the influence of an electric field. As the potential increases in the noble direction, the film thickens in order to maintain a constant electric field ($\Delta E/x$). Film thickening proceeds by transport of cations, M^{++} outward, and the combination of ions with $O^{=}$ or OH^{-} inward.

According to chemical attack and film reformation theory, the dissolution process is a chemical process and does not depend on potential. The film that is dissolved is immediately replaced by a new film, and a balance is struck between dissolution and reformation. The passive region ends at the point where oxygen is anodically evolved:

$$2H_2O \rightarrow O_2 + 4H^+ + 4e^- \quad \text{(acid)}$$

or

$$4OH^- \rightarrow O_2 + 2H_2O + 4e^- \quad \text{(neutral)}$$

The evolution of oxygen causes a sharp increase in the current. This is the transpassive region, and the potential at which it begins is the transpassive potential (E_{trans}). In some cases, transpassivity may be observed due to the breakdown of the protective film. Perhaps at more noble potentials, the film is not sufficiently protective to keep the metal in the passive state. It may become thicker, unstable, and non-adherent and eventually breakdown. It dissolves as a hydrolyzed cation in a higher oxidation state, for example, when chromium is oxidized from the +3 to the +6 state:

$$Cr^{3+} + H_2O = HCrO_4^-(aq) + 7H^+ + 3e^-.$$

The passivation of a metal can be understood by considering the relationship between the potential–pH diagram and the polarization curve as in Fig. 15.39. Figure 15.39(a) shows the Pourbaix diagram, and Fig. 15.39(b) shows the accompanying polarization plot for iron. As the potential is raised at the pH noted by the dashed vertical line, the dissolution of Fe to Fe^{++} will occur at a potential corresponding to point "a." As the potential is increased, the corrosion current rises as shown in Fig. 15.3(b). At point "c" in the Pourbaix diagram, a stable film, Fe_2O_3, will form, causing the corrosion current to drop significantly. At point "d," water begins to electrolyze. The stable form of oxygen changes from H_2O to O_2:

$$2H_2O \rightarrow O_2 + 4H^+ + 4e^-.$$

This is the anodic reaction above the oxygen line ⓑ. The dissolution is not necessarily increasing in the transpassive region just because the current increases. The current we are measuring occurs as a result of the evolution on O_2 and not the dissolution of Fe metal.

15.5.1 Theories of Passivation

There exist two basic theories of passivation. The dissolution–precipitation mechanism holds that if a metal (e.g., Ni) is immersed in acid (e.g., H_2SO_4) and the potential of the Ni electrode is increased in the positive direction, there occurs a critical potential at which a film of $Ni(OH)_2$ suddenly forms on the surface. However, the film forms negative to the passivation potential and is therefore a precursor or prepassive film. Evidence exists to suggest that the precursor film is an electrical insulator, while the passive film formed above E_{pp} is an electronic conductor. The high conductivity causes a collapse of the potential drop across the film, and without a potential gradient to drive the ions, they do not drift through the film from metal surface to the solution, so dissolution (corrosion) ceases. The evidence to support this mechanism lies in the observation of high rates of O_2 evolution in the transpassive region which requires efficient transfer of electrons from the film to the metal to occur.

The question then arises as to how the film forms? As the dissolution current rises rapidly, the interfacial concentration of dissolved ions reaches the solubility limit and a precipitate forms ($Ni(OH)_2$) in the case of nickel. This is the dissolution–precipitation process for spontaneous passivation. It must be realized that if the current density is low enough, diffusion transports the ions away as they are formed and does not allow their concentration to build up sufficiently for precipitation.

The adsorption theory says that passivation arises from the formation of a monolayer of adsorbed oxygen. The presence of oxygen may, for example, block a kink site in the dissolving metal, lowering the free energy of the initial state of the atom in its dissolution reaction so that it no longer dissolves with the former rate. That is, the exchange current density for dissolution has been reduced several orders of magnitude. In this case, the adsorbed films act as a kinetic limitation reducing the exchange current density i_0, for the dissolution reaction. Uhlig [4] postulated that chemisorbed oxygen is responsible for establishing passivity. Chemisorption of oxygen is favored by the presence of uncoupled d-electrons in the transition metals. In Fe–Cr alloys, Cr acts as an acceptor for uncoupled d-electrons from iron. When alloyed with Cr at concentrations less than 12 %, uncoupled d-electron vacancies in Cr are filled from the excess Fe and the alloy acts like unalloyed iron, which is non-passive in deaerated dilute acid solutions. Above 12 % Cr, the alloys are passive in such solutions because uncoupled d-electrons are available to foster adsorption. During film thickening, metal cations are assumed to migrate into the film from the underlying metal, as well as protons from solution.

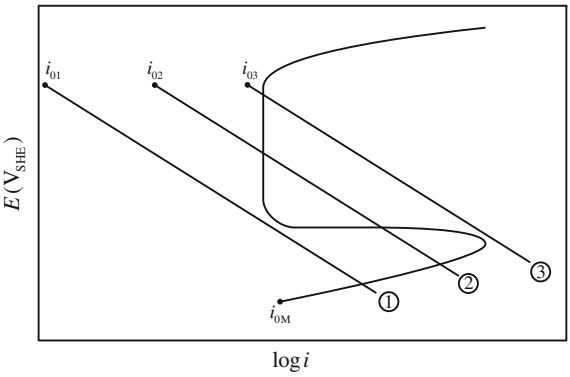

Fig. 15.40 Polarization diagram for an active–passive metal in a corrosive solution

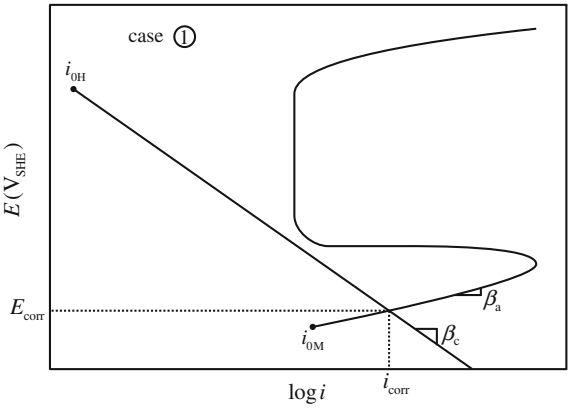

Fig. 15.41 Polarization diagram for case ① in Fig. 15.40 illustrating the condition for corrosion (e.g., stainless steel or Ti in aerated H_2SO_4)

15.5.2 Behavior of an Active–Passive Metal in Acid

Three cases may occur when an active–passive metal is exposed to a corrosive environment, shown in the polarization diagram of Fig. 15.40, and individually in Figs. 15.41, 15.42, and 15.43. In case ① in Fig. 15.40, the cathodic curve intersects the anodic curve in the active region. Figure 15.41 illustrates this case, which would occur for Ti or stainless steel immersed in deaerated H_2SO_4. Note that E_{corr} and i_{corr} occur in the active region and the metal or alloy will corrode rapidly. Case ③ (Fig. 15.42) is one of self-passivation in which SS or Ti is immersed in oxygenated acid. Note that spontaneous passivation will occur, resulting in a higher E_{corr} and a low i_{corr}. From an engineering standpoint, this is a desirable situation. However, note that spontaneous passivation only occurs if the cathodic reaction clears the tip of the anodic nose. The last case, case ② (Fig. 15.43) is one of unstable passivity as there exists three possible intersection points where $i_{ox} = i_{red}$, and three corresponding values of E_{corr}. Point "b" is unstable, and the system may exist in either the "a" (active) or "c" (passive) states.

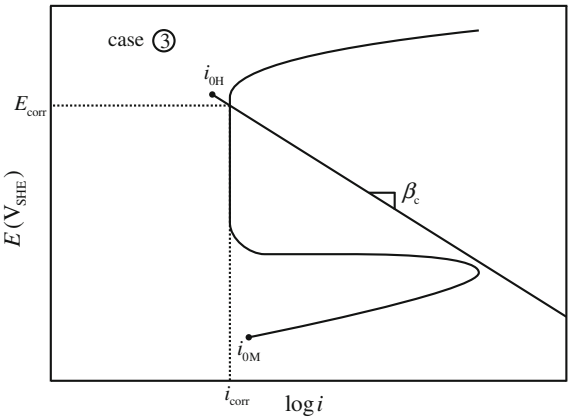

Fig. 15.42 Polarization diagram for case ③ in Fig. 15.40 illustrating spontaneous passivation (e.g., stainless steel or Ti in deaerated H_2SO_4)

15.5.3 Factors Affecting Active–Passive Corrosion Behavior

Several factors can affect the corrosion behavior of an active–passive metal. An increase in the acid concentration or the temperature of the solution results in a decrease in the passive potential range, an increase in the current density, and an increase in the corrosion rate at all potentials as in Fig. 15.44. Increasing the oxidizer concentration increases the potential of the redox half-cell according to the Nernst equation. Figure 15.45(a) shows the effect of increasing the concentration of an oxidizer on the corrosion behavior of an active–passive metal. An increase in concentration from "1" to "2" results in an increase in potential from "A" to "B." At "3," the alloy may exist in either the active "C" or passive "D" states. For concentrations "4–6," the passive state is stable and at "7" and "8," there is a transition to the transpassive state.

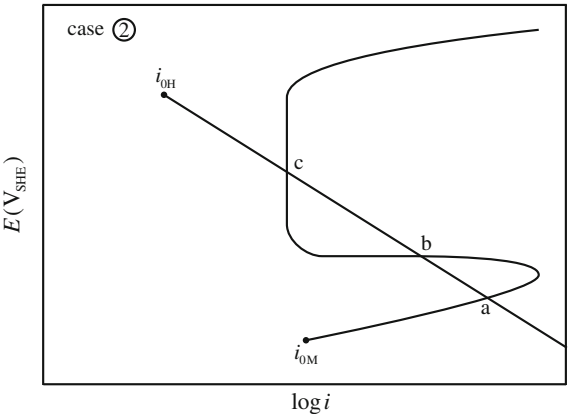

Fig. 15.43 Polarization diagram for case ② in Fig. 15.40 illustrating unstable passivity

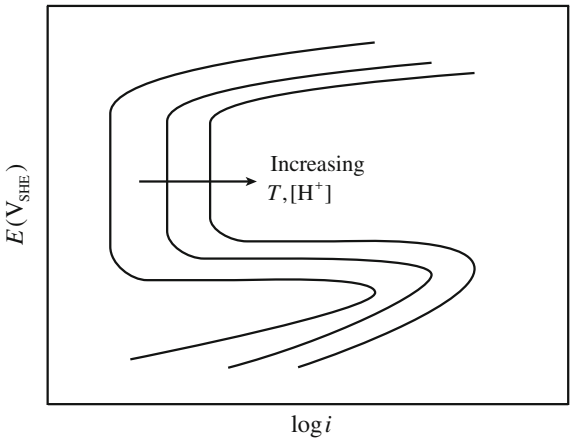

Fig. 15.44 Effect of increasing acid concentration and temperature on passivity (after [2])

Corrosion rate is plotted as a function of concentration in Fig. 15.45(b). In region BCD, either active or passive states may exist, but the film will not form until concentration D is reached. The corrosion rate stays low until the transpassive range is reached. When the process is reversed, the corrosion rate retraces its steps from transpassive to passive. But once the passive film is formed, it is retained at concentrations lower than that needed for its formation. So in region DC'B, we have borderline passivity in which any surface disturbance (scratching) will destabilize the film and corrosion can increase to the active state. This explains the behavior of iron in nitric acid. Immersion of iron into concentrated nitric acid results in the formation of a protective film as in Fig. 15.46(a). If the solution is then changed to dilute nitric acid (Fig. 15.46(b)), nothing happens unless the surface film is disturbed by, say, scratching, which will cause rapid dissolution of the iron sample Fig. (15.46(c)) Note that rapid dissolution in dilute nitric acid will occur if the bare metal sample is immersed directly into the solution since no protective film exists.

An example of the effect of solution agitation is shown in Fig. 15.47 for an active–passive metal corroding in an electrolyte under diffusion control [3]. Curves 1–5 correspond to increases in the limiting diffusion current density with increasing velocity as in Fig. 15.47(a). As the velocity is increased, the corrosion rate increases along the path ABC. When velocity is increased beyond 3, there is a rapid transition from point C in the active region to point D in the passive state. These results are shown in terms of velocity versus corrosion rate in Fig. 15.47(b). The difference in velocity dependence between an active metal (Fig. 15.32) and one demonstrating active–passive behavior (Fig. 15.47) is the result of the unusual dissolution behavior of active–passive metals. This behavior is typical of all active–passive metals that are corroding under diffusion control.

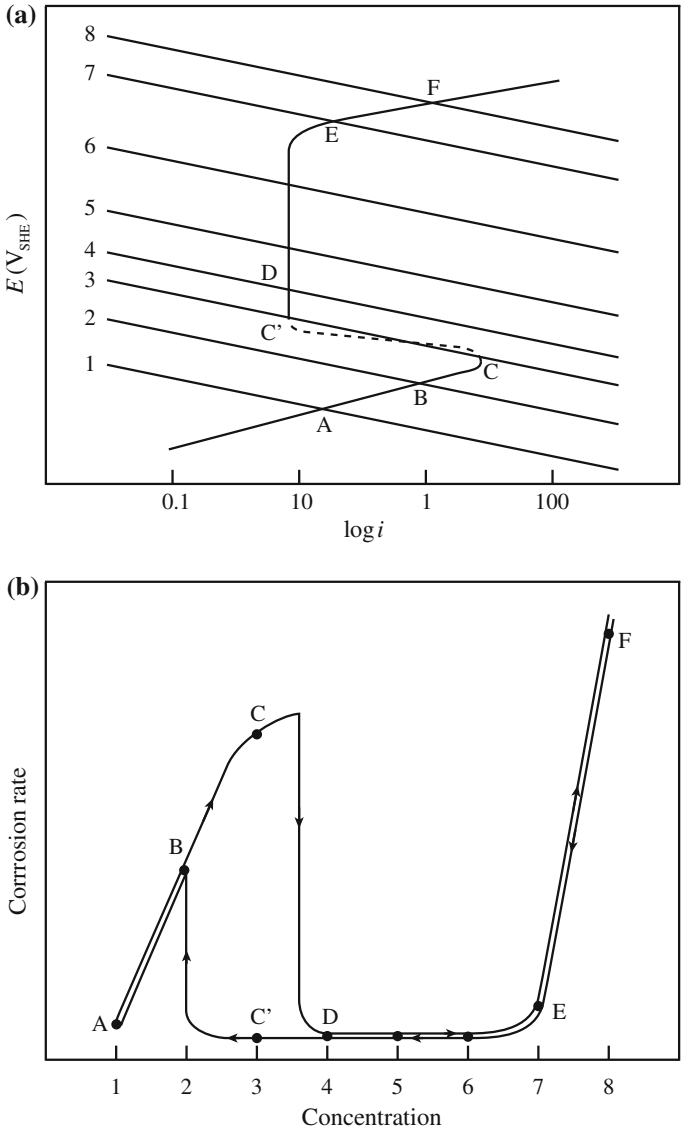

Fig. 15.45 Effect of oxidizer concentration on (**a**) corrosion, and (**b**) corrosion rate of an active–passive metal (after [2])

15.5.4 Control of Passivity

Two general rules can be applied to control passivity. If corrosion is driven by an activation-controlled reduction process, an alloy that exhibits a very active primary passive potential should be selected for use in the environment. This case is

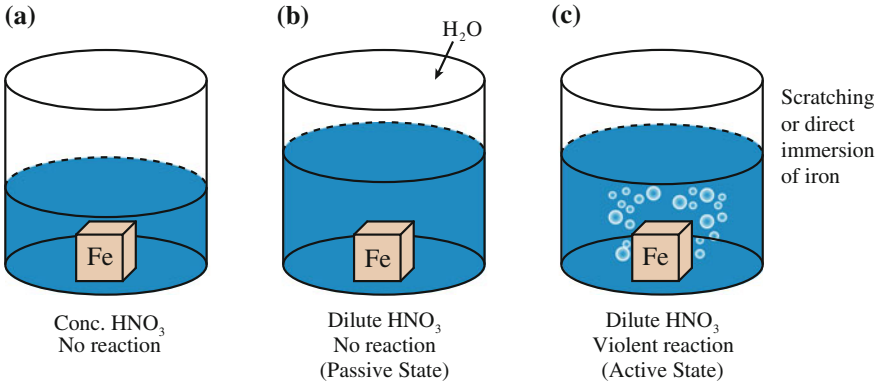

Fig. 15.46 Schematic illustration of Faraday's passivity experiment with iron (after [3])

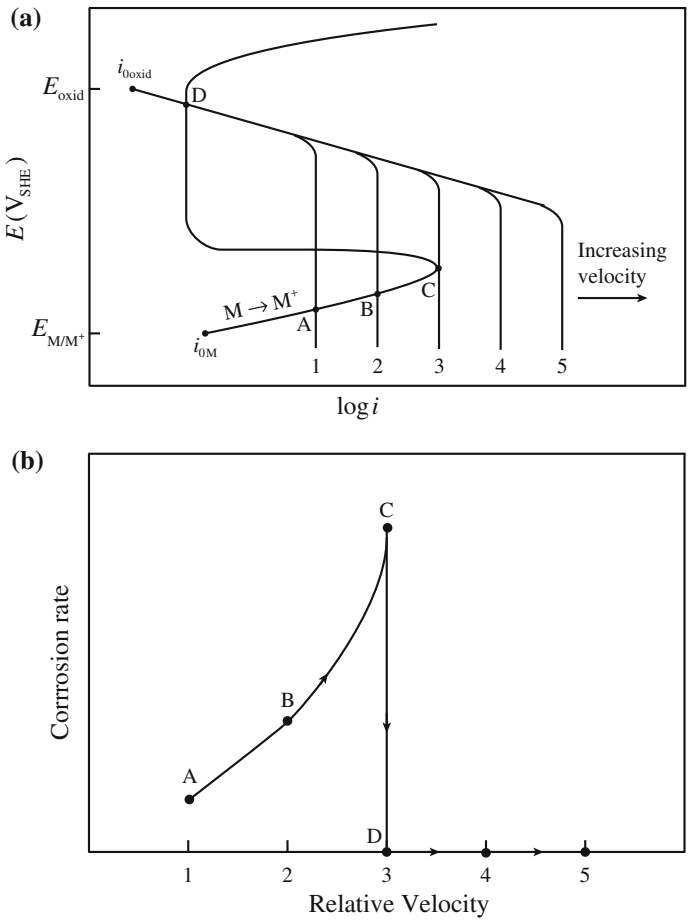

Fig. 15.47 Effect of solution velocity on (**a**) electrochemical behavior and (**b**) corrosion rate of an *active–passive* metal corroding under diffusion control (after [3]) Fontana 10.5 and 10.6

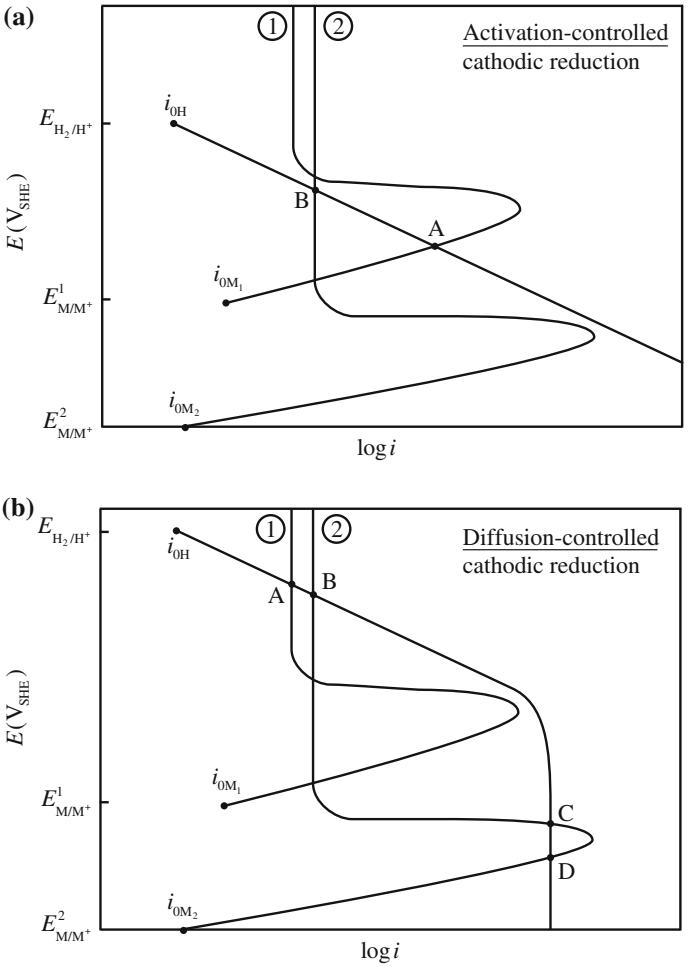

Fig. 15.48 Polarization diagram for (**a**) activation-controlled and (**b**) diffusion-controlled cathodic reduction reaction

illustrated in Fig. 15.48(a) in which alloy ② is the better selection as the corrosion current corresponding to the corrosion potential will be the passivation current which will be low (point "B") compared to that where the corrosion potential is in the active region (point "A"). If the reduction process is under diffusion control, then an alloy with a smaller critical current density is preferable. As shown in Fig. 15.48(b), alloy ① is the better choice.

The tendency for passivation can be increased by alloying additions that decrease i_{crit}. This would include additions such as Mo, Ni, Ta, and Nb to Ti and Cr. The potential of these elements is active, and their corrosion rate is low. Alloying elements that passivate more readily than the base metal will reduce i_{crit} and induce

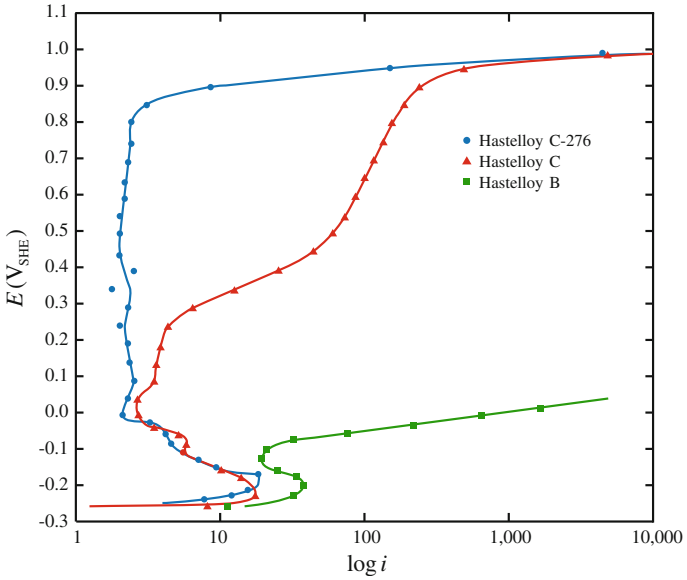

Fig. 15.49 Comparison of potentiostatic anodic polarization of nickel alloys in 1 N H_2SO_4 at ambient temperature (after [2])

passivity. Examples are Cr and Ni additions to Fe, which reduce i_{crit} and increase passivity. Ni additions to Cu (e.g., Cu–10Ni or Cu–30Ni) also promote passivity. An example of the influence of alloying elements is shown in Fig. 15.49 for nickel-base alloys. Hastelloy B is a Ni–25Mo alloy and shows only a hint of passivity. Addition of Cr and Fe at the expense of Mo to form Hastelloy C (Ni–15Cr–15Mo–5Fe) gives a low i_{crit} and an active E_{pp}, but i_{pass} increases steadily in the passive regime. Hastelloy C-276 is essentially the same as Hastelloy C but with very low Si and C levels. The restriction on Si and C reduces precipitation, which adversely affects corrosion at localized sites. Either alloy is acceptable for use in reducing conditions, Hastelloy C is acceptable in moderately oxidizing conditions, and Hastelloy C-276 is required in highly oxidizing conditions.

Consider four alloys (A–D) under three conditions: 1 = reducing, 2 = moderately oxidizing, and 3 = highly oxidizing, as shown in Fig. 15.50. Under reducing conditions (1), alloys A and B have superior corrosion resistance due to lower corrosion rates in the active state without oxidizers. Alloys C and D are passive, but this is unnecessary under reducing conditions and elements that promote passivity, such as Cr, are very expensive. In moderately oxidizing environments (2), alloy C is the obvious choice. Alloy D is borderline passive, and an active state is also possible. Alloy B is passive, but the passive current density is large compared to that for alloy C. In highly oxidizing environments (3), alloy D is best since the reduction curve exceeds the critical current density for passivation and the corrosion

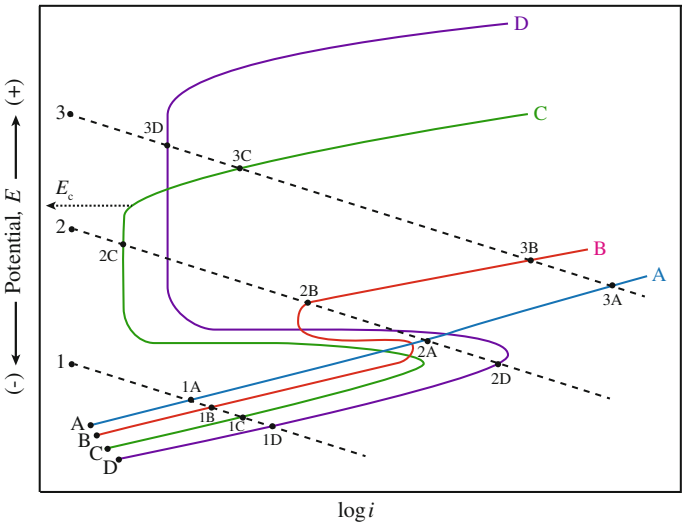

Fig. 15.50 Schematic anodic polarization curves for hypothetical alloys A, B, C, and D, illustrating behaviors in various chemical conditions: *1*—reducing, *2*—moderately oxidizing, and *3*—highly oxidizing (after [2])

rate is low. Passivity breaks down for alloy C at E_c and i_{corr} increases. Neither alloys A nor B have any resistance to corrosion in this environment.

The following rules may be adopted for the behavior of metals and alloys in aqueous media:

1. In the active state, the corrosion rate is proportional to the anodic current density whether or not the alloy is of the active–passive type.
2. The current density for the reduction reaction must exceed the critical current density for passivation, i_{crit}, to ensure a low corrosion rate in the passive state.
3. Borderline passivity in which either the active or the passive state may be stable should be avoided.
4. Breakdown of the passive film in oxidizing conditions due to transpassivity or initiation of localized corrosion should be avoided.
5. The passive state in oxidizing conditions is essential for corrosion resistance, but reasonably small variations in the passive current density may not be significant.

15.5.5 Galvanic Couples of Active–Passive Metals

Consider the coupling of Ti to Pt as shown in the polarization diagram in Fig. 15.51. Upon coupling, Ti spontaneously passivates and its corrosion rate drops to i_{corr}^{Ti-Pt}. Note that this is an exception to the rule that when coupling two metals, the

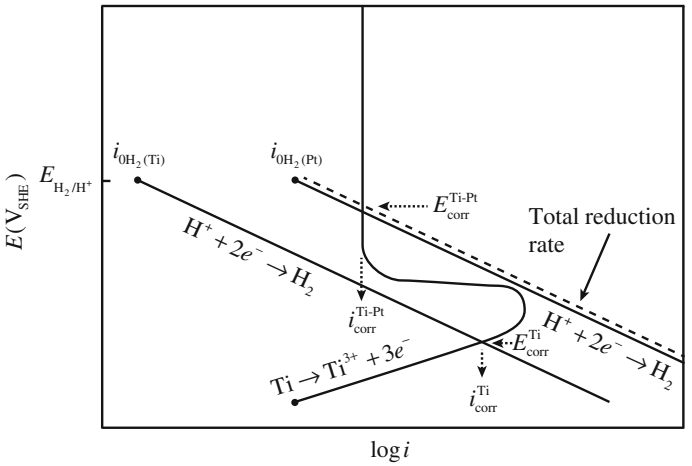

Fig. 15.51 Spontaneous passivation of titanium by galvanically coupling to platinum (after [3])

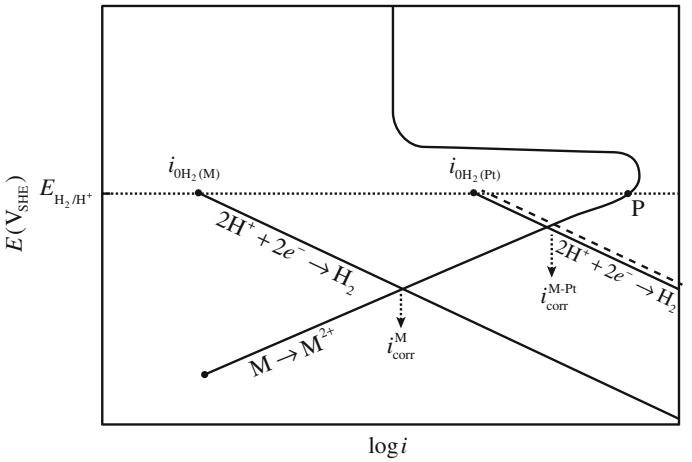

Fig. 15.52 Galvanic couple between an active–passive metal and platinum in deaerated acid (after [3])

corrosion rate of the metal with the most active corrosion potential is accelerated. The behavior in Fig. 15.51 can only occur if the passive region of the metal begins at a potential more active than the reversible potential of the redox system. In fact, only Cr and Ti exhibit this behavior. If the passive range of a metal begins at potentials more noble than the reversible hydrogen potential, coupling to Pt in the absence of oxidizers increases the corrosion rate. An example is the coupling of Fe to Pt in an acid solution as in Fig. 15.52.

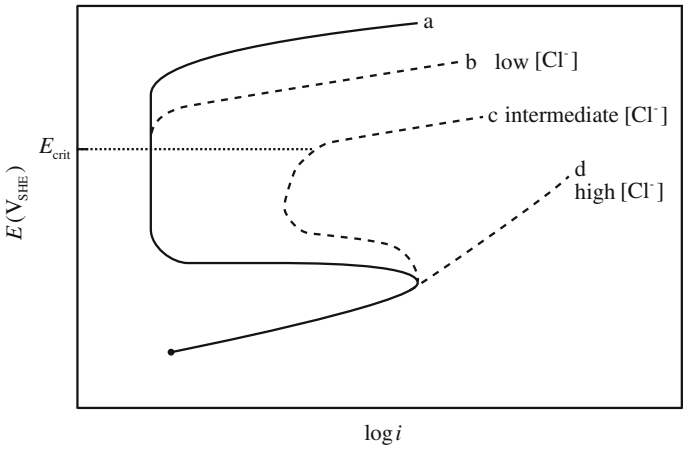

Fig. 15.53 Effect of Cl^- concentration on the polarization behavior of an active–passive metal (after [2])

15.5.6 Pitting of Passive Metals

Chloride ions and, to a lesser extent, other halogens can break down passivity or prevent its formation in Fe, Cr, Ni, Co, and stainless steels. According to the oxide film theory of passivity, Cl^- penetrates the oxide film through pores or defects easier than, e.g., $SO_4^=$. According to the adsorption theory, Cl^- adsorbs on the metal surface in competition with O_2 or OH^- and once in contact, favors hydration of metal ions, thus increasing the ease with which they enter solution. That is, they increase the exchange current for metal dissolution over that with O_2 present. The breakdown occurs locally at preferred sites. These sites become minute anodes surrounded by large cathodes (passive region). The potential difference between the two may reach ~ 0.5 V or more setting up active–passive cells. High current densities at the anode cause high rates of penetration. Note that in the presence of Cl^-, the apparent transpassive region shifts to more active potentials. Actually, this is not transpassive behavior; oxygen is not being evolved, rather there is intense local dissolution. The critical potential decreases with increasing Cl^- concentration until the surface can no longer form a passive film. Figure 15.53 shows the effect of increasing Cl^- concentration on the pitting potential. Note that in this case, the current increase above E_{pit} is *not* due to oxygen, but rather to localized corrosion at the pit.

This raises the question of the significance of a critical potential for pitting (pitting potential, E_{pit}). According to one view, this is the value needed to build up an electrostatic field within the passive or oxide film sufficient to induce Cl^- penetration to the metal surface. The incubation time for pitting is related to the time required for penetration of Cl^- through the oxide film. In terms of the adsorption theory, the metal typically has greater affinity for oxygen than for Cl^-,

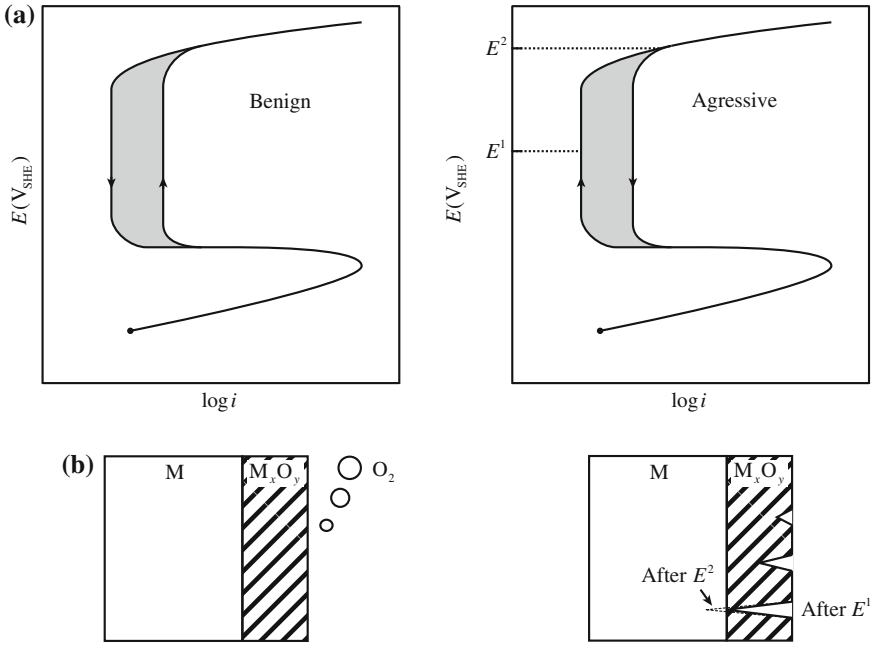

Fig. 15.54 Hysteresis effects in cyclic polarization (**a**) in an acid solution under a spontaneous passivation condition and (**b**) in the presence of Cl^- ions or other halogens

but as the potential is made more noble, the concentration of Cl^- at the surface increases to a value that allows Cl^- to displace oxygen.

The difference between aggressive and benign environments in the polarization behavior of an active–passive metal is illustrated in Fig. 15.54. In an aggressive environment containing Cl^- as in Fig. 15.54(a), pitting occurs at high potential. Upon decreasing the potential, the defective passive film is not as protective, resulting in a higher corrosion current than on voltage ascension. In a benign environment as in Fig. 15.54(b), only oxygen gas is generated at high potential and the stable oxide formed on the way up in potential provides for a lower corrosion current during descending voltage.

Inhibitors can be used to counter the effects of an aggressive environment. As shown in Fig. 15.55, in deaerated acid (non-aggressive condition), the metal is in the active state at E^a_{corr}. In an aerated acid (non-aggressive condition), the more noble corrosion potential, E^b_{corr}, results in a low corrosion current. In an aerated acid with an aggressive (Cl^-) environment, E^c_{corr} is more noble than E_{crit} and pitting occurs. The use of an inhibitor such as $NaNO_3$ for stainless steel in acetic acid (aggressive) displaces the critical pitting potential to more noble potentials such that E_{corr} is in the passive region.

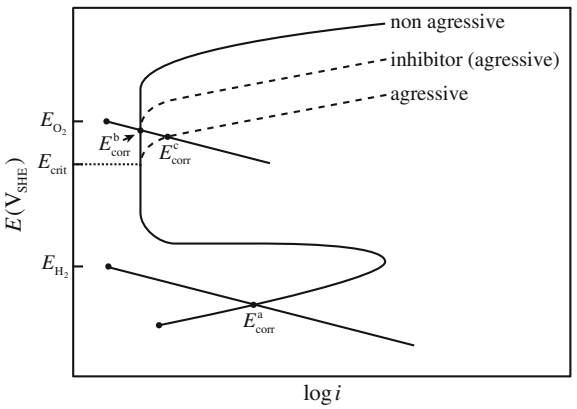

Fig. 15.55 Role of inhibitors on the polarization diagram of an active–passive alloy

15.6 Crevice Corrosion

Crevice corrosion is a form of corrosion that occurs in occluded locations where the solution in the crevice has limited exchange with that outside the crevice. It may be a region in which two metal surfaces are in close proximity but open enough to allow some solution to enter. It can also be in the form of a crack in a metal in which the crack tip is well away from the sample surface and the crack width is small. Crevice corrosion is characterized by intense localized corrosion rates and is usually associated with small volumes of stagnant solutions. In a crevice, the corrosion process consumes the dissolved oxygen, impairing passivity and increasing the concentration of metal ions, which attract negatively charged cations such as Cl^- from the bulk solution. The potential for initiation of crevice corrosion is more active than E_{pit} due to favorable geometric conditions for deaeration and chlorination. This is why any alloy that pits will exhibit crevice corrosion, but not the reverse. Although crevice corrosion can result from a difference in metal ion and oxygen concentrations, more processes are involved.

Consider a riveted metal plate immersed in aerated seawater (pH = 7), Fig. 15.56. The overall reaction is as follows:

$$\text{Oxidation:} \quad M \rightarrow M^{2+} + 2e^-$$
$$\text{Reduction:} \quad O_2 + 4H^+ + 4e^- \rightarrow 2H_2O.$$

Initially, these reactions occur uniformly over the entire metal surface and charge is conserved (Fig. 15.56(a)). After a short time, the oxygen in the crevice is depleted because of restricted access. The consumption of H^+ causes an increase in the pH. In basic environments, the anodic and cathodic reactions are as follows:

$$\text{Oxidation:} \quad M \rightarrow M^{2+} + 2e^-$$
$$\text{Reduction:} \quad O_2 + 2H_2O + 4e^- \rightarrow 4OH^-.$$

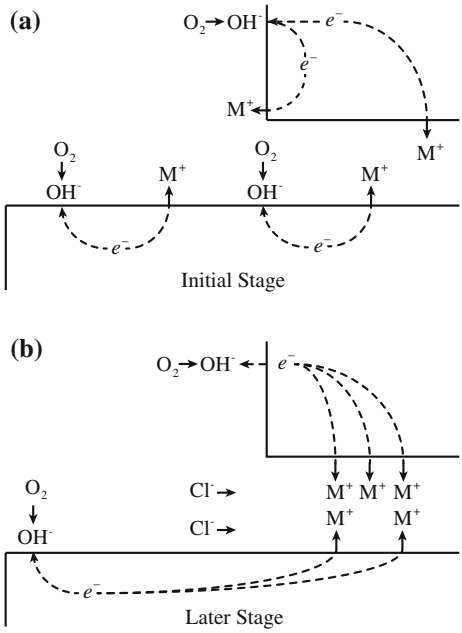

Fig. 15.56 Crevice corrosion (**a**) the initial stage and (**b**) later stage

Due to metal hydrolysis in a basic electrolyte, we have $M^{2+} + 2H_2O \rightarrow M(OH)_2 + 2H^+$ and the pH decreases (Fig. 15.56(b)). In both cases, increased resistance in the crack or crevice due to gas bubbles, for example, leads to an Ohmic drop causing a decrease in potential at the tip of the crack relative to the sample surface by up to several hundred millivolts. The result of these processes is shown in Fig. 15.57 for aerated water in which the crack tip condition is driven to a lower potential and an intermediate pH, both of which are considerably different than those at the sample surface.

As deaeration occurs in the crevice, the reduction reaction can continue, but it will be shifted to the external surface. After a while, the excess positive charge in the crevice due to continued metal dissolution will drive Cl^- migration into the crevice or crack to balance the overall charge. The increased metal chloride concentration hydrolyzes water:

$$M^+Cl^- + H_2O = MOH \downarrow + H^+Cl^-,$$

producing an insoluble hydroxide and a free acid. The pH drops and metal dissolution are accelerated, thus increasing Cl^- migration into the crevice. The process, shown in Fig. 15.57, is autocatalytic and rapidly accelerating.

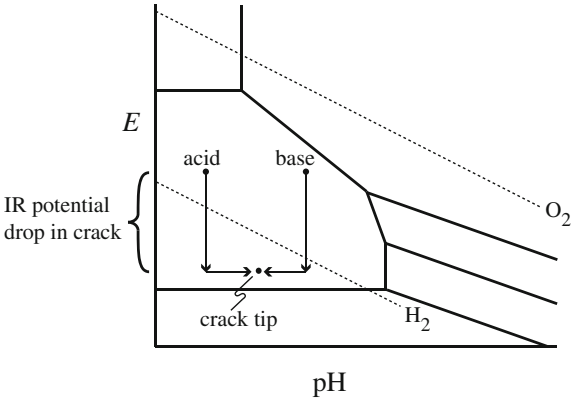

Fig. 15.57 Schematic Pourbaix diagram showing the change in potential and pH of basic and acidic bulk solutions versus the crack tip

15.7 Stress Corrosion Cracking

Stress corrosion cracking is the premature cracking of an alloy in the presence of a tensile stress and a corrosive environment. Historically, SCC was believed to occur only when three conditions were fulfilled: a susceptible alloy, a specific environment, and a tensile stress. In practice, most alloys are susceptible to SCC over a range of environments. The term *alloy* should be interpreted broadly so as to incorporate commercially pure metals since SCC is known to be a strong function of impurity content of pure metals. Similarly, the environment needs to be broadly interpreted to potentially all environments other than noble gases, since many gases, aqueous solutions, and liquid metals can promote SCC. The distinguishing characteristic of SCC is the requirement of a stress. While localized corrosion can occur in a stress-free environment, SCC can only occur with the imposition of a tensile stress. Figure 15.58 shows a stress–strain curve for an alloy in an inert environment compared to one in which the alloy is susceptible to stress corrosion cracking. SCC reduces the strain to failure as well as the maximum stress. Cracking may be either transgranular (TG) (e.g., 304 stainless steel in boiling $MgCl_2$ at 154 °C) or intergranular, IG (e.g., 304 stainless steel in 288 °C water as in Fig. 15.59). Typically, when the general corrosion rate is high, SCC susceptibility is low, and when the general corrosion rate is low, the SCC susceptibility is high.

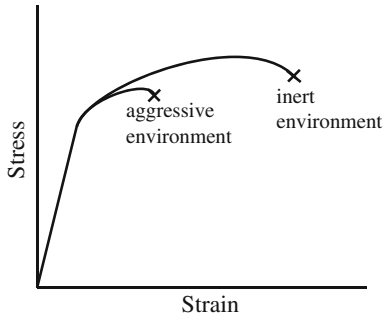

Fig. 15.58 Effect of the environment on stress–strain behavior of metals undergoing stress corrosion cracking

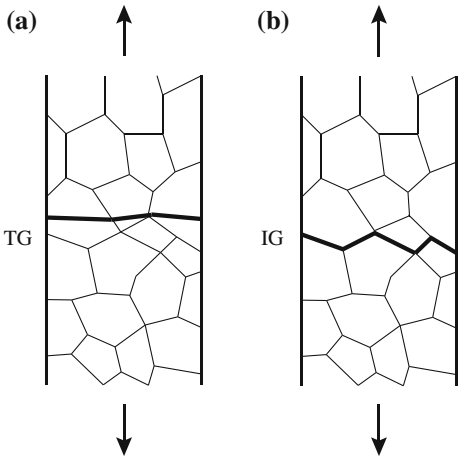

Fig. 15.59 Schematic illustrations of (**a**) transgranular stress corrosion cracking and (**b**) intergranular stress corrosion cracking

A distinction is often made between stress corrosion cracking, hydrogen embrittlement, and corrosion fatigue. Stress corrosion cracking is used here to refer to the broad category of cracking in a metal or alloy due to chemical or electrochemical processes involving the combination of environment and stress. In this context, hydrogen produced by the corrosion reaction is a form of stress corrosion cracking, yet hydrogen absorption from the gaseous state is not. SCC is often distinguished from corrosion fatigue by constant or monotonically increasing loading versus cyclic loading. Corrosion fatigue and hydrogen embrittlement will be discussed later in the chapter.

Stress corrosion cracking often exhibits some of the following characteristics [5]:

- Localization of damage is in the form of TG or IG cracks;
- Some of the most susceptible alloys are often very corrosion resistant (e.g., the corrosion rate of stainless steel in boiling $MgCl_2$ is essentially zero, but it is highly susceptible to TGSCC);
- Resistance to SCC depends on alloy composition;
- SCC exhibits a strong dependence on microstructure;
- Alloys that are ductile in an inert environment fail in a brittle manner; and
- Cathodic polarization mitigates the initiation of SCC.

Stress corrosion cracking often takes some time to occur, requiring an incubation period. Following initiation, cracks propagate at a slow rate until the stresses in the remaining ligament exceed the fracture stress and failure occurs due to overload. The SCC process is often characterized by the following stages:

- Crack initiation followed by stage 1 propagation;
- Stage 2 or steady-state crack propagation; and
- Stage 3 crack propagation or final failure.

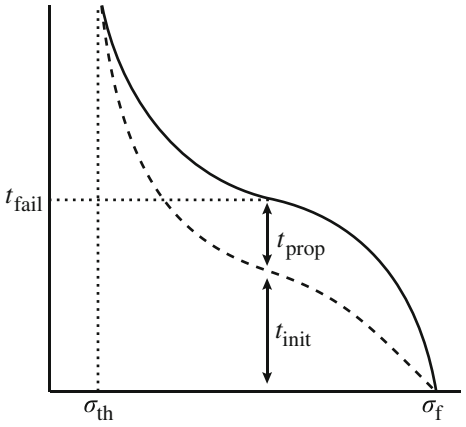

Fig. 15.60 Failure time as a function of stress for an alloy undergoing stress corrosion cracking. Failure time is the sum of the crack initiation time and the crack propagation time

However, not all alloys exhibit these stages or the stages may not be distinct or easily identifiable. To distinguish and quantify these stages of fracture, various SCC tests have been developed and are briefly summarized here.

15.7.1 SCC Tests

Stress corrosion cracking tests fall into three basic categories: static loading of smooth samples, static loading of precracked samples, and slow strain rate testing. Static loading of smooth samples provides the time to failure as a function of applied stress as the measure of the degree of stress corrosion cracking susceptibility. Figure 15.60 shows a plot of the time to failure versus stress for an alloy undergoing stress corrosion cracking. The minimum stress at which failure occurs is known as the threshold stress, σ_{th}, for SCC. The failure time includes both the initiation time, t_{init}, and the propagation time, t_{prop}, so that $t_{fail} = t_{init} + t_{prop}$. This test is useful for determining the maximum stress that can be applied without SCC failure in a specific environment. Examples of this test are the C-ring, U-bend, and the O-ring tests as shown in Fig. 15.61. In these tests, the sample is stressed to a fixed deflection and then held at that displacement for the duration of the test. In this mode, stress relaxation can occur so that the stress will decrease as the test progresses. As such, fixed load tests have been developed in which the load remains constant for the duration of the test.

In static loading of precracked samples, a constant load or fixed crack opening displacement is applied to a sample with a precrack such as a compact tension (CT) or a double cantilever beam (DCB) specimen. The crack length is measured as a function of time, yielding a crack propagation rate (or crack velocity) that can be described as a function of the stress intensity, K. Figure 15.62 shows a plot of a da/dt versus K curve in which the three stages of cracking are shown. As discussed in Chap. 14, K is a

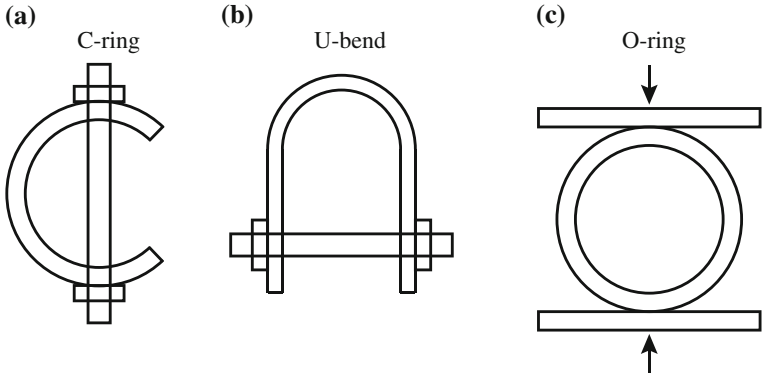

Fig. 15.61 Common constant deflection tests used to assess the relative susceptibility of an alloy to stress corrosion cracking; (**a**) C-ring, (**b**) reverse U-bend, and (**c**) O-ring

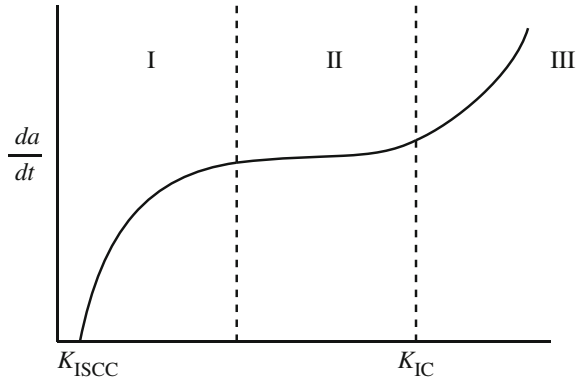

Fig. 15.62 Crack growth rate as a function of the crack tip stress intensity. Note that region II is independent of stress intensity, indicating the effect of the aggressive environment

function of applied stress, specimen geometry, and the square root of crack length. In the absence of a corrosive environment, fracture occurs when $K \geq K_{Ic}$, the plane strain fracture toughness. The effect of the corrosion environment is to lower the value of K at which cracking occurs. The existence of the plateau characteristic of stage II cracks is due to the environment. That is, in the regime where the environment has a strong impact, crack velocity is independent of the stress intensity factor.

The slow strain rate test involves the application of a slowly increasing strain, usually by applying a constant displacement rate, on a smooth bar or precracked sample. The ductility in the corrosive environment is a measure of SCC susceptibility and is plotted against the strain rate and can be compared with that in an inert environment (Fig. 15.63). As shown, various measures can be used to indicate susceptibility, such as strain to failure, reduction in area, fracture energy, or percent of the fracture surface that is due to SCC (TG or IG). Stress corrosion cracking susceptibility is manifest in a reduction in ductility at lower strain rates since there

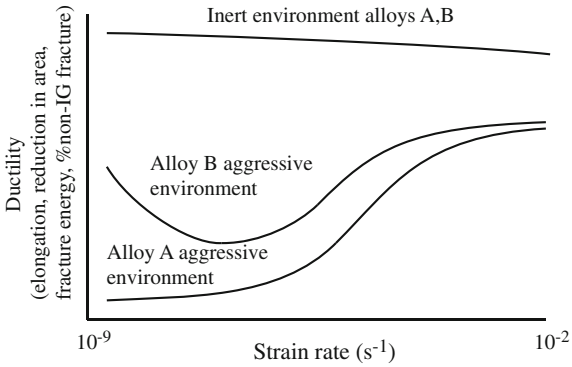

Fig. 15.63 Strain rate dependence of various measures of ductility. Alloys with no environmental effect have minimal strain rate dependence. In an aggressive environment, low strain rates are the most aggressive and cause the greatest reduction in ductility (after [5])

is sufficient time for the environment to induce SCC. As the strain rate rises, the time available for corrosion is reduced and the ductility approaches that in an inert environment. At very low rates, ductility can also increase as the strain rate is too slow to keep up with the effect of the environment. Known as constant extension rate tensile (CERT) or slow strain rate tensile (SSRT) tests, these tests are excellent indicators of the relative susceptibility of alloys to cracking in an environment, or for studying the influence of metallurgical variables. However, since they combine both the initiation and propagation stages, they are not as effective in determining the initiation stage, which is how they have traditionally been used. In most cases, they are effective in evaluating moderate to severe SCC.

15.7.2 SCC Processes

Specific mechanisms of SCC will be discussed later, but it is instructive here to consider the basic processes behind these mechanisms. Many proposed mechanisms are based on either anodic or cathodic processes, but some are purely chemical oxidation. Figure 15.64 illustrates some of the mechanisms proposed for stress corrosion crack growth. A mechanism must explain the actual crack propagation rates, fractographic features, and the formation of cracks. Atomistically, this amounts to explaining how atomic bonds are broken, which is believed to occur by either chemical oxidation or chemical solvation and dissolution or mechanical fracture (ductile or brittle). Ultimately, mechanical fracture is assumed to be stimulated or induced by interactions between the material and the environment. Certain processes or events must occur for sustained crack propagation to be possible. The potential rate-determining steps include [5]:

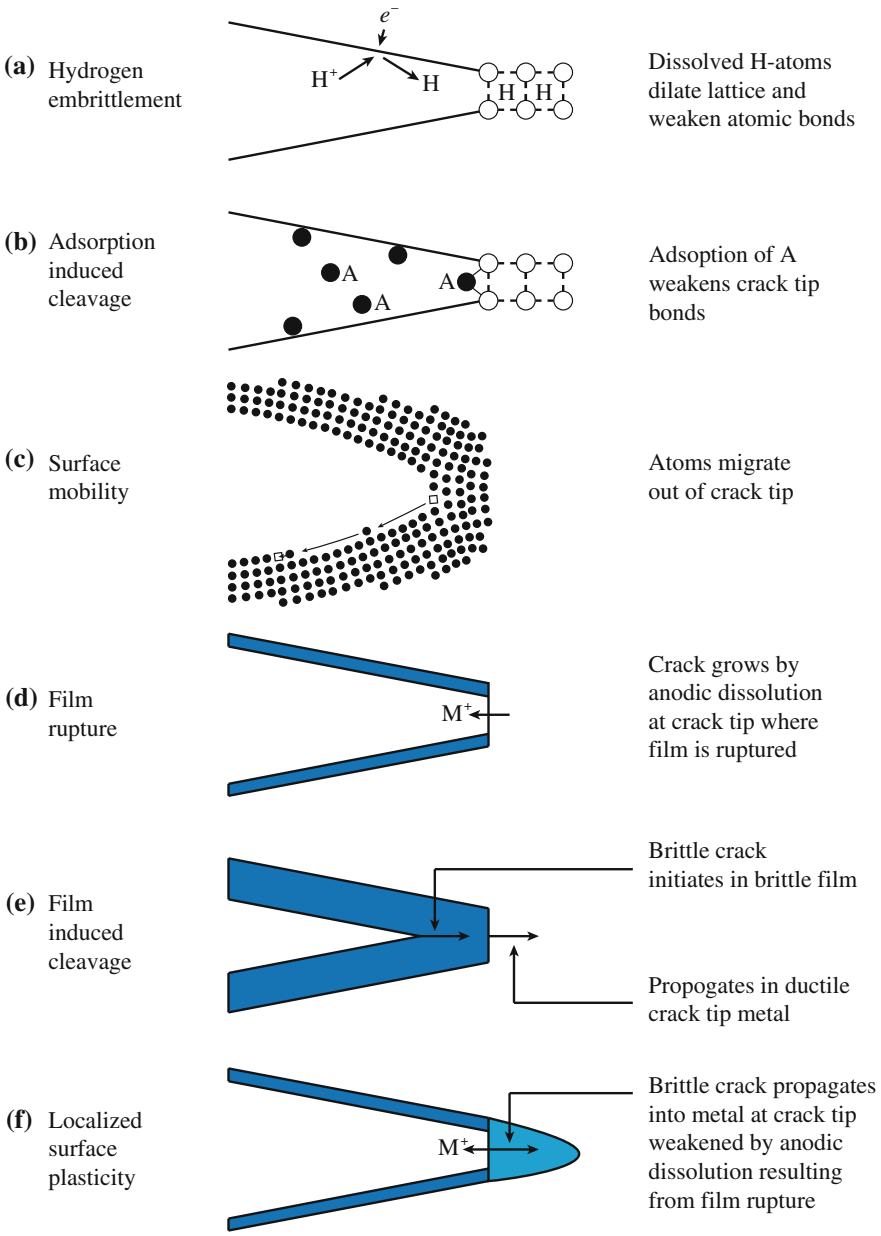

Fig. 15.64 Schematic illustration of crack tip processes that may be occur during environmentally assisted crack propagation (after [2])

- Mass transport along the crack to the crack tip;
- Reactions in the solution near the crack;
- Surface adsorption at or near the crack tip;
- Surface diffusion;
- Surface reactions;
- Adsorption into the bulk;
- Bulk diffusion to the plastic zone ahead of the crack tip;
- Chemical reactions in the bulk; and
- Rate of interatomic bond rupture.

In addition to these processes, the passivation of the surface layer by a protective oxide is an important process that can strongly affect stress corrosion cracking. Environmental parameters that affect crack propagation in aqueous solutions include:

- Temperature;
- Pressure;
- Solute species;
- Solute concentration and activity;
- pH;
- Electrochemical potential;
- Solution viscosity; and
- Agitation/flow rate.

An important factor in the cracking process is that the environment in occluded sites such as a crack tip can differ significantly from that in the bulk solution. If an alteration to the bulk environment allows the formation of a critical SCC environment at the crack nuclei, then crack propagation will result. If the bulk cannot maintain this local crack tip environment, then crack propagation will be retarded. SCC propagation rates are also influenced by a variety of mechanical and metallurgical factors, such as:

- The magnitude of the applied stress or the stress intensity factor, *K;*
- Stress state: plane stress versus plane strain;
- Loading mode at the crack tip;
- Alloy composition (nominal and local);
- Metallurgical condition (second phases in the grain boundary and matrix, phase composition and shape, grain size, grain boundary segregation, strength level, residual stress); and
- Crack geometry (length, aspect ratio, crack opening).

15.7.3 Metallurgical Condition

As stated earlier, pure metals are much less susceptible to SCC than alloys or commercial purity metals [2]. However, “pure” may mean 99.9999 % or better, so it

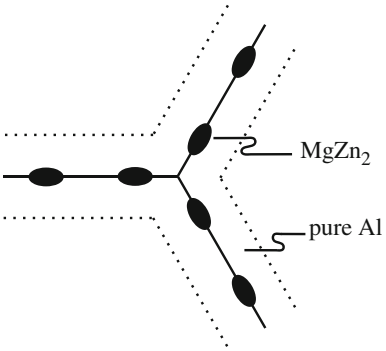

Fig. 15.65 Formation of $MgZn_2$ and depletion of Mg and Zn from the grain boundary, leading to a weak grain boundary and intergranular stress corrosion cracking in an aluminum alloy

is a very subjective term. Conversely, grain boundary chemistry and structure often play significant roles in SCC. Intergranular cracking of high purity iron is due to grain boundary impurities. Aluminum alloy 7075 (Al–Zn–Mg) fails intergranularly in chlorides and halides due to grain boundary depletion of magnesium and zinc caused by precipitation of $MgZn_2$ at the boundary (Fig. 15.65). The $MgZn_2$ phase dissolves preferentially, leaving holes in the grain boundary, and the weak aluminum bridges rupture mechanically.

The strong dependence of cracking in Fe–18Cr–xNi alloys on the nickel content in pure water or 0.1 % NaCl at high temperature is an example of the effect of bulk alloy content on SCC. The greatest susceptibility to IGSCC in pure water occurs at high concentrations of Ni (>70 wt%) and in 0.1 % NaCl at both high (IGSCC) and low (TGSCC) concentrations of Ni as in Fig. 15.66. Grain size can influence SCC, with susceptibility increasing with grain size. As grains become larger, dislocation pileups at grain boundaries become longer, producing higher local stresses and strains (according to the Hall–Petch relation), and higher susceptibility to SCC (Fig. 15.67).

15.7.4 Crack Initiation and Crack Propagation

The stress corrosion cracking process is often subdivided into initiation and propagation stages. Common sites for SCC crack initiation are as follows:

- Preexisting or corrosion-induced surface features such as grooves and burrs;
- Corrosion-induced pits;
- Intergranular corrosion or slip-dissolution processes. Intergranular corrosion-initiated SCC requires differing local grain boundary chemistry (e.g., sensitized stainless steels for grain boundary segregation). Slip dissolution-initiated SCC requires local corrosion at emerging slip planes in primarily, low stacking fault materials.

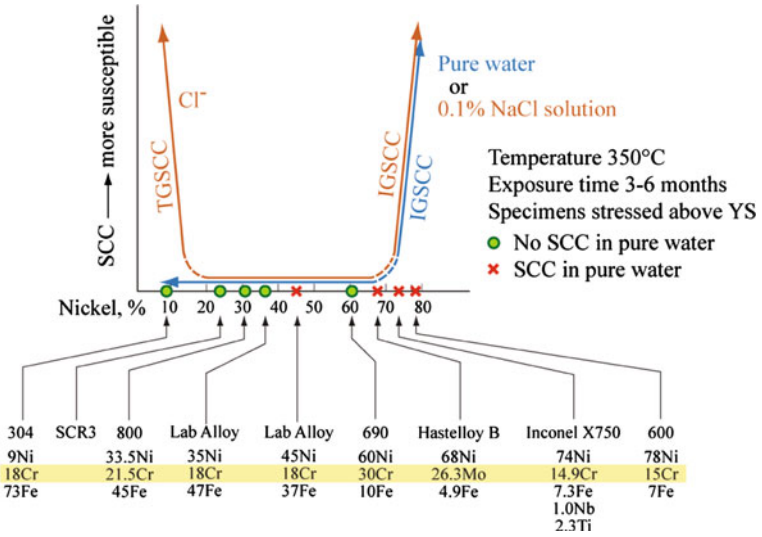

Fig. 15.66 SCC severity of austenitic alloys as a function of nickel content in pure water or 0.1 % sodium chloride solution at high temperature (courtesy of R.W. Staehle [6])

While crack initiation is of great concern, there is a distinct lack of understanding of the mechanism of stress corrosion crack initiation due to the complexity of the process and the difficulty in defining the initiation phase. Further, the distinction between crack initiation and propagation phases is not sharp. Nevertheless, the importance of the crack initiation phase cannot be overstated. Figure 15.68 shows a plot of the cumulative failure fraction of Inconel alloy 600 (Ni–16Cr–9Fe) steam generator tubes in a typical once-through steam generator as a function of effective full power years (EFPY). Note that cracking on the secondary side (freespan IGSCC) in the hot leg does not appear until about 10 years after startup. Yet, by the 13-year mark, this degradation mode grew to dominate all other failure modes in the

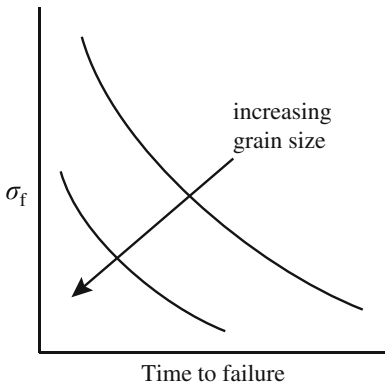

Fig. 15.67 Effect of grain size on the relation between failure stress and time to failure by SCC

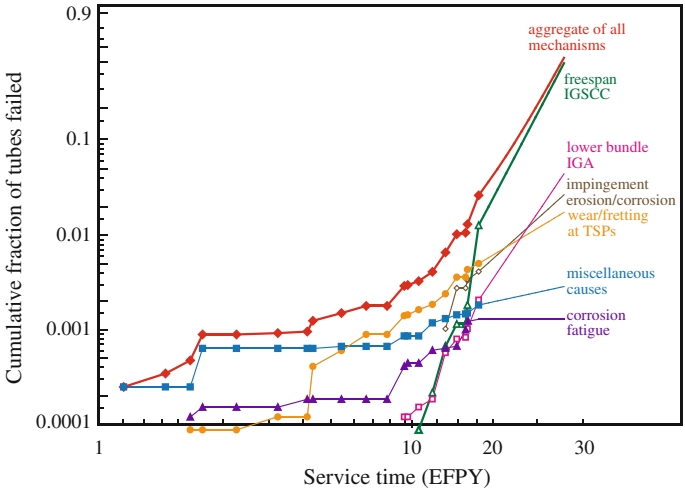

Fig. 15.68 Cumulative fraction of failed steam generator tubes for various modes of degradation of a typical once-through steam generator. Note that freespan IGSCC did not become measurable until about 10 years, and after 13 years, it accounted for more failures than all other modes combined

steam generator combined. In fact, the growth rate was so fast that the decision was made to replace the steam generator within two years after these data were accumulated. Clearly, in this case, initiation required considerable time, but once it occurred, propagation of the crack proceeded rapidly.

Cracks may initiate at preexisting surface flaws, or corrosion processes may create a surface flaw by pitting or localized corrosion, e.g., grain boundary attack or crevice corrosion. However, the conditions under which a crack will propagate are not necessarily the same. Both thermodynamic requirements and kinetic conditions must be met for a crack to initiate or to grow.

15.7.5 Thermodynamics of SCC

Without oxidation or anodic dissolution, cracks would not advance. The occurrence of simultaneous film formation and oxidation during stress corrosion crack growth can be understood from Fig. 15.69, which shows a crack in which dissolution is

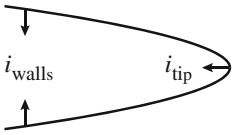

Fig. 15.69 Schematic illustration showing corrosion current from the walls and the tip of a crack

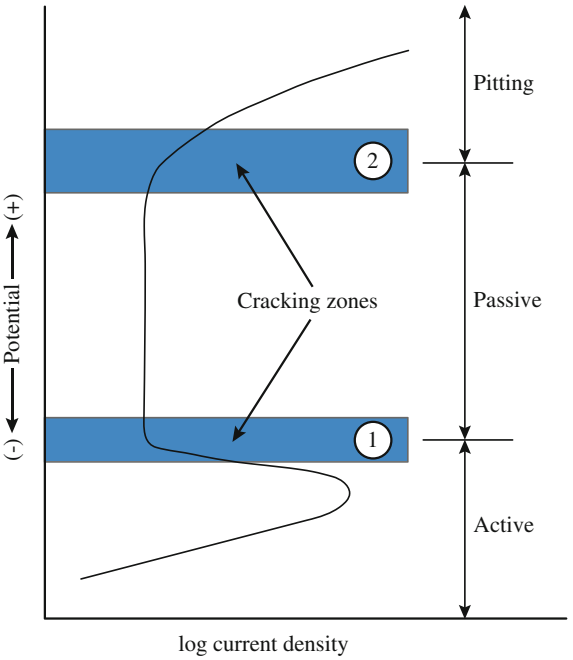

Fig. 15.70 Schematic anodic polarization curve showing the potential ranges over which susceptibility to stress corrosion cracking occurs (after [7])

occurring at both the crack tip and crack walls. The ratio of anodic currents from the walls relative to the crack tip is the critical parameter. The ratio i_{walls}/i_{tip} must be $\ll 1$ for a crack to propagate, otherwise the crack will blunt.

Figure 15.70 shows a polarization curve for an active–passive alloy. Note that there are two zones where SCC is most likely to occur. In zone ①, the alloy is in the active-to-passive film transition so that the simultaneous condition for film formation on crack walls and corrosion at the crack tip are met. In zone ②, similar conditions are met with the added factor that these potentials are above the pitting potential and cracks can initiate from pits. Practically, IGSCC can occur over the entire range between and including zones ① and ② because chemical inhomogeneities at the grain boundary produce a different electrochemical response relative to the bulk material.

An overlay of the regimes in which SCC occurs on the Pourbaix diagram will identify the phases that correlate with cracking. Figure 15.71 shows a Pourbaix diagram for nickel and iron in 300 °C water in which SCC is associated with potentials and pHs that follow the Ni/NiO stability line. The effect of many environmental parameters such as pH, oxygen concentration, and temperature on the thermodynamic conditions for SCC can be related to their effect on the potential–pH diagram. For materials in which SCC occurs by a hydrogen-induced subcritical crack growth mechanism, the thermodynamic requirement for crack growth is governed by the hydrogen reduction line ⓐ. The range of potentials at which H is available to cause crack growth increases and becomes more oxidizing with

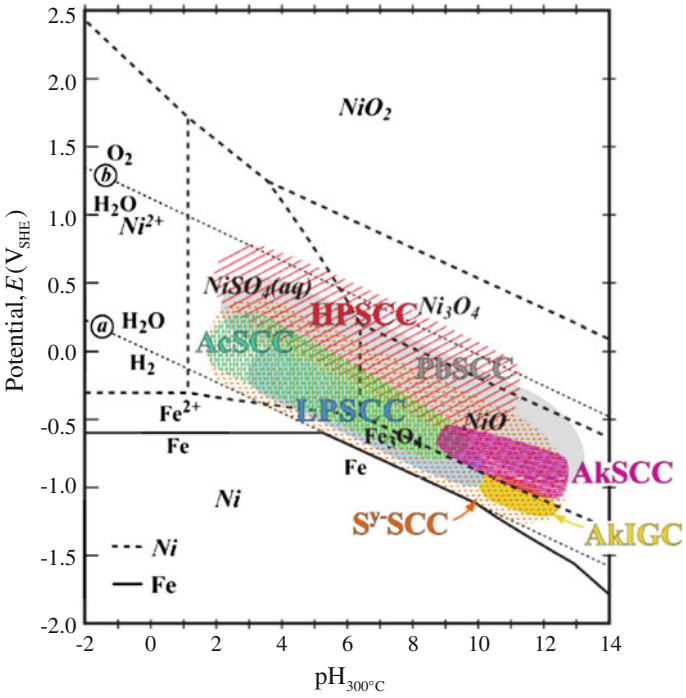

Fig. 15.71 Various SCC submodes as a function of potential and pH plotted over the Ni and Fe stability diagrams at 300 °C. Modes of SCC in Alloy 600 affected by environmental chemistry. Regimes in the figure are as follows: *AcSCC* acidic-induced SCC, *AkSCC* alkaline-induced SCC, *HPSCC* high-potential-induced SCC, *LPSCC* low-potential-induced SCC, *AkIGC* alkaline-induced intergranular corrosion, *PbSCC* lead-induced SCC, and *Sy-SCC* sulfide-induced SCC (from [8])

decreasing pH. However, the potential and pH at the tip of a crack can differ substantially from that at the free surface due to production, reaction, and diffusion of oxygen or metal ions within the crack, as described in Sect. 15.6.

15.7.6 Kinetics of SCC

As with the thermodynamic conditions for SCC, environmental parameters such as potential, pH, oxygen concentration, and temperature along with crack geometry and crack tip chemistry strongly affect crack growth kinetics. For the case of a crack growing by anodic dissolution alone, the total crack advance is a function of the total anodic charge transfer (integral of current over time) at the crack tip, and therefore, the crack velocity is a function of the average crack tip current density. A limiting velocity can be described for a crack advancing under pure anodic dissolution by the following Faradaic relationship:

$$\dot{a} = \frac{\mathrm{da}}{\mathrm{d}t} = \frac{i_{\mathrm{a}} M}{nF\rho}, \tag{15.65}$$

where i_{a} is the anodic current density of a bare surface, M is the atomic weight, n is the valence, F is Faraday's constant, and ρ is the density. Equation (15.65) assumes that the crack tip is maintained in a bare condition, while the crack walls are relatively inactive (to prevent blunting). A number of factors can reduce crack velocity, principle among them is the formation of a film which covers the crack tip. Other factors that can limit crack velocity are as follows:

- Limits on diffusion of species into or out of the crack;
- Crack growth away from the principal stress;
- Changes in local alloy chemistry; and
- Corrosion of the crack walls.

A model for crack propagation based on crack tip dissolution will be presented in Sect. 15.7.8.

15.7.7 Mechanisms of Stress Corrosion Cracking

By virtue of its nature, stress corrosion cracking refers to a chemical or electrochemical process involving oxidation and reduction reactions where the thermodynamic tendency is described by the Nernst equation. Under certain conditions, these reactions can manifest themselves in the form of a stress corrosion crack. The mechanisms by which these cracks form and propagate are not completely agreed upon. The leading theories are active path SCC and the film rupture model.

Active Path SCC

Active path SCC was first proposed in the 1940s to explain rapid grain boundary attack and is based on the establishment of galvanic cells between the base metal and anodic paths set up by heterogeneous phases (or segregated elements) along grain boundaries or slip planes. Active path SCC also refers to preferential dissolution of a phase in the alloy. The applied stress ruptures oxide films and exposes fresh metal to dissolution. The idea behind this theory is that preferred dissolution occurs at slip planes due to the increased number of preferred sites. Plastic deformation is essentially "feeding" bare material to the electrolyte for consumption with the net effect being an increase in the exchange current density and hence the rate of corrosion. Active path SCC should follow a time-to-failure dependence on current described by the plot in Fig. 15.72. However, electrochemical dissolution at a crack tip will tend to blunt the crack rather than contribute to its advance. So active path SCC is not a plausible explanation for observed stress corrosion cracks.

It should be noted, however, that active path corrosion can contribute to intergranular separation. The intergranular fracture of Ni–Cr–Fe alloys in sodium

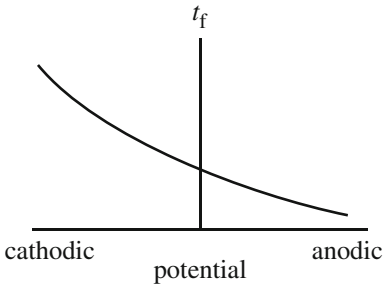

Fig. 15.72 Behavior of time-to-failure for an active path stress corrosion cracking mechanism

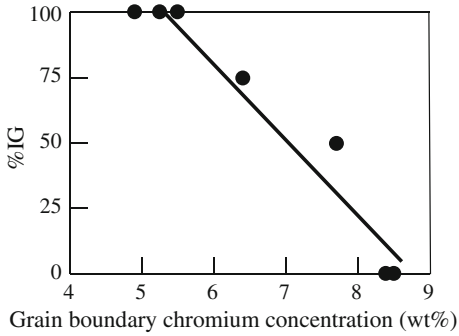

Fig. 15.73 Percent IG fracture versus grain boundary chromium concentration for Ni–16Cr–9Fe stressed in 0.017 M $Na_2S_4O_6$ at 25 °C (after [9])

tetrathionate, $Na_2S_4O_6$ (pH ~ 3–4), depends strongly on the grain boundary chromium level (Fig. 15.73). Cracking is believed to occur by stress-assisted intergranular attack in which the role of stress is to open the crack tip for access by the bulk solution, which then causes preferential dissolution along the grain boundary. This is an example of a stress-assisted anodic dissolution-driven process and is not based on film rupture.

Film Rupture Model

The corrosion resistance of most alloys is attributed to the passive film on the surface. When sufficient stress is applied, the film is ruptured or damaged by shear stresses on properly oriented glide planes (Fig. 15.74). But SCC susceptibility depends on the nature of slip. In alloys with high stacking fault energy (SFE), the separation of total dislocations into partials is unlikely. Since partials must recombine in order to cross-slip, high SFE alloys exhibit easy cross-slip, while low SFE alloys do not exhibit cross-slip. As a result, low SFE alloys exhibit planar slip in which the deformation occurs on relatively few slip planes and is characterized by regularly spaced slip bands, not unlike the morphology of dislocation channels discussed in Chap. 12. Figure 15.75 shows the effect of Ni content in austenitic

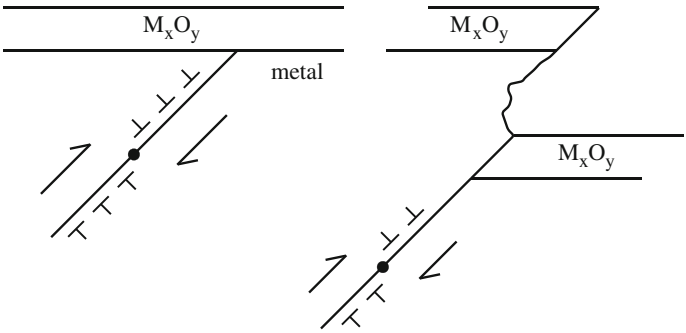

Fig. 15.74 Schematic illustration of the process by which slip can cause rupture of an oxide film, leading to accelerated corrosion before repassivation

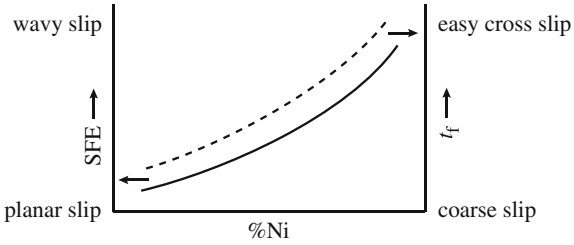

Fig. 15.75 Dependence of stacking fault energy (which determines the slip character) and time to failure on the nickel content in an austenitic, Fe–Cr–Ni alloy

alloys on the SFE and time to failure along with the role of the nature of slip. Low SFE alloys (low Ni content) exhibit coarse or *planar* slip and low time to failure, while high SFE alloys (higher Ni content) can cross-slip exhibiting *wavy* slip and a longer time to failure.

Repassivation of the exposed surface will likely occur, but the rate of repassivation will control the rate of crack propagation. If repassivation occurs too quickly, the corrosion attack causes only a very small increment of crack growth. If repassivation occurs too slowly, corrosion blunts the crack tip. Hence, there is an intermediate rate at which corrosion occurs to maximize growth crack without blunting it. Figure 15.76 shows how the rate of repassivation at a potential, and E_1 can vary with the environment. Chloride ions are effective in slowing repassivation. So while SCC of stainless steels does not occur in sulfuric acid at room temperature, the addition of Cl^- to sulfuric acid induces susceptibility to SCC, presumably by reducing the repassivation rate. In fact, alloy composition can strongly affect repassivation rate as well. Figure 15.77 shows that increasing Cr in a Ni–Cr–Fe alloy substantially increases the repassivation rate, which leads to a reduction in the SCC susceptibility.

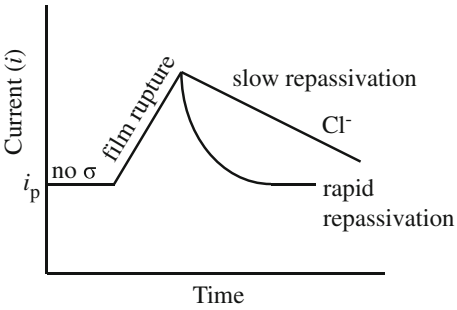

Fig. 15.76 Behavior of the corrosion current in a repassivation test in which an applied stress results in film rupture and repassivation. Aggressive species in the solution can cause slow repassivation, allowing for a greater amount of corrosion

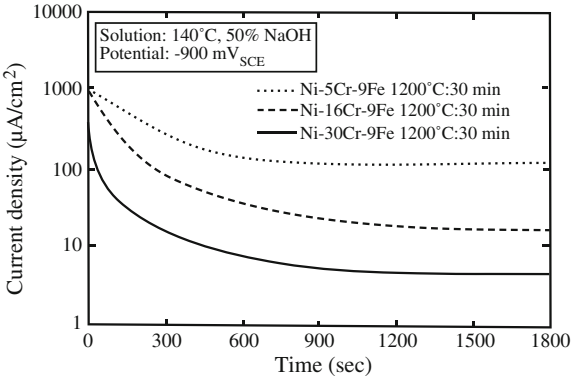

Fig. 15.77 Current decay or repassivation rate of Ni–Cr–Fe alloys as a function of chromium content, showing that repassivation occurs much more quickly with higher alloy chromium contents (after [10])

15.7.8 Predictive Model for Crack Propagation

Structural components manufactured from stainless steels, nickel-base alloys, and ferritic steels are all susceptible to environmentally assisted cracking in light water reactor environments. The phenomenology of cracking in these environments is well-recognized in terms of the effect that various material, stress, and environmental parameters have on the cracking susceptibility. For these systems, Ford and Andresen [11–14] have developed a working hypothesis for the cracking mechanism that is based on the slip oxidation/film rupture model (Fig. 15.64(d)) and the relevant crack tip environment. In this model, crack advance is related to the oxidation reactions that occur at the crack tip as the protective film is ruptured by increasing strain in the underlying matrix. Rupture events occur with a periodicity, t_f, which is determined by the fracture strain of the oxide and the strain rate at the

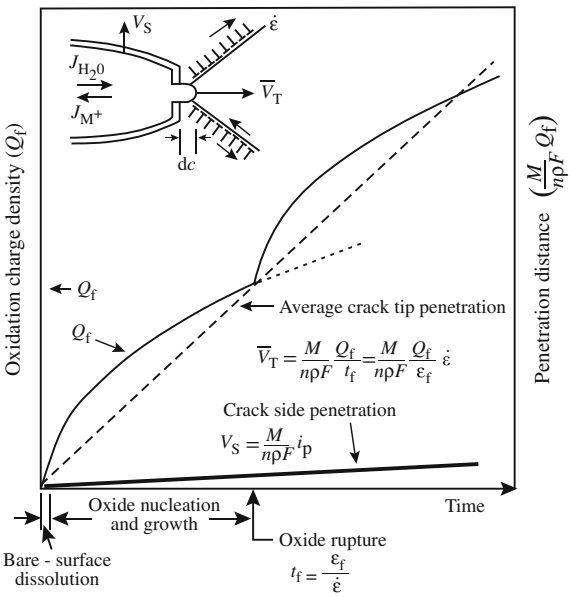

Fig. 15.78 Schematic of the oxidation charge density versus time relationship for a strained crack tip and unstrained crack sides obeying the film rupture model (after [11])

crack tip. The extent of crack advance is related (by Faraday's law) to the oxidation charge density associated with dissolution and oxide growth (passivation) on the bare metal surface, similar to that described by Eq. (15.65):

$$\dot{a} = \frac{M}{nF\rho}\frac{Q_f}{t_f}, \tag{15.66}$$

where

$$t_f = \frac{\varepsilon_f}{\dot{\varepsilon}_{ct}}, \tag{15.67}$$

giving the average crack velocity in terms of the crack tip strain rate:

$$\bar{v}_T = \dot{a} = \frac{M}{nF\rho}\frac{Q_f}{\varepsilon_f}\dot{\varepsilon}_{ct}, \tag{15.68}$$

where Q_f is the charge transfer at fracture, ε_f is the fracture strain, and $\dot{\varepsilon}_{ct}$ is the crack tip strain rate and embodies the mechanical contribution to cracking. The oxidation charge density and crack penetration rate are shown as a function of time in the schematic diagram of Fig. 15.78. Note that the oxidation charge density varies in a parabolic fashion with time according to a solid-state oxidation model [15], and the velocity of crack propagation is an average over time. The reactions at the crack tip vary with time in a complex manner for different environments and material

chemistries, and the resultant average crack growth rate, $\bar{v}_T$, is restated in a general form:

$$\bar{v}_T = \frac{M}{nF\rho}\frac{i_a t_0^m}{(1-m)\varepsilon_f^m}\dot{\varepsilon}_{ct} \tag{15.69}$$

$$= f(m)\dot{\varepsilon}_{ct}^m, \tag{15.70}$$

where i_a is the bare surface dissolution current, and t_0 and m are repassivation parameters that represent the effects of the environment and material chemistries on environmentally assisted crack growth.

The model is composed of three primary conceptual and predictive elements: (1) the rate of film rupture (proportional to the crack tip strain rate), (2) the solution chemistry at the crack tip, and (3) the resultant kinetics of oxidation/repassivation in the crack tip environment following a film rupture event. Most of the parameters that comprise the water and material chemistry effects distill into a single parameter, m, that represents the slope of the repassivation current on a log–log plot. The crack tip strain rate formulations then permit the calculation of the frequency of film rupture *events* and in turn the prediction of the environmental crack growth rate over a continuum of loading, water, and material characteristics. For example, the function, *f,* in Eq. (15.70) may be of the form, $f(m) \sim Am^{3.6}$, where m is a function of water chemistry and material chemistry and is an indicator of the level of susceptibility, where $m \rightarrow 0.3$ for high susceptibility and $m \rightarrow 1$ for low susceptibility. The crack tip strain rate is a function of the stress intensity of the crack tip and may be expressed in the form $\dot{\varepsilon}_{ct} = BK^4$. So the crack growth rate is then as follows:

$$\bar{v}_T = Am^{3.6}(BK^4)^m \tag{15.71}$$

15.7.9 Mechanical Fracture Models

Cracks occur as a result of corrosion reactions, but when their behavior is driven by the stress rather than corrosion reactions, they are considered to fail by mechanical fracture. Several models exist to explain cracking by mechanical fracture processes.

Under certain conditions, a fine array of corrosion-induced tunnels are observed at the point where slip steps emerge on the sample surface. The tunnels grow in diameter and length until stress in the remaining ligaments rises to the point where the load can no longer be sustained with the reduced cross section and fracture occurs by overload. According to the *corrosion tunnel model*, cracks propagate by alternate tunnel growth and ductile fracture. Cracks propagating by this mechanism should result in grooved fracture surfaces with evidence of microvoid coalescence. That this morphology is generally not observed suggests that the application of a

tensile stress results in thin, flat slots instead of tunnels. This morphology is very consistent with transgranular SCC fracture morphology.

Based on fractographic studies, it was concluded that cleavage fracture is not an atomically brittle process, but occurs by alternate slip at the crack tip in conjunction with formation of very small voids ahead of the crack. It was also proposed that chemisorption of environmental species facilitated the nucleation of dislocations at the crack tip, promoting shear processes responsible for brittle cleavage-like fracture. The *adsorption-enhanced plasticity* mechanism relies on adsorption of aggressive species to promote cleavage fracture.

In the *tarnish rupture* model, a brittle surface forms on the metal and fractures under an applied stress. Fracture exposes bare metal, which rapidly reacts with the environment to reform the film. The crack propagates by successive cycles of film growth and fracture. Assuming that the film penetrates along the grain boundary ahead of the crack tip, the model has been applied to intergranular cracking. The key feature of this mechanism is that fracture occurs entirely within the oxide film and not in the metal.

The *film-induced cleavage* mechanism (Fig. 15.64(e)) holds that a thin surface film or layer forms on the surface, followed by the formation of a brittle crack in the layer. The crack crosses the film–matrix interface without loss of velocity and continues to propagate in the ductile matrix along a particular crystallographic direction. The crack eventually blunts and arrests, and the cycle then repeats. This model can also explain crack arrest markings, cleavage-like facets on the fracture surface, and the discontinuous nature of crack propagation. The assumption that a brittle crack continues to propagate in a ductile matrix can be justified if the crack is sharp and propagates at high velocities.

First proposed by Uhlig, the *adsorption*(*stress-sorption*) mechanism (Fig. 15.64(b)) is related to the Griffith criterion for crack formation in glass and other brittle solids. It holds that adsorption of a species of any kind that reduces surface energy should favor crack formation. Recalling the expression for fracture stress, σ_f, from Chap. 14:

$$\sigma_f = \left(\frac{2E\gamma}{\pi c}\right)^{1/2}, \tag{15.72}$$

where E is Young's modulus, γ is the surface energy, and 2c is the crack length, then a reduction in the surface energy, e.g., as might occur by adsorption of Cl^- on a stainless steel surface, results in a lowering in the stress required for fracture. Unfortunately, the plausibility of this model is hard to establish because of the difficulty of determining the energy in the environment.

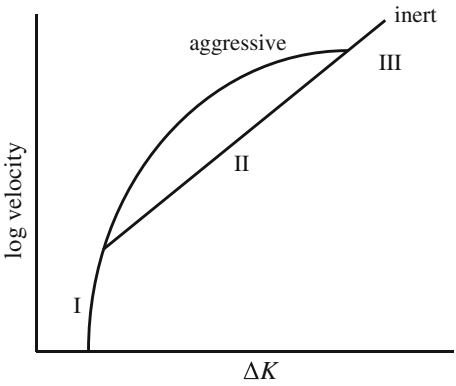

Fig. 15.79 Effect of an aggressive environment on the behavior of crack velocity with ΔK in a corrosion fatigue test

15.7.10 Corrosion Fatigue

Damage by corrosion fatigue is a conjoint action of corrosion and fatigue that is greater than that caused by the sum of both processes acting separately. In air, fatigue proceeds by localized slip within grains of the metal caused by alternating stress, resulting in slip steps at the metal surface. Adsorption of air on the exposed metal surfaces prevents rewelding on the reverse cycle (slip irreversibility). Continued application of stress produces protrusions above the metal surface (extrusions) and intrusions below. Corrosion accelerates plastic deformation by the formation of surface lattice vacancies, in particular, divacancies that rapidly diffuse into the metal at room temperature and accelerate plastic deformation by facilitating dislocation climb. The higher the rate of corrosion, the greater is the availability of divacancies, and the more pronounced is the formation of intrusions and extrusions. Lower frequencies produce greater degradation since more time is available per cycle for corrosion to occur. Figure 15.79 shows that the effect of the environment is greatest at intermediate values of ΔK.

15.7.11 Hydrogen Embrittlement

Hydrogen embrittlement is caused by the entry of hydrogen into the alloy by the corrosion process, cathodic protection, or high hydrogen overpressures. A common characteristic of hydrogen cracking is a specific delay in time for appearance of cracks after stress is applied. This is due to the time required for hydrogen to diffuse to a specific area near a crack nucleus and reach a critical concentration. Hydrogen embrittlement usually results in intergranular fracture and tends to be greatest at low strain rates.

There are several mechanisms by which hydrogen is believed to cause embrittlement. The *decohesion mechanism* (Fig. 15.64(a)) holds that atomic hydrogen

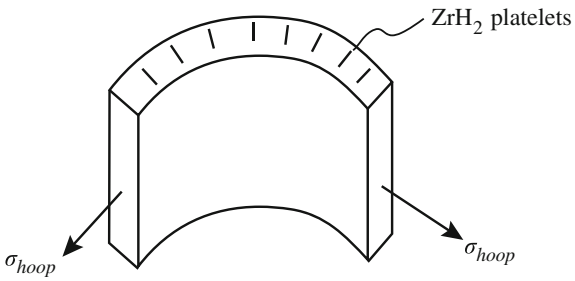

Fig. 15.80 Orientation of ZrH_2 platelets in Zircaloy fuel cladding under the application of a hoop stress

lowers or reduces the metal–metal bond strength. The *pressure theory* is based on precipitation of hydrogen as a gas at internal defects. The pressure developed by precipitation is added to the applied stress to lower the apparent fracture stress. Blisters can form if the process occurs close enough to the surface to deform the thin layer of metal above it.

A variation of the pressure theory is the *hydrogen attack* mechanism, which is due to the reaction between hydrogen and carbon to form methane. In addition to the formation of high-pressure methane gas bubbles, the reaction causes de-carburization and a weakening of the metal. Uhlig proposed that *direct adsorption* of hydrogen reduces the surface energy required to form a crack, thus lowering the fracture stress. The formation of a brittle *hydride* phase, e.g., ZrH_2 or TiH_2, can also induce embrittlement of the metal. The specific volume of the hydride is greater than the metal from which it came. Combined with the plate-like morphology of the hydride, the metal at the edge of the hydride platelet experiences a high tensile stress if the applied stress is perpendicular to the plane of the platelet. In zirconium alloys, platelets form on basal planes that are aligned in the radial direction of fuel cladding, causing a high tensile stress in the metal at the edges of the platelet due to the pressure in the cladding (Fig. 15.80). Hydrogen also interacts with dislocations. A high hydrogen fugacity at the metal surface and along grain boundaries can induce plasticity by activation of dislocation sources. The chemical driving force is responsible for the formation of dislocations, which then spread additional hydrogen into the lattice and exert a large stress intensity factor at the crack tip. This *hydrogen-induced localized plasticity* (HELP) mechanism (Fig. 15.64(f)) can explain high-temperature effects of hydrogen. Hydrogen-induced cracking is an important mechanism in ferritic steels, nickel-base alloys, and titanium and aluminum alloys.

Nomenclature

A	Atomic mass, or electron acceptor, or area
a_k	Activity of substance k
$\dot{a}$	Crack growth rate
$\mathrm{d}a/\mathrm{d}n$	Crack growth per cycle
$\mathrm{d}a/\mathrm{d}t$	Crack growth rate
c	Crack length
C_k	Concentration of substance k
D	Electron donor
i_{corr}	Corrosion current
$i_{0,\mathrm{a,c}}$	Current: exchange, anodic, cathodic
E	Electrode potential
E^e	Equilibrium electrode potential
E^0	Standard equilibrium electrode potential (at STP)
E_{corr}	Corrosion potential
E_{x}	Galvani or electrochemical potential in the phase x
F	Faraday's constant, 96,500 Coulombs/charge
G	Gibbs energy of the system
ΔG	Free energy change for a reaction
I	Current
i	Current density
K	Stress intensity
ΔK	Stress intensity range
K_{Ic}	Mode I fracture toughness
K_{th} or K_{SCC}	Threshold stress intensity for SCC
L	Path length through which a current is passed
m	Repassivation parameter
M	Atomic mass
n	Charge transfer, or number of equivalents exchanged in oxidation/reduction reaction
Q_{f}	Charge transfer at fracture
R	Gas constant or resistance
t	Time
T	Temperature
t_0	Repassivation parameter
$\bar{v}_{\mathrm{T}}$	Average crack velocity
B	Symmetry factor in expression for corrosion current
ε_{f}	Fracture strain
$\dot{\varepsilon}_{\mathrm{ct}}$	Crack tip strain rate
γ	Surface energy, or activity coefficient
h	Overpotential
μ_k^0	Standard chemical potential of species k
$(\mu_k)_x$	Electrochemical potential for the kth particle type in phase x
$(\tilde{\mu}_k)_x$	Electrochemical potential for the kth particle type in phase x

ν_i	Stoichiometric coefficients for substance i in a corrosion reaction
ρ	Density, or solution resistance
σ_f	Fracture stress
σ_{th} or σ_{SCC}	Threshold stress for SCC

Subscripts

A	Anodic
c	Chemical driving force
crit	Critical (refers to current density)
C	Cathodic
e	Reaction under an electric field
fail	Fail (refers to current density)
F	Flade
g	Gas
init	Initiation (refers to current density)
k	Substance
l	Liquid
L	Limiting
m	Metal
p, prod	Product
pp	Primary passive (refers to potential)
prop	Crack propagation (refers to current density)
r, react	Reactant, or reduction reaction designation
R	Resistance
s	Solution
tip	Tip (refers to current density)
trans	Transpassive (refers to potential)
walls	Walls (refers to current density)
x	Phase or oxidation reaction designation

Superscripts

e	Equilibrium condition
r	Reduction
x	Oxidation
0	Standard condition

Acronyms

AGR	Advanced gas reactor
AcSCC	Acidic-induced SCC
AkICG	Alkaline-induced intergranular corrosion
AkSCC	Alkaline-induced SCC

BWR	Boiling water reactor
CT	Compact tension
CERT	Constant extension rate test
DCB	Double cantilever beam
EFPY	Effective full power years
EMF	Electromotive force
ESEP	Equilibrium standard electrode potential
HPSCC	High-potential-induced SCC
HWC	Hydrogen water chemistry
IASCC	Irradiation-assisted stress corrosion cracking
IG	Intergranular
IGSCC	Intergranular stress corrosion cracking
LET	Linear energy transfer
LPSCC	Low-potential-induced SCC
LWR	Light water reactor
MSEP	Measured single electrode potential
NWC	Normal water chemistry
PbSCC	Lead-induced SCC
PWR	Pressurized water reactor
RH	Radiation hardening
RIS	Radiation-induced segregation
SCC	Stress corrosion cracking
SFE	Stacking fault energy
SHE	Standard hydrogen electrode
SGHWR	Steam-generating heavy water reactor
SSEP	Standard single electrode potential
SSRT	Slow strain rate test
STP	Standard temperature and pressure
SySCC	Sulfide-induced SCC
TG	Transgranular
TGSCC	Transgranular stress corrosion cracking

Problems

15.1 (a) Iron in an NaCl solution, pH = 1, shows a potential of +0.2 V_{SHE}. What are the possible anodic and cathodic reactions, assuming that the Pourbaix diagram in Fig. 15.7 applies.

(b) It was suggested that two possible reactions are as follows:

$$Cl_2 + 2e^- = 2Cl^-$$
$$Na = Na^+ + e^-$$

Do you agree with either or both? If so, what assumptions must you make?

15.2 Determine the equations describing the lines ① through ⑨ of the Pourbaix diagram for Ni given below and the following information.

$\mu^0_{NiO} = -51{,}610$ cal/mole
$\mu^0_{Ni_3O_4} = -170{,}150$ cal/mole
$\mu^0_{Ni_2O_3} = -112{,}270$ cal/mole
$\mu^0_{NiO_2} = -51{,}420$ cal/mole

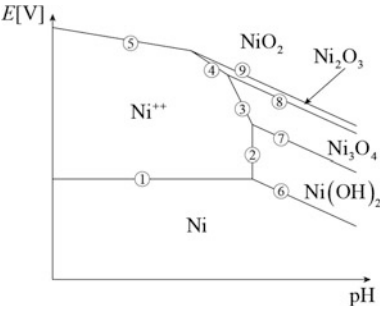

15.3 A zinc specimen exposed to an acid solution loses 25 mg during a 12 h exposure.

(a) What is the equivalent current flowing due to corrosion?
(b) If the specimen area is 200 cm^2, what is the corrosion rate in $mg/dm^2/d$ due to this current?
(c) What is the corrosion rate in mpy? μm/year?

15.4 Using appropriate polarization diagrams, determine the effect of the following parameters on the corrosion potential and corrosion rate of a metal, M, corroding to dissolved M^+ in an acid solution:

(a) Increasing i_0 of the anodic reaction;
(b) Increasing i_0 of the cathodic reaction;
(c) Increasing the concentration of dissolved H^+; and
(d) Increasing the Tafel constant of the anodic reaction.

15.5 (a) Plot the appropriate polarization curves for the following half-cell reactions and determine the corrosion potential and corrosion rate (current density) assuming activation control of both the anodic and cathodic processes. Determine the corrosion potential and corrosion rate from your plot.

$$M = M^+ + e^-, \quad E = -0.7\ V, \quad i_0 = 10^{-8}\ A/cm^2, \quad \beta_A = +0.1\ V$$
$$2H^+ + 2\ e^- = H_2, \quad E = +0.1\ V, \quad i_0 = 10^{-6}\ A/cm^2 \quad \beta_C = -0.1\ V$$

(b) Same as (a), but assume that the limiting current density for the reduction reaction is 10^{-5} A/cm^2. Again, determine the corrosion potential and corrosion rate from your plot.

15.6 Plot the following cathodic polarization data for carbon steel in 0.5 N H_2SO_4 on linear coordinates and determine the polarization resistance. From the shape of the plot, would you estimate that the absolute value of β_A is greater than or less than β_C?

Current density (μA/cm^2)	40	100	160	240	300
Cathodic overvoltage (mV)	1.0	2.5	4.1	6.3	9.0

15.7 With the following anodic and cathodic polarization data—the same conditions as Problem 15.6, but larger currents—plot the polarization curves on semilog coordinates and determine β_A, β_C, E_{corr}, and i_{corr}.

Current density, μA anodic or cathodic	Potential anode, mV_{SHE}	Potential cathode, mV_{SHE}
1.01×10^{-4}	−266	−276
2×10^{-4}	−264	−278
3×10^{-4}	−259	−286
5×10^{-4}	−255	−296
7×10^{-4}	−250	−305
1×10^{-3}	−246	−318
2×10^{-3}	−233	−341
3×10^{-3}	−226	−358
5×10^{-3}	−214	−383
7×10^{-3}	−204	−400
1×10^{-2}	−193	−416
2×10^{-2}	−176	−444

15.8 Plot schematically the polarization curve for anodic dissolution for the metal M that has the following electrochemical parameters:
$E_{corr} = -0.500\,V_{SCE}$, $i_{corr} = 10^{-4}\,A/cm^2$, $E_{pp} = 0.400\,V_{SCE}$,
$\beta_a = +0.05\,V, i_{pass} = 10^{-5}\,A/cm^2, E_{tr} = 1.000\,V.$
From the plot, determine the critical current density for passivation, i_{crit}

15.9 For the case shown in Fig. 15.43 (borderline passivity), draw the potentiostatic polarization curve ascending to higher (more noble) potentials from the corrosion potential. Carefully note changes in direction of current from anodic to cathodic.

15.10 Given active–passive alloys A and B having the following electrochemical parameters:

	E_{corr}, V	I_{corr}, A	β_a, V	E_{pp}, V	i_{pass}, A	E_{tr}, V
Alloy A	−0.400	1×10^{-6}	+0.1	0.0	1×10^{-5}	+0.7
Alloy B	−0.200	7×10^{-7}	+0.1	+0.3	1×10^{-6}	+1.2

(a) Which will be the more corrosion resistant in reducing condition (active state)? Why?
(b) Which will be the more corrosion resistant in the passive state? Why?
(c) Which is more easily passivated by dissolved oxidizers? Why?
(d) Which is more corrosion resistant in strongly oxidizing solutions? Why?
(e) Which would be more easily protected by anodic protection? Why?

15.11 Consider a 304 stainless steel pipe put into service in a boiling water reactor in 1983. The BWR used NWC (ECP = + 150 mV_{SHE}, conductivity = 0.1 μS/cm) for the first 16 years of service and then switched to HWC (ECP = −220 mV_{SHE}, conductivity = 0.1 μS/cm). The pipe was exposed to the standard water chemistry and was 6″ ID and 2″ wall thickness. The pipe experienced a constant stress and no fatigue loading (i.e., it is well supported). In 1991, a small crack was identified in the pipe during routine inspection. Given the water chemistry history of this reactor, should you expect water on the floor of this BWR?

15.12 Discuss the relative advantages and disadvantages of constant load, constant deflection, and CERT tests for assessing:

(a) The relative susceptibility of a variety of alloys to stress corrosion cracking
(b) The susceptibility of one alloy to stress corrosion cracking in several environments; and
(c) The stress and strain dependence of stress corrosion cracking.

15.13 (a) Calculate the minimum specimen width necessary for a valid fracture mechanics test of a steel of yield strength 700 MPa and fracture toughness of 170 $MPa\sqrt{m}$.
(b) Would it be practical to measure the fracture toughness of this sample?
(c) If a corrosive environment makes hydrogen embrittlement possible with K_{Ihic} of 23 $MPa\sqrt{m}$, what is the minimum specimen thickness?
(d) Would it be practical to measure the fracture toughness of this sample?

15.14 Plot the crack growth rate of an alloy over the range $10 \leq K \leq 60\,MPa\sqrt{m}$, for a crack tip strain rate given by BK^4, where B is 2×10^{-22} $MPa^{-1/4}$ $m^{-1/8}$ and A = 10 m/s for values of m = 0.1, 0.5, and 1.0.

References

1. Pourbaix M (1974) Atlas of electrochemical equilibria in aqueous solutions. NACE, Houston, TX
2. Jones DA (1996) Principles and prevention of corrosion, 2nd edn. Prentice-Hall, Upper Saddle River
3. Fontana MG (1986) Corrosion engineering, 3rd edn. McGraw-Hill, New York
4. Uhlig HH, Reive RW (2008) Corrosion and Corrosion Control: an introduction to corrosion science and engineering. Wiley-Interscience, Hoboken
5. Jones RH, Ricker RE (1992) Mechanisms of stress corrosion cracking. In: Jones RH (ed) Stress-corrosion cracking materials performance and evaluation. ASM International, Metals Park
6. Staehle RW, Personal communication
7. Staehle RW (1977) In: Staehle RW (ed) Stress Corrosion and Hydrogen Embrittlement of Iron Base Alloys, NACE-5. NACE, Houston, p 193
8. Staehle RW, Gorman JA (2002) In: Proceedings of the 10th international conference on environmental degradation of materials in nuclear power systems: water reactors. NACE International, Houston, TX, bonus paper
9. Was GS, Rajan VB (1987) Metal Trans A 18A:1313–1323
10. Sung JK, Koch J, Angeliu T, Was GS (1992) Metal Trans A 23A:2804–2887
11. Ford FP, Andresen PL, Solomon HD, Gordon GM, Ranganath S, Weinstein D, Pathania R (1990) In: Proceedings of the 4th international symposium on environmental degradation of materials in nuclear power systems: water reactors. NACE, Houston, TX, pp 4–26 to 4–51
12. Ford FP, Andresen PL (1994) Corrosion in nuclear systems: environmentally assisted cracking in light water reactors. In: Marcus P, Oudar J (eds) Corrosion mechanisms. Dekker, New York, pp 501–546
13. Ford FP, Andresen PL (1988) In: Theus GJ, Weeks JR (eds) Proceedings of the 3rd international symposium on environmental degradation of materials in nuclear power systems: water reactors. The Metallurgical Society of AIME, Warrendale, p 789
14. Andresen PL, Ford FP (1988) Mat Sci Eng vol A 1103:167
15. Wagner C (1959) Z Electrochem 63:772–782

Chapter 16
Effects of Irradiation on Corrosion and Environmentally Assisted Cracking

A growing concern for electric power utilities worldwide has been the degradation of core components in nuclear power reactors, which provide approximately 17 % of the world's electric power needs. Service failures have occurred in boiling water reactor (BWR) core components and, to a somewhat lesser extent, in pressurized water reactor (PWR) core components consisting of iron- and nickel-base stainless alloys that have achieved a significant neutron fluence in environments that span oxygenated to hydrogenated water at 270–340 °C. Because cracking susceptibility depends on many factors, such as alloy composition and microstructure, stress, radiation, and the environment, the failure mechanism has been termed irradiation-assisted stress corrosion cracking (IASCC). Initially, the affected components were either relatively small (bolts, springs, etc.) or those designed for replacement (fuel rods, control blades, or instrumentation tubes). Since these early observations, many more structural components (PWR baffle bolts and BWR core shrouds) have been identified as susceptible to IASCC. Recent reviews [1–5] describe the current state of knowledge related to IASCC service experience and laboratory investigations and highlight the limited amount of well-controlled experimentation that has been conducted on well-characterized materials.

The importance of neutron fluence on IASCC has been well established (Fig. 16.1). Observation of cracking in-core and data on post-irradiation slow strain rate tests(SSRT) on stainless steels show that there is a distinct (although not invariant) threshold fluence at which IASCC is observed under LWR conditions. Cracking is observed in BWR oxygenated water at fluences above about $2–5 \times 10^{24}$ n/m^2 ($E > 1$ MeV), which corresponds to about 0.3–0.7 displacements per atom (dpa) (Fig. 16.2). The term "threshold" is used here to characterize the regime where cracking increases steeply with fluence, but it does not mean that cracking is absent below the threshold or that cracking saturates at the threshold. Because this threshold occurs at a fraction to several dpa (depending on the alloy, stress, water chemistry, etc.), in situ effects (corrosion potential, conductivity, temperature) may be important, but only *persistent* radiation effects (microstructural and microchemical changes) can be responsible for the threshold-like behavior versus fluence in post-irradiation tests. IASCC only occurs with the confluence of irradiation and an aggressive environment. If either is absent, cracking is either eliminated or greatly reduced.

G.S. Was, *Fundamentals of Radiation Materials Science*,
DOI 10.1007/978-1-4939-3438-6_16

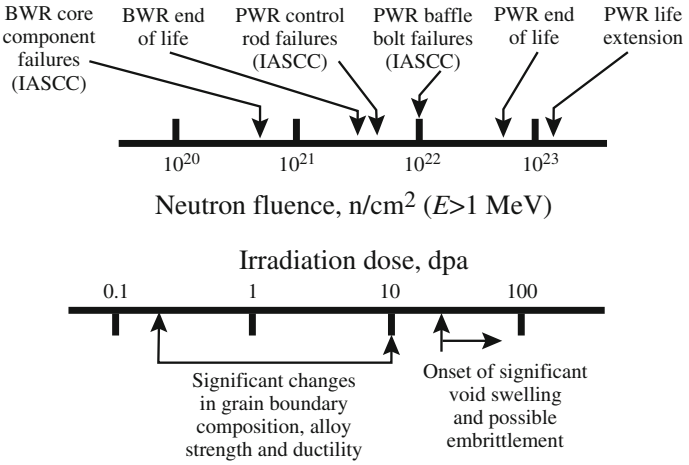

Fig. 16.1 Neutron fluence effects on irradiation-assisted stress corrosion cracking susceptibility of stainless steels in LWR environments (after [6])

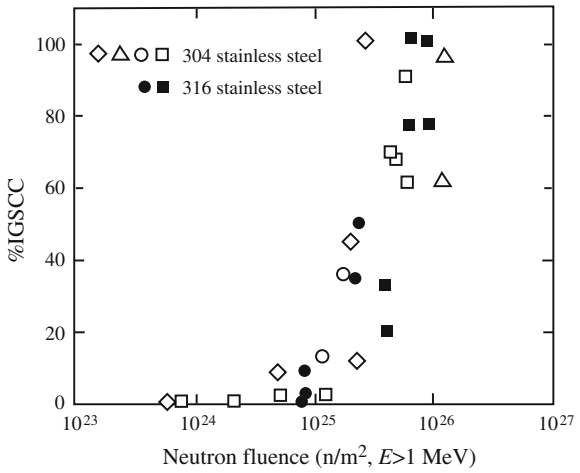

Fig. 16.2 Dependence of cracking in neutron-irradiated high-purity 304 SS and 316 SS on accumulated high-energy neutron fluence (after [4])

IASCC can be categorized into radiation effects on (1) water chemistry (radiolysis) and (2) material properties, as summarized in Fig. 16.3. The cracking response to changes in water chemistry is similar for both irradiated and unirradiated materials. In both cases, there is a steep increase in environmental cracking kinetics with a rise in the corrosion potential above about 100 mV_{SHE} [7–9]. At high corrosion potential, the CGR also increases sharply as impurities (especially chloride and sulfate) are added to pure water in either the irradiated or unirradiated

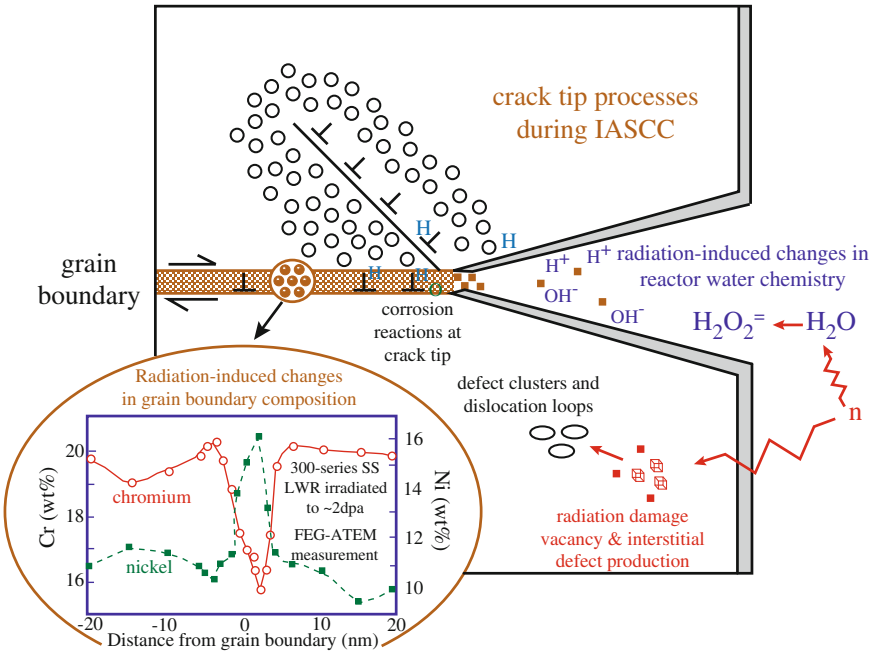

Fig. 16.3 Schematic illustration of mechanistic issues believed to influence crack advance during IASCC of austenitic stainless steels in LWRs (after [6])

cases. In post-irradiation tests, the dominant radiation-related factors are microstructural and microchemical changes, which can be responsible for *threshold-like* behavior in much the same way as corrosion potential, impurities, degree of sensitization, stress, and temperature. Other radiation phenomena, such as radiation creep relaxation and differential swelling, could also have *persistent* effects if the sources of stress present during radiation (e.g., weld residual stresses or loading from differential swelling) were also present during post-irradiation testing. In water, the effects of radiation rapidly (in seconds) achieve a dynamic equilibrium in water, primarily because of the high mobility of species in water. In the solid, dynamic equilibrium is achieved only after many dpa, typically requiring years of exposure. As radiation-induced segregation (RIS) of major elements, radiation hardening (RH), and the associated microstructural development asymptotically approach a dynamic equilibrium, other factors (e.g., RIS of Si, or precipitate formation or dissolution) may become important.

The following sections begin with a description of the effects of irradiation on water chemistry and on the oxide and how these processes can affect both oxidation and stress corrosion cracking under irradiation. The service experience of austenitic stainless steels and ferritic steels in water and under irradiation is presented, followed by a discussion of the mechanism of IASCC.

16.1 Effects of Irradiation on Water Chemistry

16.1.1 Radiolysis and Its Effect on Corrosion Potential

It is widely acknowledged that SCC susceptibility is fundamentally influenced by the corrosion potential [1, 7, 10, 11]. In this regard, what distinguishes BWRs from PWRs is the low H_2 concentration in BWRs, which permits the radiolytic formation of oxidants. Above ≈ 500 ppb (5.6 cc/kg) H_2, radiolytic formation of oxidants is effectively suppressed and the corrosion potential remains close to its thermodynamic minimum (which is a function of temperature, H_2 fugacity, and pH). BWRs cannot achieve this H_2 level because H_2 partitions to the steam phase, which begins to form about a quarter of the way up the fuel rods. Thus, radiolysis has a greater impact on BWRs and is the focus of this section.

Water is decomposed by ionizing radiation into various primary species [12–15] including both radicals (e.g., e^-_{aq}, H, OH, HO_2) and molecules (e.g., H_2O_2, H_2, O_2), which can be oxidizing (e.g., O_2, H_2O_2, HO_2) or reducing (e.g., e^-_{aq}, H, H_2). The predominant species that are stable for more than a few seconds are H_2O_2 and H_2, with O_2 forming primarily from the decomposition of H_2O_2. Because H_2 partitions to the steam phase and H_2O_2 is not volatile, the recirculated water in a BWR (≈ 87 % of the total water flow) is oxidant rich. The concentrations of radiolytic species are roughly proportional to the square root of the radiation flux in pure water. The radiation energy intensity spectrum influences the concentration of each radiolytic specie, which is described in terms of a yield, or G value (molecules produced per 100 eV absorbed by water). In LWRs, the G values for most species are within a factor of ≈ 3 for fast neutron versus gamma radiation. Despite this similarity, the influence of fast neutron radiation is much stronger than gamma radiation primarily because the energy deposition rate, or mean linear energy transfer (LET), is greater (40 eV/nm for fast neutrons versus 0.01 eV/nm for gamma radiation [15]). Also, the neutron dose rate in LWRs (e.g., ≈ 1.03×10^9 Rad/h core average and ≈ 1.68×10^9 Rad/h peak in a BWR4 of 51 W/cc power density) is also higher than the gamma dose rate (≈ 0.34×10^9 Rad/h) [5]. In fact, the moderate gamma levels present in the downcomer in the outside annulus of a BWR core actually promote recombination of hydrogen and various oxidants [13, 16]. Overall, the contribution of thermal neutrons and beta particles to radiolysis is small in LWRs.

As in many electrochemical processes, the integrated effects of various oxidants and reductants on environmental cracking are best described via changes in corrosion potential, which controls the thermodynamics and influences the kinetics of most reactions. Since electrochemical potentials are logarithmically dependent on local oxidant, reductant, and ionic concentrations via the Nernst relationship, as in Eq. (15.20), radiation-induced increases in concentrations of various species by many orders of magnitude may have comparatively small effects on the corrosion potential in hot water. Further, corrosion potentials are mixed potentials involving a balance of anodic and cathodic reactions on the metal surface, which depend on the concentrations of both oxidizing and reducing species. At low oxidant

concentrations, low corrosion potentials of ≈ −0.5 V_{SHE} result from mass transport-limited kinetics (e.g., oxygen transport to the metal surface). In this regime, more pronounced shifts in corrosion potential with radiation can occur, presumably from the radiolytic formation of oxidizing species within the mass transport-limited stagnant layer.

The relationship between dissolved oxygen concentration and corrosion potential in hot water as a function of radiation type and flux is shown in Fig. 16.4(a), in which the connected points represent data obtained in controlled, radiation on/off experiments. The data from these latter experiments are shown in Fig. 16.4(b) in terms of a radiation-induced shift in corrosion potential. The curves in Fig. 16.4(a) represent the scatter band for the data obtained under unirradiated conditions. Similar scatter also exists in the irradiated corrosion potential data in Fig. 16.4(b) and is comprised of contributions from both real effects and experimental error. These data show that little, if any, elevation in corrosion potential results from irradiation sources which do not include neutrons or simulate their contribution

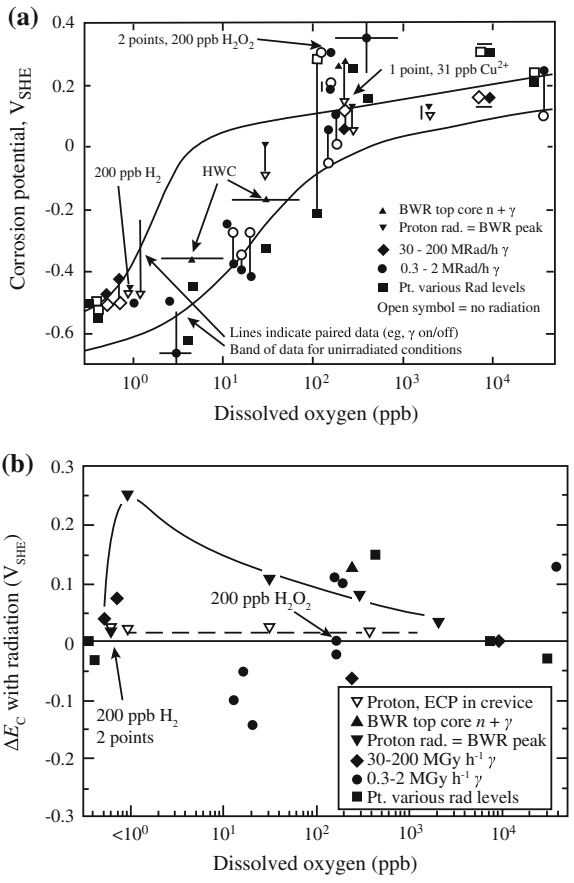

Fig. 16.4 (**a**) Effect of radiation on the corrosion potential of type 304 stainless steel in 288 °C water. The curves denote the range of typical values in the unirradiated corrosion potential data (after [1]). (**b**) Effect of radiation on the shift in corrosion potential from the value under unirradiated conditions for type 304 stainless steel in water at 288 °C (after [1])

(e.g., using high-energy protons). Some studies using gamma radiation [1, 10] showed a significant decrease in corrosion potential, especially in the intermediate (e.g., 10–200 ppb) range of dissolved oxygen. This is consistent with enhanced recombination of oxidizing and reducing species, which occurs in the downcomer region of BWRs [16] and is relied upon to produce SCC mitigation using *hydrogen water chemistry* (HWC).

In instances where neutrons or protons have been used, a consistent and significant elevation in corrosion potential is observed. It is more pronounced in hot water containing low dissolved oxygen concentrations and no dissolved hydrogen (Fig. 16.4(b)) where increases of over +0.25 V occur. At higher inlet oxygen concentrations (e.g., ≈ 200 ppb), the data still show a significant shift (typically +0.1 to 0.15 V) in corrosion potential for radiation conditions representative of peak LWR core fluxes; less increase is observed for inlet oxygen concentrations associated, e.g., with air saturation (≈ 8.8 ppm O_2) or oxygen saturation (≈ 42 ppm O_2 at STP). A similar elevation in corrosion potential is observed for additions of hydrogen peroxide (200 ppb H_2O_2, Fig. 16.4(a)), which suggests that H_2O_2 may be a major factor in increasing the corrosion potential under irradiated conditions.

In-core, in situ measurements in BWRs show that the corrosion potential, which is ≈ +0.2 to +0.25 V_{SHE} in normal water chemistry (NWC), can be decreased by over 0.5 V by sufficient additions of dissolved hydrogen in a BWR [17]. This is corroborated by other measurements [18], which show very little radiation-induced elevation in corrosion potential when the fully deaerated inlet water contains moderate dissolved hydrogen (>200 ppb H_2, 0 ppb O_2). However, at high H_2 levels, the core becomes reducing, and the small concentration of ^{16}N (transmuted from ^{16}O) changes from soluble NO_3^- to volatile NO_x and NH_3, causing a large increase in radiation level in the steam lines and turbine.

The effect of radiation on the corrosion potential within a crack or crevice is also of interest, with the possibility that a net oxidizing environment in the crack could be created that could elevate the corrosion potential above the potential at the crack mouth. In the absence of radiation, measurements in high-temperature water in artificial crevices (e.g., tubing), at the tip of growing cracks, and of short crack growth behavior show that the corrosion potential remains low (i.e., -0.5 ± 0.1 V_{SHE} in 288 °C pure water) for all bulk oxygen concentrations, indicating that complete oxygen consumption occurs within the crack, as discussed in Sect. 15.6. Recent measurements of radiation effects in crevices show that the elevation in corrosion potential is limited to less than 0.05 V in-core; this is consistent with the interpretation of available corrosion potential data on free surfaces [1, 7, 10, 19]. These small changes will not significantly affect the ≈ 0.75 V (+0.25 V_{SHE} (near mouth) minus −0.5 V_{SHE} (in crack)) potential difference in the crack under irradiated normal BWR water chemistry conditions. The potential difference, along with other factors, controls the enhancement mechanism that can lead to an increased anion activity and altered pH at the crack tip [8, 9, 11] and Fig. 15.56.

16.1.2 *Effects of Corrosion Potential on Oxidation*

The elevation of corrosion potential by radiolysis can affect the oxidation of metals. For example, γ-radiation causes the corrosion potential on the metal surface to rise substantially due to radiolytic production of oxidizing species, notably H_2O_2 [20, 21]. The increase in the corrosion potential increases the total metal oxidation rate, but the consequences of this increase vary with pH, temperature, and the type of alloy. At pH 6.0 and 25 °C, the increase results mainly in additional metal dissolution and small particle deposits on carbon steel and 316L stainless steel. At pH 10.6, dissolution is negligible and γ-radiation leads to the formation of a thicker uniform oxide [20].

Radiolytically produced redox agents can react with dissolved transition metal ions (corrosion products) to change their oxidation state. Radical radiolysis products (·OH and $\cdot e_{aq-}$), which are less effective than molecular oxidants (like H_2O_2) in promoting surface reactions, participate very effectively in these homogeneous reactions. The solubilities of hydrated transition metal ions vary by many orders of magnitude depending on their oxidation state. For example, ferrous iron (Fe^{2+}) is several orders of magnitude more soluble than ferric iron (Fe^{3+}) at acidic and neutral pHs, while Cr^{6+} species are much more soluble than Cr^{3+} species at all pHs. It has been shown that radiolytic conversion of more soluble metal ions to less soluble ions promotes precipitation of metal oxide colloidal particles [22–24]. The conversion of a dissolved ion to a particle can influence alloy corrosion rates, particularly under stagnant water conditions, because it will reduce the metal ion concentration gradient at the corroding surface. This will promote oxidative dissolution of the metal by increasing the diffusion rate of ions from the surface.

The in-reactor conversion of soluble-to-insoluble metal species has been a recognized problem in the nuclear industry since its inception. The Canadian nuclear laboratories coined the word "crud" (Chalk River unidentified deposit) that is universally used to describe the resulting deposits of the insoluble material. The formation of crud is a serious concern as it interferes with nuclear fuel heat transfer (an operation safety issue) and it promotes the neutron activation of hazardous radionuclides. While the formation of crud is qualitatively understood, the detailed mechanism for its formation and its composition is still uncertain.

An increase in corrosion potential can place the alloy in a different regime in the Pourbaix diagram. The corrosion potential of stainless steel in the primary circuit of a PWR is very low due to the addition of hydrogen to the water. In 320 °C water with 35 cc/kg H_2, the corrosion potential is approximately −600 mV_{SHE}. At this potential, the E–pH diagram in Fig. 16.5 shows that Fe_3O_4, magnetite, is the stable oxide. However, proton irradiation of 316L stainless steel at a damage rate of 7×10^{-6} dpa/s in 320 °C water with H_2 addition resulted in the formation of hematite, Fe_2O_3. This is possible if the potential increase under irradiation is at least 300 mV. Thus, irradiation can alter corrosion products by virtue of the potential elevation due to radiolysis.

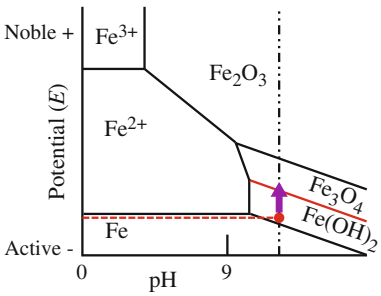

Fig. 16.5 Elevation of corrosion potential on 316L stainless steel in 320 °C water containing 35 cc/kg H_2 and irradiated at 7×10^{-6} dpa/s

16.1.3 Effects of Corrosion Potential on IASCC

Laboratory tests have been conducted on preirradiated alloys using slow strain rate testing (SSRT) in hot water with addition of oxygen and/or hydrogen peroxide to elevate the corrosion potential to simulate the effect of radiation. Tests by Jacobs et al. [25] on stainless steel irradiated to $\approx 3 \times 10^{21}$ n/cm^2 showed a strong effect of dissolved oxygen (and, by inference, corrosion potential) on IASCC (Fig. 16.6(a)). Similarly, Ljungberg [26] showed a strong effect of corrosion potential on CGR (Fig. 16.6(b)). Since the corrosion potential is a sensitive function of oxygen content, increasing oxygen content results in elevated corrosion potential and higher CGRs.

In situ data on fracture mechanics specimens of furnace-sensitized type 304 stainless steel exposed in the Nine Mile Point Unit 1 BWR showed that the higher corrosion potentials measured in-core versus in recirculation water piping induced significantly higher measured CGRs. Ex situ CGR testing on irradiated (4 dpa) type 304 SS is one of many examples of well-behaved CGR at high corrosion potential, along with the strong effect of reduced corrosion potential. These data are compared with other irradiated and unirradiated data in Fig. 16.7 based on simultaneous measurements of corrosion potential and CGR in fracture mechanics specimens; the accompanying curves represent model predictions [5]. Clearly, the in situ data compare favorably with the spectrum of unirradiated data and data obtained on a fracture mechanics specimen of furnace-sensitized type 304 stainless steel using high-energy proton irradiation to simulate the mix of neutron and gamma radiation present in power reactors. These data support the premise that increasing corrosion potential leads to higher CGR and the effect of irradiation on water chemistry is to elevate corrosion potential through the formation of radicals and higher oxygen concentration.

16.2 Effects of Irradiation on Oxidation

As shown in the previous section, radiation elevates the corrosion potential, which can change oxidation and IASCC behaviors. Irradiation can also affect the oxide directly through displacement damage of film and metal. Some recent examples

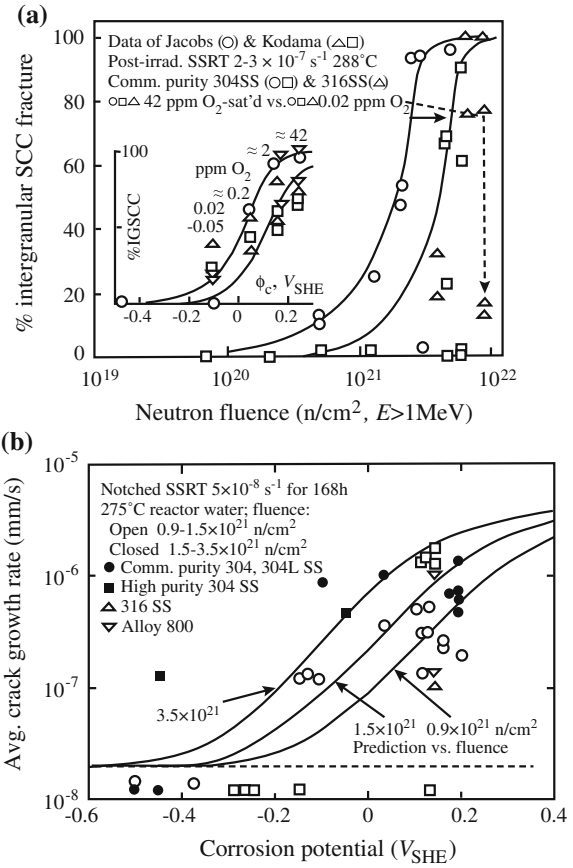

Fig. 16.6 (**a**) Dependence of IASCC on fast neutron fluence as measured in slow strain rate tests at 3.7×10^{-7} s^{-1} in 288 °C water on preirradiated type 304 stainless steel. The effect of corrosion potential via changes in dissolved oxygen is shown at a fluence of $\approx 2 \times 10^{21}$ n/cm^2 (after [25]). (**b**) Comparison of predicted and observed crack growth rates for stainless steels irradiated in a BWR at 288 °C to various fluences. Notched tensile specimens were tested at a slow strain rate in 288 °C pure water and interrupted after a given strain/time (after [26])

include the observation that irradiation of iron in moist air produced a 10× increase in oxide thickness versus the unirradiated control sample [29]. Proton irradiation of a 316 stainless steel foil in room temperature water for 4 h produced an oxide thickness that was 20× thicker than the unirradiated control [30]. In experiments conducted on 316L stainless steel in 320 °C water containing 35 cc/kg H_2 during irradiation with 3.2 MeV protons at a damage rate of 7×10^{-6} dpa/s, the outer oxide changed from magnetite to hematite (see Sect. 6.1.2), and the oxide particle size was considerably reduced. The morphology of the inner oxide was also modified [31]. The film was thinner by about a factor of ~4 compared to the unirradiated case and was more porous with inhomogeneous crystallite size. The inner oxide exhibited a depletion of Cr and a gradient in the Cr concentration from the metal–oxide interface to the oxide–solution interface. Analysis of regions on the irradiated sample, but outside of the irradiated zone, resembled those of samples exposed to the same environment with no irradiation, indicating that the changes in the morphology of

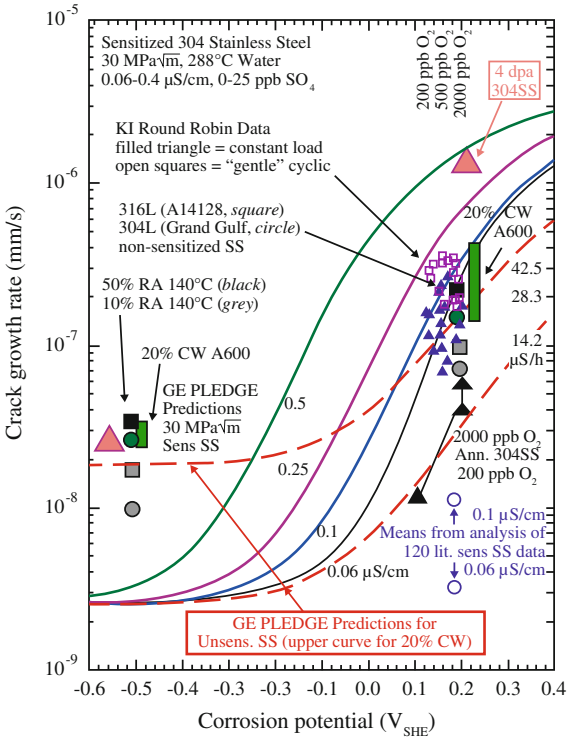

Fig. 16.7 Observed and predicted relationships of crack growth rate versus corrosion potential for furnace-sensitized type 304 stainless steel at a constant K of ≈ 27.5 MPa$\sqrt{\text{m}}$. The observed data were obtained in water of conductivity between 0.1 and 0.3 µS/cm. The predicted relationships show the sensitivity of the crack growth rate to changes in combinations of corrosion potential and water purity (0.1–0.5 µS/cm). The large triangles were obtained on 304 SS irradiated to 4 dpa. The *larger circles* and *rectangles* represent cold-worked stainless steel and alloy 600 (after [7–9, 27, 28])

the inner oxide layer are likely due to radiation effects on the water chemistry as well as the underlying metal.

Oxidation of zirconium alloys is of great importance for maintaining the integrity of fuel cladding in LWRs. Very early experiments revealed that zirconium irradiated in-reactor in moist carbon dioxide–air mixtures had oxygen weight gains of more than five times that in the unirradiated state [32]. More recently, in-reactor corrosion rates were found to be 10× greater than those conducted out-of-reactor, the difference attributed in part to greater permeability of the oxide irradiated in-reactor [33]. Data on in-reactor exposure of Zircaloy-2 have revealed increases in the oxide weight gain of 40× and a strong, linear dependence on neutron flux.

Recent experiments conducted using proton irradiation of Zircaloy-4 in situ in simulated PWR primary water (320 °C, 3 appm H_2, without addition of B and Li) at a dose rate of 4.4×10^{-7} dpa/s [34] resulted in an oxide morphology similar to that

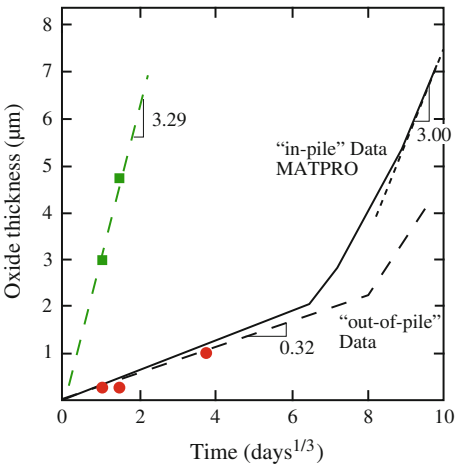

Fig. 16.8 Oxide thickness on Zr-4 as a function of corrosion time for proton-irradiated (*green-filled squares*) and unirradiated cases (*red-filled circles*), compared to in-pile and out-of-pile data (after [34])

formed under neutron irradiation and consisting of equiaxed monoclinic ZrO_2, with a preferential grain orientation. A large volume fraction of cracks and fine pores were present throughout the thickness of the oxide. Second phase particles underwent accelerated oxidation after being consumed by the oxide. Unirradiated areas of the proton-irradiated samples exhibited oxide morphology and corrosion kinetics that were in good agreement with out-of-pile test results, indicating that water radiolysis had a negligible effect on the corrosion rate of zirconium. Figure 16.8 shows oxide thickness data from the in situ irradiation–corrosion experiment compared with in-pile data [35]. The unirradiated oxide growth rate of the reference sample is in good agreement with out-of-pile data. Proton irradiation produces a growth rate that is about 10× than in the unirradiated case. This growth rate is similar to that for in-pile behavior in the post-transition regime. In this regime, the oxide growth rate should be proportional to the dose rate. Therefore, equating the ratio of oxide growth rate to dose rate for protons to that for neutrons yields a neutron dose rate of $\sim 4.4 \times 10^{-8}$ dpa/s, which is in good agreement with the range of values in expected in-pile: $3.2–6.5 \times 10^{-8}$ dpa/s [34]. This relationship suggests that oxidation under proton irradiation follows post-transition growth kinetics.

16.3 Effects of Irradiation on Stress Corrosion Cracking

16.3.1 Austenitic Alloys

A historical perspective of IASCC service experience is instructive, as the phenomenon extends back to the 1960s, and the early observations and conclusions projected an accurate image of the important characteristics, generic nature, and

broad relevance to plant components. As with other instances of environmental cracking, occasional early observations pointed the way toward a growing incidence with time and neutron fluence. IASCC was first reported in the early 1960s [1, 7, 10] and involved intergranular cracking of stainless steel fuel cladding. The findings and conclusions were that intergranular cracking morphology predominated, with initiation of multiple cracks occurring from the waterside. By contrast, only ductile, transgranular cracking was observed in post-irradiation mechanical tests performed in inert environments and at various temperatures and strain rates. Grain boundary carbide precipitation was generally not observed by optical or transmission electron microscopy (although pre-existing thermal sensitization was present in some cases). A correlation between time to failure and stress level was reported, with failure occurring first in thin-walled rods with small fuel-to-cladding gaps, where swelling strains were largest. The highest incidence of cracking occurred in peak heat flux regions, corresponding to the highest fluence and the greatest fuel cladding interaction (highest stresses and strains). Similar stainless steel cladding in PWR service exhibited fewer instances of intergranular failure. At that time, the PWR failures were attributed to off-chemistry conditions or stress rupture.

IASCC has since been observed in a growing number of other stainless steel (and nickel alloy) core components, such as neutron source holders in 1976 and control rod absorber tubes in 1978 [1]. Instrument dry tubes and control blade handles and sheaths which are subject to very low stresses also cracked, although generally in creviced locations and at higher fluences [5]. Following an initial trickle of failures in the most susceptible components, numerous incidents of IASCC have been observed since the early 1990s, perhaps most notably in BWR core shrouds [1, 7, 10, 19] and PWR baffle bolts [36, 37].

Table 16.1 presents a broad summary of reported failures of reactor internal components, showing that IASCC is not confined to a particular reactor design. For example, stainless steel fuel cladding failures were reported in early commercial PWRs and in PWR test reactors. At the West Milton PWR test loop, intergranular failure of vacuum-annealed type 304 stainless steel fuel cladding was observed in 316 °C ammoniated water (pH 10) when the cladding was stressed above yield. Similarly, IASCC was observed in creviced stainless steel fuel element ferrules in the Winfrith SGHWR, a 100-MWe plant in which light water is boiled within pressure tubes, giving rise to a coolant chemistry similar to other BWR designs.

Reactor type comparisons were also made in swelling tube tests performed in the core of a BWR and a PWR on a variety of commercial and high purity heats of types 304, 316, and 348 stainless steel and alloys X-750, 718, and 625. Swelling was controlled by varying the mix of Al_2O_3 and B_4C within the tubes; the latter swells as neutrons transmute B to He. Nominally identical strings of specimens were inserted into the core in place of fuel rods. The distinction in the IASCC response between the two reactor types was small. While the available data clearly support a linkage between IASCC in BWRs and PWRs, it is clear that the elevated corrosion potential in BWRs accelerates SCC, and to a lesser extent, the generally higher flux and temperature in PWRs also accelerates SCC.

Table 16.1 IASCC service experience (after [5])

Component	Alloy	Reactor type	Possible sources of stress
Fuel cladding	304 SS	BWR	Fuel swelling
Fuel cladding	304 SS	PWR	Fuel swelling
Fuel cladding[a]	20 %Cr/25 %Ni/Nb	AGR	Fuel swelling
Fuel cladding ferrules	20 %Cr/25 %Ni/Nb	SGHWR	Fabrication
Neutron source holders	304 SS	BWR	Welding and Be swelling
Instrument dry tubes	304 SS	BWR	Fabrication
Control rod absorber tubes	304/304L/316L SS	BWR	B_4C swelling
Fuel bundle cap screws	304 SS	BWR	Fabrication
Control rod follower rivets	304 SS	BWR	Fabrication
Control blade handle	304 SS	BWR	Low stress
Control blade sheath	304 SS	BWR	Low stress
Control blades	304 SS	PWR	Low stress
Plate-type control blade	304 SS	BWR	Low stress
Various bolts[b]	A-286	PWR and BWR	Service
Steam separator dryer bolts[b]	A-286	BWR	Service
Shroud head bolts[b]	600	BWR	Service
Various bolts	X-750	BWR and PWR	Service
Guide tube support pins	X-750	PWR	Service
Jet pump beams	X-750	BWR	Service
Various springs	X-750	BWR and PWR	Service
Various springs	718	PWR	Service
Baffle former bolts	316 SS cold-work	PWR	Torque, differential swelling
Core shroud	304/316/347L SS	BWR	Weld residual stress
Top guide	304 SS	BWR	Low stress (bending)

[a]Cracking in AGR fuel occurred during storage in spent fuel pool
[b]Cracking of core internals occurred away from high neutron and gamma fluxes

Crack initiation

As discussed earlier, IASCC is an irradiation-induced increase in susceptibility of materials to SCC with increasing neutron damage. The SCC of materials in high-temperature, high-pressure water depends on material susceptibility, high stresses, and an aggressive environment. The mechanism of IASCC in the LWR environment and the individual effect of various material and environmental parameters on IASCC will be discussed more in depth in Sect. 16.4. Although the degradation of tensile and fracture properties of austenitic SSs appears to saturate at 5–20 dpa, the susceptibility of SSs to IASCC continues to increase with neutron fluence.

Tests for the susceptibility of an alloy to the initiation of stress corrosion cracks include constant load, constant deflection, and constant extension rate tensile tests as described in Sect. 15.7.1. The most robust database is for constant load tests. Constant load IASCC initiation results in a PWR environment are plotted as stress

(as a percent of irradiated yield stress) versus dose in Fig. 16.9. The open symbols represent specimens that did not fail, and the closed symbols represent failed specimens. The results indicate that under a high enough stress, crack initiation in highly irradiated materials can occur quite rapidly (i.e., within 500 h). Furthermore, 80 % of these failures (closed symbols) occurred within 150 h. The results also indicate an apparent stress threshold below which cracks did not initiate even after several thousands of hours. That apparent threshold is between 40 and 60 % of the bulk yield stress, the average of which is shown by the dash-dot line.

Crack growth

Laboratory data support that obtained in the plant in terms of the accelerating effect of irradiation. Since laboratory data are collected post-irradiation in which radiolysis of the water is not a factor, the effects of irradiation that are responsible for the observed cracking are deduced to come from persistent changes in the microstructure. Figure 16.10 shows CGRs measured in BWR NWC (Fig. 16.10(a)) and PWR (Fig. 16.10(b)) environments as a function of the stress intensity factor. For the BWR NWC environment, the data span damage levels of 5.5–37.5 dpa. The line labeled "NUREG-0313" is the CGR disposition curve proposed in the NRC report of that name for unirradiated, sensitized austenitic stainless steels in high-purity water, and the curve labeled "EPRI NWC BWR" is proposed by EPRI for austenitic stainless steel BWR core internal components. The CGR, da/dt, in the NUREG-0313 disposition curve is expressed as:

$$\mathrm{d}a/\mathrm{d}t(\mathrm{m/s}) = A_N(K)^{2.161}, \tag{16.1}$$

where K is in MPa $\mathrm{m}^{1/2}$ and A_N is 2.1×10^{-13} in water with 8 ppm DO and 7.0×10^{-14} in water with 0.2 ppm DO. The EPRI disposition curve for use in a BWR core environment is expressed as:

$$\mathrm{d}a/\mathrm{d}t(\mathrm{m/s}) = A_E(K)^{2.5}, \tag{16.2}$$

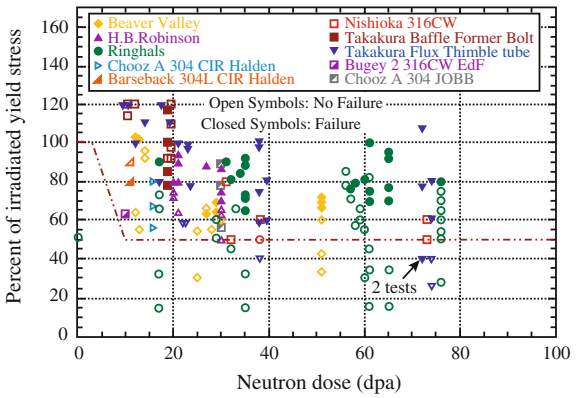

Fig. 16.9 Stress as a percent of irradiated yield stress versus neutron dose for IASCC crack initiation in austenitic stainless steels in a PWR environment (after [35])

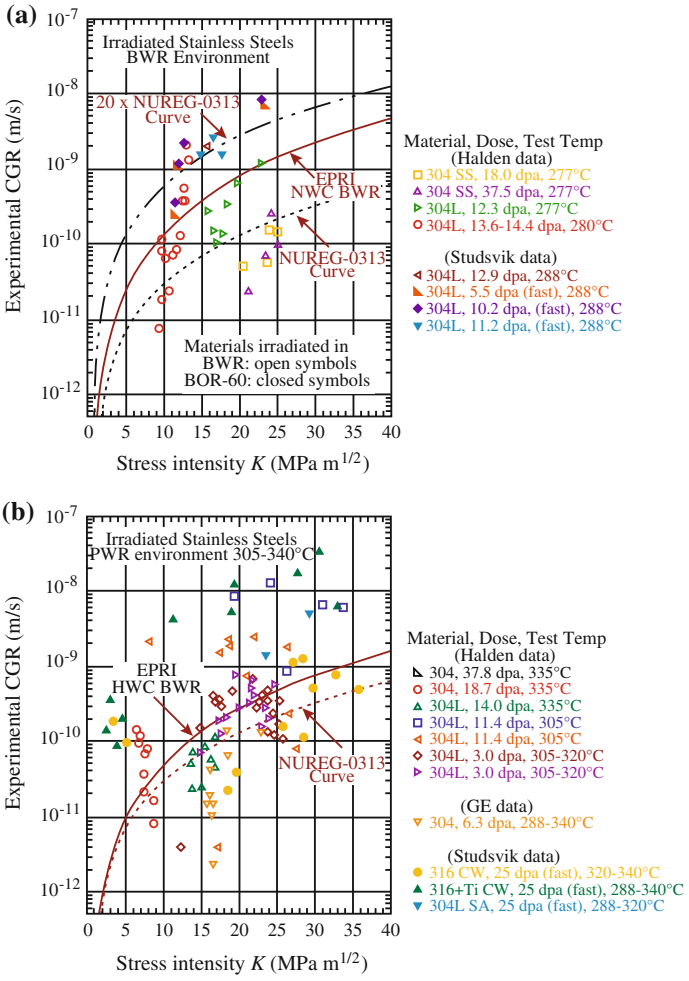

Fig. 16.10 Crack growth rates in (**a**) NWC BWR environment on austenitic steels irradiated to 5.5–37.5 dpa and (**b**) PWR environment on austenitic steels irradiated to 3.0–37.8 dpa (after [38])

where A_E is 4.565×10^{-13} in NWC BWR and 1.512×10^{-13} in BWR HWC. The values of the coefficient, A, are also found to depend on neutron dose.

Note that while there is significant scatter, overall, the CGRs are above the NRC disposition line for sensitized austenitic steels by about an order of magnitude. For the PWR environment in which steels span damage levels of 3.0–37.8 dpa, the data are slightly above the NRC disposition curve and very close to, but slightly above the EPRI disposition curve for crack growth in BWR HWC.

Data on high-purity alloys containing specific microstructures and solute additions, as in Fig. 16.11, showed a wide amount of scatter (almost $10^4\times$) but with the

bulk of the CGRs over the same range as those for the commercial alloys shown in Fig. 16.10.

Fatigue crack growth

Under cyclic loading, the CGR in an environment can be approximated as the superposition of the rate in air and the rates due to corrosion fatigue and SCC:

$$(\mathrm{d}a/\mathrm{d}t)_{\mathrm{env}} = (\mathrm{d}a/\mathrm{d}t)_{\mathrm{air}} + (\mathrm{d}a/\mathrm{d}t)_{\mathrm{cf}} + (\mathrm{d}a/\mathrm{d}t)_{\mathrm{scc}}, \tag{16.3}$$

where

$$(\mathrm{d}a/\mathrm{d}t)_{\mathrm{air}} = C_{\mathrm{ss}} S(R) \Delta K^{3.3} / t_{\mathrm{r}}, \tag{16.4}$$

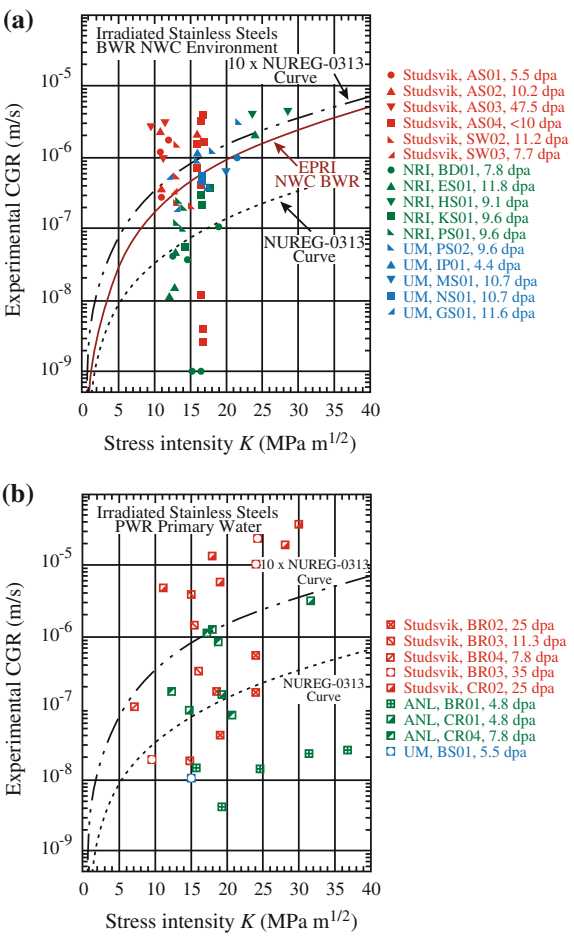

Fig. 16.11 Crack growth rate data of neutron-irradiated solute addition stainless steels irradiated in the CIR program and tested in (**a**) BWR NWC and (**b**) PWR primary water (after [39])

and ΔK is in MPa $m^{1/2}$, t_r is the rise time in sec, $S(R)$ is a function that depends on the load ratio, R, and C_{ss} is a function that captures the temperature dependence [38]. The effect of an LWR environment on fatigue was determined from non-irradiated stainless steels to be:

$$\begin{aligned}(da/dt)_{env} &= (da/dt)_{air} + 4.5 \times 10^{-5}(da/dt)_{air}^{0.5} \quad \text{for} \quad DO \sim 0.2 \text{ ppm} \\ (da/dt)_{env} &= (da/dt)_{air} + 1.5 \times 10^{-4}(da/dt)_{air}^{0.5} \quad \text{for} \quad DO \sim 8 \text{ ppm.}\end{aligned} \tag{16.5}$$

The effect of irradiation on the CGR of 304 and 316 stainless steel under fatigue loading or continuous cycling in 289 °C high-purity water with ~300 ppb dissolved oxygen as compared to that in air is shown in Fig. 16.12. The 45° line indicates no effect of the environment on cracking, and the dashed curve represents the expected CGRs for unirradiated austenitic stainless steels in high-purity water with 0.2 ppm dissolved oxygen [40]. By comparing the data at different neutron fluence levels, it is clear that both the environment and the fluence level affect the CGR. The CGR in 304 SS irradiated to 3 dpa is over an order of magnitude greater than that for irradiation to 1.35 dpa in high dissolved oxygen (8 ppm) water.

Fracture toughness

Most of all existing fracture toughness data have been obtained from tests in air and on specimens that were fatigue precracked at relatively low load ratio R, defined as the ratio of the minimum load to maximum load (typically 0.1–0.2), in room temperature air. In reactor, cracks in core components are initiated primarily by SCC and have intergranular (IG) morphology, whereas the fatigue precracks in fracture toughness tests are always transgranular (TG). Also, the corrosion/oxidation reaction could influence fracture toughness.

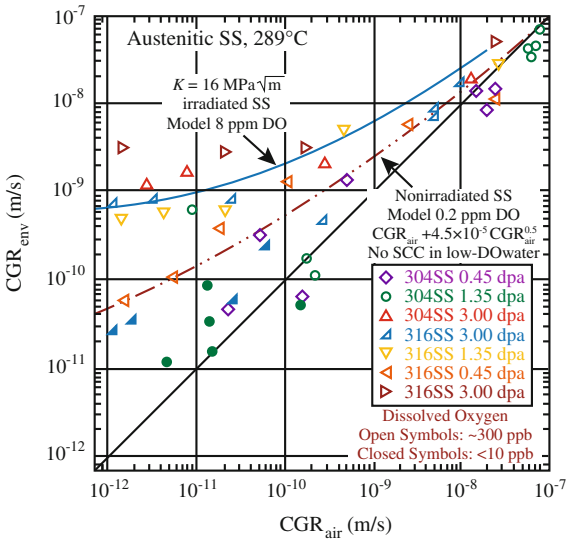

Fig. 16.12 Comparison of the crack growth rate in irradiated austenitic stainless steels under continuous cycling in 289 °C high-purity water containing <10 ppb or 300 ppb O_2 compared to that in air (after [38])

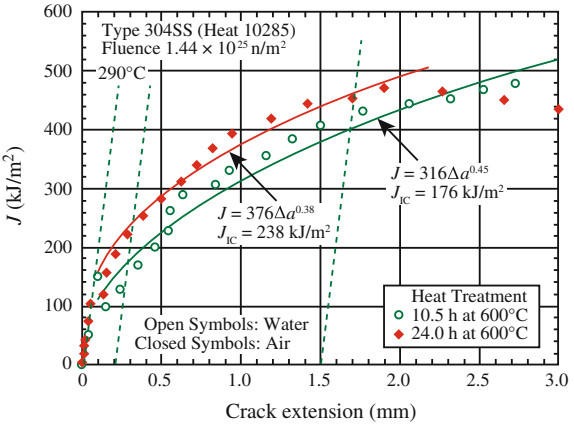

Fig. 16.13 Fracture toughness *J–R* curves for sensitized 304 stainless steel in air and BWR NWC at 289 °C (after [41])

To investigate the possible effects of the BWR coolant environment on fracture toughness (e.g., the effect of the corrosion/oxidation reaction during crack extension or use of specimens with an IG rather than TG fatigue crack), *J–R* curve tests have been conducted in BWR NWC environment [41]. The *J–R* curve data for irradiated SS weld HAZ materials showed that a BWR NWC environment had little or no effect on the fracture toughness. However, the *J–R* curves for a sensitized type 304 SS in air and water environments did show a small difference, as in Fig. 16.13. The results indicate slightly lower fracture toughness in water. Also, the material tested in water was sensitized for a shorter time than the material tested in air. Therefore, for materials with identical sensitization treatment, the difference between the *J–R* curves in air and water environments may be greater than that indicated by Fig. 16.13.

Service and laboratory experience with IASCC

Since the early 1990s, the plant and laboratory evidence of IASCC makes a compelling case that cracking is environmentally assisted and that there is a well-behaved continuum in response over ranges in fluence, corrosion potential, temperature, stress, etc. Since there is a consistent trend toward increasing IASCC susceptibility with increasing corrosion potential in BWRs (e.g., Figs. 16.6(a) and 16.7), PWRs should be less susceptible to IASCC. However, other factors distinguish PWRs from BWRs, including their higher temperatures, ≈10× higher neutron fluence in core structural components, higher hydrogen fugacity, and the borated–lithiated water chemistry (including the possibility of localized boiling and thermal concentration cells in crevices from gamma heating which could lead to aggressive local chemistries). The possible role of RIS of Si may be especially important in accounting for the limited difference in SCC response at high potential (BWR) versus low potential (PWR) at high fluence.

The two most widespread examples of irradiation-assisted SCC are BWR core shrouds and PWR baffled bolts although susceptibility clearly exists in other areas, such as control blade components, fuel components, and the BWR top guide.

SCC in the BWR core shroud occurs almost exclusively near the welds (both circumferential and vertical), and initiation is observed from both the inside (ID) and outside (OD) surfaces (the shroud separates the upward core flow from the downward recirculation flow that occurs in the annulus between the shroud and the pressure vessel). This large-diameter welded "pipe" has inherent susceptibility to SCC, related primarily to weld residual stresses and weld shrinkage strains, and cracking is observed in both low-fluence and moderate-fluence areas. Severe surface working has also been found to aggravate IASCC in core shrouds. The extent of the enhancement in SCC susceptibility by irradiation is limited, because while RH and RIS occur, radiation creep relaxes the weld residual stress.

Extensive failures of PWR baffle bolts have occurred beginning in the 1990s [36, 37] although large plant-to-plant and heat-to-heat differences are observed. Most baffle bolts are fabricated from type 316 stainless steel cold-worked to ≈ 15 % to increase their yield strength. The complex baffle former structure exists in a PWR because the fuel does not have a surrounding "channel," so the baffle former structure must conform closely to the geometry of the fuel to provide well-distributed water flow. The baffle former plates are usually made from annealed type 304 stainless steel. Because of their proximity to the fuel, very high fluences can develop, up to ~80 dpa by the end of the original design life. The high gamma flux produces significant heating in the components and in some instances estimated at 40 °C above the coolant temperature, especially in designs where the PWR coolant does not have good access to the bolt shank. Figure 16.14 shows micrographs of IG cracking in the baffle bolt described earlier in Chap. 8 on swelling. Note that the cracks are occurring where the shank meets the head. Cracks are completely intergranular and penetrate greater than half the thickness of the bolt.

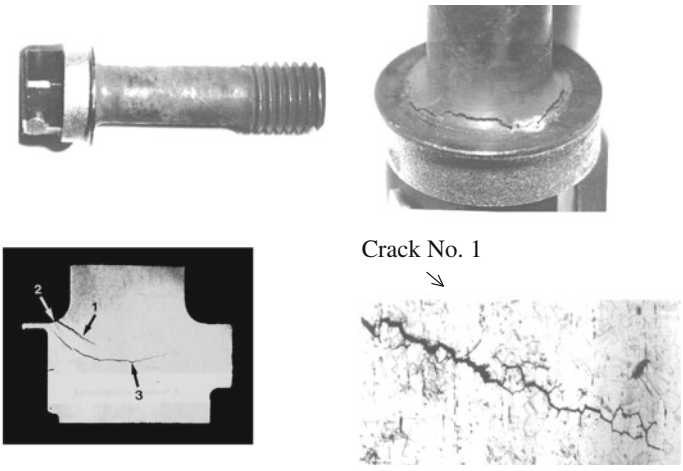

Fig. 16.14 Cracks in cold-worked 316 stainless steel baffle bolt. The location of the cracks received a neutron dose of about 7 dpa at ~310 °C (*courtesy* Electrabel)

The number of IASCC incidents has continued to grow as more and more components in LWRs are revealed to be susceptible. The overall trends and correlations for IASCC can be summarized as follows:

- While intergranular cracks related to radiation effects in solution-annealed stainless steel were once thought to occur only at fluences above $\approx 5 \times 10^{20}$ n/cm^2, significant intergranular cracking in BWR core shrouds over a broad range of fluences makes it clear that such a distinction (a true fluence threshold) is not justified. Of course, observations of SCC in unsensitized stainless steel (with or without cold-work) also render untenable the concept of a threshold fluence, below which no SCC occurs. This also holds for thresholds in corrosion potential, water impurities, etc.
- Fluence affects SCC susceptibility, but almost always in a complex fashion. SCC in BWR shrouds and PWR baffle bolts does not always correlate strongly with fluence; one important reason for this is that radiation creep produces relaxation of the stresses from welding and in bolts.
- High stresses or dynamic strains were involved in most early incidents; however, cracking has been observed at quite low stresses at high fluences and longer operating exposure. Laboratory and field data indicate that IASCC occurs at stresses below 20 % of the irradiated yield stress and at stress intensities below 10 MPa m$^{1/2}$.
- A strong effect of corrosion potential is clear from extensive laboratory and field data. Its effect is generally consistent from low to high fluence, although the quantitative change associated with changes in potential varies. Materials prone to high radiation-induced changes in Si level may exhibit a very limited effect of corrosion potential. A true threshold potential clearly does not exist, as irradiated materials exhibit IASCC in deaerated water.
- Solution conductivity (i.e., impurities, especially chloride and sulfate) strongly affects cracking propensity in BWR water. This correlation applies equally to low- and high-flux regions and to stainless steels and nickel-base alloys. Indeed, the correlation closely parallels that from out-of-core.
- Crevice geometries exacerbate cracking due primarily to their ability to create a more aggressive crevice chemistry from the gradient in corrosion potential (in BWRs) or in temperature (most relevant to PWRs).
- Cold-work often exacerbates cracking (especially abusive surface grinding), although it can also delay the onset of some radiation effects.
- Temperature has an important effect on IASCC, enhancing both crack initiation and growth rate.
- Grain boundary carbides and chromium depletion are not required for susceptibility, although furnace-sensitized stainless steels are clearly highly susceptible to cracking in-core. Cr depletion remains a primary culprit, although its effect is most pronounced in pH-shifted environments, as can develop when potential or thermal gradients exist. The role of N, S, P, and other grain boundary segregants is less clear.

– The fluence at which IASCC is observed is dependent on applied stress and strain, corrosion potential, solution conductivity, crevice geometry, etc. At sufficiently high conductivities, cracking has been observed in solution-annealed stainless steel in the field and in the laboratory. Thus, while convenient in a practical engineering sense, the concept of a "threshold" fluence (or stress, corrosion potential, etc.) is scientifically misleading as cracking susceptibility and morphology are properly considered an interdependent continuum over many relevant parameters.

The field and laboratory data available in the early 1980s, coupled with broader fundamental understanding of environmental cracking in hot water, led to the hypothesis that among innumerable possible radiation effects, the most significant factors were RIS at grain boundaries, RH (elevation of the yield strength), deformation mode, radiation creep relaxation (of constant displacement stresses, e.g., in welds and bolts), and radiolysis (elevated corrosion potential in BWRs). Other factors could also be important in some instances, such as void formation, which may also affect fracture toughness and can produce differential swelling that causes reloading of components such as baffle bolts.

16.3.2 Ferritic Alloys

Ferritic alloys are also susceptible to environmentally enhanced cracking in high-temperature water. The role of irradiation on the fatigue crack growth rate in pressure vessel steels was discussed in Chap. 14, where it was determined that irradiation alone did not accelerate crack growth rate. However, CGRs *are* affected by the environment. In fact, the environment, loading parameters, and material parameters all affect the CGR in high-temperature water. In general, crack growth per cycle increases with:

Environmental parameters	• Increased oxygen concentration • Increased conductivity • Increased temperature
Loading parameters	• Increased R ratio (higher mean stress) • Decreasing frequency • Transients and hold periods in the waveform
Material parameters	• Increasing sulfur content in the alloy

For example, Fig. 16.15 shows that lower frequency, transients, and hold times in the waveforms increase the CGR in A508 steel in a PWR environment. The effect of the environment on cracking is shown in Fig. 16.16(a), which gives the fatigue crack growth rate as a function of ΔK for A533B steels and welds in PWR water. The solid line at right is the ASME Boiler and Pressure Vessel Code bounding CGR

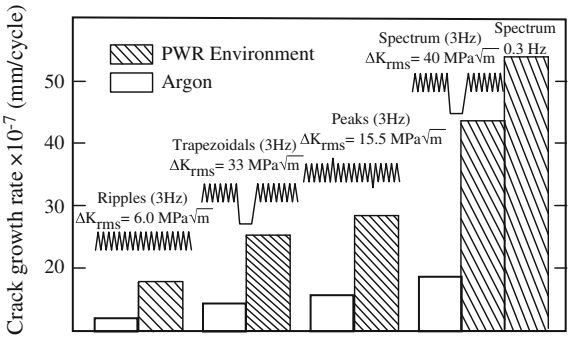

Fig. 16.15 The effect of environment, frequency, and transients on the fatigue crack growth behavior of A533B steel subjected to various loading sequences (after [42])

in air. As is evident, the environment has a significant effect on both the growth rate and the dependence of d*a*/d*N* on Δ*K*. Figure 16.16(b) also shows that in reactor grade water at 288 °C, the effect of irradiation only minimally augments the CGR due to the environment.

16.4 Mechanisms of IASCC

While the mechanism by which irradiation affects stress corrosion cracking is not precisely known, existing theories fall into five categories: (1) radiation-induced grain boundary chromium depletion, (2) radiation hardening, (3) localized deformation, (4) selective internal oxidation, and (5) irradiation creep. The difficulty in determining the role of irradiation in SCC stems from the simultaneous occurrence of several effects. Figure 16.17 shows a schematic representation of the increase in RIS, dislocation microstructure, and RH, and that all of these factors increase with approximately the same relationship with irradiation dose. Thus, the attribution of one or a combination of effects to the observed increase in cracking is complicated. The following sections describe the mechanisms by which these processes can influence IGSCC.

16.4.1 Grain Boundary Chromium Depletion

As described in Chap. 6, irradiation in the temperature range relevant to LWR core components results in grain boundary segregation, marked by a significant decrease in the chromium concentration. Chromium imparts passivity to austenitic alloys by the formation of a chromium oxide film, and its loss from the grain boundary can

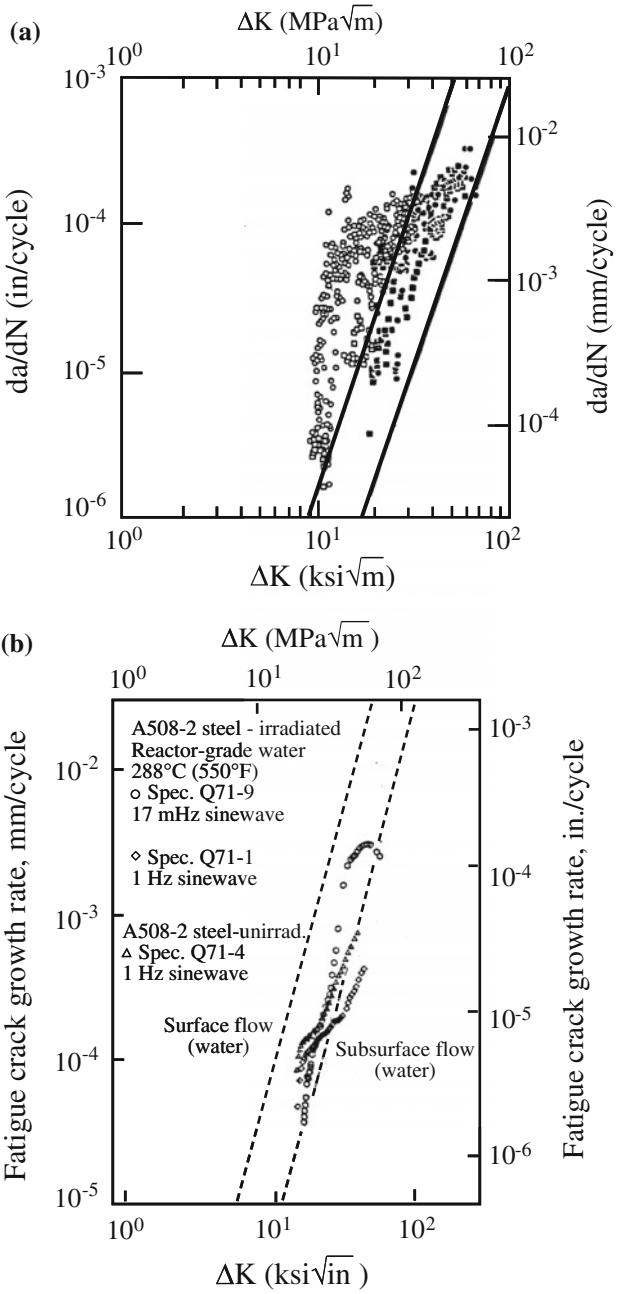

Fig. 16.16 (**a**) Compilation of fatigue crack growth data for A533B steels and weld metals in PWR water. The lower line is the 1972 ASME XI section A limit on crack growth in air. Filled circle = base metal, $R = 0.2$, filled square = welds, $R = 0.2$, open circle = base metal, $R = 0.7$, open square = welds, $R = 0.7$ (after [42]). (**b**) Fatigue crack growth rates versus applied cyclic stress intensity factor for irradiated and unirradiated A508-2 steel (after [43])

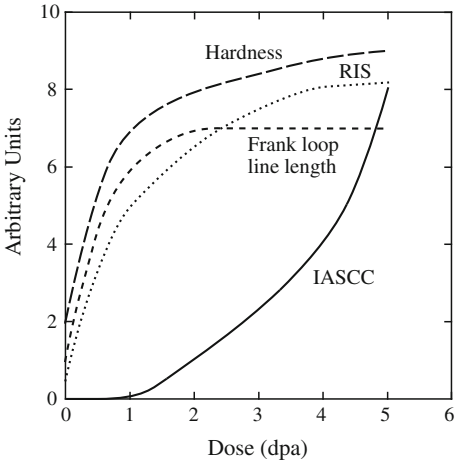

Fig. 16.17 Schematic diagram showing the increase in all parameters (RIS, loops, hardness) and SCC susceptibility with dose (after [4])

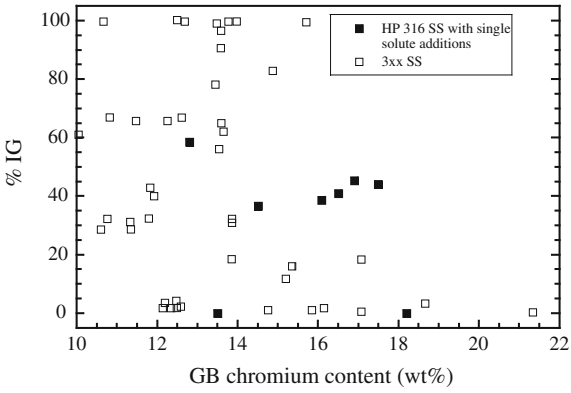

Fig. 16.18 Effect of grain boundary chromium content on IGSCC for irradiated 300 series stainless steels (after [4])

result in the loss of passivation locally. The depletion of chromium from grain boundaries in austenitic stainless steels and nickel-base alloys is a well-known cause of IGSCC in high-temperature water [44]. By analogy, the loss of chromium due to RIS is implicated as a cause of IASCC in the irradiated condition. Existing data support this premise in part, by showing that there is a general trend in increasing %IGSCC as the grain boundary chromium concentration decreases (Fig. 16.18). However, the data exhibit considerable scatter, some of which may be attributed to the stochastic nature of crack initiation that is inherent in a straining electrode test, but is unlikely to explain all of the variability.

Recently, post-irradiation annealing experiments have been utilized to separate the various effects of irradiation due to differences in their annealing characteristics. Figure 16.19 shows that of the principal irradiation-induced microstructure features. RIS is slowest to recover in isothermal anneals and is essentially unchanged over

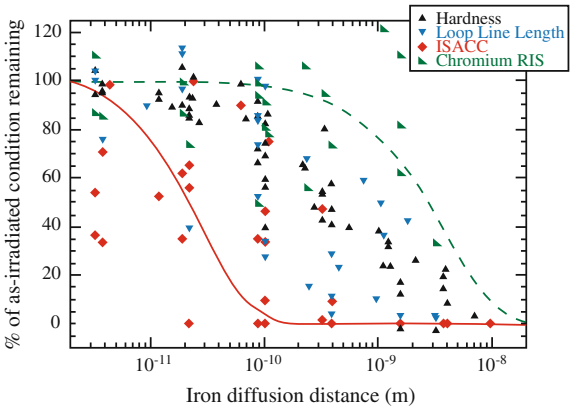

Fig. 16.19 Removal of RIS, dislocation microstructure as measured by loop line length, and hardness with annealing as measured by $(Dt)^{1/2}$ for iron, to account for annealing at different times and temperatures

the time period during which the SCC susceptibility is completely eliminated. In a systematic study, seven austenitic alloys were irradiated to 1 or 5 dpa with 2 MeV protons, followed by microstructure characterization and testing for IASCC susceptibility in simulated BWR NWC water [45]. The correlation between a microstructure feature and IASCC susceptibility was determined by the degree to which that feature explains the IASCC data, with no correlation represented by 0 and complete correlation represented by 1. The correlation strength of RIS with cracking was zero in the grain boundary Cr content range of 12–19 wt%. RIS did not play an apparent role in this study.

16.4.2 Irradiation Hardening

IGSCC has been observed to correlate with hardness as evidenced by the increase in CGR with cold-work in 300 series austenitic stainless steels tested in high-temperature water (Fig. 16.20(a)). IGSCC as measured by %IG in constant extension rate tests also correlates with hardening due to irradiation, as shown in Fig. 16.20(b). In the study described in the previous section, the correlation strength of hardness with cracking was around 0.5, indicating that it contributed to cracking but was not the dominant factor. However, as mentioned earlier, other effects occur during irradiation that make it difficult to attribute the increased cracking to hardening alone. A series of experiments conducted on a heat of stainless steel showed that in the absence of significant grain boundary chromium depletion, hardening due to irradiation results in more IGSCC than hardening from cold-work [46]. This result suggests that hardness alone is not the cause of IASCC, but rather another effect related to hardness may be operating. That factor is suspected to be the deformation mode.

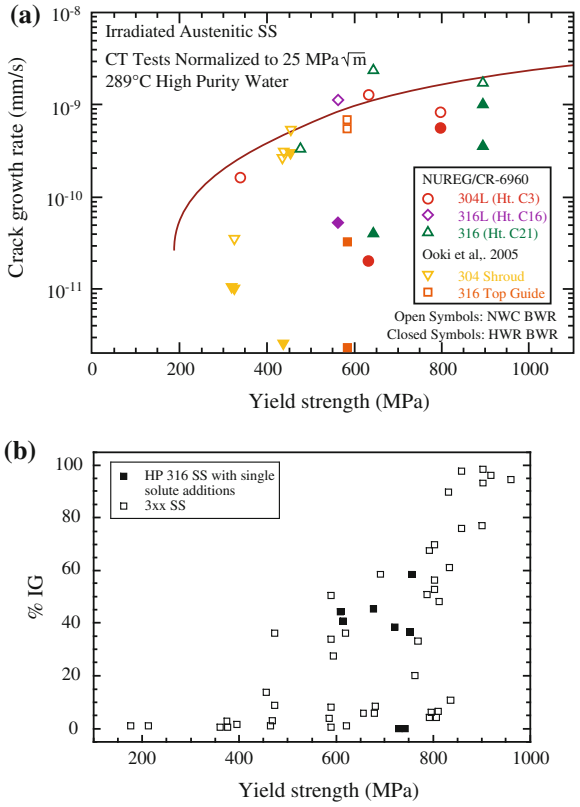

Fig. 16.20 Effect of yield strength on IGSCC. (**a**) Crack growth rates for 304 and 316 stainless steel in 289 °C high-purity water as a function of yield strength (after [38]). (**b**) %IGSCC in SSRT tests on 300 series stainless steels where hardening is by irradiation (after [4])

16.4.3 Deformation Mode

As discussed in Chap. 12, irradiated metals exhibit localized deformation characterized by the concentration of strain into dislocation channels. The strain in these channels can exceed 100 %, and while channels are believed to initiate at grain boundaries, they also must terminate there as well. As such, the considerable amount of localized strain in the channels must be accommodated at the boundary to avoid fracture. Accommodation can occur by several mechanisms including the transfer of slip across the boundary, cross-slip in the grain boundary region, and reaction of the dislocations in the channels with grain boundary dislocations to produce a resultant dislocation in the grain boundary plane that can lead to grain boundary sliding if it is mobile. Figure 16.21(a) shows a case of transfer of slip across a grain boundary from one dislocation channel to another. If slip is transferred instead to the grain boundary, then a sliding grain boundary that intersects the surface can rupture the oxide film above it and exposure of the underlying metal

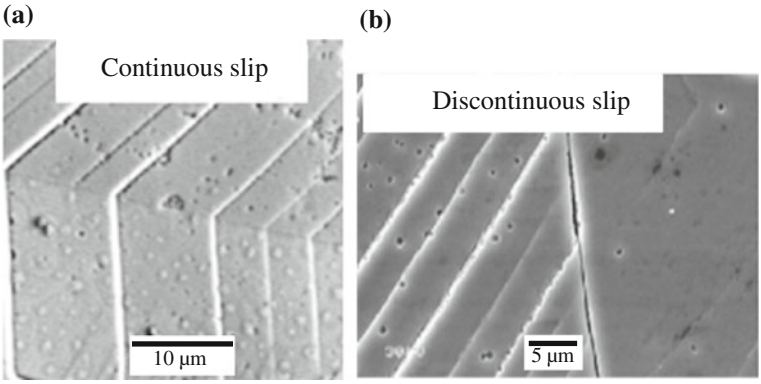

Fig. 16.21 Examples of (**a**) continuous slip across a grain boundary from one dislocation channel to another and (**b**) discontinuous slip where the dislocation channel terminates abruptly at the grain boundary

to the solution, allowing for dissolution and reoxidation. Repeated cycles of rupture, dissolution, and repassivation can then propagate a grain boundary crack by a slip oxidation-type process.

Alternatively, the strain at the dislocation channel–grain boundary (DC-GB) intersection may not be accommodated and dislocation channels may terminate there, producing a high local stress, as in Fig. 16.21(b). The high stress could rupture the oxide and promote IGSCC in much the same manner as grain boundary slip. This mechanism has support in the role of stacking fault energy in IGSCC discussed in Sect. 15.7.7, in which low-SFE alloys undergo planar slip, which is conducive to grain boundary dislocation pileups similar to, but not as severe as that in dislocation channels. Thus, as the fluence increases, localized deformation becomes more severe and IG cracking severity should follow. The correlation strength of localized deformation, which was characterized using the weighted average channel height, with IASCC was found to be 0.88 [45], which was significantly higher than others, implying that localized deformation may be the most important factor in IASCC of irradiated alloys in BWR environments. This result, which is consistent across several studies using different types of irradiation, has focused attention on hardening and deformation as potential primary factors in IASCC.

The options for the accommodation of strain at DC-GB intersections are shown in Fig. 16.22. Experiments have shown that cracking indeed occurs at DC-GB intersections, as shown in Fig. 16.23. The question is then, what type of DC-GB interaction promotes IG cracking? Digital image correlation makes it possible to characterize the nature of the intersection and correlation with cracking. As shown in Fig. 16.24(a), it is the discontinuous DC-GB interactions that have the highest cracking frequency. High-resolution TEM imaging of a discontinuous DC-GB

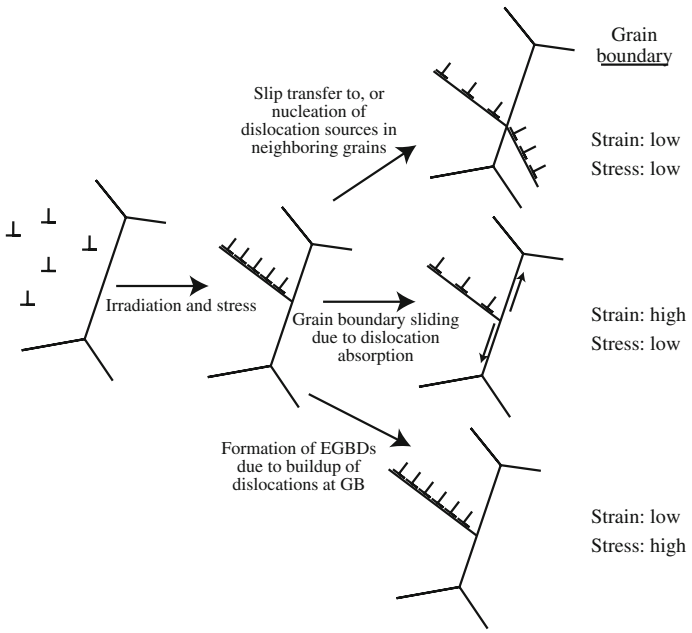

Fig. 16.22 Options for strain accommodation at dislocation channel–grain boundary intersections in an irradiated alloy

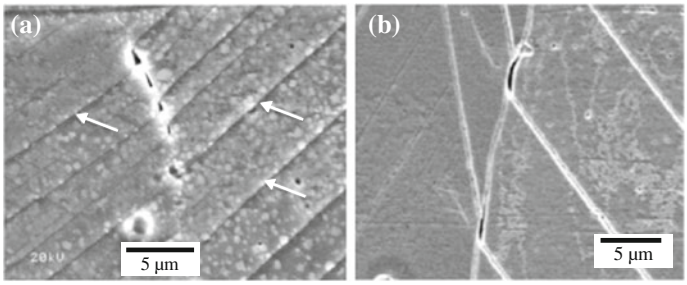

Fig. 16.23 Cracks formed at DC-GB intersections in (**a**) high-purity 304 SS containing Si irradiated to 5 dpa and strained to 6 % in simulated BWR environment at 288 °C and (**b**) 316L stainless steel irradiated and strain in supercritical water at 400 °C

interaction, as in Fig. 16.24(b), shows that when slip cannot be transferred, the result is a region of elastic distortion in the adjacent grain, indicative of a high local stress. Thus, the high stress at DC-GB intersections is a prime factor in the initiation of IASCC in irradiated stainless steels in high-temperature water.

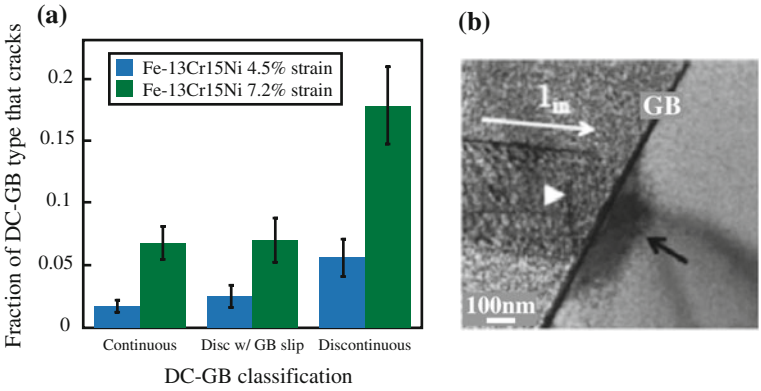

Fig. 16.24 (**a**) Cracking frequency by type of DC-GB interaction (after [47]) and (**b**) TEM image of a discontinuous DC-GB interaction producing elastic distortion in the adjacent grain (after [48])

16.4.4 Models for IASCC

Very little in the way of models for IASCC exists, primarily due to the poor level of understanding of the IASCC mechanism. One model has been developed to explain IASCC by assuming that initiation is determined by the yield strength and grain boundary chromium composition [49]. The stress at which IASCC initiates, σ_{IASCC}, is given by:

$$\sigma_{\mathrm{IASCC}} = f(\sigma_{\mathrm{y}}^{\mathrm{eff}}) \cdot g(C_{\mathrm{Cr}}), \tag{16.6}$$

$$f(\sigma_{\mathrm{y}}^{\mathrm{eff}}) = 1000 - 3.6\sigma_{\mathrm{y}}^{\mathrm{eff}}, \tag{16.7}$$

$$\begin{aligned} g(C_{\mathrm{Cr}}) &= 0.26 \cdot C_{\mathrm{Cr}} - 1.66 \quad (C_{\mathrm{Cr}} < 10.2\ \mathrm{wt}\%) \\ &= 1 \qquad\qquad\qquad\quad (C_{\mathrm{Cr}} > 10.2\ \mathrm{wt}\%), \end{aligned}$$

where

$$\sigma_{\mathrm{y}}^{\mathrm{eff}} = \sigma_{\mathrm{y}}^{0} + \Delta\sigma_{\mathrm{y}} + \Delta\sigma_{\mathrm{y}}^{\mathrm{surf}}, \tag{16.8}$$

σ_{y}^{0} is the unirradiated yield strength, $\Delta\sigma_{\mathrm{y}}$ is the RH given by Eq. (12.71), but is replaced with a simplified model based on dose and temperature:

$$\begin{aligned} \Delta\sigma_{\mathrm{y}} &= a\left\{1 - \exp\left(\frac{-\phi t}{b}\right)\right\} \\ a &= (-0.32T + 156) \cdot \ln\phi + (3810 - 7.63T) \\ b &= (0.012T - 3.46) \cdot \ln\phi + (0.183T - 49.87), \end{aligned} \tag{16.9}$$

where t is time, ϕ is neutron flux, T is temperature, and

$$\Delta\sigma_y^{surf} = 3.6\Delta H_V^{surf} \tag{16.10}$$

is the surface hardening as a function of the surface hardness, ΔH_V^{surf}.
The term C_{Cr} in the function $g(C_{Cr})$ is given by:

$$C_{Cr} = C_{Cr}^0 + \Delta C_{Cr}^0 + \Delta C_{Cr}, \tag{16.11}$$

where C_{Cr}^0 is the bulk grain boundary chromium concentration, ΔC_{Cr}^0 is the initial grain boundary chromium segregation, and the change in grain boundary Cr concentration due to irradiation, ΔC_{Cr}, is:

$$\begin{aligned}\Delta C_{Cr} &= c\phi t + d\left\{1 - \exp\left(\frac{-\phi t}{e}\right)\right\}\\ c &= (-6.28 \times 10^{-6}T + 1.14 \times 10^{-3}) \cdot \ln\phi + (2.56 \times 10^{-2} - 5.40 \times 10^{-5}T)\\ d &= (1.89 \times 10^{-3}T - 1.23) \cdot \ln\phi + (5.24 \times 10^{-2}T - 18.5)\\ e &= (-3.71 \times 10^{-3}T + 1.93) \cdot \ln\phi + (53.2 - 0.108T).\end{aligned} \tag{16.12}$$

Results of the model are plotted in Fig. 16.25 and show the same general trend as the database for constant load experiments in PWR water shown in Fig. 16.9.

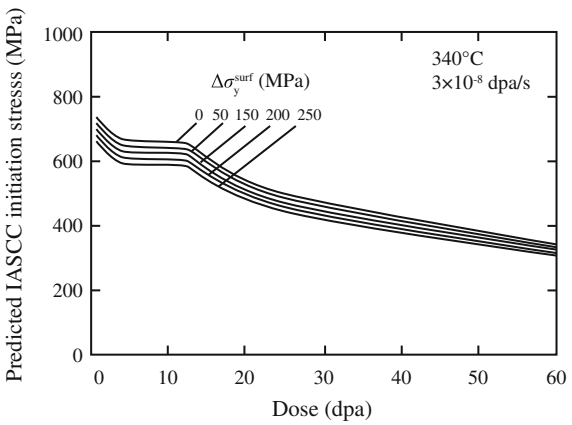

Fig. 16.25 Predicted IASCC initiation stress plotted against dose for different levels of surface hardening (after [49])

16.4.5 Selective Internal Oxidation

A final mechanism that has the potential for causing IG cracking is selective internal oxidation, which is based on the rapid transport of oxygen along grain boundaries that then oxidizes and embrittles the metal ahead of the crack tip, resulting in increased cracking along them [50]. Internal oxidation is observed in nickel-base alloys at temperatures above 600 °C [51–53], but it is not expected to occur in iron- or nickel-base alloys at LWR core temperatures. However, the combination of short-circuit diffusion paths (grain boundaries) and radiation-enhanced diffusion has increased the plausibility of this mechanism operating in the lower temperature range. Observation of oxygen penetrating ahead of an active crack tip in stainless steel core components [54] provides support to this mechanism.

16.4.6 Irradiation-Induced Creep

In contrast to the previous four effects of irradiation on SCC, irradiation-induced creep will relax residual stress, thus effectively removing the driving force for SCC. As shown in Chap. 11, the relaxation of stress depends on the dose. Figure 16.26 shows the reduction in the stress (measured as a reduction in torque) in cold-worked 316 SS PWR baffle bolts as a function of neutron dose. Note that the relaxation follows a roughly exponential behavior with neutron dose such that the stress is reduced to about half of its original value after less than 10 dpa. Stress relaxation by irradiation-induced creep is an important process to relieve stress in baffle bolts of PWRs that could experience additional stresses if swelling occurs in the plates.

Nomenclature

a	Activity of reactants/products, or crack length
$\dot{a}$	Crack growth rate
C	Concentration
$\mathrm{d}a/\mathrm{d}n$	Crack growth per cycle
$\mathrm{d}a/\mathrm{d}t$	Crack growth rate
K	Stress intensity factor
ΔK	Stress intensity range
K_{Ic}	Mode I fracture toughness
T	Temperature
R	Gas constant, or load ratio
t	Time
ϕ	Neutron flux
σ	Stress

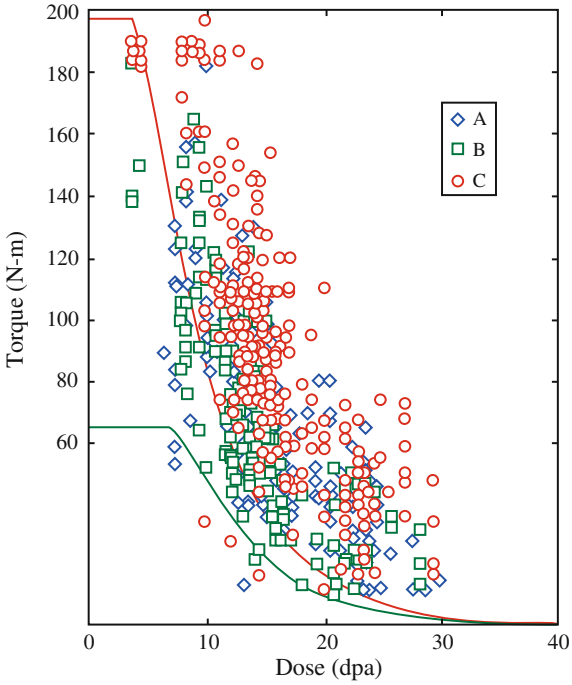

Fig. 16.26 Irradiation-induced creep causing stress relief in cold-worked 316 SS PWR baffle bolts as a function of neutron dose (after [55])

Subscripts

air	Air
Cr	Chromium
cf	Corrosion fatigue
env	Environment
IASCC	IASCC
r	Rise time
y	Yield

Superscripts

eff	Effective
0	Initial condition
surf	Surface

Acronyms

BWR	Boiling water reactor
CERT	Constant extension rate test
DC	Dislocation channel
GB	Grain boundary
HWC	Hydrogen water chemistry
IASCC	Irradiation-assisted stress corrosion cracking
IGSCC	Intergranular stress corrosion cracking
LWR	Light water reactor
NWC	Normal water chemistry
PWR	Pressurized water reactor
RH	Radiation hardening
RIS	Radiation-induced segregation
SCC	Stress corrosion cracking
SFE	Stacking fault energy
SSRT	Slow strain rate tests
STP	Standard temperature and pressure
TGSCC	Transgranular stress corrosion cracking

Problems

16.1 Consider low-alloy steel in contact with stainless steel and determine the potential difference under STP.

(a) Which will corrode?
(b) Where could such a situation arise locally due to the effects of irradiation?

16.2 For the alloys in Problem 16.1, describe how irradiation can alter the corrosion potential of the system and under what conditions.
16.3 What are the possible ways in which irradiation can lead changes in corrosion behavior?
16.4 What are the possible ways in which irradiation could induce IASCC?
16.5 Comment on the relative importance of IASCC initiation versus crack growth. Which is more important and in what circumstances?
16.6 Describe possible mitigation strategies for IASCC?

References

1. Andresen PL, Ford FP, Murphy SM, Perks JM (1990) In: Proceedings of the 4th international symposium on environmental degradation of materials in nuclear power systems: water reactors. NACE International, Houston, pp 1–83 to 1–121
2. Scott P (1994) A review of irradiation assisted stress corrosion cracking. J Nucl Mater 211:101–122

3. Andresen PL, Was GS (2012) Irradiation assisted stress corrosion cracking. In: Konings RJM, (ed) Comprehensive nuclear materials, vol 5. Elsevier, Amsterdam, pp 177–205
4. Was GS (2004) In: Proceedings of the 11th international conference on environmental degradation of materials in nuclear power systems: water reactors. American Nuclear Society, La Grange Park, pp 965–985
5. Was GS, Busby JT, Andresen PL (2006) Effect of irradiation on stress corrosion cracking and corrosion in light water reactors: corrosion in the nuclear industry. Corrosion: environments and industries, ASM handbook, vol 13c. ASM International, Metals Park, pp 386–414
6. Bruemmer SM, Simonen EP, Scott PM, Andresen PL, Was GS, Nelson JL (1999) J Nucl Mater 274:299–314
7. Ford FP, Andresen PL (1994) Corrosion in nuclear systems: environmentally assisted cracking in light water reactors. In: Marcus P, Oudar J (eds) Corrosion mechanisms. Dekker, New York, pp 501–546
8. Ford FP, Andresen PL (1988) In: Theus GJ, Weeks JR (eds) Proceedings of the 3rd international symposium on environmental degradation of materials in nuclear power systems: water reactors. The Metallurgical Society of AIME, Warrendale, p 789
9. Andresen PL, Ford FP (1988) Mat Sci Eng vol A 1103:167
10. Andresen PL (1992) In: Jones RH (ed) Stress corrosion cracking: materials performance and evaluation, ASM, Materials Park, pp 181–210
11. Andresen PL, Young LM (1995) In: Proceedings of the 7th international symposium on environmental degradation of materials in nuclear power systems: water reactors. NACE International, TX, pp 579–596
12. Lin CC (1986) Proceedings of the 2nd international symposium on environmental degradation of materials in nuclear power systems: water reactors. American Nuclear Society, La Grange Park, pp 160–172
13. Burns WG, Moore PB (1976) Rad Eff 30:233
14. Cohen P (1969) Water coolant technology of power reactors. Gordon and Breach Science, New York
15. British Nuclear Energy Society (1989) Proceedings of the conference on water chemistry of nuclear reactor systems 5, Bournemouth, UK, 23–27 October 1989, British Nuclear Energy Society, London
16. Taylor DF (1990) Paper 90501, Corrosion/90, Las Vegas. NACE, Houston, TX
17. Head RA, Indig ME, Andresen PL (1989) Measurement of in-core and recirculation system responses to hydrogen water chemistry at nine mile point unit 1 BWR, EPRI contract RP2680-5, final report. EPRI, Palo Alto, CA
18. Gordon BM (1985) Hydrogen water chemistry for BWR, task 27, Materials and environmental monitoring with in the Duane Arnold BWR, contract RP1930-1, project manager, JL Nelson. EPRI, Palo Alto, CA
19. Andresen PL, Ford FP (1995) In: Proceedings of the 7th international symposium on environmental degradation of materials in nuclear power systems: water reactors. NACE, TX, pp 893–908
20. Daub K, Zhang Z (2011) Corr Sci 53:11
21. Knapp QW, Wren JC (2012) Electrochim Acta 80:90
22. Alrehaily LM, Joseph JM, Musa AY, Guzonas DA, Wren JC (2012) Phys Chem Chem Phys 15:98
23. Daub K, Zhang (2010) Electrochim Acta 55:2767
24. Cook WG, Olive RP (2010) Corr Sci 55:326
25. Jacobs AJ, Hale DA, Siegler M (1986) Unpublished data. GE Nuclear Energy, San Jose
26. Ljungberg LG (1991) Communication. ABB Atom, Sweden
27. Ford FP, Taylor DF, Andresen DL, Ballinger RG (1987) Environmentally controlled cracking of stainless and low alloy steels in LWR environments, NP-5064M (RP2006-6). EPRI, Palo Alto
28. Angeliu TM, Andresen PL, Sutliff JA, Horn RM (1999) In: Proceedings of the 9th international symposium on environmental degradation of materials in nuclear power systems. The Minerals, Metals and Materials Society, PA, p 311

29. Lapuerta S, Moncoffre B, Millard-Pinard N, Jaffrezic H, Bererd N, Crusset D (2006) J Nucl Mater 352:174
30. Lewis MB, Hunn JD (1999) J Nucl Mater 265:423
31. Raiman SS, Wang P, Was GS (2014) In: Proceedings of Fontevraud 8, Societe Francaise d'Energie Nucleare, Paris, FR, paper 51_T02_WAS_FP
32. Asher RC, Davies D, Kirstein TBA (1973–74) J Nucl Mater 49:189
33. Bradhurst DH, Shirvington PJ, Heuer PM (1973) J Nucl Mater 46:53
34. Wang P, Was GS (2015) J Mater Res No. 9 30:1335
35. Allison CM, Berna GA, Chambers R, Coryell EW, Davis KL, Hagrman DL, Hagrman DT, Hampton NL, Hohorst JK, Mason RE, McComas ML, McNeil KA, Miller RL, Olsen CS, Reymann GA, Siefken LJ (1993) SCDAP/RELAP5/MOD3.1 code manual volume IV: MATPRO—a library of materials properties for light-water-reactor accident analysis. NUREG/CR-6150, EGG-2720, vol IV, p 4–234
36. Scott PM (1994) J Nucl Mater 211:101
37. Scott PM, Meunier M-C, Deydier D, Silvestre S, Trenty A (2000) In: Kane RD (ed) ASTMSTP 1401, environmentally assisted cracking: predictive methods for risk assessment and evaluation of materials, equipment and structures. American Society for Testing and Materials, West Conshohocken, PA, pp 210–223
38. Chopra OK, Rao AS (2011) J Nucl Mater 409:235
39. Identifying mechanisms and mitigation strategies for irradiation assisted stress corrosion cracking of austenitic steels in LWR core components, EPRI Report 3002003105, EPRI, Palo Alto CA, 2014
40. Chopra OK, Gruber EE, Shack WJ (2003) Fracture toughness and crack growth rates of irradiated austenitic steels. US Nuclear Regulatory Commission, NUREG/CR-6826, 2003, p 37
41. Chopra OK, Rao AS (2011) J Nucl Mater 412:195
42. Bulloch JH (1989) Res Mech 26:95–172
43. Cullen WH, Watson HE, Taylor RE, Loss FJ (1981) J Nucl Mater 96:261–268
44. Bruemmer SM, Was GS (1994) J Nucl Mater 216:348–363
45. Jiao Z, Was GS (2011) J Nucl Mater 408:246
46. Hash MC, Wang LM, Busby JT, Was GS (2004) In: Grossbeck ML, Allen TR, Lott RG, Kumar AS (eds) Effects of radiation on materials the 21st international symposium, ASTM STP. American Society for Testing and Materials, West Conshohocken, pp 92–104
47. McMurtrey MD, Cui B, Robertson IM, Farkas D, Was GS Curr Op Sol Stat Mater Sci (in press)
48. Cui B, McMurtrey MD, Was GS, Robertson IM (2014) Phil Mag 94(36):4197
49. Fukuya K, Fujii K, Nishioka H, Tokakura K, Nakata K (2010) Nucl Eng Des 420:473
50. Scott PM (2002) In: Ford FP, Bruemmer SM, Was GS (eds) Proceedings of the 9th international conference on environmental degradation of materials in nuclear power systems: water reactors. The Minerals, Metals and Materials Society, Warrendale, pp 3–14
51. Bricknell RH, Woodford DA (1982) Acta Metal 30:257–264
52. Iacocca RG, Woodford DA (1988) Metal Trans A 19A:2305–2313
53. Woodford DA, Bricknell RH (1983) Treatise on materials science and technology, vol 25. Academic, New York
54. Thomas LE, Gertsman VY, Bruemmer SM (2002) In: Nelson L, Was GS, King P (eds) Proceedings of the 10th international conference on environmental degradation of materials in nuclear systems: water reactors. NACE International, Houston, p 117
55. Massoud JP, Dubuisson P, Scott P, Ligneau N, Lemaire E (2002) Proc Fontevraud 5(62):417

Index

G.S. Was, *Fundamentals of Radiation Materials Science*,
DOI 10.1007/978-1-4939-3438-6

Q
Quasi-cleavage mechanism, 837
Quasicrystalline phases, 523
Quasicrystals, 523
Quasi-steady state, 210, 211, 213, 255, 402, 763
Quasi-steady state concentration, 214
Quench, 146, 152, 154, 162, 520, 567

T